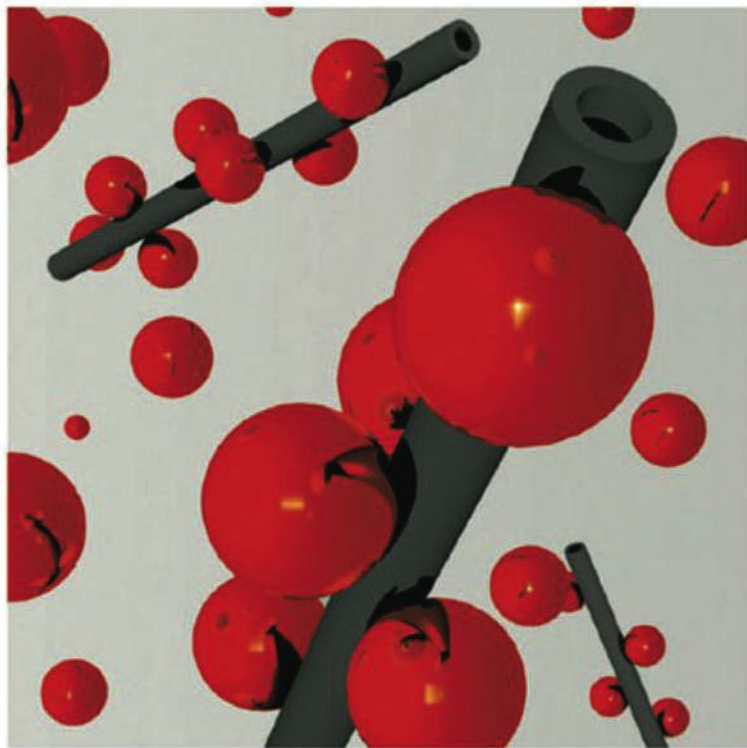


Edited by  
Kurt E. Geckeler and Hiroyuki Nishide

 WILEY-VCH

# Advanced Nanomaterials





**Advanced Nanomaterials**

*Edited by  
Kurt E. Geckeler and  
Hiroyuki Nishide*

## ***Further Reading***

Tjong, Sie Chin

### **Carbon Nanotube Reinforced Composites**

**Metal and Ceramic Matrices**

2009

ISBN: 978-3-527-40892-4

Zehetbauer, M. J., Zhu, Y. T. (eds.)

### **Bulk Nanostructured Materials**

2009

ISBN: 978-3-527-31524-6

Vollath, D.

### **Nanomaterials**

**An Introduction to Synthesis, Properties and Applications**

2008

ISBN: 978-3-527-31531-4

Astruc, D. (ed.)

### **Nanoparticles and Catalysis**

2008

ISBN: 978-3-527-31572-7

Lee, Yoon S.

### **Self-Assembly and Nanotechnology**

**A Force Balance Approach**

2008

ISBN: 978-0-470-24883-6

Eftekhari, Ali (Ed.)

### **Nanostructured Materials in Electrochemistry**

2008

ISBN: 978-3-527-31876-6

Lazzari, M. / Liu, G. / Lecommandoux, S. (eds.)

### **Block Copolymers in Nanoscience**

2006

ISBN: 978-3-527-31309-9

Kumar, Challa S. S. R. (Ed.)

### **Nanomaterials for the Life Sciences**

**10 Volume Set**

2010

ISBN: 978-3-527-32261-9

Kumar, Challa S. S. R. (Ed.)

### **Nanotechnologies for the Life Sciences**

**10 Volume Set**

2007

ISBN: 978-3-527-31301-3

Rao, C. N. R., Müller, A., Cheetham, A. K. (eds.)

### **Nanomaterials Chemistry**

**Recent Developments and New Directions**

2007

ISBN: 978-3-527-31664-9



# Advanced Nanomaterials

*Edited by*

*Kurt E. Geckeler and Hiroyuki Nishide*

*Volume 1*



WILEY-  
VCH

WILEY-VCH Verlag GmbH & Co. KGaA

## The Editors

### **Prof. Dr. Kurt E. Geckeler**

Department of Nanobio Materials and  
Electronics

World-Class University (WCU)

**and**

Department of Materials Science and  
Engineering

Gwangju Institute of Science and

Technology (GIST)

1 Oryong-dong, Buk-gu

Gwangju 500-712

South Korea

E-mail: keg@gist.ac.kr

### **Prof. Hiroyuki Nishide**

Department of Applied Chemistry

Waseda University

Ohkubo 3, Shinjuku

Tokyo 169-8555

Japan

E-mail: nishide@waseda.jp

**and**

Department of Nanobio Materials and  
Electronics

World-Class University (WCU)

Gwangju Institute of Science and

Technology (GIST)

1 Oryong-dong, Buk-gu

Gwangju 500-712

South Korea

■ All books published by Wiley-VCH are carefully produced. Nevertheless, authors, editors, and publisher do not warrant the information contained in these books, including this book, to be free of errors. Readers are advised to keep in mind that statements, data, illustrations, procedural details or other items may inadvertently be inaccurate.

**Library of Congress Card No.:** applied for

### **British Library Cataloguing-in-Publication Data**

A catalogue record for this book is available from the British Library.

### **Bibliographic information published by the Deutsche Nationalbibliothek**

The Deutsche Nationalbibliothek lists this publication in the Deutsche Nationalbibliografie; detailed bibliographic data are available on the Internet at <<http://dnb.d-nb.de>>.

© 2010 WILEY-VCH Verlag GmbH & Co. KGaA, Weinheim

All rights reserved (including those of translation into other languages). No part of this book may be reproduced in any form – by photoprinting, microfilm, or any other means – nor transmitted or translated into a machine language without written permission from the publishers. Registered names, trademarks, etc. used in this book, even when not specifically marked as such, are not to be considered unprotected by law.

**Composition** Toppan Best-set Premedia Limited

**Printing and Bookbinding** Strauss GmbH,  
Mörlenbach

**Cover Design** Schulz Grafik-Design, Fußgönheim

Printed in the Federal Republic of Germany

Printed on acid-free paper

**ISBN:** 978-3-527-31794-3

## Contents

**Preface** XV

**List of Contributors** XVII

### Volume 1

<b>1</b>	<b>Phase-Selective Chemistry in Block Copolymer Systems</b>	<b>1</b>
	<i>Evan L. Schwartz and Christopher K. Ober</i>	
1.1	Block Copolymers as Useful Nanomaterials	1
1.1.1	Introduction	1
1.1.2	Self-Assembly of Block Copolymers	3
1.1.3	Triblock Copolymers	4
1.1.4	Rod–Coil Block Copolymers	7
1.1.5	Micelle Formation	8
1.1.6	Synthesis of Block Copolymers Using Living Polymerization Techniques	9
1.1.6.1	Anionic Polymerization	10
1.1.6.2	Stable Free Radical Polymerizations	11
1.1.6.3	Reversible Addition–Fragmentation Chain Transfer (RAFT) Polymerization	12
1.1.6.4	Atom Transfer Radical Polymerization	12
1.1.6.5	Ring-Opening Metathesis Polymerization	13
1.1.6.6	Group Transfer Polymerization	13
1.1.7	Post-Polymerization Modifications	14
1.1.7.1	Active-Center Transformations	14
1.1.7.2	Polymer-Analogous Reactions	14
1.2	Block Copolymers as Lithographic Materials	15
1.2.1	Introduction to Lithography	15
1.2.2	Block Copolymers as Nanolithographic Templates	17
1.2.2.1	Creation of Nanoporous Block Copolymer Templates	20
1.2.3	Multilevel Resist Strategies Using Block Copolymers	29
1.3	Nanoporous Monoliths Using Block Copolymers	34
1.3.1	Structure Direction Using Block Copolymer Scaffolds	34
1.3.2	Nanopore Size Tunability	36

1.3.3	Functionalized Nanoporous Surfaces	38
1.4	Photo-Crosslinkable Nano-Objects	41
1.5	Block Copolymers as Nanoreactors	44
1.5.1	Polymer–Metal Solubility	44
1.5.2	Cluster Nucleation and Growth	46
1.5.3	Block Copolymer Micelle Nanolithography	47
1.6	Interface-Active Block Copolymers	48
1.6.1	Low-Energy Surfaces Using Fluorinated Block Copolymers	48
1.6.2	Patterning Surface Energies	49
1.6.3	Photoswitchable Surface Energies Using Block Copolymers Containing Azobenzene	51
1.6.4	Light-Active Azobenzene Block Copolymer Vesicles as Drug Delivery Devices	52
1.6.5	Azobenzene-Containing Block Copolymers as Holographic Materials	52
1.7	Summary and Outlook	54
	References	60
<b>2</b>	<b>Block Copolymer Nanofibers and Nanotubes</b>	<b>67</b>
	<i>Guojun Liu</i>	
2.1	Introduction	67
2.2	Preparation	69
2.2.1	Nanofiber Preparation	69
2.2.2	Nanotube Preparation	72
2.3	Solution Properties	74
2.4	Chemical Reactions	81
2.4.1	Backbone Modification	81
2.4.2	End Functionalization	85
2.5	Concluding Remarks	87
	Acknowledgements	88
	References	88
<b>3</b>	<b>Smart Nanoassemblies of Block Copolymers for Drug and Gene Delivery</b>	<b>91</b>
	<i>Horacio Cabral and Kazunori Kataoka</i>	
3.1	Introduction	91
3.2	Smart Nanoassemblies for Drug and Gene Delivery	92
3.3	Endogenous Triggers	93
3.3.1	pH-Sensitive Nanoassemblies	93
3.3.1.1	Drug Delivery	93
3.3.1.2	Gene Delivery	96
3.3.2	Oxidation- and Reduction-Sensitive Polymeric Nanoassemblies	99
3.3.3	Other Endogenous Triggers	101
3.4	External Stimuli	102
3.4.1	Temperature	102

3.4.2	Light	105
3.4.3	Ultrasound	107
3.5	Future Perspectives	108
	References	109
<b>4</b>	<b>A Comprehensive Approach to the Alignment and Ordering of Block Copolymer Morphologies</b>	<b>111</b>
	<i>Massimo Lazzari and Claudio De Rosa</i>	
4.1	Introduction	111
4.1.1	Motivation	111
4.1.2	Organization of the Chapter	112
4.2	How to Help Phase Separation	113
4.3	Orientation by External Fields	116
4.3.1	Mechanical Flow Fields	117
4.3.2	Electric and Magnetic Fields	118
4.3.3	Solvent Evaporation and Thermal Gradient	122
4.4	Templated Self-Assembly on Nanopatterned Surfaces	123
4.5	Epitaxy and Surface Interactions	126
4.5.1	Preferential Wetting and Homogeneous Surface Interactions	126
4.5.2	Epitaxy	128
4.5.3	Directional Crystallization	130
4.5.4	Graphoepitaxy and Other Confining Geometries	135
4.5.5	Combination of Directional Crystallization and Graphoepitaxy	138
4.5.6	Combination of Epitaxy and Directional Crystallization	140
4.6	Summary and Outlook	149
	Acknowledgments	150
	References	150
<b>5</b>	<b>Helical Polymer-Based Supramolecular Films</b>	<b>159</b>
	<i>Akihiro Ohira, Michiya Fujiki, and Masashi Kunitake</i>	
5.1	Introduction	159
5.2	Helical Polymer-Based 1-D and 2-D Architectures	161
5.2.1	Formation of Various 1-D Architectures of Helical Polysilanes on Surfaces	162
5.2.1.1	Direct Visualization of 1-D Rod, Semi-Circle and Circle Structures by AFM	162
5.2.1.2	Driving Force for the Formation of 1-D Architectures	165
5.2.2	Formation of Mesoscopic 2-D Hierarchical Superhelical Assemblies	167
5.2.2.1	Direct Visualization of a Single Polymer Chain	167
5.2.2.2	Formation of Superhelical Assemblies by Homochiral Intermolecular Interactions	169
5.2.3	Formation of 2-D Crystallization of Poly( $\gamma$ -L-Glutamates) on Surfaces	172

- 5.2.3.1 Direct Visualization of 2-D Self-Organized Array by AFM 173
- 5.2.3.2 Orientation in 2-D Self-Organized Array 174
- 5.2.3.3 Intermolecular Weak van der Waals Interactions in 2-D Self-Organized Arrays 175
- 5.2.3.4 Comparison of Structures between a 2-D Self-Organized Array and 3-D Bulk Phase 175
- 5.2.4 Summary of Helical Polymer-Based 1-D and 2-D Architectures 176
- 5.3 Helical Polymer-Based Functional Films 177
- 5.3.1 Chiroptical Memory and Switch in Helical Polysilane Films 178
- 5.3.1.1 Memory with Re-Writable Mode and Inversion “-1” and “+1” Switch 178
- 5.3.1.2 Memory with Write-Once Read-Many (WORM) Mode 182
- 5.3.1.3 On-Off “0” and “+1” Switch Based on Helix-Coil Transition 182
- 5.3.2 Chiroptical Transfer and Amplification in Binary Helical Polysilane Films 185
- 5.3.3 Summary of Helical Polymer-Based Functional Films 188
- Acknowledgments 189
- References 190

## **6 Synthesis of Inorganic Nanotubes 195**

*C.N.R. Rao and Achutharao Govindaraj*

- 6.1 Introduction 195
- 6.2 General Synthetic Strategies 196
- 6.3 Nanotubes of Metals and other Elemental Materials 196
- 6.4 Metal Chalcogenide Nanotubes 206
- 6.5 Metal Oxide Nanotubes 214
- 6.5.1 SiO<sub>2</sub> Nanotubes 214
- 6.5.2 TiO<sub>2</sub> Nanotubes 216
- 6.5.3 ZnO, CdO, and Al<sub>2</sub>O<sub>3</sub> Nanotubes 221
- 6.5.4 Nanotubes of Vanadium and Niobium Oxides 225
- 6.5.5 Nanotubes of other Transition Metal Oxides 228
- 6.5.6 Nanotubes of other Binary Oxides 230
- 6.5.7 Nanotubes of Titanates and other Complex Oxides 233
- 6.6 Pnictide Nanotubes 235
- 6.7 Nanotubes of Carbides and other Materials 240
- 6.8 Complex Inorganic Nanostructures Based on Nanotubes 240
- 6.9 Outlook 241
- References 241

## **7 Gold Nanoparticles and Carbon Nanotubes: Precursors for Novel Composite Materials 249**

*Thathan Premkumar and Kurt E. Geckeler*

- 7.1 Introduction 249
- 7.2 Gold Nanoparticles 249
- 7.3 Carbon Nanotubes 251

7.4	CNT–Metal Nanoparticle Composites	254
7.5	CNT–AuNP Composites	255
7.5.1	Filling of CNTs with AuNPs	255
7.5.2	Deposition of AuNPs Directly on the CNT Surface	256
7.5.3	Interaction Between Modified AuNPs and CNTs	267
7.5.3.1	Covalent Linkage	268
7.5.3.2	Supramolecular Interaction Between AuNPs and CNTs	271
7.6	Applications	288
7.7	Merits and Demerits of Synthetic Approaches	289
7.8	Conclusions	291
	Acknowledgments	292
	References	292
<b>8</b>	<b>Recent Advances in Metal Nanoparticle-Attached Electrodes</b>	<b>297</b>
	<i>Munetaka Oyama, Akrajas Ali Umar, and Jingdong Zhang</i>	
8.1	Introduction	297
8.2	Seed-Mediated Growth Method for the Attachment and Growth of AuNPs on ITO	298
8.3	Electrochemical Applications of AuNP-Attached ITO	300
8.4	Improved Methods for Attachment and Growth of AuNPs on ITO	302
8.5	Attachment and Growth of AuNPs on Other Substrates	306
8.6	Attachment and Growth of Au Nanoplates on ITO	308
8.7	Attachment and Growth of Silver Nanoparticles (AgNPs) on ITO	309
8.8	Attachment and Growth of Palladium Nanoparticles PdNPs on ITO	311
8.9	Attachment of Platinum Nanoparticles PtNPs on ITO and GC	312
8.10	Electrochemical Measurements of Biomolecules Using AuNP/ITO Electrodes	315
8.11	Nonlinear Optical Properties of Metal NP-Attached ITO	315
8.12	Concluding Remarks	316
	References	316
<b>9</b>	<b>Mesoscale Radical Polymers: Bottom-Up Fabrication of Electrodes in Organic Polymer Batteries</b>	<b>319</b>
	<i>Kenichi Oyaizu and Hiroyuki Nishide</i>	
9.1	Mesostructured Materials for Energy Storage Devices	319
9.2	Mesoscale Fabrication of Inorganic Electrode-Active Materials	322
9.3	Bottom-Up Strategy for Organic Electrode Fabrication	323
9.3.1	Conjugated Polymers for Electrode-Active Materials	323
9.3.2	Mesoscale Organic Radical Polymer Electrodes	324
9.4	Conclusions	330
	References	330
<b>10</b>	<b>Oxidation Catalysis by Nanoscale Gold, Silver, and Copper</b>	<b>333</b>
	<i>Zhi Li, Soorly G. Divakara, and Ryan M. Richards</i>	

10.1	Introduction	333
10.2	Preparations	334
10.2.1	Silver Nanocatalysts	335
10.2.2	Copper Nanocatalysts	335
10.2.3	Gold Nanocatalysts	335
10.3	Selective Oxidation of Carbon Monoxide (CO)	337
10.3.1	Gold Catalysts	337
10.3.2	Silver Catalysts	342
10.3.3	Gold–Silver Alloy Catalysts	342
10.3.4	Copper Catalysts	343
10.4	Epoxidation Reactions	344
10.4.1	Gold Catalysts	344
10.4.2	Silver Catalysts	346
10.5	Selective Oxidation of Hydrocarbons	347
10.5.1	Gold Catalysts	349
10.5.2	Silver Catalysts	350
10.5.3	Copper Catalysts	350
10.6	Oxidation of Alcohols and Aldehydes	350
10.6.1	Gold Catalysts	351
10.6.2	Silver Catalysts	351
10.7	Direct Synthesis of Hydrogen Peroxide	353
10.8	Conclusions	354
	References	355
<b>11</b>	<b>Self-Assembling Nanoclusters Based on Tetrahalometallate Anions: Electronic and Mechanical Behavior</b>	<b>365</b>
	<i>Ishenkumba A. Kahwa</i>	
11.1	Introduction	365
11.2	Preparation of Key Compounds	366
11.3	Structure of the $[(A(18C6))_4(MX_4)] [BX_4]_2 \cdot nH_2O$ Complexes	367
11.4	Structure of the $[(Na(15C5))_4Br] [TlBr_4]_3$ Complex	368
11.5	Spectroscopy of the <i>Cubic F23</i> $[(A(18C6))_4(MX_4)] [BX_4]_2 \cdot nH_2O$	368
11.6	Unusual Luminescence Spectroscopy of Some Cubic $[(A(18C6))_4(MnX_4)] [TlCl_4]_2 \cdot nH_2O$ Compounds	372
11.7	Luminescence Decay Dynamics and 18C6 Rotations	374
11.8	Conclusions	375
	Acknowledgments	377
	References	377
<b>12</b>	<b>Optically Responsive Polymer Nanocomposites Containing Organic Functional Chromophores and Metal Nanostructures</b>	<b>379</b>
	<i>Andrea Pucci, Giacomo Ruggeri, and Francesco Ciardelli</i>	
12.1	Introduction	379
12.2	Organic Chromophores as the Dispersed Phase	380



- 12.2.1 Nature of the Organic Dye 380
- 12.2.2 Polymeric Indicators to Mechanical Stress 381
  - 12.2.2.1 Oligo(*p*-Phenylene Vinylene) as Luminescent Dyes 381
  - 12.2.2.2 Bis(Benzoxazolyl) Stilbene as a Luminescent Dye 383
  - 12.2.2.3 Perylene Derivatives as Luminescent Dyes 384
- 12.2.3 Polymeric Indicators to Thermal Stress 385
  - 12.2.3.1 Oligo(*p*-Phenylene Vinylene) as Luminescent Dyes 385
  - 12.2.3.2 Bis(Benzoxazolyl) Stilbene as Luminescent Dye 387
  - 12.2.3.3 Anthracene Triaryl Amine-Terminated Diimide as Luminescent Dye 388
- 12.3 Metal Nanostructures as the Dispersed Phase 389
  - 12.3.1 Optical Properties of Metal Nanoassemblies 389
  - 12.3.2 Nanocomposite-Based Indicators to Mechanical Stress 391
    - 12.3.2.1 The Use of Metal Nanoparticles 391
    - 12.3.2.2 The Use of Metal Nanorods 395
- 12.4 Conclusions 397
  - Acknowledgments 398
  - References 398

### **13 Nanocomposites Based on Phyllosilicates: From Petrochemicals to Renewable Thermoplastic Matrices 403**

*Maria-Beatrice Coltelli, Serena Coiai, Simona Bronco, and Elisa Passaglia*

- 13.1 Introduction 403
  - 13.1.1 Structure of Phyllosilicates 404
    - 13.1.1.1 Clays 404
  - 13.1.2 Morphology of Composites 408
  - 13.1.3 Properties of Composites 411
- 13.2 Polyolefin-Based Nanocomposites 411
  - 13.2.1 Overview of the Preparation Methods 412
  - 13.2.2 Organophilic Clay and Compatibilizer: Interactions with the Polyolefin Matrix 414
  - 13.2.3 The One-Step Process 426
- 13.3 Poly(Ethylene Terephthalate)-Based Nanocomposites 429
  - 13.3.1 In Situ Polymerization 430
  - 13.3.2 Intercalation in Solution 433
  - 13.3.3 Intercalation in the Melt 434
- 13.4 Poly(Lactide) (PLA)-Based Nanocomposites 439
  - 13.4.1 Overview of Preparation Methods 439
    - 13.4.1.1 In Situ Polymerization 439
    - 13.4.1.2 Intercalation in Solution 442
    - 13.4.1.3 Intercalation in the Melt 443
- 13.5 Conclusions 447
  - Acknowledgments 449
  - References 450

## Volume 2

- 14 **Amphiphilic Poly(Oxyalkylene)-Amines Interacting with Layered Clays: Intercalation, Exfoliation, and New Applications** 459  
*Jiang-Jen Lin, Ying-Nan Chan, and Wen-Hsin Chang*
- 15 **Mesoporous Alumina: Synthesis, Characterization, and Catalysis** 481  
*Tsunetake Seki and Makoto Onaka*
- 16 **Nanoceramics for Medical Applications** 523  
*Besim Ben-Nissan and Andy H. Choi*
- 17 **Self-healing of Surface Cracks in Structural Ceramics** 555  
*Wataru Nakao, Koji Takahashi, and Kotoji Ando*
- 18 **Ecological Toxicology of Engineered Carbon Nanoparticles** 595  
*Aaron P. Roberts and Ryan R. Otter*
- 19 **Carbon Nanotubes as Adsorbents for the Removal of Surface Water Contaminants** 615  
*Jose E. Herrera and Jing Cheng*
- 20 **Molecular Imprinting with Nanomaterials** 651  
*Kevin Flavin and Marina Resmini*
- 21 **Near-Field Raman Imaging of Nanostructures and Devices** 677  
*Ze Xiang Shen, Johnson Kasim, and Ting Yu*
- 22 **Fullerene-Rich Nanostructures** 699  
*Fernando Langa and Jean-François Nierengarten*
- 23 **Interactions of Carbon Nanotubes with Biomolecules: Advances and Challenges** 715  
*Dhriti Nepal and Kurt E. Geckeler*
- 24 **Nanoparticle-Cored Dendrimers and Hyperbranched Polymers: Synthesis, Properties, and Applications** 743  
*Young-Seok Shon*
- 25 **Concepts in Self-Assembly** 767  
*Jeremy J. Ramsden*
- 26 **Nanostructured Organogels via Molecular Self-Assembly** 791  
*Arjun S. Krishnan, Kristen E. Roskov, and Richard J. Spontak*

- 27 **Self-assembly of Linear Polypeptide-based Block Copolymers** 835  
*Sébastien Lecommandoux, Harm-Anton Klok, and Helmut Schlaad*
- 28 **Structural DNA Nanotechnology: Information-Guided  
Self-Assembly** 869  
*Yonggang Ke, Yan Liu, and Hao Yan*
- Index** 881



## Preface

Nanotechnology has found an incredible resonance and a vast number of applications in many areas during the past two decades. The resulting deep paradigm shift has opened up new horizons in materials science, and has led to exciting new developments. Fundamentally, nanotechnology is dependent on the existence or the supply of new nanomaterials that form the prerequisite for any further progress in this new and interdisciplinary area of science and technology. Evidently, nanomaterials feature specific properties that are characteristic of this class of materials, and which are based on surface and quantum effects.

Clearly, the control of composition, size, shape, and morphology of nanomaterials is an essential cornerstone for the development and application of nanomaterials and nanoscale devices. The complex functions of nanomaterials in devices and systems require further advancement in the preparation and modification of nanomaterials. Such advanced nanomaterials have attracted tremendous interest during recent years, and will form the basis for further progress in this area. Thus, the major classes of novel materials are described in the twenty-eight chapters of this two-volume monograph.

The initializing concept of this book was developed at the *3rd IUPAC International Symposium on Macro- and Supramolecular Architectures and Materials (MAM-06): Practical Nanochemistry and Novel Approaches*, held in Tokyo, Japan, 2006, within the framework of the biannual MAM symposium series. This monograph provides a detailed account of the present status of nanomaterials, and highlights the recent developments made by leading research groups. A compilation of state-of-the-art review chapters, written by over sixty contributors and well-known experts in their field from all over the world, covers the novel and important aspects of these materials, and their applications.

The different classes of advanced nanomaterials, such as block copolymer systems including block copolymer nanofibers and nanotubes, smart nanoassemblies of block copolymers for drug and gene delivery, aligned and ordered block copolymers, helical polymer-based supramolecular films, as well as novel composite materials based on gold nanoparticles and carbon nanotubes, are covered in the book. Other topics include the synthesis of inorganic nanotubes, metal nanoparticle-attached electrodes, radical polymers in organic polymer batteries, oxidation catalysis by nanoscale gold, silver, copper, self-assembling

nanoclusters, optically responsive polymer nanocomposites, renewable thermoplastic matrices based on phyllosilicate nanocomposites, amphiphilic polymer-clay intercalation and applications, the synthesis and catalysis of mesoporous alumina, and nanoceramics for medical applications.

In addition, this book highlights the recent progress in the research and applications of structural ceramics, the ecological toxicology of engineered carbon nanoparticles, carbon nanotubes as adsorbents for the removal of surface water contaminants, molecular imprinting with nanomaterials, near-field Raman imaging of nanostructures and devices, fullerene-rich nanostructures, nanoparticle-cored dendrimers and hyperbranched polymers, as well as the interactions of carbon nanotubes with biomolecules. The book is completed with a series of chapters featuring concepts in self-assembly, nanostructured organogels via molecular self-assembly, the self-assembly of linear polypeptide-based block copolymers, and information-guided self-assembly by structural DNA nanotechnology.

The variety of topics covered in this book make it an interesting and valuable reference source for those professionals engaged in the fundamental and applied research of nanotechnology. Thus, scientists, students, postdoctoral fellows, engineers, and industrial researchers, who are working in the fields of nanomaterials and nanotechnology at the interface of materials science, chemistry, physics, polymer science, engineering, and biosciences, would all benefit from this monograph.

The advanced nanomaterials presented in this book are expected to result in commercial applications in many areas. As the science and technology of nanomaterials is still in its infancy, further research will be required not only to develop this new area of materials science, but also to explore the utilization of these novel materials. All new developments impart risks, and here also it is important to evaluate the risks and benefits associated with the introduction of such materials into the biosphere and ecosphere.

On behalf of all contributors to we thank the publishers and authors on behalf of all contributors for granting copyright permissions to use their illustrations in this book. It is also very much appreciated that the authors devoted their time and efforts to contribute to this monograph. Last, but not least, the major prerequisite for the success of this comprehensive book project was the cooperation, support, and understanding of our families, which is greatly acknowledged.

The Editors

## List of Contributors

### **Kotoji Ando**

Yokohama National University  
Department of Material Science  
and Engineering  
79-1 Tokiwadai  
Hohogaya-ku  
Yokohama 240-8501  
Japan

### **Besim Ben-Nissan**

University of Technology  
Faculty of Science  
Broadway  
P.O. Box 123  
Sydney  
NSW 2007  
Australia

### **Simona Bronco**

CNR-INFM-PolyLab c/o  
Dipartimento di Chimica e  
Chimica Industriale  
Università di Pisa  
Via Risorgimento 35  
56126 Pisa  
Italy

### **Horacio Cabral**

The University of Tokyo  
Department of Materials Engineering  
Graduate School of Engineering  
7-3-1 Hongo, Bunkyo-ku  
Tokyo 113-8656  
Japan

### **Ying-Nan Chan**

National Taiwan University  
Institute of Polymer Science and  
Engineering  
Taipei 10617  
Taiwan

and

National Chung Hsing University  
Department of Chemical Engineering  
Taichung 40227  
Taiwan

### **Wen-Hsin Chang**

National Taiwan University  
Institute of Polymer Science and  
Engineering  
Taipei 10617  
Taiwan

**Jing Cheng**

The University of Western  
Ontario  
Department of Civil and  
Environmental Engineering  
London, ON N6A 5B9  
Canada

**Andy H. Choi**

University of Technology  
Faculty of Science  
Broadway  
P.O. Box 123  
Sydney  
NSW 2007  
Australia

**Francesco Ciardelli**

University of Pisa  
CNR-INFN-PolyLab  
c/o Department of Chemistry,  
and Industrial Chemistry  
Via Risorgimento 35  
56126 Pisa  
Italy

**Serena Coiai**

Centro Italiano Packaging and  
Dipartimento di Chimica e  
Chimica Industriale  
Università di Pisa  
Via Risorgimento 35  
56126 Pisa  
Italy

**Maria-Beatrice Coltelli**

Centro Italiano Packaging and  
Dipartimento di Chimica e  
Chimica Industriale  
Università di Pisa  
Via Risorgimento 35  
56126 Pisa  
Italy

**Claudio De Rosa**

University of Napoli "Federico II"  
Department of Chemistry  
Complesso Monte S. Angelo  
Via Cintia  
80126 Napoli  
Italy

**Soorly G. Divakara**

Colorado School of Mines  
Department of Chemistry and  
Geochemistry  
1500 Illinois St.  
Golden, CO 80401  
USA

**Kevin Flavin**

Queen Mary University of London  
School of Biological and Chemical  
Sciences  
Mile End Road  
London E1 4NS  
UK

**Michiya Fujiki**

Nara Institute of Science and  
Technology  
Graduate School of Materials Science  
8916-5 Takayama  
Ikoma  
Nara 630-0101  
Japan

**Kurt E. Geckeler**

Gwangju Institute of Science and  
Technology (GIST)  
Department of Materials Science and  
Engineering  
1 Oryong-dong, Buk-gu  
Gwangju 500-712  
South Korea



**Achutharao Govindaraj**

International Centre for  
Materials Science  
New Chemistry Unit and CSIR  
Centre of Excellence in  
Chemistry  
Jawaharlal Nehru Centre for  
Advanced Scientific Research  
Jakkur P. O.  
Bangalore 560 064  
India

and

Solid State and Structural  
Chemistry Unit  
Indian Institute of Science  
Bangalore 560 012  
India

**Jose E. Herrera**

The University of Western  
Ontario  
Department of Civil and  
Environmental Engineering  
London, ON N6A 5B9  
Canada

**Ishenkumba A. Kahwa**

The University of the West  
Indies  
Chemistry Department  
Mona Campus  
Kingston 7  
Mona  
Jamaica

**Johnson Kasim**

Nanyang Technological  
University  
School of Physical and  
Mathematical Sciences  
Division of Physics and Applied  
Physics  
Singapore 637371  
Singapore

**Kazunori Kataoka**

The University of Tokyo  
Department of Materials Engineering  
Graduate School of Engineering  
7-3-1 Hongo  
Bunkyo-ku  
Tokyo 113-8656  
Japan

and

The University of Tokyo  
Center for Disease Biology and  
Integrative Medicine  
Graduate School of Medicine  
7-3-1 Hongo  
Bunkyo-ku  
Tokyo 113-0033  
Japan

and

The University of Tokyo  
Center for NanoBio Integration  
7-3-1 Hongo  
Bunkyo-ku  
Tokyo 113-8656  
Japan

**Yonggang Ke**

Arizona State University  
Department of Chemistry and  
Biochemistry & The Biodesign  
Institute  
Tempe, AZ 85287  
USA

**Harm-Anton Klok**

Ecole Polytechnique Fédérale de  
Lausanne (EPFL)  
Institut des Matériaux, Laboratoire des  
Polymères  
STI-IMX-LP  
MXD 112 (Bâtiment MXD), Station 12  
1015 Lausanne  
Switzerland

**Arjun S. Krishnan**

North Carolina State University  
Department of Chemical &  
Biomolecular Engineering  
Raleigh, NC 27695  
USA

**Masashi Kunitake**

Kumamoto University  
Department of Applied  
Chemistry and Biochemistry  
2-39-1 Kurokami  
Kumamoto 860-8555  
Japan

**Fernando Langa**

Universidad de Castilla-La  
Mancha  
Facultad de Ciencias del  
Medio Ambiente  
45071 Toledo  
Spain

**Massimo Lazzari**

University of Santiago de  
Compostela  
Department of Physical  
Chemistry  
Faculty of Chemistry and  
Institute of Technological  
Investigations  
15782 Santiago de Compostela  
Spain

**Sebastien Lecommandoux**

University of Bordeaux  
Laboratoire de Chimie des  
Polymères Organiques (LCPO)  
UMR CNRS 5629  
Institut Polytechnique de  
Bordeaux  
16 Avenue Pey Berland  
33607 Pessac  
France

**Zhi Li**

Colorado School of Mines  
Department of Chemistry and  
Geochemistry  
1500 Illinois St.  
Golden, CO 80401  
USA

**Jiang-Jen Lin**

National Taiwan University  
Institute of Polymer Science and  
Engineering  
Taipei 10617  
Taiwan

**Guojun Liu**

Queens University  
Department of Chemistry  
50 Bader Lane  
Kingston Ontario K7L 3N6  
Canada

**Yan Liu**

Arizona State University  
Department of Chemistry and  
Biochemistry & The Biodesign  
Institute  
Tempe, AZ 85287  
USA

**Watoru Nakao**

Yokohama National University  
Department of Energy and Safety  
Engineering  
79-5 Tokiwadai  
Hodogaya-ku  
Yokohama 240-8501  
Japan

**Dhriti Nepal**

Gwangju Institute of Science  
and Technology (GIST)  
Department of Materials Science  
and Engineering  
1 Oryong-dong, Buk-gu  
Gwangju 500-712  
South Korea

and

School of Polymer  
Textile and Fiber Engineering  
Georgia Institute of Technology  
Atlanta, GA 30332  
USA

**Jean-François Nierengarten**

Université de Strasbourg  
Laboratoire de Chimie des  
Matériaux Moléculaires  
(UMR 7509)  
Ecole Européenne de Chimie  
Polymères et Matériaux  
25 rue Becquerel  
67087 Strasbourg, Cedex 2  
France

**Hiroyuki Nishide**

Waseda University  
Department of Applied  
Chemistry  
Tokyo 169-8555  
Japan

**Christopher K. Ober**

Cornell University  
Department of Materials Science  
and Engineering  
Ithaca, NY 14853  
USA

**Akihiro Ohira**

National Institute of Advanced  
Industrial Science and Technology  
(AIST)  
Polymer Electrolyte Fuel Cell Cutting-  
Edge Research Center (FC-Cubic)  
2-41-6 Aomi, Koto-ku  
Tokyo 135-0064  
Japan

**Makoto Onaka**

The University of Tokyo  
Department of Chemistry  
Graduate School of Arts and Sciences  
Komaba, Meguro-ku  
Tokyo 153-8902  
Japan

**Ryan R. Otter**

Middle Tennessee State University  
Department of Biology  
Murfreesboro, TN 37132  
USA

**Kenichi Oyaizu**

Waseda University  
Department of Applied Chemistry  
Tokyo 169-8555  
Japan

**Munetaka Oyama**

Kyoto University  
Graduate School of Engineering  
Department of Material Chemistry  
Nishikyo-ku  
Kyoto 615-8520  
Japan

**Elisa Passaglia**

University of Pisa  
Department of Chemistry and  
Industrial Chemistry  
Via Risorgimento 35  
56126 Pisa  
Italy

**Thathan Premkumar**

Department of Materials Science  
and Engineering  
Gwangju Institute of Science  
and Technology (GIST)  
1 Oryong-dong, Buk-gu  
Gwangju 500-712  
South Korea

**Andrea Pucci**

University of Pisa  
Department of Chemistry and  
Industrial Chemistry  
Via Risorgimento 35  
56126 Pisa  
Italy

**Jeremy J. Ramsden**

Cranfield University  
Bedfordshire MK43 0AL  
UK

and

Cranfield University at  
Kitakyushu  
2-5-4F Hibikino  
Wakamatsu-ku  
Kitakyushu 808-0135  
Japan

**C.N.R. Rao**

International Centre for Materials  
Science,  
New Chemistry Unit and CSIR Centre  
of Excellence in Chemistry  
Jawaharlal Nehru Centre for Advanced  
Scientific Research  
Jakkur P. O.  
Bangalore 560 064  
India

and

Solid State and Structural Chemistry  
Unit  
Indian Institute of Science  
Bangalore 560 012  
India

**Marina Resmini**

Queen Mary University of London  
School of Biological and  
Chemical Sciences  
Mile End Road  
London E1 4NS  
UK

**Ryan M. Richards**

Colorado School of Mines  
Department of Chemistry and  
Geochemistry  
1500 Illinois St.  
Golden, CO 80401  
USA

**Aaron P. Roberts**

University of North Texas  
Department of Biological Sciences &  
Institute of Applied Sciences  
Denton, TX 76203  
USA

**Kristen E. Roskov**

North Carolina State University  
 Department of Chemical &  
 Biomolecular Engineering  
 Raleigh, NC 27695  
 USA

**Giacomo Ruggeri**

University of Pisa  
 CNR-INFM-PolyLab  
 c/o Department of Chemistry  
 and Industrial Chemistry  
 Via Risorgimento 35  
 56126 Pisa  
 Italy

**Helmut Schlaad**

Max Planck Institute of Colloids  
 and Interfaces  
 MPI KGF Golm  
 14424 Potsdam  
 Germany

**Evan L. Schwartz**

Cornell University  
 Department of Materials Science  
 and Engineering  
 Ithaca, NY 14853  
 USA

**Tsunetake Seki**

The University of Tokyo  
 Department of Chemistry  
 Graduate School of Arts and  
 Sciences  
 Komaba, Meguro-ku  
 Tokyo 153-8902  
 Japan

**Ze Xiang Shen**

Nanyang Technological University  
 School of Physical and Mathematical  
 Sciences  
 Division of Physics and Applied  
 Physics  
 Singapore 637371  
 Singapore

**Young-Seok Shon**

California State University, Long Beach  
 Department of Chemistry and  
 Biochemistry  
 1250 Bellflower Blvd  
 Long Beach, CA 90840  
 USA

**Richard J. Spontak**

North Carolina State University  
 Department of Chemical &  
 Biomolecular Engineering  
 Raleigh, NC 27695  
 USA

and

North Carolina State University  
 Department of Materials Science &  
 Engineering  
 Raleigh, NC 27695  
 USA

**Koji Takahashi**

Kyushu University  
 Hakozaki  
 Higashi-ku  
 Fukuoka 812-8581  
 Japan

**Akrajas Ali Umar**

Universiti Kebangsaan Malaysia  
 Institute of Microengineering and  
 Nanoelectronics  
 43600 UKM Bangi Selangor  
 Malaysia

**Hao Yan**

Arizona State University  
Department of Chemistry and  
Biochemistry & The Biodesign  
Institute  
Tempe, AZ 85287  
USA

**Jingdong Zhang**

Huazhong University of Science and  
Technology  
College of Chemistry and Chemical  
Engineering  
Wuhan 430074  
China

**Ting Yu**

Nanyang Technological  
University  
School of Physical and  
Mathematical Sciences  
Division of Physics and Applied  
Physics  
Singapore 637371  
Singapore

## 1

**Phase-Selective Chemistry in Block Copolymer Systems***Evan L. Schwartz and Christopher K. Ober*

## 1.1

**Block Copolymers as Useful Nanomaterials**

## 1.1.1

**Introduction**

Despite our best efforts to chemically design functional nanomaterials, we cannot yet match the brilliance of Nature. One striking example of this fact comes from a tethering structure known as a byssus created by the bivalve, *Mytilus edulis*. Byssal threads are the highly evolved materials that *M. edulis* uses to provide secure attachments to rocks and pilings during filter feeding. The threads begin at the base of the mussel's soft foot and attach to a hard surface by an adhesive plaque. Under strong tidal forces, an ordinary material would not be able to withstand the contact stresses that would result from the meeting of such soft and hard surfaces. Recent studies have shown that *M. edulis* solves this materials design problem through the creation of a "fuzzy" interface that avoids abrupt changes in the mechanical properties by gradually changing the chemical composition of the thread [1]. The chemistry that it uses to accomplish this graded material involves the elegant use of collagen-based self-assembling block copolymers (BCPs) [2]. The ventral groove of the mussel's foot contains several pores that act as channels for a reaction-injection-molding process that creates the copolymer. For this, central collagen blocks are mixed with a gradient of either elastin-like (soft) blocks, amorphous polyglycine blocks (intermediate), or silk-like (stiff) threads to form "di-block" copolymers of gradually decreasing mechanical stiffness as *M. edulis* moves farther away from the rock interface. Spontaneous self-assembly of the biopolymer seems to occur by the metal-binding histidine groups found in between each block interface that may act as ligands for metal-catalyzed polymerizations. The transition metals used for these polymerizations, such as Zn and Cu, are extracted from the ambient water through filter feeding.

*M. edulis* byssal thread is not the only example of a self-assembling chemical system found in Nature that seems perfectly suited to its environment. Self-assembly such as that found in *M. edulis* can be found in nearly every level of

nature, from cellular structures such as lipid bilayers [3], the colonization of bacteria [4], and the formation of weather systems [5]. The concept of self-assembly is defined by the automatic organization of small components into larger patterns or structures [6]. As small components, nature often uses various molecular interactions, such as hydrophilic/hydrophobic effects and covalent, hydrogen, ionic and van der Waals bonds to construct nanomaterials with specific macroscale functionalities. As scientists, we have learned an extraordinary amount about how to construct better synthetic materials from careful studies of how structure fits function in natural materials [7].

In the field of soft matter, one type of self-assembling synthetic material that has already been introduced in the *M. edulis* example is the BCP. BCPs are composed of different types of polymer connected by a covalent bond [8]. Apart from their interesting physical properties that have resulted in their use in byssal threads, upholstery foam, box tape, and asphalt [9], BCPs are also interesting due to the ability of each polymer block, or *phase*, to physically separate on the nanometer scale into various self-assembled morphologies such as spheres, cylinders, and sheets. These structures are attractive to scientists for several reasons.

- First, if one of the phases is removed from the periodic, ordered lattice, then thin films of the material could be used as stencils to etch patterns into semiconductor substrates such as silicon or gallium arsenide. This application is of great interest to the semiconductor industry, which is currently searching for alternative technologies for sub-20 nm lithography.
- Second, chemists are interested in BCP templates because they provide the power to carry out chemical reactions within specific phases of the material. This ability opens up many new areas of chemistry for nanomaterial design, including the growth of functional nanoparticle arrays for catalytic applications, the selective sequestration of chemicals for drug delivery, and the creation of mesoporous monolithic structures as low-*k* dielectric materials.
- Third, chemical functionalities attached to one phase within BCPs can be driven to segregate to the surface, where they can be affected by external stimuli such as ultraviolet (UV) light. These *surface-responsive* materials could be lithographically patterned to control the selective adsorption of biomolecules for biosensor applications.

All of the above applications use *phase-selective chemistry* to effect changes to the BCP microstructure and create useful nanostructured materials. In this chapter, we will discuss not only the recent investigations in these areas but also many other new and interesting applications.

The chapter is organized into three sections. In the first section we will discuss the basics of BCP self-assembly, and include a more detailed analysis of the morphologies possible with this class of material, along with an overview on how they are made and modified. The second section will provide a literature review of relevant studies in the field, including descriptions of BCPs as lithographic materials, as *nanoreactors*, as photo-crosslinkable nanobjects, and as surface-responsive



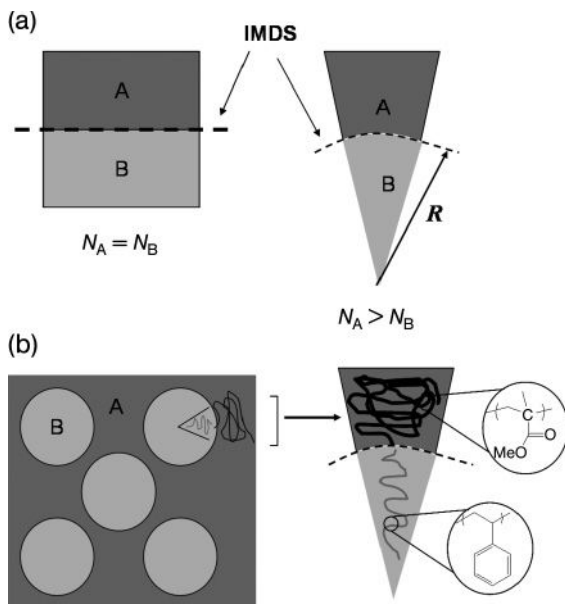
materials. The third section will conclude with a summary of the most important contributions, together with a few additional insights on the future direction of the field of phase-selective BCP systems.

### 1.1.2

#### Self-Assembly of Block Copolymers

The thermodynamics of polymer mixing plays a large role in the self-assembly of BCPs [10]. In typical binary polymer mixtures, it is entropically unfavorable for two dissimilar homopolymers to mix homogeneously, as both components feel repulsive forces that result in the formation of large “macro-phases” of each component in the mixture, akin to the mixing of oil and water. In diblock copolymers, however, the two component polymer “blocks” are chemically attached with a covalent bond. Here, the covalent bond acts as an elastic restoring force that limits the phase separation to mesoscopic length scales, thus resulting in “microphase” separated structures. The size of these phases, which are also known as microdomains, scale directly as the two-thirds power of the copolymer molecular weight [11]. The specific shape of the microdomains relies on a number of factors that control how each of the blocks interacts with each other. In the simplest argument, if there are equal amounts of each polymer, the microdomains will form into distinct layers with planar interfaces. However, if there is more of one block than the other, then curved interfaces will result. This curvature minimizes the repulsive interfacial contact between the A and B block, which also minimizes the free energy of the system. The bend that forms can be characterized by the curvature radius,  $R$ , as shown in Figure 1.1. Therefore, the equilibrium morphology of the BCP can usually be predicted based on differential geometry.

Other, more complicated, ‘self-consistent mean field’ theoretical treatments can be used to calculate the equilibrium morphology of the BCP. These theories sum the free energy contributions between (i) the repulsive polymer–polymer interactions versus (ii) the elastic restoring force energy for a particular microphase structure. The microphase structure with the lowest free energy sum will be the final equilibrium morphology. These theoretical equilibrium morphologies can be mapped out on a phase diagram, as shown in Figure 1.2. A typical BCP phase diagram plots the product  $\chi N$  on the ordinate versus the volume ratio,  $f_A$ , on the independent axis.  $\chi$  is known as the Flory–Huggins interaction parameter, which quantifies the relative incompatibility between the polymer blocks, and is inversely related to the temperature of the system.  $N$  is called the *degree of polymerization*, which is the total number of monomers per macromolecule. The volume fraction is represented by  $f_A = N_A/N$ , where  $N_A$  is the number of A monomers per molecule. For very low concentrations of A monomer, no phase separation will occur and the two polymers will mix homogeneously. However, at slightly higher compositions, where  $f_A \ll f_B$ , the A blocks form spherical microdomains in a matrix of B. The microdomains arrange on a body-centered cubic (BCC) lattice. Increasing the volume fraction to  $f_A < f_B$  leads to an increase in the connectivity of the microdomains, triggering the spheres to coalesce into cylinders that arrange on a hexago-



**Figure 1.1** (a) Equal volume fractions of A and B blocks form layered structures called lamellae with curvature radius approaching infinity. Unequal volume fractions of A and B cause a curvature at the intermaterial dividing surface (IMDS) to minimize interfacial

contact between the blocks and cause decrease of the curvature radius;

(b) Schematic representing the application of this model in a sphere-forming (PS-*b*-PMMA) block copolymer system. Adapted from Ref. [29].

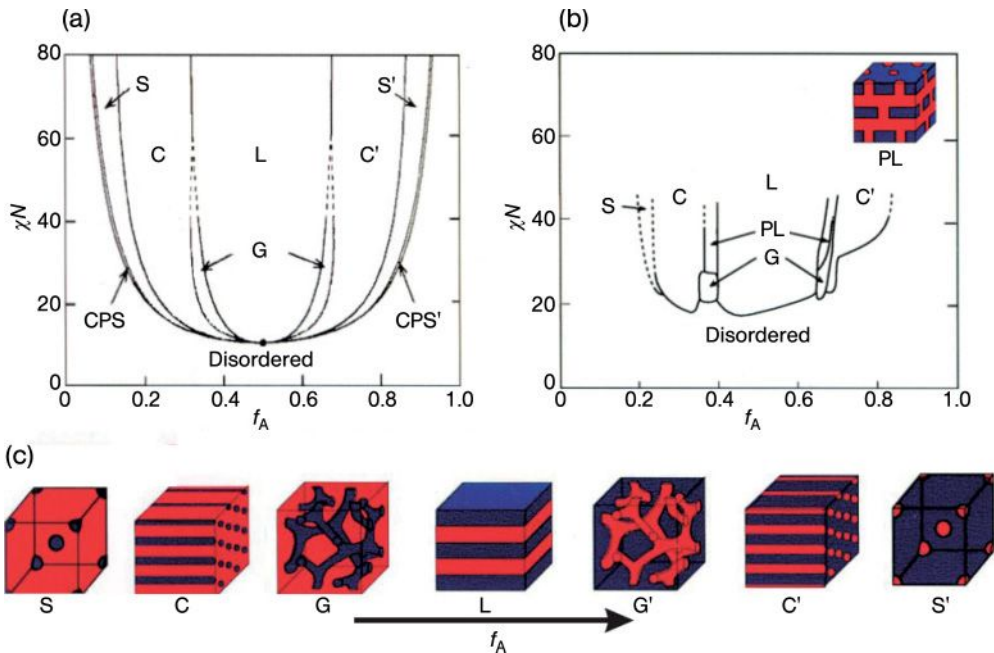
nal lattice. A roughly equal amount of both A and B blocks ( $f_A \approx f_B$ ) will result in the formation of alternating layered sheets, or lamellae, of the A and B blocks. Any further increase in  $f_A$  ( $f_A > f_B$ ), will cause the phases to invert, which means that the B block forms the microdomains in the matrix of A.

Thus, by tailoring the relative amount of A, the chemist can control the connectivity and dimensionality of the global BCP structure: spheres essentially represent zero-dimensional points in a matrix; cylinders represent one-dimensional lines; and lamellae represent two-dimensional sheets. Additionally, narrow regions of  $f_A$  exist in between the cylindrical and lamellar phase space where the two morphologies interpenetrate each other to form three-dimensional (3-D) “gyroid” [12, 13] network structures. Some reports of these morphologies have been published, and efforts have been put forth to take advantage of the added dimensionality with new applications [14, 15].

### 1.1.3

#### Triblock Copolymers

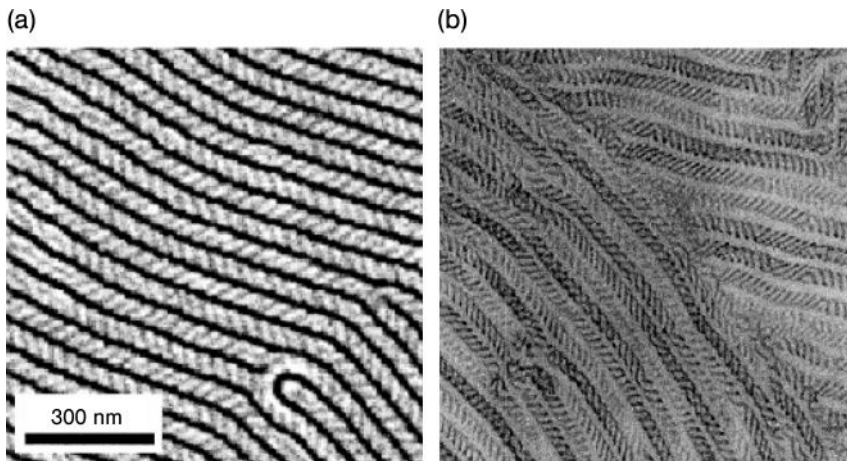
Adding extra polymer blocks to the BCP chain introduces additional levels of complexity into the self-assembled phase behavior. Core-shell morphologies [16], “knitting pattern” [17] and helical structures (Figure 1.3) are just a few of the exotic



**Figure 1.2** Phase diagram for linear AB diblock copolymers, comparing theory and experiment. (a) Self-consistent mean field theory predicts four equilibrium morphologies: spherical (S), cylindrical (C), gyroid (G), and lamellar (L), depending on the composition  $f$  and combination parameter  $\chi N$ . Here,  $\chi$  is the Flory–Huggins interaction parameter (proportional to the heat of mixing A and B segments) and  $N$  is the degree of polymerization (number of monomers of all

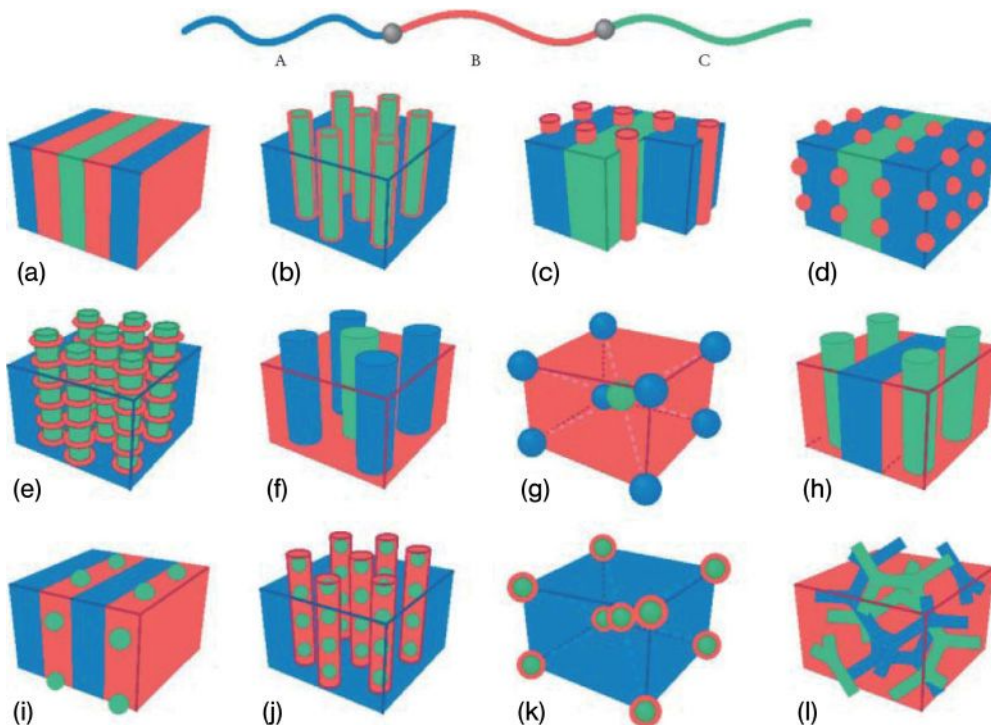
types per macromolecule); (b) Experimental phase portrait for poly(isoprene-*block*-styrene) diblock copolymers. Note the resemblance to the theoretical diagram. One difference is the observed perforated lamellae (PL) phase, which is actually metastable; (c) A representation of the equilibrium microdomain structures as  $f_A$  is increased for fixed  $\chi N$ . Reprinted with permission from Ref. [8]; © 2006, American Institute of Physics.

structures that have been found experimentally using triblock copolymers. Even more of the so-called “decorated phases” of tri-BCPs [18] have been predicted on a theoretical basis, but not yet found experimentally (Figure 1.4), offering a plethora of structures available to the chemist based on this template. In these cases, the phase behavior depends on two compositional variables and three relative incompatibility parameters ( $\chi_{AB}$ ,  $\chi_{AC}$ ,  $\chi_{BC}$ ), and thus the sequence of the components in the chain becomes important. For example, a poly(styrene-*block*-ethylene-*block*-butadiene) BCP may have completely different phase behavior than a poly(styrene-*block*-butadiene-*block*-ethylene) BCP at the same relative volume ratios. It is also possible to synthesize more than three blocks in the polymer chain—for example, a tetrablock terpolymer [19]. A more detailed look into the phase behavior and morphology of these complex systems is offered in a review by Abetz [20].



**Figure 1.3** (a) Scanning electron microscopy image of the first layers of cylinders of a thin film of a triblock copolymer containing 17% styrene, 26% vinylpyridine, and 57% *tert*-butyl methacrylate after THF vapor exposure. The surface structures indicate a helix/cylinder morphology; (b) Transmission electron microscopy cross-section of a bulk sample of a triblock copolymer containing 26% styrene, 12% butadiene, and 62% *tert*-butyl methacrylate ( $MW = 218\,000\text{ g mol}^{-1}$ ).

morphology; (b) Transmission electron microscopy cross-section of a bulk sample of a triblock copolymer containing 26% styrene, 12% butadiene, and 62% *tert*-butyl methacrylate ( $MW = 218\,000\text{ g mol}^{-1}$ ).



**Figure 1.4** Morphologies for linear ABC triblock copolymers. A combination of block sequence (ABC, ACB, BAC), composition and block molecular weights provides an

enormous parameter space for the creation of new morphologies. Reprinted with permission from Ref. [8]; © 2006, American Institute of Physics.

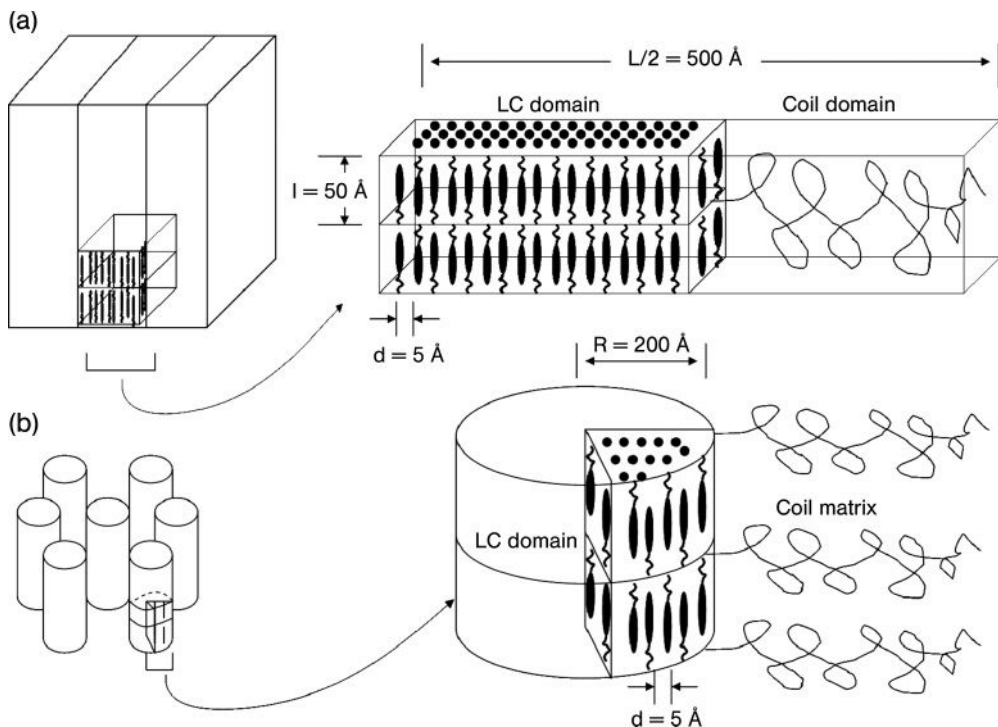
## 1.1.4

**Rod-Coil Block Copolymers**

There are essentially two types of BCP, both of which highlight interesting avenues for BCP self-assembly. “Coil-coil” BCPs, which are the most commonly studied, contain A and B blocks that can both be theoretically modeled as flexible chains. “Rod-coil” BCPs, on the other hand, have one polymer chain that is best represented as a rigid rod due to its stiff nature and anisotropic molecular shape. Rod-type molecules, also known as mesogens, can be incorporated into the main chain of a polymer backbone or appended from the polymer backbone as a side-chain substituent. Both types of rod-coil BCP have been shown to exhibit liquid crystalline (LC) behavior when placed in solution [21, 22]. These solutions are known as *lyotropic* solutions, which means that their phase behavior changes at different polymer concentrations. Initially, the polymers exhibit a disordered state called the *isotropic* phase; however, when the solution reaches a critical concentration, the molecular chains become locally packed and are forced to orient in a particular direction (*nematic* phase) due to the anisotropy of their shape. They can also arrange into several types of well-defined layers (*smectic* phases). By creating a BCP with a combination of a rod-like polymer block and a flexible polymer block, molecular level ordering characteristic of liquid crystals can be combined with the microphase-separated behavior typical of BCPs to produce hierarchical levels of self-assembly [23].

In a groundbreaking study on poly(hexylisocyanate-*block*-styrene) (PHIC-*b*-PS)—where the PHIC block represents the “rod” and the PS represents the “coil” block—it was found that, with increasing concentration of the polymer, isotropic, nematic and smectic LC phases each developed before the polymer adopted its final microphase-separated state [24]. As the PHIC chain was much longer than the PS chain in this case, the PHIC chain axis tilted with respect to the layer normal and interdigitated with the PS in order to accommodate the strain, resulting in wavy lamellae and never-before-seen zigzag and arrowhead morphologies. Electron diffraction experiments revealed  $\sim 1$  nm spacings between the PHIC chains and a smectic layer repeat distance of approximately 200 nm. Furthermore, shearing a nematic solution of the polymer on a glass substrate induced over  $10\ \mu\text{m}$  of perfect long-range ordering of the layers, thus powerfully illustrating the multiple levels of ordering possible with LC-BCPs.

In further studies conducted by Mao and coworkers [25], a LC side group was attached as a pendent unit to a modified poly(styrene-*block*-isoprene) BCP. In this material, the phase transitions occurred in the opposite direction. The microphase separation of the classical lamellae and cylinders developed first, after which smectic layering of the LC blocks developed *within* the BCP microdomains due to constraint by the intermaterial dividing surface (IMDS) (Figure 1.5). Again, by incorporating a rigid block into a BCP framework, a hierarchy of ordering is observed. Unique chemical properties such as LC behavior may turn out to be crucial for future self-assembled synthetic materials.



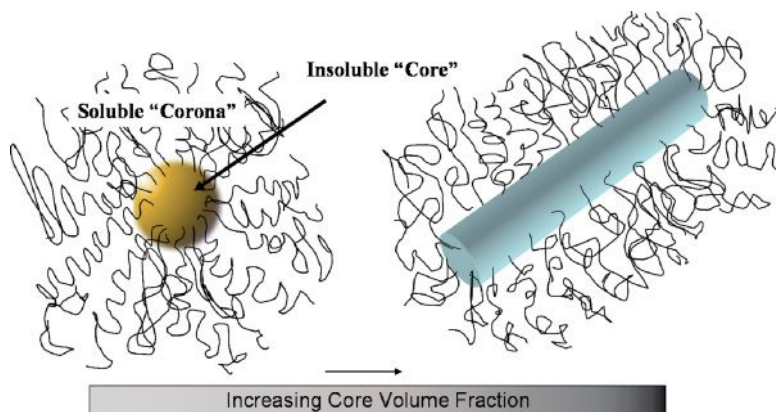
**Figure 1.5** (a) A model showing the hierarchical levels of self-assembly using rod-coil block copolymers exhibiting liquid crystalline behavior in a lamellar morphology. (b) Structures can also form in the cylindrical morphology. Adapted from Ref. [25].

### 1.1.5

#### Micelle Formation

If the BCP is dissolved in a dilute solution with a solvent that dissolves only one of the blocks, the BCP will act as a surfactant molecule and micelle formation will occur. These materials are referred to as “amphiphilic” due to their dual polar/nonpolar chemical nature, and can thus dissolve partially in polar or nonpolar media. In dilute solutions, the soluble block “corona” will wrap itself around the insoluble “core” to minimize the repulsive contact forces between the insoluble block and the solvent, as illustrated in Figure 1.6. These micelles form structures with a defined size and shape, depending on the relative molecular weight of the blocks and the ionic strength of the solution. BCPs with large soluble blocks typically form spherical micelles due to small curvature radii, but smaller soluble block lengths can also form cylindrical micelles due to their greater curvature radii. The similarity of these micellar structures to biological cell vesicles [26] and liposomes





**Figure 1.6** Schematic showing micelle structure. Amphiphilic block copolymers form micelles when dissolved in block-selective solvents. The soluble block “corona” stretches out into the solvent and masks the solvophobic “core”. Cylindrical (and other) morphologies can be formed by tuning the relative volume fraction of the blocks.

has prompted many investigators to explore their use as templates [27], encapsulating agents [28], or drug delivery systems [29].

#### 1.1.6

#### Synthesis of Block Copolymers Using Living Polymerization Techniques

BCPs are produced by the sequential addition of monomers into a “living” polymerization system [30]. Living polymerizations are characterized by a rapid initiation of the reactive chain end (e.g., carbanion, organometallic complex, etc.) and the lack of side reactions (e.g., chain termination or chain transfer) during growth of the polymer chain. In other words, a living polymer is a macromolecular species that will continue to grow as long as the monomer supply is replenished. The reactive chain end is then quenched to terminate further growth of the polymer during precipitation and purification.

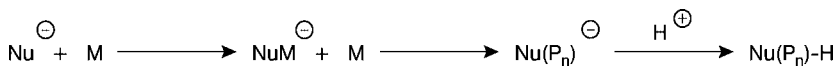
A precise control of molecular weight is possible through living polymerization strategies. The degree of polymerization ( $N$ ) is directly related to the molar amount of monomer ( $M$ ) and the molar concentration of initiator,  $[I]$ , as shown in Equation 1.1:

$$N = \frac{[M]}{[I]} \quad (1.1)$$

The living reaction will also be characterized by a narrow distribution of molecular weight, or polydispersity ( $M_w/M_n$ ), of usually between 1.02 and 1.1, which means that there is less than 30% standard deviation in the degree of polymerization of each of the chains. Many possible synthetic techniques are available to the

**Table 1.1** Common living polymerization techniques for the preparation of block copolymers.

Polymerization technique	Monomers available
Anionic	Styrenes, vinylpyridines, methacrylates, acrylates, butadiene, isoprene, <i>N</i> -carboxyanhydrides (amino acids), ethylene oxide, lactones, hexamethylcyclotrisiloxane, 1,3-cyclohexadiene, isocyanates
Cationic ring-opening	Epoxides, siloxanes, tetrahydrofuran
Group transfer	Methacrylates, acrylates, nitriles, esters, butadienes, isoprenes
Ring-opening metathesis	Norbornenes
Stable free radical	Styrene, methacrylates, acrylates, acrylamides, dienes, acrylonitrile
Atom transfer radical	Styrenes, methacrylates, acrylates, acrylonitriles
Reversible addition – fragmentation chain transfer	Methacrylates, styrene, acrylates

**Scheme 1.1** The general mechanism of anionic polymerization.

chemist wishing to prepare a BCP, each with its own advantages and disadvantages. The types of polymerization suitable for each type of monomer are listed in Table 1.1. The most common techniques used to synthesize and modify BCPs are summarized briefly in the following paragraphs.

#### 1.1.6.1 Anionic Polymerization

Anionic polymerization has become the most common technique in the synthesis of BCPs with narrow polydispersity [31]. The polymerization proceeds through the highly reactive carbanion chain end, usually created by an alkyl lithium initiator such as *sec*-BuLi or *n*-BuLi (Scheme 1.1). Due to the high reactivity of the chain end with other compounds, extremely stringent conditions must be met in order to avoid unwanted side reactions. Therefore, the polymerization must be carried out without any trace of oxygen or water, and all monomers and solvents must be extensively dried, degassed, and purified before use [32, 33]. The other main dis-



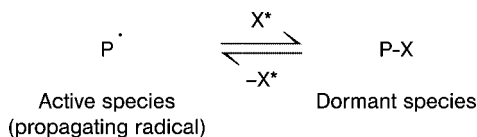
advantage to anionic polymerization is the limited range of monomers available for synthesis. Although the standard styrenes, methacrylates, butadiene, isoprene, ethylene oxide, vinylpyridines, and amino acids can all be synthesized using this technique, monomers with reactive functional groups cannot be used because they will interfere with the anionic chain end. Such monomers must therefore be protected before synthesis and then later deprotected. In some cases, such as the polymerization of acrylates, the reactions must be carried out at very low temperatures ( $-78^{\circ}\text{C}$ ) in order to avoid terminating side reactions such as intrachain cyclization or “backbiting”, caused by the reaction of the anionic center with a carbonyl group on the monomer.

For BCPs containing two distinctly different monomer types, such as the polymerization of polystyrene and polyethylene oxide, attention must be paid to the order of polymerization in order to maximize the efficiency of the reaction. For example, whilst a polystyryl lithium “macroinitiator” enables the rapid initiation of ethylene oxide, lithium-activated ethylene oxide will not efficiently initiate the polystyrene monomer and the reaction may not go to completion. This is due to the difference in relative reactivity between the oxyanion and carbanionic species.

There are, of course, many advantages to anionic polymerizations, besides the fact that they produce polymers with the lowest polydispersity. One advantage is that the chain end can be terminated with functional groups or coupling agents to produce telechelic polymers or complex macromolecular architectures, respectively. Examples of complex BCP architectures include ABA tri-BCPs, star, or graft BCPs [34].

#### 1.1.6.2 Stable Free Radical Polymerizations

The amount of growth in the area of stable free radical polymerizations (SFRPs) during the past 20 years has been astounding. Although the model for SFRP was introduced by Otsu during the early 1980s [35], more recently, alkoxyamine initiators generated by the research group of Hawker [36] at IBM have led to dramatic improvements in the technique as introduced by Georges [37, 38] at Xerox during the early 1990s. These types of initiator contain a thermally cleavable C–O bond attached to a nitroxyl radical species. Running the reaction at high temperatures ( $80\text{--}90^{\circ}\text{C}$ ) causes a reversible capping of the nitroxyl radicals, and allows monomer addition to the polymer chain only when the nitroxyl radical is in its detached state (Scheme 1.2). An advantage to SFRP is that the chemical rate of this detachment drops almost to zero at room temperature. Therefore, decreasing the temperature



**Scheme 1.2** The general mechanism of stable free radical polymerizations.

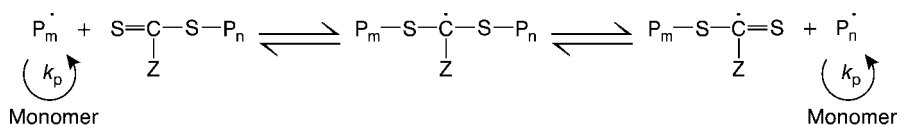
of the polymerization reactor essentially “switches off” the polymerization and allows the chemist to expose the first block to air, without terminating the reactive chain end. After precipitation, purification, and molecular weight characterization, the first block can be dissolved and heated in the presence of the second monomer to form the final product. There is a wide range of monomers available using SFRP, including styrenes, methacrylates, (meth)acrylonitriles, among others. Unfortunately, the polydispersities of the free radical polymerization process are not quite as low as anionic polymerization, and stereochemical control is not possible.

### 1.1.6.3 Reversible Addition–Fragmentation Chain Transfer (RAFT) Polymerization

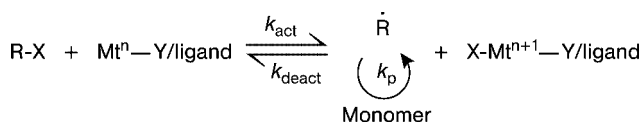
The RAFT process is a variation of the living radical process that instead uses the thermal lability of a C–S bond to provide the insertion of monomer units [39]. A general scheme of the monomer addition/fragmentation step is shown in Scheme 1.3. RAFT is used for the polymerization of methacrylates, styrenes and acrylates, and can also be successfully applied to narrow polydispersity BCPs. Interestingly, in species with dithiocarbamate end groups, such as tetraethyldithiuram disulfide, Otsu and coworkers found that the C–S bond could photochemically dissociate, offering the possibility of initiating polymerizations purely with UV light [40]. This technique was subsequently used to produce several types of BCP [41–45]. The thiocarbonyl end group can be removed by aminolysis or reduction with tri-*n*-butylstannane to leave a saturated chain end, or by thermal treatment to leave an unsaturated chain end. It may also be functionalized with amino or carboxy-functionalized end groups [46].

### 1.1.6.4 Atom Transfer Radical Polymerization

Atom transfer radical polymerization (ATRP) is another rapidly maturing technology that easily allows the production of end-functionalized and low-polydispersity polymers. It has also been shown to be a highly versatile reaction for the production of a wide variety of polymer architectures such as stars, combs, and tapered BCPs [47]. The mechanism (Scheme 1.4) functions in similar manner to typical



**Scheme 1.3** The general mechanism of reversible addition/fragmentation/transfer (RAFT) polymerization.



**Scheme 1.4** The general mechanism of atom-transfer radical polymerization (ATRP).

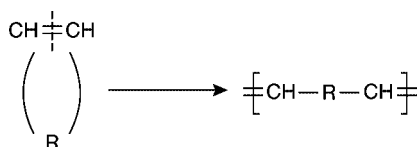
living free radical processes, except that the active radical species undergoes a reversible redox process that is catalyzed by a transition metal complex attached to an amine-based ligand. The main disadvantage of ATRP is that these transition metals are difficult (if not impossible) to remove completely from the polymer after polymerization. ATRP has a wide range of monomers available for synthesis, however, including (meth)acrylates, (meth)acrylamides, styrenes, and acrylonitriles. Initiators for the process are usually alkyl halide species (R-X), and their presence at the end of the polymer chain allows for easy substitution reactions with functional groups.

#### 1.1.6.5 Ring-Opening Metathesis Polymerization

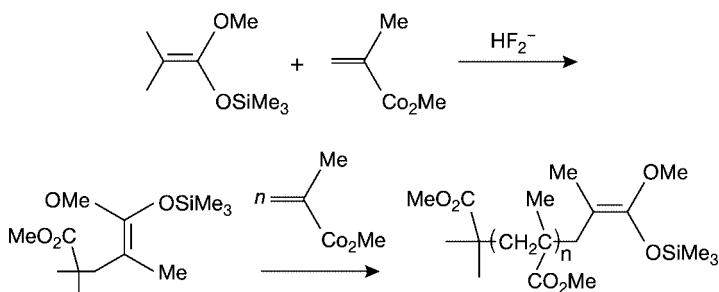
Ring-opening metathesis polymerization (ROMP) is typically used for the ring-opening polymerization of cyclic olefins such as norbornenes and cyclooctadiene [48]. A general mechanism is presented in Scheme 1.5. ROMP also uses a metal catalyst that is usually composed of titanium, tungsten, or ruthenium attached to an aluminum ligand. Based on the results obtained by Robert Grubbs and coworkers, a selection of functional group-tolerant ruthenium catalysts has been synthesized, opening up new opportunities for structurally diverse BCPs, such as amphiphilic copolymers [49] used to coat chromatographic supports, water-soluble/conducting self-assembling materials [50], and fluorescent BCPs for use in light-emitting devices [51].

#### 1.1.6.6 Group Transfer Polymerization

Group transfer polymerization (GTP) is best suited for the polymerization of methacrylate and acrylate polymers [52]. A general mechanism is shown in Scheme 1.6. Esters, nitriles, styrenes, butadienes, isoprenes, and most other  $\alpha,\beta$ -unsaturated



**Scheme 1.5** The general mechanism of ring-opening metathesis polymerization (ROMP).



**Scheme 1.6** The general mechanism for group transfer polymerizations.

compounds can also be prepared [53]. One interesting monomer that is typically prepared by GTP is poly(2-(dimethylamino)ethylmethacrylate) (PDAEMA). When polymerized with a hydrophobic methacrylate species, Billingham and coworkers found that the resulting amphiphilic BCP would easily form micelles in aqueous solution due to the water solubility of the PDAEMA block [54, 55]. Initiators often include silyl ketene acetal-type structures. Trace amounts of nucleophilic catalysts such as TASHF<sub>2</sub> are necessary to activate the silicon catalyst, along with large amounts of Lewis acids such as ZnX<sub>2</sub> (X = Cl, Br, I) to activate the monomer. A key advantage of GTP is that it can be performed at room temperature. Moreover, functionalized polymers can easily be added by the use of either: (i) a functionalized initiator or end-capping agents for functional groups attached to the end of the chain; or (ii) a functionalized monomer for functional groups evenly distributed throughout the polymer chain.

### 1.1.7

#### Post-Polymerization Modifications

Today, living polymerization techniques are available for a wide range of monomer types, and the possibilities are expanding daily. However, alternative routes are still necessary for the preparation of BCPs with highly specialized solubilities and functionalities, and this often requires post-polymerization modification steps such as active-center transformations and polymer-analogous reactions.

##### 1.1.7.1 Active-Center Transformations

Often, one type of polymerization mechanism may not be suitable for both types of monomer used in the BCP. In this case, following formation of the first block, it is possible to alter the polymerization mechanism to suit the efficient addition of a second monomer to the chain. The active center can be modified either by *in situ* reactions or by isolation of the first block, followed by chemical transformation of the active center with a separate reaction; the polymerization can then continue after addition of the second monomer. For example, an SFRP mechanism can be transformed into an anionic ring-opening system for the polymerization of poly(styrene-*block*-ethylene oxide). First, the styrene undergoes SFRP in the presence of mercaptoethanol, a chain-transfer agent. The hydroxyl functionalized PS is then used as a “macroinitiator” for the anionic ring-opening polymerization of ethylene oxide [56]. Active center transformation has been used for the formation of poly(norbornene-*block*-vinylalcohol) BCPs through a combination of ROMP and aldol GTP [57], while a combination of cationic (not discussed) and anionic procedures have been used to polymerize poly(isobutylene-*block*-methyl methacrylate) BCPs [58]. Finally, each of the above mechanisms can also be transformed into an ATRP process, as described in a review by Matyjaszewski [59].

##### 1.1.7.2 Polymer-Analogous Reactions

As we have seen, the creation of BCPs through living polymerization mechanisms restricts the number of monomers available for use. Additionally, functionalized

polymers feature delicate protecting groups that may be unsuitable for the highly reactive initiators used in living polymerizations. Polymer-analogous reactions can create copolymers that could not have been synthesized within a living polymerization. These modifications are carried out on previously synthesized, or “precursor” BCPs such as poly(styrene-*block*-isoprene) with known molecular weights and narrow molecular weight distributions. Chemical transformation of the precursor polymer can be carried out selectively on individual blocks, on the entire copolymer, or on each block in sequence. Here, careful selection of the reaction conditions is vital to avoid any harmful side reactions such as degradation or crosslinking of the original polymer. If carried out successfully, the degree of polymerization, molecular weight distribution, and main chain architecture of the precursor polymer will remain the same, but the solubility and physical properties of the polymer may be altered completely. Examples of polymer analogous reactions include hydrogenation [60], epoxidation [61], hydrolysis [62], sulfonation [63], hydroboration/oxidation [64, 65], quaternization [66], hydrosilylation [67], and chloro/bromomethylation [68, 69]. Further details for each of these reactions is also available [71].

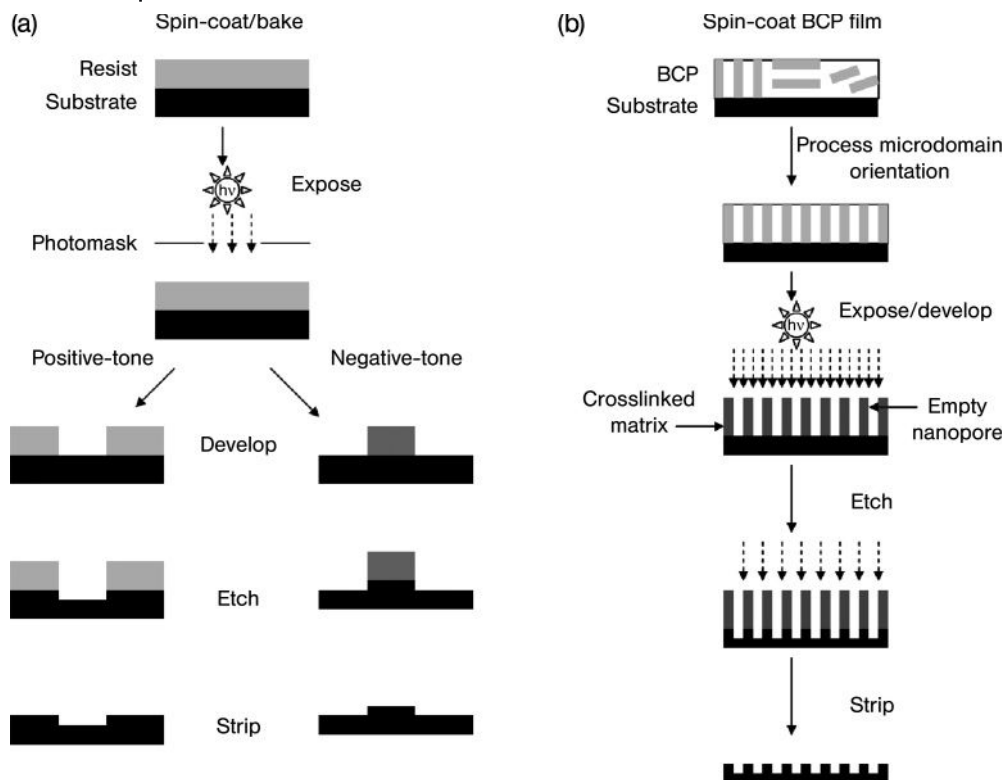
In this section, we have set the foundation for understanding how the chemistry of block copolymeric materials relates to the physics of their unique self-assembling properties. In the remainder of the chapter, it will become clear how these novel chemical strategies are used to effect practical physical applications.

## 1.2 Block Copolymers as Lithographic Materials

### 1.2.1 Introduction to Lithography

A modern integrated circuit is a complex, 3-D network of patterned wires, vias, insulators, and conductors. In order to transfer these patterns onto the silicon substrate it is first necessary to write the pattern, and for this the technique of photolithography is used, in which radiation-sensitive polymers play an integral role. Standard photolithography consists of essentially two steps: (i) writing of the pattern into a radiation-sensitive polymer thin film (resist); and (ii) transferring the pattern by etching into the underlying substrate [72]. A schematic of the traditional lithographic process is shown in Figure 1.7a. As photolithography and its associated technologies will become a recurring theme in this chapter, a brief primer on the subject will be useful at this point.

During the exposure process of a polymeric photoresist, UV radiation passes through a quartz photo mask that only allows a particular pattern of radiation to pass through and strike a thin film of photoresist. A chemical change is effected in the exposed regions of the polymer, which allows its subsequent development in a solvent, similar to the way in which photographic film is exposed and developed in a darkroom. The mechanism of the chemical change involves the forma-



**Figure 1.7** (a) Schematic of a traditional photolithography using positive-tone or negative-tone resist chemistry. (b) Schematic of block copolymer lithography, using a combination of positive-tone and negative-tone resist chemistry.

tion, rearrangement or breaking of bonds within the polymer chain. A resist's *sensitivity* is a measure of how efficiently it responds to a given amount of radiation, and might be compared to the ASA or ISO rating of a photographic film. A resist with a higher sensitivity will allow a satisfactory image to be produced for a smaller absorbed *dose* of radiation. The *resolution* of a photoresist is the size of the smallest structure that can be cleanly resolved after pattern development using standard microscopy techniques. This structure will then be used to efficiently pattern into the underlying substrate, assuming that the photoresist has sufficient *etch resistance* to withstand the harsh pattern transfer step. In this step, the patterned resist must withstand high-energy plasma sources that are designed to etch into silicon wafers. Polymers containing more carbon have stronger dry-etch resistance than those with lower amounts of carbon, whilst polymers containing high amounts of oxygen are etched easily. Even etch-resistant polymers may lose

a small amount of material during the etching step, but maintaining the structure of the pattern is important for high resolution. If less than a  $\pm 10\%$  change in the finest feature size of the polymer is etched into the substrate, the pattern transfer step is deemed successful [73]. This presents a huge challenge for the resist designer, who must tune the chemical components of the photoresist to satisfy two diametrically opposed requirements: to design a resist that is very responsive to ultraviolet radiation, but which, after the initial exposure, becomes highly resistant to the specific type of radiation and heat involved in the pattern transfer step. This is often achieved through the copolymerization of more than one type of monomer, each having its own functionality in the photoresist.

The realm of photolithography is split into two families of chemistry, based on the different physical properties possible for the exposed photoresist:

- *Positive-tone* resist chemistry refers to a photoresist that becomes *more soluble* after exposure to UV light. This can happen because of chemical deprotection, bond rearrangement, or chain-scission mechanisms.
- *Negative-tone* resist chemistry refers to a photoresist that becomes *less soluble* through the formation of crosslinked networks after exposure to UV light.

In this chapter, we will highlight the many approaches that have been used for one or both of these types of chemistries, in order to fabricate functional nanoscale-sized structures using BCPs.

### 1.2.2

#### **Block Copolymers as Nanolithographic Templates**

The lithography community has been extremely successful in its ability to pack progressively more circuit elements into a chip, as governed by the benchmark pace first predicted by Gordon Moore in 1989, which states that the transistor density of semiconductor chips will double roughly every 18 months [74]. Since then, new technologies have enabled this march down to smaller feature sizes. Photoresists with smaller pixel sizes such as molecular glass resists [75, 76], new processes such as nanoimprint lithography and step and flash lithography [77], as well as the development of smaller wavelength exposure sources [78], have catalyzed the production of feature sizes down below 50 nm.

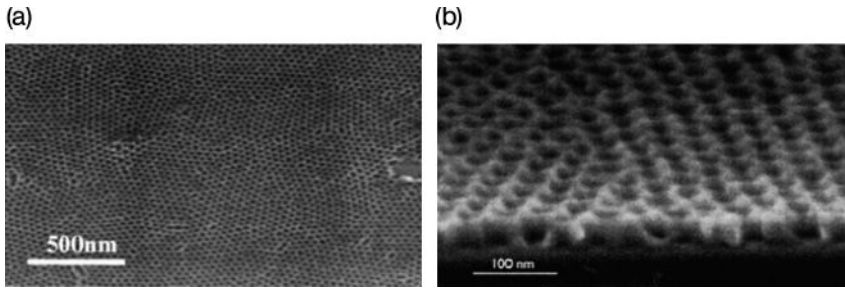
The exposure wavelength, however, has become the rate-determining step in our ability to pattern small feature sizes. Extremely small wavelength sources such as electron beams (e-beams) and X-rays do not have wavelength limitations, but e-beam systems can only write features in a slow serial process that is not amenable to large-scale commercial processes. The high cost of the incorporation of these tools into a clean room is another disadvantage to their use. X-ray lithography requires the extremely high power of synchrotron sources, or electron storage rings, which are found in only a handful of locations around the world. Both, therefore, have proven to be impractical in a production setting. It seems that extreme ultraviolet (EUV) radiation sources can carry the lithography community

down to 20 nm structures, but beyond that the semiconductor industry sees a need for innovative patterning strategies [79].

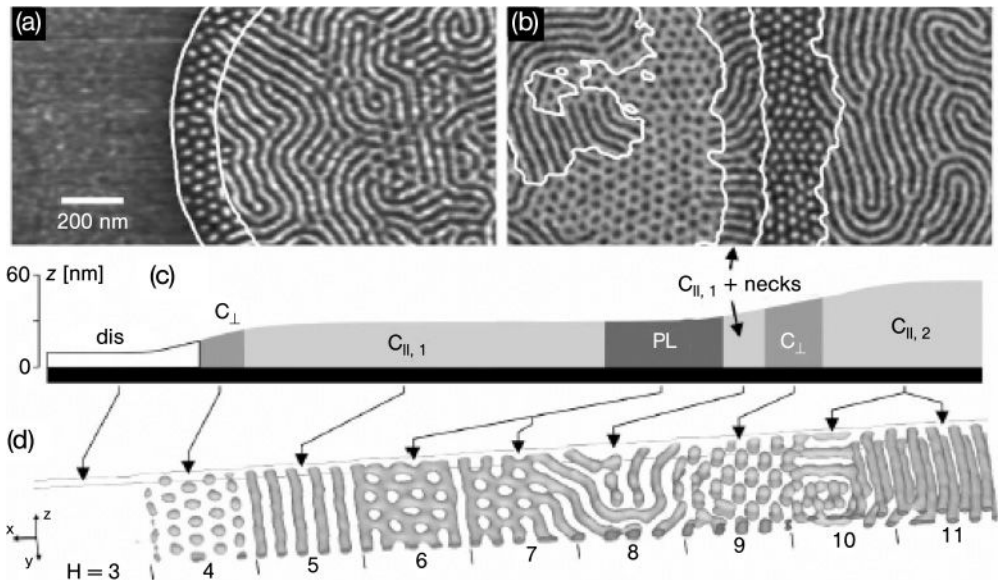
Design for modern integrated circuits usually requires a motif of several of different types of feature that may include—but are not limited to—regular patterns of straight and jogged lines and spaces, circular holes for contact openings, T-junctions, and columns of ferromagnetic media for data storage and memory applications. Interestingly, the shape of these features relate very well to the various geometries involved in BCP self-assembly (refer back to Figure 1.2). Furthermore, BCP microdomains form features that are much smaller than the current state-of-the-art standard photolithographic techniques. If one of the blocks in a BCP could be selectively degraded (i.e., positive tone chemistry), while the other block is crosslinked (i.e., negative tone chemistry) or has sufficient etch resistance, the result would be an ordered, nanoscale “stencil” that could be used to pattern circuit elements into a substrate. Theoretically, a density of over  $10^{11}$  elements per square centimeter could be achieved over a large area with this technique [80]. Starting with the pioneering work of Lee in 1989 [81], the field of BCP lithography has exploded during the past ten years. Several excellent reviews on the subject are available [82–84].

Several obstacles stand in the way of BCP lithography becoming an industrially useful technology. First, when a BCP thin film is created, the microdomains will often seem disordered, appearing in randomly oriented grains along the sample surface. Long-range ordering of the BCP nanodomains is often necessary for a few of the possible applications of BCP lithography, such as in the creation of addressable, high-density information storage media. Second, the nanodomains tend to arrange parallel to the sample surface due to preferred interfacial interactions between one of the blocks and the substrate. However, in order to be lithographically useful as etch masks that are able to transfer patterns into a wafer, nanodomains such as lamellae and cylinders must be arranged perpendicularly so that they are physically and continuously connected from the polymer/air interface through to the substrate, as shown in the plan-view and cross-sectional scanning electron microscopy (SEM) images shown in Figure 1.8. Third, the thickness of the BCP must be carefully controlled. It has been shown that, for a lamellar PS-*b*-PMMA BCP, if the initial film thickness  $t$  is thicker than the natural period of the lamellae  $L_0$  and  $t \neq (n + \frac{1}{2}) L_0$  ( $n$  an integer), then islands or holes of height  $L_0$  will form at the surface of the film and damage the homogeneity of the surface morphology. In the case where  $t < L_0$ , the situation becomes more complicated, as the lamellar chains will arrange perpendicular to the substrate due to the large entropic penalty associated with the chains having to compress to fit into the parallel orientation [85]. Other hybrid morphologies (Figure 1.9) have been found as the film thickness changes, due to the competition of several forces such as strong surface interactions, slow kinetics, and the thermodynamic driving force to arrange in layers commensurate with the height  $L_0$ . The physical complexity of block copolymer systems is staggering, and orientational control over these systems has developed into a field of its own [86]. Many research groups have achieved success in controlling the orientation of





**Figure 1.8** Field-effect scanning electron microscopy images obtained from a thin film of PS-*b*-PMMA after removal of the PMMA block. (a) Top view of the film; (b) A cross-sectional view. Reprinted with permission from Ref. [90]; © 2006, Wiley-VCH.



**Figure 1.9** (a,b) Tapping-mode atomic force microscopy phase images of thin poly(styrene-*block*-butadiene-*block*-styrene) (PS-*b*-PB-*b*-PS) films on Si substrates after annealing in chloroform vapor. The surface is covered with an 10-nm-thick PB layer. Bright regions correspond to PS microdomains below the darker top PB layer. Contour lines calculated from the corresponding height images are

superimposed; (c) Schematic height profile of the phase images shown in (a, b); (d) Simulation of a block copolymer film in one large simulation box with increasing film thickness. Reprinted with permission from Knoll A., Horvat, A., Lyakhova, K.S. *et al.* (2002) *Phys. Rev. Lett.*, **89**, 035501-1; © 2006, American Physical Society.

the self-assembled structures through special processing strategies; these include techniques such as thermal annealing [87], electric fields [88–90], mechanical shear [91–93], exposure to solvent vapor [18, 94, 95], physical confinement [96], neutral surfaces [97, 98], chemically nanopatterned surfaces [99–101], or a combination of any of the above [102].

#### 1.2.2.1 Creation of Nanoporous Block Copolymer Templates

Once a high degree of long-range ordering has been achieved on a BCP thin film, a final processing step is necessary to create the nanolithographic template. A schematic of BCP lithography is shown in Figure 1.7b. Upon exposure to UV, chemical, or reactive ion etching (RIE), these systems are designed so that one of the blocks will be selectively degraded relative to the other block(s). In fact, the second block should ideally become photochemically crosslinked and thus highly immobile during the subsequent pattern transfer step in order to avoid distortion of the photo pattern. Both “wet” and “dry” chemical processes can be used during the pattern transfer step. Wet chemical etching involves the dissolution of the first block in an aggressive acid or base solvent, whereas “dry” chemical processes refer to exposure of the film to high-energy reactive ions and plasmas such as  $\text{CF}_4$ ,  $\text{O}_2$ ,  $\text{SF}_6$ ,  $\text{Cl}_2$ , or argon gas. The etching process results from the combination of the kinetic energy of the ions (causing sputtering) and ion-induced chemical reactions that create volatile byproducts. The etching process affects polymers to different extents, depending on the chemical composition of the block. Several different types of BCP systems have been used as nanolithographic templates, such as poly(styrene-*block*-butadiene), poly(styrene-*block*-methyl methacrylate), poly(styrene-*block*-ferrocenyldimethylsilane), poly(styrene-*block*-lactic acid) and poly( $\alpha$ -methylstyrene-*block*-hydroxystyrene). The structures of the most commonly used sacrificial blocks are listed in Table 1.2.

**Poly(Styrene-*block*-Butadiene)** One of the first applications in this area also provides a model example of the concept of BCP lithography. Chaikin and coworkers [80, 111] created a thin film of microphase-separated poly(styrene-*block*-butadiene) (PS-*b*-PB), as shown in Figure 1.10a. Figure 1.10b shows how ozone was used to eliminate the PB spherical minority phase and open up windows in the PS matrix. In this instance, the minority PB block acts as a positive-tone resist due to its vulnerability to ozone chemical attack. The resulting spherical pores in the film provided less RIE resistance than the continuous PS matrix, thus creating a periodic array of 20 nm holes spaced 40 nm apart on a silicon nitride substrate. In the opposite strategy, illustrated in Figure 1.10c, the PB block was stained with osmium tetroxide vapor, which caused the PB block to exhibit a greater etch resistance than the PS block. In this case, the PB block acts like a negative-tone resist, resulting in removal of the PS matrix after RIE with  $\text{CF}_4$ . Therefore, the negative-tone system creates a pattern of raised dots on the substrate, instead of holes. This concept can easily be extended to create nanosized metal dots on any type of substrate for high-density information storage applications [127], or substrates such

**Table 1.2** Commonly used sacrificial blocks for block copolymer templates.

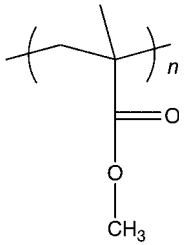
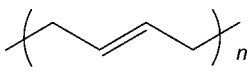
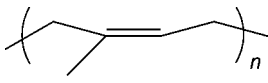
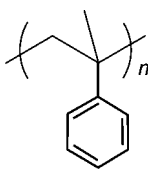
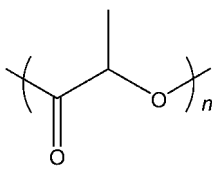
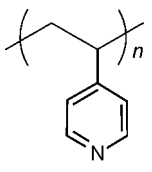
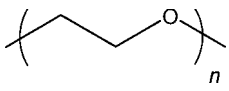
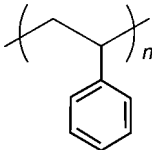
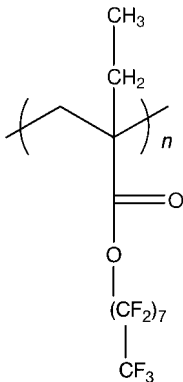
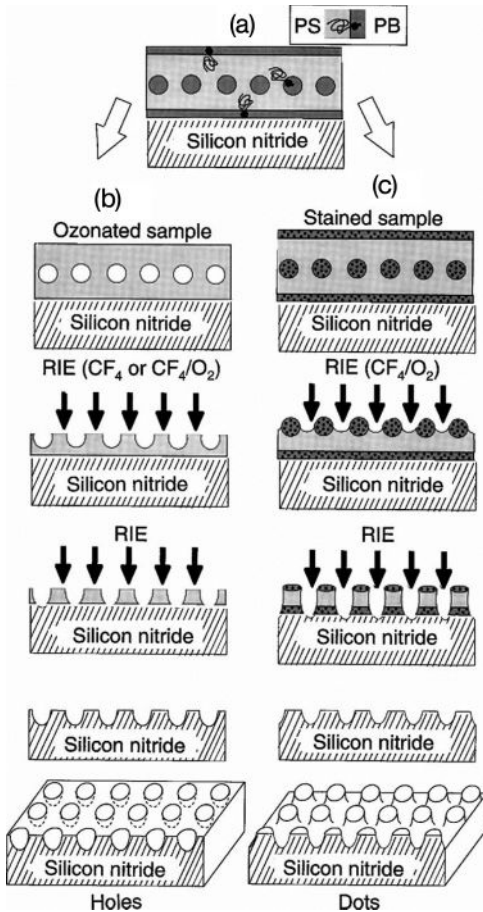
Name	Structure	Method of removal	Reference(s)
Poly(methyl methacrylate)		Photolysis Etch selectivity	[103–107] [108–110]
Poly(butadiene)		Ozonolysis	[80, 111, 112]
Poly(isoprene)		Reactive ion etching Ozonolysis	[113, 114] [14, 111, 115]
Poly( $\alpha$ -methylstyrene)		Heat/Vacuum	[116, 117]
Poly(L-lactide)		Aqueous base dissolution	[118–121]
Poly(4-vinyl pyridine)		Reactive ion etching	[96]
Poly(ethylene oxide)		Water dissolution	[122]

Table 1.2 Continued.

Name	Structure	Method of removal	Reference(s)
Polystyrene		Reactive ion etching	[123, 124]
Poly(perfluorooctyl ethyl methacrylate)		Reactive ion etching	[125, 126]

as gallium arsenide can be patterned, opening up new avenues for the production of quantum dot (QD) structures [128].

**Poly(Styrene-block-Methyl Methacrylate)** Poly(styrene-*block*-methyl methacrylate) (PS-*b*-PMMA) has been the workhorse of the field of BCP lithography for several reasons. First, it is relatively simple to produce using anionic polymerization techniques, and is commercially available [129]. Second, PMMA acts as a readily degradable positive-tone resist on exposure to deep ultraviolet (DUV) or e-beam radiation. In fact, PMMA is already well established in the semiconductor industry as a positive-tone e-beam resist. The PMMA chain breaks up into oligomers through a chain scission mechanism (Scheme 1.7), and can then be removed from the matrix through dissolution in acetic acid. Third, in the same DUV exposure step, the polystyrene matrix acts as a weak negative-tone resist, becoming photochemically crosslinked through oxidative coupling, as shown in Scheme 1.8 [130]. Immobilizing the matrix phase through crosslinking strategies is very important in the creation of nanoporous materials. The huge increase in surface area that results from the removal of the minority domain creates a concomitant increase in surface free energy. A driving force for the minimization of this free energy creates a strong tendency for the nanopores to collapse, which would result in distorted etched patterns. A high glass transition temperature ( $T_g$ ) relative to the processing temperature represents another means of stabilizing the nanoporous

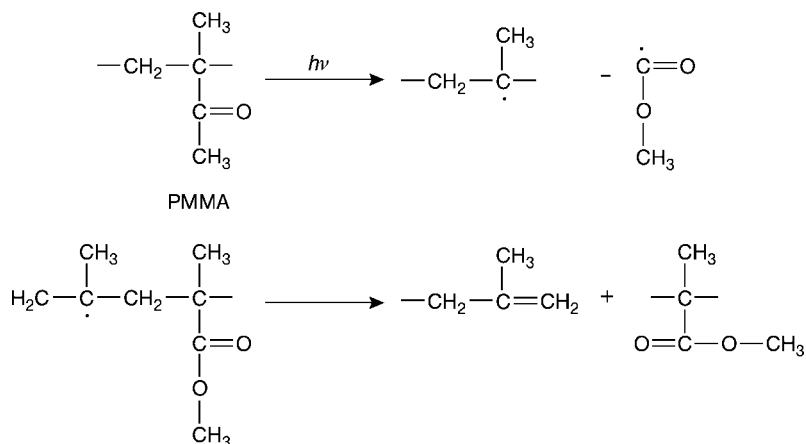


**Figure 1.10** (a) Schematic cross-sectional view of a nanolithographic template consisting of a uniform monolayer of PB spherical microdomains on silicon nitride. PB wets the air and substrate interfaces; (b) Schematic of the processing flow when an ozonated copolymer film is used, which

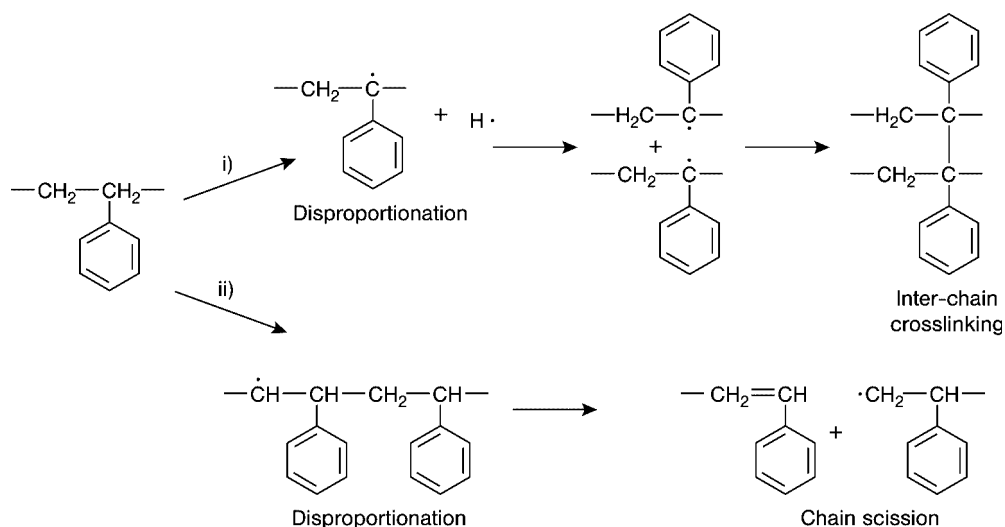
produces holes in silicon nitride; (c) Schematic of the processing flow when an osmium-stained copolymer film is used, which produces dots in silicon nitride. Reprinted with permission from Ref. [80]; © 1997, American Association for the Advancement of Science.

template; however, there must be a clear pathway in the film for the removal of degraded minority component (e.g., vertical cylinders). Otherwise, the low-molecular-weight products permeate through the matrix, leading to a decrease in  $T_g$  and collapse of the pores.

Stoykovich and colleagues in the Nealey group have substantially improved the directed self-assembly of lamellar microdomains of PS-*b*-PMMA. Traditional lithographic techniques were used to create a chemically nanopatterned surface that preferentially wets the PMMA domain. By using this preferential attraction,



Scheme 1.7 Chain scission mechanism of PMMA.

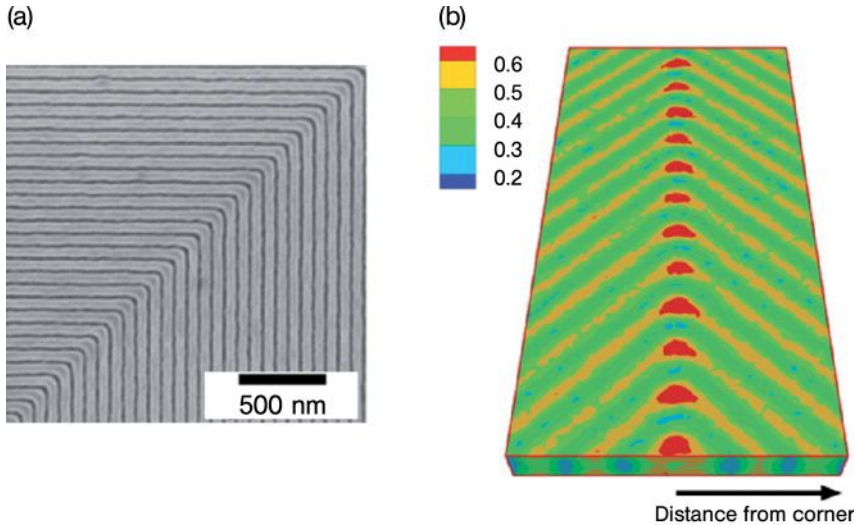


Scheme 1.8 Ultraviolet irradiation byproducts of polystyrene.

Stoykovich *et al.* were able to steer the vertically oriented lamellar morphologies through various bend angles, from 45° to 135° (Figure 1.11). The high curvature of these patterns induces a great deal of stress in the polymeric material, and leads to the formation of defects in the structure. It was found that, by blending small amounts of PMMA homopolymer, the homopolymer selectively swelled the PMMA block in the areas of high curvature (Figure 1.11b); this alleviated the stress in the material and in turn reduced the pattern defects [131].

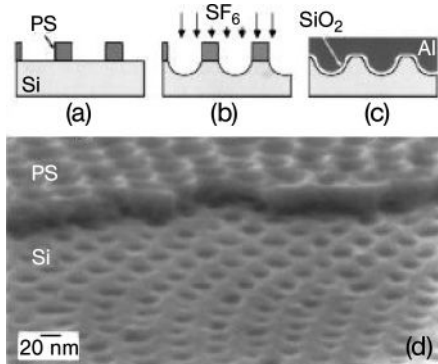
Several successful applications of PS-*b*-PMMA as a nanolithographic template have already been achieved, with C. T. Black and coworkers at IBM being among

the first to demonstrate the industrial feasibility of this technology. After optimization of the process window for maximum ordering of perpendicular-oriented nanodomains [132, 133], Black's group demonstrated the successful fabrication of metal-oxide-silicon (MOS) capacitors (Figure 1.12) [133–135], multinanowire



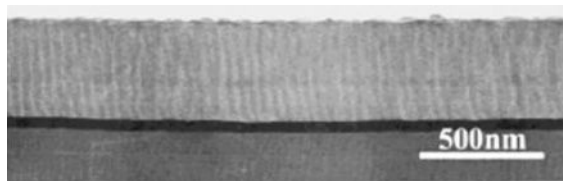
**Figure 1.11** (a) A top-down SEM image of angled lamellae in a ternary PS-*b*-PMMA/PS/PMMA blend. The chemical surface pattern is fabricated with a 70 nm line spacing to match the natural period of the copolymer; (b) Theoretical concentration map of the distribution of the homopolymers on the

surface. The homopolymers concentrate and swell the polymer at the bend area of the patterns to prevent the formation of defects. Reprinted with permission from Ref. [131]; © 2006, American Association for the Advancement of Science.



**Figure 1.12** The process flow for MOS capacitors. (a) Polymer template formation on silicon surface; (b) RIE pattern transfer of PS template into silicon, followed by removal of the PS matrix; (c) SiO<sub>2</sub> growth followed by top Al gate electrode deposition; (d) SEM image

at a 70° tilt after RIE etch. The remaining PS template is shown at the top. At the bottom, the nanoscale hexagonal array has been transferred into a Si counter electrode. Reprinted with permission from Ref. [134]; © 2006, American Institute of Physics.



**Figure 1.13** Cross-sectional transmission electron microscopy image obtained from a PS-*b*-PMMA film (800 nm) annealed in an electric field of  $25\text{ V}\mu\text{m}^{-1}$ . The block copolymer film is lying on top of a dark Au-film, which was used as the lower

electrode. The upper electrode has been removed. Cylinders oriented normal to the substrate pass all the way through the sample. Reprinted with permission from Ref. [90]; © 2006, Wiley-VCH.

silicon field effect transistors [136], and FLASH memory devices [137]. The creation of high-aspect ratio patterns has always been problematic due to the difficulty of achieving a single microdomain orientation in thick BCP films. In this area, Thurn-Albrecht and coworkers reported that the application of a strong electric field, in combination with thermal annealing, creates 500-nm-long, vertically oriented PMMA cylinders that physically connect to the substrate, as shown in Figure 1.13. After PMMA removal, the underlying conducting substrate was used for the subsequent deposition of copper into the holes to form a matrix of continuous nanowires [90].

Asakawa and coworkers from the Toshiba Corporation were the first to pattern magnetic media for hard disk applications, by using a PS-*b*-PMMA template. In these investigations, the group took advantage of the large difference in etch resistance between the aromatic and acrylic polymer to produce the BCP template using dry etching techniques [108, 109]. Spiral-shaped circumferential grooves were imprinted into a hard-baked photoresist using a nickel master plate. The spherical PMMA microdomains then aligned within the walls of the grooves, and the PMMA was preferentially etched by oxygen plasma to create holes which connected to an underlying magnetic cobalt platinum film. The size of these holes could be adjusted by changing the molecular weight of the PS-*b*-PMMA. The holes were then filled with etch-resistant spin-on-glass, which acted as a mask while the remaining PS polymer and the underlying magnetic media were patterned by ion milling. After removal of the spin-on glass, the disk featured magnetic nanodots arranged in a spiral pattern.

PS-*b*-PMMA has proved to be an excellent system to perform studies on the ability of BCPs to act as nanolithographic stencils, although doubts persist regarding its potential to enter into industrial, high-volume production. For example, as noted previously, crosslinking the matrix phase of the BCP is necessary to prevent pore collapse during the rough pattern transfer and etching step. PS, however, cannot be crosslinked (or patterned) efficiently upon exposure to UV light. A combination of different photochemical processes, such as random chain scission, oxidative coupling and crosslinking, all occur at the same time during UV expo-

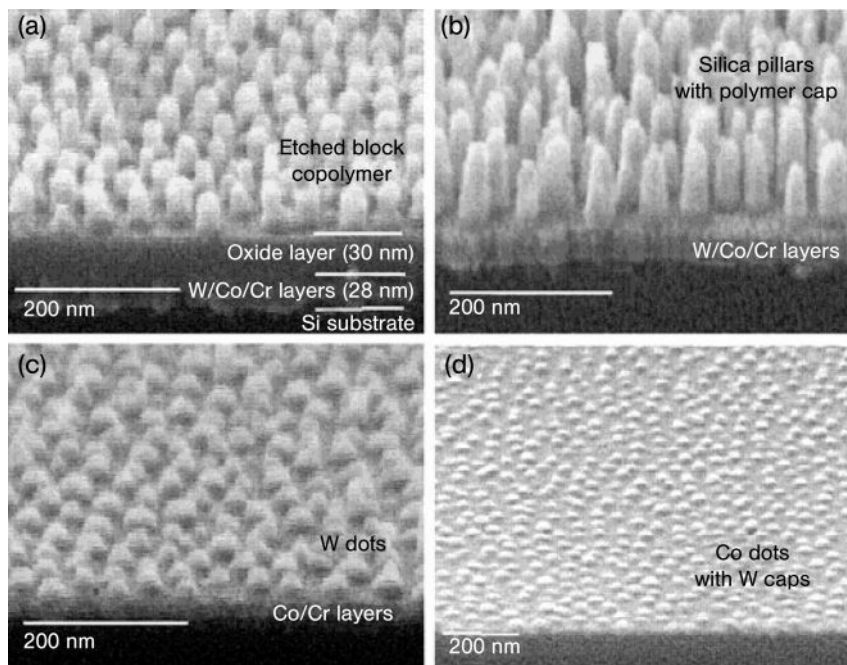


sure, as shown previously in Scheme 1.8. Several groups have taken steps to correct this problem, with Hawker and coworkers [103] having randomly copolymerized thermally crosslinkable benzocyclobutene (BCB) groups with polystyrene (PS-*ran*-BCB). The degree of crosslinking can be tuned by increasing the amount of the BCB in the random copolymer. Microdomain ordering was induced by thermally annealing the matrix at 160 °C. Raising the temperature to 220 °C caused the matrix to be crosslinked, and the PMMA was exposed and developed in the normal manner.

**Poly(Styrene-block-Lactic Acid)** Poly(styrene-*block*-lactic acid) (PS-*b*-PLA) is another copolymer that has been developed as a nanolithographic template. To synthesize this polymer, hydroxyl-terminated PS (prepared through anionic polymerization) was treated with triethylaluminum to form the corresponding aluminum alkoxide macroinitiator. This species was able to efficiently polymerize D,L-lactide through a ring-opening process [118]. The advantage of using this BCP as a nanolithographic template is that PLA undergoes main-chain cleavage simply by soaking it in an aqueous methanol mixture containing sodium hydroxide at 65 °C. The PS matrix is not affected at all by this treatment. Zalusky and coworkers have also published a complete phase diagram and characterization of PS-*b*-PLA [119]. Leiston-Balanger and coworkers used the benzocyclobutene crosslinking strategy explained in Section 1.2.2.1.2 but with PLA as the minority component, thus eliminating the photoprocessing step [138]. The group noted that, if a thermally degradable minority component were to be used, then a robust nanoporous template could be produced by using a completely thermal process.

**Poly(Styrene-block-Ferrocenyldimethylsilane)** BCPs containing organometallic elements can also function very well as nanolithographic etch masks, as shown by the studies of Thomas and coworkers [113, 114, 139]. Thomas' group was able to synthesize a BCP of poly(styrene-*block*-ferrocenyldimethylsilane) (PS-*b*-PFS) that organized into lamellar and cylindrical microdomains by using an anionic ring-opening polymerization. The PFS block contained elemental iron and silicon, which made it highly resistant to dry-etching processes due to the creation of iron and silicon oxides during oxygen etching. The resulting etching ratio between PS and PFS was estimated to be as high as 50:1. Thus, by etching through the polystyrene, the BCP patterns were transferred into the underlying substrate in only one step. By using this polymer as a masking layer, Thomas *et al.* further demonstrated that an array of cobalt single-domain magnetic particles could be created through a tri-level etching strategy (Figure 1.14). Moreover, the magnetic properties and thermal stability of the dots could be tuned simply by changing the copolymer composition and etch depth into the cobalt [123, 140].

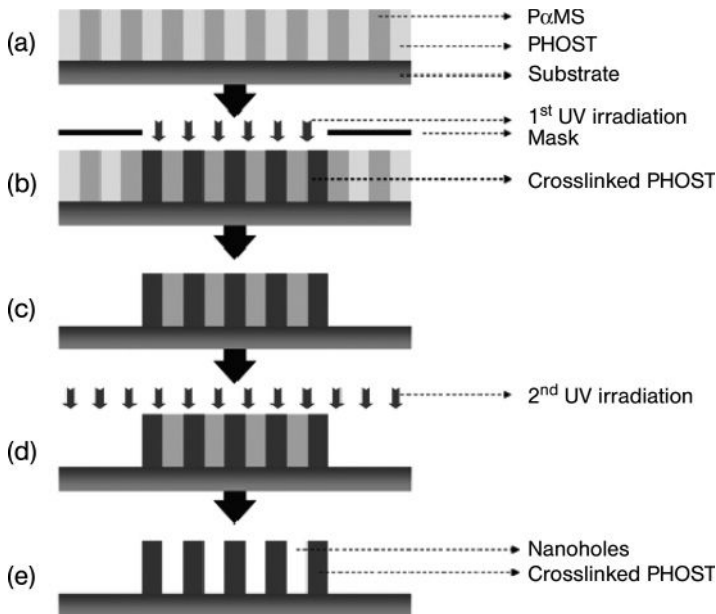
**Poly( $\alpha$ -Methylstyrene-*block*-Hydroxystyrene)** Studies conducted by the present authors' group have focused on poly( $\alpha$ -methylstyrene-*block*-hydroxystyrene) (P $\alpha$ -MS-*b*-HOST) that allows not only an efficient crosslinking of the hydroxystyrene matrix phase but also the ability to lithographically pattern the nanoporous tem-



**Figure 1.14** Tilted SEM images of the intermediate stages of lithographic processing. (a) An  $O_2$ -RIE-treated block copolymer thin film on a multilayer of silica, the metallic films, and the silicon substrate; (b) Pillars of silicon oxide capped with oxidized PFS after  $CHF_3$ -RIE; (c) Patterned

tungsten film using  $CF_4 + O_2$ -RIE on top of a cobalt layer after removing the silica and residual polymer cap; (d) W-capped cobalt dot array produced by ion beam etching (note the different magnification). Reprinted with permission from Ref. [123]; © 2006, Wiley-VCH.

plates on select areas of the wafer [116, 117]. In these studies, traditional chemical amplification strategies [141], which have been recognized among the photoresist community for over 20 years, were used in combination with BCP lithography. An overview of the processing scheme is presented in Figure 1.15. The key to chemical amplification strategies is the use of cationic catalysts known as photoacid generators (PAGs); these produce a strong acid when exposed to DUV radiation (248 and 193 nm). Triflic acid generated by the PAG molecule (triphenylsulfonium triflate) was used to catalyze a condensation reaction [142] between the hydroxyl groups of the poly(hydroxystyrene) and a crosslinking species tetramethoxymethyl glycoluril (TMMGU; Powderlink 1174) to produce, in turn, a highly crosslinked network of the matrix phase (Scheme 1.9). The areas of the wafer where nanoporous templates are not needed are washed away with a solvent development step. The crosslinked regions of PHOST contained standing, 20-nm-diameter cylinders of poly( $\alpha$ -methylstyrene), a polymer that can be depolymerized and removed from the matrix with additional UV irradiation, heat,



**Figure 1.15** Novel nanofabrication process of obtaining spatially controlled nanopores.

(a) Spin-coating of a  $P\alpha MS$ -b- $PHOST$ /PAG mixture onto a silicon wafer to form vertical cylinders of  $P\alpha MS$  in the  $PHOST$  matrix; (b) Irradiate using a 248 nm stepper with a photomask and bake; (c) Develop with a

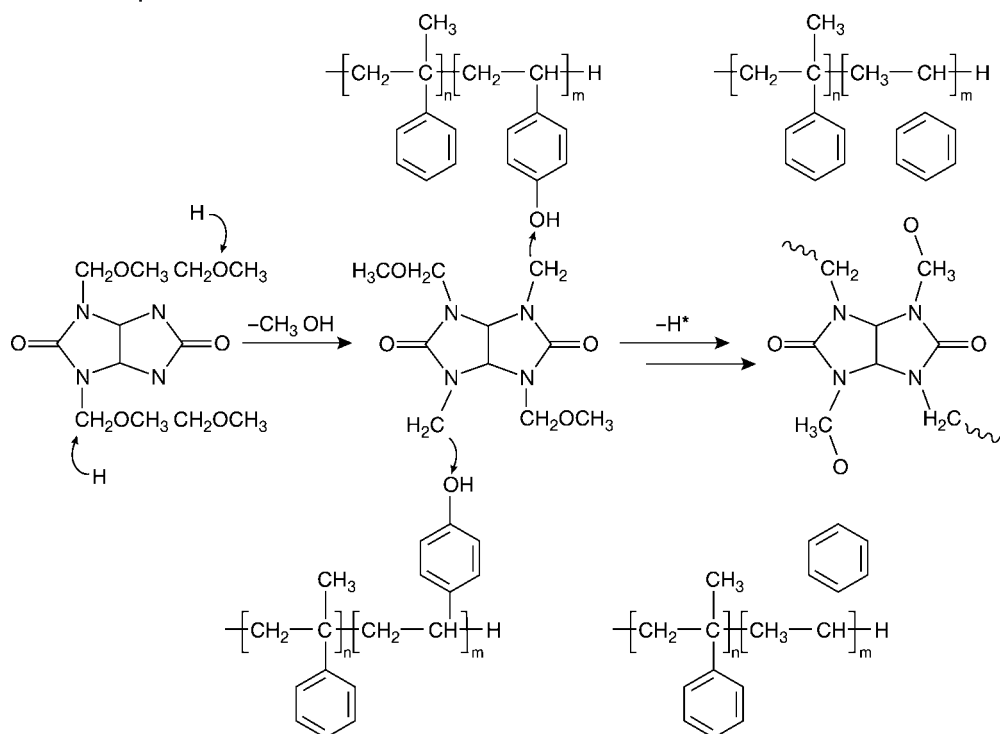
mixed solvent to form micron-sized patterns on top of the substrate; (d) Irradiate using a 365 nm lamp under vacuum; (e) Form patterns with nanoporous channels. Reprinted with permission from Ref. [117]; © 2006, American Chemical Society.

and high vacuum. Thus, by using standard lithography procedures, it was possible to generate 450 nm resolution patterns of crosslinked  $PHOST$  containing 20 nm nanoporous substructures, as shown in Figure 1.16. Further processing of this polymer in order to maximize the degree of long-range ordering is currently under way [143]. It is believed that this combination of traditional “top-down” positive- and negative-tone lithography techniques, in combination with the power of “bottom-up” BCP self-assembly, holds much promise for the future of lithography.

### 1.2.3

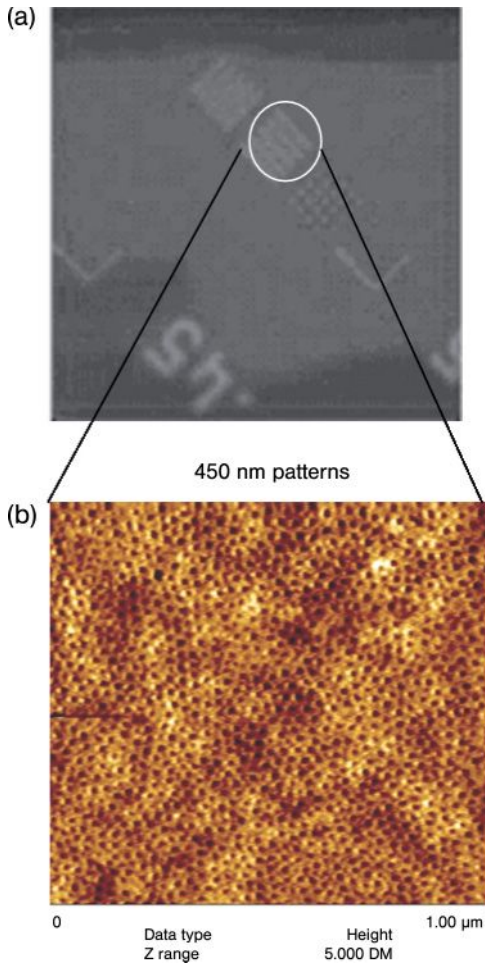
#### Multilevel Resist Strategies Using Block Copolymers

The constant drive for smaller and smaller circuit device features with higher aspect ratios and more complex substrate topographies has caused many photolithographic engineers to rethink traditional single-level resist-processing strategies. As sub-100 nm feature sizes become the norm, artifacts arising from the lithographic process that were recently deemed insignificant have now become



**Scheme 1.9** Proposed crosslinking mechanism of P $\alpha$ MS-*b*-PHOST with TMMGU. After Roschert, H., Dammel, R., Eckes, C. *et al.* (1992), *Proc. SPIE-Int. Soc. Opt. Eng.*, **1672**, 157.

major problems. One such artifact that limits resolution is the creation of the “standing wave effects” which occur when UV light reflects off the substrate surface after passing through the resist [73]. As a result, multilevel resist chemistries have been developed to incorporate polymeric planarizing layers to eliminate substrate topography variability and anti-reflection coatings to eliminate standing-wave patterns in photoresists. Commonly used multilevel strategies employ a photoresist imaging layer on top of the planarization layer. The resist used for the imaging layer is designed to provide high sensitivity to UV light exposure by providing a large number of photosensitive functional groups, and must be highly etch-resistant to the extremely harsh conditions imposed by the oxygen reactive ion-etching step. Organosilicon-containing polymers have been demonstrated to be excellent candidates as etch-resistant photoresists, due to their ability to form a protective SiO<sub>2</sub> ceramic upon exposure to oxygen plasma, as shown by Taylor and Wolf [144, 145]. The only disadvantage of these polymers is that their bulky side groups result in very low  $T_g$ -values, which make them susceptible to viscous flow and excess swelling during the development step. Photoresist engineers typically counter the problem of low  $T_g$  values by randomly copolymerizing the etch



**Figure 1.16** Atomic force microscopy height images showing: (a) the 450 nm photopattern produced through the crosslinking of the PHOST matrix; and (b) the 20 nm-diameter porous substructure generated after removal of the  $\alpha$ -methylstyrene block.

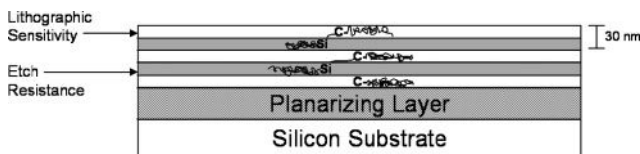
resistant, low- $T_g$  polymer with a photosensitive polymer that also has a high  $T_g$ . The copolymerization of the two monomers is necessary to avoid the inevitable macrophase separation that results when two homopolymers are mixed together. This composite style approach thereby simultaneously satisfies the requirements for high etch resistance, high sensitivity and high  $T_g$ , resulting in the best-performing photoresists.

BCPs seem to be a perfect fit for multilevel resist chemistries, due to their ability to segregate into chemically distinct levels and their intrinsic ability to avoid

macrophase separation. It is well known that a BCP film will self-assemble such that the lower surface energy block is presented at the polymer/air interface. This principle can in turn be used to design layered systems of different functionality, as will be seen in the creation of semi-fluorinated BCPs for low-surface energy applications (see Section 1.6.1). For example, to create the imaging layer a polymer containing photosensitive *tert*-butyl functional groups may be used along with an etch-resistant organosilicon polymer (Figure 1.17). Conveniently, the *tert*-butyl groups contain three low-energy methyl groups that drive the segregation of the photoactive compound to the surface, where it is most effectively exposed to UV light. The surface-segregating properties are not limited to the *tert*-butyl group, however; many other protecting groups could be used. Moreover, the functional, chemically distinct polymers used in photoresists will exist in a microphase-separated state if they are incorporated into a BCP. The microdomains form with diameters within one radius of gyration of the polymer chain, which usually is about 5–30 nm. Therefore, a patterned lithographic feature on the BCP photoresist, currently approximately 100–200 nm, will contain numerous domains of the photosensitive and etch-resistant functionalities incorporated within it to ensure optimal performance of the photoresist.

The microphase separation of BCPs also means that each one of the polymer chains is confined to its own respective domain, and can be thought of as being artificially crosslinked. Thus, in negative-tone resists, less UV light is required to cause the polymers to become insoluble compared to a homopolymer of a similar molecular weight. BCPs have also been shown to be twice as sensitive to nonphase-separated random copolymers using the same monomer units and molecular weight, due to this confinement effect [146]. Confinement might also mean that the PAG moieties used in these resists might be clustering selectively inside one of the microdomains, and this effect might be magnified if the PAG is miscible in only one of the BCP microdomains [147]. Moreover, if the usually hydrophilic photoacid segregates inside the block containing the acid-labile functional groups, the effective concentration of the acid will be increased, which means that a higher percentage of the protecting groups will be converted to base-soluble –OH groups.

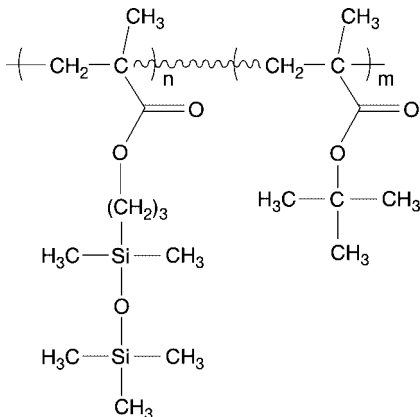
Hartney and coworkers [148] developed the first application for BCPs as bi-level e-beam resists in 1985, when they prepared a BCP of poly(chloromethylstyrene) for sensitivity and high  $T_g$ , and poly(dimethylsiloxane) (PDMS) that forms etch-resistant silicon oxide upon exposure to oxygen plasma and has a low  $T_g$ . Bowden *et al.* subsequently prepared a PDMS BCP grafted to PMMA that acted as a negative-tone resist [149, 150], while Jurek *et al.* created a novalac oligo-PDMS resist



**Figure 1.17** Multilevel resist strategy using block copolymers. Adapted from Ref. [148].

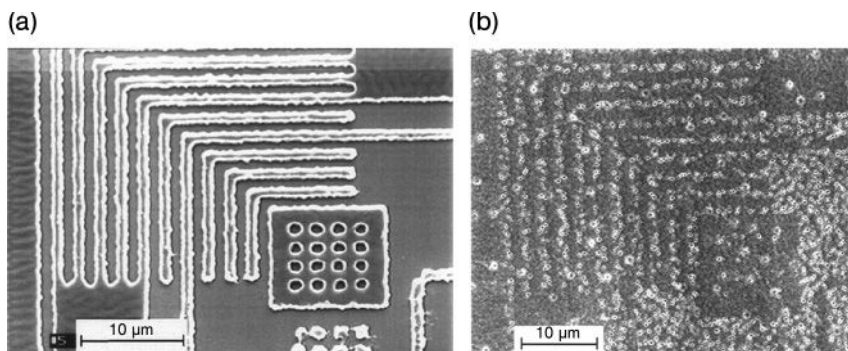
which showed resolutions of 500 nm and etch rates which were 36-fold slower than hard-baked novalac [151]. Gabor and coworkers attached a PDMS graft to the double bonds of an isoprene block in a styrene-*block*-isoprene BCP to create a negative-tone resist. In this way, Gabor *et al.* achieved line-space patterns of 200 nm using e-beam lithography, and demonstrated oxygen etching rates which were 42-fold slower than for polyimide [152]. Other resists which have incorporated PDMS for etch resistance in both block and graft copolymer architectures have also been reviewed [153].

Gabor and coworkers also prepared block and random copolymers of poly(*tert*-butyl methacrylate) and a silicon-containing methacrylate (poly(3-methacryloxy) propyl pentadimethyldisiloxane) (Figure 1.18) via group transfer polymerization for applications in 193 nm photolithography [154]. The BCP architecture allowed Gabor's group to incorporate a larger amount of the hydrophobic siloxane component for a high-oxygen RIE resistance, while maintaining solubility in an aqueous base developer. In fact, the BCPs were found to have a better development behavior in aqueous base than their random copolymer counterparts (Figure 1.19). Gabor *et al.* hypothesized that the exposed polymeric regions formed micelles in the aqueous base developer, with the silicon-containing block forming the core and the soluble methacrylic acid group forming the corona. In contrast, random copolymers would not have the ability to form these micellar structures; that is, the entire copolymer would need to be soluble in order for development to occur. However, the development behavior of these BCPs was far from perfect, presumably due to segregation of the PAG away from the surface of the film. Although their performance does not exceed commonly used industrial photoresists, the concept of using BCP architectures for multilevel photoresists is enticing, and there may be much more to learn from these types of systems.



**Figure 1.18** Block copolymer designed as a multilevel photoresist: *t*-butyl methacrylate (*t*-BMA)-*block*-3-methacryloxy-propylpentamethyldisiloxane (SiMA).





**Figure 1.19** (a) A block copolymer photoresist poly(*tert*-butyl methacrylate-*block*-[3-(methacryloxy)propyl]pentamethyldisiloxane) with 10.0wt% silicon, formulated with 5 wt% PAG. An exposure dose of  $2 \text{ mJ cm}^{-2}$  was used, and the resist was developed for 20s in a mixture of 27% 0.21 N tetramethylammonium hydroxide (TMAH) and 73% iso-propyl alcohol; (b) Random copolymer with 9.7wt% silicon, formulated

with 5 wt% PAG, after  $1.2 \mu\text{m}$  features are exposed to  $19 \text{ mJ cm}^{-2}$  and developed using the same conditions. While the random copolymer is insoluble, pinholes form during development and are thought to originate from phase-separated acid, which is removed by the developer. Reprinted with permission from Ref. [154]; © 2006, American Chemical Society.

### 1.3

#### Nanoporous Monoliths Using Block Copolymers

##### 1.3.1

##### Structure Direction Using Block Copolymer Scaffolds

Besides the potential uses of BCPs as lithographic materials, their inherent micro-phase separation and chemical dissimilarity of the blocks also leads to other applications. For example, BCPs can serve as structure-directing agents for the formation of mesoporous monolithic materials through phase-selective chemistry. Monolithic nanoporous structures have a large surface: volume ratio, which means that there is a large amount of functionalizable surface area within a small volume of material. In one of the pioneering efforts in this area, Hashimoto and coworkers created a bicontinuous morphology with poly(styrene-*block*-isoprene) and selectively removed the minority isoprene domain with ozonolysis [115]. The group showed that coating the bulk structure with nickel metal does not completely block the nanopores. Rather, metal catalysts such as nickel are known for their ability to adsorb and split  $\text{H}_2$  molecules for large-scale industrial reactions such as hydrogenation. The high surface: volume ratio of porous bicontinuous BCP morphologies make them excellent candidates for catalytic applications; indeed, one day they may even be used to make your margarine!

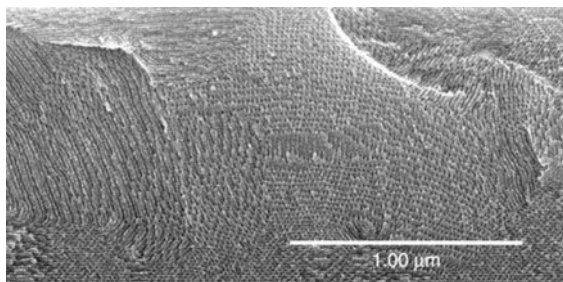
The BCPs used as structure-directing “scaffolds” to create mesoporous silicate structures could also be used as dielectric materials. Silicon dioxide ( $\text{SiO}_2$ ) is typically used as a dielectric material to reduce undesired capacitive coupling between neighboring elements of an integrated circuit, due to its low dielectric constant ( $k$ )



of approximately 4.5. Air, however, has one of the lowest dielectric constants ( $\sim 1$ ); hence, the dielectric constant of  $\text{SiO}_2$  can be dramatically decreased by filling it with voids, while maintaining good mechanical properties. So-called 'low- $k$ ' materials are highly desired by the semiconductor community because they allow faster switching speeds and lower heat dissipation in computer chipsets. Early studies conducted by Nakahama and coworkers led to the creation of monoliths of bicontinuous BCPs through a spin-coating process. This synthesis included a silyl-containing matrix block and an isoprene-based minority phase. Processing the film entailed hydrolytically crosslinking the silyl-containing block to prevent pore collapse, and ozonolysis to eliminate the isoprene minority domain [155]. Another group subsequently discovered a one-step, room-temperature UV irradiation/ozonolysis treatment to transform the matrix into a silicon oxycarbide ceramic and eliminate the polydiene minority phase. The silicon oxycarbide ceramic was stable at temperatures up to  $400^\circ\text{C}$ , and adjustment of the volume fraction of the BCP afforded an inverse bicontinuous phase to produce a nanorelief structure [14]. These mesoporous materials have also proved useful in the creation of photonic band gap materials [156], due to the possibility of tailoring the dielectric constant of the optical waveguides by sequestering optically active particles inside the matrix phase [157].

Watkins and coworkers have also demonstrated a novel technique to create mesoporous silicate structures by performing phase-selective chemistry inside one of the blocks [158]. In these studies, a tri-BCP of poly(ethylene oxide-*block*-propylene oxide-*block*-ethylene oxide) (PEO-*b*-PPO-*b*-PEO; also known as Pluronics<sup>®</sup>) was mixed with *p*-toluene sulfonic acid (pTSA) in an ethanol solution. Upon spin-casting the BCP onto a Si wafer, the BCP microphase separated into an ordered morphology containing spherical PPO microdomains. The pTSA catalyst segregated preferentially to the hydrophilic PEO matrix phase. The polymer was then placed in a chamber with humidified supercritical  $\text{CO}_2$ , so as to swell the polymer and allow the infiltration of a metal alkoxide, tetraethylorthosilicate (TEOS), into the polymer. The segregated acid in the hydrophilic domains then underwent a condensation reaction with the TEOS to form a silicon oxide network. Due to the phase selectivity of the acid segregation, no condensation reaction took place within the hydrophobic domains. The alcohol byproducts of the condensation reaction were quickly removed by the supercritical solvent, which rapidly pushed the condensation reaction to complete conversion. Finally, a calcination step in air at  $400^\circ\text{C}$  removed the organic block copolymer framework, leaving an inorganic silicon oxide replica of the original BCP (Figure 1.20). The process could also be carried out in standing cylindrical P( $\alpha$ MS-*b*-HOST) BCPs [159]. Eventually, the ability to pattern these monolithic silicate structures will lead to their use in future semiconductor fabrication paradigms.

Ulrich and coworkers reported the use of poly(isoprene-*block*-ethylene oxide) (PI-*b*-PEO) as a structure-directing agent for silica-type ceramic materials [160]. A mixture of prehydrolyzed (3-glycidyoxypropyl) trimethoxysilane (GLYMO) and aluminum *sec*-butoxide ( $\text{Al}(\text{O}i\text{Bu})_3$ ) was added to a solution of the PI-*b*-PEO and cast in a Petri dish. The  $\text{Al}(\text{O}i\text{Bu})_3$  triggered ring opening of the epoxy group that made the 3-glycidyoxypropyl ligand of the silane precursor compatible with the



**Figure 1.20** A scanning electron microscopy image showing the cross-section of a highly ordered mesoporous silicate film exhibiting a cylindrical morphology. The film was prepared by infusion and condensation of TEOS within a preorganized triblock PEO-*b*-PPO-*b*-PEO BCP film diluted with supercritical CO<sub>2</sub>. The

image reveals a preferential alignment of cylinders at the interfaces and grains of random orientation within the bulk of the film. Reprinted with permission from Ref. [158]; © 2006, American Association for the Advancement of Science.

PEO block [161]. Thus, addition of the inorganic material led to an increase in the volume fraction of the PEO block and the formation of multiple morphologies, depending on the concentration of the inorganic content in the solution. Spherical, cylindrical, lamellar and a novel type of bicontinuous morphology—called the “Plumber’s Nightmare” morphology [162]—was found and characterized using transmission electron microscopy (TEM). Surprisingly, this phase did not occur in the neat PI-*b*-PEO BCP, indicating a radical transformation of the phase space through the addition of the inorganic content, possibly through a dramatic increase in the incompatibility ( $\chi$  parameter) between the blocks. Additionally, calcination of the hybrid materials at 600 °C removed the organic phase and led to the creation of isolated nano-objects such as ceramic cylinders of the inorganic phases which ranged in size from 8.5 to 35 nm [160]. If combined with an organic ruthenium dye complex, these nano-objects could be used as fluorescent biomarkers in the field of nanobiotechnology [163].

### 1.3.2

#### Nanopore Size Tunability

Nanoporous BCP films can also be used as separation membranes or filtration devices [164, 165]. According to C.J. Hawker, “...the lateral density of pores in films prepared from block copolymers is nearly two times greater than that of aluminum oxide membranes and an order of magnitude greater than that of track-etched membranes” [82]. This increase in porosity corresponds to an ability to handle a higher flux of liquid, and thus a higher throughput filter. Furthermore, size-specific separation is possible because the nanopore size will be constant if a polymer with a low polydispersity is used. There is, however, a thermodynamic limit to how small the nanopores can be, this lower bound being based on the

position of the order–disorder transition on the phase diagram relative to  $\chi N$  (refer back to Figure 1.2). Since small molecular weights are desired for smaller microdomains, a highly immiscible pair of polymers (corresponding to a greater  $\chi$  value) is required to decrease their size. If  $\chi N$  falls below this lower bound, the copolymer will mix to form a single phase [166]. To date, structures below 12 nm have been difficult to achieve [167], although in order to tune the size of the nanopores to smaller dimensions, numerous processing methodologies have been developed.

Jeong and coworkers developed a method to alter nanopore size in PS-*b*-PMMA nanoporous films [168]. Their technique allowed the formation of two discrete sizes of nanopores, depending on the processing strategy used. A 10% blend of low-molecular-weight PMMA homopolymer into a PS-*b*-PMMA BCP resulted in the solubilization of the homopolymer into the center of the PMMA block. As the PMMA homopolymer was of a lower molecular weight than the PMMA block, it dissolved first when the film was washed with acetic acid (which is a selective solvent for PMMA). This led to the production of nanopores which were 6 nm in size, as determined by atomic force microscopy (AFM) measurements. DUV radiation, in combination with an acetic acid wash, allowed the removal of both the PMMA homopolymer and the PMMA block in the BCP matrix, which resulted in 22 nm-sized nanopores. Thus, two different size scales of nanoporous structures—6 nm and 22 nm—were created using different processing schemes. Jeong *et al.* noted that the size of the smaller length-scale nanopores could be decreased if homopolymers of smaller molecular weights were used to infiltrate the PMMA block.

In an interesting approach to the preparation of nanoporous films, Ikkala and coworkers have incorporated alkylphenols, such as pentadecylphenol (PDP), into poly(styrene-*block*-4-vinylpyridine) (PS-*b*-P4VP) to create comb–coil supramolecular structures. Here, the phenol group of the PDP forms a strong hydrogen bond with the nitrogen donor on the pyridine group of the P4VP. The hydrogen bonding introduces an additional repulsive interaction that leads to the formation of “comb-like” layered structures of the PDP side chains inside the cylindrical P4VP microdomains. By using this approach, Ikkala *et al.* witnessed hierarchical structure formations such as lamellar-within-lamellar, lamellar-within cylinders, and lamellar-within-sphere morphologies [169, 170]. This was similar to the effects seen in liquid crystalline BCPs, except that the PDP side chains could easily be dissolved in methanol to create porous membranes [171].

The tunability of nanoporous monolithic structures has also been reported through the selective infusion of supercritical CO<sub>2</sub> inside the fluorinated block of poly(styrene-*block*-perfluoro-octylethyl methacrylate) (PS-*b*-PFOMA) [125, 126]. Supercritical CO<sub>2</sub> has been shown to have a high affinity for fluorinated polymers [172]. After selective swelling of the CO<sub>2</sub> inside the PFOMA domain, quenching at 0°C to lock in the PS matrix, and controlled depressurization at 0.5 MPa min<sup>-1</sup>, nanocell formation was noted in the BCP film. It was also found that the nanocell diameter could be tuned from 10–30 nm by adjusting the saturation pressure of the CO<sub>2</sub> solvent, with low saturation pressures corresponding to small cell

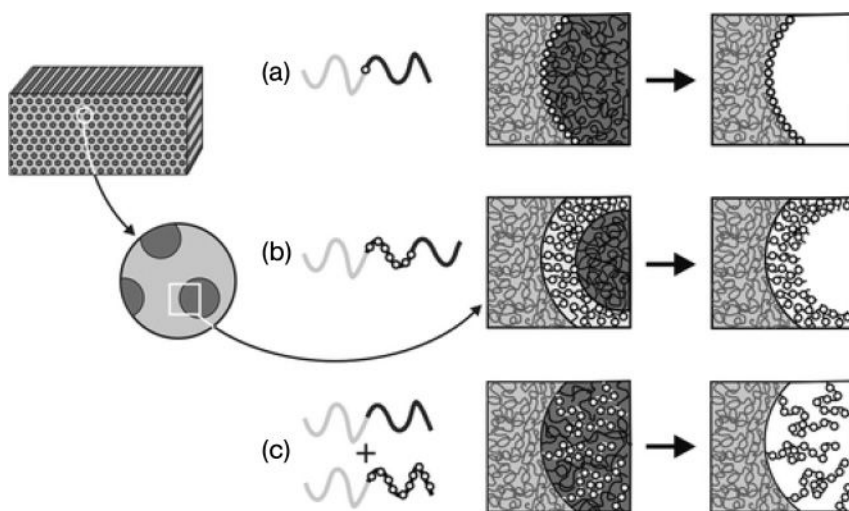
diameters, and *vice versa*. All of these approaches represent innovative means of decreasing the size scale of nanopores beyond that of the neat BCP.

### 1.3.3

#### Functionalized Nanoporous Surfaces

In nanoporous material, it may be very useful to control the chemical functionality of the nanopore wall for applications that require aqueous environments, such as microfluidic devices, water filtration, biocatalysis, or other chemical reactions that take place within the pore. In microfluidic devices, for example, compatibility between the substrate (pore wall) and the filler fluid (analyte) that passes through the nanoporous channels is necessary. Hydrophilic moieties such as hydroxyl groups attached to the pore wall will permit conduction of the aqueous solution through the membrane, as opposed to hydrophobic substrates that would hinder the flow of solution through the pores.

Several strategies are available for functionalization of the pore wall, three of which are shown in Figure 1.21. The first strategy (Figure 1.21a) is to introduce a functional group “spacer” between the covalent junction of the matrix and



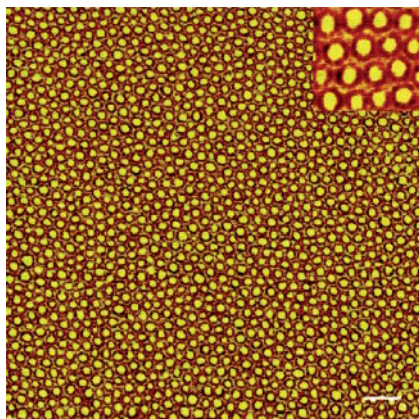
**Figure 1.21** Possible routes to nanoporous materials with controlled pore-wall functionality. (a) A functional group is incorporated into the junction between the matrix and sacrificial blocks, and is exposed upon template degradation; (b) A functionalized mid-block is inserted between the matrix and sacrificial end block, producing a functional polymer brush along the pore wall upon removal of the template; (c) An AB/AC

diblock copolymer blend is formed in which the common A block serves as the matrix, the B and C blocks are miscible, and only one of the two blocks is susceptible to degradative removal. In this manner, a functionalized nondegradable block can be introduced as a diffuse brush along the pore interior. Reproduced with permission from Ref. [176]; © 2006, Royal Society of Chemistry.

sacrificial blocks. This telechelic functionality can easily be introduced to the end of the living polymer chain during BCP synthesis, following addition of the first monomer and before addition of the second monomer. When the sacrificial block is removed through standard degradation procedures, the functional spacer will then line the pore wall. This approach has been demonstrated recently by Zalusky and coworkers [118, 119], Wolf and Hillmyer [120], and Hawker and coworkers [138]. Each of these groups made use of the hydroxyl-terminated poly(styrene) or poly(cyclohexylethylene) remaining when the PLA block had been removed. Degradation of the PLA left behind hydroxyl groups at the pore surfaces after removal, as proven by the reaction with trifluoroacetic anhydride and subsequent nuclear magnetic resonance (NMR) and infrared (IR) spectroscopic analyses. The only disadvantage to this relatively simple approach is the low density of functional groups that results, since only one  $-OH$  group exists per polymer chain. Zalusky *et al.* calculated the areal density of the hydroxyl groups to be approximately one  $-OH$  per  $4 \text{ nm}^2$  for a sample with 22 nm-diameter pores [118].

Clearly, the solution to the low density of the functional groups would be to increase their number by polymerizing the functional unit, as shown in Figure 1.21b. In other words, a tri-BCP could be synthesized in which a functional center block (B) existed between the matrix (A) and the sacrificial (C) block. The success of this strategy, of course, would depend on the morphology of the tri-BCP, which can be difficult to predict. The ideal morphology, in this case, would be a hexagonally packed core-shell cylindrical morphology, with the functional block forming a shell around the sacrificial core, surrounded by a crosslinkable matrix. The first attempt at the formation of this morphology was demonstrated by Liu *et al.* with PI-*b*-PCEMA-*b*-PtBA (CEMA = cinnamoyloxyethyl methacrylate, *t*BA = *tert*-butyl acrylate) [173]. The *tert*-butyl group was removed by hydrolysis to form gas-permeable poly(acrylic acid) nanochannels. The research results of Liu and colleagues will be presented in greater detail in Section 1.4.

Recent investigations conducted by the group of Hillmyer have demonstrated great success in functionalizing nanoporous monoliths. A poly(styrene-*block*-polydimethylacrylamide-*block*-polylactide (PS-*b*-PDMA-*b*-PLA) tri-BCP was synthesized by a combination of controlled ring-opening and free-radical polymerization techniques [174]. Aqueous base removal of the PLA minority phase and hydrolysis of the PDMA domain left carboxylic acid groups coating the pore wall, and these were used to chemically attach allylamine through carbodiimide coupling chemistry.  $^1\text{H}$  NMR spectra of the dissolved polymer film verified a successful attachment of the *N*-allylamide group, and proved that the pore wall surface was chemically active. The same group was also successful in binding other functional groups such as a pyridine, a chiral hydroxyl, and an alkene in high yields. Other studies with PS-*b*-PI-*b*-PLA triblocks [175] by the Hillmyer group have produced an isoprene shell coating the pore wall following removal of the PLA phase by treatment with NaOH solution. These studies led to the production of a beautiful AFM image of a core-shell morphology (Figure 1.22) which was due to the differing mechanical contrasts between the PS matrix and PI shell. A tri-BCP containing



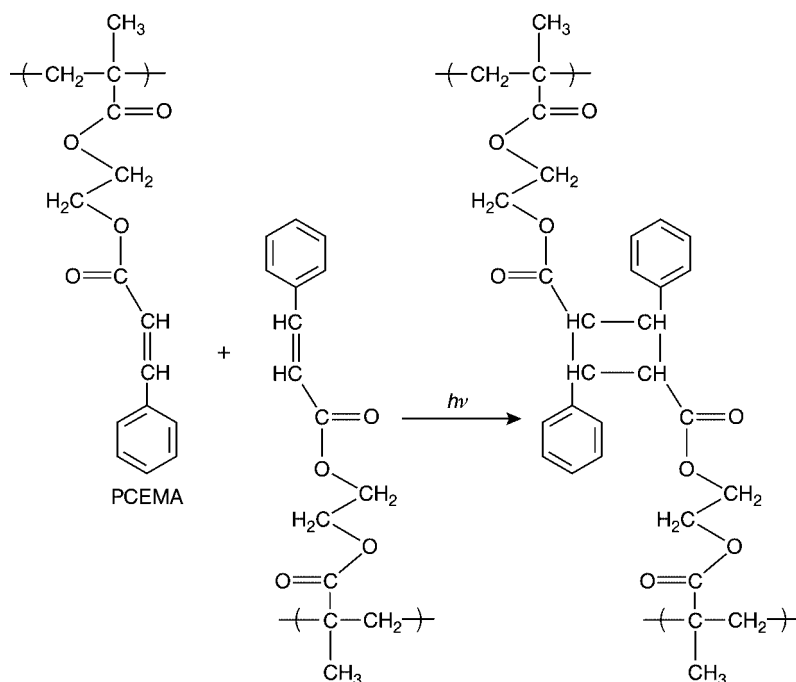
**Figure 1.22** Tapping mode AFM phase image acquired from a PS-*b*-PI-*b*-PLA thin film. The scale bar at the lower right is 200 nm. The inset at upper right is 250 × 250 nm. Reprinted with permission from Ref. [175]; © 2006, American Chemical Society.

two selectively etchable blocks, such as PI and PLA, opens up the possibility of forming hollow “nanoring” donut-shaped structures through removal of the matrix and core-forming phases. The creation of coaxial nanowires would then be conceivable through the sequential electrodeposition of metals.

The third approach to add functionality to nanoporous BCP films, as shown in Figure 1.21c, is through the blending of two diblock copolymers. This idea is based on the use of two BCPs (AB and AC), in which the A blocks mix to form the matrix phase, and the B and C blocks must be selected to be miscible with one another to form a single cylindrical domain. If either one of the B or C blocks is degradable, it is possible to form nanopore walls coated with the nondegradable block. For example, if B is degraded by UV light, C will still be attached to its parent A molecules and will form a brush extending out towards the center of the nanopore containing the end-group functionality. This approach was championed in a recent investigation by Mao and coworkers, who blended a parent PS-*b*-PLA BCP with PS-*b*-PEO to form the blended PLA/PEO microdomains in a PS matrix [176]. The PLA was degraded through hydrolysis in an aqueous methanol/NaOH solution, leaving a PEO polymer brush (containing a hydroxyl end group) which extended into the nanopore. As a test to prove the success of their strategy, Mao *et al.* floated blended (PS-*b*-PEO/PS-*b*-PLA) and nonblended (PS-*b*-PLA) films on a water surface. The blended film proceeded to sink, which meant that the pores within the film had imbibed water. In contrast, the nonblended PS-*b*-PLA BCPs floated on the water surface for an indefinite period. Chemical functionalization strategies such as these will become increasingly important as the field of BCPs moves away from fundamental science and into the realm of practical applications.

## 1.4 Photo-Crosslinkable Nano-Objects

The design and fabrication of nanometer-sized structures with well-defined size and shape has recently aroused much interest, much of which has stemmed from the need for smaller electronic devices that are not possible to produce using conventional lithographic techniques. Indeed, small nano-objects could also be useful as biosensors capable of molecular recognition. A number of groups have emerged as front-runners in this field, with their use of photoactive BCP domains to fix unique microphase-separated structures. The Liu research group, for example, has been very prolific in this area, with the majority of their investigations lying in a variety of applications stemming from the unique photo-crosslinkable polymer, poly(2-cinnamoyloxyethyl methacrylate) (PCEMA). Through a dimerization process involving a [2 + 2] cycloaddition of two double bonds in neighboring chains (see Scheme 1.10), the PCEMA becomes photochemically crosslinked. An amphiphilic BCP containing PCEMA will form micelles when placed in a solvent that dissolves only one of the blocks. The shape and size of the micelles can then be changed by altering the relative chain lengths of the soluble and insoluble blocks, to produce spherical [177], cylindrical

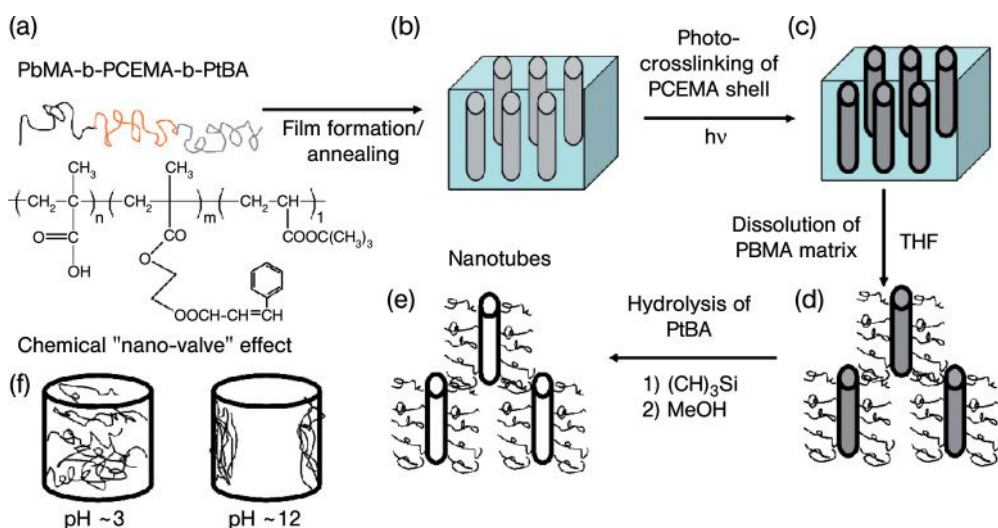


**Scheme 1.10** Photocyclodimerization (photocyclo (2+2) addition) of poly(2-cinnamoyloxyethyl methacrylate) (PCEMA).



[178, 179], vesicular [180], or donut-shaped [181] structures. These structures can then be fixed with UV light through the dimerization process to form permanent “nano-objects” that are stable in a wide variety of solvents. In an assortment of creative syntheses using this polymer, Liu’s group has developed a wide range of structures, including nanotubes [182], porous [183], “shaved” and “hairy” nanospheres [184–187], nanospheres with crosslinked shells [188], crosslinked polymer brushes [189], nanofibers [184, 190–192], and nanochannels in polymer thin films [193, 194].

As an example of the power of their photocrosslinking strategy, nanotubes with hydrophilic nanochannels have been formed using the tri-BCP *PbMA-b-PCEMA-b-PtBA* (*PbMA* = poly(butyl methacrylate); see Figure 1.23) [195]. Bulk films (~0.2 mm thick) were produced by slow evaporation of the polymer in toluene. After an annealing step, the *PtBA* formed the hexagonally packed cylindrical core, surrounded by a shell of *PCEMA* in a *PbMA* matrix. The *PCEMA* is first photocrosslinked, after which the *PtBA* cylinders are hydrolyzed in methanol to yield nanochannels filled with poly(acrylic acid) (PAA) brushes. Subsequent dissolution of the *PbMA* matrix in tetrahydrofuran (THF) led to the production of free-floating, functionalized nanotubes. These rod-like nanotubes were also shown to exhibit LC properties in solution [196].



**Figure 1.23** (a) A triblock copolymer of *PbMA-b-PHEMA-TMS-b-PtBA* was synthesized via anionic polymerization, deprotected, and then reacted with cinnamoyl chloride to form *PbMA-b-PCEMA-b-PtBA*; (b) Self-assembly of cylindrical morphologies developed upon spin-coating; (c) The *PCEMA* shells were crosslinked through a [2+2] cycloaddition upon exposure to UV light;

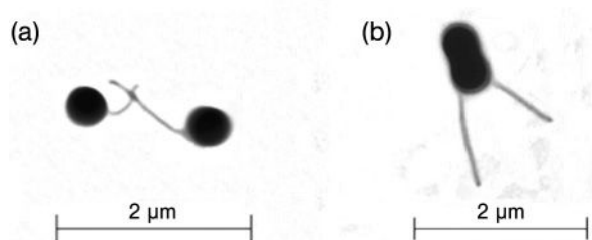
(d) The *PbMA* matrix was dissolved in THF to free the cylinders; (e) The *PtBA* was hydrolyzed to form PAA-functionalized nanotubes; (f) Schematic of the chemical “nanovalve” effect. At low pH, low water permeability was found, whereas at high pH an increased permeability was found. Adapted from Ref. [195].



These studies also had ties to the creation of functionalized nanopores (see Section 1.3.3). In what was termed a “chemical valve effect,” the permeability of the channels within the nanotubes could be tuned due to the swelling effect of the PAA brushes in water at different pH values. At low pH, the PAA chains formed a gel due to hydrogen bonding between the AA units, and prevented the flow of water through the pores. At high pH, the AA groups were converted to sodium acrylate, which did not form hydrogen bonds, and the ionized carboxyl groups were readily solvated by water. This allowed a high permeability of water through the tubes.

An obvious application for these type of functionalized material would be as a pH-sensitive membrane for filtration devices [70], although the hydrophilic PAA nanochannels may also act as hosts for the growth of inorganic nanoparticles. To demonstrate such capabilities, the authors were able to grow inorganic particles of CdS, an interesting semiconductor material, and a magnetic material,  $\text{Fe}_2\text{O}_3$ , by adding the appropriate metal salts and a reducing agent (see Section 1.5) [197, 198]. The  $\text{Fe}_2\text{O}_3$  metal-impregnated nanofibers were found to be super-paramagnetic; that is, they were attracted to each other when a magnetic field was applied, but demagnetized when the field was turned off [199].

Taking their technology one step further, Liu’s group has been successful in physically connecting the floating nanotubes to other structures, such as nanospheres. Here, a thick PS-*b*-PCEMA-*b*-P*t*BA film formed P*t*BA hexagonal cylindrical cores surrounded by a PCEMA shell and a PS matrix. After crosslinking the PCEMA, the PS was dissolved in THF to break the film up into nanotubes. Subsequent ultrasonication caused a shortening of the nanotubes and exposed the P*t*BA core chains at the ends, which were then hydrolyzed using trifluoroacetic acid to form PAA. The AA ends of the nanotubes were then grafted to polymeric spacers containing multiple amine groups on both ends. These amine-functionalized nanotubes were coupled with PCEMA-*b*-PAA nanospheres bearing surface carboxyl groups [183] through an amidation reaction, the result being the formation of “ball and chain” structures (see Figure 1.24) [182]. When a nanosphere



**Figure 1.24** Transmission electron microscopy images of nanotube and nanosphere coupling products. (a) Singular nanotubes connected to nanospheres; (b) Two nanotubes connected to a nanosphere. Reprinted with permission from Ref. [182]; © 2006, American Chemical Society.

became attached to two nanotubes (see Figure 1.24b), Liu suggested that if the nanotubes were loaded with super-paramagnetic  $\text{Fe}_2\text{O}_3$  particles they might act as “fingers,” with an opening and closing motion induced by a magnetic field. In this way they could form the chemical basis of a magnetic “nano-hand!”

## 1.5 Block Copolymers as Nanoreactors

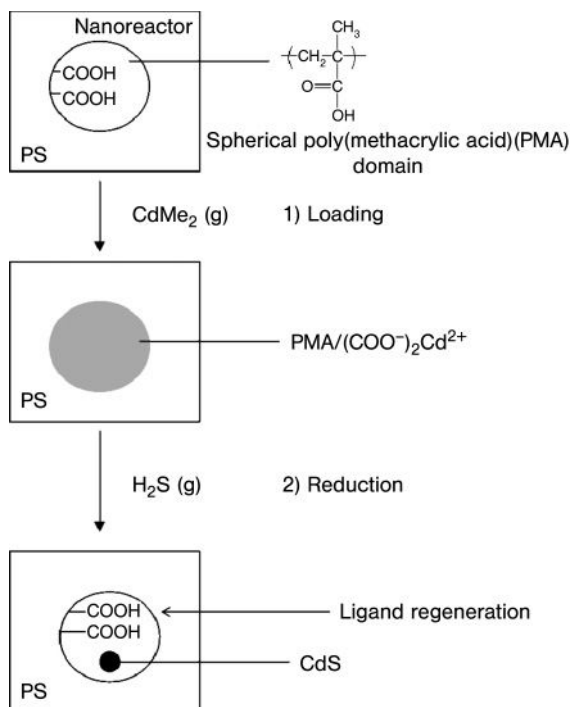
The directed self-assembly of inorganic nanoparticles into BCP templates can result in structures with interesting and useful electronic, optical, and magnetic properties. We have already seen the long-range ordering possible with BCP thin films. Yet, rather than selectively removing one of the blocks, it is also possible to use the ordered BCP pattern as a template for chemical reactions within one phase, leading to patterned clusters of functional nanoscale functional materials over large areas. Various types of functional nanostructures that could, in theory, result from these approaches include metal catalyst particles for fuel cell applications, ferromagnetic particles for high-density storage media [200], doped semiconductor clusters [201], QD structures [202, 203], and core-shell structures [204].

There are two approaches towards the use of BCPs as nanoreactors [205]. The first, most common approach uses an “*in situ*” production of metal nanoclusters inside BCP nanodomains [206]. Figure 1.25 shows a schematic of a cylindrical BCP that contains a functional group “receptor” which is located within the minority phase and is capable of selectively binding positively charged organometallic salts. Once the metal ions have been loaded, a subsequent reduction step can convert the metal ions into oxide, chalcogenide or zerovalent metal clusters, thus regenerating the receptor moiety [205]. The BCP can then accommodate repeated loading/reaction cycles [207] with the same or different metal salt.

In the second approach, the inorganic element is incorporated into an organometallic monomer, which can then be synthesized directly into the parent BCP. The previously mentioned PS-*b*-PFS (see Section 1.2.2.1.4) is an example of this type of polymer. This approach has been reviewed by Cummins *et al.* [208]. These BCPs self-assemble normally to leave an array of “pre-loaded” nanoreactors, ready and waiting for further chemical processing to form the inorganic clusters. This approach eliminates the metal salt loading step, which can take up to two weeks for bulk films, and may lead to nonselective sequestering of the reagents. However, the synthesis of new organometallic monomers for every application also presents huge challenges for the chemist.

### 1.5.1 Polymer–Metal Solubility

The solubility of inorganic compounds inside an organic matrix is made possible by careful adjustment of the polymer–metal bonding energy. Pearson’s Hard–Soft, Acid–Base (HSAB) principle effectively describes the bonding behavior [28]. The



**Figure 1.25** A typical scheme for the use of a block copolymer as a template for the selective growth of nanoparticles. Adapted from Ref. [205].

HSAB theory states that only chemicals of similar “hardness” will bond to each other; that is, soft acids will only bind to soft bases, and hard acids will only bind to hard bases. This hardness value is proportional to the difference between the materials’ highest occupied molecular orbital (HOMO) energy and the lowest unoccupied molecular orbital (LUMO) energy, which also relates to the band gap of the material. Metals are conductors and have smaller band gaps, and so are classified as chemically “soft.” Conversely, polymers are insulators with large band gaps and are classified as chemically “hard.” Therefore, hard polymers cannot bind to soft metals unless functional groups are attached to the polymer that change the bonding energy and make it chemically softer. In block copolymers, poly(vinylpyridine) (PVP), containing the electron pair-donating nitrogen species, is most commonly used to effectively solubilize metal salts. The typical design for the loading step is to choose a weakly coordinated metal salt, such as  $\text{Pd}(\text{OAc})_2$ , in which the transition metal acts as the soft acid bonded to a hard acetate base. According to the HSAB principle, this hard–soft bond is highly unstable, such that when the soft metal (Pd) encounters the functionalized soft polymer (PVP), a more stable soft–soft bond is created so as to encapsulate the metal within the block.

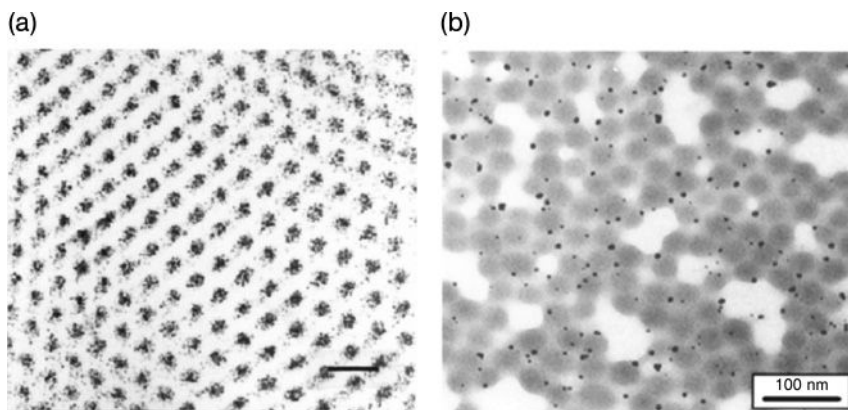
## 1.5.2

**Cluster Nucleation and Growth**

After block-selective loading of the metal salt, the next step is to reduce the salt to create the nanoparticles within each domain. Different applications may require different nanoparticle sizes and different numbers of clusters within each domain, as shown in Figure 1.26. For example, investigators in the field of electro-optics may only be interested in one nanoparticle per microdomain, whereas those in the field of catalysis might aim for a large number of nanoparticles to present a higher degree of functional surface area for subsequent chemical reactions. Formation of the nanoparticles proceeds through a nucleation and growth process. In typical nucleation and growth schemes, if the colloidal species has enough free energy to aggregate to sizes above a certain critical radius,  $R_c$ , then the particle will continue to grow; if not, the particle becomes unstable and falls apart to minimize the surface free energy. The critical radius is proportional to the interfacial tension of the polymer/particle interface ( $\gamma$ ) and the degree of supersaturation ( $c/c_0$ ), as shown in Equation 1.2 [28]:

$$R_c \propto \frac{\gamma}{\ln(c/c_0)} \quad (1.2)$$

Thus, one way to adjust the size and number of the particles is by adjustment of the degree of supersaturation of the reducing agent, which depends on the rate of chemical reaction of the reduction step [209]. Fast chemical reactions with strong



**Figure 1.26** (a) Transmission electron microscopy (TEM) image showing multiple gold nanoclusters in each domain. Scale bar = 500 Angstroms. Reprinted with permission from Chan, Y., Ng Cheong, Schrock, R.R. and Cohen, R.E. (1992) *Chem.*

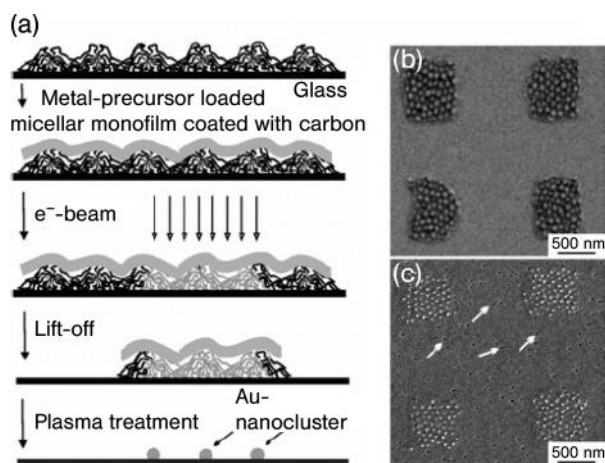
*Mater.*, **4**, 885–894; (b) TEM image showing single nanoparticles in each domain. Reprinted with permission from Klingelhofer, S., Heitz, A., Greiner, S. *et al.* (1997) *J. Am. Chem. Soc.*, **119**, 10116; © 2006, American Chemical Society.

reducing agents such as lithium aluminum hydride ( $\text{LiAlH}_4$ ) lead to high supersaturations, which in turn will mean a low critical radius for nucleation and a higher probability for particle nucleation within the microdomain. This would result in a large number of particles per domain, as shown in Figure 1.26a. In the reverse case, the use of weak reducing agents such as alkylsilanes would result in low supersaturation values. This will increase the critical radius for nucleation and decrease the probability that a nucleating event will occur, resulting usually in only one particle per microdomain, as shown in Figure 1.26b. Another way to control the critical radius is by changing the interfacial tension ( $\gamma$ ) between the particle and the polymer, which can be achieved through the selection of different metal-binding blocks.

### 1.5.3

#### Block Copolymer Micelle Nanolithography

Building on the nanoreactor approach, nanoscale devices will require the precise placement of functional materials in one- or two-dimensional arrays on semiconductor interfaces. Increased levels of control over the exact location of these inorganic nanoparticles can come from a top-down approach using UV light or e-beam lithography, as shown from a series of reports from Spatz and coworkers. Their approach, which is known as “block copolymer micelle nanolithography” [210], is shown schematically in Figure 1.27a. As an example of their strategy, poly(styrene-*block*-2-vinylpyridine) (PS-*b*-P2VP) is dissolved in a selective solvent for PS to form



**Figure 1.27** Application of monomicellar films as a negative e-beam resist on glass coverslips. (a) Schematic representation; (b) Monomicellar layers after lift-off; (c) Au-nanodots of 7 nm diameter after hydrogen plasma treatment. The white arrows point to holes which are characteristic for glass coverslips. Reprinted with permission from Glass, R., Moeller, M and Spatz, J.P. (2003) *Nanotechnology*, **14**, 1153–1160; © 2006, Institute of Physics.

micelles with P2VP cores and PS coronas. The diameter of these micelles is controlled by the molecular weight of the minority block and the interaction between the polymer blocks and the solvent. The micelles are then loaded with a metal salt of tetrachloroauric acid ( $\text{HAuCl}_4$ ), which complexes with the P2VP core. The loaded micelles are deposited as a monolayer film onto a silicon wafer. The film then is exposed to a focused electron beam that oxidizes the polymer, creating carboxylic acids, ketones, aldehydes, and ethers on the polymer surface. These reactive groups bind to the silanol groups on the Si wafer, fixing the exposed area to the substrate, while the unexposed areas are washed away in a sonicating bath. Hydrogen plasma is then used to remove the underlying polymer layer and reduce the  $\text{HAuCl}_4$ , leaving gold dots in the same shape as the previous electron beam pattern (see Figure 1.27b). It was found that the size of the gold nanoparticles could be tuned by adjusting the concentration of metal salt in the BCP solution. These gold clusters are highly mechanically stable structures, and are being pursued for applications in immobilizing single proteins for biosensor applications, or as coatings for lenses [211].

## 1.6

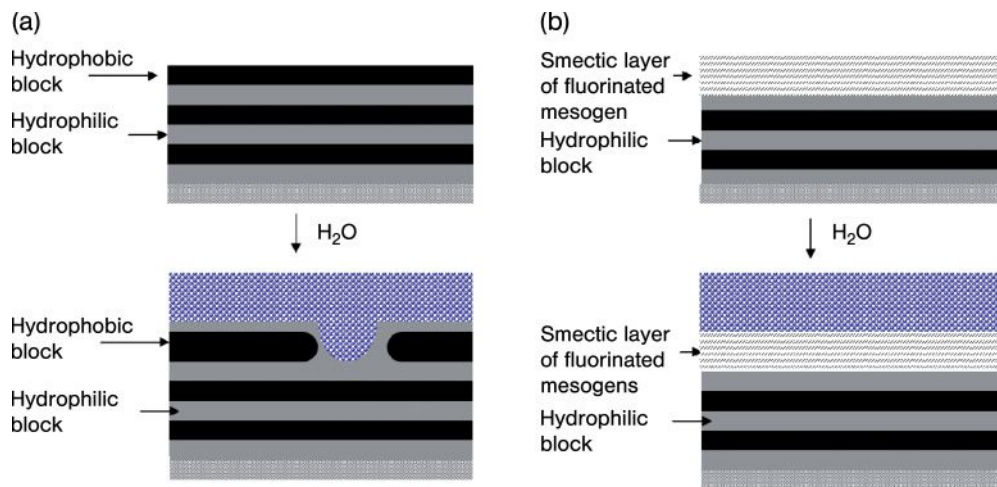
### Interface-Active Block Copolymers

#### 1.6.1

##### Low-Energy Surfaces Using Fluorinated Block Copolymers

Molecular-level control over the surface properties of polymer films has become increasingly important in current research and development strategies. Polymers with tailored surface energies are used in a wide variety of applications, from planarizing or dielectric layers for semiconductor device fabrication to nonstick cookware and surfaces for combinatorial chemistry. In each of these applications, properties such as adhesion, wetting, lubrication and adsorption behavior must be carefully tuned so as to optimize performance. In the past, scientists toiled on the effects of individual molecular interactions such as entropic frustration between polymer blocks, hydrogen bonding, molecular shape anisotropy, coulombic interactions, and surface segregation. Now, we have learned how to combine these molecular interactions to produce powerful synergistic effects on materials structure.

Semi-fluorinated polymers attached to polymer backbones are often used as surface coatings for their hydrophobic and lipophobic behavior due to the highly chemically resistant nature of the C–F bond. They can also be used as surfactants, lubricating agents, emulsifiers, or photoresists. It has been found that the semi-fluorinated mesogens segregate to the polymer/air interface due to their low surface energy, and are often tilted with respect to the surface normal [212]. One problem with these highly hydrophobic materials, however, is the tendency for surface reconstruction to occur when placed in a highly polar solvent such as water (see Figure 1.28a). Surface reconstruction severely impairs the hydrophobic properties of the material.



**Figure 1.28** (a) Lamellar morphologies of a block copolymer consisting of hydrophobic and hydrophilic blocks self-assembled with the hydrophobic block situated at the air interface due to its lower surface energy. Exposure of the film to water causes a surface reconstruction that brings the hydrophilic block into contact with the water; (b) Block

copolymers containing a hydrophobic fluorinated mesogen resist surface reconstruction due to the formation of a highly stable liquid crystalline smectic phase at the surface. Adapted from Gabor, A.H., Pruette, L.C. and Ober, C.K. (1996), *Chem. Mater.*, **8** (9), 2282–2290.

BCPs provide a solution to the problem of surface reconstruction. It has been found that the incorporation of semi-fluorinated chemical groups into micro-phase-separated BCPs produces materials that resist surface reconstruction due to the formation of a stable liquid crystalline smectic phase at the surface (as shown in Figure 1.28b). Since this discovery, semi-fluorinated BCPs have become very popular candidates as longlasting, nonbiofouling surface coatings for marine vessels, due to the inability of aquatic organisms to stick to their surfaces [65, 213]. A recent report showed that the surface hydrophobicity of fluorinated BCPs can be enhanced with supercritical CO<sub>2</sub> annealing due to a thickening of the smectic layer [214]. According to Langmuir's *Principle of Independent Surface Action*, the unique hydrophobic properties of a surface depend on: (i) the *nature*; and (ii) the *physical arrangement* of the atoms populating the surface of the material [215]. In the following examples, we will discuss how the surface energy of block copolymer films have been manipulated by changing these two variables.

### 1.6.2

#### Patterning Surface Energies

The facility to alter the hydrophobicity of a polymer in precise patterns would be a highly desirable trait for the formation of biologically active surfaces. This would allow the selective adsorption of biomolecules [216] or recombinant proteins [217] onto specific locations of a polymer film, which could then be used for biosensors



or other “lab-on-a-chip” applications. By definition, the patterning of a photoresist readily accomplishes this solubility switch (see Section 1.2.1). Hayakawa and coworkers synthesized a hydroxylated poly(styrene-*block*-isoprene) BCP using polymer-analogous chemistry, followed by the grafting of a semi-fluorinated side chain onto the hydroxylated isoprene block [218]. The surface-segregated semi-fluorinated chains were capped with an acid-labile *tert*-butoxycarbonyl (TBOC) protecting group that masks a hydroxyl functionality at the end of the chain. To tailor the surface energy of the polymer surface layer, a chemical amplification strategy was used. A photoacid generator mixed into the polymer thin film produced a photoacid that deprotected the TBOC groups, such that the nonpolar methyl end group from the TBOC switched to a polar hydroxyl group during photoprocessing. This resulted in a decrease in the advancing and receding water contact angles by 14° and 15°, respectively. Annealing the film also induced a greater degree of surface ordering of the semi-fluorinated chain and increased the hydrophilicity of the exposed material by a small amount.

Other similar approaches have been used to accomplish the same effect. Böker *et al.* demonstrated that the highly hydrophobic perfluorinated side chains grafted to a hydroxylated poly(styrene-*b*-isoprene) BCP became completely removed after thermal annealing to dramatically alter the surface properties of the film [219]. Annealing at 340 °C for 15 min in a vacuum oven caused a thermal ester cleavage that resulted in decomposition of the perfluorodecanoyl side chains, but left the parent polymer backbone intact. This resulted in a considerable change of the advancing contact angle of the film, from 122° to 87°. As thermal heating could also be carried out locally on a polymer film, the author suggested that this approach could be used to pattern hydrophobic and hydrophilic regions on the master template of a printing press to control the dispersion of aqueous inks.

In a similar approach, Yang *et al.* used group transfer polymerization to synthesize a variety of methacrylate-based BCPs with semi-fluorinated chains functionalized with protecting groups, with the intent to use them as surface-active materials as well as photoresists [220]. Due to their transparency under 193 nm wavelength light, the semiconductor industry has shown great interest in fluorinated methacrylate polymers as 193 nm wavelength photoresists. Prior studies have also shown that fluorine-containing BCPs can outperform their random copolymer counterparts [154], and are able to develop in environmentally friendly supercritical CO<sub>2</sub> [221]. To investigate the effect of BCP microstructure on wetting behavior, an assortment of volume ratios for these copolymers were synthesized to provide a wide range of different microstructures and solubilities, but these did not have any effect on the surface energy of the films. The polymers with six –CF<sub>2</sub>– units and a –CF<sub>3</sub> end group showed the lowest critical surface tension, at approximately 7 mNewtons per meter. Rather than the commonly used *tert*-butyl protecting group, the acetal-type tetrahydropyranyl (THP) protecting group was used on the basis of its more polar and labile nature. Thermal deprotection of the THP groups formed acid and left –OH groups on the polymer chain ends that reduced the advancing water contact angle by 30°. After a period of annealing, it was also reported that the free acid caused by the THP deprotection interacted with



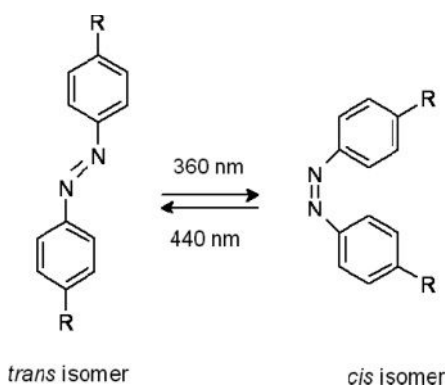
the Si–OH substrate and led to the formation of highly stable, nonreconstructing surfaces.

### 1.6.3

#### Photoswitchable Surface Energies Using Block Copolymers Containing Azobenzene

It is well known that polymers containing azobenzene groups attached to one of the blocks can exhibit light-responsive effects [222]. These chemical structures undergo a reversible *cis*–*trans* isomerization upon exposure to specific wavelengths of light (Figure 1.29), which also changes the molecular orientation of the LC azobenzene mesogens. It has also been found that the mesogens align perpendicular to the incident light polarization, which means that they will align in the film plane and along the direction of the propagation of radiation. Therefore, if the irradiation source is slanted at a given angle, the mesogens then align at the same angle within the film. This field is full of exciting potential for applications in the fields of holographic data storage, optical signal processing, and optical switching.

Light-induced molecular reorganization can also be used to tailor surface properties. Returning to the principle of independent surface action, there are two ways to change the wettability of a surface: (i) to change the nature of the end-group atoms; or (ii) to change the molecular orientation of the end-group atoms. Expanding on the latter point brings us to the topic of photoisomerizable fluorinated mesogens. Thin films of BCPs containing LC fluorinated mesogens have been shown to segregate into well-organized smectic layers on the surface, due to the low energy of the fluorinated block (see Section 1.6.1). Recently, the details have been reported of azobenzene BCPs with semi-fluorinated alkyl side chains that would allow structural modification of the fluorinated mesogens at the surface,



**Figure 1.29** The chemical structure of an azobenzene chromophore and the reversible photoisomerization between *trans* and *cis* isomers.

and thus selective patterning of the films' wetting behavior [223]. It has also been shown that the copolymers with longer fluoroalkyl chain lengths resulted in a high degree of orientational order, but were highly resistant to molecular restructuring with photoisomerization. The copolymers with short fluoroalkyl segments showed a small change in advancing/receding contact angle measurements upon exposure to UV light, corresponding to changes from a hydrophobic to a slightly less hydrophobic surface.

Möller and coworkers have also investigated the behavior of a BCP consisting of a PHEMA block and a poly(methacrylate) block with 4-trifluoromethoxyazobenzene side groups for photoswitchable wetting applications [224]. The group found that the photoswitchable effect depended heavily on the packing density of the chromophores, which are higher in the *trans* state than in the *cis* state. Films that were switched to the *cis* state before film formation had a lower packing density and were more susceptible to photoinduced motions, due to the increased free volume in the film. Another group reported an 8° difference in water contact angles between the *cis* and *trans* states in 4-trifluoromethylazobenzene-containing BCPs [225].

#### 1.6.4

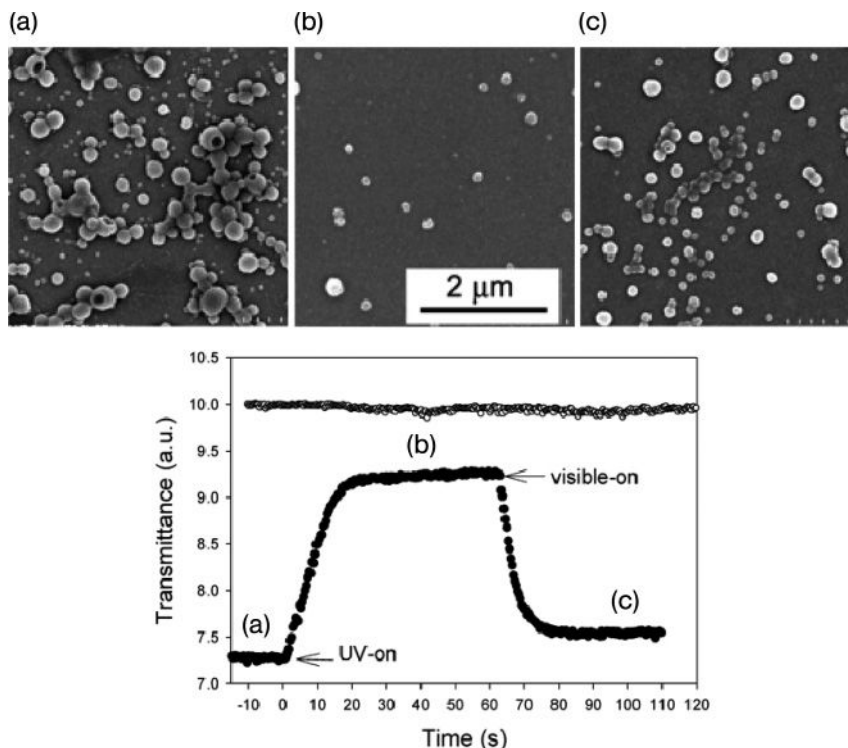
#### **Light-Active Azobenzene Block Copolymer Vesicles as Drug Delivery Devices**

Tong and coworkers have shown that amphiphilic, azobenzene-containing BCP micelles are highly responsive to UV light [226]. In their ATRP synthesis, the hydrophobic block is a methacrylate-based, azobenzene-containing LC polymer, and the hydrophilic block is a random copolymer of poly(*tert*-butyl acrylate-co-acrylic acid). The BCP forms micelles in solution. Under UV light, the azobenzene groups in the core undergo a *trans*-*cis* photoisomerization that induces a change in the dipole moment in the BCP vesicle. This shift in the delicate hydrophilic/hydrophobic balance between the chains causes dissociation of the micelle. Subsequent exposure to visible light irradiation switches the azo molecule back to its *trans* state, restores the thermodynamic balance, and causes the micelles to reform (Figure 1.30). Tong *et al.* note that other groups [227] had found little effect of UV light irradiation on other azo-based amphiphilic BCPs, but hinted that the success of their system might be due to the thermodynamic lever made possible by the tunability of the hydrophilic random copolymer block. Combined with the ability for micelles to solubilize anticancer drugs [228] and to act as carriers for the site-specific transport of drugs [229], these UV light-responsive micelles are very exciting.

#### 1.6.5

#### **Azobenzene-Containing Block Copolymers as Holographic Materials**

In the effort to store data on smaller and smaller length scales, volume holographic data storage has become an area of intense study in the scientific community. Recently, attention has turned to BCPs as a potential holographic material. In



**Figure 1.30** Changes in transmittance for a vesicle solution of PAzo74-*b*-(tBA46-AA22) exposed to UV (360 nm,  $18 \text{ mW cm}^{-2}$ ) and visible (440 nm,  $24 \text{ mW cm}^{-2}$ ) light irradiation. The vesicles are formed by adding 16% (v/v) of water in a dioxane solution with an initial polymer concentration of  $1 \text{ mg ml}^{-1}$ . (a–c) Typical SEM images for samples cast from the solution at different times: (a) before and (b) during UV light exposure, while (c) shows their reformation after visible light

exposure. For comparison, also shown is the transmittance of the diblock copolymer solution in dioxane (no water added to induce the aggregation) subjected to the same conditions of UV and visible light irradiation. The abscissa of time is shifted to have the origin correspond to the application of UV irradiation. Reprinted with permission from Ref. [226]; © 2006, American Chemical Society.

order to understand where they fit in, some background into the technology will be necessary. Holography is a revolutionary technique to store and view data in which an optical interference pattern is produced by the intersection of two coherent laser beams. At the point of intersection, the phase and amplitude of the wave fields induce a chemical or physical change in the material, and are thus “recorded” onto the holographic material [230].

High-capacity holographic data storage requires precise, 3-D control over the index of refraction of the material. Among many potential candidates for holographic materials, azobenzene-containing polymers seem to be the best suited for

holographic data storage for several reasons, including their high diffraction efficiency, resolution, and sensitivity, but mainly for the nematic–isotropic phase transition that occurs when the rod-like *trans* isomer is switched to the contracted *cis* isomer (refer to Figure 1.29). The disruption of LC ordering in the molecule takes place on a time scale of about 200  $\mu\text{s}$ , which is a reasonable period for writing data. In 1995, in a landmark study conducted by Ikeda and coworkers [231], this phenomenon was used to record holographic gratings inside the bulk of a polymer film.

One drawback to the use of azobenzene-containing homopolymers and random copolymers is the astonishing formation of surface relief gratings [232]. Here, the polymer becomes physically displaced in the areas of the most intense illumination, due to a massive macroscopic motion of the azo-polymer chains. Despite an increased diffraction efficiency created by these photopatterned ridges, surface relief structures are permanent physical effects that are highly detrimental to the angular selectivity and rewritability required for volume holograms.

BCPs containing azobenzene side chains do not form surface relief gratings due to the confining effect of the microdomains on the azobenzene side chains [233]. This confinement effect, however, seems to have detrimental effects on the speed and magnitude of the *cis*–*trans* photoisomerization [234]. Häckel *et al.* synthesized a series of BCPs containing a polystyrene block and a polybutadiene block containing the photo-addressable azobenzene components [235]. The photo-addressable phase consisted of a statistical distribution of azobenzene side groups and benzoylbiphenyl side groups. The latter rod-type mesogen was introduced to increase the difference in refractive index between the illuminated and nonilluminated areas of the volume and to improve the stability of the orientation. Different azo:mesogen ratios were used to identify the polymer with the highest degree and stability of molecular reorientation. The polymer containing 35% of the mesogenic side groups showed a slight increase of the refractive index modulation over the period of a year. This strategy posted remarkable improvements over the stability of the recorded orientations.

## 1.7

### Summary and Outlook

In this chapter we have brought to light many interesting chemical and physical applications possible using BCP-directed self-assembly (see Table 1.3). Unfortunately, however, many other fascinating applications have been omitted in the interest of space. An extraordinary amount of progress has been made in our ability to manipulate and optimize BCP structural ordering in various forms, including thin films, micelles, and monolithic bulk structures. The ordered microdomains may contain chemical functionality that can be used in a variety of fashions, such as templates for the nucleation and growth of inorganic nanoparticles, chemical valves inside cylindrical pores, monolithic nanoporous structures, or as removable components to form lithographic stencils. We have also seen how BCPs

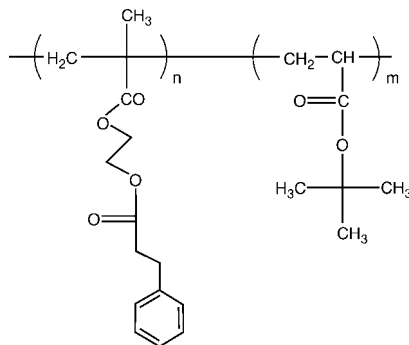
**Table 1.3** Block copolymers used for phase-selective chemistry.

Name	Structure	Function
Poly(styrene- <i>block</i> -isoprene) modified with 4-perfluoroalkyl azobenzene side groups	<p style="text-align: center;"> <math display="block">R = \text{---C(=O)---(CH}_2\text{)}_5\text{---O---C}_6\text{H}_4\text{---N=N---C}_6\text{H}_4\text{---(CF}_2\text{)}_n\text{F}</math> </p>	Photoswitchable surface engineering
Poly(styrene- <i>block</i> -methyl methacrylate)		Nanolithographic patterning
Poly(styrene- <i>block</i> -4-vinyl pyridine)		Micelle nanoreactors, nanolithographic patterning
Polystyrene- <i>block</i> -butadiene		Nanolithographic patterning

Table 1.3 Continued.

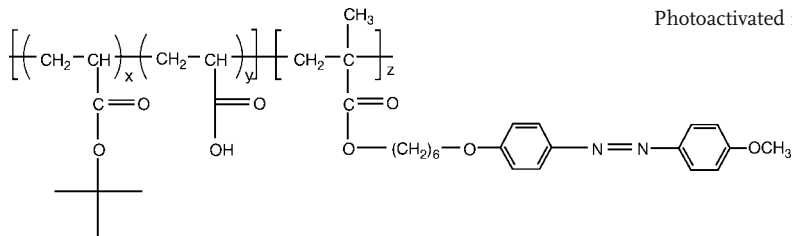
Name	Structure	Function
Poly( $\alpha$ -methylstyrene- <i>block</i> -hydroxystyrene)		Nanolithographic patterning
Poly(isoprene- <i>block</i> -ethylene oxide)		Structure-directing scaffolds for inorganic chemistry
Poly(styrene- <i>block</i> -L-lactide)		Functionalized nanoporous surfaces, nanolithographic patterning
<i>t</i> -butyl methacrylate ( <i>t</i> -BMA)- <i>block</i> -3-methacryloxypropylpentamethyldisiloxane (SiMA).		Bilevel block copolymer photoresists

Poly(cinnamoylethylmethacrylate-*block-tert*-butyl acrylate)



Functionalized nanoporous surfaces ; crosslinked polymeric nanostructures

Poly(*tert*-butyl acrylate-*co*-acrylic acid)-*block*-azo methacrylate)



Photoactivated micelle formation

Table 1.3 Continued.

Name	Structure	Function
Modified poly(styrene- <i>block</i> -1,2-butadiene)		Holographic patterning



can behave as multilevel photoresists due to their ability to combine different polymers without macrophase separation. BCPs have also been used for their ability to segregate into distinct chemical levels for the tailoring of surface properties. Lastly, we have seen how the incorporation of LC moieties such as fluorinated mesogens or azobenzene chromophores into BCPs widens their repertoire to low-energy surface patterning and holographic data storage applications.

In all of these studies, novel chemical strategies have been used to generate functional results. Chemistry is at the heart of every physical effect arising from BCP self-assembly. Using myriad living polymerization strategies in combination with polymer-analogous reactions, BCPs with a vast range of functionalities can be synthesized with low polydispersity and well-defined molecular weights. Exquisite levels of control over the BCP can be achieved by altering the degree of polymerization of each of the blocks, through which the chemist can dial in any type of morphology from spheres, cylinders, bicontinuous networks, and lamellar phases. Even more morphologies are possible through micellization strategies, such as spherical, cylindrical, or onion-like structures. The physical and functional likeness of these structures to biological vesicles and lysosomes is uncanny. Moreover, these technologies are just starting to see the first of their applications as containers for drug delivery, and excellent reviews have been produced that highlight this area [29, 236].

In the field of BCP lithography, we have just begun to see the first practical uses emerge from all of the fundamental studies. The formation of cobalt magnetic dot arrays, flash memory devices, and MOS capacitors are only the “tip of the iceberg” of applications that can arise from this technology. Whilst industry has not overlooked these results, several key requirements are required in order for the semiconductor industry to take directed self-assembly seriously. Among these requirements are “improved long-range dimensional control ... improved resolution and linear density by at least a factor of two over that achieved by top down lithography [~11 nm by 2010] ... fabricated features with multiple sizes and pitches in the same layer in different regions of a chip ....” and so on [79]. If improvements in these areas are not made in the next four years, the field of directed self-assembly may miss its chance for widespread industrial use.

In the future, nothing stands in the way of our ability to pattern individual, isolated lines of perpendicular lamellar morphologies. To this end, the work of Ober and coworkers with the P( $\alpha$ MS-*b*-HOST) system, in combination with small molecular additives that undergo phase-selective photocrosslinking chemistry, seems very promising. One day, the rapidly growing field of organic electronics may converge with BCP lithography, and the ability to create patterned, well-ordered arrays of conducting nanowires may become possible [237–239]. In theory, the chemical nanopatterning approach mastered by the Nealey group should allow us to effectively control BCP self-assembly by forcing microdomains to organize into any type of lattice, such as simple cubic lattices. It should also be possible with chemical nanopatterning to pattern some of the more complicated features in semiconductor device components, such as nested and embedded jog structures, and t-junctions. Furthermore, if we consider the immense 3-D complexity

of protein molecules, which are formed from various combinations of the 20 amino acids, we have only begun to scratch the surface of the dimensional control made possible by block copolymers. The incorporation of multiple blocks, hydrogen-bonded [240] and LC blocks [21] will be immensely rewarded by the ability to manipulate and exert control over multiple length scales of molecular self-assembly. Nor should we be constrained by the type of BCP that we use. PS-*b*-PMMA is a great lithographic system, but other, better-performing BCP systems may be on the horizon. New and improved chemistry will be vital for improvement in this field. It will certainly be exciting to follow the field of BCP research as it reaches its full maturity in the coming years.

## References

- 1 Waite, J.H., Lichtenegger, H.C., Stucky, G.D. and Hansma, P. (2004) *Biochemistry*, **43**, 7653–7662.
- 2 Coyne, K.J., Qin, X. and Waite, J.H. (1997) *Science*, **277**, 1830.
- 3 Jones, M.N. and Chapman, D. (1995) *Micelles, Monolayers and biomembranes*, John Wiley & Sons, Inc., New York.
- 4 Shapiro, J.A. (1998) *Annu. Rev. Microbiol.*, **52**, 81.
- 5 Phillip, D. and Stoddart, J.F. (1996) *Angew. Chem. Int. Ed. Engl.*, **35**, 1155.
- 6 Whitesides, G.M., Mathias, J.P. and Seto, C.T. (1991) *Science*, **254**, 1312–1319.
- 7 Ball, P. (2001) *Nature*, **413**, 667–668.
- 8 Bates, F.S. and Fredrickson, G.H. (1999) *Phys. Today*, **52**, 32–38.
- 9 Holden, G., Legge, N.R., Quirk, R. and Schroeder, H.E. (1996) *Thermoplastic Elastomers*, 2nd edn, Schoder Druck GmbH & Co KG, Gersthofen.
- 10 Bates, F.S. and Fredrickson, G.H. (1990) *Annu. Rev. Phys. Chem.*, **41**, 525–557.
- 11 Hashimoto, T., Shibayama, M. and Kawai, H. (1980) *Macromolecules*, **13**, 1237.
- 12 Hajduk, D.A., Harper, P.E., Gruner, S.M., Honeker, C.C., Kim, G., Thomas, E.L. and Fetters, L.J. (1994) *Macromolecules*, **27**, 4063.
- 13 Zhao, J., Majumdar, B., Schulz, M.F., Bates, F.S., Almdal, K., Mortensen, K., Hajduk, D.A. and Gruner, S.M. (1996) *Macromolecules*, **29**, 1024.
- 14 Chan, V.Z.H., Hoffman, J., Lee, V.Y., Latrou, H., Avgeropoulos, A., Hadjichristidis, N. and Miller, R.D. (1999) *Science*, **286**, 1716–1719.
- 15 Urbas, A.M., Maldovan, M., DeRege, P. and Thomas, E.L. (2002) *Adv. Mater.*, **14**, 1850–1853.
- 16 Blomberg, S., Ostberg, S., Harth, E., Bosman, A.W., Van Horn, B. and Hawker, C.J. (2002) *J. Polym. Sci., Part A: Polym. Chem.*, **40**, 1309–1320.
- 17 Stadler, R., Auschra, C., Beckmann, J., Krappe, U., Voight-Martin, I. and Leibler, L. (1995) *Macromolecules*, **28**, 3080–3097.
- 18 Zheng, W. and Wang, Z.G. (1995) *Macromolecules*, **28**, 7215–7223.
- 19 Takahashi, K., Hawegawa, H., Hashimoto, T., Bellas, V., Iatrou, H. and Hadjichristidis, N. (2002) *Macromolecules*, **36**, 4859.
- 20 Abetz, V. and Simon, P.F.W. (2005) *Adv. Polym. Sci.*, **189**, 125–212.
- 21 Adams, J. and Gronski, W. (1989) *Makromol. Chem. Rapid Commun.*, **10**, 553–557.
- 22 Gallot, B. (1996) *Prog. Polym. Sci.*, **21**, 1035–1088.
- 23 Muthukumar, M., Ober, C.K. and Thomas, E.L. (1997) *Science*, **277**, 1225–1232.
- 24 Chen, J.T., Thomas, E.L., Ober, C.K. and Mao, G.P. (1996) *Science*, **273**, 343–346.
- 25 Mao, G.P., Wang, J., Clingman, S.R., Ober, C.K., Chen, J.T. and Thomas, E.L. (1997) *Macromolecules*, **30**, 2556–2567.
- 26 Discher, B.M., Won, Y.Y., Ege, D.S., Lee, J.C.M., Bates, F.S., Discher, D.E. and

- Hammer, D.A. (1999) *Science*, **284**, 1143–1146.
- 27 Foerster, S. (2003) *Top. Curr. Chem.*, **226**, 1–28.
- 28 Forster, S. and Antonietti, M. (1998) *Adv. Mater.*, **10**, 195–217.
- 29 Forster, S. and Plantenberg, T. (2002) *Angew. Chem. Int. Ed. Engl.*, **41**, 688–714.
- 30 Hadjichristidis, N., Pitsikalis, M. and Iatrou, H. (2005) *Adv. Polym. Sci.*, **189**, 124.
- 31 Hsieh, H. and Quirk, R. (1996) *Anionic Polymerization: Principles and Practical Applications*, Vol. **34**, Marcel Dekker, Inc., New York.
- 32 Hadjichristidis, N., Pitsikalis, M., Iatrou, H. and Pispas, S. (2000) *J. Polym. Sci., Part A: Polym. Chem.*, **38**, 3211–3234.
- 33 Ndoni, S., Papadakis, C.M., Bates, F.S. and Almdal, K. (1995) *Rev. Sci. Instrum.*, **66**, 1090–1095.
- 34 Hadjichristidis, N., Pitsikalis, M., Pispas, S. and Iatrou, H. (2001) *Chem. Rev.*, **101**, 3747–3792.
- 35 Otsu, T., Yoshida, M. and Tazaki, T. (1982) *Makromol. Chem., Rapid Commun.*, **3**, 133.
- 36 Hawker, C.J., Bosman, A.W. and Harth, E. (2001) *Chem. Rev.*, **101**, 3661–3688.
- 37 Georges, M.K., Veregin, R.P.N., Kazmaier, P.M., Hamer, G.K. and Saban, M. (1994) *Macromolecules*, **27**, 7228–7229.
- 38 Georges, M.K., Veregin, R.P.N., Kazmaier, P.M. and Hamer, G. (1993) *Macromolecules*, **26**, 2987–2988.
- 39 Otsu, T. and Matsumoto, A. (1998) *Adv. Polym. Sci.*, **136**, 75–136.
- 40 Otsu, T., Yoshida, M. and Kuriyama, A. (1982) *Polym. Bull.*, **7**, 45.
- 41 Otsu, T., Kuriyama, A. and Yoshida, M. (1983) *J. Polym. Sci. Tech. (Japan)*, **40**, 583.
- 42 Otsu, T. and Yoshida, M. (1982) *Polym. Bull.*, **7**, 197.
- 43 Haque, S.A. (1994) *J. Macromol. Sci., Pure Appl. Chem. A*, **31**, 827.
- 44 Liu, F.T., Cao, S.Q. and Yu, X.D. (1993) *J. Appl. Polym. Sci.*, **48**, 425.
- 45 Oprešnik, M. and Sebenik, A. (1995) *Polym. Int.*, **36**, 13.
- 46 Moad, G., Chong, Y.K., Postma, A., Rizzardo, E. and Thang, S.H. (2005) *Polymer*, **46**, 8458–8468.
- 47 Matyjaszewski, K. and Xia, J. (2001) *Chem. Rev.*, **101**, 2921–2990.
- 48 Gibson, V.C. (1994) *Adv. Mater.*, **6**, 37–42.
- 49 Buchmeiser, M.R., Seeber, G., Mupa, M. and Bonn, G.K. (1999) *Chem. Mater.*, **11**, 1533–1540.
- 50 Royappa, A.T., Saunders, R.S., Rubner, M.F. and Cohen, R.E. (1998) *Langmuir*, **14**, 6207–6214.
- 51 Fogg, D.E., Radzilowski, L.H., Blanski, R., Schrock, R.R. and Thomas, E.L. (1997) *Macromolecules*, **30**, 417–426.
- 52 Brittain, W. (1992) *Rubber Chem. Technol.*, **65**, 580.
- 53 Sogah, D.Y., Hertler, W.R., Webster, O.W. and Cohen, G.M. (1987) *Macromolecules*, **20**, 1473–1488.
- 54 Mykytiuk, J., Armes, S.P. and Billingham, N.C. (1992) *Polym. Bull.*, **29**, 139.
- 55 Rannard, S.P., Billingham, N.C., Armes, S.P. and Mykytiuk, J. (1993) *Eur. Polym. J.*, **29**, 407.
- 56 AG and Goldschmidt, T. (1992), Germany.
- 57 Risse, W. and Grubbs, R.H. (1989) *Macromolecules*, **22**, 1558–1562.
- 58 Feldthusen, J., Ivan, B. and Muller, A.H.E. (1998) *Macromolecules*, **31**, 578–585.
- 59 Matyjaszewski, K. and Xia, J. (2001) *Chem. Rev.*, **101**, 2963.
- 60 McGrath, M.P., Sall, E.D. and Tremont, S.J. (1995) *Chem. Rev.*, **95**, 381.
- 61 Jian, X. and Hay, A.S. (1991) *J. Polym. Sci., Part A: Polym. Chem.*, **29**, 1183.
- 62 Ramireddy, C., Tuzar, Z., Prochazka, K., Webber, S.E. and Munk, P. (1992) *Macromolecules*, **25**, 2541.
- 63 Valint, P.L. and Bock, J. (1988) *Macromolecules*, **21**, 175.
- 64 Chung, T.C., Raate, M., Berluche, E. and Schulz, D.N. (1988) *Macromolecules*, **21**, 1903–1907.
- 65 Krishnan, S., Wang, N., Ober, C.K., Finlay, J.A., Callow, M.E., Callow, J.A., Hexemer, A., Sohn, K., Kramer, E.J. and Fischer, D. (2006) *Biomacromolecules*, **7**, 1449–1462.

- 66 Selb, J. and Gallot, Y. (1985) In *Developments in Block Copolymers*, Vol. 2 (ed. I. Goodman), Elsevier, London, p. 27.
- 67 Cameron, G.G. and Qureshi, M.Y. (1981) *Makromol. Chem.*, **2**, 287.
- 68 Pepper, K.W., Paisley, H.M. and Young, M.A. (1953) *J. Am. Chem. Soc.*, 4097.
- 69 Rahlwes, D., Roovers, J.E.L. and Bywater, S. (1977) *Macromolecules*, **10**, 604.
- 70 Liu, G., Ding, J., Guo, A., Herfort, M. and Bazett-Jones, D. (1997) *Macromolecules*, **30**, 1851–1853.
- 71 Hadjichristidis, N., Pispas, S. and Floudas, G. (2003) *Block Copolymers: Synthetic Strategies, Physical Properties, and Applications*, John Wiley & Sons, Inc., Hoboken, NJ.
- 72 Reichmanis, E. (1993) In *Polymers for Electronic and Photonic Applications* (ed. C.P. Wong), Academic Press, pp. 67–116.
- 73 Thompson, L.F. and Bowden, M.J. (1983) In *Introduction to Microlithography*, ACS Symposium Series, Vol. 412, 1st edn, American Chemical Society, Washington, DC, pp. 162–214.
- 74 Moore, G.E. (1965) *Electronics*, **38**. [ftp://download.intel.com/museum/Moores\\_Law/Articles-Press\\_Releases/Gordon\\_Moore\\_1965\\_Article.pdf](ftp://download.intel.com/museum/Moores_Law/Articles-Press_Releases/Gordon_Moore_1965_Article.pdf)
- 75 Chang, S.W., Ayothi, R., Bratton, D., Yang, D., Felix, N., Cao, H.B., Deng, H. and Ober, C.K. (2006) *J. Mater. Chem.*, **16**, 1470–1474.
- 76 Yang, D., Chang, S.W. and Ober, C.K. (2006) *J. Mater. Chem.*, **16**, 1693–1696.
- 77 Xia, Y., Rogers, J.A., Paul, K.E. and Whitesides, G.M. (1999) *Chem. Rev.*, **99**, 1823–1848.
- 78 McCord, M. and Rooks, M. (1997) In *Handbook of Microlithography, Micromachining and Microfabrication*, Vol. 1, Ch. 2 (ed. P. Rai-Choudhury), SPIE Press, Bellingham, WA.
- 79 Garner, M.C., Herr, D. and Krautschik, C. (2006) Semiconductor Research Corporation Internal Document.
- 80 Park, M., Harrison, C., Chaikin, P.M., Register, R.A. and Adamson, D.H. (1997) *Science*, **276**, 1401–1404.
- 81 Lee, J.S., Hirao, A. and Nakahama, S. (1989) *Macromolecules*, **22**, 2602.
- 82 Hawker, C.J. and Russell, T.P. (2005) *MRS Bull.*, **30**, 952–966.
- 83 Harrison, C.H., Dagata, J.A. and Adamson, D.H. (2004) In *Developments in Block Copolymer Science and Technology* (ed. I.W. Hamley), John Wiley & Sons, pp. 295–323.
- 84 Li, M., Coenjarts, C.A. and Ober, C.K. (2005) *Adv. Polym. Sci.*, **190**, 183–226.
- 85 Fasolka, M.J. and Mayes, A.M. (2001) *Annu. Rev. Mater. Res.*, **31**, 323–355.
- 86 Segalman, R.A. (2005) *Mater. Sci. Eng., R*, **48**, 191–226.
- 87 Hahm, J. and Sibener, S.J. (2001) *J. Chem. Phys.*, **114**, 4730–4740.
- 88 Amundson, K., Helfand, E., Quan, X., Hudson, S.D. and Smith, S.D. (1994) *Macromolecules*, **27**, 6559–6570.
- 89 Thurn-Albrecht, T., DeRouchey, J., Russell, T.P. and Kolb, R. (2002) *Macromolecules*, **35**, 8106–8110.
- 90 Thurn-Albrecht, T., Steiner, R., DeRouchey, J., Stafford, C.M., Huang, E., Bal, M., Tuominen, M.T., Hawker, C.J. and Russell, T.P. (2000) *Adv. Mater.*, **12**, 787–790.
- 91 Daniel, C., Hamley, I.W., Mingvanish, W. and Booth, C. (2000) *Macromolecules*, **33**, 2163–2170.
- 92 Fredrickson, G.H. (1994) *J. Rheol.*, **38**, 1045–1067.
- 93 Hamley, I.W. (2000) *Curr. Opin. Colloid Interface Sci.*, **5**, 342–350.
- 94 Xuan, Y., Peng, J., Cui, L., Wang, H., Li, B. and Han, Y. (2004) *Macromolecules*, **37**, 7301–7307.
- 95 Fukunaga, K., Elbs, H., Magerle, R. and Krausch, G. (2000) *Macromolecules*, **33**, 947–953.
- 96 Segalman, R.A., Yokoyama, H. and Kramer, E.J. (2001) *Adv. Mater.*, **13**, 1152–1155.
- 97 Huang, E., Pruzinsky, S., Russell, T.P., Mays, J. and Hawker, C.J. (1999) *Macromolecules*, **32**, 5299–5303.
- 98 Huang, E., Russell, T.P., Harrison, C., Chaikin, P.M., Register, R.A., Hawker, C.J. and Mays, J. (1998) *Macromolecules*, **31**, 7641–7650.
- 99 Peters, R.D., Yang, X.M., Wang, Q., de Pablo, J.J. and Nealey, P.F. (2000) *J. Vac. Sci. Tech., B*, **18**, 3530–3534.
- 100 Kim, S.O., Solak, H.H., Stoykovich, M.P., Ferrier, N.J., de Pablo, J.J. and Nealey, P.F. (2003) *Nature*, **424**, 411–414.

- 101 Yang, X.M., Peters, R.D., Nealey, P.F., Solak, H.H. and Cerrina, F. (2000) *Macromolecules*, **33**, 9575–9582.
- 102 Kim, S.H., Misner, M.J., Xu, T., Kimura, M. and Russell, T.P. (2004) *Adv. Mater.*, **16**, 226–231.
- 103 Drockenmuller, E., Li, L.Y.T., Ryu, D.Y., Harth, E., Russell, T.P., Kim, H.C. and Hawker, C.J. (2005) *J. Polym. Sci., Part A: Polym. Chem.*, **43**, 1028–1037.
- 104 Russell, T.P., Thurn-Albrecht, T., Tuominen, M., Huang, E. and Hawker, C.J. (2000) *Macromol. Symp.*, **159**, 77–88.
- 105 Xu, T., Stevens, J., Villa, J.A., Goldbach, J.T., Guarini, K.W., Black, C.T., Hawker, C.J. and Russell, T.P. (2003) *Adv. Funct. Mater.*, **13**, 698–702.
- 106 Kim, H.C., Jia, X., Stafford, C.M., Kim, D.H., McCarthy, T.J., Tuominen, M., Hawker, C.J. and Russell, T.P. (2001) *Adv. Mater.*, **13**, 795–797.
- 107 Shin, K., Leach, K.A., Goldbach, J.T., Kim, D.H., Jho, J.Y., Tuominen, M., Hawker, C.J. and Russell, T.P. (2002) *Nano Lett.*, **2**, 933–936.
- 108 Asakawa, K. and Hiraoka, T. (2002) *J. Appl. Phys.*, **1** (Japan), **41**, 6112–6118.
- 109 Asakawa, K., Hiraoka, T., Hieda, H., Sakurai, M., Kamata, Y. and Naito, K. (2002) *J. Photopolym. Sci. Technol.*, **15**, 465–470.
- 110 Naito, K., Hieda, H., Sakurai, M., Kamata, Y. and Asakawa, K. (2002) *IEEE Trans. Magn.*, **38**, 1949–1951.
- 111 Harrison, C., Park, M., Chaikin, P.M., Register, R.A. and Adamson, D.H. (1998) *J. Vac. Sci. Tech.*, **B**, **16**, 544–552.
- 112 Mansky, P., Harrison, C.K., Chaikin, P.M., Register, R.A. and Yao, N. (1996) *Appl. Phys. Lett.*, **68**, 2586–2588.
- 113 Lammertink, R.G.H., Hempenius, M.A., Van Den Enk, J.E., Chan, V.Z.H., Thomas, E.L. and Vancso, G.J. (2000) *Adv. Mater.*, **12**, 98–103.
- 114 Lammertink, R.G.H., Hempenius, M.A., Chan, V.Z.H., Thomas, E.L. and Vancso, G.J. (2001) *Chem. Mater.*, **13**, 429–434.
- 115 Hashimoto, T., Tsutsumi, K. and Funaki, Y. (1997) *Langmuir*, **13**, 6869–6872.
- 116 Du, P., Li, M., Douki, K., Li, X., Garcia, C.B.W., Jain, A., Smilgies, D.M., Fetters, L.J., Gruner, S.M., Wiesner, U. and Ober, C.K. (2004) *Adv. Mater.*, **16**, 953–957.
- 117 Li, M., Douki, K., Goto, K., Li, X., Coenjarts, C., Smilgies, D.M. and Ober, C.K. (2004) *Chem. Mater.*, **16**, 3800–3808.
- 118 Zalusky, A.S., Olayo-Valles, R., Taylor, C.J. and Hillmyer, M.A. (2001) *J. Am. Chem. Soc.*, **123**, 1519–1520.
- 119 Zalusky, A.S., Olayo-Valles, R., Wolf, J.H. and Hillmyer, M.A. (2002) *J. Am. Chem. Soc.*, **124**, 12761–12773.
- 120 Wolf, J.H. and Hillmyer, M.A. (2003) *Langmuir*, **19**, 6553–6560.
- 121 Rzayev, J. and Hillmyer, M.A. (2005) *Macromolecules*, **38**, 3–5.
- 122 Lin, Z., Kim, D.H., Wu, X., Boosahda, L., Stone, D., LaRose, L. and Russell, T.P. (2002) *Adv. Mater.*, **14**, 1373–1376.
- 123 Cheng, J.Y., Ross, C.A., Chan, V.Z.H., Thomas, E.L., Lammertink, R.G.H. and Vancso, G.J. (2001) *Adv. Mater.*, **13**, 1174–1178.
- 124 Cheng, J.Y., Ross, C.A., Thomas, E.L., Smith, H.I. and Vancso, G.J. (2002) *Appl. Phys. Lett.*, **81**, 3657–3659.
- 125 Yokoyama, H., Li, L., Nemoto, T. and Sugiyama, K. (2004) *Adv. Mater.*, **16**, 1542–1546.
- 126 Li, L., Yokoyama, H., Nemoto, T. and Sugiyama, K. (2004) *Adv. Mater.*, **16**, 1226–1229.
- 127 Park, M., Chaikin, P.M., Register, R.A. and Adamson, D.H. (2001) *Appl. Phys. Lett.*, **79**, 257–259.
- 128 Li, R.R., Dapkus, P.D., Thompson, M.E., Jeong, W.G., Harrison, C., Chaikin, P.M., Register, R.A. and Adamson, D.H. (2000) *Appl. Phys. Lett.*, **76**, 1689–1691.
- 129 Poly(styrene-block-methylmethacrylate). Polymer Source, Inc. Available at: <http://www.polymersource.com/shoppingCart/product.asp?ID=408>
- 130 Ranby, B. and Rabek, J.F. (1975) *Photodegradation, Photo-oxidation and Photostabilization of Polymers*, John Wiley & Sons, Inc., New York.
- 131 Stoykovich, M.P., Mueller, M., Kim, S.O., Solak, H.H., Edwards, E.W., de Pablo, J.J. and Nealey, P.F. (2005) *Science*, **308**, 1442–1446.
- 132 Guarini, K.W., Black, C.T. and Yeung, S.H.I. (2002) *Adv. Mater.*, **14**, 1290–1294.
- 133 Guarini, K.W., Black, C.T., Milkove, K.R. and Sandstrom, R.L. (2001) *J. Vac. Sci. Tech.*, **B**, **19**, 2784–2788.
- 134 Black, C.T., Guarini, K.W., Milkove, K.R., Baker, S.M., Russell, T.P. and

- Tuominen, M.T. (2001) *Appl. Phys. Lett.*, **79**, 409–411.
- 135** Guarini, K.W., Black, C.T., Zhang, Y., Kim, H., Sikorski, E.M. and Babich, I.V. (2002) *J. Vac. Sci. Tech., B*, **20**, 2788–2792.
- 136** Black, C.T. (2005) *Appl. Phys. Lett.*, **87**, 163116.
- 137** Guarini, K.W., Black, C.T., Zhang, Y., Babich, I.V., Sikorski, E.M. and Gignac, L.M. (2003) Low voltage, scalable nanocrystal FLASH memory fabricated by templated self assembly. *Technical Digest—International Electron Devices Meeting*, pp. 541–544.
- 138** Leiston-Belanger, J.M., Russell, T.P., Drockenmuller, E. and Hawker, C.J. (2005) *Macromolecules*, **38**, 7676–7683.
- 139** Lammertink, R.G.H., Hempenius, M.A., Thomas, E.L. and Vancso, J. (1999) *J. Polym. Sci., Part B: Polym. Phys.*, **37**, 1009–1021.
- 140** Cheng, J.Y., Ross, C.A., Thomas, E.L., Smith, H.I., Lammertink, R.G.H. and Vancso, G.J. (2002) *IEEE Trans. Magn.*, **38**, 2541–2543.
- 141** Ito, H. and Willson, C.G. (1982) *Polym. Eng. Sci.*, **23**, 1021.
- 142** Shaw, J.M. and Gelorme, J.D. (1997) *IBM J. Res. Dev.*, **41**, 81.
- 143** Bosworth, J.K., Paik, M.Y., Ruiz, R. *et al.* (2008) *ACS Nano*, **2** (7), 1396.
- 144** Taylor, G.N. and Wolf, T.M. (1980) *Polym. Eng. Sci.*, **20**, 1087.
- 145** Taylor, G.N., Wolf, T.M. and Moran, J.M. (1981) *J. Vac. Sci. Tech.*, **19**, 872.
- 146** Gabor, A.H., Pruette, L.C. and Ober, C.K. (1996) *Chem. Mater.*, **8**, 2282–2290.
- 147** Uhrich, K.E., Reichmanis, E. and Baiocchi, F.A. (1994) *Chem. Mater.*, **6**, 295–301.
- 148** Hartney, M.A., Novembre, A.E. and Bates, F.S. (1985) *J. Vac. Sci. Tech., B*, **3**, 1346–1351.
- 149** Bowden, M.J., Gozdz, A.S., Desimone, J.M., McGrath, J.E., Ito, S. and Matsuda, M. (1992) *Makromol. Chem., Macromol. Symp.*, **53**, 125.
- 150** DeSimone, J.M., York, G.A., McGrath, J.E., Gozdz, A.S. and Bowden, M.J. (1991) *Macromolecules*, **24**, 5330.
- 151** Jurek, M.J. and Reichmanis, E. (1989) In *Polymers in Microlithography*, ACS Symposium Series, Vol. **412** (eds E. Reichmanis, S.A. MacDonald and T. Iwayanagi), American Chemical Society, Washington DC, p. 158.
- 152** Gabor, A.H., Lehner, E.A., Mao, G.P., Schneggenburger, L.A. and Ober, C.K. (1994) *Chem. Mater.*, **6**, 927–934.
- 153** Gabor, A.H. and Ober, C.K. (1995) In *Microelectronics Technology: Polymers in Advanced Imaging and Packaging*, ACS Symposium Series, Vol. **614** (eds E. Reichmanis, S.A. MacDonald, T. Iwayanagi, C.K. Ober and T. Nishikubo), American Chemical Society, Washington, DC, pp. 281–298.
- 154** Gabor, A.H., Pruette, L.C. and Ober, C.K. (1996) *Chem. Mater.*, **8**, 2282–2290.
- 155** Lee, J.S., Hirao, A. and Nakahama, S. (1989) *Macromolecules*, **22**, 2602–2606.
- 156** Fink, Y., Urbas, A.M., Bawendi, M.G., Joannopoulos, J.D. and Thomas, E.L. (1999) *J. Lightwave Technol.*, **17**, 1963–1969.
- 157** Maldovan, M., Bockstaller, M.R., Thomas, E.L. and Carter, W.C. (2003) *J. Appl. Phys., B*, **76**, 877–889.
- 158** Pai, R.A., Humayun, R., Schulberg, M.T., Sengupta, A., Sun, J.N. and Watkins, J.J. (2004) *Science*, **303**, 507–511.
- 159** Nagarajan, S., Pai, R.A., Russell, T.P., Watkins, J.J., Li, M., Bosworth, J.K., Busch, P., Smilgies, D.M. and Ober, C.K. (2008) *Adv. Mater.*, **20** (2), 246.
- 160** Ulrich, R., Du Chesne, A., Templin, M. and Wiesner, U. (1999) *Adv. Mater.*, **11**, 141–146.
- 161** Simon, P.F.W., Ulrich, R., Spiess, H.W. and Wiesner, U. (2001) *Chem. Mater.*, **13**, 3464–3486.
- 162** Finnefrock, A.C., Ulrich, R., Toombes, G.E.S., Gruner, S.M. and Wiesner, U. (2003) *J. Am. Chem. Soc.*, **125**, 13084–13093.
- 163** Ulrich, R. (2000) *Morphologien und Eigenschaften strukturierter organisch-anorganischer Hybridmaterialien*, Logos-Verlag, Berlin.
- 164** Li, M. (2004) In *Materials Science and Engineering*, Cornell University, Ithaca, NY, p. 216.
- 165** Li Minqi, Development of functional block copolymers for nanotechnology. PhD Dissertation (2004), Cornell



- University Materials Science and Engineering.
- 166** Hamley, I.W. (1998) *The Physics of Block Copolymers*, Oxford University Press, Oxford.
- 167** Xu, T., Kim, H.-C., DeRouchey, J., Seney, C., Levesque, C., Martin, P., Stafford, C.M. and Russell, T.P. (2001) *Polymer*, **42**, 9091–9095.
- 168** Jeong, U., Kim, H.C., Rodriguez, R.L., Tsai, I.Y., Stafford, C.M., Kim, J.K., Hawker, C.J. and Russell, T.P. (2002) *Adv. Mater.*, **14**, 274–276.
- 169** Ruokolainen, J., ten Brinke, G. and Ikkala, O. (1999) *Adv. Mater.*, **11**, 777–780.
- 170** Ikkala, O. and ten Brinke, G. (2002) *Science*, **295**, 2407–2409.
- 171** Maki-Ontto, R., de Moel, K., de Odorico, W., Ruokolainen, J., Stamm, M., ten Brinke, G. and Ikkala, O. (2001) *Adv. Mater.*, **13**, 117–121.
- 172** DeSimone, J.M., Guan, Z. and Elsbernd, C.S. (1992) *Science*, **257**, 945.
- 173** Liu, G., Ding, J. and Stewart, S. (1999) *Angew. Chem. Int. Ed. Engl.*, **38**, pp. 835–838.
- 174** Rzayev, J. and Hillmyer, M.A. (2005) *J. Am. Chem. Soc.*, **127**, 13373–13379.
- 175** Guo, S., Rzayev, J., Bailey, T., Zalusky, A., Olayo-Valles, R. and Hillmyer, M.A. (2006) *Chem. Mater.*, **18**, 1719–1721.
- 176** Mao, H., Arrechea, P.L., Bailey, T.S., Johnson, B.J.S. and Hillmyer, M.A. (2004) *Faraday Discuss.*, **128**, 149–162.
- 177** Tuzar, Z. and Kratochvil, P. (1993) *Colloids Surf. A*, **15**, 1–83.
- 178** Canham, P.A., Lally, T.P., Price, C. and Stubbersfield, R.B. (1980) *Faraday Trans.*, **55**, 1857.
- 179** Jenekhe, S.A. and Chen, X.L. (1998) *Science*, **279**, 1903.
- 180** Ding, J. and Liu, G. (1997) *Macromolecules*, **30**, 655.
- 181** Ding, J., Liu, G. and Yang, M. (1997) *Polymer*, **38**, 5497.
- 182** Liu, G., Yan, X., Li, Z., Zhou, J. and Duncan, S. (2003) *J. Am. Chem. Soc.*, **125**, 14039–14045.
- 183** Henselwood, F. and Liu, G. (1998) *Macromolecules*, **31**, 4213.
- 184** Ding, J. and Liu, G. (1998) *J. Phys. Chem. B*, **102**, 6107–6113.
- 185** Stewart, S. and Liu, G. (1999) *Chem. Mater.*, **11**, 1048–1054.
- 186** Guo, A., Liu, G. and Tao, J. (1996) *Macromolecules*, **29**, 2487–2493.
- 187** Tao, J., Liu, G., Ding, J. and Yang, M. (1997) *Macromolecules*, **30**, 4084–4089.
- 188** Ding, J. and Liu, G. (1998) *Macromolecules*, **31**, 6554.
- 189** Ding, J. and Liu, G. (1999) *Langmuir*, **15**, 1738–1747.
- 190** Liu, G. (1997) *Adv. Mater.*, **9**, 437–439.
- 191** Liu, G., Ding, J., Qiao, L., Guo, A., Dymov, B.P., Gleeson, J.T., Hashimoto, T. and Saijo, K. (1999) *Chem. Eur. J.*, **5**, 2740–2749.
- 192** Liu, G., Qiao, L. and Guo, A. (1996) *Macromolecules*, **29**, 5508–5510.
- 193** Liu, G. and Ding, J. (1998) *Adv. Mater.*, **10**, 69.
- 194** Liu, G., Ding, J., Guo, A., Herfort, M. and Bazett-Jones, D. (1997) *Macromolecules*, **30**, 1851.
- 195** Yan, X., Liu, F., Li, Z. and Liu, G. (2001) *Macromolecules*, **34**, 9112–9116.
- 196** Stewart, S. and Liu, G. (2000) *Angew. Chem. Int. Ed. Engl.*, **39**, 340–344.
- 197** Liu, G., Ding, J., Hashimoto, T., Kimishima, K., Winnik, F.M. and Nigam, S. (1999) *Chem. Mater.*, **11**, 2233–2240.
- 198** Underhill, R.S. and Liu, G. (2000) *Chem. Mater.*, **12**, 2082–2091.
- 199** Xiaohu, Y., Liu, G., Liu, F., Tang, B.Z., Peng, H., Pakhomov, A.B. and Wong, C.Y. (2001) *Angew. Chem. Int. Ed. Engl.*, **40**, 3593–3596.
- 200** Abes, J.I., Cohen, R.E. and Ross, C.A. (2003) *Chem. Mater.*, **15**, 1125–1131.
- 201** Kane, R.S., Cohen, R.E. and Silbey, R. (1999) *Chem. Mater.*, **11**, 90–93.
- 202** Fogg, D.E., Radzilowski, L.H., Dabbousi, B.O., Schrock, R.R., Thomas, E.L. and Bawendi, M.G. (1997) *Macromolecules*, **30**, 8433–8439.
- 203** Fogg, D.E., Radzilowski, L.H., Blanski, R., Schrock, R.R. and Thomas, E.L. (1997) *Macromolecules*, **30**, 417–426.
- 204** Aizawa, M. and Buriak, J. (2006) *J. Am. Chem. Soc.*, **128**, 5877–5886.
- 205** Cohen, R.E. (2000) *Curr. Opin. Solid State Mater. Sci.*, **4**, 587–590.
- 206** Ciebien, J.F., Clay, R.T., Sohn, B.H. and Cohen, R.E. (1998) *New J. Chem.*, **22**, 685–691.

- 207 Kane, R.S., Cohen, R.E. and Silbey, R. (1996) *Chem. Mater.*, **8**, 1919–1924.
- 208 Cummins, C.C., Beachy, M.D., Schrock, R.R., Vale, M.G., Sankaran, V. and Cohen, R.E. (1991) *Chem. Mater.*, **3**, 1153–1163.
- 209 Kane, R.S., Cohen, R.E. and Silbey, R.J. (1999) *Langmuir*, **15**, 39–43.
- 210 Spatz, J.P., Herzog, T., Moessmer, S., Ziemann, P. and Moeller, M. (1999) *Adv. Mater.*, **11**, 149–153.
- 211 Arnold, M., Calvacanti, A.A., Glass, R., Blummel, J., Eck, W., Kessler, H. and Spatz, J.P. (2004) *ChemPhysChem*, **5** (3), 383.
- 212 Genzer, J. and Kramer, E.J. (1997) *Phys. Rev. Lett.*, **78**, 4946–4949.
- 213 Youngblood, J.P., Andruzzi, L., Ober, C.K., Hexemer, A., Kramer, E.J., Callow, J.A., Finlay, J.A. and Callow, M.E. (2003) *Biofouling*, **19**, 91–98.
- 214 Yokoyama, H. and Sugiyama, K. (2004) *Langmuir*, **20**, 10001–10006.
- 215 Langmuir, I. (1916) *J. Am. Chem. Soc.*, **38**, 2221.
- 216 Pan, F., Wang, P., Lee, K., Wu, A., Turro, N.J. and Koberstein, J.T. (2005) *Langmuir*, **21**, 3605–3612.
- 217 Cresce, A.V., Silverstein, J.S., Bentley, W.E. and Kofinas, P. (2006) *Macromolecules*, **39**, 5826–5829.
- 218 Hayakawa, T., Wang, J., Sundararajan, N., Xiang, M., Li, X., Glusen, B., Leung, G.C., Ueda, M. and Ober, C.K. (2000) *J. Phys. Org. Chem.*, **13**, 787–795.
- 219 Boker, A., Reihns, K., Wang, J., Stadler, R. and Ober, C.K. (2000) *Macromolecules*, **33**, 1310–1320.
- 220 Yang, S., Wang, J., Valiyaveetil, S. and Ober, C.K. (2000) *Chem. Mater.*, **12**, 33–40.
- 221 Sundararajan, N., Yang, S., Ogino, K., Valitaveetil, S., Wang, J., Zhou, X. and Ober, C.K. (2000) *Chem. Mater.*, **12**, 41–48.
- 222 Natansohn, A. and Rochon, P. (2002) *Chem. Rev.*, **102**, 4139.
- 223 Paik, M.Y., Krishnan, S., You, F., Li, X., Hexemer, A., Ando, Y., Ho Kang, S., Fischer, D.A., Kramer, E.J. and Ober, C.K. (2007) *Langmuir*, **23** (9), 5110.
- 224 Moller, G., Harke, M., Motschmann, H. and Prescher, D. (1998) *Langmuir*, **14**, 4955.
- 225 Feng, C.L., Jin, J., Zhang, Y.J., Song, Y.L., Xie, L.Y., Qu, G.R., Xu, Y. and Jiang, L. (2001) *Surf. Interface. Anal.*, **32**, 121.
- 226 Tong, X., Wang, G., Soldera, A. and Zhao, Y. (2005) *J. Phys. Chem.*, **109**, 20281–20287.
- 227 Ravi, P., Sin, S.L., Gan, L.H., Gan, Y.Y., Tam, K.C., Xia, X.L. and Hu, X. (2005) *Polymer*, **46**, 137.
- 228 Yokoyama, M., Inoue, S., Kataoka, K., Yui, N. and Sakurai, Y. (1987) *Makromol. Chem. Rapid Commun.*, **8**, 431–435.
- 229 Kwon, G.S. (1998) *Crit. Rev. Therap. Drug Carr. Sys.*, **15**, 481–512.
- 230 Ashley, J., Bernal, M.P., Burr, G.W., Coufal, H., Guenther, H., Hoffnagle, J.A., Jefferson, C.M., Marcus, B., Macfarlane, R.M., Shelby, R.M. and Sincerbox, G.T. (2000) *IBM J. Res. Dev.*, **44**, 341–368.
- 231 Ikeda, T. and Tsutsumi, O. (1995) *Science*, **268**, 1873–1875.
- 232 Yamamoto, T., Hasegawa, M., Kanazawa, A., Shiono, T. and Ikeda, T. (1999) *J. Phys. Chem. B*, **103**, 9873–9878.
- 233 Frenz, C., Fuchs, A., Schmidt, H.W., Theissen, U. and Haarer, D. (2004) *Macromol. Chem. Phys.*, **205**, 1246–1258.
- 234 Tong, X., Cui, L. and Zhao, Y. (2004) *Macromolecules*, **37**, 3101–3112.
- 235 Hackel, M., Kador, L., Kropp, D., Frenz, C. and Schmidt, H.W. (2005) *Adv. Funct. Mater*, **15**, 1722–1727.
- 236 Kita-Tokarczyk, K., Grumelard, J., Haefele, T. and Meier, W. (2005) *Polymer*, **46**, 3540–3563.
- 237 Liu, J., Sheina, E., Kowalewski, T. and McCullough, R.D. (2002) *Angew. Chem. Int. Ed. Engl.*, **41**, 329–332.
- 238 Li, M., Li, X. and Ober, C.K. (2001) *Polym. Mater. Sci. Eng.*, **84**, 715.
- 239 Hempenius, M.A., Langeveld-Voss, B.M.W., van Haare, J.A.E.H., Janssen, R.A.J., Sheiko, S.S., Spatz, J.P., Moller, M. and Meijer, E.W. (1998) *J. Am. Chem. Soc.*, **120**, 2798–2804.
- 240 Ruokolainen, J., Makinen, R., Torkkeli, M., Makela, T., Serimaa, R., ten Brinke, G. and Ikkala, O. (1998) *Science*, **280**, 557–560.



## 2

# Block Copolymer Nanofibers and Nanotubes

*Guojun Liu*

### 2.1

#### Introduction

Block copolymer nanofibers in this chapter refer to cross-linked cylindrical structures that are made from block copolymers with diameters below 100 nm and lengths up to hundreds of micrometers. Figure 2.1 depicts the structures of nanofibers prepared from an A-B diblock and an A-B-C triblock copolymer, respectively. In the case of diblock nanofibers, either the core or the corona [1, 2] can be cross-linked. Once dried, nanofibers with cross-linked coronas may not re-disperse readily in solvents, the same as for block copolymer nanospheres with cross-linked shells [3]. Hence, our discussion in this chapter will be mainly on diblock nanofibers with cross-linked cores. For nanofibers with cross-linked cores, the soluble corona chains stretch into the solvent phase helping disperse the fibers, and the cross-linked core provides the structural stability. Although the nanofibers are depicted in Figure 2.1 as being rigid and straight, in reality, they can bend or contain kinks.

Three scenarios can be differentiated for triblock nanofibers. In scenario one, the corona block is cross-linked. Again because of dispersibility considerations we have not prepared and studied such fibers. Our focus so far has been on scenario two where the middle layer of the nanofiber is cross-linked. In scenario three, the innermost block is cross-linked. The structure of such a nanofiber bears close resemblance to block copolymer cylindrical brushes [4] when the inner most block is short relative to the other blocks. Block copolymer cylindrical brushes can be obtained by polymerizing a diblock macromer. There have been a number of reports on the properties and applications of block copolymer cylindrical brushes [4]. While this chapter will not go beyond triblock nanofibers, except for one case when nanofibers of a tetrablock copolymer are discussed, the methodologies developed for di- and triblock copolymer nanofiber preparations should apply equally well to a preparation of nanofibers from tetra- and pentablock copolymers and to more complex copolymers.



**Figure 2.1** Structural illustration of a diblock nanofiber (top) and a triblock nanofiber (bottom).



**Figure 2.2** Two configurations for a nanotube.

In principle, nanotubes can be prepared by cross-linking tubular micelles [5–8] of diblock copolymers. The focus of discussion here is, however, on nanotubes derived from triblock copolymers. Two possible configurations for such nanotubes are depicted in Figure 2.2.

In case one, the tubular core is void. Such a nanotube is derived from a triblock nanofiber with a cross-linked intermediate layer by degrading the innermost block [9]. In case two, the tubular core is lined by a polymer. In this instance, a nanotube is derived from a triblock nanofiber with a cross-linked intermediate layer by cleaving pendant groups off the core block [10].

The preparation of block copolymer nanofiber [11] and nanotube [9] structures were only reported for the first time a few years ago. Over the years, there have been reports on the use of block copolymer nanofibers and nanotubes as vehicles for drug delivery [12], as scaffolds for cell growth [13, 14], as precursors for ceramic magnetic nanowires [15, 16] and as precursors for carbon nanofibers [17, 18], etc. While finding novel applications for such structures is of paramount importance, the emphasis of this chapter will be on research undertaken in my group aimed at achieving a fundamental understanding of the physical and chemical properties of these materials. In Section 2.2, the preparation of block copolymer nanofibers and nanotubes will be described and the solution properties of the nanofibers and nanotubes will be discussed in Section 2.3. The different reaction patterns of nanofibers and nanotubes will be examined in Section 2.4. In Section 2.5, some conclusions will be drawn and my perspectives on where block copolymer nanofiber and nanotubes research is going will be presented.

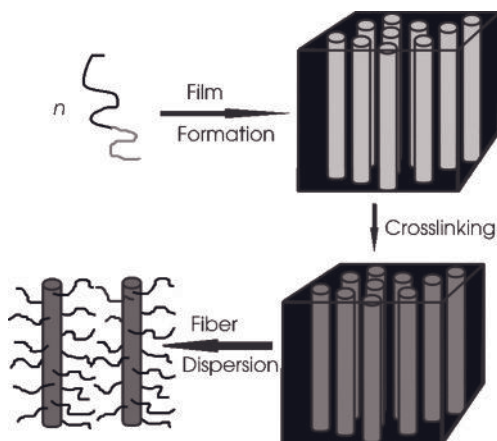
## 2.2 Preparation

### 2.2.1 Nanofiber Preparation

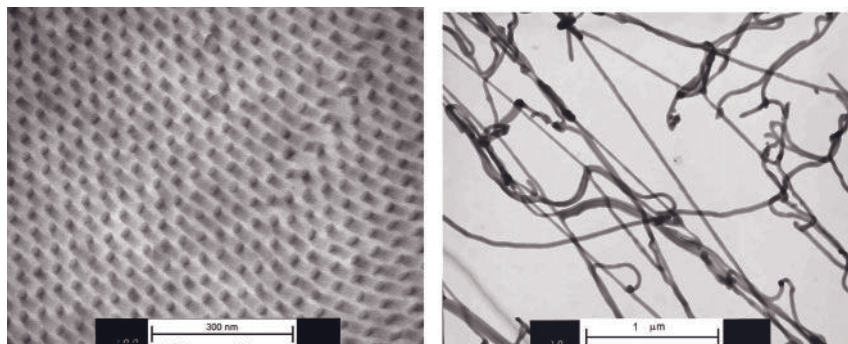
Nanofibers can be prepared from chemically processing either a block-segregated copolymer solid [19] or block copolymer cylindrical micelles [20] formed in a block-selective solvent. Figure 2.3 depicts the processes involved to obtain nanofibers from a block-segregated diblock solid.

The first step involves casting a film from a diblock with an appropriate composition so that the minority block segregates from the majority block forming hexagonally packed cylinders. This is followed by cross-linking the cylindrical domains. The cross-linked cylinders are then levitated from the film or separated from one another by stirring the film in a solvent that solubilizes the uncross-linked diblock.

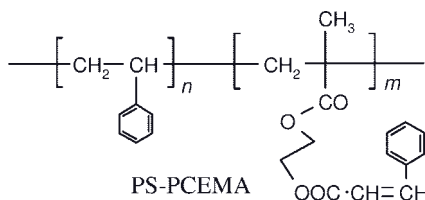
Our literature search revealed that the first report on block copolymer nanofiber synthesis appeared in 1996 [11]. In that report, block-segregated solids of two polystyrene-*block*-poly(2-cinnamoyloxyethyl methacrylate), or PS-PCEMA, samples were used as the precursor. The two PS-PCEMA samples used had 1250 and 160 units of PS and PCEMA for polymer 1 and 780 and 110 for polymer 2, respectively. Thus, the volume fraction of PCEMA was  $\approx 26\%$  in both samples. After film formation from a diblock by evaporating a toluene solution slowly, the film was annealed at  $90^\circ\text{C}$  for days to ensure clean phase segregation between PS and PCEMA. This film was then sectioned by ultra-microtoming to yield thin slices for transmission electron microscopic (TEM) examination. Shown in the left panel of Figure 2.4 is



**Figure 2.3** Schematic illustration of the steps involved in the preparation of diblock copolymer nanofibers from a block-segregated solid.



**Figure 2.4** Left: Thin-section TEM image of a solid  $\text{PS}_{1250}\text{-PCEMA}_{160}$  sample. The dark PCEMA cylinders are slanted diagonally (from bottom right to top left). Right: TEM image of the  $\text{PS}_{1250}\text{-PCEMA}_{160}$  nanofibers on a carbon-coated copper grid aspirated from THF.

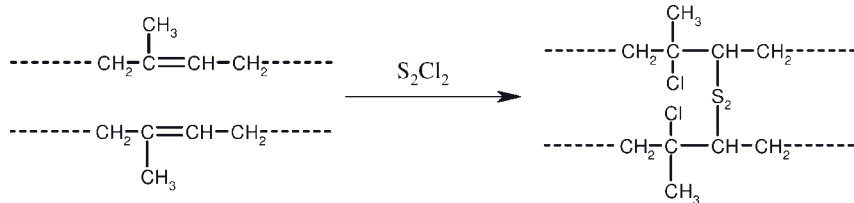


**Scheme 2.1**

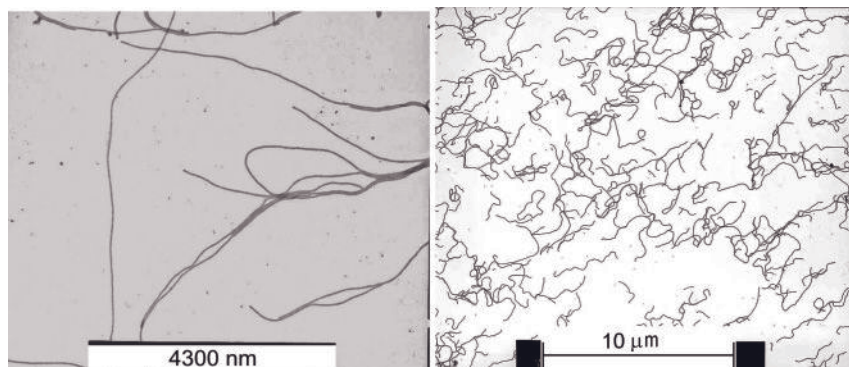
a TEM image of a thin section for polymer 1 or  $\text{PS}_{1250}\text{-PCEMA}_{160}$ , where the subscripts denote the numbers of styrene and CE MA units, respectively (Scheme 2.1). It can be seen that the  $\text{OsO}_4$ -stained dark PCEMA phase consist of hexagonally packed cylinders dispersed in the PS matrix and that the cylinders slant, aligned along a diagonal direction of the image. A similar PCEMA block segregation pattern was found for polymer 2. Such films were then irradiated by UV light to cross-link the PCEMA cylindrical domains. Stirring the irradiated samples in THF helped levitate the cross-linked PCEMA cylinders from the films to yield solvent-dispersible nanofibers. In the right panel, a TEM image of the resultant nanofibers is shown. It can be observed that the fibers in this sample are still entangled.

The groups working with Wiesner [21], Ishizu [22], Muller [23] and my group [24], have also used chemical rather than photochemical methods to cross-link the cylindrical domains of block copolymer solids to prepare nanofibers. To prepare nanofibers from polystyrene-*block*-polyisoprene (PS-PI), we utilized a diblock that had 220 styrene and 140 isoprene units, respectively, which corresponded to a volume fraction of  $\approx 30\%$  for PI. The cylindrical domains were then cross-linked by exposing the film to sulfur monochloride (Scheme 2.2).

Isolated nanofibers were obtained by separating the cross-linked cylindrical domains in THF. The left panel of Figure 2.5 shows a TEM image of such nanofibers.



Scheme 2.2

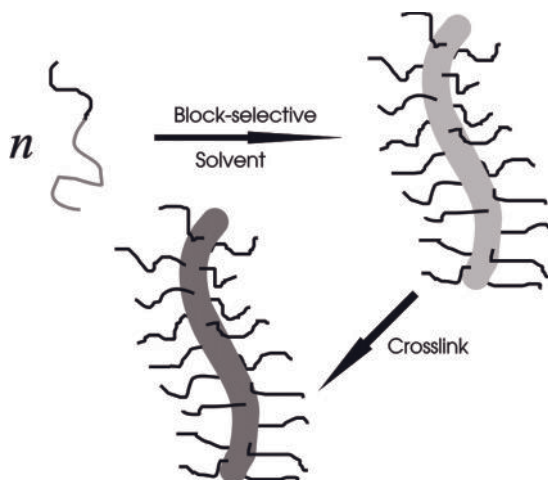


**Figure 2.5** Left: TEM image of PS-PI nanofibers prepared from the cross-linking of block-segregated PS<sub>220</sub>-PI<sub>140</sub> solid. The length of the white box is 4300 nm. Right: TEM image of PS-PI nanofibers prepared from the cross-linking of PS<sub>130</sub>-PI<sub>370</sub> cylindrical micelles.

A drawback with chemical cross-linking of block-segregated solids is the long diffusion time required for the cross-linker to penetrate the film. Insufficient reaction time leads to non-uniform cross-linking with higher degrees of cross-linking found close to the surfaces. Such non-uniform cross-linking can occur with photocross-linking for the short penetration distance of the light. These complications can be avoided by preparing nanofibers starting from block copolymer cylindrical micelles formed in a block-selective solvent.

Figure 2.6 depicts processes involved in preparation of diblock nanofibers starting from cylindrical micelles. Firstly, this requires the preparation of a diblock with an appropriate composition. Then, a selective solvent has to be found that solubilizes only one block of the diblock copolymer. In such a block-selective solvent, the insoluble blocks of different chains aggregate to form a cylindrical core stabilized by chains of the soluble block. Nanofibers are obtained by cross-linking the core chains.

A report on the preparation of block copolymer nanofibers from the cross-linking of cylindrical micelles first appeared in 1997 [25]. The cylindrical micelles were prepared also from PS-PCEMA in refluxing cyclopentane, which solubilized PS and not PCEMA. Nanofibers were obtained after the photocross-linking of the



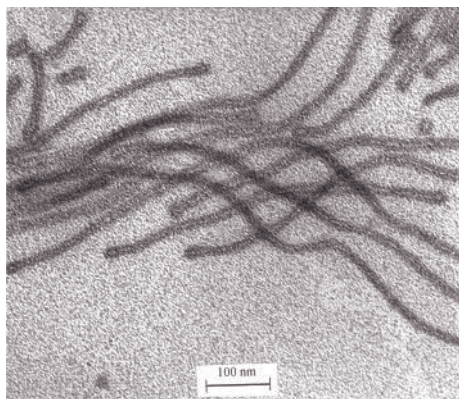
**Figure 2.6** Schematic illustration of the steps involved in the preparation of diblock copolymer nanofibers from cylindrical micelles formed in a block-selective solvent.

PCEMA cores. Aside from photocross-linking, the groups working with Bates [26], Discher [27], Manner [2], Wooley [28] and Stupp [13], in addition to my group [29, 30], have reported on the chemical cross-linking of cylindrical micelles to prepare nanofibers. For example, recently we prepared nanofibers by cross-linking PS-PI cylindrical micelles formed in a block-selective solvent, *N,N*-dimethyl acetamide, for PS [24, 31]. For cylindrical micelle formation with PI as the core, the PI weight fraction should be relatively high. We followed the recipe of Price [32] and used a sample consisting of 130 styrene units and 370 isoprene units. The cylindrical fibers were cross-linked using  $S_2Cl_2$ . The right-hand panel of Figure 2.5 shows a TEM image of such nanofibers. Compared with fibers prepared from the solid-state syntheses described above, the fibers in the right-hand panel of Figure 2.5 are shorter. A more quantitative analysis of the length distributions revealed that the fibers from the solution preparation approach are more monodisperse. Furthermore, the preparation yield can be high, approaching 100%.

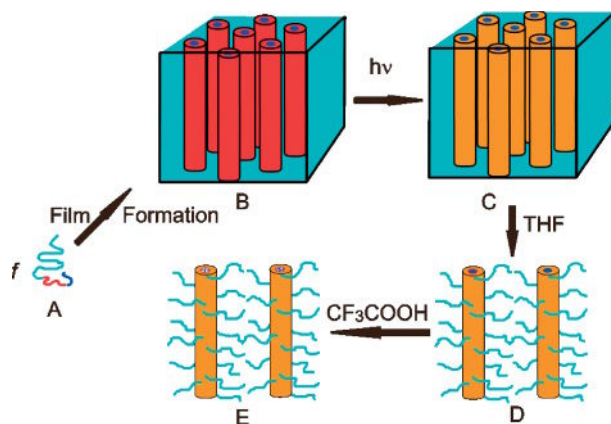
### 2.2.2

#### Nanotube Preparation

Nanotubes have been prepared by my group mainly via the derivatization of triblock nanofibers. The first block copolymer nanotubes were prepared from  $PI_{130}$ -PCEMA<sub>130</sub>-P*t*BA<sub>800</sub> [9], where P*t*BA denotes poly(*tert*-butyl acrylate). This involved firstly dispersing the triblock in methanol. As only the P*t*BA block was soluble in methanol, the triblock self-assembled into cylindrical micelles consisting of a PI core encapsulated in an insoluble PCEMA intermediate layer and a P*t*BA corona. After photocross-linking the PCEMA intermediate layer, the PI core block was



**Figure 2.7** TEM image of PCEMA-PtBA nanotubes where the PI core has been degraded.



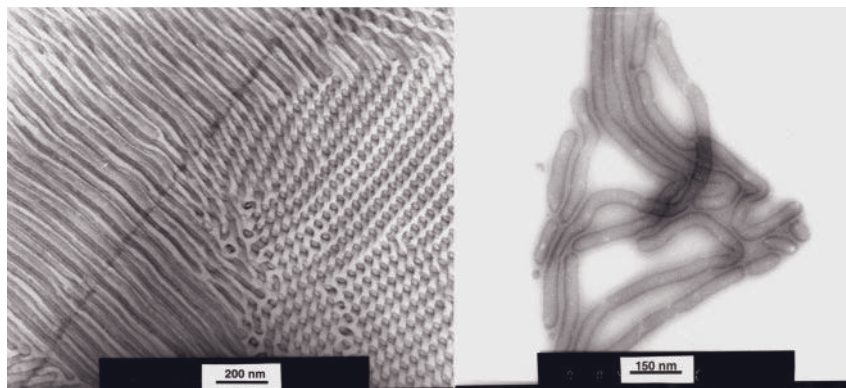
**Figure 2.8** Schematic illustration of processes involved in preparing PS-PCEMA-PAA nanotubes.

degraded by ozonolysis to yield nanotubes. The removal of the PI block was demonstrated by infrared absorption and TEM analyses. More importantly, Rhodamine B could be loaded into the tubular core. Figure 2.7 shows a TEM image of such nanotubes stained by  $\text{OsO}_4$ . The center of each tube appears lighter than the PCEMA intermediate layer because the PI block was decomposed.

To facilitate the incorporation of inorganic species into the tubular core, nanotubes containing PAA-lined cores were more desirable. Figure 2.8 depicts the steps involved in the preparation of PS-PCEMA-PAA nanotubes from  $\text{PS}_{690}\text{-PCEMA}_{170}\text{-PtBA}_{200}$  via a solid-state precursor approach [10].

Step 1 (A  $\rightarrow$  B in Figure 2.8) involved casting films from the triblock containing concentric PtBA and PCEMA core-shell cylinders dispersed in the matrix of PS. This required the PS volume fraction to be  $\approx 70\%$  [33] and was achieved by mixing some PS homopolymers (hPS) with the triblock to increase the PS volume fraction.





**Figure 2.9** Left: TEM image of a thin section of the PS<sub>690</sub>-PCEMA<sub>170</sub>-PtBA<sub>200</sub> solid. Right: TEM image of the PS-PCEMA-PAA nanotubes.

The left-hand panel of Figure 2.9 shows a TEM image of a thin section of an hPS/PS-PCEMA-PtBA solid. On the right-hand side of this image we can see numerous concentric light and dark ellipses with short stems. These represent projections of cylinders with PCEMA shells and PtBA cores aligned slightly off the normal direction of the image. The PCEMA shells appear darker, because OsO<sub>4</sub> stained the PCEMA selectively. The diameter of the PtBA core is  $\approx 20$  nm. On the left of this image we see cylinders lying in the plane of the picture. Thus, the orientation of the cylindrical domains varied from grain to grain, in the micrometer size range, because we did not take special measures to effect their macroscopic alignment.

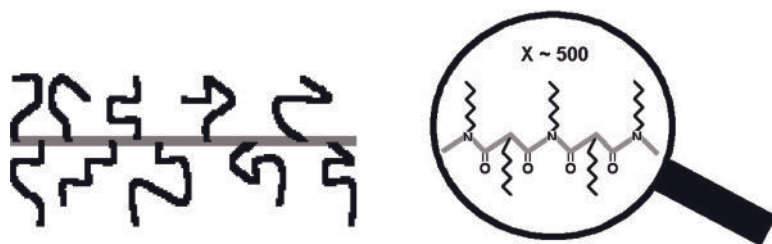
In step 2 (B  $\rightarrow$  C, in Figure 2.8), the block-segregated copolymer film was irradiated with UV light to cross-link the PCEMA shell cylinder. The cross-linked cylinders were levitated from the film by stirring in THF (C  $\rightarrow$  D). PS-PCEMA nanotubes containing PAA-lined tubular cores were prepared by hydrolyzing the PtBA block in methylene chloride and trifluoroacetic acid (D  $\rightarrow$  E). The right-hand panel of Figure 2.9 shows a TEM image of the intestine-like nanotubes. The stained PCEMA layer does not have a uniform diameter across the nanotube length because of its uneven collapse during solvent evaporation. The presence of PAA groups inside the tubular core was demonstrated by our ability to carry out various aqueous reactions inside the tubular core, as will be discussed later.

## 2.3

### Solution Properties

Figure 2.10 shows a comparison between the structures of a PS-PI nanofiber and a poly(*n*-hexyl isocyanate), PHIC, chain. In a PHIC chain, the backbone is made of imide units joined linearly and the hairs are the hexyl groups. Their counterparts in a PS-PI nanofiber are the cross-linked PI cylinder and PS chains, respec-





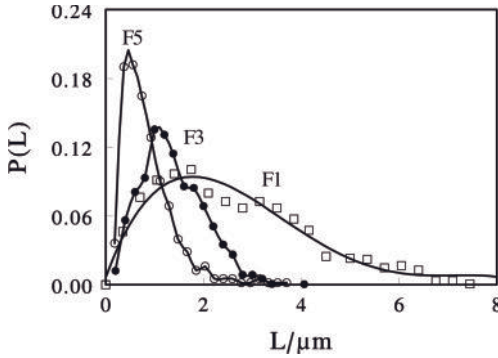
**Figure 2.10** Structural comparison between a PS-PCEMA nanofiber (left) and a PHIC chain (right) at different magnifications.

tively. Other than a large size difference, a nanofiber bears remarkable structural resemblance to PHIC. Thus, block copolymer nanofibers can be viewed as a macroscopic counterpart of a polymer chain or a “suprapolymer” chain or “giant” polymer chain [34]. In this subsection, preliminary results showing the similarities and dissimilarities between the solution properties of polymer chains and diblock nanofibers will be reviewed.

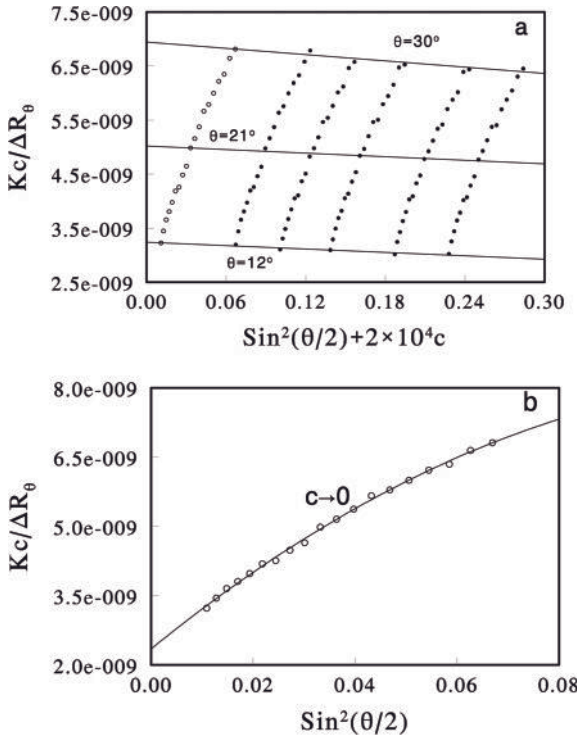
To study the dilute solution properties of nanofibers and polymer chains, the fibers should be made sufficiently short, so that they remain dispersed in the solvent for a long, or even an infinitely long, period of time. The use of relatively short nanofibers also ensured their characterization by classic techniques, such as light scattering (LS) and viscometry. While we have studied nanofibers prepared from several block copolymer families, for clarity, the discussion will be restricted to PS-PI nanofibers obtained by cross-linking cylindrical micelles of PS<sub>130</sub>-PI<sub>370</sub> formed in *N,N*-dimethyl acetamide [24]. The preparation of such fibers has been discussed previously and the right-hand panel of Figure 2.5 shows a TEM image of the nanofibers thus prepared in THE after aspiration onto a carbon-coated copper grid. As the magnification was known for such images, we were able to measure manually the lengths of more than 500 fibers for this sample. The data from such measurements allowed us to construct the length distribution function of this sample denoted as fraction 1 or F1 in Figure 2.11. From the length distribution function, we obtained the weight- and number-average lengths and  $L_w$  and  $L_n$ . The  $L_w$  and  $L_w/L_n$  values are 3490 nm and 1.35 for this sample.

While ultracentrifugation [34] or density gradient centrifugation could have been used, in principle, to separate the fibers into fractions of different lengths, we obtained nanofiber fractions with shorter lengths by breaking up the longer nanofibers by ultrasonication [26]. By adjusting the ultrasonication time, we produced fibers of different lengths. Also shown in Figure 2.11 are the length distribution functions for samples denoted as F3 and F5, which were ultrasonicated for 4 and 20 h, respectively. As ultrasonication time increased, the distribution shifted to shorter lengths.

These fiber fractions were sufficiently short and allowed us to determine their weight-average molar,  $M_w$ , by light scattering. Figure 2.12 shows a Zimm plot

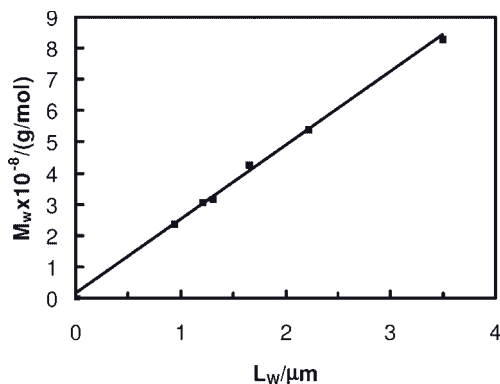


**Figure 2.11** Plot of fiber population density  $P(L)$  versus length  $L$  for  $\text{PS}_{130}\text{-PI}_{370}$  nanofiber fractions 1 ( $\square$ ), 3 ( $\bullet$ ) and 5 ( $\circ$ ) generated from TEM image analysis.



**Figure 2.12** Zimm plot for the light scattering data of F3 in the scattering angle range of 12 to 30°. The solid circles represent the experimental data. The hollow circles represent the extrapolated  $Kc/\Delta R_\theta|_{c \rightarrow 0}$  data.

(a) Linear extrapolation of data to zero concentration at the highest and lowest scattering angles of 30 and 12° is illustrated. (b) The result of curve fitting of the  $Kc/\Delta R_\theta|_{c \rightarrow 0}$  data using Equation (2.1).



**Figure 2.13** Increase in LS  $M_w$  with TEM  $L_w$  for PS<sub>130</sub>-PI<sub>370</sub> nanofiber fractions.

for the light scattering data for sample F3 in the scattering angle,  $\theta$ , range of 12 to 30°.

The data quality appears high. Multiple runs of the same sample indicated that the data precision was high.

For the large-sized fibers, the  $Kc/\Delta R_\theta$  data varied with  $\sin^2(\theta/2)$  or the square of the scattering wave vector  $q$  non-linearly, despite the low angles used. We fitted the data using Equation (2.1):

$$\frac{Kc}{\Delta R_\theta} = \frac{1}{M_w} [1 + (1/3)q^2 R_G^2 - kq^4 R_G^4] + 2A_2c \quad (2.1)$$

and obtained  $M_w$ , the radii of gyration  $R_G$  and the second Virial coefficient  $A_2$  for the different fractions. Figure 2.13 plots the resultant  $M_w$ , versus  $L_w$ , where the values for  $L_w$  were obtained from TEM length distribution functions  $P(L)$ . The linear increase in  $M_w$  with  $L_w$  suggests the validity of the  $M_w$  values determined. The validity of the  $M_w$  value for F3 was further confirmed recently by Professor Chi Wu's group at the Chinese University of Hong Kong, who performed a light scattering analysis of a nanofiber sample down to  $\theta = 7^\circ$ . At such low angles, the  $kq^4 R_G^4$  term in Equation (2.1) was not required for curve fitting and data analysis by the Zimm method should yield accurate  $M_w$  and  $R_G$  values.

After nanofiber characterization, we then proceeded to check the dilute solution viscosity properties. Our experiments indicated that the nanofiber solutions were analogous to polymer solutions and were shear thinning, i.e., the viscosity of a sample decreased with increasing shear rate. This occurred for the alignment of the nanofibers along the shearing direction above a shear rate  $\dot{\gamma}$  of  $\approx 0.1 \text{ s}^{-1}$  [35]. While both nanofiber and polymer solutions are shear thinning, the fields required for shear thinning are dramatically different. Polymers of ordinary molar mass, e.g.  $< 10^6 \text{ g mol}^{-1}$ , would experience shear thinning only if  $\dot{\gamma} \gtrsim 10^{-4} \text{ s}^{-1}$  [36].

The huge difference should be a direct consequence of the drastically different sizes between the two.

To minimize the shear-thinning effect, we measured the viscosities of dilute solutions of the nanofiber fractions in THF using a laboratory-built rotating cylinder viscometer at  $\gamma = 0.082 \text{ s}^{-1}$  [37]. Figure 2.14 shows the  $(\eta_r - 1)/c$  data plotted against nanofiber concentrations  $c$ , where  $\eta_r$ , the relative viscosity, is defined as the ratio between the viscosities of the nanofiber solution and solvent THF. The solid lines represent the best fit to the experimental data by Equation (2.2):

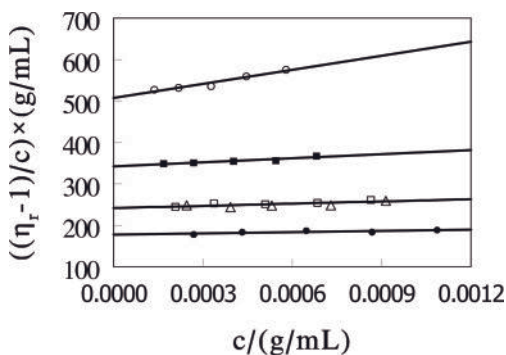
$$(\eta_r - 1)/c = [\eta] + k_h [\eta]^2 c \quad (2.2)$$

where  $[\eta]$  is the intrinsic viscosity and  $k_h$  is the Huggins coefficient. The linear dependence between  $(\eta_r - 1)/c$  and  $c$  is in striking agreement with the behavior of polymer solutions. Even more interesting,  $k_h$  took values mostly between 0.20 and 0.60 in agreement with those found for polymers [36].

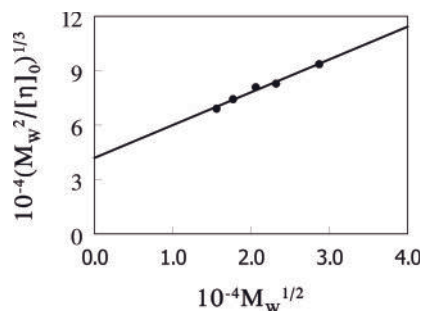
We further treated the  $[\eta]$  data with the Yamakawa–Fujii–Yoshizaki (YFY) theory, originally developed for wormlike chains [38, 39]. According to Bohdanecky [40], the YFY theory could be cast in a much simpler form, Equation (2.3):

$$(M_w^2/[\eta])^{1/3} = A + BM_w^{1/2} \quad (2.3)$$

for chains with a wide range of reduced chain lengths. In Equation (2.3),  $A$  and  $B$  are fitting parameters that are related to the persistence length  $l_p$  and the hydrodynamic diameter  $d_h$  of the chains, respectively. Figure 2.15 shows the data that we obtained for the PS<sub>130</sub>-PI<sub>370</sub> nanofibers in THF plotted following Equation (2.3). From the intercept  $A$  and slope  $B$  of the straight line, we calculated  $l_p$  and  $d_h$  for the nanofibers to be  $(1040 \pm 150)$  and  $(69 \pm 18)$  nm, respectively.



**Figure 2.14** From top to bottom, plot of  $(\eta_r - 1)/c$  versus  $c$  for PS<sub>130</sub>-PI<sub>370</sub> nanofiber fractions 2, 3, 4 and 6 in THF. All the  $\eta_r$  data were obtained using the viscometer at a shear rate of  $0.082 \text{ s}^{-1}$  with the exception of those denoted by  $(\Delta)$ , which were obtained at a shear rate of  $0.047 \text{ s}^{-1}$ .



**Figure 2.15** Nanofiber viscosity data plotted following the Bohdanecky method.

**Table 2.1** Persistence length  $l_p$ , and hydrodynamic diameter  $d_h$  of the nanofibers calculated from the viscosity data for PS<sub>130</sub>-PI<sub>370</sub> nanofiber fractions in various solvents.

Solvent	$d_h/\text{nm}$	$l_p/\text{nm}$
THF	$69 \pm 18$	$1040 \pm 150$
THF – DMF = 50/50	$61 \pm$	$850 \pm 90$
THF – DMF = 30/70	$51 \pm 12$	$830 \pm 60$

This procedure was repeated for the nanofibers in different solvents. Table 2.1 summarizes the  $l_p$  and  $d_h$  values that we determined in three different solvents for the PS<sub>130</sub>-PI<sub>370</sub> nanofibers. The  $d_h$  value in THF compares well with what we estimated from the sum between the diameter of the cross-linked PI core determined from TEM and the root-mean-square end-to-end distance of the PS coronal chains, and thus suggests the applicability of the FYF theory to the nanofiber solutions. What is more convincing is the decreasing trend for the determined  $d_h$  values with increasing DMF content in THF–DMF mixtures. While both THF and DMF solubilize PS,  $d_h$  decreased with increasing DMF content because the extent of swelling for the cross-linked PI core decreased with increasing DMF content.

The  $l_p$  values reported in Table 2.1 are comparable to those reported by Discher and coworkers [41, 42] and by Bates and coworkers [43, 44] for PEO-PI cylindrical micelles with a core diameter of  $\approx 20$  nm prepared in water, where PEO denotes poly(ethylene oxide). While Bates and coworkers deduced the  $l_p$  values from small-angle neutron scattering, Discher and coworkers determined the  $l_p$  values from fluorescence microscopy. In the latter case, they compared the dynamic behavior of single cylindrical micelles before and after PI core cross-linking. After micelle cross-linking, the micelles became much more rigid dynamically, which means that the contour or conformation of the fibers, in contrast to the micelles, changed or flexed very little with time, despite their rotation in space as approximate rigid rotors. By performing a dynamic analysis of the flexion motion by subtracting off the spontaneously curved average shape of the fibers, they concluded that the

*dynamic*  $l_p$  values of the fibers were about 50 times higher than those of the cylindrical micelles. From viscometry, one deduces the *static*  $l_p$  values of the nanofibers, which measure on average how much an ensemble of fibers bends. Therefore, one should not compare the viscometry  $l_p$  values determined by us with those determined by Discher and coworkers, who totally ignored the locked-in curvatures of the fibers in their analysis.

To get a clue to the static  $l_p$  values of the PEO-PI fibers studied by Discher and coworkers, from their fluorescence microscopy images we noticed that the kinks in the original cylindrical micelles were locked in after micelle cross-linking and the fibers assumed conformations similar to those before micelle cross-linking. Thus, the static  $l_p$  values of the nanofibers should be similar to those of the cylindrical micelles. The fact that the  $l_p$  values that we determined from viscometry are comparable to those of the PEO-PI cylindrical micelles with similar core diameters again suggests the validity of the YFY theory in treating the nanofiber viscosity data.

The above study demonstrates that block copolymer nanofibers have dilute solution properties similar to those of polymer chains. In an earlier report [45], we also demonstrated that block copolymer nanofibers have concentrated solution properties similar to those of polymer chains. According to the theories of Onsager [46] and Flory [47], polymer chains with  $l_p/d_h > 6$  would form a liquid crystalline phase above a critical concentration. We did show the presence of such a liquid crystalline phase by polarized optical microscopy for PS-PCEMA nanofibers dissolved in bromoform at concentrations above  $\approx 25$  wt-% [45]. Furthermore, we observed that such liquid crystalline phases disappeared as the temperature was raised and the liquid crystalline to disorder transition was fairly sharp.

While block copolymer nanofibers behave similarly to polymer chains in many aspects, the drastic size difference between the two dictates that they have substantial property differences. Because of the large size of the nanofibers, they obviously move more sluggishly. Hence, we observed that a liquid crystalline phase was formed only after the PS-PCEMA nanofiber solution was sheared mechanically. Also, because of their sluggishness, the liquid crystalline phase could not reform spontaneously after cooling a system if it had been heated above the liquid crystalline to disorder transition temperature. Thus, we can predict, without performing any sophisticated experiments, that the analogy between nanofibers and polymer chains will fail after the molar mass or the size of the nanofibers exceeds a critical value. As the size of the nanofiber increases, the gravitational force driving the settling of the nanofiber increases and the dispersibility of the nanofiber decreases. Furthermore, the van der Waals forces between different nanofibers increase [48], which can cause different nanofibers to cluster and settle.

We recently examined the stability of nanofibers dispersed in THF prepared from PS<sub>130</sub>-PI<sub>370</sub>. This particular nanofiber sample had  $L_w = 1650$  nm,  $L_w/L_n = 1.21$  and  $M_w = 4.3 \times 10^8$  g mol<sup>-1</sup>, respectively. At a concentration of  $\approx 8 \times 10^{-3}$  g mL<sup>-1</sup> and under gentle stirring, no nanofiber settling was observed during 4 days of observation by light scattering. Without stirring, we noticed a 10% decrease in the light

scattering intensity of the solution, which corresponded to  $\approx 10$  wt-% settling of the nanofibers in the first 4 days. No noticeable further settling was observed in another 8 days [24]. This could indicate that the longer fibers in this sample exceeded the critical size for settling. Our light scattering and centrifugation experiments suggested that the longer fibers first clustered and then settled. The fact that the clustering could be prevented by gentle stirring suggests that only a very shallow attraction potential existed between the fibers.

Although the critical length for settling was short for this sample, several micrometers, the critical length depends on many factors including the relative length between the core and soluble block and the absolute diameter of the cores. Methods of increasing the nanofiber dispersity may include increasing the length of the soluble block relative to the core block and decreasing the core diameter.

Because of the differences between the polymer chains and the nanofibers, we expect differences in the performances of these two classes of bulk materials. Unfortunately, the mechanical properties of block copolymer nanofibers or nanofiber composites have not been studied so far. We have not performed any detailed studies of solution properties of block copolymer nanotubes. As a result of the structural similarities between the two, we expect the nanofibers and nanotubes to have many similar solution properties.

## 2.4 Chemical Reactions

The similarities between the structure and the properties of the solutions between nanofibers and polymer chains prompted us to ask the question as to whether nanofibers and nanotubes would have chemical reaction patterns similar to those of polymer chains. A PI chain can be hydrogenated via “backbone modification” to yield a polyolefin chain. Through techniques such as anionic polymerization, etc., one can readily prepare “end-functionalized” polymers. The end-groups can be further derivatized or used for additional end-functionalization. This section will show that block copolymer nanotubes can also undergo backbone modification and end-functionalization.

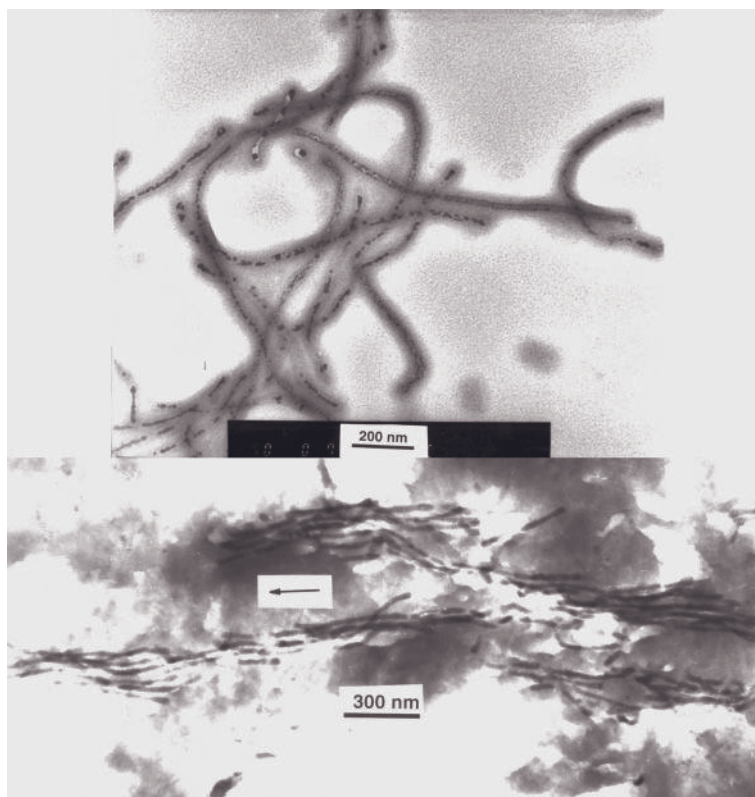
### 2.4.1 Backbone Modification

Backbone modification has already been involved to convert triblock nanofibers into nanotubes. Apart from the performance of organic reactions to the nanofibers and nanotubes, this sub-section discusses the performance of inorganic reactions in the cores of the nanotubes to convert them into polymer–inorganic hybrid nanofibers. Block copolymer nanofibers and nanotubes are soft materials. They will most probably find applications in bio-related disciplines, such as in the medical, pharmaceutical and cosmetic industries. For applications in nanoelectronic devices, polymer–inorganic hybrid nanofibers would be more desirable [49,

50]. The first report on the preparation of block copolymer–inorganic hybrid nanofibers appeared in 2001, which dealt with filling of the core of the PS-PCEMA-PAA nanotubes by  $\gamma\text{-Fe}_2\text{O}_3$  [10].

The preparation first involved the equilibration between the nanotubes and  $\text{FeCl}_2$  in THF.  $\text{Fe(II)}$  entered the nanotube core to bind with the core carboxyl groups. The extraneous  $\text{FeCl}_2$  was then removed by precipitating the  $\text{Fe(II)}$ -containing nanotubes into methanol. Adding  $\text{NaOH}$  dissolved in THF containing 2 vol-% of water precipitated  $\text{Fe(II)}$  trapped in the nanotube core as ferrous oxide. The ferrous oxide was subsequently oxidized to  $\gamma\text{-Fe}_2\text{O}_3$  via the addition of hydrogen peroxide [51]. The top panel in Figure 2.16 shows a TEM image of the hybrid nanofibers. The  $\gamma\text{-Fe}_2\text{O}_3$  particles can be seen to be produced exclusively inside the nanotube cores.

The production of  $\gamma\text{-Fe}_2\text{O}_3$  in the confined space of the “nanotest-tubes” resulted in particles that were nanometer-sized. Hence the particles were superparamag-



**Figure 2.16** Top: TEM image of PS-PCEMA-PAA/ $\text{Fe}_2\text{O}_3$  hybrid nanofibers. Bottom: Bundling and alignment of the nanofibers in a magnetic field. The arrow indicates the magnetic field direction.

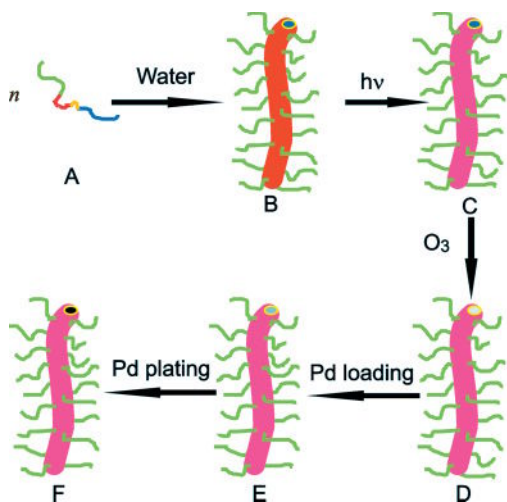


netic, as demonstrated by the results of our magnetic property measurement [10]. This meant that they were magnetized only in the presence of an external magnetic field and were demagnetized when the field was removed. To see how such fibers behaved in a solvent in a magnetic field, we dispersed the fibers in a solvent mixture consisting of THF, styrene, divinylbenzene, and a free radical initiator AIBN. The fiber dispersion was then dispensed into an NMR tube and mounted in the sample holder of an NMR instrument. In the 4.7-T magnetic field of the NMR, the solvent phase was gelled by raising the temperature to 70°C to polymerize styrene and divinylbenzene. Thin sections were obtained from the gelled sample by ultramicrotoming. Shown in the bottom panel of Figure 2.16 is a TEM image of nanofibers in a gelled sample. One consequence of the induced magnetization of the fibers is that they attracted one another and bundled in a magnetic field. Also clear from this image is that the fibers aligned along the magnetic field direction.

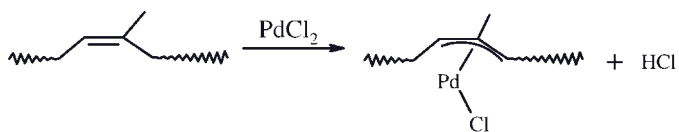
The bundling and alignment of the hybrid nanofibers in a magnetic field have important practical implications. For example, the controlled bundling of several nanofibers may form the basis of magnetic nanomechanical devices. For the construction of water-dispersible magnetic nanomechanical devices, the superparamagnetic nanofibers need to be water dispersible. We recently prepared water-dispersible polymer–Pd hybrid catalytic nanofibers from a tetrablock copolymer [52] and more recently polymer–Pd–Ni superparamagnetic nanofibers from a triblock copolymer [53]. The tetrablock that we used was PI-*Pt*BA-P(CEMA-HEMA)-PGMA, where PGMA, being water soluble, denotes poly(glycerol methacrylate) and P(CEMA-HEMA) denotes a random copolymer of CEMA and 2-hydroxyethyl methacrylate. The hydroxyl groups of the precursory PHEMA block was not fully cinnamated because P(CEMA-HEMA) facilitated the transportation of Pd<sup>2+</sup> and Ni<sup>2+</sup>.

We prepared the polymer–Pd hybrid nanofibers following the scheme depicted in Figure 2.17 [52]. This involved first dispersing freshly-prepared PI-*Pt*BA-P(CEMA-HEMA)-PGMA in water to yield cylindrical aggregates (A → B in Figure 2.17). Such aggregates consisted of a PGMA corona and a PI core. Sandwiched between these two layers are a thin *Pt*BA layer and a P(CEMA-HEMA) layer. Such cylindrical aggregates were then irradiated to cross-link the (CEMA-HEMA) layer (B → C). The PI core was degraded by ozonolysis (C → D). By controlling the ozonolysis time, we could control the degree of PI degradation. When not fully degraded, the residual double bonds of the PI fragments trapped inside the nanotubular core were able to sorb Pd(II), most probably via  $\pi$ -allyl complex formation, Scheme 2.3.

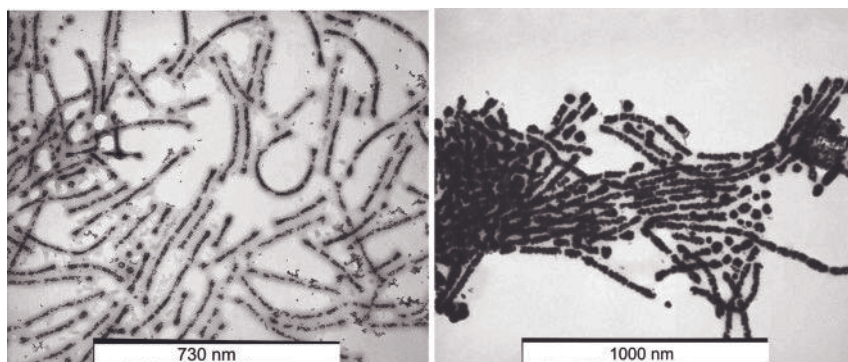
The complexed Pd(II) was then reduced by NaBH<sub>4</sub> to Pd (D → E). The left panel of Figure 2.18 is a TEM image for such nanotubes containing 4.0 wt-% reduced Pd nanoparticles. The Pd-loaded nanofibers were dispersible in water where many water-based electroless plating reactions occur. Thus, Pd could serve as a catalyst for the further electroless deposition of other metals. We, for example, loaded more Pd into the tubular core via electroless Pd plating onto the initially formed Pd nanoparticles to yield essentially continuous Pd nanowires (E → F,



**Figure 2.17** Schematic illustration of the processes involved to produce water-dispersible polymer-Pd hybrid nanofibers.



**Scheme 2.3**



**Figure 2.18** TEM image of nanofibers containing 4 wt-% Pd (left); TEM image of nanofibers containing 18.4 wt-% Pd (right). The scale bars in the form of white boxes are 730 and 1000 nm long, respectively.

Figure 2.17). The right-hand image in Figure 2.18 shows a TEM image of such hybrid nanofibers after the incorporation of Pd to a total of 18.4 wt-%. In fact, we could tune the amount of Pd loaded into the nanotubes by adjusting the relative amounts of the Pd-loaded nanotubes and Pd<sup>2+</sup> in a plating bath. As the Pd content increased, eventually the hybrid fibers could not be dispersed in water. In addition to Pd plating, we have also succeeded in the plating of Ni into the core of such nanotubes, as evidenced by our recent success in preparing water-dispersible triblock-Pd-Ni magnetic nanofibers [53].

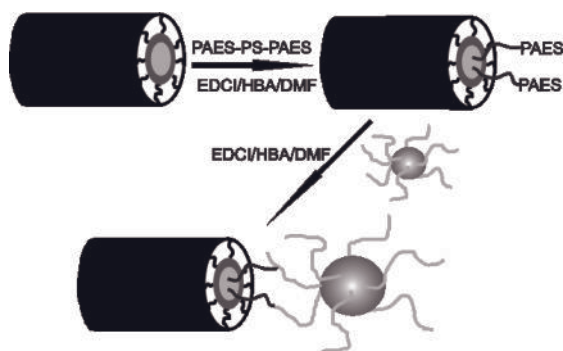
The use of a tetrablock copolymer for the above project seems to be an over kill, as in the end the P*t*BA block was not used at all. This was, however, not by design. Our initial plan was to fully degrade the PI block and then to hydrolyze the P*t*BA block. We planned to introduce Pd(II) via its binding with the carboxyl groups of PAA. The binding between Pd(II) and the residual double bonds of PI was a surprise to us and should be useful in the future as a staining method for PI in the elucidation of complex segregation patterns of block copolymers.

#### 2.4.2

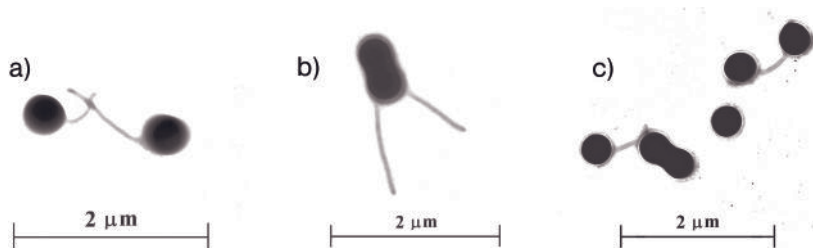
##### End Functionalization

In the “supramolecular chemistry” of nanotubes and nanofibers, the end-functional groups should not be interpreted as the traditional carboxyl or amino groups, etc. Rather, they should be other nano “building blocks”, including nanospheres and nanofibers or nanotubes of a different composition. We first end-functionalized PS-PCEMA-PAA nanotubes by attaching to them water-dispersible PAA-PCEMA nanospheres and spheres bearing surface carboxyl groups that were prepared from emulsion polymerization [54]. Figure 2.19 shows the steps involved in coupling the nanotubes and PCEMA-PAA nanospheres.

To ensure that the PAA core chains were exposed at the ends, we ultrasonicated the pristine nanotubes to shorten them. The carboxyl groups of the nanotubes were then reacted with the amino groups of a triblock PAES-PS-PAES, where PAES denotes poly[4(2-aminoethyl)styrene], in the presence of catalyst 1-[3-



**Figure 2.19** End-functionalization of PS-PCEMA-PAA nanotubes by PAA-PCEMA nanospheres.

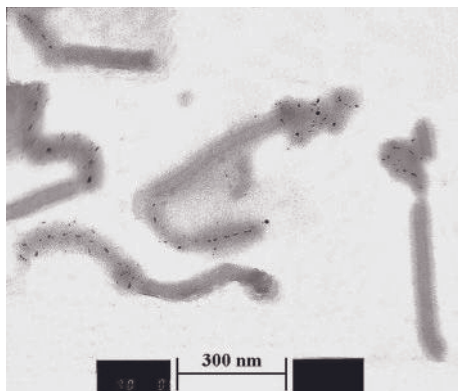


**Figure 2.20** TEM images of nanotube and emulsion nanosphere coupling products.

(dimethyl-amino)propyl]-3-ethylcarbodiimide hydrochloride (EDCI) and co-catalyst 1-hydroxy-benzotriazole (HBA). As PAES-PS-PAES was used in excess, it was grafted onto the nanotubes mainly via one end only. We then purified the sample. Nanotubes bearing terminal PAES chains were subsequently reacted with the carboxyl groups on the surfaces of the nanospheres again using EDCI and HBA as the catalysts. Coupling between the nanotubes and emulsion spheres containing surface carboxyl group was achieved in a similar manner.

Figure 2.20 shows the typical products obtained from coupling the PAES-PS-PAES-treated nanotubes with a batch of emulsion nanospheres bearing surface carboxyl groups. The product in Figure 2.20a resulted from the coupling between one tube and one sphere. As the spherical “head” is water-dispersible and the tube “tail” is hydrophobic, this structure may be viewed as a macroscopic counterpart of a surfactant molecule or a “super-surfactant”. Figure 2.20b shows the attachment of two tubes to one sphere, which had fused with another sphere probably during TEM specimen preparation. “Dumbbell-shaped molecules” were formed from the attachment of one tube to two spheres at the opposite ends, as seen in Figure 2.20c. The products depicted in Figure 2.20a–c co-existed regardless of whether we changed the tube to microsphere mass ratio from 20/1 to 1/20. At the high tube to emulsion sphere mass ratio of 20/1, the super-surfactant and dumbbell-shaped species were the major products. At a mass ratio of 1/1 and 1/20, the dumbbell-shaped product dominated. Other than product control by adjusting the stoichiometry, an effective method to eliminate the dumbbell-shaped product was to use nanotubes labeled at only one end by PAES-PS-PAES. These tubes were obtained by using ultrasonication to break up nanotubes that contained end-grafted PAES-PS-PAES chains. For example, the ultrasonication of the PAES-PS-PAES-grafted nanotubes for 8 h reduced the  $L_w$  of a nanotube sample from 701 to 252 nm and  $L_n$  from 515 to 187 nm. The reaction between the shortened tubes and the nanospheres at a tube to sphere mass ratio of 1/20 yielded almost exclusively the supersurfactant structure with unreacted nanospheres. The content of the multi-armed structure increased as the nanotube to microsphere mass ratio increased.

More recently, we have used the same chemistry to couple PS-PCEMA-PAA nanotubes with PGMA-PCEMA-PAA nanotubes [55]. Figure 2.21 shows the nano-



**Figure 2.21** TEM image of nanotube multiblocks.

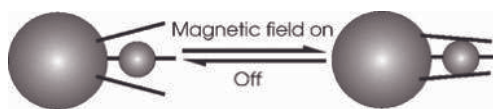
tube multiblocks that we prepared. To facilitate the easy differentiation between the two types of nanotubes, we loaded Pd nanoparticles into the PGMA-PCEMA-PAA nanotubes. Using this method, we succeeded in preparing both nanotube di- and triblocks with structures similar to di- and triblock copolymers. The nanotube multiblocks should self-assemble in a manner similar to the block copolymers.

## 2.5 Concluding Remarks

Block copolymer nanofibers and nanotubes can now be readily prepared with high yields. Such nanofibers have interesting chemical and physical properties. More pressing challenges in this area of research are to find and to realize the commercial applications for these nanostructures. The latter will be greatly facilitated with more participation from industrial partners.

On the fundamental research side, the construction and study of superstructures prepared from the coupling of different nano- and micro-components are a very interesting and promising area of frontier research. The super-surfactants of Figure 2.20a may, for example, self-assemble as do surfactant molecules to form supermicelles or artificial cells, which contain structural order to several length scales. The multi-armed structure of Figure 2.20b and its analogues will be of particular interest if the nanotubes are replaced by PS-PCEMA-PAA/ $\gamma$ -Fe<sub>2</sub>O<sub>3</sub> hybrid nanofibers. Figure 2.22 shows, for example, just such an interesting structure, which can be prepared by attaching three PS-PCEMA-PAA/ $\gamma$ -Fe<sub>2</sub>O<sub>3</sub> hybrid nanofibers to one microsphere.

These fibers will attract one another in a magnetic field due to their magnetization and thus grab a nanoobject. Such a nanoobject can be moved around by focussing a laser beam on the microsphere that is trapped through an optical



**Figure 2.22** Schematic illustration of the operation of an optical magnetic nanohand.

tweezing mechanism. The nanoobject can then be released at a desired spot by turning off the magnetic field. Thus, such a device can function as an “optical magnetic nanohand”. Last but not the least, studies on the concentrated solution properties and nanofiber composite properties should be performed to see if there are any novel desirable applications for these materials.

### Acknowledgements

G. L. is very grateful for financial support from the Natural Sciences and Engineering Research Council of Canada, Defense Research and Development Canada, Canada Research Chairs Program, Canada Foundation for Innovations, Ontario Innovation Trust. G. L. would also like to thank Drs. Xiaohu Yan, Zhao Li, Sean Stewart, Jianfu Ding, and Lijie Qiao for carrying out the work reviewed in this chapter.

This Chapter has been published previously in:  
Lazzari, Massimo / Liu, Guojun / Lecommandoux, Sébastien (eds.)

### Block Copolymers in Nanoscience

2006

ISBN-13: 978-3-527-31309-9-Wiley-VCH, Weinheim

### References

- 1 Wang, X.S., Wang, H., Coombs, N., Winnik, M.A. and Manners, I. (2005) *J. Am. Chem. Soc.*, **127**, 8924–8925.
- 2 Wang, X.S., Arsenault, A., Ozin, G.A., Winnik, M.A. and Manners, I. (2003) *J. Am. Chem. Soc.*, **125**, 12686–12687.
- 3 Ding, J.F. and Liu, G.J. (1998) *Macromolecules*, **31**, 6554–6558.
- 4 Zhang, M.F., Muller, A.H.E. (2005) *J. Polym. Sci. A: Polym. Chem.*, **43**, 3461–3481.
- 5 Yu, K., Zhang, L.F., Eisenberg, A. (1996) *Langmuir*, **12**, 5980–5984.
- 6 Raez, J., Manners, I. and Winnik, M.A. (2002) *J. Am. Chem. Soc.*, **124**, 10381–10395.
- 7 Jenekhe, S.A. and Chen, X.L. (1999) *Science*, **283**, 372–375.
- 8 Grumelard, J., Taubert, A. and Meier, W. (2004) *Chem. Commun.*, 1462–1463.
- 9 Stewart, S. and Liu, G. (2000) *Angew. Chem., Int. Ed. Engl.*, **39**, 340–344.
- 10 Yan, X.H., Liu, G.J., Liu, F.T., Tang, B.Z., Peng, H., Pakhomov, A.B. and Wong, C.Y. (2001) *Angew Chem., Int. Ed. Engl.*, **40**, 3593–3596.

- 11 Liu, G.J., Qiao, L.J. and Guo, A. (1996) *Macromolecules*, **29**, 5508–5510.
- 12 Kim, Y., Dalhaimer, P., Christian, D.A. and Discher, D.E. (2005) *Nanotechnology*, **16**, S484–S491.
- 13 Silva, G.A., Czeisler, C., Niece, K.L., Beniash, E., Harrington, D.A., Kessler, J.A. and Stupp, S.I. (2004) *Science*, **303**, 1352–1355.
- 14 Stupp, S.I. (2005) *MRS Bull.*, **30**, 546–553.
- 15 Massey, J.A., Winnik, M.A., Manners, I., Chan, V.Z.H., Ostermann, J.M., Enchelmaier, R., Spatz, J.P. and Moller, M. (2001) *J. Am. Chem. Soc.*, **123**, 3147–3148.
- 16 Garcia, C.B.W., Zhang, Y.M., Mahajan, S. DiSalvo, F. and Wiesner, U. (2003) *J. Am. Chem. Soc.*, **125**, 13310–13311.
- 17 Kowalewski, T., Tsarevsky, N.V. and Matyjaszewski, K. (2002) *J. Am. Chem. Soc.*, **124**, 10632–10633.
- 18 Tang, C.B., Tracz, A., Kruk, M., Zhang, R., Smilgies, D.M., Matyjaszewski, K. and Kowalewski, T. (2005) *J. Am. Chem. Soc.*, **127**, 6918–6919.
- 19 Bates, F.S. and Fredrickson, G.H. (1999) *Phys. Today*, **52**, 32–38.
- 20 Cameron, N.S., Corbierre, M.K. and Eisenberg, A. (1999) *Can. J. Chem.*, **77**, 1311–1326.
- 21 Templin, M., Franck, A., DuChesne, A., Leist, H., Zhang, Y.M., Ulrich, R., Schadler, V. and Wiesner, U. (1997) *Science*, **278**, 1795–1798.
- 22 Ishizu, K., Ikemoto, T. and Ichimura, A. (1999) *Polymer*, **40**, 3147–3151.
- 23 Liu, Y.F., Abetz, V. and Muller, A.H.E. (2003) *Macromolecules*, **36**, 7894–7898.
- 24 Yan, X., Liu, G. and Li, H. (2004) *Langmuir*, **20**, 4677–4683.
- 25 Tao, J., Stewart, S., Liu, G.J. and Yang, M.L. (1997) *Macromolecules*, **30**, 2738–2745.
- 26 Won, Y.Y., Davis, H.T. and Bates, F.S. (1999) *Science*, **283**, 960–963.
- 27 Dalhaimer, P., Bermudez, H. and Discher, D.E. (2004) *J. Polym. Sci. B: Polym. Phys.*, **42**, 168–176.
- 28 Ma, Q.G., Remsen, E.E., Clark, C.G., Kowalewski, T. and Wooley, K.L. (2002) *Proc. Natl. Acad. Sci. USA*, **99**, 5058–5063.
- 29 Liu, G.J., Li, Z. and Yan, X.H. (2003) *Polymer*, **44**, 7721–7727.
- 30 Yan, X.H. and Liu, G.J. (2004) *Langmuir*, **20**, 4677–4683.
- 31 Liu, G.J. and Zhou, J.Y. (2003) *Macromolecules*, **36**, 5279–5284.
- 32 Price, C. (1983) *Pure Appl. Chem.*, **55**, 1563–1572.
- 33 Breiner, U., Krappe, U., Abetz, V. and Stadler, R. (1997) *Macromol. Chem. Phys.*, **198**, 1051–1083.
- 34 Liu, G.J., Yan, X.H., Qiu, X.P. and Li, Z. (2002) *Macromolecules*, **35**, 7742–7747.
- 35 Liu, G.J., Yan, X.H. and Duncan, S. (2003) *Macromolecules*, **36**, 2049–2054.
- 36 Moore, W.R. (1969) *Progr. Polym. Sci.*, **1**, 3–43.
- 37 Zimm, B.H. and Crothers, D.M. (1962) *Proc. Natl. Acad. Sci. USA*, **48**, 905.
- 38 Yamakawa, H. and Fujii, M. (1974) *Macromolecules*, **7**, 128–135.
- 39 Yamakawa, H. and Yoshizaki, T. (1980) *Macromolecules*, **13**, 633–643.
- 40 Bohdanecky, M. (1983) *Macromolecules*, **16**, 1483–1492.
- 41 Dalhaimer, P., Bates, F.S. and Discher, D.E. (2003) *Macromolecules*, **36**, 6873–6877.
- 42 Geng, Y., Ahmed, F., Bhasin, N. and Discher, D.E. (2005) *J. Phys. Chem. B*, **109**, 3772–3779.
- 43 Won, Y.Y., Davis, H.T., Bates, F.S., Agamalian, M. and Wignall, G.D. (2000) *J. Phys. Chem. B*, **104**, 9054.
- 44 Won, Y.Y., Paso, K., Davis, H.T. and Bates, F.S. (2001) *J. Phys. Chem. B*, **105**, 8302–8311.
- 45 Liu, G.J., Ding, J.F., Qiao, L.J., Guo, A., Dymov, B.P., Gleeson, J.T., Hashimoto, T. and Saijo, K. (1999) *Chem. Eur. J.*, **5**, 2740–2749.
- 46 Onsager, L. (1949) *Ann. N.Y. Acad. Sci.*, **51**, 627–659.
- 47 Flory, P.J. (1956) *Proc. R. Soc. London, Ser. A: Math. Phys. Sci.*, **234**, 73–89.
- 48 Hunter, R.J. (1989) *Foundations of Colloid Science*, Vol. 1, Oxford University Press, Oxford.
- 49 Xia, Y.N., Yang, P.D., Sun, Y.G., Wu, Y.Y., Mayers, B., Gates, B., Yin, Y.D., Kim, F. and Yan, Y.Q. (2003) *Adv. Mater.*, **15**, 353–389.
- 50 Lieber, C.M. (2003) *MRS Bull.*, **28**, 486–491.

- 51 Ziolo, R.F., Giannelis, E.P., Weinstein, B.A., Ohoro, M.P., Ganguly, B.N., Mehrotra, V., Russell, M.W. and Huffman, D.R. (1992) *Science*, **257**, 219–223.
- 52 Li, Z. and Liu, G.J. (2003) *Langmuir*, **19**, 10480–10486.
- 53 Yan, X.H., Liu, G.J., Haeussler, M. and Tang, B.Z. (2005) *Chem. Mater.*, **17**, 6053–6059.
- 54 Liu, G., Yan, X., Li, Z., Zhou, J. and Duncan, S. (2003) *J. Am. Chem. Soc.*, **125**, 14039–14045.
- 55 Yan, X., Liu, G. and Li, Z. (2004) *J. Am. Chem. Soc.*, **126**, 10059–10066.



## 3 Smart Nanoassemblies of Block Copolymers for Drug and Gene Delivery

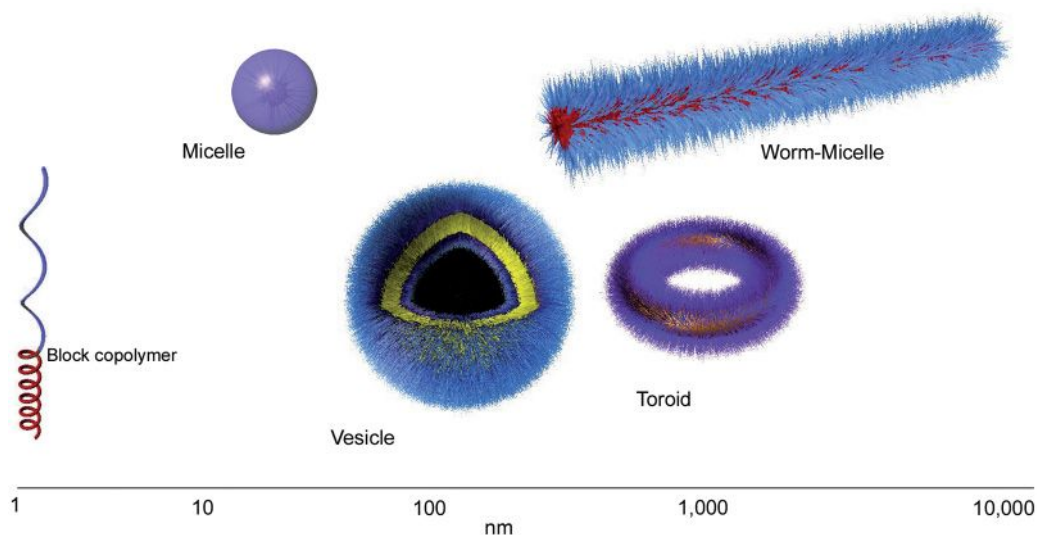
*Horacio Cabral and Kazunori Kataoka*

### 3.1 Introduction

In Nature, various complex architectures are formed from a limited choice of building units such as lipids or amino acids. These natural assemblies form a large variety of biological devices with specific cellular functions. Conversely, synthetic polymers can be prepared from a wide range of monomers, and these macromolecules can construct singular architectures and shapes. The interest in these structures relies on their characteristic sizes in the mesoscopic range (<100 nm), and that their constitution and shape lead to materials with particular properties and functions. Nevertheless, these artificial structures could not yet attain the complexity achieved by the natural assemblies.

One particular example of man-made nanoassemblies is that of block copolymers. The reason for using block copolymeric systems to prepare nanostructures is their simplicity to form nanoscale objects with expected shapes and sizes, without any additional trigger. Block copolymers consist of two or more covalently bonded blocks with different physical and chemical properties. In addition, each block should have the features to control the self-assembly process. The driving force for core-shell-structured self-assembly consists of repulsive interactions between incompatible domains, such as the case of amphiphilic diblock copolymers, which contain a hydrophobic and a hydrophilic block. Moreover, the covalent link between the blocks is responsible for the microphase separation, and prevents the system from further separation on a macroscopic scale. The self-assembled nanostructures can be finely tuned to a variety of morphologies by altering the molecular parameters of the block copolymers or the environment (Figure 3.1). These self-assembled block copolymer systems have already been found to be appropriate for several applications in nanotechnology, including detergents, paints, electronics, cosmetics, lubricants, tissue engineering, and drug delivery, as determined by the morphology of the structures [1–3].

In an attempt to create synthetic structures that somehow approach natural assemblies in terms of their complexity, functionality, and performance,



**Figure 3.1** Block copolymer nanoassemblies. Several structures ranging from 10 nm to 10 000 nm can be formed using block copolymers as the building units.

nanostructures have been designed to respond in a controlled manner to external stimuli. Stimulus-responsive nanostructures, which are also referred to as “smart,” “intelligent”, or “environmentally sensitive” nanostructures, are systems that exhibit sharp changes in response to physical stimuli such as heat, ultrasound, and light, or to chemical stimuli such as pH, ions in solution, and chemical substances. These responses depend on the stimulus applied, and they may comprise modifications in the properties of the assemblies such as shape, volume, and permeation rates.

### 3.2 Smart Nanoassemblies for Drug and Gene Delivery

An “ideal” drug carrier should emulate a system that is capable of residing *in vivo* for long periods of time, targeting particular cell types, incorporating a large set of therapeutic agents, and releasing those molecules in the appropriate environment. Micelles, rods, or polymersomes have been used as carriers of therapeutic agents to target specific sites in the body [3, 4]. Moreover, several micellar delivery systems for anticancer drugs are currently undergoing clinical trials [5]. Rods, threads, and fibers have also been shown to be useful as support media for cell growth *in vitro*, and have been used to direct nerve regrowth *in vivo* or as the basis of more complex mechanical systems [6–8].

Polymeric self-assembled nanostructures have a great potential to reach pathological sites while avoiding biological barriers in the human, due to their nano-

scopic size (typically between 10 and 100 nm). It has been determined that the so-called enhanced permeability and retention (EPR) effect plays a major role in tissue targeting to, for example, tumor tissues [9, 10]. The EPR effect is attributed to the angiogenic tumor vasculature, which has a higher permeability compared to normal tissues due to its discontinuous endothelium, and to the somewhat undeveloped lymphatic drainage in tumors. These characteristics lead to the extravasation of colloidal particles in tumor and other inflamed tissues, and their subsequent retention there. Moreover, the polymeric nanostructures must circulate in the bloodstream for a sufficient time in order to achieve this targeting. Thus, the surface properties of polymeric micelles represent important factors as they determine the biological fate of the material. The reduction of nonspecific recognition and uptake by the reticuloendothelial system (RES) is critical for the prolonged circulation of the carrier. Colloidal carriers bearing hydrophilic polymers on the surface of particles have been shown to reduce the opsonization and subsequent uptake by the RES cells of the liver, spleen, and bone marrow [11–13].

The development of smart nanoassemblies that dynamically morph their properties due to sensitivity to chemical or physical stimuli, magnifies to an even greater extent the significance of block copolymer nanostructures in biological applications. In this way, smart polymeric nanostructures can respond either to pathological or physiological endogenous stimuli present in the body, or to externally applied stimuli such as temperature, light, or ultrasound. One sophisticated and rational approach is a conversion of the core-forming segment of polymeric micelles from a hydrophobic to a more hydrophilic state under a stimulus, which causes an eventual dissolution of the micelles. The therapeutic agent should be stably associated with the hydrophobic core, and release of the drug would be expected to occur along with destabilization of the nanostructure. Irreversible changes in the structure of the nanoassemblies can be induced by cleavage of the covalent bonds, whereas reversible changes can result from changes in hydrogen-bonding capability, in the solubility-temperature of polymers, the protonation, the pH-sensitivity of polymers, and from changes in the redox potential.

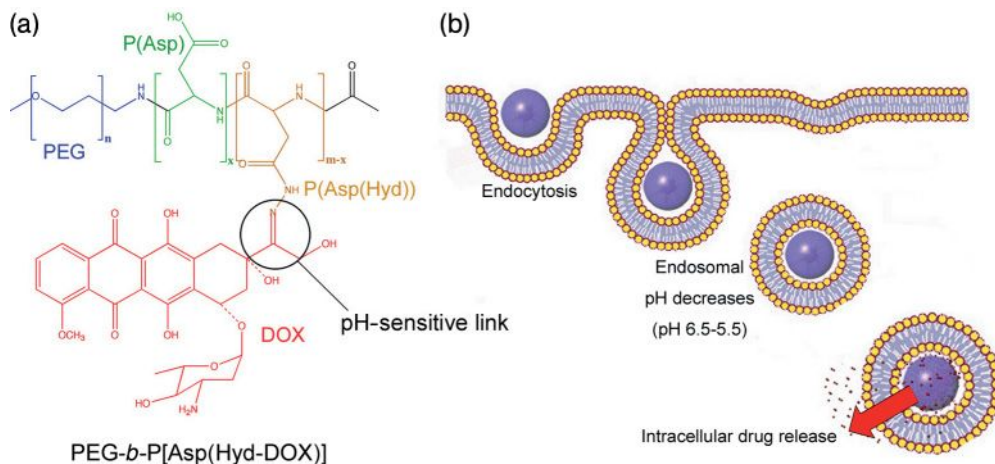
In this chapter we will introduce smart nanoassemblies as applied to drug and gene delivery fields, organized in groups depending on their stimuli sensitivity.

### 3.3 Endogenous Triggers

#### 3.3.1 pH-Sensitive Nanoassemblies

##### 3.3.1.1 Drug Delivery

The mildly acidic pH of solid tumors and inflammatory tissues [14] (pH ~6.8), and the pH of the endosomal and lysosomal compartments of cells [15] (pH 5–6), provides a potential trigger for the release of systemically administered drugs from a pH-sensitive carrier, as blood and normal tissues have a pH of 7.4. Moreover, as macromolecular carriers enter the cells via endocytosis and are localized in



**Figure 3.2** PEG-P(ASP(Hyd))/DOX conjugate forming pH-sensitive micelles. At endosomal pH, the micelles release DOX molecules [17].

the endosomes or in the lysosomes [16], the pH represents a very useful stimulus for the design of drug carriers that release their contents only within the intracellular environment. Conversely, drug-loaded nanoassemblies that are stable at low pH (i.e., in the stomach) and degrade at near-physiological pH (i.e., in the intestines) are very attractive for controlled drug release following their oral administration.

pH-sensitive nanoassemblies can be constructed by the use of an acid-labile bond between the drug and the carrier polymer. As drug release is dependent on the chemical or enzymatic hydrolysis of the bond between the drug and the polymer backbone, drug release from these nanoconstructs is usually slower than that of physically loaded drugs. Recently, pH-sensitive doxorubicin (DOX)-loaded polymeric micelles were prepared by chemically conjugating DOX to the side chain of poly(ethylene glycol)-*b*-poly(aspartic acid) (PEG-*b*-P(Asp)) copolymers via an acid-labile hydrazone bond (Figure 3.2) [17]. These micelles specifically released DOX at endosomal pH conditions (pH 5.0), whereas DOX was retained in the micelle core at physiological pH. These pH-sensitive DOX micelles were very effective against subcutaneous murine colon adenocarcinoma 26 *in vivo*, while their toxicity proved to be negligible due to minimal drug leakage [18].

Gillies *et al.* reported the construction of PEG-*b*-P(Asp) functionalized with trimethoxybenzylidene acetals as acid-labile linkages [19]. The cyclic benzylidene acetals and the copolymer backbone increased the hydrophobicity of the core due to the aromatic rings, while the acetal groups hid the polarity of the diol. Although these micelles were relatively stable at physiological pH, hydrolysis of the acetal bonds occurred at pH 5. In addition, the generation of diols increased the hydrophilicity of the polymers. During this process, disassembly of the micelles occurred as the hydrophobic dye was released.

Protonation of the block copolymer backbone can also trigger destabilization of the micelles. Block copolymers with such characteristics normally contain L-histidine [20, 21], pyridine [22], and tertiary amine groups in their hydrophobic segments [23]. In these systems, polymeric micelles are formed at a pH above the  $pK_a$  of the protonatable group, and therefore the hydrophobic segment essentially is uncharged. As the pH falls below the  $pK_a$ , however, ionization of the polymer causes increased hydrophilicity and electrostatic repulsions of the polymers, leading to destabilization of the micelles. In this way, PEG-*b*-poly(L-histidine) (PEG-*b*-P(His)) was used to prepare pH-sensitive polymeric micelles incorporating DOX [20]. The prepared micelles showed an accelerated release of drug as the pH was decreased, with ionization of the P(His) block forming the micelle core determining the pH-dependent critical micelle concentration (CMC) and stability of the system. Moreover, control of the transition pH is possible by combining different block copolymers. In light of these findings, Lee *et al.* prepared mixed micelles from PEG-*b*-P(His) and PEG-*b*-poly(lactic acid) (PEG-*b*-PLA) [21]. The PEG-*b*-P(His) micelles destabilized at physiological pH, whereas the mixed polymeric micelles of PEG-*b*-P(His) and PEG-*b*-PLA showed improved micellar stability at pH 7.4 and dissociated over a pH range of 6.0 to 7.2, depending on the proportion of PEG-*b*-PLA present. Similar pH-sensitive mixed micelles were prepared from biotin-P(His)-*b*-PEG-*b*-PLLA (poly(L-lactic acid)) and PEG-*b*-P(His). At pH >7, the P(His) attached to the biotin was mostly deionized and became hydrophobic, thus interacting with the micellar PLA core. However, as the pH was slowly decreased the P(His) segments became progressively ionized and extended outwards through the polyethylene (PEG) brush surrounding the core, thus exposing the biotin moieties for ligand–receptor interactions. At pH values <6.5, protonation of P(His) in the PEG-*b*-P(His) block copolymer contained in the core caused the induction of micellar dissociation.

The above-described pH-sensitive nanoassemblies release their contents after dissociation of the micelles. However, a different type of pH-sensitive nanoassembly was designed to release the encapsulated contents after aggregation or collapse of the nanoassemblies. As an example, Leroux *et al.* prepared random copolymers of *N*-isopropylacrylamide (NIPAAm) and methacrylic acid (MAA) substituted with alkyl chains at either the terminal chain ends, or distributed randomly over the copolymer chain to induce micelle formation [24]. When chloroaluminum phthalocyanine (AlClPc), a widely used photosensitizer for the photodynamic treatment of cancer, was incorporated into these micelles [25], the addition of 5 mol% MAA to the copolymers caused the hydrophobic core to distort following neutralization of the MAA as the pH fell below 5.7–5.8 at 37 °C. This phenomenon was thought to cause the release of the entrapped photosensitizer and to alter the intracellular localization of the drug in a favorable way, making it more photoactive.

Smart polymeric micelles may also represent a promising approach for the oral delivery of hydrophobic drug molecules. Sant *et al.* developed pH-sensitive micelles composed of block copolymers of PEG as the hydrophilic block and poly(alkyl acrylate-*co*-methacrylic acid) [PEG-*b*-(PAA-*co*-MAA)] [26]. Due to the presence of

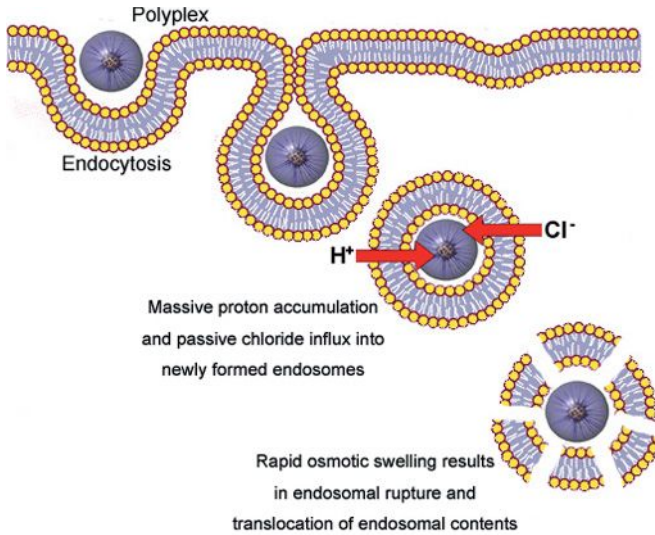
pendant carboxylic groups on the MAA segments in the core, the copolymers self-assembled at pH <4.7, whereas, above this value the micelles dissociated owing to ionization of the COOH moieties. The pH at which micellization occurred was decreased with a reduction in the length of the hydrophobic block. Three poorly water-soluble drugs, namely indomethacin, fenofibrate, and progesterone, were successfully loaded into these micelles. It was also possible to trigger drug release in a pH-dependent manner by changing the pH of the release medium from 1.2 to 7.2; this clearly demonstrated the potential of pH-responsive polymeric micelles for targeting drugs to the intestine following oral administration.

### 3.3.1.2 Gene Delivery

Gene therapy refers to the potential use of nucleic acids, irrespective of whether this involves plasmid DNA, antisense oligonucleotides or siRNA, to modulate the expression of genes in cells for therapeutic purposes. Among the highlights of gene therapy are:

- The replacement of a deficient gene in a genetically inherited disease, with a normal copy restoring the production of a functional protein.
- The correction of genetic defects beyond inherited disorders, as modulation of the regulation of gene expression is involved in numerous acquired diseases.
- The integration of functions in cells that are not originally present, and which could serve a therapeutic purpose.

Gene delivery may be divided into two main categories, depending on the vectors used for nucleic acid transfer, namely *viral* and *nonviral*. The first vectors to be developed were based on the use of viruses or pseudoviral particles. Viral vectors may pose serious problems in terms of immunogenicity, toxicity and potential oncogenicity, thus risking their use as therapeutic drugs [27]. Nonviral gene delivery involves the use of cationic lipids and cationic polymers to deliver the genes. Synthetic self-assembled gene vectors based on cationic polymers, termed polyplexes, are considerably safer and easier to produce. Polyplexes have also been progressively ameliorated as gene vectors, and specific DNA delivery to several tissues has been achieved *in vivo* by using either systemic or localized delivery [28]. Cationic polymers mask the negative charge of the plasmid DNA (pDNA) and package it into small particles, thus protecting the pDNA from both enzymatic and hydrolytic degradation [29–31]. Polycations with a relatively low  $pK_a$  value, such as poly(ethylenimine) (PEI), present a high transfection activity, most likely because they buffer the endosomal acidification and produce an increase in the ion osmotic pressure in endosomes. This is followed by protonation of the amines, which leads in turn to a disruption of the endosomal membranes and release of the endosomal contents into the cytoplasm. This whole process is referred to as the “proton-sponge effect” (Figure 3.3) [32]. Such polycations require a high ratio of cationic amino groups in the polycations to phosphate anions in the DNA (N/P ratio), in order to form a polyplex which has a high stability and efficient transfection activity. Moreover, although free PEI contributes to the increased gene expression, it also produces a considerable increase in the toxicity of the carrier [33].



**Figure 3.3** The “proton sponge effect.” Polyplexes containing weak base components buffer the endosomal acidification and produce an increase in the ion osmotic

pressure in endosomes; this leads to disruption of the endosomal membranes. Finally, the endosomal contents are delivered into the cytoplasm.

Conversely, polycations with a  $pK_a > 9.0$ , such as poly(L-lysine) (P(Lys)), form stable polyplexes even at a relatively lower N/P ratios [34]. The introduction of buffering units into a polycation with high  $pK_a$  value improves the transfection efficiency based on the proton-sponge effect, but decreases the stability of the complex due to a lower affinity towards DNA [35]. The buffering capacity of these units is also lessened due to protonation of the polycations following their complexation with DNA. Thus, as the efficiencies of the polyplexes are still too low for clinical use, the next crucial point of gene delivery will be to construct virus-like polyplexes using smart polymer conjugates. By using that approach, the creation of effective gene vectors for clinical applications should resolve the problems of poor stability and high toxicity of the current polyplexes, and also provide the buffering capacity to enhance transfection, without an excess of free polymers.

It is essential that the smart gene nanostructures recognize the biological signals and undergo designed structural changes which match the different steps of gene delivery. In this respect, Oishi *et al.* reported the creation of hepatocyte-targeted polyion complex (PIC) micelles with a pH-sensitive PEG shell as a smart delivery system for antisense oligodeoxynucleotides (ODNs) [36]. These PIC micelles were prepared from P(Lys) and a lactosylated PEG-ODN conjugate (Lac-PEG-ODN), which had an acid-labile linkage ( $\beta$ -thiopropionate) between the PEG and ODN segments. The lactose-PIC micelles achieved an elevated antisense effect against luciferase gene expression in human hepatoma (HuH-7) cells, this being significantly higher than that produced by either ODN or Lac-PEG-ODN alone,

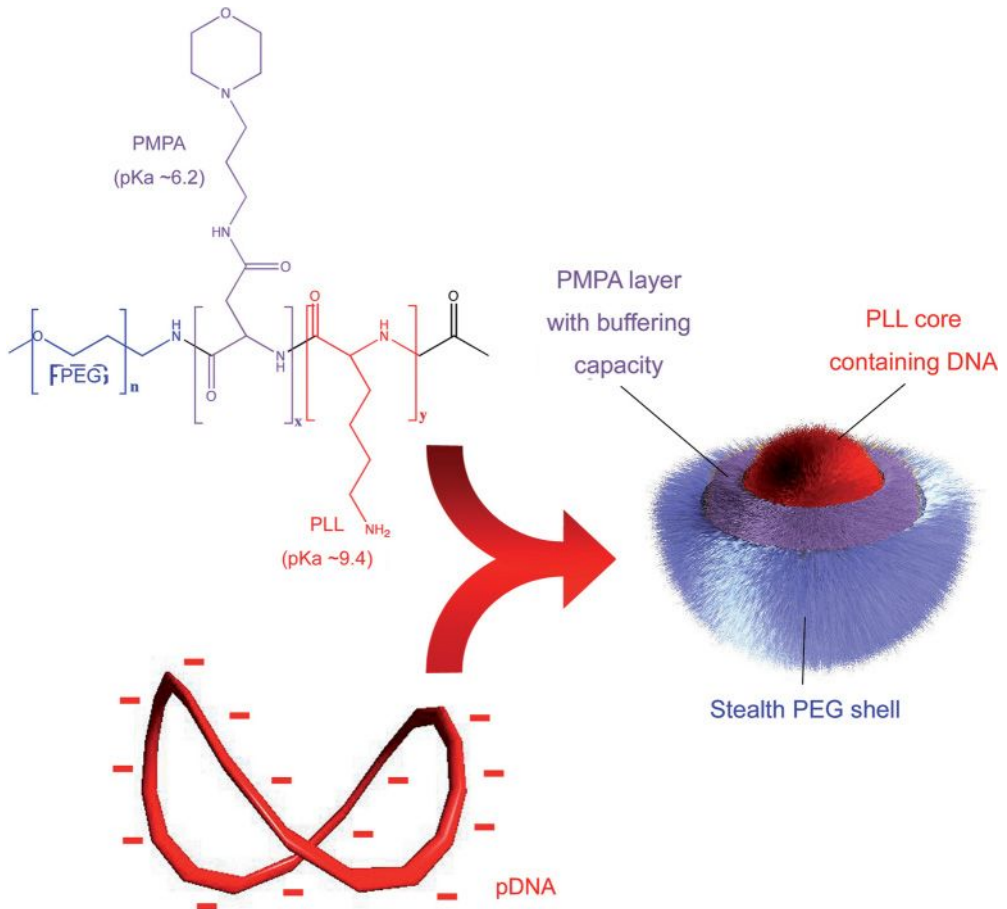


and also the lactose-free PIC micelle, most likely due to an asialoglycoprotein receptor-mediated endocytosis process. In addition, a significant decrease in the antisense effect was observed for a lactosylated PIC micelle without the acid-labile linkage. This suggested that the pH-sensitive release of the active antisense ODN molecules into the cytoplasm is a key event in the antisense effect of this micelle. Conversely, the use of a polycation with low  $pK_a$ , such as branched PEI instead of the P(Lys), to prepare the PIC micelle led to a decrease in the antisense effect, most likely due to a buffer effect of the branched PEI in the endosomal compartment that prevented cleavage of the acid-labile linkage in the conjugate.

Another approach for developing a smart gene delivery system consists of an A–B–C-type triblock copolymer using a biocompatible fragment in the A-fragment, a polycation with low  $pK_a$  value and buffering effect as the B-fragment, and a polycation with high  $pK_a$  to condense the DNA as the C-fragment. Fukushima *et al.* showed that PEG-*b*-poly[(3-morpholinopropyl) aspartamide] (PMPA;  $pK_a = 6.2$ )-*b*-P(Lys) (PEG-*b*-PMPA-*b*-P(Lys)) formed smart PIC micelles where the P(Lys) backbone condensed DNA and the uncomplexed PMPA backbone covered the P(Lys)/DNA polyplex core (Figure 3.4) [37]. These PIC micelles had a diameter of 88.7 nm, a zeta potential of 7.3 mV, and exhibited much higher transfection efficiency against HuH-7 cells than did micelles prepared from PEG-*b*-PLL (poly(lactic acid)) or the combination of PEG-*b*-PLL and PEG-*b*-PMPA. The improvement in transfection efficiency of these three-layered polyplex micelles can be related to the buffering capacity of the PMPA segment in the polyplex micelle. Nevertheless, positively charged polyplexes might potentially induce cytotoxicity and form aggregates with the plasma proteins present in the biological media, thus restricting their *in vivo* applicability. In order to overcome this problem, two strategies have been followed:

- The first approach consists of using a block copolymer of a PEG segment and a cationic polyaspartamide segment carrying an ethylenediamine unit at the side chain (PEG-*b*-P[Asp(DET)]) (Figure 3.5) [38]. This block copolymer led to the formation of stable polyplexes with a core of tightly packed pDNA. Ethylenediamine undergoes a clear, two-step protonation with a characteristic *gauche–anti* conformational transition providing an effective buffering function in the acidic endosomal compartment. Thus, after endocytosis of these polyplexes, the ethylenediamine unit in the block copolymer is expected to facilitate the efficient translocation of the micelle towards the cytoplasm due to the proton-sponge effect. The PIC micelles prepared from PEG-*b*-P[Asp(DET)] accomplished an appreciably high gene transfection efficacy and a remarkably low cytotoxicity against several cell lines, including primary osteoblasts. Moreover, these polyplexes showed a high efficiency *in vivo* for the treatment of vascular lesions, with markedly reduced cytotoxicity and thrombogenicity [39].
- A second approach was proposed by Lee *et al.* using polymeric micelles of PEG-*b*-poly[(*N'*-citraconyl-2-aminoethyl)aspartamide] (PEG-*b*-P(Asp(EDA-Cit))) [40]. This block copolymer has the ability to switch the charge from anionic to cationic at the endosomal pH due to degradation of the citraconic amide side chain at pH 5.5. This rapid charge-conversion can cause the PIC micelles to





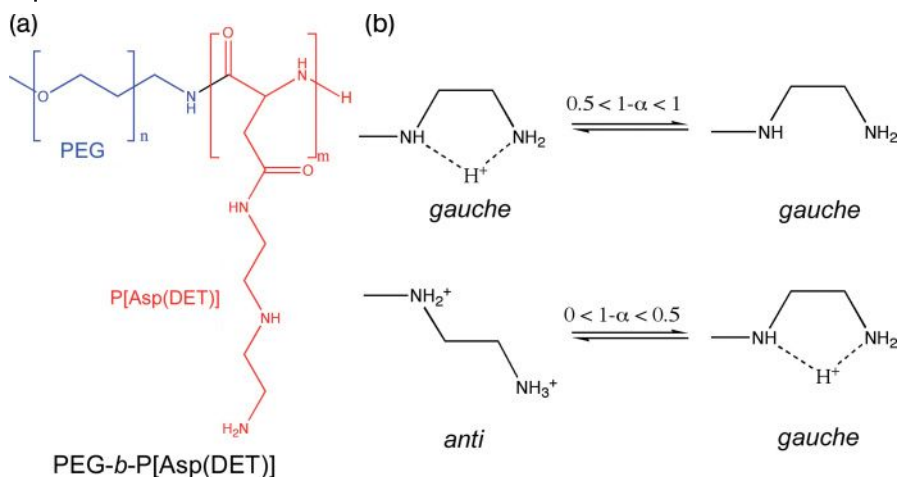
**Figure 3.4** Chemical structure of the PEG-PMPA-PLL triblock copolymer, and schematic illustration of the three-layered polyplex micelles with spatially regulated structure [37].

promptly release the loaded protein in response to the endosomal pH. Consequently, this pH-sensitive charge-conversion polymer has shown great promise for the design of gene carriers that become cationic at the early endosomal stage, yet still have the ability to achieve endosomal escape due to the proton-sponge effect.

### 3.3.2

#### Oxidation- and Reduction-Sensitive Polymeric Nanoassemblies

Redox-sensitive nanostructures from block copolymers can result in a change of the assembly morphology and the selective release of encapsulated drugs when an electric current is applied externally. Moreover, the redox-triggering can occur

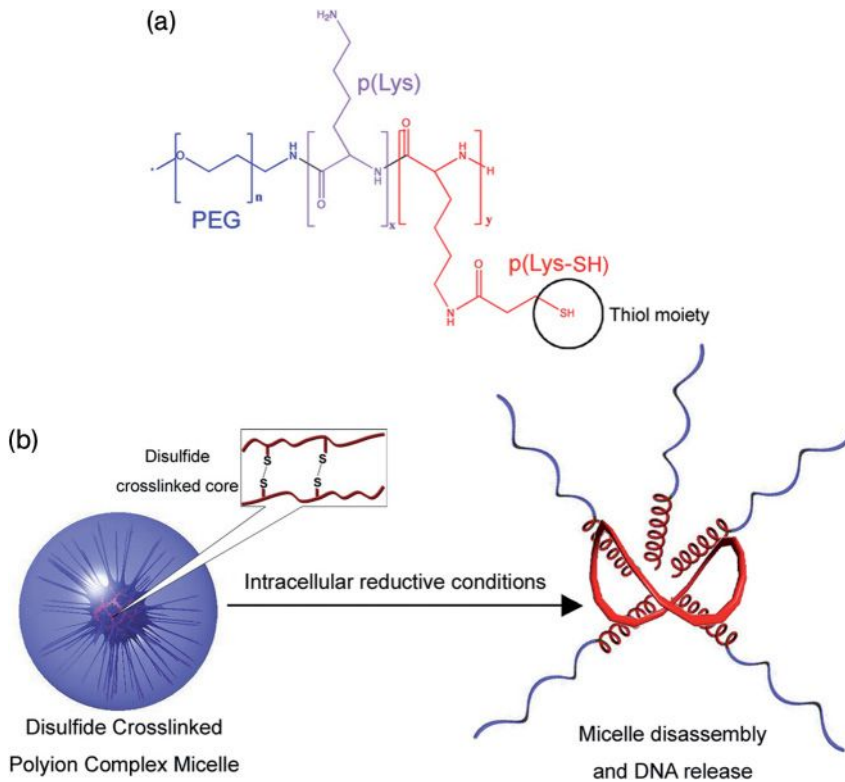


**Figure 3.5** (a) PEG-*b*-P[Asp(DET)] copolymer bearing an ethylenediamine unit at the side chain leads to the formation of stable polyplexes with smart buffering properties; (b) Ethylenediamine presents a two-step

protonation with a unique *gauche*–*anti* conformational transition providing an effective buffering function at the endosome. The proton-free form may take both *gauche* and *anti* conformation [38].

at inflammation sites and solid tumors, since those pathologies present activated macrophages that release oxygen-reactive species. Hubbell *et al.* synthesized amphiphilic A–B–A block copolymers which consisted of the hydrophobic poly(propylene sulfide) and PEG (PEG-*b*-PPS-*b*-PEG), which formed polymeric vesicles in water [41]. Following exposure of these vesicles to oxidative agents, the thioethers in the PPS block were oxidized to poly(propylene sulfoxide) and eventually to poly(propylene sulfone), leading in turn to hydrophilization of the originally hydrophobic block. As a result, the vesicles became destabilized. This oxidative conversion was also accomplished by incorporating glucose oxidase (GOx) into the vesicles [42]. After incubation in 0.1 M glucose solution, the GOx-containing polymeric vesicles were disassembled due to the oxidation of glucose by GOx to produce H<sub>2</sub>O<sub>2</sub>. Another possibility would be to take advantage of the redox tunability of metal-containing compounds. In this way, redox-active micelles were prepared from amphiphilic block copolymers bearing a hydrophobic ferrocenylalkyl moiety (FPEG) [43]. Oxidation of the ferrocenyl moiety caused the micelles to be disrupted into unimers. However, when loaded with perylene, these redox-active FPEG micelles released the drug in a controlled manner by applying a selective and electrochemical oxidation of the FPEG.

Another type of reduction-sensitive nanostructures is represented by polymeric assemblies containing disulfide bonds. Polyplex micelles with a disulfide-crosslinked core efficiently release the loaded pDNA in response to reductive intracellular conditions; that is, at 50- to 1000-fold higher glutathione concentrations than are encountered in the extracellular environment (Figure 3.6) [44–47].



**Figure 3.6** Disulfide crosslinking is used to stabilize PIC micelles. (a) Molecular structure of the PEG-P(Lysine-SH) block copolymer; (b) Under intracellular reductive conditions, the disulfide bonds are cleaved and the PIC micelles release their contents.

The intracellular glutathione reductively cleaves the disulfide links, which leads to a destabilization of the system. This type of micelle also achieved sufficient tolerability against destabilization by anionically charged biocomponents, and induced an efficient transfection in the cell. As a result, the transfection efficiencies achieved *in vivo* were relatively high [47].

### 3.3.3

#### Other Endogenous Triggers

Several other internal triggers, including enzymes or peptides, can be used to control the structure and properties of smart block copolymer nanoassemblies. The construction of smart polyplexes with two types of gene-transfection activation has been reported [48]. These systems utilize cationic polymers which are responsive to cyclic AMP-dependent protein kinase A (PKA) or to caspase-3, PAK, and

PAC, respectively. The PAK polymer incorporates a substrate for PKA, ARRASLG, while the PAC polymer has a substrate sequence for caspase-3, DEVD, and a cationic oligolysine, KKKKKK. These polymers formed stable complexes with DNA. However, the PKA or caspase-3 signal breaks up the PAK–DNA or PAC–DNA complexes, respectively, releasing the DNA and activating the gene transfection activity.

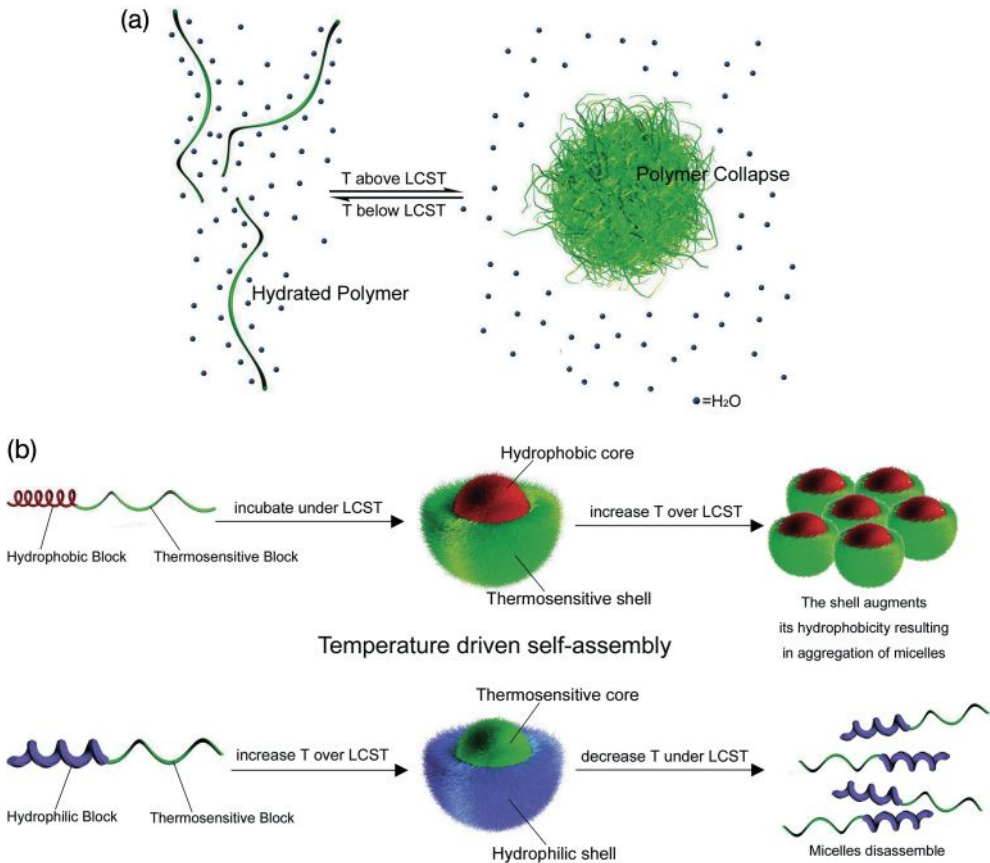
### 3.4

#### External Stimuli

##### 3.4.1

##### Temperature

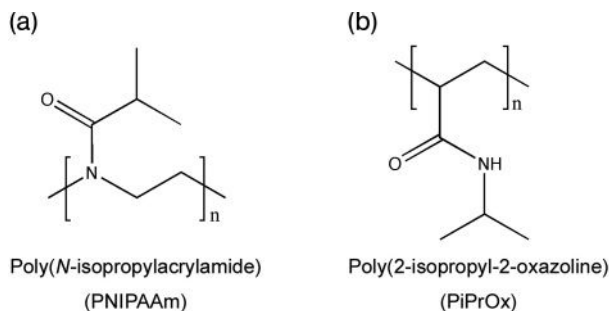
As local heating can also be exploited to destabilize smart nanoassemblies, several thermosensitive copolymers that use this approach are currently undergoing investigation for biomedical applications. The thermosensitive nanoassemblies are characterized by a lower critical solution temperature (LCST), below which water is bound to the thermosensitive polymer block so as to prevent both intrapolymer and interpolymer interactions, thus rendering the nanoassembly water-soluble. Whilst the formation of hydrogen bonds between the thermosensitive polymer and water lowers the free energy of mixing, the ordered molecular orientations of water on the polymer lead to negative entropy changes and positive contributions to free energy. The nonpolar hydrophobic groups in the thermosensitive polymer are incompatible with water, and facilitate an ordered clustering of the surrounding water molecules so as to decrease the entropy. Increasing the temperature of the system causes the water cluster to become destabilized to compensate the thermal energy. Above the LCST, water is released from the polymer chain (Figure 3.7a). The positive entropic contribution then grows and dominates the heat term, which causes the monophasic system to become unbalanced and leads to phase separation due to polymer association. To date, the most extensively investigated thermosensitive polymer is poly(*N*-isopropylacrylamide) (PNIPAAm; Figure 3.8a); this molecule has a sharp LCST in water at approximately 32°C (slightly lower than body temperature), which makes it extremely attractive for the design of thermosensitive drug delivery systems [49]. The LCST of a thermosensitive polymer can also be modulated by copolymerizing it with hydrophobic comonomers to reduce the LCST, or with hydrophilic comonomers to increase the LCST. PNIPAAm copolymers may be used either as a hydrophilic segment or as a hydrophobic segment of polymeric micelles, switching the dispersivity depending on the LCST (Figure 3.7b). By using this approach, Okano *et al.* were able to prepare DOX-loaded polymeric micelles of PNIPAAm-*b*-poly(butyl methacrylate) (PNIPAAm-*b*-PBMA) and PNIPAAm-*b*-poly(styrene) (PNIPAAm-*b*-PS) [50]. Below the LCST of PNIPAAm, this system demonstrated a core-shell micellar structure, but on heating above the LCST the DOX was rapidly released from the PNIPAAm-*b*-PBMA micelles as a result of structural distortion of the relatively flexible PBMA core, caused by collapse of the PNIPAAm shell. In con-



**Figure 3.7** (a) Thermosensitive polymers can undergo reversible transformation from hydrated to hydrophobic/collapse state upon heating; (b) Several strategies can be used with thermosensitive polymers, such as using them as the micelle shell below the LCST or the micelle core over the LCST.

trast, the PNIPAAm-*b*-PS micelles did not show any enhanced DOX release when the temperature was increased above the LCST, mainly because the rigid PS core was insensitive to collapse of the PNIPAAm. As PNIPAAm exists in its precipitated form at body temperature, this system proved not to be suitable for *in vivo* application without modification. Nevertheless, the copolymerization of NIPAAm with the hydrophilic dimethylacrylamide (DMAAm) resulted in a random copolymer (P(NIPAAm-*co*-DMAAm)) with a LCST slightly above body temperature (40°C) [51]. The release of DOX from P(NIPAAm-*co*-DMAAm)-*b*-PLA micelles was very slow at 37°C, but showed a sudden increase at 42.5°C, which suggested that this system might have potential benefit for hyperthermic treatments.

A system in which PNIPAAm was utilized as the core-forming block was reported by Feijen *et al.* [52]. Here, the PEG-*b*-PNIPAAm block copolymer was



**Figure 3.8** Two examples of thermosensitive polymers having a LCST. (a) Poly(*N*-isopropylacrylamide) (PNIPAAm); (b) Poly(2-isopropyl-2-oxazoline) (PiPrOx). Both polymers have been used in the construction of nanoassemblies of block copolymers.

water-soluble below the LCST of PNIPAAm, but above this temperature it formed polymeric micelles with a collapsed PNIPAAm core and a PEG outer shell. The temperature at which micelles are formed is known as the critical micelle temperature (CMT). The heating rate is a critical parameter for the size of PEG-*b*-PNIPAAm micelle, as a higher heating rate causes rapid dehydration of the thermosensitive segments. Any subsequent collapse of these segments precedes the aggregation between polymers and, as a result, micelles with a well-defined core-shell structure are formed.

Poly(2-isopropyl-2-oxazoline) (PiPrOx) is another promising thermosensitive polymer (Figure 3.8b). This material possess an isopropyl group in the side position and, as PNIPAAm, the aqueous solutions of PiPrOx have a LCST at near-physiological conditions [53, 54]. Park *et al.* prepared novel thermosensitive PIC micelles in an aqueous medium via the complexation of a pair of oppositely charged block copolymers containing the thermosensitive PiPrOx segments, PiPrOx-*b*-P(Lys) and PiPrOx-*b*-P(Asp) [55]. These PIC micelles had a constant cloud-point temperature of approximately 32°C under physiological conditions, regardless of their concentration. Since the LCST of PiPrOx can be modulated by copolymerization [56], these PiPrOx-PIC micelles have high potential as a size-regulated, temperature-responsive nanocontainers for loading charged compounds.

The main drawback of thermosensitive drug delivery systems is that the thermal treatment required for the controlled destabilization of the micelles and subsequent drug release is not always feasible in clinical practice. However, this issue can be overcome using secondary external triggers. Sershen *et al.* developed a photothermally modulated hydrogel using NIPAAm-*b*-acrylamide in combination with photoactive gold nanoshells [57]. The nanoshells strongly absorbed near-infrared (NIR) irradiation (1064 nm) and converted it to heat, resulting in a collapse of the hydrogel. As an example, laser irradiation of this system led to the controlled release of methylene blue and proteins.

## 3.4.2

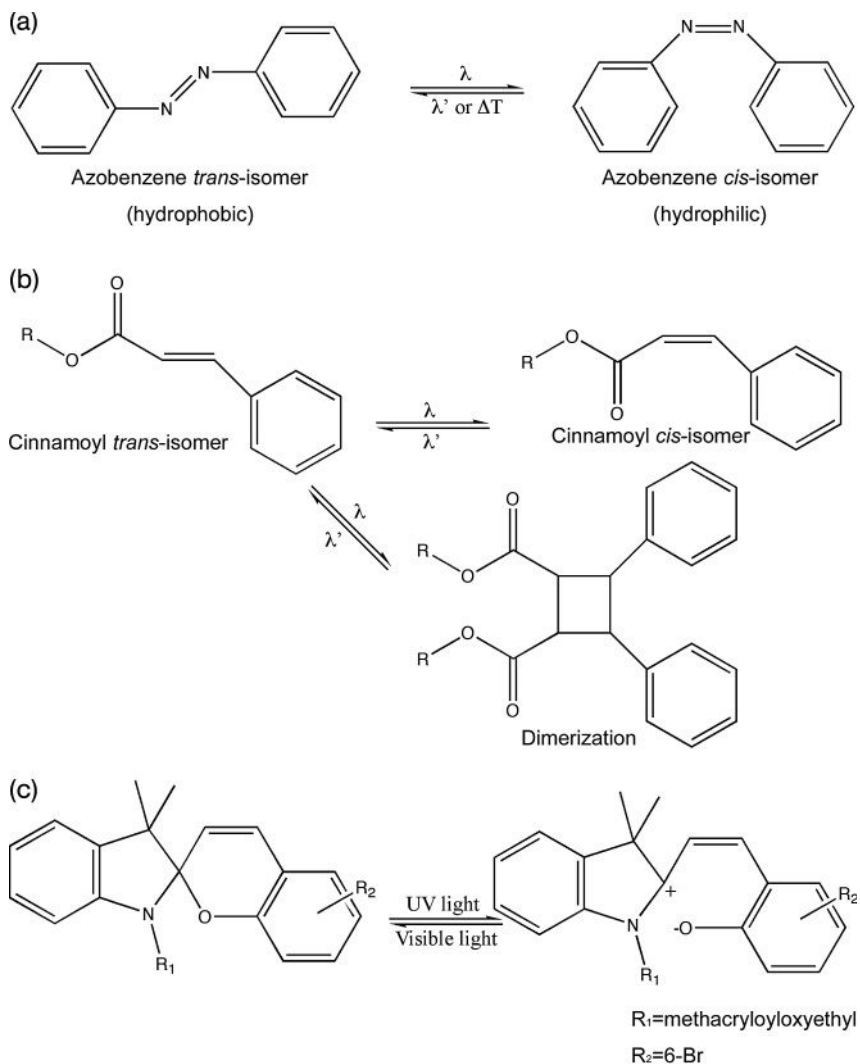
**Light**

The attractive feature of light-responsive polymeric assemblies is that the drug release can be induced at a specific time and site of light exposure, with ultraviolet (UV), visible (VIS) or NIR light being applied as the trigger. Since NIR light shows a deeper tissue penetration and minimal damage to healthy cells, its use is of particular interest for biomedical applications [58]. The structural changes of the nanoassemblies induced by light can be either irreversible or reversible; for example, cleavage of the side chains of the block copolymers induced an irreversible destabilization of the structures. The micelles prepared from PEG-*b*-polymethacrylate copolymers bearing a photolabile pyrene chromophore moiety in the side chain (PPy) demonstrated photosensitivity [59]. Likewise, pyrenyl methyl esters were cleaved following UV irradiation, thus transforming the hydrophobic polymethacrylate segment to hydrophilic poly(methacrylic acid) (PMA). The same group also developed a PEG-*b*-poly(2-nitrobenzyl methacrylate) system [60], where the cleavage of 2-nitrobenzyl moieties occurred by photolysis either via one-photon UV (365 nm) or two-photon NIR (700 nm) excitation. The formation of carboxylic acid after irradiation shifted the hydrophilic/hydrophobic balance and resulted in either break-up of the micelles or in swelling of the micelle core when it was crosslinked with a diamine.

The exposure of photoactive groups to light may also generate reversible structural changes due to deviations in the hydrophilic–hydrophobic balance. The molecular units showing photochemical-induced transitions include azobenzenes (Figure 3.9a), cinnamoyl derivatives (Figure 3.9b), and spirobenzopyran (Figure 3.9c).

A reversible isomerization between the *trans* (*E*) and *cis* (*Z*) geometric isomers of azobenzenes can be induced by light or heat (Figure 3.9a). The *cis* isomer is thermodynamically less stable, and isomerizes to the *trans* form due to thermal energy; the illumination can reduce this conversion time to minutes. Moreover, the photoisomerization wavelengths can be tuned by modulating the substituent groups at the chromophores. In that way, azo-functionalized hyperbranched polyesters [61] and polypeptides [62] showed photoinduced transformations. Photosensitive polymeric rods were formed with helical polypeptides by the hydrophobic interactions between the azo groups in a planar, apolar, *trans* configuration [63]. The photoisomerization of these azo-moieties to the skewed, polar, *cis* configuration, inhibited the interactions between azo-groups, leading to a disintegration of the nanoassemblies. Moreover, azobenzene–polymethacrylate-*b*-poly(acrylic acid) copolymers self-assembled in dioxane–water mixtures into micelles and vesicles [64], although the nanoassemblies broke up after UV irradiation. Subsequent illumination with visible light led to all of the nanoassemblies being reformed due to the *cis*-to-*trans* isomerization of the azobenzene, thus indicating the reversibility of the system.

Cinnamate undergoes either *trans*-to-*cis* photoisomerization, thus generating cinnamate residues with an increased hydrophilicity, or photodimerization after



**Figure 3.9** Light-sensitive groups normally used to modify block copolymers in order to obtain light-sensitive nanostructures.

(a) Azobenzenes undergo isomerization by light and heat between the *trans* and *cis* geometric isomers; (b) Cinnamate undergoes

*trans*-to-*cis* photoisomerization, producing residues with higher hydrophilicity or dimers; (c) Spirobenzopyran undergoes reversible photoisomerization into a zwitterionic merocyanine.

irradiation with UV light (Figure 3.9b). Accordingly, the partial modification of poly(HPMA) by cinnamate (9 mol%) produced both temperature- and light-sensitive polymers [65]. UV irradiation of the polymer in aqueous solution resulted in a 6°C increase in the LCST due to *trans*-to-*cis* isomerization. However, at a high cinnamate content the polymer was photocrosslinked due to the photodimeriza-



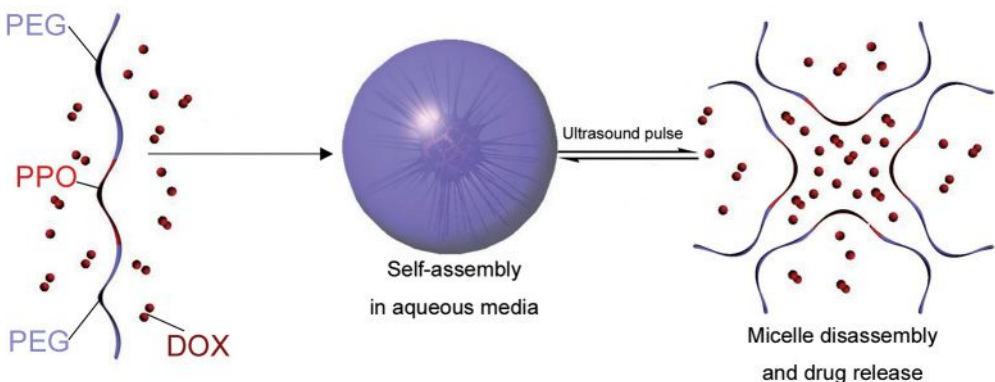
tion. The parameters that affect the LCST in this system are the polymer concentration, the amount of cinnamate moieties per polymer chain, and the extent of isomerization. Moreover, photocrosslinked cinnamoyl microcapsules were used to encapsulate cyclodextrin, and subsequently release it by UV illumination as a result of photocleavage and microcapsular break-up [66].

Block copolymers bearing merocyanine were self-assembled due to the attractive electrostatic dipole–dipole interaction of the zwitterionic moieties. The zwitterionic merocyanine is the photoisomerization product from spirobenzopyran (SBP) after UV irradiation (Figure 3.9c). For example, HPMA copolymers bearing various amounts of spirobenzopyran moieties aggregated into large clusters after UV exposure in water due to zwitterionic formation after 20 min illumination [67]. After incubation under visible light, however, the rapid reversal of the metastable zwitterionic form to the neutral form caused the nanostructures to be dissociated. As the neutral form of this copolymer had a low solubility at high ionic strength, this photoreversible cluster behavior was of completely opposite nature in 1 M NaCl.

### 3.4.3

#### Ultrasound

Ultrasound has been used successfully as a noninvasive trigger for the *in vitro* and *in vivo* release of drugs from PEG-*b*-poly(propylene oxide) (PPO)-*b*-PEG (poloxamer) micelles (Figure 3.10) [68–70]. Ultrasound not only causes the release of drug from these micelles but also enhances the intracellular uptake of both the released and encapsulated drug. Moreover, ultrasound can penetrate deeply into the interior of the body, and can also be focused and precisely controlled. The application of ultrasound in the frequency range of 20 to 90 kHz to pluronic micelles loaded with DOX or ruboxyl (a paramagnetic anthracyclin, an analogue of Rubomicin; Rb)



**Figure 3.10** Poloxamers (Pluronic<sup>®</sup>) have been used for the preparation of DOX-loaded polymeric micelles [68–70]. Upon ultrasound application, the micelles release the drug, whereas eliminating the ultrasound leads to reformation of the micelle.

caused release of the drug. The highest rate of release was observed at 20 kHz, but fell with increasing ultrasonic frequency, despite much higher power densities. The release of DOX was also higher than that of Rb, due to a stronger interaction and a deeper incorporation of Rb into the micelle cores. When using pulsed ultrasound, there is a rapid release and re-encapsulation behavior that takes within half a second for each pulse. The released drug is quickly re-encapsulated between ultrasound pulses; this suggests that, on leaving the sonicated volume, the non-extravasated and noninternalized drug would circulate in the encapsulated form, thus preventing any unwanted drug interactions with normal tissues. The *in vivo* enhancement of cellular drug uptake for this system was attributed to an increase in drug release from the micelles, which implied that ultrasound could be focused on a localized tumor and an anti-cancer agent released from the micelles and delivered directly to the malignant tissues. Unfortunately, ultrasound may also promote permeabilization of the cell membrane, followed by an increase in cellular drug incorporation.

### 3.5 Future Perspectives

Several approaches to the development of smart nanoassemblies have been discussed in this chapter, with a combination of stimuli-sensitive processes being used to control the properties of the nanostructures and provide a precise customization of drug delivery behavior *in vivo*.

Moreover, external stimuli-responsive nanoassemblies— the fate of which can be followed *in vivo* (e.g., smart drug delivery systems loaded with magnetic resonance imaging (MRI) contrast agents [71], or fluorescent dyes for NIR imaging [72])—will facilitate the use of an external trigger and enhance the therapeutic effects of smart drug carriers.

The incorporation of molecules that target specific cellular signals on the outer surfaces of smart nanoconstructs [21, 36, 73–76], or the construction of nanoassemblies with copolymers that have specific interaction with cells [77], is essential for designing carrier systems with specific cellular recognition. Such recognition can be precisely tuned by constructing end-functionalized block copolymers, the self-assembly of which will lead to the formation of nanostructures with pilot molecules on their exterior. In this way, a specific drug delivery to a target tissue and specific activation of that delivered drug within the targeted cell, may enhance the efficacy and minimize any adverse side effects during drug targeting. The combination of a specific cellular uptake of nanoassemblies with intracellular drug release might also permit the accurate management of drug distribution, leading to an enhanced or innovative therapeutic activity. Although several of the pilot molecule-directed block-copolymer assemblies reported here have still to be optimized, in some cases the activities achieved are elevated to a significant extent, thus highlighting the huge potential of cell-targeted, smart nanoassemblies.

## References

- 1 Lazzari, M. and López-Quintela, M.A. (2003) *Adv. Mater.*, **15**, 1583–1594.
- 2 Hamley, I.W. (2003) *Angew. Chem. Int. Ed. Engl.*, **42**, 1692–1712.
- 3 Kataoka, K., Harada, A. and Nagasaki, Y. (2001) *Adv. Drug Deliv. Rev.*, **47**, 113–131.
- 4 Allen, C., Maysinger, D. and Eisenberg, A. (1999) *Colloids Surf. B Biointerfaces*, **16**, 3–27.
- 5 Matsumura, Y. (2007) *J. Drug Target.*, **15**, 507–517.
- 6 Martina, M. and Hutmacher, D.W. (2007) *Polym. Int.*, **56**, 145–157.
- 7 Hasirci, V., Vrana, E., Zorlutuna, P., Ndreu, A., Yilgor, P., Basmanav, F.B., and Aydin, E. (2006) *J. Biomater. Sci. Polym. Ed.*, **17**, 1241–1268.
- 8 Jagur-Grodzinski, J. (2006) *Polym. Adv. Tech.*, **17**, 395–418.
- 9 Matsumura, Y. and Maeda, H. (1986) *Cancer Res.*, **46**, 6387–6392.
- 10 Maeda, H., Wu, J., Sawa, T., Matsumura, Y. and Hori, K. (2000) *J. Control. Release*, **65**, 271–284.
- 11 Stolnik, S., Illum, L. and Davis, S.S. (1995) *Adv. Drug Deliv. Rev.*, **16**, 195–214.
- 12 Kwon, G., Suwa, S., Yokoyama, M., Okano, T., Sakurai, Y. and Kataoka, K. (1994) *J. Control. Release*, **29**, 17–23.
- 13 Avgoustakis, K., Beletsi, A., Panagi, Z., Klepetsanis, P., Livaniou, E., Evangelatos, G. and Ithakissios, D.S. (2003) *Int. J. Pharm.*, **259**, 115–127.
- 14 Engin, K., Leeper, D.B., Cater, J.R., Thistlethwaite, A.J., Tupchong, L. and McFarlane, J.D. (1995) *Int. J. Hyperthermia*, **11**, 211–216.
- 15 Murphy, R.F., Powers, S. and Cantor, C.R. (1984) *J. Cell Biol.*, **98**, 1757–1762.
- 16 Savic, R., Luo, L., Eisenberg, A. and Maysinger, D. (2003) *Science*, **300**, 615–618.
- 17 Bae, Y., Fukushima, S., Harada, A. and Kataoka, K. (2003) *Angew. Chem. Int. Ed. Engl.*, **42**, 4640–4643.
- 18 Bae, Y., Nishiyama, N., Fukushima, S., Koyama, H., Yasuhori, M. and Kataoka, K. (2005) *Bioconj. Chem.*, **16**, 122–130.
- 19 Gillies, E.R. and Frechet, J.M. (2003) *Chem. Commun.*, **14**, 1640–1641.
- 20 Lee, E.S., Shin, H.J., Na, K. and Bae, Y.H. (2003) *J. Control. Release*, **90**, 363–374.
- 21 Lee, E.S., Na, K. and Bae, Y.H. (2003) *J. Control. Release*, **91**, 103–113.
- 22 Martin, T.J., Prochazka, K., Munk, P. and Webber, S.E. (1996) *Macromolecules*, **29**, 6071–6073.
- 23 Tang, Y., Liu, S.Y., Armes, S.P. and Billingham, N.C. (2003) *Biomacromolecules*, **4**, 1636–1645.
- 24 Leroux, J., Roux, E., Le Garrec, D., Hong, K. and Drummond, D.C. (2001) *J. Control. Release*, **72**, 71–84.
- 25 Taillefer, J., Jones, M.C., Brasseur, N., van Lier, J.E. and Leroux, J.C. (2000) *J. Pharm. Sci.*, **89**, 52–62.
- 26 Sant, V.P., Smith, D. and Leroux, J.-C. (2004) *J. Control. Release*, **97**, 301–312.
- 27 Merdan, T., Kopecek, J. and Kissel, T. (2002) *Adv. Drug Deliv. Rev.*, **54**, 715–758.
- 28 Wagner, E. (2004) *Pharm. Res.*, **21**, 8–14.
- 29 De Smedt, S.C., Demeester, J. and Hennink, W.E. (2000) *Pharm. Res.*, **17**, 113–126.
- 30 Brown, M.D., Schatzlein, A.G. and Uchegbu, I.F. (2001) *Int. J. Pharm.*, **229**, 1–21.
- 31 Han, S., Mahato, R.I., Sung, Y.K. and Kim, S.W. (2000) *Mol. Ther.*, **2**, 302–317.
- 32 Behr, J.P. (1997) *Chimia*, **51**, 34–36.
- 33 Boeckle, S. (2004) *J. Gene Med.*, **6**, 1102–1111.
- 34 Zauner, W. (1998) *Adv. Drug Deliv. Rev.*, **30**, 97–113.
- 35 Putnam, D. (2001) *Proc. Natl Acad. Sci. USA*, **98**, 1200–1205.
- 36 Oishi, M., Nagatsugi, F., Sasaki, S., Nagasaki, Y. and Kataoka, K. (2005) *Chembiochem*, **6**, 718–725.
- 37 Fukushima, S., Miyata, K., Nishiyama, N., Kanayama, N., Yamasaki, Y. and Kataoka, K. (2005) *J. Am. Chem. Soc.*, **127**, 2810–2811.
- 38 Kanayama, N., Fukushima, S., Nishiyama, N., Itaka, K., Jang, W.-D., Miyata, K. and Kataoka, K. (2006) *ChemMedChem*, **1**, 439–444.
- 39 Akagi, D., Oba, M., Koyama, H., Nishiyama, N., Fukushima, S., Miyata, T., Nagawa, H. and Kataoka, K. (2007) *Gene Ther.*, **14**, 1029–1038.

- 40 Lee, Y., Fukushima, S., Bae, Y., Hiki, S., Ishii, T. and Kataoka, K. (2007) *J. Am. Chem. Soc.*, **129**, 5362–5363.
- 41 Napoli, A., Valentini, M., Tirelli, N., Muller, M. and Hubbell, J.A. (2004) *Nat. Mater.*, **3**, 183–189.
- 42 Napoli, A., Boerakker, M.J., Tirelli, N., Nolte, R.J., Sommerdijk, N.A. and Hubbell, J.A. (2004) *Langmuir*, **20**, 3487–3491.
- 43 Takeoka, Y., Aoki, T., Sanui, K., Ogata, N., Yokoyama, M., Okano, T., Sakurai, Y. and Watanabe, M. (1995) *J. Control. Release*, **33**, 79–87.
- 44 Kakizawa, Y., Harada, A. and Kataoka, K. (1999) *J. Am. Chem. Soc.*, **121**, 11247–11248.
- 45 Kakizawa, Y., Harada, A. and Kataoka, K. (2001) *Biomacromolecules*, **2**, 491–497.
- 46 Miyata, K., Kakizawa, Y., Nishiyama, N., Harada, A., Yamasaki, Y., Koyama, H. and Kataoka, K. (2004) *J. Am. Chem. Soc.*, **126**, 2355–2361.
- 47 Miyata, K., Kakizawa, Y., Nishiyama, N., Yamasaki, Y., Watanabe, T., Kohara, M. and Kataoka, K. (2005) *J. Control. Release*, **109**, 15–23.
- 48 Katayama, Y., Fujii, K., Ito, E., Sakakihara, S., Sonoda, T., Murata, M. and Maeda, M. (2002) *Biomacromolecules*, **3**, 905–909.
- 49 Schild, H.G. (1992) *Prog. Polym. Sci.*, **17**, 163–249.
- 50 Chung, J.E., Yokoyama, M. and Okano, T. (2000) *J. Control. Release*, **65**, 93–103.
- 51 Kohori, F., Sakai, K., Aoyagi, T., Yokoyama, M., Yamato, M., Sakurai, Y. and Okano, T. (1999) *Colloids Surf. B Biointerface*, **16**, 195–205.
- 52 Topp, M.D.C., Dijkstra, P.J., Talsma, H. and Feijen, J. (1997) *Macromolecules*, **30**, 8518–8520.
- 53 Uyama, H. and Kobayashi, S. (1992) *Chem. Lett.*, 1643–1646.
- 54 Park, J.-S., Akiyama, Y., Winnik, F.M. and Kataoka, K. (2004) *Macromolecules*, **37**, 6786–6792.
- 55 Park, J.-S., Akiyama, Y., Yamasaki, Y. and Kataoka, K. (2007) *Langmuir*, **23**, 138–146.
- 56 Park, J.-S. and Kataoka, K. (2007) *Macromolecules*, **40**, 3599–3609.
- 57 Sershen, S.R., Westcott, S.L., Halas, N.J. and West, J.L. (2000) *J. Biomed. Mater. Res.*, **5**, 293–298.
- 58 Weissleder, R. (2001) *Nat. Biotechnol.*, **19**, 327–331.
- 59 Jiang, J. and Tong, Z. (2005) *J. Am. Chem. Soc.*, **127**, 8290–8291.
- 60 Jiang, J., Tong, X., Morris, D. and Zhao, Y. (2006) *Macromolecules*, **39**, 4633–4640.
- 61 Wang, G. and Wang, X. (2002) *Polym. Bull.*, **49**, 1–8.
- 62 Pieroni, O., Fissi, A. and Popova, G. (1998) *Prog. Polym. Sci.*, **23**, 81–123.
- 63 Minoura, N., Higuchi, M. and Kinoshita, T. (1997) *Mater. Sci. Eng. C Biomim. Mater. Sens. Syst.*, **4**, 249–254.
- 64 Wang, G., Tong, X. and Zhao, Y. (2004) *Macromolecules*, **37**, 8911–8917.
- 65 Laschewsky, A. and Rekaei, E.D. (2000) *Macromol. Rapid Commun.*, **21**, 937–940.
- 66 Yuan, Z., Fischer, K. and Schärfl, W. (2005) *Langmuir*, **21**, 9374–9380.
- 67 Konak, C., Rathi, R.C., Kopeckova, P. and Kopecek, J. (1997) *Macromolecules*, **30**, 5553–5556.
- 68 Pitt, W.G., Husseini, G.A. and Staples, B.J. (2004) *Expert Opin. Drug Deliv.*, **1**, 37–56.
- 69 Husseini, G.A., Myrup, G.D., Pitt, W.G., Christensen, D.A. and Rapoport, N.Y. (2000) *J. Control. Release*, **69**, 43–52.
- 70 Marin, A., Muniurazzaman, M. and Rapoport, N. (2001) *J. Control. Release*, **10**, 69–81.
- 71 Nakamura, E., Makino, K., Okano, T., Yamamoto, T. and Yokoyama, M. (2006) *J. Control. Release*, **114**, 325–333.
- 72 Ghoroghchian, P.P., Frail, P.R., Susumu, K., Blessington, D., Brannan, A.K., Bates, F.S., Chance, B., Hammer, D.A. and Therien, M.J. (2005) *Proc. Natl Acad. Sci. USA*, **102**, 2922–2927.
- 73 Yamamoto, Y., Nagasaki, N., Kato, M. and Kataoka, K. (1999) *Colloids Surf. B Biointerfaces*, **16**, 135–146.
- 74 Nagasaki, Y., Yasugi, K., Yamamoto, Y., Harada, A. and Kataoka, K. (2001) *Biomacromolecules*, **2**, 1067–1070.
- 75 Torchilin, V., Lukyanov, A.N., Gao, Z. and Papahadjopoulos-Sternberg, B. (2003) *Proc. Natl Acad. Sci. USA*, **100**, 6039–6044.
- 76 Bae, Y., Nishiyama, N. and Kataoka, K. (2007) *Bioconj. Chem*, **18**, 1131–1139.
- 77 Holowka, E.P., Sun, V.Z., Kamei, D.T. and Deming, T.J. (2007) *Nat. Mater.*, **6**, 52–57.

## 4

# A Comprehensive Approach to the Alignment and Ordering of Block Copolymer Morphologies

*Massimo Lazzari and Claudio De Rosa*

### 4.1

#### Introduction

##### 4.1.1

#### Motivation

Self-assembly is an enormously powerful concept in modern materials science, which was first associated with the use of synthetic strategies for the preparation of nanostructures only about 15 years ago [1–3]. Since then, a large variety of carefully designed building blocks have been proposed and employed for working “from atoms up” with the aim of fabricating two-dimensional (2-D) and three-dimensional (3-D) structures. In particular, within the past decade, interest in a potentially ideal nanoscale tool has been growing exponentially, namely phase-separated block copolymers (BCs) [4–17].

Immiscibility among the BC constituents is common, and phase separation results in the series of morphologies, for example, lamellar, gyroid, hexagonal and body-centered cubic for diblock copolymers [4, 7, 9], the size and shape of which may be conveniently tuned by changing the molecular weights and compositions of the BCs [5, 18–20]. Part of the enormous potential for nanomaterial fabrication of these self-organized patterns of chemically distinct domains that have periodicity in the mesoscale—that is, between a few tens and hundreds of nanometers—has already been demonstrated [21–40]. However, in our opinion their development into practical routes suitable for industrial applications will probably only be fully exploited when a few key limitations have been efficiently overcome. As an example, writing and replication processes in microelectronics require spatial and orientational control of patterns which, in the case of BCs, entails the solution of the nontrivial problem of large-area ordering and precise orientation of domains.

Regular structures can be generated by controlling the typical disadvantages of spontaneous phase separation. First, similar to polycrystalline materials, the self-assembly of BCs in bulk is prone to form grains with a high level of local order but a very short persistence length, especially in the case of cylinders and lamellae

which, on a larger scale, correspond to bulk materials with isotropic properties. Although annealing permits a consistent annihilation of the corresponding grain boundary defects, in addition to other defects such as dislocation, disclination, terracing and asymmetry defects [41–47], the formation of defect-free structures points to more efficient strategies based on the application of external forces or spatial constraints. In the same way, long-range oriented patterns, for example, cylindrical or lamellae domains parallel to the substrate, with all of the axes aligned in a single direction rather than randomly in the parallel plane, may only be induced through a careful engineering of surface effects or by well-oriented fields.

It could be stated that for many technological applications such an appealing spontaneous organization has to be directed by some form of templating (in this context considered in its broader sense), where the BC components could not only interact with each other but also take advantage of external controlling interactions.

Numerous methods to induce and control BC domain orientation have been explored, particularly for substrate-supported films to create perfectly periodic 2-D patterns, ranging from the first demonstration of the effectiveness of the application of electric fields [48] to the recent combination of both active and passive forces to obtain laterally ordered arrays of cylindrical domains with areal densities of up to 1.5 terabits per  $\text{cm}^2$  [39], through the elegant application of chemically nanopatterned templates [31]. Most methods proposed to date will be critically presented in this chapter, and special attention will be given to the combination of techniques to yield 3-D control.

#### 4.1.2

##### **Organization of the Chapter**

The scope of this chapter is to provide an overview of the variety of methods that can induce long-range ordered BC morphologies, focusing on the most promising areas of ongoing research. The main strategies applied so far may be classified into three different approaches:

1. Control of orientation by applying external fields, such as electric, magnetic, thermal, mechanical and solvent evaporation. Depending on the field imposed, thin films and/or samples in bulk may be oriented.
2. Induction of large-area ordering by facilitating the self-assembly, generally of thin films, on templates either topographically or chemically nanopatterned.
3. Modulation of substrate and surface interactions as a result of:
  - a) Preferential interaction of one block with the surface.
  - b) Neutralization of attractions to the substrate or to the surface.
  - c) Epitaxial crystallization of domains onto a crystalline substrate.
  - d) Directional eutectic crystallization of a BC solvent.
  - e) Graphoepitaxy.
  - f) 2-D geometric confinements.

Before highlighting recent advances in such control strategies, a preliminary section specifically for all researchers who are new to this field will offer practical information on film preparation, and on the methods used in practice to achieve thermodynamic equilibrium morphologies. Because one of the aims of this book is to offer solutions to experimental difficulties and research needs, the decision was taken to highlight the practical aspects of phase separation and orientation with respect to the theoretical concepts.

## 4.2

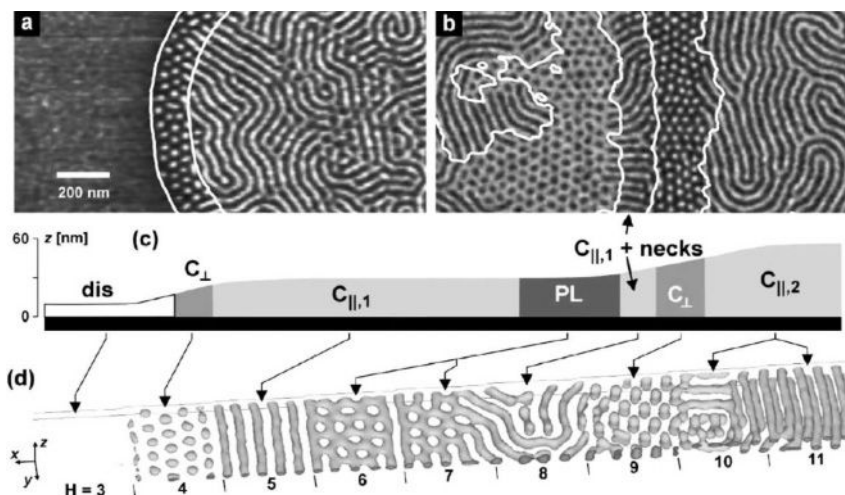
### How to Help Phase Separation

Except for some specific instances—for example, direct use as photonic crystals or in the case of amphiphilic BC for drug and genetic delivery—applications of BCs require the preparation of thin films with thicknesses ranging from a few tens of nanometers (in some cases down to thicknesses of less than the corresponding equilibrium period of the BC) to several micrometers. Films with low surface roughness may be produced by spin-coating or dip-coating from relatively dilute solutions, that is, approximately 1–5% by weight, onto solid substrates with uniform flatness. The thickness and the uniformity of the film surface mainly depend on the concentration of the solution, the volatility of the solvent, and the specific instrumental speed—that is, the spin speed or withdrawal speed, respectively. Silicon wafers, eventually coated with metals, semiconductors, carbon or polymers are often utilized as the support. During dip-coating processes, and also for films prepared from direct casting, the solvent may evaporate slowly, thus allowing a stable organization of macromolecules close to thermodynamic equilibrium. In contrast, in the case of spun-cast films the solvent is driven off so quickly that nonequilibrium structures could be observed. Moreover, the concentration gradient due to fast solvent evaporation can in fact have a significant effect on domain orientation, as discussed in Section 4.

In thin films, the self-assembled BC morphologies are influenced not only by molecular weights, polydispersity and composition, but also by other variables such as the selectivity of the solvent for one block, surface–interfacial interactions, and the interplay between structure periodicity and film thickness, which can cause significant deviations from the predicted phases in the bulk state. An elegant demonstration and a didactic example of the influence of surface effects in thin films has been reported by Krausch and coworkers [49]. Their experimental data for a triblock copolymer of ABA type are compared with those of the simulated film in Figure 4.1. Several more studies have demonstrated the importance of confinement effects, and will be treated in detail later.

Independently of the casting techniques, even for a film prepared taking all necessary precautions, it is not possible to obtain a perfectly ordered morphology over a large area. In fact, an optimization of the nanostructures is almost indispensable and can be carried out by different annealing processes, with the double objective of obtaining the equilibrium morphology and eliminating the





**Figure 4.1** (a,b) Tapping-mode scanning force microscopy phase images of thin films of a cylinder-forming polystyrene-*block*-polybutadiene-*block*-polystyrene (PS-*b*-PB-*b*-PS) after solvent annealing, showing a sequence of phases as a function of the height profile (c), which is in good agreement with the simulation of an  $A_3B_{12}A_3$  copolymer film (d). Owing to preferential wetting, the

silicon substrate is covered with a homogeneous 10-nm-thick PB layer which, with increasing thickness from left to right, is followed by isolated domains of PS, parallel-oriented PS cylinders, perforated lamella, parallel-oriented PS cylinders again, and finally two layers of parallel-oriented cylinders. Reproduced with permission from Ref. [49]; © 2002, The American Physical Society.

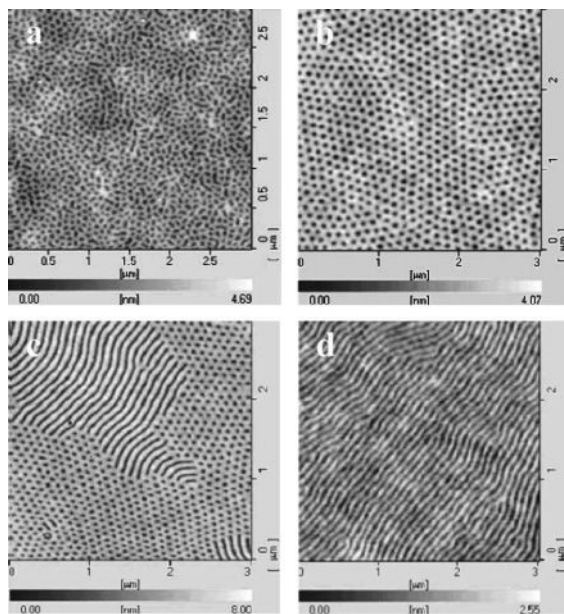
defects. Annealing is usually performed before any further manipulation, even though some approaches include the alignment of domains within the orientation process.

In principle, *thermal annealing* is the simplest option and the most commonly used method. This consists of controlled heating at a temperature above the glass transition temperature ( $T_g$ ) of the constituent blocks, preferably in an inert atmosphere or under vacuum, for a specific time. For polymers with high molecular weights and complex architectures, the high degree of chain entanglements and the difficult diffusion of one polymer block through the domains of the other blocks pose large kinetic barriers to equilibrium. In such cases, and for partially crystalline BCs with high fusion temperatures, the annealing window for the relevant conditions of temperature and time that are theoretically necessary and those of the order–disorder transition or polymer decomposition, may be insufficient to reach equilibrium. On the other hand, the degradation of one or more blocks has been used to stabilize the morphologies for further applications, through decomposition, partial oxidation or crosslinking [23, 26, 27, 50–53], or even to induce a hierarchical transition of morphologies [54].

Alternative annealing approaches entail an increase in chain mobility by the addition of some type of plasticizer, either transient, such as a solvent, or low-



molecular-weight homopolymers [55, 56], which also swell each domain. Exposing thin films to vapors of a good solvent potentially allows long-range equilibrium morphologies to be produced without any thermal treatment. However, as genuinely neutral solvents are rare, the use of solvents selective for one block may induce structures far removed from the equilibrium situation [49, 57–62], which remain frozen after solvent removal and are sometimes difficult to obtain by other methods [60]. As a conjecture, a fully selective solvent should lead to a micellar-like microdomain phase. Once more, Krausch and coworkers were the first to demonstrate for a polystyrene-*block*-poly(2-vinylpyridine)-*block*-poly(*t*-butyl acrylate) (PS-*b*-P2VP-*b*-PtBA) triblock copolymer, that the choice of annealing solvent strongly influenced the types of metastable structures observed, and also investigated the time development of the microdomain structure [60]. More recently, the morphology evolution has been followed in other BCs, for example in polystyrene-*block*-poly(methyl methacrylate) (PS-*b*-PMMA) thin films with different thicknesses exposed to PMMA-selective solvent vapors (Figure 4.2) [63, 64].



**Figure 4.2** Atomic force microscopy topographic images of PS-*b*-PMMA ( $M_n$  PS = 133 000,  $M_n$  PMMA = 130 000) thin films cast onto an Si substrate with an SiO<sub>x</sub> surface layer exposed to chloroform vapor. (a) After 40 h, the initially featureless structure shows a disordered microstructure that evolves, at 60 h (b), into a hexagonally packed nanocylinder structure. (c) Further treatment, 80 h, promotes the evolution after 100 h (d) to a

mixed morphology, which completely develops into stripes having the repeat spacing ( $L_0$ ), of 90 nm. For longer annealing times, the film returns to a flat surface. It has also been shown that only when the film thickness is less than  $1/2L_0$  can the packed nanocylinder structures form. Reproduced with permission from Ref. [63]; © 2004, The American Chemical Society.

Other representative examples in controlling the orientation and lateral ordering of microstructures are poly(ethylene oxide) (PEO)-containing block copolymers. A simple solvent annealing of cylinder-forming PS-*b*-PEO and PS-*b*-PMMA-*b*-PEO BC thin films can lead to a perpendicular orientation with a high degree of lateral ordering [65, 66]. In these systems, the relative humidity of the vapor during solvent annealing was shown to play a fundamental role in achieving such order [67], while the addition of small amounts of an alkali halide or metal salts to cylinder-forming PS-*b*-PEO, where the salt complexes with the PEO block, was found to significantly enhance the long-range positional order [68]. In a similar way, the incorporation of diverse PEO additives into PS-*b*-PMMA diblock copolymer thin films gave a vertical alignment of the PMMA cylinder, due mainly to an interaction with the water vapor under the high humidity, solvent-swollen processing conditions, as a direct consequence of the miscibility of the PEO with PMMA block [69, 70].

Finally, an in-depth understanding of the formation of either equilibrium structures or kinetically trapped morphologies during solvent annealing requires not only an accurate choice of solvent but also the proper control of experimental parameters, such as vapor pressure, treatment time, solvent extraction rate and, in case, relative humidity. In practice, this knowledge facilitates the preparation of reproducible nanopatterns in thin films, which also, in the case of metastable assemblies, show a long-term stability, at least for  $T_g$ s of all the components that are well above room temperature.

Another plasticizing agent that presents a modest equilibrium sorption and can be easily removed is supercritical CO<sub>2</sub>. Although its rapid diffusion in most polymers allows an equally rapid equilibrium distribution in thin films, CO<sub>2</sub> annealing has so far been limited to a surprisingly low number of BCs, essentially PS-*b*-PMMA, having molecular weights up to 300 000 g mol<sup>-1</sup> [71, 72].

### 4.3

#### Orientation by External Fields

Since the first macroscopic alignment of cylindrical domains of an industrial tri-block copolymer (a PS-*b*-PB-*b*-PS; Kraton 102) by extrusion carried out by the Keller group during the early 1970s [73, 74], many more mechanical flow fields have been proposed to control BC alignment. Following the Keller belief that BC microstructuring and orientation were exciting research subjects, but with very limited applicability (E. Pedemonte, personal communication), and after the shear flow experiments on the same copolymer by Skolios and coworkers [75–77], during the 1990s research interests returned strongly to alignment by relatively weak external fields. Another reason for this was the greater availability of BCs with different architectures and chemical compositions [5, 18–20]. Particularly in recent years, most investigations moved from bulk materials to thin films, due to their nanotechnological potential, with a special focus on the use of electric fields. Active

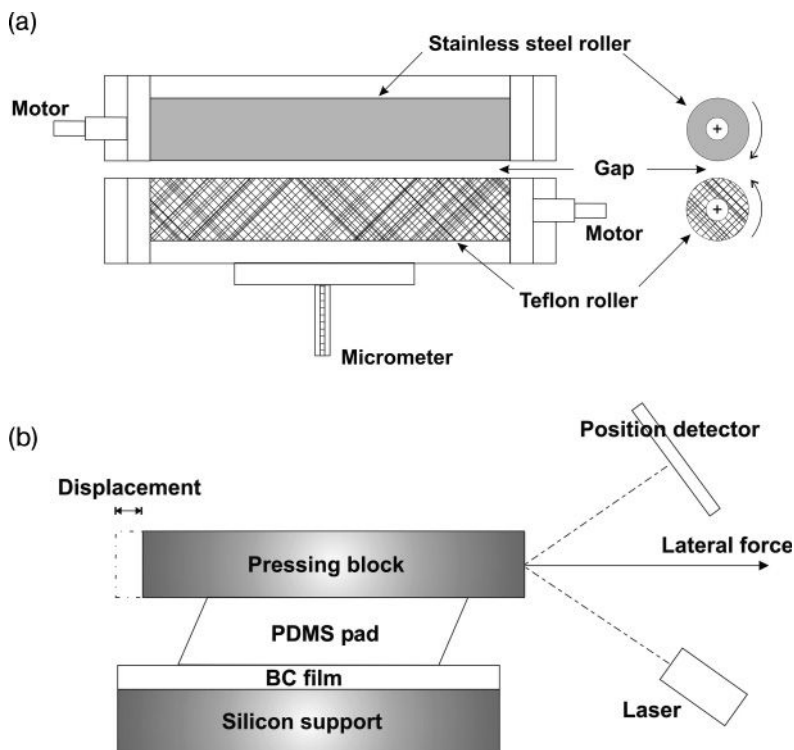
external fields will be discussed later in the chapter, while those that are passive, such as with interfacial interactions, are considered in the next sections.

#### 4.3.1

##### Mechanical Flow Fields

Extrusion [73, 74], compression [78–82], flows involving oscillatory shearing [75–77, 82–91] and other steady shearing [92–98], and techniques that combine different flow fields [99–104] have been successfully applied to induce alignment in BCs, either in a microphase-separated molten state or, to a lesser extent, in gels of solvent-swollen microdomains [105–112], with the objective of forming single crystal structures. Large-amplitude oscillatory shear (LAOS), which was first proposed at the end of the 1980s to orient commercial triblock copolymers [82, 83], is the most widely employed technique, also due to the easy characterization of the shear field with respect to other methods. As an example, common parallel plate-type rheometers enable the modulation of valuable experimental variables to be carried out, such as shear rate, frequency, strain amplitude, and temperature.

Early studies on the effect of mechanical flow fields on the orientation of BC domains have already been summarized in many excellent publications and books, for example, by Fasolka and Mayes [9], Hamley [4, 113], the group working with Thomas [12, 114] and others [84, 115, 116], and so need not be reviewed here. Di-, tri-, and multiblock copolymers in bulk with different microstructures, such as lamellar [74, 78, 79, 84–91, 96, 98], cylindrical [80–82, 94, 95, 97, 101, 103], spherical [92, 93, 97] and gyroid [102], can be preferentially oriented parallel or, where applicable, perpendicular or mixed-perpendicular to the flow direction. Most experimental observations have been supported and even anticipated by theory, with several good theoretical works being published in recent years [117–126]. Further developments concerned the extension of the shearing techniques to thin films. Albalak and Thomas [99, 100] proposed a novel casting method, termed *roll-casting*, in which a BC solution is subjected to a flow between two counter-rotating rolls (Figure 4.3a). The solution is compressed and, as a result of solvent evaporation and shearing, the microphase separates into a film with a high degree of orientation and close to single-crystal characteristics. Only cylinder morphology from triblock commercial polymers has been oriented in this way [101, 102], with a film thickness intrinsically limited by the geometry of the device to hundreds of nanometers. Thinner films of sphere- and cylinder-forming polystyrene-*b*-poly(ethylene propylene) (PS-*b*-PEP) have been shear-aligned by simple flowing techniques [93, 94], and extended to arbitrarily large areas. Films of 30–50 nm spread onto a silicon substrate are covered by an elastomer pad, which is then slowly pulled forward by a constant force (Figure 4.3b). The steady shear must be applied at temperatures between the  $T_g$  and the temperature of order–disorder transition,  $T_{ODT}$ , of the copolymer, thus providing an essentially infinite orientational order in all directions without the typical limitations of sheared bulk samples, related to the presence of multigrains.



**Figure 4.3** Schematic of apparatus used to induce alignment in BC thin films. (a) In the roll-caster (upper view and section), two independent rollers—one of stainless steel and the other of Teflon—are driven at the same angular velocity by two independent motors and separated by a micrometer-

controlled gap; (b) In the shear-alignment set-up, the polydimethylsiloxane (PDMS) pad is pressed with a constant weight against the film; the support is heated at the annealing temperature while the displacement of the pressing block is continuously monitored with a laser-mirror-optical sensor assembly.

Unconventional methods, which to some extent are based on shearing and a stretching field, such as electrospinning [127–130] and orientation by spin coating [131, 132], have been proposed in the past few years, but still need to be investigated in depth. *Electrospinning* in particular [133, 134] seems to offer great potential for the fabrication of nanofibers with internal oriented structuring from cylinder-forming copolymers with at least one partially crystalline block.

#### 4.3.2

##### Electric and Magnetic Fields

Following the pioneering studies of Amundson *et al.* on lamellar diblock copolymer thin films [135–137], static electric fields have been widely used in copolymer melts to macroscopically orient lamellar or cylindrical morphologies [48, 138–146],

with most of the investigations being focused on PS-*b*-PMMA. Although morphologies parallel to the substrate could be obtained using an in-plane field, a uniaxial orientation along the field and perpendicular to the substrate is preferably induced between the electrodes compressing the film. As initially proposed by Russell and coworkers, a convenient procedure consists of the preparation of films between two Kapton sheets coated on one side with aluminum, with the film thickness controlled through Kapton spacers. Kapton is a commercially available polyimide with excellent mechanical properties that allows further manipulation after alignment of the domains [23], and also facilitates sample characterization, such as for microtoming. In order to avoid electric shorting, one of the electrodes must be placed in contact with the polymer, while the second is inverted with the Kapton side facing the polymer.

The general statement that the orientation of BC microdomains is possible if the applied field is high enough for a given difference in the dielectric constant between blocks, can be expressed by Equation 4.1 [147, 148]:

$$E_c = \Delta\gamma^{1/2} \frac{2(\varepsilon_A + \varepsilon_B)^{1/2}}{\varepsilon_A - \varepsilon_B} t^{-1/2} \quad (4.1)$$

where  $E_c$  is the critical electric field strength,  $\varepsilon_A$  and  $\varepsilon_B$  are the dielectric constants of blocks, and  $t$  is the film thickness, which also takes into account the surface interactions through the difference between the interfacial energies of each block with the substrate,  $\Delta\gamma$ . In the absence of preferential interactions with the substrate—that is,  $\Delta\gamma = 0$ —the domains do not need any external field to orient normal to the substrate (see Section 4.5.1). From a practical point of view, Equation 4.1 permits the evaluation of the critical parameter for a given set of the different parameters, eventually imposed by the same experimental design. The thickness of the region to be oriented is limited to a few millimeters by the electric field strengths, in the range of approximately 1 to 100 V $\mu\text{m}^{-1}$ , considered as the upper limit that prevents dielectric breakdown.

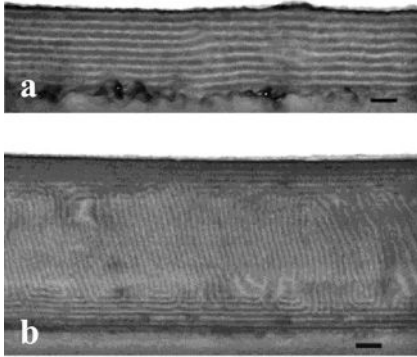
In addition, large-scale topographic structures could be generated by electrohydrodynamic (EHD) film instability, a technique in which a liquid dielectric interface is destabilized by a perpendicular electric field [149]. The interplay between EHD structure formation and the structural control over BC microphases allowed lithographically controlled micrometer-sized features to be obtained, where the cylindrical or lamellar domains are oriented parallel to the patterned structure axis; that is, normal to the substrate [144, 150].

Theoretical studies have been conducted to investigate various aspects of the dynamics of mesophase formation and orientation, mainly in diblock copolymer melts [147, 148, 151–154]; here, special mention should be made of the capacitor analogy proposed by Pereira and Williams for symmetric BCs [147]. The appeal of this model actually lies in its simplicity which, at a more qualitative level, also permits justification of the alignment of lamellae perpendicular to the electrodes on the basis of preferential travel of the electric field lines along easy paths, though each and every block has the highest polarizability. In the same way, parallel

orientation is unfavorable, as the electric field lines would be forced to cross both blocks evenly. Tsori *et al.* have recently proposed that, in these systems, alignment may also occur by other strong orienting forces, such as by the presence of a conductivity or mobility contrast [155], postulating an important role for the ions remaining in the polymers after synthesis in the reorientation mechanism [153].

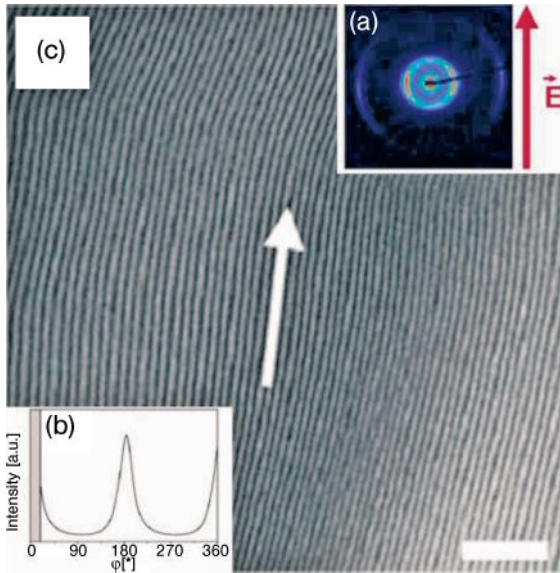
The alignment pathways in thin films of BCs with various morphologies have been recently followed using *in situ* small-angle X-ray scattering (SAXS) [140, 143] and scanning force microscopy (SFM) [145]. The application of an electric field (perpendicular to the plane of the film) to the disordered melt of an asymmetric BC induced the progressive growth of microphase-separated structures oriented parallel to the field only at temperatures below the order–disorder transition temperature. This occurs up to a stationary, equilibrium state, and also for a copolymer already having ordered domains parallel to the substrate, either a cylindrical PS-*b*-PMMA [140] or a lamellar polystyrene–polyisoprene (PS-PI) system [143], alignment parallel to the field could be achieved within minutes. An analysis of the scattering patterns suggested that, during the reorientation, the initial large grains are broken up into smaller pieces by the amplification of interfacial fluctuations, which are then able to rotate in the field. The final state of the symmetric BCs of PS and PI consists of many small grains with a high degree of orientation of the lamellae parallel to the electric field, but with a random orientation in the perpendicular plan. This observation also finds some theoretical support in the prediction by Tsori [148, 153, 154]. The limits imposed by the film thickness and the interfacial energy effects, as predicted in Equation 4.1, have been faced experimentally by the Russell group for symmetric and asymmetric BC thin films between substrates with modulated interfacial interactions [142, 156, 157]. In the presence of a preferential interaction of one block with the substrate (see Section 4.5.1) such effects are dominant for film thicknesses up to approximately  $10 L_0$ , regardless of the electric field applied normal to the surface (see, e.g., Figure 4.4a). For thicker films, the effects dissipate with distance from the surface and the domains orient in the direction of the electric field, at least in the interior of the film (Figure 4.4b), with a distance of propagation inversely proportional to the strength of the interfacial interactions [157].

All of these melt-based procedures suffer severe limitations because of the melt viscosity itself, which is directly dependent on the molecular weight and architecture of BCs, and the thickness of the region to be oriented. In addition, the achievement of high degrees of orientation eventually requires high temperatures and electric field strengths close to the decomposition conditions. An alternative approach to circumvent such restrictions consists in the addition of a neutral solvent with the effect of increasing chain mobility, as already discussed above for thermal annealing, thus facilitating large-scale domain alignment [158–160]. Concentrated diblock (PS-*b*-PI) [158] and triblock [polystyrene-*block*-poly(hydroxyethyl methacrylate)-*block*-poly(methyl methacrylate), PS-*b*-PHEMA-*b*-PMMA] [159] copolymer solutions have been aligned under a dc electric field during solvent evaporation, leading to highly anisotropic bulk samples (Figure 4.5). The orientation kinetics and mechanisms of alignment—that is, grain orientation and nuclea-



**Figure 4.4** Cross-sectional transmission electron microscopy images of  $\approx 300$  nm (a) and  $\approx 700$  nm (b) symmetric PS-*b*-PMMA films between PDMS-coated Kapton electrodes annealed at  $170^\circ\text{C}$  under

$\approx 40\text{V}\mu\text{m}^{-1}$  electric field for 6 and 16 h, respectively. The scale bar represents 100 nm. Reproduced with permission from Ref. [142]; © 2004, The American Chemical Society.



**Figure 4.5** (a) 2-D small-angle X-ray scattering pattern; (b) Azimuthal intensity distribution for a first-order reflection; (c) TEM image of a bulk sample prepared from a 40wt% solution in toluene of symmetric PS-*b*-PI ( $M_n = 80\,000$ ).

The arrows indicate the direction of the electric field. Scale bar = 400 nm. Reproduced with permission from Ref. [158]; © 2003, The American Chemical Society.

tion and growth of domains—have been corroborated by simulations [158] based on dynamic density functional theory (DFT) [161]. In summary, several groups have demonstrated that the application of unidirectional electric fields, coupled with an appropriate choice of materials and experimental conditions, allow an effective fabrication of patterns with a high degree of orientation and high aspect



ratio, suitable for nanotechnological applications. However, the orientation of domains is azimuthally degenerate and a further improvement to achieve morphologies with orientation controlled in the three dimensions logically requires the application of a second, orthogonal, external field. The first sequential combination toward long-range, 3-D ordered thin films was shown to control the orientation of lamellar microdomains through the application of an elongational flow field to obtain an in-plane orientation in  $\approx 30\mu\text{m}$ -thick films, and an electric field normal to the surface [162]. The concurrent application of the orthogonal field (e.g., a mechanical shearing) is expected to reduce the presence of defects and grain boundaries in an even more effective fashion.

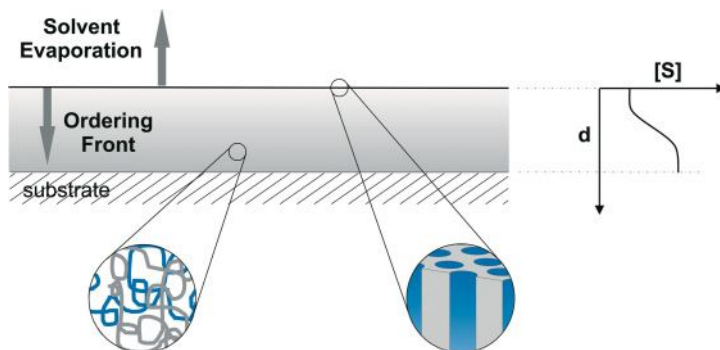
A further alignment approach is available for materials that exhibit anisotropic susceptibility due to an anisotropic molecular structure. Magnetic field-induced orientation has been achieved for liquid crystalline (LC) diblock copolymers with a dielectric diamagnetic isotropy, possibly through the magnetic alignment of LC mesogens [163–165], and also for BCs with a crystallizable block through an accurate control of the crystallization process [166]. The latter investigation is particularly likely to open a new fruitful research field and, at the same time, pave the way to an alternative method of relatively wide applicability, which only has the prerequisite of a high nucleation density during crystallization. Magnetic fields also offer the ability to apply very high fields without the risks of electric fields, associated with the danger and limit of electric breakdown. In addition, the orientation of PEO-based diblock copolymers with a poly(methacrylate) containing an azobenzene moiety in the side chain as a hydrophobic LC segment was produced by using a LASER beam, that induced the alignment of photoresponsive azobenzenes and transferred the molecular ordering at supramolecular level [167]. Macroscopic parallel array of nanocylinders can be obtained over an arbitrary area, in principle even on curved surfaces.

### 4.3.3

#### **Solvent Evaporation and Thermal Gradient**

The observation of lamellar and cylindrical microdomains in thin films perpendicular to the surface as a result of solvent evaporation was first reported by Turturro and coworkers [168], and subsequently investigated in more detail by Kim and Libera for a similar triblock copolymer [169, 170]. On the basis of these and other studies on either spun-cast or solution-cast films from solutions in a good solvent for all the blocks, a reasonable mechanism of orientation could be proposed (Figure 4.6). In the first moments after deposition, the  $T_g$  of the swollen film is still well below room temperature, thus allowing free chain mobility. With the decrease in the solvent concentration, the BC undergoes a transition from the disordered to the ordered state and, as in thin films the diffusion of the solvent produces a gradient of concentration, the ordering front rapidly propagates from the air surface to the substrate. The consequent decrease of  $T_g$  below room temperature, for at least one block, locks in the structures which, due to the high





**Figure 4.6** Schematic of the solvent evaporation in a diblock copolymer thin film. The diffusion produces a gradient in the concentration of the solvent,  $[S]$ , as a function of depth,  $d$ , which induces an ordering front from the film surface to the substrate.

directionality of the solvent gradient, are highly oriented normal to the surface. This behavior has been reported so far for films of less than one-half micron thick, for example, on PS-PB systems [168–170], PS-*b*-PEO [65, 171, 172], polystyrene-*block*-polyferrocenyldimethylsilane (PS-*b*-PFS) [173], and PS-*b*-P4VP [174], whereas the applicability of these conditions can be extended to any BCs having the  $T_g$  of one block above room temperature. Commonly, the short-range order of cylindrical microdomains of as-spun films may be significantly enhanced by solvent annealing. In the case of PS-*b*-PEO thin films, a better control over domain orientation was obtained by resorcinol complexation of the PEO cylinder-forming block [175]. This is possibly due to a lower degree of crystallinity of the PEO/resorcinol complexes with respect to the pure PEO, that has the effect of enhancing the mobility of polymers during film formation, and therefore also the orientation of domains parallel to the solvent gradient.

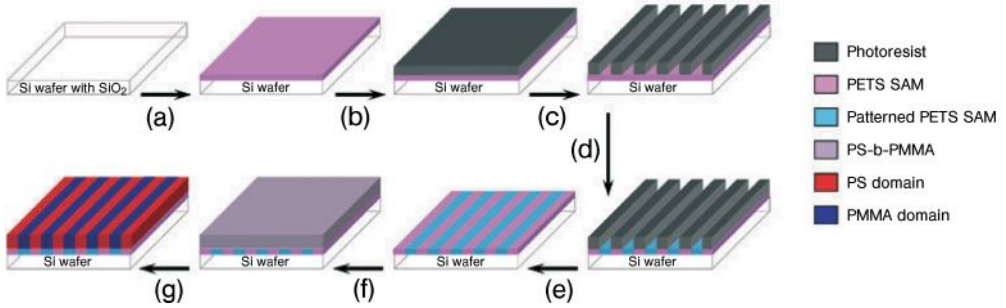
After the excellent results obtained by the Hashimoto group [176, 177], the use of temperature gradient apparatus to produce highly oriented single crystals was also reported for thin films [178, 179]. As an example, square-millimeter well-oriented samples of a cylinder-forming BC were obtained, with a density of disclinations estimated at  $4 \times 10^{-4} \mu\text{m}^{-2}$  (corresponding to an average disclination separation of  $50 \mu\text{m}$ ) [178].

#### 4.4 Templated Self-Assembly on Nanopatterned Surfaces

The combination of top-down strategies to fabricate patterns that direct the bottom-up organization of organic or inorganic building blocks is a strategy often

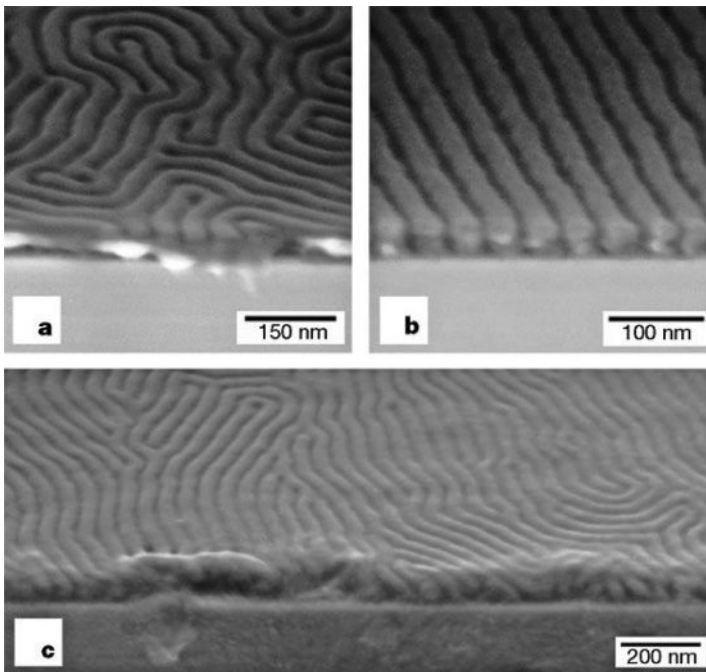
used in the micrometer and, to a minor extent, in the nanometer regime. Also, in the case of BCs, long-range order and orientation may be induced if self-assembly is forced to occur into/onto a guide, either topographically or chemically patterned, or in other 2-D or 3-D confinements. In this section, only the effect of surfaces with features having periodicity commensurable with those of the BC morphologies is considered. The study of the control of the registration and orientation of domains by topographic confinements (in the form of surface relief or groove structures) with a length scale much larger than the BC lattice parameters had a somehow different theoretical and historical development, and is better known as *graphoepitaxy*. It will therefore be discussed later as it follows such different nomenclature.

Rockford and coworkers decorated miscuit silicon wafers with gold to fabricate striped and essentially flat surface of nonpolar gold and polar silicon oxide, with periodicity ranging from 40 to 70 nm [180, 181]. Films of symmetric PS-*b*-PMMA solution cast onto such substrates showed, after thermal annealing, lamellar orientation normal to the plane and parallel to the striping, with the greatest ordering for patterns commensurable with the bulk lamellar period of the BC. A mismatch in the length scale of 10% and 25% in thick and ultrathin films, respectively, appeared to be sufficient to lose control over orientation. A novel integrated fabrication strategy that makes use of advanced lithographic techniques has been tuned, by Nealey and coworkers, to produce perfect periodic domain ordering [182, 183]. Although Nealey actually discussed epitaxial self-assembly, we prefer to reserve that term for a different methodology to control spatial and orientation order, as introduced by De Rosa *et al.* [184] (for a definition of epitaxy, see Section 4.5.2). As schematically reported in Figure 4.7, in the first essential step of this procedure a self-assembled monolayer (SAM) is precisely patterned throughout the photoresist using extreme ultraviolet interferometric lithography [185, 186]. Following the conversion of the topographic pattern to a chemical pattern and the photoresist removal, a symmetric PS-*b*-PMMA is spin-coated onto the chemical pattern and, as the modified regions present polar groups that preferentially wet the PMMA block, the self-assembly results in lamellae oriented perpendicular to the substrate. High-quality, defect-free BC films require pretty much the same period of the chemical pattern and the BC, with commensurability within just a few percent. For values within approximately 10%, the morphology can still be surface-directed but it is not perfect (Figure 4.8). An extension of this method, through the use of ternary blends of diblock copolymers and the corresponding homopolymers, showed that is possible to pattern chemical templates with periodicities substantially deviating from those of the BC [31]. The redistribution of homopolymer macromolecules during thermal annealing facilitates defect-free assembly of the blend as a whole, to form 50–80 nm periodic arrays in addition to pattern structures with different bend geometries. More recently, the validity of this approach was proven by other groups, which demonstrated that PS-*b*-PMMA can self-assemble in a well-aligned, long-range ordered hexagonal lattice commensurate with chemically prepatterned templates prepared by electron beam lithography (EBL) [187] or into a laterally



**Figure 4.7** Schematic representation of the fabrication process of chemically nanopatterned surfaces that template the self-assembly of symmetric PS-*b*-PMMA ( $M_n = 104\,000$ ). (a) A self-assembled monolayer of phenylethyltrichlorosilane is deposited on a silicon wafer; (b) A photoresist is then spin-coated and patterned with alternating lines and spaces by ultraviolet interferometric lithography (c); (d) The

topographic pattern is converted into a chemical pattern by irradiation with soft X-rays in the presence of oxygen; (e) After the photoresist removal, a toluene solution of PS-*b*-PMMA is spin-coated onto the patterned SAM (f). (g) Thermal annealing facilitates surface-directed self-assembly. Reproduced with permission from Ref. [183]; © 2003, Nature Publishing Group.



**Figure 4.8** Cross-sectional images of symmetric PS-*b*-PMMA ( $M_n = 104\,000$ ;  $L_0 = 48$  nm) films on unpatterned surfaces (a) and chemically nanopatterned surfaces with 47.5 nm periodicity (b), prepared as

reported in Figure 4.7. When the surface pattern is greater than  $L_0$  (c), lamellae exhibit an imperfect ordering. Reproduced with permission from Ref. [183]; © 2003, Nature Publishing Group.

stacked one-dimensional (1-D) lamellar assembly along surfaces chemically stripe patterned by conventional lithography [188]. A further optimization of blend composition, polymer chemistry and lithographic techniques will make it possible to fabricate nonregular shaped structures of different types, which implicitly afford the production of nanodevices requiring patterns more complex than simple periodic arrays.

## 4.5

### Epitaxy and Surface Interactions

Control of the orientation of microdomains in the microstructure of BCs can be obtained through a bias field induced by surface interactions. It is well known that a certain type of substrate strongly influences the structure of polymers. A trivial example is the action of nucleating agents on the crystallization, which has often been attributed to epitaxy of the growing polymer crystal. The interactions between the surfaces of a substrate or of confining walls and the molecules of amorphous or semicrystalline block copolymers, determine the orientation of domains on the substrate. Different types of interaction can be established depending on the nature of the surface and of the BC.

Specific interactions, such as epitaxy and directional crystallization, are involved in semicrystalline or amorphous BCs and crystalline substrates. It will be shown in the following sections that epitaxy and/or graphoepitaxy can be used in combination with the directional crystallization providing powerful methods for creating regular surface patterns in BC thin films.

#### 4.5.1

##### Preferential Wetting and Homogeneous Surface Interactions

The microstructures in thin films block copolymers generally depend on additional variables such as thickness of the film and two types of surface interactions—that is, interactions of the BC with the superstrate (often air) and with the substrate. In particular, the behavior of BC thin films depends primarily on the interfacial interactions and commensurability of the period of the BC with the film thickness. The chemical modification of BCs and various surface-patterning techniques (e.g., soft lithography and holography) allow a better control of the microdomain structures of BC thin films. The simplest interaction of a BC film deposited on a substrate is the preferential wetting of one block at an interface so as to minimize the interfacial and surface energies. As a consequence, a parallel orientation of microdomains, lamellae and cylinders is often induced at the interface, and this orientation tends to propagate throughout the entire film [9, 189–200]. Quantization of the film thickness occurs in thin films with dimensions of the order of only a few microdomain repeats, when the thickness is incommensurate with the natural period of the block copolymer. For lamellar-forming block copolymers,

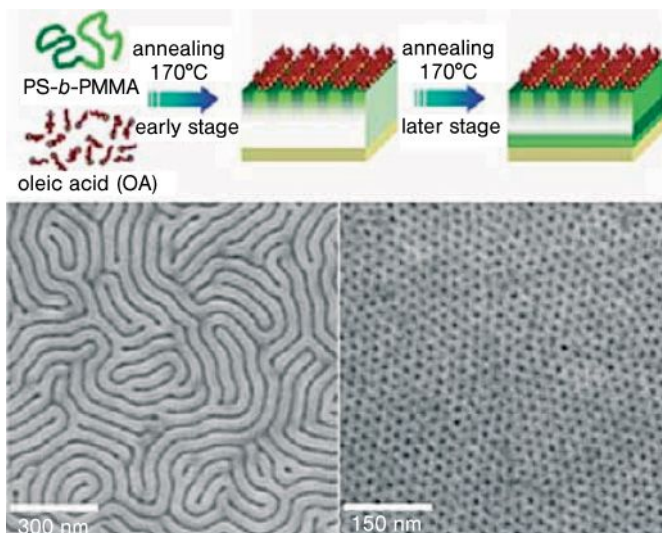
discrete integer or half-integer values of the repeat period occur, leading to the formation of terraces (i.e., islands and holes) at the polymer/air interface [193–196].

The microstructure can be altered by variation of the film thickness on the substrate and preferential interactions of blocks with the substrate [59, 198, 199, 201–203]. Symmetric boundary conditions are established when one of the blocks interacts preferentially with both the substrate and the air surface [193], whereas asymmetric conditions pertain when one block is preferentially wetted by the substrate and the other block by the superstrate [197].

The control of orientation of the microdomains can also be achieved by confining a BC between two surfaces; that is, adding a superstrate to a BC film supported on a substrate [204–207]. Strong or weak interactions of BCs with the surfaces can be created by coating the surface walls with a homopolymer or a random copolymer, respectively, containing the same chemical species as the confined BC [206]. In the case of a neutral surface, for example, by using a random copolymer, the lamellar microdomains rearrange themselves so that the direction of periodicity is parallel to the substrate [206, 208–210]. Moreover, decreasing the confined film thickness—that is, creating a large incompatibility strain of the natural domain period of the BC and the film thickness—induces a heterogeneous in-plane structure where both parallel and perpendicular lamellae are located near the confining substrate [207]. Various theoretical studies have predicted the structural behavior of BC thin films in a confined geometry [211–220] and are basically consistent with experimental results.

Great influences of both film thickness and surface interaction on the orientations of the microdomains have also been found for BCs forming cylinder [190, 221–229] and sphere [230, 231] morphologies. A parallel-to-vertical transition of cylindrical PB microdomains was observed, depending on film thickness [190, 223, 224, 228]. Moreover, strong preferential interactions between one block and the substrate in the case of confined and supported block copolymer thin film, induce a transition from cylindrical microdomains to a layered structure near the substrate surface [221, 222, 224]. It has also been shown that in cylinder-forming PS-*b*-PB BC thin films, the PS cylinders transformed into a perforated interlayer, penetrated by PB channels that connect the two outermost PB surface layers, for film thicknesses that are significantly less than their respective unperturbed chain dimensions [224]. For the reverse structure—that is, PB cylinders in a polystyrene matrix—the cylinders transformed into spheres as the film thickness decreased, then to hemispheres, and finally to a bilayer of surface-segregated PB covering a PS-rich interlayer [224].

The alignment of microdomains in both substrate-supported and -confined films has also been achieved by tuning the specific interaction between the BC and the substrate through modification of the surface [27, 139, 210, 232, 238]. An example is the application of a random copolymer brush anchored on the substrate, which allows the orientation of the domains to be changed from parallel to perpendicular by altering the composition of the random copolymer [238]. A new approach



**Figure 4.9** Schematic on the surfactant-assisted orientation of PS-*b*-PMMA thin film. Reproduced with permission from Ref. [239]; © 2008, Wiley-VCH.

developed by Char and coworkers is based in the addition of a low-molecular-weight surfactant, oleic acid, that has the effect to mediate the self-assembly of the BC thin film (Figure 4.9) [239]. At the early stage of the thermal annealing, oleic acid (whose acid groups have a preferential affinity with the hydrophobic part of the PMMA block) segregates to the upper part of the film, and preferentially in the PMMA domains. The energetically neutral conditions at the surface rapidly induce the perpendicular orientation of microdomains into the inner film.

#### 4.5.2

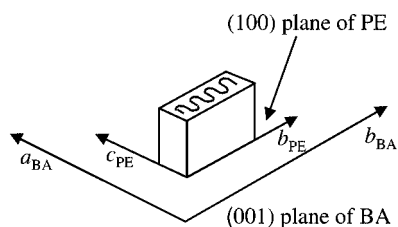
##### Epitaxy

Epitaxy is defined as the oriented growth of a crystal on the surface of a crystal of another substance (the substrate). The growth of the crystals occurs in one or more strictly defined crystallographic orientations defined by the crystal lattice of the crystalline substrate [240–242]. The resulting mutual orientation is due to a 2-D or, less frequently, a 1-D structural analogy, with the lattice matching in the plane of contact of the two species [240]. The term epitaxy, literally meaning “on surface arrangement,” was introduced in the early theory of organized crystal growth based on structural matching [240–242]. Discrepancy between atomic or molecular spacings is measured by the quantity  $100(d - d_0)/d_0$ , where  $d$  and  $d_0$  are the lattice periodicities of the adsorbed phase and the substrate, respectively. In general 10–15% discrepancies are considered as an upper limit for epitaxy to occur in polymers [242].

Inorganic substrates were first used for the epitaxial crystallization of polymers [243–257]. Successive studies have demonstrated the epitaxial crystallizations of polyethylene (PE) and linear polyesters onto crystals of organic substrates, such as condensed aromatic hydrocarbons (naphthalene, anthracene, phenanthrene, etc.), linear polyphenyls, and aromatic carboxylic acids [258–262]. In the case of PE, a unique orientation of the crystals grown on all the substrates is observed, with different contact planes depending on the substrate [258–260].

An example of an epitaxial relationship between PE crystals and an organic substrate is shown in Figure 4.10, with the substrate constituted by a crystal of benzoic acid (BA) [259] (monoclinic structure with  $a = 5.52 \text{ \AA}$ ,  $b = 5.14 \text{ \AA}$ ,  $c = 21.9 \text{ \AA}$  and  $\beta = 97^\circ$ , with a melting temperature of  $123^\circ\text{C}$ ). A clear match between the PE interchain distance (the  $b$ -axis of PE equal to  $4.95 \text{ \AA}$ ) and the  $b$ -axis periodicity of benzoic acid crystal ( $5.14 \text{ \AA}$ ), and between the  $c$ -axis periodicity of PE ( $2.5 \text{ \AA}$ ) and the  $a$ -axis of benzoic acid crystal ( $5.52 \text{ \AA}$ ), produces the crystallization of PE onto preformed crystals of benzoic acid with lamellae standing edge-on, that is, normal to the surface of benzoic acid crystal (Figure 4.10). The PE polymer chains lie flat on the substrate surface with their chain axis parallel to the substrate surface and parallel to the  $a$ -axis of benzoic acid crystal, and the  $b$ -axis of PE parallel to the  $b$ -axis of the benzoic acid crystal [259]. The (100) plane of PE is in contact with the (001) exposed face of benzoic acid.

In order to apply epitaxial control, BCs need to have at least one crystalline block, which can interact with a crystalline surface. The morphology of semicrystalline block copolymers is the result of the interaction between microphase separation of the component blocks and crystallization of the crystallizable block. The process pathway of structure formation is of primary importance, in the sense that the forming structures set off those emerging to the described geometry into which the new structure must evolve. The final morphology is therefore path-dependent; different microdomain structures are obtained if the crystallization occurs from a homogeneous melt (in this case the crystallization drives the



$$(100)_{PE} \parallel (001)_{BA} \quad b_{PE} \parallel b_{BA} \quad \text{and} \quad c_{PE} \parallel a_{BA}$$

**Figure 4.10** PE lamella oriented edge-on on the (001) face of a BA crystal substrate after epitaxial crystallization. The (100) plane of PE is in contact with the (001) plane of BA, and  $b$ - and  $c$ -axes of PE are parallel to  $b$ - and  $a$ -axes of BA, respectively [259].



microphase separation), or it occurs from an already microphase-separated heterogeneous melt (in this case microphase separation precedes crystallization and provides a microstructure within which crystallization takes place.) In the latter case, crystallization is confined to occur within the pre-existing microseparated domains; crystallization confined in preformed lamellar, spherical or within and outside cylindrical microdomains has been observed [12, 78, 80]. Different situations occur when the crystallization is controlled by epitaxy. Although the versatility of epitaxy in the case of crystallization of polymers has clearly been shown, the method of using organic substrates to control the crystallization and the morphology of semicrystalline BCs was introduced only in 2000, when De Rosa and coworkers [184–263] first used epitaxy to control the molecular and microdomain orientation of PE-*b*-PEP-*b*-PE and PS-*b*-PE semicrystalline BC thin films. These authors used BA [184, 263, 264] or anthracene (AN) [264, 265] and obtained precise control of the molecular orientation of the crystalline block and subsequent overall long-range order of the BC microdomains.

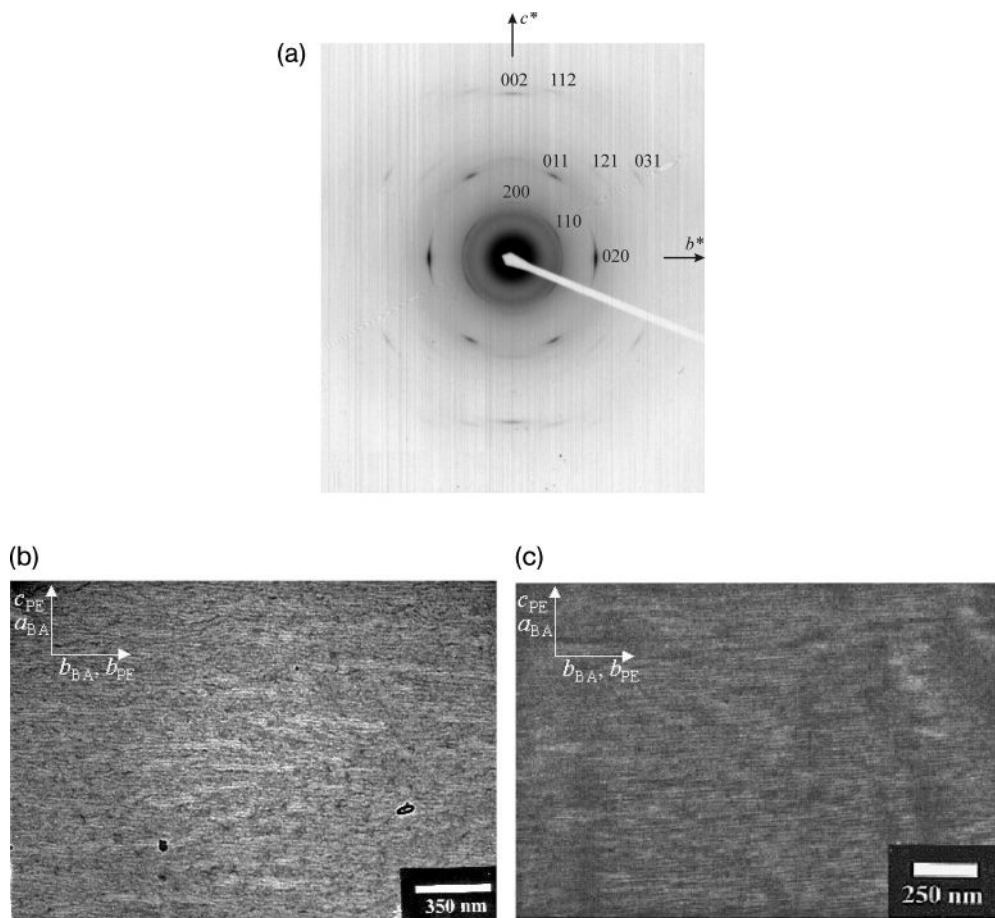
The selected area electron diffraction pattern and the transmission electron microscopy (TEM) bright-field image of a thin film of PE-*b*-PEP-*b*-PE epitaxially crystallized onto a BA crystal are shown in Figure 4.11a and b, respectively. The diffraction pattern essentially presents only the  $0kl$  reflections of PE, and therefore corresponds to the  $b^*c^*$  section of the reciprocal lattice of PE (Figure 4.11a). This indicates that the chain axis of the crystalline PE lies flat on the substrate surface and is oriented parallel to the  $a$ -axis of the BA crystals, as in the case of the PE homopolymer (Figure 4.10) [184]. The (100) plane of PE is in contact with the (001) plane of BA; therefore, the crystalline PE lamellae stands edge-on on the substrate surface, with the  $b$ - and  $c$ -axes of PE oriented parallel to the  $b$ - and  $a$ -axes of BA, respectively. The bright-field TEM image (Figure 4.11b) indicates that epitaxy has produced, instead of a spherulitic structure, a highly aligned lamellar structure with long, thin crystalline PE lamellae with a thickness of 10–15 nm, evidenced as dark regions, oriented along the  $[010]_{\text{PE}}||[010]_{\text{BA}}$  direction. The dark-field image created by using the strongest 110 reflection (see Figure 4.11c) reveals the same parallel array of crystalline edge-on PE lamellae oriented along the  $b$ -axis of BA crystals. This can be seen as bright regions due to the lamellae all being arranged in Bragg diffraction conditions determined by the 2-D epitaxy [184]. A scheme of the orientation of the PE-*b*-PEP-*b*-PE obtained on BA crystals is shown in Figure 4.12 [184]. The biaxial matching of the BA and PE lattices creates a highly ordered lamellar BC microdomain state. The widths of the crystalline PE lamellae are highly uniform, the PE crystals and the intervening noncrystalline PEP are all parallel, and the orientations of both the  $c$ - and  $b$ -axes of PE crystals over many micron-sized regions are very high [184].

#### 4.5.3

##### Directional Crystallization

In polymer–diluent binary mixtures, if both the polymer and solvent are crystallizable above room temperature, then a eutectic-like behavior can be observed. In



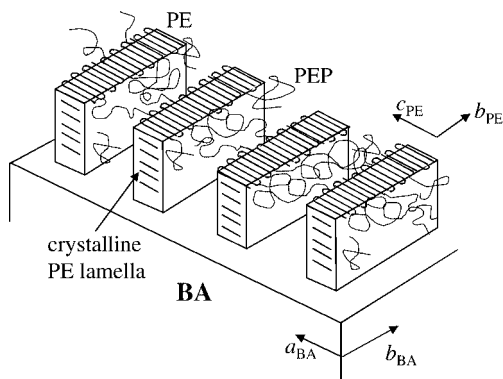


**Figure 4.11** (a) Selected area electron diffraction pattern, (b) TEM bright-field image, and (c) TEM (110) dark-field image of a thin film of PE-*b*-PEP-*b*-PE epitaxially crystallized onto a BA crystal. In the TEM bright-field image, the dark regions correspond to the denser crystalline PE phase, which form long lamellae standing edge-on on the substrate

surface and preferentially oriented with the *b*-axis of PE parallel to the *b*-axis of the BA (panel b). In the dark-field image, the bright regions correspond to the crystalline PE lamellae in the Bragg condition (panel c). Reproduced with permission from Ref. [184]; © 2000, The American Chemical Society.

fact, the melting temperatures of both the polymer and solvent are depressed up to the eutectic composition [266–271].

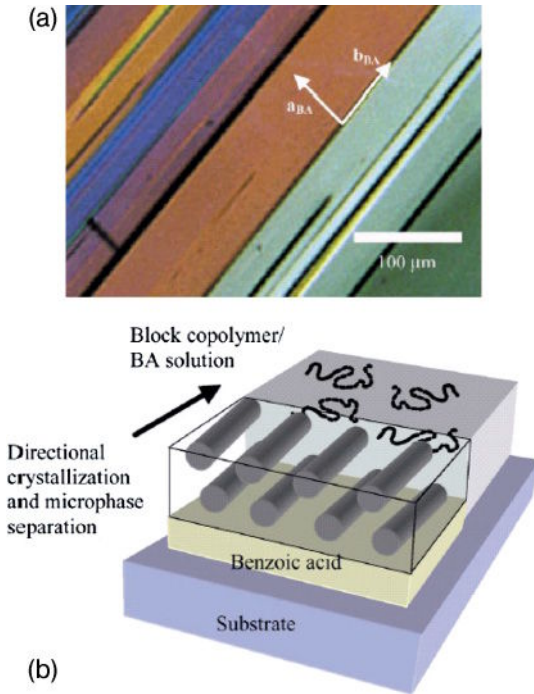
The presence of solvent in a noncrystalline BC depresses the order–disorder temperature of the BC, depending on the solvent quality. Several theories predict the phase behavior of BC–organic solvent mixtures [272–274]. Therefore, it can be expected that mixtures of BCs with crystallizable solvents exhibit eutectic behavior. In theory, the two liquidus lines of the binary mixture of a block copolymer and



**Figure 4.12** Schematic model of the crystalline and amorphous microdomains in the PE-*b*-PEP-*b*-PE triblock copolymer epitaxially crystallized on the BA crystal. The epitaxy shows the relative orientation of

crystalline PE lamellae on the BA crystal:  $(100)_{PE} || (001)_{BA}$  and  $c_{PE} || a_{BA}, b_{PE} || b_{BA}$ .  
Reproduced with permission from Ref. [184];  
© 2000, The American Chemical Society.

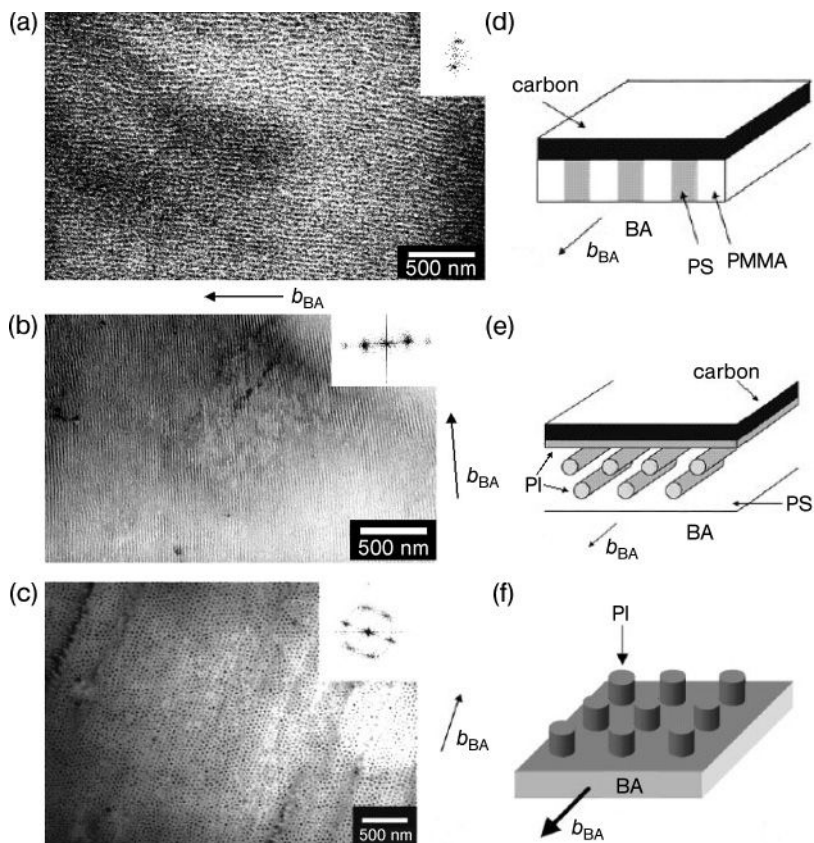
an organic diluent—that is, the freezing point depression curve of the organic diluent and the order–disorder temperature depression curve of the BC—can meet each other at a certain composition and induce the characteristic eutectic transformation of a liquid to two solids: the crystalline solvent and the phase-separated solid block copolymer. Since the order–disorder transition in a block copolymer is a weak first-order transition, the phase-separated block copolymer at the invariant point can have some nonzero diluent content, as seen in the mixtures of block copolymer and solvents [274]. If this were the case, the phase separation at the invariant point would be from homogeneous liquid into a pure solid (crystalline solvent) and another solid (solvent-swollen BC microdomains). Park *et al.* [275] used this hypothesis of eutectic formation to globally organize the eutectic mixture for the first time and induce the alignment of microdomains in the solid BC. These authors used organic diluents, such as BA and AN, and amorphous asymmetric PS-*b*-PI and symmetric PS-*b*-PMMA diblock copolymers [275]. In this process, the first requirement is that the diluent must dissolve the BC above the melting temperature of the solvent. Second, the diluent must have a tendency to crystallize directionally into large, plate-like crystals. When the organic diluent, which initially was a solvent for the BC, directionally crystallizes along its fast growth direction under a temperature gradient, the BC undergoes microphase separation, due to a rapid decrease in the solvent concentration. At the same time, the orientation of the microdomains nucleated from the eutectic transforming solution is determined by the fast directional growth of the organic diluent. In the case of BA and AN, the fast growth directions are both *b*-axis, and consequently the intermaterial dividing surface of the microdomains of the BC tends to orient along this direction, which also corresponds to the temperature gradient direction [275]. A polarized optical microscope image of directionally crystallized BA crystal is shown in Figure 4.13a [275]. The BA crystal is elongated along the fast growth *b*-axis and presents



**Figure 4.13** (a) Polarized optical microscopy image of directionally crystallized BA crystals. The large, flat and elongated BA crystals are aligned with the  $b$ -axis parallel to the growth front direction. Reproduced with permission from Ref. [275]; © 2001, The American Chemical Society; (b) Schematic model of the microstructure formation of a cylinder forming BC under directional crystallization of the BA from homogeneous solution. Reproduced with permission from Ref. [12]; © 2003, Elsevier.

a flat (001) surface. The different thicknesses of the BA crystals lead to the different colors under the microscope. A schematic model of cylindrical microdomains well aligned from the directional eutectic transformation of the homogeneous BC solution is shown in Figure 4.13b [12]. This process occurs within a few seconds (the growth velocity of the BA crystal is nearly  $1\text{ cm s}^{-1}$ ) and the microstructure is formed and then kinetically trapped.

Examples of the ordered microstructures obtained by this process are shown in Figure 4.14 for symmetric PS- $b$ -PMMA (Figure 4.14a) and asymmetric PS- $b$ -PI (Figure 4.14b,c) diblock copolymers prepared by directional solidification with BA crystals [275]. In the case of PS- $b$ -PMMA, the darker regions correspond to the RuO<sub>4</sub>-stained PS microdomains (Figure 4.14a). Edge-on parallel lamellae of PS and PMMA are well aligned along the fast growth direction of the BA crystals (the  $b$ -axis), as shown in the schematic model of Figure 4.14d [275]. The well-aligned parallel lamellae extend over regions larger than  $50\mu\text{m}^2$ . The fast Fourier transform (FFT) power spectrum in the inset of Figure 4.14a shows a spotlike first reflection located on the meridian, indicating the nearly



**Figure 4.14** TEM bright-field images of thin films directionally solidified with BA of the symmetric PS-*b*-PMMA (20-nm thick) stained with RuO<sub>4</sub> (a), the asymmetric PS-*b*-PI stained with OsO<sub>4</sub> with a thickness of 50 nm (b) and 20 nm (c). The dark regions correspond to the stained PS lamellae (a), parallel PI cylinders (b) and vertically oriented PI cylinders (c) well aligned along the fast

growth direction of the BA crystals (*b*-axis). The insets show the FFT power spectrum of the TEM micrographs. Schematic models of the microstructures of PS-*b*-PMMA (d), PS-*b*-PI (e) and ultrathin film of PS/PI (f) processed with BA. Reproduced with permission from Ref. [275]; © 2001, The American Chemical Society; and with permission from Ref. [12]; © 2003, Elsevier.

single-crystal-like microdomain structure. The fast directional microstructure formation during the phase separation with a thin film thickness approximately less than a half-lamellar period avoids preferential wetting of one of the blocks on the substrate, leading to the oriented lamellae microdomain structure where the interface of the microdomains is parallel to the normal of the substrate surface [275]. The structure is kinetically driven and subsequently vitrified at room temperature. Importantly, for regions thicker than approximately a half-lamellar period, the perpendicular lamellae orientation switches to an in-plane parallel one, and large planar regions are produced. The bright-field TEM image of a film of the asymmetric PS-*b*-PI with a thickness of approximately 50 nm,

directionally solidified with BA (Figure 4.14b) shows OsO<sub>4</sub>-stained darker PI cylinders, lying in-plane and well oriented along the crystallographic *b*-axis of the BA, as reported in the scheme of Figure 4.14e [275]. The ordered parallel cylinder structure also extends over regions larger than 50 μm<sup>2</sup>. The average diameter of the PI cylindrical microdomains is approximately 20 nm, while the average distance between the cylinders is 40–50 nm. In both of these examples, the initial homogeneous solution confined between the glass substrates transforms due to the imposed directional solidification of large crystals of BA having (001) surfaces coexisting with a thin liquid layer near the eutectic composition. Dropping the temperature further then causes this layer also to directionally solidify by thickening the preexisting BA crystal with the simultaneous formation of a thin, metastable vertically oriented *lamellar* microdomain film (Figure 4.13b) [275]. In the case of the PS-*b*-PMMA, the vertical lamellar structure is vitrified due to the high glass transition temperatures of both blocks. In the case of PS-*b*-PI with a low volume fraction of PI block, however, it has been hypothesized that the vertical lamellar microstructure is transformed into in-plane cylindrical microstructure due to the interfacial instability of thin lamellae, film thickness, and preferential wetting of the PI block [275]. Similar ordered microstructures have been obtained employing other organic crystallizable solvents as AN which has a melting temperature of 216 °C, about 100 °C higher than that of BA [275].

This process has also been used in combination with thickness effects to achieve vertically aligned cylinders employing ultrathin films [275]. Cylindrical microdomains, indeed, orient vertically for relatively thin films due to incommensurability effects, which is similar to what was observed for lamellar diblock copolymers [276]. A bright-field TEM image of a thinner film (of approximately 20 nm thickness) of PS-*b*-PI, prepared from a more dilute solution, directionally solidified with BA and stained with OsO<sub>4</sub>, is shown in Figure 4.14c [275]. The dark OsO<sub>4</sub>-stained vertically aligned cylindrical PI microdomains are oriented into rows along the *b*-axis of the BA crystal and packed in an approximate hexagonal lattice, as shown in the schematic model of the microstructure reported in Figure 4.14f [275]. The aligned vertical cylinders extend over regions larger than 50 μm<sup>2</sup>. The FFT power spectrum in the inset of Figure 4.14c shows spotlike first reflections with sixfold symmetry, indicating approximate hexagonal packing of the cylindrical PI microdomains.

Various di- and tri-block copolymers with different architecture and properties such as rubbery–glassy, glassy–glassy, amorphous–crystalline, amorphous–liquid crystalline, and ABC-type terpolymers have been successfully organized with this process [275].

#### 4.5.4

#### Graphoepitaxy and Other Confining Geometries

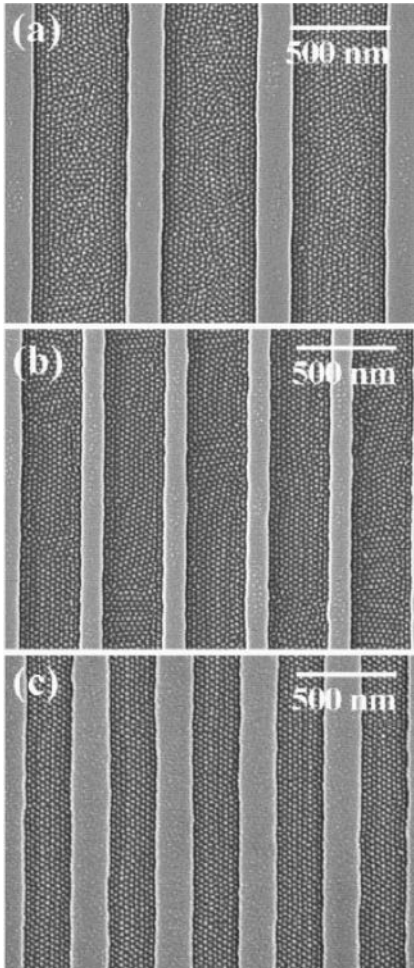
Graphoepitaxy is a process whereby an artificial surface topography of a crystalline or amorphous substrate influences and controls the orientation of the crystal growth in thin films [277–280]. Graphoepitaxy has been used (often in combination with epitaxy) to obtain high orientation of polymeric crystals onto substrates

constituted by films of other polymers [281–285]. For instance, a variety of polymers, including PE, nylons, polyesters, and liquid crystalline polymers, have been grown in highly oriented form on the oriented surface of poly(tetrafluoroethylene) (PTFE) crystals [281]. In the case of PE, the orientation of the crystals is such that the *c*-axis lies in the plane of the film and the *bc* plane of the unit cell is in contact with the substrate surface [285]. Different orientations, for instance, a fiber-like alignment, have been observed for other polymers [285]. This suggests that the alignment of materials on PTFE films can occur by graphoepitaxial or epitaxial mechanisms, depending on the materials. In some instances both the lattice structure and the surface topography of the PTFE films promote the alignment, so that the two mechanisms can operate in conjunction [285].

Graphoepitaxy was utilized by Segalman and coworkers [286, 287] to control the orientation of BC microdomains. The procedure is an example of the combined top-down and bottom-up approaches to patterning. Segalman's group used topographically alternating mesa and well patterns fabricated by conventional photolithography and chemical etching techniques to align spherical P2VP microdomains of a PS-*b*-P2VP diblock copolymer. A large area single crystal of the P2VP spheres was obtained on the mesas and wells [286].

Nanostructures with long-range order were also developed using graphoepitaxy in combination with BC lithography [288, 289]. Cheng *et al.* employed a diblock copolymer of PS-*b*-PFS, in which the organometallic PFS block provides an excellent (10:1) etching contrast in an oxygen plasma [287]. A topographically patterned silica substrate was fabricated by interference lithography, after which the substrate was used for a templating BC self-assembly. Monolayer films of the BC were deposited by spin-casting and annealed onto the patterned silica substrate. The film was then oxidized by etching in an oxygen plasma. Scanning electron microscopy (SEM) images of annealed and etched PS-*b*-PFS films, reported in Figure 4.15, revealed ordered arrays of PFS spheres in grooves of different widths [288]. A thin PFS-PS brush layer is present at the groove edge and bottom where the PFS block wets the silica substrate. This surface-induced thin layer was shown to drive the ordering of the PS-PFS block copolymer microdomains, and resulted in PFS spherical microdomains parallel to the groove edges. In the microstructure with grooves having a width of 240 nm (Figure 4.15c), and comparable to the typical block copolymer grain size, a near-perfect alignment of PFS spherical microdomains was achieved. The microdomain patterns were transferred onto the underlying silica substrate using a reactive ion etcher (RIE) process with a CHF<sub>3</sub> plasma, so as to create well-ordered arrays of silica posts [288]. The oxidized PFS domains are perfectly ordered by the guided self-assembly of the BC in the prepatterned substrate, and can potentially be useful for fabricating 2-D photonic crystal waveguide structures. More recently, other investigations have confirmed the general applicability of this approach employing spherical, cylindrical or lamellar diblock copolymers to yield 2-D patterns into different lithographic features [35, 36, 38, 290, 291]. However, as the pre-pattern size should be determined by the grain size of the block copolymers, only patterns with a small periodicity are applicable. To overcome this problem, graphoepitaxy should be combined with





**Figure 4.15** SEM images of annealed and oxygen plasma-treated PS-*b*-PFS films on silica gratings with (a) 500 nm-wide grooves, (b) 320 nm-wide grooves, and (c) 240 nm-wide grooves. Reproduced with permission from Ref. [288]; © 2002, The American Institute of Physics.

methods that allow the grain size of the BCs to be increased, which can then in turn be controlled with the micron size patterns available, for example, from soft lithography [12]. As discussed in the next sections, the combination of graphoepitaxy or epitaxy with directional crystallization provides possible routes to achieve this result.

Unlike graphoepitaxy, which can be considered to approximate a 1-D confinement of a thin film between (often parallel) solid walls, the 2-D confinement of BCs has been predicted to induce more complicated effects on phase-separation

and morphology orientation [292–294]. Recent investigations have confirmed for various PS-based diblock copolymers that, in the case of a nonplanar geometry of confinements, such as in cylindrical pores, the confining of dimensions incommensurable with the copolymer period and the imposed curvature leads to the production of unusual morphologies [295–297]. The self-assembly of asymmetric diblock copolymers introduced as a melt into nanoporous alumina templates occurs with an alignment of the cylinders along the pore axis, favored by the preferential wetting of the pore with the majority block [296]. Furthermore, for symmetric BCs, concentric lamellae oriented parallel to the long axes of the pores have been observed, with an overall number of lamellae and forbidden segregations that are directly dependent on the pore diameter and the preferential wetting of one block, respectively [296, 297].

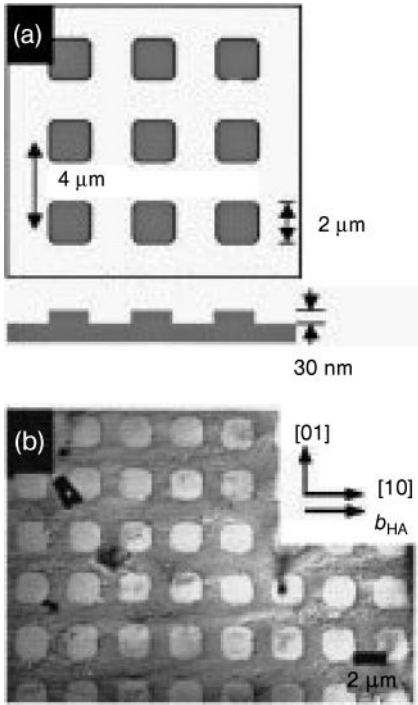
#### 4.5.5

##### Combination of Directional Crystallization and Graphoepitaxy

The idea of combining graphoepitaxy from a topographical pattern fabricated by conventional photolithography procedures and the directional crystallization of a solvent was first introduced by Park *et al.* [298]. The thin film of the BC was confined between crystals of BA, obtained from a directional eutectic crystallization of the homogeneous BC solution, and the topographic substrate pattern. The confinement induced a thickness variation of the BC film, and resulted in the two different orientations of the microdomains [298]. The patterned substrate was produced via standard lithographic techniques, and consisted of 30 nm-high,  $2\ \mu\text{m} \times 2\ \mu\text{m}$  mesas arranged in a square array with a  $4\ \mu\text{m}$  spacing, as shown in the schematic diagram of Figure 4.16a. The square-shaped mesas are made by selective etching of a thermally grown silicon oxide on a 10 cm wafer. A PS-*b*-PI diblock copolymer was directionally solidified with benzoic acid on the patterned substrate [298]. A low-magnification, bright-field TEM micrograph of the OsO<sub>4</sub>-stained BC film is shown in Figure 4.16b. The prepatterned substrate structure produces thickness variations in the directionally solidified BC thin films; the films are thinner on the mesas and thicker in the plateau regions. As described in Section 4.5.3 (see Figure 4.14b,c), the directional eutectic solidification produces an orientation of PI cylinders along the *b*-axis of the benzoic acid crystal or normal to the substrate, depending on the thickness [275, 298].

The BC film directionally solidified on the patterned substrate was then subjected to O<sub>2</sub>-RIE to selectively remove the cylindrical PI microdomains [298]. A higher-magnification atomic force microscopy (AFM) image after O<sub>2</sub>-RIE, shown in Figure 4.17a, reveals the double orientation of the cylindrical PI microdomains. In the thicker film regions (ca. 50 nm thick), the cylindrical PI microdomains are well aligned along the *b*-axis of the BA crystal, with the cylinder axis parallel to the substrate and to the walls of the mesas. In the thinner film regions (ca. 20 nm thick), the PI cylinders are hexagonally packed with their cylinder axes perpendicular to the substrate and with the *a*<sub>1</sub> hexagonal lattice direction parallel to *b*-axis of BA; that is, along the [10] direction of the square substrate pattern [298]. The SEM



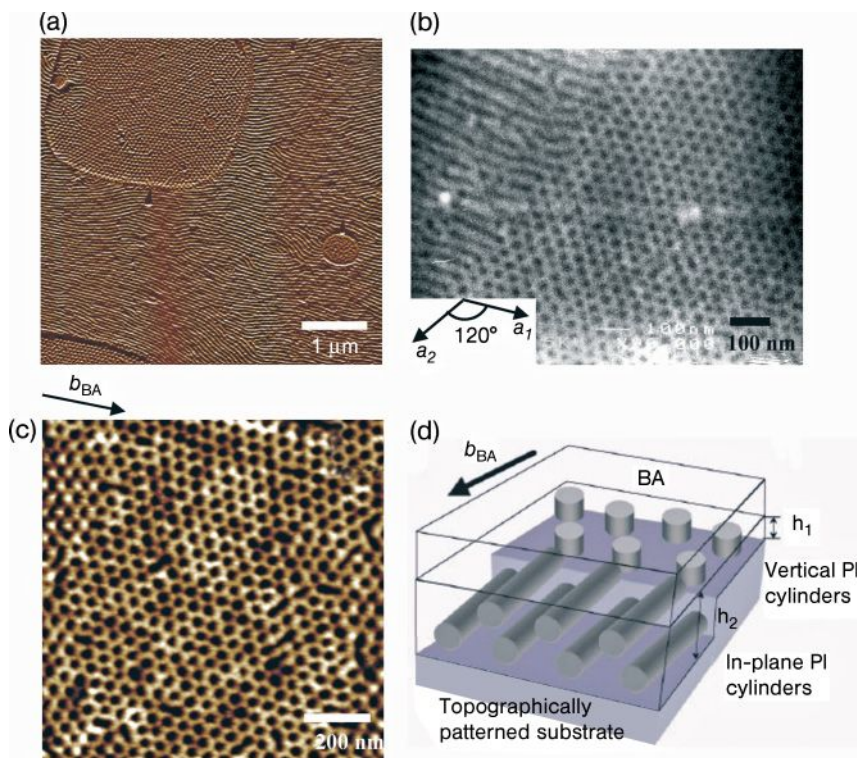


**Figure 4.16** (a) Schematic of the topographically patterned silicon oxide substrate; (b) Bright-field TEM image of a thin film of PS/PI block copolymer, directionally solidified with BA on the prepatterned substrate. The low-magnification image depicts a typical region larger than  $1000\mu\text{m}^2$  where the cylindrical PI microdomains are aligned via directional solidification. The

replicated micron-scale pattern structure is seen due to the different film thicknesses in the two types of region. The inset shows the basis vectors of the cylindrical PI microdomain lattice and the fast growth direction of the BA crystal ( $b$  axis).

Reproduced with permission from Ref. [298]; © 2001, The American Institute of Physics.

image of Figure 4.17b shows that the microdomains successively transform from parallel to vertical when they pass from the plateau into the mesa regions [298]. The in-plane PI cylindrical microdomains aligned along the  $b$ -axis direction of the BA crystal in the plateau regions transform abruptly into hexagonally packed, vertically oriented cylinders. The cylindrical hole structures on the mesa areas after  $\text{O}_2$ -RIE are also shown in Figure 4.17c, in height-contrast AFM. The vertically ordered PI cylindrical domains, which appear dark, on the mesa regions are essentially empty. A scheme of this process of directional solidification of the BC, combined with topographically mediated substrate patterning, is shown in Figure 4.17d. The BC films confined between the top BA crystal and the bottom prepatterned substrate undergo thickness variation ( $h_1$  and  $h_2$ ), leading to two different microdomain orientations. Control over the position and orientation of cylindrical



**Figure 4.17** (a,c) AFM and (b) SEM images of a thin film of asymmetric PS-*b*-PI, directionally solidified with BA on the prepatterned substrate and subsequently etched by O<sub>2</sub>-RIE. The tapping mode AFM image (panel a) shows that the cylindrical PI microdomains, with two different orientations with respect to the substrate, are well aligned along the fast growth direction of the BA crystals, as indicated by the arrow. The square-shaped mesa regions exhibit vertically oriented, hexagonally packed PI cylinders. The thicker matrix regions show the in-plane PI cylinders. The SEM image reveals that aligned PI cylinders transform their in-plane to vertical

orientation with respect to the substrate. The two hexagonal lattice directions of the vertically ordered PI cylinders are shown in inset (b). The height mode AFM image on a mesa region (c) indicates that vertically ordered cylindrical PI microdomains are selectively removed by O<sub>2</sub>-RIE, which appear dark. Reproduced with permission from Ref. [298]; © 2001, The American Institute of Physics; (d) Scheme of the orientation of microdomains of PS-*b*-PI between the top BA crystal and the bottom prepatterned substrate. Reproduced with permission from Ref. [12]; © 2003, Elsevier.

domains on the patterned substrate provides nanolithographic templates for micromagnetics and microphotonics [298].

#### 4.5.6

#### Combination of Epitaxy and Directional Crystallization

The method of combination of directional crystallization and epitaxy was introduced by De Rosa *et al.* [263]. The process is based on the directional solidification

of the eutectic solution of a semicrystalline BC in a crystallizable organic solvent and subsequent epitaxial crystallization of the crystalline block onto the organic crystalline substrate [263]. The organic substrate (e.g., BA or AN) at a temperature higher than its melting temperature is a solvent for the BC, and becomes a substrate, when it crystallizes at lower temperatures, for the epitaxial crystallization of the BC [263–265, 299].

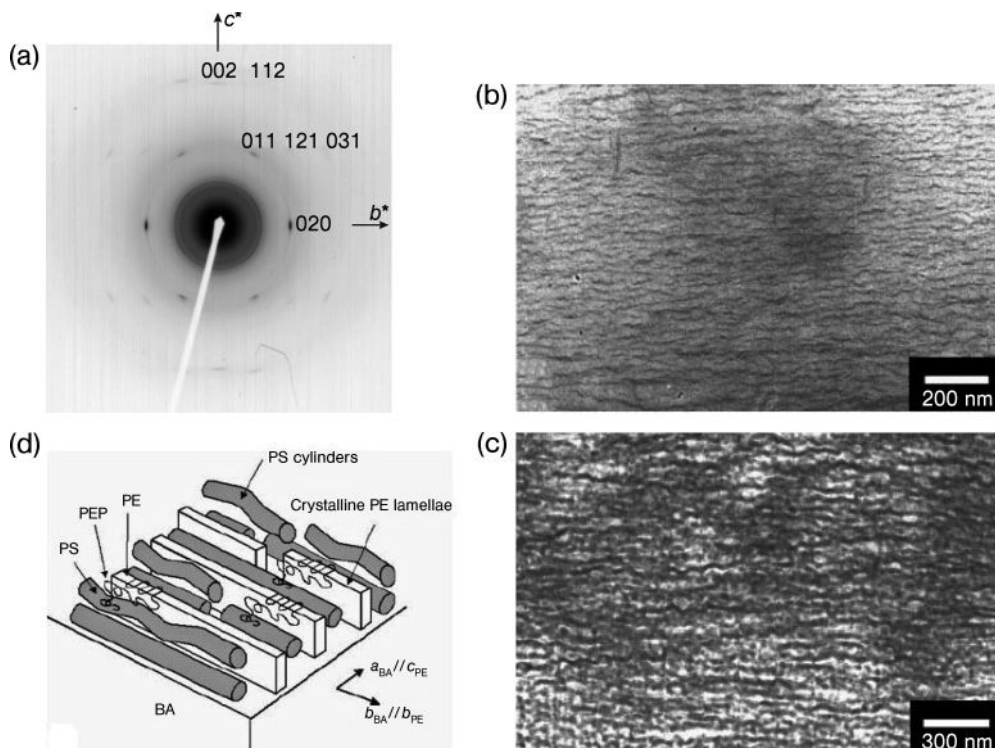
Examples of the ordered microstructures obtained with this method are provided by PS-*b*-PEP-*b*-PE and PS-*b*-PE semicrystalline BCs containing crystallizable PE blocks directionally solidified with BA or AN [263–265].

The electron diffraction pattern of PS-*b*-PEP-*b*-PE triblock copolymer film directionally solidified and epitaxially crystallized with BA is shown in Figure 4.18a [264]. As in the case of the melt-compatible PE-*b*-PEP-*b*-PE (see Figure 4.11a) [184], the pattern of Figure 4.18a essentially presents only the  $0kl$  reflections of PE, indicating orientation of the PE crystals similar to that found for the PE-*b*-PEP-*b*-PE triblock copolymer [184], and for the homopolymer, as shown in Figures 4.10 and 4.12. The crystalline PE lamellae are oriented edge-on on the substrate surface with the (100) plane of PE in contact with the (001) plane of BA. The *b*- and *c*-axes of PE are parallel to the *b*- and *a*-axes of benzoic acid, respectively.

The bright-field TEM image of the unstained film directionally solidified and epitaxially crystallized onto BA, reported in Figure 4.18b [264], shows the highly oriented lamellar structure with long thin crystalline lamellae oriented along the  $[010]_{\text{PE}}||[010]_{\text{BA}}$  direction. The bright-field image of the same sample after staining with RuO<sub>4</sub>, as shown in Figure 4.18c, indicates that the PS blocks, corresponding to the darker-stained regions, are organized in parallel cylinders the axes of which are generally oriented along the elongated direction  $[010]_{\text{PE}}||[010]_{\text{BA}}$  of the crystalline lamellae [264].

As the order–disorder temperature of PS-*b*-PEP-*b*-PE (>250 °C) is much higher than the crystallization temperature of the PE block (almost 65 °C) [300, 301], the directional crystallization of BA induces the orientation of the cylindrical PS microdomains along the fast growth direction of the BA crystal (*b*-axis) [264] (as discussed in Section 4.5.3 for amorphous BCs) [275]. Subsequently, epitaxial crystallization of the crystalline PE block onto the BA crystalline substrate induces molecular orientation of the PE chains, leading to oriented crystalline PE lamellae in the presence of pre-existing ordered PS cylinders [264]. A schematic model (Figure 4.18d) displays the final microstructure generated by a combination of the directional crystallization and epitaxy. The process induces alignment of the PS cylinders and PE lamellae along the same direction, resulting in a multilayered ordering of the PS cylinders [264].

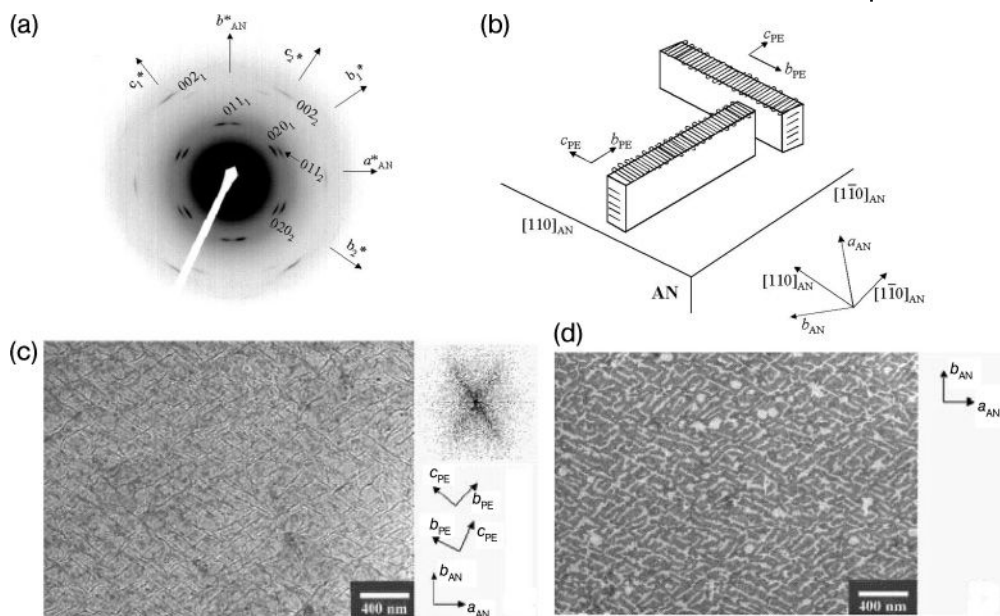
A different microstructure of the same PS-*b*-PEP-*b*-PE is obtained when AN is used as the crystallizable solvent [265], due to a different epitaxial relationship between PE and AN crystals [258]. The selected area diffraction (SAD) pattern of the PS-*b*-PEP-*b*-PE film epitaxially crystallized onto AN is shown in Figure 4.19a [265]. The pattern exhibits  $0kl$  reflections of two sets of PE crystals having two different orientations [265], corresponding to the  $b^*c^*$  sections of the PE reciprocal lattice symmetrically rotated by an angle of almost 70° with respect to the  $a^*$ -axis of the AN. This angle of 70° corresponds to the angle made by the [1 1 0] and



**Figure 4.18** Selected area diffraction pattern (a), TEM bright-field image of unstained (b) and stained with  $\text{RuO}_4$  (c) thin film of PS-*b*-PEP-*b*-PE triblock copolymer directionally solidified and epitaxially crystallized onto BA. The dark regions in the TEM bright-field image of the unstained film (panel b) correspond to the crystalline PE phase, which form long lamellae oriented edge-on, and aligned with the *b*-axis parallel to the *b*-axis of BA. The dark regions in the TEM bright-field image of the film stained with  $\text{RuO}_4$  (panel c) correspond to the PS phase, which form cylinders aligned parallel to the crystalline lamellae; (d) Schematic

model of the microstructure in thin films of the PS-*b*-PEP-*b*-PE terpolymer directionally solidified and epitaxially crystallized onto BA. The directional solidification induces in-plane cylindrical PS microdomains aligned along the fast growth direction of BA crystals. The following epitaxial crystallization of PE blocks onto the BA crystals induces the formation of long, thin crystalline PE lamellae in between the PS cylinders. The PE crystals have their (100) planes in contact with the (001) plane of the BA crystal with  $a_{\text{BA}} \parallel c_{\text{PE}}$  and  $b_{\text{BA}} \parallel b_{\text{PE}}$ . Reproduced with permission from Ref. [264]; © 2003, Wiley-VCH.

$[1 \bar{1} 0]$  directions in the *ab*-plane of the AN crystal ( $a_{\text{AN}} = 8.65 \text{ \AA}$ ;  $b_{\text{AN}} = 6.04 \text{ \AA}$ ;  $c_{\text{AN}} = 11.18 \text{ \AA}$ ;  $\beta = 124.7^\circ$ ; melting temperature of  $216^\circ\text{C}$ ). The *c*-axis of PE is therefore oriented parallel to two equivalent  $[1 \ 1 \ 0]$  and  $[1 \bar{1} 0]$  directions of the AN crystal, and two sets of PE lamellae oriented edge-on on the AN crystals are produced, with the (100) plane of PE in contact with the (001) plane of AN (Figure 4.19b) [265]. The epitaxial relationship between PE and AN crystals can be readily explained in terms of matching between the *b*-axis of PE and the inter-row spacing



**Figure 4.19** (a) Selected area electron diffraction pattern of a thin film of PS-*b*-PEP-*b*-PE block terpolymer epitaxially crystallized onto AN; (b) Scheme showing the two orientations of edge-on PE lamellae onto the (001) exposed face of the AN crystals. The (100) plane of PE is normal to the electron beam and parallel to the (001) face of the AN crystals. The *c*-axes of the two sets of PE crystals are parallel to the  $[1\ 0\ 9]$  and  $[1\ \bar{1}\ 0]$  direction of the AN crystal; (c) TEM bright-field image of an unstained thin film of

PS-*b*-PEP-*b*-PE epitaxially crystallized on AN. The dark regions correspond to the crystalline PE phase, which forms cross-oriented PE lamellae standing edge-on; (d) TEM bright-field image of the film of PS-*b*-PEP-*b*-PE epitaxially crystallized on AN and stained with RuO<sub>4</sub>. The dark regions correspond to the PS phase, which forms a double-oriented structure similar to that of the PE microdomains. Reproduced with permission from Ref. [265]; © 2001, Wiley-VCH.

of the (110) plane of AN and a second matching of  $2c$  of PE with the Bragg distance of the (110) plane ( $d_{110}$ ) of AN [258]. Similar lattice matching occurs between PE and other aromatic substances [258].

The bright-field TEM image of the unstained film of the PS-*b*-PEP-*b*-PE epitaxially crystallized onto AN (Figure 4.19c) provides a direct visualization of the crystalline PE lamellae that presents a cross-oriented texture. The lamellae having a thickness of 10–20 nm are oriented along the two different  $[1\ 1\ 0]$  and  $[1\ \bar{1}\ 0]$  directions of the AN crystals [265]. A bright-field image of a different region of the same sample after staining with RuO<sub>4</sub> (Figure 4.19d) indicates that the PS blocks (the darker regions) are organized into a similar, double-oriented pattern [265]. The directional solidification of the mixture of the terpolymer and AN develops the orientation of the cylindrical PS microdomains along the fast growth direction of the AN crystals (*b*-axis direction) before crystallization of the PE. The epitaxial



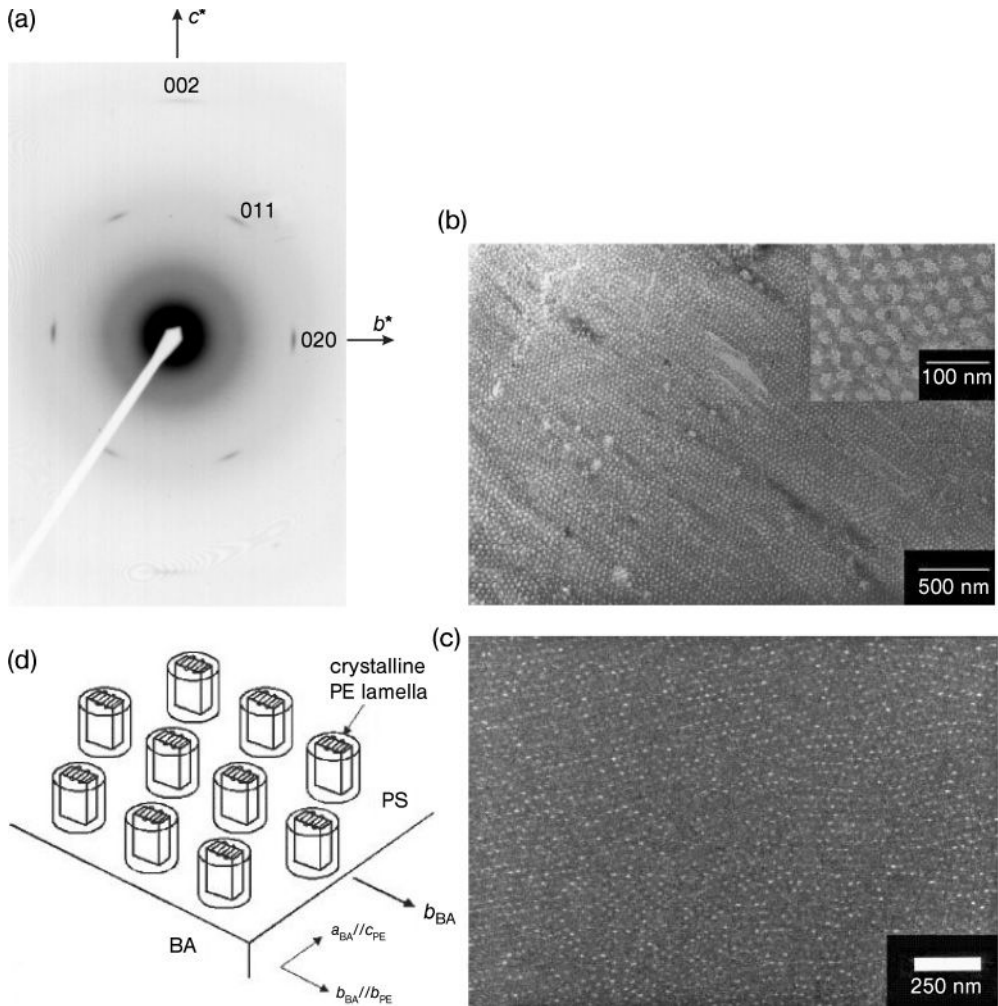
crystallization induces a high orientation of the molecular chains of the crystalline phase, resulting in PE lamellae standing edge-on on the substrate surface, oriented in two directions due to the crystallographic degeneracy. This structure in turn induces reorganization and reorientation of the pre-existing PS cylinders [265].

This thin-film process suggests the possibility of creating new 2-D microdomain textures via self-assembled semicrystalline BCs using a combination of one or more crystallizable blocks and various crystalline organic substrates [265].

The asymmetric PS-*b*-PE diblock copolymer is an interesting example of crystallization of PE confined in PE cylinders formed by self-assembly in the melt [263, 264]. The electron diffraction pattern of an unstained film of PS-*b*-PE film epitaxially crystallized onto BA is shown in Figure 4.20a. The pattern is similar to those obtained for the PS-*b*-PEP-*b*-PE (Figure 4.18a) [264] and PE-*b*-PEP-*b*-PE (Figure 4.11a) [184] epitaxially crystallized onto BA and presents only the  $0kl$  reflections of PE. This indicates that the PE lamellae are oriented edge-on on the (001) surface of BA, with the (100) plane of PE in contact with the (001) plane of BA and the *b*- and *c*-axes of PE parallel to the *b*- and *a*-axes of BA, respectively, as shown in Figures 4.10 and 4.12. A bright-field image of a thin film of PS-*b*-PE directionally solidified and epitaxially crystallized onto BA and stained with RuO<sub>4</sub>, is shown in Figure 4.20b [263]. The presence of a very well-ordered array of light-unstained PE cylinders in the dark-stained PS matrix is apparent [263]. The cylinders are vertically aligned and packed on a hexagonal lattice, having an average lattice constant of almost 40 nm. The order extends to large distances (>20 μm).

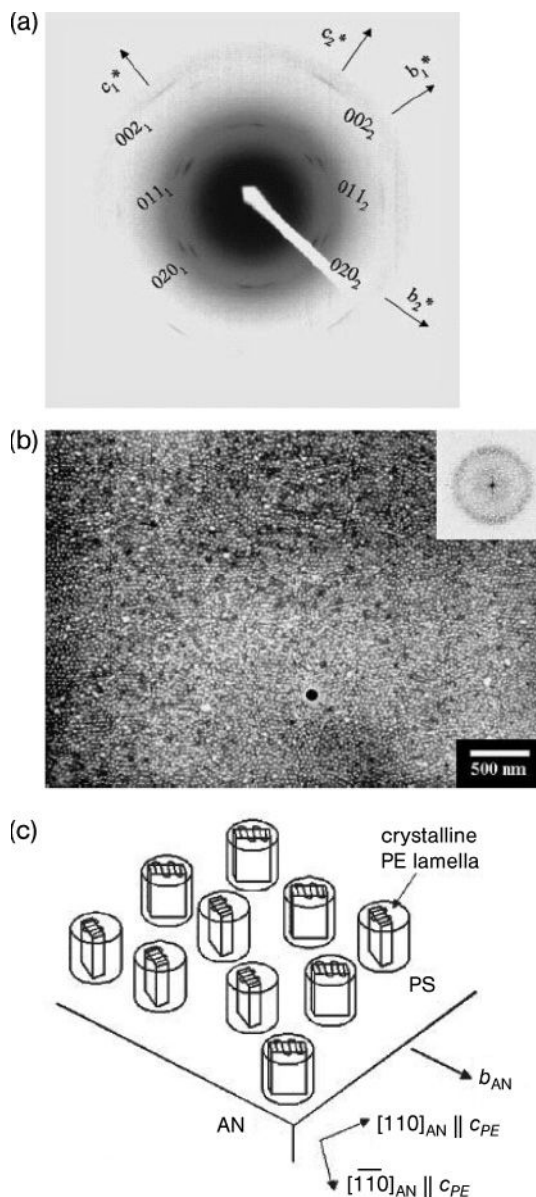
The PE crystals have been visualized with dark-field imaging, employing the strong 110 reflection of PE (Figure 4.20c). Small rectangular PE crystals are observed in the dark-field image of Figure 4.20c (the light regions), well aligned along the *b*-axis direction of the BA crystals and packed on a pseudo-hexagonal lattice, the size and orientation of which are the same as seen in the bright-field image of Figure 4.20b [263]. The PE crystals are 7 nm thick and 20 nm long, with their longest dimension parallel to the  $[1\ 1\ 0]^*$  reciprocal lattice direction [263]. The size and spacing of PE microdomains observed in bright- and dark-field images show that there is precisely one crystalline PE lamella centered in each cylinder, with the *b*-axis of the lamella oriented parallel to the *b*-axis of the BA, confirming the epitaxy of PE on BA demonstrated by the electron diffraction pattern (Figure 4.12a). A scheme of the nanostructure obtained in PS/PE thin film is shown in Figure 4.20d [263, 264].

The same PE-*b*-PS was also processed with AN to manipulate both molecular and microstructure orientation [264]. The electron diffraction pattern of an unstained film is shown in Figure 4.21a. As in the case of Figure 4.19a for the PS-*b*-PEP-*b*-PE triblock copolymer, the pattern exhibits the  $0kl$  reflections of two sets of PE crystals in two different orientations, indicating that PE lamellae stand edge-on on the substrate surface with the *c*-axes of PE oriented parallel to the  $[1\ 1\ 0]$  or  $[1\ \bar{1}\ 0]$  directions (Figure 4.19b) [264]. A RuO<sub>4</sub>-stained bright-field TEM image of the PS-*b*-PE diblock copolymer directionally solidified and epitaxially crystallized onto AN is shown in Figure 4.21b. Also, in this case the light-unstained



**Figure 4.20** Selected area electron diffraction pattern (a), TEM bright-field image (b) and TEM dark-field image (c) of a thin film of PS-*b*-PE directionally solidified and epitaxially crystallized onto BA. In the TEM bright-field image, the film of PS-*b*-PE was stained with RuO<sub>4</sub>; therefore, the darker regions correspond to the stained PS matrix, while the light regions correspond to the crystalline PE microdomains, which form hexagonally packed cylinders oriented perpendicular to the substrate surface. Inset, magnified region of (panel b) showing the noncircular shape of the PS-PE interface. The dark-field image (panel c) of the unstained film was created using the (110) diffraction reflection. Small

rectangular PE crystals are observed, well aligned along the *b*-axis direction of the BA crystals and packed on a pseudohexagonal lattice, the size and orientation of which is the same as seen in panel (b). Reproduced with permission from Ref. [263]; © 2000, Nature Publishing Group; (d) Schematic models of the microstructures in thin films of PS-*b*-PE directionally solidified and epitaxially crystallized onto BA. Vertically oriented PE cylinders are packed on a hexagonal lattice and contain one crystalline PE lamella oriented edge-on on the substrate with the *b*-axis parallel to the *b*-axis of the BA crystal. Reproduced with permission from Ref. [264]; © 2003, Wiley-VCH.



**Figure 4.21** Selected area electron diffraction pattern (a) and TEM bright-field image (b) of a thin film of PS-*b*-PE directionally solidified and epitaxially crystallized onto AN. In the TEM bright-field image the film of PS-*b*-PE was stained with RuO<sub>4</sub>; therefore, the darker regions correspond to the stained PS matrix, while the light regions correspond to the crystalline PE microdomains, which form hexagonally packed cylinders oriented perpendicular to the substrate surface;

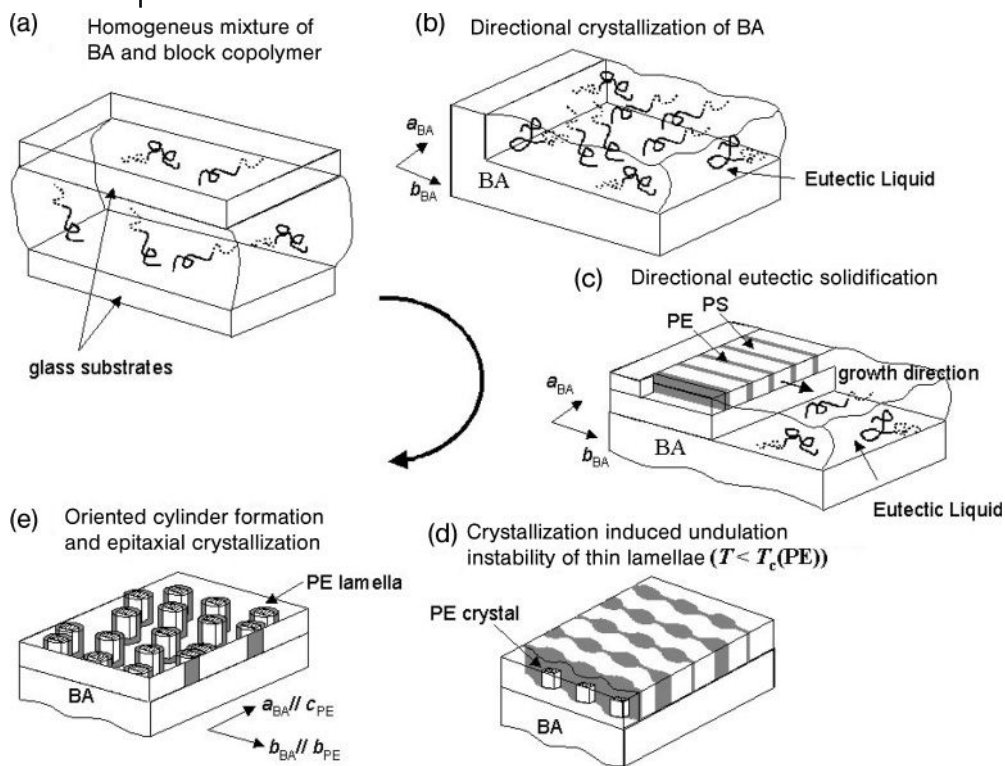
(c) Schematic model of the microstructure in thin films of PS-*b*-PE, directionally solidified and epitaxially crystallized onto AN. Vertically oriented PE cylinders are packed on a hexagonal lattice and contain one crystalline PE lamella oriented edge-on on the substrate with two different orientations, in which the *c*-axes of PE lamellae are parallel to the [1 1 0] or [1  $\bar{1}$  0] directions of AN crystals. Reproduced with permission from Ref. [264]; © 2003, Wiley-VCH.



PE cylinders are vertically aligned but the order in the lateral packing is lower than that observed for the same BC crystallized onto BA (Figure 4.20b) [264]. The lattice has, indeed, many defects, resulting in very small grain size with short-range order. This is probably because the shape anisotropy of AN crystals in the growth process is lower than that of BA crystals and the epitaxial crystallization of the PE block on AN, which causes the double texture of the crystalline PE lamellae, may disturb the lateral ordering of the PE cylinders [264]. A scheme of the microstructure obtained is shown in Figure 4.21c. The PE cylinders are vertically aligned and contain one PE crystalline lamella oriented along two equivalent crossed directions [264].

It has been suggested by De Rosa *et al.* [263] that the mechanism of the pattern formation of PS-*b*-PE on BA or AN is based on the combination of epitaxy and directional crystallization, and is basically similar to that for PS-*b*-PEP-*b*-PE (Figure 4.18) [263, 264]. The directional crystallization of the organic crystal (BA or AN) produces the formation of the globally oriented PE cylindrical microdomains due to the polymer first undergoing the order–disorder transition. However, in this instance the subsequent epitaxial crystallization of the PE block influences the final microstructure, where vertically oriented cylindrical PE microdomains [263] (Figure 4.20d) instead of in-plane PS cylinders are formed (Figure 4.18d) [264]. The morphological evolution of the system is depicted schematically in Figure 4.22. The initial homogeneous solution confined between the glass substrates (Figure 4.22a) transforms, due to the imposed directional eutectic solidification, into large crystals of BA having (001) surfaces coexisting with a thin liquid layer near the eutectic composition (Figure 4.22b). Decreasing the temperature also causes this layer to solidify directionally, by thickening the pre-existing BA crystal, and the formation of a thin, metastable vertically oriented lamellar microdomain film (Figure 4.22c). The PE microdomains are aligned along the fast growth direction of substrate crystals, as shown in Figure 4.13b. Many sequences of events are possible, depending on the affinity of the respective blocks for the substrate surfaces, the polymer film thickness, the microdomain period, and the type of subsequent epitaxy and orientation of chains in the crystallizable block with respect to the crystalline substrate. In the case of the PS-*b*-PE/BA system, the structure transforms due to the instability of the flat interface at this composition and from the in-plane PE *c*-axis orientation induced by the epitaxy, so that vertical cylinders readily form (Figure 4.22d). The depression of the  $T_g$  of PS by plasticization from the BA allows the intermediate structure to reorganize when the crystallization of PE occurs, even at 60°C. The domains evolve from an aligned precursor state (Figure 4.22d), into the final structure with vertical cylinders containing one PE crystalline lamella (Figure 4.22e) [263].

In the case of PS-*b*-PEP-*b*-PE, due to the presence of the PEP mid-block and the appropriate condition for the epitaxy of the PE block, in-plane crystalline PE lamellae were produced without hindering the pre-existing PS cylinders (see Figure 4.18d) [264]. However, in the case of PS-*b*-PE, the fact that the epitaxial crystallization of the PE block must take place inside the cylindrical microdomains and the



**Figure 4.22** Structural evolution during the directional eutectic solidification and epitaxial crystallization of the BC from the crystallizable solvent. (a) Homogeneous solution of PS-*b*-PE in BA between two glass substrates; (b) Directional solidification forms crystals of BA coexisting with a liquid layer of more concentrated polymer; (c) Second directional solidification, showing the eutectic liquid layer transforming into a BA crystal (which grows on the pre-eutectic BA crystal) and an ordered lamellar BC; (d) Because of the highly asymmetric composition of the BC and the epitaxial crystallization of the PE in contact

with the BA substrate, the flat interfaces of vertically oriented lamellae are unstable, and spontaneously deform in order to achieve a more preferred interfacial curvature and allow epitaxial growth of PE; (e) The layers transform into an array of vertically oriented, pseudo-hexagonally packed semicrystalline PE cylinders. A single, chain-folded PE lamella is formed in each cylinder. The PE crystals have their (100) planes contacting the (001) plane of the BA crystal with  $a_{\text{BA}} \parallel c_{\text{PE}}$  and  $b_{\text{BA}} \parallel b_{\text{PE}}$ . Reproduced with permission from Ref. [263]; © 2000, Nature Publishing Group.

*c*-axis of the PE block must contact with the crystalline BA or AN surface, make the two controlling forces of directional crystallization and epitaxy determine the final microstructure orientation in a more cooperative manner. Indirect evidence of the contribution of the PE epitaxy to the vertically ordered microstructure is given by the results reported by Park *et al.* [275], who introduced the method of directional crystallization (see Section 4.5.3) using a PS-*b*-PI that has a volume fraction and molecular weight similar to those of the PS-*b*-PE. The authors found

in-plane PI cylinder orientation with the same experimental conditions due to the absence of the epitaxy (see Figure 4.14b) [275]. Plasticization of the PS matrix from BA or AN enables the subsequent epitaxial crystallization to transform the microstructure into vertical cylinders [263, 264].

## 4.6 Summary and Outlook

The importance of developing methods which allow control over the alignment of domains arises from the opportunities that they provide for the exploitation of BCs in nanotechnological applications, such as in nanolithography or for the fabrication of photonic materials and other optical and electronic devices. In this chapter we have attempted to describe most of techniques proposed essentially during the past decade to induce long-range ordered and preferentially oriented morphologies, considering as seminal work the partial alignment of cylindrical domains in BC melts obtained during the early 1970s by the application of a mechanical field [73].

Macroscopically oriented thin films have been achieved by methods of general applicability, including roll-casting, shearing, and through the use of unidirectional electric fields. Less-direct approaches have established a control of surface interactions or entail a fine-tuning of surface topography and geometric confinements, eventually through lithographically patterned substrates. Moreover, when BCs fulfill specific structural or molecular requirements, other strategies are available: (i) semicrystalline BCs or copolymers having the  $T_g$  of one block above room temperature may undergo morphology alignment by epitaxy or solvent evaporation, respectively; (ii) BCs soluble in a crystallizable solvent are suitable for alignment by directional crystallization, eventually in combination with epitaxy or graphoepitaxy. Other approaches, essentially proposed for bulk BC systems, achieve only moderate orientation with multigrain structures, for example, through the application of different mechanical flow fields, or appear to be too complicated to assume nimble developments (e.g., for orientation by temperature gradients).

Finally, a scenario could be foreseen in which only a few of the techniques proposed so far will allow the development of processes for the preparation of defect-free nanostructured materials suitable for technological applications. This is despite the fact that most of them are of remarkable interest as model studies which, in the best case, could assist researchers working in this field and on the development of other complementary technologies, or they may simply be intended for academic exercises. In particular, there is a considerable interest in the combination of different methods of alignment for the production of “truly” defect free 3-D nanostructures, with the goal of overcoming the azimuthal degeneration of domains, intrinsic for unidirectional interactions. The best potential is logically offered by the simultaneous application or orthogonal directing interactions. However, in our opinion, it is worth devoting additional effort to further explore

the integration of ultraviolet interferometric lithography and, more generally, the implementation of the combination of top-down and bottom-up approaches.

### Acknowledgments

M.L. and C.D.R. gratefully acknowledge financial support from the Ministerio de Ciencia e Innovación (MAT2008-06503 and the program Ramón y Cajal) and MIUR (Prin 2007), respectively. M.L. has also benefited from useful discussions with Prof. M. A. Lopez-Quintela, University of Santiago, Spain.

### References

- 1 Seto, C.T. and Whitesides, G.M. (1990) *J. Am. Chem. Soc.*, **112**, 6409.
- 2 Manka, J.S. and Lawrence, D.S. (1990) *J. Am. Chem. Soc.*, **112**, 2440.
- 3 Koert, U., Harding, M.M. and Lehn, J.-M. (1990) *Nature (London)*, **346**, 339.
- 4 Hamley, I.W. (1998) *The Physics of Block Copolymers*, Oxford University Press, Oxford.
- 5 Hadjichristidis, N., Pispas, S. and Floudas, G. (2003) *Block Copolymers. Synthetic Strategies, Physical Properties and Applications*, John Wiley & Sons, Inc., New York.
- 6 Lazzari, M., Liu, G. and Lecommandoux, S. (eds) (2006) *Block Copolymers in Nanoscience*, Wiley-VCH Verlag GmbH, Weinheim.
- 7 Bates, F.S. and Fredrickson, G.H. (1999) *Phys. Today*, **52**, 32.
- 8 Fasolka, M.J. and Mayes, A.M. (2001) *Annu. Rev. Mater. Res.*, **31**, 323.
- 9 Krausch, G. and Magerle, R. (2002) *Adv. Mater.*, **14**, 1579.
- 10 Ryu, D.Y., Jeong, U., Kim, J.K. and Russell, T.P. (2002) *Nat. Mater.*, **1**, 114.
- 11 Hamley, I.W. (2003) *Angew. Chem., Int. Ed.*, **42**, 1692.
- 12 Park, C., Yoon, J. and Thomas, E.L. (2003) *Polymer*, **44**, 6725.
- 13 Lazzari, M. and Lopez-Quintela, M.A. (2003) *Adv. Mater.*, **15**, 1583.
- 14 Segalman, R.A. (2005) *Mater. Sci. Eng. R Rep.*, **48**, 191.
- 15 Ruzette, A.-V. and Leibler, L. (2005) *Nat. Mater.*, **4**, 19.
- 16 Cheng, J.Y., Ross, C.A., Smith, H.I. and Thomas, E.L. (2006) *Adv. Mater.*, **18**, 2505.
- 17 Lazzari, M., Rodríguez-Abreu, C., Rivas, J. and Lopez-Quintela, M.A. (2006) *J. Nanosci. Nanotechnol.*, **6**, 892.
- 18 Hatada, K., Kitayama, T. and Vogl, O. (eds) (1997) *Macromolecular Design of Polymeric Materials*, Marcel Dekker, New York.
- 19 Hadjichristidis, N., Pitzikalis, M., Pispas, S. and Iatrou, H. (2001) *Chem. Rev.*, **101**, 3747.
- 20 Matyjaszewski, K. and Davis, T.P. (eds) (2002) *Handbook of Radical Polymerization*, John Wiley & Sons, Inc., New York.
- 21 Park, M., Harrison, C., Chaikin, P.M., Register, R.A. and Adamson, D.H. (1997) *Science*, **276**, 1401.
- 22 Li, R.R., Dapkus, P.D., Thompson, M.E., Jeong, W.G., Harrison, C., Chaikin, P.M., Register, R.A. and Adamson, D.H. (2000) *Appl. Phys. Lett.*, **76**, 1689.
- 23 Thurn-Albrecht, T., Schotter, J., Kästle, G.A., Emley, N., Shibauchi, T., Krusin-Elbaum, L., Guarini, K., Black, C.T., Tuominen, M.T. and Russell, T.P. (2000) *Science*, **290**, 2126.
- 24 Park, M., Chaikin, P.M., Register, R.A. and Adamson, D.H. (2001) *Appl. Phys. Lett.*, **79**, 257.
- 25 Cheng, J.Y., Ross, C.A., Chan, V.Z.-H., Thomas, E.L., Lammertink, R.G.H. and Vancso, G.J. (2001) *Adv. Mater.*, **13**, 1174.

- 26 Guarini, K.W., Black, C.T., Milkove, K.R. and Sandstrom, R.L. (2001) *J. Vac. Sci. Technol. B*, **19**, 2784.
- 27 Kim, H.-C., Jia, X., Stafford, C.M., Kim, D.H., McCarthy, T.J., Tuominen, M.T., Hawker, C.J. and Russell, T.P. (2001) *Adv. Mater.*, **13**, 795.
- 28 Naito, K., Hieda, H., Sakurai, M., Kamata, Y. and Asakawa, K. (2002) *IEEE Trans. Magn.*, **38**, 1949.
- 29 Cheng, J.Y., Meyes, A.M. and Ross, C.A. (2004) *Nat. Mater.*, **3**, 823.
- 30 Yoon, J., Lee, W. and Thomas, E.L. (2005) *MRS Bull.*, **30**, 721.
- 31 Stokytovich, M.P., Müller, M., Kim, S.O., Solak, H.H., Edwards, E.W., de Pablo, J.J. and Nealey, P.F. (2005) *Science*, **308**, 1442.
- 32 Han, E., In, I., Park, S.-M., La, Y.-H., Wang, Y., Nealey, P.F. and Gopalan, P. (2007) *Adv. Mater.*, **19**, 4448.
- 33 Chen, F., Akasaka, S., Inoue, T., Takenaka, M., Hasegawa, H. and Yoshida, H. (2007) *Macromol. Rapid Commun.*, **28**, 2137.
- 34 Lazzari, M., Scaroni, D., Hoppe, C.E., Vazquez-Vazquez, C. and López-Quintela, M.A. (2007) *Chem. Mater.*, **19**, 5818.
- 35 Bitá, I., Yang, J.K.W., Jung, Y.S., Ross, C.A., Thomas, E.L. and Berggren, K.K. (2008) *Science*, **321**, 939.
- 36 Bosworth, J.K., Paik, M.Y., Schwartz, E.L., Huang, J.Q., Ko, A.W., Smilgies, D.-M., Black, C.T. and Ober, C.K. (2008) *ACS Nano*, **2**, 1396.
- 37 Kim, T.H., Hwang, J., Hwang, W.S., Huh, J., Kim, H.-C., Kim, S.H., Hong, J.M., Thomas, E.L. and Park, C. (2008) *Adv. Mater.*, **20**, 522.
- 38 Yamaguchi, T. and Yamaguchi, H. (2008) *Adv. Mater.*, **20**, 1684.
- 39 Park, S., Lee, D.Y., Xu, J., Kim, B., Hong, S.W., Jeong, U., Xu, T. and Russell, T.P. (2009) *Science*, **323**, 1030.
- 40 Liu, X. and Stamm, M. (2009) *Nanoscale Res. Lett.*, **4**, 459.
- 41 Thomas, E.L., Anderson, D.M., Henkee, C.S. and Hoffman, D. (1988) *Nature (London)*, **334**, 598.
- 42 Gido, S.P. and Thomas, E.L. (1994) *Macromolecules*, **27**, 6137.
- 43 Gido, S.P. and Thomas, E.L. (1997) *Macromolecules*, **30**, 3739.
- 44 Hahm, J., Lopes, W.A., Jaeger, H.M. and Sibener, S.J. (1998) *J. Chem. Phys.*, **109**, 10111.
- 45 Goldacker, T., Abetz, V., Stadler, R., Erukhimovich, I. and Leibler, L. (1999) *Nature (London)*, **398**, 138.
- 46 Hahm, J. and Sibener, S.J. (2001) *J. Chem. Phys.*, **114**, 4730.
- 47 Tsarkova, L., Knoll, A., Krausch, G. and Magerle, R. (2006) *Macromolecules*, **39**, 3608.
- 48 Morkved, T.L., Lu, M., Urbas, A.M., Ehrichs, E.E., Jaeger, H.M., Mansky, P. and Russell, T.P. (1996) *Science*, **273**, 931.
- 49 Knoll, A., Horvat, A., Lyakhova, K.S., Krausch, G., Sevink, G.J.A., Zvelindovsky, A.V. and Magerle, R. (2002) *Phys. Rev. Lett.*, **89**, 035501.
- 50 Hashimoto, T., Tsutsumi, K. and Funaki, Y. (1997) *Langmuir*, **13**, 6869.
- 51 Liu, G., Ding, J., Guo, A., Hertfort, M. and Bazett-Jones, D. (1997) *Macromolecules*, **30**, 1851.
- 52 Liu, G., Ding, J., Hashimoto, T., Kimishima, K., Winnik, F.M. and Nigam, S. (1999) *Chem. Mater.*, **11**, 2233.
- 53 Leiston-Belanger, J.M., Russell, T.P., Drockenmuller, E. and Hawker, C.J. (2005) *Macromolecules*, **38**, 7676.
- 54 La, Y.-H., Edwards, E.W., Park, S.-M. and Nealey, P.F. (2005) *Nano Lett.*, **5**, 1379.
- 55 Jeong, U., Ryu, D.Y., Kho, D.H., Kim, J.K., Goldbach, J.T., Kim, D.H. and Russell, T.P. (2004) *Adv. Mater.*, **16**, 533.
- 56 Ahn, D.U. and Sancaktar, E. (2008) *Soft Matter*, **4**, 1454.
- 57 Meiners, J.-C., Quintel-Ritzi, A., Mlinek, J., Elbs, H. and Krausch, G. (1997) *Macromolecules*, **30**, 4945.
- 58 Kim, G. and Libera, M. (1998) *Macromolecules*, **31**, 2569.
- 59 Faselka, M.J., Banerjee, P., Mayes, A.M., Pickett, G. and Balazs, A.C. (2000) *Macromolecules*, **33**, 5702.
- 60 Elbs, H., Drummer, C., Abetz, V. and Krausch, G. (2002) *Macromolecules*, **35**, 5570.
- 61 Buck, E. and Fuhrmann, J. (2001) *Macromolecules*, **34**, 2172.

- 62 Peng, J., Xuan, Y., Wang, H.F., Li, B.Y. and Han, Y.C. (2005) *Polymer*, **46**, 5767.
- 63 Xuan, Y., Peng, J., Cui, L., Wang, H., Li, B. and Han, Y. (2004) *Macromolecules*, **37**, 7301.
- 64 Chen, Y., Huang, H., Hu, Z. and He, T. (2004) *Langmuir*, **20**, 3805.
- 65 Kim, S.H., Misner, M.J., Xu, T., Kimura, M. and Russell, T.P. (2004) *Adv. Mater.*, **16**, 226.
- 66 Bang, J., Kim, S.H., Drogenmuller, E., Misner, M.J., Russell, T.P. and Hawker, C.J. (2006) *J. Am. Chem. Soc.*, **128**, 7622.
- 67 Bang, J., Kim, S.H., Stein, G.E., Russell, T.P., Li, X., Wang, J., Kramer, E.J. and Hawker, C.J. (2007) *Macromolecules*, **40**, 7019.
- 68 Kim, S.H., Misner, M.J., Yang, L., Gang, O., Ocko, B.M. and Russell, T.P. (2006) *Macromolecules*, **39**, 8473.
- 69 Park, S.C., Kim, B.J., Hawker, C.J., Kramer, E.J., Bang, J. and Ha, J.S. (2007) *Macromolecules*, **40**, 8119.
- 70 Park, S.C., Jung, H., Fukukawa, K., Campos, L.M., Lee, K., Shin, K., Hawker, C.J., Ha, J.S. and Bang, J. (2008) *J. Polym. Sci. Part A: Polym. Chem.*, **46**, 8041.
- 71 RamachandraRao, V.S., Gupta, R.R., Russell, T.P. and Watkins, J.J. (2001) *Macromolecules*, **34**, 7923.
- 72 Vogt, B.D., RamachandraRao, V.S., Gupta, R.R., Lavery, K.A., Francis, T.J., Russell, T.P. and Watkins, J.J. (2003) *Macromolecules*, **36**, 4029.
- 73 Keller, A., Pedemonte, E. and Willmouth, F.M. (1970) *Nature (London)*, **225**, 538.
- 74 Folkes, M.J., Keller, A. and Scalisi, F.P. (1973) *Colloid Polym. Sci.*, **251**, 1.
- 75 Skoulios, A. (1977) *J. Polym. Sci. Polym. Symp.*, **58**, 369.
- 76 Hadziioannou, G., Mathis, A. and Skoulios, A. (1979) *Colloid Polym. Sci.*, **257**, 15.
- 77 Hadziioannou, G., Mathis, A. and Skoulios, A. (1979) *Colloid Polym. Sci.*, **257**, 136.
- 78 Kofinas, P. and Cohen, R.E. (1995) *Macromolecules*, **28**, 336.
- 79 Drzal, P.L., Barnes, J.D. and Kofinas, P. (2001) *Polymer*, **42**, 5633.
- 80 (a) Quiram, D.J., Register, R.A., Marchand, G.R. and Adamson, D.H. (1998) *Macromolecules*, **31**, 4891.  
(b) Quiram, D.J., Register, R.A. and Marchand, G.R. (1997) *Macromolecules*, **30**, 4551.  
(c) Quiram, D.J., Register, R.A., Marchand, G.R. and Ryan, A.J. (1997) *Macromolecules*, **30**, 8338.
- 81 van Asselen, O.L.J., van Casteren, I.A., Goossens, J.G.P. and Meijer, H.E.H. (2004) *Macromol. Symp.*, **205**, 85.
- 82 Morrison, F.A. and Winter, H.H. (1989) *Macromolecules*, **22**, 3533.
- 83 Morrison, F.A., Winter, H.H., Gronski, W. and Barnes, J.D. (1990) *Macromolecules*, **23**, 7200.
- 84 Wiesner, U. (1997) *Macromol. Chem. Phys.*, **198**, 3319.
- 85 Pinheiro Scott, B. and Winey, K.I. (1998) *Macromolecules*, **31**, 4447.
- 86 Leist, H., Maring, D., Thurn-Albrecht, T. and Wiesner, U. (1999) *J. Chem. Phys.*, **110**, 8225.
- 87 Hermel, T.J., Wu, L.F., Hahn, S.F., Lodge, T.P. and Bates, F.S. (2002) *Macromolecules*, **35**, 4685.
- 88 Stangler, S. and Abetz, V. (2003) *Rheol. Acta*, **42**, 569.
- 89 Wu, L., Lodge, T.P. and Bates, F.S. (2004) *Macromolecules*, **37**, 8184.
- 90 Oelschlaeger, C., Gutmann, J.S., Wolkenhauer, M., Spiess, H.-W., Knoll, K. and Wilhelm, M. (2007) *Macromol. Chem. Phys.*, **208**, 1719.
- 91 Mendoza, C., Pietsch, T., Gindy, N. and Fahmi, A. (2008) *Adv. Mater.*, **20**, 1179.
- 92 Sebastian, J.M., Graessley, W.W. and Register, R.A. (2002) *J. Rheol.*, **46**, 863.
- 93 Angelescu, D.E., Waller, J.H., Register, R.A. and Chaikin, P.M. (2005) *Adv. Mater.*, **17**, 1878.
- 94 Angelescu, D.E., Waller, J.H., Adamson, D.H., Deshpande, P., Chou, S.Y., Register, R.A. and Chaikin, P.M. (2004) *Adv. Mater.*, **16**, 1736.
- 95 Luo, K.F. and Yang, Y.L. (2004) *Polymer*, **45**, 6745.
- 96 Lisal, M. and Brennan, J.K. (2007) *Langmuir*, **23**, 4809.
- 97 Register, R.A., Angelescu, D.E., Pelletier, V., Asakawa, K., Wu, M.W., Adamson, D.H. and Chaikin, P.M. (2007) *J. Photopolym. Sci. Technol.*, **20**, 493.

- 98 Hong, Y.-R., Adamson, D.H., Chaikin, P.M. and Register, R.A. (2009) *Soft Matter*, **5**, 1687.
- 99 Albalak, R.J. and Thomas, E.L. (1993) *J. Polym. Sci.: Part B, Polym. Phys.*, **31**, 37.
- 100 Albalak, R.J. and Thomas, E.L. (1994) *J. Polym. Sci.: Part B, Polym. Phys.*, **32**, 341.
- 101 Honeker, C.C., Thomas, E.L., Albalak, R.J., Hajduk, D.A., Gruner, S.M. and Capel, M.C. (2000) *Macromolecules*, **33**, 9395.
- 102 Dair, B.J., Avgeropoulos, A. and Hadjichristidis, N. (2000) *Polymer*, **41**, 6231.
- 103 Villar, M.A., Rueda, D.R., Ania, F. and Thomas, E.L. (2002) *Polymer*, **43**, 5139.
- 104 Kwon, Y.K., Ko, Y.S. and Okamoto, M. (2008) *Polymer*, **49**, 2334.
- 105 Mortensen, K., Brown, W. and Norden, B. (1992) *Phys. Rev. Lett.*, **68**, 2340.
- 106 Hamley, I.W., Koppi, K.A., Rosedale, J.H., Bates, F.S., Almdal, K. and Mortensen, K. (1993) *Macromolecules*, **26**, 5959.
- 107 Hamley, I.W., Pople, J.A., Fairclough, J.P.A., Ryan, A.J., Booth, C. and Yang, Y.W. (1998) *Macromolecules*, **31**, 3906.
- 108 Daniel, C., Hamley, I.W., Mingvanish, W. and Booth, C. (2000) *Macromolecules*, **33**, 2163.
- 109 Hamley, I.W. (2000) *Curr. Opin. Colloid Interface Sci.*, **5**, 342.
- 110 Hamley, I.W. (2001) *Phyl. Trans. R. Soc.*, **359**, 1017.
- 111 Mortensen, K., Theunissen, E., Kleppinger, R., Almdal, K. and Reynaers, H. (2002) *Macromolecules*, **35**, 7773.
- 112 Castelletto, V., Hamley, I.W., Crothers, M., Attwood, D., Yang, Z. and Booth, C. (2004) *Macromol. Sci. Phys. B*, **43**, 13.
- 113 Hamley, I.W. (2001) *J. Phys.: Condens. Matter*, **13**, R643.
- 114 Honeker, C.C. and Thomas, E.L. (1996) *Chem. Mater.*, **8**, 1702.
- 115 Fredrikson, G.H. and Bates, F.S. (1996) *Annu. Rev. Mater. Sci.*, **26**, 501.
- 116 Watanabe, H. (1997) *Acta Polym.*, **48**, 215.
- 117 Morozov, A.N., Zvelindovsky, A.V. and Fraaije, J.G.E. (2001) *Phys. Rev. E*, **64**, 051803.
- 118 Corberi, F., Gonnella, G. and Lamura, A. (2002) *Phys. Rev. E*, **66**, 016114.
- 119 Zvelindovsky, A.V.M. and Sevink, G.J.A. (2003) *Europhys. Lett.*, **62**, 370.
- 120 Fraser, B., Denniston, C. and Muser, M.H. (2005) *J. Polym. Sci. Pol. Phys.*, **43**, 970.
- 121 Zvelindovsky, A.V. and Sevink, G.J.A. (2005) *J. Chem. Phys.*, **123**, 074903.
- 122 Chen, P.L. (2005) *Phys. Rev. E*, **71**, 061503.
- 123 Rychkov, I. (2005) *Macromol. Theory Simul.*, **14**, 207.
- 124 Huang, Z.F. and Vinals, J. (2006) *Phys. Rev. E*, **73**, 060501.
- 125 Daud, A., Morais, F.M., Morgado, W.A.M. and Martins, S. (2007) *Physica A*, **374**, 517.
- 126 Kindt, P. and Briels, W.J. (2008) *J. Phys. Chem.*, **128**, 124901.
- 127 Fong, H. and Reneker, D.H. (1999) *J. Polym. Sci. Polym. Phys.*, **37**, 3488.
- 128 Ruotsalainen, T., Turku, J., Heikkilä, P., Ruokolainen, J., Nykänen, A., Laitinen, T., Torkkeli, M., Serimaa, R., Harlin, ten Brinke, G., Harlin, A. and Ikkala, O. (2005) *Adv. Mater.*, **17**, 1048.
- 129 Ma, M.L., Hill, R.M., Lowery, J.L., Fridrikh, S.V. and Rutledge, G.C. (2005) *Langmuir*, **21**, 5549.
- 130 Kalra, V., Mendez, S., Lee, J.H., Nguyen, H., Marquez, M. and Joo, Y.L. (2006) *Adv. Mater.*, **18**, 3299.
- 131 Hahn, J. and Sibener, S.J. (2000) *Langmuir*, **16**, 4766.
- 132 Li, X., Han, Y.C. and An, L.J. (2002) *Langmuir*, **18**, 5293.
- 133 Li, D. and Xia, Y. (2004) *Adv. Mater.*, **16**, 1151.
- 134 Dzenis, Y. (2004) *Science*, **304**, 1917.
- 135 Amundson, K., Helfand, E., Davis, D.D., Quan, X., Patel, S. and Smith, S.D. (1991) *Macromolecules*, **24**, 6546.
- 136 Amundson, K., Helfand, E., Davis, D.D., Quan, X. and Smith, S.D. (1993) *Macromolecules*, **26**, 2698.
- 137 Amundson, K., Helfand, E., Davis, D.D., Quan, X., Hudson, S.D. and Smith, S.D. (1994) *Macromolecules*, **27**, 6559.
- 138 Onuki, A. and Fukuda, J. (1995) *Macromolecules*, **28**, 8788.
- 139 Thurn-Albrecht, T., Steiner, R., DeRouchey, J., Stafford, C.M., Huang, E., Bal, M., Tuominen, M., Hawker, C.J.



- and Russell, T.P. (2000) *Adv. Mater.*, **12**, 787.
- 140 Thurn-Albrecht, T., DeRouchey, J., Russell, T.P. and Kolb, R. (2002) *Macromolecules*, **35**, 8106.
- 141 Elhadj, S., Woody, J.W., Niu, V.S. and Saraf, R.F. (2003) *Appl. Phys. Lett.*, **82**, 872.
- 142 Xu, T., Zhu, Y., Gido, S.P. and Russell, T.P. (2004) *Macromolecules*, **37**, 2625.
- 143 DeRouchey, J., Thurn-Albrecht, T., Russell, T.P. and Kolb, R. (2004) *Macromolecules*, **37**, 2538.
- 144 Xiang, H., Lin, Y., Russell, T.P. and Kolb, R. (2004) *Macromolecules*, **37**, 5358.
- 145 Olszowka, V., Hund, M., Kuntermann, V., Scherdel, S., Tsarkova, L., Boker, A. and Krausch, G. (2006) *Soft Matter*, **2**, 1089.
- 146 Wang, J.-Y., Chen, W. and Russell, T.P. (2008) *Macromolecules*, **41**, 7227.
- 147 Pereira, G.G. and Williams, D.R.M. (1999) *Macromolecules*, **32**, 8115.
- 148 Tsori, Y. and Andelman, D. (2002) *Macromolecules*, **35**, 5161.
- 149 Schaeffer, E., Thurn-Albrecht, T., Russell, T.P. and Steiner, U. (2000) *Nature (London)*, **403**, 874.
- 150 Voicu, N.E., Ludwigs, S. and Steiner, U. (2008) *Adv. Mater.*, **20**, 3022.
- 151 Ashok, B., Muthukumar, M. and Russell, T.P. (2001) *J. Chem. Phys.*, **115**, 1559.
- 152 Kyrilyuk, A.V., Zvelindovsky, A.V., Sevink, G.J.A. and Fraaije, J.G.E.M. (2002) *Macromolecules*, **35**, 1473.
- 153 Tsori, Y., Tournilhac, F. and Leibler, L. (2003) *Macromolecules*, **36**, 5873.
- 154 Tsori, Y., Tournilhac, F., Andelman, D. and Leibler, L. (2003) *Phys. Rev. Lett.*, **90**, 145504.
- 155 Dürr, O., Dietrich, W., Maas, P. and Nitzan, A. (2002) *J. Phys. Chem.*, **106**, 6149.
- 156 Thurn-Albrecht, T., DeRouchey, J., Russell, T.P. and Jaeger, H.M. (2000) *Macromolecules*, **33**, 3250.
- 157 Xu, T., Hawker, C.J. and Russell, T.P. (2003) *Macromolecules*, **36**, 6178.
- 158 Böker, A., Elbs, H., Hänsen, H., Knoll, A., Ludwigs, S., Zettl, H., Zvelindovsky, A.V., Sevink, G.J.A., Urban, V., Abetz, V., Müller, A.H.E. and Krausch, G. (2003) *Macromolecules*, **36**, 8078.
- 159 Böker, A., Knoll, A., Elbs, H., Abetz, V., Müller, A.H.E. and Krausch, G. (2002) *Macromolecules*, **35**, 1319.
- 160 Boker, A., Schmidt, K., Knoll, A., Zettl, H., Hansel, H., Urban, V., Abetz, V. and Krausch, G. (2006) *Polymer*, **47**, 849.
- 161 Zvelindovski, A.V. and Sevink, G.J.A. (2003) *Phys. Rev. Lett.*, **90**, 049601.
- 162 Xu, T., Goldbach, J.T. and Russell, T.P. (2003) *Macromolecules*, **36**, 7296.
- 163 Osuji, C., Ferreira, P.J., Mao, G., Ober, C.K., Vander Sande, J.B. and Thomas, E.L. (2004) *Macromolecules*, **37**, 9903.
- 164 Tomikawa, N., Lu, Z.B., Itoh, T., Imrie, C.T., Adachi, M., Tokita, M. and Watanabe, J. (2005) *Jpn. J. Appl. Phys.*, **2**, 44, L711.
- 165 Tao, Y., Zohar, H., Olsen, B.D. and Segalman, R.A. (2007) *Nano Lett.*, **7**, 2742.
- 166 Grigorova, T., Pispas, S., Hadjichristidis, N. and Thurn-Albrecht, T. (2005) *Macromolecules*, **38**, 7430.
- 167 Yu, H., Iyoda, T. and Ikeda, T. (2006) *J. Am. Chem. Soc.*, **128**, 11010.
- 168 Turturro, A., Gattiglia, E., Vacca, P. and Viola, G.T. (1995) *Polymer*, **21**, 3987.
- 169 Kim, G. and Libera, M. (1998) *Macromolecules*, **31**, 2569.
- 170 Kim, G. and Libera, M. (1998) *Macromolecules*, **31**, 2670.
- 171 Kimura, M., Mister, M.J., Xu, T., Kim, S.H. and Russell, T.P. (2003) *Langmuir*, **19**, 9910.
- 172 Lin, Z., Kim, D.H., Wu, X., Boosahda, L., Stone, D., LaRose, L. and Russell, T.P. (2002) *Adv. Mater.*, **14**, 1373.
- 173 Temple, K., Kulbaba, K., Power-Billard, K.N., Manners, I., Leach, K.A., Xu, T., Russell, T.P. and Hawcker, C.J. (2003) *Adv. Mater.*, **15**, 297.
- 174 Park, S., Wang, J.-Y., Kim, B., Xu, J. and Russell, T.P. (2008) *ACS Nano*, **2**, 766.
- 175 Scalarone, D., Tata, J., Lazzari, M. and Chiantore, O. (2009) *Eur. Polym. J.*, **45**, 2520.
- 176 Hashimoto, T., Bodycomb, J., Funaki, Y. and Kimishima, K. (1999) *Macromolecules*, **32**, 952.
- 177 Hashimoto, T., Bodycomb, J., Funaki, Y. and Kimishima, K. (1999) *Macromolecules*, **32**, 2075.



- 178 Angelescu, D.E., Waller, J.H., Adamson, D.H., Register, R.A. and Chaikin, P.M. (2007) *Adv. Mater.*, **19**, 2687.
- 179 Mita, K., Takenaka, M., Hasegawa, H. and Hashimoto, T. (2008) *Macromolecules*, **41**, 8789.
- 180 Rockford, L., Liu, Y., Mansky, P., Russell, T.P., Yoon, M. and Mochrie, S.G.J. (1999) *Phys. Rev. Lett.*, **82**, 2602.
- 181 Rockford, L., Mochrie, S.G.J. and Russell, T.P. (2001) *Macromolecules*, **34**, 1487.
- 182 Yang, X.M., Peters, R.D., Nealey, P.F., Solak, H.H. and Cerrina, F. (2000) *Macromolecules*, **33**, 9575.
- 183 Kim, S.O., Solak, H.H., Stoykovich, M.P., Ferrier, N.J., de Pablo, J.J. and Nealey, P.F. (2003) *Nature (London)*, **424**, 411.
- 184 De Rosa, C., Park, C., Lotz, B., Fetters, L.J., Wittmann, J.C. and Thomas, E.L. (2000) *Macromolecules*, **33**, 4871.
- 185 Yang, X.M., Peters, R.D., Kim, T.K. and Nealey, P.F. (1999) *J. Vac. Sci. Technol. B*, **17**, 3203.
- 186 Solak, H.H., David, C., Gobrecht, J., Golovkina, V., Cerrina, F., Kim, S.O. and Nealey, P.F. (2003) *Microelectron. Eng.*, **56**, 67–68.
- 187 Tada, Y., Hakasaka, S., Yoshida, H., Hasegawa, H., Dobisz, E., Kercher, D. and Takenaka, M. (2008) *Macromolecules*, **41**, 9267.
- 188 Shin, D.O., Kim, B.H., Kang, J.-H., Jeong, S.-J., Park, S.H., Lee, Y.-H. and Kim, S.O. (2009) *Macromolecules*, **42**, 1189.
- 189 Matsen, M.W. (1998) *Curr. Opin. Colloid Interface Sci.*, **3**, 40.
- 190 Henkee, C.S., Thomas, E.L. and Fetters, L.J. (1988) *J. Mater. Sci.*, **23**, 1685.
- 191 Coulon, G., Deline, V.R., Russell, T.P. and Green, P.F. (1989) *Macromolecules*, **22**, 2581.
- 192 Anastasiadis, S.H., Russell, T.P., Satija, S.K. and Majkrzak, C.F. (1989) *Phys. Rev. Lett.*, **62**, 1852.
- 193 Russell, T.P., Coulon, G., Deline, V.R. and Miller, D.C. (1989) *Macromolecules*, **22**, 4600.
- 194 Anastasiadis, S.H., Russell, T.P., Satija, S.K. and Majkrzak, C.F. (1990) *J. Chem. Phys.*, **92**, 5677.
- 195 Russell, T.P., Menelle, A., Anastasiadis, S.H., Satija, S.K. and Majkrzak, C.F. (1991) *Macromolecules*, **24**, 6269.
- 196 Collin, B., Chatenay, D., Coulon, G., Ausserre, D. and Gallot, Y. (1992) *Macromolecules*, **25**, 1621.
- 197 Coulon, G., Dailant, J., Collin, B., Benattar, J.J. and Gallot, Y. (1993) *Macromolecules*, **26**, 1582.
- 198 Mayes, A.M., Russell, T.P., Bassereau, P., Baker, S.M. and Smith, G.S. (1994) *Macromolecules*, **27**, 749.
- 199 Carvalho, B.L. and Thomas, E.L. (1994) *Phys. Rev. Lett.*, **73**, 3321.
- 200 Joly, S., Ausserre, D., Brotons, G. and Gallot, Y. (2002) *Eur. Phys. J. E*, **8**, 355.
- 201 Walton, D.G., Kellogg, G.J., Mayes, A.M., Lambooy, P. and Russell, T.P. (1994) *Macromolecules*, **27**, 6225.
- 202 Smith, A.P., Douglas, J.F., Meredith, J.C., Amis, E.J. and Karim, A. (2001) *Phys. Rev. Lett.*, **87**, 015503.
- 203 Smith, A.P., Douglas, J.F., Meredith, J.C., Amis, E.J. and Karim, A. (2001) *J. Polym. Sci. Part B Polym. Phys.*, **39**, 2141.
- 204 Lambooy, P., Russell, T.P., Kellogg, G.J., Mayes, A.M., Gallagher, P.D. and Satija, S.K. (1994) *Phys. Rev. Lett.*, **72**, 2899.
- 205 Koneripalli, N., Singh, M., Levicky, R., Bates, F.S., Gallagher, P.D. and Satija, S.K. (1995) *Macromolecules*, **28**, 2897.
- 206 Kellogg, G.J., Walton, D.G., Mayes, A.M., Lambooy, P., Russell, T.P., Gallagher, P.D. and Satija, S.K. (1996) *Phys. Rev. Lett.*, **76**, 2503.
- 207 Koneripalli, N., Levicky, R., Bates, F.S., Ankner, J., Kaiser, H. and Satija, S.K. (1996) *Langmuir*, **12**, 6681.
- 208 In, I., La, Y.H., Park, S.M., Nealey, P.F. and Gopalan, P. (2006) *Langmuir*, **22**, 7855.
- 209 Ji, S., Liu, C.-C., Son, J.G., Gotrik, K., Craig, G.S.W., Gopalan, P., Himpfel, F.J., Char, K. and Nealey, P.F. (2008) *Macromolecules*, **41**, 9098.
- 210 Kim, S.H., Misner, M.J. and Russell, T.P. (2008) *Adv. Mater.*, **20**, 4851.
- 211 Turner, M.S. (1992) *Phys. Rev. Lett.*, **69**, 1788.
- 212 Shull, K.R. (1992) *Macromolecules*, **25**, 2122.
- 213 Pickett, G.R., Witten, T.A. and Nagel, S.R. (1993) *Macromolecules*, **26**, 3194.

- 214 Kikuchi, M. and Binder, K. (1994) *J. Chem. Phys.*, **101**, 3367.
- 215 Brown, G. and Chakrabarti, A. (1995) *J. Chem. Phys.*, **102**, 1440.
- 216 Pickett, G.T. and Balazs, A.C. (1997) *Macromolecules*, **30**, 3097.
- 217 Matsen, M.W. (1997) *J. Chem. Phys.*, **106**, 7781.
- 218 Tang, W.H. and Witten, T.A. (1998) *Macromolecules*, **31**, 3130.
- 219 Geisinger, T., Muller, M. and Binder, K. (1999) *J. Chem. Phys.*, **111**, 5251.
- 220 Frischknecht, A.L., Curro, J.G. and Frink, L.J.D. (2002) *J. Chem. Phys.*, **117**, 10398.
- 221 Liu, Y., Zhao, W., Zheng, X., King, A., Singh, A., Rafailovich, M.H., Sokolov, J., Dai, K.H., Kramer, E.J., Schwarz, S.A., Gebizlioglu, O. and Sinha, S.K. (1994) *Macromolecules*, **27**, 4000.
- 222 Turner, M.S., Rubinstein, M. and Marques, C.M. (1994) *Macromolecules*, **27**, 4986.
- 223 van Dijk, M.A. and van den Berg, R. (1995) *Macromolecules*, **28**, 6773.
- 224 Radzilowski, L.H., Carvalho, B.L. and Thomas, E.L. (1996) *J. Polym. Sci. B Polym. Phys.*, **34**, 3081.
- 225 Kim, H.C. and Russell, T.P. (2001) *J. Polym. Sci. B Polym. Phys.*, **39**, 663.
- 226 Suh, K.Y., Kim, Y.S. and Lee, H.H. (1998) *J. Chem. Phys.*, **108**, 1253.
- 227 Huinink, H.P., Brokken-Zijp, J.C.M., van Dijk, M.A. and Sevink, G.J.A. (2000) *J. Chem. Phys.*, **112**, 2452.
- 228 Konrad, M., Knoll, A., Krausch, G. and Magerle, R. (2000) *Macromolecules*, **33**, 5518.
- 229 Knoll, A., Magerle, R. and Krausch, G. (2004) *J. Chem. Phys.*, **120**, 1105.
- 230 Szamel, G. and Muller, M. (2003) *J. Chem. Phys.*, **118**, 905.
- 231 Yokoyama, H., Mates, T.E. and Kramer, E.J. (2000) *Macromolecules*, **33**, 1888.
- 232 Mansky, P., Russell, T.P., Hawker, C.J., Pitsikalis, M. and Mays, J. (1997) *Macromolecules*, **30**, 6810.
- 233 Mansky, P., Liu, Y., Huang, E., Russell, T.P. and Hawker, C. (1997) *Science*, **275**, 1458.
- 234 Huang, E., Russell, T.P., Harrison, C., Chaikin, P.M., Register, R.A., Hawker, C.J. and Mays, J. (1998) *Macromolecules*, **31**, 7641.
- 235 Huang, E., Rockford, L., Russell, T.P. and Hawker, C.J. (1998) *Nature (London)*, **395**, 757.
- 236 Huang, E., Pruzinsky, S., Russell, T.P., Mays, J. and Hawker, C.J. (1999) *Macromolecules*, **32**, 5299.
- 237 Huang, E., Mansky, P., Russell, T.P., Harrison, C., Chaikin, P.M., Register, R.A., Hawker, C.J. and Mays, J. (2000) *Macromolecules*, **33**, 80.
- 238 Harrison, C., Chaikin, P.M., Huse, D.A., Register, R.A., Adamson, D.H., Daniel, A., Huang, E., Mansky, P., Russell, T.P., Hawker, C.J., Egolf, D.A., Melnikov, I.V. and Bodenschatz, E. (2000) *Macromolecules*, **33**, 857.
- 239 Son, J.G., Bulliard, X., Kang, H., Nealey, P.F. and Char, K. (2008) *Adv. Mater.*, **20**, 3643.
- 240 Royer, L. (1928) *Bull. Soc. Fr. Mineral. Crystallogr.*, **51**, 7.
- 241 van deer Mere, J.H. (1949) *Discuss. Faraday Soc.*, **5**, 206.
- 242 Swei, G.S., Lando, J.B., Rickert, S.E. and Mauritz, K.A. (1986) *Encyclopedia Polym. Sci. Eng.*, **6**, 209.
- 243 Willems, J. (1955) *Naturwissenschaften*, **42**, 176.
- 244 Willems, J. and Willems, L. (1957) *Experientia*, **13**, 465.
- 245 Willems, J. (1958) *Discuss. Faraday Soc.*, **25**, 111.
- 246 Fischer, E.W. (1958) *Discuss. Faraday Soc.*, **25**, 204.
- 247 Wellinghoff, S.H., Rybnikar, F. and Baer, E. (1974) *J. Macromol. Sci. (Phys.)*, **B10**, 1.
- 248 Koutsky, J.A., Walton, A.C. and Baer, E. (1967) *J. Polym. Sci. Polym. Lett. Ed.*, **5**, 177.
- 249 Koutsky, J.A., Walton, A.C. and Baer, E. (1967) *J. Polym. Sci. Polym. Lett. Ed.*, **5**, 185.
- 250 Ashida, M., Uedn, Y. and Watanabe, T. (1978) *J. Polym. Sci. Polym. Phys. Ed.*, **16**, 179.
- 251 Rickert, S.E. and Baer, E. (1978) *J. Mater. Sci. Lett.*, **13**, 451.
- 252 Lovinger, A.J. (1980) *Polym. Prep. Am. Chem. Soc.*, **21**, 253.
- 253 Martinez-Salazzas, J., Barham, P.J. and Keller, A. (1984) *J. Polym. Sci. Polym. Phys. Ed.*, **22**, 1085.

- 254 Wittmann, J.C. and Lotz, B. (1986) *J. Mater. Sci.*, **21**, 659.
- 255 Tuinstra, F. and Baer, E. (1970) *J. Polym. Sci. Polym. Lett. Ed.*, **8**, 861.
- 256 Lovinger, A.J. (1983) *J. Polym. Sci. Polym. Phys. Ed.*, **21**, 97.
- 257 Hobbs, S.Y. (1971) *Nature Phys. Sci.*, **12**, 234.
- 258 Wittmann, J.C. and Lotz, B. (1981) *J. Polym. Sci. Polym. Phys. Ed.*, **19**, 1837.
- 259 Wittmann, J.C., Hodge, A.M. and Lotz, B. (1983) *J. Polym. Sci. Polym. Phys. Ed.*, **21**, 2495.
- 260 Wittmann, J.C. and Lotz, B. (1989) *Polymer*, **30**, 27.
- 261 Wittmann, J.C. and Lotz, B. (1990) *Prog. Polym. Sci.*, **15**, 909.
- 262 Kopp, S., Wittmann, J.C. and Lotz, B. (1995) *Makromol. Chem. Macromol. Symp.*, **98**, 917.
- 263 De Rosa, C., Park, C., Lotz, B. and Thomas, E.L. (2000) *Nature (London)*, **405**, 433.
- 264 Park, C., De Rosa, C., Lotz, B., Fetters, L.J. and Thomas, E.L. (2003) *Macromol. Chem. Phys.*, **204**, 1514.
- 265 Park, C., De Rosa, C., Lotz, B., Fetters, L.J. and Thomas, E.L. (2001) *Adv. Mater.*, **13**, 724.
- 266 Smith, P. and Pennings, A.J. (1974) *Polymer*, **15**, 413.
- 267 Smith, P. and Pennings, A.J. (1976) *J. Mater. Sci.*, **11**, 1450.
- 268 Hodge, A.M., Kiss, G., Lotz, B. and Wittmann, J.C. (1982) *Polymer*, **23**, 985.
- 269 Wittmann, J.C. and St. John Manley, R. (1977) *J. Polym. Sci. Polym. Phys. Ed.*, **15**, 1089.
- 270 Wittmann, J.C. and St. John Manley, R. (1977) *J. Polym. Sci. Polym. Phys. Ed.*, **15**, 2277.
- 271 Dorset, D.L., Hanlon, J. and Karet, G. (1989) *Macromolecules*, **22**, 2169.
- 272 Fredrickson, G.H. and Leibler, L. (1989) *Macromolecules*, **22**, 1238.
- 273 Lodge, T.P., Pan, C., Jin, X., Liu, Z., Zhao, J., Maurer, W.W. and Bates, F.S. (1995) *J. Polym. Sci. Polym. Phys.*, **33**, 2289.
- 274 Hamley, I.W., Fairclough, J.P.A., Ryan, A.J., Ryu, C.Y., Lodge, T.P., Gleeson, A.J. and Pedersen, J.S. (1998) *Macromolecules*, **31**, 1188.
- 275 Park, C., De Rosa, C. and Thomas, E.L. (2001) *Macromolecules*, **34**, 2602.
- 276 Van Dijk, M.A. and van den Berg, R. (1995) *Macromolecules*, **28**, 6773.
- 277 Smith, H.I. and Flanders, D.C. (1978) *Appl. Phys. Lett.*, **32**, 349.
- 278 Smith, H.I., Geis, M.W., Thompson, C.V. and Atwater, H.A. (1983) *J. Cryst. Growth*, **63**, 527.
- 279 Kobayashi, T. and Takagi, K. (1984) *Appl. Phys. Lett.*, **45**, 44.
- 280 Flanders, D.C., Shaver, D.C. and Smith, H.I. (1978) *Appl. Phys. Lett.*, **32**, 597.
- 281 Wittmann, J.C. and Smith, P. (1991) *Nature (London)*, **352**, 414.
- 282 Hansma, H., Motamedi, F., Smith, P., Hansma, P. and Wittmann, J.C. (1992) *Polym. Commun.*, **33**, 647.
- 283 Dietz, P., Hansma, P.K., Ihn, K.J., Motamedi, F. and Smith, P. (1993) *J. Mater. Sci.*, **28**, 1372.
- 284 Fenwick, D., Ihn, K.J., Motamedi, F., Wittmann, J.C. and Smith, P. (1993) *J. Appl. Polym. Sci.*, **50**, 1151.
- 285 Fenwick, D., Smith, P. and Wittmann, J.C. (1996) *J. Mater. Sci.*, **31**, 128.
- 286 Segalman, R.A., Yokoyama, H. and Kramer, E.J. (2001) *Adv. Mater.*, **13**, 1152.
- 287 Segalman, R.A., Hexemer, A., Hayward, R.C. and Kramer, E.J. (2003) *Macromolecules*, **36**, 3272.
- 288 Cheng, J.Y., Ross, C.A., Thomas, E.L., Smith, H.I. and Vancso, G.J. (2002) *Appl. Phys. Lett.*, **81**, 3657.
- 289 Cheng, J.Y., Ross, C.A., Thomas, E.L., Smith, H.I. and Vancso, G.J. (2003) *Adv. Mater.*, **15**, 1599.
- 290 Cheng, J.Y., Zhang, F., Chuang, V.P., Mayes, A.M. and Ross, C.A. (2006) *Nano Lett.*, **6**, 2099.
- 291 Ruiz, R., Ruiz, N., Zhang, Y., Sandstrom, R.L. and Black, C.T. (2007) *Adv. Mater.*, **19**, 2157.
- 292 He, X.-H., Song, M., Liang, H.-J. and Pan, C.-Y. (2001) *J. Chem. Phys.*, **114**, 10510.
- 293 Sevink, G.J.A., Zvelindovsky, A.V., Fraaije, J.G.E.M. and Huinink, H.P. (2001) *J. Chem. Phys.*, **115**, 8226.
- 294 Bosse, A.W., Garcia-Cervera, C.J. and Fredrickson, G.H. (2007) *Macromolecules*, **40**, 9570.

- 295** Shin, K., Xiang, H., Moon, S.I., Kim, T., McCarthy, T.J. and Russell, T.P. (2004) *Science*, **306**, 76.
- 296** Xiang, H., Shin, K., Kim, T., Moon, S.I., McCarthy, T.J. and Russell, T.P. (2004) *Macromolecules*, **37**, 5660.
- 297** Sun, Y., Steinhartm, M., Zschech, D., Adhikari, R., Michler, G.H. and Gösele, U. (2005) *Macromol. Rapid Commun.*, **26**, 369.
- 298** Park, C., Cheng, J.Y., De Rosa, C., Fasolka, M.J., Mayes, A.M., Ross, C.A. and Thomas, E.L. (2001) *Appl. Phys. Lett.*, **79**, 848.
- 299** Thomas, E.L., De Rosa, C., Park, C., Fasolka, M., Lotz, B., Mayes, A.M. and Yoon, J. (2005) US Patent No. 6, 893, 705 (MIT).
- 300** Park, C., Simmons, S., Fetters, L.J., Hsiao, B., Yeh, F. and Thomas, E.L. (2000) *Polymer*, **41**, 2971.
- 301** Park, C., De Rosa, C., Fetters, L.J. and Thomas, E.L. (2000) *Macromolecules*, **33**, 7931.

## 5

# Helical Polymer-Based Supramolecular Films

Akihiro Ohira, Michiya Fujiki, and Masashi Kunitake

### 5.1

#### Introduction

Nature's elegant bottom-up fabrication of hierarchical superhelical assemblies over a wide range of scales has inspired the development of functional advanced materials from efficient approaches [1].

In natural systems, hierarchical helical architectures, such as the double helix of DNA, the triple helix of collagen, and the  $\alpha$ -helical coiled-coils of myosin and keratin on the molecular level, are ubiquitous [2]. They also occur frequently in artificial systems, and it is well known that amphiphilic compounds, such as phospholipids, amino acids, nucleic acid derivatives, and carbohydrate compounds, fabricate a variety of helical superstructures including tubes, disks, bundles, fibers, and cholesteric liquid crystals [1, 3]. Until recently, extensive studies have been conducted into the helical supramolecular assemblies of organic molecular materials [1, 3–5] and, indeed, recent progress in the areas of polymer and supramolecular sciences has led us to construct highly ordered and well-defined helical architectures for synthetic helical polymers [6]. Akagi *et al.* reported the synthesis of hierarchical helical polyacetylene fiber under an asymmetric reaction field consisting of a chiral nematic ( $N^*$ ) liquid crystal [7]. Nolte *et al.* demonstrated that the formation of various helical superstructures of amphiphilic block copolymer containing a polystyrene tail and a charged helical polyisocyanide head group derived from isocyano-L-alanine-L-alanine and isocyano-L-alanine-L-histidine [8]. Yashima *et al.* succeeded in the construction of both two-dimensional (2-D) and three-dimensional (3-D) smectic self-assemblies composed of helical polyisocyanides [9]. The same group also created a one-dimensional (1-D) helical supramolecular architecture of double-stranded helical polyacetylenes, which can form 2-D, self-assembled structures on the substrate [10]. Today, the control of such highly ordered and hierarchical helical assemblies of synthetic helical polymers is a major challenge in polymer and supramolecular sciences, especially from the point of view of developing the materials sciences. Generally, the driving forces in the formation of helical assembled structures are varied, including a

chiral interaction and a polar interaction between solute–solvent and solute–solute, such as hydrogen bonding, electrostatic interactions, coordination bonding, and  $\pi$ - $\pi$  stacking. If a simple system were to organize a hierarchical helical structure only by weak intermolecular interactions such as van der Waals interactions, it might be helpful to understand the chiral interactions between the molecules. In this chapter, we will review several helical polymer-based supramolecular assemblies in order to provide a better understanding of the driving forces in the formation of these helical assemblies. First, we describe helical polymer-based 1-D and 2-D architectures from the perspective of the construction of supramolecular organization with helical polymers. Next, we describe helical polymer-based functional films, focusing on the functionalities, such as switch, memory, transfer and amplification, that are derived from the intrinsic chirality of helical polymers. Two different types of well-known helical polymer were chosen. A poly( $\gamma$ -L-glutamate)-derivative polypeptide and a synthetic helical polysilane polymer were selected because these are well studied and possess ideal helical conformation, thus allowing us to investigate both the intramolecular and intermolecular interactions. Studies of the crystal structure of poly( $\gamma$ -L-glutamate) derivatives have focused primarily on the packing structure of the  $\alpha$ -helices. Kaufman *et al.* initially reported that long *n*-alkyl side chains of polymers based on acrylic and methacrylic acids can pack into paraffin-like crystallites [11]. Watanabe *et al.* discovered the thermotropic liquid crystal nature of these polymers and investigated the molecular packing and thermotropic behaviors for a series of poly( $\gamma$ -L-glutamate)s with *n*-alkyl side chains, ranging from amyl to octadecyl [12].

Polysilane can be prepared by an easy synthetic route, and exhibits unique electronic and optical properties that are attributed to the delocalized  $\sigma$  electrons along the Si–Si main chain [13]. Much research has been conducted on the behavior of polysilane in solution in order to elucidate polymer conformation [14]. Consequentially, it has been found that the optical and electronic properties of polysilane may change easily with the side chain structure, solvent, or temperature. Optically active polysilanes with various chiral substituents in the side chains adopt helical conformations with a preferential screw-sense [14]. Furthermore, it has been found that helical polysilanes exhibit many interesting characteristics both in solution and in solid states [15]. The relationship between the global conformation of a polymer chain and the physical properties in dilute solution has already been established from spectroscopic evidence in helical polysilanes [16].

Research into the supramolecular assembly based on a helical polymer is expected to contribute significantly to developments within the life sciences and materials sciences. In the field of life sciences, it is important to clarify how the existence of the helical configuration is related to human vital activity. In the field of materials sciences, a helical conformation is used for functional materials, for example in electronic and/or ionic conductors, using the directivity with a well-defined helical conformation, molecular sensing and sensor systems using the regularity of the helical conformation. Helical and superhelical assemblies are ubiquitous in nature, as exemplified in biological polymers such as DNA and structural proteins, wherein the information stored in the molecular building

blocks is utilized for supramolecular organization into higher-order helical architectures at different hierarchical levels, from nanoscopic to macroscopic lengths. Inspired by this elegant spontaneous fabrication into higher-order helical architectures at different hierarchical levels in nature, the self-organization of synthetic organic molecules has been widely exploited to generate novel functional supramolecular architectures. However, in order to achieve this system, it is necessary to design a programmed molecule which can self-organize spontaneously into higher-ordered supramolecular structures with controlled morphology, dimension, and size. As the helical polymer possesses a programmed and well-organized structure, a supramolecular assembly based on a helical polymer would be promising for controlling the hierarchy in multi-scale so as to create a natural system.

## 5.2 Helical Polymer-Based 1-D and 2-D Architectures

Today, the precise control of topology at the single polymer chain level (1-D), especially for helical polymers, is a “hot issue,” because understanding the 1-D change of topology is the ultimate goal for the development of polymer-based nanomaterials, and will take advantage of the solubility, flexibility, stability, and electronic properties of these materials [17]. The 2-D, self-organized microscopic and/or mesoscopic structures composed of helical polymers are also of considerable interest both for advancing the fundamental understanding of structural properties, such as helicity and rigidity, and for developing potential applications, including liquid crystals and molecular sensing and sensory systems at the monolayer level [18]. In addition to the structural properties, understanding the interactions that operate between the molecules is also crucial for self-organization. The results of this research will be useful for the construction of hierarchical 3-D bulk phases.

In general, the supramolecular 1-D and 2-D architectures composed of helical polymers can be visualized by using scanning probe microscopy (SPM) techniques, such as scanning tunnel microscopy (STM) and atomic force microscopy (AFM). These not only provide the opportunity for direct observations on atomic flat substrates with submolecular resolution, but also reveal the structural information of individual polymer chains, whereas most spectroscopic characterizations have provided averaged data for multiple molecules or aggregates. Observations of biopolymers and synthetic polymers [19–22] in the isolated or aggregated state using SPM (mainly AFM) have been conducted in order to analyze molecular characteristics such as chain length, end-to-end length, polymer diameters, and chain rigidity [23, 24]. In fact, AFM has proved very advantageous for observing helical characteristics, such as helicity, helical pitch, and helix reversal [9].

In this section, as examples of 1-D structures, such as rods and circles, we describe the changes in the 1-D architectures of isolated helical polysilanes with different chain lengths on the surfaces. Additionally, we describe a mesoscopic 2-D superhelical assembly of polysilane formed by homochiral intermolecular

interactions. The observation of the associated superstructure of the synthetic helical polymers was significant, especially for a wide range of scales, and also provided a better understanding of the mechanism of formation of the highly ordered and hierarchical architectures. We also present details of the formation of 2-D epitaxial adlayers of poly( $\gamma$ -L-glutamate)s as examples of 2-D helical, polymer-assembled structures. It should be noted here that not only the observation of both 1-D and 2-D architectures but also the direct visualization of intramolecular and intermolecular interactions existing between helical polymers were clearly demonstrated by AFM, with molecular-level resolution.

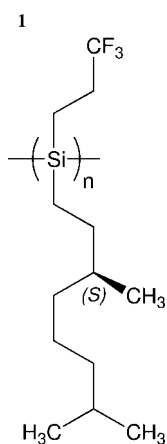
### 5.2.1

#### Formation of Various 1-D Architectures of Helical Polysilanes on Surfaces

The topology of an isolated helical polysilane chain bearing a fluoroalkyl side group (Scheme 5.1, polymer **1**) changes from a rod-like to a circular structure on a mica surface, with the main chain length determined by means of AFM [25]. Polymer **1** is an ideal model molecule with different lengths; it is a 1-D, semi-flexible semiconductor that has exhibited unique properties that have contributed to intramolecular CF/Si interactions [26].

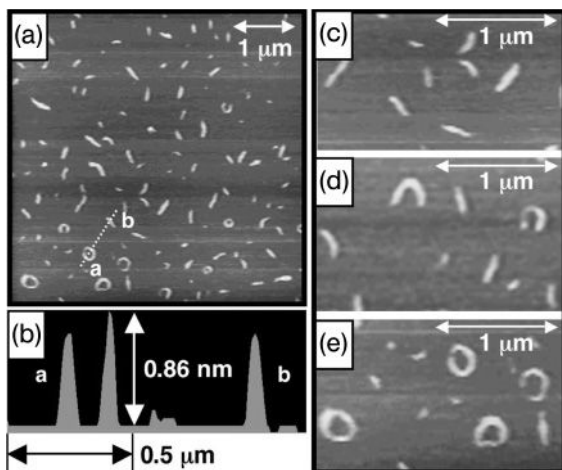
##### 5.2.1.1 Direct Visualization of 1-D Rod, Semi-Circle and Circle Structures by AFM

Figure 5.1 exemplifies typical AFM images of **1** on mica surfaces. In these images, three different forms of topology—namely, rod, semi-circle, and circle structures—coexisted and can be clearly distinguished. Figures 5.1c, d, and e show AFM images of rod, semi-circle, and circle structures of isolated **1**, respectively, in a relatively narrow area. The average height of both the rod and circle structures was approximately 0.86 nm and was almost uniform, which corresponds to the real height of adsorbates.



**Scheme 5.1** Chemical structure of fluoroalkyl-containing helical polysilane **1**.



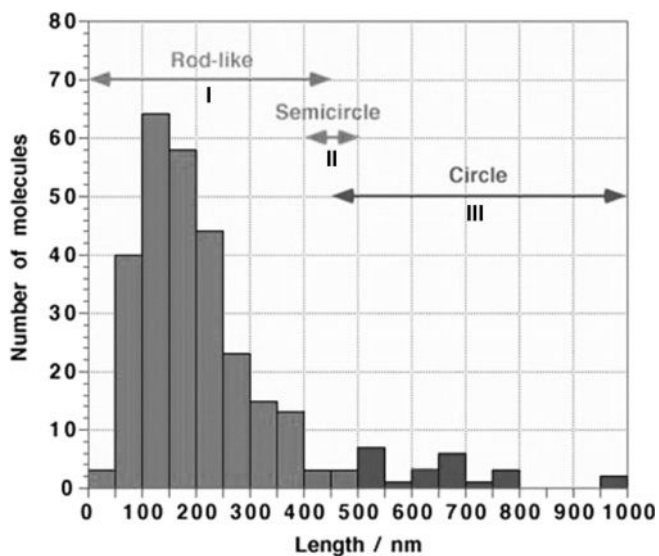


**Figure 5.1** Typical atomic force microscopy (AFM) images of isolated polysilane **1** chains on mica surfaces in (a) large area, (b) cross-sectional profile of line a–b in (a), (c) rod-like structure, (d) rod-like and semi-circle structures, and (e) rod-like, semi-circle, and circle structures.

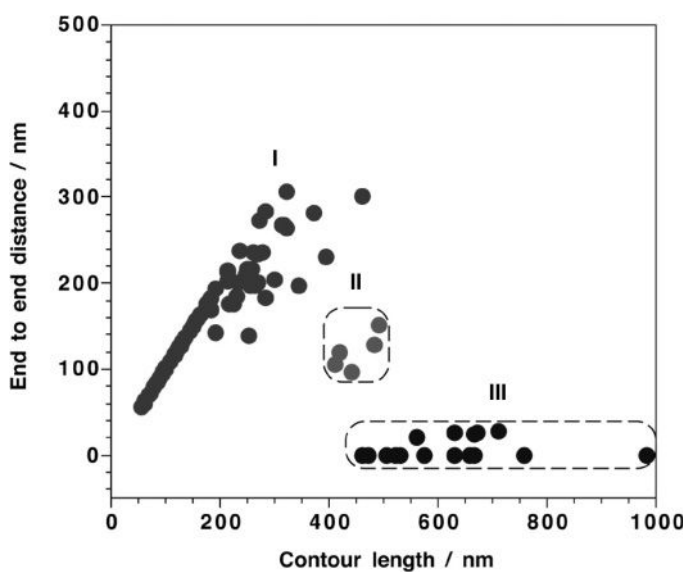
All of the observed rod, semi-circle, and circle structures were not aggregated forms but isolated single polymer chains. The distribution of the average number of contour lengths ( $L_n$ ) is shown in Figure 5.2.

In the region of shorter lengths in Figure 5.2 (region I), only rod-like structures were observed (see Figure 5.1c), and this was essentially consistent with the results that **1** possesses a stable, semi-rigid, helical conformation by the intramolecular CF/Si interaction in the solution system [26]. However, it should be emphasized here that the chain topology eventually transformed from rod to circle structures as the main chain length increased on the surfaces. In particular, semi-circle structures were observed in the very narrow region of medium length (400–500 nm) in Figure 5.2 (region II), thereby showing that the topological switching between the rod and circle structures is attributable to the discontinuous transition phenomenon. The distribution of the end-to-end distance also exhibited a discrete decrease as contour length increased, as shown in Figure 5.3.

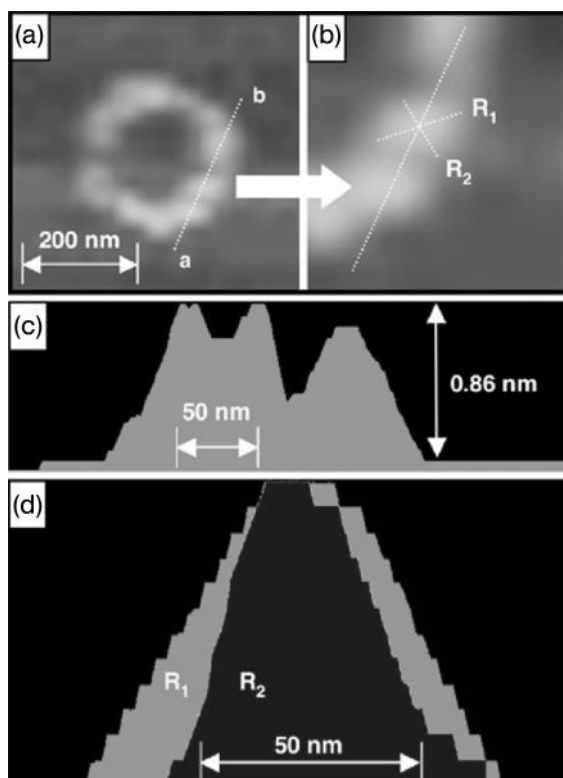
Figure 5.4 shows a high-resolution AFM image of the higher-order helical conformation in a circle structure. The observed helical pitch in the AFM images was determined to be approximately  $44.2 \pm 4.2$  nm, although it was much longer than that expected from the  $7_3$  helical structure model (0.45 nm). This might be attributed not only to a tip broadening effect but also to an intramolecular CF/Si interaction, leading to a long-period macromolecular right-handed helicity [27]. Except for the limitation of the AFM spatial resolution, and because such helical conformations cannot be seen within the rod and semi-circle structures, significant long



**Figure 5.2** Contour length distribution of **1** estimated from AFM images. Regions I, II, and III indicate the existence of rod-like, semi-circle, and circle structures, respectively.



**Figure 5.3** Distribution of the end-to-end distance of **1** obtained from AFM images as a function of contour length. The numbers I, II, and III correspond to the rod, semi-circle, and circle structures, respectively.



**Figure 5.4** High-resolution AFM image of **1**. (a) Circle structure; (b) Highly zoomed image of (a); (c) Cross-section profile of line a–b in (a); (d) Cross-sectional profiles of segments  $R_1$  and  $R_2$ . The greater width of  $R_1$  in the profile indicates that the polymer chain possesses a right-handed helical structure.

Each bright spot and its cross-sectional profile clearly indicate that the polymer chain has a helical structure. From the cross-sectional profile, it can be seen that the local conformation of  $R_2$  is flat on the bottom, but  $R_1$  is bulged on the top [33].

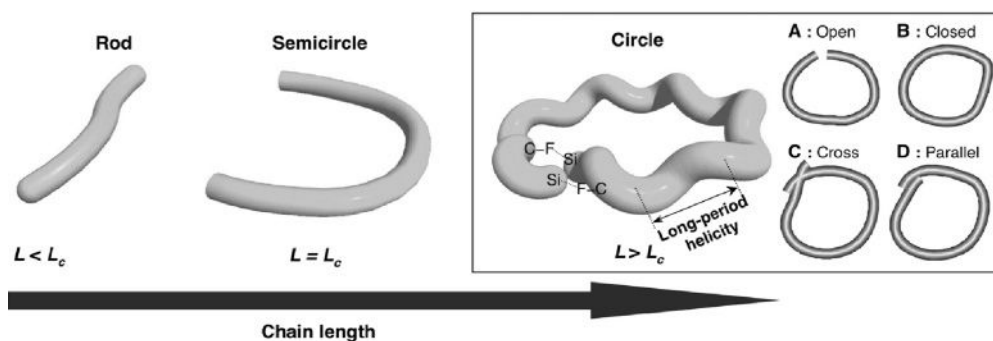
chains might be required to configure the long-period helicity. In several AFM images and their cross-section profiles, the height and width were frequently different at the right and left or up and down points in the circle structure (e.g., Figure 5.1b).

### 5.2.1.2 Driving Force for the Formation of 1-D Architectures

The chain dynamics were realized on the surfaces, and not in the solution system. Although these structures cannot be formed in the solution system due to thermal fluctuation, the mechanism of topology switching of single polymer chains is different from that of the associated forms. The dominant driving force of topology switching would originate from a degree of freedom, as the topology of a single polymer chain on the surface depends heavily on the chain length.

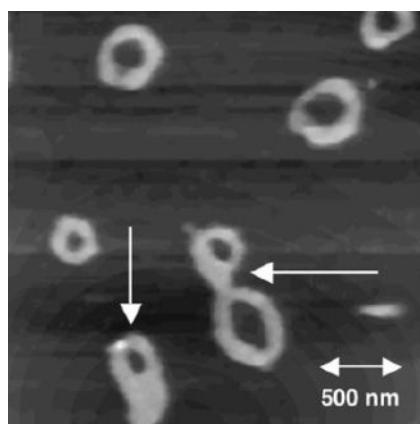
The proposed structural models regarding the circle structure are shown in Figure 5.5. Imperfect open-circle structures with a narrow end-to-end gap were frequently observed, as illustrated in Figure 5.5 (open circle A). In the case of B, it is hypothesized that the intramolecular CF/Si interaction allows it to form and stabilize a perfect closed-circle structure, because the fluorine atoms on the side chains may attach to the Si atoms on the main chain, close to the end groups. Besides this effect, a Si–O–Si bond may be formed between the end-termini via hydrolysis of the SiH end group by water adsorbed onto the mica surfaces [28]. In the case of circle C, the end-termini of the polymer chain are crossing each other, while in circle D the end-termini are not crossing but are parallel to each other. These structural models can be the precursors of toroidal structures.

As expected, much longer polymer chains frequently formed toroid-like structures, as shown in Figure 5.6. These circle and toroid-like architectures may be



**Figure 5.5** Schematic representation of morphology switching of single polysilane chain **1** with chain length dependence based on AFM observations. Here,  $L_c$  indicates the critical length of the semi-circle structure as

an intermediate state between the rod and circle structures. In the circle structure, (a), (b), (c), and (d) indicate the proposed models (open, closed, cross, and parallel, respectively).



**Figure 5.6** Typical AFM image of toroid-like structures adsorbed onto mica surfaces.

useful in device applications because a nanoscaled circle architecture composed of organic/inorganic materials has been expected to provide a superior device performance due to the lack of defects in the end-terminus part, which strongly affects energy loss [29].

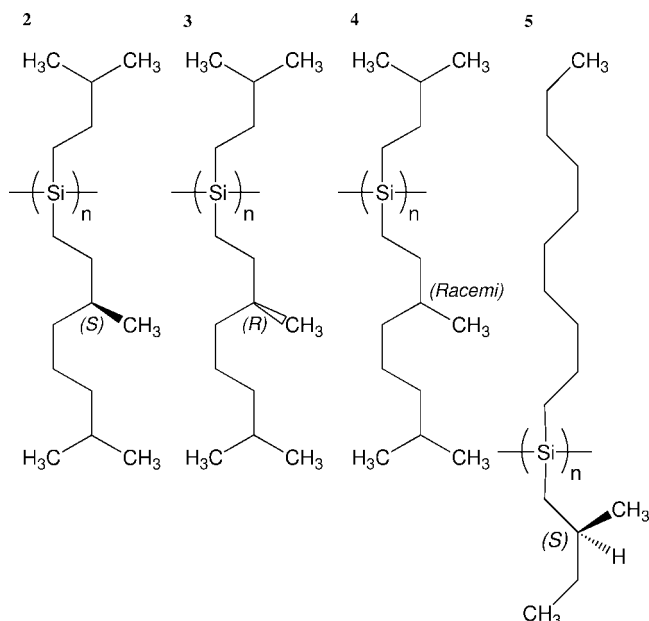
### 5.2.2

#### Formation of Mesoscopic 2-D Hierarchical Superhelical Assemblies

Optically active polysilanes, such as poly[(*S*)-3,7-dimethyloctyl-3-methylbutylsilane] (**2**) and poly[(*R*)-3,7-dimethyloctyl-3-methylbutylsilane] (**3**), which are able to undergo the helix–helix transition [30] at  $-20^{\circ}\text{C}$  in iso-octane (as shown in Scheme 5.2) were used in this study. Notably, we present here both the construction of mesoscopic highly ordered and hierarchical–superhelical assemblies based on only weak homochiral intermolecular interactions.

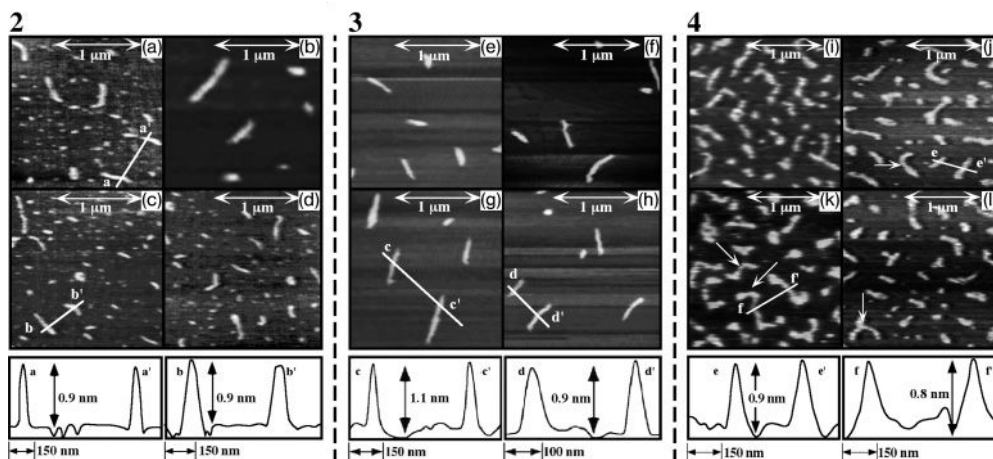
##### 5.2.2.1 Direct Visualization of a Single Polymer Chain

Figure 5.7 shows the typical AFM images of single polymer chains of polymers **2**, **3**, and racemic **4**, deposited onto the freshly cleaved mica surfaces and their section analysis. The samples were prepared by casting a dilute iso-octane solution of polymer sample (approximate range of  $5\text{--}10\mu\text{gml}^{-1}$ ), after which the strands



**Scheme 5.2** Chemical structures of optically active poly[(*S*)-3,7-dimethyloctyl-3-methylbutylsilane] **2**, poly[(*R*)-3,7-dimethyloctyl-3-methylbutylsilane] **3**, which can undergo a

helix–helix transition at  $-20^{\circ}\text{C}$  in iso-octane, poly[(*rac*)-3,7-dimethyl-octyl-3-methylbutylsilane] **4**, and poly[*n*-decyl-(*S*)-2-methylbutylsilane] **5**.

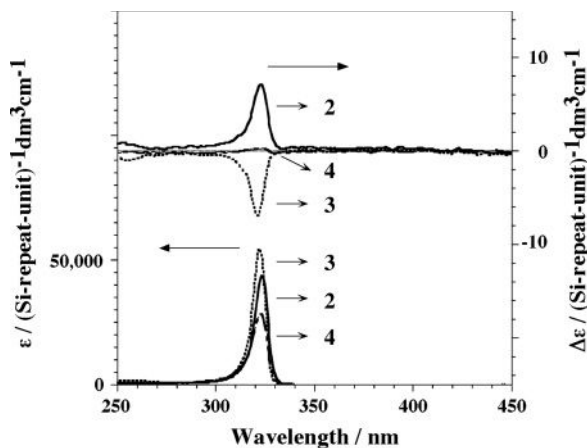


**Figure 5.7** Typical AFM images of single polymer chains of **2**, **3**, and **4**, and their cross-sectional profiles [lines a–a' in (c) and b–b' in (d) of **2**, lines c–c' in (g) and d–d' in (h) of **3**, and lines e–e' in (j) and f–f' in (k) of **4**] onto the mica surfaces. **2**:  $M_w = 2.9 \times 10^5$ ,

$M_w/M_n = 3.43$ . **3**:  $M_w = 2.6 \times 10^5$ ,  
 $M_w/M_n = 3.53$ . **4**:  $M_w = 3.2 \times 10^5$ ,  
 $M_w/M_n = 5.39$ . The concentrations of casting solution were ca.  $7 \mu\text{g ml}^{-1}$  for **2**, ca.  $5 \mu\text{g ml}^{-1}$  for **3**, and ca.  $10 \mu\text{g ml}^{-1}$  for **4**.

corresponding to the single polymer chains were randomly and separately adsorbed onto the mica surface. Both, the **2** and **3** polymer chains typically possessed an isolated and stretched conformation. Although the information on the helical conformation, such as the helicity and helical pitch, could not be obtained due to a lack of resolution, these AFM images demonstrate the rod-like conformation, which is expected from the empirical relationship between the molar extinction coefficient  $\epsilon$ , the viscosity index  $\alpha$  (**2**: 1.47, **3**: 1.32 in toluene at  $70^\circ\text{C}$ ), and the relatively long persistence length ( $\sim 60$  nm) [31]. A different polysilane, poly(*n*-decyl-(*S*)-2-methylbutylsilane) (**5**), which is a stiff polymer with a persistence length of 70 nm, was observed by means of AFM as a rod-like chain onto the sapphire surfaces [23b]. Therefore, these results were consistent with the previous report.

However, slightly bent chains were frequently observed when the polymer chains of the racemic polymer **4** ( $M_w: 5.2 \times 10^5$ ,  $M_w/M_n: 5.39$ ), which is a random copolymer system composed of equal amounts of *R*-comonomer and *S*-comonomer, were compared to those of **2** and **3** (marked by arrows in Figure 5.7j, k, and l). Additionally, the molar absorption coefficient  $\epsilon$  was lower than that of **2** and **3** ( $2.8 \times 10^4$  (Si repeat unit) $^{-1}$ ) in iso-octane at  $20^\circ\text{C}$ , and the  $\alpha$  value, which indicates the rigidity of the polymer chain, was also relatively lower than that of **2** and **3** (1.15 in tetrahydrofuran at  $40^\circ\text{C}$ ), as shown in Figure 5.8. In addition to the empirical relationship between  $\epsilon$  and the viscosity index of polysilanes [14b], the present AFM observations suggest that the topology of **4** is more flexible than that of **2** and **3**.



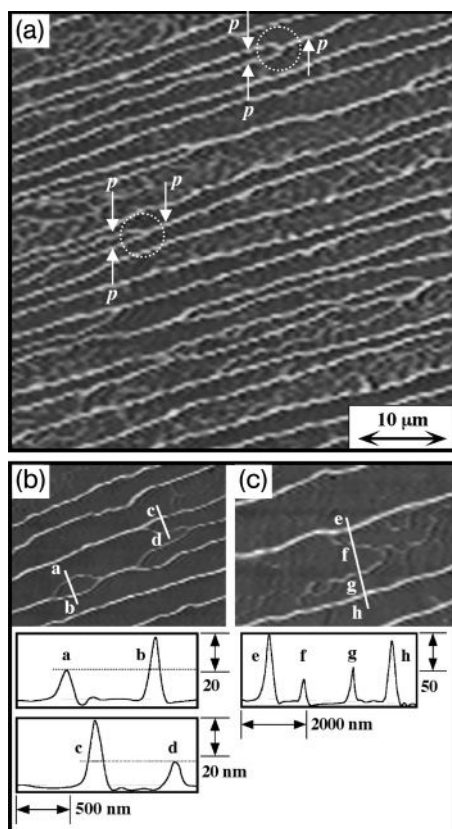
**Figure 5.8** Circular dichroism and UV absorption spectra in homogeneous iso-octane solutions of **2** (at 20 °C, solid line), **3** (at -5 °C, dotted line) and **4** (at 20 °C, broken line). Either the  $\epsilon$  or  $\Delta\epsilon$  value was normalized (Si repeat unit) $^{-1}$ .

#### 5.2.2.2 Formation of Superhelical Assemblies by Homochiral Intermolecular Interactions

The polymer chain, which is much longer than the persistence length of **2** ( $M_w$ :  $3.9 \times 10^5$ ,  $M_w/M_n$ : 3.02), formed a unique aggregated structure. Figure 5.9 shows the typical AFM images of the superhelical assemblies of **2**. The highly oriented assembled polymer chains were observed on the mica surfaces (Figure 5.9a), which might be attributed to a dewetting property and evaporation process of iso-octane on the mica surfaces. In the case of a fast evaporation process at 80 °C, no uniform superhelical assemblies were found.

Figures 5.9b and c show the assembled polymer chains and cross-section analysis in the narrow area. The lines a–b and c–d in Figure 5.9b indicate the height and width, respectively, of the branching points in the main assembled polymer chain. The height of two different polymer chains splitting from the branching points was approximately 17 nm at the lower part and 39 nm at the higher part. The lines e–h in Figure 5.9c indicate the height and width of the main assembled polymer chain. The height of the main assembled polymer chain, corresponding to approximately 70 nm, is higher than the total of the branching chain (17 + 39 nm), and shows that the main assembled coil is formed by a twisting of branches. These results reveal that the assembled polymer chain is composed of several twined polymer chains.

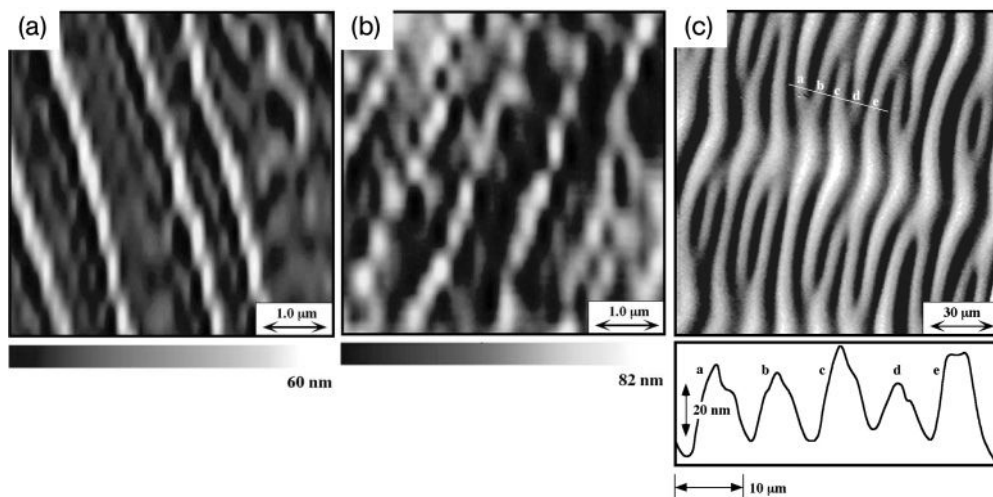
Figure 5.10a shows the high-resolution AFM image of coiled-coil assemblies of polymer **2**. Right-handed superhelical polymer chains, which possess a long helical pitch, were clearly observed. In the case of the coiled-coil forms of polymer **3** ( $M_w$ :  $7.9 \times 10^5$ ,  $M_w/M_n$ : 4.78), superhelical polymer assemblies were also observed, which have the opposite handedness (left-handed) as polymer **2**, as shown in



**Figure 5.9** AFM images and cross-sectional profiles [lines a–b and c–d in (b) and e–f–g–h in (c)] of highly ordered superhelical assemblies of **2** onto the mica surfaces.  $M_w = 3.9 \times 10^5$ ,  $M_w/M_n = 3.02$ . The concentration of the casting solution was ca.  $500 \mu\text{g ml}^{-1}$ .

Figure 5.10b. It should be noted that each helical (*S* or *R*) polysilane was configured in its corresponding unidirectional superhelical structure. It has been suggested that the **2** and **3** chains possess the *P* (right-handed) and *M* (left-handed) helical screw-senses, respectively. In our case, large-scaled, right-handed and left-handed superhelical fibers are composed of right-handed **2** and left-handed **3**, respectively [32]. In Figure 5.9a, here again, it was found that the branched chains (branching points are denoted by a dotted circle), which are components of the main assembled chain, also possessed a right-handed helical structure (marked by arrows). Each branched chain and its small aggregate maintained the same helicity, leading to the formation of uniform and hierarchical superhelical assemblies with the same helicity as the components. It has been reported that, in both natural and artificial systems, heretofore, the helicities of the components were





**Figure 5.10** AFM images of superhelical structures of **2**, **3**, and **4** polymer chains onto mica surfaces. (a) **2** ( $M_w = 3.9 \times 10^5$ ,  $M_w/M_n = 3.02$ ); (b) **3** ( $M_w = 7.9 \times 10^5$ ,  $M_w/M_n = 4.78$ ); (c) **4** ( $M_w = 3.2 \times 10^5$ ,  $M_w/M_n = 5.39$ ).

**Table 5.1** Numerical data of assembled fibers of **2**, **3**, and **4** polymer on the mica surfaces (see Scheme 5.2).

Polymer	$M_w \times 10^5$	$M_w/M_n$	Height of aggregate (nm)	Helical pitch (nm)	Screw-sense of fibers
2	3.9	3.02	$65 \pm 12$	$646 \pm 82$	Right-handed
3	7.9	4.78	$49 \pm 10$	$636 \pm 77$	Left-handed
4	3.2	5.39	$51 \pm 9.5$	–	–

different from that of the hierarchical superstructure that eventually formed; for example, the right-handed superhelix of collagen is composed of three left-handed helices [2a, 5k, 33]. Given that the same helicity was maintained during the process of association without reference to the state of the aggregate (number of polymer chains), homochiral intermolecular interactions would be a dominant driving force for the formation of uniform and hierarchical superhelical assemblies. The data reporting on the height, helical pitch and handedness of the coiled-coil chains are listed in Table 5.1.

A comparison of the helical fibers constructed from **2** and **3** showed, surprisingly, almost the same value for the heights and helical pitches, but a difference in the handedness. A similar phenomenon has been reported in a biological system, where Larson and coworkers observed the left-handed superhelical structure composed of RecA and double-stranded DNA by means of AFM [33]. In that

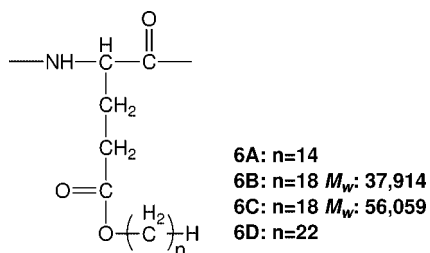
case, the pitches of the superhelices of the complexes (RecA and DNA filament) were very similar to each other, regardless of the number of component filaments. Moreover, from observations of the heights of the helical fibers of **2** and **3**, it is believed that the formation of the highly ordered structure in the large scale is achieved by the assembly of several polymer chains. This observation is an example of mesoscopic large-scaled, highly ordered superhelical assemblies that possess both of the helical senses constructed by a synthetic helical polymer. Most of the synthetic helical polymers have a polar functional group in the main or side chain, and therefore an associated structure is formed by the combination of various strong intermolecular interactions, such as hydrogen bonding, electrostatic interactions, coordination bonding, and  $\pi$ - $\pi$  stacking. In the present case, only weak intermolecular interactions can account for the polymer association, because the polysilanes **2** and **3** are composed of nonpolar groups with side chains. It is noteworthy that no assembled superhelical structures were observed with **4**. As for the morphology of the observed structure of **4**, although large-scaled stripe patterns were formed on the substrate, the structures possessed no helicity. As discussed above, there was no major difference between **2** or **3** and **4** in the conformation of a single polymer chain. These results suggest that the homochirality of the single helical polymer chain rather than the chain conformation structure contributes to the formation of the large-scaled, highly ordered superhelical assembly [34]. Similar phenomena have been observed in the 2-D crystallization of small chiral organic molecules on the surfaces. For example, homochiral enantioselective crystallization from racemic mixture has been reported [34a]. Kühnle and coworkers have shown that cysteine molecules formed homochiral pairs (D-D and L-L) from racemic mixture using STM. Chiral transfer from single molecules into self-assembled monolayers on the metal surfaces has also reported by Fasel *et al.* [34b]; here, enantiopure *P* and *M* chiral single molecules on the surfaces formed the enantiopure self-assembled monolayers with clockwise and anticlockwise formats, respectively. In addition to the enantiopure self-assembly, it has been reported that the enhancement of chiral interactions in two dimensions was observed in the enantioseparation of chiral molecules, using STM [34c]. These results also suggested that homochiral intermolecular interaction would be an important factor to form the 2-D chiral surfaces.

### 5.2.3

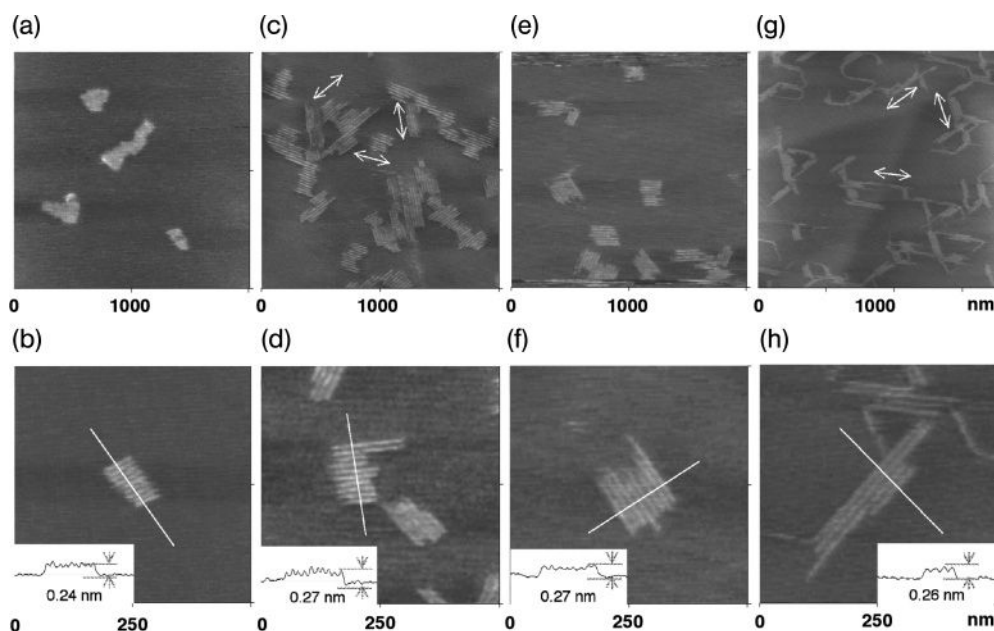
#### Formation of 2-D Crystallization of Poly( $\gamma$ -L-Glutamates) on Surfaces

Poly( $\gamma$ -L-glutamate) (**6**) is a polypeptide that is well known for forming a stable  $\alpha$ -helical conformation, even when the substituted side chains are varied, as shown in Scheme 5.3. Polymers of **6** have longer alkyl side chains and can form 2-D self-organized arrays on highly oriented pyrolytic graphite (HOPG) [20c].

In the following section, the formation of 2-D epitaxial arrays on surfaces and a comparison of structures between 2-D epitaxial arrays and 3-D bulk phases will be described, based on the results of AFM and wide-angle X-ray diffraction (XRD) studies.



**Scheme 5.3** Chemical structure of poly( $\gamma$ -L-glutamate) derivatives **6**, where  $n$  is defined as the number of methylene units in the alkyl group.



**Figure 5.11** Typical AFM images and cross-sectional profiles (insets) of polymers **6** adsorbed onto HOPG substrate. (a, b) **6A**; (c, d) **6B**; (e, f) **6C**; (g, h) **6D**. The Z-scale of the images is constant at 4 nm. Cross-sectional profiles of the island structures are shown in the insets of the images. The arrows indicated the running directions of the rods in

the 2-D array, and the directions corresponded to  $\langle \bar{1}2\bar{1}0 \rangle$  directions of the graphite basal plane. In whole images, the entire surface is uniformly covered by bright islands, representing the polymer adsorbates, and the dark portion surrounding islands is bare graphite surface.

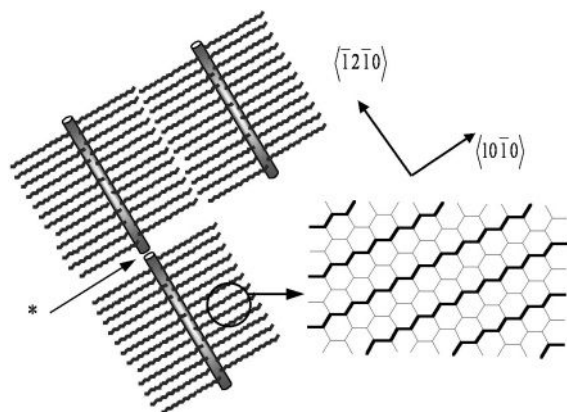
### 5.2.3.1 Direct Visualization of 2-D Self-Organized Array by AFM

Figure 5.11 shows a collection of high-resolution island images for the **6** series, which all revealed a similar island structure. The island-like arrays consisted of rods, which possessed an entirely straight conformation in a parallel arrangement. A single rod, which was separated from the islands, was not found at all. It is

important to emphasize here that the corrugations of the islands were constant for each of the members within the **6** series; this suggests that the alkyl chains on **6** were flat and contacted graphite in the same manner. It also indicates that the polymers adsorbed on the HOPG were not in an aggregated form, but rather in a monolayer form. The stripped patterns in the arrays were triangular in arrangement, with the running stripes directly rotated  $60^\circ$  from each other (see Figure 5.11c and g, where the marked arrows indicate the running direction of the stripes in the islands). This clearly indicated that the formation of the island structures is by epitaxial adsorption.

### 5.2.3.2 Orientation in 2-D Self-Organized Array

The orientation of the adsorbed structure was estimated by the relationship between the alignment of the alkyl chain and the graphite substrate. Figure 5.12 shows the schematic representation of the structural model proposed for **6**. In the array model, the intervals of the rods correspond to intermolecular distances between flat-oriented adjacent polymers. Extended alkyl side chains with the *all-trans* conformation are divided to both sides of the helical main chain, and align perpendicular to the main chain. The driving force for the formation of the array is predominantly an epitaxial interaction between the alkyl side chains and the graphite surface. The rods of the **6** polymers run in the  $\langle \bar{1}2\bar{1}0 \rangle$  direction. When the rod model was superimposed on a graphite lattice, the alkyl side chains, which were angled at  $90^\circ$  to the direction of the rods, were aligned in the  $\langle 10\bar{1}0 \rangle$  direction. It is well known that alkyl chains adsorb epitaxially onto HOPG, and that the alkyl chains are aligned in the  $\langle 10\bar{1}0 \rangle$  direction [35], clearly showing the accuracy of the proposed model and indicating that the formation of the array is predominantly due to epitaxial adsorption of the side groups.



**Figure 5.12** Schematic representation of the proposed structural models for the 2-D array, displaying the rod structure and the epitaxial alignment of alkyl side chains on the HOPG substrate of **6**.

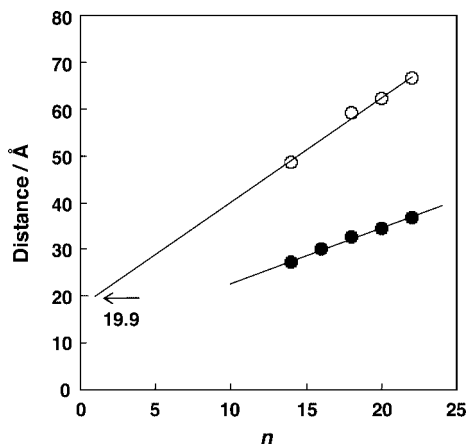
### 5.2.3.3 Intermolecular Weak van der Waals Interactions in 2-D

#### Self-Organized Arrays

Although the interactions between the alkanes and graphite are stronger than the intermolecular interactions, the lateral intermolecular interactions are important in the formation of an ordered 2-D structure [36]. In addition to the epitaxial interaction between the alkyl side chains and the graphite surface, the formation of an island structure composed of rods suggests the existence of the attractive intermolecular interactions, including van der Waals interactions, between the alkyl chains of adjacent rods. Alkyl chains have also been reported to align “side by side” with parallel or perpendicular conformations at the surface [36, 37]. In the case of the **6** series, the interval between the alkyl chains is very close to that reported for a flat conformation. From the model, it was expected that the length of the rods was attributable to the length of each helical polymer. However, the observed lengths of the strings were regularly several times longer than expected, and often overestimated even by gel permeation chromatography (GPC). For example, the observed lengths of the rods for **6B** ( $M_w = 37900$ ;  $M_w/M_n = 1.1$ ; expected length = 15 nm) and **6C** (56100; 1.2; 22 nm) were 27–44 and 17–98 nm, respectively, indicating that each rod consisted of several polymers to form “head-to-head” or “head-to-tail” structures, shown by the arrow in Figure 5.11. The interpolymer “side-by-side” arrangement is due to the intermolecular interactions between the alkyl chains of adjacent rods. Although the average degree of polymerization for **6D** was almost the same as that of **6C** (Figure 5.1e), the rods of **6D** (Figure 5.1g) were longer than those of other **6s**. This observation was due not to differences in the molecular masses of the polymers, but rather to the enhancement of intermolecular interactions with increasing alkyl chain length. More interestingly, the rods seem to have a tendency to align with the edges of rods. The islands in Figure 5.11b, d and f are typical examples, with relatively ordered rod ends. This suggests that attractive lateral intermolecular interactions exist between rods at the surface.

### 5.2.3.4 Comparison of Structures between a 2-D Self-Organized Array and 3-D Bulk Phase

The interval distances between the parallel rods depend on the length of the alkyl side chains of the polymers. Figure 5.13 shows plots of the intervals between the parallel rods against the number of alkyl side chains. The intervals increase linearly with the length of the alkyl side chains, and from the slope of the linear plot the length per methylene unit is approximately 2.2 Å; this corresponds to increments of an extended alkyl chain with all-*trans* conformations, and indicates that the alkyl side chains are perpendicular to the helical main chain. The extrapolated value of the interval to  $n = 1$ , which should correspond to the interval for poly( $\gamma$ -methyl-L-glutamates) (PMLG,  $n = 1$ ), was 19.9 Å. This value is appropriate for the diameter of PMLG, and validates the model subsequently proposed. In Figure 5.13, the results of the bulk crystal analysis were plotted with those of the 2-D array. The slope for the PG $n$  bulk crystal, in which the side chains were crystallized, was approximately 1.3 Å/CH<sub>2</sub> (a methylene unit), which is almost half the



**Figure 5.13** Variations in the interval distances (○) between neighboring rods in the 2-D array and the corresponding distances (●) between the center of **6** in the bulk crystal, which was revealed through (100) reflections.

value of that for the 2-D crystal. This difference is due to the interdigitating structure of the bulk crystal.

The 2-D array of **6** on HOPG forms under submonolayer coverage conditions. All results, including the correlation between the interval of rods and alkyl chain lengths, clearly proved the proposed model for the epitaxial adsorption of **6**. Furthermore, epitaxial helical polymer–substrate and polymer–polymer interactions were also found which can lead to the formation of controllable architectures. In particular, the existence of some of the intermolecular interactions between the end-termini of polymers was quite interesting and important for the design of 1-D supramolecular architectures.

#### 5.2.4

#### Summary of Helical Polymer-Based 1-D and 2-D Architectures

In this section, attention will be focused on the formation of 1-D and 2-D self-organized structures composed of helical polymers. From Section 5.2.1, the proper adsorbate–substrate interaction, which should be neither too weak nor too strong, enables the detection of the topology switching and 2-D self-organization. The control of chain length leads to the construction of various 1-D helical architectures onto surfaces; these have the rigid characteristics of helical polymers, which are unique and advantageous for constructing various hierarchical systems from 1-D to 3-D. In Section 5.2.2, the rigidity of a single polymer chain and the mesoscopic hierarchical helical superstructures in the polysilane aggregates were observed, using AFM. The dominant driving force for the formation of right- and left-handed superhelical structures is based on homochiral weak intermolecular interactions.

Furthermore, it should be noted that a helical polymer chain that is much longer than the persistence length could easily form the entangled structure, consequently leading to the formation of mesoscopic highly ordered superhelical structures. In Section 5.2.3, in addition to adsorbate–substrate interactions, the interactions of lateral (alkyl side chain) and longitudinal (end-termini of main chain) directions were shown to also be required for 2-D self-organization.

It should be emphasized here that both the polymer–substrate and polymer–polymer interactions can lead to the formation of controllable architectures. Furthermore, these interactions are not exceptionally strong, but they are sufficient to form well-organized structures.

In the following section, as an example of functional 3-D architecture, attention will be focused on a unique optical activity based on a helical conformation, which has potential use for functional materials in the solid state.

### 5.3

#### Helical Polymer-Based Functional Films

Previously, we have described the formation of 1-D and 2-D architectures composed of helical polymers. These well-defined helical, polymer-based supramolecular architectures can be designed and controlled, except for some limitations, and therefore expanding these to the life sciences and/or materials sciences applications based on optical activity remains a major challenge [1b]. As noted above, synthetic helical polymers exhibit many unique phenomena, including chiroptical memory, amplification [38], formation of thermotropic cholesteric liquid crystals [12, 39], molecular chirality recognition [40], and helix–helix (*PM*) transition [30, 32, 41–49]. The *PM* transition phenomenon, which involves the reversible switching between the *P*-(plus, right-handed) and *M*-(minus, left-handed) screw-sense segments along the helical backbone, is especially promising for chiroptical materials [30, 32, 38, 40–49]. The *PM* transition, driven by external stimuli such as temperature [30, 32, 45, 49], photoradiation [46] and additives [40], is currently understood to be one of the general characteristics of helical polymers.

Molecule-based chiroptical properties, such as memory and the helicity switch using the *PM* transition phenomenon in helical polymers, will be useful for data storage, optical devices, chromatographic chiral separation and liquid crystals for display [50]. In addition to memory and the helicity switch using the *PM* transition phenomenon, chirality transfer and/or amplification in polymer systems have also been studied extensively in aggregates, while the complexation of achiral polymers with chiral additives has been investigated in solution systems [40], 51, 52].

In this section, attention is focused on the fabrication of helical polymer-based solid films as supramolecular assemblies that possess functionality based on chiroptical properties, such as switch [30, 53], memory [30], transfer, and amplification [54]. A focus on these chiroptical properties, either in bulk thin film or in a polymer matrix, is required from a practical viewpoint [48, 55]. In the present system, a temperature control is used as the “trigger” to realize the memory,

switch, and chirality transfer/amplification. Those chiroptical properties can be detected by using circular polarized light (CPL), which is able to distinguish between right- or left-handed polarity (helicity), thus highlighting their potential application as circular polarization recording/erasing systems.

### 5.3.1

#### Chiroptical Memory and Switch in Helical Polysilane Films

The *PM* transition phenomenon in helical polymer films is primarily applied for molecular-based chiroptical memory and switches. In general, there are two types of memorizing system which function by means of a *PM* transition phenomenon in the solid state. One system is in the Re-Writable (RW) mode, while the other is in the Write-Once Read-Many (WORM) mode. In the RW mode, the right- or left-handed helicity can be erased when data are renewed. In contrast, in the WORM mode the right- or left-handed helicity is immobilized once for the storage of data, and these are then read (detected) using CPL.

The basic requirement for a switching system is the bistable state of a molecule, which can be assigned as either the chiroptical inversion “-1 and +1” switch through the helix–helix (*PM*) transition or the on-off “0 and +1” switch through the helix–coil transition. Normally, these chiroptical properties can be characterized by using circular dichroism (CD). The conformational transition temperature ( $T_c$ ), such as for the helix–helix or helix–coil transition, is the critical factor when designing the chiroptical memory and switch in the solid state. Since below  $T_c$  the segmental motion of the polymer chain is frozen, polymers having relatively low  $T_c$  values may represent good candidates for practical application.

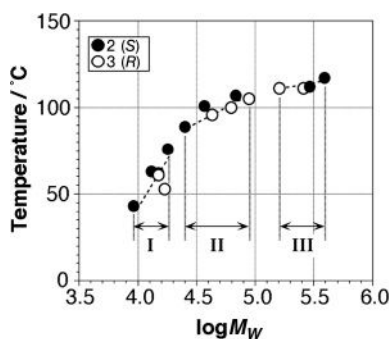
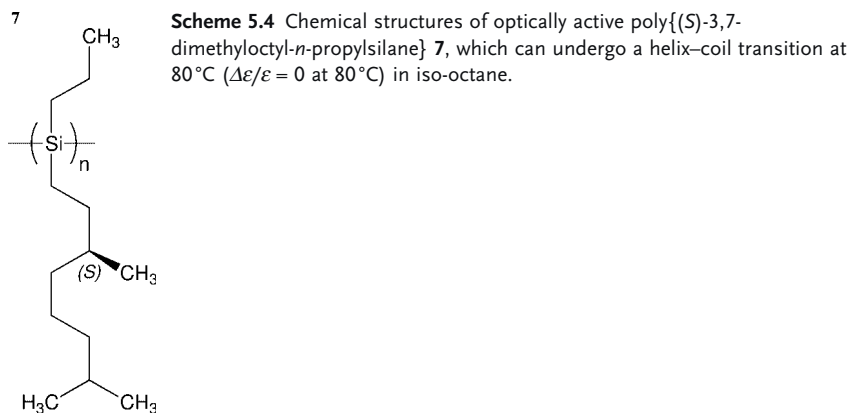
Polysilanes possessing relevant enantiopure chiral side chains will be successful candidates for chiroptical memory and switches at the molecular level. Furthermore, the  $T_c$  of polysilanes in the solid state can easily be designed by adjusting the molecular mass.

In this section, we present some examples of easy, versatile approaches for chiroptical memory with RW and WORM modes, and chiroptical switches based on the inversion “-1” and “+1” and on-off “0” and “+1” switch in solid films. Certain polysilanes, including poly{(*S*)-3,7-dimethyloctyl-3-methylpentylsilane} (**2**) and poly{(*S*)-3,7-dimethyloctyl-*n*-propylsilane} (**7**), were used, each of which can undergo helix–helix or helix–coil transitions at a certain temperature in dilute solution states by controlling their molecular mass and/or thermal modulation (Scheme 5.4).

##### 5.3.1.1 Memory with Re-Writable Mode and Inversion “-1” and “+1” Switch

Polymers **2** and **3** exhibited a strong molecular mass dependence on the phase transition temperature  $T_c$  (estimated using differential scanning calorimetry; DSC) due to the *PM* transition, as shown in Figure 5.14. The enthalpy change ( $\Delta H$ ) estimated from the heating was only approximately  $0.05 \text{ kcal mol}^{-1}$  per repeat unit [15a]. Given that the helix–helix transition of polysilane is caused by the order–disorder transition of side chain groups in solution, the entropy gain based on the





**Figure 5.14** Change of transition temperature ( $T_c$ ) estimated from DSC thermograms as a function of logarithmic function of molecular mass. Filled and open circles indicate **2** and **3**, respectively. Regions I, II, and III indicate reversible, irreversible, and no change of CD signals for the cast films in the heating and cooling process, respectively.

order-disorder transition of side chains could easily overcome the tiny amount of enthalpy, thus paving the way for the induction of a helix-coil transition, even in the solid state.

For the cast film of **2** onto quartz substrate comprising the low-molecular-mass fraction ( $M_w$ :  $1.3 \times 10^4$ ,  $M_w/M_n$ : 1.16, corresponding to region I in Figure 5.14), a typical bisignate CD signal based on exciton coupling was clearly observed, and seen reversibly to switch between almost mirror-imaged CD spectra in the heating-cooling cycles (see Figure 5.15).

In this case,  $T_c$  was approximately 47°C, which was estimated from the temperature dependence of Kuhn's dissymmetry ratio ( $g_{solid} = \Delta OD/OD$ ), where  $OD$  is the optical density of the UV absorbance at  $\lambda_{max}$  and  $\Delta OD/OD$  is defined as  $2(OD_L - OD_R)/(OD_L + OD_R)$  of the CD intensity at the extremum ( $\lambda_{ext}$ ) of the first Cotton band, as shown in Figure 5.16. The transition temperature estimated from CD almost corresponded to that estimated by DSC.

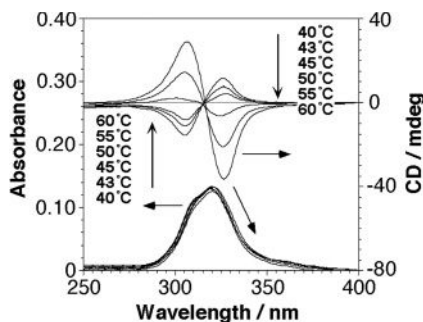


Figure 5.15 Ultraviolet (UV) and CD spectra of the solid film of **2** in the heating process.

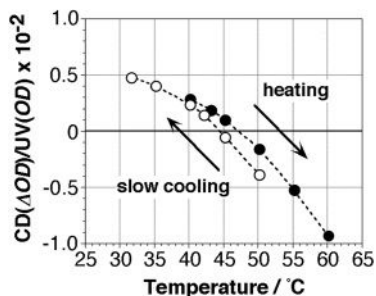
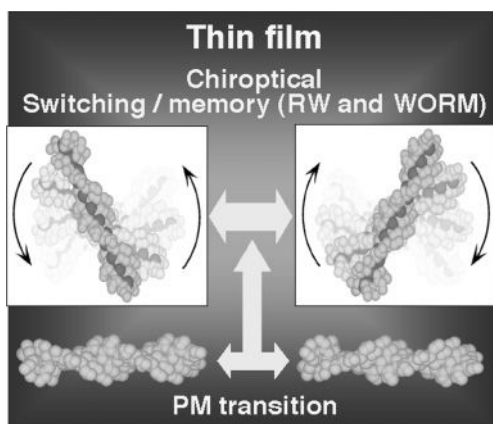


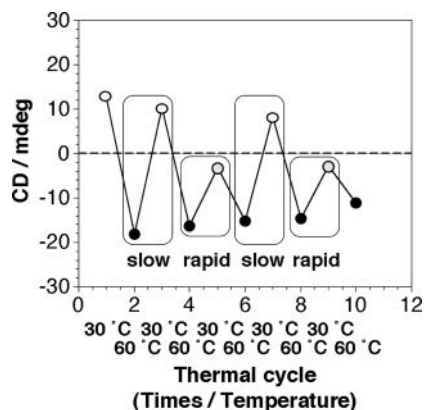
Figure 5.16 Temperature dependence of relative Kuhn's dissymmetry ratios  $\Delta OD/OD$  for the cast film of **2** in the heating (●) and cooling (○) processes.  $M_w = 1.3 \times 10^4$ ,  $M_w/M_n = 1.16$ . The heating rate was  $20^\circ\text{C min}^{-1}$ , and the cooling rate  $2^\circ\text{C min}^{-1}$ .

In this case, the phase transition temperature in the film state seemed to be approximately  $60^\circ\text{C}$  higher than the *PM* transition temperature in iso-octane. A higher transition energy might be required to induce the phase transition in the solid state, and therefore the phase transition would originate from a macroscopic geometric change, such as a twisted superhelical structure, among the polymeric backbones based on exciton coupling in the films [1b, 56]. The reversible switch occurs between the *laevo* and *dextro* helical polymer shapes, which is followed by changes in the helical supramolecular geometry, as observed in the CD spectrum and illustrated in Figure 5.17. The molecular mass control alone is sufficient to change the transition temperature of **2** in region I of Figure 5.14. Moreover, the chiroptical property of the inversion “-1” and “+1” switch can make it possible to obtain chiroptical memory with RW mode.

Chiroptical memory with RW mode can be achieved by controlling the cooling rate of the film with a low molecular mass. Figure 5.18 shows the multiple thermal cycle responses of the CD intensities at the extrema for the cast film of **2**. Cycling



**Figure 5.17** Schematic representation of helical supramolecular geometry switch on the basis of the helix–helix transition of **2**.



**Figure 5.18** Thermal cycle responses of extrema of CD intensities for the solid film of **3**. Thermal cycles were conducted by heating to 60 °C (●) and followed by slow (○) or rapid (shaded circle) cooling to 30 °C. Rapid

cooling was achieved by dipping the film into the ice water. The heating rate was 20 °C min<sup>-1</sup>, and the slow cooling rate 2 °C min<sup>-1</sup>.  $M_w = 1.3 \times 10^4$ ,  $M_w/M_n = 1.16$ .

was conducted between by heating above the  $T_c$  and by slow cooling or rapid quenching below the  $T_c$ . In the slow cooling process, the sign of the CD signal changed, indicating a chiroptical inversion “–1” and “+1” switch. On the other hand, a chiroptical memory with RW mode occurred during the rapid quenching from above the  $T_c$ . However, the sign of the CD signal did not change during the rapid quenching. This memory effect was resettable by heating to above the  $T_c$ . The chiroptical inversion “–1” and “+1” switch and chiroptical memory with RW mode are feasible by controlling both the cooling conditions in the solid film and the molecular mass of **2**.

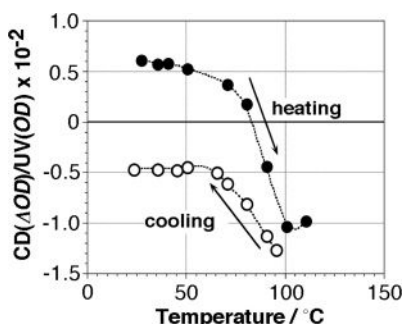
### 5.3.1.2 Memory with Write-Once Read-Many (WORM) Mode

Another memory state, the WORM mode, can be achieved by controlling the molecular mass only, although in this case the management of cooling conditions is not required. With regards to the cast films in region II in Figure 5.14, the phase transition was seen only on heating, and the state above the  $T_c$  remained unchanged during the cooling process. This irreversible transition behavior can be confirmed by the  $g_{solid}$ -value (defined as  $\Delta OD/OD$ ), as shown in Figure 5.19. This irreversible change in the CD signal indicates the nonerasable memory as the WORM mode. It should be noted that the transition temperature of the WORM mode in region II of Figure 5.14 is also adjustable by controlling the molecular mass.

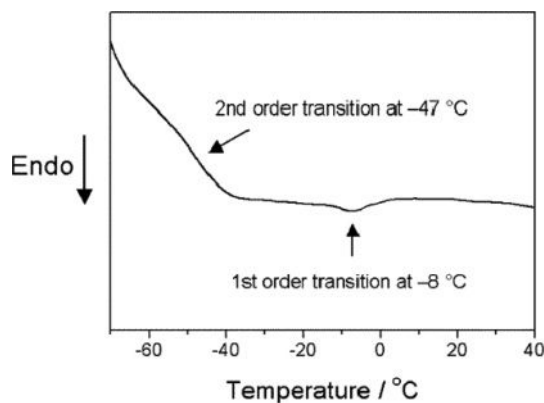
The dynamic chiroptical properties of polysilanes in the solid state, such as inversion switching and memory with RW and WORM modes, can be managed by a combination of molecular mass control and thermal modulation.

### 5.3.1.3 On-Off “0” and “+1” Switch Based on Helix–Coil Transition

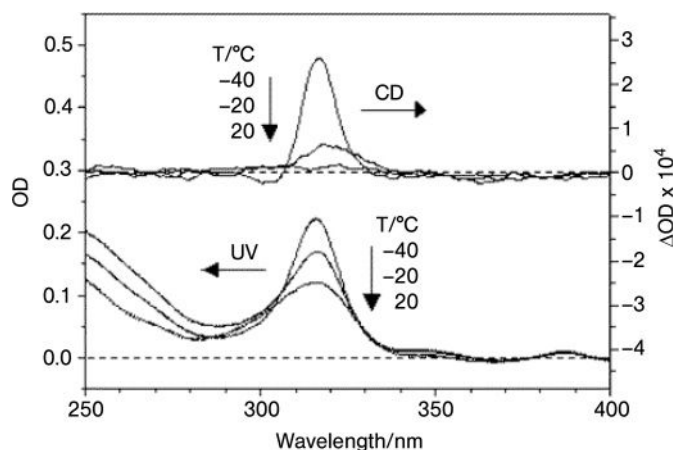
As noted above, the basic requirement for a switching system is the bistable state of a molecule, which can be rapidly interconverted by an external stimulus, even in the solid state. In addition to the achievement of a chiroptical inversion “–1 and +1” switch in polymer **2** and **3** solid films by means of molecular mass control and thermal modulation, an on-off “0 and +1” switch, based on changes in the magnitude of the helicity in polymer **7** film, can also be achieved by thermal modulation. The DSC thermogram of **7** displayed a second-order transition at  $-47^\circ\text{C}$  and a first-order transition at  $-8^\circ\text{C}$  corresponding to the glass and helix–coil transitions, respectively, as shown in Figure 5.20. The heat flow ( $\Delta H$  is  $\sim 0.004\text{kcal mol}^{-1}$  per repeat unit) for the helix–coil transition in **7** was relatively small, with only weak van der Waals interactions likely to permit the helix–coil transition, even in the solid state (this is the same as the previously discussed case in Section 5.3.1.1).



**Figure 5.19** Temperature dependence of relative Kuhn's dissymmetry ratios  $\Delta OD/OD$  for the cast film of **2** in the heating (●) and cooling (○) processes.  $M_w = 2.5 \times 10^4$ ,  $M_w/M_n = 1.25$ .



**Figure 5.20** DSC thermogram of **7** obtained on second heating with a heating rate of  $10^{\circ}\text{Cmin}^{-1}$ .



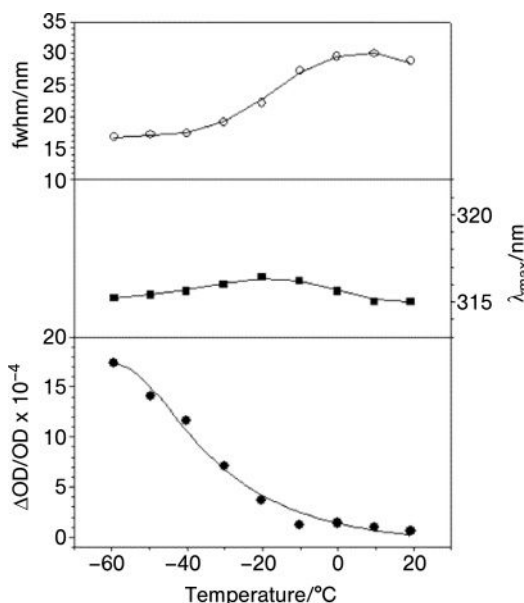
**Figure 5.21** Ultraviolet (UV) and CD spectra of the solid film of **7**.  $M_w = 330\,000$ ,  $M_w/M_n = 1.87$ .

Figure 5.21 shows the UV and CD spectra of the **7** film cast from iso-octane onto a quartz substrate. Although there was no detectable CD absorption at  $20^{\circ}\text{C}$ , **7** showed a strong Cotton effect at  $-40^{\circ}\text{C}$ , indicating a coil-to-helix transition of **7** in the solid state with decreasing temperature. This transition can be well correlated with DSC results. The positive Cotton effect could result from a single polymer chain because of the similarity between the UV and CD absorption profiles. Furthermore, no bisignate CD signal attributable to exciton coupling was observed, even at  $-60^{\circ}\text{C}$ , which is completely different from the cases of the previous Sections 5.3.1.1 and 5.3.1.2. Although **7** showed a strong Cotton effect at low temperatures both in solution and in the solid state, the global conformations of polymer chains in both states may be significantly different. Due to the excluded

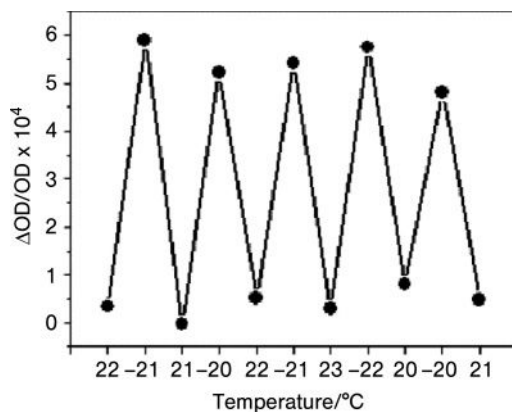
volume of other chains and the chain entanglements, the entire conformation of the polymer chains in the solid state would be difficult to change with decreasing temperature, even above their glass transition temperature ( $T_g$ ). These results clearly indicate that the macroscopic geometric changes in the inversion “-1” and “+1” switch and the on-off “0” and “+1” switch are different.

The helix-coil transition in the thin solid film can be explained by some parameters, such as  $fwhm$ ,  $\lambda_{max}$  and  $\Delta OD/OD$ , as shown in Figure 5.22. The  $fwhm$  of the UV absorption band became narrower when the temperature decreased from 20 to  $-40^\circ\text{C}$  and remained constant below  $-40^\circ\text{C}$  (around  $T_g$ ), indicating that the homogeneity of the polymer backbone was induced due to the decreasing degree of freedom in the Si-Si bond rotations. The  $\lambda_{max}$  shifted slightly to a longer wavelength with decreasing temperature from 20 to  $-20^\circ\text{C}$ , and shifted to a shorter wavelength below  $-20^\circ\text{C}$ . It is likely that the chiroptical property in the solid state would be induced through the movement and/or disappearance of the helical reversal within the localized segments, which is in stark contrast to that of the solution state.

Figure 5.23 shows the multiple thermal cycle responses of  $\Delta OD/OD$  in the range from  $-20$  to  $20^\circ\text{C}$ . The intensity changed during heating and cooling, indicating a switching property. The helix-coil transition in the solid state is highly reversible, can be applicable to the on-off switching system, and is assigned as “0 and +1”.



**Figure 5.22** Temperature dependence of relative Kuhn's dissymmetry ratios  $\Delta OD/OD$ ,  $\lambda_{max}$ , and  $fwhm$  of the solid film of **7**.  $M_w = 330000$ ,  $M_w/M_n = 1.87$ .



**Figure 5.23** Thermal cycle responses of relative Kuhn's dissymmetry ratios  $\Delta OD/OD$  of the solid film of **7**. Thermal cycles were conducted by heating to 20°C, followed by cooling to -20°C.

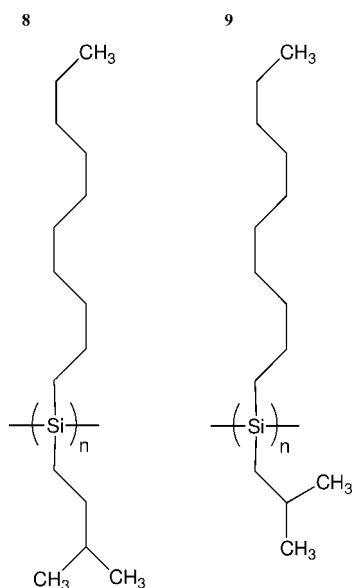
### 5.3.2

#### Chiroptical Transfer and Amplification in Binary Helical Polysilane Films

In addition to controlling the chiroptical properties such as memory and switch, chiroptical transfer and amplification have also been achieved based on the concept of the “sergeants and soldiers” principle [57] in binary helical polysilane films.

Optically active poly(*n*-decyl-(*S*)-2-methylbutylsilane} (as “sergeants”, **5**:  $M_w = 2.11 \times 10^5$ ,  $M_w/M_n = 1.77$ ) with an almost  $7_3$  helix and optically inactive poly(*n*-decyl-3-methylbutyl-silane) (as “soldiers”, **8**:  $M_w = 1.11 \times 10^5$ ,  $M_w/M_n = 1.75$ ) and poly(*n*-decyl-*i*-butylsilane) (as “soldiers”, **9**:  $M_w = 3.36 \times 10^4$ ,  $M_w/M_n = 1.17$ ) were used for this study, as shown in Scheme 5.5. Polymers **8** and **9** have equal populations of right and left  $7_3$  helices; however, the rigidities of **5**, **8**, and **9** are different. The polymers **5** and **9**, with  $\beta$ -branching methyl groups in the side chains, were classified into rigid rod-like polymers with a persistent length of about 70 nm, while **8** belonged to a semi-rigid polymer with a persistent length of only 6 nm [31].

The CD spectra of a grafted 5-spin-coated **8** bilayer system prepared on quartz substrate were measured before and after annealing, as shown in Figure 5.24. The CD spectra of both the grafted 5-spin-coated **8** bilayer system and a grafted **5** system alone showed a bisignate CD signal with a positive Cotton band at about 309 nm and a negative Cotton band at about 324 nm, as shown in Figure 5.24. For the grafted 5-spin-coated **8** bilayer system, both positive- and negative-Cotton CD intensity were greatly increased after thermal annealing. The enhancement in the CD signal intensities was a result of a chiroptical transfer to spin-coated **8** either from the chiral side chain of grafted **5** or the polymer backbone itself, and it was drastically amplified after annealing. On the other hand, no significant changes

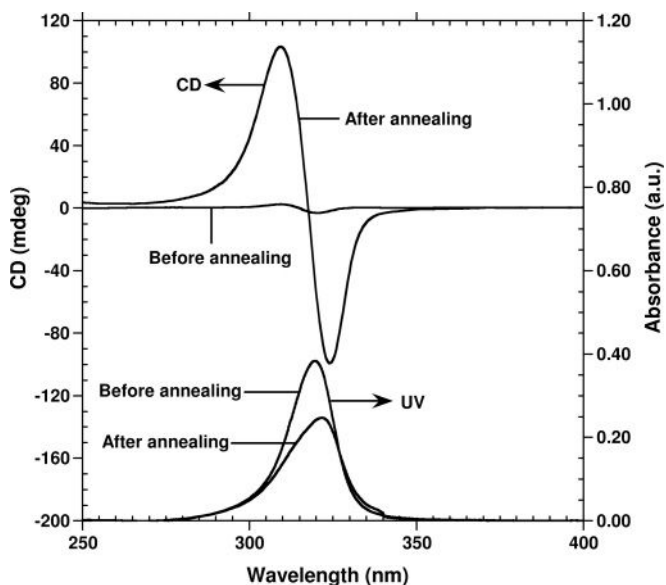


**Scheme 5.5** Chemical structures of optically inactive poly(*n*-decyl-3-methylbutylsilane) (as “soldiers”, **8**) and poly(*n*-decyl-*i*-butylsilane) (as “soldiers”, **9**).

of CD signal intensities were observed for only immobilized grafted **5** after annealing. In Figure 5.24, a decrease of the UV absorbance of the grafted **5**-spin-coated **8** bilayer system was observed after the annealing treatment. This result implies that most of the polymer chains lie down before annealing in the quartz substrate plane, as the film was prepared by a spin-coating technique. The thermal annealing treatment may impact some of the polymer chain segments of semi-rigid spin-coated **8** in the perpendicular orientation and/or tilt of the substrate plane, leading to the decrease of the apparent UV absorbance at 321 nm, as illustrated in Figure 5.25 [58].

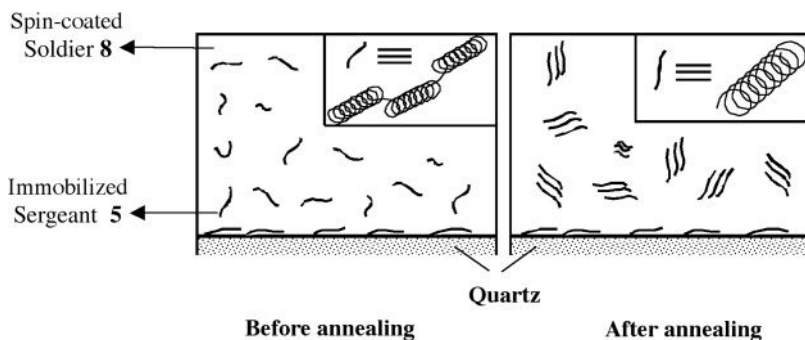
Figure 5.26 shows the change in the relative Kuhn’s dissymmetry ratios ( $g_{\text{solid}} = \Delta OD/OD$ ), after ( $g_{\text{AA}}$ ) and before ( $g_{\text{BA}}$ ) annealing with the varied film thickness. As was evident, the ratios increased with the decrease in the thickness of **8**. The magnitude of the  $g_{\text{AA}}/g_{\text{BA}}$  value was found to be significantly higher in grafted **5** (filled squares) than in spin-coated **5** (filled circles), presumably due to the partial penetration of spin-coated **5** polymer chains into the surface during the spin-coating process of **8**, leading to the similar solvent solubility behaviors of **5** and **8**. A tiny amount of immobilized, optically active **5** could induce and effectively amplify the optical activity in the optically inactive **8** layer by thermal treatment. Weak van der Waals interactions at the surface between these two polymers might be responsible for the transfer and amplification of the optical activity in **8**. The positional segmental movement of polymer chains in **8** (melting point 40°C, as estimated by DSC) would easily occur, which would be responsible for the helical





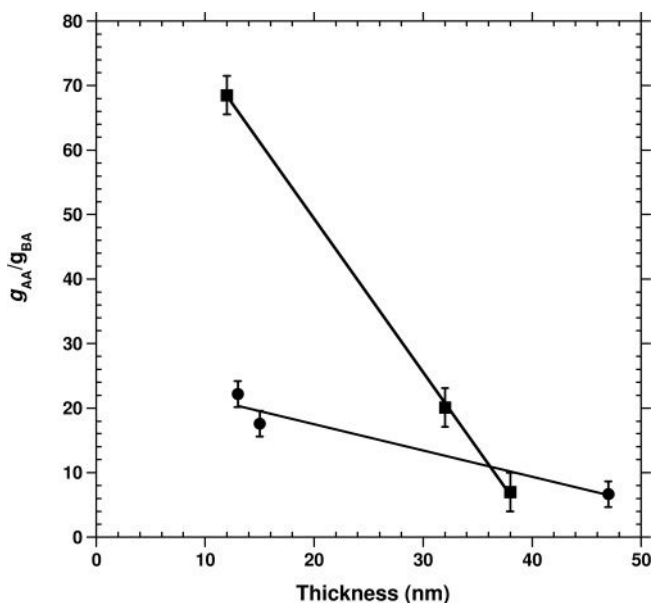
**Figure 5.24** Circular dichroism (CD) and UV spectra of grafted 5-spin-coated 8 bilayer system onto quartz substrate before and after annealing. The initial UV absorbance of 8 was 0.04, and total UV absorbance of grafted

5-spin-coated 8 bilayer system was 0.39. In this case, the spectra do not significantly affect the spectral intensity with rotation of the solid films at different angles.



**Figure 5.25** Schematic representation of thermo-driven chiroptical transfer and amplification in the “soldier” optically inactive polysilane 8 from the “sergeant” optically active helical polysilane 5 on quartz.

transfer from 5 to 8 in the solid film. This could be regarded as a “sergeants and soldiers” system in the solid state. In the case of the 5-spin-coated 9 bilayer system, the optical activity transfer phenomenon was not seen, due to the higher transition energy barrier (no transition was observed by DSC) originating from the rigid rod-like conformation by the help of  $\beta$ -branched side chain.



**Figure 5.26** Relative Kuhn's dissymmetry ratios  $\Delta OD/OD$  of a grafted **8**-spin-coated **9** bilayer system (■) and spin-coated **8**-spin-coated **9** (●) on a quartz surface before ( $g_{BA}$ ) and after ( $g_{AA}$ ) annealing, as a function of the film thickness.

### 5.3.3

#### Summary of Helical Polymer-Based Functional Films

In this section, attention is focused on the fabrication of helical polymer-based solid films as supramolecular assemblies that possess functionality based on chiroptical properties, such as switch, memory, transfer, and amplification. In Section 5.3.1, simple molecular mass control and thermal modulation were shown to be capable of realizing various chiroptical properties, such as the inversion “−1” and “+1” switch and memory with RW and WORM modes. Furthermore, different types of polysilane were used to construct on-off “0” and “+1” switching. For practical use of those systems, without the threat of polymer degradation by UV light for example, a laser-assisted heat-mode RW system which is based on a dye dispersed in the switchable polysilanes may be feasible, provided that the applied wavelengths of the dye and laser are much longer than those of the polysilanes. A high-power, circularly polarized laser-diode would be effective to directly heat the dye, leading to an indirect heating of the polysilane film above the  $T_c$ . Controlling the cooling rate of the film would enable the switching or memorizing of the chiroptical state above the  $T_c$ . In order to access data from the polysilane film, a controlled modulation of the laser to the dye, including the power, pulse irradiation time, and periods, would be effective to erase with a heat mode and to read with a photon mode.

In Section 5.3.2, the optical activity of rigid rod-like polysilane was discussed, both in terms of grafted and spin-coated films, with a preferential helical sense, which was transferred and greatly amplified to an optically inactive semi-rigid, helical spin-coated polysilane layer at the solid surface by thermal annealing. Selection of the correct rigidity of the optically inactive helical polysilane was important for the emergence of a helical polymer command surface of the “sergeants and soldiers” type, a chiroptical amplification system in the solid film states.

It should be emphasized here that the weak van der Waals interactions between polymers are key to the assembly of various chiroptical systems that possess switch, memory, transfer, and amplification properties. Optically active polysilane is unique in natural and synthetic helical polymers, and allows for the possibility of creating a wide variety of supramolecular architectures with a range of chiroptical properties.

### Acknowledgments

The authors thank Professors M. M. Green (Polytechnic University), J. Michl (University of Colorado), R. West (University of Wisconsin), K. Tamao (Kyoto University), G. Basu (Bose Institute), R. G. Jones (University of Kent), T. M. Swager (Massachusetts Institute of Technology), Y. Kawakami (JAIST), A. Teramoto (Ritsumeikan University), T. Sato (Osaka University), and E. Yashima (Nagoya University) for collaborations and fruitful discussions on the consideration of optical properties of polysilanes in solution and in the solid state. They also thank Professors J. Watanabe and S. Kawauchi of the Tokyo Institute of Technology for collaborations and discussions on the structural properties of poly( $\gamma$ -L-glutamates). Thanks are also extended to T. Hagihara, and F. Asanoma for technical assistance and discussion, and to Doctors T. Imase, S.-Y. Kim, A. Saxena, K. Okoshi, M. Naito, G. Kwak, M. Ishikawa, T. Kawabe, G.-Q. Guo, and Y.-G. Yang for fruitful discussions.

A.O., M.F., and M.K. are supported by grants from CREST-JST, “Syntheses of the Cooperative Hyper Helical Polymers and Understanding of Structure-Property-Functionality Relationship” and “Nanoelectronic-Device Fabrication Based on the Fine Molecular Design.” A.O. is also supported by grants from the Ministry of Economy, Trade and Industry, Japan. M.F. is supported in part by grants from the Ministry of Education, Science, Sports, and Culture of Japan and by a Grant-in-Aid for Scientific Research “Experimental Test of Parity Nonconservation at Helical Polymer Level” (No. 16655046) and “Design, Synthesis, Novel Functionality of Nanocircle and Nanorod Conjugating Macromolecules” (No. 16205017).

## References

- 1 (a) Lehn, J.-M. (1995) *Supramolecular Chemistry*, VCH Verlag GmbH, Weinheim.  
 (b) Green, M.M., Nolte, R.J.M. and Meijer, E.W. (2003) *Materials Chirality: Topics in Stereochemistry*, John Wiley & Sons, Inc., New York.
- 2 (a) Pauling, L. and Corey, R.B. (1953) *Nature*, **4341**, 59.  
 (b) Eyre, D.R. (1980) *Science*, **207**, 1315.  
 (c) Dickerson, R.E., Drew, H.R., Conner, B.N., Wing, R.M., Fratini, A.V. and Kopka, M.L. (1982) *Science*, **216**, 475–485.  
 (d) Watanabe, J. and Ono, H. (1986) *Macromolecules*, **19**, 1079.
- 3 (a) Sommerdijk, N.A.J.M., Lambermon, M.H.L., Feiters, M.C., Nolte, R.J.M. and Zwanenburg, B. (1997) *Chem. Commun.*, 1423.  
 (b) Nakashima, N., Asakuma, S. and Kunitake, T. (1985) *J. Am. Chem. Soc.*, **107**, 509.  
 (c) Sommerdijk, N.A.J.M., Lambermon, M.H.L., Feiters, M.C., Nolte, R.J.M. and Zwanenburg, B. (1997) *Chem. Commun.*, 455.  
 (d) Yanagawa, H., Ogawa, Y., Furuta, H. and Tsuno, K. (1989) *J. Am. Chem. Soc.*, **114**, 3414.  
 (e) Fuhrhop, J.H. and Helfrich, W. (1993) *Chem. Rev.*, **93**, 1565, and references therein.
- 4 Rai, R., Saxena, A., Ohira, A. and Fujiki, M. (2005) *Langmuir*, **21**, 3957.
- 5 (a) Kunitake, T. (1992) *Angew. Chem. Int. Ed. Engl.*, **31**, 709.  
 (b) Fuhrhop, J.H. and Helfrich, W. (1993) *Chem. Rev.*, **93**, 1565.  
 (c) Schunr, J.M. (1993) *Science*, **262**, 1669.  
 (d) Engelkamp, H., Middlebeek, S. and Nolte, R.J.M. (1999) *Science*, **284**, 785.  
 (e) Prins, L.J., Huskens, J., de Jong, F., Timmerman, P. and Reinhoudt, D.N. (1999) *Nature*, **398**, 498.  
 (f) Hirschberg, J.H.K.K., Brunsveld, L., Vekemans, J.A.J.M. and Meijer, E.W. (2000) *Nature*, **407**, 167.  
 (g) Volker, B., Huc, I., Khoury, R.G., Krische, M.J. and Lehn, J.-M. (2000) *Nature*, **407**, 720.  
 (h) Brunsveld, L., Meijer, E.W., Prince, R.B. and Moore, J.S. (2001) *J. Am. Chem. Soc.*, **123**, 7978.  
 (i) Koga, T., Matsuoka, M. and Higashi, N. (2005) *J. Am. Chem. Soc.*, **127**, 17596.  
 (j) Lohr, A., Lysetska, M. and Würthner, F. (2006) *Angew. Chem. Int. Ed. Engl.*, **44**, 5071.  
 (k) Ajayaghosh, A., Varghese, R., Jacob, S. and Vijayakumar, C. (2006) *Angew. Chem. Int. Ed. Engl.*, **45**, 1141.
- 6 (a) Ikeda, Y., Jmshidi, K., Tsuji, H. and Hyon, S.-H. (1987) *Macromolecules*, **20**, 906.  
 (b) Brizzolara, D., Cantow, H.-J., Diederichs, K., Keller, E. and Domb, A.J. (1996) *Macromolecules*, **29**, 191.
- 7 Akagi, K., Piao, G., Kaneko, S., Sakamaki, K., Shirakawa, H. and Kyotani, M. (1998) *Science*, **282**, 1683.
- 8 Cornelissen, J.J.L.M., Fischer, M., Sommerdijk, N.A.J.M. and Nolte, R.J.M. (1998) *Science*, **280**, 1427.
- 9 (a) Maeda, K., Takeyama, Y., Sakajiri, K. and Yashima, E. (2004) *J. Am. Chem. Soc.*, **126**, 16284.  
 (b) Kajitani, T., Okoshi, K., Sakurai, S., Kumaki, J. and Yashima, E. (2006) *J. Am. Chem. Soc.*, **128**, 708.
- 10 Yashima, E., Maeda, K. and Furusho, Y. (2008) *Acc. Chem. Res.*, **41**, 1166 and references therein.
- 11 Kaufman, H.S., Sacher, S., Alfrey, T. and Frakuchen, I. (1948) *J. Am. Chem. Soc.*, **70**, 3147.
- 12 (a) Watanabe, J., Fukuda, Y., Gehani, R. and Uematsu, I. (1984) *Macromolecules*, **17**, 1004.  
 (b) Watanabe, J., Ono, H., Uematsu, I. and Abe, A. (1985) *Macromolecules*, **18**, 2141.  
 (c) Watanabe, J. and Ono, H. (1986) *Macromolecules*, **19**, 1079.  
 (d) Watanabe, J., Goto, M. and Nagase, T. (1987) *Macromolecules*, **20**, 298.  
 (e) Watanabe, J. and Nagase, T. (1987) *Polym. J.*, **19**, 781.  
 (f) Watanabe, J. and Nagase, T. (1987) *Macromolecules*, **21**, 171.
- 13 (a) Miller, R.D. and Michl, J. (1989) *Chem. Rev.*, **89**, 1359.

- (b) Michl, J. and West, R. (2000) In *Silicon-Containing Polymers: The Science and Technology of Their Synthesis and Applications* (eds R.G. Jones, W. Ando and J. Chojnowski), Kluwer, Dordrecht, p. 499.
- 14** (a) Fujiki, M. (1994) *J. Am. Chem. Soc.*, **116**, 6017.  
 (b) Fujiki, M. (1996) *J. Am. Chem. Soc.*, **118**, 7424.  
 (c) Fujiki, M. (2001) *Macromol. Rapid Commun.*, **22**, 539.  
 (d) Fujiki, M.J. (2003) *Organomet. Chem.*, **685**, 15.
- 15** (a) Yuan, C.-H. and West, R. (1994) *Macromolecules*, **27**, 629.  
 (b) Frey, H., Möller, M., Turetskii, A., Lotz, B. and Matyjaszewski, K. (1995) *Macromolecules*, **28**, 5498.  
 (c) Terao, K., Terao, Y., Teramoto, A., Nakamura, N., Terakawa, I., Sato, T. and Fujiki, M. (2001) *Macromolecules*, **34**, 2682.  
 (d) Terao, K., Terao, Y., Teramoto, A., Nakamura, N., Fujiki, M. and Sato, T. (2001) *Macromolecules*, **34**, 4519.  
 (e) Teramoto, A., Terao, K., Terao, Y., Nakamura, N., Sato, T. and Fujiki, M. (2001) *J. Am. Chem. Soc.*, **123**, 12303.  
 (f) Natsume, T., Wu, L., Sato, T., Terao, K., Teramoto, A. and Fujiki, M. (2001) *Macromolecules*, **34**, 7899.
- 16** Sato, T., Terao, K., Teramoto, A. and Fujiki, M. (2003) *Polymer*, **44**, 5477.
- 17** (a) Sheiko, S.S. and Möller, M. (2001) *Chem. Rev.*, **101**, 4099.  
 (b) Brunsveld, L., Folmer, B.J.B., Meijer, E.W. and Sijbesma, R.P. (2001) *Chem. Rev.*, **101**, 4071.  
 (c) Ungar, G. and Zeng, X.-B. (2001) *Chem. Rev.*, **101**, 4157.
- 18** (a) Satrijo, A. and Swager, T.M. (2005) *Macromolecules*, **38**, 4054.  
 (b) Satrijo, A., Meskers, S.C.J. and Swager, T.M. (2006) *J. Am. Chem. Soc.*, **128**, 9030.  
 (c) Thomas, S.W. III, Joly, G.D. and Swager, T.M. (2007) *Chem. Rev.*, **107**, 1339.  
 (d) Maeda, K., Morioka, K. and Yashima, E. (2007) *Macromolecules*, **40**, 1349.
- 19** (a) Kanno, T., Tanaka, H., Miyoshi, N. and Kawai, T. (2000) *Jpn. J. Appl. Phys.*, **39**, L269–L270.  
 (b) Hamai, C., Tanaka, H. and Kawai, T. (2000) *J. Phys. Chem.*, **104**, 9894–9897.  
 (c) Hansma, H.G. (2001) *Annu. Rev. Phys. Chem.*, **52**, 71–92.
- 20** (a) Ohnishi, S., Hara, M., Furuno, T. and Sasabe, H. (1996) *Jpn. J. Appl. Phys.*, **35**, 6233.  
 (b) Takeda, S., Ptak, A., Nakamura, C., Miyake, J., Kageshima, M., Jarvis, S.P. and Tokumoto, H. (2001) *Chem. Pharm. Bull.*, **49**, 1512.  
 (c) Imase, T., Ohira, A., Okoshi, K., Sano, N., Kawauchi, S., Watanabe, J. and Kunitake, M. (2003) *Macromolecules*, **36**, 1865–1869.
- 21** (a) Nakajima, K., Ikehara, T. and Nishi, T. (1996) *Carbohydr. Polym.*, **30**, 77.  
 (b) Kibry, A.R., Gunning, A.P. and Morris, V.J. (1996) *Biopolymers*, **38**, 355.  
 (c) Balnois, E., Stoll, S., Wilkinson, K.J., Buffle, J., Rinaudo, M. and Milas, M. (2000) *Macromolecules*, **33**, 7440.  
 (d) Comesano, T.A. and Wilkinson, K.J. (2001) *Biomacromolecules*, **2**, 1184.
- 22** (a) Callroll, D.L., Czerw, R., Teklead, D. and Smith, D.W. Jr. (2000) *Langmuir*, **16**, 3574.  
 (b) Hasegawa, T., Matsuura, K., Ariga, K. and Kobayashi, K. (2000) *Macromolecules*, **33**, 2772.  
 (c) Cornelissen, J.J.L.M., Donners, J.J.J.M., de Gelder, R., Graswinckel, W.S., Metselaar, G.A., Rowan, A.E., Sommerdijk, N.A.J.M. and Nolte, R.J.M. (2001) *Science*, **293**, 676.  
 (d) Nishimura, T., Takatani, K., Sakurai, S., Maeda, K. and Yashima, E. (2002) *Angew. Chem. Int. Ed. Engl.*, **41**, 3602.  
 (e) Samori, P., Ecker, C., Gössl, I., de Witte, P.A.J., Cornelissen, J.J.L.M., Metselaar, G.A., Otten, M.B.J., Rowan, A.E., Nolte, R.J.M. and Rabe, J.P. (2002) *Macromolecules*, **35**, 5290.  
 (f) Li, B.S., Cheuk, K.K.L., Yang, D., Lam, J.W.Y., Wan, L.J., Bai, C. and Tang, B.Z. (2003) *Macromolecules*, **36**, 5447.  
 (g) Kiriya, N., Jähne, E., Adler, H.-J., Schneider, M., Kiriya, A., Gorodyska, G., Minko, S., Jehnichen, D., Simon, P.,

- Fokin, A.A. and Stamm, M. (2003) *Nano Lett.*, **3**, 707.
- (h) Sakurai, S., Kuroyanagi, K., Morino, K., Kunitake, M. and Yashima, E. (2003) *Macromolecules*, **36**, 9670.
- 23** (a) Kumaki, J., Nishikawa, Y. and Hashimoto, T. (1996) *J. Am. Chem. Soc.*, **118**, 3321.
- (b) Ebihara, K., Koshihara, S., Yoshimoto, M., Maeda, T., Ohnishi, T., Koinuma, H. and Fujiki, M. (1997) *Jpn. J. Appl. Phys.*, **36**, L1211.
- 24** (a) Shinohara, K., Yasuda, S., Kato, G., Fujita, M. and Shigekawa, H. (2001) *J. Am. Chem. Soc.*, **123**, 3619.
- (b) Sakurai, S., Okoshi, K., Kumaki, J. and Yashima, E. (2006) *Angew. Chem. Int. Ed. Engl.*, **45**, 1245.
- 25** Ohira, A., Kim, S.-Y., Fujiki, M., Kawakami, Y., Naito, M., Kwak, G. and Saxena, A. (2006) *Chem. Commun.*, 2705.
- 26** Kim, S.-Y., Saxena, A., Kwak, G., Fujiki, M. and Kawakami, Y. (2004) *Chem. Commun.*, 538.
- 27** Sakurai, S., Ohira, A., Suzuki, Y., Fujito, R., Nishimura, T., Kunitake, M. and Yashima, E. (2004) *J. Polym. Sci. A*, **42**, 4621.
- 28** Saxena, A., Okoshi, K., Fujiki, M., Naito, M., Guo, G., Hagihara, T. and Ishikawa, M. (2004) *Macromolecules*, **36**, 367.
- 29** (a) Donley, C.L., Zaumseil, J., Andreasen, J.W., Nielsen, M.M., Sirringhaus, H., Friend, R.H. and Kim, J.-S. (2005) *J. Am. Chem. Soc.*, **127**, 12890.
- (b) Mano, T., Kuroda, T., Sanguinetti, S., Ochiai, T., Tateno, T., Kim, J., Noda, T., Kawabe, M., Sakoda, K., Kido, G. and Koguchi, N. (2005) *Nano Lett.*, **5**, 425.
- 30** (a) Fujiki, M. (2000) *J. Am. Chem. Soc.*, **122**, 3336.
- (b) Fujiki, M., Koe, J.R., Montonaga, M., Nakashima, H., Terao, K. and Teramoto, A. (2001) *J. Am. Chem. Soc.*, **123**, 6253; Addition/Correction, (2001), *J. Am. Chem. Soc.*, **123** (35), 8644.
- 31** Fujiki, M., Koe, J.R., Terao, K., Sato, T., Teramoto, A. and Watanabe, J. (2003) *Polym. J.*, **35**, 297.
- 32** (a) Ohira, A., Okoshi, K., Fujiki, M., Kunitake, M., Naito, M. and Hagihara, T. (2004) *Adv. Mater.*, **16**, 1645.
- (b) Ohira, A., Kunitake, M., Fujiki, M., Naito, M. and Saxena, A. (2004) *Chem. Mater.*, **16**, 3919.
- 33** Shi, W.-X. and Larson, R.G. (2006) *Nano Lett.*, **6**, 144.
- 34** (a) Kühnle, A., Linderoth, T.R., Hammer, B. and Besenbacher, A. (2002) *Nature*, **415**, 891. Recently, two-dimensional crystallization of small chiral organic molecules on the surfaces has attracted much attention in the field of "surface chirality". For example, homochiral enantioselective crystallization from racemic mixture has been reported. Kühnle and coworkers have demonstrated that cysteine molecules formed homochiral pairs (D-D and L-L) from racemic mixture by using scanning tunneling microscopy (STM).
- (b) Fasel, R., Parschau, M. and Ernst, K.-H. (2003) *Angew. Chem. Int. Ed. Engl.*, **42**, 5178. Chiral transfer from single molecules into self-assembled monolayers on the metal surfaces has been reported by Fasel and coworkers. In that case, enantiopure *P* and *M* chiral single molecules on the surfaces formed the enantiopure self-assembled monolayers with clockwise and anticlockwise, respectively.
- (c) Fasel, R., Parschau, M. and Ernst, K.-H. (2006) *Nature*, **439**, 449. In addition to the enantiopure self-assembly, these authors have more recently reported that the enhancement of chiral interactions in two dimensions was observed in the enantioseparation of chiral molecules by STM study. These results also suggested that homochiral intermolecular interaction is an important factor to form the 2-D chiral surfaces.
- 35** (a) Percec, P., Ahn, C.-H., Ungar, G., Yeardley, D.J.P., Moeller, M. and Sheiko, S.S. (1998) *Nature*, **391**, 161–164.
- (b) Percec, V., Holerca, M.N., Magonov, S.N., Yeardley, D.J.P., Ungar, G., Duan, H. and Hudson, S.D. (2001) *Biomacromolecules*, **2**, 706–728.
- 36** Yin, S., Wang, C., Qiu, X., Xu, B. and Bai, C. (2001) *Surf. Interface Anal.*, **32**, 248.
- 37** Rabe, J.P. and Buchholz, S. (1991) *Science*, **253**, 424.
- 38** (a) Mayer, S., Maxein, G. and Zentel, R. (1998) *Macromolecules*, **31**, 8522.

- (b) Langeveld-Voss, B.M.W., Janssen, R.A.J. and Meijer, E.W. (2000) *J. Mol. Struct.*, **521**, 285.
- (c) Nagai, K., Maeda, K., Takeyama, Y., Sakajiri, K. and Yashima, E. (2005) *Macromolecules*, **38**, 5444.
- (d) Ousaka, N., Inai, Y. and Kuroda, R. (2008) *J. Am. Chem. Soc.*, **130**, 12266.
- 39** Okoshi, K., Kamee, H., Suzaki, G., Tokita, M., Fujiki, M. and Watanabe, J. (2002) *Macromolecules*, **35**, 4556.
- 40** (a) Yashima, E., Matsushima, T. and Okamoto, Y. (1995) *J. Am. Chem. Soc.*, **117**, 11596.
- (b) Yashima, E., Nimura, T., Matsushima, T. and Okamoto, Y. (1996) *J. Am. Chem. Soc.*, **118**, 9800.
- (c) Yashima, E., Matsushima, T. and Okamoto, Y. (1997) *J. Am. Chem. Soc.*, **119**, 6345.
- (d) Yashima, E., Maeda, K. and Okamoto, Y. (1998) *J. Am. Chem. Soc.*, **120**, 8895.
- (e) Yashima, E., Maeda, K. and Okamoto, Y. (1999) *Nature*, **399**, 449.
- (f) Nakako, H., Mayahara, Y., Nomura, R., Tabata, M. and Masuda, T. (2000) *Macromolecules*, **33**, 3978.
- (g) Nakako, H., Nomura, R. and Masuda, T. (2001) *Macromolecules*, **34**, 1496.
- (h) Maeda, K., Goto, H. and Yashima, E. (2001) *Macromolecules*, **34**, 1160.
- (i) Onouchi, H., Maeda, K. and Yashima, E. (2001) *J. Am. Chem. Soc.*, **123**, 7441.
- (j) Yashima, E., Maeda, K. and Sato, O. (2001) *J. Am. Chem. Soc.*, **123**, 8159.
- (k) Kumaki, J., Kawachi, T., Ute, K., Kitayama, T. and Yashima, E. (2008) *J. Am. Chem. Soc.*, **130**, 6373.
- (l) Nishino, T. and Umezawa, Y. (2008) *Anal. Chem.*, **80**, 6968.
- 41** (a) Pohl, F.M. and Jovin, T.M. (1972) *J. Mol. Biol.*, **67**, 375.
- (b) Pohl, F.M. (1976) *Nature*, **260**, 365.
- (c) Pohl, F.M., Thomae, R. and DiCapua, E. (1982) *Nature*, **300**, 545.
- 42** Toriumi, H., Saso, N., Yasumoto, Y., Sasaki, S. and Uematsu, I. (1979) *Polym. J.*, **11**, 977.
- 43** (a) Maeda, K. and Okamoto, Y. (1998) *Macromolecules*, **31**, 5164.
- (b) Maeda, K. and Okamoto, Y. (1999) *Macromolecules*, **32**, 974.
- 44** (a) Cheon, K.S., Selinger, J.V. and Green, M.M. (2000) *Angew. Chem. Int. Ed. Engl.*, **39**, 1482.
- (b) Tang, K., Green, M.M., Cheon, K.S., Selinger, J.V. and Garetz, B.A. (2003) *J. Am. Chem. Soc.*, **125**, 7313.
- 45** Schenning, A.P.H.J., Franssen, M. and Meijer, E.W. (2002) *Macromol. Rapid Commun.*, **23**, 265.
- 46** Maxein, G. and Zentel, R. (1995) *Macromolecules*, **28**, 8438.
- 47** Nakashima, H., Fujiki, M., Koe, J.R. and Motonaga, M. (2001) *J. Am. Chem. Soc.*, **123**, 1963.
- 48** Watanabe, J., Okamoto, S., Satoh, K., Sakajiri, K., Furuya, H. and Abe, A. (1996) *Macromolecules*, **29**, 7084.
- 49** (a) Koe, J.R., Fujiki, M., Nakashima, H. and Motonaga, M. (2000) *Chem. Commun.*, 389.
- (b) Fujiki, M. (2001) *Macromol. Rapid Commun.*, **22**, 539.
- (c) Fujiki, M., Tang, H.-Z., Motonaga, M., Torimitsu, K., Koe, J.R., Watanabe, J., Sato, T. and Teramoto, A. (2002) *Silicon Chem.*, **1**, 67.
- 50** Feringa, B.L., van Delden, R.A., Koumura, N. and Geertsema, E.M. (2000) *Chem. Rev.*, **100**, 1789.
- 51** (a) Okamoto, Y. and Nakano, T. (2001) *Chem. Rev.*, **101**, 4013.
- (b) Cornelissen, J.J.L.M., Rowan, A.E., Nolte, R.J.M. and Sommerdijk, N.A.J.M. (2001) *Chem. Rev.*, **101**, 4039.
- 52** (a) Aoki, T., Kaneko, T., Maruyama, N., Sumi, A., Takahashi, M., Sato, T. and Teraguchi, M. (2003) *J. Am. Chem. Soc.*, **125**, 6346.
- (b) Nakano, T., Nakagawa, O., Tsuji, M., Tanikawa, M., Yade, T. and Okamoto, Y. (2004) *Chem. Commun.*, 144.
- 53** Kim, S.-Y., Fujiki, M., Ohira, A., Kwak, G. and Kawakami, Y. (2004) *Macromolecules*, **37**, 4321.
- 54** Saxena, A., Guo, G., Fujiki, M., Yang, Y., Ohira, A., Okoshi, K. and Naito, M. (2004) *Macromolecules*, **37**, 3081.
- 55** (a) Muellers, B.T., Park, J.-W., Brookhart, M.S. and Green, M.M. (2001) *Macromolecules*, **34**, 527.
- (b) Mayer, S. and Zentel, R. (2000)

- Macromol. Rapid Commun.*, **21**, 927.
- (c) Catellani, M., Luzzati, S., Bertini, F., Bolognesi, A., Lebon, F., Longhi, G., Abbate, S., Famulari, A. and Meille, S.V. (2002) *Chem. Mater.*, **14**, 4819.
- (d) Roux, C. and Leclere, M. (1992) *Macromolecules*, **25**, 2141.
- 56** Nakanishi, K. and Berova, N. (1994) in *Circular Dichroism: Principles and Applications*, Chapters 5 and 13 (eds K. Nakanishi, N. Berova and R.W. Woody), John Wiley & Sons, Inc., New York.
- 57** (a) Green, M.M., Reidy, M.P., Johnson, R.D., Darling, G., O'Leary, D.J. and Willson, G. (1989) *J. Am. Chem. Soc.*, **111**, 6452.
- (b) Green, M.M., Park, J.-W., Sato, T., Teramoto, A., Lifson, S., Selinger, R.L.B. and Selinger, J.V. (1999) *Angew. Chem. Int. Ed. Engl.*, **38**, 3138.
- 58** (a) Fukuda, K., Seki, T. and Ichimura, K. (2002) *Macromolecules*, **35**, 2177.
- (b) Ichimura, K. (2000) *Chem. Rev.*, **100**, 1847.



## 6 Synthesis of Inorganic Nanotubes

*C.N.R. Rao and Achutharao Govindaraj*

### 6.1 Introduction

Zero-dimensional nanoparticles and one-dimensional (1D) nanowires and nanotubes are important classes of nanomaterials [1, 2]. The first family of nanotubes is that of carbon nanotubes described by Iijima [3]. Nanotubes are, however, no longer confined to carbon but encompass a variety of inorganic materials [4, 5], and peptides [6]. In this article, our concern is with nanotubes of inorganic materials excluding carbon.

The early examples of inorganic nanotubes synthesized in the laboratory are those of molybdenum and tungsten sulfides by Tenne and coworkers [7]. These layered sulfides form fullerene-type structures and hence also nanotubes. Several methods to prepare nanotubes of Mo and W sulfides and of the analogous selenides have been reported in the last few years [1, 2]. The synthesis of BN nanotubes has also received considerable attention because of the similarity of the structure of BN to graphite. In the last few years, nanotubes of several inorganic materials including binary oxides, nitrides, halides as well as metals and non-metallic elemental materials have been prepared and characterized [1, 2, 4, 5]. Besides nanotubes of binary compounds, those of complex materials such as perovskite titanates and spinels have also been reported. Composites that involve nanotubes, nanowires, and nanoparticles are also known. In this article, we shall provide a status report on the synthesis of inorganic nanotubes. In doing so, we shall cover the synthetic strategies employed for the different classes of inorganic nanotubes. In view of the vast literature that has emerged in the last 2–3 years, we were unable to cite all the papers in this area and have restricted ourselves to representative ones. We apologize for any oversight or error in judgement.

## 6.2

### General Synthetic Strategies

Several strategies have been employed for the synthesis of inorganic nanotubes. In the case of molybdenum and tungsten sulfides and such layered chalcogenides, decomposition of precursor compounds such as the trisulfides (e.g.,  $\text{MoS}_3$  or  $\text{WS}_3$ ) and ammonium thiometallate or selenometallate has been successful. An important method, used particularly in the case of oxide nanotubes, is the hydrothermal and solvothermal route, carried out in the presence of surfactants or other additives in certain instances. Electric arcing and laser ablation have been used to synthesize nanotubes of BN and other materials. Sol-gel chemistry is useful for the synthesis of nanotubes, especially of oxides. Chemical vapor deposition (CVD) is commonly used for the synthesis of some of the nanotubes.

A popular method of synthesis in the last few years has employed templates. The templates can be porous membranes of alumina or polycarbonate. The pores are used to deposit the relevant materials or these precursors, followed by annealing and removal of the template. Deposition of the material in the porous channels is carried out by the sol-gel method or by an electrochemical procedure. Electrochemical anodization is commonly used for the synthesis of nanotubes of  $\text{TiO}_2$ , ZnO, and such oxides. The porous membrane method has emerged to be a general means of preparing a large variety of inorganic nanotubes and nanowires. Carbon nanotubes, surfactants, polymer gels, and liquid crystals have all been used as templates, wherein the precursor material is covered over the templates, followed by annealing and removal (burning or dissolution) of the template. In what follows, we shall discuss the synthesis of various inorganic nanomaterials where we will indicate the method and give the most essential aspects of the procedure. In order for the reader to obtain greater details, we have provided a large list of references.

## 6.3

### Nanotubes of Metals and other Elemental Materials

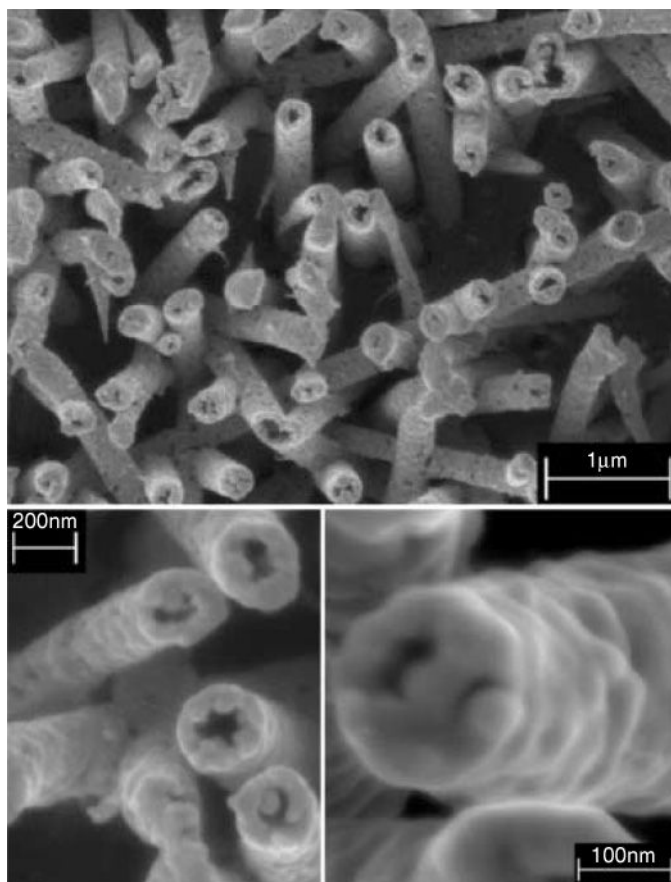
Synthesis of gold nanotubes was reported by Martin and co-workers [8, 9] in the 1990s. They prepared Au tubules with lengths of up to a few micrometers and diameters of a few hundred nanometers by electrochemically depositing gold into the pores of a microporous alumina membrane (AM). To obtain gold tubules, initially the AM pore walls were chemically derivatized by attaching a molecular anchor such as a cyanosilane, so that the electrodeposited metal preferentially deposits on the pore wall, which leads to tubule formation.

Electrodeposition in membrane pores is an important method for the synthesis of metal nanotubes. Thus, Au nanotube arrays have been prepared by direct electrodeposition in the nanochannels of alumina templates. The nanochannel alumina templates with pore diameters of about 105 nm and 45 nm were used to synthesize nanotubes with average outer diameters respectively of 105 nm and

45 nm and a wall thickness of 15 nm. The lengths went up to several micrometers. The alumina templates are readily removed by treatment with NaOH. The nanotube arrays so obtained have a well-controlled microstructure and are polycrystalline with a face-centered cubic structure [10]. Au nanotubes have also been prepared by electroless deposition in the pores of track-etched polycarbonate membranes that contain 10  $\mu\text{m}$  thick and 220 nm diameter pores [11]. The inner surfaces of the polycarbonate membranes were first sensitized with a  $\text{Sn}^{2+}$  salt and then activated by forming a layer of Ag, before depositing Au for a period of 2 h. The gold nanotubes were cleaned with 25%  $\text{HNO}_3$  solution for 15 h. Hydrophobic or hydrophilic self-assembled monolayers on gold nanotubes can be formed by rinsing the samples in ethanol for 20 min, followed by immersion in a solution of ethanol that contains  $\text{HS}(\text{CH}_2)_{15}\text{CH}_3$  or  $\text{HS}(\text{CH}_2)_{15}\text{COOH}$ . The Au nanotubules are polycrystalline and have lengths of up to 6  $\mu\text{m}$  and inner diameters of  $\sim 1$  nm. By controlling the Au deposition time, Au nanotubules of effective inside diameters of molecular dimensions ( $< 1$  nm) can be prepared. They found electroless deposition allows for more uniform gold deposition in a short duration of time. Since the electroless plating method used to deposit Au nanotubes in polymeric templates does not work in AMs, Martin and coworkers [12] have developed a modified electroless plating strategy that can be used to deposit high-quality Au nanotubes within the pores of alumina templates.

Three-dimensional (3D) Au nanotube arrays with smooth as well as nanoporous walls have been obtained by using anodic alumina and conducting polyaniline nanorod templates [13]. In this procedure, polyaniline nanorods were predeposited electrochemically in the interior of a porous alumina membrane, which was then used as a template for the formation of vertically aligned Au nanotubes. For the synthesis of Au nanotube arrays with nanoporous walls, gold/silver alloy nanowalls were electrodeposited from cyanide solutions that contain gold/silver ions (mole ratio,  $\text{Au}^+/\text{Ag}^+ = 1:3$ ). The nanoporous walls were generated by de-alloying (selective dissolution of the less noble metal) the gold/silver alloy shells with concentrated nitric acid, which also dissolves the polyaniline nanorods. The porous architecture is formed because of an intrinsic dynamic pattern formation process, in which the more noble metal (Au) atoms tend to aggregate into two-dimensional clusters through a phase separation process at the solid–acid interface. The length, average inner diameter, and wall thickness of the Au nanotubes with smooth walls was  $\sim 4 \mu\text{m}$ ,  $\sim 196$  nm, and  $62 (\pm 18)$  nm, respectively. The Au nanotubes with smooth nanoporous walls (nanopore diameter of  $\sim 8$  nm) had similar physical dimensions as the nanotubes.

Gold nanotubes embedded within the pores of the polycarbonate template membranes were subjected to reactive ion etching (RIE) using an oxygen plasma to selectively etch approximately 2.3 mm of the polycarbonate, leaving the polycrystalline gold nanotubes intact. Figure 6.1 shows field-emission scanning electron microscopy (FESEM) images of the top surface of a template membrane after electroless deposition of gold followed by RIE [14]. Single crystalline and bamboo-like Au nanotube arrays growing in the [111] direction, with a diameter of 100–150 nm and a length of 10  $\mu\text{m}$ , and standing perpendicular to the Ti metal foil



**Figure 6.1** Field-emission SEM images of gold nanotubes at different magnifications. Micrographs were taken on the etched side of the membrane. Reproduced with permission from [14]. Copyright 2004, Wiley-VCH.

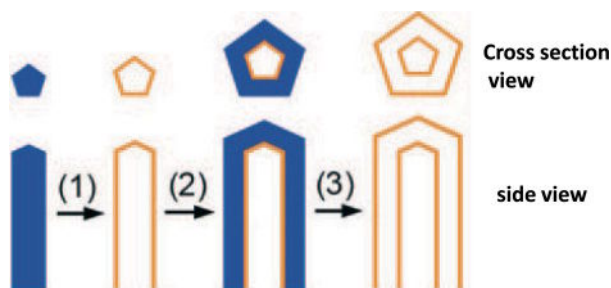
substrates are obtained by using a radiation track-etched hydrophilic polycarbonate membrane [15]. By using water-dissolvable  $\text{Na}_2\text{SO}_4$  nanowires as templates, Au nanoparticle tubes have been obtained by the self-assembly of Au nanoparticles [16]. The as-synthesized Au nanoparticle tubes were further calcined at  $300^\circ\text{C}$  ( $5^\circ\text{C min}^{-1}$ ) for 30 min to transform them into polycrystalline Au nanotubes. At this temperature, the Au nanoparticles (3–5 nm diameter) melt and form nanotubes of  $\sim 1\ \mu\text{m}$  length and  $\sim 80\ \text{nm}$  diameter. Using an electroless deposition procedure, continuous, polycrystalline Au nanotubes with controllable shape, size (tens of nanometer in diameter), shell thickness ( $\sim 5\ \text{nm}$ ), and length (up to  $5\ \mu\text{m}$ ) can be grown by using Co nanoparticles as sacrificial templates [17]. Here, the alignment of Co nanoparticles into a 1D structure is induced by manipulation of

the magnetic field. In this reaction,  $\text{Au}^{3+}$  is reduced to  $\text{Au}^0$  by the  $\text{Co}^0$  nanoparticles as given by the following reaction:



Goethite ( $\text{FeOOH}$ ) nanorods have been used as templates to grow Au nanotubes with a length of a few hundred nanometers and an aspect ratio between 3 and 4 [18]. The uniform growth of gold nanoshells on goethite nanorods was achieved by  $\text{SiO}_2$ -mediated assembly/attachment of Au nanoparticles/seeds on these rods, followed by a one-step seeded growth by the catalyzed reduction of  $\text{HAuCl}_4$  using formaldehyde. The successful attachment of small Au seeds on goethite nanorods requires modification of the nanorod surface, which was carried out by depositing a thin layer of silica using tetraethoxysilane (TEOS), followed by silanization using (3-aminopropyl)trimethoxysilane (APS). Gold nanoparticles (~3 nm in diameter) are prepared by the reduction with tetrakis(hydroxymethyl)phosphonium chloride (THPC), which were used for the self-assembly of Au seeds on the surface of goethite rods. The growth of Au shells on the goethite surface was accomplished by the selective reduction of  $\text{HAuCl}_4$  with a weak reducing agent such as formaldehyde, catalyzed by the Au seeds. In a typical synthesis, 100 mL of the dispersion of goethite was added to 48 g of poly(vinyl pyrrolidone) (PVP) and the mixture stirred for 24 h before transferring to ethanol (100 mL). Twelve millilitres of the goethite–PVP dispersion was diluted with 200 mL of ethanol that contained 20 mL of ammonium hydroxide and 0.75 mL of TEOS, under mechanical stirring. The goethite nanorods coated with silica were washed several times with ethanol. Silanization was carried out by adding 0.6 mL of pure APS to 10 mL of the goethite@silica dispersion under magnetic stirring, followed by additional washing with ethanol to remove excess APS. For the assembly of Au nanoparticles on the nanorod surface, 5 mL of the solution of silanized goethite particles was centrifuged and re-dispersed in 5 mL of the Au colloid solution in an ultrasound bath for 1 to 2 min. This step was repeated until no further adsorption of gold on the surface of the particles was observed. Further growth of the Au coating on the nanorods was carried out as follows. A mixture of 0.425 mL of 0.01 M  $\text{HAuCl}_4$  and 10 mL of  $1.8 \times 10^{-3}$  M  $\text{K}_2\text{CO}_3$  was aged in the dark for a day so that  $\text{Au}^{\text{III}}$  ions were reduced to  $\text{Au}^{\text{I}}$  ions. This solution (5 mL) was mixed with 0.01–0.03 mL of the Au-covered goethite solution and 0.01 mL of formaldehyde solution. The thickness and surface roughness of the obtained shells could be adjusted by simply varying the concentration ratio between the seeds (modified goethite rods) and the growth reagents ( $\text{HAuCl}_4$  and formaldehyde).

Platinum and PtPd alloy nanotubes with polycrystalline walls and a face-centered cubic structure (50 nm in diameter, 5–20  $\mu\text{m}$  long, and 4–7 nm wall thickness) can be synthesized by the galvanic replacement reaction of Ag nanowires [19]. In this procedure, Ag nanowires are refluxed for 10 min with platinum acetate in aqueous solution. When an aqueous platinum acetate solution is mixed with a dispersion of Ag nanowires, the galvanic replacement reaction generates a tubular sheath whose morphology is complementary to that of the Ag nanowire (step 1 in



**Scheme 6.1** Schematic representation for the fabrication of multiple-walled nanotubes composed of Pt/Ag alloys.

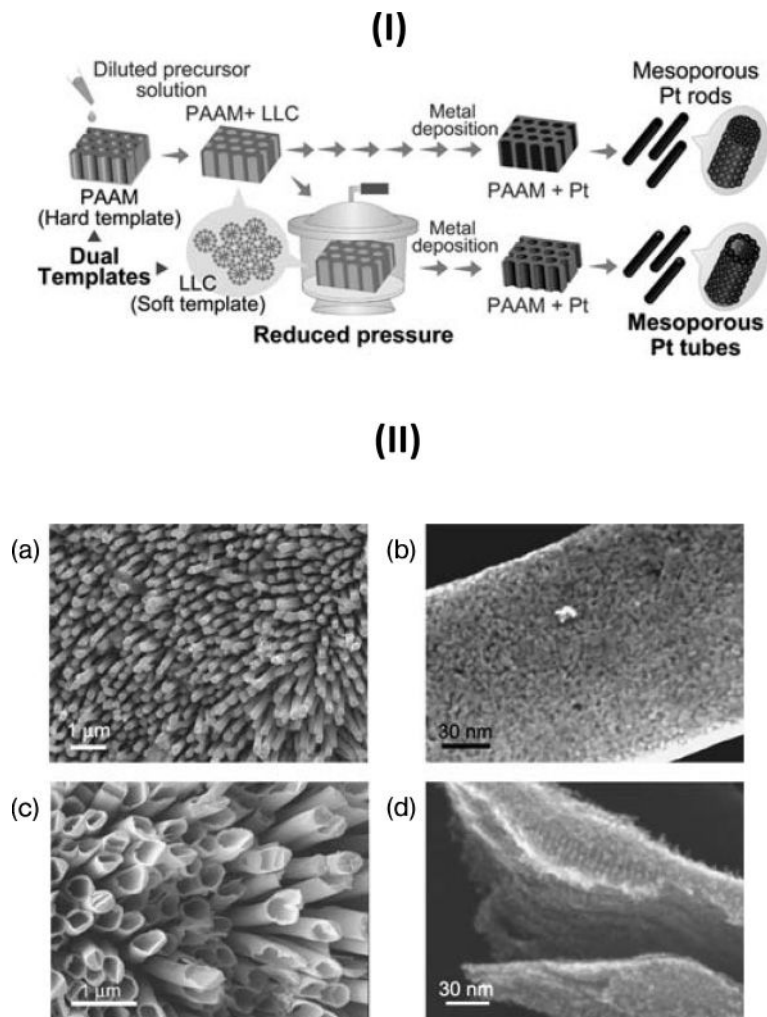
Scheme 6.1). Following the same scheme for multiple-walled nanoshells, coaxial nanotubes with more than two walls can be prepared. Mesoporous Pt nanotubes have been prepared by incorporating lyotropic liquid crystals in the pores of an AM before depositing the metal (Fig. 6.2) [20]. By using a mixed non-ionic–cationic liquid crystalline surfactant (nonaethylene glycol monododecyl ether ( $C_{12}EO_9$ ), polyoxyethylene (20) sorbitan monostearate (Tween 60) and water), polycrystalline Pt nanotubes (with a face-centered cubic structure) with small inner (3–4 nm) and outer (6–7 nm) diameters have been obtained [21]. In a typical synthesis, the liquid crystalline phase that contains hexachloroplatinic acid ( $H_2PtCl_6$ ),  $C_{12}EO_9$ , Tween 60, and water at a molar ratio of 1 : 1 : 1 : 60 was treated with hydrazine to cause the reduction of the metal salts confined in the lyotropic mixed crystals of the two different surfactants to yield the metal nanotubes. The resulting solid was separated, and washed with water and ethanol prior to drying in air. The same procedure has been used to prepare nanotubes of other metals such as Pd and Ag.

Hierarchical assemblies of hollow Pd nanostructures have been grown by using Co nanoparticles as self-sacrificial templates [22]. Assemblies of hollow Pd nanostructures (from 80 nm Pd nanoparticles) are obtained with raspberry-like or nanotube-like geometries, by the replacement reaction between  $H_2PdCl_4$  and Co nanoparticles, which occurs rapidly, wherein the reduced Pd atoms nucleate and grow into very small particles, and eventually evolve into a thin shell around the cobalt nanoparticles. The replacement reaction is given by:



The polycrystalline 1D Pd nanostructures have a face-centered cubic structure with lengths that run to several micrometers and diameters up to ~60 nm.

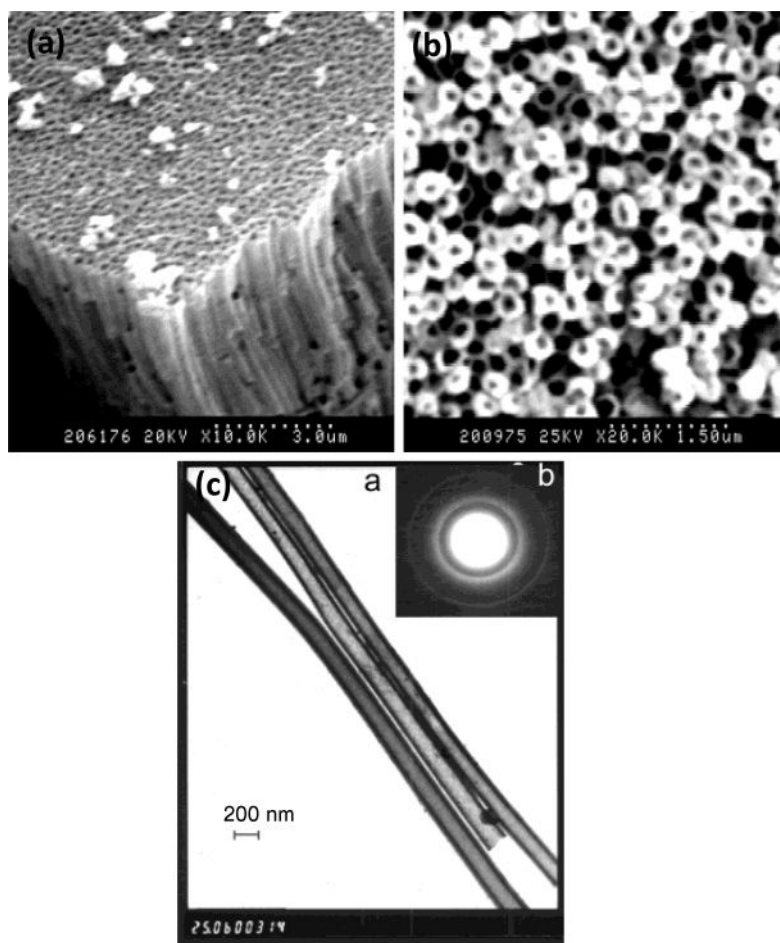
Ni and Co microtubules were prepared by Han *et al.* [23], by the pyrolysis of composite fibers consisting of a poly(ethylene terephthalate) (PET) core fiber with the electroless-plated metal at the exterior. Ni microtubules prepared by this method were single-crystalline, but the Cu microtubules were polycrystalline. Electrodeposition in the pores of AMs has been carried out by Bao *et al.* [24], to obtain ordered arrays of Ni nanotubules. The pore walls were modified by these



**Figure 6.2** I) Schematic view of the preparative procedure for mesoporous Pt nanorods and nanotubes. II) SEM images of: a,b) mesoporous Pt nanorods, and c,d) mesoporous Pt nanotubes. Figures (b) and (d) are highly magnified images of (a) and (c), respectively. Reproduced with permission from [20]. Copyright 2008, RSC.

workers with an organic amine to assist the formation of nanotubes (Fig. 6.3). In the absence of the amine, nickel nanowires were obtained. Nickel, when electrodeposited in the pores, binds preferentially to the pore walls because of its strong affinity towards the amine. The AM is removed by treatment with NaOH. The top-view SEM image in Figure 6.3b shows open-ends of the Ni nanotubules after the removal of the top layer of the AM with NaOH solution. The electron

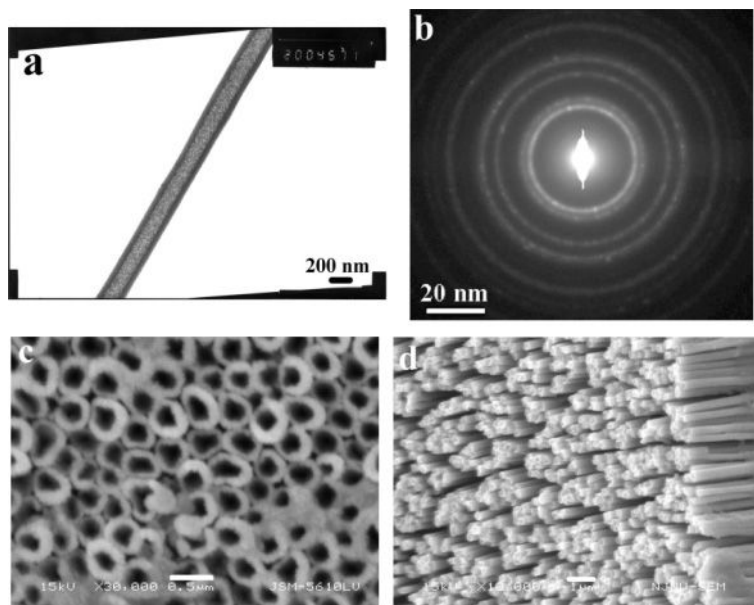




**Figure 6.3** SEM images of a) Ni nanotubes after dissolution of the alumina template, b) showing the top-view of an array of Ni nanotubes after partial removal of the template, and c) transmission electron microscopy (TEM) image of the Ni nanotubes after dissolution of the alumina template. Inset shows electron diffraction pattern of the Ni nanotubes. Reproduced with permission from [24]. Copyright 2001, Wiley-VCH.

diffraction pattern of the Ni nanotubes in the inset of Figure 6.3c shows diffuse rings, which indicates that the Ni nanotubes are polycrystalline and have a face-centered cubic structure. The transmission electron microscopy (TEM) image of the Ni nanotubes in Figure 6.3c shows that the diameter of the Ni nanotubes are uniform with average outer diameter of  $160 \pm 20$  nm. The deposition follows a bottom-up approach. Thus, the growth of nanotubes starts at the Au cathode at the bottom of the pores. The length and the wall thickness of the Ni nanotubes depend on experimental conditions, such as pore-wall modifying agent, and electrodeposition parameters. A low current density appears to be a key factor. For



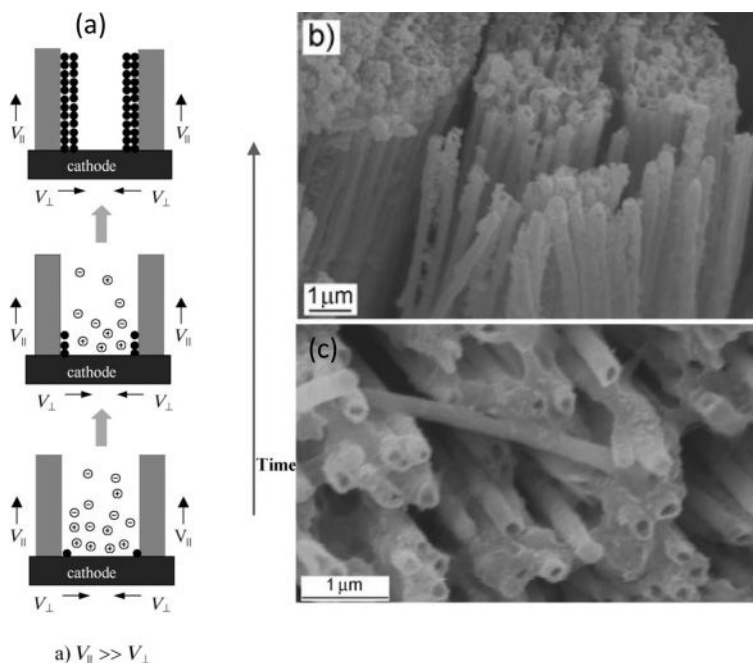


**Figure 6.4** a) TEM image and b) SAED pattern of a Ni nanotube after removing the alumina template. c) Top-view and d) side-view SEM images of an ordered array of Ni nanotubes after partial removal of the

template. The experimental parameters are: current density,  $0.13 \text{ mA cm}^{-2}$ , concentration of P123 of  $37 \text{ g L}^{-1}$ , and deposition time of 48 h. Reproduced with permission from [25]. Copyright 2006, Wiley-VCH.

instance, with a current density of  $0.3 \text{ mA cm}^{-2}$  and an electrodeposition time of 24 h, Ni nanotubules of  $20 \mu\text{m}$  in length and  $30 \text{ nm}$  in wall thickness were obtained, while with electrodeposition for 48 h, Ni nanotubules grow up to  $35 \mu\text{m}$  in length and  $60 \text{ nm}$  in wall thickness. Ordered magnetic Ni nanotubes have been prepared by employing electrodeposition by adding an amphiphilic triblock co-polymer (Pluronic P123) to the electrodeposition solution [25]. By adjusting experimental parameters such as current density and electrodeposition time, the wall thickness and length of the nanotube are controlled (Fig. 6.4). The Ni nanotubes prepared at a current density of  $0.13 \text{ mA cm}^{-2}$  with an electrodeposition solution that contains  $37 \text{ g L}^{-1}$  of P123 and a deposition time of 48 h yielded uniform tubes of about  $50 \text{ nm}$  wall thickness,  $60 \mu\text{m}$  length, and an outer diameter of  $\sim 250 \text{ nm}$ , which corresponds to the pore diameter of the alumina template. Weak, diffuse rings in the selected-area electron diffraction (SAED) pattern of the nanotubes showed they were polycrystalline.

The preparation and growth mechanism of Ni, Co, and Fe nanotubes have been reported by Cao *et al.* [26], wherein the nanotubes are actually constructed from non-layered materials of the metal, and the tubular growth is directed by the current in the template-based electrodeposition process (Fig. 6.5). Typically, the length of the as-synthesized tubular structures can reach about  $60 \mu\text{m}$ , which



**Figure 6.5** a) Schematic diagram of the steps in the growth of metal nanotubes by template-based electrochemical deposition method. b, c) SEM images of cobalt and iron nanotube arrays, respectively. Reproduced with permission from [26]. Copyright 2006, Wiley-VCH.

corresponds to the thickness of the AM. Most of them have an outer diameter of 50–100 nm, which corresponds to the pore diameter of the AM, and an inner diameter of about 30–50 nm. The electron diffraction patterns reveal that the nanotubes are single-crystalline and have a body-centered cubic structure for iron, a face-centered cubic structure for nickel, and a hexagonal close packed structure for cobalt. Employing AMs, aligned Fe nanotubes have been grown electrochemically [27]. The wall thickness of the nanotubes could be controlled by changing the deposition parameters. Co nanotubes have also been grown by electrodeposition in an AM [28]. Electrodeposition in a rotating electric field produces dense arrays of single crystalline Cu nanotubes [29]. The applied rotating field makes the ions graze the surface of the pores in helical paths and makes the deposition occur selectively in the region near the wall of the nanopores. The wall thickness of the metal nanotubes so obtained are in the range of 15–20 nm and can be controlled by changing the amplitude of the rotating field. The nanotubes had a diameter of ~230 nm with lengths going up to several micrometers.

Electrochemical deposition methods have also been used for the synthesis of nanotubes of many other metals including Zn, Sn, and Ag having polycrystalline structures [30]. In order to fabricate these metal nanotube arrays, a thin layer of

Au was deposited on the bottom surface of the porous AM, for use as a working electrode. The circular step edges of the Au nanorings so formed at the bottom of the AM serve as the preferential sites for the deposition of metal ions. Nanotube arrays of Zn and Sn were then obtained within the porous AM by preferentially plating at circular step edges of the Au nanorings. This was accompanied by the evolution of hydrogen gas, which is critical for nanotube formation. It is well known that circular step edges have the ability to catalyze electron transfer to metal ions in solutions. Since the reductive potential of hydrogen is higher than that of Zn and Sn, evolution of hydrogen gas accompanies metal deposition. Hydrogen gas evolves continuously from the cathode through the central region of the nanopores while the metallic elements become attached to the pore walls, which results in the formation of nanotubes. The nanotubes have open ends on top and are arranged in a well-ordered manner. The outer diameter of the nanotubes is in the range 90–110 nm, which corresponds to the pore diameter of the membrane. The inner diameter of the nanotubes is in the range of 40–60 nm. The length of the nanotubes goes up to several micrometers. The compactness of the nanotubes is quite high, about  $1 \times 10^9 \text{ cm}^{-2}$ , which corresponds to the pore density of the membrane.

Metallic indium nanotubes can be prepared by direct thermal evaporation of the metal [31]. A metal source is heated in an Ar atmosphere between 900–1100 °C and the vapor is passed over a catalyst such as a Au-coated silicon substrate to obtain crystalline nanotubes. The length of the nanotubes increases with temperature. The diameter of the head portion (100–300 nm) is approximately three times larger than the tail diameter. The diameter of the tail portion remains uniform throughout the nanostructure. Electrodeposition in AMs has been employed to prepare polycrystalline nanotubes of alloys such as BiSb [32], FeCo [33], FeNi [34], and CoCu [35].

Lyotropic liquid crystal templates along with surfactants are used to synthesize metal–boron nanotubes (M–B (M = Fe, Co, and Ni)) [36]. The non-ionic surfactants used are Tween 40 (polyoxyethylene sorbitan monopalmitate), Tween 60, and Tween 80 (polyoxyethylene sorbitan monooleate), and the anionic surfactant is camphorsulfonic acid. In a typical synthesis,  $\text{FeCl}_3 \cdot 6\text{H}_2\text{O}$  was dissolved in water that contained (1S)-(+)-10-camphorsulfonic acid (CSA) and Tween 40 at 60 °C and the mixture cooled to 20 °C. To this a mixture of 4 M  $\text{NaBH}_4$  and 0.1 M NaOH was added and the mixture kept for 48 h in an inert atmosphere. The resulting solid was collected, washed with distilled water and ethanol, and dried in flowing nitrogen. Non-crystalline Co–B and Ni–B nanotubes were prepared from  $\text{CoCl}_2 \cdot 6\text{H}_2\text{O}$  or  $\text{NiCl}_2 \cdot 6\text{H}_2\text{O}$  and Tween 60 in place of  $\text{FeCl}_3 \cdot 6\text{H}_2\text{O}$  and Tween 40 under similar conditions. This method provides a route for the synthesis of metal–boron nanotubes and can also be extended to other tubular materials of non-crystalline alloys. Fe–B nanotubes prepared using Tween 40 and CSA are several micrometers in length and have inner and outer diameters of around 50–55 and 60–65 nm, respectively. The continuous broad halo rings in the SAED pattern further suggest a non-crystalline nature of the Fe–B nanotubes.

One-dimensional nanostructures of Se and Te were reported some time ago by Gautam *et al.* [37, 38]. Recently, *t*-Se nanotubes have been grown hydrothermally

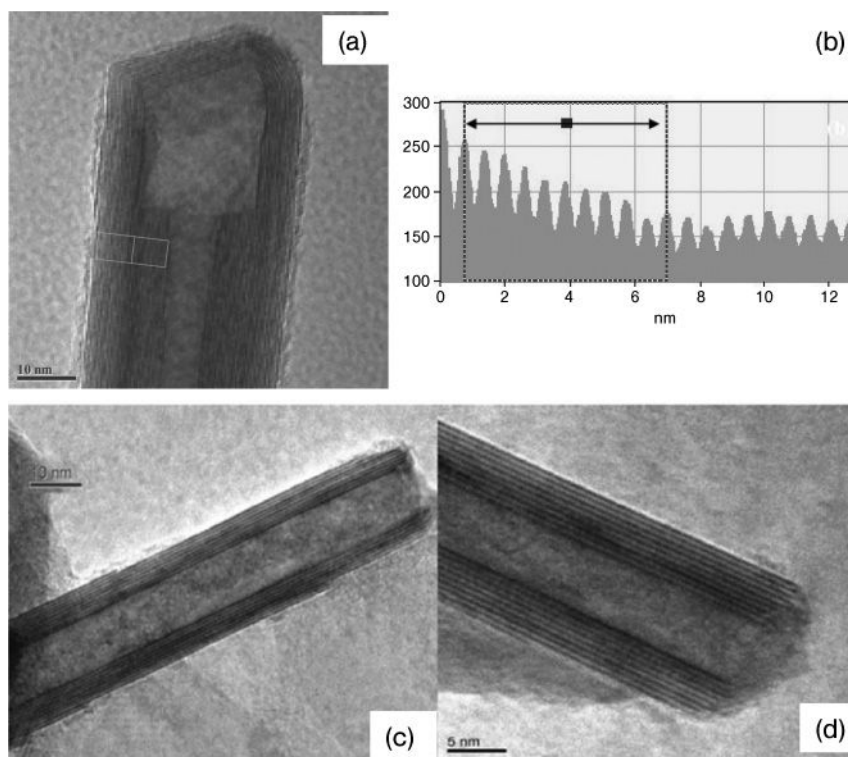
in the absence of a surfactant or a polymer [39]. In this procedure, an aqueous solution of sodium selenite ( $\text{Na}_2\text{SeO}_3$ ), NaOH, and sodium formate ( $\text{NaCHO}_2$ ) is reacted in a hydrothermal bomb at  $100^\circ\text{C}$  for 25 h. Zhang *et al.* [40]. have reported the fabrication of *t*-Se nanotubes by a hydrothermal-ultrasonic route. Ma *et al.* [41]. synthesized *t*-Se nanotubes in micelles of a non-ionic surfactant, while Li *et al.* [42]. synthesized them by a sonochemical process. Single-crystalline Te nanotubes have been prepared by a solvothermal method using PVP to modulate the reaction time, the reactants being  $\text{TeO}_2$  and ethanolamine [43].

## 6.4

### Metal Chalcogenide Nanotubes

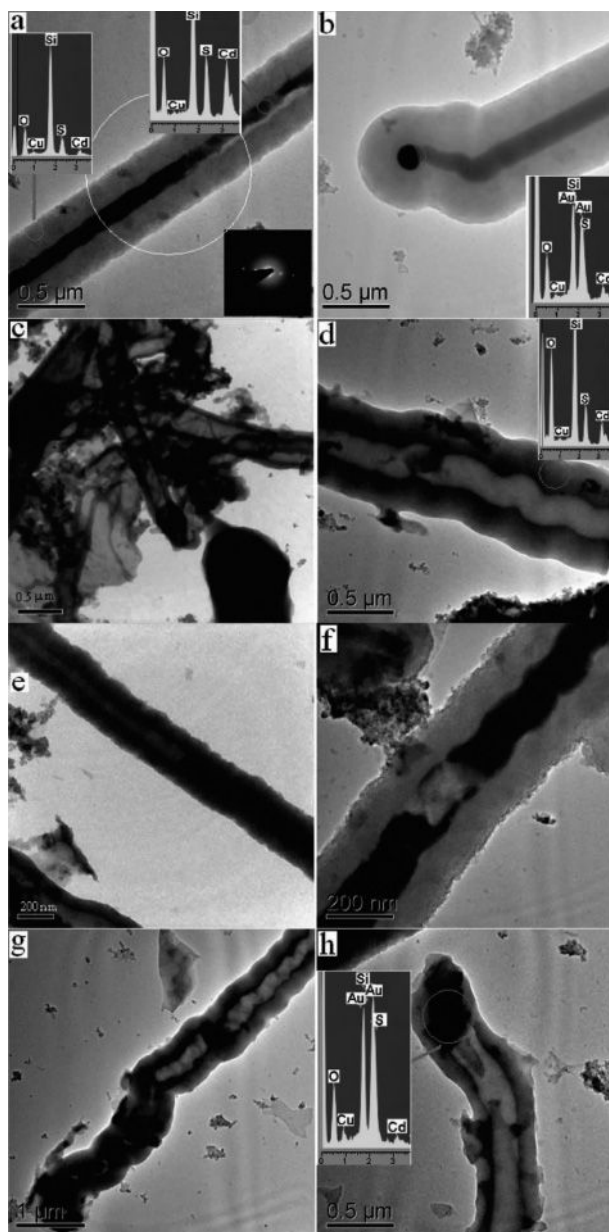
$\text{MoS}_2$  and  $\text{WS}_2$  are the first chalcogenides whose fullerene type structures and nanotubes were prepared in the laboratory [44, 45]. The method involved heating of metal oxide nanorods in  $\text{H}_2\text{S}$ . A similar strategy was also employed to prepare the corresponding selenide nanotubes. Recognizing that amorphous  $\text{MoS}_3$  and  $\text{WS}_3$  are the likely intermediates in the formation of the disulfides, the trisulfides have been directly decomposed in a  $\text{H}_2$  atmosphere to obtain the disulfide nanotubes [46]. Diselenide nanotubes were similarly obtained by the decomposition of metal triselenides [47]. The trisulfide route provides a general route for the synthesis of the nanotubes of many metal disulfides such as  $\text{NbS}_2$  and  $\text{HfS}_2$  that have a single crystalline nature [48, 49]. The decomposition of precursor ammonium salts  $(\text{NH}_4)_2\text{MX}_4$  ( $\text{X} = \text{S}, \text{Se}; \text{M} = \text{Mo}, \text{W}$ ), is even better, all the products, except the dichalcogenides, being gases [46, 47]. Metal trichalcogenides are intermediates in the decomposition of the ammonium salts as well. These nanotubes have a hexagonal structure with a layer spacing of  $\sim 0.6\text{ nm}$ , which corresponds to a *d*-spacing of (002), with an external diameter of  $\sim 25\text{ nm}$ , a wall thickness of  $\sim 10\text{ nm}$ , and lengths of up to several micrometers. Employing trisulfides and triselenides as starting materials, nanotubes of  $\text{TiS}_2$ ,  $\text{HfS}_2$ ,  $\text{NbS}_2$ ,  $\text{NbSe}_2$  and related layered metal chalcogenide nanotubes have been prepared [50]. Recently,  $\text{MoS}_2$  and  $\text{WS}_2$  have been made by using gas phase reactions using metal chlorides and carbonyls (Fig. 6.6) [51]. Solar ablation can also be used to generate  $\text{MoS}_2$  nanotubes [52]. Nanotubes and onions of GaS and GaSe have been generated through laser and thermally induced exfoliation of the bulk powders [53].

CdS nanotubes and related structures have been prepared by the thermal evaporation of CdS powder (Fig. 6.7) [54]. Nanotubes of CdS and CdSe had earlier been prepared by using surfactants as templates [55]. CdS occurs in the hexagonal structure in the nanotubes. The diameter and length are in the ranges of 40–160 nm and 3–4  $\mu\text{m}$ , respectively. The CdSe nanotubes are generally long, with lengths up to 5  $\mu\text{m}$ . The outer diameter of the nanotubes is in the 15–20 nm range while the diameter of the central tubule is in the 10–15 nm range. These nanotubes are polycrystalline and form through the oriental attachment of nanoparticles. Recently, CdS, ZnS, and CuS nanotubes have been made by the hydrogel-assisted route (Fig. 6.8) [56]. The TEM image of CdS in Figure 6.8a, obtained



**Figure 6.6** a) HRTEM image of the MoS<sub>2</sub> nanotube, b) the line profile of the boxed area in (a) gives an interlayer spacing of 6.2 Å. Reproduced with permission from [51a] c,d) TEM images of WS<sub>2</sub> nanotubes obtained in the reaction between WCl<sub>5</sub> and H<sub>2</sub>S in the vertical reactor. Reproduced with permission from [51b].

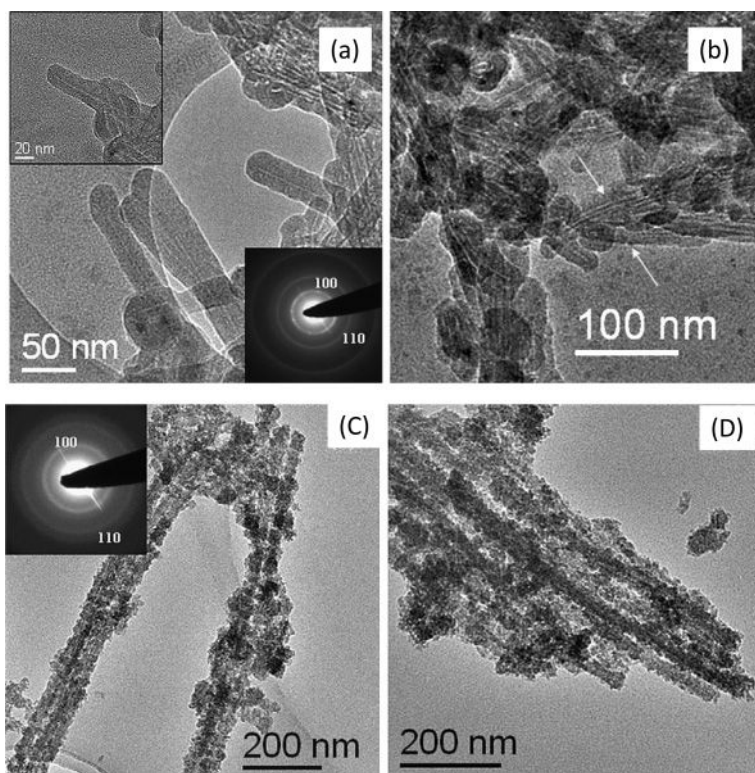
after the removal of the hydrogel template, demonstrates the hollow nature of the nanotubes. The lengths of the nanotubes extend to a few hundred nanometers, while the diameter of the inner tubule is ~2–3 nm, the outer diameter being in the 20–25 nm range. A SAED pattern of a single nanotube is given in the bottom inset of Figure 6.8a. The diffuse rings correspond to the (100) and (110) Bragg planes of hexagonal CdS showing the nanotubes to be generally polycrystalline. Clearly, the tripodal cholanamide hydrogel fibers act as templates, on which the CdS particles get deposited, giving rise to the nanotubes. The low magnification TEM image in Figure 6.8b suggests a possible assembly or attachment of the initially formed shorter nanotubes to form linear chains (indicated by arrows in the figure). The hydrogel might be responsible for such an attachment, the hydrogel playing a dual role of being a template to produce hollow nanotubes as well as favoring the attachment or assembly of the nanotubes. The ZnS nanotubes prepared similarly (Figs 6.8c and d) have an inner diameter in the ~4–6 nm range,



**Figure 6.7** TEM images of the 1D CdS nanostructures: a) a core–sheath nanowire with insets that contain the energy dispersive X-ray analysis (EDX) of the core and the sheath and SAED of the core, b) the top of a core–sheath nanowire with an inset of the EDX of the catalyst, c,d) CdS nanotubes,

e) tube–wire nanojunction, f) wire–tube–wire nanojunction, g) top part of a nanotube with nanoparticles with the channel, and (h) top part of one nanotube with the catalyst with the inset showing the EDX of the particle. Reproduced with permission from [54]. Copyright 2008, ACS.





**Figure 6.8** a) TEM image of CdS nanotubes obtained after the removal of the hydrogel template. Top inset is a high-magnification image of a single nanotube. Bottom inset is the SAED pattern of the nanotubes. b) TEM image showing a bunch of nanotubes

assembled spontaneously, indicated by the arrows. c,d) TEM images showing nanotubes of ZnS obtained using 0.02 mmol of  $\text{Zn}(\text{OAc})_2$ . Reproduced with permission from [56]. Copyright 2006, Elsevier.

with lengths going up to a micrometer. The TEM image shows tiny nanocrystals of ZnS (Fig. 6.8c) making up the walls of the nanotubes. The electron diffraction patterns also reveal the nanotubes to be polycrystalline and of hexagonal structure. The CuS nanotubes prepared by this route have an inner diameter of  $\sim 5$  nm with lengths extending to a few hundreds of nanometers. The outer diameter is in the 20–30 nm range. The nanotubes are polycrystalline as found from electron diffraction as well as the TEM images. The polycrystalline nanotubes are formed through the oriented attachment of nanoparticles. CuS nanotubes have also been made by the solution reaction of Cu nanowires in ethylene glycol with a suitable sulfur source such as thiourea and thioacetamide at  $80^\circ\text{C}$  [57]. The CuS nanotubes so-produced in large quantities possess a hexagonal structure and have an inner diameter of 30–90 nm, a wall thickness of 20–50 nm, and a length of more than  $40\mu\text{m}$ . The straight nanotubes are made up of nanoparticles of around 30 nm

diameter. This study also shows that sulfur sources such as thiourea and thiacetamide, which release ionic sulfur rather than molecular sulfur at their decomposition temperature, are favorable for the formation of CuS nanotubes, compared with sulfur powder.

CdSe nanotubes have been prepared by a sono-electrochemical method [58], while CuSe nanotubes have been prepared by using trigonal Se nanotubes as templates [59]. The CdSe nanostructures (with a cubic structure) were formed by electrodeposition onto the sonic probe cathode [58]. The deposit could be spheroidal or have a 2D structure. Subsequent sonic shock waves remove the deposit from the probe surface. The sonochemical treatment provides the required energy to roll the nanosheets to form tubular nanoscrolls. After the 2D nanosheets are ejected from the probe, because of the high surface energy of the ends of the nanosheets, the flexible and unstable nanosheets easily roll-up in the sonochemical process. It is well known that collapsing bubbles produced in a liquid solution during sonication can instantaneously generate local spots of high temperature, pressure, and cooling rates. The worm-like morphology of the CdSe prepared by this method involves a tubular structure and the nanotubes (diameter: 80 nm, wall thickness: 10 nm) are entangled with each other. The nanotube with a straight part reveals a round open tip, which is not completely seamed. This indicates that the nanotubes were probably formed through a roll-up process. The CdSe nanotubes show many stacking faults and missing layers in the nanotube walls. The appearance of defects is mainly a result of the high stress and strain present in the nanotubes.

CuSe with a tubular nanostructure is formed by the template mechanism wherein diffusion of Cu atoms occur into t-Se nanotubes [59]. The synthesis process involves the t-Se nanotubes acting as templates and reactants were converted into crystalline nanotubes of CuSe by reacting with Cu nanoparticles freshly produced from an aqueous  $\text{CuSO}_4$  solution. Apart from CuSe nanotubes, 1D nanocrystallites of  $\text{Cu}_3\text{Se}_2$ ,  $\text{Cu}_{2-x}\text{Se}$ , and  $\text{Cu}_2\text{Se}$  were also obtained by changing the atom ratio of Cu and Se in the precursors. The tubular nanostructures have the hexagonal structure of CuSe. The wall thickness and diameter of the CuSe nanotubes were around 80 and 300 nm, respectively.

CdTe nanotubes of controlled diameter are prepared by first reacting  $\text{CdCl}_2$  with thioglycolic acid (TGA) to obtain 1D Cd-TGA nanowires (thickness ~8 nm), the aqueous dispersion of which is then used as a sacrificial template to generate long CdTe nanotubes by reaction with  $\text{NaHTe}$  [60]. The length of the nanotubes is typically hundreds of micrometers, similar to the initial length of the precursor. The inner and outer diameters of the nanotubes are in the ranges of 12–20 nm and 30–50 nm, respectively. The CdTe nanotubes are polycrystalline and adopt a cubic structure. The average diameter of the nanowires of the 1D Cd-TGA precursors obtained in the presence of poly(acrylic acid) (PAA), could substantially be increased as a function of the amount of PAA. During the formation of CdTe, 1D Cd-TGA precursors are gradually consumed to finally lead to hollow structures, preserving the original shape, size, and morphology of the precursor.

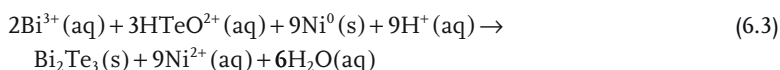


Photochemical decomposition of  $\text{CSe}_2$  adsorbed on Ag nanowires yields  $\text{Ag}_2\text{Se}$  nanotubes [61]. The evolution of Ag nanowires to core–shell structures and finally to hollow  $\text{Ag}_2\text{Se}$  nanotubes was studied in detail by TEM analysis. Upon irradiation for 15 min, the TEM image of the nanowires began to show evidence of core–shell nanowires with mean diameters of  $\sim 85$  nm and  $\sim 45$  nm cores. The shell grew thicker at the expense of the core with increasing irradiation time, and voids were observed to grow from both ends of the nanowires along the longitudinal axis, ultimately merging to form hollow nanotubes of mean diameters of  $\sim 90$  nm with  $\sim 45$  nm voids. The nanotubes are polycrystalline with a structure corresponding to the orthorhombic phase of  $\text{R-Ag}_2\text{Se}$ . Trigonal Se nanotubes can be used as templates to prepare  $\text{Ag}_2\text{Se}$  nanotubes [62].  $\text{Ag}_2\text{Te}$  nanotubes have been generated by the reaction of  $\text{AgNO}_3$  with sodium tellurate ( $\text{Na}_2\text{TeO}_3$ ) in the presence of hydrazine and ammonia by a hydrothermal process in the absence of a template or a surfactant [63]. All these nanotubes are bent and curled, with diameters of 80–250 nm and several tens of micrometers in length. They show the characteristics of tubular structures with open-ended and uncovered hollow interiors. The nanotubes are single-crystalline, and free of dislocations and stacking faults. A structural phase transition of the as-prepared  $\text{Ag}_2\text{Te}$  nanotubes from the low-temperature monoclinic structure ( $\beta\text{-Ag}_2\text{Te}$ ) to the high-temperature face-centered cubic structure ( $\alpha\text{-Ag}_2\text{Te}$ ) has been observed.

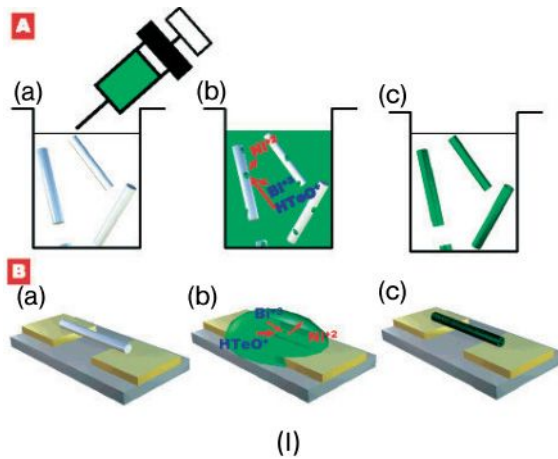
$\text{Bi}_2\text{S}_3$  nanotubes and nanorods are prepared solvothermally at a low temperature of  $120^\circ\text{C}$ , using a mixed solvent (acetone–water, methanol–water, ethanol–water, water, ethylene glycol–water, or glycerol–water) as the reaction medium and urea as the mineralizer [64]. In a typical synthesis,  $\text{Bi}(\text{NO}_3)_3 \cdot 5\text{H}_2\text{O}$  is dissolved in the mixed solvent and aqueous  $\text{Na}_2\text{S} \cdot 9\text{H}_2\text{O}$  ( $\text{S}/\text{Bi} = 3:1$ ) solution added drop by drop into the solution under vigorous stirring. The mixture of precursors and urea is transferred into a Teflon-lined autoclave and heated solvothermally. The gray-black powder so obtained is washed with distilled water and ethanol several times and dried. A mixture of nanorods and nanotubes is found in the final product synthesized in methanol–water mixtures. The diameter of the nanotubes was more than that of the nanorods (in the 80–100 nm range) with lengths up to a micrometer. The powders synthesized in water are nanotubes, which are polycrystalline with a diameter of 200 nm and a length of about  $1\ \mu\text{m}$ .  $\text{Bi}_2\text{S}_3$  nanotubes synthesized in ethylene glycol–water mixtures are single crystalline, with a diameter in the 200–500 nm range and the lengths up to several micrometers. The inner diameter of the single hollow nanotube is about 100 nm and the walls of the tube are around 100 nm thick.  $\text{Bi}_2\text{S}_3$  microtubes synthesized in the mixed solvent of glycerol–water have a diameter of about  $1\ \mu\text{m}$  and a length of about  $7\ \mu\text{m}$ . During the process of solvothermal synthesis, there is a dynamic equilibrium between the  $\text{Bi}_2\text{S}_3$  solid particles or nuclei and the  $\text{Bi}^{3+}$  and  $\text{S}^{2-}$  ions in solution ( $2\text{Bi}^{3+} + 3\text{S}^{2-} \rightleftharpoons \text{Bi}_2\text{S}_3$ ). In such an equilibrium,  $\text{Bi}^{3+}$  and  $\text{S}^{2-}$  ions tend to dissolve from the small particles into the solution and precipitate onto the surfaces of large particles so that the total energy of the interface between the particles and the solution is decreased.  $\text{Bi}_2\text{S}_3$  has a layered structure and the weak bonds between the layers give rise to an anisotropic growth of  $\text{Bi}_2\text{S}_3$  particles during the solvothermal synthesis. At the

low reaction temperature, the rate of crystal growth is greater than that of crystal nucleation. The growth of  $\text{Bi}_2\text{S}_3$  nanosheets is favoured at higher viscosity and surface tension of the reaction medium. The powders synthesized in the mixed solvent of water, ethylene glycol–water, and glycerol–water possess nanosheet structures and the nanosheet nanostructures self-roll to form tube-like structures. The interface energy between bismuth sulfide and the mixed solvent of water, ethylene glycol–water, and glycerol–water with a high surface tension appears to be higher than that between bismuth sulfide and the mixed solvent of acetone–water, ethanol–water, and methanol–water. A solvent with higher viscosity and surface tension favours the formation of tube-like structures and a solvent with lower viscosity and surface tension favours the formation of a rod-like structure during the synthesis. Hence the morphology of the nanostructure depends on the viscosity and surface tension of the mixed solvent used in the solvothermal synthesis.  $\text{Bi}_2\text{S}_3$  nanotubes have also been prepared by the conventional evaporation method [65], as well as by employing the micelle-template method at  $115^\circ\text{C}$  [66].

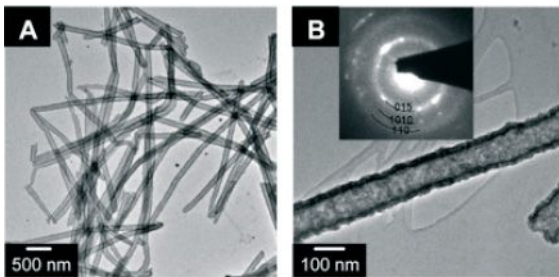
$\text{Bi}_2\text{Se}_3$  nanotubes can be prepared solvothermally starting with ammonium bismuth citrate and elemental Se in dimethylformamide solution [67]. However, the diameters of the nanotubes are not uniform and vary in the range of 15–150 nm with the wall thickness in the 5–20 nm range. These polycrystalline nanotubes have a rhombohedral structure.  $\text{Bi}_2\text{Te}_3$  nanotubes have been obtained by the galvanic displacement of nickel nanowires in nitric acid that contains  $\text{Bi}^{3+}$  and  $\text{HTeO}_2^+$  ions (Fig. 6.9) [68]. When Ni nanowires are immersed in a nitric acid solution that contains  $\text{Bi}^{3+}$  and  $\text{HTeO}_2^+$  ions, the Ni nanowires are galvanically displaced to form  $\text{Bi}_2\text{Te}_3$ , because of the difference in the reduction potentials. The nanotubes have diameters in the 100–130 nm range, a wall thickness of approximately 20 nm, and lengths running to several micrometers. The nanotubes are formed out of highly crystalline rhombohedral  $\text{Bi}_2\text{Te}_3$  crystals without obvious preferential orientation. The composition of  $\text{Bi}_2\text{Te}_3$  nanotubes was precisely tuned by adjusting the  $[\text{Bi}^{3+}]/[\text{HTeO}_2^+]$  ratio. The galvanic displacement reaction can be written as:



Nanotubular  $\text{Bi}_2\text{Te}_3$ , as well as its alloys with Se and Sb, are obtained by electrodeposition in the nanochannels of alumina templates [69].  $\text{Sb}_2\text{S}_3$  nanotubes with thin walls (1.5 nm–2 nm) have been made by the solvothermal reaction of  $\text{SbCl}_3$  with sulfur in oleylamine solution at a relatively low temperature ( $175^\circ\text{C}$ ) [70]. The average diameter of the  $\text{Sb}_2\text{S}_3$  nanotubes (orthorhombic structure) was 10.4 nm, and the length was in the 100 to 300 nm range with an atomic ratio of Sb to S of 1 : 1.51. By changing the concentration of sulfur, the aspect ratios of the initially formed  $\text{Sb}_2\text{S}_3$  nanoribbons were delicately controlled. Reducing the number of equivalents of sulfur results in a decrease in the length of the nanoribbons with a simultaneous increase in the width. In addition to the wider nanoribbons, a significant amount of nanotubes with 6.7 nm average width were observed.



(I)



(II)

**Figure 6.9** I) Schematic illustrations of  $\text{Bi}_2\text{Te}_3$  nanowire ( $\sim 100$  nm in diameter). Tube thickness was approximately 20 nm (B). Reproduced with permission from [68]. Copyright 2007, ACS.

nanotube synthesis (A) and individual  $\text{Bi}_2\text{Te}_3$  nanotube laid across electrodes (B). TEM images and SAED pattern of high aspect ratio  $\text{Bi}_2\text{Te}_3$  nanotubes (A) synthesized from nickel

Further reduction in sulfur yields pure small aspect ratio nanotubes. Clearly, the nanotubes are formed by the rolling of the nanoribbons.

Nanotubes of lead chalcogenides are prepared by the reaction of  $\text{Pb}(\text{NO}_3)_2$  with cysteine in ethanolamine solution followed by the subsequent reaction of the nanowire product with the chalcogenide source solution at room temperature [71]. The nanowires are formed by the self-assembly of nanocrystals (10 nm diameter) and the nanowires act as templates for the subsequent formation of lead chalcogenide nanotubes. The nanotubes are polycrystalline, have a typical diameter of about 200 nm and are several micrometers long. The lead chalcogenide nanotubes show face-centered cubic phases with a disorderly aggregation of the nanocrystals. The lead chalcogenide nanocrystals are formed on the surface of the precursor

nanowires by an anion-replacement reaction that is the result of the lower solubility of lead chalcogenide in solution. An ion exchange solvothermal reaction between  $\text{Na}_4\text{P}_2\text{S}_6$  and  $\text{MnCl}_2$  gives rise to nanotubes of  $\text{Mn}_2\text{P}_2\text{S}_6$  [72]. These nanotubes are single-crystalline (monoclinic) and have uniform outer diameters of 40–50 nm and lengths that range from 110 to 170 nm.

## 6.5

### Metal Oxide Nanotubes

Metal oxide nanotubes have been investigated widely in the last 2–3 years because of the potential applications of some of these materials. They have been prepared by employing several methods including sol–gel chemistry, hydrothermal reactions and use of templates. The template method is used particularly widely in combination with electrodeposition. Besides the popular porous alumina template, carbon nanotubes and other materials are used in the preparation of oxide nanotubes. The template-directed synthesis of oxide nanotubes has been reviewed by Bae *et al.* [73].

#### 6.5.1

##### $\text{SiO}_2$ Nanotubes

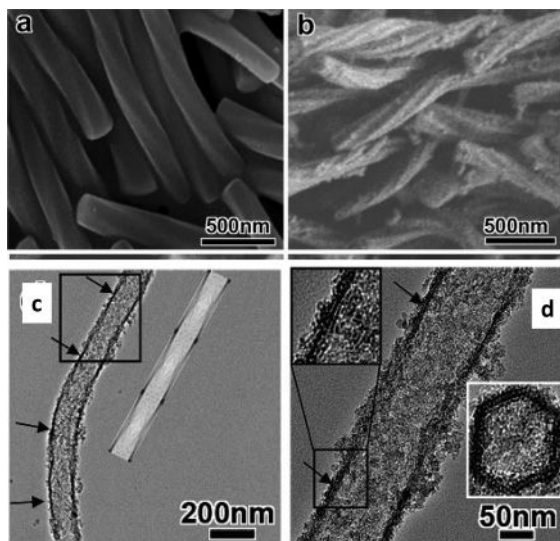
$\text{SiO}_2$  nanotubes are readily prepared by using a variety of templates wherein the templates are coated with the oxide precursor followed by hydrolysis and heat treatment. Besides carbon nanotubes, carbon nanofibres have been used as templates to obtain  $\text{SiO}_2$  nanotubes. The same method is also applicable for the synthesis of  $\text{ZrO}_2$  and  $\text{Al}_2\text{O}_3$  nanotubes [74]. Peptide amphiphile (PA) nanofibres have been successfully used as templates. The catalytic activities of PAs that contain lysine, histidine, or glutamic acid have been compared and only the PAs that contain lysine or histidine found to be good as catalytic templates. Depending on the reaction conditions and the size of the PA assembler, the nanotube wall thickness can be varied between 5–9 nm [75]. Self-assembled peptidic lipids that form tubular structures are also used as templates to prepare silica nanotubes [76]. The use of self-assembled structures as templates for preparing silica nanotubes and other nanostructured oxides generally involves the coating of the super-structure with metal alkoxides, sol–gel condensation, and the removal of the templates. This template method has been used to prepare nanotubes of silica and other materials using organogelators including those that are fluorinated [77].

Thermal evaporation of  $\text{SiO}$  yields  $\text{SiO}_2$  nanotubes [78]. This in-situ template-like process (carried out in the presence of GaN and ZnS) in a vertical induction furnace gives amorphous  $\text{SiO}_2$  nanotubes wherein both the diameters and lengths can be tuned by changing the reaction temperature. The  $\text{SiO}_2$  nanotubes are amorphous, with a diameter of 30 nm and length of several hundred micrometers at 1450 °C, change to a diameter of 100 nm and length of 2–10 micrometers at 1300 °C. At high reaction temperatures, GaN decomposes to give Ga and the

newly formed Ga is in the form of small-sized liquid clusters. The Ga clusters are transported by the Ar gas to the low temperature region, where they deposit as liquid droplets on the inner walls of the graphite crucible. The Ga droplets are the favored sites for the adsorption of ZnS vapor generated in the system. On supersaturation, ZnS segregates and gives rise to ZnS nanowires. With an increase in temperature, the decomposition of the SiO results in the formation of Si vapor, which is oxidized by the residual O<sub>2</sub> to SiO<sub>2</sub>. This is transported by the Ar gas and is deposited on the surface of the ZnS nanowires, which results in ZnS/SiO<sub>2</sub> hetero-nanowires. Because of the high temperature, the inner ZnS nanowires evaporate, and hollow SiO<sub>2</sub> nanotubes remain. This method can also be used for nanotubes of other inorganic nanomaterials such as ZnS and GaN. CdSe nanocrystals are used as seeds in a one-step thermal evaporation process to prepare long, high density SiO<sub>2</sub> nanotubes [79]. SiO<sub>2</sub> nanotubes generally have smooth surfaces, uniform thickness, and round cross sections of both the interiors and exteriors which are amorphous in nature. The nanotubes are open-ended and have diameters of about 80–110 nm and a length of several hundreds of micrometers. High purity SiO<sub>2</sub> nanotubes are obtained by using track-etched membrane templates that involve O<sub>2</sub> plasma treatment. Oxygen plasma pre-treatment ensures pore-filling of the precursor solution and covalent bonding between template and precursor, while pyrolysis of the template–nanostructure composite completely removes organics and produces inorganic nanostructures [80]. These nanotubes are also amorphous and have diameters of 100 nm and lengths of 2–6 micrometers.

Hybrid SiO<sub>2</sub> nanotubes with walls that contain chiral aromatic rings are obtained by using self-assemblies of appropriate amphiphiles [81]. Mesoporous SiO<sub>2</sub> nanotubes with helical channels have been prepared by the self-assembly of surfactants in the presence of chiral molecules [82]. These are formed by the self-assembly of the achiral surfactant sodium dodecyl sulfate (SDS) in the presence of (*R*)-(+)- and (*S*)-(–)-2-amino-3-phenylpropan-1-ol (APP) (Fig. 6.10). TEM combined with computer simulations confirm the presence of ordered chiral channels winding around the central axis of the tubes with an inner diameter of 100 nm.

Double-walled silica nanotubes have been obtained by biomimetic synthesis under mild conditions. Pouget *et al.* [83]. use the peptide lanreotide in which the silica phase and the lanreotide nanotube grow synergistically in a concerted manner by mutually neutralizing their charges (positive on the lanreotide and negative on on the silica) (Fig. 6.11). This requires kinetic coupling of the two chemical processes. The presence of an X-ray diffraction peak at 0.35 Å<sup>-1</sup>, characteristic of the β-sheet organization in the lanreotide wall surface, gives a mean diameter of 24.6 nm. The walls of the tubes are separated by 2 nm, which corresponds to the thickness of the lanreotide tube. The walls of the silica tubes are thin (1.4 nm) with lengths up to 3 μm, in agreement with the TEM data shown in Figure 6.11. Calcination at 600 °C converts hybrid organic–inorganic nanostructures into pure silica double-walled nanotubes. A dynamic template mechanism can explain these results. Silica deposition occurs on both sides of the lanreotide molecule, and stops immediately after neutralization of the surface charge. This



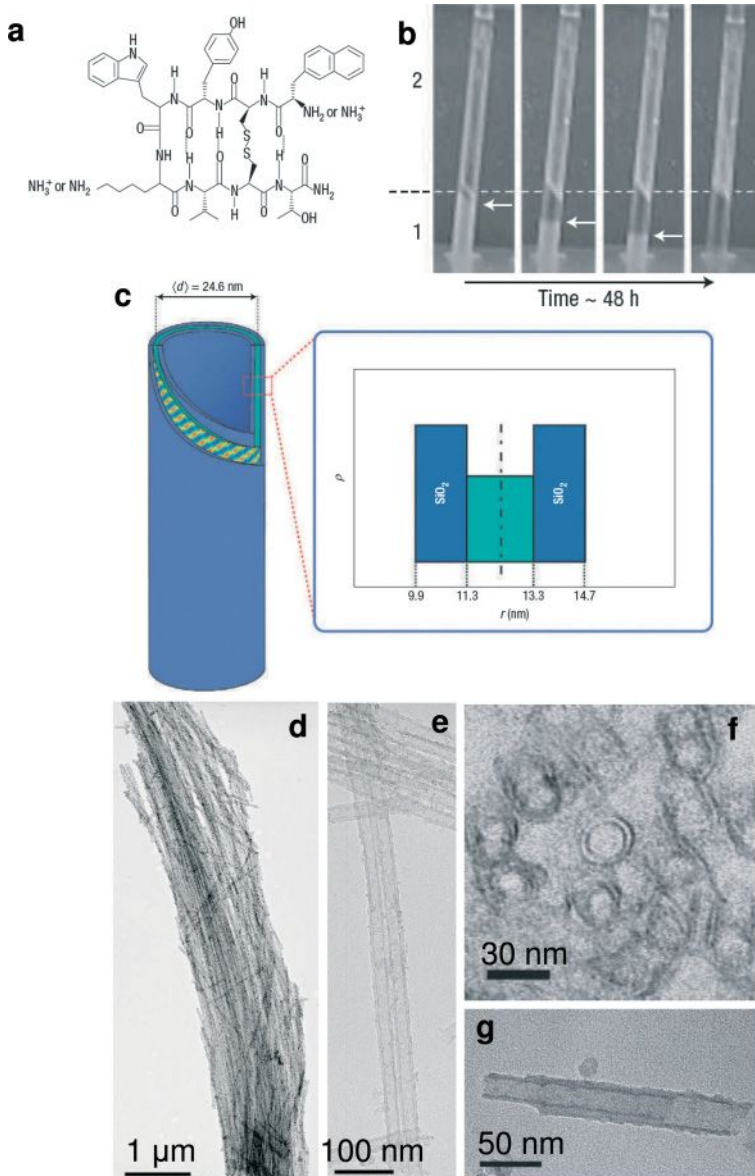
**Figure 6.10** a,b) SEM images of calcined silica nanotubes with chiral mesoporous wall structure synthesized with different (*R*)-(+)-APP/SDS molar ratios of 0 and 0.2, respectively. These materials were synthesized at 30 °C for 6 h and then allowed to age for 1 day at 90 °C. c) Low and d) high magnification TEM images of calcined samples. Reproduced with permission from [82]. Copyright 2007, ACS.

is a well-controlled process and yields a hierarchical structure from the nanometer-scale to the macroscopic level. The double-walled silica tubes form bundles 1–3  $\mu\text{m}$  in length, and bundles of closely packed aligned nanotubes as much as a centimetre long. Shape-coded  $\text{SiO}_2$  nanotubes are obtained by using porous alumina along with the sol–gel method [84]. The template synthesis of shape-coded nanotubes begins with the fabrication of a porous alumina film that contains well-defined cylindrical pores with two or more different diameter segments created by multistep anodization of the aluminum substrate. The nanotubes are fabricated with a surface sol–gel method that controls the wall thickness at a single-nanometer level. Amorphous silica nanotubes seeded by copper sulfide nanoparticles have been synthesized by using a supercritical organic solvent [85]. Addition of copper sulfide nanocrystals, monophenylsilane, and small amounts of water and oxygen to supercritical toluene at 500 °C at 10.3 MPa yields silica nanotubes.

### 6.5.2

#### **TiO<sub>2</sub> Nanotubes**

Amongst the nanotubes of various metal oxides, those of  $\text{TiO}_2$  have been investigated most widely.  $\text{TiO}_2$  nanotubes can be prepared hydrothermally, by anodization of titanium by template-assisted growth as well as seeded growth. Porous alumina templates are specially useful for fabricating dense, uniform, aligned



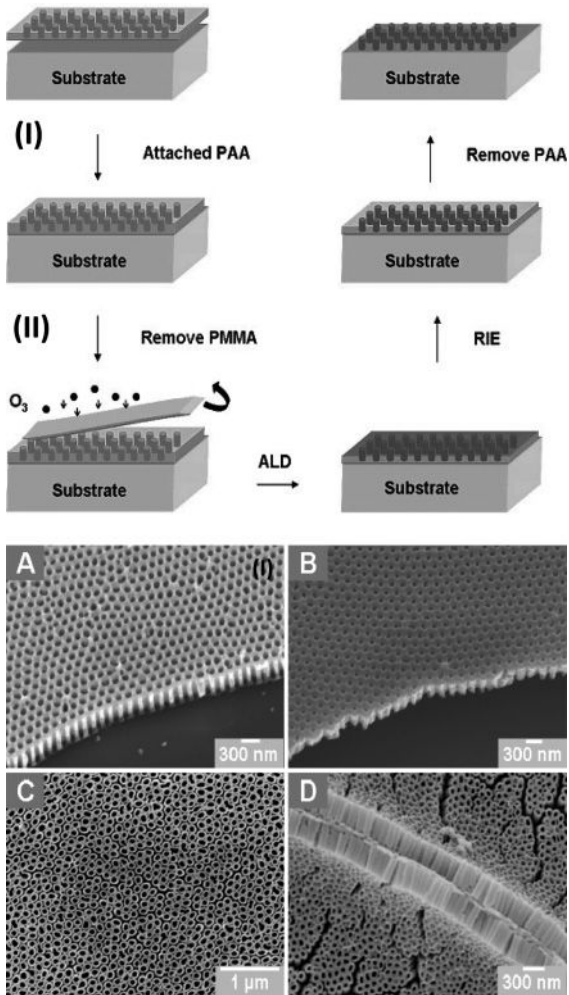
**Figure 6.11** Silica mineralization of lanreotide: a) Structure of the lanreotide octapeptide showing the two charged amine sites. b) Time-lapsed pictures of the capillaries during the mineralization process. Initially, a volume of lanreotide gel at 5% (w/w) poured into the bottom of the capillary (region 1) and is covered with the same volume of a 30% (w/w) TEOS/water mixture (region 2) (tube 1). On ageing, the lanreotide turbid gel recedes (white arrows), to yield a transparent region, while long white fibres appear in region 2, starting from the interface (tubes 2 and 3). After 48 h, the lanreotide gel has completely disappeared and only two phases separated by a white ring are observed: the lower clear one containing a dilute lanreotide solution and the upper one filled with mineralized fibres (tube 4). c) Schematic representation of a multi-scale organization of a silica-lanreotide nanotube with an inner and an outer 1.4 nm thick silica shell and a central 2.0 nm thick lanreotide tube as deduced from radial density ( $\rho$ ) profiles. d) TEM image of double-walled silica nanotube replica obtained after the calcination of silica-lanreotide nanotubes. e) TEM image of a 7  $\mu\text{m}$  long bundle of dried mineralized nanotubes. f) Cross-sectional TEM image of dried fibres, revealing several concentric circles attributable to the double-wall structure. g) TEM image of a fragment of dried nanotube, showing that the internal and external cylinders are independent and free to slide. Reproduced with permission from [83]. Copyright 2007, Nature Publishing Group.



arrays of TiO<sub>2</sub> nanotubes on substrates such as glass, silicon, and polymers. Free-standing porous alumina templates have been employed for atomic layer deposition (ALD) of ordered TiO<sub>2</sub> nanotube arrays on various substrates (Fig. 6.12) [86]. The diameter and length of the nanotubes, as well as the distance between two neighboring nanotubes, can be controlled by varying the dimensions of the template and the anodization conditions. Typically, hexagonally packed pores with a diameter of ~65 nm and interpore distance of ~110 nm are used. The synthesis of highly ordered arrays of TiO<sub>2</sub> nanotubes by potentiostatic anodization of Ti has been reviewed by Grimes [87]. This appears to be an excellent method wherein anodic oxidation is carried out in a dimethyl sulphoxide (DMSO) medium that contains hydrofluoric acid, potassium fluoride, or ammonium fluoride as the electrolyte [88]. Self-aligned, hexagonally close packed TiO<sub>2</sub> nanotube arrays, 1000 μm in length with high aspect ratios (~10 000) are obtained by the anodization of titanium. These are polycrystalline in the anatase structure after annealing in oxygen at 280 °C for 1 h. Such nanotubes can be transformed into self-standing membranes [89].

The formation of TiO<sub>2</sub> membranes by the anodization of Ti foil in fluorine-containing ethylene glycol has been described [90]. This method yields self-organized, free-standing TiO<sub>2</sub> nanotube arrays with ultra-high aspect ratio of the diameter/length (~1500) by simply using solvent-evaporation-induced delamination of the TiO<sub>2</sub> barrier layer formed between the TiO<sub>2</sub> membrane and Ti foil during anodization. The resulting membrane consists of highly ordered, vertically aligned, one-side open TiO<sub>2</sub> nanotube arrays with pore diameter, wall thickness, and length of around 90 nm, 15 nm, and 135 μm, respectively. The as-grown TiO<sub>2</sub> nanotubes are amorphous and transform into the anatase structure after annealing at high temperature in air. Aligned TiO<sub>2</sub> nanotubes with novel morphologies, such as bamboo-type reinforced nanotubes and 2D nanolace sheets, obtained by an anodization process carried out under alternating-voltage conditions in fluoride-containing electrolytes, have been reported [91]. The experiment was carried out under constant voltage conditions, and after 2 h of anodization at 120 V in an electrolyte that consists of 0.2 mol L<sup>-1</sup> HF in ethylene glycol, yielded a regular layer of aligned, individual TiO<sub>2</sub> nanotubes with thickness of about 10 μm and diameter of 150 nm. If the voltage is lowered to 40 V, the growth of the nanotubes slows down and may even stop. A bamboo-type structure can be grown under certain conditions (i.e., when the voltage is alternated between 120 and 40 V). The spacing between the bamboo rings can be altered by means of changing the time for which the sample is held at 120 V, and spacing is reduced from 200 to 70 nm by reducing the holding time. If anodization takes place for a long time at a low voltage, nanotubular features with a reduced diameter start to grow. This can be exploited to grow a double-layer structure. In this case, branching of the main tube with a diameter of 150 nm into several (typically 2–3) smaller tubes of about 50 nm in diameter occurs. The structures can be transformed to the anatase structure without losing structural integrity by annealing in air at 450 °C. Anodization under constant-voltage conditions leads to an ordered layer that consists of smooth tubes with a defined cylindrical or hexagonal cross section [92, 93]. Fluoride-free aqueous





**Figure 6.12** I) Schematic of the process to fabricate highly ordered  $\text{TiO}_2$  nanotube arrays on substrates using ALD on a free-standing porous alumina template. Free-standing AM supported with a poly(methyl methacrylate) (PMMA) layer was first attached onto the substrate. The PMMA was then removed for ALD on the AM template. Substrates were alternatively exposed to  $\text{TiCl}_4$  and water vapor for ALD at a pressure of  $1 \times 10^{-3}$  Torr. The  $\text{TiO}_2$  overlayer was etched by RIE, and finally highly ordered ALD  $\text{TiO}_2$  nanotube arrays were

released from the AM template. II) Dense, uniform, highly ordered, and well-aligned ALD  $\text{TiO}_2$  nanotube arrays on Si and a flexible polyimide film. SEM images of a highly ordered free-standing AM template ( $\sim 300$  nm) attached on Si before (A) and after (B) 150-cycle  $\text{TiO}_2$  ALD. C) Highly ordered  $\text{TiO}_2$  nanotube arrays released from the template on the Si substrate. D) Cross-section of well-aligned  $\text{TiO}_2$  nanotube arrays on a bending polyimide film. Reproduced with permission from [86]. Copyright 2008, ACS.

HCl electrolyte is also used to obtain vertically oriented TiO<sub>2</sub> nanotube arrays [94]. These nanotube arrays, obtained by using a 3 M HCl aqueous electrolyte with an anodization potential of 20 V, have an inner pore diameter of 15 nm, wall thickness of 10 nm, and length up to 600 nm. The nanotubes are polycrystalline and have an anatase structure, with a rutile barrier layer separating the tubes from the underlying metal foil.

Sulfur-doped TiO<sub>2</sub> nanotubular arrays are obtained by potentiostatic anodization of Ti foils followed by the annealing of TiO<sub>2</sub> tubular arrays in a flow of H<sub>2</sub>S at 380 °C [95]. Ordered, vertically oriented B-doped TiO<sub>2</sub> nanotube arrays are prepared by forming a nanotube-like TiO<sub>2</sub> film in the anodization process on a Ti sheet followed by CVD treatment with trimethylborate vapor [96]. A double-template-assisted sol-gel method has been used to prepare TiO<sub>2</sub> nanotube arrays with nanopores on their walls [97]. In this method, poly(ethylene glycol) dissolved in a TiO<sub>2</sub> sol is used as a soft template to form nanopores on the walls of TiO<sub>2</sub> nanotube arrays, which were templated from ZnO nanorod hard templates by the dip-coating technique. The microstructure of nanoporous TiO<sub>2</sub> nanotube arrays can change from end-opened to end-closed by increasing the number of dip-coating cycles.

Gas-phase ALD of metal oxides in combination with a micro-contact printing ( $\mu$ -CP) technique has been used to attain precise atomic-level control over the dimensions (wall thickness) of nanotubes as well as the one-step fabrication of the free-standing oxide nanotubes [98]. In this procedure, octadecyltrichlorosilane (OTS) molecules were transferred onto both sides of the surfaces of the template by the  $\mu$ -CP technique and self-assembled monolayers (SAMs) formed on the surfaces, thus exposing chemically inert methyl surfaces. The ALD process allows atomic-level control over the thickness of the wall of the nanotubes, and the OTS self-assembled mono-layers function as resistant layers to materials deposition, thus allowing free-standing cylindrical nanotubes to be collected after dissolution of the template without an additional polishing step. This method has been used to obtain high aspect ratio (~300) nanotubes of TiO<sub>2</sub>, ZrO<sub>2</sub>, and Al<sub>2</sub>O<sub>3</sub>. Crystalline and homogeneous CeO<sub>2</sub> nanoparticles have been used as seeds to grow TiO<sub>2</sub> nanotubes from the hydrolysis of aqueous titanium sulfate solution [99]. Layer-by-layer deposition of a water-soluble titania precursor (titanium(IV) bis(ammonium lactato) dihydroxide, along with the oppositely charged poly(ethylenimine) gives rise to multilayer films. The tubular structure is obtained by depositing inside the cylindrical pores of a polycarbonate membrane followed by calcination [100]. Nanotubular TiO<sub>2</sub> can be obtained by using uncharged or negatively charged L-lysine-based organic gelators as templates [101]. By heating nanotubes of titanic acid (obtained by heating P25-TiO<sub>2</sub> (Degussa) with an NaOH solution at 110 °C) in ammonia, N-doped TiO<sub>2</sub> nanotubes with an anatase structure are obtained [102].

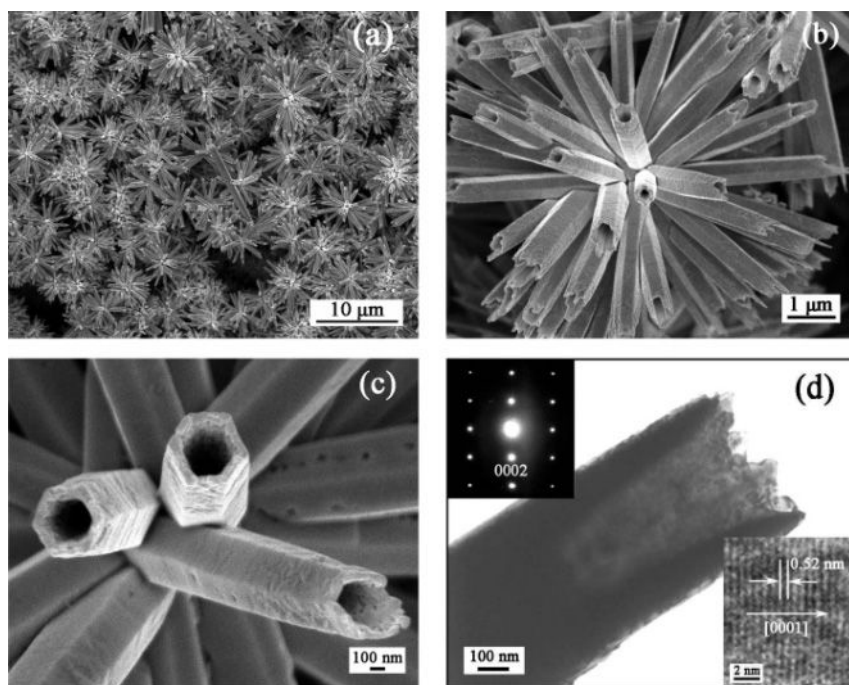
The use of carbon nanotubes to obtain oxide nanotubes is well documented [103, 104]. This method has been used to obtain pure rutile nanotubes [105]. The method involves coating of the carbon nanotubes with amorphous titania through a sol-gel process followed by heating in air to convert titania into anatase. Further heating in nitrogen transforms the anatase predominantly to rutile and finally

heating in air again at a higher temperature removes the carbon nanotubes and transforms the remaining anatase to rutile. Brookite-type  $\text{TiO}_2$  nanotubes are obtained by heating titanate nanotubes obtained by the reaction of  $\text{TiO}_2$  powder with  $\text{NaOH}$  solution, followed by hydrothermal treatment [106]. Transparent thin films of titanate nanotube arrays with super-hydrophilic characteristics are grown on sapphire substrates by the hydrothermal reaction of sputter-deposited Ti films in an aqueous  $\text{NaOH}$  solution [107].

### 6.5.3

#### ZnO, CdO, and $\text{Al}_2\text{O}_3$ Nanotubes

ZnO nanotubes have been prepared by CVD and thermal evaporation, as well as by hydrothermal and solution methods. For example, large-scale ZnO nanotube bundles have been synthesized by a simple wet chemical approach (Fig. 6.13) [108]. In this method, an aqueous solution of  $\text{Zn}(\text{NO}_3)_2$  and hexamethylenetetramine is stirred over long periods and heated at  $90^\circ\text{C}$ . This method yields nanotubes with an inner diameter of  $\sim 350$  nm and a wall thickness of  $\sim 60$  nm, and forms radiating



**Figure 6.13** Morphological and structural characterization of ZnO nanotube bundles: a,b) Low-magnification FE-SEM images. c) High-magnification FE-SEM image. d) TEM image. The upper left and lower right inset

images of (d) are the SAED pattern and the high-resolution transmission electron microscopy (HRTEM) image of a single nanotube, respectively. Reproduced with permission from [108]. Copyright 2007, ACS.

structures. These ZnO nanotubes are single crystalline in nature, having the wurtzite structure, and preferentially grow along the [0001] direction. High aspect ratio nanotubes are obtained by a three-step low temperature process that involves ionic layer absorption, deposition of the ZnO seed layer, followed by hydrothermal annealing of the seed layer and deposition of the 1D ZnO nanostructures [109]. The uniform ZnO nanotubes have a single-crystalline wurtzite structure with lengths that exceed 10  $\mu\text{m}$  and diameters of around 27 nm. By hydrothermal annealing, ZnO nanotubes grown along the  $\langle 001 \rangle$  direction have been obtained [109]. Nanotube-based paint-brush structures of ZnO have been prepared on Zn foils by solvothermal means by adjusting the pH of the solution [110].

Electrochemical deposition from aqueous solution into porous alumina membranes can be employed to prepare ZnO nanotube arrays [111]. Single-crystalline ZnO nanotube arrays with an hexagonal wurtzite structure have been generated on glass substrates by a two-step solution approach [112]. The method involves the electrodeposition of oriented ZnO nanorods and subsequent coordination-assisted selective dissolution along the  $c$ -axis to form tubular structures caused by the preferential adsorption of ethylenediamine (EDA) and  $\text{OH}^-$  on different crystal faces. After dissolution in aqueous EDA solution for 10–15 h, the inner/outer wall surfaces of the ZnO nanotubes become smooth with a wall thickness of  $\sim 10$ –30 nm.

Reaction of  $\text{Zn}(\text{NO}_3)_2$  with methenamine in aqueous medium under hydrothermal conditions gives rise to ZnO nanotubes [113]. These nanotubes are hollow with rough surfaces, which indicates a layer-stack structure. The ZnO nanotubes have an hexagonal wurtzite structure with lengths in the range of 1–3  $\mu\text{m}$  and wall thickness in the 50–100 nm range. The cross section is hexagonally faceted, which provides strong evidence that the single nanotube grows along the  $c$ -axis direction. ZnO nanotube structures have been obtained by the hydrothermal self-assembly of zinc ions at the interface of surfactants, such as cetyltrimethylammonium bromide (CTAB) and the triblock copolymer of poly(ethylene oxide)–poly(propylene oxide)–poly(ethylene oxide) (P123) [114]. These molecules are suitable for the assembly of layered zinc species–surfactant hybrids that can be exfoliated into intermediate single sheets that roll to form tubular ZnO nanostructures because of the heat stress and the crystallization of ZnO sheets. The size of the tubular ZnO is determined by the type of surfactants, the concentration of the surfactant, and the Zn species/surfactant molar ratio. Tubular products can be obtained at a relatively high  $\text{Zn}^{2+}$ /surfactant molar ratio as the concentrations of CTAB and P123 are higher than their critical micelle concentrations. The hydrophobic side of each surfactant layer is connected through a weak bond, which gives rise to an organic layer, while the hydrophilic side of each surfactant layer adsorbs metal ions or hydrates, to form an inorganic layer. Dehydration and crystallization of amorphous inorganic layers cause the volume to shrink and results in stress in the inorganic layers, and breaks the equilibrium between the organic and the inorganic layers. Crystallography of these ZnO nanotubes is determined by how the nanosheets exfoliate and roll. The large cylindrical ZnO nanotubes have diameters ranging from 200 to 400 nm (wall thickness, 80 nm) with lengths going up to 14  $\mu\text{m}$ . The

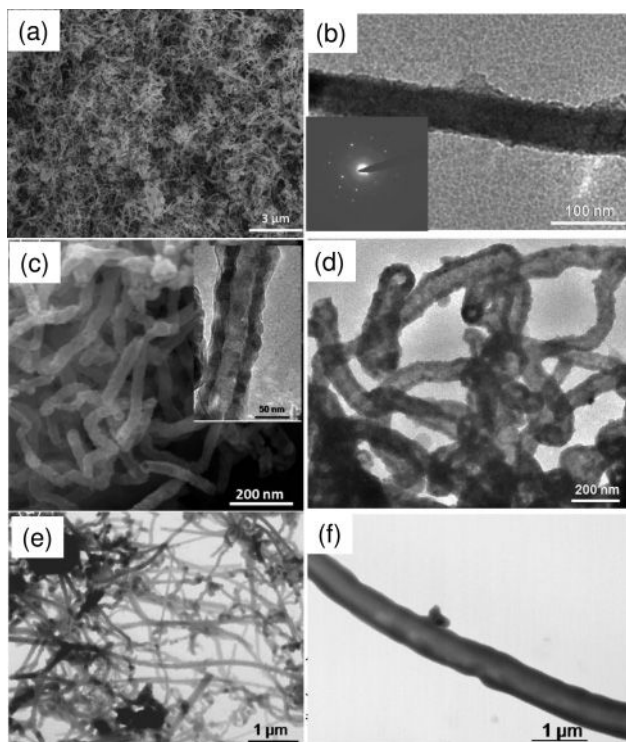
nanotubes are single-crystalline and possess a wurtzite structure. With an increase in the amount of  $\text{Zn}(\text{CH}_3\text{COO})_2 \cdot 2\text{H}_2\text{O}$ , middle-size ZnO nanotubes with diameters in the range from 40 to 70 nm and lengths up to 550 nm are obtained. The inner diameter of these nanotubes varies from 14 to 30 nm.

ZnO nanotubes with nanometer-scaled holes on the side-walls are obtained by a low-temperature hydrothermal procedure based on a preferential etching strategy [115]. The procedure is as follows. By a two-step heating of a solution mixture of  $\text{ZnCl}_2$  and ammonia hydrothermally, nanotubes of nearly homogeneous size with ~250 nm diameter, 40 nm wall thickness, and 500 nm length are formed. The first stage involves the transformation of the precursor  $\text{Zn}(\text{NH}_3)_4^{2+}$  to ZnO through hydrothermal decomposition at 95 °C, which leads to the formation of single crystal ZnO nanorods. At the same time, ZnO dissolves as the equilibrium moves to the left. The growth of ZnO rods becomes dominant since the high concentration of  $\text{Zn}(\text{NH}_3)_4^{2+}$  favors the precipitation of ZnO. As the temperature goes down (95 to 75 °C), along with the partial consumption of the  $\text{Zn}(\text{NH}_3)_4^{2+}$ , etching of the ZnO nanorods occurs. Formation of porous ZnO nanotubes with nanoholes, which are single crystalline with a wurtzite structure, result from the preferential etching along the *c*-axis and slow etching along the radial directions. Nanoholes are created on the side-walls of the tubular structure. ZnO nanotubes have been assembled into microsphere superstructures by employing a mixture of poly(ethylene glycol) (PEG), ethanol, and water [116]. Addition of metallic zinc species into the solution mixture leads to aggregation of the PEG polymer coils to  $\text{Zn}^{\text{II}}$ /PEG globules with a diameter of ~500 nm. The globules turn into tube-like-structured ZnO–PEG microsphere assemblies (~2 mm) after ultrasonic pretreatment.

ZnO nanotubes are also produced by the oxidation of Zn nanowires because of the Kirkendall effect. This effect has also been used to produce nanotubes of  $\text{SiO}_2$ ,  $\text{Co}_3\text{O}_4$ , and  $\text{ZnCr}_2\text{O}_4$  as well as of ZnS, CdS, and CdSe (Fig. 6.14) [117]. It is observed that there is a distribution in the diameters of the nanotubes just as in the case of the diameters of the starting nanowires. The Zn nanowires possess a smooth surface with an average diameter of 50 nm and lengths of several tens of micrometers with a zig-zag morphology. The ZnO nanotubes formed from the thermal oxidation of the Zn nanowires have an outer diameter that goes up to 90 nm with lengths that vary from 400 nm to a few micrometers. The ZnO nanotubes have a wall thickness of around 20 nm and an inner diameter close to the diameter of the starting metal nanowires.

CdO nanotubes with a mean diameter of 50 nm have been obtained by the thermal evaporation of Cd powder without using any catalyst or template [118]. The CdO nanotubes are single-crystalline with a cubic structure and have diameters of around 40–65 nm, a wall thickness of around 15 nm, and lengths of over a few tens of micrometers. Some of the nanotubes appear straight in morphology, while others are twisted with some straight parts.

Well-defined uniform  $\text{Al}_2\text{O}_3$  nanotubes are obtained by the pulse anodization of aluminium in  $\text{H}_2\text{SO}_4$  solution [119]. Periodic galvanic pulses were employed to achieve mild and hard anodization (HA) conditions, where the pulse duration for

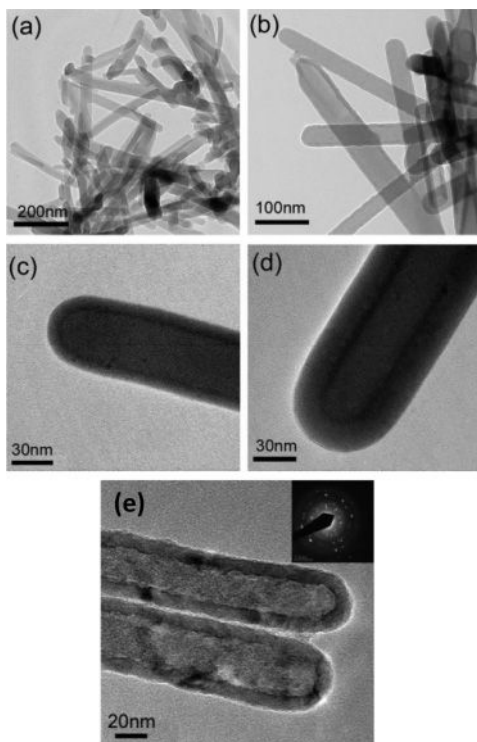


**Figure 6.14** Nanowire–nanotube transformation as a result of the Kirkendall effect: a) Low-magnification FESEM images of Zn nanowires. b) TEM image of a Zn nanowire (the inset is the SAED pattern). c) FESEM image of ZnO nanotubes (inset

shows the TEM image of a ZnO nanotube). d) TEM image of ZnS nanotubes. e, f) Scanning transmission electron microscope images of Si nanowires and SiO<sub>2</sub> nanotubes, respectively. Reproduced with permission from [117]. Copyright 2008, ACS.

HA determines the length of nanotubes. By properly choosing the pulse parameters, continuous tailoring of the pore structure of the resulting nanoporous anodic alumina (i.e., periodic modulation of pore diameters along the pore axis) is achieved. This also enables weakening of the junction strength between cells, thereby helping in the separation of individual alumina nanotubes from the porous anodic alumina. The average inner and outer diameter of the nanotubes is estimated to be 80 and 95 nm, respectively, with lengths of up to several tens of micrometers. The inner diameter of the alumina nanotubes can be controlled by varying the etching time of the pore walls by using an appropriate etching solution (e.g., H<sub>3</sub>PO<sub>4</sub>). Aluminium oxide nanotubes have been fabricated by using tris(8-hydroxyquinoline) gallium organic nanowires (GaQ<sub>3</sub>) as soft templates to coat alumina using ALD [120]. By dissolving the template in toluene or by heat treatment, alumina nanotubes are prepared, where the alumina shell thickness is controlled by the number of precursor/purge cycles (Fig. 6.15).





**Figure 6.15** TEM images of a)  $\text{GaQ}_3$  nanowires prepared by thermal evaporation. b,c)  $\text{GaQ}_3\text{-Al}_2\text{O}_3$  core-shell nanowires fabricated by 100 cycles of ALD, and (d) same as (c), after 200 cycles of ALD. e) TEM image of the alumina nanotubes after heat treatment at  $900^\circ\text{C}$  for 1 h. The inset shows the electron diffraction pattern of alumina. Reproduced with permission from [120]. Copyright 2007, ACS.

#### 6.5.4

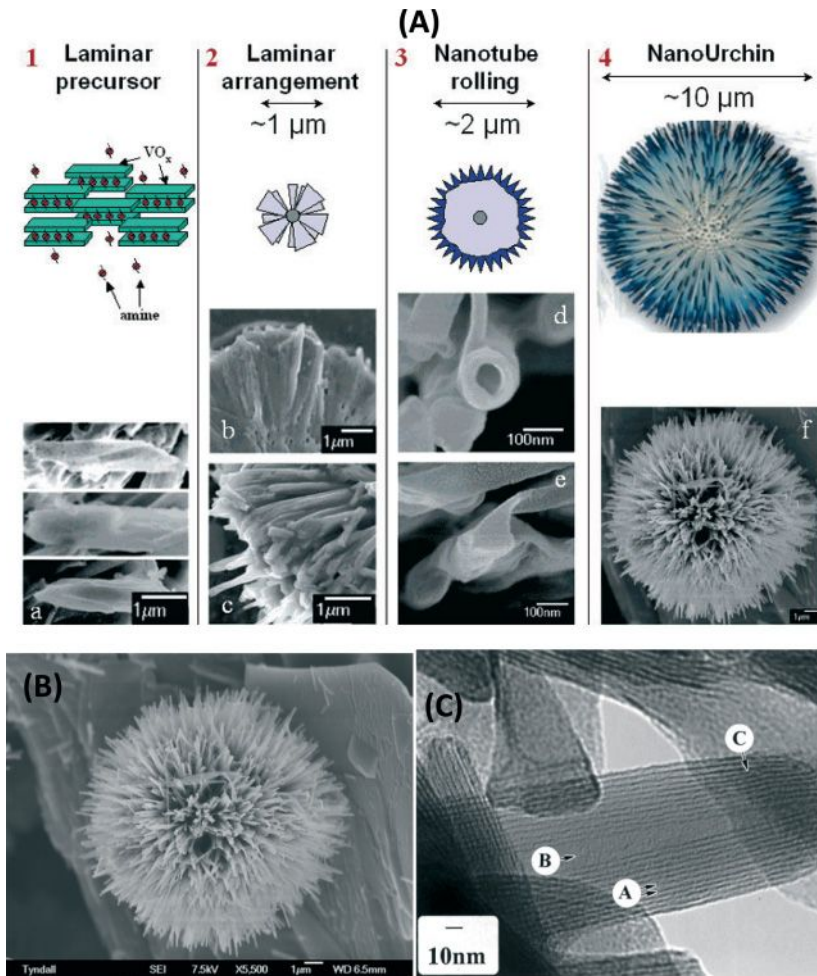
#### Nanotubes of Vanadium and Niobium Oxides

Vanadium oxides have received considerable attention because of their structural flexibility and useful catalytic, electrochemical, and other properties. The structure of  $\text{V}_2\text{O}_5$  permits the intercalation of various cationic species in the interlamellar space [121]. The cations include alkylammonium ions, which are readily intercalated between the layers under hydrothermal conditions [122]. This system is thus analogous to graphite and layered dichalcogenides. Nesper and coworkers [123, 124] synthesized nanotubules of alkylammonium intercalated  $\text{VO}_x$  by hydrothermal means. The vanadium alkoxide precursor was hydrolyzed in the presence of hexadecylamine and the hydrolysis product (lamellar structured composite of the

surfactant and the vanadium oxide) yielded  $\text{VO}_x$  nanotubes along with the intercalated amine under hydrothermal conditions. Vanadium in these materials is in the mixed-valent state, and is redox active. The template cannot be removed by calcination as the structural stability is lost above 523 K. It is possible to partially extract the surfactant under mild acidic conditions. Nesper *et al.* have shown that the alkylamine intercalated in the intertubular space could be exchanged with other alkylamines of varying chain lengths as well as  $\alpha,\omega$ -diamines [124]. Such mixed valent  $\text{VO}_x$  nanotubes are also obtained under hydrothermal conditions using  $\text{V}_2\text{O}_5$  and 3-phenylpropylamine [125]. Most of the  $\text{VO}_x$  nanotubes obtained by the hydrothermal method are open ended. Very few closed tubes had flat or pointed conical tips. Cross-sectional TEM images of the nanotubular phases show that instead of concentric cylinders (i.e., layers that fold and close within themselves), the tubes are made up of single or double layer scrolls that provide a serpentine-like morphology [124, 126]. Non-symmetric fringe patterns in the tube walls exemplify that most of the nanotubes are not rotationally symmetric and carry depressions and holes in the walls. Diamine-intercalated  $\text{VO}_x$  nanotubes are multilayer scrolls with narrow cores and thick walls, composed of vanadium oxide layers. Diamine-containing  $\text{VO}_x$  nanotubes show a smaller number of holes in the wall structure and the tubes are well ordered with uniform distances throughout the tube length [124]. The scroll-like structures of  $\text{VO}_x$  are not real nanotubes of the type formed by carbon or metal dichalcogenides. Vanadium oxide nanotubes that contain primary monoamines with long alkyl chains have been prepared by employing non-alkoxide vanadium precursors such as  $\text{VOCl}_3$  and  $\text{V}_2\text{O}_5$ . The amine complexes of the vanadium precursors are then hydrolyzed. Hydrothermal treatment of the precursors gives good yields of  $\text{VO}_x$  nanotubes that incorporate the amines [127]. In general the inner diameter varies between 15 and 50 nm in the  $\text{VO}_x$  nanotubes, independent of the precursor. The outer diameters are similar, generally between 50 and 150 nm, with a range of tube lengths. Starting from the alkoxides, the tube length varies from 1 to 15  $\mu\text{m}$ . In the samples obtained starting with  $\text{VOCl}_3$  and  $\text{V}_2\text{O}_5$ , the average length of the tubes is shorter (1–3  $\mu\text{m}$ ). The distribution of the number of layers is similar in all the nanotubes, generally between 6 and 15 layers. The layers are preformed in the lamellar phase and roll up during the autoclave treatment, because the tetragonal structure of the layers gives rise to a more or less square-shaped growth. However, since many scrolls consist of multiple independent layers and the maximum length approaches 15  $\mu\text{m}$ , growth along the tube axis may occur as well. Mn–V oxides have been prepared by mixing  $\text{V}_2\text{O}_5$  with dodecylamine in the presence of ethanol and water. The amine templates are easily substituted or ion-exchanged with ions like  $\text{Mn}^{2+}$  in an aqueous alcohol solution to yield Mn–V–O nanotubes [128]. Most of the nanotubes had open ends, while some of them had closed ends, with the side of the tubes wrapped around the end to close it. The  $\text{Mn}^{2+}$  ions replace the organic cations in the structures and hence are intercalated in between the layers.

Arrays of  $\text{V}_2\text{O}_5 \cdot n\text{H}_2\text{O}$  nanotubes with diameters of 200 nm and 5  $\mu\text{m}$  length have been fabricated by template-based physical wetting of  $\text{V}_2\text{O}_5$  sols [129]. Urchine-like





**Figure 6.16** Schematic summary of the stages of growth of  $\text{VO}_x$  nano-urchins. FESEM image of an individual nano-urchin. This fully grown nano-urchin is  $12\mu\text{m}$  in diameter and is covered in  $\text{VO}_x$  nanotubes with a volumetric density of  $\sim 40\text{sr}^{-1}$ . HRTEM image of an early stage nanotube. Lattice planes are resolved

(A) and have a measured lattice spacing  $a = 2.85\text{ nm}$ . The hollow center (B) extends to the tip of the nanotube. A lattice plane termination dislocation is also observed (C). Reproduced with permission from [130]. Copyright 2006, ACS.

nanostructures (Fig. 6.16) that consist of high-density spherical nanotube radial arrays of vanadium oxide nanocomposites, were successfully synthesized by a simple chemical route using an ethanolic solution of vanadium tri-isopropoxide and alkylamine hexadecylamine for 7 days at  $180^\circ\text{C}$  [130].  $\text{M-Nb}_2\text{O}_5$  nanotube arrays have been prepared starting from  $\text{H-Nb}_2\text{O}_5$  nanorods, taking advantage of the phase transformation accompanied by the formation of voids [131].

## 6.5.5

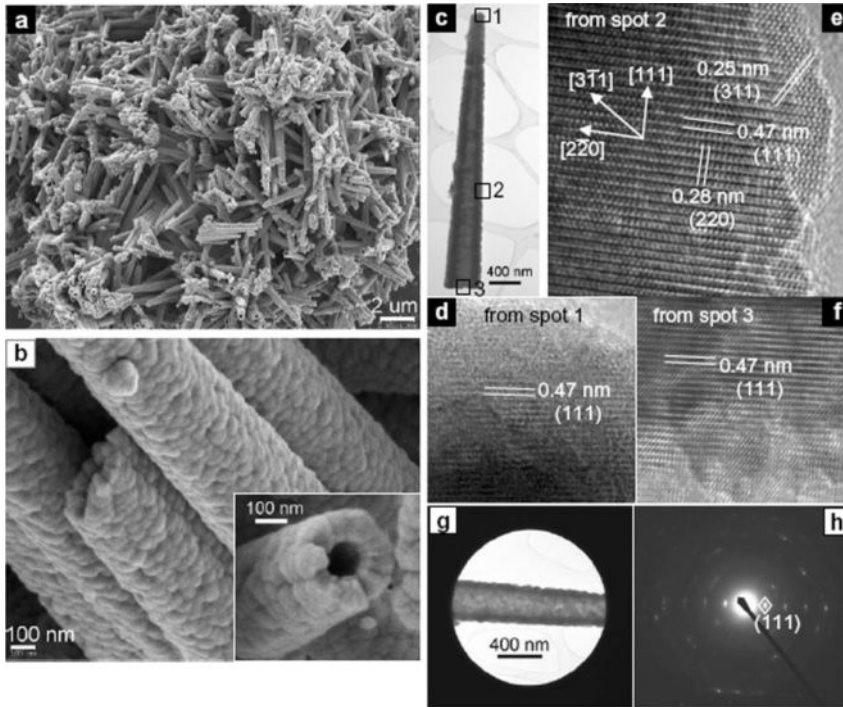
**Nanotubes of other Transition Metal Oxides**

A hydrothermal reaction of  $\text{KMnO}_4$  in HCl gives rise to  $\alpha\text{-MnO}_2$  nanotubes [132]. These  $\text{MnO}_2$  nanotubes are single-crystalline and possess a tetragonal structure, with an average outer diameter of around 100 nm. The wall thickness is 30 nm and the length goes up to several micrometers. The nanotubes show nearly perfect tetragonal cross sections, consistent with the crystal structure.

By the reaction of  $\text{FeCl}_3$  with water in the presence of polyisobutylene bis-succinimide (L113B) or the surfactant span80 as well as butanol under solvothermal conditions,  $\text{Fe}_2\text{O}_3$  nanotubes are produced [133].  $\text{Fe}_2\text{O}_3$  nanotubes (rhombohedral structure) prepared from the surfactant (span80 as the template) were tube-like with diameters of 18–29 nm, wall thickness of 3–7 nm, and lengths of 110–360 nm. They have a multi-walled structure, with an interlayer spacing of 2.76 Å.  $\alpha\text{-Fe}_2\text{O}_3$  nanotubes are also obtained by the deposition of a metal salt solution and NaOH/ $\text{NH}_3$  in the pores of templates with the initial formation of an insoluble metal hydroxide precursor, and its subsequent transformation by dehydration and crystallization to metal oxide nanotubular structures [134]. The  $\alpha\text{-Fe}_2\text{O}_3$  nanotubes so obtained are polycrystalline and have diameters and lengths of  $\sim 260 \pm 60$  nm and  $6 \pm 3$   $\mu\text{m}$ , respectively. These nanotubes possess a rhombohedral structure and consist of small mis-oriented single-crystalline nanocrystalline domains. Ordered  $\text{Fe}_2\text{O}_3$  nanotube arrays can also be prepared by ALD in an AM [135]. In this method, the thermal decomposition of a homoleptic dinuclear iron(III) *tert*-butoxide complex ( $\text{Fe}_2(\text{O}t\text{Bu})_6$ ) is carried out in the presence of water inside a self-ordered porous anodic AM to yield arrays of nanocrystalline  $\text{Fe}_2\text{O}_3$  tubes with aspect ratios up to 100. Polycarbonate membranes are used to obtain nanoparticle–nanotube arrays of  $\text{Fe}_2\text{O}_3$  by employing electrodeposition followed by calcination [136]. The arrays have lengths in the 5–6  $\mu\text{m}$  range and a diameter of  $\sim 200$  nm, which corresponds closely to the pore dimension and pore diameter, respectively, of the membrane. The open ends of the arrays demonstrate the hollow structure of the product. The nanotubes have a hexagonal structure.

Ferromagnetic  $\gamma\text{-Fe}_2\text{O}_3$  nanotubes have been synthesized by a template process with the aid of a high magnetic field [137]. These are polycrystalline, with a cubic spinel structure and lengths of about 30  $\mu\text{m}$ , a wall thickness of 20 nm, and a diameter in the 300–400 nm range.  $\alpha\text{-Fe}_2\text{O}_3$  is first formed at 500 °C by the thermal decomposition of  $\text{Fe}(\text{NO}_3)_3$  inside the template and  $\alpha\text{-Fe}_2\text{O}_3$  is then transformed into  $\gamma\text{-Fe}_2\text{O}_3$  in the presence of the high magnetic field. Porous alumina templates are also used to obtain  $\text{Fe}_3\text{O}_4$  nanotubes [138]. The hydrothermal reaction of  $\text{Fe}(\text{NO}_3)_2$  in ethanol at pH 12 gives rise to  $\alpha\text{-FeOOH}$  nanotubes [139]. The so obtained  $\alpha\text{-FeOOH}$  nanotubes were  $\sim 10$  nm in outer diameter and  $\sim 6$  nm in inner diameter. Electron microscopic images of the nanotubes clearly show the resolved interplanar spacing of about 4.18 Å, which corresponds to the spacing between the (110) planes of orthorhombic  $\alpha\text{-FeOOH}$ .

Needle-like  $\text{Co}_3\text{O}_4$  nanotubes have been prepared by employing a one-step self-supported topotactic transformation of nanoneedles of  $\beta\text{-Co}(\text{OH})_2$  (Fig. 6.17) [140].



**Figure 6.17** a,b) FE-SEM images of needle-like  $\text{Co}_3\text{O}_4$  nanotubes. The inset in (b) shows a cross-sectional view of a nanotube. c) Low-magnification TEM image of an individual needlelike  $\text{Co}_3\text{O}_4$  nanotube. d–f) HREM images taken from spots 1–3, respectively, of the nanotube shown in (c). g) TEM image showing a selected area of a  $\text{Co}_3\text{O}_4$  nanotube for electron diffraction and h) the corresponding SAED pattern. Reproduced with permission from [140]. Copyright 2008, Wiley-VCH.

The nanotubes can be as long as  $10\ \mu\text{m}$  with a variable diameter in the range of 150–400 nm. The nanotubes are cylindrical and constructed from  $\text{Co}_3\text{O}_4$  building blocks of less than 100 nm. The high-resolution (HR) TEM images in Figures 6.17d–f correspond to spots 1 to 3, respectively, of an individual nanotube (Fig. 6.17c). All show (111) lattice fringes perpendicular to the tube axis with an interplane spacing of 0.47 nm, while the two other sets of lattice fringes seen in Figure 6.17e are (220) and (311) planes, which correspond to interplanar spacings of 0.28 and 0.25 nm, respectively. On the basis of structural analysis, it is found that the tube axis is along the [111] direction with possible small mis-orientations for individual  $\text{Co}_3\text{O}_4$  nanocrystals. The quasi-single-crystallinity of the cubic  $\text{Co}_3\text{O}_4$  nanotubes is also confirmed by the SAED pattern (Fig. 6.17h) and the corresponding TEM image in Figure 6.17g.  $\text{Co}_3\text{O}_4$  nanotubes are also prepared in the pores of AM by CVD, starting with cobaltacetylacetonate [141]. These nanotubes are highly ordered with a uniform diameter in the range of 100–300 nm and lengths of up to tens of micrometers. The nanotubes are composed of cubic polycrystalline

Co<sub>3</sub>O<sub>4</sub>. Porous AMs have been used to obtain CoFe<sub>2</sub>O<sub>4</sub> nanotube arrays by employing a sol-gel procedure [142]. These nanotubes are several micrometers in length with a mean outer diameter of 50 nm, which corresponds to the diameter of the alumina pore. The wall thickness is 15 nm.

NiO nanotubes can be fabricated through a MOCVD route using an AM as the template and Ni(tta)<sub>2</sub>tmeda (Htta = 2-thenoyl-trifluoroacetone, tmeda = tetramethylenediamine) as the Ni source [143]. The nanotubes are polycrystalline and have the bunsenite structure of NiO. The length is around 1 μm, with an outer diameter of ~200 nm with a wall thickness of 20 nm. The nickel-ammine complex (Ni(NH<sub>3</sub>)<sub>x</sub><sup>2+</sup>) has also been used as a precursor to produce NiO nanotubes in an AM [144]. These NiO nanotubes are about 60 μm in length, with an outer diameter of about 200 nm and a wall thickness of 60 nm. They are polycrystalline with a face-centered cubic structure.

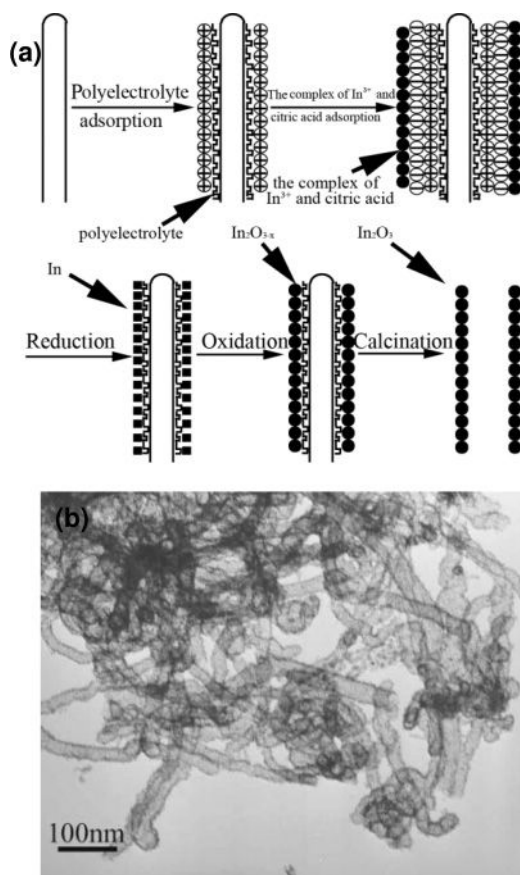
Synthesis of WO<sub>3</sub> nanotubes has been carried out by various methods, in particular starting from tungstic acid hydrate nanotubes without using any templates [145]. WO<sub>3</sub> nanotubes are obtained on slow calcination at 450 °C. The tungstic acid hydrate nanotubes obtained from the solvothermal reaction have outer diameters of 300–1000 nm and lengths of 2–20 μm. The nanotubes have a nearly rectangular pore of around 250 nm and the surface of the nanotube is not smooth. The polycrystalline nanotubes when calcined at 450 °C for 3 h, retain the open ended tubular structure and the overall dimensions of their precursor nanotubes. The nanotubes have a triclinic structure. The calcined nanotubes are free-standing and show no signs of aggregation. The annealed nanotube walls consist of individual nanoparticles arranged one-dimensionally with numerous self-supported pores, which are formed by the incomplete aggregation of nanoparticles. The sidewalls of the nanotubes are, therefore, porous. Although the diameter of the nanoparticles is approximately 40–80 nm, the nanotubes are 2–20 μm long. HR-TEM images of WO<sub>3</sub> nanotubes show that the lattice fringes of the nanocrystals have a spacing of 0.309 nm, which corresponds to the interplanar distance of the (112) plane of triclinic tungsten trioxide.

#### 6.5.6

##### Nanotubes of other Binary Oxides

MgO nanotubes can be synthesized by introducing Sn as a catalyst in the CVD process. The nanotubes are formed by the vapor-liquid-solid (VLS) mechanism [146]. MgO nanotubes can also be formed by the thermal evaporation of a mixture of Zn and Mg powders [147]. In<sub>2</sub>O<sub>3</sub> nanotubes are prepared by annealing InOOH nanotubes [148], having obtained the latter under solvothermal conditions starting with InCl<sub>3</sub> in the presence of a surfactant and formamide in anhydrous ethanol. In<sub>2</sub>O<sub>3</sub> tubular nanotubes are also generated by CVD starting with nanoporous structures of InP [149]. The In<sub>2</sub>O<sub>3</sub> nanotubes are single crystalline with a cubic structure and have outer diameters of around 200–300 nm and lengths of around 2–6 μm and retain the size and square shape of the pores. Porous In<sub>2</sub>O<sub>3</sub> nanotubes can also be prepared by layer-by-layer assembly/deposition on carbon nanotube templates followed by calcination. The layer-by-layer assembly is used to form a

polyelectrolyte on the surface of pristine nanotubes, which enhances the adsorption of the metal-complex species on the surface of the carbon nanotube as a result of electrostatic attraction between the charged species [150]. In a typical procedure, the layer-by-layer assembly is formed with a polyelectrolyte such as sodium poly(styrene sulfonate) (PSS) and poly(diallyldimethylammonium chloride) (PDDA) on the surface of pristine carbon nanotubes. A solution mixture of  $\text{InCl}_3$  and citric acid is added into the solution of the polyelectrolyte-modified carbon nanotubes. A solution of  $\text{NaBH}_4$  is added into the above-mentioned solution to reduce  $\text{In}^{3+}$  into indium, which is readily oxidized into  $\text{In}_2\text{O}_{3-x}$  because of the oxygen dissolved in the solution from the surrounding ambient air. The porous  $\text{In}_2\text{O}_3$  nanotubes are obtained by calcinations (Fig. 6.18). Thus, uniform, porous and polycrystalline  $\text{In}_2\text{O}_3$  nanotubes with diameters of 30–60 nm can be formed



**Figure 6.18** a) Schematic diagram for the growth process of  $\text{In}_2\text{O}_3$  nanotubes. b) TEM image of regular  $\text{In}_2\text{O}_3$  nanotubes prepared by the calcination of  $\text{In}_2\text{O}_3$ /polyelectrolyte/carbon nanotube nanocomposites at  $550^\circ\text{C}$  in  $\text{O}_2$  for 3 h. Reproduced with permission from [150]. Copyright 2007, Wiley-VCH.

using layer-by-layer assembly on carbon nanotube templates, followed by calcination.  $\text{In}_2\text{O}_3$  nanotubes have a cubic structure and comprise nanoparticles of about 5 nm. The wall thickness is about 9 nm. This technique can also be used for the preparation of nanotubes of other oxides such as NiO,  $\text{SnO}_2$ ,  $\text{Fe}_2\text{O}_3$ , and CuO [150].

$\text{Y}_2\text{O}_3$  nanotubes are prepared by a non-aqueous electrochemical method involving oxide transfer to  $\text{Y}^{\text{III}}$  precursors [151]. These horn-shaped nanotubes (nanohorns) with a narrow size distribution coexist with small nodular deposits. The horn-shaped structures are hollow. The diameter of these structures tapers from approximately 900 nm at the base to less than 100 nm at the tip. The nanohorns have lengths that range from 3.9 to 16.5  $\mu\text{m}$ . The thickness of the walls of the cylinder is approximately 250 nm, and the inner diameter is approximately 400 nm. These open cap structures have diameters similar to the nanohorn base diameters and are commonly observed at the initial stages of growth. A hydrothermal procedure has also been employed starting with  $\text{Y}(\text{OH})_3$  nanotubes, followed by calcination of the hydroxide [152].

The one-pot synthesis of  $\text{SnO}_2$  nanotubes has been accomplished at room temperature starting from Sn nanorods [153]. The method involves the Kirkendall effect. The  $\text{SnO}_2$  nanotubes are polycrystalline, tetragonal with diameters that range from 50 to 60 nm, and lengths from 300 to 500 nm. A 10–20 nm increase in the diameter of  $\text{SnO}_2$  nanotubes compared with that of the starting Sn nanorods is seen as a result of the outward flow of Sn during the oxidation. A solution phase synthesis of  $\text{SnO}_2$  nanotubes using surfactant-assisted micelles as templates has been reported [154]. In this method, a mixture of  $\text{SnCl}_4$  with PVP and dimethyl sulfoxide (DMSO) is refluxed in the presence of  $\text{Na}_2\text{S}$ . The nanotubes consist of nanocrystalline particles that have a face-centered cubic structure, a diameter of ~200 nm, and lengths up to a few micrometers. Electrosynthesis of  $\text{SnO}_2$  nanotubes employing the track-etched polymer polycarbonate membranes has been carried out [155]. A gold electrode modified with a porous polycarbonate membrane is immersed in an aqueous tin chloride solution. Electrochemistry is employed to control the local pH within the pores and drive the precipitation reaction. Removal of the gold and dissolution of the polymer yields 1D polycrystalline tin oxide particles. The crystallinity of the material is enhanced by annealing at 650 °C. The particles are hollow, with a wall thickness of approximately 10 nm. Nanotubes result from the continuous side-wall precipitation along a reaction front, which are polycrystalline  $\text{SnO}_2$  (rutile structure), with a diameter in the 100 nm range and a length between 0.4 and 1.4  $\mu\text{m}^2$ . Nanotubular indium-tin oxide (ITO) has been prepared by the sol-gel process using cellulose paper as a template [156].

$\text{ZrO}_2$  nanotube arrays with diameters of about 130 nm and lengths up to 190  $\mu\text{m}$  are obtained by anodizing zirconium foil in a mixture of formamide and glycerol that contains  $\text{NH}_4\text{F}$  and 3 wt% water [157]. The as-prepared  $\text{ZrO}_2$  nanotube arrays are amorphous, with the coexistence of monoclinic and tetragonal phases when annealed from 400 to 600 °C. Monoclinic zirconia nanotubes were obtained at 800 °C with retention of shape. By employing a sol-gel method and AM, yttria-stabilized  $\text{ZrO}_2$  nanotubes have been prepared [158]. The length and the diameter



of these nanotubes are 50  $\mu\text{m}$  and 200 nm, respectively, in agreement with the dimensions of the template pores. The wall thickness of the nanotubes depends on the impregnation time. The nanotubes after sintering at 800  $^{\circ}\text{C}$  are polycrystalline with a cubic structure.

Formation of  $\text{CeO}_2$  nanotubes has been reported by a few workers.  $\text{CeO}_2$  nanotubes are produced by a two-step procedure involving precipitation at 100  $^{\circ}\text{C}$  and ageing at 0  $^{\circ}\text{C}$  for 45 days [159].  $\text{CeO}_{2-x}$  nanotubes are crystalline, having a cubic fluorite structure. They tend to align the (111) planes parallel to the axis direction. The diameter of the nanotubes ranges from 5 to 30 nm, while the length goes up to several micrometers. The thickness of the wall of the nanotubes is about 5.5 nm.  $\text{CeO}_2$  nanotubes are also obtained by annealing layered  $\text{Ce}(\text{OH})_3$  nanotubes by a simple oxidation–coordination–assisted dissolution process of the  $\text{Ce}(\text{OH})_3$  nanotubes/nanorods. One-dimensional structures of  $\text{Ce}(\text{OH})_3$  are synthesized by the hydrothermal treatment of  $\text{Ce}_2(\text{SO}_4)_3 \cdot 9\text{H}_2\text{O}$  with a 10 M NaOH solution at 130  $^{\circ}\text{C}$ . Starting from  $\text{Ce}(\text{OH})_3$  nanorods (as well as from narrow cavity nanotubes), it is possible to obtain  $\text{CeO}_2$  nanotubes with large cavities by a simple oxidation and dissolution process [160]. These nanotubes with open ends have a cubic structure and display an outer diameter of about 15–25 nm and a length of about 100 nm. Nanoparticles of about 8 nm are attached to the walls and the thickness of the wall is about 5–7 nm. The inner diameter of the nanotubes is about 10–15 nm. In this method, freshly prepared 1D  $\text{Ce}(\text{OH})_3$  is exposed to air at room temperature for 24 h. The partially oxidized  $\text{Ce}(\text{OH})_3$  nanotubes with narrow cavities are dispersed in distilled water and subjected to ultrasonication for 2 h after adding 15%  $\text{H}_2\text{O}_2$ . Partial oxidation of the  $\text{Ce}(\text{OH})_3$  is essential to form the ceria tubular structures. Electrosynthesis of  $\text{CeO}_2$  nanotubes using AMs has been reported by employing a non-aqueous electrolyte [161].  $\text{ThO}_2$  nanotubes are reported by the sol–gel method by using a porous alumina template [162].

### 6.5.7

#### Nanotubes of Titanates and other Complex Oxides

The hydrothermal method has been employed to synthesize nanotubes of monocrystalline  $\text{BaTiO}_3$  [163], and tubular  $\text{PbTiO}_3$  [164]. Pulsed laser ablation also yields  $\text{PbTiO}_3$  nanotubes within the pores of an AM [165], while sol–gel electrophoretic deposition of an acetic acid-based highly stabilized lead zirconate titanate (PZT) sol in AMs gives rise to PZT nanotubes [166]. The PZT sol with a near-morphotropic phase boundary composition and no polymeric addition was prepared using lead acetate trihydrate, zirconium, and titanium tetra-butoxides. By anodization of a Ti–Zr alloy,  $\text{ZrTiO}_3$  nanotubes are obtained [167].

Mallouk *et al.* [168], and Peng *et al.* [169], have reported the synthesis of niobate-based nanotubes at low temperatures by the exfoliation of acid-exchanged  $\text{K}_4\text{Nb}_6\text{O}_{17}$  with tetra(*n*-butyl)ammonium hydroxide ( $\text{TBA}^+\text{OH}^-$ ) in aqueous solution. In the presence of excess acid, around 80% of the potassium ions in  $\text{K}_4\text{Nb}_6\text{O}_{17}$  are replaced by protons. The remaining potassium ions appear to reside in the slowly exchanging interlayer galleries that alternate along the stacking axis [168]. The

bilamellar colloid initially formed by reacting this material with  $\text{TBA}^+\text{OH}^-$  is unstable relative to the formation of unilamellar sheets and tubules. Exfoliation initially produces a bilayer colloid and then transforms (depending on conditions) irreversibly into tubules, unilamellar sheets, or a mixture of the two. The concentration of the colloid and the pH are important factors in controlling the coiling equilibrium. Both  $\text{H}^+$  and alkali ions help to precipitate the aggregated tubules. The individual tubules are formed by the rolling of sheets of exfoliated  $\text{K}_{4-x}\text{H}_x\text{Nb}_6\text{O}_{17}$  ( $x \approx 3.2$ ). The tubules are 0.1–1  $\mu\text{m}$  in length, with outer diameters that range from 15 to 30 nm. The colloids and the precipitated tubules are both highly stable.

Potassium hexaniobate nanotubes have also been fabricated from polycrystalline  $\text{K}_4\text{Nb}_6\text{O}_{17}$  at room temperature using the intercalating and exfoliating methods [169]. These are multilayer crystalline nanotubes with interlayer spacings from 0.83 to 3.6 nm, depending on the intercalating molecules such as tetra(*n*-butyl) ammonium hydroxide ( $\text{TBA}^+\text{OH}^-$ ) and alkylamines ( $\text{C}_n\text{H}_{2n+1}\text{NH}_2$ ). The number of layers in the wall is in the range of 3 to 8. The outer diameter varies between 20 and 90 nm for the nanotubes obtained with different alkylamines, and the length of the nanotubes ranges from a few hundred nanometers to several micrometers. When a single-layer  $(-\text{Nb}_6\text{O}_{17}-)_n$  sheet rolls up into a nanotube,  $\text{C}_n\text{H}_{2n+1}\text{NH}_2$  ( $n \neq 1$ ) molecules are already adsorbed on both sides of the sheet and then reside in the interlayer spaces of the nanotube. A model of the spiral structural growth of these nanotubes has been proposed and the tube axis found to be parallel to the [100] direction of the  $\text{K}_4\text{Nb}_6\text{O}_{17}$  crystal. Spiral nanotubes of potassium niobate are obtained by introduction of a polyfluorinated cationic azobenzene derivative, *trans*-[2-(2, 2, 3, 3, 4, 4, 4-heptafluorobutylamino)ethyl] {2-[4-(4-hexylphenylazo)phenoxy]ethyl} dimethylammonium (abbreviated as  $\text{C}_3\text{F}_7\text{-Azo}^+$ ), into the layered niobate interlayer by a two-step guest–guest exchange method, with methyl viologen ( $\text{MV}^{2+}$ )- $\text{K}_4\text{Nb}_6\text{O}_{17}$  as the precursor [170]. When  $\text{MV}^{2+}$ -intercalated niobate was used as the precursor, the polyfluorinated  $\text{C}_3\text{F}_7\text{-Azo}^+$  results in the quantitative formation of spiral nanotubes from exfoliated nanosheets of the niobate, by rolling along the sandwiched microstructure. Nanotubes of  $\text{FePO}_4$  have been prepared under solvothermal conditions in the presence of a sodium dodecyl sulfate (SDS) surfactant [171]. Iron phosphate nanotubes have mesoporous walls and diameters of 50–400 nm and lengths of several micrometers. The walls of the nanotubes range from 20 to 40 nm in thickness. The removal of the surfactant by acetate exchange and heat treatment results in amorphous mesoporous nanotubes of  $\text{FePO}_4$ . Mesoporous  $\text{NiPO}_4$  nanotubes have been prepared in the presence of a cationic surfactant and different bases by the sol–gel method [172]. The solution–liquid–solid (SLS) method has been exploited to obtain tin-filled  $\text{In}(\text{OH})_3$  nanotubes using liquid droplets of an In–Sn mixture [173].

Nanotubes and how they are formed of other complex oxides reported are:  $\text{In}_2\text{Ge}_2\text{O}_7$  by thermal evaporation [174],  $\text{InVO}_4$  nanotubes using templates [175],  $\text{WO}_3\text{-H}_2\text{O}$  nanotubes with the aid of intercalated polyaniline [176], chrysotile nanotubes by the hydrothermal method [177], aluminogermanate nanotubes by a simple solution procedure [178],  $\alpha\text{-FeOOH}$  nanotubes by employing reverse



micelles [179], boehmite nanotubes by a hydrothermal procedure [180], and hydroxyapatite nanotubes by a sol-gel procedure in an AM [181].

$\text{La}_{0.5}\text{Sr}_{0.5}\text{CoO}_3$  nanotubes have been prepared using an AM template by the sol-gel method [182], while  $\text{ZnAl}_2\text{O}_4$  spinel nanotubes have been obtained by making use of the Kirkendall effect [183].  $\text{ZrCr}_2\text{O}_4$  has also been prepared by this method [117]. Nanotubes of  $\text{SrAl}_2\text{O}_4$  [184], as well as  $\text{AgIn}(\text{WO}_4)_2$  [185], are produced under hydrothermal conditions. By controlling the pH, single-walled aluminogermanate nanotubes have been synthesized by the reaction of tetraethylorthogermanate and  $\text{AlCl}_3$  in NaOH solution [186]. Nickel hexacyanoferrate nanotubes have been fabricated in an AM using the electrokinetic method [187]. Single-crystal calcium sulfate nanotubes can be generated by the reverse micelle method at room temperature [188]. Self-assembled supramolecular  $\text{C}_{32}\text{H}_{70}\text{N}_2\text{ZnSO}_4$  nanotubes with high thermal stability have been prepared [189]. Bismuth subcarbonate nanotubes are prepared by a simple reflux of bismuth citrate and urea in ethylene glycol [190].

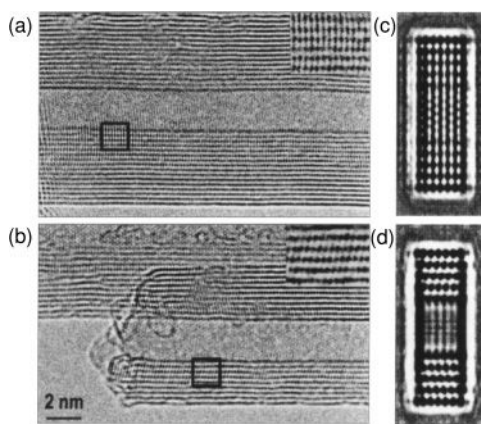
## 6.6 Pnictide Nanotubes

Several methods to synthesize BN nanotubes including CVD and electrical discharge, as well as templating have been described in the literature [4]. Thin BN tubes of less than 200 nm diameter were first obtained by arc discharge with hollow tungsten electrodes filled with h-BN powder. Following this initial report, a variety of methods have been employed to prepare BN nanotubes. The other methods of synthesis of BN nanotubes include those that are far from equilibrium, such as the electrical arc method [191, 192], arcing between h-BN and Ta rods in a  $\text{N}_2$  atmosphere [193], laser ablation of h-BN [194], and continuous laser heating of BN [195]. The last method produces long ropes of BN nanotubes with thin walls. Single-walled BN nanotubes are formed in some cases [191, 196]. Single-walled nanotubes of BN have been deposited on polycrystalline W substrates by using electron-cyclotron resonance nitrogen and electron beam boron sources [197].

Bando and coworkers [198, 199], have carried out extensive work on BN nanotubes. They prepared the nanotubes by the reaction of MgO and B in the presence of ammonia at 1300 °C [198].  $\text{B}_2\text{O}_2$  (obtained by heating B and MgO at 1300 °C) was heated in the presence of  $\text{NH}_3$  in a long BN boat, which was placed into a graphite susceptor that was heated from the outside by an RF furnace to obtain BN nanotubes. The BN nanotubes exhibit a 1D nanostructure and have diameters that range from several nanometers to about 70 nm, and lengths that go up to 10 micrometers. They show the presence of mixed hexagonal and rhombohedral BN phases. The nanotubes of diameter around 10 nm exhibit a perfectly cylindrical structure, although edge dislocations are occasionally observed from the rhombohedrally stacking, ordered nanotubes. The concentric tube structures do not contain internal wall closures or internal cap structures. Bando and coworkers [199], have also prepared BN nanotubes by the reaction of MgO, FeO, and B in the presence of  $\text{NH}_3$  at 1400 °C. The nanotubes are in the pure h-BN phase and

have diameters of  $\sim 50$  nm and lengths of up to several tens of micrometers. The reaction of boric acid or  $B_2O_3$  with  $N_2$  or  $NH_3$  at high temperatures in the presence of carbon or catalytic metal particles has also been employed in the preparation of BN nanotubes [200]. BN nanotubes can be grown directly on substrates at 873 K by a plasma-enhanced laser-deposition technique [201].

$B_2O_3$ -coated multi-walled carbon nanotubes, on reaction with  $NH_3$  at high temperatures, yield BN nanotubes [202]. Bando and coworkers have reviewed various aspects of BN nanotubes and cite methods involving arc-discharge, laser ablation, and the plasma jet method (Fig. 6.19) [203]. Straight BN nanotubes have been grown by heating a mixture of  $Mg(BO_2)_2 \cdot H_2O$ ,  $NH_4Cl$ ,  $NaN_3$ , and Mg powder in an autoclave at  $600^\circ C$  for 20–60 h. These BN nanotubes had diameters mainly in the range of 30–300 nm and lengths of up to  $\sim 5 \mu m$ , and a majority of them had at least one closed end [204]. Multi-walled BN nanotubes have been obtained by a reduction–nitridation route wherein the reaction of boron trifluoride etherate and sodium azide was carried out in the presence of Fe–Ni powder in a sealed autoclave at  $600^\circ C$  for 12 h. The BN nanotubes so obtained have an average outer diameter of 60 nm, an inner diameter of 30 nm, and lengths up to 300 nm [205]. By annealing an Fe film evaporated on boron pellets at  $1000^\circ C$  in  $N_2$  gives rise to BN nanotubes [206]. Microwave plasma-enhanced CVD has been employed to obtain BN nanotube arrays [207]. In this method, AM are used (for confinement) along with borane and ammonia or nitrogen. BN nanotubes that are 1 mm long are obtained by an optimized ball-milling and annealing method [208]. The annealing tempera-



**Figure 6.19** a,b) HRTEM images of two zig-zag BN MWNTs. A different stacking order is apparent in the marked areas in (a) and (b), as highlighted in the insets. Hexagonal- (a) and rhombohedral-type (b) stacking (in  $12.5^\circ$  fringe inclinations with respect to the tube axis) are verified by the corresponding computer-simulated HRTEM

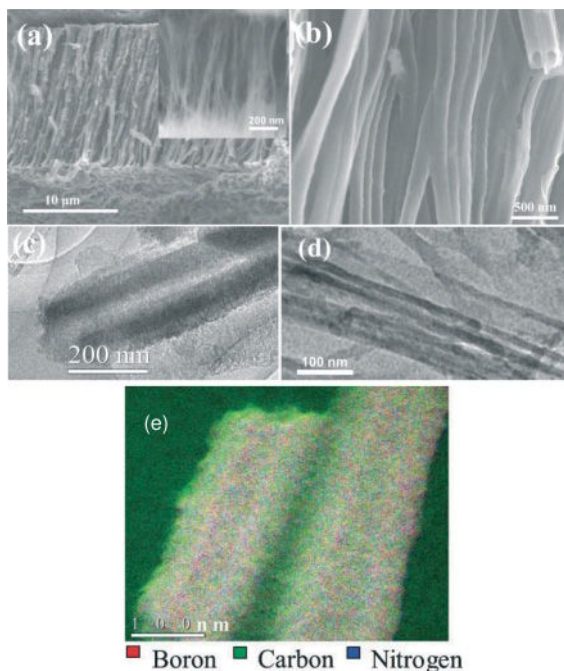
images (c and d, respectively) for BN MWNTs having the axes strictly parallel to the  $[10\bar{1}0]$  orientations (“zig-zag” NTs). Note a characteristically open tip-end of a BNNT in (b). This feature is frequently seen in BNNTs obtained from high-temperature chemical syntheses. Reproduced with permission from [203b]. Copyright 2007, Wiley-VCH.

ture of 1100 °C is crucial for the growth of the long BN nanotubes because at this temperature there is a fast nitrogen dissolution rate in Fe and the B/N ratio in Fe is 1.

By combining polymer thermolysis and the use of templates, ordered arrays of BN nanotubes have been obtained [209]. In this method, liquid borazine in AM is thermolyzed at high temperatures in a nitrogen atmosphere. Double-walled BN nanotubes are obtained by the reaction of a flowing stream of borazine and ammonia with a nickelocene catalyst vapor in the hot zone of a furnace maintained at 1200 °C [210]. The mechanism of growth of single-walled BN nanotubes by laser vaporization has been examined in detail [211]. It appears that the root-growth model that involves a droplet of B is applicable for this growth. It may be noted that laser vaporization is a unique route for the synthesis of single-walled BN nanotubes.

Single-walled BCN nanotubes are obtained by bias-assisted hot-filament CVD [212]. In this method, a Fe–Mo catalyst supported on MgO powder is used for the decomposition of a mixture of CH<sub>4</sub>, B<sub>2</sub>H<sub>6</sub>, and ethylenediamine. The as-grown SWNTs have clean and smooth surfaces with diameters in the range of 0.8–2.5 nm and lengths up to micrometers. Homogeneous BC<sub>4</sub>N nanotube brushes have been obtained recently by the reaction of amorphous carbon nanotubes with boric acid and urea (Fig. 6.20) [213]. The BCN nanotubes have open ends with a diameter of 170 nm, a length of 15 mm, and thickness of around 50 nm. The SAED pattern shows faint rings and a few spots. The X-ray diffraction (XRD) pattern of the BCN nanotube brushes shows broad reflections with *d*-spacings of 3.43 Å and 2.13 Å, which correspond to the (002) and (100) planes, respectively, similar to the pattern reported for BC<sub>3</sub>N. The broad reflections in the XRD pattern and the diffuse rings in the electron diffraction pattern suggest the turbo static nature of the nanotubes.

GaN nanotubes have been grown in AMs by employing MOCVD. The reactants used are trimethylgallium and NH<sub>3</sub> [214]. The diameter of the GaN nanotubes is approximately 200–250 nm and the wall thickness is about 40–50 nm. Nanotubular GaN consists of numerous fine GaN particulates with a size range of 15–30 nm. XRD and TEM analyses indicate that the grains in the GaN nanotubular material is nanocrystalline with a hexagonal structure. By the reaction of GaCl<sub>3</sub> with excess NaN<sub>3</sub> in dry benzene, GaN nanotubes with branched tubules have been grown in mesoporous MCM 48 [215]. These GaN nanotubes are polycrystalline with a wurtzite structure and an outer diameter of 50–150 nm. The tube wall thickness is ~10 nm and the lengths go up to several micrometers. Amorphous carbon nanotube brushes, on reaction with GaCl<sub>3</sub> followed by reaction with NH<sub>3</sub>, give rise to GaN nanotube brushes (Fig. 6.21) [216]. The close packing of 1D GaN nanotube-nanobristles have diameters from 100 to 230 nm and lengths in the 7–10 μm range. The tubes are open at one end and their surface appears to be smooth. The nanotube brushes have a wurtzite structure. The TEM images in Figures 6.21c–e shows a nanotube with an outer diameter of 200 nm and the wall thickness is in the range of 10–15 nm. The HRTEM image of the nanotube wall in Figure 6.21f shows



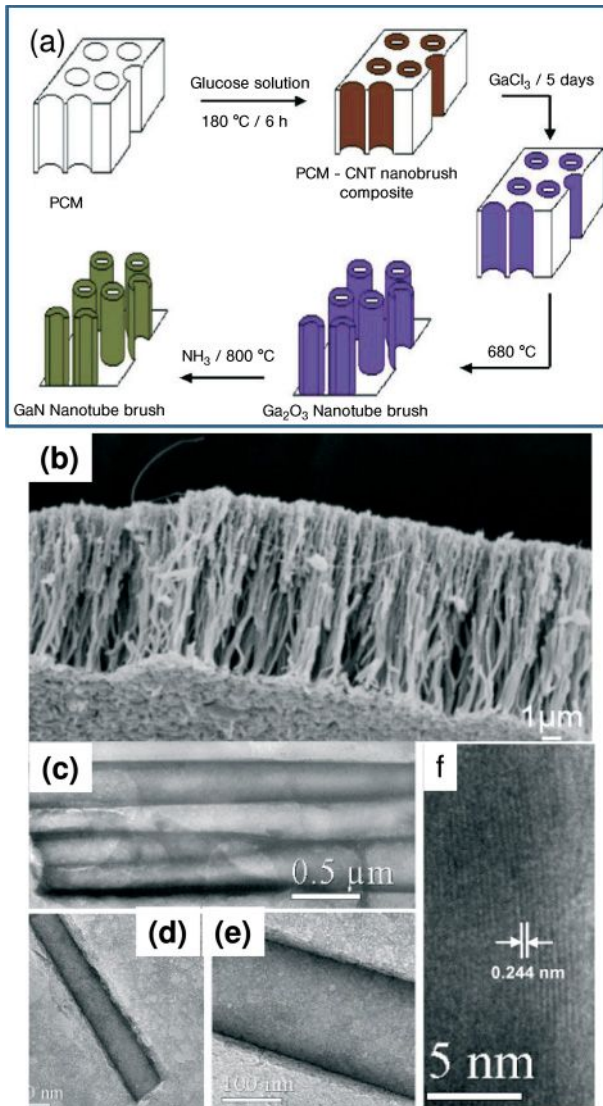
**Figure 6.20** a) FESEM images of BCN nanotube brushes with the average diameter of a single tube being around 170 nm. The inset shows a FESEM image of BCN nanotube brushes of 40 nm diameter. b) Higher magnification FESEM images of BCN

nanotube brushes. TEM images of a BCN nanotube: c) 170 nm diameter and d) 40 nm diameter. e) Elemental mapping of the boron, carbon, and nitrogen of BCN nanotubes obtained from EELS. Reproduced with permission from [213]. Copyright 2008, RSC.

interplanar spacing of 0.244 nm, which indicates the single crystalline nature of the GaN nanotube.

$\text{Si}_3\text{N}_4$  nanotubes can be prepared by the sol-gel route in which tetraethoxysilane (TEOS) and phenolic resin are used to prepare a carbonaceous silica xerogel, and ferric nitrate is employed as an additive. The xero-gel is heated at 1300 °C for 10 h in nitrogen [217]. Molybdenum nitride nanotubes have been obtained by depositing a nitride film on anodic alumina and etching away the template with NaOH [218].

Single crystalline nanotubes of  $\text{Cd}_3\text{P}_2$  and  $\text{Zn}_3\text{P}_2$  have been obtained by a template process in which Cd and Zn nanorods formed in-situ act as self-sacrificing templates [219]. A mixture of reactants that contain CdS (or ZnS), P, and  $\text{Mn}_3\text{P}_2$  is heated to 1350 °C in an induction furnace to obtain nanotubes. Single-crystalline, single-walled,  $\text{SbPS}_{4-x}\text{Se}$  nanotubes with a tunable band-gap have been prepared by taking a mixture of stoichiometric amounts of the elements Sb, P, S, for  $\text{SbPS}_4$ , and the corresponding amounts for  $\text{SbPS}_3\text{Se}$ ,  $\text{SbPS}_2\text{Se}_2$ , and  $\text{SbPSSe}_3$  in fused silica tubes sealed under vacuum, and heated [220].



**Figure 6.21** a) Schematic showing the formation of nanotube brushes of carbon,  $\text{Ga}_2\text{O}_3$ , and GaN. b) SEM image of a GaN nanotube brush. c–e) TEM images of GaN nanotubes and f) HRTEM image of the wall of a GaN nanotube. Reproduced with permission from [216]. Copyright 2007, ACS.

## 6.7

### Nanotubes of Carbides and other Materials

SiC nanowires, SiC/SiO<sub>2</sub> core-shell nanocables, and SiC nanotubes have been synthesized simultaneously by directly heating Si powder and multiwall carbon nanotubes (MWCNTs) [221]. Single-phase TiC nanotubes are prepared by the reaction of carbon nanotubes with Ti powder at 1300 °C for 30 h [222].

Silicon oxycarbide ceramic nanotubes can be obtained by the pyrolysis of polysilicone nanotubes using a sacrificial AM as a template [223]. In a typical synthesis, the AM templates were immersed in a mixture of low-molecular-weight silicone starting materials, such as {CH<sub>3</sub>(CH=CH)SiO}<sub>n</sub> (*n* = 3–7), named VC4, and a cyclic-type silicone bearing vinyl groups, and (CH<sub>3</sub>)<sub>3</sub>SiO{CH<sub>3</sub>(H)SiO}<sub>m</sub> (*m* = 20), named KF-99 and heated in an oven at two different temperatures, 50 and 200 °C. Large-scale aligned silicon carbonitride nanotube arrays have been synthesized by microwave-plasma-assisted CVD using SiH<sub>4</sub>, CH<sub>4</sub>, and N<sub>2</sub> as precursors. The nanotubes are 6–7 μm in length and 100–200 nm in diameter [224].

Transition metal halides such as NiCl<sub>2</sub> crystallize in the CdCl<sub>2</sub> structure, with the metal halide layers held together by weak van der Waals forces. NiCl<sub>2</sub> has been shown to form closed cage structures and nanotubes [225]. These were prepared by heating NiCl<sub>2</sub>·6H<sub>2</sub>O initially in air to remove the water of crystallization, and heated further at 960 °C under Ar. Zeng *et al.* [226]. have carried out UV-light-induced fabrication of CdCl<sub>2</sub> nanotubes starting from CdSe solid nanocrystals through a Kirkendall effect. In this procedure, CdCl<sub>2</sub> nanotubes are obtained starting with a solution of CdSe nanocrystals in *o*-dichlorobenzene (which generates chlorine free radicals on photolysis).

## 6.8

### Complex Inorganic Nanostructures Based on Nanotubes

In addition to the simple nanotube structures, more complex nanotubular structures of various inorganic materials such as coaxial cables, heterojunctions, and nanotube-nanowire or nanotube-nanoparticle composites have been prepared and characterized by several workers. Typical examples of such nanostructures are the following: Integration of ZnO nanotubes with ordered nanorods [227], conversion of ZnO nanorod arrays into ZnO–ZnS nanocable and ZnS nanotube arrays [228], core–sheath heterostructure CdS–TiO<sub>2</sub> nanotube arrays [229], ZnS nanotube–In nanowire core–shell heterostructures [230], ZnO–ZnS core–shell nanotube arrays [231], Cu nanotube–Bi nanowire heterojunctions [232], carbon nanotubes in TiO<sub>2</sub> nanotubes [233], TiO<sub>2</sub>–Pt coaxial nanotube arrays [234], Sn nanowires on TiO<sub>2</sub> nanotubes [235], Fe<sub>2</sub>O<sub>3</sub>–TiO<sub>2</sub> nanorod–nanotube arrays [236], SiO<sub>2</sub>–Ta<sub>2</sub>O<sub>5</sub> core–shell nanowires and nanotubes [237], multi-walled BCN–carbon nanotube junctions [238], and BN nanotubes with periodic iron nanoparticles [239].

## 6.9

## Outlook

The preceding presentation should suffice to demonstrate the great progress made in the synthesis of inorganic nanotubes. It would appear that today we are able to synthesize almost any inorganic material in tubular form. Not only do we have an arsenal of inorganic nanotubes but also several strategies to synthesize them. There are still many synthetic challenges. One of them relates to the need to synthesize single-walled single-crystalline nanotubes of inorganic materials. There are hardly one or two reports of single-walled inorganic nanotubes at present. With the availability of inorganic nanotubes in sufficient quantities, there is much scope to measure their properties and investigate phenomena associated with them.

This Chapter has been published previously online in

*Advanced Materials* 3 Aug 2009

Doi: 10.1002/adma.200803720

Copyright © 2009 WILEY-VCH Verlag GmbH & Co. KGaA, Weinheim

## References

- 1 Rao, C.N.R., Muller, A., Cheetham, A.K. (2007) *Nanomaterials Chemistry: Recent Developments*, Wiley-VCH, Weinheim.
- 2 Rao, C.N.R., Govindaraj, A. (2005) *Nanotubes and Nanowires*, RSC series on Nanoscience, Royal Society of Chemistry, London.
- 3 Iijima, S. (1991) *Nature*, **354**, 56.
- 4 Rao, C.N.R. and Nath, M. (2003) *Dalton Trans*, **1**.
- 5 Tenne, R. and Rao, C.N.R. (2004) *Phil. Trans. Royal. Soc. (London)* **362**, 2099.
- 6 a) Ghadiri, M.R., Granja, J.R., Milligan, R.A., McRee, D.E. and Kazanovich, N. (1993) *Nature*, **366**, 324.  
b) Gazit, E. (2007) *Chem. Soc. Rev.*, **36**, 1263.
- 7 a) Tenne, R. (2002) *Chem. Eur. J.*, **8**, 5296, and the references, there, in.  
b) Deepak, F.L. and Tenne, R. (2008) *Cent. Eur. Chem.*, **6**, 373.
- 8 Brumlik, C.J. and Martin, C.R. (1991) *J. Am. Chem. Soc.*, **113**, 3174.
- 9 Hultheen, J.C. and Martin, C.R. (1997) *J. Mater. Chem.*, **7**, 1075.
- 10 Zhang, X., Wang, H., Bourgeois, L., Pen, R., Zhao, D. and Webby, P.A. (2008) *J. Mater. Chem.*, **18**, 463.
- 11 a) Martin, C.R., Nishizawa, M., Jirage, K. and Kang, M. (2001) *J. Phys. Chem. B*, **105**, 1925. b) Wirtz, M., Martin, C. R. (2003) *Adv. Mater.*, **15**, 455.
- 12 Kohli, P., Wharton, J.E., Braide, O. and Martin, C.R. (2004) *J. Nanosci. Nanotechnol.*, **4**, 605.
- 13 Shin, T.-Y., Yoo, S.-H. and Park, S. (2008) *Chem. Mater.*, **20**, 5682.
- 14 Sanchez-Castillo, M.A., Couto, C., Kim, W.B. and Dumesic, J.A. (2004) *Angew. Chem. Int. Ed.*, **43**, 1140.
- 15 Wang, H.-W., Sheih, C.-F., Chen, H.-Y., Shiu, W.-C., Russo, B. and Cao, G. (2006) *Nanotechnology*, **17**, 2689.
- 16 Pu, Y.-C., Hwu, J.R., Su, W.-C., Shieh, D.-B., Tzeng, Y. and Yeh, C.-S. (2006) *J. Am. Chem. Soc.*, **128**, 11606.
- 17 Schwartzberg, A.M., Olson, T.Y., Talley, C.E. and Zhang, J.Z. (2007) *J. Phys. Chem. C*, **111**, 16080.
- 18 Calvar, M.S., Pacifico, J., Juste, J.P. and Liz-Marzan, L.M. (2008) *Langmuir*, **24**, 9675.
- 19 Chen, Z., Waje, M., Li, W. and Yan, Y. (2007) *Angew. Chem. Int. Ed.*, **46**, 4060.



- 20 Takai, A., Yamauchi, Y. and Kuroda, K. (2008) *Chem. Commun.*, 4171.
- 21 Kijima, T., Yoshimura, T., Uota, M., Ikeda, T., Fujikawa, D., Mouri, S. and Uoyama, S. (2004) *Angew. Chem. Int. Ed.*, **43**, 228.
- 22 Liang, H.-P., Lawrence, N.S., Wan, L.-J., Jiang, L., Song, W.-G. and Jones, T.G.J. (2008) *J. Phys. Chem. C*, **112**, 338.
- 23 Han, C.C., Bai, M.Y. and Lee, J.T. (2001) *Chem. Mater.*, **13**, 4260.
- 24 Bao, J., Tie, C., Xu, Z., Zhou, Q., Shen, D. and Ma, Q. (2001) *Adv. Mater.*, **13**, 1631.
- 25 Tao, F., Guan, M., Jiang, Y., Zhu, J., Xu, Z. and Xue, Z. (2006) *Adv. Mater.*, **18**, 2161.
- 26 Cao, H., Wang, L., Qiu, Y., Wu, Q., Wang, G., Zhang, L. and Liu, X. (2006) *ChemPhysChem*, **7**, 1500.
- 27 Xu, X.J., Yu, S.F., Lau, S.P., Li, L. and Zhao, B.C. (2008) *J. Phys. Chem. C*, **112**, 4168.
- 28 Narayanan, T.N., Shaijumon, M.M., Ajayan, P.M. and Anantharaman, M.R. (2008) *J. Phys. Chem. C*, **112**, 14281.
- 29 Kamalakar, M.V. and Raychaudhuri, A.K. (2008) *Adv. Mater.*, **20**, 149.
- 30 Cheng, C.-L., Lin, J.-S. and Chen, Y.-F. (2008) *Mater. Lett.*, **62**, 1666.
- 31 Kar, S., Santra, S. and Chaudhuri, S. (2008) *Cryst. Growth. Des.*, **8**, 344.
- 32 Dou, X., Li, G., Huang, X. and Li, L. (2008) *J. Phys. Chem. C*, **112**, 8167.
- 33 Li, F.S., Zhou, D., Wang, T., Wang, Y., Song, L.J. and Xu, C.T. (2007) *J. Appl. Phys.*, **101**, 014309.
- 34 Zhou, D., Cai, L.-H., Wen, F.-S. and Li, F.-S. (2007) *Chi. J. Chem. Phys.*, **20**, 821.
- 35 Liu, L., Zhou, W., Xie, S., Song, L., Luo, S., Liu, D., Shen, J., Zhang, Z., Xiang, Y., Ma, W., Ren, Y., Wang, C. and Wang, G. (2008) *J. Phys. Chem. C*, **112**, 2256.
- 36 Zhu, Y., Liu, F., Ding, W., Guo, X. and Chin, Y. (2006) *Angew. Chem. Int. Ed.*, **45**, 7211.
- 37 Gautam, U.K., Nath, M. and Rao, C.N.R. (2003) *J. Mater. Chem.*, **13**, 2845.
- 38 Gautam, U.K. and Rao, C.N.R. (2004) *J. Mater. Chem.*, **14**, 2530.
- 39 Xi, G., Xiong, K., Zhao, Q., Zhang, R., Zhang, H. and Qian, Y. (2006) *Cryst. Growth Des.*, **6**, 577.
- 40 Zhang, H., Yang, D., Ji, Y.J., Ma, X.Y., Xu, J. and Que, D.L. (2004) *J. Phys. Chem. B*, **108**, 1179.
- 41 Ma, Y.R., Qi, L.M., Ma, J.M. and Cheng, H.M. (2004) *Adv. Mater.*, **16**, 1023.
- 42 Li, X.M., Li, S.Q., Zhou, W.W., Chu, H.B., Chen, W., Li, I.L. and Tang, Z.K. (2005) *Cryst. Growth Des.*, **5**, 911.
- 43 Xi, B., Xiong, S., Fan, H., Wang, X. and Qian, Y. (2007) *Cryst. Growth, Des.*, **7**, 1185.
- 44 Tenne, R., Margulis, L., Genut, M. and Hodes, G. (1992) *Nature*, **360**, 444.
- 45 Feldman, Y., Wasserman, E., Srolovitch, D.J. and Tenne, R. (1995) *Science*, **267**, 222.
- 46 Nath, M., Govindaraj, A. and Rao, C.N.R. (2001) *Adv. Mater.*, **13**, 283.
- 47 Nath, M. and Rao, C.N.R. (2001) *Chem. Commun.*, 2336.
- 48 Nath, M. and Rao, C.N.R. (2001) *J. Am. Chem. Soc.*, **123**, 4841.
- 49 Nath, M. and Rao, C.N.R. (2002) *Angew. Chem. Int. Ed.*, **41**, 3451.
- 50 Nath, M. and Rao, C.N.R. (2002) *Pure Appl. Chem.*, **74**, 1545.
- 51 a) Deepak, F.L., Margolin, A., Wiesel, I., Bar-Sadan, M., Popovitz-Biro, R. and Tenne, R. (2006) *Nano*, **1**, 167.  
b) Margolin, A., Deepak, F.L., Popovitz-Biro, R., Bar-Sadan, M., Feldman, Y. and Tenne, R. (2008) *Nanotechnology*, **19**, 095601.
- 52 Gordon, J.M., Katz, E.A., Feuermann, D., Yaron, A.A., Levy, M. and Tenne, R. (2008) *J. Mater. Res.*, **18**, 458.
- 53 Gautam, U.K., Vivekchand, S.R.C., Govindaraj, A., Kulkarni, G.U., Selvi, N.R. and Rao, C.N.R. (2005) *J. Am. Chem. Soc.*, **127**, 3658.
- 54 Pan, H., Poh, C.K., Zhu, Y., Xing, G., Chin, K.C., Feng, Y.P., Lin, J., Sow, C.H., Ji, W. and Wee, A.T.S. (2008) *J. Phys. Chem. C*, **112**, 11227.
- 55 Rao, C.N.R., Govindaraj, A., Deepak, F.L., Gunari, N.A. and Nath, M. (2001) *Appl. Phys. Lett.*, **78**, 1853.
- 56 Kalyaniketty, K.P., Nikhila, M., Maitra, U. and Rao, C.N.R. (2006) *Chem. Phys. Lett.*, **432**, 190.
- 57 Wu, C., Yu, S.-H., Chen, S., Liu, G. and Liu, B. (2006) *J. Mater. Chem.*, **16**, 3326.
- 58 Shen, Q., Jiang, L., Miao, J., Hou, W., Zhu, J.-J. (2008) *Chem. Commun.*, 1683.



- 59 Zhang, S.-Y., Fang, C.-X., Tian, Y.-P., Zhu, K.-R., Jin, B.-K., Shen, Y.-H. and Yang, J.-X. (2006) *Cryst. Growth Des.*, **6**, 2089.
- 60 Niu, H. and Gao, M. (2006) *Angew. Chem. Int. Ed.*, **45**, 6462.
- 61 Ng, C.H.B., Tan, H. and Fan, W.Y. (2006) *Langmuir*, **22**, 9712.
- 62 Zhang, S.-Y., Fang, C.-X., Wei, W., Jin, B.-K., Tian, Y.-P., Shen, Y.-H., Yang, J.-X. and Gao, H.-W. (2007) *J. Phys. Chem. C*, **111**, 4168.
- 63 Qin, A., Fang, Y., Tao, P., Zhang, J. and Su, C. (2007) *Inorg. Chem.*, **46**, 7403.
- 64 Zhu, G., Liu, P., Zhou, J., Bian, X., Wang, X., Li, J. and Chen, B. (2008) *Mater. Lett.*, **62**, 2335.
- 65 Ye, C.H., Meng, G.W., Jiang, Z., Wang, Y.H., Wang, G.Z. and Zhang, L.D. (2002) *J. Am. Chem. Soc.*, **124**, 15 180.
- 66 Jyoti, R.O. and Suneel, K.S. (2005) *Nanotechnology*, **16**, 2415.
- 67 Batabyal, S.K., Basu, C., Das, A.R. and Sanyal, G.S. (2006) *Mater. Lett.*, **60**, 2582.
- 68 Xiao, F., Yoo, B., Lee, K.H. and Myung, N.V. (2007) *J. Am. Chem. Soc.*, **129**, 10068.
- 69 Li, X.-H., Zhou, B., Pu, L. and Zhu, J.-J. (2008) *Cryst. Growth, Des.*, **8**, 771.
- 70 Park, K.H., Choi, J., Kim, H.J., Lee, J.B. and Uk Son, S. (2007) *Chem. Mater.*, **19**, 3861.
- 71 Tong, H., Zhu, Y.-J., Yang, L.-X., Li, L. and Zhang, L. (2006) *Angew. Chem. Int. Ed.*, **45**, 7739.
- 72 Li, C., Wang, X., Peng, Q. and Li, Y. (2005) *Inorg. Chem.*, **44**, 6641.
- 73 Bae, C., Yoo, H., Kim, S., Lee, K., Kim, J., Sung, M.M. and Shin, H. (2008) *Chem. Mater.*, **20**, 756.
- 74 Ogihara, H., Sadakane, M., Nodasaka, Y. and Ueda, W. (2006) *Chem. Mater.*, **18**, 4981.
- 75 Yuwono, V.M. and Hartgerink, J.D. (2007) *Langmuir*, **23**, 5033.
- 76 Ji, Q., Iwaura, R. and Shimizu, T. (2007) *Chem. Mater.*, **19**, 1329.
- 77 Yamanaka, M., Miyake, Y., Akita, S. and Nakano, K. (2008) *Chem. Mater.*, **20**, 2072.
- 78 Shen, G., Bando, Y. and Golberg, D. (2006) *J. Phys. Chem. B*, **110**, 23170.
- 79 Zhai, T., Gu, Z., Dong, Y., Zhong, H., Ma, Y., Fu, H., Li, Y. and Yao, J. (2007) *J. Phys. Chem. C*, **111**, 11 604.
- 80 Chen, H., Elabd, Y.A. and Palmese, G.R. (2007) *J. Mater. Chem.*, **17**, 1593.
- 81 Chen, Y., Li, B., Wu, X., Zhu, X., Suzuki, M., Hanabusa, K. and Yang, Y. (2008) *Chem. Commun.*, 4948.
- 82 Wu, X., Ruan, J., Ohsuna, T., Terasaki, O. and Che, S. (2007) *Chem. Mater.*, **19**, 1577.
- 83 Pouget, E., Dujardin, E., Cavalier, A., Moreac, A., Valéry, C., Marchi-Artzner, V., Weiss, T., Renault, A., Paternostre, M. and Artzner, F. (2007) *Nature Mater.*, **6**, 434.
- 84 He, B., Son, S.J. and Lee, S.B. (2006) *Langmuir*, **22**, 8263.
- 85 Tuan, H.-Y., Ghezlbash, A. and Korgel, B.A. (2008) *Chem. Mater.*, **20**, 2306.
- 86 Tan, L.K., Chong, M.A.S. and Gao, H. (2008) *J. Phys. Chem. C*, **112**, 69.
- 87 Grimes, C.A. (2007) *J. Mater. Chem.*, **17**, 1451.
- 88 Yoriya, S., Paulose, M., Varghese, O.K., Mor, G.K. and Grimes, C.A. (2007) *J. Phys. Chem. C*, **111**, 13 770.
- 89 Paulose, M., Prakasam, H.E., Varghese, O.K., Peng, L. and Popat, K.C. (2007) *J. Phys. Chem. C*, **111**, 14 992.
- 90 Wang, J. and Lin, Z. (2008) *Chem. Mater.*, **20**, 1257.
- 91 Albu, S.P., Kim, D. and Schmuki, P. (2008) *Angew. Chem. Int. Ed.*, **47**, 1916.
- 92 Albu, S.P., Ghicov, A., Macak, J.M. and Schmuki, P. (2007) *Phys. Status Solidi RRL*, **1**, R65.
- 93 Macak, J.M., Albu, S.P. and Schmuki, P. (2007) *Phys. Status Solidi RRL*, **1**, 181.
- 94 Allam, N.K. and Grimes, C.A. (2007) *J. Phys. Chem. C*, **111**, 13 028.
- 95 Tang, X. and Li, D. (2008) *J. Phys. Chem. C*, **112**, 5405.
- 96 Lu, N., Quan, X., Li, J.Y., Chen, S., Yu, H.T. and Chen, G.H. (2007) *J. Phys. Chem. C*, **111**, 11 836.
- 97 Qiu, J., Yu, W., Gao, X. and Li, X. (2007) *Nanotechnology*, **18**, 295 604.
- 98 Bae, C., Kim, S., Ahn, B., Kim, J., Sung, M.M. and Shin, H. (2008) *J. Mater. Chem.*, **18**, 1362.

- 99 Yue, L., Gao, W., Zhang, D., Guo, X., Ding, W. and Chen, Y. (2006) *J. Am. Chem. Soc.*, **128**, 11042.
- 100 Yu, A., Lu, G.Q.M., Drennan, J. and Gentle, I.R. (2007) *Adv. Funct. Mater.*, **17**, 2600.
- 101 Suzuki, M., Nakajima, Y., Sato, T., Shirai, H. and Hanabusa, K. (2006) *Chem. Commun.*, 377.
- 102 Feng, C., Wang, Y., Jin, Z., Zhang, J., Zhang, S., Wu, Z. and Zhang, Z. (2008) *New J. Chem.*, **32**, 1038.
- 103 Satishkumar, B.C., Govindaraj, A., Vogl, E.M., Basumallick, L. and Rao, C.N.R. (1997) *J. Mater. Res.*, **12**, 604.
- 104 Satishkumar, B.C., Govindaraj, A., Nath, M. and Rao, C.N.R. (2000) *J. Mater. Chem.*, **10**, 2115.
- 105 Eder, D., Kinloch, I.A. and Windle, A.H. (2006) *Chem. Commun.*, 1448.
- 106 Deng, Q., Wei, M., Ding, X., Jiang, L., Ye, B. and Wei, K. (2008) *Chem. Commun.*, 3657.
- 107 Miyauchi, M. and Tokudome, H. (2007) *J. Mater. Chem.*, **17**, 2095.
- 108 Yu, Q., Fu, W., Yu, C., Yang, H., Wei, R., Li, M., Liu, S., Sui, Y., Liu, Z., Yuan, M., Zou, G., Wang, G., Shao, C. and Liu, Y. (2007) *J. Phys. Chem. C*, **111**, 17521.
- 109 Ku, C.-H. and Wu, J.-J. (2006) *J. Phys. Chem. B*, **110**, 12981.
- 110 Kar, S. and Santra, S. (2008) *J. Phys. Chem. C*, **112**, 8144.
- 111 Li, L., Pan, S., Dou, X., Zhu, Y., Huang, X., Yang, Y., Li, G. and Zhang, L. (2007) *J. Phys. Chem. C*, **111**, 7288.
- 112 Xu, L., Liao, Q., Zhang, J., Ai, X. and Xu, D. (2007) *J. Phys. Chem. C*, **111**, 4549.
- 113 Tong, Y., Liu, Y., Shao, C., Liu, Y., Xu, C., Zhang, J., Lu, Y., Shen, D. and Fan, X. (2006) *J. Phys. Chem. B*, **110**, 14714.
- 114 Shen, L., Bao, N., Yanagisawa, K., Domen, K., Grimes, C.A. and Gupta, A. (2007) *J. Phys. Chem. C*, **111**, 7280.
- 115 Wang, H., Li, G., Jia, L., Wang, G. and Tang, C. (2008) *J. Phys. Chem. C*, **112**, 11738.
- 116 Zhou, X.F., Hu, Z.L., Chen, Y. and Shang, H.Y. (2008) *Mater. Res. Bull.*, **43**, 2790.
- 117 Raidongia, K. and Rao, C.N.R. (2008) *J. Phys. Chem. C*, **112**, 13366.
- 118 Lu, H.B., Liao, L., Li, H., Tian, Y., Wang, D.F., Li, J.C., Fu, Q., Zhu, B.P. and Wu, Y. (2008) *Mater. Lett.*, **62**, 3928.
- 119 Lee, W., Scholz, R. and Gosele, U. (2008) *NanoLett.*, **8**, 2155.
- 120 Wang, C.-C., Kei, C.-C., Yu, Y.-W. and Perng, T.-P. (2007) *NanoLett.*, **7**, 1566.
- 121 Galy, J. (1992) *J. Solid State Chem.*, **100**, 229.
- 122 Whittingham, M.S., Guo, J., Chen, R., Chirayil, T., Janauer, G. and Zavalji, P.Y. (1995) *Solid State Ionics*, **75**, 257.
- 123 Spahr, M.E., Bitterli, P., Nesper, R., Müller, M., Krumeich, F., Nissen, H.U. (1998) *Angew. Chem. Int. Ed.*, **37**, 1263; *Angew. Chem.*, **110**, 1339.
- 124 Krumeich, F., Muhr, H.-J., Niederberger, M., Bieri, F., Schnyder, B. and Nesper, R. (1999) *J. Am. Chem. Soc.*, **121**, 8324.
- 125 Sediri, F., Touati, F. and Gharbi, N. (2007) *Mater. Lett.*, **61**, 1946.
- 126 Muhr, H.-J., Krumeich, F., Schönholzer, U.P., Bieri, F., Niederberger, M., Gauckler, L.J. and Nesper, R. (2000) *Adv. Mater.*, **12**, 231.
- 127 Niederberger, M., Muhr, H.-J., Krumeich, F., Bieri, F., Günther, D. and Nesper, R. (2000) *Chem. Mater.*, **12**, 1995.
- 128 Doble, A., Ngala, K., Yang, S., Zavalji, P.Y. and Whittingham, M.S. (2001) *Chem. Mater.*, **13**, 4382.
- 129 Zhou, C., Mai, L., Liu, Y., Qi, Y., Dai, Y. and Chen, W. (2007) *J. Phys. Chem. C*, **111**, 8202.
- 130 O'Dwyer, C., Navas, D., Lavayen, V., Benavente, E., Santa Ana, M.A., Gonza'lez, G., Newcomb, S.B. and Torres, C.M.S. (2006) *Chem. Mater.*, **18**, 3016.
- 131 Yan, C. and Xue, D. (2008) *Adv. Mater.*, **20**, 1055.
- 132 Luo, J., Zhu, H.T., Fan, H.M., Liang, J.K., Shi, H.L., Rao, G.H., Li, J.B., Du, Z.M. and Shen, Z.X. (2008) *J. Phys. Chem. C*, **112**, 12594.
- 133 Liu, L., Kou, H.-Z., Mo, W., Liu, H. and Wang, Y. (2006) *J. Phys. Chem. B*, **110**, 15218.
- 134 Zhou, H. and Wong, S.S. (2008) *ACS Nano*, **2**, 944.
- 135 Bachmann, J., Jing, J., Knez, M., Barth, S., Shen, H., Mathur, S., Gosele, U. and

- Niensch, K. (2007) *J. Am. Chem. Soc.*, **129**, 9554.
- 136 Yu, X., Cao, C. and An, X. (2008) *Chem. Mater.*, **20**, 1936.
- 137 Wang, J., Ma, Y. and Watanabe, K. (2008) *Chem. Mater.*, **20**, 20.
- 138 Wang, T., Wang, Y., Li, F., Xu, C. and Zhou, D. (2006) *J. Phys. Condens. Matter*, **18**, 10545.
- 139 Geng, F., Zhao, Z., Geng, J., Cong, H. and Cheng, H.-M. (2007) *Mater. Lett.*, **61**, 4794.
- 140 Lou, X.W., Deng, D., Lee, J.Y., Feng, J. and Archer, L.A. (2008) *Adv. Mater.*, **20**, 258.
- 141 Shen, X.-P., Miao, H.-J., Zhao, H. and Xu, Z. (2008) *Appl. Phys. A*, **91**, 47.
- 142 Xu, Y., Wei, J., Yao, J., Fu, J. and Xue, D. (2008) *Mater. Lett.*, **62**, 1403.
- 143 Malandrino, G., Perdicaro, L.M.S., Fragala, I.L., Nigro, R. Lo, Losurdo, M. and Bruno, G. (2007) *J. Phys. Chem. C*, **111**, 3211.
- 144 Shi, C., Wang, G., Zhao, N., Du, X. and Li, J. (2008) *Chem. Phys. Lett.*, **454**, 75.
- 145 Zhao, Z.-G. and Miyauchi, M. (2008) *Angew. Chem. Int. Ed.*, **47**, 7051.
- 146 Yan, Y., Zhou, L., Zhang, J., Zeng, H., Zhang, Y. and Zhang, L. (2008) *J. Phys. Chem. C*, **112**, 10412.
- 147 Lu, H.B., Liao, L., Li, H., Tian, Y., Li, J.C., Wang, D.F. and Zhu, B.P. (2007) *J. Phys. Chem. C*, **111**, 10273.
- 148 Chen, C., Chen, D., Jiao, X. and Wang, C. (2006) *Chem. Commun.*, 4632.
- 149 Zhong, M., Zheng, M., Ma, L., Li, Y. (2007) *Nanotechnology*, **18**, 465605.
- 150 Du, N., Zhang, H., Chen, B., Ma, X., Liu, Z., Wu, J. and Yang, D. (2007) *Adv. Mater.*, **19**, 1641.
- 151 Rajasekharan, V.V. and Buttry, D.A. (2006) *Chem. Mater.*, **18**, 4541.
- 152 Mao, Y., Huang, J.Y., Ostroumov, R., Wang, K.L. and Chang, J.P. (2008) *J. Phys. Chem. C*, **112**, 2278.
- 153 Du, N., Zhang, H., Chen, B., Ma, X. and Yang, D. (2008) *Chem. Commun.*, 3028.
- 154 Wang, N., Cao, X. and Guo, L. (2008) *J. Phys. Chem. C*, **112**, 12616.
- 155 Lai, M., Martinez, J.A.G., Gratzel, M. and Riley, D.J. (2006) *J. Mater. Chem.*, **16**, 2843.
- 156 Aoki, Y., Huang, J. and Kunitake, T. (2006) *J. Mater. Chem.*, **16**, 292.
- 157 Zhao, J., Wang, X., Xu, R., Meng, F., Guo, L. and Li, Y. (2008) *Mater. Lett.*, **62**, 4428.
- 158 Meng, X., Tan, X., Meng, B., Yang, N. and Ma, Z.-F. (2008) *Mater. Chem. Phys.*, **111**, 275.
- 159 Han, W.Q., Wu, L.J. and Zhu, Y.M. (2005) *J. Am. Chem. Soc.*, **127**, 12814.
- 160 Zhou, K., Yang, Z. and Yang, S. (2007) *Chem. Mater.*, **19**, 1215.
- 161 Inguanta, R., Piazza, S. and Sunseri, C. (2007) *Nanotechnology*, **18**, 485605.
- 162 Lin, Z.-W., Kuang, Q., Lian, W., Jiang, Z.-Y., Xie, Z.-X., Huang, R.-B. and Zheng, L.-S. (2006) *J. Phys. Chem. B*, **110**, 23007.
- 163 Bao, N., Shen, L., Srinivasan, G., Yanagisawa, K. and Gupta, A. (2008) *J. Phys. Chem. C*, **112**, 8634.
- 164 Yang, Y., Wang, X., Zhong, C., Sun, C. and Li, L. (2008) *Appl. Phys. Lett.*, **92**, 122907.
- 165 Singh, S. and Krupanidhi, S.B. (2007) *Appl. Phys. A*, **87**, 27.
- 166 Nourmohammadi, A., Bahrevar, M.A. and Hietschold, M. (2008) *Mater. Lett.*, **62**, 3349.
- 167 Yasuda, K. and Schmuki, P. (2007) *Adv. Mater.*, **19**, 1757.
- 168 Saupe, G.B., Waraksa, C.C., Kim, H.N., Han, Y.J., Kaschak, D.M., Skinner, D.M. and Mallouk, T.E. (2000) *Chem. Mater.*, **12**, 1556.
- 169 Du, G., Chen, Q., Yu, Y., Zhang, S., Zhu, W. and Peng, L.M. (2004) *J. Mater. Chem.*, **14**, 1437.
- 170 Tong, Z., Takagi, S., Shimada, T., Tachibana, H. and Inoue, H. (2006) *J. Am. Chem. Soc.*, **128**, 684.
- 171 Yu, D., Qian, J., Xue, N., Zhang, D., Wang, C., Guo, X., Ding, W. and Chen, Y. (2007) *Langmuir*, **23**, 382.
- 172 Yu, J., Wang, A., Tan, J., Li, X., Bokhoven, J.A.V. and Hu, Y. (2008) *J. Mater. Chem.*, **18**, 3601.
- 173 Fang, Y., Wen, X. and Yang, S. (2006) *Angew. Chem. Int. Ed.*, **45**, 4655.
- 174 Yan, C., Zhang, T. and Lee, P.S. (2008) *Cryst. Growth, Des.*, **8**, 3144.
- 175 Wang, Y. and Cao, G. (2007) *J. Mater. Chem.*, **17**, 894.
- 176 Wang, Z., Zhou, S. and Wu, L. (2007) *Adv. Funct. Mater.*, **17**, 1790.

- 177 Olson, B.G., Decker, J.J., Nazarenko, S., Yudin, V.E., Otaigbe, J.U., Korytkova, E.N. and Gusarov, V.V. (2008) *J. Phys. Chem. C*, **112**, 12943.
- 178 Levard, C., Rose, J., Masion, A., Doelsch, E., Borschneck, D., Olivi, L., Dominici, C., Grauby, O., Woicik, J.C. and Bottero, J.-Y. (2008) *J. Am. Chem. Soc.*, **130**, 5862.
- 179 Yu, T., Park, J., Moon, J., An, K., Piao, Y. and Hyeon, T. (2007) *J. Am. Chem. Soc.*, **129**, 14558.
- 180 Zhao, Y., Frost, R.L., Martens, W.N. and Zhu, H.Y. (2007) *Langmuir*, **23**, 9850.
- 181 Yuan, Y., Liu, C., Zhang, Y. and Shan, X. (2008) *Mater. Chem. Phys.*, **112**, 275.
- 182 Liu, W., Wang, S., Chen, Y., Fang, G., Li, M. and Zhao, X.-Z. (2008) *Sensors Actuators B*, **134**, 62.
- 183 Fan, H.J., Knez, M., Scholz, R., Nielsch, K., Pippel, E., Hesse, D., Zacharias, M. and Gosele, U. (2006) *Nat. Mater.*, **5**, 627.
- 184 Ye, C., Bando, Y., Shen, G. and Golberg, D. (2006) *Angew. Chem. Int. Ed.*, **45**, 4922.
- 185 Song, S., Zhang, Y., Xing, Y., Wang, C., Feng, J., Shi, W., Zheng, G. and Zhang, H. (2008) *Adv. Funct. Mater.*, **18**, 2328.
- 186 Mukherjee, S., Kim, K. and Nair, S. (2007) *J. Am. Chem. Soc.*, **129**, 6820.
- 187 Chen, W. and Xia, X.-H. (2007) *Adv. Funct. Mater.*, **17**, 2943.
- 188 Chen, Y. and Wu, Q. (2008) *Colloids, Surf. A*, **325**, 33.
- 189 Huang, K.-W., Wang, J.-H., Chen, H.-C., Hsu, H.-C., Chang, Y.-C., Lu, M.-Y., Lee, C.-Y. and Chen, L.-J. (2007) *J. Mater. Chem.*, **17**, 2307.
- 190 Chen, R., So, M.H., Yang, J., Deng, F., Che, C.-M. and Sun, H. (2006) *Chem. Commun.*, 2265.
- 191 Loiseau, A., Williams, F., Demoncey, N., Hug, G. and Pascard, H. (1996) *Phys. Rev. Lett.*, **76**, 4737.
- 192 Chopra, N.G., Luyken, R.G., Cherrey, K., Crespi, V.H., Cohen, M.L., Louie, S.G. and Zettl, A. (1995) *Science*, **269**, 966.
- 193 Terrones, M., Hsu, W.K., Terrones, H., Zhang, J.P., Ramos, S., Hare, J.P., Castillo, R., Prassides, K., Cheetham, A.K., Kroto, H.W., Walton, D.R.M. (1996) *Chem. Phys. Lett.*, **259**, 568.
- 194 a) Yu, D.P., Sun, X.S., Lee, C.S., Bello, I., Lee, S.T., Gu, H.D., Leung, K.M., Zhou, G.W., Dong, Z.F. and Zhang, Z. (1998) *Appl. Phys. Lett.*, **72**, 1966. b) Zhou, G.W., Zhang, Z., Bai, Z.G. and Yu, D.P. (1999) *Solid, State, Commun.*, **109**, 555. c) Terauchi, M., Tanaka, M., Matsuda, H., Takeda, M. and Kimura, K. (1997) *J. Electron Microsc.*, **1**, 75.
- 195 Laude, T., Matsui, Y., Marraud, A. and Jouffrey, B. (2000) *Appl. Phys. Lett.*, **76**, 3239.
- 196 a) Golberg, D., Bando, Y., Han, W., Kurashima, K. and Sato, T. (1999) *Chem. Phys. Lett.*, **308**, 337. b) Fowler, P.W., Rogers, K.M., Seifert, G., Terrones, M. and Terrones, H. (1999) *Chem. Phys. Lett.*, **299**, 359.
- 197 Bengu, E. and Marks, L.D. (2001) *Phys. Rev. Lett.*, **86**, 2385.
- 198 Tang, C.C., Bando, Y., Sato, T. and Kurashima, K. (2002) *Chem. Commun.*, 1290.
- 199 Zhi, C.Y., Bando, Y., Tang, C. and Golberg, D. (2005) *Solid State Commun.*, **135**, 67.
- 200 Deepak, F.L., Vinod, C.P., Mukhopadhyay, K., Govindaraj, A. and Rao, C.N.R. (2002) *Chem. Phys. Lett.*, **353**, 345.
- 201 Wang, J., Kayastha, V.K., Yap, Y.K., Fan, Z., Lu, J.G., Pan, Z., Ivanov, I.N., Puzos, A.A. and Geoghegan, D.B. (2005) *Nano Lett.*, **5**, 2528.
- 202 Pal, S., Vivekchand, S.R.C., Govindaraj, A. and Rao, C.N.R. (2007) *J. Mater. Chem.*, **17**, 450.
- 203 a) Golberg, D., Bando, Y., Tang, C. and Zhi, C. (2007) *Adv. Mater.*, **19**, 2413. b) Golberg, D., Bando, Y., Bourgeois, L., Kurashima, K. and Sato, T. (2000) *Appl. Phys. Lett.*, **77**, 1979.
- 204 Dai, J., Xu, L., Fang, Z., Sheng, D., Guo, Q., Ren, Z., Wang, K. and Qian, Y. (2007) *Chem. Phys. Lett.*, **440**, 253.
- 205 Chen, X., Wang, X., Liu, J., Wang, Z. and Qian, Y. (2005) *Appl. Phys. A*, **81**, 1035.

- 206 Oku, T., Koi, N. and Suganuma, K. (2008) *Diamond Relat. Mater.*, **17**, 1805.
- 207 Wang, X.Z., Wu, Q., Hu, Z. and Chen, Y. (2007) *Electrochem. Acta*, **52**, 2841.
- 208 Chen, H., Chen, Y., Liu, Y., Fu, L., Huang, C. and Llewellyn, D. (2008) *Chem. Phys. Lett.*, **463**, 130.
- 209 Bechelany, M., Bernard, S., Brioude, A., Cornu, D., Stadelmann, P., Charcosset, C., Fiaty, K. and Miele, P. (2007) *J. Phys. Chem. C*, **111**, 13 378.
- 210 Kim, M.J., Chatterjee, S., Kim, S.M., Stach, E.A., Bradley, M.G., Pender, M.J., Sneddon, L.G. and Maruyama, B. (2008) *NanoLett.*, **8**, 3298.
- 211 Arenal, R., Stephan, O., Cochon, J.-L. and Loiseau, A. (2007) *J. Am. Chem. Soc.*, **129**, 16183.
- 212 Wang, W.L., Bai, X.D., Liu, K.H., Xu, Z., Golberg, D., Bando, Y. and Wang, E.G. (2006) *J. Am. Chem. Soc.*, **128**, 6530.
- 213 Raidongia, K., Jagadeesan, D., Upadhyay-Kahaly, M., Waghmare, U.V., Pati, S.K., Eswaramoorthy, M. and Rao, C.N.R. (2008) *J. Mater. Chem.*, **18**, 83.
- 214 Jung, W.-G., Jung, S.-H., Kung, P. and Razeghi, M. (2006) *Nanotechnology*, **17**, 54.
- 215 Gai, L., Jiang, H., Ma, W., Cui, D., Lun, N., Wang, Q. (2007) *J. Phys. Chem. C*, **111**, 2386.
- 216 Dinesh, J., Eswaramoorthy, M. and Rao, C.N.R. (2007) *J. Phys. Chem. C*, **111**, 510.
- 217 Wang, F., Jin, G.-Q. and Guo, X.-Y. (2006) *Mater. Lett.*, **60**, 330.
- 218 Miiikkulainen, V., Suvanto, M. and Pakkanen, T.A. (2008) *Thin Solid Films*, **516**, 6041.
- 219 Shen, G., Bando, Y., C.Ye, Yuan, X., Sekiguchi, T. and Golberg, D. (2006) *Angew. Chem. Int. Ed.*, **45**, 7568.
- 220 Malliakas, C.D. and Kanatzidis, M.G. (2006) *J. Am. Chem. Soc.*, **128**, 6538.
- 221 Li, B., Wu, R., Pan, Y., Wu, L., Yang, G., Chen, J. and Zhu, Q. (2008) *J. Alloys Compounds*, **462**, 446.
- 222 Taguchi, T. and Yamamoto, H. (2007) *J. Phys. Chem. C*, **111**, 18888.
- 223 Wan, C., Guo, G., Zhang, Q. (2008) *Mater. Lett.*, **62**, 2776.
- 224 Liao, L., Xu, Z., Liu, K.H., Wang, W.L., Liu, S., Bai, X.D., Wang, E.G., Li, J.C. and Liu, C. (2007) *J. Appl. Phys.*, **101**, 114306.
- 225 Hacothen, Y.R., Grunbaum, E., Tenne, R., Sloan, J. and Hutchison, J.L. (1998) *Nature*, **395**, 336.
- 226 Zeng, J., Liu, C., Huang, J., Wang, X., Zhang, S., Li, G. and Hou, J. (2008) *Nano Lett.*, **8**, 1318.
- 227 Fan, D.H., Shen, W.Z., Zheng, M.J., Zhu, Y.F. and Lu, J.J. (2007) *J. Phys. Chem. C*, **111**, 9116.
- 228 Yan, C. and Xue, D. (2006) *J. Phys. Chem. B*, **110**, 25850.
- 229 Yin, Y., Jin, Z. and Hou, F. (2007) *Nanotechnology*, **18**, 495608.
- 230 Gautam, U.K., Fang, X., Bando, Y., Zhan, J. and Golberg, D. (2008) *ACS Nano*, **2**, 1015.
- 231 Liao, H.-C., Kuo, P.-C., Lin, C.-C. and Chen, S.-Y. (2006) *J. Vac. Sci. Technol.*, **24**, 2198.
- 232 Yang, D., Meng, G., Zhang, S., Hao, Y., An, X., Wei, Q., Ye, M. and Zhang, L. (2007) *Chem. Commun.*, 1733.
- 233 Yang, L., Luo, S., Liu, S. and Cai, Q., (2008) *J. Phys. Chem. C*, **112**, 8939.
- 234 Chen, H., Chen, S., Quan, X., Yu, H., Zhao, H. and Zhang, Y. (2008) *J. Phys. Chem. C*, **112**, 9285.
- 235 Djenizian, T., Hanzu, I. and Premchand, Y.D. (2008) *Nanotechnology*, **19**, 205601.
- 236 Mohapatra, S.K., Banerjee, S. and Misra, M. (2008) *Nanotechnology*, **19**, 315601.
- 237 Chueh, Y.-L., Chou, L.-J. and Wang, Z.L. (2006) *Angew. Chem. Int. Ed.*, **45**, 7773.
- 238 Liao, L., Liu, K., Wang, W., Bai, X., Wang, E., Liu, Y., Li, J. and Liu, C. (2007) *J. Am. Chem. Soc.*, **129**, 9562.
- 239 Chen, Z.-G., Zou, J., Li, F., Liu, G., Tang, D.-M., Li, D., Liu, C., Ma, X., Cheng, H.-M., Lu, G.Q. and Zhang, Z. (2007) *Adv. Funct. Mater.*, **17**, 3371.



## 7

# Gold Nanoparticles and Carbon Nanotubes: Precursors for Novel Composite Materials

*Thathan Premkumar and Kurt E. Geckeler*

### 7.1

#### Introduction

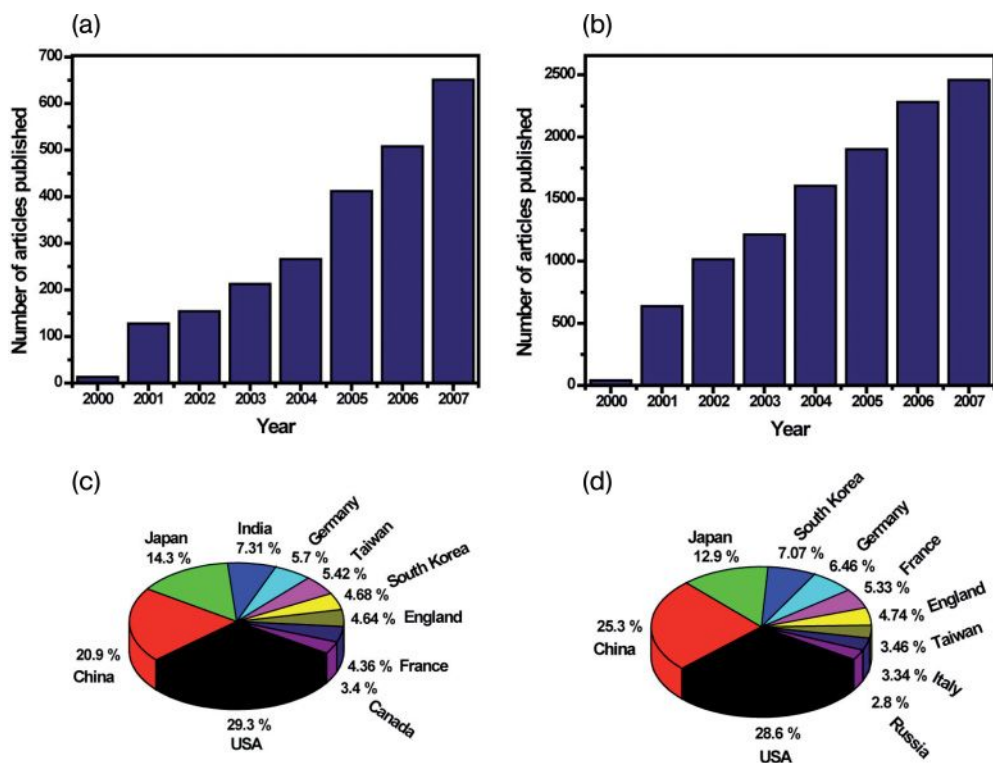
One of the most stimulating challenges in modern chemistry, materials science, and nanotechnology is the manipulation and assembly at the nanoscale. Carbon nanotubes (CNTs) constitute a novel class of nanomaterials with remarkable applications in diverse domains. The attachment of metal nanoparticles to CNTs represents a new means of obtaining novel hybrid materials with exciting characteristics for a variety of applications such as catalysts and gas sensors, as well as electronic and magnetic devices. These exceptional characteristics, which include excellent electronic properties, good chemical stability, and a large surface area, make CNTs good candidates as support materials for gold nanoparticles in many key applications, ranging from advanced catalytic systems through very sensitive electrochemical sensors and biosensors to highly efficient fuel cells. In this chapter, we focus on the recent progress in this area by exploring the various synthetic approaches and types of assemblies and interactions, in which gold nanoparticles can be attached to CNTs, and also survey the various applications of the resulting composites.

### 7.2

#### Gold Nanoparticles

The name of gold (Au) is derived from the Latin *aurum* (meaning “shining dawn”). Gold has the atomic number 79 (electron configuration, [Xe] 4f<sup>14</sup>, 5d<sup>10</sup>, 6s<sup>1</sup>), and is one of the so-called “noble” metals, which are resistant to both corrosion and oxidation. Gold is the most malleable and ductile of the known elements, with characteristic properties of being dense, soft, and shiny. Gold nanoparticles (AuNPs), which are also known as “colloidal gold” or “nanogold”, are a colloid of nanosized gold particles in a liquid (generally water). The first description of

colloidal gold was reported by the philosopher and medical doctor Francisci Antonii in 1618 [1]. Subsequently, in 1676, the chemist Johann Kunckles [2] described "... drinkable gold that contains metallic gold in a neutral, slightly pink solution that exert curative properties for several diseases." Although colloidal gold has been known from ancient times, when it was used as for staining glass, the modern scientific development of colloidal gold did not begin until Michael Faraday's pioneering studies in the nineteenth century. In 1857, Faraday prepared a red-colored solution of colloidal gold in a two-phase system by the reduction of an aqueous solution of chloroaurate ( $\text{AuCl}_4^-$ ) using phosphorus in carbon disulfide [3, 4]. The AuNPs are the most stable metal nanoparticles, and have been studied extensively during the past decade owing to their fascinating aspects in materials science, size-related electronics, and optical properties (quantum size effect), as well as their applications in catalysis and biology. This is clearly evident from a literature survey of published articles relating to AuNPs with respect to years [5]. This analysis reveals that reports on AuNPs have increased significantly each year (Figure 7.1a), and indicates that remarkable attention—from both fundamental



**Figure 7.1** Statistical survey of articles published on (a) AuNPs and (b) CNTs. Contributions from the top ten countries in percentage for (c) AuNPs and (d) CNTs.



and applied aspects—has been paid to the synthesis, characterization, and potential application of AuNPs.

When reducing the first, second or third dimensions (1-D, 2-D or 3-D) of bulk material to the nanometer scale, nanometer-thick 2-D layers, 1-D nanowires, or 0-D nanoclusters, respectively, are produced. Nanoparticles have diameters of <100 nm and demonstrate new or enhanced size-dependent properties when compared to larger particles, or to the bulk entity of the same material. Metal nanoparticles—and especially AuNPs—appeared as a new class of materials which were of interest not only in the fields of materials science and chemistry but also in nanotechnology, on the basis of their exceptional catalytic, electronic, and optical properties. Notably, these features related neither to the bulk metal nor to the molecular compounds, but depended heavily on the particle size, the nature of the protecting organic shell, and the shape of the nanoparticle [6]. For example, gold nanocrystals of different shapes possess unique optical scattering responses. Whilst symmetric spherical particles display a single scattering peak, anisotropic shapes such as rods [7], triangular prisms [8], and cubes [9] exhibit multiple scattering peaks in the visible wavelengths due to highly localized charge polarizations at their corners and edges.

With regards to metallic gold, the nucleation and growth of nanoparticles have been most widely achieved using colloidal methods rather than a variety of other approaches [4]. In these techniques, the general approach is to reduce a gold salt precursor in solution (mostly aqueous) in the presence of a stabilizing or protecting agent; this improves the chemical stability of the AuNPs formed by avoiding the aggregation among the particles. The advantages of these methods are: (i) large quantities of nanoparticles can be synthesized; (ii) solution-based processing and assembly can be readily implemented; (iii) no specialized equipment is necessary; (iv) the technique is comparatively low-cost in nature; and (v) the preparation is both facile and user-friendly. The aforesaid reasons are particularly important when considering the real applications of AuNPs; in order to utilize AuNPs as catalytic, electronic, or optical materials a large-scale synthesis and assembly process is required.

### 7.3

#### Carbon Nanotubes

Carbon nanotubes, a new carbon allotrope, were discovered by Sumio Iijima in 1991 [10] and have attracted wide and interdisciplinary attention. CNTs are fullerene-related, tube-like structures which may be considered as a rolled-up sheet of graphene. Every carbon atom is covalently bonded to three of its neighbors, and the fourth electron is free to move over the whole structure; that is, it is delocalized ( $sp^2$ -hybridization). There are two main types of CNT with high structural perfection: single-walled carbon nanotubes (SWNTs), and multiwalled carbon nanotubes (MWNTs). While the SWNTs consist of a single  $sp^2$ -bonded graphene sheet seamlessly wrapped into a hollow cylindrical tube, MWNTs include an array

of concentric cylinders (a collection of several concentric SWNTs). Both of these are typically a few nanometers in diameter (ca. between 0.4 and 3 nm for SWNTs, and between 1.4 and 100 nm for MWNTs [11]), and up to several micrometers to millimeters in length. The SWNTs represent a very important type of CNT as they exhibit significant electric properties that are not shared by the MWNT variants. In analogy to the graphite modification of carbon, the unit cells of CNTs are planar hexagons. CNTs may have a variety of helical structures [12], depending on the graphene sheet rolling-up phenomenon. The CNTs form bundles, which are entangled together in the solid state, giving rise to a highly complex network. Depending on the arrangement of the hexagon rings along the tubular surface, CNTs can be either metallic or semiconducting.

The history of CNTs may be traced back to 1976, with the fabrication of very small-diameter (<10 nm) carbon filaments [13, 14]. Nevertheless, until the discovery of fullerene chemistry [15] in 1985, the importance of these as-prepared carbon materials was not well documented. The discovery and development of fullerenes led to an increased interest in carbon materials, and this in turn induced the systematic study of carbon filaments. The CNT structure was first observed by Iijima in 1991, using high-resolution transmission electron microscopy (HR-TEM) [10]. Although the first CNTs to be discovered were MWNTs, subsequently—in 1993—smaller-diameter SWNTs were independently observed by Iijima [16] and Bethune [17]. Since then, efficient methods for the synthesis of large-quantity [18] and high-quality [19] CNTs, with their exciting electronic, mechanical, and structural properties, as well as their diverse potential applications, have paved the way for global research interest and development activities. Today, these materials form the subject of intensive investigation due not only to their academic and industrial characteristics but also the scope of their application. Indeed, both the number of studies on, and scientific interest in, CNTs have increased dramatically and continue to increase since their discovery—as demonstrated by the huge numbers of articles relating to this topic which are published each year (Figure 7.1b).

Both, SWNTs and MWNTs may generally be synthesized using methods which include arc-discharge [18, 20], laser ablation [19, 21], chemical vapor deposition (CVD) [22], and the gas-phase catalytic process (HiPco) method [23]. Unfortunately, no method has yet been introduced for the synthesis of pure CNTs; rather, all of the methods proposed to date for the synthesis of CNTs lead not only to impure products, such as carbon-coated metal catalysts, carbon-coated metal, and carbon nanoparticles/amorphous carbon, but also to structural defects such as dangling bonds. The impurities may generally be removed using a variety of purification techniques, including: the oxidation of contaminants [24]; flocculation and selective sedimentation [25]; filtration [26]; size-exclusion chromatography [27]; selective interaction with organic polymers [28]; and microwave irradiation [29]. Despite such a variety of techniques, each has been shown to have its own limitations, such that problems persist in the purification of CNTs.

As CNTs can be synthesized with extreme aspect ratios (i.e., length-to-diameter ratios), they are particularly appropriate for applications in electronics and semi-

conductor devices. The inherent size, hollow geometry and extraordinary electronic properties of CNTs make them promising building blocks for molecular or nanoscale devices. Further, the well-defined geometry, exceptional mechanical properties and remarkable electrical characteristics, in addition to their outstanding physical properties [10] (see Table 7.1), qualify them for potential applications [30] in nanoelectronic circuits, field emitters, nanoelectronic devices, nanotube aquators, batteries, probe tips for scanning probe microscopy, nanotube-reinforced materials, nanoelectromechanical systems (NEMS), and nanorobotic systems [31].

**Table 7.1** Important properties of CNTs.

Property	Item	Data	Potential application
Geometric	Layers	Single/multiple	Structures, probes, grippers/tweezers, scissors
	Aspect ratio	10–1000	
	Diameter	~0.4–3 nm (SWNTs) ~1.4–100 nm (MWNTs)	
	Length	Several $\mu\text{m}$ to mm	
Mechanical	Young's modulus	~1 TPa (steel: 0.2 TPa)	Actuators, bearings, syringes, switches, memories
	Tensile strength	45 GPa (steel: 2 GPa)	
	Density	~1.33–1.4 $\text{g cm}^{-3}$ (Al: 2.7 $\text{g cm}^{-3}$ )	
	Interlayer friction	Ultra-small	
Electronic	Conductivity	Metallic/ semi-conducting	Diodes, transistors, switches, logic gates Wires/cables
	Current carrying capacity	~1 TA $\text{cm}^{-3}$ (Cu: 1 GA $\text{cm}^{-3}$ )	
	Field emission	Activate phosphorus at ~1–3 V	Proximity/position sensors
	Band gap	$E_g$ (eV) $\approx 1 \text{ d}^{-1}$ (nm)	
	Electron transport	Ballistic, no scattering	
	Maximum current density	$10^{10} \text{ A cm}^{-2}$	
Electromechanical	Piezoresistivity	Positive/negative	Deformation/ displacement sensors
Thermal	Heat transmission	>3 kW $\text{mK}^{-1}$ (Diamond: 2 kW $\text{mK}^{-1}$ )	Circuits, sensors, thermal actuators

TPa, Tera-Pascal; GPa, Giga-Pascal; TA, Tera-Ampere; GA, Giga-Ampere.

#### 7.4 CNT–Metal Nanoparticle Composites

In nanocomposites, different materials such as metal nanoparticles, CNTs and clay may be combined with another material, usually a polymer. Nanocomposites have recently attracted considerable interest in both academic and industrial fields due to their unique mechanical, thermal and electronic properties. Nanoscaled particulates such as CNTs have been investigated as fillers in a variety of polymeric matrices to produce enhanced properties. Because of their exceptionally small diameters (several nm), as well as their high Young's modulus (~1 TPa), tensile strength (~200 GPa) and high elongation (10–30%), in addition to a high chemical stability, CNTs represent attractive reinforcement materials for lightweight and high-strength metal matrix composites. Metallic composites (especially with noble metals) containing CNTs would offer distinct advantages over polymeric composites. However, the development of metal matrix composites remains in its infancy, despite its great potential, primarily because of the high fabrication costs involved and difficulties in scaling-up the production process.

It has been predicted, based on computer stimulations, that open nanotubes may be filled with liquid by capillary suction [32]. This has provided much speculation that the filling of extraneous materials into the hollow nanotube cavities might have interesting effects on the physical and electronic properties of the encapsulated materials. The modification of CNTs into composite nanofibers by filling them with molten materials through capillary action has been reported [33, 34], and subsequently metal carbides have been entrapped into the hollow cavities of CNTs by using an arc discharge method [35, 36]. In contrast, in 1994 Ajayan and coworkers [37] reported for the first time that a combination of CNTs and metal nanoparticles could also be achieved by depositing the metal cluster on the surface (outside the tube) of the CNTs; this was termed the “decoration” of CNTs with metal clusters. The method involved the use of SWNTs as a support material for dispersing ruthenium nanoparticles that would then serve as a catalyst in heterogeneous catalysis. As a result, ~0.2% (w/w) of Ru nanoparticles were deposited on the surface of the CNTs. Following these successes, a variety of hybrid composites was introduced and developed with either metal or metal oxide or semiconductor nanoparticles. It is envisaged that these composite materials might find practical uses as nanowires and novel catalysts.

The combination of metal nanoparticles (notably AuNPs) and CNTs may lead to the development of a new class of nanocomposite materials, and lead in turn to the successful integration of the properties of these two components in new hybrid materials that present significant features for catalysis and nanotechnology. The combination of two classes of novel material may be obtained as either particles coated on the surface of the CNTs (exohedral), or encapsulated in the nanotube cavity (endohedral). Here, the CNT surface acts as a template where nanoparticles (either naked or stabilized by protecting agents) are absorbed or, in the case of a functionalized CNT, the nanoparticles may be linked through a functional group of the organic moieties attached to the CNTs. This new type

of composite material is important not only for fundamental and academic studies of the interactions between the matrix and the metallic nanoparticles, but also for various applications such as catalysts as well as electronic, optical, and sensor devices.

## 7.5

### CNT–AuNP Composites

A variety of resourceful techniques has been reported for the production of CNT–AuNP composites (in general, the deposition of AuNPs onto the surface of the CNT substrate), each offering different degrees of particle size control and distribution along the CNTs. By changing the size and concentration of the AuNPs deposited/incorporated, the electronic properties of the CNTs can in turn be controlled. Composites of CNTs with AuNPs may be created via different pathways. One approach is to grow and/or incorporate the AuNPs into the hollow cavities of the CNTs, while a second approach is to grow and/or deposit naked AuNPs directly onto the terrace of the CNTs. In yet another process, the AuNPs may be prepared and modified with suitable functional groups that can be connected to the CNT surface via covalent bonding through organic moieties; alternatively, the modified AuNPs may simply be linked to the surface of the CNTs via supramolecular interactions.

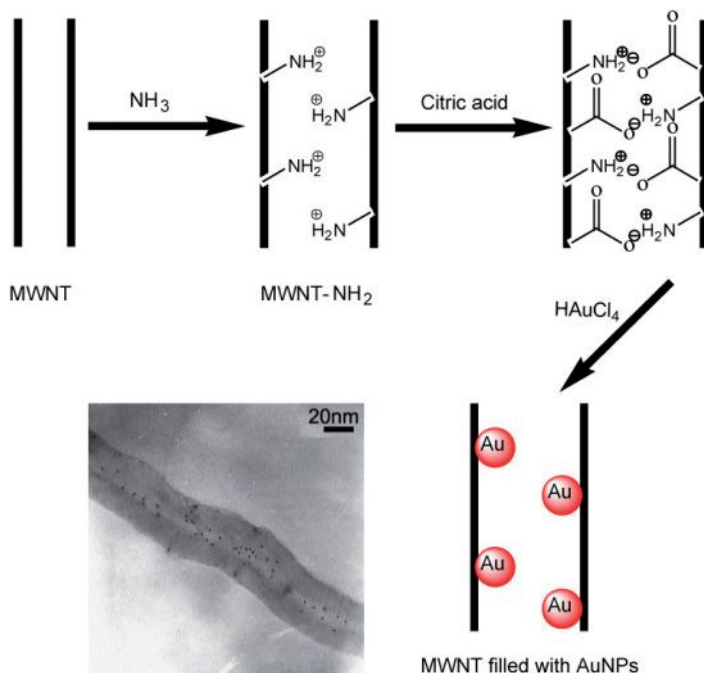
#### 7.5.1

##### Filling of CNTs with AuNPs

In order to synthesize CNTs with predetermined characteristics, it is essential to identify and control the mechanisms that direct CNT growth. The major challenge here is to identify effective ways in which to fill the metal nanoparticles (notably AuNPs) into the hollow CNT cavities, without affecting the latter's individual characteristic properties.

A simple procedure for producing a composite is to fill the MWNTs with AuNPs, simply by mixing an aqueous citric acid solution containing  $\text{NH}_3$ -treated MWNTs and aqueous auric chloride solution [38]. Heat treatment in  $\text{NH}_3$  causes most of the nanotubes to be open, such that functional basic groups are created on their inner walls. Mixing and ultrasonication will then help the citric acid to combine strongly with the basic groups via electrostatic attraction, thus facilitating the *in situ* reduction and subsequent attachment of AuNPs (1–2 nm) inside the nanotubes (Figure 7.2). These hybrid materials may in time become important for investigating and creating a rich variety of electrical and sensor devices.

In another “wet chemistry” technique, a two-step procedure was used to produce a composite material by filling gold metal into the cavities of the CNTs. Here, the nanotubes were opened by oxidation with  $\text{HNO}_3$  [39] and then stirred overnight with a concentrated aqueous solution of  $\text{AuCl}_3$ . The resultant CNTs, when separated from excess concentrated solution, were calcined in a furnace under argon



**Figure 7.2** Schematic illustration for the attachment of AuNPs to  $\text{NH}_3$ -treated CNTs and the TEM image of AuNP-filled CNTs. Adopted and modified according to Ref. [38]; TEM image reprinted with permission from Ref. [38].

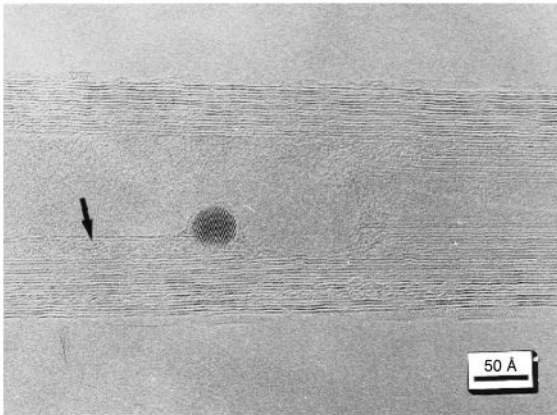
at  $600^\circ\text{C}$ , whereby the  $\text{AuCl}_3$  was decomposed to produce elemental gold [40]. Most of the gold entrapped within the hollow CNTs was seen to be crystalline in nature, spherical in shape, and to range in size from 1 to 5 nm diameter. A HR-TEM image of a CNT encapsulated with a gold crystal, together with the analytical energy-dispersive spectrum (EDS) of the gold particle, are shown in Figure 7.3. More importantly, by using this method it was possible to produce a relatively high percentage ( $\sim 70\%$ ) of opened nanotubes to be filled with metallic gold [33, 39].

### 7.5.2

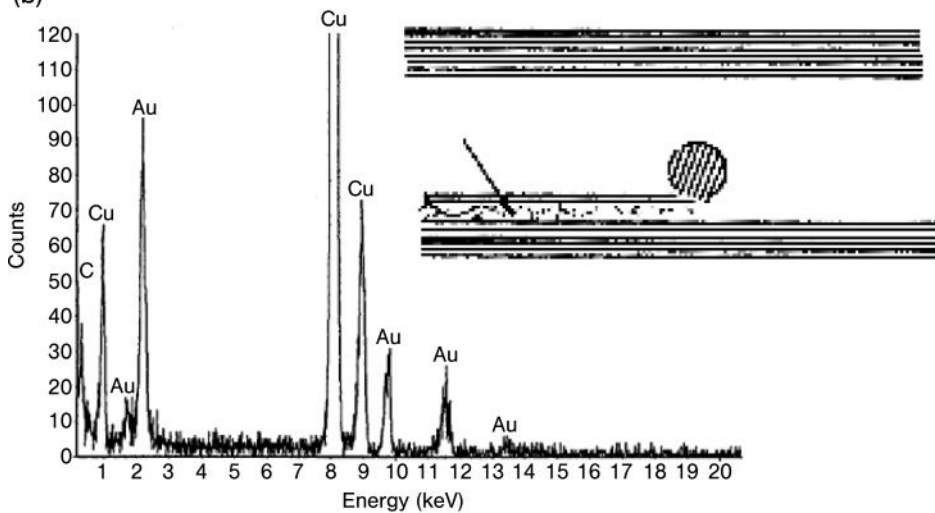
#### Deposition of AuNPs Directly on the CNT Surface

When depositing AuNPs onto the terrace of the CNTs, it is possible to use gold salts as the precursors for the AuNPs; these salts are produced by a variety of reduction processes, using either reducing agents and/or external energies such as heat (thermal), photochemical, and light, in the presence of the CNTs. The interactions between the AuNPs and CNTs are mostly based on van der Waals forces which, in some cases, appear to be sufficiently strong so as to ensure significant adhesion.

(a)



(b)

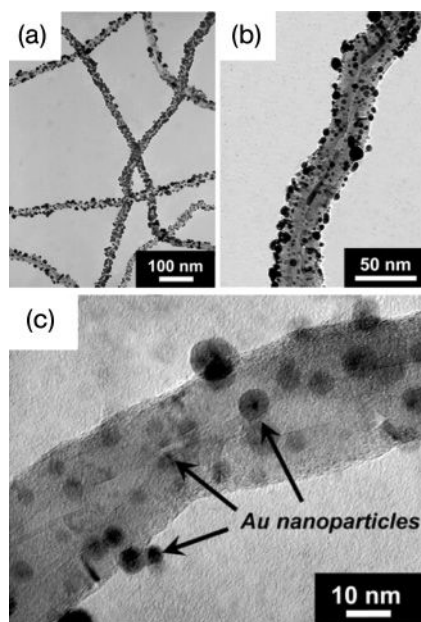


**Figure 7.3** (a) High-resolution transmission electron microscopy (HR-TEM) image of a carbon nanotube filled with a spherical Au crystal. The solid arrow shown in the HR-TEM image indicates where there has been intercalation into the gaps where carbon layers are missing; (b) ED spectrum of the Au particle. Reprinted with permission from Ref. [40].

An effective method was introduced by Xue and coworkers for depositing AuNPs onto the walls of CNTs [41]. For this, AuNPs (average size 8 nm) were grown on the surface of the CNTs by the thermal decomposition (400 °C) of gold salts under a hydrogen atmosphere. This synthetic strategy has also been shown to be a generalized process that can easily be extended to the synthesis of different types of metal nanoparticle (Pt, Ag, Pd) onto the CNT surface. It appears

that the CNTs play a vital role here, not only as a template for tuning the metal nanoparticles size but also acting as a support material. This finding was supported by the fact that larger particles were observed when metal salts were reduced in the presence of graphite or amorphous carbon. Xue and coworkers suggested that these composite materials might be used as efficient catalysts for certain environmentally advantageous reactions, as well as certain applications in electronic devices.

Raghuveer and coworkers established a novel “eco-friendly” strategy of utilizing microwave irradiation for the rapid introduction of carboxyl, carbonyl, hydroxyl, and allyl terminal groups onto the surface of MWNTs, without using any aggressive oxidants such as  $\text{HNO}_3$  and/or ultrasonication [42]. Here, the functional groups served as the preferred nucleation points for reducing gold ions from solution by a microwave-assisted reduction reaction. MWNTs were dispersed in water and added to an aqueous solution containing  $\text{HAuCl}_4$  and ethylene glycol. After microwave irradiation, the surfaces of the MWNTs were seen to be decorated by uniformly dispersed AuNPs (Figure 7.4) that ranged in size from 3 to 10 nm (average  $\sim 6$  nm). The MWNTs were derivatized with nanoparticles synthesized by an *in situ* gold-ion reduction during functionalization, all in a single-step process. The notable point here was that the overall tubular structure of the MWNTs remained intact, as was evident from TEM images. This was in great contrast to

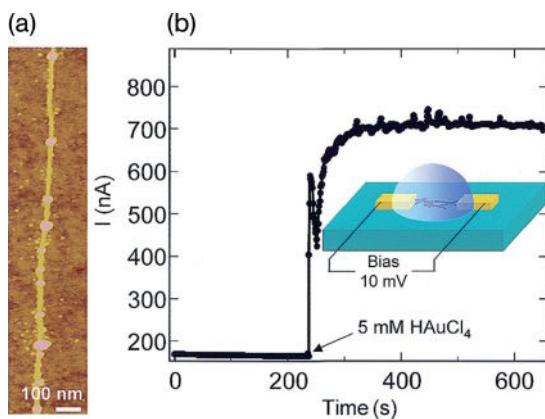


**Figure 7.4** (a, b) Low- and (c) high-magnification bright-field TEM images showing the decoration of MWNTs with AuNPs of 3–10 nm diameter. Reprinted with permission from Ref. [42].

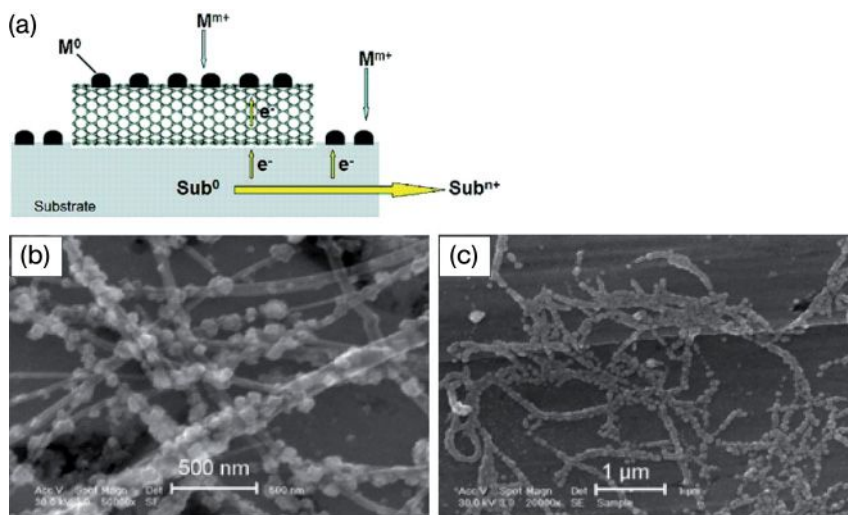


the rupture and tube breakage observed during functionalization by aggressive sonication and acid treatment [43].

A different strategy for the formation of AuNPs on the surface of SWNTs, based on the spontaneous reduction of metal ions in solution without the use of a reducing agent, was reported by Choi and coworkers [44]. This approach differed from a typical electroless deposition, which requires either a reducing agent or a catalyst, as a result of direct redox reactions between the ions and nanotubes. Electroless deposition methods rely on a chemical (as opposed to an electrochemical) reduction process, whereby a chemical species with a redox potential suitably lower than that of the metal species being reduced provides the driving force for the reaction [45]. A spontaneous decoration of AuNPs (average size 7 nm) on the sidewalls of the SWNTs was observed following their immersion in  $\text{HAuCl}_4$  ( $\text{Au}^{3+}$ ) solution for 3 min (Figure 7.5a). The  $\text{Au}^{3+}$  ion reduction and SWNT oxidation during electroless metal deposition was investigated by measuring the electrical conductance of SWNTs immersed in solutions (Figure 7.5b). When the SWNTs act as electron donors, hole insertion into SWNTs would be expected to cause an increase in the electrical conductance [46] to the already p-type nanotubes due to  $\text{O}_2$  doping under ambient conditions [47]. Spontaneous metal deposition onto the SWNTs by an electroless process allows for a facile, efficient, and selective immobilization of metal species on nanotubes, which may be useful for sensor and catalysis applications. However, this selective electroless metal deposition on SWNTs was shown to be effective only for Au or Pt; other metal ions such as  $\text{Ag}^+$ ,  $\text{Ni}^{2+}$ , and  $\text{Cu}^{2+}$ , could not be reduced in the same way, perhaps due to their lower redox potentials.



**Figure 7.5** (a) Atomic force microscopy image of AuNPs formed on an individual SWNT; (b) Monitoring the change in current across a SWNT during exposure to a 5 mM  $\text{HAuCl}_4$  solution. The period before the exposure corresponds to the nanotube in a mixture of ethanol and water (1:1). Inset: Schematic for the experimental set-up. Spacing between points = 1 s. Reprinted with permission from Ref. [44].



**Figure 7.6** (a) Schematic illustration of the metal nanoparticle deposition on CNTs via the substrate-enhanced electroless deposition process; (b, c) Scanning electron microscopy images of (b) MWNTs and (c) SWNTs supported by a copper foil after immersion in an aqueous solution of HAuCl<sub>4</sub> (3.8 mM). Reprinted with permission from Ref. [48].

Qu and Dai introduced for the first time another facile, but versatile and effective, method for the electroless deposition of AuNPs on both SWNTs and MWNTs in the absence of any additional reducing agent [48]. Upon immersion of the copper-supported MWNTs or SWNTs into an aqueous solution of HAuCl<sub>4</sub> (3.8 mM), the AuNPs were deposited spontaneously onto the terrace of the nanotubes. The advantage of this technique over the previous method is that a large variety of metal nanoparticles (even for metals with a lower redox potential than that of the CNTs, such as Cu and Ag) could be reduced and decorated onto the surface of both MWNTs and SWNTs. The general scheme of the reaction process, together with scanning electron microscopy (SEM) images of AuNPs decorated onto MWNTs and SWNTs, are shown in Figure 7.6.

The deposition of metal nanoparticles is achieved via the redox reaction of a galvanic cell, in which the nanotube acts as a cathode for the metal nanoparticle deposition (M<sup>0</sup>, e.g., Au<sup>0</sup>) from the reduction of metal ions (M<sup>m+</sup>, e.g., Au<sup>3+</sup>) in solution, while the metal substrate (e.g., Cu) serves as an anode where metal atoms (Sub<sup>0</sup>) are oxidized into corresponding ions (Sub<sup>n+</sup>) followed by dissolution [49] (Figure 7.6). This process, which is known as substrate-enhanced electroless deposition (SEED), allows the electroless deposition of many metal nanoparticles onto conducting CNTs, and indicates a great potential for the functionalization of CNTs with various metal nanoparticles.

Geckeler and coworkers have established an unprecedented approach to prepare SWNT–AuNP hybrids in homogeneous phase by using the reaction of gold salts

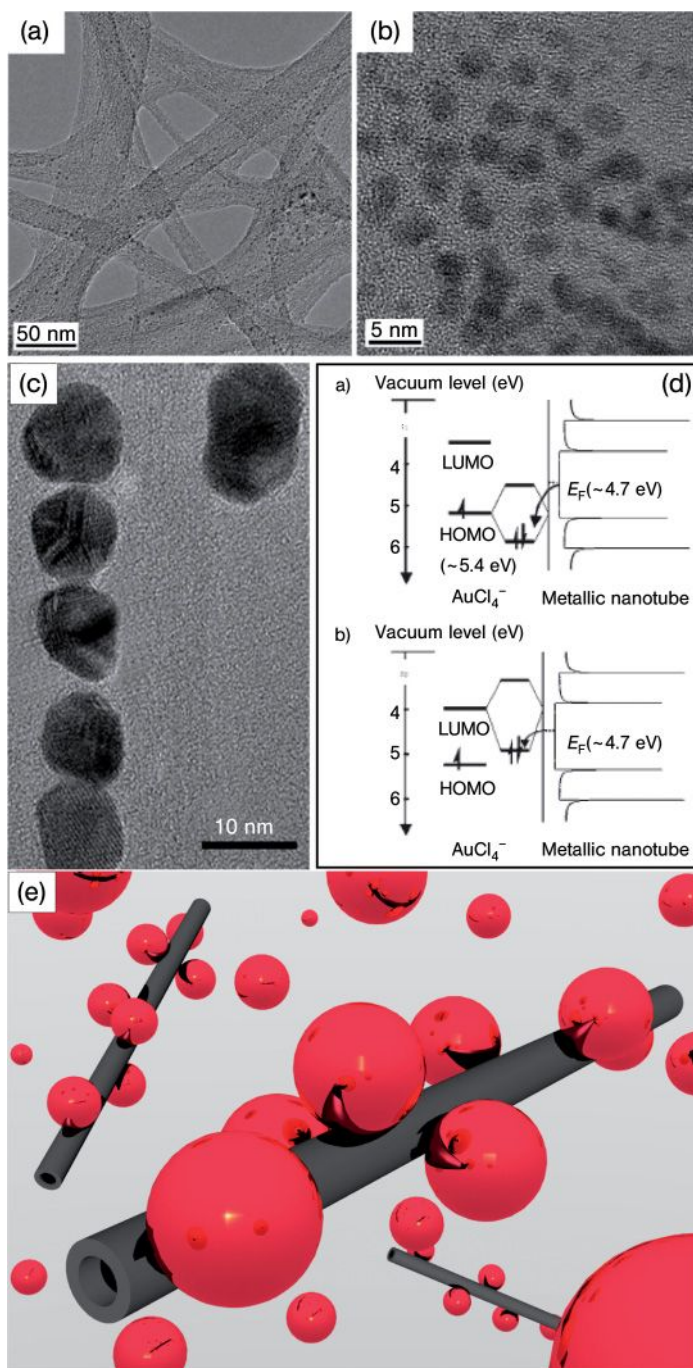
and SWNTs in the presence of a surfactant in aqueous solution, without the addition of a reducing agent [50]. The AuNPs decorated on the sidewalls of the SWNTs were uniform in size and well dispersed (Figure 7.7). Statistical calculations indicated the average AuNP size to be  $2.94 \pm 0.75$  nm, with  $7.5 \times 10^{-17}$  g of gold being coated on an individual nanotube that in turn contained approximately 300 AuNPs. Interestingly, the size of the AuNPs decorated on the surface of the SWNTs could be tailored by altering the concentration of the gold salt solution.

The chemistry of the hybrid material was described by using a frontier-orbital picture. As the relative position of the Fermi level of nanotubes with respect to the mixed metal ion/nanotube highest occupied molecular orbital (HOMO) and lowest unoccupied molecular orbital (LUMO) is suitable for charge transfer, both semiconducting and metallic CNTs may establish attractive interactions with the metal ions, either by four-electron interactions involving two occupied orbitals, or by zero-electron interactions involving two empty orbitals (Figure 7.7d). It was noted that the HOMO level of  $\text{AuCl}_4^-$  is partly occupied with electrons. This method is easy to scale-up, such that a uniform size of AuNPs may be decorated on the walls of the SWNTs, and size of the AuNPs can also be controlled. More importantly, as the method yields water-soluble composite materials, a much greater variety of applications can be envisaged.

A simple method has been developed recently to prepare hybrid materials from SWNTs and AuNPs, including Pt and Rh nanoparticles. For this, nanoparticles were deposited on the surface of the SWNTs by the mild reduction of metal salts using poly(ethylene glycol)-200 as the reducing agent [51]. The free surface of the nanoparticles attached to the SWNTs was then coated with organic aliphatic molecules such as oleylamine, which enhanced the dispersion of the resulting hybrid material in organic solvents. This method avoids chemical functionalization of the sidewalls and open ends of the SWNTs, and the final hybrid material may be used for the application in the catalysis of organic reactions.

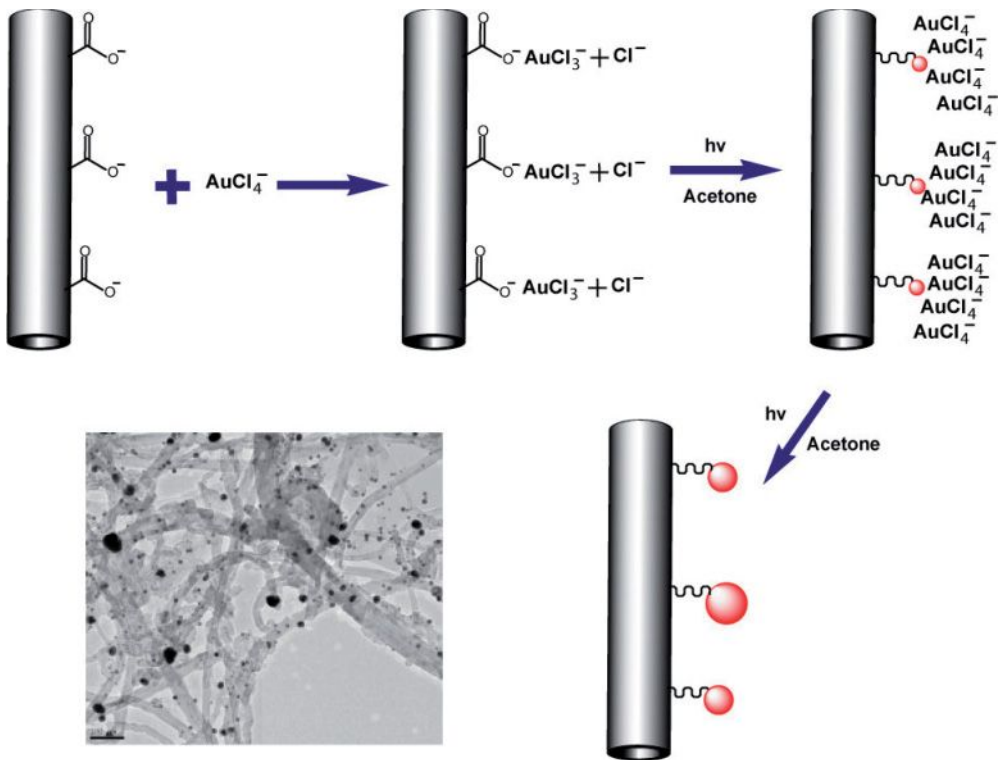
Recently, a simple UV irradiation method was developed to grow uncoated naked AuNPs on carboxy-modified MWNTs by performing UV irradiation on mixed solution containing oxidized MWNTs,  $\text{HAuCl}_4$ , and acetone (acting as a photosensitive agent) at room temperature (Figure 7.8) [52]. The size of AuNPs deposited on the terrace of the MWNTs was found to depend heavily on the diameter of MWNTs and the solution pH. The size of the AuNPs was indirectly proportional to the diameter of MWNTs and the solution pH. As a high catalytic activity (especially for AuNPs) mainly depends on the steps, edges, and corner sites of surface, and also on the electrical interactions between AuNPs and supporting materials, the resultant composites may prove to be advantageous in catalytic reactions.

Although a variety of ingenious strategies to decorate AuNPs onto CNTs is available, the electrodeposition method has its own advantages. Electrochemistry represents a potent technique for the deposition of diverse metals and/or the surface modification of CNTs, being both rapid and facile, and thus allowing the chemist and materials scientist to control with ease the nucleation and growth of the metal nanoparticles [45, 53, 54]. It is very feasible to control the size and distribution of



**Figure 7.7** (a) Transmission electron microscopy (TEM) image, and (b, c) HR-TEM images of the CNT/AuNPs hybrid; (d) Frontier-orbital picture representation of four-electron interactions (plot a), and zero-electron interactions (plot b) between  $\text{AuCl}_4^-$  and a metallic CNT. The  $\text{AuCl}_4^-$  frontier-orbitals are designated as HOMO and

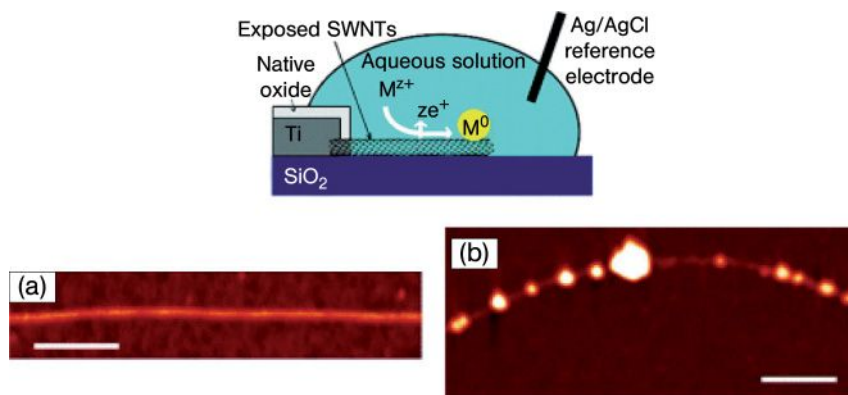
LUMO, and the nanotube orbitals are represented by the density of states plots.  $E_F$  = Fermi level. (Reprinted with permission from Ref. [50]); (e) Schematic showing decoration of the surface of CNTs with AuNPs. (Kyungjae Lee is gratefully acknowledged for his support in the preparation of this image).



**Figure 7.8** Scheme showing the growth of AuNPs on the surface of MWNTs initiated by UV irradiation, and a TEM image of AuNPs attached to the surface of MWNTs at pH 12. Scale bar = 100nm. Adopted and modified according to Ref. [52]; TEM image reprinted with permission from Ref. [52].

metal nanoparticles simply by varying the deposition potential, time, and substrate. However, the other imaginative methods of depositing nanoparticles onto the CNTs surface involve some tricky, tedious, and time-consuming treatments that allow the impurities in the bath solutions to be included either into the nanoparticles or onto the terrace of the CNTs themselves, thus affecting the optical or catalytic properties of the nanoparticles [54]. Electrochemically deposited nanoparticles—particularly of noble metals such as Au, Pt, or Pd—are often of very high purity, are formed rapidly, and have good adhesion to the CNT substrate [53, 54].

Quinn and coworkers [53] reported a general electrodeposition method for depositing noble metals such as Au, Pt, and Pd onto the surface of the SWNTs by immersing the latter in a solution of the respective metal salts, namely  $\text{HAuCl}_4$ ,  $\text{K}_2\text{PtCl}_4$ , and  $(\text{NH}_4)_2\text{PdCl}_4$ . Whilst the size of the nanoparticles was tuned by the concentration of the metal precursor salt and the electrochemical deposition parameters, the coverage of the nanoparticles on the surface of the SWNTs was controlled by the nucleation potential. The resultant composite material was

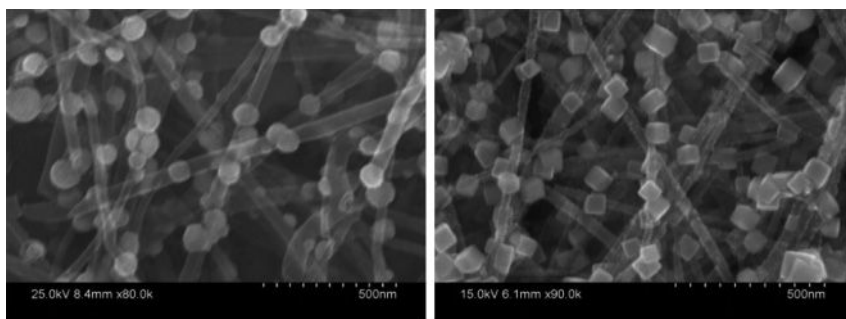


**Figure 7.9** General schematic illustration of the SWNT as an electrode used for the electrodeposition of metal nanoparticles, and AFM images of the predeposition (a) and postdeposition (b) of Au. The deposition time was 20 s. Scale bar = 300 nm. Reprinted with permission from Ref. [53].

considered as a metallic wire, as the surface of the SWNTs was thoroughly decorated by the metal nanoparticles (Figure 7.9). It was noted that, under the experimental conditions, both the sidewalls and ends of the SWNTs were coated equally by metal nanoparticles, even though it is believed that the CNTs sidewalls are less reactive than the tube ends. The SWNT serves a dual function in such a way that initially acts as the electrodeposition template, and subsequently as a wire to electrically connect the deposited Au, Pt, and Pd nanoparticles.

The cubic and spherical nanoparticles of gold, with a fairly narrow size distribution, deposited on the surface of the CNTs were produced by immersing copper foil-supported CNTs into an aqueous solution of  $\text{HAuCl}_4$  with and without  $\text{CuCl}_2$  at room temperature under different reaction conditions (e.g., different concentration and reaction time) [55, 56]. Both, the shape and size of the AuNPs were found to depend heavily on the gold salt concentration and reaction time, providing considerable room for regulating the morphological features of the resultant nanoparticles. The size of the AuNPs deposited on the surface of CNTs is approximately 60–100 nm, although their size can be tailored by controlling the reaction conditions, especially the deposition time [56]. Gold nanospheres and nanocubes were multisite deposited along the CNT length, with individual nanotubes even threading through the nanoparticles (Figure 7.10). The facile and versatile technique for the shape- and size-controlled syntheses of AuNPs for the site-selective modification of CNTs is very attractive for producing various multicomponent nanoparticle–nanotube hybrid structures that might be useful in a wide range of potential applications, including fuel cells, catalytic, sensing, and optoelectronic systems. Further, in order to investigate and explain the optical response of the CNT–AuNP hybrid from a theoretical standpoint, a 3-D electrodynamic model was built using the finite-difference time-domain [56]. These studies proposed an anisotropic





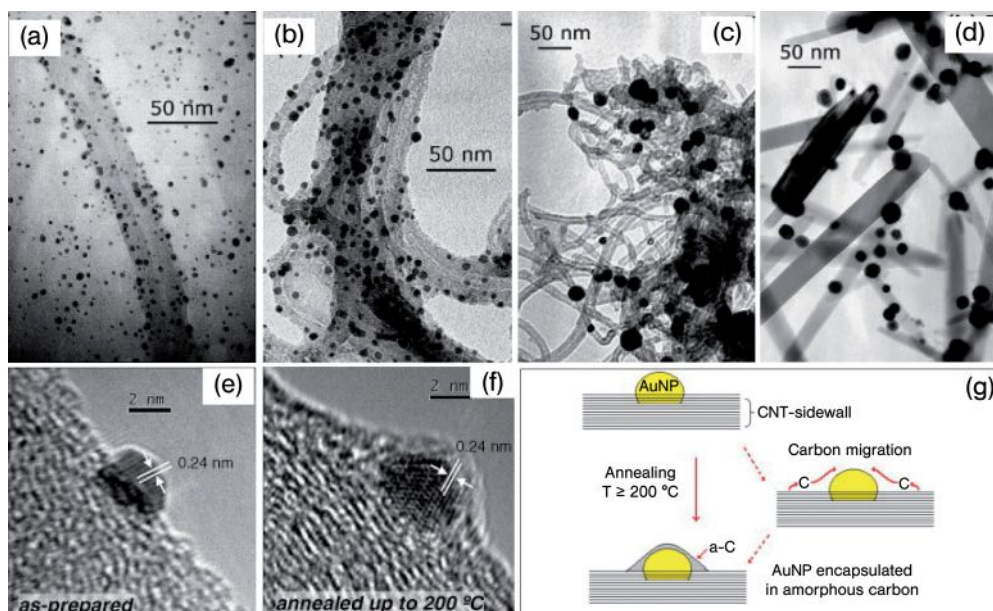
**Figure 7.10** Scanning electron microscopy images of synthesized CNTs that are grafted with gold nanosphere and nanocube systems. Reprinted with permission from Ref. [56].

response, in line with the experimentally observed absorption peaks of such systems in the optical range.

Tello and coworkers introduced a new method, known as solvated metal atom dispersion (SMAD), in combination with CVD, to prepare MWNT and AuNP hybrid materials, and subsequently investigated their thermal stabilities [57]. In the SMAD protocol, a colloid with small and highly reactive gold clusters was prepared by co-evaporation of the gold metal and acetone. The colloid was subsequently condensed into a frozen matrix in a liquid nitrogen atmosphere, and the matrix then allowed to warm to room temperature. The as-prepared gold clusters were reacted with previously incorporated MWNTs in the reactor to yield MWNT–AuNP hybrid materials which were thermally stable up to 400 °C. Moreover, no appreciable changes in particle size were detected as the AuNPs were covered with amorphous carbon after annealing at 200 °C (Figure 7.11).

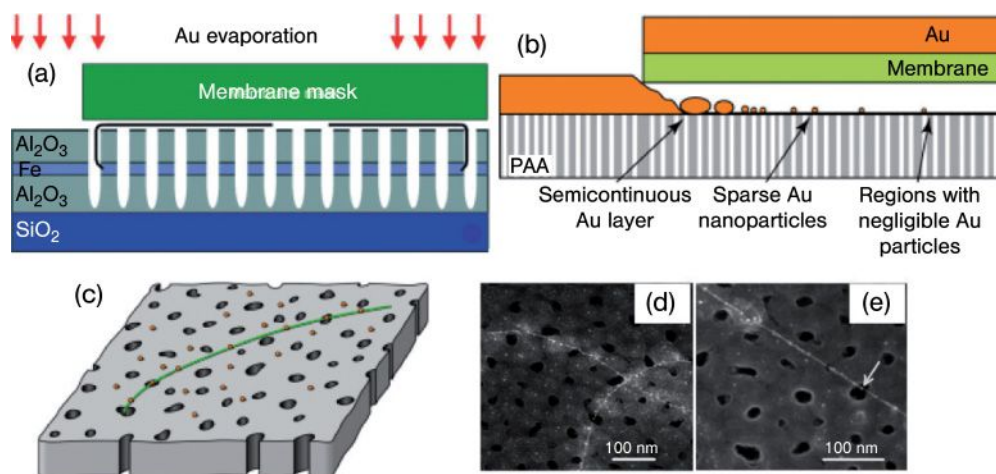
Interestingly, whilst the average AuNP size was increased approximately from 4 to 20 nm and the nanoparticles were detached from the MWNTs, no damage was induced on the MWNTs when the hybrid material was annealed beyond 600 °C (Figure 7.11c). Surprisingly, further heating (annealing up to 800 °C) induced a severe transformation of the MWNTs (perhaps due to a catalytic activity of the AuNPs) into cylindrical solid carbon nanorods (Figure 7.11d). It would appear that this method provides a new approach to the synthesis of both carbon nanorods and MWNT–AuNP composites that are useful in a variety of key applications.

A new and important approach was developed recently to form naked sub-10-nm AuNPs on individual 2 nm bare CNTs [58]. These assemblies were produced on the terrace of a porous anodic alumina (PAA) template, on which the CNTs (single- or double-walled) were grown by using plasma-enhanced chemical vapor deposition (PECVD). The AuNPs were obtained via an indirect evaporation method using a membrane mask, consisting of a suspended, patterned silicon nitride film; the AuNPs then diffused along the PAA surface into the regions containing CNTs (Figure 7.12a). Three distinct regions were observed on the PAA surface: (i) a semi-continuous gold film composed of multiple grains; (ii) a transition region,



**Figure 7.11** Transmission electron microscopy images for the as-prepared AuNP-CNT hybrids (a), and annealed up to 200°C (b), 600°C (c), and 800°C; (d) HR-TEM images of AuNPs anchored on the CNT-walls (e, f); for the as-prepared AuNP-CNT hybrids (e, f), and annealed up to 200°C (f). A carbon

layer is encapsulating the AuNPs after the thermal process. Lattice fringes on gold particles are consistent with the (111) fcc orientation (0.235 nm); (g) A schematic representation of the process. Reprinted with permission from Ref. [57].



**Figure 7.12** (a) Diagram of a cross-section of the experimental set-up; (b) Schematic representation of the three regions with different Au particle distribution on the porous anodic alumina (PAA) film after Au evaporation through a nitride membrane mask; (c) Enlarged view of region sparse AuNPs, showing one CNT emerging from a pore and growing along the PAA surface. The

AuNPs diffuse into this region and attach to the CNT; (d) Field-emission scanning electron microscopy images of an area from region sparse AuNPs, showing two crossed CNTs decorated with AuNPs; (e) A sub-5-nm AuNP (indicated by a white arrow) is on a CNT and above the pore in the PAA film. Scale bar = 100 nm. Reprinted with permission from Ref. [58].



in which a sparse coverage of small AuNPs was observed; and (iii) a region where negligible gold was observed. The schematic illustration of the three regions with different gold particle distributions on the PAA film after the evaporation of gold through a nitride membrane mask is shown in Figure 7.12b. The presence of the various regions is attributed to the migration of gold on the surface; as the gold atoms migrate they also aggregate, forming grains (at large surface coverage) and small nanoparticles (at lower surface coverage) [59]. As shown schematically in Figure 7.12c, within region (b) the AuNPs were observed on the PAA surface and on the CNTs. The field-emission scanning electron microscopy (FESEM) image of an area within region (b) shows the presence of a number of well-defined particles with diameters  $\sim 5$  nm along the CNTs, most likely due to AuNPs (Figure 7.12d). In addition, somewhat diffuse bright regions with the dimensions of 20–40 nm nearer to CNTs were also observed, though these may be due to local charging effects arising during the FESEM imaging. The AuNPs attached strongly to the CNTs, as substantiated by the observations of nanoparticles that were suspended over pores or that moved along with the CNTs (Figure 7.12e). The strong mechanical binding between the AuNPs and the CNTs revealed a comparatively close contact between the two objects, and also showed that this binding energy was larger than that between the cluster and the alumina surface. This behavior is significant for understanding a strongly coupled electronic system. In contrast to most other general methods for the direct evaporation of gold onto CNTs, defect sites on the CNTs are not necessary in this method of creating preformed AuNPs. This approach may provide a new strategy for functionalizing CNTs for chemical or biological sensing and also for fundamental studies of nanoscale contacts to CNTs. Thus, drawbacks such as the complexity in directly functionalizing CNTs, and the inability to obtain individual SWNTs by using common bulk synthesis methods are avoided, which confine the applicability of CNTs as primary elements in sensors.

### 7.5.3

#### **Interaction Between Modified AuNPs and CNTs**

A significant feature of nanoscience and nanotechnology concerns the progress of experimental protocols for the preparation of nanoparticles of diverse chemical compositions, sizes, shapes, and controlled dispersity with a facile approach and no environmental risk [60]. There are many established methods for the synthesis of AuNPs, including conventional chemical reduction, heat-treatment, microwave irradiation, sonochemical, photolytical, seeding growth approaches, and self-reduction using surfactants [4, 61]. It is well known that the reaction medium, reducing agent, and capping or protecting agent are the three key factors for the synthesis and stabilization of metal nanoparticles in general, and for AuNPs in particular. By selecting these factors appropriately, it would be possible to modify the nanoparticles according to their convenient purposes. Therefore, it should also be possible to connect the AuNPs to the surface of the CNTs through either covalent linking or supramolecular (noncovalent) interaction. Hence, the AuNPs

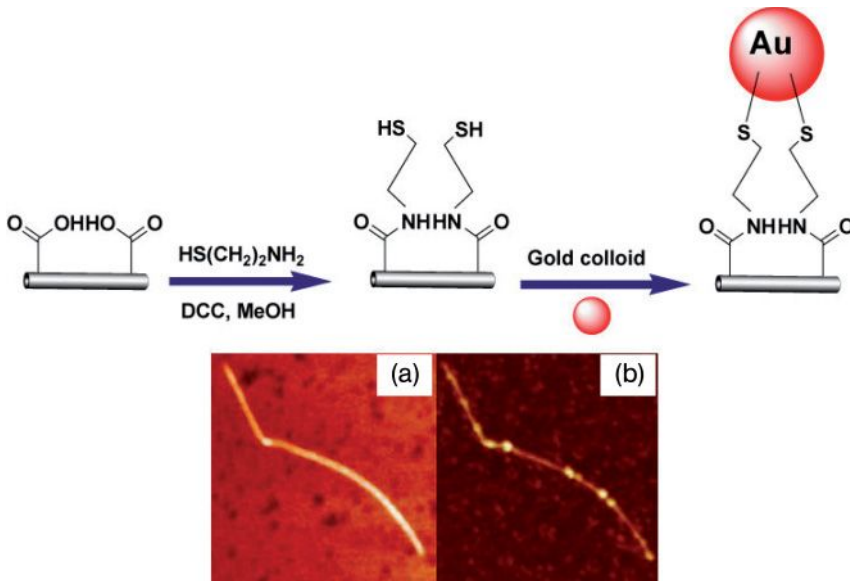
prepared are modified with suitable functional groups so as to link the AuNPs to the CNT surface. These connections can be attained by using the functional groups of the modified AuNPs to covalently link with functional groups present on the surface of the CNTs. An alternative method would be simply to adhere the linker onto the CNT surface via supramolecular interactions such as hydrophobic interactions, hydrogen bond linkage,  $\pi$ - $\pi$  interactions, or electrostatic attraction.

#### 7.5.3.1 Covalent Linkage

As CNTs are chemically inert, the triggering of their surface is a vital prerequisite for linking the metal nanoclusters to them. Chemical functionalization is the most common and widely used way to introduce the linkers, as well as to improve dispersibility of CNTs, which is also significant for the proficient and uniform deposition of nanoparticles. The functionalization of SWNTs by a chemical method (covalent linkage) to enhance its dispersibility was introduced by Chen and coworkers [62].

Azamian and coworkers [63] employed carboxylate chemistry to covalently link the AuNPs to defect sites in controllably oxidized SWNT termini and/or sidewalls. The carboxylic acid groups created on a SWNT were converted to amides by reaction with carbodiimide reagents [*N,N'*-dicyclohexyl-carbodiimide (DCC) or 1-ethyl-3-(3-dimethyl-amino-propyl)-carbodiimide (EDC)] and 2-aminoethanethiol. Generally, carbodiimide catalyzes the formation of amide bonds between carboxylic acids or phosphates and amines by activating carboxyl or phosphate to form an *O*-urea derivative. The introduced thiol functionality was consequently linked with well-dispersed gold colloids (Figure 7.13). The attachment of AuNPs to SWNTs sidewalls was corroborated by imaging the pristine SWNTs with atomic force microscopy (AFM) before and after exposure to the coupling reagent and colloidal AuNPs. This technique may be extended to test, with ease, the functionalization of SWNTs with a range of groups.

A simple, direct, solvent-free approach was reported for decorating AuNPs onto the surface of MWNTs functionalized with aliphatic dithiols such as 1,4-butanedithiol, 1,6-hexanedithiol, 1,8-octanedithiol, and 2-aminoethanethiol [64]. While AuNPs (~1.7 nm) with a narrow particle size distribution were produced on the 1,6-hexanedithiol-functionalized MWNTs, the average size of AuNPs was 5.5 nm, obtained on MWNTs derivatized with aminothiols. This difference in the AuNPs size was apparently due to a coalescence phenomenon of AuNPs in aminothiols-functionalized MWNT samples; this could be the result of a nonuniform capping of the aminothiols over the AuNPs surface, avoiding the passivated AuNPs. The main drawback of this approach is that attempts to attach AuNPs to the derivatized MWNTs using water as a solvent medium were not particularly successful, giving rise to a considerable agglomeration of gold over the nanotube bundles, obviously due to the poor CNT dispersibility in water. Instead, the MWNTs nicely decorated with well-dispersed AuNPs can be prepared only when water is substituted by 2-propanol. It is anticipated that this method may be useful for attaching CNTs to gold tips for AFM and scanning tunneling microscopy

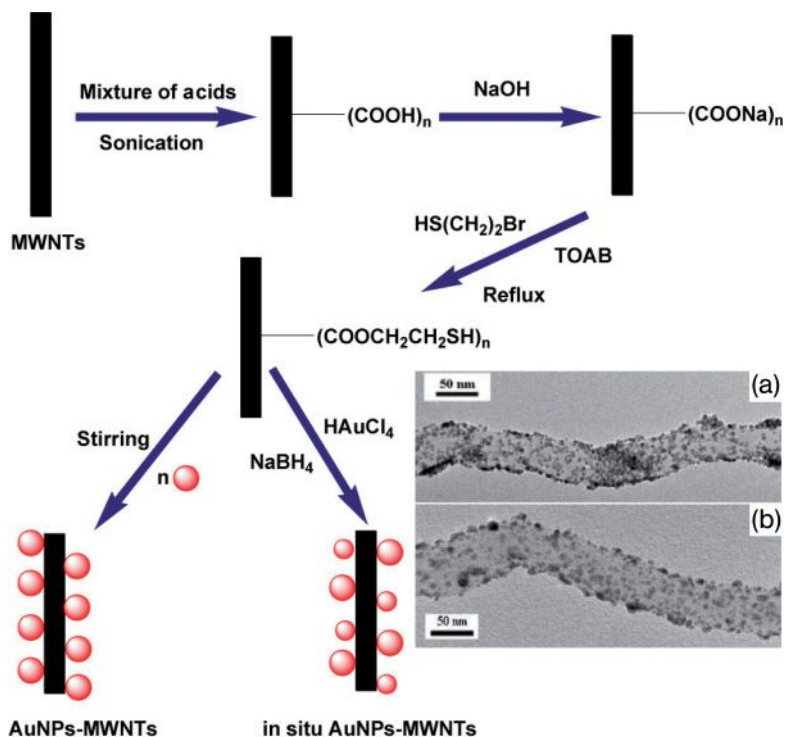


**Figure 7.13** The chemistry used to connect the AuNPs to oxidized SWNTs. AFM images of SWNTs before (a) and after (b) exposure to the coupling reagents and colloidal gold particles. DCC = *N,N'*-dicyclohexyl-carbodiimide. Adopted and modified according to Ref. [63]; AFM images reprinted with permission from Ref. [63].

(STM), and also potentially for monitoring the adsorption and concentration of trace metal ions.

An efficient method was developed to functionalize MWNTs with thiol groups, after which AuNPs were anchored onto them to fabricate new composite materials. Two different simple procedures were followed to produce MWNT–AuNP composite materials, as summarized in the Figure 7.14. The thiol-functionalized MWNTs were stirred with already prepared AuNPs in toluene at room temperature, and in another way AuNPs were produced in the presence of thiol-functionalized MWNTs (*in situ* formation of MWNT–AuNP composite) [65]. The TEM images showed self-assembly of the AuNPs on the MWNTs, where the AuNPs (Figure 7.14a) of 25 nm were dispersed on the MWNTs. The shape and size of the AuNPs obtained using the *in situ* method were different (Figure 7.14b) from those obtained with the former method. This might be explained by the existence of thiol groups surrounded by  $\text{AuCl}_4^-$  anions, which were reduced to AuNPs in the presence of reducing agents. These AuNPs represent the cores for further growth, as the thiol groups did not cover the whole particles.

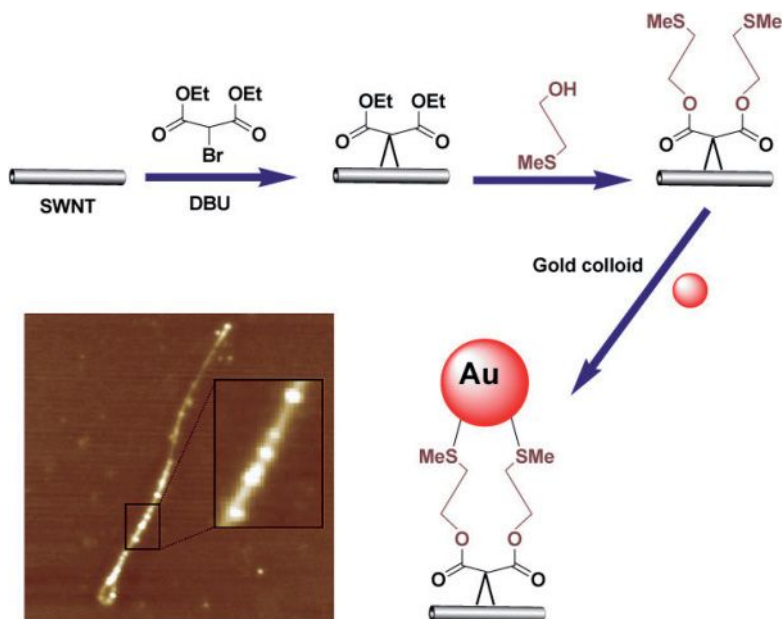
Coleman and coworkers used the Bingel reaction to functionalize the SWNTs with a cyclopropane group [66]. For this, the cyclopropane group was tagged using



**Figure 7.14** Experimental procedure for the fabrication of AuNP–MWNT composites and TEM images of AuNP–MWNT (a) and *in situ* AuNP–MWNT (b). TOAB = Tetraoctylammonium bromide. Adopted and modified according to Ref. [65]; TEM images reprinted with permission from Ref. [65].

performed  $\sim 5$  nm gold colloids by exploiting the gold sulfur binding interaction, as shown in the Figure 7.15. AuNPs were observed both on the sidewalls and at the ends of the SWNTs. The Bingel reaction is an example of a [2+1] cycloaddition reaction, and is a popular method in fullerene chemistry.

Recently, a novel DNA biosensor was fabricated for the detection of DNA hybridization based on the layer-by-layer (LBL) self-assembly of MWNTs and AuNPs via covalent linkage, which exhibited an excellent specificity and chemical stability under the DNA-hybridization conditions [67]. The LBL assembly represents one of the simplest ways of producing fundamentally and practically interesting multilayer films with unique mechanical properties; it also provides a precise control over film composition and thickness, which in turn opens up many new opportunities for achieving the ideal model surface, the properties of which are controllable. For this, the cysteamine molecules simply act as a glue to connect activated MWNTs and AuNPs into a 3-D hybrid network on the Au electrode, after which  $\text{NH}_2$ -ssDNA (ssDNA; single-stranded DNA) was immobilized onto multi-



**Figure 7.15** Schematic illustration of the chemistry used to connect AuNPs to SWNTs and AFM image of as-formed AuNP–SWNT composites by using the Bingel reaction. DBU = 1,8-diazabicyclo[5.4.0]undec-7-ene. Adopted and modified according to Ref. [66]; AFM image reprinted with permission from Ref. [66].

layer films via the amino link at the 5' end. Owing to the electron-transfer ability of the CNTs and the catalytic activities of the AuNPs, the sensitivity of DNA biosensors was improved and this DNA biosensor showed an excellent reproducibility and stability under DNA hybridization conditions.

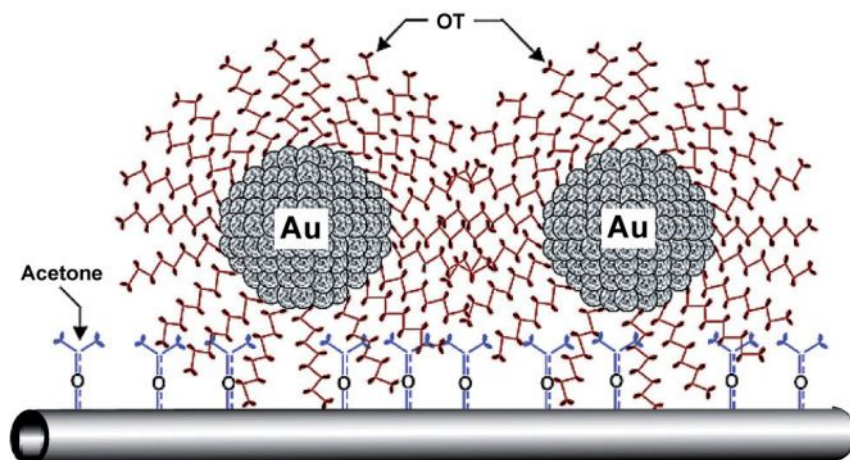
### 7.5.3.2 Supramolecular Interaction Between AuNPs and CNTs

Another strategy for preparing CNT–AuNP composites is that of the supramolecular or noncovalent functionalization of CNTs, and the subsequent attachment of AuNPs based on noncovalent interaction such as hydrophobic–hydrophobic interaction, weak hydrogen bond linkage,  $\pi$ – $\pi$  stacking interaction, or electrostatic attraction.

**Hydrophobic Interactions and Hydrogen Bonding** Hydrophobic interaction is the attractive force between molecules owing to the close positioning of the nonhydrophilic portions of the two or more molecules. Hydrogen bonding is a type of supramolecular interaction or a type of weak attractive (dipole–dipole) interaction between an electronegative atom and a hydrogen atom bonded to another electronegative atom such as nitrogen, oxygen, or fluorine. It can occur between

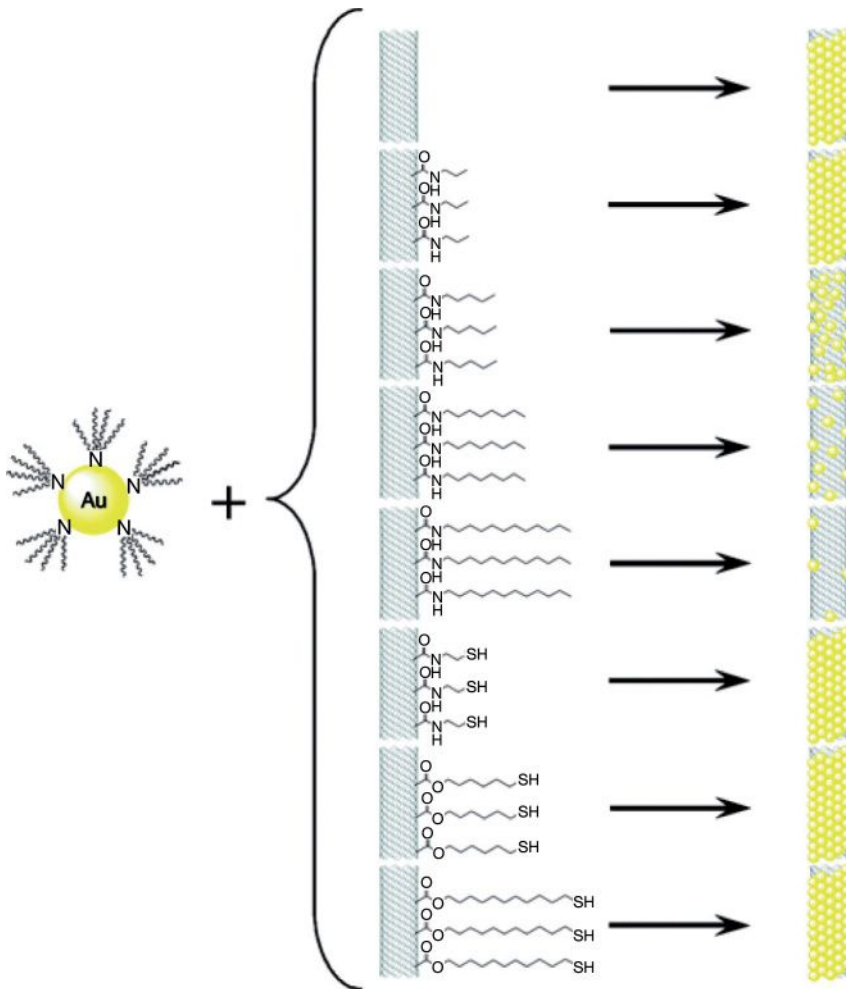
molecules, or within parts of a single molecule. A hydrogen bond tends to be weaker than a covalent or ionic bond, but stronger than van der Waals forces. One method of noncovalent functionalization of CNTs involves their association with amphiphilic molecules through hydrophobic interaction in aqueous medium [68]. Hydrophobic interactions between the ligands forming the monolayer that passivate the metal surface have been used to deposit the metal nanoparticles onto the surface of the CNTs. A novel strategy was reported to link monolayer-protected gold nanoclusters of 1–3 nm diameter to the sidewalls of nonoxidized CNTs through hydrophobic interactions between acetone-activated CNTs and octanethiol-protected gold nanoclusters [69]. The anchorage was provided by the interdigitation of alkyl chains of self-assembled molecular layers protecting the gold nanoclusters and molecular moieties adsorbed on the surface of CNTs (Figure 7.16). These molecularly interlinked hybrid nanoblocks may be significant for exploring and manufacturing a rich variety of molecular nanostructures for potential device applications.

In addition to experimental studies, a theoretical model has been developed to provide a detailed account of the interactions (charge transfer, van der Waals, osmotic, elastic, nonelastic, and covalent) between tetraoctylammonium bromide-stabilized AuNPs and alkyl- and alkythiol-modified MWNTs, so as to estimate the coverage of AuNPs at the surface of the MWNTs under different experimental conditions [70]. A quantitative description of the interactions between AuNPs and MWNTs was made by comparing between the predictions of the theoretical model and the experimental results. From such a comparison, it was concluded that as the length of the alkyl chains at the surface of the MWNTs increased, coverage of



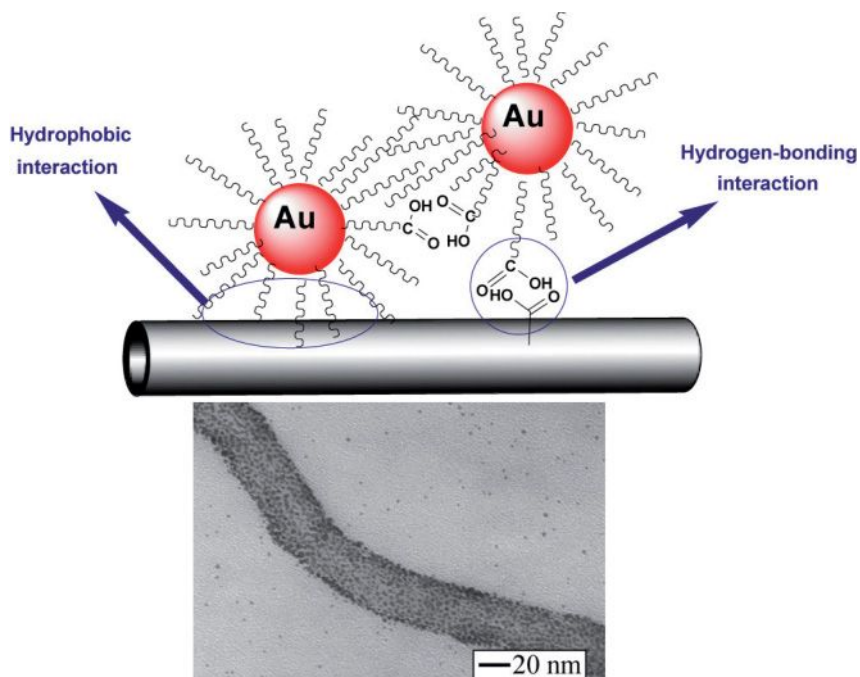
**Figure 7.16** Schematic illustrating the attachment of octanethiol (OT)-capped Au nanoclusters to acetone-activated MWNTs. Reprinted with permission from Ref. [69].

the AuNPs decreased (i.e., noncovalent adsorption). In contrast, for alkylthiol-modified MWNTs, coverage of the AuNPs at their surface remained constant, irrespective of the length of the alkyl-thiol chain (covalent adsorption) (Figure 7.17). The theoretical model assumption was in good agreement with the experimental findings, which proved the validity of the predictive model. A significant insight is that, under certain conditions, the coverage of AuNPs is very sensitive to the nature of the MWNT surface modification and the environment, pointing



**Figure 7.17** Scheme showing the templated assembly of tetraoctylammonium bromide-stabilized AuNPs at the surface of unmodified, alkyl-modified, and alkylthiol-modified MWNTs. Reprinted with permission from Ref. [70].





**Figure 7.18** Schematic representation of the molecularly mediated assembly of monolayer-capped AuNPs on CNTs, and the characteristic TEM image of the AuNP-CNT composite. Adopted and modified according to Ref. [71]; TEM image reprinted with permission from Ref. [71].

the way to a rational design of functional CNT-based nanoscale devices with potentially widespread applications.

A molecularly mediated assembly of alkanethiolate-capped AuNPs onto the surface of MWNTs through a combination of hydrophobic interactions between the alkyl chains of the capping/linking molecules and the hydrophobic backbones of a nanotube and the hydrogen-bonding interaction between carboxylic groups of the capping/linking molecules and the functional groups on the surface of the nanotube, has been described [71] (Figure 7.18).

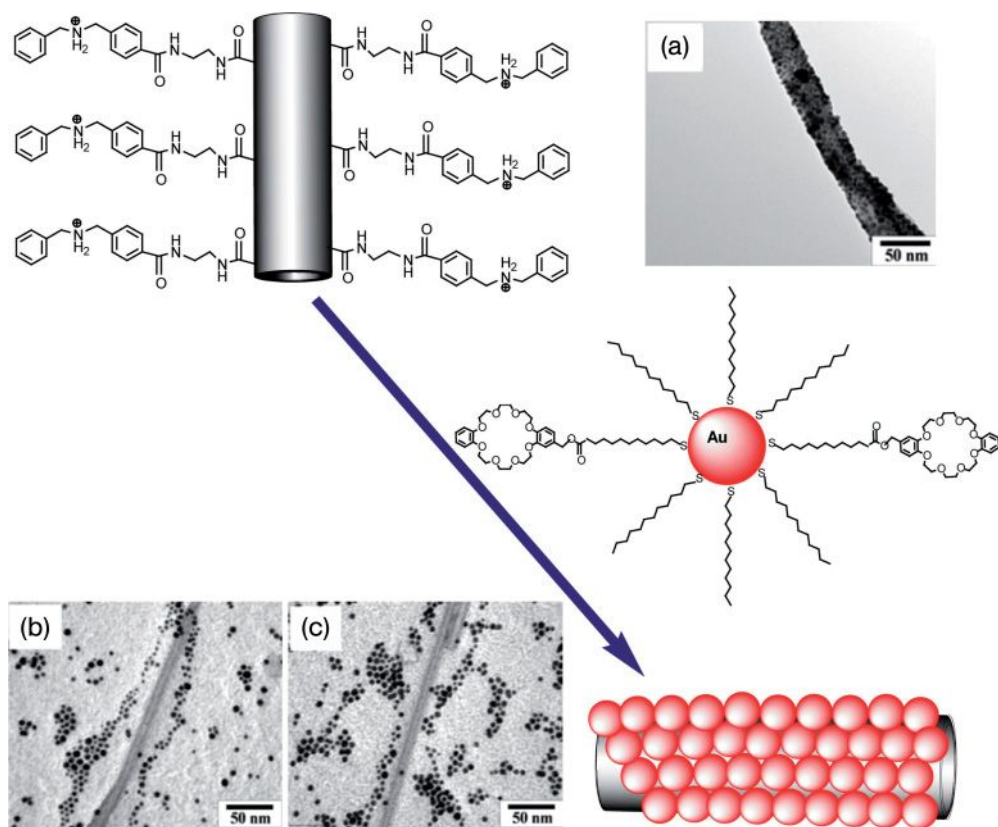
Here, the simplicity and effectiveness for assembling alkanethiolate-capped AuNPs of 2–5 nm core size onto CNTs with controllable coverage and spatially isolated character were achieved by adopting such a combination of interfacial chemistry—that is, a combination of hydrophobic and hydrogen-bonding interactions between the organic shells and the CNT surfaces. The benefit of this pathway is that it does not require any difficult and tedious surface modification of CNTs. Rather, the assembly, packing density and distribution of the AuNPs onto the surface of the CNTs depended on the relative concentrations of the AuNPs, CNTs, and capping or linking agents. A thermal treatment to remove any organic



capping/linking shells of the AuNPs induced an agglomeration of the AuNPs that attached effectively to the CNTs surface. These composite materials were very stable, with even sonication in hydrophobic solvents being unsuccessful in dissociating the composite material. In time, this approach may find important implications for the design of nanostructured and nanocomposite catalyst and sensory materials. Since it is possible to control the size, shape, loading, and dispersion of the AuNPs on the surface of the conductive CNTs by using a combination of hydrophobic and hydrogen-bonding interactions, this system might also become important for addressing some of the fundamental issues in fuel cell catalysis applications.

Sainsbury and Fitzmaurice [72] reported a smart, noncovalent, self-assembly coverage of dibenzylammonium-cation-modified MWNTs with crown-modified (dibenzo[24]crown) AuNPs, where ammonium cations thread the crown ethers present on the AuNPs surface (Figure 7.19). From the different experimental conditions utilized, it was found that the MWNT-templated self-assembly of a solid nanowire was observed only when uncomplexed cations were present on the surface of the MWNTs and uncomplexed crown was present on the surface of the AuNPs (Figure 7.19a–c). This significant observation led to the perception that the possibility of driving force for the templated nanowire assembly via charge transfer from the crown-modified AuNPs to the cation-modified MWNT could be excluded. Therefore, it was concluded that the templated self-assembly of nanowires was driven by the formation of the surface-confined pseudorotaxanes that resulted from the electron-poor cation threading the electron-rich crown. In order to initiate the templated self-assembly of a gold nanowire in solution, a dispersion of crown-modified AuNPs in chloroform was added to a freshly sonicated suspension of cation-modified MWNTs in chloroform. The stable dispersion of dodecane-thiol-modified AuNPs was prepared using the well-known method introduced by Brust and coworkers [73]. The nearly size-monodisperse fraction was subsequently modified by the exchange of the adsorbed thiol for thiol-incorporating crown molecules (dodecanethiol incorporating a crown moiety in the terminal position) [74]. The MWNTs were modified by amide-coupling reactions either between the carboxy-modified MWNTs and ethylenediamine, or between the remaining amine of the coupled ethylenediamine and the cation precursor [*N*-(4-carboxydibenzylamine) carbamate]. This approach may offer the vision of diverse nanoscale components for which many applications can be anticipated.

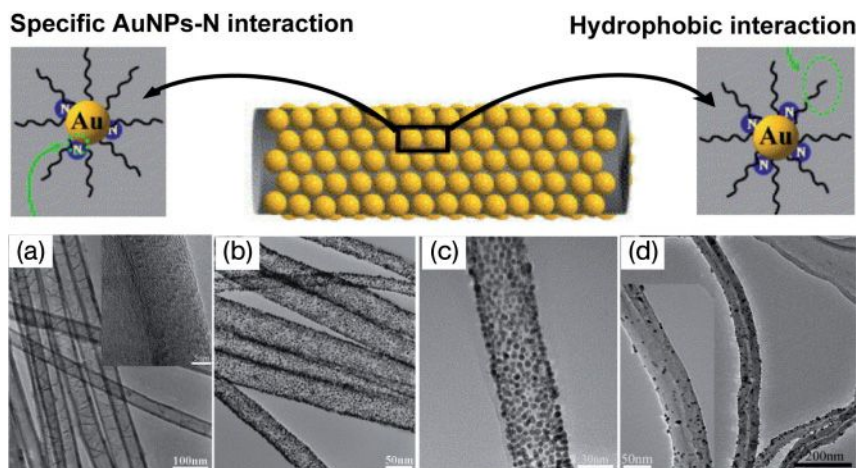
A facile approach has been developed to prepare a hybrid material of dodecanethiol-protected AuNPs decorated on the surfaces of SWNTs and MWNTs simply by reacting dispersions of both components in dichloromethane [75]. The as-prepared AuNP–SWNT and AuNP–MWNT systems exhibited a strong electronic coupling, which may influence important physico-chemical properties. Although the nature of the electronically coupled state was not clearly understood, it was anticipated that it might involve a charge-transfer character, in which the AuNPs functioned as an electron acceptor, receiving additional electron density from the SWNTs or MWNTs. The well-known absorption features of SWNTs led



**Figure 7.19** A cation-modified MWNT and the noncovalent self-assembly of AuNPs with a crown ether-modified monolayer, and TEM images of (a) crown-modified AuNPs adsorbed at the surface of a cation-modified MWNT. The same AuNPs are not adsorbed at the surface of (b) a cation-precursor-modified MWNTs or (c) an unmodified MWNTs. Adopted and modified according to Ref. [72]; TEM images reprinted with permission from Ref. [72].

to considering the dispersion of AuNP–SWNT instead of the less-explored and less-understood MWNTs characteristics.

In contrast to normal CNTs, Li and coworkers [76] produced bamboo-like carbon nanotubes (BCNTs) that were decorated with a high-density and uniform assembly of AuNPs on the surface, by using a simple and effective method. BCNTs produced by the pyrolysis of iron(II) phthalocyanine were sonicated in toluene for homogeneous dispersion, and then mixed, by gentle shaking, with the toluene solution of AuNPs protected by organic shell. The resultant composite materials, AuNP–BCNTs, were separated by centrifugation and washed repeatedly with toluene. Apart from the hydrophobic interaction between the alkyl chains of the capping/linking molecules and the hydrophobic backbones of the nanotubes, the specific interaction between AuNPs and the nitrogen atoms present on the surface

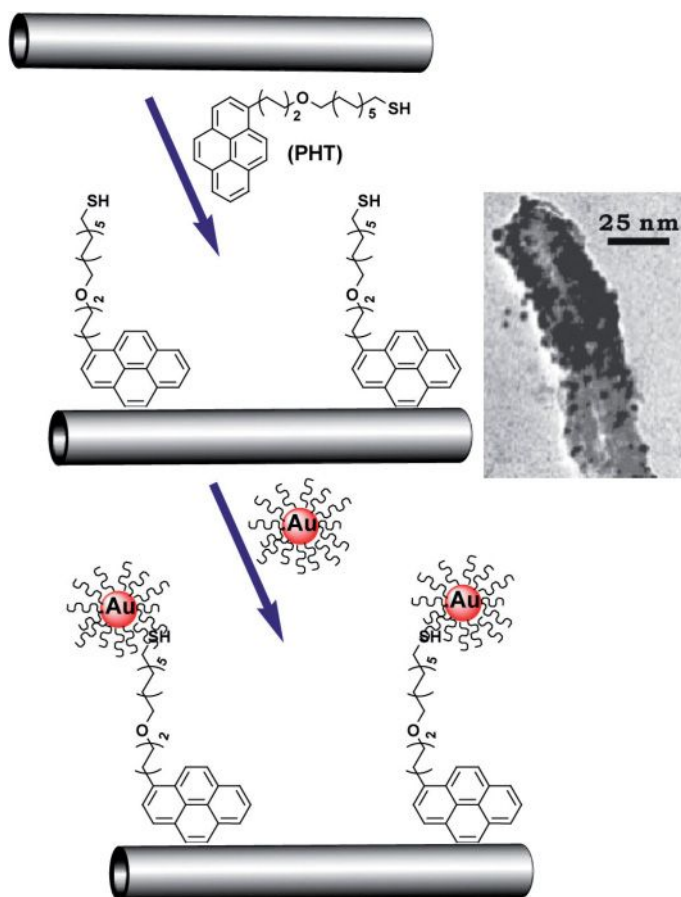


**Figure 7.20** Schematic illustration of the direct assembly of AuNPs on BCNTs. (a) TEM image of BCNTs; (b, c) BCNT–AuNP nanohybrids; (d) AuNPs supported on an undoped CNTs. The inset in (a) shows a higher-magnification image. Reprinted with permission from Ref. [76].

of the BCNTs is responsible for the high-density and uniform assembly of AuNPs on BCNTs (Figure 7.20). It is important to note that, compared to the N-doped BCNTs, the pristine undoped CNTs were not efficient for the direct, highly dense and uniform immobilization of AuNPs, due mainly to an absence of specific AuNP–N interactions or other activation processes. As evidently seen from the TEM images, the assembled AuNPs (average size 3.9 nm) were quite uniform, well dispersed, and decorated or packed onto the walls and ends of BCNTs with high density. The unique properties of the BCNTs, combined with this simple and straightforward assembly approach, may facilitate the use of CNTs in a variety of pivotal fields, including biosensors and fuel cell catalysis.

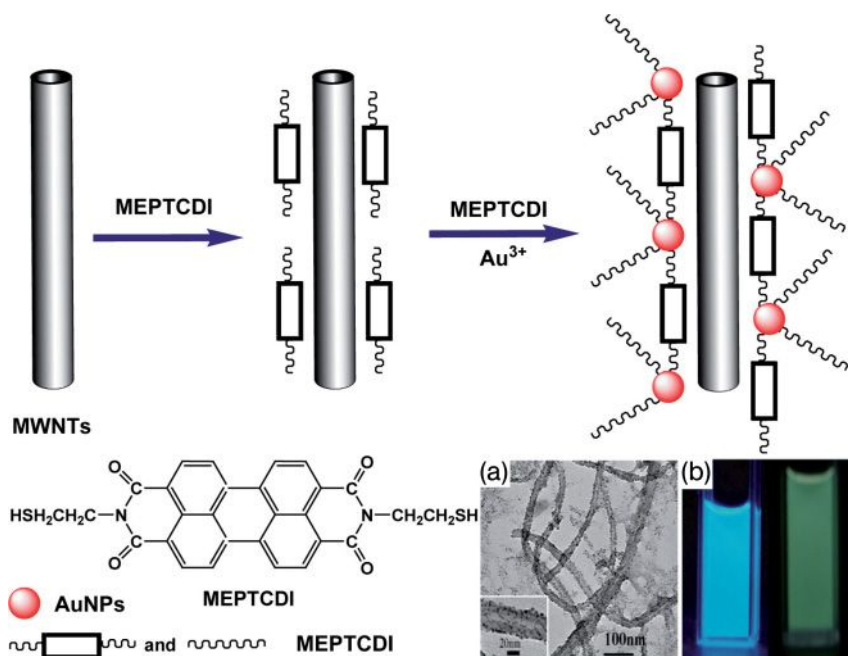
**$\pi$ – $\pi$  Stacking Interactions** This is a type of noncovalent interaction, which is mainly caused by the intermolecular overlapping of p-orbitals in  $\pi$ -conjugated systems (e.g., organic compounds or polymers containing aromatic moieties). The results of different studies [68, 77] have confirmed that organics or polymers with phenyl groups could interact with CNTs through  $\pi$ – $\pi$  stacking, which is a stronger interaction than the van der Waals forces. Compared to various aromatic compounds, pyrene derivatives are more susceptible to stack on the surface of the CNTs via  $\pi$ – $\pi$  stacking interactions [78–80]. In this way, the intrinsic electronic properties of the CNTs are preserved, and the surface functional groups on the nanotubes can easily be varied by changing the pyrene derivatives.

By using bifunctionalized pyrene derivatives such as 17-(1-pyrenyl)-13-oxo-hepta-decanethiol (PHT) as an interlinker, AuNPs were decorated on the



**Figure 7.21** Illustration of the connection of AuNPs onto MWNTs through pyrene derivatives as an interlinker, and TEM image of MWNTs decorated with AuNPs. PHT = 17-(1-pyrenyl)-13-oxo-heptadecanethiol. Adopted and modified according to Ref. [78]; TEM image reprinted with permission from Ref. [78].

surface of the didecylamine-modified MWNTs, where PHT bound to the surface of MWNTs via a  $\pi$ - $\pi$  stacking interaction between its pyrenyl unit at one end and the sidewall of MWNTs, while the other terminal thiol group was interacted to the surface of AuNPs (Figure 7.21). In this way, AuNPs were self-assembled onto the surface of nanotubes via an organic linker. It should be noted that, while the fluorescence of the resultant composite material was entirely quenched, the Raman response of the CNTs was enhanced considerably. These important consequences imply that there are charge-transfer interactions between the CNTs and AuNPs through the organic interlinker.



**Figure 7.22** Representation for the fabrication processes of the AuNP–MWNT hybrids and molecular structure of MEPTCDI. (a) TEM image of AuNP–MWNT hybrids; (b) Emission from the AuNP–MWNT hybrid with MEPTCDI in water (left) and MEPTCDI in DMF (right) under UV irradiation at 365 nm. MEPTCDI = *N,N'*-bi(2-mercaptoethyl)-perylene-3,4,9,10-tetracarboxylic diimide. Reprinted with permission from Ref. [81].

Very recently, the *in situ*-solution method was proposed for the synthesis of water-dispersible AuNP–MWNT hybrids with high density and well-distributed AuNPs by using an optoelectronic-active compound of *N,N'*-bi(2-mercaptoethyl)-perylene-3,4,9,10-tetra-carboxylic diimide (MEPTCDI) as an interlinker and stabilizer for the formation of the AuNP–MWNT hybrids [81]. Here, the MEPTCDI with both phenyl and mercapto groups, played a dual role as an interlinker (Figure 7.22) between the MWNTs and AuNPs (noncovalently wrapping of the MWNTs through  $\pi$ - $\pi$  stacking) and as a stabilizer for controlling the nucleation and growth of AuNPs on the surface of the MWNTs. This endowed the AuNPs anchored on the surface of the MWNTs with a good stability and dispersability, as well as flexibility of size-control (Figure 7.22a).

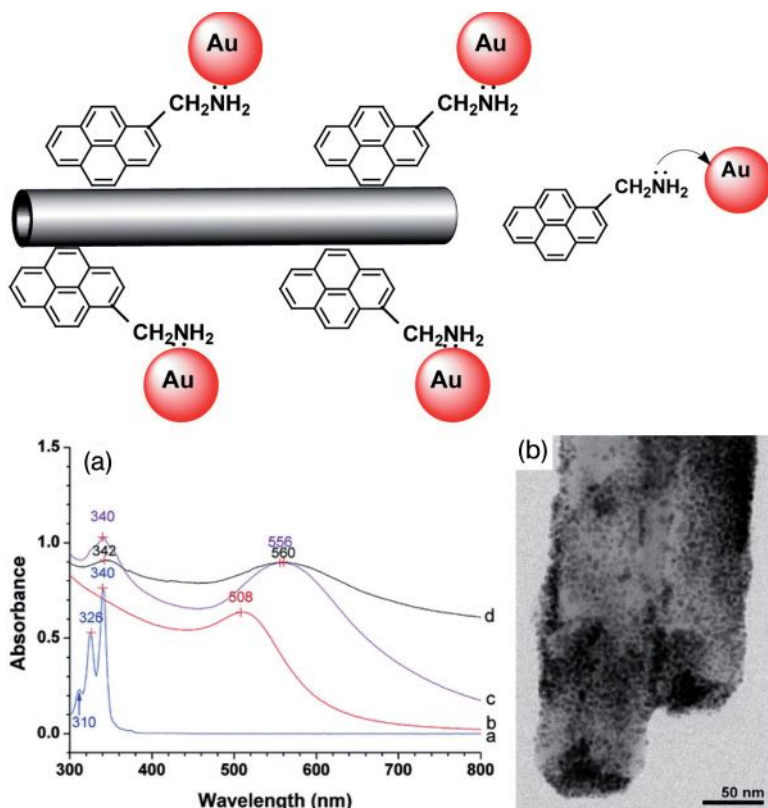
AuNP–MWNT hybrids were prepared using an *in situ* procedure in such a way that the MWNTs were dispersed in aqueous solution containing sodium dodecyl benzen sulfonate (SDBS) by sonication and a dimethylformamide (DMF) solution of MEPTCDI was added to the MWNTs suspension, followed by the addition of an aqueous solution of HAuCl<sub>4</sub>, and stirred for 12 h at room temperature. The nanohybrids formed were further purified by centrifugation and redispersed in water for further characterization. The as-prepared AuNP–MWNT hybrid with

MEPTCDI showed an interesting photoluminescence property under UV irradiation at 365 nm (Figure 7.22b). Based on several blank experiments and reported information [82], it was concluded that the strong luminescence of the hybrids did not result from the atomic Au clusters or from defects of the CNTs or from the organically functionalized CNT hybrids, but rather originated from the AuNP–MWNT hybrids with MEPTCDI, which may be due to energy transfer occurring between the MWNTs and AuNPs or between AuNPs and the MEPTCDI. This property of AuNP–MWNT hybrids in water may expand the potential applications as building blocks to a wider range such as light-emitting sources, biomedical labels, or even tracking materials for drug delivery, and so on.

AuNPs of 2–4 nm diameter were densely decorated on the walls of MWNTs using pyrenealkylamine derivatives such as 1-pyrenemethylamine as the interlinker in aqueous solution [83]. While the pyrene chromophore is noncovalently attached to the terrace of nanotubes through a  $\pi$ – $\pi$  stacking interaction, the alkylamine substituent of 1-pyrene-methylamine connects to the AuNPs (Figure 7.23). UV-visible absorption and luminescence spectroscopy were employed to monitor the formation of functionalized AuNPs and AuNP–CNT composites. Following surface modification of the AuNPs with 1-pyrenemethylamine, the absorption value of the pyrene chromophore was greatly decreased and the surface plasmon resonance (SPR) of AuNPs showed a red shift from 508 to 556 nm (Figure 7.23a), owing to interparticle plasmon coupling. Further, the photoluminescence property of 1-pyrenemethylamine and its emission intensity were drastically quenched after formation of the AuNP–CNT composites, most likely due to the energy and/or electron transfer from the excited pyrene fluorophore to the AuNPs. This facile strategy for the formation of a high-density assembly of AuNPs onto the surface of CNTs (Figure 7.23b) has been applied to other linking organic molecules with similar structures, such as *N*-(1-naphthyl)ethylenediamine and phenethylamine, thus demonstrating the general applicability of this approach for preparing AuNP–CNT composites. The resultant composites may become important for applications in low-temperature CO oxidation and other catalytic reactions. Further, the present strategy of depositing spherical AuNPs may be extended to produce CNT–Au nanorod heterojunctions for electronic connection and molecular sensing applications.

**Electrostatic Interactions** Electrostatic interactions are noncovalent dipole–dipole or induced dipole–dipole interactions that can be either stabilizing or destabilizing. A simple and proficient method has been introduced for the selective anchoring of AuNPs on the surface of nitrogen-doped MWNTs by electrostatic adsorption [84]. Nitrogen-doped MWNTs produced using a pyrolysis method were initially chemically modified by acid treatment (mixture of  $\text{H}_2\text{SO}_4$  and  $\text{HNO}_3$ ) and the resultant oxidized MWNTs subsequently treated with a cationic polyelectrolyte, namely poly-(diallyldimethylammoniumchloride) (PDDA). The polyelectrolyte was adsorbed onto the surface of the nanotubes by an electrostatic interaction between the carboxyl groups on the chemically oxidized nanotube surface and the polyelectrolyte chains. Negatively charged AuNPs of 10 nm were attached



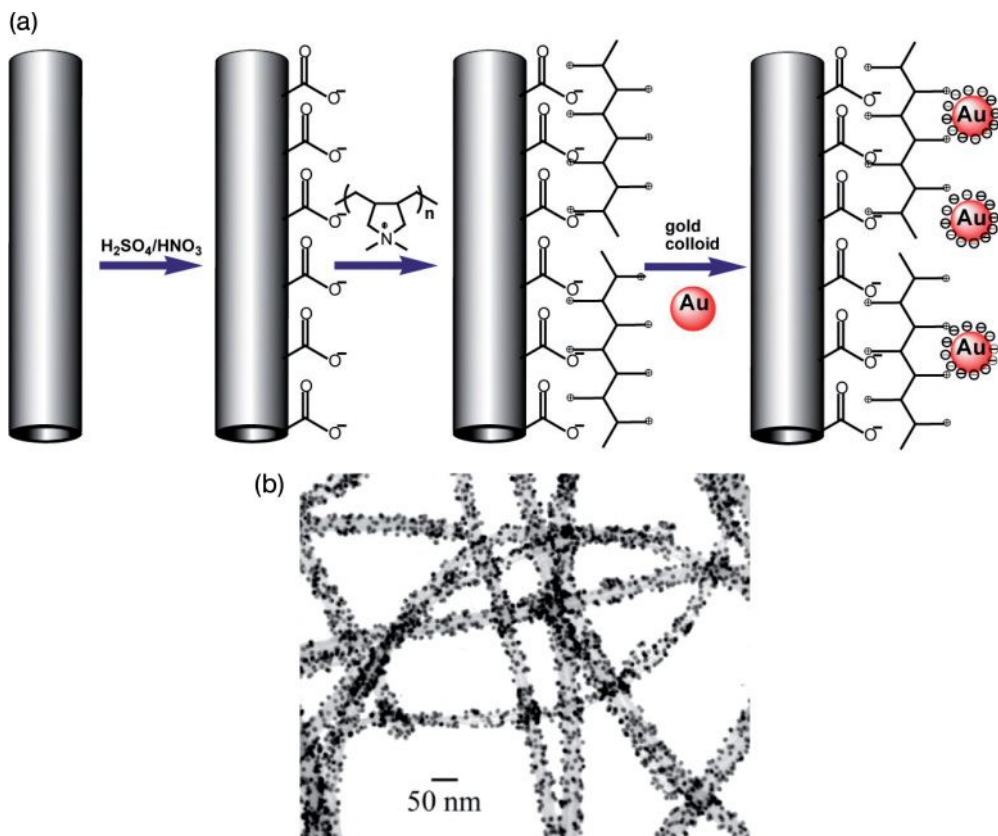


**Figure 7.23** AuNP assembly on CNTs through the 1-pyrenemethylamine interlinker. (a) UV-visible absorption spectra of: (curve a) free 1-pyrenemethylamine in ethanol; (curve b) aqueous AuNP solution; (curve c) a

mixture of 1-pyrenemethylamine and AuNPs; (curve d) solution containing AuNP–CNT composites; (b) TEM image of the resulting AuNP–CNT composites. Reprinted with permission from Ref. [83].

to the surface of the nanotubes via electrostatic interactions between the polyelectrolyte and AuNPs (Figure 7.24). In this way, novel composites with homogeneously distributed AuNPs on the surface of nitrogen-doped MWNTs were obtained. Therefore, by selecting different types of polyelectrolytes the surfaces of the CNTs can be modified to be either negatively or positively charged, such that accordingly different types of other nanoparticle (e.g., semiconductor nanocrystals, magnetic nanoparticles) can be selectively anchored to the nanotube surfaces. This strategy of decorating nanotubes can be used to identify the location of functional groups on the CNT surfaces, while the resultant composite materials may be used in various domains such as catalytic, electronic, optical, and magnetic applications.

Another example of the electrostatic approach is the formation of AuNP–MWNT composites by the LBL self-assembly technique using polyelectrolytes [85]. To this

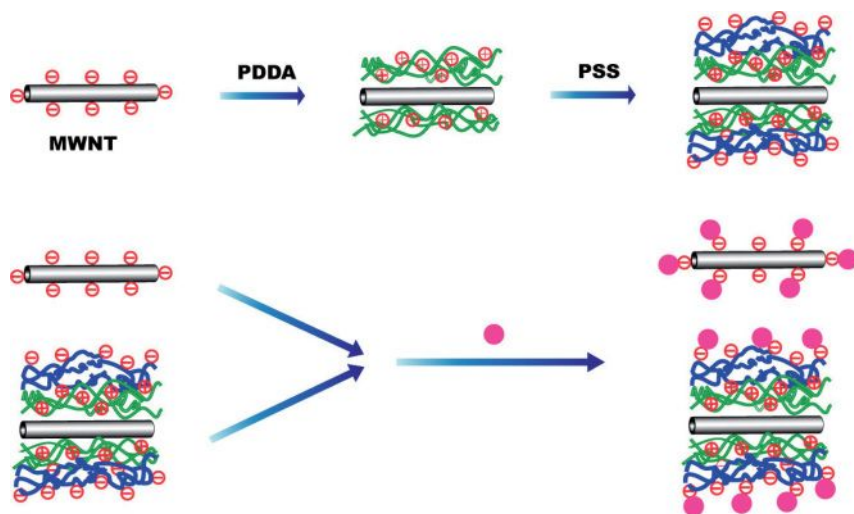


**Figure 7.24** (a) Schematic view of the process for anchoring AuNPs onto CNTs; (b) TEM image of AuNP-CNT hybrid structures. Reprinted with permission from Ref. [84].

end, chemically functionalized MWNTs were wrapped with a layer of a positively charged polyelectrolyte (PDDA), followed by a layer of a negatively charged polyelectrolyte such as poly(sodium 4-styrene sulfonate) (PSS). Consequently, positively charged AuNPs prepared by the phase-transfer method [86] were immobilized on negatively charged MWNTs prepared by LBL self-assembly due to electrostatic interactions (Figure 7.25). Positively charged AuNPs also interacted with chemically functionalized MWNTs alone (without polyelectrolyte coating) through electrostatic interaction with the carboxylic acid groups present on MWNTs sidewalls. Hence, it is expected that positively charged AuNPs could be used to detect negatively charged defect sites on CNTs. However, the binding interaction between MWNTs and AuNPs is much more powerful and effective for the LBL approach than the direct approach.

The noncovalent attachment of silica-coated AuNP monolayers and multilayers onto CNT templates was achieved by using the polymer-wrapping technique,

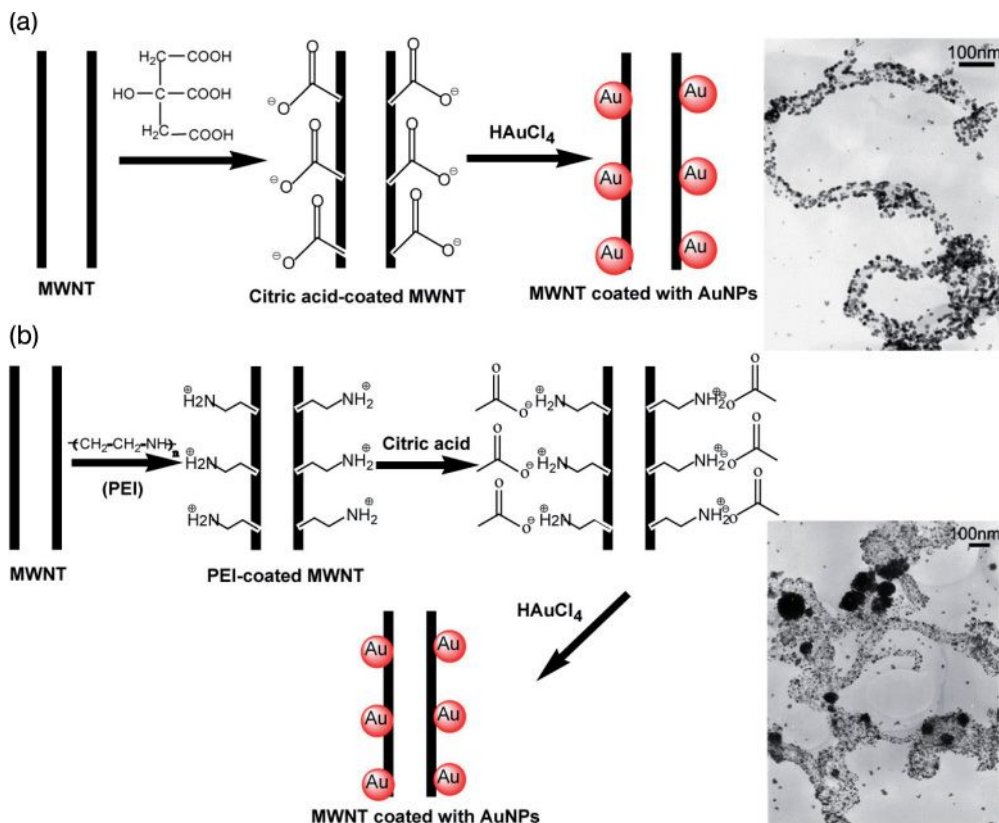




**Figure 7.25** Schematic illustration of the LBL self-assembly technique. PDDA = poly(diallyldimethylammoniumchloride); PSS = poly(sodium 4–styrene sulfonate). Adopted and modified according to Ref. [85].

combined with the LBL assembly process [87]. First, a stable dispersion of individual CNTs was obtained by dispersing the MWNTs in water by sonication in the presence of PSS, which acts as the wrapping polymer. PSS has negatively charged sulfonate groups, which serve as primers for the homogeneous adsorption of the cationic polyelectrolyte PDDA. In the LBL approach, the interactions accountable for the assembly are mostly electrostatic, and permit an exploitation of the surface properties of silica to obtain close-packed monolayers and multilayers. As a result, the MWNTs were entirely packed with dense monolayers of silica-coated AuNPs. Such composite nanowires were optically labeled and might have key applications as components of nanoelectronic circuits and waveguides. The repetition of the LBL process allows a good control of the thickness of the nanocomposites by increasing the number of layers deposited. Another strategy for functionalizing SWNT or MWNT surfaces noncovalently with polymer multilayers and AuNPs was also reported by Carrillo and coworkers [88].

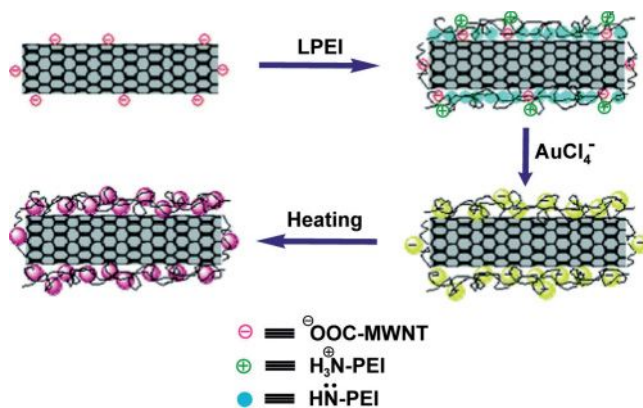
Jiang and Gao reported a versatile method for the selective attachment of AuNPs onto the surface of the MWNTs [38]. By using cationic poly(ethyleneimine) (PEI) or anionic citric acid (CA) as the dispersant, the surface properties of the MWNTs were modified to yield a basic or acidic surface. Then, by electrostatic interactions, AuNPs of approximately 10 nm were successfully anchored onto the sidewalls of the MWNTs (Figure 7.26). In the case of the CA-coated MWNTs, the CA forms an adsorption layer around the outer walls of the CNTs and then reduces *in situ* the  $\text{HAuCl}_4$  to produce the AuNPs. The PEI treatment of the nanotubes and exposure to the  $\text{HAuCl}_4$  solution generated nitrogen-containing functional groups on



**Figure 7.26** The process for attaching AuNPs to: (a) Citric acid-coated CNTs; (b) Poly(ethyleneimine) (PEI)-coated CNTs. The TEM images show the respective products. Adopted and modified according to Ref. [38]; TEM images reprinted with permission from Ref. [38].

the outer walls of the MWNTs. This strategy may be extended to attach other nanoparticles (e.g., semiconductor, electrical and magnetic nanoparticles) onto the terrace of the CNTs by choosing different types of suitable dispersant.

Another straightforward *in situ* reduction procedure for the fabrication of CNT-supported AuNP composite nanomaterials was demonstrated by Hu and coworkers [89]. Here, linear PEI had a dual role as a functionalizing agent for the MWNTs as well as a reducing agent for the formation of AuNPs (Figure 7.27). The driving force involved in the functionalization of PEI on the surface of CNTs is a combination of the electrostatic interaction between the oppositely charged CNTs and the PEI and the physisorption process, which is analogous to the polymer-wrapping process [87]. This synthetic method engages a mild heat-treatment process, which persuades the *in situ* reduction of  $\text{HAuCl}_4$  on the MWNTs sidewalls and does not require the additional steps of oxidizing the MWNTs with mixed acids and

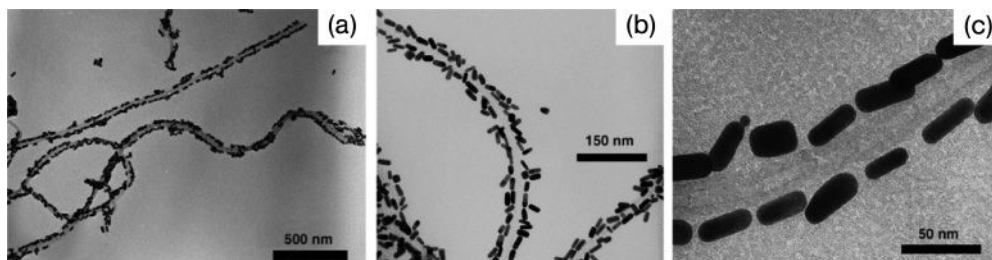


**Figure 7.27** Experimental procedure, in which poly(ethyleneimine) possibly interacts with acid-functionalized MWNTs through electrostatic interaction and a physisorption process. Reprinted with permission from Ref. [89].

introducing other reducing agents. More importantly, the dense package of AuNPs on the surface of CNTs was tailored by simply changing the experimental parameters, such as the initial molar ratio of PEI to HAuCl<sub>4</sub>, the relative concentration of PEI and HAuCl<sub>4</sub> to MWNTs, and both the temperature and duration of the heat treatment. This approach is anticipated to become universal for preparing composites of CNTs and other noble metals, as well as heterogeneous CNT–AuNP composite nanowires, and also shows potential for applications such as electronic nanodevices.

Fullam and coworkers have shown that CNTs can be used as templates for the formation of Au nanowires—a new type of composite material which may have the potential for a wide range of applications. The CNT-templated self-assembly of gold nanocrystals and subsequent thermal processing of the nanocrystal assemblies to form continuous polycrystalline gold nanowires extending over many micrometers were described [90]. The AuNPs were decorated on the surface of the CNTs, when mixing the CNTs to a dispersion of tetraoctylammonium bromide-stabilized gold nanocrystals ( $\sim 6 \pm 1$  nm) in chloroform. A monolayer coverage of gold nanocrystals on the surface of the CNTs was obtained after precipitation from solution. It was anticipated that the deposition of Au nanocrystals on the CNT surface would be similar to that of phase-transfer catalyst-stabilized gold nanocrystals adsorbed as a monolayer onto the surface of [60]fullerene [91]. Subsequent heat treatment of the gold nanocrystal-coated CNTs yielded a continuous polycrystalline gold nanowire with a CNT core. These findings were of general interest as they showed that nanometer-scale structures self-assembled from nanocrystals might subsequently be processed to yield polycrystalline, nanoscale structures.

In contrast to the use of MWNTs to template the assembly of aligned nanoparticles, which is a relatively common practice, Correa-Duarete and coworkers [92] showed for the first time that the nanorods were assembled with a preferential

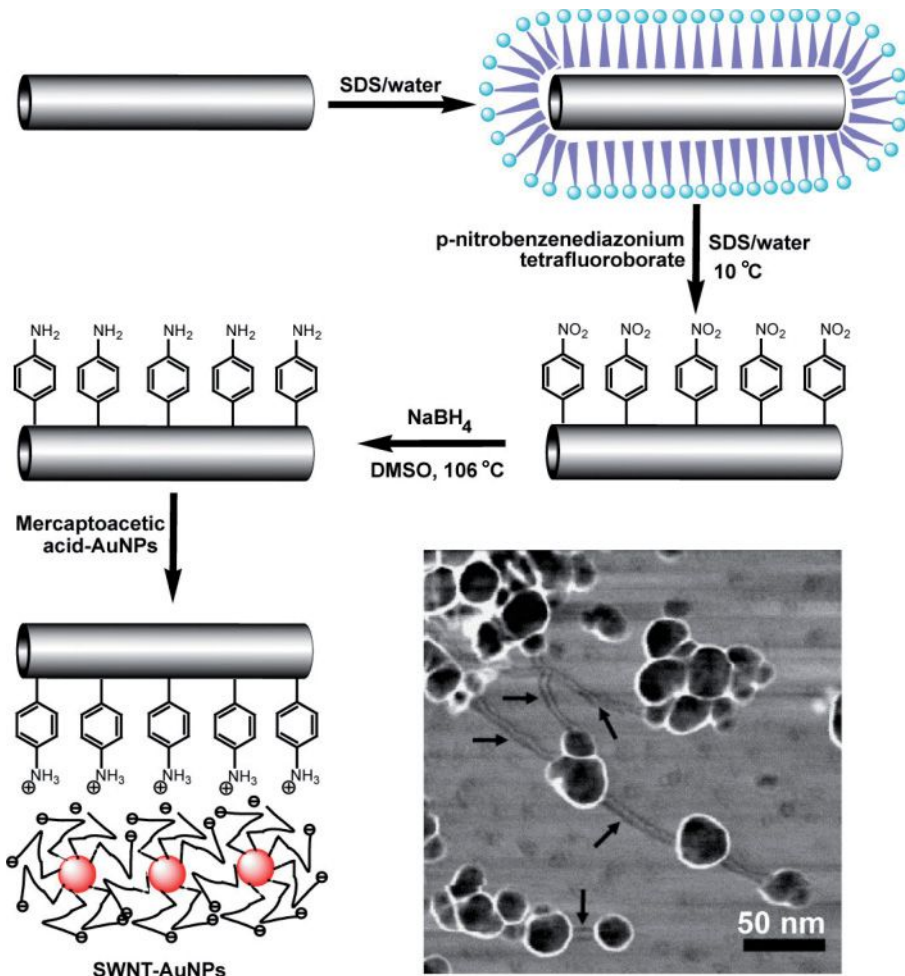


**Figure 7.28** (a–c) TEM images of Au nanorods (average aspect ratio 2.94), assembled on MWNTs (average diameter 30 nm) at various magnifications. Reprinted with permission from Ref. [95].

string-like alignment on the surface of MWNTs. The group showed that the formation of uniform electrostatic assembly of Au nanorods on MWNTs occurred in such a way that the nanorods formed strings with end-to-end contacts (Figure 7.28). Such a morphology would result in uniaxial plasmon coupling, and the nanorods could serve as a label to monitor the alignment of CNTs within polymer films or other nanostructured systems, as demonstrated through optical absorption measurements on stretched poly(vinyl alcohol) films loaded with the nanocomposite arrays. Fabrication of the aligned Au nanorods was achieved using the LBL technique. Prior to the assembly of gold nanorods, the MWNTs were wrapped with the negatively charged polyelectrolyte PSS, followed by an electrostatic assembly of the positively charged polyelectrolyte PDDA.

A different approach to fabricate MWNT–AuNPs was proposed via the noncovalent functionalization of MWNTs with surfactants such as sodium dodecyl sulfate (SDS) using the LBL-mediated assembly of a MWNT multilayer film onto indium tin oxide (ITO)-coated glass plates [93]. The supramolecular interactions [94] between the alkyl chains of the SDS and the surface of the MWNTs leads to a good dispersion of MWNTs in water and, on the other hand, creates a distribution of electronic charges at the tube surface. This is very useful for the LBL assembly of uniform MWNT multilayer films on the solid substrate and the fabrication of MWNT–AuNP composites. Hence, it was possible to assemble the MWNT multilayer film onto the ITO plate via the electrostatic interaction of oppositely charged, SDS-modified MWNTs and polyelectrolyte (e.g., PDDA). The same properties of the SDS-functionalized MWNTs were also shown to be useful for mediating the attachment of AuNPs onto the surface of the tubes. This approach to assembling CNT multilayer films and the resultant composites may both find application in the development of bioelectronic nanodevices such as biosensors and biofuel cells.

Biju and coworkers [95] used the functionalization of SWNTs to produce a hierarchical nanoscale composite material of SWNT–AuNPs as well as SWNT–CdSe–ZnS quantum dots (QDs), and studied the photoluminescence properties of the resulting hybrid materials. The excessive sidewall functionalization of the SWNTs into nitro and amino derivatives provided water-solubility to the SWNT



**Figure 7.29** Steps involved in the functionalization of SWNTs, including successive conjugation to AuNPs and AFM phase image of SWNT–AuNP conjugates dispersed on a mica plate. Adopted and modified according to Ref. [95]; AFM image reprinted with permission from Ref. [95].

derivatives. The AuNPs modified with mercaptoacetic acid, which provides free surface carboxylic acid groups, were attached to SWNTs through quaternary ammonium salt formation (Figure 7.29). Based on absorption and photoluminescence spectroscopic measurements, it was observed that the conjugation of AuNPs to the SWNT templates induced electronic interactions between the components, which perturbed their energy states, absorption, and photoluminescence properties. The hierarchical nanoscale hybrid structures based on the SWNT and nanoparticle hybrid materials, together with an understanding of their optical properties,

were suggested to represent promising building blocks for a light-harvesting system [96] and nanoscale optoelectronic devices.

Another novel method was demonstrated by which to electroporate Gram-negative bacteria (e.g., *Acidithiobacillus ferrooxidans*) through MWNTs [97]. The addition of MWNTs into a solution containing bacteria and AuNPs, and subsequent exposure to microwave radiation, facilitated a rapid transport of AuNPs across the cell wall, without affecting cell viability. In fact, both cell viability and growth provided an insight into the stability of cell under microwave exposure, the reversibility of electroporation via MWNTs, and demonstrated the cells' ability to withstand a high intake of AuNPs. Upon the random addition of MWNTs to a bacteria–AuNPs solution, both the MWNTs and AuNPs remained uniformly suspended, without any strong tendency to accumulate on the bacterial cells. However, upon exposure to microwaves, a large fraction of MWNTs and AuNPs was seen to accumulate on the cell surfaces.

## 7.6 Applications

It is well known that much attention has been paid to metal nanoparticles based on their pivotal applications as advanced materials in an ample diversity of areas such as catalysis, optical devices, nanotechnology, and the biological sciences [98–100]. Today, many applications of metal nanoparticles are close to profitable implementation, with AuNPs in particular having attracted most attention based on their potential use in applications such as catalysis [101, 102], chemical sensors [103], biological and/or medical areas [104, 105], and the miniaturization of electronic devices due to their unique optical and electrical properties [4]. The applications of thiol-stabilized AuNPs in catalysis comprise asymmetric dihydroxylation reactions [106], carboxylic ester cleavage [107], electrocatalytic reductions [108], and particle-bound ring-opening metathesis polymerization [109], among others [4]. These catalytic applications have in common an exploitation of the carefully designed chemical functionality of the ligand shell, rather than the potential catalytic activity of a nanostructured clean metal surface. From a biological aspect, a color change of AuNP aggregates, from ruby-red to blue, has been exploited in the development of a highly sensitive calorimetric technique for DNA analysis, capable of detecting trace amounts of oligonucleotide sequences. The same effect has also been used to distinguish between perfectly complementary DNA sequences and those exhibiting different degrees of base pair mismatches [110]. One of the most famous potential long-term applications of AuNPs is the fabrication of new (eventually small) electronic devices [111, 112]; for example, a single-electron transistor action has been demonstrated for systems that contain ideally only one particle in the gap between two contacts separated by only few nanometers.

CNTs are of great interest due to their unique mechanical, electronic, and optical properties, as well as their interesting applications [68, 77]. Both, SWNTs and MWNTs have been investigated in numerous promising areas such as field emit-



ters [113], memory elements [114], sensors [46], and nanotube aquators [115]. In order to optimize the applications of CNTs, it is necessary to modify the sidewalls by chemical functionalization and to attach suitable nanoclusters to the nanotubes [90, 116]. In this way, functionalized nanoparticles could be used as versatile building blocks in the construction of nanodevices. An example of this includes the decoration of AuNPs on to the surface of CNT sidewalls, which has shown particular promise towards the development of novel, highly, efficient photoelectrochemical cells, fuel cells, or sensor devices. The noble metal nanoparticles in general—and AuNPs in particular—have become the focal point for many research groups on the basis of their special optical properties [117], their unusual electronic properties, including conductivity by activated electron hopping [118], and their remarkably high catalytic activity [119]. Hybrid nanostructures combining these two types of material might improve these performances, and further extend the applications.

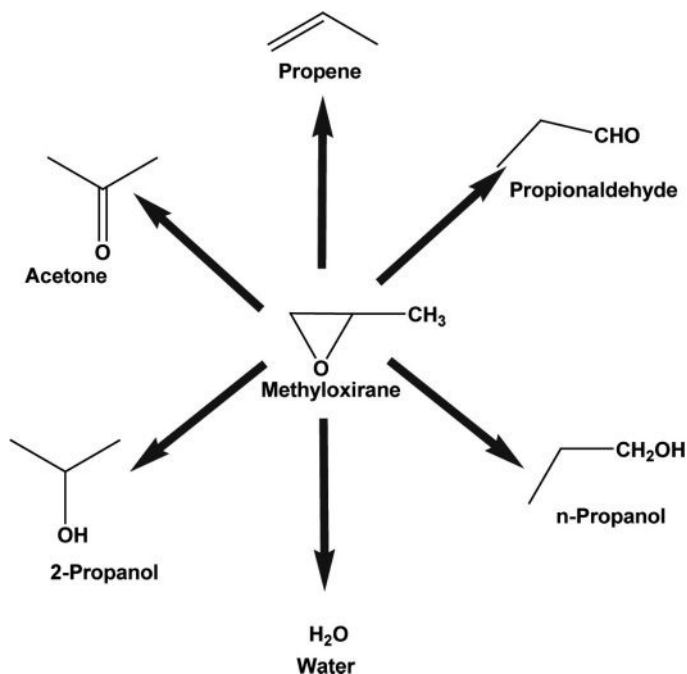
Considering that the broad spectrum of studies connecting metal nanoparticles and CNTs composites are mainly focused on the noble metals (e.g., Pt, Pd, Au, Ag, Ru), it is hardly surprising that the most potential applications of these composite materials are in the field of catalysis. The anchoring of metal nanoparticles in general (and of AuNPs in particular) to CNTs represents another means of producing new types of composite materials with useful properties for gas sensors and catalytic applications [45, 120]. For example, Fasi and coworkers [121] have shown that AuNPs deposited on the surface of the MWNTs were active catalysts in the transformation of methyloxirane (Figure 7.30).

Methyloxirane, which can react in more than one direction and has a versatile functionality, is a favorite of synthetic chemists when creating complicated molecules from relatively simple synthons. It has also been reported that AuNP–CNT composites have been used as catalysts for some environmentally advantageous reactions [41, 71]. Gold-covered MWNTs were proposed as the basic element of a glucose biosensor [122], while the attachment of SWNTs to gold tips not only allowed observations to be made with both AFM and STM [123, 124], but also permitted an investigation of the potential of MWNTs as a solid phase for the adsorption and concentration of true metal ions [125]. A key element when exploring the use of nanoparticle–CNT composites as sensors or catalytic materials is the possibility of an effective and controllable assembly of AuNPs on the surface of CNTs. Such attachment might also serve to detect the presence of certain functional groups on the CNT surface, thus proving that the derivatization had been successful.

## 7.7

### Merits and Demerits of Synthetic Approaches

Several pathways have been introduced to either decorate or attach AuNPs onto the outer walls of CNTs, including processes of reduction, deposition, and chemical linking. By comparing and analyzing these different techniques, it can be



**Figure 7.30** Experimentally proven products obtained in the ring-opening reaction of methyloxirane by using AuNP–CNT composite as a catalyst. Reprinted with permission from Ref. [121].

concluded that each and every approach has its merits and demerits. Although, on each occasion the preferred approach can be selected depending on the conditions and specific application purposes, a direct reduction or deposition of AuNPs on the surface of CNTs is generally the easiest and most effective way of ensuring that large quantities of nanoparticles are coated or deposited onto the CNT surfaces. Controlling the shape, size, and distribution of the nanoparticles, as well as the number deposited on the CNT surface, may be very difficult when using this approach, however.

The alternative approach, to link already modified AuNPs with the CNT surface, is a rather complicated, expensive, multistep procedure that typically would include the synthesis and modification of AuNPs, chemical modification of the CNTs, and then linking of the two components. As well as being a very time-consuming process, the formation of composite materials by covalent linking is highly complex, as the number of AuNPs anchored covalently to the surface of the CNTs will be associated with the number of carboxyl groups or other chemical functionalities of the CNT surface. The major advantages of such a linking procedure are that the size and shape of AuNPs can be tuned; likewise, under certain conditions the connection between AuNPs and CNTs is reversible.



The linking of AuNPs to the CNT surface through hydrophobic or electrostatic interactions may be more beneficial, as a fine dispersion with a high density of composite materials can be achieved if previously modified AuNPs are deposited onto the CNT surface in this way. This is especially the case if the CNTs are pre-modified by polymers or surfactants, which enhance such interactions.

## 7.8 Conclusions

Owing to their unique geometry, exceptional properties and large surface area, CNTs are excellent candidates as support materials for metal nanoparticles in general, and for AuNPs in particular. The blending of these materials to create new composites should in turn lead to the generation of new hybrid materials with applications in catalysis, electronics, and nanotechnology. Moreover, the formation of such composites can be achieved either by the deposition or attachment of AuNPs onto the CNT surface, or by their entrapment within the nanotube cavities.

In this chapter, we have discussed not only the synthetic approaches, assembly and interaction related to AuNP–CNT composites, but also their potential applications. The strategies used to create hybrid materials are variable and depend on the requirements and applications of the composite product. The interaction of CNTs with AuNPs provides the ability to generate significant composite derivatives with numerous potential applications, including advanced catalytic systems, biosensors, electronic nanodevices, probe tips for scanning probe microscopy, electrochemical sensors, and gas sensors. It is perhaps surprising to note that most potential applications for these composites involve catalytic systems, with the high surface area : volume ratio, excellent mechanical properties, thermal and electrical conductivity, chemical stability and inertness, and lack of porosity forming the basis of CNTs being used to support AuNPs. Indeed, with remarkable advances having been made in the area of catalysis, the efficient industrial use of AuNP–CNT composites as catalysts will inevitably attract much interest in the future. Yet, perhaps the most significant point for the future development of these hybrid materials would be to determine influential synthetic protocols and methodologies for the fabrication of composite materials with reproducible properties and performances. Extensive studies are also required with regards to the possible re-use of the composites as catalysts, and consequently attention must be focused on their catalytic reaction mechanisms. Moreover, the spectrum of catalytic activity for AuNP–CNT composites must be extended to the production of industrially important compounds. In addition, simple but effective methods must be identified to deposit gold nanowires and nanorods onto the CNT surface, creating high-density packaging suitable for both electrical and electronic applications. The electron-transfer phenomenon that occurs between deposited AuNPs and CNTs should also be addressed in greater detail, as this may open new opportunities for the development of optoelectronic and light-to-energy-conversion devices. Another

future task will be to explore multicomponent systems that contain several different types of structurally cooperating component, including combinations of metal semi-conductor nanoparticles. This may lead in turn to the development of new materials and structures with functional properties that are superior to those of currently available, “conventional” materials. It is envisaged, therefore, that the future will bear witness to a whole range of novel alloys related to AuNP and CNTs, while the list of applications of CNTs that have been functionalized with AuNPs, other metals, metal oxides and semiconductor nanoparticles, should expand significantly in the near future. Undoubtedly, the great attraction of these composite materials will lead to many research groups undertaking increasing numbers of investigations into their properties and practical applications.

In conclusion, it is clear that the extraordinary diversity of structures, properties, and applications of the AuNP–CNT composites will stimulate many investigations into the fundamental properties and applications of these materials. Moreover, such studies will be conducted in association with other molecular, inorganic, and biological areas of research involving chemistry, physics, biology, and medicine.

### Acknowledgments

The authors acknowledge financial support from the “Brain Korea 21” project from the Ministry of Education, Science, and Technology, as well as from the World-Class University (WCU), Ministry of Education, Science and Technology (MEST) of Korea (Project No. R31-2008-000-10026-0).

### References

- 1 Antonii, F. (1618) *Panacea Aurea-Auro Potibile*, Bibliopoli Frobeniano, Humberg.
- 2 Kunckles, J. (1676) *Nuetlicke Observationes oder Anmerkungen von Auro und Argento otabili*, Schutzens, Humberg.
- 3 Faraday, M. (1857) *Philos. Trans. London*, **147**, 145.
- 4 Daniel, M.-C. and Astruc, D. (2004) *Chem. Rev.*, **104**, 293 and references there in.
- 5 Source–ISI web of knowledge. Available at: <http://isiknowledge.com>
- 6 Brust, M. and Kiely, C.J. (2002) *Physicochem. Eng. Asp.*, **202**, 186.
- 7 Yu, Y.Y., Chang, S.S., Lee, C.L. and Wang, C.R.C. (1997) *J. Phys. Chem. B*, **101**, 6661.
- 8 Shankar, S.S., Rai, A., Ankamwar, B., Singh, A., Ahmad, A. and Sastry, M. (2004) *Nat. Mater.*, **3**, 482.
- 9 Sun, Y. and Xia, Y. (2002) *Science*, **298**, 2176.
- 10 Iijima, S. (1991) *Nature*, **354**, 56.
- 11 Tang, Z.K., Zhang, L., Wang, N., Zhang, X.X., Wen, G.H., Li, G.D., Wang, J.N., Chan, C.T. and Sheng, P. (2001) *Science*, **292**, 2462.
- 12 Ajayan, P.M. (1999) *Chem. Rev.*, **99**, 1787.
- 13 Oberlin, A., Endo, M. and Koyama, T. (1976) *J. Cryst. Growth*, **32**, 335.
- 14 Oberlin, A., Endo, M. and Koyama, T. (1976) *Carbon*, **14**, 133.
- 15 Kroto, H.W., Heath, J.R., O’Brien, S.C., Curl, R.F. and Smalley, R.E. (1985) *Nature*, **318**, 162.
- 16 Iijima, S. and Ichihashi, T. (1993) *Nature*, **363**, 603.
- 17 Bethune, D.S., Kiang, C.H., de Vries, M.S., Gorman, G., Savoy, R., Vazquez, J. and Beyers, R. (1993) *Nature*, **363**, 605.

- 18 Ebbesen, T.W. and Ajayan, P.M. (1992) *Nature*, **358**, 220.
- 19 Thess, A., Lee, R., Nikolaev, P., Dai, H.J., Petit, P., Robert, J., Xu, C., Lee, Y.H., Kim, S.G., Rinzler, A.G., Colbert, D.T., Scuseria, G.E., Tomanek, D., Fisher, J.E. and Smalley, R.E. (1996) *Science*, **273**, 483.
- 20 Journet, C., Maser, W.K., Bernier, P., Loiseau, A., Lamy de la Chapelle, M., Lefrant, A., Denard, P., Lee, R. and Fischer, J.E. (1997) *Nature*, **388**, 756.
- 21 Rinzler, A.G., Liu, J., Dai, H., Nikolaev, P., Huffman, C.B., Rodriguez-Macias, F.J., Boul, P.J., Lu, A.H., Heymann, D., Colbert, D.T., Lee, R.S., Fischer, J.E., Rao, A.M., Eklund, P.C. and Smalley, R.E. (1998) *Appl. Phys. A*, **67**, 29.
- 22 Endo, M., Takeuchi, K., Kobori, K., Takahashi, K., Kroto, H.W. and Sarkar, A. (1995) *Carbon*, **33**, 873.
- 23 Nikolaev, P., Bronikowski, M., Bradley, R., Rohmund, F., Colbert, D.T., Smith, K. and Smalley, R.E. (1999) *Chem. Phys. Lett.*, **313**, 91.
- 24 Chiang, I.W., Brinson, B.E., Huang, A.Y., Willis, P.A., Bronikowski, M.J., Margrave, J.L., Smalley, R.E. and Hauge, R.H. (2001) *J. Phys. Chem. B*, **105**, 8297.
- 25 Bonard, J.M., Stora, T., Salvétat, J.-P., Maier, F., Stockli, T., Duschl, C., Forro, L., de Heer, W.A. and Chatelain, A. (1997) *Adv. Mater.*, **9**, 827.
- 26 Bandow, S., Rao, A.M., Williams, K.A., Thess, A., Smalley, R.E. and Eklund, P.C. (1997) *J. Phys. Chem. B*, **101**, 8839.
- 27 Duesberg, G.S., Burghard, M., Muster, J., Philipp, G. and Roth, S. (1998) *Chem. Commun.*, 435.
- 28 Coleman, J.N., Dalton, A.B., Curran, S., Rubio, A., Davey, A.P., Drury, A., McCarthy, B., Lahr, B., Ajayan, P.M., Roth, S., Barklie, R.C. and Blau, W.J. (2000) *Adv. Mater.*, **12**, 213.
- 29 Vazquez, E., Georgakilas, V. and Prato, M. (2002) *Chem. Commun.*, 2308.
- 30 Baughman, R.H., Zakhidov, A.A. and de Heer, W.A. (2002) *Science*, **297**, 787.
- 31 Dong, L., Subramanian, A. and Nelson, B.J. (2007) *Nanotoday*, **2**, 12.
- 32 Pederson, M.R. and Broughton, J.Q. (1992) *Phys. Rev. Lett.*, **69**, 2689.
- 33 Ajayan, P.M. and Iijima, S. (1993) *Nature*, **361**, 333.
- 34 Seshadri, R., Govindaraj, A., Aiyer, H.N., Sen, R., Subbanna, G.N., Raju, A.R. and Rao, C.N.R. (1994) *Curr. Sci.*, **66**, 839.
- 35 Liu, M. and Cowley, J.M. (1995) *Carbon*, **33**, 225.
- 36 Liu, M. and Cowley, J.M. (1993) *Carbon*, **33**, 749.
- 37 Planeix, J.M., Coustel, N., Coq, J., Brotons, V., Kumbhar, P.S., Dutartre, R., Geneste, P., Bernier, P. and Ajayan, P.M. (1994) *J. Am. Chem. Soc.*, **116**, 7935.
- 38 Jiang, L. and Gao, L. (2003) *Carbon*, **41**, 2923.
- 39 Tsang, S.C., Chen, Y.K., Harris, P.J.F. and Green, M.L.H. (1994) *Nature*, **372**, 159.
- 40 Chu, A., Cook, J., Heesom, R.J.R., Hutchison, J.L., Geen, M.L.H. and Sloan, J. (1996) *Chem. Mater.*, **8**, 2751.
- 41 Xue, B., Chen, P., Hong, Q., Lin, J. and Tan, K.L. (2001) *J. Mater. Chem.*, **11**, 2378.
- 42 Raghuvver, M.S., Agrawal, S., Bishop, N. and Ramanath, G. (2006) *Chem. Mater.*, **18**, 1390.
- 43 Chen, J., Rao, A.M., Lyuksyutove, S., Itkis, M.E., Hamon, M.A., Hu, H., Cohn, R.W., Eklund, P.C., Colbert, D.T., Smalley, R.E. and Haddon, R.C. (2001) *J. Phys. Chem. B*, **105**, 2525.
- 44 Choi, H.C., Shim, M., Bangsaruntip, S. and Dai, H. (2002) *J. Am. Chem. Soc.*, **124**, 9058.
- 45 Wildgoose, G.G., Banks, C.E. and Compton, R.G. (2006) *Small*, **2**, 182.
- 46 Kong, J., Franklin, N., Zhou, C., Chapline, M., Peng, S., Cho, K. and Dai, H. (2000) *Science*, **287**, 622.
- 47 Collins, P.G., Bradley, K., Ishigami, M. and Zettl, A. (2000) *Science*, **287**, 622.
- 48 Qu, L. and Dai, L. (2005) *J. Am. Chem. Soc.*, **127**, 10806.
- 49 Wen, X. and Yang, S. (2002) *Nano Lett.*, **2**, 451.
- 50 Kim, D.S., Lee, T. and Geckeler, K.E. (2006) *Angew. Chem. Int. Ed. Engl.*, **45**, 104.
- 51 Tzitzios, V., Georgakilas, V., Oikonomou, E., Karakassides, M. and Petridis, D. (2006) *Carbon*, **44**, 848.
- 52 Zhang, R., Wang, Q., Zhang, L., Yang, S., Yang, Z. and Ding, B. (2008) *Colloid Surf. A*, **312**, 136.

- 53 Quinn, B.M., Dekker, C. and Lemay, S.G. (2005) *J. Am. Chem. Soc.*, **127**, 6146.
- 54 Guo, D.J. and Li, H.L. (2004) *J. Electroanal. Chem.*, **573**, 197.
- 55 Qu, L., Dai, L. and Osawa, E. (2006) *J. Am. Chem. Soc.*, **128**, 5523.
- 56 Heltzel, A.J., Qu, L. and Dai, L. (2008) *Nanotechnology*, **19**, 245702.
- 57 Tello, A., Cardenas, G., Haberle, P. and Segura, R.A. (2008) *Carbon*, **46**, 884.
- 58 Hang, Q., Maschmann, M.R., Fisher, T.S. and Janes, D.B. (2007) *Small*, **3**, 1266.
- 59 Zhang, Y., Franklin, N.W., Chen, R.J. and Dai, H. (2000) *Chem. Phys. Lett.*, **331**, 35.
- 60 Geckeler, K.E. and Rosenberg, E. (eds) (2006) *Functional Nanomaterials*, American Scientific Publishers, Valencia, USA.
- 61 Premkumar, T., Kim, D.S., Lee, K.J. and Geckeler, K.E. (2007) *Gold Bull.*, **40**, 321.
- 62 Chen, J., Hamon, M.A., Hu, H., Chen, Y.S., Rao, A.M., Ecklund, P.C. and Haddon, R.C. (1998) *Science*, **282**, 95.
- 63 Azamian, B.R., Coleman, K.S., Davis, J.J., Hanson, N. and Green, M.L.H. (2002) *Chem. Commun.*, 366.
- 64 Zanella, R., Basiuk, E.V., Santiago, P., Basiuk, V.A., Mireles, E., Puente-Lee, I. and Saniger, J.M. (2005) *J. Phys. Chem. B*, **109**, 16290.
- 65 Hu, J., Shi, J., Li, S., Qin, Y., Guo, Z.X., Song, Y. and Zhu, D. (2005) *Chem. Phys. Lett.*, **401**, 352.
- 66 Coleman, K.S., Bailey, S.R., Fogden, S. and Green, M.L.H. (2003) *J. Am. Chem. Soc.*, **125**, 8722.
- 67 Ma, H., Zhang, L., Pan, Y., Zhang, K. and Zhang, Y. (2008) *Electroanalysis*, **20**, 1220.
- 68 Tasis, D., Tagmatarchis, N., Bianco, A. and Prato, M. (2006) *Chem. Rev.*, **106**, 1105.
- 69 Ellis, A.V., Vijayamohanam, K., Goswami, R., Chakrapani, N., Ramanathan, L.S., Ajayan, P.M. and Ramanath, G. (2003) *Nano Lett.*, **3**, 279.
- 70 Sainsbury, T., Stolarczyk, J. and Fitzmaurice, D. (2005) *J. Phys. Chem. B*, **109**, 16310.
- 71 Han, L., Wu, W., Kirk, F.L., Luo, J., Maye, M.M., Kariuki, N.N., Lin, Y., Wang, C. and Zhong, C.J. (2004) *Langmuir*, **20**, 6019.
- 72 Sainsbury, T. and Fitzmaurice, D. (2004) *Chem. Mater.*, **16**, 2174.
- 73 Brust, M., Walker, M., Buthell, D., Schiffrin, D. and Whyman, R. (1994) *J. Chem. Soc. Chem. Commun.*, 801.
- 74 Ahern, D., Rao, S. and Fitzmaurice, D. (1999) *J. Phys. Chem. B*, **103**, 1821.
- 75 Rahman, G.M.A., Guldi, D.M., Zambon, E., Pasquato, L., Tagmatarchis, N. and Prato, M. (2005) *Small*, **1**, 527.
- 76 Li, X., Liu, Y., Fu, L., Cao, L., Wei, D., Yu, G. and Zhu, D. (2006) *Carbon*, **44**, 3139.
- 77 Tasis, D., Tagmatarchis, N., Georgakilas, V. and Prato, M. (2003) *Chem. Eur. J.*, **9**, 4000.
- 78 Liu, L., Wang, T., Li, J., Guo, Z.-X., Dai, L., Zhang, D. and Zhu, D. (2003) *Chem. Phys. Lett.*, **367**, 747.
- 79 Yang, D.Q., Hennequin, B. and Sacher, E. (2006) *Chem. Mater.*, **18**, 5033.
- 80 Guldi, D.M., Rahman, G.M.A., Jux, N., Prato, M., Qin, S.H. and Ford, W. (2005) *Angew. Chem. Int. Ed. Engl.*, **44**, 2015.
- 81 Zhou, R., Shi, M., Chen, X., Wang, M., Yang, Y., Zhang, X. and Chen, H. (2007) *Nanotechnology*, **48**, 485603.
- 82 Lee, T.H., Gonzalez, J.I., Zheng, J. and Dickson, R.M. (2005) *Acc. Chem. Res.*, **38**, 534.
- 83 Ou, Y.Y. and Huang, M.H. (2006) *J. Phys. Chem. B*, **110**, 2031.
- 84 Jiang, K., Eitan, A., Schadler, L.S., Ajayan, P.M., Siegel, R.W., Grobert, N., Mayne, M., Reyes-Reyes, M., Terrones, H. and Terrones, M. (2003) *Nano Lett.*, **3**, 275.
- 85 Kim, B. and Sigmund, W.M. (2004) *Langmuir*, **20**, 8239.
- 86 Gittins, D.I. and Caruso, F. (2001) *Angew. Chem. Int. Ed. Engl.*, **40**, 3001.
- 87 Correa-Duarte, M.A., Sobal, N., Liz-Marzan, L.M. and Giersig, M. (2004) *Adv. Mater.*, **16**, 2179.
- 88 Carrilo, A., Swartz, J.A., Gamba, J.M., Kare, R.S., Chakrapani, N., Wei, B. and Ajayan, M. (2003) *Nano Lett.*, **3**, 1437.
- 89 Hu, X., Wang, T., Qu, X. and Dong, S. (2006) *J. Phys. Chem. B*, **110**, 853.
- 90 Fullam, S., Cottell, D., Rensmo, H. and Fitzmaurice, D. (2000) *Adv. Mater.*, **12**, 1430.

- 91 Brust, M., Kiely, C.J., Bethell, D. and Schiffrin, D.J. (1998) *J. Am. Chem. Soc.*, **120**, 12367.
- 92 Correa-Duarte, M.A., Perez-Juste, J., Sanchez-Iglesias, A., Giersig, M. and Liz-Marzan, L.M. (2005) *Angew. Chem. Int. Ed. Engl.*, **44**, 4375.
- 93 Zhang, M., Su, L. and Mao, L. (2006) *Carbon*, **44**, 276.
- 94 Geckeler, K.E. (ed.) (2003) *Advanced Macromolecular and Supramolecular Materials and Processes*, Kluwer Academic/Plenum, New York.
- 95 Biju, V., Itoh, T., Makita, Y. and Ishikawa, M. (2006) *J. Photochem. Photobiol. A-Chem.*, **183**, 315.
- 96 Ichiya, L.S.H., Basner, B. and Willner, I. (2005) *Angew. Chem. Int. Ed. Engl.*, **44**, 78.
- 97 Rajas-Chapana, J.A., Correa-Duarte, M.A., Ren, Z., Kempa, K. and Giersig, M. (2004) *Nano Lett.*, **4**, 985.
- 98 Moreno-Manas, M. and Pleixats, R. (2003) *Acc. Chem. Res.*, **36**, 638.
- 99 Van Dijk, M.A., Lippitz, M. and Orrit, M. (2005) *Acc. Chem. Res.*, **38**, 594.
- 100 Han, M., Gao, X., Su, J.Z. and Nie, S. (2001) *Nat. Biotechnol.*, **19**, 631.
- 101 Haruta, M. (2002) *CATTECH*, **6**, 102.
- 102 Remediakis, I.N., Lopez, N. and Norskov, J.K. (2005) *Angew. Chem. Int. Ed. Engl.*, **44**, 1824.
- 103 Zayats, M., Kharitonov, A.B., Pogorelova, S.P., Lioubashevski, O., Katz, E. and Willner, I. (2003) *J. Am. Chem. Soc.*, **125**, 16006.
- 104 Ghosh, P., Han, G., De, M., Kim, C.K. and Rotello, V.M. (2008) *Adv. Drug Deliv. Rev.*, **60**, 1307.
- 105 Bhattacharya, R. and Mukherjee, P. (2008) *Adv. Drug Deliv. Rev.*, **60**, 1289.
- 106 Li, H., Luk, Y.Y. and Mrksich, M. (1999) *Langmuir*, **15**, 4957.
- 107 Pasquato, L., Rancan, F., Scrimin, P., Mancin, F. and Frigeri, C. (2000) *Chem. Commun.*, 2253.
- 108 Pietron, J.J. and Murray, R.W. (1999) *J. Phys. Chem. B*, **103**, 4440.
- 109 Bartz, M., Kuther, J., Scshadri, R. and Tremel, W. (1998) *Angew. Chem. Int. Ed. Engl.*, **37**, 2466.
- 110 Storhoff, J.J., Elghanian, R., Mucic, R.C., Mirkin, C.A. and Letsinger, R.L. (1998) *J. Am. Chem. Soc.*, **120**, 1959.
- 111 Sato, T., Ahmed, H., Brown, D. and Johanson, B.F.G. (1997) *J. Appl. Phys.*, **82**, 1007.
- 112 Person, S.H.M., Olofsson, L. and Hedberg, L. (1999) *Appl. Phys. Lett.*, **74**, 2546.
- 113 De Heer, W.A., Chatelain, A. and Ugarte, D. (1995) *Science*, **270**, 1179.
- 114 Rueckes, T., Kim, K., Joselevich, E., Tseng, G.Y., Cheung, C. and Lieber, C.M. (2000) *Science*, **289**, 94.
- 115 Baughman, R.H., Cui, C.X., Zakhidov, A.A., Lqbal, Z., Barisci, J.N., Spinks, G.M., Wallace, G.G., Mazzoldi, A., De Rossi, D., Rinzler, A.G., Jaschinski, O., Roth, S. and Kertesz, M. (1999) *Science*, **284**, 1340.
- 116 Chen, Q., Dai, L., Gao, M., Huang, S. and Mau, A. (2001) *J. Phys. Chem. B*, **105**, 618.
- 117 Dirix, Y., Bastiaansen, C., Caseri, W. and Smith, P. (1999) *Adv. Mater.*, **11**, 233.
- 118 Terrill, R.H., Postlethwaite, T.A., Chem, C.H., Poon, C.D., Terzis, A., Chen, A., Hutchison, J.E., Clark, M.R., Wignall, G., Landono, J.D., Superfine, R., Falvo, M., Johnson, C.S. Jr., Samulski, E.T. and Murray, R.W. (1995) *J. Am. Chem. Soc.*, **117**, 12537.
- 119 Haruta, M. and Date, M. (2001) *Appl. Catal. A, General*, **222**, 427.
- 120 Georgakilas, V., Gournis, D., Tzitzios, V., Pasquato, L., Guldi, D.M. and Prato, M. (2007) *J. Mater. Chem.*, **17**, 2679.
- 121 Fasi, A., Palinko, I., Seo, J.W., Konya, Z., Hernadi, K. and Kiricsi, I. (2003) *Chem. Phys. Lett.*, **372**, 848.
- 122 Wang, S.G., Zhang, Q., Wang, R., Yoon, S.F., Ahm, J., Yang, J.D., Tian, J.Z., Li, J.Q. and Zhou, Q. (2003) *Electrochem. Commun.*, **5**, 800.
- 123 Yang, Y., Zhang, J., Nan, X. and Liu, Z. (2002) *J. Phys. Chem. B*, **106**, 4139.
- 124 Nishino, T., Ito, T. and Umezawa, Y. (2002) *Anal. Chem.*, **74**, 4275.
- 125 Liang, P., Liu, Y., Gue, L., Zeng, I. and Lu, H. (2004) *J. Anal. Atomic Spectrom.*, **19**, 1489.



## 8

# Recent Advances in Metal Nanoparticle-Attached Electrodes

*Munetaka Oyama, Akrajas Ali Umar, and Jingdong Zhang*

### 8.1

#### Introduction

Metal nanoparticles (NPs) have attracted vast attention during the past decade on the basis of their unique optical, electronic, magnetic, and catalytic properties. In the case of gold NPs (AuNPs), their assembly, supermolecular chemistry, quantum-size related properties, and applications to biology, catalysis, and nanotechnology have been summarized by Daniel and Astruc [1].

Within the field of electrochemistry, and in particular of electroanalysis, metal NPs have been actively utilized in the modification of electrodes as functional nanomaterials, and this subject has been extensively reviewed [2–4].

In order to utilize metal NPs as unique devices in functional electrodes, they must normally be attached onto the electrode surfaces. Consequently, a wide variety of methods is available for preparing NP-attached functional electrodes with respect to the metal NPs used, the nature of the substrate electrode materials, and the method of attachment. One well-known method of modification is that of electrochemical deposition, which involves the electrochemical reduction of metal ions onto the surfaces of a conducting material, such that the nanoparticles become attached to the surfaces. This procedure is used in the case of AuNPs [5, 6].

A second, “chemical,” method is also available for preparing metal NPs. For this, bottom-up-type preparation strategies for metal NPs in solution are well known and well established, again as reported for AuNPs [7–9]. In terms of regularity and uniformity of NP size, the chemical approach is generally superior to electrochemical deposition, although certain difficulties may be encountered when attaching metal NPs which have been formed in solution onto the electrode surfaces. It is possible that the more interesting characteristics of metal NPs might be diminished when they aggregate to form larger clusters, and consequently it is necessary to either fix or attach the NPs while retaining a moderate degree of NP dispersion. The development of such attachment methods with appropriate



degrees of dispersion are, therefore, very important if the best use is to be made of the characteristics of metal NPs for electrode modification. But this situation is also true for the preparation of nanocomposites, as are used in electronic, sensing, and optical devices.

When attaching AuNPs to the electrode surfaces, a number of peculiar binding molecules that are suitable for connecting AuNPs with substrates have been used. For example, when connecting AuNPs with a glass surface, both 3-mercaptopropyl-trimethoxysilane (MPTMS) and 3-aminopropyl-trimethoxysilane (APTMS) have been adopted; this process utilizes not only the bonding ability of the silanol group towards the glass surfaces but also the affinity of the  $-SH$  or  $-NH_2$  group for AuNPs [10–12]. The AuNP-attached surfaces thus formed were successfully applied to surface-enhanced Raman spectroscopic measurements.

Although today, the use of these peculiar binder molecules has become standard strategy when attaching AuNPs to electrode surfaces [13, 14], it is to be expected that the characteristics of metal NPs—notably their conductivity and catalytic ability—might be greatly affected by the chemical reagents that surround or bind them. Hence, although the use of these bridging reagents is clearly effective in some respects (e.g., size-uniformity and rigid-fixation of metal NPs), they may interfere in the process of utilizing the characteristics of the metal NPs.

If it were possible to attach metal NPs to a conducting substrate without the use of a binder molecule, it might be expected that novel conducting nanodispersed materials with unique electrochemical properties involving both the metal NPs and the conducting substrates, could be fabricated. Consequently, our group has recently developed a seed-mediated growth method for surface modification with metal NPs, notably on the surfaces of indium tin oxide (ITO).

In this chapter, we summarize the development and applications of seed-mediated growth methods for the modification of electrode surfaces. Examples include the wet chemical preparation of advanced functional nanomaterials composed of metal NPs and a conducting substrate.

## 8.2

### Seed-Mediated Growth Method for the Attachment and Growth of AuNPs on ITO

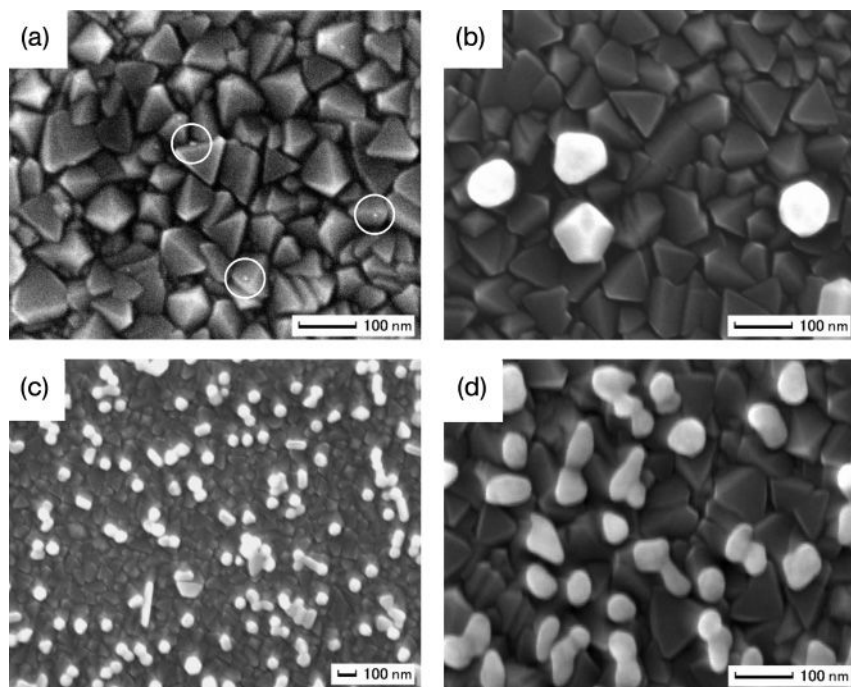
During the early stages of the studies, a seed-mediated growth method was used which originally had been developed by Murphy and coworkers to synthesize Au nanorods in aqueous solution, by the chemical reduction of  $HAuCl_4$  [15, 16]. This approach was applied to the formation of AuNPs on the ITO surfaces [17].

In the actual procedure, a piece of ITO-coated glass was washed first by sonication in acetone, and then in pure water. The washed ITO substrate was dried in air and prepared for immersion in a seed solution produced by adding 0.5 ml of a cooled pure aqueous solution of 0.1 M  $NaBH_4$  to 19.5 ml of a pure aqueous solution of 0.25 mM  $HAuCl_4$  and 0.25 mM trisodium citrate, with stirring. When using this procedure, it has been reported that Au nanoseed particles of 3.5 nm were formed in the seed solution [15].

The ITO substrate was then immersed in the seed solution so as to attach the Au nanoseed particles onto the surface. Typically, immersion in the seed solution was maintained for 2 h, and without any particular treatments. The ITO substrate was then removed from the seed solution, and the surface washed carefully by flushing pure water over the surface several times. Any water retained on the surface was removed with tissue paper, simply by touching the edges of the glass.

After blowing the surface of the ITO with  $N_2$  gas until dry, the substrate was immersed in the growth solution. This was prepared by adding 2.5 ml of a pure aqueous solution of 0.01 M  $H AuCl_4$ , 0.5 ml of a pure aqueous solution of 0.1 M ascorbic acid, and 0.5 ml of a pure aqueous solution of 0.1 M NaOH into 90 ml of a pure aqueous solution of 0.1 M cetyltrimethylammonium bromide (CTAB). Again, the ITO substrate was retained in the growth solution typically for a period of 24 h in order to promote the growth of AuNPs from the attached Au nanoseed particles. Finally, the sample was washed by flushing with pure water.

The real surface nanoscale images were recorded using field emission scanning electron microscopy (FE-SEM). Figure 8.1a shows the FE-SEM image observed



**Figure 8.1** FE-SEM images of the ITO surfaces. (a) After immersion of the ITO into the seed solution for 2 h. The white circles indicate areas of attachment of small seed particles; (b) After subsequent immersion of the ITO in the growth solution for 24 h; (c) A low-magnification image of the ITO surface of

panel (b); (d) The ITO substrate was modified initially with MPTMS, after which seed-mediated growth was performed in the same manner as for (b). Reproduced with permission from Ref. [17]; © 2005, American Chemical Society.

after seeding, while the images in Figures 8.1b and c were observed after the seed-mediated growth treatment. In the later images, the AuNPs grown on ITO were seen as white particles in the images against a background of ITO crystals. The AuNPs clearly grew to approximately 50–70 nm on the ITO surface from the Au nanoseed particles attached on ITO (Figure 8.1a), following immersion in the growth solution (i.e., by applying the seed-mediated growth method), while retaining a moderate dispersion [17].

The initial attachment of nanoseed particles would be expected to be promoted via the physisorption of ultrasmall NPs which had been dispersed in the seed solution by simply dipping the substrates [18]. The second process should involve crystal growth via the chemical reduction of metal ions in the growth solution, which is inferred to proceed gradually around the nanoseed particles on the substrates.

As shown in Figure 8.1d, the FE-SEM image of AuNPs on the ITO surfaces premodified with MPTMS revealed significant differences in the morphology of the grown AuNPs [17]. Because the crystal-like structures of AuNPs were observed in the absence of MPTMS (Figures 8.1b and c), the seed-mediated growth method was proposed as a unique means of attaching Au nanocrystals onto the ITO surfaces, without the use of binder molecules.

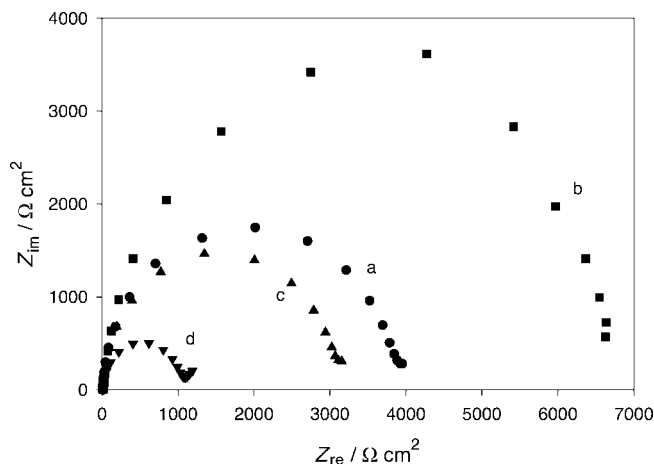
### 8.3

#### Electrochemical Applications of AuNP-Attached ITO

The AuNP-directly attached ITO (AuNP/ITO) electrodes were then applied to electrochemical measurements. As inferred by the fact that as-prepared AuNPs on the ITO surface (Figure 8.1c) displayed a different morphology than the MPTMS-linked AuNPs modified on ITO (Figure 8.1d), the AuNP/ITO electrodes provided attractive electrochemical and electrocatalytic properties to promote heterogeneous electron transfer kinetics [19, 20]. In particular, the electrochemical impedance measurements performed to evaluate the effects of AuNPs on the interfacial electron transfer property revealed that the presence of a MPTMS layer caused a significant increase in charge transfer resistance. The relatively low charge transfer resistances of the AuNP/ITO electrodes were clarified from the impedance results, with the typical charge transfer resistance of the AuNP/ITO electrode being approximately one-third that of the AuNP/MPTMS/ITO electrode (Figure 8.2) [20].

The AuNP/ITO electrodes were used for observing the electro-oxidation of uric acid, ascorbic acid, dopamine, norepinephrine (noradrenaline), and epinephrine (adrenaline) [20]. Whilst the AuNP/MPTMS/ITO electrodes caused a depression in selectivity when determining epinephrine in the presence of ascorbic acid, due to the existence of the thiol monolayer, the AuNP/ITO electrodes were able to improve the detection sensitivity while retaining the selectivity [20].

The AuNP/ITO electrodes also provided a biocompatible matrix for the immobilization of hemoglobin (Hb). By using electrochemical impedance



**Figure 8.2** Electrochemical impedance spectra of ITO (●), MPTMS/ITO (■), Au/MPTMS/ITO (▲) and Au/ITO (▼) electrodes in 0.1 M phosphate-buffered saline (pH 7.4) containing 1 mM  $K_3Fe(CN)_6$  and 1 mM  $K_4Fe(CN)_6$ . Electrode potential = 0.22 V; Frequency range = 100 kHz to 100 mHz; Voltage amplitude = 5 mV. Reproduced with permission from Ref. [20]; © 2005, Wiley-VCH.

measurements, the modification of AuNPs, followed by the immobilization of Hb on the electrode surfaces, was characterized with the  $[Fe(CN)_6]^{3-}/[Fe(CN)_6]^{4-}$  redox probe [21]. Due to the promoted electron transfer of Hb by AuNPs, the Hb-immobilized AuNP/ITO electrodes exhibited an effective catalytic response to the reduction of  $H_2O_2$  with good reproducibility and stability. A linear relationship existed between the catalytic current and the  $H_2O_2$  concentration in the range of  $1 \times 10^{-5}$  to  $7 \times 10^{-3}$  M, with a detection limit [signal-to-noise ratio (SNR) = 3] of  $4.5 \times 10^{-6}$  M [21].

A mediator-free  $H_2O_2$  sensor was also developed along with the application of AuNP/ITO electrodes for the immobilization of myoglobin (Mb) [22]. The Mb-modified AuNP/ITO electrodes showed good reproducibility and stability in pH 7.0 buffer, this being based on the catalytic activity of Mb immobilized on AuNP/ITO towards the reduction of  $H_2O_2$ . A linear relationship existed between the catalytic current and the  $H_2O_2$  concentration in the range of  $2.5 \times 10^{-6}$  to  $5 \times 10^{-4}$  M, with a detection limit (SNR = 3) of  $4.8 \times 10^{-7}$  M. In this case, the direct electron transfer of Mb was recorded as a stable and well-behaved voltammetric response, with the Mb-immobilized AuNP/ITO electrodes in buffer solutions [22].

The effects of capping reagents on electron transfer reactions on the AuNP/ITO electrodes were also investigated using cyclic voltammetry [23]. In addition to the conventional preparation, with CTAB present in the growth solution, the presence of sodium dodecyl sulfate (SDS) was investigated to determine whether the fabrication of AuNP/ITO was also possible. Systematic cyclic voltammetry was then carried out using the AuNP/ITO electrodes prepared with different

surfactants—namely cationic CTAB and anionic SDS—for the oxidation of anionic  $[\text{Fe}(\text{CN})_6]^{4-}$  and reduction of cationic  $[\text{Ru}(\text{NH}_3)_6]^{3+}$ . The results showed that the electrochemical responses were significantly improved on both the AuNP/ITO electrodes, but did not depend on the charges of the capping surfactants and the redox species. Thus, the capping of CTAB and SDS on AuNP/ITO was concluded to be quite weak, so that the electron-transfer reactions of both  $[\text{Fe}(\text{CN})_6]^{4-}$  and  $[\text{Ru}(\text{NH}_3)_6]^{3+}$  were not disturbed [23].

The electrocatalytic activity of a three-dimensional (3-D) monolayer of 3-mercaptopropionic acid (MPA) assembled on AuNPs on the surface of ITO was investigated by using the weak capping of CTAB on the grown AuNPs [24]. The electrochemical behavior of nicotinamide adenine dinucleotide hydrate (NADH) on the 3-D MPA monolayer assembled on the AuNP/ITO electrodes indicated that the MPA layer promoted the electron transfer, which was similar to that of a two-dimensional (2-D) MPA monolayer assembled on planar gold electrodes. However, for the electro-oxidation of ascorbic acid and dopamine, the 3-D MPA monolayer showed an obvious electrocatalytic promotion, while the 2-D MPA monolayer exhibited a blocking effect. The catalytic activity of the 3-D MPA monolayer would be an interesting feature of the proposed AuNP/ITO electrodes.

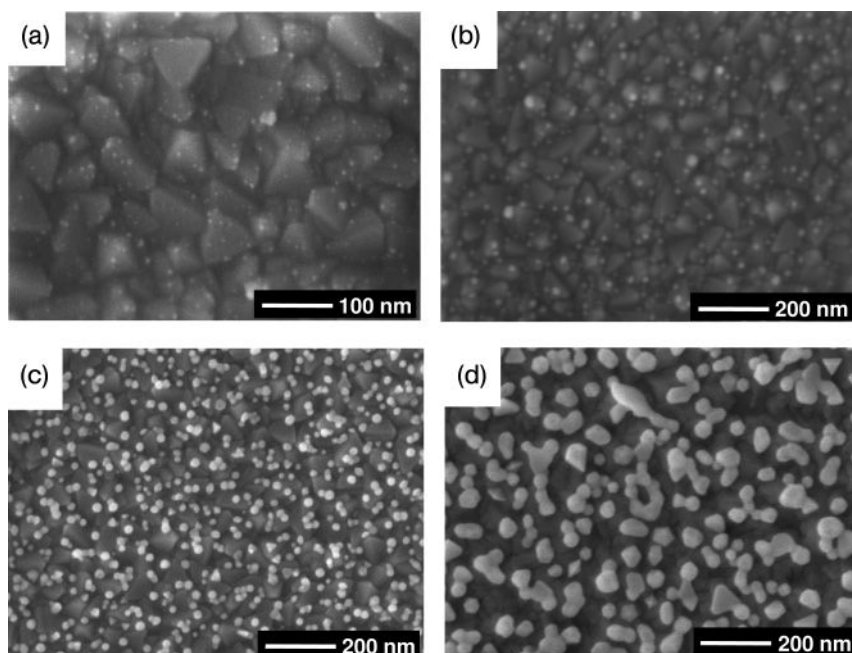
## 8.4

### Improved Methods for Attachment and Growth of AuNPs on ITO

A number of refined methods for improving or perturbing the seeding processes, namely the attachment of Au nanoseed particles, have been proposed by the present authors' group in order to recognize the significance of the seeding treatment.

The first approach involved an *in situ* reduction method, rather than seeding in the Au colloid solution. Here, it was shown that, when the seeding procedure was modified to be carried out by the impregnation reduction of  $\text{AuCl}_4^-$  in the presence of the ITO substrate, the density of AuNPs grown directly on the surface was greatly improved [25]. Figure 8.3 shows the FE-SEM images of the AuNP-attached ITO surfaces prepared using the *in situ* reduction method. The initial attachments of the seed particles were recognized on the ITO crystals (Figure 8.3a), after which the AuNP growth could be seen with time on the nanostructured ITO surface. After a 24-h growth period, the smaller AuNPs were found to be attached densely on the ITO surfaces (Figure 8.3c). Repeating the growth treatment was also effective in increasing the size of the AuNPs (Figure 8.3d), although an increasing time for the repeated treatment led to a decrease in the monodispersion properties of the AuNPs on the electrode surface. In other words, the particle size difference became larger, indicating that the AuNPs had not grown uniformly.

The facile heterogeneous electron transfer kinetics resulting from the deposition and growth of the AuNP-arrays was then monitored by using the  $[\text{Fe}(\text{CN})_6]^{3-}/[\text{Fe}(\text{CN})_6]^{4-}$  redox probe for cyclic voltammetry measurements. In addition, the



**Figure 8.3** FE-SEM images of AuNP-attached ITO surfaces.

For seeding, the ITO substrate was immersed into the solution containing  $\text{AuCl}_4^-$  and citrate ions before the reduction by  $\text{NaBH}_4$ . (a) Observed just after seeding; (b, c) After growth treatment for (b) 15 min and (c) 24 h; (d) After repeating 24-h growth three times. Reproduced with permission from Ref. [25]; © 2005, Elsevier.

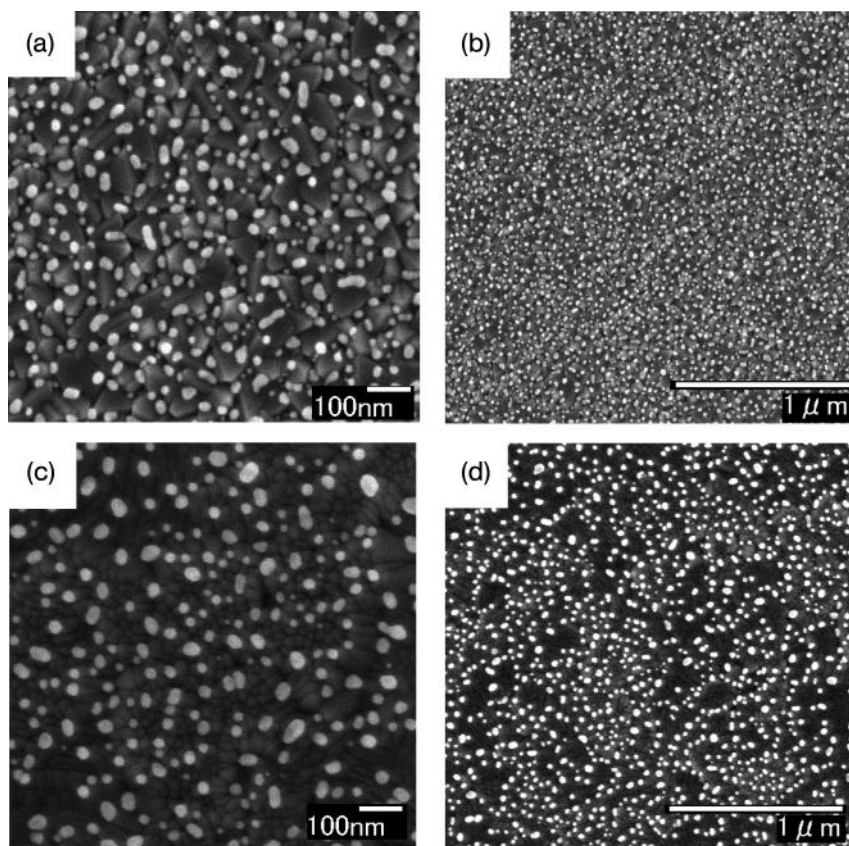
AuNP/ITO electrodes thus prepared exhibited a high catalytic activity for the electro-oxidation of nitric oxide (NO), which in turn led to electroanalytical applications for NO sensing [25].

For the second approach, an attempt was made to grow high-density AuNPs on the ITO surfaces by using a “touch” seeding technique rather than the “normal” seeding in the seed-mediated growth procedure [26]. This approach provided a simple and useful strategy to promote the growth of AuNPs on ITO surfaces by simply touching the surface that had already been covered with a drop of Au nanoseed solution with tissue paper.

Subsequent FE-SEM characterization of the growth of AuNPs on two different structured ITOs—namely, rough and smooth structures (Figure 8.4)—has confirmed that this approach was commonly effective and prospective for fostering the growth of high-density AuNPs with a relatively small size (ca. 10–30 nm) of spherical particle [26].

Based on optical absorption measurements of the AuNP-densely attached ITO samples, it was confirmed that the modified ITO substrates could be used for

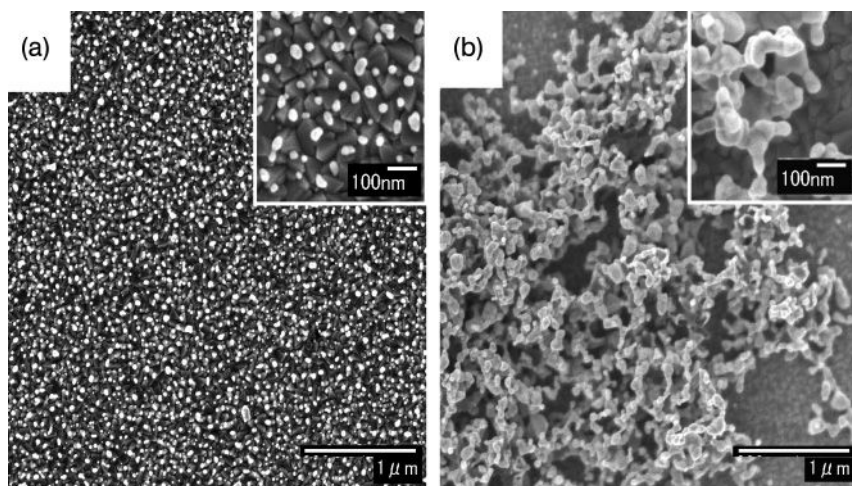




**Figure 8.4** FE-SEM images of AuNP-attached ITO surfaces prepared using the touch seed-mediated growth method. (a, c) High-magnification and (b, d) low-magnification images of the surfaces of (a, b) rough ITO and (c, d) smooth ITO. Reproduced with permission from Ref. [26]; © 2005, American Chemical Society.

photoelectrochemical applications, an example being the optically transparent electrode [26]. In addition, the densely attached AuNP/ITO electrodes thus fabricated were applied to observe the electrochemical responses of hydroquinone and *p*-aminophenol in phosphate buffered solutions [27]. Although the electron-transfer reactions of these compounds were sluggish on bare ITO electrodes, improved electrochemical responses could be remarkably observed on the AuNP/ITO electrodes fabricated with the “touch” seed-mediated growth method [27].

The dense attachment of AuNPs could be also carried out using a cast seed-mediated growth method [28]. Cast seeding which involved three cycles of dropping the seed solution containing Au nanoseed particles and evaporation at 30°C, followed by treatment in the growth solution containing HAuCl<sub>4</sub>, CTAB, and ascorbic acid, was found to be suitable for preparing the AuNP-attached ITO



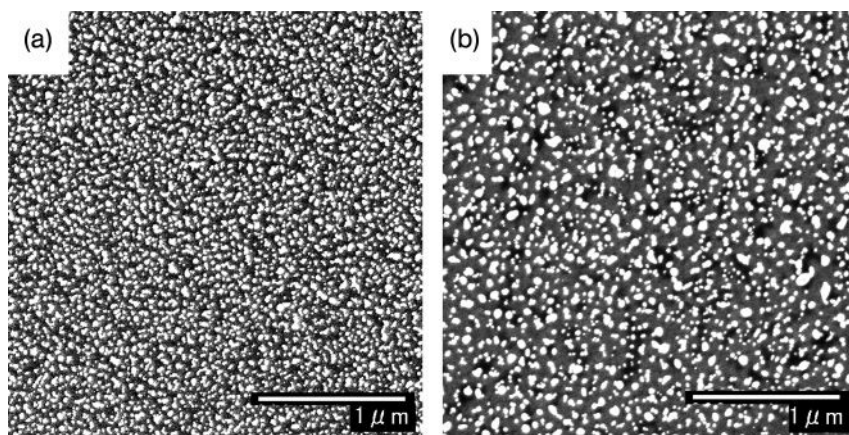
**Figure 8.5** FE-SEM images of AuNP-attached ITO surfaces prepared using the cast seed-mediated growth method. The repeated cycles of casting were (a) three times and (b) 10 times. The insets show the higher-magnification images. Reproduced with permission from Ref. [28]; © 2006, Elsevier.

surfaces having a higher density and a narrower size distribution. The FE-SEM image is shown in Figure 8.5a. On the other hand, a 10-cycle cast seeding process formed the connected or networked nanostructures of AuNPs (see Figure 8.5b), while the optical properties were also different from those of the dispersed AuNP-attached ITO [28]. The cast seeding approach provided a facile and practical strategy for attaching AuNPs on the ITO surfaces while controlling the amount of Au loading and without using certain organic binder molecules.

Furthermore, by adjusting the concentration of citrate ions in the seed solution from 1 mM to 50 mM by adding trisodium citrate after the preparation of the Au nanoseed solution, dramatic changes could be observed in the SEM images and in the actual colors of the ITO substrates, which in turn indicated changes in the nanostructures of the AuNPs formed on the ITO surfaces [29]. The attachment of smaller AuNPs with a higher density was observed when 25 mM citrate ions were added in the seed solution (see Figure 8.6). In contrast, larger AuNPs were seen to attach when the concentration of citrate ions was increased to 50 mM. On the basis of this difference and the FE-SEM images observed just after seeding, it was inferred that the citrate ions affected not only the growth process but also the seeding process [29].

Whilst the repulsive power expected from the increased negative charges of citrate ions was not significant, a rather dense attachment was promoted as the particular effect of citrate ions. Such control of the AuNP attachment on ITO would be practically effective because the dense attachment could be achieved by simply changing the composition of the seed solution.





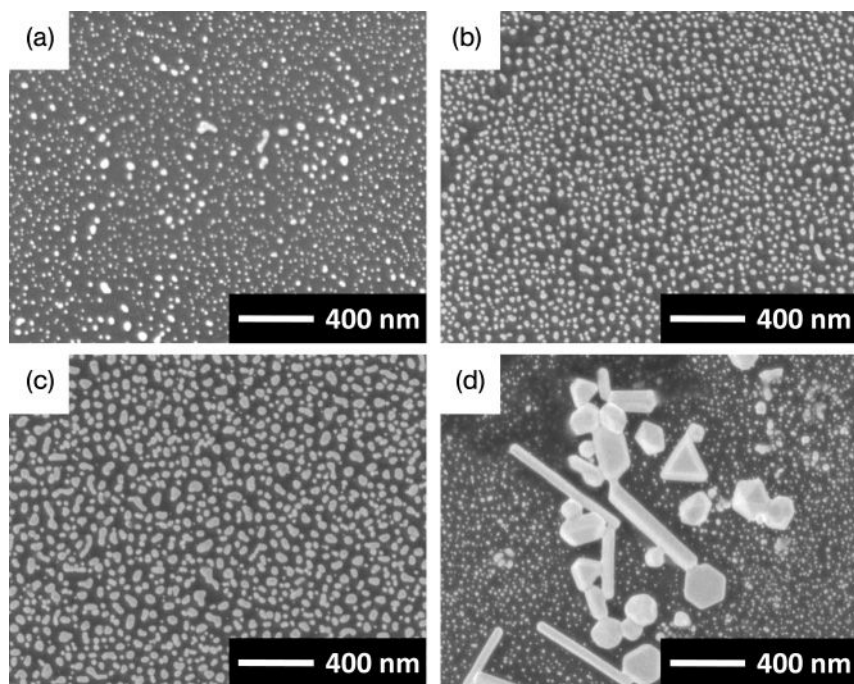
**Figure 8.6** FE-SEM images of AuNP-attached ITO surface. The sample was prepared by adding (a) 25 mM and (b) 50 mM citrate ions into the seed solution before seeding, followed by the growth treatment. Reproduced with permission from Ref. [29]; © 2006, Elsevier.

## 8.5

### Attachment and Growth of AuNPs on Other Substrates

The seed-mediated growth method for surface modification with AuNPs could be applicable to the surface treatments of various types of substrate, mainly because that the modification of AuNPs was found to be possible on all of the examined materials, including glassy carbon (GC), mica, stainless, epoxy resin, phenol resin, simple glass, and ZnO film. FE-SEM observations of these materials revealed that the AuNPs attached and grew on the surfaces, although the grown size of the AuNPs and the formation of rod-like particles varied depending on the substrates. Thus, attachment of the Au nanoseed particles by simple immersion into the Au colloid solutions is considered to proceed commonly via physisorption, and not by specific chemical bonding.

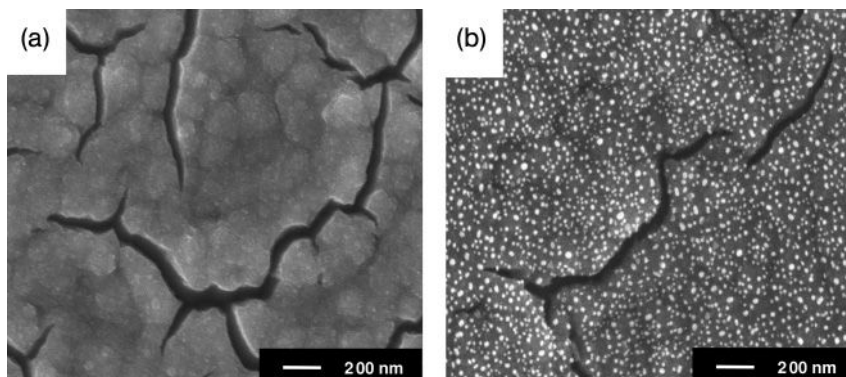
As an example, Figure 8.7 shows the FE-SEM images of AuNP-attached GC surfaces observed after seed-mediated growth treatment [30]. Here, although the seeding time was fixed at 2 h for all samples, the growth period was changed from 5 min to 24 h. This resulted in the dense attachment of AuNPs on the GC surfaces, and shorter growth times when compared to the cases where the ITO surfaces were modified. In addition, flat and smaller AuNPs were clearly formed on the GC surfaces (see Figure 8.7a–c). Interestingly, a longer (24 h) treatment in the growth solution promoted the growth of some microcrystals in local areas, as shown in Figure 8.7d. This would be a reflection of ripening in the growth solution, to promote crystal growth and to form the bold bodies. The AuNP-attached



**Figure 8.7** FE-SEM images of AuNP-attached GC surfaces. Samples were prepared using the seed-mediated growth method, with seeding for 2 h. The growth period was (a) 5 min, (b) 2 h, (c) 8 h, and (d) 24 h. The observation of (d) was focused on an area where bold crystals were dominantly formed. Reproduced with permission from Ref. [30]; © 2009, Japan Society for Analytical Chemistry.

GC electrodes prepared using the seed-mediated growth method were used for the electrochemical detection of nitrite [31].

The method of attachment used for AuNPs on solid surfaces was applied to the slightly different fabrication of a functional electrode. The technique was used to attach AuNPs onto mesoporous  $\text{TiO}_2$  films prepared via a liquid-phase deposition process on GC substrates [32]. Whilst the  $\text{TiO}_2$  film strongly inhibited the electron transfer process of the  $[\text{Fe}(\text{CN})_6]^{3-}/[\text{Fe}(\text{CN})_6]^{4-}$  redox couple, electrochemical measurements indicated that the overpotential for the reduction of maleic acid was significantly decreased when the electrode surface was covered with  $\text{TiO}_2$  film, due to the electrocatalytic activity. After attaching the AuNPs by the seed-mediated growth method (Figure 8.8), however, the sluggish heterogeneous electron transfer kinetics at the  $\text{TiO}_2$  film was effectively improved while the catalytic activity of the  $\text{TiO}_2$  film was retained [32]. This example showed the effect of AuNPs on the nature of less-conducting electrode materials.



**Figure 8.8** FE-SEM images of (a)  $\text{TiO}_2$  film and (b) AuNPs attached and grown on the surfaces of  $\text{TiO}_2$  film. When the  $\text{TiO}_2$  film had been prepared on the GC substrate by liquid-phase deposition, the AuNPs were attached and grown using the seed-mediated growth method. Reproduced with permission from Ref. [32]; © 2005, Electrochemical Society.

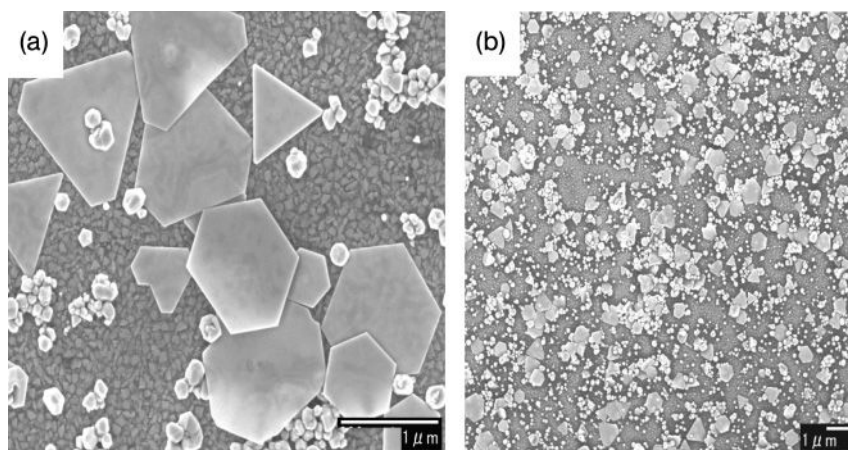
## 8.6

### Attachment and Growth of Au Nanoplates on ITO

Although previously, all approaches and trials for preparation have focused on the seeding process, it is likely that a modification of the growth process should, potentially, also be capable of altering the nanostructures of AuNPs on the ITO electrode surfaces.

As a new strategy for attaching Au nanoplates onto the ITO surfaces, a 2-D crystal growth of Au was permitted through a liquid-phase reduction from Au nanoseed particles attached to the ITO surface, using poly(vinylpyrrolidone) (PVP) rather than CTAB as a capping reagent in the growth solution [33]. By controlling the PVP concentration it was possible to form Au nanoplates (see Figure 8.9) with a surface coverage of up to 30%, although variously shaped Au nanocrystals were formed concurrently on the ITO surface. The Au nanoplates were single crystalline in nature, with (111) basal planes and an edge-length of up to approximately  $\sim 2\mu\text{m}$ , growing parallel to the ITO surface [33]. The concentration of PVP in the growth solution was a key factor in the Au nanoplate formation, as spherical or irregularly shaped AuNPs were formed at either higher or lower concentrations of PVP [33]. The absorption spectra of the Au nanoplate-attached ITO implied anisotropic and specific optical characteristics of the modified ITO glasses.

The Au nanoplate-attached ITO electrode showed some interesting characteristics; for example, an electrochemical response to cytochrome c was observed without using promoter molecules. However, in order to better examine the functions of the Au nanoplates, an increase in their coverage is important. Hence, improved attachment and coverage methods for Au nanoplates are currently under investigation.



**Figure 8.9** FE-SEM images of Au nanoplates attached and grown on ITO surfaces. (a) High-magnification and (b) low-magnification images. Reproduced with permission from Ref. [33]; © 2006, American Chemical Society.

## 8.7

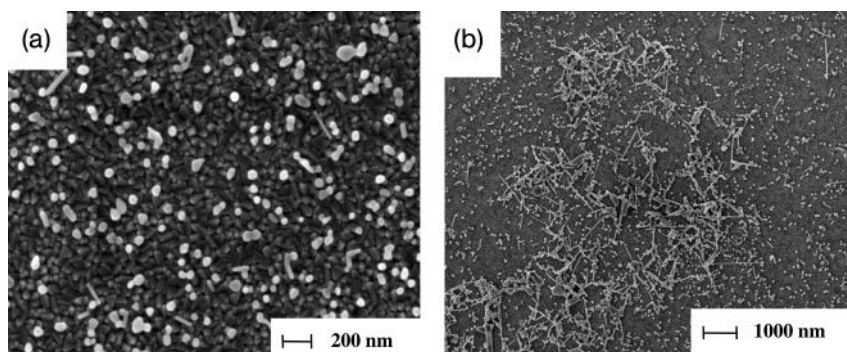
### Attachment and Growth of Silver Nanoparticles (AgNPs) on ITO

By applying the same seed-mediated growth method, silver nanosphere and nanorod particles were successfully attached to the ITO surfaces [34]. As with AuNPs, the attachment of AgNPs could be performed without using a bridging reagent (such as MPTMS), by a simple two-step immersion into first the seed solution, and second into the growth solution containing  $\text{AgNO}_3$ , CTAB, and varying amounts of ascorbic acid [34].

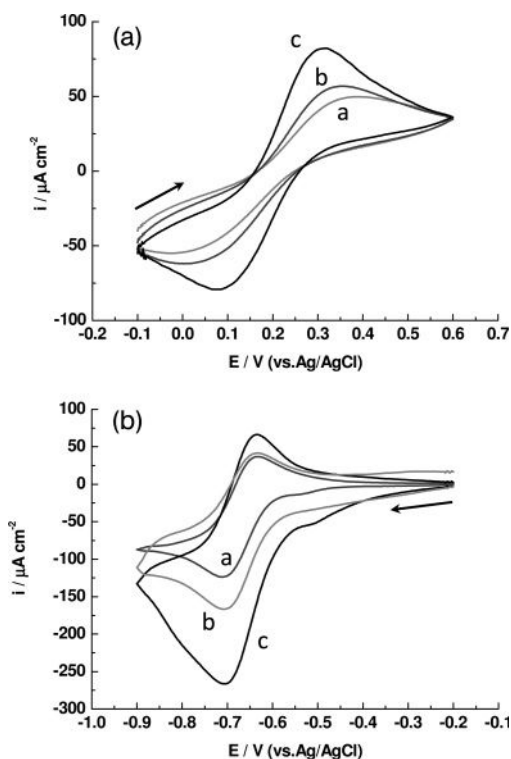
The formed nanostructures were found to be very sensitive to the ascorbic acid content of the growth solution. For example, with an ascorbic acid concentration of 0.64 mM the AgNPs grew on the ITO surface but retained a moderate dispersion (Figure 8.10a). However, when the concentration was raised to 0.86 mM, Ag nanorod and nanowire formation on the ITO surfaces was much less dispersed (Figure 8.10b).

The attachment of AgNPs onto the ITO surfaces was sufficiently strong for further use, for example as a working electrode, and consequently AgNP/ITO electrodes were used in a number of electrochemical measurements. As a result, it was confirmed that the outer spheres of the Ag nanoparticles involved in the redox reaction showed the typical oxidation and reduction waves of Ag metal [34]. In addition, the redox behavior of  $[\text{Fe}(\text{CN})_6]^{3-}/[\text{Fe}(\text{CN})_6]^{4-}$  was improved on the AgNP/ITO electrode, reflecting the low electron transfer resistance of Ag (see Figure 8.11a). This, in turn, indicated that the AgNPs promoted electron transfer reactions by their presence on the conducting ITO surface. The AgNP/ITO electrode was also investigated for reduction of the methyl viologen dication





**Figure 8.10** FE-SEM images of AgNP-attached ITO surfaces. The ITO substrate was first immersed in the seed solution for 2 h and then into the growth solution containing (a) 0.64 mM or (b) 0.86 mM ascorbic acid for 24 h. Reproduced with permission from Ref. [34]; © 2005, American Chemical Society.



**Figure 8.11** (a) Cyclic voltammograms of 0.5 mM  $[\text{Fe}(\text{CN})_6]^{3-}$  and 0.5 mM  $[\text{Fe}(\text{CN})_6]^{4-}$  in 0.1 M phosphate-buffered solution (pH 7.0) recorded using: (curve a) a bare ITO electrode; (curve b) an Ag seed-attached ITO electrode; and (curve c) an AgNP/ITO electrode. Scan rate = 50  $\text{mV s}^{-1}$ ; (c) Cyclic

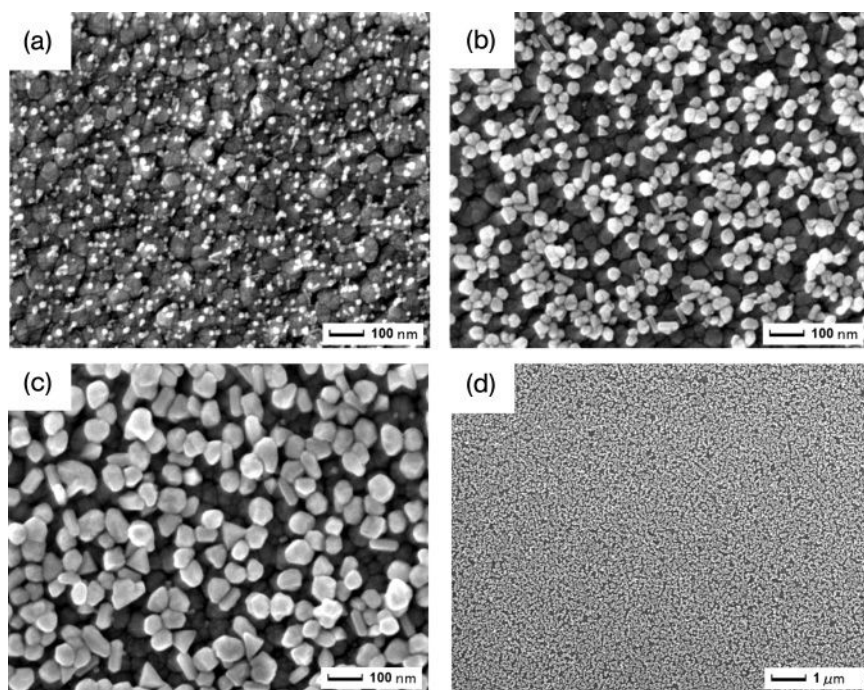
voltammograms of 0.5 mM methyl viologen in 0.1 M  $\text{Na}_2\text{SO}_4$  recorded using: (curve a) a bare ITO electrode; (curve b) a conventional Ag electrode; and (curve c) an AgNP/ITO electrode. Scan rate = 100  $\text{mV s}^{-1}$ . Reproduced with permission from Ref. [35]; © 2006, American Chemical Society.

(Figure 8.11b), in order to determine the native adsorption features of the fabricated AgNP/ITO electrodes [34].

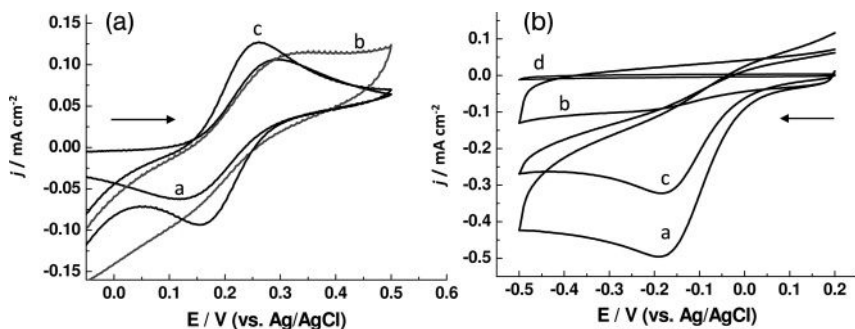
## 8.8

### Attachment and Growth of Palladium Nanoparticles PdNPs on ITO

Palladium nanoparticles (PdNPs) were also successfully attached and grown on ITO surfaces using the seed-mediated growth method [35]. The FE-SEM images recorded after treating the Pd nanoseed particle-attached ITO substrates in a growth solution for 4 and 12 h, respectively, are shown in Figures 8.12a and b. Crystal growth of PdNPs occurred as the immersion time in the growth solution was increased, with Pd nanocrystals of 60–80 nm being identified after 24 h (Figures 8.12c and d). The major characteristic of the formed nanostructure of Pd was that the nanocrystals tended to adhere to each other. Moreover, such aggregation occurred not only on the surface but was also 3-D in nature; that is, some nanocrystals were seen to grow above the basal nanocrystals. The nanostructure



**Figure 8.12** FE-SEM images of PdNP-attached ITO surfaces. The ITO substrates were immersed into the seed solution for 2 h and then into the growth solution for: (a) 4 h; (b) 12 h; and (c) 24 h; (d) A low-magnification image of the surface of panel (c). Reproduced with permission from Ref. [35]; © 2006, American Chemical Society.



**Figure 8.13** (a) Cyclic voltammograms of  $1.0\text{ mM } [\text{Fe}(\text{CN})_6]^{4-}$  in  $0.1\text{ M}$  phosphate-buffered solution ( $\text{pH } 7.0$ ) with: (curve a) a bare ITO electrode; (curve b) a bulk Pd electrode; and (curve c) a PdNP/ITO electrode prepared via 24 h growth. Scan rate =  $50\text{ mV s}^{-1}$ ; (b) Cyclic voltammograms recorded with: (curves a, b) the PdNP/ITO

electrode prepared via 24 h growth in (curve a) air-saturated and (curve b)  $\text{N}_2$ -saturated  $0.1\text{ M}$  KCl solutions, and with (curve c) a Pd bulk electrode and (curve d) a bare ITO electrode in air-saturated  $0.1\text{ M}$  KCl solution. Scan rate =  $50\text{ mV s}^{-1}$ . Reproduced with permission from Ref. [35]; © 2006, American Chemical Society.

of Pd grown on ITO was quite different from that of Au and Ag, mainly because the AuNPs and AgNPs tended to form in dispersed states (see above). Hence, the inference was that the identity of the metal changed the aggregation characteristics during the growth process, despite using CTAB as the same capping reagent in all growth procedures.

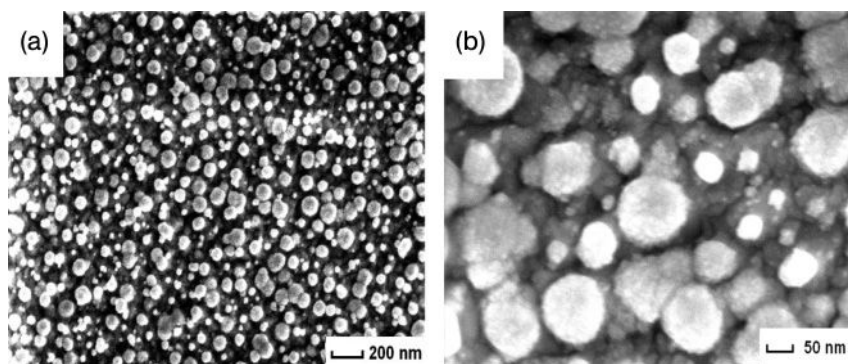
Due to the dense nanoparticle attachment (see Figure 8.12c), the PdNP/ITO electrodes had a significantly lowered charge transfer resistance compared to that of a bare ITO, and the redox reaction of  $[\text{Fe}(\text{CN})_6]^{3-}/[\text{Fe}(\text{CN})_6]^{4-}$  was observed to be reversible in  $0.1\text{ M}$  phosphate-buffered solution (Figure 8.13a) [35]. The electrocatalytic property of PdNPs attached on ITO was confirmed for the reduction of oxygen (Figure 8.13b). In addition, some typical responses were observed in  $0.5\text{ M}$   $\text{H}_2\text{SO}_4$  with the PdNP/ITO electrodes, reflecting both the characteristics of the NPs and the thin layer on a nanoscale [35]. The proposed preparation method for PdNP-attached ITO surfaces should be promising for catalytic applications, as well as electrochemical uses.

## 8.9

### Attachment of Platinum Nanoparticles PtNPs on ITO and GC

Although attempts were made to prepare platinum nanoparticles (PtNPs) on ITO surfaces using the seed-mediated growth method, some preliminary studies showed this approach to be difficult [36]. The problems were caused by the appearance of brown precipitates in the growth solution, despite using the same principle (i.e., the mixing of  $\text{K}_2\text{PtCl}_4$ , CTAB and ascorbic acid), before the seed-attached ITO was immersed.



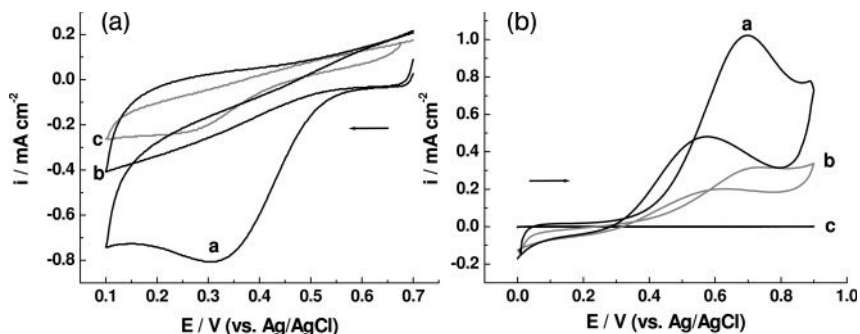


**Figure 8.14** FE-SEM images of PtNP-attached ITO surfaces. The ITO substrate was immersed in the growth solution containing 0.25 mM  $K_2PtCl_4$  and 5 mM ascorbic acid for 24 h. (a) Low-magnification and (b) high-magnification images of the same surface. Reproduced with permission from Ref. [36]; © 2006, American Chemical Society.

However, with further investigation the attachment of PtNPs on ITO was achieved by employing a rather simple method, namely a one-step *in situ* chemical reduction of  $PtCl_4^{2-}$  by ascorbic acid, but without using CTAB [36]. The FE-SEM images of the PtNP-attached ITO surfaces prepared via this *in situ* reduction method are shown in Figure 8.14. Here, the attached PtNPs were spherical and showed an agglomerated nanostructure which was composed of small nanoclusters. Based on the morphological changes which were dependent on the growth time, PtNPs were shown to grow via a progressive nucleation mechanism [36].

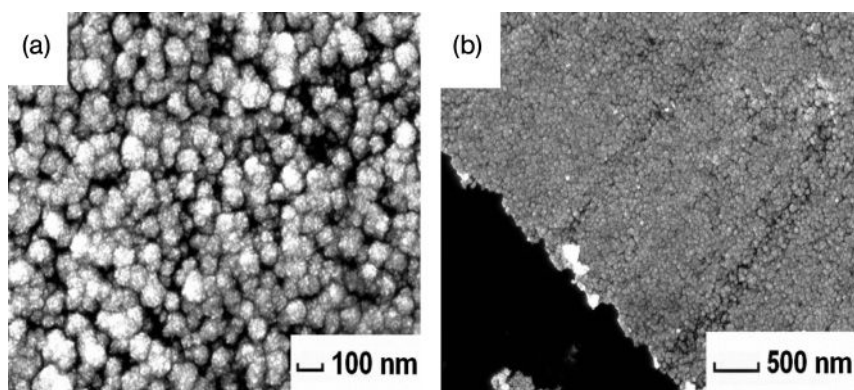
Characteristically, when PtNP/ITO was used as a working electrode, the charge transfer resistances were found to be significantly lowered due to the PtNP growth. Hence, for the typical redox system of  $[Fe(CN)_6]^{3-}/[Fe(CN)_6]^{4-}$ , the PtNP/ITO electrodes exhibited electrochemical responses which were similar to that of a bulk Pt electrode [36]. It was also apparent that the PtNP/ITO electrodes had significant electrocatalytic properties for oxygen reduction and methanol oxidation (see Figures 8.15a and b, respectively) [36]. Those PtNPs which demonstrated an agglomerated nanostructure should show promise as a new type of electrode material.

The *in situ* reduction method used to prepare PtNPs was also applied to the modification of GC surfaces. This resulted in a thin continuous Pt film which was composed of small nanoclusters that had a further agglomerated nanostructure of small grains, and could be attached onto the GC surface [37]. FE-SEM images of the Pt nanocluster film (PtNCF) are shown in Figure 8.16. The electrochemical results obtained indicated that the current values for Pt oxidation, Pt oxide reduction and hydrogen-related redox reactions, when recorded with the PtNCF electrode, were almost twice those with the Pt nanocluster dispersedly-attached GC (PtNC/GC) electrode, but this reflected the higher Pt loading (Figure 8.17a) [37]. The electrocatalytic ability of the PtNCF for methanol oxidation was also



**Figure 8.15** (a) Cyclic voltammograms recorded using (curves a, b) a PtNP/ITO electrode prepared via 24 h growth in: (curve a) air-saturated and (curve b)  $N_2$ -saturated  $0.5\text{ M H}_2\text{SO}_4$  solutions, and (curve c) a Pt bulk electrode for the air-saturated  $0.5\text{ M H}_2\text{SO}_4$  solution. Scan rate =  $50\text{ mV s}^{-1}$ ; (b) Cyclic voltammograms obtained for  $0.1\text{ M}$  methanol

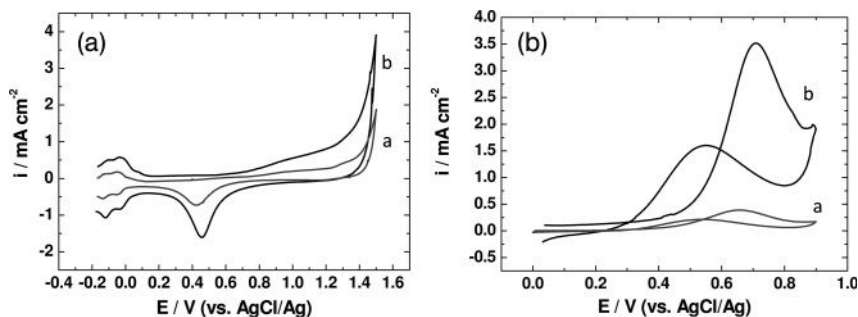
oxidation in the  $N_2$ -saturated  $0.5\text{ M H}_2\text{SO}_4$  solution recorded with: (curve a) the prepared PtNP/ITO electrode; (curve b) a Pt bulk electrode; and (curve c) a bare ITO electrode. Scan rate =  $50\text{ mV s}^{-1}$ . Reproduced with permission from Ref. [36]; © 2006, American Chemical Society.



**Figure 8.16** FE-SEM images of PtNCF attached on GC. The concentration of ascorbic acid for preparation was  $5.1\text{ mM}$ . (a) High-magnification and (b) low-magnification images. The left lower corner of (b) was scratched to show the film thickness. Reproduced with permission from Ref. [37]; © 2007, Elsevier.

apparently higher than that of the PtNC/GC or PtNP/ITO electrodes (Figure 8.17b). In addition, the electrocatalytic performance of PtNCF, when expressed in term of Pt content, was clearly superior to that of Pt black formed on GC [37].

Taken together these results indicated that, in spite of the continuous nanostructures, the nanograins of PtNCF functioned effectively for catalytic electrolysis. At present, PtNCF may be regarded as an interesting thin-film material, which can be easily prepared via a one-step chemical reduction.



**Figure 8.17** (a) Cyclic voltammograms recorded using (a) PtNC/GC and (b) PtNCF electrodes in a solution containing 0.5 M  $\text{H}_2\text{SO}_4$ . Scan rate =  $50 \text{ mV s}^{-1}$ ; (b) Cyclic voltammograms obtained for 1.0 M methanol oxidation in  $\text{N}_2$ -saturated 0.5 M  $\text{H}_2\text{SO}_4$  recorded using (a) PtNC/GC and (b) PtNCF electrodes. Scan rate =  $50 \text{ mV s}^{-1}$ . Reproduced with permission from Ref. [37]; © 2007, Elsevier.

## 8.10

### Electrochemical Measurements of Biomolecules Using AuNP/ITO Electrodes

It has been shown that the AuNP/ITO electrodes can be used for the electrochemical measurements of biomolecules and, in collaboration with Professor Goyal in India, we have acquired a host of data using our AuNP/ITO electrodes, albeit with a differential pulse voltammetry technique. Examples include the electrochemical analysis of uric acid [38], paracetamol (acetaminophen) [39], atenolol [40], nandrolone [41], methylprednisolone acetate [42], and salbutamol [43]. In addition, the simultaneous electrochemical determination of guanosine and guanosine 5'-triphosphate [44], adenosine and adenosine 5'-triphosphate [45], and dopamine and serotonin [46] have been successfully achieved with the AuNP/ITO electrodes.

Although the AuNP/ITO electrodes are not robust, and the modified surfaces are difficult to renew if damaged, Professor Goyal's group used the AuNP/ITO electrodes (which were sent from Japan) with great care and so obtained excellent results. Yet, this may in fact provide evidence of the practical strength of the AuNP/ITO electrodes prepared using the seed-mediated growth method.

## 8.11

### Nonlinear Optical Properties of Metal NP-Attached ITO

Beyond application as electrodes, the metal NP-attached ITO materials exhibit interesting nonlinear optical characteristics, and in order to investigate these properties we are presently collaborating with Professor Kityk in Poland and Professor Ebothé in France. To date, a variety of interesting nonlinear optical

properties of AuNPs [47–51] and AgNPs [52, 53], attached either on ITO or glass, have been reported. In addition, PdNPs [54, 55], PtNPs [54], and NiNPs [56] attached to ITO surfaces have also been investigated.

Because the seed-mediated growth technique includes a chemical reduction process in solution, the doping of second ions can be easily carried out. Consequently, the luminescence properties of not only the NPs of pure metals but also of erbium ion-doped AgNPs have been reported [57]. In addition, due to the universal applicability of the seed-mediated method, a ZnO film was modified with AuNPs and the nonlinear optical properties reported [58, 59].

In addition to the nonlinear optical properties of metal NPs, the modification of glasses with metal NPs has the potential for use as a new type of substrate for spectroscopic detection. As an example, AuNP-attached glass plates were described for use in surface plasmon resonance spectroscopy [60].

## 8.12

### Concluding Remarks

In this chapter, we have summarized the wet chemical preparation methods—notably seed-mediated growth—for fabricating various metal NP (or nanostructured crystal)-attached electrodes. It has been shown that small metal seed-NPs can be attached to the surfaces of substrates (typically ITO and GC, but also other materials) without the use of binding reagents, and the seed-NPs can then be grown via chemical reductions while retaining a strong attachment. The simplicity of the preparation method—that is, a two-step immersion first into the seed solution, and second into the growth solution (both of which are aqueous and at ambient temperature)—would be of significant merit in any proposed seed-mediated method for nanofabrication.

The thus-fabricated metal NP-attached electrodes have demonstrated interesting properties in terms of their electrochemical applications, which differ from those of bulk metals. The lower charge transfer resistances should represent a key advantage when constructing electrode materials with metal NPs. Consequently, nanocomposites consisting of metal NPs and base substrates, when prepared using the seed-mediated growth method, should be regarded as advanced-function materials, with potential applications also in nonlinear optics.

### References

- 1 Daniel, M.-C. and Astruc, D. (2004) *Chem. Rev.*, **104**, 293.
- 2 Hernández-Santos, D., González-García, M.B. and Costa-García, A. (2002) *Electroanalysis*, **14**, 1225.
- 3 Katz, E., Willner, I. and Wang, J. (2004) *Electroanalysis*, **16**, 19.
- 4 Welch, C.M. and Compton, R.G. (2006) *Anal. Bioanal. Chem.*, **384**, 601.
- 5 Finot, M.O., Braybrook, G.D. and McDermott, M.T. (1999) *J. Electroanal. Chem.*, **466**, 234.
- 6 El-Deab, M.S., Okajima, T. and Ohsaka, T. (2003) *J. Electrochem. Soc.*, **150**, A851.

- 7 Frens, G. (1973) *Nature*, **241**, 20.
- 8 Slot, J.W. and Geuze, H.J. (1985) *Eur. J. Cell Biol.*, **38**, 87.
- 9 Brust, M., Walker, M., Bethell, D., Schiffrin, D.J. and Whyman, R. (1994) *J. Chem. Soc., Chem. Commun.*, 802.
- 10 Freeman, R.G., Grabar, K.C., Allison, K.J., Bright, R.M., Davis, J.A., Guthrie, A.P., Hommer, M.B., Jackson, M.A., Smith, P.C., Walter, D.G. and Natan, M.J. (1995) *Science*, **267**, 1629.
- 11 Grabar, K.C., Freeman, R.G., Hommer, M.B. and Natan, M.J. (1995) *Anal. Chem.*, **67**, 735.
- 12 Chumanov, G., Sokolov, K., Gregory, B.W. and Cotton, T.M. (1995) *J. Phys. Chem.*, **99**, 9466.
- 13 Cheng, W., Dong, S. and Wang, E. (2002) *Anal. Chem.*, **74**, 3599.
- 14 Cheng, W., Dong, S. and Wang, E. (2002) *Langmuir*, **18**, 9952.
- 15 Jana, N.R., Gerheart, L. and Murphy, C.J. (2001) *J. Phys. Chem. B*, **105**, 4065.
- 16 Busbee, B.D., Obare, S. and Murphy, C.J. (2003) *Adv. Mater.*, **15**, 414.
- 17 Kambayashi, M., Zhang, J. and Oyama, M. (2005) *Cryst. Growth Des.*, **5**, 81.
- 18 Bönemann, H., Braun, G., Brijoux, W., Brinkmann, R., Schulze Tilling, A., Seevogel, K. and Siepen, K. (1996) *J. Organomet. Chem.*, **520**, 143.
- 19 Zhang, J., Kambayashi, M. and Oyama, M. (2004) *Electrochem. Commun.*, **6**, 683.
- 20 Zhang, J., Kambayashi, M. and Oyama, M. (2005) *Electroanalysis*, **17**, 408.
- 21 Zhang, J. and Oyama, M. (2004) *Electrochem. Acta*, **50**, 85.
- 22 Zhang, J. and Oyama, M. (2005) *J. Electroanal. Chem.*, **577**, 273.
- 23 Horibe, T., Zhang, J. and Oyama, M. (2007) *Electroanalysis*, **19**, 847.
- 24 Zhang, J. and Oyama, M. (2007) *Electrochem. Commun.*, **9**, 459.
- 25 Zhang, J. and Oyama, M. (2005) *Anal. Chim. Acta*, **540**, 299.
- 26 Ali Umar, A. and Oyama, M. (2005) *Cryst. Growth Des.*, **5**, 599.
- 27 Ali Umar, A. and Oyama, M. (2005) *Indian J. Chem. A*, **44**, 938.
- 28 Ali Umar, A. and Oyama, M. (2006) *Appl. Surf. Sci.*, **253**, 2196.
- 29 Ali Umar, A. and Oyama, M. (2006) *Appl. Surf. Sci.*, **253**, 2933.
- 30 Oyama, M., Yamaguchi, S. and Zhang, J. (2009) *Anal. Sci.*, **25**, 249.
- 31 Cui, Y., Yang, C., Zeng, W., Oyama, M., Pu, W. and Zhang, J. (2007) *Anal. Sci.*, **23**, 1421.
- 32 Zhang, J. and Oyama, M. (2005) *Electrochem. Solid-State Lett.*, **8**, E49.
- 33 Ali Umar, A. and Oyama, M. (2006) *Cryst. Growth Des.*, **6**, 818.
- 34 Chang, G., Zhang, J., Oyama, M. and Hirao, K. (2005) *J. Phys. Chem. B*, **109**, 1204.
- 35 Chang, G., Oyama, M. and Hirao, K. (2006) *J. Phys. Chem. B*, **110**, 20362.
- 36 Chang, G., Oyama, M. and Hirao, K. (2006) *J. Phys. Chem. B*, **110**, 1860.
- 37 Chang, G., Oyama, M. and Hirao, K. (2007) *Thin Solid Films*, **515**, 3311.
- 38 Goyal, R.N., Oyama, M., Sangal, A. and Singh, S.P. (2005) *Indian J. Chem. A*, **44**, 945.
- 39 Goyal, R.N., Gupta, V.K., Oyama, M. and Bachheti, N. (2005) *Electrochem. Commun.*, **7**, 803.
- 40 Goyal, R.N., Gupta, V.K., Oyama, M. and Bachheti, N. (2006) *Electrochem. Commun.*, **8**, 65.
- 41 Goyal, R.N., Oyama, M., Tyagi, A. and Singh, S.P. (2007) *Talanta*, **72**, 140.
- 42 Goyal, R.N., Oyama, M., Ali Umar, A., Tyagi, A. and Bachheti, N. (2007) *J. Pharm. Biomed. Anal.*, **44**, 1147.
- 43 Goyal, R.N., Oyama, M. and Singh, S.P. (2007) *J. Electroanal. Chem.*, **611**, 140.
- 44 Goyal, R.N., Oyama, M. and Tyagi, A. (2007) *Anal. Chim. Acta*, **581**, 32.
- 45 Goyal, R.N., Oyama, M. and Singh, S.P. (2007) *Electroanalysis*, **19**, 575.
- 46 Goyal, R.N., Gupta, V.K., Oyama, M. and Bachheti, N. (2007) *Talanta*, **72**, 976.
- 47 Kityk, I.V., Ali Umar, A. and Oyama, M. (2005) *Physica E*, **27**, 420.
- 48 Kityk, I.V., Ali Umar, A. and Oyama, M. (2005) *Physica E*, **28**, 178.
- 49 Kityk, I.V., Ebothé, J., Fuks-Janczarek, I., Ali Umar, A., Kobayashi, K., Oyama, M. and Sahraoui, B. (2005) *Nanotechnology*, **16**, 1687.
- 50 Kityk, I.V., Plucinski, K.J., Ebothé, J., Ali Umar, A. and Oyama, M. (2005) *J. Appl. Phys.*, **98**, 084304.
- 51 Kityk, I.V., Ali Umar, A. and Oyama, M. (2005) *Appl. Opt.*, **44**, 6905.

- 52 Kityk, I.V., Ebothé, J., Chang, G. and Oyama, M. (2005) *Phil. Mag. Lett.*, **85**, 549.
- 53 Kityk, I.V., Ebothé, J., Ozgac, K., Plucinski, K.J., Chang, G., Kobayashi, K. and Oyama, M. (2006) *Physica E*, **31**, 38.
- 54 Ebothé, J., Kityk, I.V., Chang, G., Oyama, M. and Plucinski, K.J. (2006) *Physica E*, **35**, 121.
- 55 Ebothé, J., Kityk, I.V., Nzoghe-Mendon, L., Chang, G., Oyama, M., Sahraoui, B. and Miedzinski, R. (2008) *J. Mod. Opt.*, **55**, 187.
- 56 Zamorskii, M.K., Nouneh, K., Kobayashi, K., Oyama, M., Ebothé, J. and Reshak, A.H. (2008) *Opt. Laser Technol.*, **40**, 499.
- 57 Ebothé, J., Ozga, K., Ali Umar, A., Oyama, M. and Kityk, I.V. (2006) *Appl. Surf. Sci.*, **253**, 1626.
- 58 Ozga, K., Kawaharamura, T., Ali Umar, A., Oyama, M., Nouneh, K., Slezak, A., Fujita, S., Piasecki, M., Reshak, A.H. and Kityk, I.V. (2008) *Nanotechnology*, **19**, 18709.
- 59 Ozga, K., Kawaharamura, T., Ali Umar, A., Oyama, M., Slezak, A., Fujita, S. and Kityk, I. (2008) *J. Nano Res.*, **2**, 31.
- 60 Hamamoto, K., Micheletto, R., Oyama, M., Ali Umar, A., Kawai, S. and Kawakami, Y. (2006) *J. Opt. A Pure Appl. Opt.*, **8**, 268.

## 9

**Mesoscale Radical Polymers: Bottom-Up Fabrication of Electrodes in Organic Polymer Batteries***Kenichi Oyaizu and Hiroyuki Nishide*

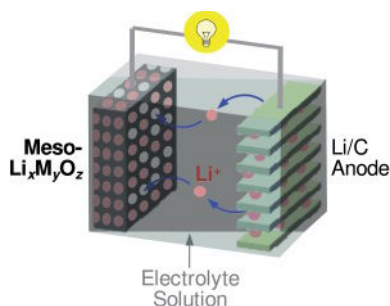
## 9.1

**Mesostructured Materials for Energy Storage Devices**

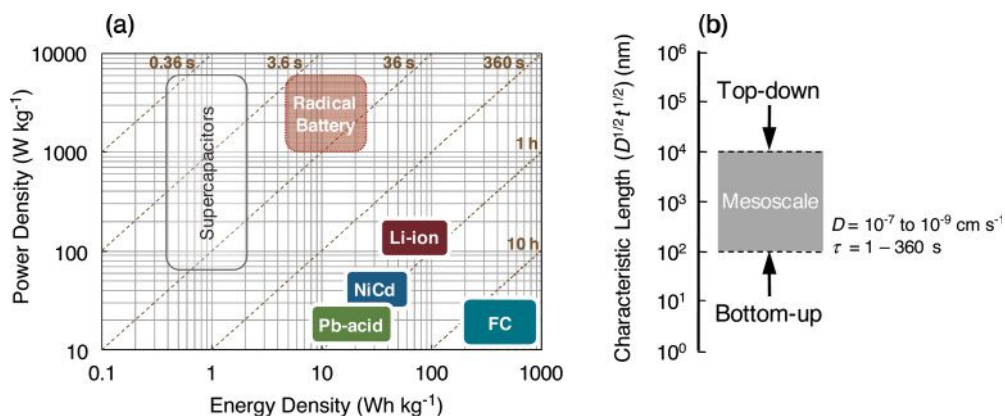
Energy storage is one of the most important worldwide concerns of the twenty-first century, and it is essential that new, low-cost, and environmentally benign (i.e., sustainable) materials for energy conversion and storage purposes are found [1, 2]. Energy-related nanostructured materials have attracted much attention because of the unusual electrical properties that originate from their confined nanoscale dimensions and combined bulk/interfacial properties, which affect their overall behavior [3]. On the other hand, a new trend in materials research has begun to emerge recently, focusing on the fabrication of mesoscale structures [4], which is a broader term (or superordinate concept) of the ordered fine structures, characterized by dimensions larger than those in nanomaterials that typically consist of nanoparticles and top-down nanoarchitected structures. The exploration of properties of materials on the mesoscale has led to new technological perspectives of electrochemical devices such as batteries and sensors, which rely on ion transport and, thus, are strongly influenced by the size effects of composing materials on mass transfer, transport, and storage. In particular, mesoscale materials are becoming increasingly important for electrochemical energy storage applications, due to the limited distance of diffusion for the mass transfer during charging/discharging processes. A typical example is that of lithium-ion batteries, which consist of a Li-ion intercalating anode (e.g., graphite) and a cathode (e.g.,  $\text{LiCoO}_2$ ), separated by Li-ion-conducting electrolyte layers such as a solution of  $\text{LiPF}_6$  in an ethylene carbonate/diethylcarbonate (EC/DEC) mixture (Figure 9.1) [5].

The advantages of ordered mesostructures for these electrode-active materials are the improved accommodation of the lattice transformation resulting from the  $\text{Li}^+$  intercalation/deintercalation to improve cycle life, the increased electrode/electrolyte contact area leading to higher charging/discharging rates, and—most importantly—the short path length for electronic and ionic transport which permit operation with low electric conductivity and hence at high power [6].





**Figure 9.1** Li-ion battery using mesoscale lithium metal oxide cathodes for an improved rate performance.



**Figure 9.2** (a) Ragone plot for batteries, fuel cells, and supercapacitors. The dashed lines represent the time parameter,  $\tau$ , which is characteristic of the rate performance; (b) Characteristic length of electrode-active materials defined as the layer thickness of

diffusing ions and/or propagating charges during the charging/discharging process, showing the top-down and bottom-up strategies to fabricate the target mesoscale materials.

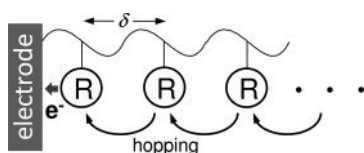
Ragone plots (Figure 9.2a) of specific power density versus specific energy density for various batteries, displayed with those of fuel cells and supercapacitors as references, show their specific time parameter,  $\tau$ , that characterizes the period of time required for charging/discharging operations [2]. The diffusion length  $(D\tau)^{1/2}$  of ions and propagating charges within the electrode-active materials corresponds to their characteristic dimensional scales, where  $D$  is the diffusion coefficient for the mass transfer processes. For cathode-active materials in Li-ion batteries, the lithium cobalt oxide ( $\text{LiCoO}_2$ ) is characterized by a relatively large diffusion coefficient of  $D = 10^{-7}$  to  $10^{-9} \text{ cm}^2 \text{ s}^{-1}$  [7], but the recently investigated less expensive and/or less toxic oxides show lower diffusivities for the  $\text{Li}^+$  ion, such as those in  $\text{Li}_{1-x}\text{Ni}_{0.5}\text{Mn}_{0.5-x}\text{Ti}_x\text{O}_2$  ( $x = 0-0.3$ ,  $D = 10^{-9}$  to  $10^{-14} \text{ cm}^2 \text{ s}^{-1}$ ) [8],  $\text{Li}_7\text{BiO}_6$  ( $D = 5 \times 10^{-13} \text{ cm}^2 \text{ s}^{-1}$ ) [9],  $\text{LiFePO}_4$  ( $D = 1.8 \times 10^{-14} \text{ cm}^2 \text{ s}^{-1}$ ) [10], and  $\text{LiV}_3\text{O}_8$  ( $D = 2-8 \times 10^{-10} \text{ cm}^2 \text{ s}^{-1}$ ) [11]. The resulting dimensional scale, or the

characteristic length, is typically in the order of  $10^2 < (D\tau)^{1/2} < 10^4$  nm, thus revealing the importance of fabricating mesostructured materials (Figure 9.2b), which are in-between nanoscopic and macroscopic materials in dimension.

Fabrication of the mesostructured oxides has been accomplished by using top-down methods, although mesoscale cathodes are less developed than the mesostructured anodes. For example, a similar approach to the formation of silicon nanopillars has been applied for cathode-active materials. By using suitable templates such as porous alumina and porous polymeric materials, nanopillars of  $V_2O_5$  and  $LiMn_2O_4$  have been successfully grown on metal substrates as the current collectors [6]. The mesostructured materials have additional advantages over the conventional electrode-active materials, to accommodate relatively large volumetric changes during charging/discharging cycles, thus improving the overall power-rate performance of the resulting batteries.

Organic molecule-based electrode-active materials are more advantageous than inorganic materials in terms of their potential capability for the molecule-based “bottom-up” fabrication of mesostructures (Figure 9.2b), in addition to their inherent flexibility, safety, and accessibility from unlimited resources [12]. The organic polymers most typically examined for batteries are conducting polymers such as polyacetylene, polyaniline, polypyrrole, polythiophene, and polyphenylene [13–17]. Sulfur and redox polymerization electrodes have also been reported as electroactive materials [13]. However, the low doping levels in conducting polymers result in a small theoretical capacity. Moreover, the charging/discharging processes have often been impeded by the slow kinetics of electrode reactions [13]. Another group of molecules investigated for charge storage is a series of redox polymers with nonconjugated backbones and redox centers localized in pendant groups, such as tetrathiafulvalene [18], ferrocene [19, 20], and carbazole [21, 22]. In this case, the redox centers, rather than the polymer backbones, govern the redox behaviors. Conductivity arises when these redox centers can exchange charge, through for example electron hopping between the redox isolated sites within the polymers (Figure 9.3).

It has been found recently that organic robust radicals are potentially useful as the redox centers due to their rapid one-electron-redox reactions [23, 24]. Moreover, excellent film-forming properties of the organic radical polymers by simple wet processes allow various mesoscale fabrication such as homogeneous layers with precisely controlled thicknesses and ordered mesostructures supported on carbon fiber matrices. This aim of this chapter is to provide a concise overview of recent



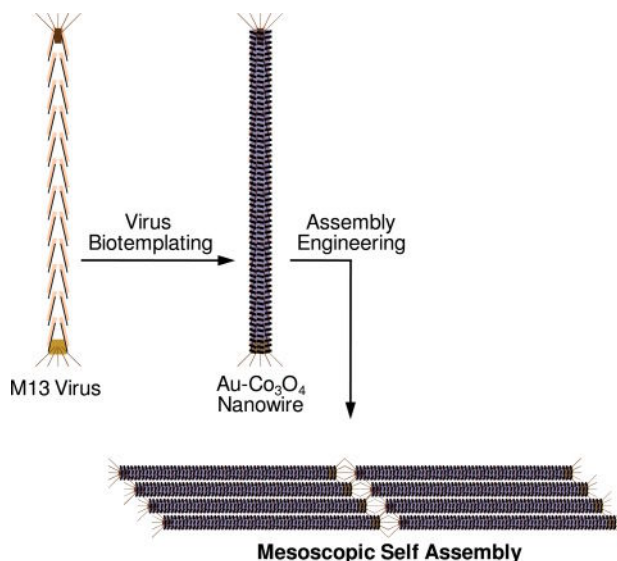
**Figure 9.3** Charge propagation within redox polymer layers, swollen in electrolyte solutions, by an electron self-exchange (hopping) mechanism.

approaches to fabricate mesoscale electrode-active materials, with emphasis placed on the organic polymers for the radical polymer battery [25], which is characterized by an excellent rate performance and capability of fabricating flexible, paper-like, and (semi)transparent rechargeable energy-storage devices.

## 9.2

### Mesoscale Fabrication of Inorganic Electrode-Active Materials

The top-down fabrication of inorganic electrode-active materials has been motivated by the possibility of producing a film-like, bendable lithium-ion battery, which depends in turn on the development of soft electrode-active materials such as those composed of nanoparticles and nanocoatings of metal oxides for the cathodes, and lithium foil or nanocarbon materials for the anodes [1, 26]. The top-down fabrication has also been driven by the recent challenge to maximize transport rates by employing mesostructured inorganic-based materials. The electrode reaction of inorganic-based materials is often rate-determined by the slow kinetics of ion intercalation and migration that accompany lattice transformation [6]. The power-rate properties have been improved by employing the top-down strategy so as to produce a large surface area and suitable path length for the mass transfer processes [27]. Recent interesting approaches have included the virus-enabled synthesis and assembly of cobalt oxide nanowires (Figure 9.4). This has been accomplished by incorporating gold-binding peptides into a filament coat to



**Figure 9.4** Virus-enabled synthesis of Au-Co<sub>3</sub>O<sub>4</sub> nanowire and self-assembly strategy to form an ordered monolayer of Co<sub>3</sub>O<sub>4</sub> nanowires [28].

form mesoscale gold–cobalt oxide hybrid wires that improve battery capacity as a new cathode-active material [28]. Indeed, engineered electrode mesostructures to enhance electrode kinetics have been a target of intense research, including those based on the electrochemically assisted template growth of Cu nanorods onto a current collector, followed by electrochemical plating of  $\text{Fe}_3\text{O}_4$  to form the ordered structure at a mesoscale level [27]. The significant effect of the mesoscopic size on transport rates and flexibility has been demonstrated recently by Li-ion batteries made from nanocomposite papers [26, 29]. These are obtained by infiltrating cellulose into carbon nanotubes (CNTs) grown on a silicon substrate and impregnated with the electrolyte, allowing the combination of the cathode (the nanotubes) and the separator (the cellulose) in a single unit [26].

### 9.3

#### Bottom-Up Strategy for Organic Electrode Fabrication

##### 9.3.1

##### Conjugated Polymers for Electrode-Active Materials

Research into organic electrode-active materials was prompted by the discovery of the electric conductivity of doped polyacetylene, which in turn led to the exploration of organic batteries by employing the redox capacity of polyacetylene. This was based on the reversible *p*-type and *n*-type doping/de-doping processes for the cathode and the anode, respectively, as the principal electrode reactions [30]. Electrically conducting polymers such as polyaniline, polypyrrole, polythiophene, and their related derivatives, have been similarly examined as electrode-active materials, based on their reversible electrochemical doping behaviors. The limitations of conducting polymers are based on their insufficient doping levels, the resulting low redox capacities, and the chemical instability of the doped states that frequently lead to the self-discharge and degradation of the rechargeable properties of the resulting batteries.

Another concept of using conjugated polymers for batteries is to explore a charge–storage configuration in which the electrolyte layer is sandwiched by thin layers of even less conductive polymers incorporating redox-active groups, with a view to increasing the overall redox capacity. In this case, the polymer backbones provide a matrix and/or a conducting path to interconnect innumerable redox sites for the hopping of electrons by a self-exchange mechanism, and this results in the storage and transport of charge in a homogeneous solid. Along with this concept, polythiophene-based conjugated polymers bearing redox sites such as tetrathiafulvalene derivatives [31] and polypyrrole coupled with redox-active dopants such as indigo carmine derivatives [32–35], have been recently designed. However, the chemical bond cleavage and the formation that are often accompanied by the redox reaction of these closed-shell molecules are frequently electrochemically irreversible or nonreversible, and hence are unfavorable for application as electrode-active materials. Simple methods to fabricate mesostructures by the bottom-up strategies

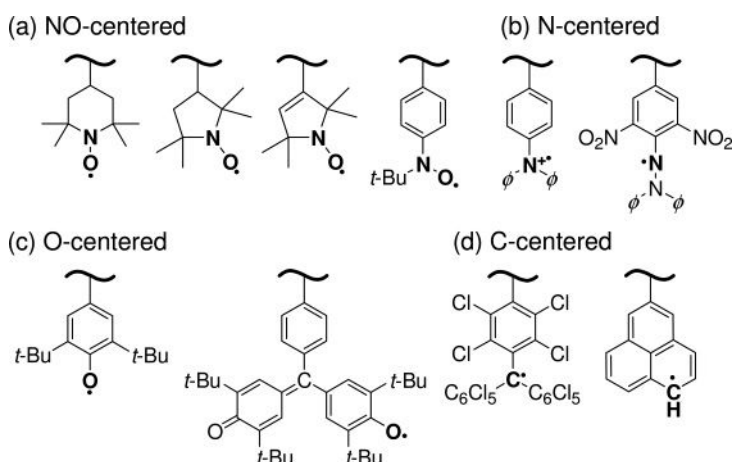
have been also awaited, in order to bring out the performance of the organic polymers.

### 9.3.2

#### Mesoscale Organic Radical Polymer Electrodes

A new concept, applicable to the mesostructure fabrication, has been proposed for the organic electrode-active materials, based on the sufficiently large redox capacity of aliphatic redox polymers—that is, organic polymers densely populated with pendant redox-isolated sites. The principal finding to permit the use of the non-conjugated redox polymers is the capability of organic robust radicals, or open-shell molecules, to allow fully reversible, one-electron redox reactions featuring fast electrode kinetics and reactant recyclability. While the chemically inert organic radicals constitute an important and extensively studied group of functional materials, such as organic ferromagnets [36–39], metal-free redox mediators for synthetic applications [40–44], and electron and hole transport materials for organic devices [45, 46], the idea of using them as electroactive materials for rechargeable batteries has never been proposed, except in our recent reports [47–52] and those from other groups [53–64]. Hence, we have focused on organic radicals stabilized thermodynamically by an effective delocalization of the unpaired electron and/or kinetically by bulky substituents to employ them as the redox centers. Radical groups such as the NO-centered nitroxides, N-centered triarylaminium cation radicals, and diphenylpicrylhydrazyl derivatives, O-centered phenoxyls and galvinoxyls, and C-centered trityls and phenalenyls, are typically examined as the pendant group of the radical polymers (Scheme 9.1).

These radicals are persistent at ambient temperatures under air and are characterized by a rapid and reversible one-electron-electrode reactions, typically with heterogeneous electron-transfer rate constants of  $k_0 = 10^{-1} \text{ cm s}^{-1}$  in the



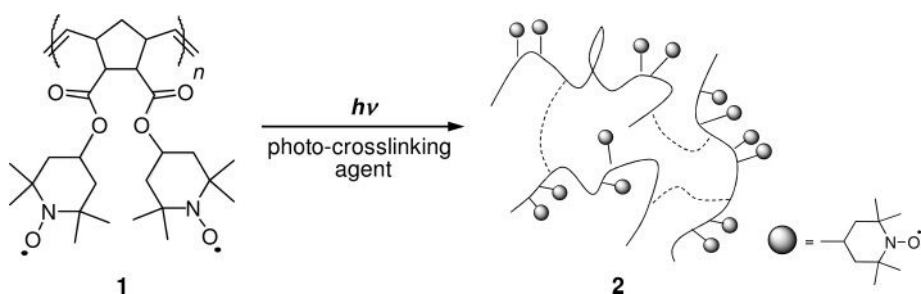
**Scheme 9.1** Chemical structures of organic robust radicals in the radical polymers.

case of 2,2,6,6-tetramethylpiperidine-1-oxyl (TEMPO) derivatives [23, 24]. A variety of polymer backbones have been employed to bind the radicals, such as poly(methacrylate)s, polystyrene derivatives, poly(vinyl ether)s, polyethers, and poly(norbornene)s. The unpaired electron density of the polymers, as determined by superconducting quantum interference device (SQUID) measurements, has revealed the presence of radicals substantially per repeating unit. Theoretical redox capacities based on the formula mass of the repeating unit are in the range of 50 to 150 mAh g<sup>-1</sup>.

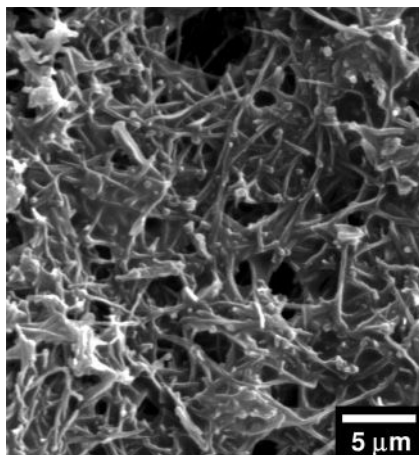
For mesoscale electrode fabrication, the radical polymers are conveniently placed on the surface of an electrode or a current collector by a solution-based wet process such as the spin-coating method. The contact stylus profile near a scratched edge provides a layer thickness under dry conditions in the range of 10 to 10<sup>3</sup> nm, according to the concentration of the polymer in the mother liquor and the spinning velocity, and has revealed a flat surface with a roughness of less than several nanometers. The polymer backbones are suitably modified by photocrosslinking, for example, thus, to be swollen but not to be dissolved in the electrolyte solutions, as typically shown for the TEMPO-substituted polynorbornene **1** in Scheme 9.2 [47].

The capability of forming stable films by the crosslinking method has allowed a novel design of a mesostructure fabrication processes, in which the polymer is coated on the surface of conducting mesoscale matrices as the support. The scanning electron microscopy (SEM) image of the resulting electrode surface, prepared on a Au quartz crystal microbalance (QCM) assembly for simultaneous electrochemical and resonant frequency-based gravimetric analysis (*vide infra*), demonstrates the ordered three-dimensional (3-D) structure successfully fabricated on the mesoscale (Figure 9.5) and which is suitable for ion transport throughout the polymer layer.

The unpaired electron density of the radical polymers amounts to a number of several molar in the bulk of the swollen polymer equilibrated in electrolyte



**Scheme 9.2** Photo-crosslinking of the TEMPO-substituted polynorbornene **1** to form a polymer layer of **2**, which is insoluble but swellable in electrolyte solutions. The spin density by SQUID measurements amounts to 10<sup>21</sup> spin per gram of **2**, indicating that most of the radicals survive during the photo-crosslinking reaction.

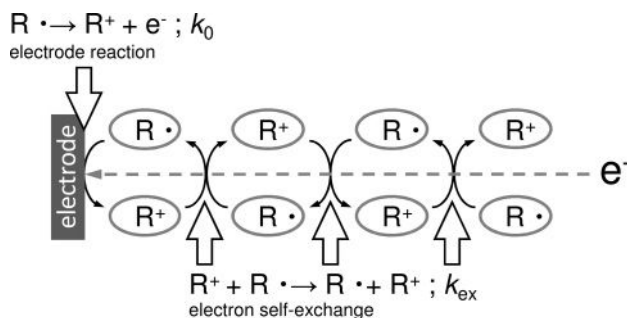


**Figure 9.5** Scanning electron microscopy image of the photo-crosslinked polymer **2**/carbon composite electrode coated on the surface of a QCM electrode assembly.

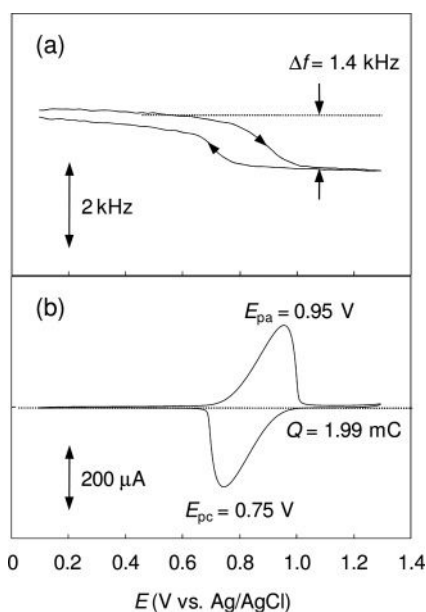
solutions. Under these conditions, charge propagation within the polymer layer is sufficiently fast, leading to high-density charge storage, because the redox sites are so populated that the electron self-exchange reaction goes to completion within a finite distance of the polymer layer attached to the carbon fiber. The concentration gradient-driven charge propagation is accomplished by the electron self-exchange reaction. The apparent diffusion coefficient,  $D$ , of the charge produced at the surface of the electrode is determined by the bimolecular rate constant,  $k_{\text{ex}}$ , for the self-exchange reaction. Thus, when the sites are immobilized in the layer, allowing only diffusional collision of the neighboring sites to undergo an electron self-exchange reaction, this process involves an electron-hopping mechanism with a diffusion coefficient formulated by  $D = k_{\text{ex}}\delta^2 C^*/6$ , where  $k_{\text{ex}}$  is the bimolecular rate constant,  $\delta$  is the site distance, and  $C^*$  is the site concentration in the polymer layer [65, 66]. The electron self-exchange reaction is sufficiently fast for diffusion-limited outer-sphere redox reactions, resulting in the efficient transfer of charge produced at the surface of the electrode (Figure 9.6).

The electrochemical behavior of the radical polymer layers attached to an electrode have revealed an efficient charge propagation process with diffusion coefficients in the order of  $10^{-8}$  to  $10^{-10}$   $\text{cm}^2 \text{s}^{-1}$ . The electrolytes examined are typically tetrabutylammonium or the lithium salts of perchlorate or hexafluorophosphate, dissolved in conventional organic solvents such as  $\text{CH}_3\text{CN}$  and propylene carbonate. The cyclic voltammogram obtained for the electrode (as in Figure 9.5), with a sufficient crosslinking density of 11%, persists without change for several days of continued charging/discharging cycling in  $\text{CH}_3\text{CN}$ , in which the layer appears completely insoluble (Figure 9.7). Wave shapes with a peak-to-peak separation of  $\Delta E_p = \text{ca. } 200 \text{ mV}$  suggest some contribution from diffusion across the thick layer (Figure 9.7b). In the QCM response, the resonant frequency decreases during the





**Figure 9.6** Electrode and chemical reactions related to the charge transfer in radical redox polymers.



**Figure 9.7** (a) QCM response and (b) cyclic voltammogram obtained for the photocrosslinked polymer **2**/carbon composite electrode coated on the surface of a QCM electrode assembly. The Au electrode surface area A was 0.196 cm<sup>2</sup>. The content of **2** in the

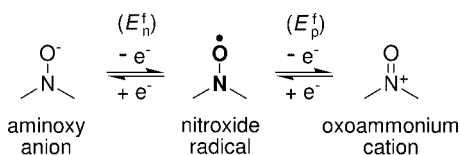
composite electrode was 10 wt%. The crosslinking density was 11%. The electrolyte was a solution of 0.1 mol l<sup>-1</sup> tetrabutylammonium hexafluorophosphate in CH<sub>3</sub>CN. Scan rate = 20 mV s<sup>-1</sup>.

oxidation and attains its original value after the reduction, indicating reversibility to the mass change (Figure 9.7a). The galvanostatic  $E-t$  curves show a plateau region, which agrees with the formal potential. The amount of charge consumed during the potential scan and the constant-current electrolysis both coincide well with the formula weight-based redox capacity, which reveal that almost all of the sites in the layer undergo the redox reaction.

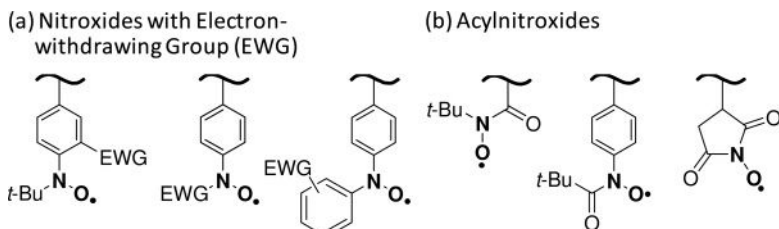
The redox process of the polymer layer is accompanied by the rapid injection and rejection of solvated counterions that compensate the charges produced by the redox reaction. Electroneutrality requires that the removal of each electron from the polymer layer results in the insertion of one electrolyte anion into the layer and/or the Donnan exclusion of the electrolyte cation. The mass change,  $\Delta m$ , associated with the redox reaction is obtained from the resonant frequency change  $\Delta f$  in Figure 9.7a using the Sauerbrey equation ( $\Delta f = -C_f \Delta m$ ), where the sensitive factor  $C_f$  is  $0.183 \text{ Hz cm}^2 \text{ ng}^{-1}$  for the QCM assembly employed in this study. The redox capacity  $Q$  is determined from the area under the waves in Figure 9.7b. The mass change relative to the redox capacity ( $\Delta m F / Q \sim 71 \text{ g mol}^{-1}$ ) is smaller than the formula mass of the  $\text{PF}_6^-$  anion, indicating the slight contribution from the nonpermselective incorporation of the electrolyte cation during the mass transfer process.

Nitroxide radicals are potentially reducible to aminoxy anions by a one-electron-transfer process, which corresponds to the  $n$ -type doping of the neutral radical polymer (Scheme 9.3).

Attempts have been made to synthesize the  $n$ -dopable polymers and to use them as the anode-active material, with a view to employing only nitroxide radicals at both electrodes [48]. It has been demonstrated that suitable electron-withdrawing groups (EWG)s such as trifluoromethyl and cyano substituents, bound proximally to the NO redox center (Scheme 9.4a), shift the  $n$ -doping potential positively up to approximately  $-0.8 \text{ V}$ . Acylnitroxides (Scheme 9.4b) are also potentially useful as the anode material. The nitroxide radical polymer can thus be switched from the  $p$ -type material for use in cathodes to the  $n$ -type anode-active material, by tuning the substituent effect.



**Scheme 9.3** Redox couples related to nitroxide radicals.



**Scheme 9.4**  $n$ -Type nitroxide polymers.

The radical polymers act as both cathode- and anode-active materials, because of their capability to tune the redox potentials by the bottom-up strategy based on the molecular design. A couple of polymers, different in redox potentials, are used as the electroactive materials in the organic radical battery. The charging process corresponds to the oxidation of the radical to the cation at the cathode, and the reduction of the radical to the anion at the anode (Figure 9.8). The electromotive force is close to the potential gap between the two redox couples, which typically amounts to 0.5–1.5 V. The radical polymers are reversibly converted to the corresponding polyelectrolytes during the charging process. The rapid electrode reaction of the radicals and the efficient charge propagation within the polymer layer lead to a high rate performance, allowing rapid charging and large discharge currents without any substantial loss of output voltage. The amorphous radical polymers also allow the fabrication of flexible, thin-film devices. A curious feature is the capability of forming a “see-through” battery, due to the absence of significant chromophores in the radical polymer. Here, use could also be made of the slight color changes accompanied by radical redox reactions as an indicator of the charging level.

Efforts have also been directed towards further increasing the theoretical redox capacity of the radical polymer. For this purpose, radical polymers with even smaller formula masses per repeating unit have been designed (Scheme 9.5). The dinitroxide-functionalized polystyrene in Scheme 9.5 with a theoretical capacity of  $193 \text{ mAh g}^{-1}$  has been typically characterized by a notably high radical density of  $4.3 \times 10^{21}$  unpaired electrons per gram, which leads to the high capacity charging/discharging characteristics of the polymer membrane.

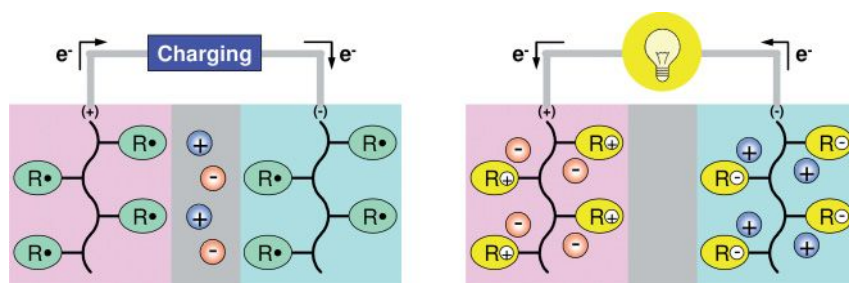
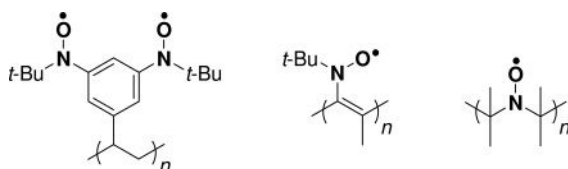


Figure 9.8 Charging (left) and discharging (right) processes of the organic radical battery.



Scheme 9.5 Typical radical polymers designed for high redox capacity.

## 9.4

## Conclusions

Radical polymers have been identified as a new class of redox polymers, which are characterized by a fast kinetics of electrode reactions. The suitably designed polymer backbone allows efficient swelling in conventional electrolyte solutions, which in turn enables an efficient charge propagation by a site-hopping mechanism within the mesostructured polymer layer. The use of radical polymers as electroactive materials leads to the first fabrication of organic electrode-active materials ordered in a mesoscale. The organic radical batteries have several advantages over the Li-ion batteries, such as higher safety, adaptability to wet fabrication processes, easy disposability, and capability of fabrication from less-limited resources. While organic batteries have an intrinsically lower volumetric energy density, this limitation can surely be overcome in the near future so that they can be designed to be compatible with, and installable in, a wide variety of electronic equipment.

## References

- 1 Tarascon, J.-M. and Armand, M. (2001) *Nature*, **414**, 359–367.
- 2 Service, R.F. (2006) *Science*, **313**, 902.
- 3 Maier, J. (2005) *Nat. Mater.*, **4**, 805–14.
- 4 Yamauchi, Y., Takai, A., Nagaura, T., Inoue, S. and Kuroda, K. (2008) *J. Am. Chem. Soc.*, **130**, 5426–5427.
- 5 Alper, J. (2002) *Science*, **296**, 1224–1226.
- 6 Aricò, A.S., Bruce, P., Scrosati, B., Tarascon, J.-M. and van Schalkwijk, W. (2005) *Nat. Mater.*, **4**, 366–367.
- 7 Manthiram, A. and Kim, J. (1998) *Chem. Mater.*, **10**, 2895–2909.
- 8 Myung, S.-T., Komaba, S., Hosoya, K., Hirosaki, N., Miura, Y. and Kumagai, N. (2005) *Chem. Mater.*, **17**, 2427–2435.
- 9 Wilkening, M., Mühle, C., Jansen, M. and Heitjans, P. (2007) *J. Phys. Chem. B*, **111**, 8691–8694.
- 10 Zhang, P., Wu, Y., Zhang, D., Xu, Q., Liu, J., Ren, X., Luo, Z., Wang, M. and Hong, W. (2008) *J. Phys. Chem. A*, **112**, 5406–5410.
- 11 Yang, G., Wang, G. and Hou, W. (2005) *J. Phys. Chem. B*, **109**, 11186–11196.
- 12 Nishide, H. and Oyaizu, K. (2008) *Science*, **319**, 737–738.
- 13 Novák, P., Müller, K., Santhanam, K.S.V. and Haas, O. (1997) *Chem. Rev.*, **97**, 207–281.
- 14 Coppo, P. and Turner, M.L. (2005) *J. Mater. Chem.*, **15**, 1123–1133.
- 15 Roncali, J., Blanchard, P. and Frère, P. (2005) *J. Mater. Chem.*, **15**, 1589–1610.
- 16 Roncali, J. (1997) *J. Mater. Chem.*, **7**, 2307–2321.
- 17 Roncali, J. (1997) *Chem. Rev.*, **97**, 173–205.
- 18 Kaufman, F.B., Schroeder, A.H., Engler, E.M., Kramer, S.R. and Chambers, J.Q. (1980) *J. Am. Chem. Soc.*, **102**, 483–488.
- 19 Iwakura, C., Kawai, T., Nojima, M. and Yoneyama, H. (1987) *J. Electrochem. Soc.*, **134**, 791–795.
- 20 Hunter, T.B., Tyler, P.S., Smyrl, W.H. and White, H.S. (1987) *J. Electrochem. Soc.*, **134**, 2198–2204.
- 21 Compton, R.G., Davis, F.J. and Grant, S.C. (1986) *J. Appl. Electrochem.*, **16**, 239–249.
- 22 Skompska, M. and Peter, L.M. (1995) *J. Electroanal. Chem.*, **383**, 43–52.
- 23 Yonekuta, Y., Oyaizu, K. and Nishide, H. (2007) *Chem. Lett.*, **36**, 866–867.
- 24 Suga, T., Pu, Y.-J., Oyaizu, K. and Nishide, H. (2004) *Bull. Chem. Soc. Jpn.*, **77**, 2203–2204.
- 25 Nishide, H. and Suga, T. (2005) *Electrochem. Soc. Interface*, **14**, 32–36.

- 26 Scrosati, B. (2007) *Nat. Nanotechnol.*, **2**, 598–599.
- 27 Taberna, P.L., Mitra, S., Poizot, P., Simon, P. and Tarascon, J.-M. (2006) *Nat. Mater.*, **5**, 567–573.
- 28 Nam, K.T., Kim, D.-W., Yoo, P.J., Chiang, C.-Y., Meethong, N., Hammond, P.T., Chiang, Y.-M. and Belcher, A.M. (2006) *Science*, **312**, 885–888.
- 29 Pushparaj, V.L., Shaijumon, M.M., Kumar, A., Murugesan, S., Ci, L., Vajtai, R., Linhardt, R.J., Nalamasu, O. and Ajayan, P.M. (2007) *Proc. Natl Acad. Sci. USA*, **104**, 13574–13577.
- 30 Nigrey, P.J., MacDiarmid, A.G. and Heeger, A.J. (1979) *J. Chem. Soc., Chem. Commun.*, 594–595.
- 31 Berridge, R., Skabara, P.J., Pozo-Gonzalo, C., Kanibolotsky, A., Lohr, J., McDouall, J.J.W., McInnes, E.J.L., Wolowska, J., Winder, C., Sariciftci, N.S., Harrington, R.W. and Clegg, W. (2006) *J. Phys. Chem. B*, **110**, 3140–3152.
- 32 Song, H.-K. and Palmore, G.T.R. (2006) *Adv. Mater.*, **18**, 1764–1768.
- 33 Song, H.-K. and Palmore, G.T.R. (2005) *J. Phys. Chem. B*, **109**, 19278–19287.
- 34 Fei, J., Song, H.-K. and Palmore, G.T.R. (2007) *Chem. Mater.*, **19**, 1565–1570.
- 35 Song, H.-K., Toste, B., Ahmann, K., Hoffman-Kim, D. and Palmore, G.T.R. (2006) *Biomaterials*, **27**, 473–484.
- 36 Murata, H., Miyajima, D. and Nishide, H. (2006) *Macromolecules*, **39**, 6331–6335.
- 37 Fukuzaki, E. and Nishide, H. (2006) *Org. Lett.*, **8**, 1835–1838.
- 38 Kaneko, T., Makino, T., Miyaji, H., Teraguchi, M., Aoki, T., Miyasaka, M. and Nishide, H. (2003) *J. Am. Chem. Soc.*, **125**, 3554–3557.
- 39 Nishide, H., Kaneko, T., Nii, T., Katoh, K., Tsuchida, E. and Lahti, P.M. (1996) *J. Am. Chem. Soc.*, **118**, 9695–9704.
- 40 Knoop, C.A. and Studer, A. (2003) *J. Am. Chem. Soc.*, **125**, 16327–16333.
- 41 Georges, M.K., Lukkarila, J.L. and Szkurhan, A.R. (2004) *Macromolecules*, **37**, 1297–1303.
- 42 Dijkstra, A., Marino-Gonzalez, A., Mairatai Payeras, A., Arends, I.W.C.E. and Sheldon, R.A. (2001) *J. Am. Chem. Soc.*, **123**, 6826–6833.
- 43 Cameron, N.R. and Reid, A.J. (2002) *Macromolecules*, **35**, 9890–9895.
- 44 Huang, W., Chiarelli, R., Charleux, B., Rassat, A. and Vairon, J.-P. (2002) *Macromolecules*, **35**, 2305–2317.
- 45 Pu, Y.-J., Soma, M., Kido, J. and Nishide, H. (2001) *Chem. Mater.*, **13**, 3817–3819.
- 46 Yonekuta, Y., Susuki, K., Oyaizu, K., Honda, K. and Nishide, H. (2007) *J. Am. Chem. Soc.*, **129**, 14128–14129.
- 47 Suga, T., Konishi, H. and Nishide, H. (2007) *Chem. Commun.*, 1730–1732.
- 48 Suga, T., Pu, Y.-J., Kasatori, S. and Nishide, H. (2007) *Macromolecules*, **40**, 3167–3173.
- 49 Oyaizu, K., Suga, T., Yoshimura, K. and Nishide, H. (2008) *Macromolecules*, **41**, 6646–6652.
- 50 Takahashi, Y., Hayashi, N., Oyaizu, K., Honda, K. and Nishide, H. (2008) *Polym. J.*, **40**, 763–767.
- 51 Nishide, H., Iwasa, S., Pu, Y.-J., Suga, T., Nakahara, K. and Satoh, M. (2004) *Electrochim. Acta*, **50**, 827–831.
- 52 Suga, T., Yoshimura, K. and Nishide, H. (2006) *Macromol. Symp.*, **245-246**, 416–422.
- 53 Kim, J.-K., Cheruvally, G., Choi, J.-W., Ahn, J.-H., Choi, D.S. and Song, C.E. (2007) *J. Electrochem. Soc.*, **154**, A839–A843.
- 54 Zhang, X., Li, H., Li, L., Lu, G., Zhang, S., Gu, L., Xia, Y. and Huang, X. (2008) *Polymer*, **49**, 3393–3398.
- 55 Bugnon, L., Morton, C.J.H., Novak, P., Vetter, J. and Nesvadba, P. (2007) *Chem. Mater.*, **19**, 2910–2914.
- 56 Suguro, M., Iwasa, S., Kusachi, Y., Morioka, Y. and Nakahara, K. (2007) *Macromol. Rapid Commun.*, **28**, 1929–1933.
- 57 Yoshikawa, H., Kazama, C., Awaga, K., Satoh, M. and Wada, J. (2007) *Chem. Commun.* 3169–3170.
- 58 Endo, T., Takuma, K., Takata, T. and Hirose, C. (1993) *Macromolecules*, **26**, 3227–3229.
- 59 Nakahara, K., Iwasa, S., Iriyama, J., Morioka, Y., Suguro, M., Satoh, M. and Cairns, E.J. (2006) *Electrochim. Acta*, **52**, 921–927.
- 60 Allgaier, J. and Finkelmann, H. (1993) *Makromol. Chem., Rapid Commun.*, **14**, 267–271.

- 61 Nakahara, K., Iriyama, J., Iwasa, S., Suguro, M., Satoh, M. and Cairns, E.J. (2007) *J. Power Sources*, **163**, 1110–1113.
- 62 Nakahara, K., Iwasa, S., Satoh, M., Morioka, Y., Iriyama, J., Suguro, M. and Hasegawa, E. (2002) *Chem. Phys. Lett.*, **359**, 351–354.
- 63 Nakahara, K., Iriyama, J., Iwasa, S., Suguro, M., Satoh, M. and Cairns, E.J. (2007) *J. Power Sources*, **165**, 398–402.
- 64 Nakahara, K., Iriyama, J., Iwasa, S., Suguro, M., Satoh, M. and Cairns, E.J. (2007) *J. Power Sources*, **165**, 870–873.
- 65 Murray, R.W. (ed.) (1992) *Molecular Design of Electrode Surfaces*, John Wiley & Sons, Inc., New York.
- 66 Bard, A.J. and Faulkner, L.R. (2001) *Electrochemical Methods, Fundamentals and Applications*, 2nd edn, John Wiley & Sons, Inc., New York.

## 10

# Oxidation Catalysis by Nanoscale Gold, Silver, and Copper

Zhi Li, Soorly G. Divakara, and Ryan M. Richards

### 10.1

#### Introduction

Catalysis by nanoscale materials is a rapidly growing field which involves the use of nanoparticles as catalysts for a variety of organic and inorganic reactions. Although the application of nanoscale catalysts has a long history in industry, the ability to engineer catalysts on the nanoscale and to explore the related phenomena in a controlled manner has evolved considerably in recent years. Numerous reviews have been published during the past decade on both heterogeneous catalysis in which nanoparticles are supported on solid surfaces (e.g., silica, alumina, MgO) and “soluble heterogeneous” or “quasi-homogeneous” catalysis with colloidal nanoparticles [1–8].

The catalytic performances of nanoparticles can be finely tuned either by their composition, which mediates electronic structure, or by their shape, which determines surface atomic arrangement and coordination. Beyond the exciting potential for tailoring catalysts, nanostructured materials introduce additional challenges to catalyst design. Being small, and with surface atoms of different unsaturated valencies, nanoparticles of specific shape are more liable to change their shape in the harsh medium of chemical reactions; this in turn raises concerns about durability, what the true active species is, and what approaches can be taken to control this phenomena. The surface reconstruction and/or dissolution of active atoms on corners or edges by one or more of the reactants, or even by the solvent, is an additional concern that requires attention. Despite these challenges, several types of chemical reaction have been catalyzed using transition metal nanomaterials, including crosscouplings, electron transfers, hydrogenations, fuel cell electrocatalysis and oxidations. In this chapter, attention will be focused on oxidation reactions, with particular emphasis on the Group 11 metals of the Periodic Table, namely silver, gold, and copper.

The Group 11 metals have a long history for their uses in jewelry, ornaments and as “coinage metals,” as well being particularly interesting on the nanoscale for the colors they display as a function of size. However, as research has



progressed with regards to both size- and shape-related chemical reactivities, the rich chemistry of this group of metals is emerging, and particularly their application as catalysts. Gold, in its bulk state, has long been thought to be far less catalytically active than other transition metals, such as silver, platinum, and palladium. However, many research groups [9–11] have reported pioneering studies to indicate that gold could catalyze hydrogenation, hydrogen exchange, hydrocracking, and carbon monoxide oxidation reactions. These initial findings have inspired numerous investigations into the nature of ultrafine gold particles dispersed on supports, using a wide variety of approaches [12, 13].

For many years, the chemistry of silver and gold was believed to be more similar than is now known to be the case. Silver (Ag) is the best conductor among these metals, and so silver nanoparticles facilitate more electron transfer than do gold (Au) nanoparticles. Silver has a reduction potential of +0.79 V (versus NHE) for an  $\text{Ag}^{\text{I}}$  (aqueous)/ $\text{Ag}_{\text{metal}}$  system, but for an  $\text{Ag}^{\text{I}}$  (aqueous)/ $\text{Ag}_{\text{atom}}$  system it is –1.80 V (versus NHE). Among the many different metal nanoparticles under investigation, silver nanoparticles are emerging as one of the most intensively studied, largely because of the broad range of applications that they exhibit. These properties include shape- and size-dependent optical, electronic, and chemical properties, and present many possibilities with respect to technological applications. Currently, copper (Cu) is one of the most widely used materials worldwide, being of major significance in all industries, especially in the electrical sector due to its low cost. Moreover, Cu continues to gain importance on the basis of it being an essential component in future nanodevices due to its excellent conductivity, its good biocompatibility, and its surface-enhanced Raman scattering (SERS) activity. Further, copper nanoparticles smaller than 50 nm in size are also considered “superhard” materials, as they do not exhibit the same malleability and ductility as bulk copper.

## 10.2

### Preparations

There are two general paradigms for the preparation of nanoscale materials, namely “top down” and “bottom up”. Those preparations characterized by the breaking down of larger starting materials are classified as “top down,” while those which are built up from atomic or molecular starting materials are termed “bottom up.” Chemical procedures such as alcohol reduction [14–16], hydrogen reduction [17–19], and sodium borohydride reduction [20–22] have in the past been recognized as the most common methods for synthesizing colloidal metal nanoparticles. Other reduction methods such as electrochemical [23, 24], photochemical [25–27], and sonochemical [28, 29] have also been used, but to a smaller extent. Many different stabilizers have been used as capping agents for the synthesis of colloidal metal nanocatalysts, including polymers [30, 31], dendrimers [32, 33], block copolymer micelles [31, 34], and surfactants [35, 36]. Supported metal nanocatalysts have been prepared by the adsorption of colloidal metal nanocatalysts

onto supports [37–39], and/or by grafting the nanoparticles onto the support [40]. Supported metal nanocatalysts can also be fabricated lithographically, using electron beam lithography [41, 42].

### 10.2.1

#### **Silver Nanocatalysts**

By using the above-described methods, silver materials with zero-, one-, or two-dimensional nanostructures, including monodisperse nanoparticles, nanowires, nanodisks, nanoprisms, nanoplates, and nanocubes, have each been prepared and are recognized as having great potential for applications in optics, catalysis, and other fields [43–47].

### 10.2.2

#### **Copper Nanocatalysts**

Copper nanoparticles have been synthesized and characterized by different methods. Notably, chemical reduction, pulsed laser ablation, radiolytic reduction, and the reduction of copper ions using supercritical fluids have been developed to synthesize spherical and different-shaped nanoparticles [48–50]. Stability and reactivity are the two important factors that impede the use and development of metal clusters. In contrast to noble metals, such as Ag and Au, pure metallic copper particles usually cannot be obtained via the reduction of simple copper salts (e.g., copper chloride or copper sulfate) in aqueous solution, because the reduction tends to stop at the  $\text{Cu}_2\text{O}$  stage due to the presence of a large number of oxygenous water molecules. However, this problem can be overcome by the addition of other reagents carrying functional groups that can form complexes with copper ions, or by using soluble surfactants as capping agents to prepare copper particles in aqueous solution. Although zero-valent copper forms initially in the solvent, ultimately it can be transformed relatively easily into oxides, in solvents with high dipole moments and under ambient conditions. The use of reverse micelles as microreactors and protecting shells has also helped to overcome some of these complications. Likewise, electrolytic techniques have been used to synthesize a variety of transition metal colloids of either decahedral or isohedral shape, by controlling the electrode potential. The extreme air-sensitivity of copper nanoparticles requires that care be taken during such preparation in order to avoid oxidation.

### 10.2.3

#### **Gold Nanocatalysts**

Beyond preparing nanoscale materials in the form of colloids, considerable effort has been expended in the preparation of supported heterogeneous catalysts, and in particular the nature of the support and the process to immobilize an active metal on the support (mostly metal oxides and active carbon). The use of gold

nanocatalysts is cited as an example here when introducing different methods for preparing nanocatalysts.

Due to the lower melting point of gold, and its poor affinity for metal oxides, it is difficult to prepare stable gold catalysts that are well dispersed on metal oxides. The typical impregnation methods that are widely used to prepare supported Pd or Pt catalysts are ineffective in the case of gold, because the presence of chloride ions can cause a significant enhancement in the coagulation of gold particles during the calcination of  $\text{HAuCl}_4$ .

Haruta has summarized the methods used to prepare supported gold catalysts (Table 10.1), and categorized them into four groups [51]:

- The first group includes coprecipitation [54], amorphous alloying [55], and cosputtering [56]. These procedures generally consist of two steps: (i) the preparation of well-mixed gold/metal oxide precursors; and (ii) transformation of the gold precursor into gold particles, normally by calcinations in air above 550 K. Well-mixed precursors and high-temperature calcination are equally

**Table 10.1** Preparation techniques for nanoparticulate gold catalysts[51].

Categories	Preparation techniques	Support materials	Reference(s)
Preparation of mixed precursors of Au and the metal component of supports	Coprecipitation (hydroxides or carbonates) (CP)	$\text{Be}(\text{OH})_2$ , $\text{TiO}_2$ , $\text{Mn}_2\text{O}_3$ , $\text{Fe}_2\text{O}_3$ , $\text{Co}_3\text{O}_4$ , $\text{NiO}$ , $\text{ZnO}$ , $\text{In}_2\text{O}_3$ , $\text{SnO}_2$	[52–54]
	Amorphous alloy (metals) (AA)	$\text{ZrO}_2$	[55]
	Cosputtering (oxides) in the presence of $\text{O}_2$ (CS)	$\text{Co}_3\text{O}_4$	[56]
Strong interaction of Au precursors with support materials	Deposition–precipitation ( $\text{HAuCl}_4$ in aqueous solution) (DP)	$\text{Mg}(\text{OH})_2$ , $\text{Al}_2\text{O}_3$ , $\text{TiO}_2$ , $\text{Fe}_2\text{O}_3$ , $\text{Co}_3\text{O}_4$ , $\text{NiO}$ , $\text{ZnO}$ , $\text{ZrO}_2$ , $\text{CeO}_2$ , $\text{Ti-SiO}_2$	[57]
	Liquid-phase grafting (organogold complex in organic solvents) (LG)	$\text{TiO}_2$ , $\text{MnOx}$ , $\text{Fe}_2\text{O}_3$	[58, 59]
	Gas-phase grafting (organogold complex) (GG)	All types, including $\text{SiO}_2$ , $\text{Al}_2\text{O}_3$ - $\text{SiO}_2$ , and activated carbon	[60, 61]
Mixing colloidal Au with support materials	Colloid mixing (CM)	$\text{TiO}_2$ , activated carbon	[13]
Model catalysts using single crystal supports	Vacuum deposition (at low temperature) (VD)	Defects are the sites for deposition, $\text{MgO}$ , $\text{SiO}_2$ , $\text{TiO}_2$	[62–64]

important to ensure a strong contact between the Au particles and the crystalline metal oxides.

- The strategy for the second group is based on the concept of depositing or adsorbing Au compounds onto metal oxide surfaces. Among the three methods referred to here, deposition–precipitation (DP) is widely used to produce active Au catalysts. By controlling the pH and concentration of the  $\text{HAuCl}_4$  solution, the deposition of  $\text{Au}(\text{OH})_3$  can be controlled on the surfaces of the support metal oxides so as to prevent precipitation in the liquid phase. Aggregation of the gold nanoparticles, induced by chloride ions, can be prevented by washing the gold compound before drying, and this represents one of the main reasons for the high activity of these catalysts. The primary limitation here is that DP can only be applied to metal oxides with an isoelectric point  $>5$ . Although previously it was shown that  $\text{Au}(\text{OH})_3$  could not be deposited on  $\text{SiO}_2$  and active carbon, recent studies have found that this constraint may be overcome by correct surface modification [65].
- In the third group, the procedure involves the direct immobilization of Au colloids on modified metal oxide surfaces. In theory, this method could be applied to all metal oxides, and the catalysts prepared would normally have a good gold particle size distribution. However, there is often a relatively poor contact between the gold particles and the support.
- In the fourth group, vacuum deposition is considered to be an important method for preparing model catalysts that play a critical role when studying reaction mechanisms, and especially the active sites of the supported gold catalysts. Au anion clusters can be deposited with homogeneous dispersion at relatively low temperatures [62, 64] on single crystals of MgO and  $\text{TiO}_2$  (rutile). Surface defects or specific surface cages have been suggested as possible sites for stabilizing the Au clusters [62, 63].

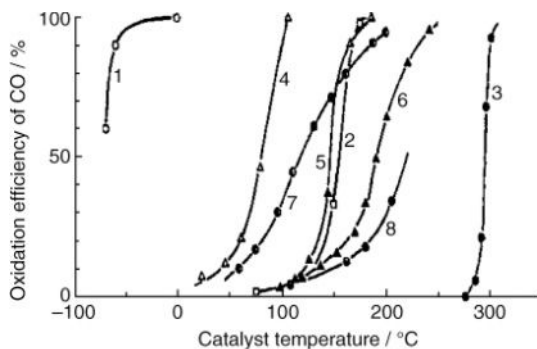
## 10.3

### Selective Oxidation of Carbon Monoxide (CO)

#### 10.3.1

#### Gold Catalysts

During the 1980s, Haruta *et al.* [66] found that gold nanoparticles, when supported on  $\alpha\text{-Fe}_2\text{O}_3$ , were highly active in the oxidation of CO, and especially at very low temperatures, although this surprisingly high activity was not replicated by other metals (Figure 10.1). In a later series of investigations conducted by the same group [52], Au/ $\text{TiO}_2$  was found to be an equally effective catalyst, and this in turn led to extensive studies of gold nanocatalysts supported on a variety of metal oxides.



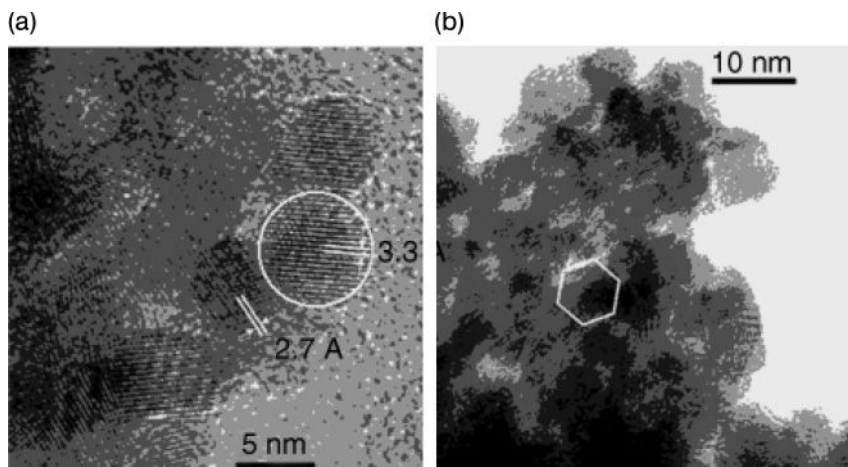
**Figure 10.1** CO conversion over various catalysts as a function of temperature. Curve 1, Au/ $\alpha$ -Fe<sub>2</sub>O<sub>3</sub> (Au/Fe = 1/19, coprecipitation, 400 °C); Curve 2, 0.5 wt% Pd/ $\gamma$ -Al<sub>2</sub>O<sub>3</sub> (impregnation, 300 °C); Curve 3, fine Au powder; Curve 4, Co<sub>3</sub>O<sub>4</sub> (carbonate, 400 °C);

Curve 5, NiO (hydrate, 200 °C); Curve 6,  $\alpha$ -Fe<sub>2</sub>O<sub>3</sub> (hydrate, 400 °C); Curve 7, 5 wt% Au/ $\alpha$ -Fe<sub>2</sub>O<sub>3</sub> (impregnation, 200 °C); Curve 8, 5 wt% Au/ $\gamma$ -Al<sub>2</sub>O<sub>3</sub> (impregnation, 200 °C). Reproduced with permission from Ref. [66]; © 1987, Chemical Society of Japan, Tokyo.

Owing to the possible applications of polymer electrolyte fuel cells to automobiles and also to residential electricity-heat delivery systems, the low-temperature water-gas-shift reaction continues to attract renewed interest. When compared to commercial catalysts that are based on Ni or Cu and operated at 900 K or 600 K, respectively, supported Au catalysts appear to have a clear operational advantage in that they function at temperatures as low as 473 K [67]. During the course of investigating the hydrogenation of CO<sub>2</sub> over supported Au catalysts, it was found that Au/TiO<sub>2</sub> was selective towards the formation of CO, in that the reverse water-gas-shift reaction could be conducted at a temperature as low as 473 K [67]. Later, Au/TiO<sub>2</sub> was confirmed also to be active for the water-gas-shift reaction [68].

The oxidation of CO is a typical reaction for which Au catalysts are extraordinarily active at room temperature, and indeed are much more active than other noble metal catalysts at temperatures below 400 K. One focal point of recent studies has been the elaboration of the mechanism for CO oxidation [69, 70]. Although the available data on this topic are vast—and occasionally contradictory—several pieces of information were identified that were critical to developing an understanding of the mechanism. For example, active catalysts always contain metallic Au particles which produce a CO absorption band at 2112 cm<sup>-1</sup>, whereas oxidic Au species that produce a CO absorption band at 2151 cm<sup>-1</sup> are not responsible for steady-state, high catalytic activity [71]. However, as the smooth surfaces of metallic Au do not adsorb CO at room temperature [72], this indicates that CO is adsorbed only on steps, edges, and corner sites. As a consequence, the smaller metallic Au particles are preferable [73].

A theoretical calculation [74] has been used to explain why the smooth surface of Au is noble in the dissociative adsorption of hydrogen. However, when Au is deposited as nanoparticles on metal oxides by means of coprecipitation and DP techniques, it exhibits a surprisingly high catalytic activity for CO oxidation at a



**Figure 10.2** High-resolution transmission electron microscopy images of the 2.8% Au/CeO<sub>2</sub> sample. (a) The white lines correspond to the (202) Ce<sub>2</sub>O<sub>11</sub> (3.3 Å) and the (200) CeO<sub>2</sub> (2.7 Å) lattice spacing; (b) A hexagonal

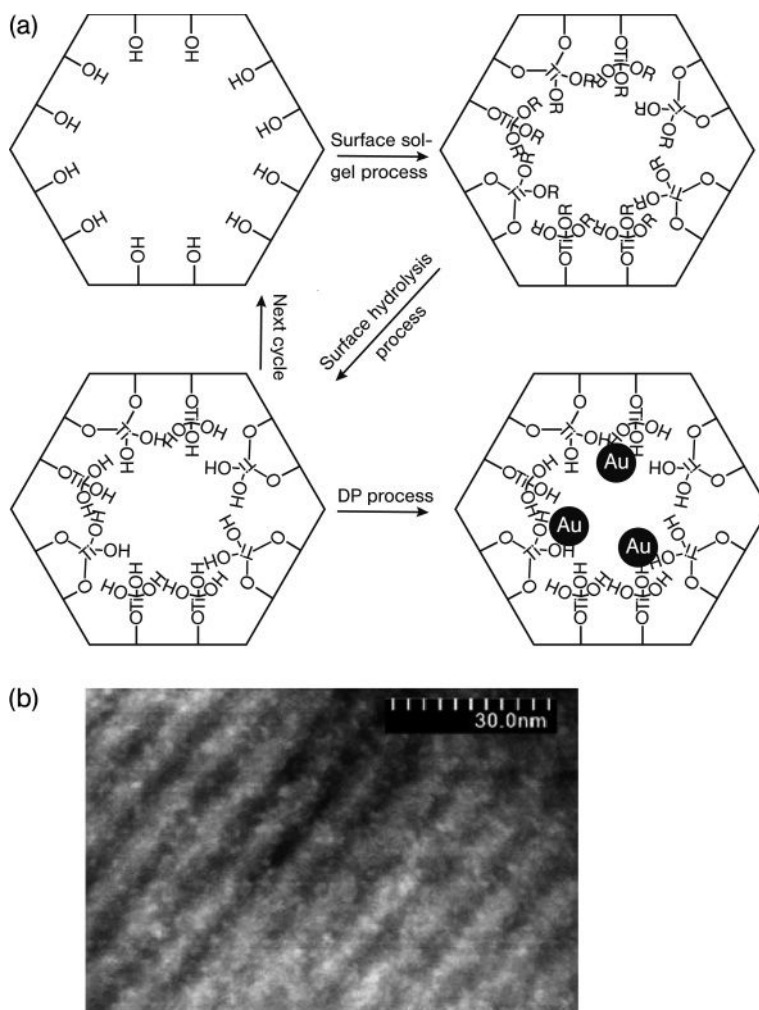
faceted (111) Au crystal is indicated. Reproduced with permission from Ref. [75]; © 2005, WILEY-VCH Verlag GmbH & Co. KGaA, Weinheim.

temperature as low as 200 K [12, 52]. During the 1990s, this finding led to many research groups conducting extensive investigations into the catalysis of Au.

One remarkable study among many was conducted by Corma and coworkers [75], who showed that gold nanoparticles supported on nanocrystalline CeO<sub>2</sub>, in conjunction with the DP method, proved to be a very active catalyst for CO oxidation (Figure 10.2). Indeed, the catalysts were found to be an order of magnitude more active for CO oxidation than comparable catalysts prepared using a non-nanocrystalline support. The Au/CeO<sub>2</sub> catalyst also showed excellent selectivity for CO oxidation in the presence of H<sub>2</sub> at 60 °C (close to the operating temperature of fuel cell), where the selectivity of normal Au active catalysts would be negatively affected [76].

Most gold catalysts which have been reported as active for CO oxidation were prepared using the DP method, which provides catalysts with a strong interaction between the gold and the metal oxide matrix. However, a major drawback of this method is that it cannot be used to deposit gold at metal oxides with an isoelectric point (IEP) <5, such as SiO<sub>2</sub>. Subsequently, Sheng Dai and coworkers [65] successfully deposited gold at the surface of mesoporous SiO<sub>2</sub> by using the DP method following a sol-gel surface modification with TiO<sub>2</sub>. The results showed the gold nanoparticles (0.8–1.0 nm) in the mesopores to be highly active in terms of CO oxidation (Figure 10.3).

Today, whilst it is widely recognized that these supported gold nanocatalysts show a high activity in the low-temperature oxidation of CO, many questions remain unanswered concerning the relatively simple reaction of CO oxidation. The most notable of these are “What is the reaction mechanism?”, and “What is the nature of the active site?”

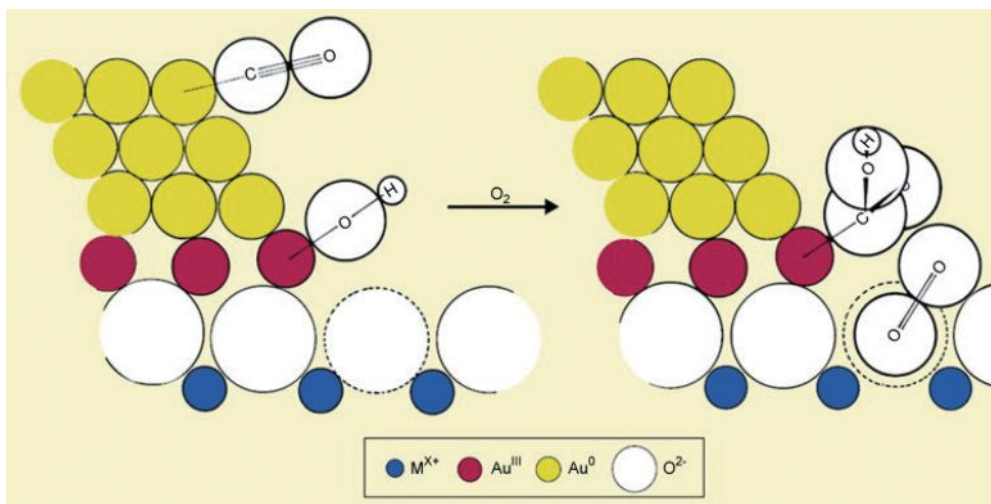


**Figure 10.3** (a) Scheme of preparation of gold/mesoporous material catalysts; (b) Z-contrast TEM image of ultrasmall gold nanoparticles on ordered mesoporous

materials. The bright spots (0.8–1.0 nm) correspond to gold nanoparticles. Reproduced with permission from Ref. [65]; © 2004, ACS Publications, Washington.

A substantial proportion of the research into CO oxidation catalyzed by supported gold has been motivated by the goal of identifying those catalyst properties which affect the activity. In this respect, two early classes of observation were important in determining the approaches used recently to investigate supported gold catalysts: (i) that various preparation routes lead to catalysts with different activities [52, 77]; and (ii) that catalysts consisting of gold supported on reducible metal oxides (e.g.,  $\text{Fe}_2\text{O}_3$ ,  $\text{CeO}_2$ ,  $\text{TiO}_2$ ) are typically more active than those





**Scheme 10.1** Schematic representation of an active site and possible reaction mechanism for CO oxidation catalyzed by supported gold. Reproduced with permission from Ref. [77]; © 2000, World Gold Council, London.

supported on nonreducible metal oxides (e.g.,  $\gamma$ - $\text{Al}_2\text{O}_3$ ,  $\text{MgO}$ ,  $\text{SiO}_2$ ). Such observations led to a wide acceptance of the inferences that the preparation method influenced activity [12], and that the support played a role in the catalysis.

Bond and Thompson [77], in their review of the literature which extended to the year 2000, and in an attempt to reconcile some apparently contradictory hypotheses, proposed a mechanism for CO oxidation that was catalyzed by supported gold (Scheme 10.1). The proposed active site consisted of nanoparticles incorporating both zero-valent and cationic gold, with the latter positioned at the metal–support interface. The suggestion by Bond and Thompson of the presence of cationic gold was based on observations by various authors of  $\nu\text{CO}$  infrared (IR) bands that were characteristic of CO bonded to cationic gold. However, evidence was lacking not only of any such species in working catalysts, but also of the suggestion that cationic gold was a “glue” which held the nanoclusters to the support.

In 2002, Haruta [78] presented a review of the literature and proposed, on the basis of measurements of the kinetics of CO oxidation catalyzed by supported gold, that there were three temperature regions, each with different kinetics and activation energies of the CO oxidation reaction. Haruta suggested that, at temperatures below 200 K, the reaction catalyzed by  $\text{Au}/\text{TiO}_2$  took place at the surfaces of small gold nanoparticles dispersed on the support, but at temperatures above 300 K the reaction occurred at gold atoms at the perimeter sites of the supported gold nanoparticles.

## 10.3.2

**Silver Catalysts**

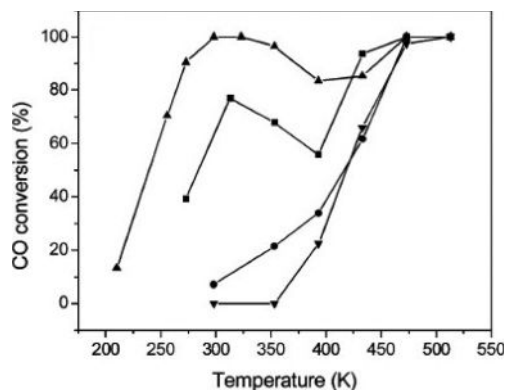
Silver catalysts also have a relatively high activity for the selective oxidation of CO at low temperatures. A silver catalyst was deactivated remarkably following pretreatment in H<sub>2</sub> at high temperatures, but could be reactivated by treatment in oxygen at similarly high temperatures. Interestingly, these changes in activities were mostly reversible. The structures of the silver particles were seen to experience massive changes during the course of various pretreatments, and the existence of subsurface oxygen resulting from an oxygen treatment at high temperatures was shown to be crucial for high selectivity and activity in CO selective oxidation [79, 80]. As CO oxidation is generally claimed to be a structure-sensitive reaction, restructuring of the silver particles is likely to exert an influence on the activity of the catalyst. Yang and Aoyama [81, 82] studied the thermal stability of uniform silver clusters supported on oxidized silicon or aluminum surfaces in both oxidizing and reducing atmospheres, and found the thermal stability of the silver clusters to be significantly lowered under oxidizing conditions. Moreover, heating above 350 °C under oxidizing condition could induce a migration of the silver clusters.

Size selectivity in catalysis was reported for propylene partial oxidation and low-temperature CO-oxidation, with Ag nanoparticles of <5 nm diameter being shown to have equal activity as the Au nanoparticles. In contrast, for ethylene epoxidation only those Ag particles >30 nm could catalyze the reaction [83]. Recently, much attention has been focused on the use of spherical or undetermined-shape nanoparticles for catalyzing reactions. Very few studies have been undertaken in which catalysis was conducted with nanoparticles of known shapes [84], for example, using truncated octahedral Pt nanoparticles to catalyze the electron-transfer reaction, and cubic Pt nanoparticles in the decomposition of the oxalate capping agent. The formation of different oxygen species, depending on the Ag particle size sputtered on the highly ordered pyrolytic graphite (HOPG) surface, resulted in a variation in catalytic activity of CO oxidation using oxygen under (ultra-high vacuum) UHV conditions revealed CO oxidation to be sensitive towards the size of particle [85]. The oxygen uptake of a smaller Ag nanoparticle was seen to be significantly higher than that of a larger particle and a bulk-like Ag which enhanced the reactivity of CO oxidation.

## 10.3.3

**Gold–Silver Alloy Catalysts**

The recent progress in polymer electrolyte membrane fuel cells has particularly motivated the search for a highly efficient catalyst for CO selective oxidation at low temperatures. Thus, combinations of metals in the forms of alloys, core–shell and “decorated” surfaces (Pt, Pd, Rh, Ru, Au, Ag, Cu, Co, Fe, In, Ga) with different supports, such as zeolite, Al<sub>2</sub>O<sub>3</sub>, SiO<sub>2</sub>, and activated carbon, have produced active catalysts for the CO reaction. One such alternative catalyst, namely gold–silver



**Figure 10.4** CO conversion over reaction temperatures at various molar ratios of Au:Ag. ▲, ratio 3:1; ■, ratio 1:1; ●, ratio 1:0; ▼, ratio 0:1. Reproduced with permission from Ref. [88]; © 2005, ACS Publications, Washington.

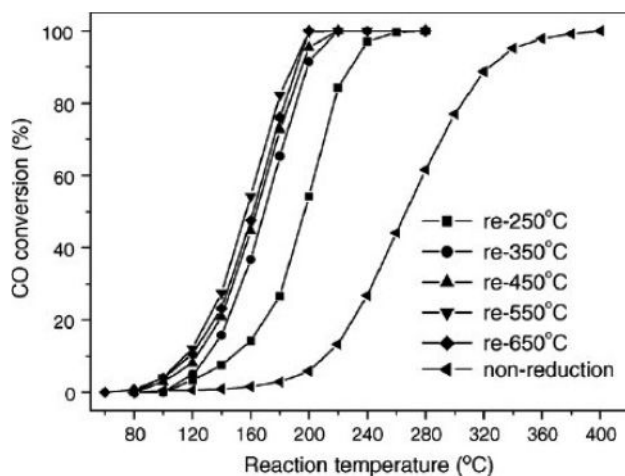
alloy nanoparticles deposited on MCM-41, demonstrated an exceptionally high catalytic activity which was comparable to the most active catalysts (Figure 10.4) such as Au/TiO<sub>2</sub> and Au/Fe<sub>2</sub>O<sub>3</sub> [86, 87]. The alloying of Au and Ag showed a strong synergistic effect in promoting the low-temperature oxidation of CO [88]. The alloy catalyst activation was shown to depend on the composition (the Ag ratio was crucial), the aluminum content in the support, and the pretreatment conditions.

#### 10.3.4

##### Copper Catalysts

Copper nanoparticles are also active for the selective oxidation of CO. The majority of studies with copper particles have been performed with finely dispersed copper on various supports, and have demonstrated high catalytic activities for CO oxidation. Likewise, CuO mixed with ZnO or with CeO<sub>2</sub> have also shown promise as catalysts. The results of a recent density functional theory (DFT) study showed that gold and copper had a lower barrier for CO oxidation than for H<sub>2</sub> oxidation.

Ceria has a promoting effect on the activity of the Au/Al<sub>2</sub>O<sub>3</sub> catalyst in CO oxidation [89]. The addition of Li<sub>2</sub>O and/or CeOx to copper, silver, and gold catalysts of 3 nm size on  $\gamma$ -Al<sub>2</sub>O<sub>3</sub> for the preferential oxidation of CO in a hydrogen atmosphere [90], have shown significant changes in the conversion. The nanoscale metal particles or metal complexes in polymer matrices show quite interesting chemical and catalytic reactivity towards a variety of small gas molecules under relatively mild conditions that differ from those of the corresponding free transition metal complexes, or from those in inorganic oxide-supported systems. The incorporation of copper nanoparticles into cellulose acetate, and the subsequent oxidation of small gas molecules (e.g., CO, H<sub>2</sub>, D<sub>2</sub>, O<sub>2</sub>, NO, and olefins) over a temperature range of 25 to 160 °C, has also been examined [91]. Nanoparticles of various sizes prepared by different routes and hosted in the channels of SBA-15, exhibited a



**Figure 10.5** CO conversions versus reaction temperature over Cu/SBA-15 (post grafted) calcined at 500°C and reduced at different temperatures. Reproduced with permission from Ref. [92]; © 2006, Elsevier B.V., Amsterdam.

high catalytic activity for CO oxidation, with complete conversion at 190°C (Figure 10.5) [92]. Such high catalytic activity was mainly influenced by the size and dispersion of the Cu particles.

## 10.4

### Epoxidation Reactions

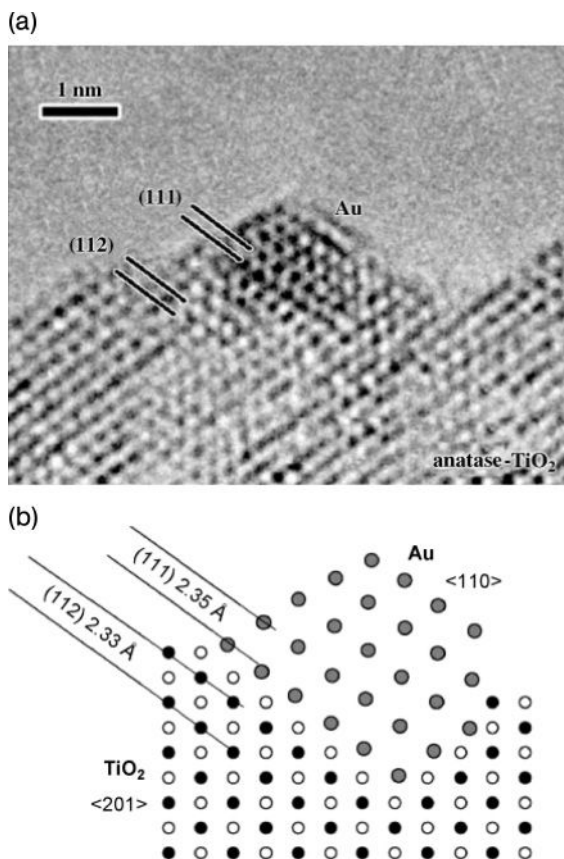
#### 10.4.1

##### Gold Catalysts

Since the first recognition by Hayashi [93] that Au supported on TiO<sub>2</sub> could catalyze the epoxidation of propylene in the gas phase containing O<sub>2</sub> and H<sub>2</sub>, the catalytic properties of Au/TiO<sub>2</sub> and related systems have attracted interest not only from the chemical industries but also from academia. Today, propylene oxide (PO) is recognized as one of the world's most important bulk chemicals, and is used in the production of polyurethane and polyols. The current industrial processes utilize two-staged chemical reactions, using either Cl<sub>2</sub> or organic peroxides to yield the byproducts stoichiometrically.

From both environmental and economic points of view, the direct synthesis of PO by using molecular oxygen has long been a major academic challenge, although supported noble metal catalysts such as Ag/carbonates and/or titanates, Pd/TS-1, Pd-Pt/TS-1 [94–96], and Au/TiO<sub>2</sub> (Figure 10.6) [93, 97], have each been reported to be active in this process.

In 1998, using the DP technique, Haruta and coworkers [97] produced nanoscale gold catalysts that showed a high activity towards CO oxidation, based on the



**Figure 10.6** (a) Transmission electron microscopy image of the Au/TiO<sub>2</sub> contact interface; (b) A schematic representation of the interface. Reproduced with permission from Ref. [97]; © 1998, VSP, Leiden.

strong contact with the support at highly dispersed isolated tetrahedral Ti<sup>4+</sup> sites. Moreover, this catalyst also provided a very high PO selectivity (>99%) in a gas phase containing O<sub>2</sub> and H<sub>2</sub>, at ambient pressure. The same group also demonstrated the formation of PO over an Au-based catalyst to be a typical structure-sensitive reaction [97], with the selective production of PO being catalyzed only by hemispherical Au particles of a suitable size (2 nm < diameter Au nanoparticle < 10 nm). In more recent investigations, these authors also showed an organically modified mesoporous titanosilicate to be an efficient support [98], providing a reasonably efficient H<sub>2</sub> consumption, high yields, and PO selectivities in excess of 90% [99].

These studies initiated a growing research interest from both industry and academia [100–103], with one of the more remarkable investigations being conducted by Hutchings and coworkers [102]. This group used catalytic amounts of peroxides to initiate the oxidation of alkenes with O<sub>2</sub>, and making it unnecessary

to sacrifice  $H_2$  in order to activate the  $O_2$ . Here, Au/graphite was found to be very active in catalyzing the epoxidation of cyclohexene, styrene, *cis*-stilbene, and cyclooctene, even in a solvent-free system. Although the selectivity could be increased by using the correct solvent (e.g., toluene), the environment-friendly epoxidation in solvent-free systems would be much more attractive to the chemical industry and is certain to become another hot topic of research in the near future.

#### 10.4.2

##### Silver Catalysts

Silver is considered to be an almost uniquely effective catalyst for heterogeneous epoxidation reactions, and the mechanism of the epoxidation of ethylene with oxygen over a silver catalyst has been the subject of extensive investigation [104–111]. However, despite such numerous studies and its wide use, a number of questions remain unanswered regarding this catalytic system, including: “How do the supports and promoters affect the reaction?”; “What is the mechanism of the primary and secondary reactions?”; and “What relationship exists between the electron and structure factors?” The interaction of oxygen with metal surfaces has been suggested as one of the most important elementary steps in heterogeneous catalysis, and several reviews of oxygen adsorption, active oxygen species, promoter effects and reaction mechanisms on silver catalysts have been produced [112]. The oxygen species on silver were found to play a key role in ethylene epoxidation, and extensive studies have been performed to establish details of the interaction of oxygen with silver surfaces, namely whether the chemisorbed oxygen is atomic or molecular [113]. Details of surface molecular, surface atomic, subsurface atomic, and bulk atomic oxygen species have each been reported in the literature.

Significant efforts to improve selectivity have included the use of different silver precursors, of different preparation techniques, and of different promoters. Such information is gathered following the continuous addition of a chlorine-containing hydrocarbon species to the gaseous reactants as a moderator, which also acts to depress the overall reaction rates. Campbell reported that small amounts of promoters (e.g., Cl) would increase the ethylene oxide selectivity [114, 115]. For an industrial oxidation of ethylene, alkali metal ions are an important additive when using a silver catalyst, and alkali or alkaline earth promoters (e.g., cesium) can provide further substantial improvements [116–118]. Campbell [116] reported the role of a cesium promoter in silver catalysts for the selective oxidation of ethylene. The oxidation of ethylene in solution, catalyzed by polymer-protected silver colloids, and the promotion effect by alkali metal ions on colloidal silver catalysts, have also been studied [119]. Colloidal dispersions of silver nanoclusters, when protected by poly(sodium acrylate), caused increases in the rate of oxidation, the reaction temperature and also the catalytic activity following the addition of Cs(I) and Re(VII) ions [120].

The influence of silver nanoparticle size on catalytic activity is due not only to an enhanced surface area but also to particular electronic properties, which differ from those of bulk silver. The effect of silver particle size on the reaction rate is a well-

known property of supported silver catalysts [121, 122]. For example, when monitoring the distribution of Ag supported on alumina, silver particles of 30–70 Å on alumina or silica showed higher activities. Previously, small silver clusters had been shown to be the most effective, probably due to the electronic and other properties of silver (atomic environment, electron work function, electric conductance, etc.), and differed considerably from bulk silver in this respect. Although the majority of studies have used bulk silver samples, uncertainty remains as to the nature of the active sites for ethylene epoxidation on a commercial catalyst. Enlargement of the silver particles has been found to decrease the amount of subsurface oxygen, and result in the appearance of nucleophilic oxygen. These findings have been used to provide a possible explanation for the size effect in ethylene epoxidation over Ag/Al<sub>2</sub>O<sub>3</sub> catalysts (Figure 10.7) [123–126]. The kinetic study and shape-controlled catalytic epoxidation of olefins by these nanoparticles on several supports such as  $\alpha$ -Al<sub>2</sub>O<sub>3</sub>, CaCO<sub>3</sub> and spherical particles of TiO<sub>2</sub> (all obtained using the Stöber method) were investigated for a non-allylic olefin (e.g., styrene) and for an allylic olefin (e.g., propene), using molecular oxygen and N<sub>2</sub>O as oxidants.

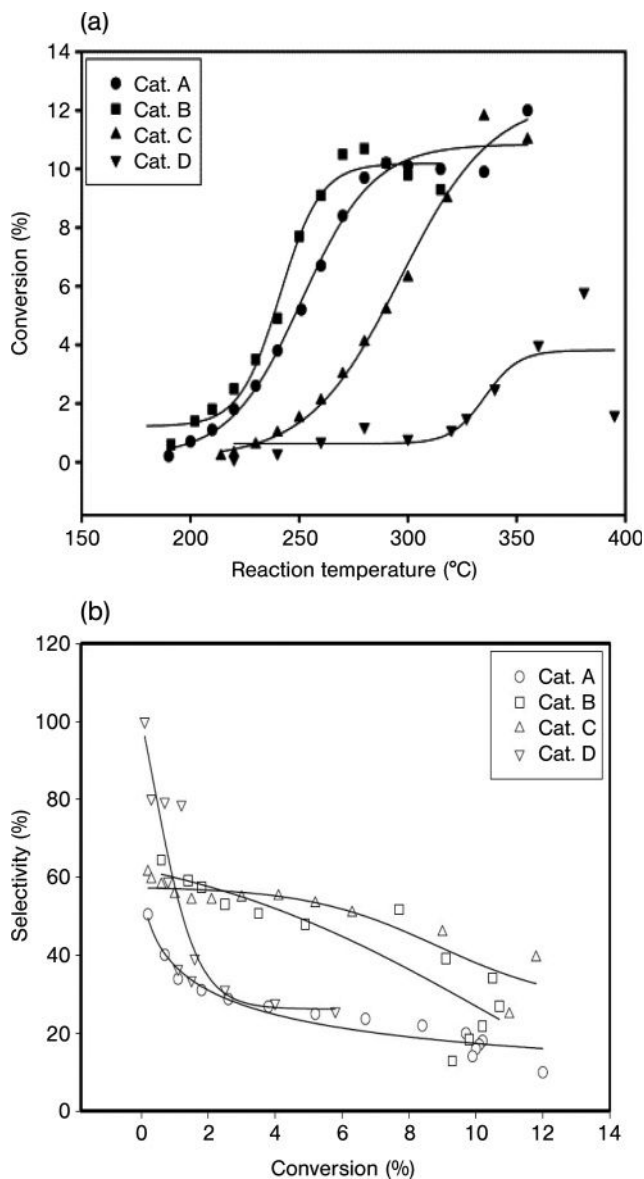
Silver supported on titania was found to be active for propene epoxidation using hydrogen/oxygen mixtures at 50 °C [127, 128]. The direct aerobic oxidation of various alkenes catalyzed by H<sub>3</sub>PV<sub>2</sub>Mo<sub>10</sub>O<sub>40</sub> polyoxometalate-stabilized silver nanoparticles supported on Al<sub>2</sub>O<sub>3</sub> showed a higher selectivity towards epoxide in the liquid phase [129]. Styrene represents a useful alkene model for studying the reaction mechanism of terminal alkene epoxidation; the size and morphology of the nanoparticles was reported to affect the catalytic behavior of silver catalysts supported on  $\alpha$ -Al<sub>2</sub>O<sub>3</sub> and MgO, in the selective oxidation of styrene in the gas phase [130–134]. The epoxidation of styrene to its oxide by molecular oxygen was studied using a Cs-loaded silver nanowire catalyst, and resulted in the desired product with greater selectivity.

## 10.5 Selective Oxidation of Hydrocarbons

The selective oxidation of alkanes with molecular oxygen represents a major challenge [135, 136], as the production of the more valuable oxidized products relative to the low cost of the raw materials is of economic interest. The chemical inertness of hydrocarbons makes the activation of C–H bonds especially difficult, and usually requires dramatic reaction conditions such as high temperature and pressure. The oxidation of cyclohexane is of special interest industrially, because the process produces KA-oil as an intermediate; this is a mixture of cyclohexanone and cyclohexanol that is important in the petroleum chemical industry. KA-oil is used for the production of adipic acid and  $\epsilon$ -caprolactam, which are key materials in the respective manufacture of 6,6-nylon and 6-nylon [137].

Modern industrial methods typically require both high pressure and temperature when using a soluble cobalt catalyst. A high selectivity for cyclohexanone and cyclohexanol can only be achieved at a low conversion, as these products are





**Figure 10.7** (a) Conversion of ethylene; (b) Selectivity and conversion of Ag on  $\gamma\text{-Al}_2\text{O}_3$  with catalysts prepared by different methods: A, precipitation; B, modified precipitation; C, water-alcohol; D, microemulsion silver loading (7.5–8.6%). Reproduced with permission from Ref. [126]; © 2003, Elsevier B.V., Amsterdam.

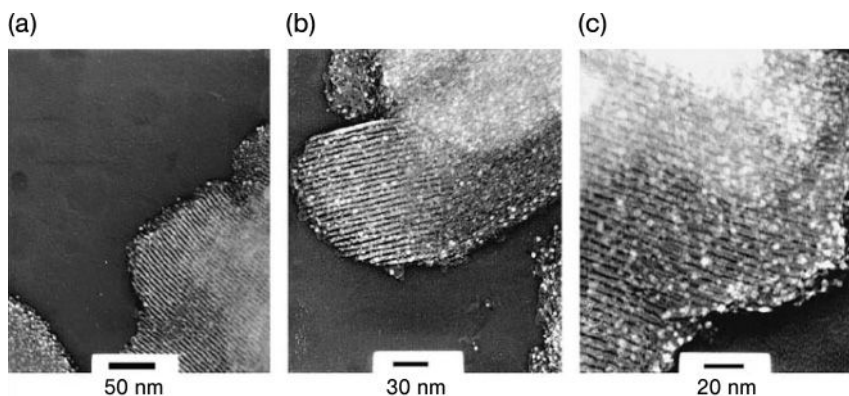
substantially more reactive than the cyclohexane reactant. Thus, under mild conditions it is difficult to achieve, simultaneously, a high conversion and selectivity.

Whilst it is desirable to identify a good catalyst in order to activate the reaction between oxygen and cyclohexane, the technology by which cyclohexane is oxidized by  $O_2$  to produce KA-oil has not yet been improved [138]. In an effort to reduce the use of environmentally harmful elements, heterogeneous catalysts prepared by immobilizing  $Mn^{III}$ ,  $Co^{III}$ ,  $Cr^{III}$  and  $Fe^{III}$  ions on metal oxides have been developed for the oxidation of cyclohexane [139–141], although these systems were subsequently found to suffer from leaching under the reaction conditions used. Mesoporous materials were reported as efficient support materials because in the pores, cyclohexane is oxidized more readily than cyclohexanol, such that the selectivity is enhanced.

### 10.5.1

#### Gold Catalysts

Zhao and coworkers were the first to apply gold nanoparticles for this application, and reported that a supported gold catalyst could activate cyclohexane at  $150^\circ C$ , with selectivities in the region of 90% [142, 143]. Under similar reaction conditions, Kake Zhu and coworkers found that gold nanoparticles immobilized by a variety of methods in the channels of SBA-15 showed a good performance in catalyzing the aerobic oxidation of cyclohexane in a solvent-free system (Figure 10.8) [144], with the highest conversion being reported as 32%. In order to enhance selectivity, the aerobic oxidation of cyclohexane was performed below  $100^\circ C$  and catalyzed by supported Au, Pt, and Pd catalysts [145]. Although, the selectivity for cyclohexanone and cyclohexanol was found to decline rapidly with the enhanced conversion and longer reaction times, the gold catalysts provided an identical performance to the Pt and Pd catalysts.



**Figure 10.8** Representative transmission electron microscopy images. (a) Au-APS/SBA-15; (b, c) Au-SH/SBA-15 at low (b) and high (c) magnification. Reproduced with permission from Ref. [144]; © 2005, Springer, Netherlands.

## 10.5.2

**Silver Catalysts**

Silver catalysts have also found use in hydrocarbon oxidation reactions. Since the granting of the first patent in 1931 for the manufacture of ethylene oxide with an Ag catalyst [146], the industrial production of ethylene oxide by direct oxidation in gas phase has become widely used, with ethylene being converted into ethylene glycol or a variety of other derivatives. In fact, the selective oxidation of ethylene over a supported material represents one of the few uses of silver as an industrially important catalyst, whilst also providing fundamental interests in the surface sciences [112, 147].

Silver has, however, rarely been considered as a catalyst for the selective oxidation of saturated hydrocarbons. Yet, nanoscale silver supported on MCM-41 for the liquid-phase oxidation of cyclohexane was found to be an effective catalyst in the absence of a solvent [148], with a higher turnover number and improved selectivity compared to other support systems of Ag/TS-1 and Ag/Al<sub>2</sub>O<sub>3</sub>.

## 10.5.3

**Copper Catalysts**

Copper nanoparticles supported on natural zeolites of different structure and origin have been utilized for the complete oxidation of hydrocarbons over a temperature range of 170 to 250 °C. Although a complete conversion was reported, this was shown to depend on the Si/Al ratio of the zeolite matrix and the different nanospecies of copper present [149].

## 10.6

**Oxidation of Alcohols and Aldehydes**

The oxidations of alcohols and polyols are important processes in industrial chemistry, and it is not surprising that a significant effort is currently being expended within the scientific community to improve present-day technologies, and in particular to create processes that are more “green.” The objective of these research investigations has been the development of a catalytic system that would compete against a stoichiometric approach involving concentrated and toxic oxidizing agents. Supported platinum and palladium catalysts are well known as effective catalysts for the oxidation of polyols under acidic or basic conditions. Yet, supported gold nanoparticles were also found to be very effective for the oxidation of alcohols, including diols, in the presence of a base [150–157]. These catalysts could also be used in the oxidation of sugars, glucose, and sorbitol [158, 159]. When using dioxygen as the oxidant, Carrettin *et al.* reported a 100% selectivity for the oxidation of glycerol to glycerate, this being catalyzed by an Au catalyst supported on graphite under relatively mild conditions, and with yields approaching 60% [160–162]. In these studies the presence of a base was also found to be essential for both activity and selectivity.

### 10.6.1

#### Gold Catalysts

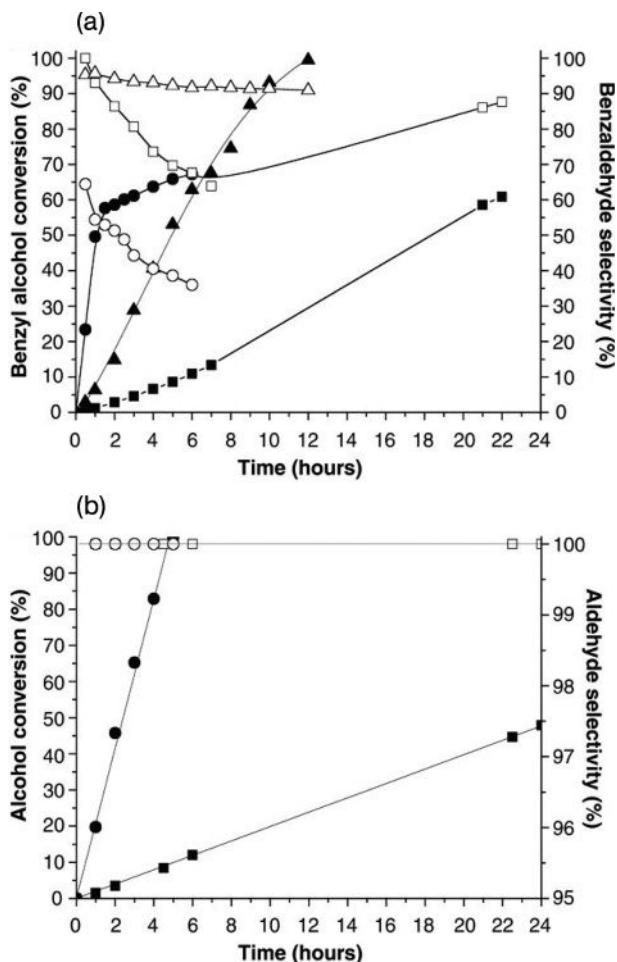
It has been commonly observed that the oxidation of alcohols catalyzed by supported gold catalysts show better performances under basic conditions in terms of high selectivities and reasonable activities, although the mechanism behind this chemistry remains unclear. Another interesting observation is that the types of support used for the gold catalysts, which have important roles in the oxidation of CO and epoxidation, appear to have little effect in the oxidation of alcohols. In fact Rossi and coworkers [163], when monitoring the oxidation of glucose to gluconic acid, found that unsupported colloidal Au particles were equally active as Au nanoparticles supported on active carbon, under the same conditions. A subsequent study extended the application of colloidal gold catalysts to the oxidation of 1,2-diols [164, 165]. The disadvantage of an unsupported colloidal gold catalyst is its poor long-term performance compared to a supported gold nanocatalyst, due to problems of aggregation. Recently, gold nanoclusters stabilized by polymers [166] showed good activity in the aerobic oxidation of benzyl alcohol in aqueous media. However, Corma and coworkers [167, 168] proposed that the support of Au/CeO<sub>2</sub> catalysts could help to stabilize a reactive peroxy intermediate from O<sub>2</sub>, and thus could enhance the activities of gold catalysts in the selective oxidation of alcohols to aldehydes/ketones, and of aldehydes to acids. One further interesting point here was that the gold catalysts functioned well in solvent-free systems without any additional base, a point which differed considerably from earlier findings.

One of the most significant advances in the field of alcohol oxidation, provided by the group of Hutchings [169], indicated that an Au/Pt alloy supported on TiO<sub>2</sub> was a highly active catalyst for the oxidation of benzyl alcohol, cinnamyl alcohol, and vanillyl alcohol. In particular, for the oxidation of benzyl alcohol, the performance of the Au-Pd/TiO<sub>2</sub> catalyst was remarkably superior to that of Au/TiO<sub>2</sub> and Pd/TiO<sub>2</sub> in terms of both conversion and selectivity (Figure 10.9).

### 10.6.2

#### Silver Catalysts

The silver-catalyzed partial oxidation of methanol to formaldehyde, which is an industrially important chemical transformation of alcohols to carbonyls in the gas phase, and is significant in the synthesis of drugs, vitamins, fragrances, and many complex syntheses, was first employed on an industrial scale by BASF AG in 1905 [170, 171]. Since that time, several silver-based catalysts, including bulk and supported systems, have been developed for the oxidation of alcohols. The main problems encountered with bulk silver are low catalytic activities at low temperatures, or the products of cracking and/or overoxidation at higher reaction temperatures. Various attempts have been made to improve the catalytic performance of silver-based catalysts, either by adding additives to the bulk silver catalysts or by dispersing the silver particles on supports [172–175]. Supported silver would be expected to enhance the dispersion and stability of silver, and thus also enhance its catalytic activity at relatively low temperatures. The design of a catalyst combin-



**Figure 10.9** (a) Benzyl alcohol conversion and selectivity in benzaldehyde with the reaction time at 373 K and 0.1 MPa  $pO_2$ . Squares indicate Au/TiO<sub>2</sub>; circles indicate Pd/TiO<sub>2</sub>; triangles indicate Au-Pd/TiO<sub>2</sub>. Solid symbols indicate conversion, open symbols indicate selectivity; (b) Au-Pd/TiO<sub>2</sub>-catalyzed reactions at 363 K, 0.1 MPa  $pO_2$ , for cinnamyl alcohol (squares) and vanillyl alcohol (circles). Solid symbols indicate conversion, open symbols indicate selectivity to the corresponding aldehydes. Reproduced with permission from Ref. [169]; © 2005, RSC Publishing, Cambridge.

ing the advantages of both bulk silver catalysts (conventional electrolytic silver) and supported silver catalysts, with better performance, remains a major research challenge in the area of alcohol catalytic oxidation [176].

Supported platinum and palladium nanoparticles are generally acknowledged as effective catalysts for the oxidation of polyols [177]. *In situ* electrolytic nanosilver/zeolite film/copper grid catalysts have shown higher catalytic oxidation properties towards mono, di, and other types of alcohols, and with higher selectivities

[176, 178]. The silver nanoparticles, when generated *in situ*, highly dispersed on the zeolite film and then precoated on a copper grid, demonstrated excellent activities towards polyhydric alcohol at low temperature. Such performance effectively avoids the problems of both overoxidation and C–C bond cracking at high temperatures, or mild oxidation at low temperatures (as in the case of the practical electrolytic silver catalyst). Au–Ag alloy clusters (size range 1.6–2.2 nm) with various Ag contents (5–30%) and prepared using a coreduction method in the presence of poly(*N*-vinyl-2-pyrrolidone), were investigated in the aerobic oxidation of *p*-hydroxybenzyl alcohol as a model reaction to understand the effect of Ag on the catalytic activity of Au clusters [179]. The rate constants per unit surface area for the Au–Ag:PVP clusters with a small Ag content (<10%) were larger than those of monometallic Au:PVP clusters of comparable size. Spherical nanoparticles anchored on the external walls of a multiwalled carbon nanotube (Ag/MWNT) composite electrode exhibited a high catalytic activity for the electro-oxidation of methanol [180].

## 10.7

### Direct Synthesis of Hydrogen Peroxide

As noted above, there has been much recent interest in the design of new heterogeneous catalysts for selective oxidation under ambient conditions, and these typically use hydrogen peroxide as the oxidant [96]. At present, hydrogen peroxide is produced by the sequential hydrogenation and oxidation of alkyl anthraquinone, with the annual global production approximating  $1.9 \times 10^6$  tons. However, a number of problems are associated with the anthraquinone route, including the cost of the quinone solvent system and a periodic need to replace the anthraquinone because of hydrogenation. In view of this, considerable interest has been expressed in the direct manufacture of hydrogen peroxide from the catalyzed reaction of hydrogen and oxygen. At present, a degree of success has been achieved using Pd as a catalyst, especially when halides are used as promoters. Typically, dilute solutions of hydrogen peroxide are produced, with earlier studies indicating that the Pd catalyst could be combined with an oxidation catalyst, TS-1, such that the hydrogen peroxide produced could be used *in situ*. To date, however, no commercial process exists for the direct manufacture of hydrogen peroxide. Hutchings and coworkers were the first to show that Au/Al<sub>2</sub>O<sub>3</sub> catalysts were effective for the direct reaction, and thus far the best catalysts identified have been Pt–Au alloy supported catalysts (Table 10.2); these showed a better performance than pure Pd or Au catalysts [181, 182]. The suggestion was made that the enhanced activity observed by the addition of Pd to Au was due to an enhanced activation of hydrogen. However, if too much Pd was added, the decomposition activity of the hydrogen peroxide was also enhanced, such that the rate declined.

Subsequently, Ishihara *et al.* [183] have shown that Au/SiO<sub>2</sub> and Au–Pd/SiO<sub>2</sub> catalysts are also effective for this reaction at only 10 °C. In recent studies, Hutchings and coworkers have shown that the selectivity for H<sub>2</sub> utilization could be

**Table 10.2** Formation of H<sub>2</sub>O<sub>2</sub> from the reaction of H<sub>2</sub>/O<sub>2</sub> over Au and Pd catalysts[182].

Catalyst	Solvent <sup>a</sup>	Temperature (°C)	Pressure (MPa)	O <sub>2</sub> /H <sub>2</sub> (molar ratio)	H <sub>2</sub> O <sub>2</sub> mmol g (catalyst) <sup>-1</sup> h <sup>-1</sup>
Au/Al <sub>2</sub> O <sub>3</sub>	CH <sub>3</sub> OH	2	3.7	1.2	1530
Au: Pd (1:1)/ Al <sub>2</sub> O <sub>3</sub>	CH <sub>3</sub> OH	2	3.7	1.2	4460
Pd/Al <sub>2</sub> O <sub>3</sub>	CH <sub>3</sub> OH	2	3.7	1.2	370
Au/ZnO	scCO <sub>2</sub>	35	9.2	1.0	9
Au: Pd (1:3)/ ZnO	scCO <sub>2</sub>	35	9.2	1.1	7
Au: Pd (1:1)/ ZnO	scCO <sub>2</sub>	35	9.2	0.8	12
Au: Pd (3:1)/ ZnO	scCO <sub>2</sub>	35	9.2	0.9	8
Pd/ZnO	scCO <sub>2</sub>	35	9.2	1.3	0

a scCO<sub>2</sub> = supercritical CO<sub>2</sub>.

significantly enhanced when Fe<sub>2</sub>O<sub>3</sub> and TiO<sub>2</sub> were used as supports [184, 185]. Indeed, with short reaction times the selectivity may exceed 95% for the reaction of dilute H<sub>2</sub>/O<sub>2</sub> mixtures (1:1; 5 vol%) diluted with CO<sub>2</sub> (95 vol%). Very high rates of reaction were observed with noncalcined Au–Pd/TiO<sub>2</sub> catalysts, but these proved to be unstable as they lost both Au and Pd during the reaction and could not be successfully reused. However, if the catalysts were calcined at 400 °C prior to use, very stable reusable materials were obtained. Detailed structural investigations of these active stable catalysts, using X-ray photoelectron spectroscopy (XPS) and transmission electron microscopy (TEM), showed that the catalysts have a core–shell structure with a gold-rich core and a palladium-rich shell. It was concluded that the Au was acting as an electronic promotor for the Pd-rich surface of the Au–Pd nanocrystals.

## 10.8

### Conclusions

Although the catalytic processes described in this chapter have provided a good overview of the oxidation catalysis properties of Group 11 metals, this is a far from comprehensive survey of the field. However, this group of metals has provided



the basis for some of the most interesting size- and shape-dependent catalytic phenomena on the nanoscale. Whilst copper and silver have shown interesting and employable properties, the chemistry exhibited by gold on the nanoscale has truly sparked a whole subfield of research that has regularly yielded exciting and unexpected results. As the research groups continue to unravel the chemistry of these nanomaterials, it is likely that revolutionary technologies will follow.

## References

- Burda, C., Chen, X.B., Narayanan, R. and El-Sayed, M.A. (2005) Chemistry and properties of nanocrystals of different shapes. *Chem. Rev.*, **105** (4), 1025–1102.
- Min, B.K. and Friend, C.M. (2007) Heterogeneous gold-based catalysis for green chemistry: low-temperature CO oxidation and propene oxidation. *Chem. Rev.*, **107** (6), 2709–2724.
- Daniel, M.C. and Astruc, D. (2004) Gold nanoparticles: assembly, supramolecular chemistry, quantum-size-related properties, and applications toward biology, catalysis, and nanotechnology. *Chem. Rev.*, **104** (1), 293–346.
- Wieckowski, A., Savinova, E.R. and Vayenas, C.G. (2003) *Catalysis and Electrocatalysis at Nanoparticle Surfaces*, Dekker, New York.
- Bonnemann, H. and Richards, R.M. (2001) Nanoscopic metal particles—Synthetic methods and potential applications. *Eur. J. Inorg. Chem.*, **10**, 2455–2480.
- Xu, Y.P., Tian, Z.J. and Lin, L.W. (2004) Nanostructure and catalytic performance of noble metal solid catalysts. *Chin. J. Catal.*, **25** (4), 331–338.
- Welch, C.W. and Compton, R.G. (2006) The use of nanoparticles in electroanalysis: a review. *Anal. Bioanal. Chem.*, **384** (3), 601–619.
- Thomas, J.M. and Raja, R. (2001) Nanopore and nanoparticle catalysts. *Chem. Rec.*, **1** (6), 448–466.
- Bond, G.C. and Sermon, P.A. (1973) Gold catalysts for olefin hydrogenation. *Gold Bull.*, **6** (1), 102–105.
- Bond, G.C., Sermon, P.A., Webb, G., Buchanan, D.A. and Wells, P.B. (1973) Hydrogenation over supported gold catalysts. *J. Chem. Soc., Chem. Commun.*, (13), 444b–445b.
- Huber, H., McIntosh, D. and Ozin, G.A. (1977) A metal atom model for the oxidation of carbon monoxide to carbon dioxide. The gold atom-carbon monoxide-dioxygen reaction and the gold atom-carbon dioxide reaction. *Inorg. Chem.*, **16** (5), 975–979.
- Haruta, M., Tsubota, S., Kobayashi, T., Kageyama, H., Genet, M.J. and Delmon, B. (1993) Low-temperature oxidation of Co over gold supported on TiO<sub>2</sub>, alpha-Fe<sub>2</sub>O<sub>3</sub>, and Co<sub>3</sub>O<sub>4</sub>. *J. Catal.*, **144** (1), 175–192.
- Grunwaldt, J.D., Kiener, C., Wogerbauer, C. and Baiker, A. (1999) Preparation of supported gold catalysts for low-temperature CO oxidation via “size-controlled” gold colloids. *J. Catal.*, **181** (2), 223–232.
- Teranishi, T. and Miyake, M. (1998) Size control of palladium nanoparticles and their crystal structures. *Chem. Mater.*, **10** (2), 594–600.
- Li, Y., Boone, E. and El-Sayed, M.A. (2002) Size effects of PVP-Pd nanoparticles on the catalytic Suzuki reactions in aqueous solution. *Langmuir*, **18** (12), 4921–4925.
- Narayanan, R. and El-Sayed, M.A. (2003) Effect of catalysis on the stability of metallic nanoparticles: Suzuki reaction catalyzed by PVP-palladium nanoparticles. *J. Am. Chem. Soc.*, **125** (27), 8340–8347.
- Ahmadi, T.S., Wang, Z.L., Green, T.C., Henglein, A. and ElSayed, M.A. (1996) Shape-controlled synthesis of colloidal platinum nanoparticles. *Science*, **272** (5270), 1924–1926.

- 18 Narayanan, R. and El-Sayed, M.A. (2004) Changing catalytic activity during colloidal platinum nanocatalysis due to shape changes: electron-transfer reaction. *J. Am. Chem. Soc.*, **126** (23), 7194–7195.
- 19 Narayanan, R. and El-Sayed, M.A. (2005) Effect of colloidal nanocatalysis on the metallic nanoparticle shape: the Suzuki reaction. *Langmuir*, **21** (5), 2027–2033.
- 20 Sau, T.K., Pal, A. and Pal, T. (2001) Size regime dependent catalysis by gold nanoparticles for the reduction of eosin. *J. Phys. Chem. B*, **105** (38), 9266–9272.
- 21 Crooks, R.M., Zhao, M.Q., Sun, L., Chechik, V. and Yeung, L.K. (2001) Dendrimer-encapsulated metal nanoparticles: synthesis, characterization, and applications to catalysis. *Acc. Chem. Res.*, **34** (3), 181–190.
- 22 Schulz, J., Roucoux, A. and Patin, H. (2000) Stabilized rhodium(0) nanoparticles: a reusable hydrogenation catalyst for arene derivatives in a biphasic water-liquid system. *Chem. Eur. J.*, **6** (4), 618–624.
- 23 Reetz, M.T. and Helbig, W. (1994) Size-selective synthesis of nanostructured transition-metal clusters. *J. Am. Chem. Soc.*, **116** (16), 7401–7402.
- 24 Reetz, M.T. and Quaiser, S.A. (1995) A new method for the preparation of nanostructured metal-clusters. *Angew. Chem. Int. Ed. Engl.*, **34** (20), 2240–2241.
- 25 Michaelis, M. and Henglein, A. (1992) Reduction of Pd(II) in aqueous-solution-stabilization and reactions of an intermediate cluster and Pd colloid formation. *J. Phys. Chem.*, **96** (11), 4719–4724.
- 26 Toshima, N., Takahashi, T. and Hirai, H. (1985) Colloidal platinum catalysts prepared by hydrogen-reduction and photo-reduction in the presence of surfactant. *Chem. Lett.*, **8**, 1245–1248.
- 27 Kurihara, K., Kizling, J., Stenius, P. and Fendler, J.H. (1983) Laser and pulse radiolytically induced colloidal gold formation in water and in water-in-oil microemulsions. *J. Am. Chem. Soc.*, **105** (9), 2574–2579.
- 28 Caruso, R.A., Ashokkumar, M. and Grieser, F. (2000) Sonochemical formation of colloidal platinum. *Colloids Surf. A Physicochem. Eng. Asp.*, **169** (1–3), 219–225.
- 29 Fujimoto, T., Terauchi, S., Umehara, H., Kojima, I. and Henderson, W. (2001) Sonochemical preparation of single-dispersion metal nanoparticles from metal salts. *Chem. Mater.*, **13** (3), 1057–1060.
- 30 Borsla, A., Wilhelm, A.M. and Delmas, H. (2001) Hydrogenation of olefins in aqueous phase, catalyzed by polymer-protected rhodium colloids: kinetic study. *Catal. Today*, **66** (2–4), 389–395.
- 31 Bronstein, L.M., Chernyshov, D.M., Volkov, I.O., Ezernitskaya, M.G., Valetsky, P.M., Matveeva, V.G. and Sulman, E.M. (2000) Structure and properties of bimetallic colloids formed in polystyrene-block-poly-4-vinylpyridine micelles: catalytic behavior in selective hydrogenation of dehydrolinalool. *J. Catal.*, **196** (2), 302–314.
- 32 Scott, R.W.J., Dartye, A.K. and Crooks, R.M. (2003) Bimetallic palladium-platinum dendrimer-encapsulated catalysts. *J. Am. Chem. Soc.*, **125** (13), 3708–3709.
- 33 Pittelkow, M., Moth-Poulsen, K., Boas, U. and Christensen, J.B. (2003) Poly(amidoamine)-dendrimer-stabilized Pd(0) nanoparticles as a catalyst for the Suzuki reaction. *Langmuir*, **19** (18), 7682–7684.
- 34 Lu, Z.H., Liu, G.J., Phillips, H., Hill, J.M., Chang, J. and Kydd, R.A. (2001) Palladium nanoparticle catalyst prepared in poly(acrylic acid)-lined channels of diblock copolymer microspheres. *Nano Lett.*, **1** (12), 683–687.
- 35 Mevellec, V., Roucoux, A., Ramirez, E., Philippot, K. and Chaudret, B. (2004) Surfactant-stabilized aqueous iridium(0) colloidal suspension: an efficient reusable catalyst for hydrogenation of arenes in biphasic media. *Adv. Synth. Catal.*, **346** (1), 72–76.
- 36 Lin, Y. and Finke, R.G. (1994) Novel polyoxoanion-stabilized and bu(4) n(+)-stabilized, isolable, and redissolvable, 20–30-angstrom ir-similar-

- to(300)-(900) nanoclusters—the kinetically controlled synthesis, characterization, and mechanism of formation of organic solvent-soluble, reproducible size, and reproducible catalytic activity metal nanoclusters. *J. Am. Chem. Soc.*, **116** (18), 8335–8353.
- 37 Chen, S.L. and Kucernak, A. (2004) Electrocatalysis under conditions of high mass transport rate: oxygen reduction on single submicrometer-sized Pt particles supported on carbon. *J. Phys. Chem. B*, **108** (10), 3262–3276.
- 38 Liu, Z.L., Ling, X.Y., Lee, J.Y., Su, X.D. and Gan, L.M. (2003) Nanosized Pt and PtRu colloids as precursors for direct methanol fuel cell catalysts. *J. Mater. Chem.*, **13** (12), 3049–3052.
- 39 Fachini, E.R., Diaz-Ayala, R., Casado-Rivera, E., File, S. and Cabrera, C.R. (2003) Surface coordination of ruthenium clusters on platinum nanoparticles for methanol oxidation catalysts. *Langmuir*, **19** (21), 8986–8993.
- 40 Chen, C.W., Serizawa, T. and Akashi, M. (1999) Preparation of platinum colloids on polystyrene nanospheres and their catalytic properties in hydrogenation. *Chem. Mater.*, **11** (5), 1381–1389.
- 41 Eppler, A.S., Rupprechter, G., Anderson, E.A. and Somorjai, G.A. (2000) Thermal and chemical stability and adhesion strength of Pt nanoparticle arrays supported on silica studied by transmission electron microscopy and atomic force microscopy. *J. Phys. Chem. B*, **104** (31), 7286–7292.
- 42 Grunes, J., Zhu, J., Anderson, E.A. and Somorjai, G.A. (2002) Ethylene hydrogenation over platinum nanoparticle array model catalysts fabricated by electron beam lithography: determination of active metal surface area. *J. Phys. Chem. B*, **106** (44), 11463–11468.
- 43 Rashid, H. and Mandal, T.K. (2007) Synthesis and catalytic application of nanostructured silver dendrites. *J. Phys. Chem. C*, **111** (45), 16750–16760.
- 44 Zhang, W., Qiao, X. and Chen, J. (2007) Synthesis and UV-Vis spectral properties of silver nanoparticles. *Rare Metal Mater. Eng.*, **36**, 64–70.
- 45 Zhang, T.W., Zhang, L., Yang, S.C., Yang, Z.N. and Ding, B.J. (2007) Shape-controlled synthesis and applications of silver nano-particles. *Rare Metal Mater. Eng.*, **36** (8), 1495–1499.
- 46 Eastoe, J., Hollamby, M.J. and Hudson, L. (2006) Recent advances in nanoparticle synthesis with reversed micelles. *Adv. Colloid Interface Sci.*, **128**, 5–15.
- 47 Bajpai, S.K., Mohan, Y.M., Bajpai, M., Tankhiwale, R. and Thomas, V. (2007) Synthesis of polymer stabilized silver and gold nanostructures. *J. Nanosci. Nanotechnol.*, **7** (9), 2994–3010.
- 48 Anandan, S. and Yang, S.H. (2007) Emergent methods to synthesize and characterize semiconductor CuO nanoparticles with various morphologies—an overview. *J. Exp. Nanosci.*, **2** (1–2), 23–56.
- 49 Aymonier, C., Loppinet-Serani, A., Reveron, H., Garrabos, Y. and Cancsall, F. (2006) Review of supercritical fluids in inorganic materials science. *J. Supercrit. Fluids*, **38** (2), 242–251.
- 50 Salzemann, C., Lisiecki, L., Urban, J. and Pileni, M.P. (2004) Anisotropic copper nanocrystals synthesized in a supersaturated medium: Nanocrystal growth. *Langmuir*, **20** (26), 11772–11777.
- 51 Haruta, M. (2004) Gold as a novel catalyst in the 21st century: preparation, working mechanism and applications. *Gold Bull.*, **37** (1–2), 27–36.
- 52 Haruta, M., Yamada, N., Kobayashi, T. and Iijima, S. (1989) Gold catalysts prepared by coprecipitation for low-temperature oxidation of hydrogen and of carbon-monoxide. *J. Catal.*, **115** (2), 301–309.
- 53 Kageyama, H., Kamijo, N., Kobayashi, T. and Haruta, M. (1989) XAFS studies of ultra-fine gold catalysts supported on hematite prepared from coprecipitated precursors. *Physica B*, **158** (1–3), 183–184.
- 54 Sanchez, R.M.T., Ueda, A., Tanaka, K. and Haruta, M. (1997) Selective oxidation of CO in hydrogen over gold supported on manganese oxides. *J. Catal.*, **168** (1), 125–127.

- 55 Shibata, M., Kawata, N., Masumoto, T. and Kimura, H. (1985) CO hydrogenation over an amorphous gold-zirconium alloy. *Chem. Lett.*, **11**, 1605–1608.
- 56 Kobayashi, T., Haruta, M., Tsubota, S., Sano, H. and Delmon, B. (1990) Thin-films of supported gold catalysts for CO detection. *Sens. Actuators B Chem.*, **1** (1–6), 222–225.
- 57 Vogel, W., Cunningham, D.A.H., Tanaka, K. and Haruta, M. (1996) Structural analysis of Au/Mg(OH)(2) during deactivation by Debye function analysis. *Catal. Lett.*, **40** (3–4), 175–181.
- 58 Yuan, Y.Z., Kozlova, A.P., Asakura, K., Wan, H.L., Tsai, K. and Iwasawa, Y. (1997) Supported Au catalysts prepared from Au phosphine complexes and As-precipitated metal hydroxides: characterization and low-temperature CO oxidation. *J. Catal.*, **170** (1), 191–199.
- 59 Okumura, M. and Haruta, M. (2000) Preparation of supported gold catalysts by liquid-phase grafting of gold acetylacetonate for low-temperature oxidation of CO and of H<sub>2</sub>. *Chem. Lett.*, **4**, 396–397.
- 60 Okumura, M., Tanaka, K., Ueda, A. and Haruta, M. (1997) The reactivities of dimethylgold(III)beta-diketone on the surface of TiO<sub>2</sub>—a novel preparation method for Au catalysts. *Solid State Ionics*, **95** (1–2), 143–149.
- 61 Okumura, M., Tsubota, S., Iwamoto, M. and Haruta, M. (1998) Chemical vapor deposition of gold nanoparticles on MCM-41 and their catalytic activities for the low-temperature oxidation of CO and of H<sub>2</sub>. *Chem. Lett.*, **4**, 315–316.
- 62 Wallace, W.T. and Whetten, R.L. (2000) Carbon monoxide adsorption on selected gold clusters: highly size-dependent activity and saturation compositions. *J. Phys. Chem. B*, **104** (47), 10964–10968.
- 63 Kishi, K., Date, M. and Haruta, M. (2001) Effect of gold on the oxidation of the Si(111)-7 × 7 surface. *Surf. Sci.*, **486** (3), L475–L479.
- 64 Valden, M., Pak, S., Lai, X. and Goodman, D.W. (1998) Structure sensitivity of CO oxidation over model Au/TiO<sub>2</sub> catalysts. *Catal. Lett.*, **56** (1), 7–10.
- 65 Yan, W.F., Chen, B., Mahurin, S.M., Hageman, E.W., Dai, S. and Overbury, S.H. (2004) Surface sol-gel modification of mesoporous silica materials with TiO<sub>2</sub> for the assembly of ultrasmall gold nanoparticles. *J. Phys. Chem. B*, **108** (9), 2793–2796.
- 66 Haruta, M., Kobayashi, T., Sano, H. and Yamada, N. (1987) Novel gold catalysts for the oxidation of carbon-monoxide at a temperature far below 0-degrees-C. *Chem. Lett.*, **2**, 405–408.
- 67 Sakurai, H. and Haruta, M. (1995) Carbon-dioxide and carbon-monoxide hydrogenation over gold supported on titanium, iron, and zinc-oxides. *Appl. Catal. A Gen.*, **127** (1–2), 93–105.
- 68 Sakurai, H., Ueda, A., Kobayashi, T. and Haruta, M. (1997) Low-temperature water-gas shift reaction over gold deposited on TiO<sub>2</sub>. *Chem. Commun.*, (3), 271–272.
- 69 Cosandey, F., Zhang, L. and Madey, T.E. (2001) Effect of substrate temperature on the epitaxial growth of Au on TiO<sub>2</sub>(110). *Surf. Sci.*, **474** (1–3), 1–13.
- 70 Kozlov, A.I., Kozlova, A.P., Liu, H.C. and Iwasawa, Y. (1999) A new approach to active supported Au catalysts. *Appl. Catal. A Gen.*, **182** (1), 9–28.
- 71 Dekkers, M.A.P., Lippits, M.J. and Nieuwenhuys, B.E. (1998) CO adsorption and oxidation on Au/TiO<sub>2</sub>. *Catal. Lett.*, **56** (4), 195–197.
- 72 Boccuzzi, F., Chiorino, A., Manzoli, M., Lu, P., Akita, T., Ichikawa, S. and Haruta, M. (2001) Au/TiO<sub>2</sub> nanosized samples: a catalytic, TEM, and FTIR study of the effect of calcination temperature on the CO oxidation. *J. Catal.*, **202** (2), 256–267.
- 73 Mavrikakis, M., Stoltze, P. and Norskov, J.K. (2000) Making gold less noble. *Catal. Lett.*, **64** (2–4), 101–106.
- 74 Hammer, B. and Norskov, J.K. (1995) Why gold is the noblest of all the metals. *Nature*, **376** (6537), 238–240.
- 75 Guzman, J., Carrettin, S., Fierro-Gonzalez, J.C., Hao, Y.L., Gates, B.C. and Corma, A. (2005) CO oxidation catalyzed by supported gold: cooperation

- between gold and nanocrystalline rare-earth supports forms reactive surface superoxide and peroxide species. *Angew. Chem. Int. Ed. Engl.*, **44** (30), 4778–4781.
- 76** Qiao, B.T. and Deng, Y.Q. (2003) Highly effective ferric hydroxide supported gold catalyst for selective oxidation of CO in the presence of H<sub>2</sub>. *Chem. Commun.*, (17), 2192–2193.
- 77** Bond, G.C. and Thompson, D.T. (2000) Gold-catalysed oxidation of carbon monoxide. *Gold Bull.*, **33** (2), 41–51.
- 78** Haruta, M. (2002) Catalysis of gold nanoparticles deposited on metal oxides. *CatTech*, **6** (3), 102–115.
- 79** Qu, Z.P., Cheng, M.J., Dong, X.L. and Bao, X.H. (2004) Kx, CO selective oxidation in H<sub>2</sub>-rich gas over Ag nanoparticles—effect of oxygen treatment temperature on the activity of silver particles mechanically mixed with SiO<sub>2</sub>. *Catal. Today*, **93–95**, 247–255.
- 80** Qu, Z., Huang, W., Cheng, M. and Bao, X. (2005) Restructuring and redispersion of silver on SiO<sub>2</sub> under oxidizing/reducing atmospheres and its activity toward CO oxidation. *J. Phys. Chem. B*, **109** (33), 15842–15848.
- 81** Yang, M.X., Jacobs, P.W., Yoon, C., Muray, L., Anderson, E., Attwood, D. and Somorjai, G.A. (1997) Thermal stability of uniform silver clusters prepared on oxidized silicon and aluminum surfaces by electron beam lithography in oxidizing and reducing ambients. *Catal. Lett.*, **45** (1–2), 5–13.
- 82** Aoyama, N., Yoshida, K., Abe, A. and Miyadera, T. (1997) Characterization of highly active silver catalyst for NOx reduction in lean-burning engine exhaust. *Catal. Lett.*, **43** (3–4), 249–253.
- 83** Jin, L., Qian, K., Jiang, Z.Q. and Huang, W.X. (2007) Ag/SiO<sub>2</sub> catalysts prepared via gamma-ray irradiation and their catalytic activities in CO oxidation. *J. Mol. Catal. A Chem.*, **274** (1–2), 95–100.
- 84** Narayanan, R. and El-Sayed, M.A. (2004) Shape-dependent catalytic activity of platinum nanoparticles in colloidal solution. *Nano Lett.*, **4** (7), 1343–1348.
- 85** Lim, D.C., Lopez-Salido, I. and Kim, Y.D. (2005) Size selectivity for CO-oxidation of Ag nanoparticles on highly ordered pyrolytic graphite (HOPG). *Surf. Sci.*, **598** (1–3), 96–103.
- 86** Wang, A.Q., Hsieh, Y., Chen, Y.F. and Mou, C.Y. (2006) Au-Ag alloy nanoparticle as catalyst for CO oxidation: effect of Si/Al ratio of mesoporous support. *J. Catal.*, **237** (1), 197–206.
- 87** Wang, A.Q., Chang, C.M. and Mou, C.Y. (2005) Evolution of catalytic activity of Au-Ag bimetallic nanoparticles on mesoporous support for CO oxidation. *J. Phys. Chem. B*, **109** (40), 18860–18867.
- 88** Liu, J.H., Wang, A.Q., Chi, Y.S., Lin, H.P. and Mou, C.Y. (2005) Synergistic effect in an Au-Ag alloy nanocatalyst: CO oxidation. *J. Phys. Chem. B*, **109** (1), 40–43.
- 89** Arena, F., Famulari, P., Trunfio, G., Bonura, G., Frusteri, F. and Spadaro, L. (2006) Probing the factors affecting structure and activity of the Au/CeO<sub>2</sub> system in total and preferential oxidation of CO. *Appl. Catal. B Environ.*, **66** (1–2), 81–91.
- 90** Lippits, M.J., Gluhoi, A.C. and Nieuwenhuys, B.E. (2007) A comparative study of the effect of addition of CeOx and Li<sub>2</sub>O on gamma-Al<sub>2</sub>O<sub>3</sub> supported copper, silver and gold catalysts in the preferential oxidation of CO. *Top. Catal.*, **44** (1–2), 159–165.
- 91** Shim, I.W., Noh, W.T., Kwon, J., Cho, J.Y., Kim, K.S. and Kang, D.H. (2002) Preparation of copper nanoparticles in cellulose acetate polymer and the reaction chemistry of copper complexes in the polymer. *Bull. Korean Chem. Soc.*, **23** (4), 563–566.
- 92** Tu, C.H., Wang, A.Q., Zheng, M.Y., Wang, X.D. and Zhang, T. (2006) Factors influencing the catalytic activity of SBA-15-supported copper nanoparticles in CO oxidation. *Appl. Catal. A Gen.*, **297** (1), 40–47.
- 93** Hayashi, T., Tanaka, K. and Haruta, M. (1998) Selective vapor-phase epoxidation of propylene over Au/TiO<sub>2</sub> catalysts in the presence of oxygen and hydrogen. *J. Catal.*, **178** (2), 566–575.
- 94** Meiers, R., Dingerdissen, U. and Holderich, W.F. (1998) Synthesis of propylene oxide from propylene, oxygen,

- and hydrogen catalyzed by palladium-platinum-containing titanium silicalite. *J. Catal.*, **176** (2), 376–386.
- 95** Laufer, W. and Hoelderich, W.F. (2001) Direct oxidation of propylene and other olefins on precious metal containing Ti-catalysts. *Appl. Catal. A Gen.*, **213** (2), 163–171.
- 96** Jenzer, G., Mallat, T., Maciejewski, M., Eigenmann, F. and Baiker, A. (2001) Continuous epoxidation of propylene with oxygen and hydrogen on a Pd-Pt/Ts-1 catalyst. *Appl. Catal. A Gen.*, **208** (1–2), 125–133.
- 97** Haruta, M., Uphade, B.S., Tsubota, S. and Miyamoto, A. (1998) Selective oxidation of propylene over gold deposited on titanium-based oxides. *Res. Chem. Intermed.*, **24** (3), 329–336.
- 98** Sinha, A.K., Seelan, S., Tsubota, S. and Haruta, M. (2004) A three-dimensional mesoporous titanosilicate support for gold nanoparticles: vapor-phase epoxidation of propene with high conversion. *Angew. Chem. Int. Ed. Engl.*, **43** (12), 1546–1548.
- 99** Sinha, A.K., Seelan, S., Okumura, M., Akita, T., Tsubota, S. and Haruta, M. (2005) Three-dimensional mesoporous titanosilicates prepared by modified sol-gel method: ideal gold catalyst supports for enhanced propene epoxidation. *J. Phys. Chem. B*, **109** (9), 3956–3965.
- 100** Mul, G., Zwijnenburg, A., van der Linden, B., Makkee, M. and Moulijn, J.A. (2001) Stability and selectivity of Au/TiO<sub>2</sub> and Au/TiO<sub>2</sub>/SiO<sub>2</sub> catalysts in propene epoxidation: an in situ FT-IR study. *J. Catal.*, **201** (1), 128–137.
- 101** Zwijnenburg, A., Saleh, M., Makkee, M. and Moulijn, J.A. (2002) Direct gas-phase epoxidation of propene over bimetallic Au catalysts. *Catal. Today*, **72** (1–2), 59–62.
- 102** Hughes, M.D., Xu, Y.J., Jenkins, P., McMorn, P., Landon, P., Enache, D.I., Carley, A.F., Attard, G.A., Hutchings, G.J., King, F., Stitt, E.H., Johnston, P., Griffin, K. and Kiely, C.J. (2005) Tunable gold catalysts for selective hydrocarbon oxidation under mild conditions. *Nature*, **437** (7062), 1132–1135.
- 103** Stangland, E.E., Stavens, K.B., Andres, R.P. and Delgass, W.N. (2000) Characterization of gold-titania catalysts via oxidation of propylene to propylene oxide. *J. Catal.*, **191** (2), 332–347.
- 104** Lambert, R.M., Williams, F.J., Cropley, R.L. and Palermo, A. (2005) Heterogeneous alkene epoxidation: past, present and future. *J. Mol. Catal. A Chem.*, **228** (1–2), 27–33.
- 105** Sachtler, W.M.H., Backx, C. and Vansanten, R.A. (1981) On the mechanism of ethylene epoxidation. *Catal. Rev. Sci. Eng.*, **23** (1–2), 127–149.
- 106** Sajkowski, D.J. and Boudart, M. (1987) Structure sensitivity of the catalytic-oxidation of ethene by silver. *Catal. Rev. Sci. Eng.*, **29** (4), 325–360.
- 107** Vansanten, R.A. and Kuipers, H. (1987) The mechanism of ethylene epoxidation. *Adv. Catal.*, **35**, 265–321.
- 108** Verykios, X.E., Stein, F.P. and Coughlin, R.W. (1980) Oxidation of ethylene over silver—adsorption, kinetics, catalyst. *Catal. Rev. Sci. Eng.*, **22** (2), 197–234.
- 109** Yong, Y.S. and Cant, N.W. (1990) Ethylene oxidation over silver catalysts—a study of mechanism using nitrous-oxide and isotopically labeled oxygen. *J. Catal.*, **122** (1), 22–33.
- 110** Tan, S.A., Grant, R.B. and Lambert, R.M. (1987) Pressure-dependence of ethylene oxidation-kinetics and the effects of added CO<sub>2</sub> and Cs—a study on Ag(111) and Ag/alpha-Al<sub>2</sub>O<sub>3</sub> catalysts. *Appl. Catal.*, **31** (1), 159–77.
- 111** Tan, S.A., Grant, R.B. and Lambert, R.M. (1987) Secondary chemistry in the selective oxidation of ethylene—effect of Cl and Cs promoters on the adsorption, isomerization, and combustion of ethylene-oxide on Ag(111). *J. Catal.*, **106** (1), 54–64.
- 112** Serafin, J.G., Liu, A.C. and Seyedmonir, S.R. (1998) Surface science and the silver-catalyzed epoxidation of ethylene: an industrial perspective. *J. Mol. Catal. A Chem.*, **131** (1–3), 157–168.
- 113** Nagy, A., Mestl, G., Ruhle, T., Weinberg, G. and Schlögl, R. (1998) The dynamic restructuring of electrolytic silver during the formaldehyde synthesis reaction. *J. Catal.*, **179** (2), 548–559.

- 114 Campbell, C.T. (1986) Chlorine promoters in selective ethylene epoxidation over Ag(111)—a comparison with Ag(110). *J. Catal.*, **99** (1), 28–38.
- 115 Campbell, C.T. and Koel, B.E. (1985) Chlorine promotion of selective ethylene oxidation over Ag(110)—kinetics and mechanism. *J. Catal.*, **92** (2), 272–283.
- 116 Campbell, C.T. (1985) Cs-promoted Ag(111)—model studies of selective ethylene oxidation catalysts. *J. Phys. Chem.*, **89** (26), 5789–5795.
- 117 Goncharova, S.N., Paukshtis, E.A. and Balzhinimaev, B.S. (1995) Size effects in ethylene oxidation on silver catalysts—influence of support and Cs promoter. *Appl. Catal. A Gen.*, **126** (1), 67–84.
- 118 Grant, R.B., Harbach, C.A.J., Lambert, R.M. and Tan, S.A. (1987) Alkali-metal, chlorine and other promoters in the silver-catalyzed selective oxidation of ethylene. *J. Chem. Soc., Faraday Trans. I*, **83**, 2035–2046.
- 119 Shiraishi, Y. and Toshima, N. (1999) Colloidal silver catalysts for oxidation of ethylene. *J. Mol. Catal. A Chem.*, **141** (1–3), 187–192.
- 120 Shiraishi, Y. and Toshima, N. (2000) Oxidation of ethylene catalyzed by colloidal dispersions of poly(sodium acrylate)-protected silver nanoclusters. *Colloids Surf. A Physicochem. Eng. Asp.*, **169** (1–3), 59–66.
- 121 Verykios, X.E., Stein, F.P. and Coughlin, R.W. (1980) Influence of metal crystallite size and morphology on selectivity and activity of ethylene oxidation catalyzed by supported silver. *J. Catal.*, **66** (2), 368–382.
- 122 Lee, J.K., Verykios, X.E. and Pitchai, R. (1989) Support and crystallite size effects in ethylene oxidation catalysis. *Appl. Catal.*, **50** (2), 171–188.
- 123 Bukhtiyarov, V.I. and Kaichev, V.V. (2000) The combined application of XPS and TPD to study of oxygen adsorption on graphite-supported silver clusters. *J. Mol. Catal. A Chem.*, **158** (1), 167–172.
- 124 Podgornov, E.A., Prosvirin, I.P. and Bukhtiyarov, V.I. (2000) XPS, TPD and TPR studies of Cs-O complexes on silver: their role in ethylene epoxidation. *J. Mol. Catal. A Chem.*, **158** (1), 337–343.
- 125 Minahan, D.M., Hoflund, G.B., Epling, W.S. and Schoenfeld, D.W. (1997) Study of Cs-promoted, alpha-alumina-supported silver, ethylene epoxidation catalysts. 3. Characterization of Cs-promoted and nonpromoted catalysts. *J. Catal.*, **168** (2), 393–399.
- 126 Kim, Y.C., Park, N.C., Shin, J.S., Lee, S.R., Lee, Y.J. and Moon, D.J. (2003) Partial oxidation of ethylene to ethylene oxide over nanosized Ag/alpha-Al<sub>2</sub>O<sub>3</sub> catalysts. *Catal. Today*, **87** (1–4), 153–162.
- 127 de Oliveira, A.L., Wolf, A. and Schuth, F. (2001) Highly selective propene epoxidation with hydrogen/oxygen mixtures over titania-supported silver catalysts. *Catal. Lett.*, **73** (2–4), 157–160.
- 128 Nijhuis, T.A., Makkee, M., Moulijn, J.A. and Weckhuysen, B.M. (2006) The production of propene oxide: catalytic processes and recent developments. *Ind. Eng. Chem. Res.*, **45** (10), 3447–3459.
- 129 Maayan, G. and Neumann, R. (2005) Direct aerobic epoxidation of alkenes catalyzed by metal nanoparticles stabilized by the H5PV2Mo10O40 polyoxometalate. *Chem. Commun.*, (36), 4595–4597.
- 130 Chimentao, R.J., Medina, F., Sueiras, J.E., Fierro, J.L.G., Cesteros, Y. and Salagre, P. (2007) Effects of morphology and cesium promotion over silver nanoparticles catalysts in the styrene epoxidation. *J. Mater. Sci.*, **42** (10), 3307–3314.
- 131 Chimentao, R.J., Kirm, I., Medina, F., Rodriguez, X., Cesteros, Y., Salagre, P., Sueiras, J.E. and Fierro, J.L.G. (2005) Sensitivity of styrene oxidation reaction to the catalyst structure of silver nanoparticles. *Appl. Surf. Sci.*, **252** (3), 793–800.
- 132 Chimentao, R.J., Kirm, I., Medina, F., Rodriguez, X., Cesteros, Y., Salagre, P. and Sueiras, J.E. (2004) Different morphologies of silver nanoparticles as catalysts for the selective oxidation of styrene in the gas phase. *Chem. Commun.*, (7), 846–847.



- 133 Chimentao, R.J., Medina, F., Fierro, J.L.G., Sueiras, J.E., Cesteros, Y. and Salagre, P. (2006) Styrene epoxidation over cesium promoted silver nanowires catalysts. *J. Mol. Catal. A Chem.*, **258** (1–2), 346–354.
- 134 Chimentao, R.J., Barrabes, N., Medina, F., Fierro, J.L.G., Sueiras, J.E., Cesteros, Y. and Salagre, P. (2006) Synthesis, characterization and catalytic activity of metal nanoparticles in the selective oxidation of olefins in the gas phase. *J. Exp. Nanosci.*, **1** (4), 399–418.
- 135 Suresh, A.K., Sharma, M.M. and Sridhar, T. (2000) Engineering aspects of industrial liquid-phase air oxidation of hydrocarbons. *Ind. Eng. Chem. Res.*, **39** (11), 3958–3997.
- 136 Thomas, J.M., Raja, R., Sankar, G. and Bell, R.G. (1999) Molecular-sieve catalysts for the selective oxidation of linear alkanes by molecular oxygen. *Nature*, **398** (6724), 227–230.
- 137 Schuchardt, U., Cardoso, D., Sercheli, R., Pereira, R., de Cruz, R.S., Guerreiro, M.C., Mandelli, D., Spinace, E.V. and Fires, E.L. (2001) Cyclohexane oxidation continues to be a challenge. *Appl. Catal. A Gen.*, **211** (1), 1–17.
- 138 Sheldon, R.A., Arends, I. and Lempers, H.E.B. (1998) Liquid phase oxidation at metal ions and complexes in constrained environments. *Catal. Today*, **41** (4), 387–407.
- 139 Nowotny, M., Pedersen, L.N., Hanefeld, U. and Maschmeyer, T. (2002) Increasing the ketone selectivity of the cobalt-catalyzed radical chain oxidation of cyclohexane. *Chem. Eur. J.*, **8** (16), 3724–3731.
- 140 Yuan, H.X., Xia, Q.H., Zhan, H.J., Lu, X.H. and Su, K.X. (2006) Catalytic oxidation of cyclohexane to cyclohexanone and cyclohexanol by oxygen in a solvent-free system over metal-containing ZSM-5 catalysts. *Appl. Catal. A Gen.*, **304** (1), 178–184.
- 141 Anand, R., Hamdy, M.S., Gkourgkoulas, P., Maschmeyer, T., Jansen, J.C. and Hanefeld, U. (2006) Liquid phase oxidation of cyclohexane over transition metal incorporated amorphous 3D-mesoporous silicates M-TUD-1 (M = Ti, Fe, Co and Cr). *Catal. Today*, **117** (1–3), 279–283.
- 142 Zhao, R., Ji, D., Lv, G.M., Qian, G., Yan, L., Wang, X.L. and Suo, J.S. (2004) A highly efficient oxidation of cyclohexane over Au/ZSM-5 molecular sieve catalyst with oxygen as oxidant. *Chem. Commun.*, (7), 904–905.
- 143 Lu, G.M., Zhao, R., Qian, G., Qi, Y.X., Wang, X.L. and Suo, J.S. (2004) A highly efficient catalyst Au/MCM-41 for selective oxidation cyclohexane using oxygen. *Catal. Lett.*, **97** (3–4), 115–118.
- 144 Zhu, K.K., Hu, J.C. and Richards, R. (2005) Aerobic oxidation of cyclohexane by gold nanoparticles immobilized upon mesoporous silica. *Catal. Lett.*, **100** (3–4), 195–199.
- 145 Xu, Y.J., Landon, P., Enache, D., Carley, A., Roberts, M. and Hutchings, G. (2005) Selective conversion of cyclohexane to cyclohexanol and cyclohexanone using a gold catalyst under mild conditions. *Catal. Lett.*, **101** (3–4), 175–179.
- 146 Lefort, T.E. (1931) Société Française de Catalyse Generalisée, French Patent 729952, p. 562.
- 147 van Santen, R.A. and Kuipers, H.P.C.E. (1987) *Advances in Catalysis*, Vol. 35, Academic Press, London, pp. 265–321.
- 148 Zhao, H., Zhou, J.C., Luo, H., Zeng, C.Y., Li, D.H. and Liu, Y.J. (2006) Synthesis, characterization of Ag/MCM-41 and the catalytic performance for liquid-phase oxidation of cyclohexane. *Catal. Lett.*, **108** (1–2), 49–54.
- 149 Petranovskii, V.P., Pestryakov, A.N., Kazantseva, L.K., Barraza, F.F.C. and Farias, M. (2005) Formation of catalytically active copper nanoparticles in natural zeolites for complete oxidation of hydrocarbons. *Int. J. Mod. Phys. B*, **19** (15–17), 2333–2338.
- 150 Prati, L. and Rossi, M. (1997) Chemoselective catalytic oxidation of polyols with dioxygen oil gold supported catalysts, in *3rd World Congress on Oxidation Catalysis*, Vol. 110, Elsevier, Amsterdam, pp. 509–516.
- 151 Prati, L. and Rossi, M. (1998) Gold on carbon as a new catalyst for selective

- liquid phase oxidation of diols. *J. Catal.*, **176** (2), 552–560.
- 152** Prati, L. and Martra, G. (1999) New gold catalysts for liquid phase oxidation. *Gold Bull.*, **32** (3), 96–101.
- 153** Porta, F., Prati, L., Rossi, M., Coluccia, S. and Martra, G. (2000) Metal sols as a useful tool for heterogeneous gold catalyst preparation: reinvestigation of a liquid phase oxidation. *Catal. Today*, **61** (1–4), 165–172.
- 154** Porta, F., Prati, L., Rossi, M. and Scari, G. (2002) New Au(0) sols as precursors for heterogeneous liquid-phase oxidation catalysts. *J. Catal.*, **211** (2), 464–469.
- 155** Bianchi, C.L., Biella, S., Gervasini, A., Prati, L. and Rossi, M. (2003) Gold on carbon: influence of support properties on catalyst activity in liquid-phase oxidation. *Catal. Lett.*, **85** (1–2), 91–96.
- 156** Biella, S., Porta, F., Prati, L. and Rossi, M. (2003) Surfactant-protected gold particles: new challenge for gold-on-carbon catalysts. *Catal. Lett.*, **90** (1–2), 23–29.
- 157** Dimitratos, N., Lopez-Sanchez, J.A., Morgan, D., Carley, A., Prati, L. and Hutchings, G.J. (2007) Solvent free liquid phase oxidation of benzyl alcohol using Au supported catalysts prepared using a sol immobilization technique. *Catal. Today*, **122** (3–4), 317–324.
- 158** Comotti, M., Della Pina, C., Matarrese, R., Rossi, M. and Siani, A. (2005) Oxidation of alcohols and sugars using Au/C catalysts—Part 2. Sugars. *Appl. Catal. A Gen.*, **291** (1–2), 204–209.
- 159** Beltrame, P., Comotti, M., Della Pina, C. and Rossi, M. (2006) Aerobic oxidation of glucose II. Catalysis by colloidal gold. *Appl. Catal. A Gen.*, **297** (1), 1–7.
- 160** Carrettin, S., McMorn, P., Johnston, P., Griffin, K. and Hutchings, G.J. (2002) Selective oxidation of glycerol to glyceric acid using a gold catalyst in aqueous sodium hydroxide. *Chem. Commun.*, (7), 696–697.
- 161** Carrettin, S., McMorn, P., Johnston, P., Griffin, K., Kiely, C.J. and Hutchings, G.J. (2003) Oxidation of glycerol using supported Pt, Pd and Au catalysts. *Phys. Chem. Chem. Phys.*, **5** (6), 1329–1336.
- 162** Carrettin, S., McMorn, P., Johnston, P., Griffin, K., Kiely, C.J., Attard, G.A. and Hutchings, G.J. (2004) Oxidation of glycerol using supported gold catalysts. *Top. Catal.*, **27** (1–4), 131–136.
- 163** Comotti, M., Della Pina, C., Matarrese, R. and Rossi, M. (2004) The catalytic activity of “Naked” gold particles. *Angew. Chem. Int. Ed. Engl.*, **43** (43), 5812–5815.
- 164** Mertens, P.G.N., Bulut, M., Gevers, L.E.M., Vankelecom, I.F.J., Jacobs, P.A. and De Vos, D.E. (2005) Catalytic oxidation of 1,2-diols to alpha-hydroxy-carboxylates with stabilized gold nanocolloids combined with a membrane-based catalyst separation. *Catal. Lett.*, **102** (1–2), 57–61.
- 165** Mertens, P.G.N., Vankelecom, I.F.J., Jacobs, P.A. and De Vos, D.E. (2005) Gold nanoclusters as colloidal catalysts for oxidation of long chain aliphatic 1,2-diols in alcohol solvents. *Gold Bull.*, **38** (4), 157–162.
- 166** Tsunoyama, H., Sakurai, H., Negishi, Y. and Tsukuda, T. (2005) Size-specific catalytic activity of polymer-stabilized gold nanoclusters for aerobic alcohol oxidation in water. *J. Am. Chem. Soc.*, **127** (26), 9374–9375.
- 167** Abad, A., Concepcion, P., Corma, A. and Garcia, H. (2005) A collaborative effect between gold and a support induces the selective oxidation of alcohols. *Angew. Chem. Int. Ed. Engl.*, **44** (26), 4066–4069.
- 168** Corma, A. and Domine, M.E. (2005) Gold supported on a mesoporous CeO<sub>2</sub> matrix as an efficient catalyst in the selective aerobic oxidation of aldehydes in the liquid phase. *Chem. Commun.*, (32), 4042–4044.
- 169** Enache, D.I., Edwards, J.K., Landon, P., Solsona-Espriu, B., Carley, A.F., Herzing, A.A., Watanabe, M., Kiely, C.J., Knight, D.W. and Hutchings, G.J. (2006) Solvent-free oxidation of primary alcohols to aldehydes using Au-Pd/TiO<sub>2</sub> catalysts. *Science*, **311** (5759), 362–365.
- 170** Reuss, G., Disteldorf, D., Grundler, O. and Hilt, A. (1988) “Formaldehyde” in *Ullmann’s Encyclopedia of Industrial Chemistry*, Vol. A11, 5th edn, VCH Verlag GmbH, Weinheim.

- 171 Gerberich, H.R. and Seaman, G.C. (1994) Formaldehyde. In *Kirk-Othmer Encyclopedia of Chemical Technology*, Vol. 11, 4th edn, John Wiley & Sons, Inc., New York.
- 172 Pestryakov, A.N., Petranovskii, V.P., Pfander, N. and Knop-Gericke, A. (2004) Supported foam-copper catalysts for methanol selective oxidation. *Catal. Commun.*, 5 (12), 777–781.
- 173 Dai, W.L., Yong, C., Ren, L.P., Yang, X.L., Xu, J.H., Li, H.X., He, H.Y. and Fan, K.N. (2004) Ag-SiO<sub>2</sub>-Al<sub>2</sub>O<sub>3</sub> composite as highly active catalyst for the formation of formaldehyde from the partial oxidation of methanol. *J. Catal.*, 228 (1), 80–91.
- 174 Pestryakov, A.N. (1996) Modification of silver catalysts for oxidation of methanol to formaldehyde. *Catal. Today*, 28 (3), 239–244.
- 175 Pestryakov, A., Davydov, A. and Tsyrlunikov, P. (1996) Role of electronic states of silver and copper catalysis in processes of selective or deep oxidation of alcohols and hydrocarbons. *Abst. Papers Am. Chem. Soc.*, 211, 64-COLL.
- 176 Shen, J., Shan, W., Zhang, Y.H., Du, J.M., Xu, H.L., Fan, K.N., Shen, W. and Tang, Y. (2006) Gas-phase selective oxidation of alcohols: in situ electrolytic nano-silver/zeolite film/copper grid catalyst. *J. Catal.*, 237 (1), 94–101.
- 177 Besson, M. and Gallezot, P. (2000) Selective oxidation of alcohols and aldehydes on metal catalysts. *Catal. Today*, 57 (1–2), 127–141.
- 178 Shen, J., Shan, W., Zhang, Y.H., Du, J.M., Xu, H.L., Fan, K.N., Shen, W. and Tang, Y. (2004) A novel catalyst with high activity for polyhydric alcohol oxidation: nanosilver/zeolite film. *Chem. Commun.*, (24), 2880–2881.
- 179 Chaki, N.K., Tsunoyama, H., Negishi, Y., Sakurai, H. and Tsukuda, T. (2007) Effect of Ag-doping on the catalytic activity of polymer-stabilized Au clusters in aerobic oxidation of alcohol. *J. Phys. Chem. C*, 111 (13), 4885–4888.
- 180 Dao Jun Guo, H.L.L. (2005) *Carbon*, 43, 1259–1264.
- 181 Landon, P., Collier, P.J., Papworth, A.J., Kiely, C.J. and Hutchings, G.J. (2002) Direct formation of hydrogen peroxide from H<sub>2</sub>/O<sub>2</sub> using a gold catalyst. *Chem. Commun.*, (18), 2058–2059.
- 182 Landon, P., Collier, P.J., Carley, A.F., Chadwick, D., Papworth, A.J., Burrows, A., Kiely, C.J. and Hutchings, G.J. (2003) Direct synthesis of hydrogen peroxide from H<sub>2</sub> and O<sub>2</sub> using Pd and Au catalysts. *Phys. Chem. Chem. Phys.*, 5 (9), 1917–1923.
- 183 Ishihara, T., Ohura, Y., Yoshida, S., Hata, Y., Nishiguchi, H. and Takita, Y. (2005) Synthesis of hydrogen peroxide by direct oxidation of H<sub>2</sub> with O<sub>2</sub> on Au/SiO<sub>2</sub> catalyst. *Appl. Catal. A Gen.*, 291 (1–2), 215–221.
- 184 Edwards, J.K., Solsona, B.E., Landon, P., Carley, A.F., Herzing, A., Kiely, C.J. and Hutchings, G.J. (2005) Direct synthesis of hydrogen peroxide from H<sub>2</sub> and O<sub>2</sub> using TiO<sub>2</sub>-supported Au-Pd catalysts. *J. Catal.*, 236 (1), 69–79.
- 185 Edwards, J.K., Solsona, B., Landon, P., Carley, A.F., Herzing, A., Watanabe, M., Kiely, C.J. and Hutchings, G.J. (2005) Direct synthesis of hydrogen peroxide from H<sub>2</sub> and O<sub>2</sub> using Au-Pd/Fe<sub>2</sub>O<sub>3</sub> catalysts. *J. Mater. Chem.*, 15 (43), 4595–4600.

## 11

# Self-Assembling Nanoclusters Based on Tetrahalometallate Anions: Electronic and Mechanical Behavior

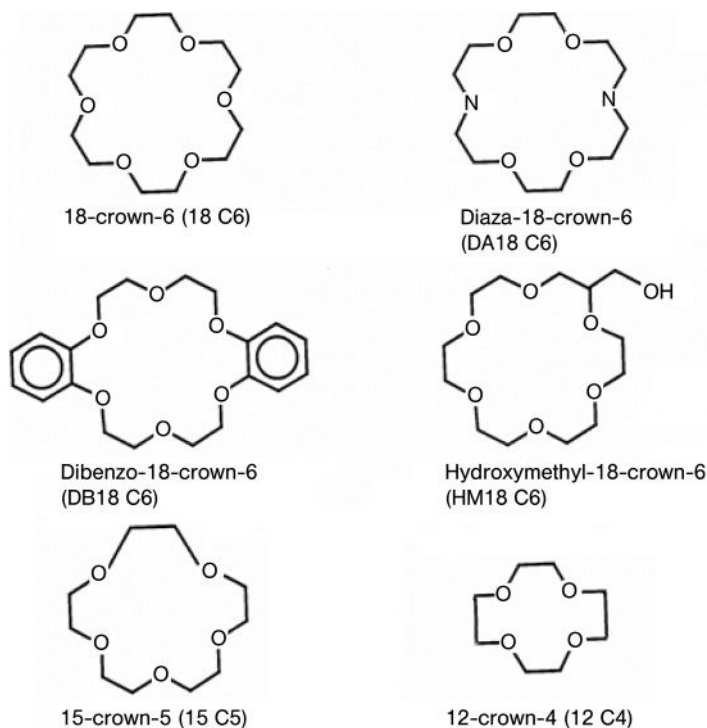
Ishenkumba A. Kahwa

### 11.1

#### Introduction

Self-assembling systems are invaluable sources of novel materials with diverse architectures, morphologies, physical and chemical properties, as well as potential applications [1–9]. The relative simplicity of some preparative procedures, and the precision with which thermodynamic and kinetic factors operate to produce such materials, make self-assembly an intensely studied phenomenon [4, 7]. The major aim of the present author's research has been the preparation of novel multi-metal materials that could: (i) efficiently immobilize toxic metals from the environment [10]; (ii) trap and transport metal ions in human and animal bodies for diagnostic, imaging, or therapeutic benefits [11]; or (iii) simply act as dispersion media for metal ions in the efficient synthesis of multicomponent metal oxides with interesting properties, such as the superconducting oxides,  $\text{YBa}_2\text{Cu}_3\text{O}_7$  [12]. These studies have covered self-assembling coordination compounds of multiple metal ions of the 3d-, 4f-, some p-, and nearly all of the s-block series [10–21]. This chapter provides a review of the synthesis of multinuclear self-assembling compounds facilitated by crown ethers, their structures, electronic behavior, and their thermally activated mechanical properties [10–21].

Interest in these compounds was inspired by the potential of crown ether chelates to bind metal ions such as  $\text{M}^+$ ,  $\text{M}^{2+}$ , and  $\text{M}^{3+}$ , the charge of which can then be counterbalanced by, among others, negatively charged, metalloanions such as  $[\text{CuX}_4]^{2-}$  and  $[\text{Cu}_2\text{X}_6]^{2-}$  to produce mixed-metal compounds for the preparation of superconducting ceramic oxides such as  $\text{YBa}_2\text{Cu}_3\text{O}_7$  and their derivatives [10]. For thallium-based superconducting ceramic oxide systems, the toxicity of thallium and ensuing environmental health concerns were important considerations [10]. Thus, as thallium-based superconducting ceramics demonstrated a superior potential based on a higher transition temperature ( $T_c$ ) (e.g.,  $T_c = 120\text{--}125\text{ K}$  and  $100\text{--}105\text{ K}$  for  $\text{Tl}_2\text{Ba}_2\text{Ca}_2\text{Cu}_3\text{O}_{10}$  and  $\text{Tl}_2\text{Ba}_2\text{CaCu}_2\text{O}_8$ , respectively) [22] compared to  $90\text{ K}$  for  $\text{YBa}_2\text{Cu}_3\text{O}_7$ ) [23], self-assembling systems that could immobilize large amounts of toxic thallium ions achieved greater significance.



**Scheme 11.1** Crown ethers used in these studies.

In this chapter, a review is provided of the studies conducted on the syntheses of metal-rich *Cubic F23* supramolecular complexes  $[(A(18\text{-Crown-6}))_4(MX_4)] [BX_4]_2 \cdot nH_2O$ , where A is a monovalent metal or  $NH_4^+$  ion; M is a divalent metal ion (normally of 3d element); B is a trivalent metal ion ( $Tl^{3+}$  or  $Fe^{3+}$ ); and X is a halogen (Cl or Br). The 18-crown-6 chelate (Scheme 11.1) in these and other complexes exhibits a thermally activated rotation conformation reorientation motion, which is of interest as a trigger for luminescence and magnetic on/off switching and mechanical nanodevices. The effectiveness of  $Mn^{2+}$  to serve as an efficient probe for a variety of coordination environments was also successfully explored, and the results are reported.

## 11.2

### Preparation of Key Compounds

The general preparation of the  $[(A(18C6))_4(MX_4)] [BX_4]_2 \cdot nH_2O$  series has been reported previously [10–21]. The procedure involves a simple refluxing of chelate 18C6 in alcoholic solutions containing the corresponding quantities of metal salts (e.g.,  $RbBr$ ,  $MnBr_2$ , and  $TlBr_3$ , when the complex  $(Rb(18C6))_4(MnBr_4)] [TlBr_4]_2 \cdot nH_2O$  is desired), and then evaporating off the excess solvent to deposit the crystalline

- (1)  $\text{Tl}^+ + 18\text{-crown-6} \rightleftharpoons [\text{Tl}(18\text{-crown-6})]^+$   
 (2)  $[\text{M}(\text{H}_2\text{O})_6]^{2+} + 4\text{X}^- \rightleftharpoons [\text{MX}_4]^{2-} + 6\text{H}_2\text{O}$   
 (3)  $[\text{Tl}(18\text{-crown-6})]^+ + 4\text{X}^- \rightleftharpoons [\text{TX}_4]^- + 18\text{-crown-6} + 2\text{e}^-$   
 (4)  $4[\text{Tl}(18\text{-crown-6})]^+ + [\text{MX}_4]^{2-} \rightleftharpoons [(\text{Tl}(18\text{-crown-6}))_4\text{MX}_4]^{2+}$   
 (5)  $[(\text{Tl}(18\text{-crown-6}))_4\text{MX}_4]^{2+} + 2[\text{TX}_4]^- \rightleftharpoons [(\text{Tl}(18\text{-crown-6}))_4\text{MX}_4][\text{TX}_4]_2$

**Scheme 11.2** Pertinent reactions leading to supramolecular systems:  $[(\text{Tl}(18\text{-Crown-6}))_4(\text{CuCl}_4)][\text{TlCl}_4]_2 \cdot n\text{H}_2\text{O}$ . The solvent shells are removed, and reactions occur in air.

materials. For the complex  $(\text{Tl}(18\text{C6}))_4(\text{MX}_4)[\text{TX}_4]_2 \cdot n\text{H}_2\text{O}$ , auto-oxidation of  $\text{Tl}^+$  to  $\text{Tl}^{3+}$  or auto-reduction of  $\text{Tl}^{3+}$  to  $\text{Tl}^+$  occurs in the refluxing mixture when the reaction vessels are open to the atmosphere (Scheme 11.2).

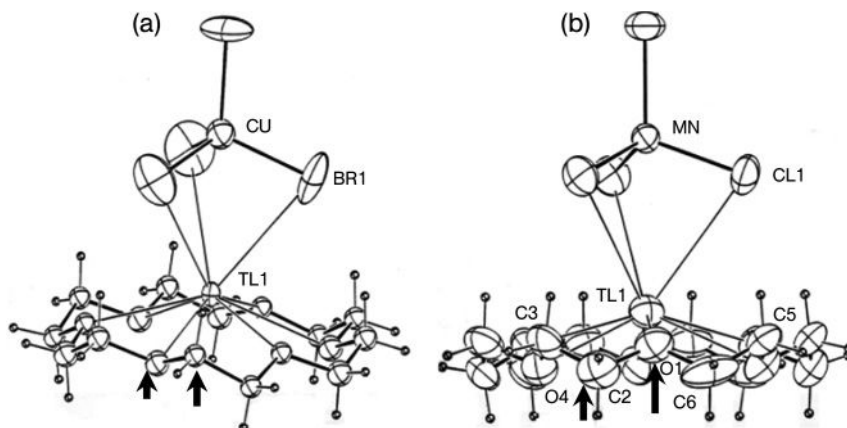
Hence, there is no need for both  $\text{Tl}^{3+}$  and  $\text{Tl}^+$  to be added into the reaction mixture. If  $\text{Fe}^{3+}$  and  $\text{Tl}^+$  are used, no auto-oxidation of  $\text{Tl}^+$  is observed. Overall, compounds  $[(\text{A}(18\text{C6}))_4(\text{MX}_4)][\text{BX}_4]_2 \cdot n\text{H}_2\text{O}$  with  $\text{A} = \text{Tl}, \text{Na}, \text{K}, \text{Rb}, \text{NH}_4, \text{BaX}$  ( $\text{X} = \text{halide or OH}$ );  $\text{M} = \text{Mn}, \text{Fe}, \text{Co}, \text{Ni}, \text{Cu}, \text{Zn}$ , and  $\text{B} = \text{Tl or Fe}$  have been prepared. Similar results were recently obtained by another group, which demonstrated that for  $\text{M}^{2+} = \text{Fe}^{2+}$  reducing conditions are required; otherwise, oxidation to  $\text{Fe}^{3+}$  occurs and the cubic compounds are not formed [24]. The crown ethers used in the study are shown in Scheme 11.1.

Changing the crown from 18C6 to DA18C6 or HM18C6 resulted in the formation of compounds similar to those of  $[(\text{Rb}(18\text{Crown}))_4(\text{MnX}_4)][\text{TX}_4]_2 \cdot n\text{H}_2\text{O}$ , while DB18C6, 15C5 and 12C4 failed to produce the cubic series. However, the reaction of NaBr, 15C5, and  $\text{TlBr}_3$  in the presence or absence of  $[\text{MX}_4]^{2-}$  anions yielded an elegant self-assembling compound  $[(\text{Na}(15\text{C5}))_4\text{Br}][\text{TlBr}_4]_3$  in which the  $\text{Br}^-$  anion played the role of concentrating  $[\text{Na}(\text{Crown})]^+$  cations in a manner similar to that of tetrahedral  $[\text{MX}_4]^{2-}$  anions  $[(\text{A}(18\text{C6}))_4(\text{MX}_4)][\text{BX}_4]_2 \cdot n\text{H}_2\text{O}$ .

### 11.3

#### Structure of the [(A(18C6))<sub>4</sub>(MX<sub>4</sub>)] [BX<sub>4</sub>]<sub>2</sub> · nH<sub>2</sub>O Complexes

The structure of compounds of the  $[(\text{A}(18\text{C6}))_4(\text{MX}_4)][\text{BX}_4]_2 \cdot n\text{H}_2\text{O}$  is *Cubic F23*, with the  $[\text{A}(18\text{C6})]^+$  cation perched on the triangular surfaces of the  $[\text{MX}_4]^{2-}$  anions, as shown in Figure 11.1 for one of the four such links. While the structures remained *Cubic F23* throughout the series  $[(\text{A}(18\text{C6}))_4(\text{MX}_4)][\text{BX}_4]_2 \cdot n\text{H}_2\text{O}$ , there were subtle differences in the orientation of the 18C6 in some cases, which are temperature-dependent. For instance, for the compound  $[(\text{Tl}(18\text{C6}))_4(\text{CuBr}_4)][\text{TlBr}_4]_2 \cdot n\text{H}_2\text{O}$ , the room temperature structure is similar to that of the  $\text{Mn}^{2+}$  analogue, but when it is cooled to 115 K a switch in the O and C positions was found to have occurred (Figure 11.1). The structures of many compounds were studied, and the switch from the low-temperature form (that of  $[(\text{Tl}(18\text{C6}))_4(\text{CuBr}_4)][\text{TlBr}_4]_2$  at 115 K) to the high-temperature form (that of  $[(\text{Tl}(18\text{C6}))_4(\text{CuBr}_4)][\text{TlBr}_4]_2$



**Figure 11.1** Partial structures of the  $[(\text{Tl}(18\text{-Crown-6}))_4(\text{MX}_4)]^{2+}$  supramolecular cations, showing the two orientations.

(a)  $T = 115\text{ K}$ ,  $M = \text{Cu}$ ,  $X = \text{Br}$ ; (b) Room temperature,  $M = \text{Mn}$ ,  $X = \text{Cl}$ . The difference is in the  $30^\circ$  rotation for 18C6 ligand resulting in carbon and oxygen switching positions (compare the positions marked by the arrows). Adopted from Ref. [15].

at room temperature) was found to depend on several factors, including the nature of the halide, the presence or absence of crystal water, and the temperature (Table 11.1) [16].

The extended cubic structure of members of the  $[(\text{A}(18\text{C}6))_4(\text{MX}_4)] [\text{BX}_4]_2 \cdot n\text{H}_2\text{O}$  was recently [24] analyzed in detail (Figure 11.2a); the study revealed an  $\text{M}^{2+}$  nucleus trapped in a tetrahedron of four  $\text{X}^-$  anions; the resultant  $[\text{MX}_4]^{2-}$  is coordinated on each of its four triangular faces by  $[\text{A}(18\text{C}6)]^+$  cations with resulting  $[(\text{A}(18\text{C}6))_4(\text{MX}_4)]^{2+}$  cations secured inside a cavity made up of a cyclic adamantane-like network of ten  $[\text{TX}_4]^-$  anions constituting six-member rings in chair conformations, as shown in Figure 11.2b [24].

#### 11.4

##### Structure of the $[(\text{Na}(15\text{C}5))_4\text{Br}] [\text{TlBr}_4]_3$ Complex

Like the  $[(\text{A}(18\text{C}6))_4(\text{MX}_4)] [\text{BX}_4]_2 \cdot n\text{H}_2\text{O}$ , the elegant structure of the  $[(\text{Na}(15\text{C}5))_4\text{Br}] [\text{TlBr}_4]_3$  complex reveals that it is stabilized by multiple complexation networks, as shown in Figure 11.3 [18].

#### 11.5

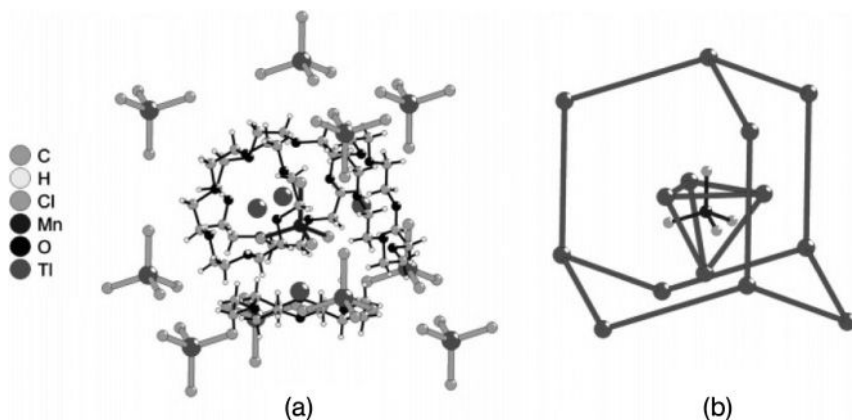
##### Spectroscopy of the Cubic F23 $[(\text{A}(18\text{C}6))_4(\text{MX}_4)] [\text{BX}_4]_2 \cdot n\text{H}_2\text{O}$

The Cubic F23 structure  $[(\text{A}(18\text{C}6))_4(\text{MX}_4)] [\text{BX}_4]_2 \cdot n\text{H}_2\text{O}$  requires additional support because it requires the  $[\text{MX}_4]^{2-}$  anion, including the  $[\text{CuX}_4]^{2-}$ , which is



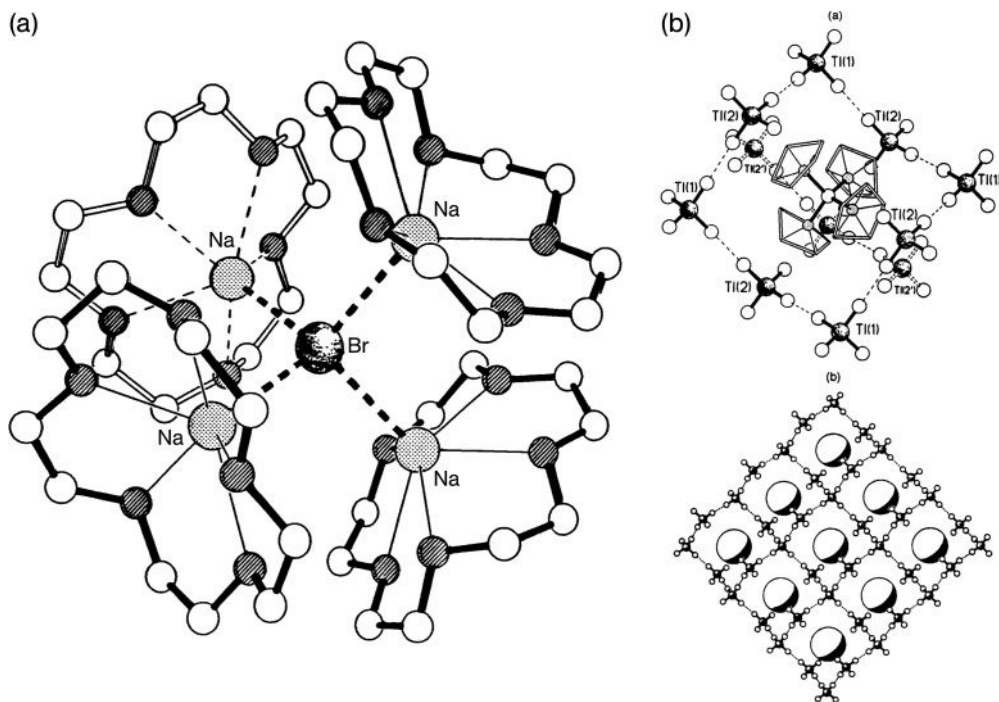
**Table 11.1** 18-Crown-6 orientations for structures of  $[(A(18\text{-Crown-6}))_4(MX_4)][TX_4]_2$ . The crown orientation is seen to depend on many factors.

A	M	X	T (K)	Orientation
Tl	Cu	Br	295	HT
Tl	Mn	Cl	295	HT
Tl	Cu	Cl	295	HT
K	Fe	Cl	293	HT
Tl	Cu	Br	115	LT
Tl	Cu	Cl (with 0.25 H <sub>2</sub> O)	297	LT
K	Mn	Br	295	LT
K	Zn	Br	297	LT

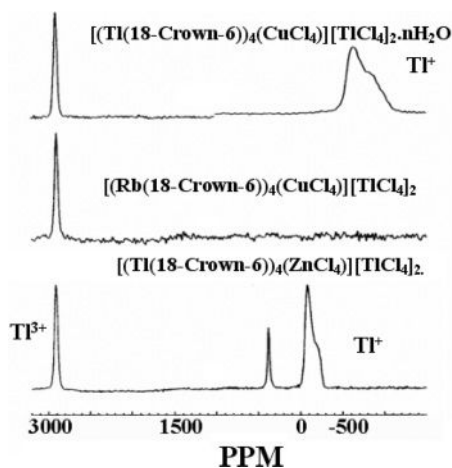


**Figure 11.2** (a) The partial extended structure of  $[(A(18C6))_4(MX_4)][BX_4]_2 \cdot nH_2O$  members; (b) The network of ten  $[TX_4]^-$  anions in an adamantine-type arrangement [24].

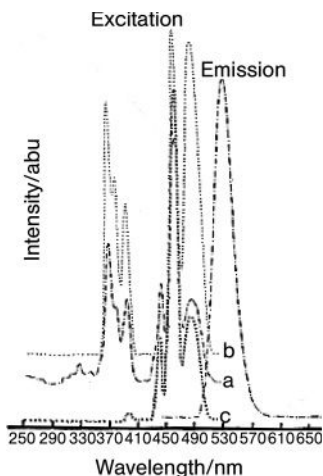
highly susceptible to Jahn–Teller distortion [25–27], to occupy a 23T site of perfect  $T_d$  symmetry [10]. We thus sought to determine whether the A, M, and B sites were of the indicated oxidation states and coordination geometries by spectroscopic means to complement the X-ray structural evidence. The presence of mixed valence thallium centers in  $[(Tl(18C6))_4(MCl_4)][TlCl_4]_2 \cdot nH_2O$  was established using solid-state nuclear magnetic resonance (NMR) of  $^{205}Tl$  (Figure 11.4), which showed  $Tl^{3+}$  with chemical shifts of approximately 2900 ppm relative to  $Tl(NO_3)$ , while that of  $Tl^+$  occurred at  $-782$  ppm and  $-117$  ppm for the paramagnetic  $[(Tl(18C6))_4(CuCl_4)][TlCl_4]_2 \cdot nH_2O$  and diamagnetic  $[(Tl(18C6))_4(ZnCl_4)][TlCl_4]_2 \cdot nH_2O$  compounds, respectively. The larger chemical shift and broader resonance of  $Tl^+$  in  $[(Tl(18\text{-Crown-6}))_4(CuCl_4)][TlCl_4]_2 \cdot nH_2O$ , relative to that of  $[(Tl(18\text{-Crown-6}))_4(ZnCl_4)][TlCl_4]_2$ , being indicative of the cation's proximity to the paramagnetic  $Cu^{2+}$  center.



**Figure 11.3** An elegant structure of  $[(\text{Na-Crown-5})_4\text{Br}][\text{TlX}_4]_3$ . (a) The cation  $[(\text{Na-Crown-5})_4\text{Br}]^{3+}$ ; (b) Upper: the cation in a network of  $[\text{TlBr}_4]^-$  anions. Lower: one layer of stacking egg-tray networks of  $[\text{TlBr}_4]^-$  anions and their  $[(\text{Na-Crown-5})_4\text{Br}]^{3+}$  guest, shown as a partially shaded ball.



**Figure 11.4** Solid-state  $^{205}\text{Tl}$  NMR spectra for some members of the  $[(\text{A}(18\text{C}6))_4(\text{MCl}_4)][\text{BCl}_4]_2 \cdot n\text{H}_2\text{O}$  series, showing the presence of the thallium(I) ( $\text{Tl}^+$ ) and thallium(III) ( $\text{Tl}^{3+}$ ) sites [10].



**Figure 11.5** Emission and excitation spectra of  $[(Rb(18C6))_4(MnCl_4)_{1-x}(CuCl_4)_x][TlCl_4]_{1-y}(FeCl_4)_y]_2 \cdot nH_2O$ . Spectrum a:  $x = 0$ ,  $y = 0$ ; spectrum b:  $x = 0.056$ ,  $y = 0$ ; spectrum c:  $x = 0$ ,  $y > 0$  [14].

While the structural details of the copper complexes  $[(A(18C6))_4(MX_4)][BX_4]_2 \cdot nH_2O$ ,  $M = Cu$ , were similar to those of  $M = Co, Mn, Fe, Ni$  and  $Zn$ , it was necessary to determine whether the 23T site is really  $T_d$  or is an average of various geometries at room temperature. The deep-blue  $Co^{2+}$  cubic compound  $[(Tl(18C6))_4(CoCl_4)][TlCl_4]_2 \cdot nH_2O$  is consistent with  $Co^{2+}$  being in a  $T_d$  environment.

The manganese (II) emission from the  $[(A(18C6))_4(MnCl_4)][TlCl_4]_2 \cdot nH_2O$  ( $A = Tl$  or  $Rb$ ) compounds peaked at about 535 nm, as is typical of the tetrahedral  $[MnCl_4]^{2-}$  anions [14]; the corresponding excitation spectra were also characteristic of  $T_d$   $[MnCl_4]^{2-}$  anions (Figure 11.5 for  $A = Rb$ ). The excitation spectrum of  $[MnCl_4]^{2-}$  emission in  $[(Rb(18C6))_4(MnCl_4)][TlCl_4]_2 \cdot nH_2O$  (Figure 11.5a) is attributed to electronic transitions from the  ${}^6A_1$  ground state to accessible higher-energy quartets derived from the crystal field splitting of  ${}^4G$ ,  ${}^4D$ ,  ${}^4P$ , and  ${}^4F$  levels. Emission spectra from compounds with  $Cu^{2+}$  and  $Fe^{3+}$  were also typical of  ${}^4T_1({}^4G) \rightarrow {}^6A_1$  emission for  $[MnCl_4]^{2-}$  ions. However, the inner-filter due to charge transfer bands of  $Cu^{2+}$  and  $Fe^{3+}$  led to significant changes on the excitation spectra (Figure 11.5).

Thus, as required by *Cubic F23* symmetry, the 23T site occupied by the  $[MX_4]^{2-}$  anions in crystalline  $[(A(18C6))_4(MX_4)][BX_4]_2 \cdot nH_2O$  compounds is indeed of  $T_d$  character. However, the  $Cu^{2+}$  charge transfer bands exhibited by the  $[(A(18C6))_4(CuCl_4)][TlCl_4]_2 \cdot nH_2O$  compounds at 27 000 to 30 000  $cm^{-1}$  ( ${}^2E \leftarrow {}^2B_2$ ) and 21 000 to 23 000  $cm^{-1}$  ( ${}^2A_2 \leftarrow {}^2B_2$  and  ${}^2E \leftarrow {}^2B_2$ ) are in regions generally expected of  $D_{2d}$   $[CuCl_4]^{2-}$  [10]. This ion may be distorted, but this requires additional proof.

## 11.6

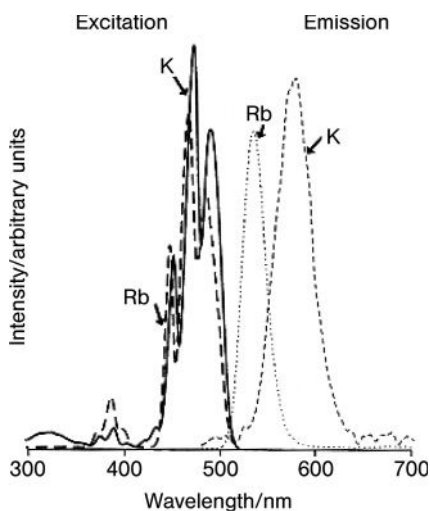
Unusual Luminescence Spectroscopy of Some Cubic  $[(A(18C6))_4(MnX_4)] [TlCl_4]_2 \cdot nH_2O$  Compounds

Whereas, the spectral profiles of  $[(A(18C6))_4(MnCl_4)] [TlCl_4]_2 \cdot nH_2O$  ( $A = Tl$  or  $Rb$ ) compounds (Figure 11.5) were typical of  $Mn^{2+}$  in  $T_d$  environments, the spectra of several other  $[(A(18C6))_4(MnX_4)] [TlX_4]_2 \cdot nH_2O$  compounds exhibited very interesting dynamics and features that depended on the nature of the halide  $X^-$  and the large cation  $A$ . The spectra of the  $[(A(18C6))_4(MnBr_4)] [TlBr_4]_2 \cdot nH_2O$  compounds with  $A = K$  and  $Rb$  (Figure 11.6) show the excitation spectra being similar. However, the emission spectrum of rubidium ( $A = Rb$ ) features a green emission peaking at 535 nm, as is normal for  $Mn^{2+}$  in  $T_d$  environments, while the potassium ( $A = K$ ) compound exhibits an unusual orange emission peaking at 575 nm, with the normal green emission being too weak to observe.

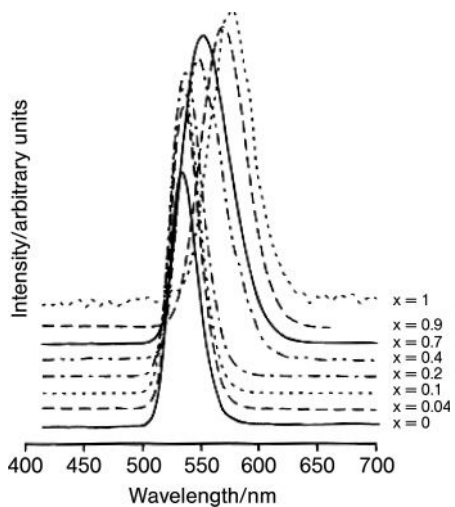
The emission spectra indeed do depend on the nature of the  $A$  cation, as shown in Figure 11.7, where a progressive spectral shift from the 535 nm to 575 nm emission is observed as the concentration of  $K^+$  ions ( $x$ ) increases from 0 (pure  $Rb$  complex) to 1 (pure  $K$  complex).

Most interestingly, the ammonium compound  $[(NH_4(18C6))_4(MnCl_4)] [TlCl_4]_2 \cdot nH_2O$ , which features temperature-independent spectra, shows both emissions. The normal emission for  $Mn^{2+}$  in  $T_d$  environments is seen at room temperature, while the strange orange emission dominates at 77 K (Figure 11.8a).

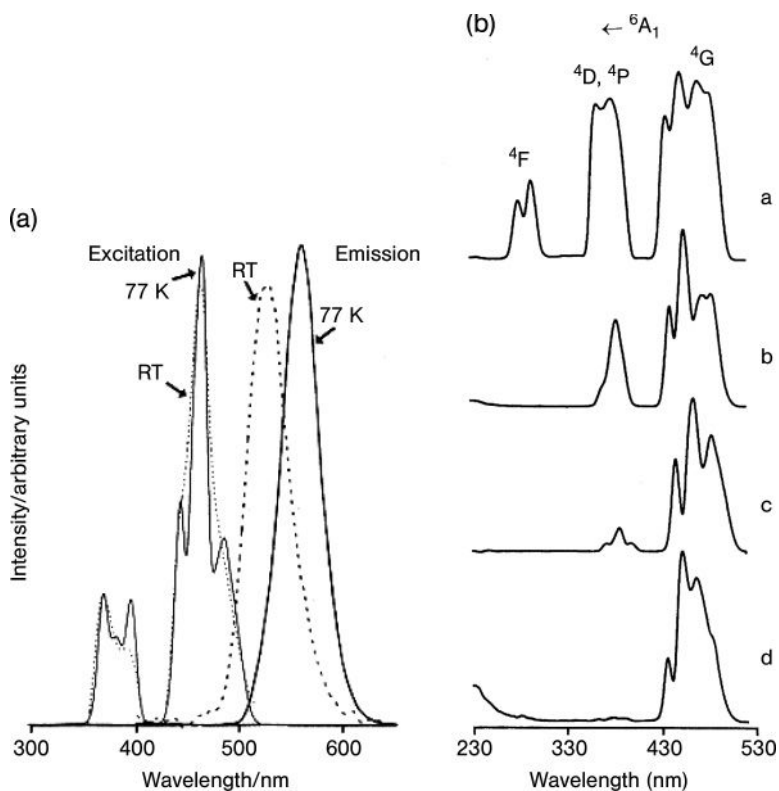
The emission from the bromide complex  $[(NH_4(18C6))_4(MnBr_4)] [TlBr_4]_2 \cdot nH_2O$  was normal, but the excitation spectrum featured an unusual broad absorption at 330 nm that was attributed to defects [21]. This led to the conclusion that the



**Figure 11.6** Emission and excitation spectra of  $[(A(18C6))_4(MnBr_4)] [TlBr_4]_2 \cdot nH_2O$  ( $A = K$  or  $Rb$ ) [16].



**Figure 11.7** Dependence of emission spectra of  $[(Rb_{1-x}K_x(18C6))_4(MnBr_4)] [TlBr_4]_2 \cdot nH_2O$  on the molar fraction of K [16].



**Figure 11.8** (a) The unusual emission behavior of the  $[(NH_4(18C6))_4(MnBr_4)] [TlBr_4]_2 \cdot nH_2O$  complex [16]; (b) Compared to  $[(NH_4(18C6))_2(MnBr_4)]$  (spectrum a), the inner-filter effect of defect sites on the

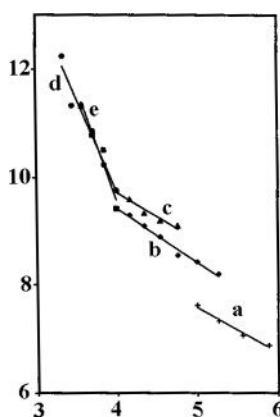
excitation spectral profile of [21]: spectrum b =  $(Rb(HM18C6))_4(MnBr_4) [TlBr_4]_2 \cdot nH_2O$ ; spectrum c =  $[(K(18C6))_4(MnBr_4)] [TlBr_4]_2 \cdot nH_2O$ ; spectrum d =  $[(Ba(HM18C6))_4(MnBr_4)] [TlBr_4]_2 \cdot nH_2O$ .

strange orange emission and broad UV absorptions were associated with defect sites. The electronic states of defect sites yielding orange emission are capable of quenching the normal  $[\text{MnX}_4]^{2-}$  green emission, especially at 77 K. At room temperature, back energy transfer from the defect site to the normal  $\text{Mn}^{2+}$  seems to be dominant in the case of the  $[(\text{NH}_4(18\text{C}6))_4(\text{MnBr}_4)] [\text{TlBr}_4]_2 \cdot n\text{H}_2\text{O}$  compound. Indeed, these defect sites were traced through a variety of compounds of  $[\text{MnX}_4]^{2-}$  where their ability to act as inner-filters for  $[\text{MnBr}_4]^{2-}$  UV absorptions is evident (Figure 11.8a).

### 11.7 Luminescence Decay Dynamics and 18C6 Rotations

The above temperature-dependent structural and luminescence behavior prompted the study of the temperature evolution of luminescence decay dynamics of the  $[(\text{A}(18\text{C}6))_4(\text{MnX}_4)] [\text{BX}_4]_2 \cdot n\text{H}_2\text{O}$  compounds. As these fascinating decay dynamics have been investigated and reported in detail elsewhere [14, 16, 21], at this point only the main aspects of our observations and conclusions will be presented.

The luminescence decay rates of  $[(\text{A}(18\text{C}6))_4(\text{MnX}_4)] [\text{BX}_4]_2 \cdot n\text{H}_2\text{O}$  compounds are influenced by the nature of the halogen X and metal A for spin-orbit coupling reasons, and also the nature of defect sites, their proximity to the  $\text{Mn}^{2+}$  site, and the efficiency with which they interact with the emitting  ${}^4\text{T}_1({}^4\text{G}) \rightarrow {}^6\text{A}_1$  process of  $\text{Mn}^{2+}$ . Whilst the decay rates change with the composition of the manganese(II) compound, the general features are a temperature-independent component up to approximately 200 K, followed by a rapid decay which involves energy migration over the  $\text{Mn}^{2+}$  sublattice. The Arrhenius plots (Figure 11.9) show biphasic emission quenching processes, with activation energies of 8–14 kJ mol<sup>-1</sup> at the start of the emission quenching, followed by a more rapid quenching process with a thermal barrier of 30–50 kJ mol<sup>-1</sup> [14, 16, 21].



**Figure 11.9** Arrhenius plots ( $\ln k$ , versus  $1/T$ ) for  $170 < T < 300$  K for  $[(\text{NH}_4(18\text{C}6))_4(\text{MnCl}_4)] [\text{TlCl}_4]_2 \cdot n\text{H}_2\text{O}$ . Normal  $[\text{MnCl}_4]^{2+}$  emission monitored at 510 nm: plots b = 8 kJ mol<sup>-1</sup> and e = 35 kJ mol<sup>-1</sup>. Unusual emission monitored at 590 nm: plot a = 7 kJ mol<sup>-1</sup>; plot c = 8 kJ mol<sup>-1</sup>; plot d = 29 kJ mol<sup>-1</sup>.  $E$  (kJ mol<sup>-1</sup>)  $\approx 0.155 T_c$  (where  $T_c$  = transition temperature, i.e.,  $\approx 210$  K from the above luminescence studies).

The thermal barrier of 9–14 kJ mol<sup>-1</sup> was attributed to the energy required to bridge the gap between the Stokes shifted exciton-donating <sup>4</sup>T<sub>1</sub>(<sup>4</sup>G) state of [MnX<sub>4</sub>]<sup>2-</sup> anions and the energy-accepting <sup>4</sup>T<sub>1</sub>(<sup>4</sup>G) levels of the [MnX<sub>4</sub>]<sup>2-</sup> neighbors, this being a key requirement for the energy migration process over the [MnCl<sub>4</sub>]<sup>2+</sup> sublattice. The difference between the absorption and emission energies was about 1060 cm<sup>-1</sup> (or 12.7 kJ mol<sup>-1</sup>), which was in good agreement with the measured thermal barriers of 9–14 kJ mol<sup>-1</sup>. The higher thermal barrier of 30–50 kJ mol<sup>-1</sup> was attributed to the energy required for the onset of the 18C6 rotation–conformation reorientation. These reorientation motions can generate a dynamic electric field at the Mn<sup>2+</sup> centers, thereby enhancing the electronic transition involved in the energy transfer process from Mn<sup>2+</sup> to defect sites. The measured thermal barriers of 30–50 kJ mol<sup>-1</sup> were in good agreement with the Waugh–Fedin approximation for hindered solid-state orientations within the assumptions made in deriving the relationship [16, 25].

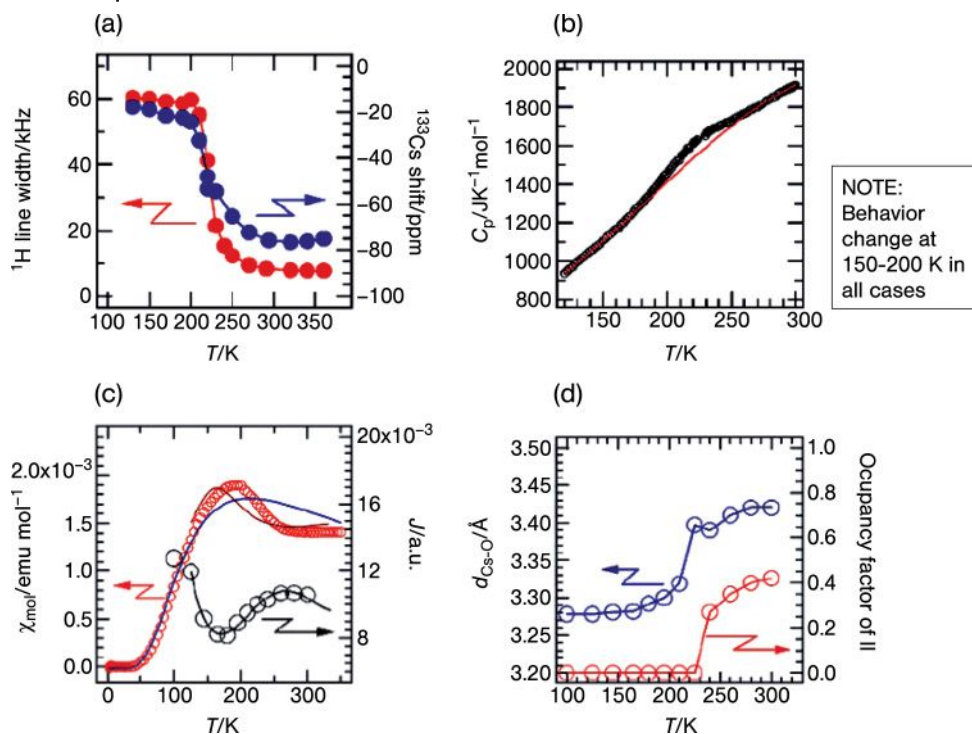
The cross-polarization-magic angle spinning (CP-MAS) <sup>13</sup>C NMR spectrum of the [(K(18C6))<sub>4</sub>(ZnBr<sub>4</sub>)] [TlBr<sub>4</sub>]<sub>2</sub> · nH<sub>2</sub>O compound showed one –CH<sub>2</sub>– resonance instead of the pair expected to result from the differential shielding of the up-and-down –CH<sub>2</sub>– functionalities of 18C6 in D<sub>3d</sub> symmetry [16]. The single resonance is consistent with –CH<sub>2</sub>– positions being equilibrated by the rotation–conformational reorientation of the 18C6 ring.

This conclusion is supported by a large body of solid-state NMR data on the compounds of 18C6 and other crown ether ligands in a variety of compounds, and is consistent with the merry-go-round 18C6 motion proposed by Buchanan, Ratcliff *et al.* [26] and supported by Dye *et al.* [27], to account for unusual solid-state NMR behavior. Recent detailed magnetic susceptibility, solid-state NMR and heat capacity measurements on 18C6 sandwich complexes of cesium, [(18C6)Cs(18C6)Cs(18C6)]<sup>+</sup> with magnetic [Ni(dmit<sub>2</sub>)]<sup>-</sup> identified 18C6 in these compounds as a rotor (Figure 11.10), the onset motion of which has influence on the physical characteristics of the compounds, including the magnetic behavior of the [Ni(dmit<sub>2</sub>)]<sup>-</sup> anion [28, 29] (Figure 11.9).

## 11.8 Conclusions

The [(A(18C6))<sub>4</sub>(MX<sub>4</sub>)] [BX<sub>4</sub>]<sub>2</sub> · nH<sub>2</sub>O supramolecular systems have the interesting properties of concentrating and immobilizing toxic metal ions such as thallium(I/III), and are accessible via a relatively simple synthetic procedure. The [(A(18C6))<sub>4</sub>(MnX<sub>4</sub>)] [BX<sub>4</sub>]<sub>2</sub> · nH<sub>2</sub>O compounds hold a total of six thallium ions—four as [Tl(18C6)]<sup>+</sup> and two as [TlX<sub>4</sub>]<sup>-</sup>. The structural, luminescence, and CP-MAS <sup>13</sup>C NMR spectroscopic evidence for 18C6 mechanical activity in the [(A(18C6))<sub>4</sub>(MnX<sub>4</sub>)] [BX<sub>4</sub>]<sub>2</sub> · nH<sub>2</sub>O compounds is compelling. Indeed, when taken together with published reports on heat capacity, magnetic susceptibility and NMR evidence for such mechanical activity in a variety of crown ether compounds, the possibility of developing potentially useful nanodevices becomes of major interest. For example, the





**Figure 11.10** (a) Solid-state  $^1H$  NMR, (b) heat capacity, (c) magnetic susceptibility, and (d) crystal structural parameters of compounds of  $[(18C6)Cs(18C6)Cs(18C6)]^+$  with magnetic  $[Ni(dmit_2)]^-$  anions, showing behavioral changes at approximately 150–200 K in all cases [28].

changes in physical behavior associated with the onset of rotation–conformation reorientation motion could be used in the form of switches. Indeed, new opportunities for fabricating mechanical nanodevices in which the 18C6 chelate performs useful work as it rotates with  $-CH_2-$  and  $-O-$  moieties flipping up and down can be envisaged. In this regard, it is noteworthy that the behavior of compounds of HM18C6 and 18C6 were similar, as studying the behavior of other substituted 18C6 molecules is important in the search for nanodevices based on the 18C6 motion.

The remarkable sensitivity of  $Mn^{2+}$  emission in detecting molecular motion within its environments is also of great interest. It is possible that the defect sites which dominated the emission behavior of  $[(A(18C6))_4(MnX_4)] [BX_4]_2 \cdot nH_2O$  compounds were of manganese(II), in unusual coordination environments. The sensitivity of  $Mn^{2+}$  to changing coordination and supramolecular environments was convincingly demonstrated by comparing the luminescence spectroscopy (Figure 11.11) and decay dynamics of compounds featuring  $Mn^{2+}$  in coordination numbers 4, 6, 7, and 8. The potential of  $Mn^{2+}$  as a luminescence probe for structural and supramolecular environmental deserves further development.

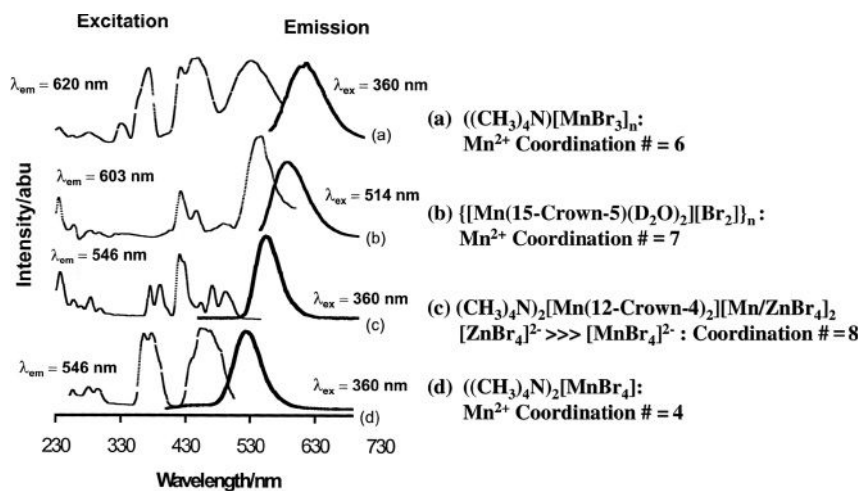


Figure 11.11 Manganese(II) luminescence spectroscopy as a structural probe [19].

### Acknowledgments

Contributions made by coauthors of the original publications are greatly appreciated, and especially those of Drs H.O. Reid and N.S. Fender as former students. These studies were funded by the UWI, the Inter-American Development Bank (IADB), and the US NSF.

### References

- Guan, Z. (2007) *Polym. Int.*, **56**, 467.
- Lehn, J.-M. (2007) *Chem. Soc. Rev.*, **36**, 151.
- Loeb, S.J. (2007) *Chem. Soc. Rev.*, **36**, 226.
- Gale, P.A. (ed.) (2007) *Chem. Soc. Rev., Supramolecular Anniversary Issue*, **36**, 125.
- Yang, Z. and Xu, B. (2007) *J. Mater. Chem.*, **17**, 2385.
- Schneider, H.-J. and Yatsimirsky, A.K. (2008) *Chem. Soc. Rev.*, **37**, 263.
- Monti, S. and De Schryver, F. (eds) (2007) *Photochem. Photobiol. Sci., Special Issue*, **6**, 333.
- Miyata, M., Tohnai, N. and Hisaki, I. (2007) *Acc. Chem. Res.*, **40**, 694.
- Flood, A.H., Ramirez, R.J.A., Deng, W.-Q., Muller, R.P., Goddard, W.A. and Stoddart, J.F. (2004) *Aust. J. Chem.*, **57**, 301.
- Kahwa, I.A., Miller, D., Mitchell, M., Fronczek, F.R., Goodrich, R.G., Williams, D.J., O'Mahoney, C.A., Slawin, A.M.Z., Ley, S.V. and Groombridge, C.J. (1992) *Inorg. Chem.*, **31**, 3963.
- Kahwa, I.A., Folkes, S., Williams, D.J., Ley, S.V., O'Mahoney, C.A. and McPherson, G.L. (1989) *J. Chem. Soc., Chem. Commun.*, 1531.
- Kahwa, I.A. and Goodrich, R.G. (1989) *J. Mater. Sci. Lett.*, **8**, 755.
- Kahwa, I.A., Miller, D., Mitchell, M. and Fronczek, F.R. (1993) *Acta Crystallogr. Sect. C, Cryst. Struct. Commun.*, **49**, 320–321.
- Fairman, R.A., Gallimore, W.A., Spence, K.V.N. and Kahwa, I.A. (1994) *Inorg. Chem.*, **33**, 823–828.
- Fender, N.S., Finnegan, S.A., Miller, D., Mitchell, M., Kahwa, I.A. and Fronczek,

- F.R. (1994) *Inorg. Chem.*, **33**, 4002–4008.
- 16 Fender, N.F., Fronczek, F.R., John, V., Kahwa, I.A. and McPherson, G.L. (1997) *Inorg. Chem.*, **37**, 5539–5547.
- 17 Reid, H.O.N., Kahwa, I.A., White, A.J.P. and Williams, D.J. (1998) *Inorg. Chem.*, **37**, 3868–3873.
- 18 Fender, N.S., Kahwa, I.A., White, A.J.P. and Williams, D.J. (1998) *J. Chem. Soc., Dalton. Trans.*, 1729–1730.
- 19 Reid, H.O.N., Kahwa, I.A., White, A.J.P. and Williams, D.J. (1999) *Chem. Commun.*, 1565–1566.
- 20 Reid, H.O.N., Kahwa, I.A., Mague, J.T. and McPherson, G.L. (2001) *Acta Crystallogr.*, **E57**, m3–m4.
- 21 Fender, N.S., Kahwa, I.A. and Fronczek, F.R. (2002) *J. Solid State Chem.*, **163**, 286–293.
- 22 Subramanian, M.A., Calabresse, J., Toradi, C.C., Askew, T.R., Flippen, R.B., Morrissey, K.J., Chahudhuri, U. and Sleight, A.W. (1988) *Nature*, **332**, 420.
- 23 Wu, M.K., Ashburn, J.R., Tomg, C.J., Hor, P.H., Meng, R.L., Gao, L., Huang, Z.J., Wang, Y.Q. and Chu, C.W. (1987) *Phys. Rev. Lett.*, **58**, 908.
- 24 Rieger, S.F. and Mudring, A.-V. (2005) *Inorg. Chem.*, **44**, 9340.
- 25 Waugh, J.S. and Fedin, É.I. (1963) *Sov. Phys. Solid State*, **4**, 1633.
- 26 Ratcliffe, C.I., Ripmester, J.A., Buchanan, G.W. and Denike, J.K. (1992) *J. Am. Chem. Soc.*, **114**, 3294 and references therein.
- 27 Wagner, M.J., McMills, L.E.H., Ellaboudy, A.S., Elgin, J.L., Dye, J.L., Edward, P.P. and Pyper, N.C. (1992) *J. Phys. Chem.*, **96**, 9656 and references therein.
- 28 Nishihara, S., Akutagawa, T., Sato, D., Takeda, S., Noro, S.-I. and Nakamura, T. (2005) *J. Am. Chem. Soc.*, **127**, 4397.
- 29 Takeda, S., Akutagawa, T., Nishihara, S., Nakamura, T. and Saito, K. (2005) *J. Chem. Phys.*, **123**, 044514.

## 12

# Optically Responsive Polymer Nanocomposites Containing Organic Functional Chromophores and Metal Nanostructures

*Andrea Pucci, Giacomo Ruggeri, and Francesco Ciardelli*

### 12.1

#### Introduction

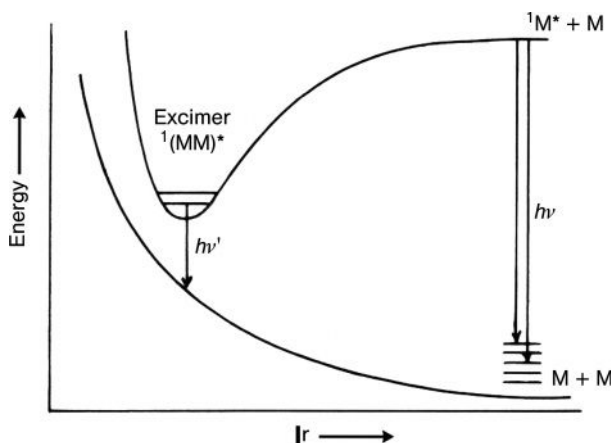
Responsive “smart” materials are certainly one of the most intriguing research areas in modern polymer science and technology, as molecularly designed materials based on macromolecules offer unique opportunities in this connection. Indeed, macromolecules are able to transmit and amplify small signals through involvement of the whole chain, conferring to the material a change in properties of various level and type. We can learn from Nature how these effects may be obtained according to two distinct routes, based either on the covalent bonding of highly responsive molecular species to the chains, or on the nanodispersion of such responsive species within the polymer bulk. In the latter case, those materials based on macromolecules may also affect the behavior of guest low-molecular-weight molecules or noble metal assemblies. In addition to the molecular features of both host and guest, the supramolecular arrangement of the guest can be modulated by external events on the host material. These effects can be identified and conveniently used when easily detected and field-sensitive species are present in the low-molecular-weight component. In this chapter, we review those investigations conducted not only in our laboratory but also by others, that have provided clear examples of the concepts which drive the original idea. In particular, we report our data relating to the effects of external stimuli (i.e., mechanical stretching such as polymer drawing, temperature, and pressure) on the optical properties (absorption and emission) of (nano)composite materials. The (nano)dispersion of active dyes and metal nanoparticles (guest) in inert polymers (host) will then be presented as an example of the effect of the macromolecular environment on respectively the dye or metal atom aggregates (metal nanoparticles), in terms of induced optical properties.

## 12.2 Organic Chromophores as the Dispersed Phase

### 12.2.1 Nature of the Organic Dye

Highly sensitive optical techniques based on the luminescence of conjugated aromatic molecular additives dispersed at low concentration (e.g., in Scheme 12.2, less than 1–2 wt%) into the amorphous phase of thermoplastic polymers have been successfully applied to the detection of thermal and mechanical solicitations on plastic films. In fact, a growing interest was devoted to the optical characteristics of macromolecules due to the sensitive response of the photophysical techniques for the study of the dynamic physical properties of macromolecules (i.e., energy transfer, polarization, and trapping phenomena). For example, when luminescent dyes are incorporated into polymers as thermodynamically stable micro-/nano-sized aggregates of a few molecules, emission characteristics are observed which derive mainly from the fluorescence of interacting chromophores through  $\pi$ – $\pi$  stacking interactions among the planar aromatic backbones. Interactions between the excited state of an aromatic molecule and the ground state of the same molecule actually give rise to the excimer (excited dimer) formation, which represent a powerful diagnostic tool for interacting chromophores (Scheme 12.1) [1–3].

For small molecules separations ( $r < 4 \text{ \AA}$ ), with interactions between ground-state and excited-state molecules, an attractive potential may be obtained due to the configurational interaction between resonance and exciton–resonance states. According to Scheme 12.1, fluorescence from the excimer state will thus be unstructured and at a lower energy than the corresponding monomer emission [2].



**Scheme 12.1** Energy diagram for excimer formation.  
 M = molecule in the ground state;  $M^*$  = molecule in the excited state;  $r$  = distance between molecules.

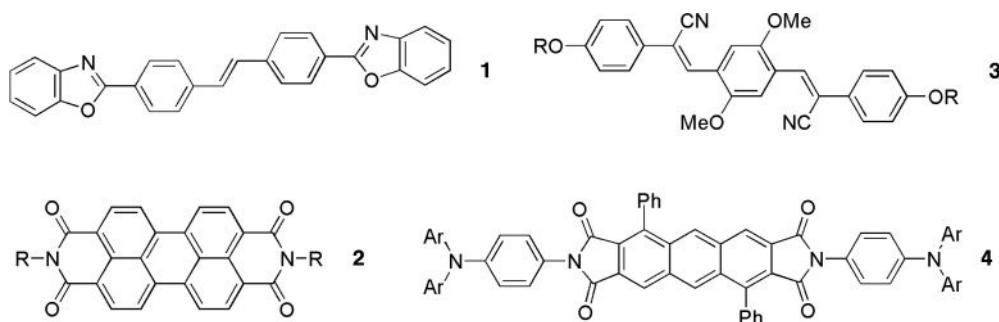
Comparisons between the signal intensities of monomeric fluorescence (defined as the contribution of an isolated chromophore covalently attached to the polymer chain or dispersed herein) and the excimer contribution are used very efficiently to obtain accurate information not only on polymer structure and conformation [4–9] but also on mixing at the molecular level in polymer blends [9–16]. Excimer formation in polymer solutions is widely considered to be a diffusion-controlled process, and is influenced by a variety of factors including the solvent, the chromophore microstructure, and the macromolecular conformation [2, 17, 18]. In contrast, in polymer films the formation of aggregates or excimers (static excimers) arises from the structural constraints of the polymer chains. In this case, the static excimers react very sensitively to chromophore aggregation and, as might be expected, also to any variations in the spatial distribution and alignment of molecules within the local environment [19–23].

### 12.2.2

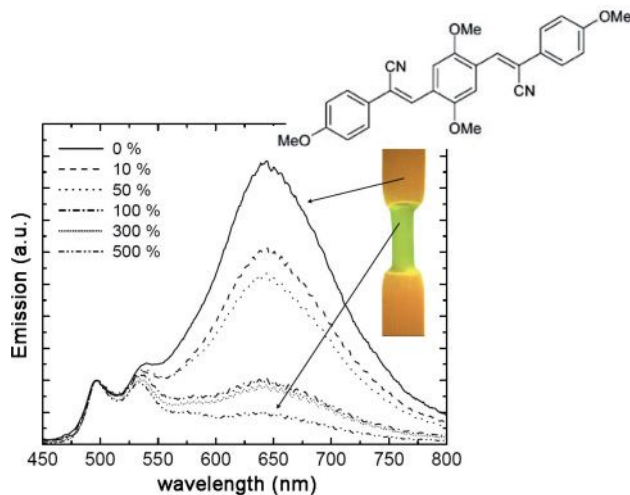
#### Polymeric Indicators to Mechanical Stress

##### 12.2.2.1 Oligo(*p*-Phenylene Vinylene) as Luminescent Dyes

Recently, the possibility of applying the formation of excimers inside polymer matrices, in order to prepare polymers with “built-in” stress–strain deformation sensors, has been effectively demonstrated [24–27]. Weder *et al.* reported that small amounts (0.01–3 wt%) of excimer-forming oligo(*p*-phenylene vinylene) synthetic chromophores (Scheme 12.2, 3) dispersed into a ductile host polymer matrix (e.g., linear low-density polyethylene, LLDPE) as very small (nano)aggregates of dyes may be produced either by guest diffusion or by processing the components in the melt. The authors demonstrated that the phase behavior of the LLDPE/dye blends depended strictly on the supramolecular structure of the dye, which may be easily tuned as a function of the processing conditions and chromophore concentration. On applying a mechanical deformation of the film, a shear-induced mixing between the two phases promoted the break up of the dye’s supramolecular



**Scheme 12.2** Examples of excimer-forming dyes: 1, stilbene; 2, perylene; 3, cyano-oligo(*p*-phenylene vinylene); 4, anthracene diimide derivatives. R = alkyl groups, Ar = aryl groups; Ph = Phenyl.



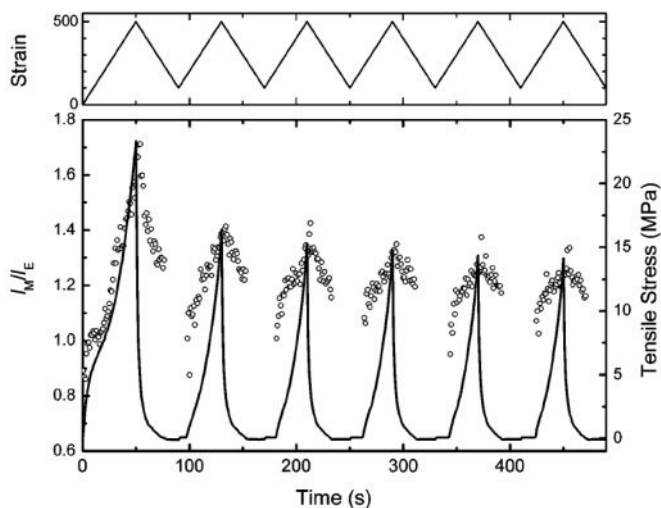
**Figure 12.1** Emission spectra of a 0.20 wt% linear low-density polyethylene/1,4-bis( $\alpha$ -cyano-4-methoxystyryl)-2,5-dimethoxybenzene (inset) blend as a function of draw ratio, and image of the same blend after orientation (inset, draw ratio = 500%,  $\lambda_{exc.} = 365$  nm). Adapted with permission from Ref. [27]; © 2003, American Chemical Society.

structure, and led to a mixing of the two components (polymer and dye) and a change in the material's emission properties, from orange-red excimers to the molecularly dissolved green monomers of the dye (Figure 12.1) [26, 27].

According to Weder *et al.* [28], the extent of the color change observed upon deformation, and thus the ability of the polymer host to break up the dye aggregates, is influenced primarily by three parameters: dye aggregate size; polymer crystallinity; and strain rate. The nucleation rate of dye aggregates, and consequently the size of the aggregates, can be controlled via the structure of the groups attached to the dye. That is, long aliphatic alkyl groups lead to much higher nucleation rates, which in turn promotes the formation of small aggregates. Most importantly, the mechanically induced dispersion of the excimer-forming sensor molecules upon deformation is considered to be related to the plastic deformation process of the polyethylene (PE) crystallites, and thus increases with increasing polymer crystallinity.

In order to determine whether the sensing scheme could be exploited also for elastomers (which change their luminescent color reversibly as a function of the applied strain), Weder *et al.* recently investigated different polyurethanes that comprised cyano-oligo(*p*-phenylene vinylene)s (cyano-OPVs) as built-in deformation sensors [29]. The covalent integration of cyano-OPVs into the backbone of the polyurethane led to materials in which large-scale phase separation of the dye was prevented, while the formation of a large population of (presumably very small) ground-state dye aggregates was still allowed. Consequently, these polymers





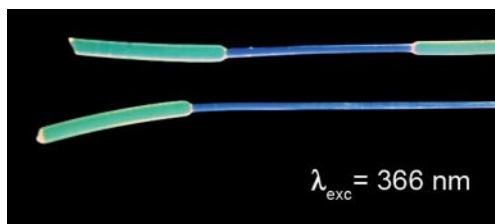
**Figure 12.2** Ratio of monomer to excimer emission,  $I_M/I_E$  (circles, measured at 540 and 650 nm), and tensile stress (solid line) for a covalent incorporation of cyano-oligo(*p*-phenylene vinylene)s in polyurethane under a triangular strain cycle between 100% and 500% at a frequency of 0.0125 Hz. Reproduced with permission from Ref. [29]; © 2006, American Chemical Society.

displayed a predominantly excimer emission in the unstretched state, and exhibited a pronounced fluorescence color change upon deformation. The optical change appeared mostly reversible, and reflected the stress–strain behavior of the polymeric material (Figure 12.2).

Recently, properly substituted cyano-OPVs were also discovered as a new class of piezochromic material [30]. Liquid-crystalline cyano-OPV dyes showed emission properties which could be switched reversibly and repeatedly from monomer to excimer fluorescence upon compression or quenching of the compounds from a nematic state. In particular, if the powder was either briefly compressed (1 min at 1500 p.s.i. in an IR pellet press) or ground using a mortar and pestle, then a significant bathochromic shift ( $\geq 50$  nm) occurred and the emission band was seen to broaden. Once compressed, the “excimer form” (turquoise emission) was found to be stable for months if stored under ambient conditions. Rapid heating (ca. 3 min) of the compressed material to 130 °C fully restored the original “monomer” form (green emission).

#### 12.2.2.2 Bis(Benzoxazoly) Stilbene as a Luminescent Dye

A similar approach to the preparation of stress–strain polymeric indicators was reported by Pucci *et al.*, who developed polypropylene (PP) films that contained different concentrations of the food-grade, luminescent dye bis(benzoxazoly) stilbene (BBS) (Scheme 12.2, 1) [31]. Notably, it was clear that the emission



**Figure 12.3** Partially stretched linear low-density polyethylene rods prepared in a corotating twin screw extruder (THERMO, Polylab) at a fixed barrel temperature of 180°C for first zone and 200°C for the following zones, and with screw speed fixed at 50 r.p.m. with increasing (from top to bottom) amounts of BBS (from 0.2 to 0.5 wt%), examined under UV light.

characteristics of the PP films depended on the BBS concentration and the polymer deformation. A well-defined excimer band was observed with more than 0.2 wt% of BBS, and this conferred to the film a green luminescence. During drawing (130°C), the PP reorganization caused a break in the BBS excimer-type arrangement, leading to a prevalent blue emission of the single molecules.

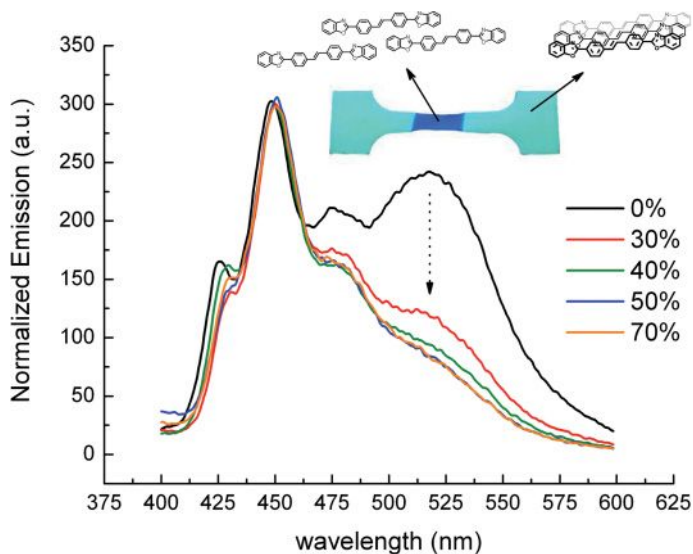
In a subsequent phase, the same formulation was obtained by continuous compounding of the components mixture in a co-rotating, twin-screw extruder with a screw diameter of 24 mm and a length-to-diameter (L/D) ratio of 40 [32]. The films obtained through off-line melt-compression molding confirmed the optical responsive properties demonstrated by laboratory-scale, batch-compounded materials (Figure 12.3).

Intelligent films from thermoplastic materials, based on excimer luminescence and responsiveness to mechanical stress, were also obtained through the dispersion (melt-processing) of moderate amounts (0.02–0.2 wt%) of BBS into a thermoplastic, aliphatic, biodegradable polyester [poly(1,4-butylene succinate), PBS] (Figure 12.4) [33].

As reported for PP blends, the PBS morphology reorganization occurred during the drawing process, thus breaking the BBS excimer-type arrangement and leading to a prevalence of blue emission for the single molecules.

### 12.2.2.3 Perylene Derivatives as Luminescent Dyes

Very recently, analogous thermoplastic films sensitive to mechanical stress were prepared by using a different luminescent probe based on the perylene core (Scheme 12.2, 2) [34]. Perylene dyes containing different peripheral alkyl chains were synthesized and efficiently dispersed at low loadings (from 0.01 to 0.1 wt%) into LLDPE by processing in the melt. Both perylene bisimides were found to generate supramolecular aggregates promoted by  $\pi$ - $\pi$  intermolecular interactions between the conjugated planar structure of the dyes, as indicated by spectroscopic investigations on heptane solutions or dispersions into the LLDPE polymer matrix. The occurrence of this phenomenon effectively changed the emission of the dyes from yellow-green (noninteracting dyes) to red (interacting dyes). In particular,



**Figure 12.4** Fluorescence emission spectra ( $\lambda_{exc.} = 277$  nm) of 0.1 wt% poly(1,4-butylene succinate)/bis(benzoxazolyl)stilbene film (PBSBBS-0.1), before (0%) and after solid-state drawing (from 30 to 70% elongation). The spectra are normalized to

the intensity of the isolated BBS molecules peak (430 nm). Inset: digital image of the uniaxially oriented PBSBBS film containing the 0.1 wt% of BBS molecules, recorded under excitation at 366 nm (50% elongation).

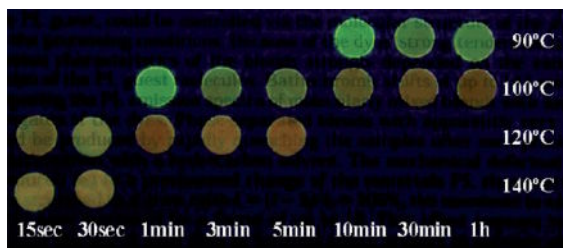
the data (provided by optical experiments and by quantum-mechanical calculations) acquired for dispersion of the dyes into the polymer matrix, revealed that the optical properties and responsiveness to mechanical stimuli were heavily dependent on the compactness of the perylene aggregates provided by the different molecular structures of the dyes.

### 12.2.3

#### Polymeric Indicators to Thermal Stress

##### 12.2.3.1 Oligo(*p*-Phenylene Vinylene) as Luminescent Dyes

Another sensing mechanism may be produced, in contrast, by mixing the cyano-OPVs dyes (or other suitable excimer-forming dyes) with a macromolecular system characterized by a glass transition temperature ( $T_g$ ) which is above the operating temperature. Hence, molecularly mixed, glassy composites can readily be produced via melt processing and rapid quenching of the melts. In this case, the sensor dyes were kinetically trapped inside the glassy amorphous phase of the host polymers, namely poly(methyl methacrylate) (PMMA) and poly(bisphenyl A carbonate) (PC), with the formation of thermodynamically stable excimers occurring just after annealing above  $T_g$  [24]. Subjecting blends of sufficiently high dye concentrations to temperatures above their  $T_g$ -values (130 °C for PMMA, 150 °C for PC) led to permanent and significant changes in the materials' emission spectra,



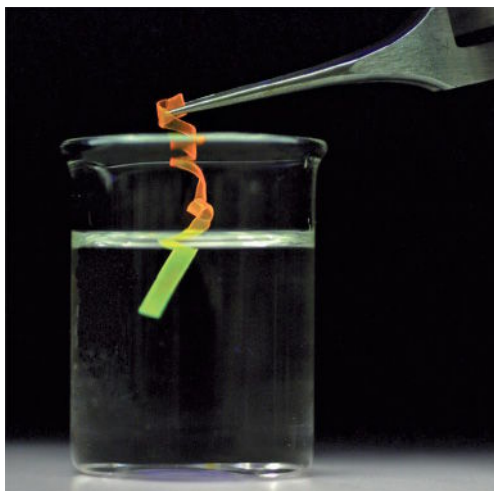
**Figure 12.5** Images of initially quenched blends films of 0.9 wt% poly(ethylene terephthalate)/cyano-oligo(*p*-phenylene vinylene) upon annealing for the time and at the temperature indicated ( $\lambda_{\text{exc.}} = 365 \text{ nm}$ ). Reproduced with permission from Ref. [25]; © 2006, American Chemical Society.

due to phase separation of the polymer and the excimer-forming dye. This effect appears to bear significant potential for technological applications, including the use of dye/polymer blends as time-temperature indicators (TTIs). In fact, kinetic experiments performed as a function of time, temperature and dye concentration, resulted in some well-fitted, monoexponential growth functions. In particular, plotting the rate of aggregation against the inverse of the annealing temperature indicated the presence of a linear, Arrhenius-type behavior, which suggested that an aggregation of the dye molecules might be predicted when dispersed into a polymer film. Moreover, the derived thermodynamic parameters could easily be determined via luminescence experiments.

Recently, additional data have been acquired by using semicrystalline [poly(ethylene terephthalate); PET] and poly(alkyl methacrylate) -based matrices [25, 35]. Homogeneous blends can be produced by conventional melt-processing protocols that are concluded with a quenching step, with the materials thus prepared displaying emission spectra characteristic of the dyes' monomer emission. For example, annealing above the  $T_g$ -value of the polyester ( $80^\circ\text{C}$ ) led to the formation of excimers and caused significant changes in the materials' emission characteristics. The aggregation processes in the semicrystalline PET/cyano-OPVs blends investigated appeared to be well-described by single-exponential transformation kinetics, while the fluorescence color of these materials was characteristic of their thermal history (Figure 12.5).

In particular, cyano-OPV dyes with a longer, rigid conjugated core showed slower aggregation rates due to their limited mobility within the polymer matrix [35].

An extreme, yet intriguing, application of the multifunctional chromogenic cyano-OPV dyes was recently reported by Weder *et al.* [36]. The group reported the preparation and characterization of a new shape memory polymer (SMP) with built-in temperature-sensing capabilities, by incorporating a cyano-OPV dye into a semi-crystalline crosslinked poly(cyclo-octene) (PC'O) by guest diffusion. SMPs have the ability to memorize a permanent shape, and so can be manipulated and fixed to a temporary shape under specific conditions of temperature and stress,



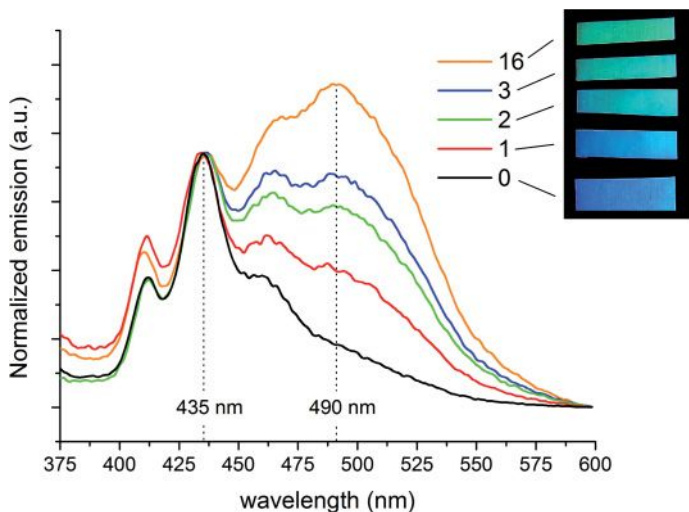
**Figure 12.6** Image of the recovery from temporary shape (spiral, orange emission) to the permanent shape (rod, green emission) for a crosslinked poly(cyclo-octene)/cyano-oligo(*p*-phenylene vinylene) blend. The sample was immersed in silicon oil at  $\sim 75^\circ\text{C}$  (under illumination at 365 nm) [36]. Reproduced with permission of the Royal Society of Chemistry.

yet subsequently relax to the original, stress-free state upon application of an external stimulus [37]. Weder's group described a new SMP/dye system in which a built-in sensor provided additional functionality. The material was based on a chromogenic sensor dye that provided a simple and clear signal indicating if the set/release temperature had been reached. The dye concentration was chosen to allow dye aggregation upon drying, which resulted in the formation of excimers. Exposure of these phase-separated blends to temperatures above the melting point ( $T_m = 47\text{--}48^\circ\text{C}$ ) of the polymer led to dissolution of the dye molecules, yielding a pronounced change in their optical characteristics.

Briefly, the permanent rod-shaped PCO/dye blend was heated to  $80^\circ\text{C}$ , deformed to a temporary shape (spiral), and fixed by cooling to room temperature. The spiral was slowly immersed into a silicon oil bath (ca.  $75^\circ\text{C}$ ), allowing recovery of the rod shape which was flanked by a color change from orange to yellow-green (Figure 12.6).

#### 12.2.3.2 Bis(Benzoxazoly) Stilbene as Luminescent Dye

Polymeric film sensors that were based on excimer luminescence and responsive to temperature stress were also obtained through the dispersion of moderate amounts (0.02–0.2 wt%) of the food-grade dye BBS into the thermoplastic aliphatic biodegradable polyester, PBS, by melt-mixing [33]. Analogous to the cyano-OPVs polymer blends, rapid quenching at  $0^\circ\text{C}$  of the PBS-BBS mixtures from the melt promoted the very fine molecular dispersion of BBS dyes that were kinetically



**Figure 12.7** Fluorescence emission spectra ( $\lambda_{\text{exc.}} = 277 \text{ nm}$ ) of initially quenched 0.05 wt% poly(1,4-butylene succinate)/bis(benzoxazolyl)stilbene film, and its color evolution as a function of the annealing time at  $65^\circ\text{C}$ . Inset: The same films, with images recorded under irradiation at  $366 \text{ nm}$  for specified times (h).

trapped within the PBS matrix, thus avoiding the formation of excimers. The luminescent behavior of PBS-BBS-quenched films was thermally controlled, with BBS aggregation tendencies and emission color changes proportional to the increasing annealing temperature (from  $50$  to  $80^\circ\text{C}$ ). The thermal stress applied to films led to the generation of thermodynamically stable aggregates among BBS dyes, promoting the color change of the material from blue (emission at  $435 \text{ nm}$ ) to green (emission at  $490 \text{ nm}$ ) (Figure 12.7).

The molecular dispersion of BBS dyes into quenched PBS films should allow a prompt optical response to thermal stimuli, that was faster with respect to the isolated dyes incorporated into a glassy amorphous polymer matrix. In the case of PMMA, this occurred at a lower annealing temperature due to the  $T_g$  value ( $-34^\circ\text{C}$ ) of the PBS supporting matrix.

#### 12.2.3.3 Anthracene Triaryl Amine-Terminated Diimide as Luminescent Dye

Another example of thermochromic flexible materials based on polyethylene was recently reported [38] in which the authors described the synthesis and incorporation into PE of a novel anthracene triaryl, amine-terminated diimide fluorescent sensor (Scheme 12.2, 4). When incorporated into the polymer (0.1 wt%, by melt-mixing), the films showed an emission at approximately  $620 \text{ nm}$  which was progressively red-shifted by increasing the annealing temperature to  $543 \text{ nm}$  (green color) at  $150^\circ\text{C}$ . Although it is likely that room-temperature emission from the anthracene diimide-doped PE was due to the formation of molecular aggregates,

this mechanism cannot fully explain the material's thermochromic behavior in these films. The authors suggested that heating at 150°C led to disruption of the dye aggregates, while the highly viscous medium of the polymer hampered full conjugation of the molecule, thus providing the same green emission.

## 12.3

### Metal Nanostructures as the Dispersed Phase

#### 12.3.1

##### Optical Properties of Metal Nanoassemblies

Today, nanoscience represents one of the most rapidly growing research areas, allowing the manipulation of matter at the nanoscale and allowing the controlled fabrication of such systems and devices. Engineered nanoparticles offer potential applications in many areas beneficial for humankind, including sensors, medical imaging, drug delivery systems, sunscreens, cosmetics, and many others [39–41]. Ever since the birth of nanotechnology, it has been clear that the optical properties of nanostructured metal particles depend heavily not only on their dimensions but also their shape [42, 43]. The absorption of visible light by metal nanoparticles was attributed to the induction of a collective oscillation of the free conduction electrons, promoted by their interaction with electromagnetic field. Indeed, when the wavelength of an incident radiation is comparable with the mean free path of the conduction electrons of a metal particle, the electric component of the electromagnetic incident field induces a polarization of the conduction electrons, giving rise to surface plasmon absorption [43, 44].

In particular, noble metal nanoparticles or semi-conducting nanocrystals embedded in bulk polymer matrices demonstrate enhanced optical (absorption, luminescence, and nonlinearity) [42, 43, 45–51] and magnetic properties [52], due to the stabilizing effects of size and aggregation provided by the macromolecular support. When dispersed into polymers in a nonaggregated form, however, those metal nanoparticles with very small diameters (a few nanometers) will allow the preparation of materials with much-reduced light scattering properties for applications as optical filters, linear polarizers, and optical sensors [53, 54].

For example, clusters of noble metals such as gold, silver, or copper, assume a real and natural color due to the absorption of visible light at the surface plasmon resonance (SPR) frequency. The application of composites based on polymeric materials and containing noble metal nanoparticles depends strictly on an ability to control and to modulate their size, shape, and extent of aggregation. As described by the Drude–Lorentz–Sommerfeld theory [42, 43], a decrease in metal particle size leads to a broadening of the absorption band, a decrease in the maximum intensity, and often also to a hypsochromic (blue) shift of the peak. These effects may also depend on cluster topology and packing [44, 55].

In addition, the anisotropic orientation of dipoles in nanoparticles by a uniaxially oriented host polymer matrix leads to the generation of two different

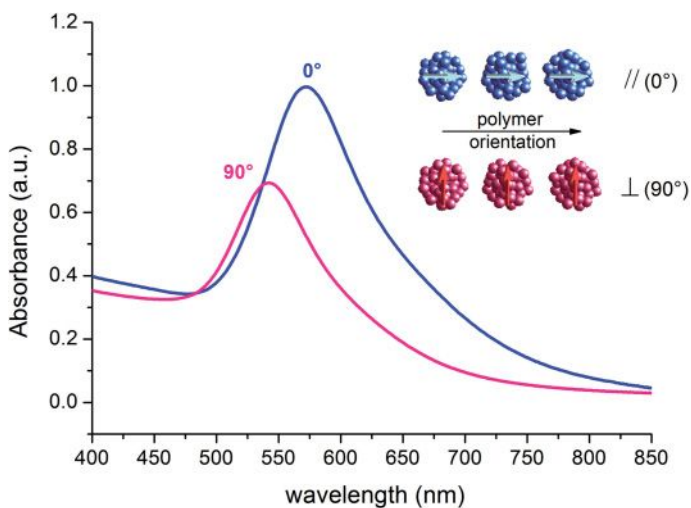


excitation modes: (i) with photons polarized along the aggregation direction, leading to a bathochromic (red) shift of the SPR; or (ii) with photons polarized orthogonally to the aggregation direction, resulting in a hypsochromic (blue) shift (Figure 12.8) [53].

The most common procedure for obtaining a dispersion of metal nanoparticles (MNPs) in a polymer matrix is to prepare a colloidal solution of stabilized MNPs, to mix this with the desired polymer in a mutual solvent, and then to cast a film by evaporation from the solution [53]. In contrast, few examples have been reported demonstrating the dispersion of preformed MNPs in a polymer matrix by melt-mixing at high temperature [56, 57].

Usually, a water-soluble metal salt is moved into an organic solvent by using tetra-alkylammonium bromide as phase-transfer agent, followed by successive reduction with sodium borohydride in the presence of an alkylthiol as surface stabilizer to prevent coalescence of the growing nanoparticles [58, 59]. In addition to thiols, a number of different surface stabilizers have been used, including amines [60], poly(vinyl pyrrolidone) (PVP) [61], and sodium poly(acrylate) [62]. By using the above-described colloid chemistry technique, MNPs have been dispersed in ultra-high molecular-weight polyethylene (UHMWPE) [11, 45], high-density polyethylene (HDPE) [57], poly(vinyl alcohol) (PVA) [53, 63, 64], poly(dimethylsiloxane) (PDMS) [65, 66], and poly(styrene-*b*-ethylene/propylene) [67].

An alternative approach for preparing nanocomposites containing metal nanoparticles involves an *in situ* formation of nanoparticles directly within the



**Figure 12.8** Influence of the polarization direction of light on the surface plasmon resonance (SPR) band of uniaxially oriented polymer film containing gold nanoparticles. The polarization direction was either parallel ( $0^\circ$ ) or perpendicular ( $90^\circ$ ) to the drawing axis.

polymer matrix [63, 68–80]. This process is relatively straightforward and requires simply a reduction of the metal ions precursors by either a photochemical or a thermally induced process. However, in contrast to nanoparticles prepared via colloid chemistry, controlling the size distribution of these *in situ*-prepared particles is often more difficult due to influential factors such as the polymer matrix composition, and the time and energy density of the photo- or thermo-irradiation process.

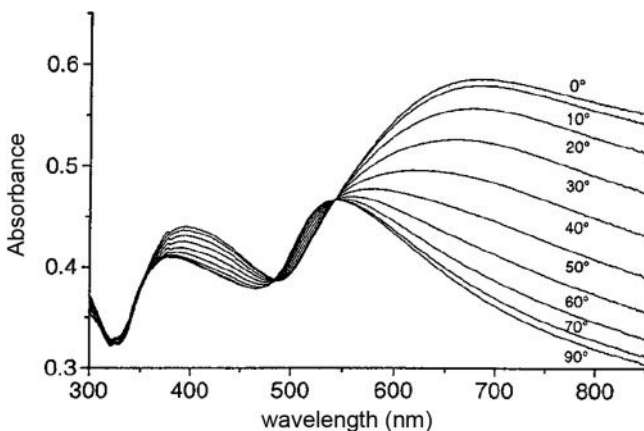
### 12.3.2

#### Nanocomposite-Based Indicators to Mechanical Stress

##### 12.3.2.1 The Use of Metal Nanoparticles

Nanoparticle dispersions in a polymer matrix can be rendered macroscopically anisotropic, a feature that has allowed their use in nonlinear optical devices and linear absorbing polarizers, for example, in display applications [11, 45, 53, 57, 81–83]. Highly dichroic noble metal nanoparticles are efficiently obtained after mechanical drawing of the polymer matrix. The uniaxial orientation of the macromolecular fibers promotes the anisotropic distribution of both the crystalline and amorphous phases, which then determines the alignment of the metal particles along the direction of drawing [53, 84].

Examples of this include PVA and HDPE film composites with alkyl thiol-coated gold and silver particles which, once uniaxially oriented by stretching, present angular dependencies of the absorption intensity and the color of the transmitted light [53] (Figure 12.9).



**Figure 12.9** UV-visible spectra of drawn nanocomposites comprising high-density polyethylene and gold nanoparticles, taken in linearly polarized light at different angles between the polarization direction of the incident light and the drawing direction [53]. Reproduced with permission of John Wiley & Sons, Ltd.

The absorption of photons is dominated by the excitation of surface plasmons in the metal particles and their aggregates [42, 43]. For example, drawn polyethylene/silver nanocomposites exhibited a strongly polarization-dependent color. Yet, the color of the light transmitted through the oriented nanocomposite shifted from red to yellow when the angle between the polarization axis of an interposed polarizer and the drawing direction of the film was varied from 0° to 90° [57].

Moreover, the optical response of metal nanoparticles can be strongly enhanced through the introduction of photoactive organic molecules, possibly combined with control of the nanoparticle dimensions [85]. The presence of direct electronic interactions between metal and metal-bound chromophores is of particular interest, because it could allow for a fine modulation of the optical properties by inducing an energy transfer from the excited state of the chromophore to the SPR of the metal [86, 87].

For example, the dispersion of gold nanoparticles and gold-binding chromophores in a stretched polymer matrix of PE produces nanocomposites with unusual and anisotropic optical properties [45]. Strongly dichroic, terthiophene-based chromophores, which previously had been used in anisotropic PE dispersions for the preparation of linear polarizers [88], were modified with a thiol group and used for the preparation of gold nanoparticles. These authors demonstrated that the electronic systems of the chromophores were coupled with the gold nanoparticles, and that the polarization of the absorbed radiation could be preserved during energy transfer between a chromophore and a metal particle.

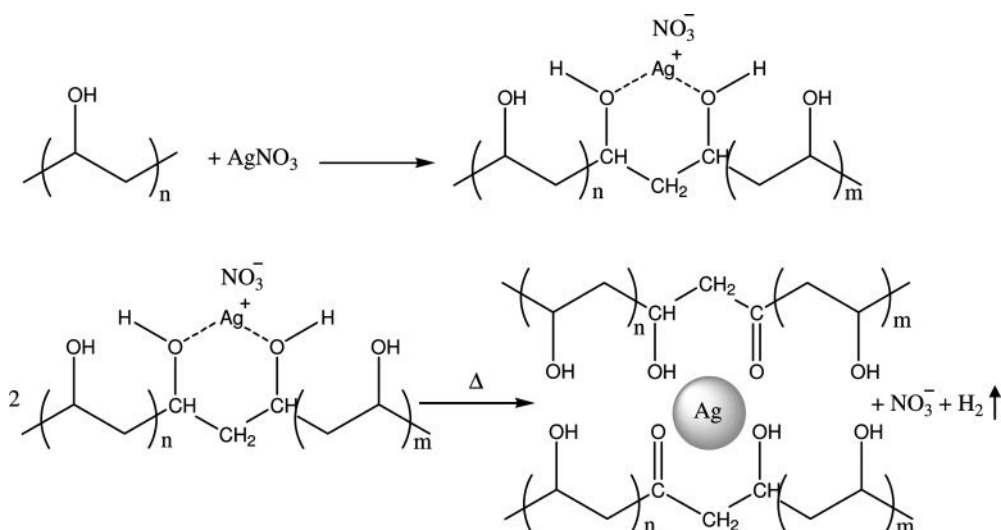
An interesting method for the production of dichroic nanocomposites with a reversible optical response to mechanical stress has been recently reported [65, 66]. Here, Caseri *et al.* [65] based their studies on the difference in the transmitted color of gold and silver elastomeric nanocomposites in dry and in swollen samples, based on the change in interparticle distances which resulted from the swelling process. Caseri's group showed that a given dry gold-polymer nanocomposite could adopt not only one but several colors, and that these colors could be switched through swelling processes, including reversible and irreversible dichroic-monochroic color transitions. A lightly crosslinked rubber such as PDMS was selected as the supporting polymer matrix, as it can take up large quantities of solvent without dissolution, and might also afford reversible dichroic effects upon deformation. The oriented PDMS composite films appeared blue-gray with light polarized parallel to the drawing axis, and red with light in a perpendicular orientation; the dichroism was preserved upon removing the strain. Swelling (with toluene) of the dichroic oriented films caused the specimens to become pink, indicating that the individual particles in the linear assemblies had disconnected and turned blue and nondichroic following evaporation of the toluene.

Recently, nanocomposites based on PVA and poly [ethylene-*co*-vinyl alcohol] polymers and nanostructured gold have been efficiently prepared using a UV photoreduction process [89]. In this case, the polymer matrix based on vinyl alcohol repeating units, acted both as a coreducing agent, as a protective agent against particle agglomeration, and as a macroscopic support. The very rapid process provided dispersed gold nanoparticles with average diameters ranging

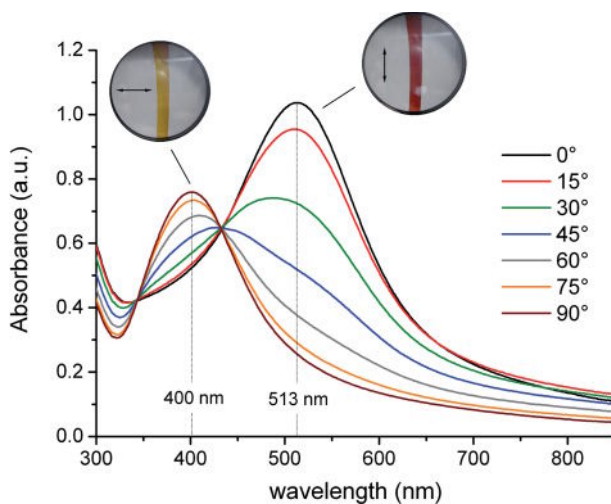
from 3 to 20 nm, depending on the host polymer matrix and the irradiation time. Uniaxial drawing of the Au/polymer composites promoted anisotropic packing of the embedded gold nanoparticles along the stretching direction of the film, and this resulted in a shift of the SPR of gold well above 30–40 nm (83 nm maximum), thus producing a well-defined polarization-dependent color change from blue to purple [89]. The optical responsiveness to mechanical stimuli appeared similar to that reported previously by Smith *et al.* for optically anisotropic polyethylene-gold nanocomposites obtained by introducing preformed and annealed alkyl-thiol-protected gold nanoparticles into polyethylene [81]. The UV photogeneration of gold nanoparticles directly into a polymer film precursor represents an easier, faster, and highly competitive technique for the preparation of optically responsive nanocomposites to mechanical stimuli, however.

Among the large number of hybrid organic-inorganic systems investigated, those nanocomposites based on PVA and silver have attracted great interest because of their specific optical, catalytic, electronic, magnetic, and antimicrobial properties [64, 68, 76, 90–97]. Recent developments have been focused in this direction in order to optimize the preparation Ag/PVA nanostructured films by using alternative “*in situ*” methods such as sun-(UV) [76, 98, 99] or thermally promoted reduction processes [100].

These simple and very rapid methods provide dispersed Ag nanoparticles (<4 wt%) with average diameters that range from 15 to 150 nm, depending on the type of preparation [101]. Thermal annealing and UV irradiation in fact form the basis for these very efficient methodologies, because they take advantage of the formation of a complex between the PVA matrix, while silver nitrate [102]: Ag<sup>+</sup> ions can easily be chelated by the hydroxyl groups of the polymer and then reduced directly in the host matrix (Scheme 12.3).



**Scheme 12.3** Thermally promoted formation of silver nanoparticles within the PVA matrix.



**Figure 12.10** UV-visible spectra of oriented sun-promoted Ag/PVA nanocomposite films as a function of the angle between the polarization of light and the drawing direction of the film. The insets show images of the same films under polarized light.

Ag(0) formation was progressively followed using both UV-visible and Fourier transform-infrared (FT-IR) spectroscopies, monitoring the evolution of the SPR of silver (ca. 430 nm) and the carbonyl absorption band of PVA (ca.  $1720\text{ cm}^{-1}$ ), respectively [101].

After uniaxial orientation, the Ag/PVA nanocomposites showed a pronounced dichroic behavior, based on the anisotropic distribution of the silver assemblies along the stretching direction. In uniaxially oriented samples, the light absorption was seen to depend heavily on the angle between the polarization direction of the incident light and the orientation of the particles embedded onto the host polymeric matrix. Simply by observing oriented samples through a linear polarizer, it is possible to observe that the color of the films depends markedly on the relative orientation between the polarizer and the drawing direction of the film (Figure 12.10).

The maximum shifts measured for the oriented films were more than 100 nm, while the spectra showed a well-defined isosbestic point, thus confirming the existence of two different populations of absorbing nanoparticles [89]. Interestingly, the shift in wavelength of the silver SPR band also occurred at moderate drawings (draw ratio  $\geq 2$ ). The nanocomposite films thus produced were highly optically responsive to mechanical stimuli as uniaxial deformations.

Analogously, thermochromic films based on silver/polystyrene nanocomposites have been reported, these being prepared by the thermal annealing of silver dodecylmercaptide/polystyrene blends at approximately  $200\text{ }^\circ\text{C}$  [103–105]. It was shown that alkanethiolates of transition metals dissolved in polymers would

undergo thermolysis reactions at moderately low temperatures (120–200 °C), producing polymer-embedded metal or metal sulfide clusters. The rapid and reversible color switch (from dark brown to light yellow) that was observed when exposing the nanocomposite films at approximately 80 °C was attributed to a change in the surface-plasmon absorption of silver nanoparticles that follows the variation of inter-particle distances due to polymer matrix expansion [104].

#### 12.3.2.2 The Use of Metal Nanorods

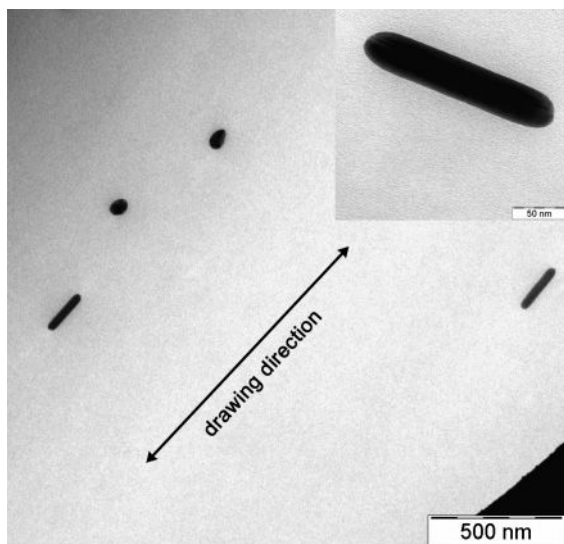
During the past few years, there has been an increasing interest towards the optical properties of elongated nanostructures, as nanorods or nanowires, mainly because their absorption spectrum is characterized by a longitudinal and a transverse SPR, rather than the single resonance, as observed for spherical nanoparticles [40, 106–109]. In other words, despite spherical particles having the greatest symmetry, they have only one plasmon resonance (all modes are degenerate). However, by extending a particle in one dimension, a second, lower-energy resonance band in the longitudinal direction (longitudinal mode) becomes apparent, while the original plasmon resonance (transversal mode) remains unaffected. In general, the number of SPR peaks will increase as the particle symmetry decreases.

In general, those one-dimensional (1-D) structures that range in size from a few hundreds of nanometers to several micrometers, or which have a high aspect ratio (the ratio between the longest and shortest structure axes), are referred to as nanowires, and smaller more elongated structures as nanorods.

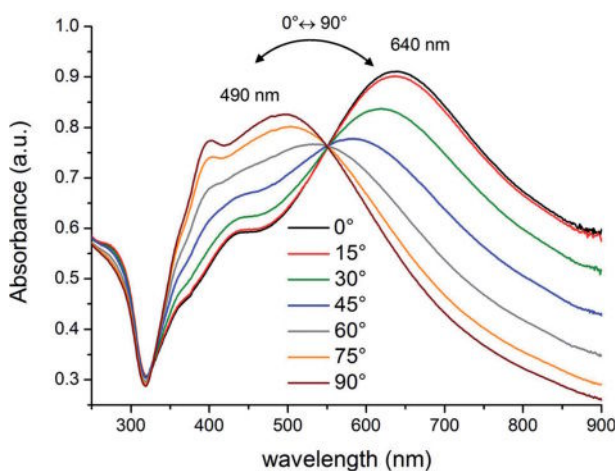
In the past, many techniques have been developed for the preparation of 1-D nanostructures, and in order to understand this basic growth process it will first be necessary to consider the spontaneous growth process [110]. In a previous report [44] silver nanorods were prepared via a seed-mediated process and, depending on the surfactant (capping material) used, it was possible to produce shapes other than spheres during seed-mediated growth. Several theories [111] have centered on a preferential adsorption of the surfactant to certain crystal facets on seed particles; in other words, the surfactant binds to the surface radially, but not axially. Unfortunately, however, this behavior blocks crystal growth on these surfaces, such that the particle can grow only in the axial direction.

As reported by the present authors' group and elsewhere [109, 112, 113], in order to produce nanocomposite-containing metal nanostructures which are anisotropic and thus potentially more sensitive and responsive to any mechanical stimuli applied to the polymer matrix, silver nanorods were mixed with an aqueous solution of PVA, such that a homogeneous film was obtained after solvent evaporation.

Following uniaxial stretching, the elongated silver nanostructures (mostly nanorods, but mixed with other spherical assemblies generated during solution casting as a consequence of particle coalescence) that were embedded into the polymer matrix assumed the direction of the drawing, as indicated using transmission electron microscopy (TEM) (Figure 12.11). These dispersed nanorods had diameters between 30 and 35 nm, and a length <180 nm.



**Figure 12.11** Bright-field TEM image of PVA-oriented film containing silver nanostructures [114].



**Figure 12.12** UV-visible spectra of oriented Ag nanorods/PVA film as a function of the angle between the light polarization and the drawing direction [114].

As expected, the oriented nanocomposite films showed a strong dichroism when irradiated with a linearly polarized light (Figure 12.12). Changing the relative orientation between the stretching direction of the film and the polarization vector of the incident light induced a suppression of the longitudinal SPR at 640 nm in favor of the transversal SPR at 420 nm. The two isosbestic points, placed at 327





**Figure 12.13** Images of oriented Ag nanorods/PVA film with polarization direction of the incident light parallel (blue,  $0^\circ$ ) and perpendicular (brown-red,  $90^\circ$ ) to the drawing direction [114].

and 550 nm, were originated by the two independent optical modes (transversal and longitudinal) that characterized the optical absorption of silver nanorods. The large, reversible variation ( $\sim 220$  nm) in wavelength of the two absorption maxima was also flanked by an increase in a red component placed at 500 nm and coupled with a strong decreasing of the blue contribution located at 640 nm. Accordingly, the film changed its color under linearly polarized light from blue (parallel configuration,  $0^\circ$ ) to brown-red (perpendicular configuration,  $90^\circ$ ), with only a moderate drawing (draw ratio  $\geq 2$ ) (Figure 12.13).

Another recently reported and highly interesting example concerned the application of gold nanorods to polymers [115]. This group described the generation of gold nanorod (GNR)–elastin-like polypeptide (ELP) nanoassemblies, the optical responses of which could be manipulated based on their exposure to near-infrared (NIR) light. Cysteine-containing ELPs were actually self-assembled on GNRs mediated by gold–thiol bonds, which led to the generation of GNR–ELP nanoassemblies. Exposure of these assemblies to NIR light at 720 nm resulted in a heating of the GNRs due to SPR (directed in the NIR region of the absorption spectrum at 710 and 820 nm). Subsequent heat transfer from the GNRs led to an increase in the temperature of the self-assembled ELP above its  $T_g$ -value (i.e.,  $33\text{--}34^\circ\text{C}$ ), which in turn led to a phase transition and aggregation of the GNR–ELP assemblies and a clear change in the optical density of the system. Based on these findings, it was suggested that polypeptides might be interfaced with GNRs to produce optically responsive nanoassemblies for sensing and drug delivery applications.

## 12.4

### Conclusions

The information provided in this chapter provides a clear demonstration of the potential offered by controlling the dispersion of luminescent aromatic molecules and noble metal nanoaggregates into a wide range of polymer matrices, down to the nanometer scale. Whilst most of the polymers have been characterized by their excellent thermomechanical properties, a lack of any particular optical response was apparent wavelengths above 200 nm. In contrast, the addition of very small

(<4 wt%) amounts of correctly selected active dyes or noble metal (nano)assemblies allowed the production of flexible or rigid polymeric thin films which demonstrated remarkable optical responses towards external stimuli. Luminescent, excimer-forming dyes have been described as a new class of optical indicators for many thermoplastic and elastomeric polymer matrices for mechanical and thermal uses. However, the greater the interaction and asymmetry of the metal nanostructures, the higher is the dichroic response of the SPR following mechanical stimulation of the nanocomposite film. Thus, these hybrid materials may be regarded as extremely important for future advanced applications, including the possibility of inducing a nanophase organization through external stresses.

### Acknowledgments

These studies were supported financially by the FIRB Project RBNE03R78E\_005 of the Italian Ministry of University and Research (MIUR).

### References

- 1 Birks, J.B. (1975) *Rep. Prog. Phys.*, **38**, 903–974.
- 2 Phillips, D. (1985) *Polymer Photophysics: Luminescence, Energy Migration, and Molecular Motion in Synthetic Polymers*, Chapman & Hall Ltd, London.
- 3 Lakowicz, J.R. (1986) *Principles of Fluorescent Spectroscopy*, Plenum Press, New York.
- 4 Ceroni, G.B.P., Marchioni, F. and Balzani, V. (2005) *Prog. Polym. Sci.*, **30**, 453–473.
- 5 Duhamel, J. (2004) *Macromolecules*, **37**, 1987–1989.
- 6 Vangani, V., Drage, J., Mehta, J., Mathew, A.K. and Duhamel, J. (2001) *J. Phys. Chem. B*, **105**, 4827–4839.
- 7 Siu, H. and Duhamel, J. (2004) *Macromolecules*, **37**, 9287–9289.
- 8 Naciri, J. and Weiss, R.G. (1989) *Macromolecules*, **22**, 3928–3936.
- 9 Morawetz, H. (1999) *J. Polym. Sci., Part A Polym. Chem.*, **37**, 1725.
- 10 Semerak, S.N. and Frank, C.W. (1984) *Adv. Polym. Sci.*, **54**, 31–85.
- 11 Pucci, A., Elvati, P., Ruggeri, G., Liuzzo, V., Tirelli, N., Isola, M. and Ciardelli, F. (2003) *Macromol. Symp.*, **204**, 59–70.
- 12 Frank, C.W., Gashgari, M.A. and Semerak, S.N. (1986) *NATO ASI Ser., Ser. C*, **182**, 523–546.
- 13 Semerak, S.N. and Frank, C.W. (1984) *Adv. Chem. Ser.*, **206**, 77–100.
- 14 Semerak, S.N. and Frank, C.W. (1984) *Macromolecules*, **17**, 1148–1157.
- 15 Semerak, S.N. and Frank, C.W. (1983) *Adv. Chem. Ser.*, **203**, 757–771.
- 16 Semerak, S.N. and Frank, C.W. (1981) *Polym. Prep. (Am. Chem. Soc., Div. Polym. Chem.)*, **22**, 314–315.
- 17 Birks, J.B. (1970) *Photophysics of Aromatic Molecules*, John Wiley & Sons, New York.
- 18 Birks, J.B., Dyson, D.J. and Munro, I.H. (1963) *Proc. Roy. Soc. (London)*, **275**, 575–588.
- 19 Halkyard, C.E., Rampey, M.E., Kloppenburg, L., Studer-Martinez, S.L. and Bunz, U.H.F. (1998) *Macromolecules*, **31**, 8655–8659.
- 20 Wilson, J.N., Smith, M.D., Enkelmann, V. and Bunz, U.H.F. (2004) *Chem. Commun.*, 1700–1701.
- 21 Yang, J., Li, H., Wang, G. and He, B. (2001) *J. Appl. Polym. Sci.*, **82**, 2347–2351.

- 22 van Hutten, P.F., Krasnikov, V.V., Brouwer, H.J. and Hadziioannou, G. (1999) *Chem. Phys.*, **241**, 139–154.
- 23 Pucci, A., Biver, T., Ruggeri, G., Itzel Meza, L. and Pang, Y. (2005) *Polymer*, **46**, 11198–11205.
- 24 Crenshaw, B.R. and Weder, C. (2005) *Adv. Mater.*, **17**, 1471–1476.
- 25 Kinami, M., Crenshaw, B.R. and Weder, C. (2006) *Chem. Mater.*, **18**, 946–955.
- 26 Lowe, C. and Weder, C. (2002) *Adv. Mater.*, **14**, 1625–1629.
- 27 Crenshaw, B.R. and Weder, C. (2003) *Chem. Mater.*, **15**, 4717–4724.
- 28 Crenshaw, B.R., Burnworth, M., Khariwala, D., Hiltner, A., Mather, P.T., Simha, R. and Weder, C. (2007) *Macromolecules*, **40**, 2400–2408.
- 29 Crenshaw, B.R. and Weder, C. (2006) *Macromolecules*, **39**, 9581–9589.
- 30 Kunzelman, J., Kinami, M., Crenshaw, B.R., Protasiewicz, J.D. and Weder, C. (2008) *Adv. Mater.*, **20**, 119–122.
- 31 Pucci, A., Bertoldo, M. and Bronco, S. (2005) *Macromol. Rapid Commun.*, **26**, 1043–1048.
- 32 Andreotti, L., Pucci, A., Ruggeri, G., Scatto, M. and Sterner, M. (2007) Monitoring polyethylene films orientation during melt-processing through UV-vis and IR spectroscopy in polarized light. Presented at *European Polymer Congress, Portoroz, Slovenia*, p. 263.
- 33 Pucci, A., Di Cuia, F., Signori, F. and Ruggeri, G. (2007) *J. Mater. Chem.*, **17**, 783–790.
- 34 Donati, F., Pucci, A., Cappelli, C., Mennucci, B. and Ruggeri, G. (2008) *J. Phys. Chem. B*, **112**, 3668–3679.
- 35 Crenshaw, B.R., Kunzelman, J., Sing, C.E., Ander, C. and Weder, C. (2007) *Macromol. Chem. Phys.*, **208**, 572–580.
- 36 Kunzelman, J., Chung, T., Mather, P.T. and Weder, C. (2008) *J. Mater. Chem.*, **18**, 1082–1086.
- 37 Lendlein, A. and Kelch, S. (2002) *Angew. Chem. Int. Ed. Engl.*, **41**, 2034–2057.
- 38 Tyson, D.S., Carbaugh, A.D., Ilhan, F., Santos-Perez, J. and Meador, M.A. (2008) *Chem. Mater.*, **20**, 6595–6596.
- 39 Baker, C.C., Pradhan, A. and Shah, S.I. (2004) in *Encyclopedia of Nanoscience and Nanotechnology*, American Scientific Publisher, Stevenson Ranch, California, Vol. 5, pp. 449–473.
- 40 Jain, P.K., Huang, X., El-Sayed, I.H. and El-Sayed, M.A. (2008) *Acc. Chem. Res.*, **41**, 1578–1586.
- 41 Nair, L.S. and Laurencin, C.T. (2007) *J. Biomed. Nanotechnol.*, **3**, 301–316.
- 42 Klabunde, K.J. (2001) *Nanoscale Materials in Chemistry*, John Wiley & Sons, Inc., New York.
- 43 Kreibitz, U. and Genzel, L. (1985) *Surf. Sci.*, **156**, 678–700.
- 44 Schwartzberg, A.M. and Zhang, J.Z. (2008) *J. Phys. Chem. C*, **112**, 10323–10337.
- 45 Pucci, A., Tirelli, N., Willneff, E.A., Schroeder, S.L.M., Galembeck, F. and Ruggeri, G. (2004) *J. Mater. Chem.*, **14**, 3495–3502.
- 46 Beecroft, L.L. and Ober, C.K. (1997) *Chem. Mater.*, **9**, 1302–1317.
- 47 Gehr, R.J. and Boyd, R.W. (1996) *Chem. Mater.*, **8**, 1807–1819.
- 48 Godovsky, D.Y. (2000) *Adv. Polym. Sci.*, **153**, 163–205.
- 49 Trindade, T., O'Brien, P. and Pickett, N.L. (2001) *Chem. Mater.*, **13**, 3843–3858.
- 50 Caseri, W.R. (2006) *Mater. Sci. Technol.*, **22**, 807–817.
- 51 Ni, Y., Hao, H., Cao, X., Su, S., Zhang, Y. and Wei, X. (2006) *J. Phys. Chem. B*, **110**, 17347–17352.
- 52 de la Venta, J., Pucci, A., Pinel, E.F., Garcia, M.A., de Julian Fernandez, C., Crespo, P., Mazzoldi, P., Ruggeri, G. and Hernando, A. (2007) *Adv. Mater.*, **19**, 875–877.
- 53 Caseri, W. (2000) *Macromol. Rapid Commun.*, **21**, 705–722.
- 54 Heilmann, A. (2003) *Polymer Films with Embedded Metal Nanoparticles*, Vol. 52, Springer, Berlin.
- 55 El-Sayed, M.A. (2001) *Acc. Chem. Res.*, **34**, 257–264.
- 56 Dirix, Y., Bastiaansen, C., Caseri, W. and Smith, P. (1999) *J. Mater. Sci.*, **34**, 3859–3866.
- 57 Dirix, Y., Bastiaansen, C., Caseri, W. and Smith, P. (1999) *Adv. Mater.*, **11**, 223–227.
- 58 Brust, M., Walker, M., Bethell, D., Schiffrin, D.J. and Whyman, R. (1994)

- J. Chem. Soc., Chem. Commun.*, 801–802.
- 59 Lu, A.H., Lu, G.H., Kessinger, A.M. and Foss, C.A. Jr. (1997) *J. Phys. Chem. B*, **101**, 9139–9142.
- 60 Leff, D.V., Brandt, L. and Heath, J.R. (1996) *Langmuir*, **12**, 4723–4730.
- 61 Carotenuto, G. (2001) *Appl. Organomet. Chem.*, **15**, 344–351.
- 62 Hussain, I., Brust, M., Papworth, A.J. and Cooper, A.I. (2003) *Langmuir*, **19**, 4831–4835.
- 63 Perez-Juste, J., Rodriguez-Gonzalez, B., Mulvaney, P. and Liz-Marzan, L.M. (2005) *Adv. Funct. Mater.*, **15**, 1065–1071.
- 64 Mbhele, Z.H., Salemane, M.G., van Sittert, C.G.C.E., Nedeljkovic, J.M., Djokovic, V. and Luyt, A.S. (2003) *Chem. Mater.*, **15**, 5019–5024.
- 65 Uhlenhaut, D.I., Smith, P. and Caseri, W. (2006) *Adv. Mater.*, **18**, 1653–1656.
- 66 Pastoriza-Santos, I., Perez-Juste, J., Kicckelbick, G. and Liz-Marzan, L.M. (2006) *J. Nanosci. Nanotechnol.*, **6**, 453–458.
- 67 Bockstaller, M.R. and Thomas, E.L. (2003) *J. Phys. Chem. B*, **107**, 10017–10024.
- 68 Mallick, K., Witcomb, M.J. and Scurrall, M.S. (2004) *J. Mater. Sci.*, **39**, 4459–4463.
- 69 Salvati, R., Longo, A., Carotenuto, G., De Nicola, S., Pepe, G.P., Nicolais, L. and Barone, A. (2005) *Appl. Surf. Sci.*, **248**, 28–31.
- 70 Raikher, Y.L., Stepanov, V.I., Depeyrot, J., Sousa, M.H., Tourinho, F.A., Hasmonay, E. and Perzynski, R. (2004) *J. Appl. Phys.*, **96**, 5226–5233.
- 71 Dong, S., Tang, C., Zhou, H. and Zhao, H. (2004) *Gold Bull.*, **37**, 187–195.
- 72 Kaneko, K., Sun, H.-B., Duan, X.-M. and Kawata, S. (2003) *Appl. Phys. Lett.*, **83**, 1426–1428.
- 73 Henneke, D.E., Malyavanatham, G., Kovar, D., O'Brien, D.T., Becker, M.F., Nichols, W.T. and Keto, J.W. (2003) *J. Chem. Phys.*, **119**, 6802–6809.
- 74 Callegari, A., Tonti, D. and Chergui, M. (2003) *Nano Lett.*, **3**, 1565–1568.
- 75 Seibel, M. (2001) In PCT Int. Application (Plasco Ehrlich Plasma-Coating GmbH, Germany), WO2001083596, p. 12.
- 76 Gaddy, G.A., McLain, J.L., Steigerwalt, E.S., Broughton, R., Slaten, B.L. and Mills, G. (2001) *J. Cluster Sci.*, **12**, 457–471.
- 77 Tanahashi, I. and Kanno, H. (2000) *Appl. Phys. Lett.*, **77**, 3358–3360.
- 78 Zhou, Y., Wang, C.Y., Zhu, Y.R. and Chen, Z.Y. (1999) *Chem. Mater.*, **11**, 2310–2312.
- 79 Itakura, T., Torigoe, K. and Esumi, K. (1995) *Langmuir*, **11**, 4129–4134.
- 80 Porel, S., Singh, S. and Radhakrishnan, T.P. (2005) *Chem. Commun.*, 2387–2389.
- 81 Dirix, Y., Darribere, C., Heffels, W., Bastiaansen, C., Caseri, W. and Smith, P. (1999) *Appl. Opt.*, **38**, 6581–6586.
- 82 Crespo, P., Litran, R., Rojas, T.C., Multigner, M., de la Fuente, J.M., Sanchez-Lopez, J.C., Garcia, M.A., Hernando, A., Penades, S. and Fernandez, A. (2004) *Phys. Rev. Lett.*, **93**, 087204.
- 83 Hao, E., Schatz, G.C. and Hupp, J.T. (2004) *J. Fluoresc.*, **14**, 331–341.
- 84 Caseri, W. (2003) *Chemistry of Nanostructured Materials*, World Scientific Publishing Co., Mountain View, CA, pp. 359–386.
- 85 Chandrasekharan, N., Kamat, P.V., Hu, J. and Jones, G. II (2000) *J. Phys. Chem. B*, **104**, 11103–11109.
- 86 Thomas, K.G. and Kamat, P.V. (2003) *Acc. Chem. Res.*, **36**, 888–898.
- 87 Thomas, K.G. and Kamat, P.V. (2000) *J. Am. Chem. Soc.*, **122**, 2655–2656.
- 88 Tirelli, N., Amabile, S., Cellai, C., Pucci, A., Regoli, L., Ruggeri, G. and Ciardelli, F. (2001) *Macromolecules*, **34**, 2129–2137.
- 89 Pucci, A., Bernabò, M., Elvati, P., Meza, L.I., Galembeck, F., de Paula Leite, C.A., Tirelli, N. and Ruggeri, G. (2006) *J. Mater. Chem.*, **16**, 1058–1066.
- 90 Kim, J.-H. and Lee, T.R. (2007) *Langmuir*, **23**, 6504–6509.
- 91 Lin, W.-C. and Yang, M.-C. (2005) *Macromol. Rapid Commun.*, **26**, 1942–1947.
- 92 Kong, H. and Jang, J. (2006) *Chem. Commun.*, 3010–3012.
- 93 Khanna, P.K., Singh, N., Charan, S., Subbarao, V.V.V.S., Gokhale, R. and Mulik, U.P. (2005) *Mater. Chem. Phys.*, **93**, 117–121.

- 94 Karthikeyan, B. (2005) *Physica B*, **364**, 328–332.
- 95 Cascaval, C.N., Cristea, M., Rosu, D., Ciobanu, C., Padurarau, O. and Cotofana, C. (2007) *J. Optoelectron. Adv. Mater.*, **9**, 2116–2120.
- 96 Badr, Y. and Mahmoud, M.A. (2006) *J. Mater. Sci.*, **41**, 3947–3953.
- 97 Fornasiero, D. and Grieser, F. (1987) *Chem. Phys. Lett.*, **139**, 103–108.
- 98 Gaddy, G.A., Korchev, A.S., McLain, J.L., Slaten, B.L., Steigerwalt, E.S. and Mills, G. (2004) *J. Phys. Chem. B*, **108**, 14850–14857.
- 99 Gaddy, G.A., McLain, J.L., Korchev, A.S., Slaten, B.L. and Mills, G. (2004) *J. Phys. Chem. B*, **108**, 14858–14865.
- 100 Clemenson, S., David, L. and Espuche, E. (2007) *J. Polym. Sci., Part A Polym. Chem.*, **45**, 2657–2672.
- 101 Bernabo, M., Ciardelli, F., Pucci, A. and Ruggeri, G. (2008) *Macromol. Symp.*, **270**, 177–186.
- 102 Zidan, H.M. (1999) *Polym. Test.*, **18**, 449–461.
- 103 Carotenuto, G., Nicolais, L. and Perlo, P. (2006) *Polym. Eng. Sci.*, **46**, 1016–1021.
- 104 Carotenuto, G., La Peruta, G. and Nicolais, L. (2006) *Sens. Actuators B*, **B114**, 1092–1095.
- 105 Carotenuto, G., Martorana, B., Perlo, P. and Nicolais, L. (2003) *J. Mater. Chem.*, **13**, 2927–2930.
- 106 Maier, S.A., Kik, P.G., Atwater, H.A., Meltzer, S., Harel, E., Koel, B.E. and Requicha, A.A.G. (2003) *Nat. Mater.*, **2**, 229–232.
- 107 Gluodenis, M. and Foss, C.A. Jr. (2002) *J. Phys. Chem. B*, **106**, 9484–9489.
- 108 Mohamed, M.B., Volkov, V., Link, S. and El-Sayed, M.A. (2000) *Chem. Phys. Lett.*, **317**, 517–523.
- 109 Perez-Juste, J., Rodriguez-Gonzalez, B., Mulvaney, P. and Liz-Marzan, L.M. (2005) *Adv. Funct. Mater.*, **15**, 1065–1071.
- 110 Cao, G. (2004) *Nanostructures and Nanomaterials, Synthesis, Properties and Applications*, Imperial College Press, London.
- 111 Gole, A. and Murphy, C.J. (2004) *Chem. Mater.*, **16**, 3633.
- 112 Wilson, O., Wilson, G.J. and Mulvaney, P. (2002) *Adv. Mater.*, **14**, 1000–1004.
- 113 Zhou, Y., Yu, S.H., Wang, C.Y., Li, X.G., Zhu, Y.R. and Chen, Z.Y. (1999) *Adv. Mater.*, **11**, 850–852.
- 114 Bernabo, M. (2009) Synthesis and characterization of optical and magnetic properties of nanostructured metal-polymer systems. PhD Thesis, University of Pisa, Italy.
- 115 Huang, H.-C., Koria, P., Parker, S.M., Selby, L., Megeed, Z. and Rege, K. (2008) *Langmuir*, **24**, 14139–14144.



## 13

# Nanocomposites Based on Phyllosilicates: From Petrochemicals to Renewable Thermoplastic Matrices

*Maria-Beatrice Coltelli, Serena Coiai, Simona Bronco, and Elisa Passaglia*

### 13.1

#### Introduction

Polymer–phyllosilicate nanocomposites, which are characterized by the presence of fillers that are less than 100 nm in at least one dimension, have been the subject of many reviews and reports during the past decade [1, 2]. The excellent balance between performance and filler content (2–5% by weight of phyllosilicates is sufficient to provide clear improvements in properties) makes these composites especially interesting as innovative materials for a variety of applications. Such improvements, which include high moduli, increased strength and heat resistance, and decreased gas permeability and flammability, can be ascribed to a fundamental feature of polymer nanocomposites, namely that the small size of the fillers leads to a dramatic increase in interfacial area when compared to traditional composites [3].

Many studies have been initiated by considering conventional petrochemical-derived polymer matrices, such as polyolefins, polyamides, and polyesters. Typically, the preparation methods underwent intense examination, the aim being to correlate the structure and morphology of these new nanostructured materials with their ultimate properties.

Today, the development of renewable polymeric materials with excellent properties forms the subject of active research interest worldwide [4], with aliphatic polyesters being among the most promising materials for the production of high-performance, environment-friendly, biodegradable plastics [5]. The need to optimize their properties, in order that in time they can replace present-day commodities, requires the assessment of new, selective, efficient, and sustainable preparation methods. Hence, a comparative review of the preparation methods for both commodities and renewable polyester-based materials should allow comparisons to be made of these two classes of material in terms of their potential and future opportunities.



## 13.1.1

**Structure of Phyllosilicates**

Phyllosilicates [6] are an essential constituent of argillaceous sedimentary rocks and of some low-grade metamorphic rocks. The group includes micas, clays, and serpentine, which are soft minerals with a variable, but generally low, density. Minerals belonging to the phyllosilicate group are characterized by their possessing layers of  $[\text{SiO}_4]^{4-}$  tetrahedra linked together to form a flat sheet. Rings of tetrahedra are linked by shared oxygens to other rings in a two-dimensional (2-D) plane that produces a sheet-like structure. Typically, the sheets are then connected to each other by layers of cations, together with water or other low molecules devoid of any electrical charge. In some substrates, the sheets are rolled into tubes that produce fibers, as in asbestos serpentine. The silicon: oxygen ratio is generally 1: 2.5, because only one oxygen is bonded exclusively to the silicon, while the other three oxygens are half-shared (1.5) with other silicons.

13.1.1.1 **Clays**

In the case of polymeric composites [7], the most important subcategory is that of clays [8], including kaolinite, montmorillonite/smectite, illite (mica) and chlorite subgroups (Table 13.1). The clay minerals form part of a general, but important, group that contain a high percentage of water trapped between the silicate sheets. Most clays are chemically and structurally analogous to other phyllosilicates, but contain varying amounts of water and so allow more substitution of their cations. Clay minerals tend to form microscopic to submicroscopic crystals, with the percentage of water changing as a function of the humidity change. In the presence of water, clays become plastic and can be molded and formed. The expansion of clay is due to a progressive inclusion of water between the stacked silicate layers. Clays are usually mixed not only with other clays but also with microscopic crystals of carbonates, feldspars, micas, and quartz.

In the case of polymer nanocomposites, the most important fillers belong to the group of smectites. The term “smectite” is used to describe a family of expandable 2:1 phyllosilicate minerals. Specific minerals included in the smectite family [9] include pyrophyllite, talc, vermiculite, saunonite, saponite, nontronite, montmorillonite, and several less common species. Smectites [10] consist of a single octahedral sheet sandwiched between two tetrahedral sheets, with the octahedral sheet sharing the apical oxygens of the tetrahedral sheet. The octahedral sheet may be either dioctahedral or trioctahedral. Some minerals of the smectite groups are neutral (e.g., kaolinite, pyrophyllite, talc), but others are characterized by negatively charged layers. The charge arises from substitutions in either the octahedral sheet (typically from the substitution of low-charge species such as  $\text{Mg}^{2+}$ ,  $\text{Fe}^{2+}$ , or  $\text{Mn}^{2+}$  for  $\text{Al}^{3+}$  in dioctahedral species), or in the tetrahedral sheet (where  $\text{Al}^{3+}$  or occasionally  $\text{Fe}^{3+}$  substitutes for  $\text{Si}^{4+}$ ), thus producing one negative charge for each such substitution. The charge, which usually expressed as a charge/unit formula, is fundamental to correlate the type of mineral with its final use (Table 13.2).

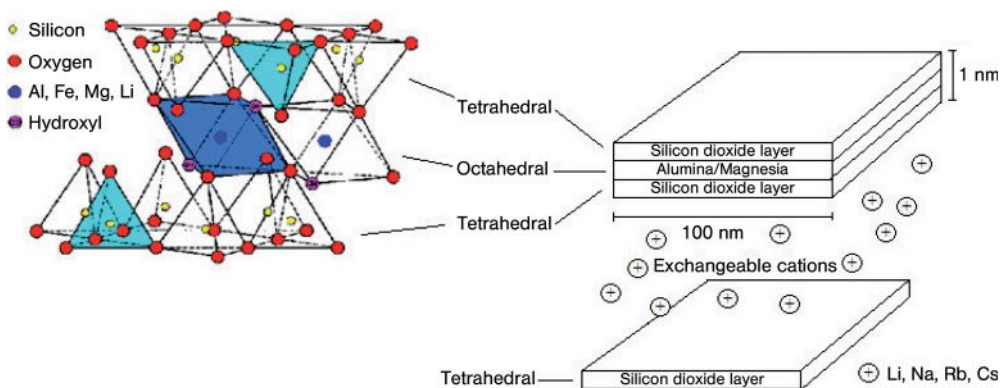
**Table 13.1** Groups, formula, structural description and specific minerals of the clay group.

	Group	Formula	Description	Mineral(s)
Clays	Kaolinite	$\text{Al}_2\text{Si}_2\text{O}_5(\text{OH})_4$	Silicate sheets ( $\text{Si}_2\text{O}_5$ ) bonded to aluminum oxide/hydroxide layers ( $\text{Al}_2(\text{OH})_4$ )	Kaolinite Dickite Nacrite
	Smectite	$(\text{Ca}, \text{Na}, \text{H})(\text{Al}, \text{Mg}, \text{Fe}, \text{Zn})_2(\text{Si}, \text{Al})_4\text{O}_{10}(\text{OH})_2 - x\text{H}_2\text{O}$	Silicate layers sandwiching a gibbsite [ $\text{Al}_2(\text{OH})_4$ ] (or brucite [ $\text{Mg}_2(\text{OH})_4$ ]) layer in between, in an <b>s-g-s</b> stacking sequence. Variable amounts of water molecules lie between the <b>s-g-s</b> sandwiches	Pyrophyllite <b>Talc</b> Vermiculite Sauconite Saponite Nontronite <b>Montmorillonite</b>
	Illite (Mica)	$(\text{K}, \text{H})\text{Al}_2(\text{Si}, \text{Al})_4\text{O}_{10}(\text{OH})_2 - x\text{H}_2\text{O}$	Silicate layers sandwiching a gibbsite-like layer in between, in an <b>s-g-s</b> stacking sequence. The variable amounts of water molecules would lie between the <b>s-g-s</b> sandwiches as well as the potassium ions	Biotite Lepidolite Muscovite Paragonite Phlogopite Zinnwaldite
	Chlorite	$\text{X}_{4-6}\text{Y}_4\text{O}_{10}(\text{OH}, \text{O})_8^a$	Silicate layers sandwiching a brucite or brucite-like layer in between, in an <b>s-b-s</b> stacking sequence similar to the above groups. There is an extra weakly bonded brucite layer in between the <b>s-b-s</b> sandwiches. This gives the structure an <b>s-b-s b s-b-s b</b> sequence. The variable amounts of water molecules would lie between the <b>s-b-s</b> sandwiches and the brucite layers	Amesite Baileychlore clinochlore Cookeite corundophilite Daphnite Delessite Gonyerite Nimite Odinite Orthochamosite penninite Pannantite Rhipidolite (prochlore) Sudoite Thuringite etc.

a The X represents either aluminum, iron, lithium, magnesium, manganese, nickel, zinc or, rarely, chromium. The Y represents either aluminum, silicon, boron, or iron but mostly aluminum and silicon.

**Table 13.2** Charge/unit formula for different phyllosilicates minerals.

	Mineral species	Interlayer cations	Charge/unit formula
Kaolinite-serpentine	Kaolinite, Halloysite	–	0.0
Pyrophyllite-talc	Antigorite, Chrysotile	–	0.0
Smectite	Montmorillonite, Beidelite, Nontronite, Saponite, Hectorite	Na, Ca	0.25–0.6
Vermiculite	Di-octahedral-vermiculite  Tri-octahedral-Vermiculite	Mg	0.6–0.9
Mica	Muscovite, Biotite, Phlogopite	K	1.0

**Figure 13.1** Structure of montmorillonite clay.


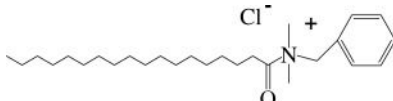
*Montmorillonite* (MMT) a member of the smectite group, is commonly used in polymer–clay nanomaterials. The layered structure of MMT (Figure 13.1) consists of two silica tetrahedral (corner-shared) sheets fused to one (edge-shared) octahedral sheet of alumina (aluminosilicate) or magnesia (magnesium silicate). The lateral dimensions of these layers vary from 100 nm to a few microns, and about 1 nm in thickness, depending on the particular silicate. Due to an isomorphous substitution of alumina into the silicate layers ( $\text{Al}^{3+}$  for  $\text{Si}^{4+}$ ) or magnesium for aluminum ( $\text{Mg}^{2+}$  for  $\text{Al}^{3+}$ ), each unit cell has a negative charge of between 0.5 and 1.3. The layers are held together with a layer of charge-compensating cations, such as  $\text{Li}^+$ ,  $\text{Na}^+$ ,  $\text{K}^+$ , and  $\text{Ca}^{2+}$ ; the charge-compensating cations help the intercalation and surface modification of clays, which is required to disperse clays at the

nanoscale into polymers. The cation-exchange capacity (CEC), which is indicative of the intercalation capacity, is defined as the number of exchangeable interlayer cations, and has units of  $\text{mEq } 100 \text{ g}^{-1}$ . Typically, MMT has a CEC ranging from approximately 75 to  $115 \text{ mEq } 100 \text{ g}^{-1}$  [11].

Other clays are saponite, a synthetic material that closely resembles MMT, and hectrite, which is a magnesium silicate ( $\text{CEC } 55 \text{ mEq } 100 \text{ g}^{-1}$ ) and its synthetic equivalent, Laponite®. Typically, sheets of Laponite are 25–30 nm wide, whereas MMT has sheets that are approximately 200 nm in width.

The dispersion of a hydrophilic nanofiller into a hydrophobic polymer matrix requires a preliminary modification of the clay to render it more organophilic. Consequently, a treatment is often carried out with suitable chemicals to replace the inorganic exchange ions in the galleries between the layers with alkylammonium surfactants or other organic cations. Clays treated in this way are referred to as “organoclays”. The number of onium ions that can be packed into the galleries depends on the charge density of the clay and the CEC. In fact, at lower charge densities the surfactants pack in monolayers while, as the charge increases, bilayers and trilayers can be formed with different orientations of packed alkyl chains. The intercalation of organophilic cations into the layers can be followed using X-ray diffraction (XRD) analysis, with the distance between a plane in the unit layer and the corresponding plane in the next unit layer being defined as the “basal plane spacing”  $d_{001}$ , often known as the “interlayer distance”. When a surfactant replaces sodium in the galleries, an increase in interlayer distance can be observed. The organic moiety used for preparing organoclays depends on the host polymer to be used as a matrix for the nanocomposites. Both, the structural and physical characteristics of two common ammonium salts (hexadecyltrimethylammonium bromide and stearyldimethylbenzylammonium chloride) are reported in Table 13.3 [7].

**Table 13.3** Structure and physical characterization of two organoclays.

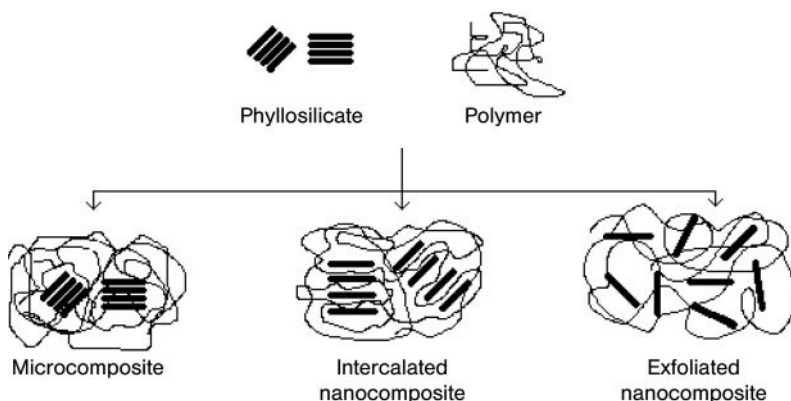
Organic moiety	CEC ( $\text{mEq kg}^{-1}$ )	Moisture content (wt%)	Loss on ignition	Basal Spacing (nm)
HDTM 	0.91	1.13	29.98	1.9
Hexadecyltrimethylammoniumbromide SMB 	0.91	1.05	34.19	2.5
Stearyldimethylbenzylammoniumchloride				

The aim of the ion exchange process is to enlarge the interlayer distance so as to promote the accommodation of monomers or polymers, thus affording an organophilic surface and improving wetting between the clays and polymers.

### 13.1.2

#### Morphology of Composites

Polymer–clay composites based on layered silicates can be classified into three types, depending on the extent of separation of the silicate layers [12], namely conventional microcomposites, intercalated nanocomposites, and exfoliated nanocomposites (these are shown schematically in Figure 13.2). If the polymer does not enter the galleries, the  $d_{001}$  of the clay will remain unchanged, in agreement with the achievement of a microcomposite. If an organic species enters the galleries and causes an increase in  $d_{001}$ , but the clay layers remain stacked, then the composite is considered “intercalated.” However, if the clay layers are completely pushed apart to create a disordered array, the composite is termed “exfoliated.” Usually, a composite for which  $d_{001} > 10$  nm (a spacing that cannot be determined by conventional XRD analysis) is designated as exfoliated. Recently, Sinha Ray *et al.* [13] defined another type of nanocomposite within the set of “intercalated nanocomposites” that they termed intercalated-and-flocculated nanocomposites, and which contained aggregates of intercalated silicate layers due to the hydroxylated edge–edge interaction of the silicate layers. In fact, most intercalated tactoids include both single stacks and several connected stacks of clay layers, such that the distinction between flocculation and intercalation will rest on an electron microscopic analysis of the structure. Moreover, the “flocculation” could be attributed to the long molecular chains that intercalate into two or more clay galleries and play a bridging role. Electron microscopy studies have often shown that most nanocomposites are both intercalated and exfoliated, but this cannot be readily deduced from XRD measurements. This situation may occur because the preparation method has not allowed sufficient time for adsorption and penetration



**Figure 13.2** Classification of morphologies for polymer–clay composites.

of the galleries to be completed, or because the dispersive mixing has been less effective and that, if more time were available, the polymer–clay system might develop either fully intercalated or exfoliated structures. The extent of clay dispersion in polymer is dependent on the intrinsic properties of the polymer and clay, including the aspect ratio of the clay platelets, the volume fraction of the clay, the nature/structure of polymer, the interactions between the polymer, clay and clay modifier, and the processing conditions used. Fully exfoliated polymer–clay nanocomposites are, in theory, only found for volume fractions of clay less than 3%, as calculated by considering the small size of clay platelets [14].

Three principal methods are available to determine the exfoliated fraction:

- Quantitative XRD, using a strong and independent reflection from an internal standard, can potentially be used to track the decrease in the ratio  $d_{001}$  for the clay to the standard peak as exfoliation proceeds.
- A method based on NMR, which was recently established [15].
- Transmission electron microscopy (TEM) provides an indication, but is difficult to use for precise measurement unless very thin specimens are prepared, a large number of images are captured, and quantitative microscopy coupled with stereology is used.

Recently, Luo *et al.* [16] developed a statistical TEM image analysis methodology to evaluate the dispersion parameters  $D_{0.1}$ , based on measurement of the free-path spacing distance between the single clay sheets. Drummy *et al.* [17] reported a morphological characterization of layered silicate nanocomposites by using both electron tomography and small-angle X-ray scattering (SAXS). The latter method has the advantage of providing complementary results with respect to the electron tomography. In fact, it can be used to probe materials with subnanometer resolution while at the same time sampling a large number of nanoparticles, thus providing more than adequate statistics.

*Rheological testing* [18] might also be developed to measure the degree of exfoliation, but at present this is only used for semi-quantitative analysis. Hence, the morphological characterization of layered silicate nanocomposites requires the use of different techniques in order to achieve a relevance not only in the three-dimensional (3-D) representation of the nanometer-scale part of the sample, but also regarding the average distribution of platelets in the systems.

The characterization of layered silicate polymer blends is complicated by the need to study both the phase and filler distribution. In miscible systems, such as poly(methyl methacrylate) (PMMA)/poly(ethylene oxide) (PEO) [19, 20], the morphological analysis can be carried out as in a general polymeric matrix. However, in immiscible systems, such as poly(propylene) (PP)/poly(styrene) (PS), both XRD patterns and TEM observations have shown that the silicate layers were either intercalated or exfoliated, depending on their interactions with the polymer pair, and were located at the interface between the two polymers [21]. In this case, the compatibilizing action of an organically modified layered silicate resulted in a decrease in the interfacial tension and particle size, and in a remarkable increase

in the mechanical properties of the modified immiscible blends. A similar result was obtained by Fang *et al.* [22], who investigated the morphology of nanocomposites based on 80/20 and 20/80 (w/w) poly( $\epsilon$ -caprolactone) (PCL)/PEO immiscible blends and organophilic layered silicates prepared by melt extrusion. From the TEM analysis, it was observed that the exfoliated silicate platelets were located preferentially at the interface between the two blend phases. However, when the blend-based nanocomposites were prepared via a two-step process, in which the silicates were first premixed with the PEO component or with the PCL component, the silicate layers migrated from the PEO phase or PCL phase to the interface. The emulsifying capability of layered silicates in immiscible blends depends on the structure and physical properties of the couple of polymer components. In fact, in PP/poly(amide) (PA) blends [23], it was shown, using electron microscopy, that in all cases the inorganic filler was enriched in the PA phase, and this resulted in a phase coarsening in comparison with the unfilled PP/PA blend. In contrast, in blends of a poly(vinylidene fluoride)/nylon-6 (PVDF/PA6) 30:70 melt compounded with various organoclays either directly or sequentially [24], the nanocomposite with the best mechanical properties was characterized by a good dispersion of particles throughout the matrix (PA6) and at the PVDF/PA6 interface. The authors ascribed this good result to a suppression of the coalescence of PVDF domains. Moreover, the crystallization of the PVDF domains was suppressed, ultimately creating a blend nanocomposite that was stiffer, stronger, and tougher than the blend without nanoparticles.

In agreement with the latter results, organoclay strongly influences the dynamic evolution of phase morphology, both in partially miscible and immiscible blends. A partially miscible blend was examined by investigating the poly(vinyl methyl ether) (PVME)/poly(styrene) (PS) [25] demixing in the presence of organically modified Laponite. The phase separation of these near-critical blends proceeds by a spinodal decomposition, even with added nanoparticles. However, the presence of nanoparticles slowed the phase-separation kinetics. In immiscible systems, such as poly(ethylene) (PE)/PA6 blends, the presence of an organoclay, preferentially distributed in the polyamide phase, effectively stabilized a co-continuous phase morphology [26] which persisted for more than 500 s. The authors explained this experimental evidence by suggesting that the co-continuous morphology could evolve to a phase-separated morphology in the timescale of their experiments, as the organoclay framework would radically slow down the melt state dynamics of the percolating network formed during the melt processing.

The presence of a compatibilizer [e.g., ethylene-propylene random copolymers (EPM), functionalized with maleic anhydride (EPM-g-MAH), or maleic anhydride-functionalized PP (PP-g-MAH)] in PP/PA6 blends containing organoclay, improves the phase morphology of the blends and promotes the formation of exfoliated nanocomposites, with the nanoplatelets preferentially distributed in the polyamide phase [27, 28]. In particular, atomic force microscopy (AFM) studies [29] carried out after selective chemical or physical etching of PP-g-MAH compatibilized PA6/PP/organoclay polished sample surface, showed that the organoclay was embedded in the PA6-g-PP phase of the PA6/PP blends compatibilized with PP-g-MAH. The preferential location of the clay in the PA6-g-PP phase was attributed to pos-



sible chemical interactions between the PA6 and the organic surfactant of the clay. The use of a proper organoclay, modified with the reactive (glycidoxypropyl)trimethoxy silane, in poly(lactic acid) (PLA)/poly(butylene succinate) (PBS) blends [30], allowed an exfoliated blend to be obtained contemporarily, and improved the phase adhesion between the two polymers. The authors ascribed this result to the formation of a grafted hybrid in the interphase region, based on the reaction of a glycidyl unit with the terminal hydroxyl or carboxylic groups of the polyesters.

In general, the phase morphology development and the compatibilization of nanofilled blends requires more studies to be conducted, in order to create a rational scheme concerning the effect of nanoscaled interactions, physical features, and rheological properties on filler and phase distribution, with the aim of modulating the final properties of the composites.

### 13.1.3

#### Properties of Composites

The dispersion of phyllosilicates into polymer or blends at nanometer scale allows improvements to be made to the properties of the polymer matrix [31]. In particular:

- the barrier properties to gases are enhanced [32], not only when an exfoliated morphology is obtained [33], but also in an intercalated morphology [34]. In fact, the results of fitting of experimental data with proper models showed that the chain confinement enhanced the barrier properties of the intercalated nanocomposites [35].
- Flame retardancy is improved, based on the dispersion of nanoclays, such that char formation is favored on the burning surface [36, 37].
- Stiffness is improved, with an increase in tensile modulus frequently being observed in phyllosilicate–polymer nanocomposites [21].
- Thermal stability, as degradation temperature, determined via thermogravimetric analysis (TGA), shows an increase of at least 7–8°C when an exfoliated nanocomposite is tested [38].

Other properties of nanocomposites are currently the object of much research, and in some cases—an example is that of thermal behavior [39, 40]—these investigations have begun to establish new properties that might be exploited such that the nanocomposites can be used for a variety of industrial applications.

## 13.2

### Polyolefin-Based Nanocomposites

The polyolefins (POs) represent one of the most widely used classes of thermoplastic materials, as they offer a unique combination of high thermomechanical properties and good environmental compatibility, at low cost.

Currently, a huge effort is being devoted to extend the field of application for POs and to satisfy their market demand, the latter point being based on these materials having specific and advanced properties, and being adaptable to the environment and, ideally, recyclable. In particular, the preparation of PO nanocomposites by the addition of very small amounts of layered silicate loadings is a very common approach that provides drastic improvements in the elasticity modulus, strength and heat resistance of the materials, as well as a substantial decrease in their gas permeability, when compared to either virgin POs or conventional microcomposites [41–49].

Attempts have been made to prepare either intercalated and exfoliated nanocomposites, through different routes, and extensive studies have been conducted to promote an understanding of the fundamental aspects associated with the clay dispersion, the resultant physical properties, and the inter-relationship between both. Indeed, the properties of polymer–clay nanocomposites depend largely on the synergistic effect of nanoscale structure and interactions occurring between the clay and polymer.

The achievement of a desired level of clay dispersion into the polymer, and interaction between the phases, involves numerous chemical and technological implications. Generally, the chemical modification of one or both system phases is necessary. For this, the hydrophilic clay is often changed to hydrophobic either by the cation exchange or grafting of alkoxy silanes, by exploiting the cation-exchange capability in one case and the reactivity of silanol groups present on the edges of the clay platelets in the other case. Typically, a compatibilizer—that is, a functionalized PO or copolymer—is added to assist in this situation. At present, it is not completely clear which conditions lead to exfoliated layers and which cause only the intercalation of polymer chains into the gallery spacing of the stacked silicate layers. However, what does appear well established is that the interface is not only fundamental for the adhesion between the two phases and stabilization of the attained morphology, but also plays a major role in the bulk properties, due to its large extension [39].

Clearly, the ability to predict and control the morphology of nanocomposites would be of major interest, by virtue of the strict connection between structural control and the final properties of the nanocomposite [49, 50]. Consequently, the main objective of this section is to review the concepts and methods relating to the optimization of layered silicate dispersion in PO matrices by melt intercalation, notably with regard to the use of a compatibilizer and identification of the preferred process conditions.

### 13.2.1

#### **Overview of the Preparation Methods**

Two major synthetic strategies are generally followed for preparing PO/layered silicates nanocomposites: (i) polymer intercalation (including melt intercalation [51–56] and solution intercalation methods [57]); and (ii) *in situ* intercalative polymerization [58–62].

The *in situ* intercalative polymerization method, which is based on the thermo-mechanical forces generated during the process of olefin polymerization inside the interlayers of the silicate, and the energy released during the polymerization, is reported to promote silicate layer dispersion and exfoliation in the nonpolar PO matrix. However, a very poor interaction between the polar silicate layers and the hydrophobic PO matrix makes the nanocomposite structure thermodynamically instable. In fact, it has been demonstrated that melting processes of this type of nanocomposite material cause agglomeration of the silicate layers and collapse of the nanocomposite structure. Even the more recently developed *polymerization filling technique*, which consists of attaching the polymerization catalyst to the surface and into the interlayers of the silicate and polymerizing the olefin *in situ*, although favoring exfoliated structures does not allow thermodynamically stable nanocomposites to be prepared [63]. The method which should be adopted for stabilizing the morphology is to copolymerize the olefin with a functionalized comonomer, thus improving the necessary interaction with the clay. However, many challenges remain for the catalytic polymerization of polar monomers with both traditional Ziegler–Natta and metallocene catalysts, due mainly to the catalyst deactivation.

For *solution intercalation*, the enthalpy of dispersion of the silicate layers in solution must balance the entropy loss of the solvent molecules which intercalate into the silicate layers [64]. Moreover, this method is poorly sustainable because it requires a large amount of organic solvent to ensure a good clay dispersion.

*Melt intercalation* is the most commonly applied process for preparing PO nanocomposites, because it is sustainable, versatile, and inexpensive. This methodology is limited by the low interaction enthalpy between the nonpolar PO chains and the polar silicate layers. In fact, when using polymer chain intercalation between the silicate layers, an effective and stable morphology is achieved only if the interaction enthalpy balances the entropy loss of the polymer chains confined within the silicate interlayers. However, it has been recognized that the entropy loss due to such polymer confinement is only partially compensated by the entropy gain associated with the increased conformational freedom of the surfactant tails as the interlayer distance increases with polymer intercalation [65, 66], whereas favorable enthalpic interactions are critical for determining the nanocomposite structure [67]. Hence, even if a good dispersion of the clay can be achieved simply by applying strong shear forces during the process, the structure will be unstable and reagglomeration of the particles may occur quite rapidly if an effective interaction between the polymer and clay surface is not ensured [44].

It is somewhat evident that the PO hydrophobicity makes it almost impossible to obtain intercalation without chemical modification of the clay or polymer, or both. In order to overcome the above-described thermodynamic obstacles, and to promote the interaction between the hydrophobic PO and the polar silicate layers, the general approach is to use either: (i) organophilic layered silicates (OLSs), obtained via cation exchange; or (ii) polymer compatibilizers (i.e., functionalized polyolefins).

Whilst the dispersal of layered silicates in polar polymers is relatively straightforward, the achievement of comparable results with hydrophobic POs remains a challenge. Favorable interactions at the inorganic/organic interface are necessary in order to separate the clay monolayers and to successively grant cohesion forces between the exfoliated layers and polymer chains, thus achieving a stable nanostructure.

### 13.2.2

#### **Organophilic Clay and Compatibilizer: Interactions with the Polyolefin Matrix**

Two main methods can be applied for clay modification: (i) to replace the metallic cations that were originally present on the clay surface with large organic cations; and (ii) to graft alkoxy silanes onto the clay by exploiting the reactivity of the silanol groups [64].

The first of these methods has been widely applied, using several types of cation (mostly dialkyldimethyl- or alkyltrimethyl-ammonium cations). The introduction of quaternary ammonium salts with long alkyl chains between the layers (as discussed above) allows the interlamellar space to be expanded, reduces the interaction among the silicate sheets, and also facilitates the diffusion and accommodation of the polymeric matrix. In contrast, the grafting of alkoxy silanes has been used only rarely with layered silicates, due to the small number of reactive-edge silanols present. Moreover, it has been shown recently, by using a combination of morphological analysis and multinuclear solid-state nuclear magnetic resonance (NMR) experiments [68], that the modification of a synthetic Laponite with a combination of organic ammonium cations and alkoxy silanes will result in a disordered arrangement of the clay platelets (which favors interplatelet interactions). This effect was due to self-condensation occurring among clay silanols at the platelet edges, thus limiting dispersion into the polymer matrix.

Several reports have described the use of OLSs modified with alkylammonium surfactants of different nature and length for the preparation of PO/OLS nanocomposites [52, 69]. In particular, the effect of factors such as the length and number of alkyl groups of the cationic surfactant was investigated. It became apparent that the equilibrium structure of the polymer/OLS depended on the nature of the polymer, on the charge density of the layered silicate, and also on the chain length and structure of the cationic surfactant. Balazs *et al.* [70, 71] showed that an increase in surfactant length improved the separation of the layers by allowing the polymer to adopt more conformational degrees of freedom. Both, exfoliated and intercalated PE/OLS nanocomposites were obtained when the number of methylene units in the alkylammonium chain exceeded 16 [72], whereas it was reported that an excessive density of tethered chains would prevent the formation of intercalated structures. The dispersion level was found to depend strictly on the amount of OLS; in particular, it was shown that the morphology of the PO/OLS systems could be shifted from disordered exfoliated to predominantly intercalated by varying the OLS content from 6 to 36wt% [73]. Finally, from a thermodynamic point of view, OLSs modified with alkylammonium salts were

shown to be adequate in offering a surplus enthalpy for promoting OLS dispersion into a nonpolar matrix, as did a PO. In fact, the surfactant/silicate interactions were more favorable compared to those of PO/silicates. Hence, the synthetic approach was directed towards reducing the enthalpic interactions between the clay and surfactant by using semi-fluorinated surfactants [52] as clay modifiers. Although, in the case of PP/OLS composites this approach led to a significant improvement in miscibility, this type of surfactant was seen to be much too expensive for use in the mass production of PO nanocomposites.

A more general approach for improving the compatibility of a PO with OLS was to introduce into the system a compatibilizer as the coupling agent. In general, the compatibilizer was a functionalized PO, such as a maleic anhydride (MAH) or maleate ester-grafted PO, an oligomeric-functionalized PO, or an ammonium-terminated or OH-terminated PO, as well as a suitable block or random copolymer (Table 13.4). These types of polymer or oligomer reflected some of the theoretical calculations carried out to probe the interactions between polymers and clay sheets, and were used substantially to design the ideal compatibilizer [70, 71]. It became clear that for the simple penetration of polymer chains into the clay gallery, the compatibilizer should contain a fragment which would be highly attracted by the clay surface. In addition, it should incorporate a longer fragment that was not attracted by the sheets, but rather would attempt to gain entropy by pushing the layers apart. Subsequently, when the layers had separated, the surfaces would be sterically hindered from coming into close contact. In this way the compatibilizer could be seen to behave as a steric stabilizer for the PO/OLS colloidal suspension. Thus, the role of the compatibilizer is not only to favor a layered silicate dispersion and to enhance the polarity of the polymer matrix, but also to stabilize the final morphology. The strong interactions between the compatibilizer and clay are not only fundamental for the dispersion step, but also for maintaining the morphology.

Initial attempts to improve the interactions between nonpolar PO and layered silicates were carried out by melt-mixing the polymer and clay with modified oligomers, so as to mediate the polarity [51, 55–57, 74]. Usuki *et al.* [55] were first to report the preparation of PP/layered silicate nanocomposites using a functional oligomer (PP–OH) with polar telechelic –OH groups as compatibilizer. In this approach, PP–OH was intercalated between the layers of an OLS, after which the PP–OH/OLS was melt-mixed with PP to obtain nanocomposites with an intercalated structure. Another typical example to be reported was that of PP/layered silicate nanocomposites; these were prepared by Toyota, using PP oligomers modified with approximately 10wt% of MAH groups [51, 56] and clays exchanged with stearyl ammonium cations. Wide-angle X-ray diffraction (WAXD) analyses and TEM observations established the intercalated structure for all of these nanocomposites. Here, the driving force of the intercalation was considered to have originated from the interaction between the MAH group and the oxygen groups of the silicate, through the formation of hydrogen bonding (Figure 13.3).

In general, the compatibilizer is a polymer in which the functional groups are distributed randomly along the backbone, or functionalized at the chain end. Both,

Table 13.4 Some examples of compatibilizers for the preparation of PO/OLS nanocomposites.

Types of compatibilizer for PO/OLS systems	Examples	Main characteristics	Reference(s)
End-functionalized oligomers (i.e., OH-; MAH- terminated)	OH end-functionalized PP oligomer	$M_w$ (by GPC) 20 000; OH value 54 mg KOH g <sup>-1</sup>	[52, 56, 58]
	MAH end-functionalized PP oligomer	$M_w$ (by GPC) 12 000–30 000. Acid value 7–52 mg KOH g <sup>-1</sup>	[52, 56, 58]
	MAH end-functionalized PE oligomer	$M_n$ 5700. Acid value; weight fraction of polar comonomer 0.01). This PE-g-MA has a low anhydride content so that, on average, there is one anhydride moiety per two molecules. It can be considered as an end-functionalized PE oligomer.	[64]
End-functionalized polymers (i.e., NH <sub>2</sub> -, OH-, COOH- terminated)	Linear end-functionalized polyethylene with dimethyl ammonium chloride end groups	Narrow molecular weight distribution	[74, 75]
	Polyethylene with multiple quaternized amine groups along the polymer chain	Narrow molecular weight distribution	[75]

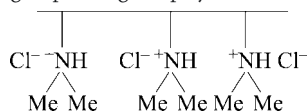


Table 13.4 Continued.

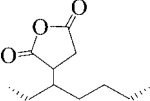
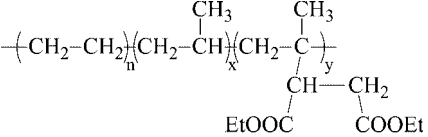
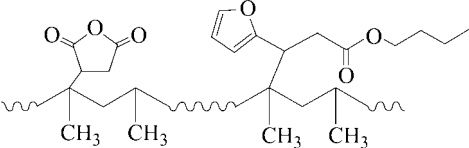
Types of compatibilizer for PO/OLS systems	Examples	Main characteristics	Reference(s)
Block copolymers	<p>Poly(ethylene-block-methacrylic acid)</p> $\text{~~~~~CH}_2\text{CH}_2\text{CH}_2\text{CH}_2\text{~~~~~CH}_2\text{C}\begin{matrix} \text{CH}_3 \\   \\ \text{C}=\text{O} \\   \\ \text{OH} \end{matrix}\text{~~~~~}$	Narrow molecular weight distribution	[75]
	<p>Poly(ethylene-block-ethylene glycol)</p> $\text{H} \left[ \text{---CH}_2\text{---CH}_2\text{---} \right]_n \left[ \text{---O---CH}_2\text{---CH}_2\text{---} \right]_m \text{OH}$	<p><math>M_n</math> (575 mol<sup>-1</sup>); 0.20 molar fraction of polar comonomer; PE-<i>b</i>-PEG is a block-copolymer, the chains of which contain 33 methylene groups and 2.6 ethylene oxide units per molecule on average</p>	[64]
	<p>Poly(propylene- block -methyl methacrylate)</p> $\left( \text{CH}_2\text{---CH} \begin{matrix}   \\ \text{CH}_3 \end{matrix} \right)_y \text{---} \left( \text{CH}_2\text{---C} \begin{matrix} \text{CH}_3 \\   \\ \text{C} \\   \\ \text{O} \end{matrix} \text{---OCH}_3 \right)_x$	<p><math>M_w</math> around 200 000; molar fraction of MMA units 1 or 5</p>	[52]
	<p>Styrene-<i>b</i>-ethylene/butylenes-<i>b</i>-styrene block copolymer</p>	<p>A triblock copolymer based on hydrogenated polybutadiene (10 wt% ethyl branches, <math>M_n = 37\,000\text{ g mol}^{-1}</math>) central block and polystyrene (30 wt%, <math>M_n = 7000\text{ g mol}^{-1}</math>)</p>	[76]

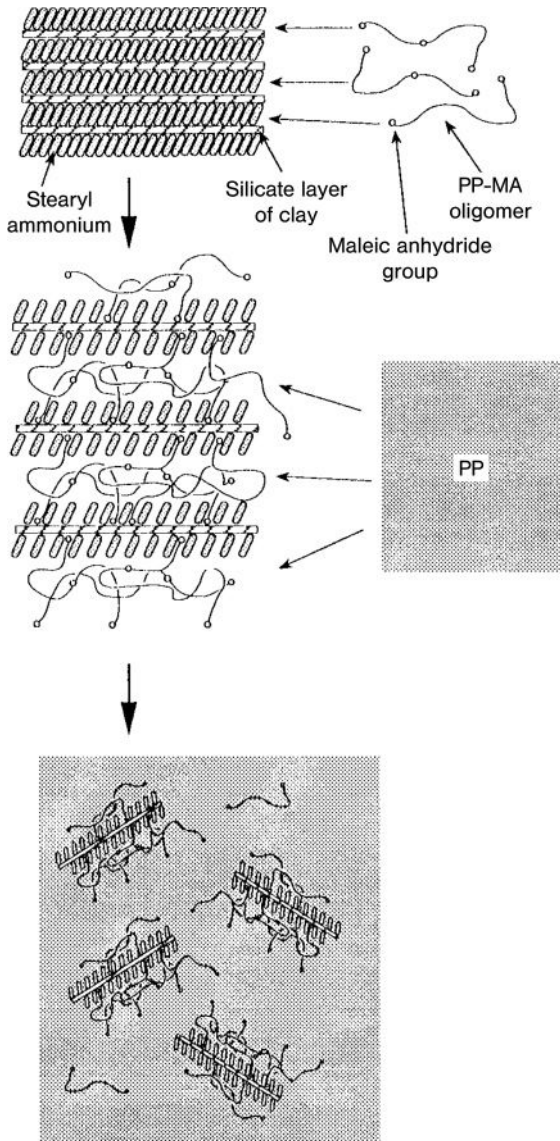


Table 13.4 Continued.

Types of compatibilizer for PO/OLS systems	Examples	Main characteristics	Reference(s)
Random copolymers	Poly(ethylene-co-vinyl alcohol)	0.69 weight fraction of polar comonomer	[64, 76]
	Poly(ethylene-co-methacrylic acid)	$M_n$ 68 000; 0.11 weight fraction of polar comonomer.	[64]
	PP-r-(PP-OH) <sub>x</sub>	These copolymers derive from a random polypropylene copolymer which contains 1 mol% <i>p</i> -methylstyrene comonomer. $M_w$ around 200 000; molar fraction of polar units 0.5	[52]
	PP-r-(PP-MA) <sub>x</sub>		

Table 13.4 Continued.

Types of compatibilizer for PO/OLS systems	Examples	Main characteristics	Reference(s)
Randomly functionalized polyolefins	Maleic anhydride (MAH)-functionalized polyolefins 	Functionalization degree ranging between 0.1 and 2% by mol	[32, 48, 51–55, 72, 77–82]
	Diethyl maleate (DEM)-functionalized polyolefins 	Functionalization degree ranging between 0.1 and 2% by mol	[32, 79–81, 83–85]
	Maleic anhydride (MAH) and Butyl furanyl propenoate (BFA)-functionalized polypropylene 	Functionalized polypropylene having high molecular weight	[86–89]



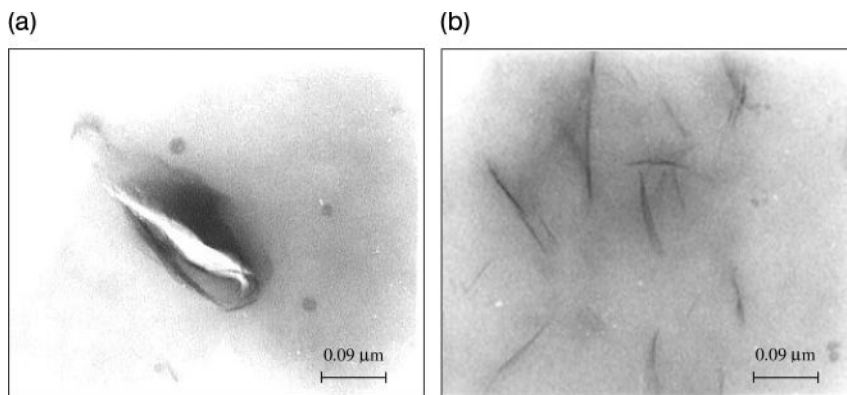
**Figure 13.3** Schematic representation of the dispersion process of the organo layered silicate (OLS) in the poly(propylene) (PP) matrix with the aid of a maleic anhydride functionalized PP oligomers. Reproduced with permission from Ref. [51]; © 1997, American Chemical Society.

simulation studies and experimental results [74, 90, 91] produced evidence that end-functionalized polymers—unlike more functionalized polymer systems—assumed a special configuration on the clay surface which allowed complete exfoliation of the clay. In particular, in the case of the PP/OLS nanocomposites, it was shown that by using an ammonium group-terminated PP (PP-NH<sub>3</sub><sup>+</sup>) as compatibilizer, the terminal hydrophilic NH<sub>3</sub><sup>+</sup> groups would be attached by cation exchange on the inorganic surfaces, while the hydrophobic high-molecular-weight PP tails would aid exfoliation of the structure, though this would be maintained even after further mixing with undiluted PP [74]. In contrast, side chain-functionalized PPs or PP block copolymers were seen to form multiple contacts with each of the clay surfaces, which resulted not only in the polymer chains being aligned parallel to the clay surfaces, but also consecutive clay platelets being bridged, thus promoting the production of intercalated structures. This bridging effect was established, for example, by using side chain-functionalized polyolefins characterized by large (>2 wt%) amounts of grafted polar groups [74, 90, 91].

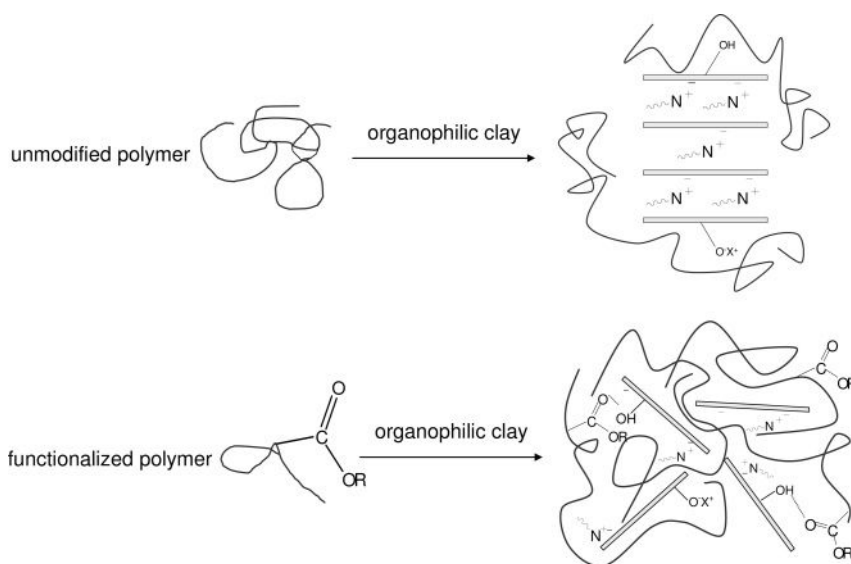
Without doubt, however, the most popular compatibilizers are POs functionalized with MAH by free radical processes. PP functionalized with MAH (PP-g-MAH) was shown to intercalate into the inter-galleries of OLS, much like the analogous oligomers [77]. In fact, a WAXD analysis of the PP/OLS nanocomposites revealed an absence of any peaks representing dispersed OLS in the PP-g-MAH matrix; hence, in this case also, the strong hydrogen bonds between the MAH-grafted groups and the polar clay surface promoted dispersion of the layers. Similar results were obtained for PE-PP rubber (EPM)/OLS nanocomposites which had been prepared by melt blending EPM-g-MAH and OLS modified with C18 alkyl ammonium chains, in a twin-screw extruder [78]. Confirmation of the intense interactions between the functional groups of the compatibilizer and the lamellae of OLS was obtained from experiments with nanocomposites that had been prepared by blending an EPM functionalized with diethylmaleate (DEM) (with 1 mol% grafted functional groups) with increasing amounts (up to 20 wt%) of OLS. The use of a functionalized, rather than virgin, EPM allowed (in the case of 5 wt% OLS nanocomposites) the shift to be made from an intercalated morphology to an almost completely exfoliated morphology [83] (Figure 13.4).

It was hypothesized that the hydrogen bonds between the -OH groups present on the OLS surface and the carbonyl groups of the functionalized EPM allowed both optimization and stabilization of the clay dispersion (Figure 13.5). Most likely, the compatibilizer was placed between the polar silicate layers and contemporarily mixed with the nonpolar polymer chains, thus creating a concentration gradient suitable for providing an exfoliated morphology and avoiding phase separation.

The strong interactions between the OLS and the EPM-g-DEM were confirmed by extracting the nanocomposites with hot toluene; a significant proportion of the rubber proved to be insoluble (up to 55 wt% for 15–20 wt% OLS), and the amount of nonextractable polymer was increased by raising the OLS loading [32, 84]. The occurrence of strong polymer/clay interactions was also proved by comparing the infrared (IR) spectra of the composite and residue (Figure 13.6). The

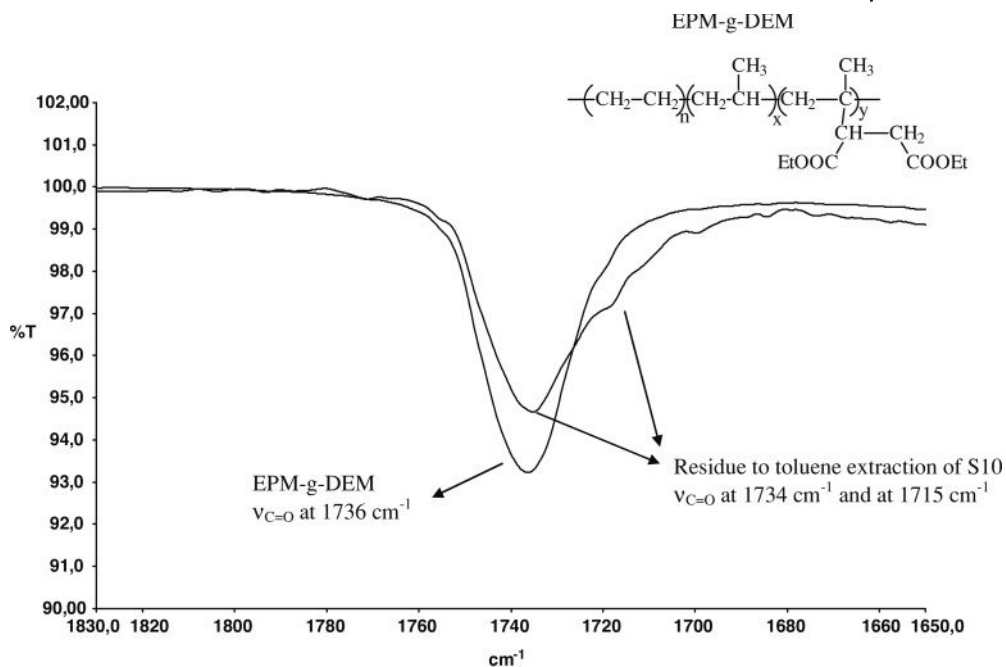


**Figure 13.4** Transmission electron microscopy images of (a) ethylene propylene rubber (EPM)/organo-layered silicate (OLS) and (b) EPM functionalized with diethyl maleate (EPM-g-DEM)/OLS 5 wt% nanocomposites. Reproduced with permission from Ref. [84]; © 2005, John Wiley & Sons, Ltd.



**Figure 13.5** Effect of organophilic and polar interactions on the morphologies of ethylene-propylene rubber (EPM) and EPM functionalized with diethyl maleate (EPM-g-DEM)/organo-layered silicate (OLS) composites.

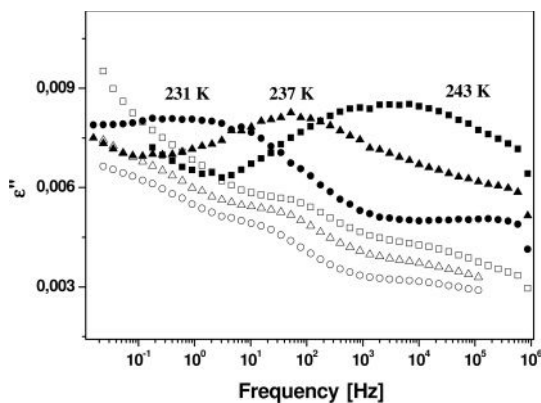
C=O stretching band of the carbonyl ester group of the EPM-g-DEM, when retained in the toluene-extracted residue, was significantly broad and was shifted to lower wavenumbers compared to neat EPM-g-DEM. Moreover, the shoulder at approximately  $1715\text{ cm}^{-1}$  suggested a hydrogen-bond interaction between the EPM functional groups and the silicate surface [85].



**Figure 13.6** Attenuated total reflectance (ATR) spectra of ethylene-propylene rubber functionalized with diethyl maleate (EPM-g-DEM) and residue to toluene extraction of a PE-g-DEM/organo-layered silicate (OLS) nanocomposite 10 wt% OLS. Note the enlargement of the C=O stretching region. Reproduced with permission from Ref. [84]; © 2008, Elsevier Ltd.

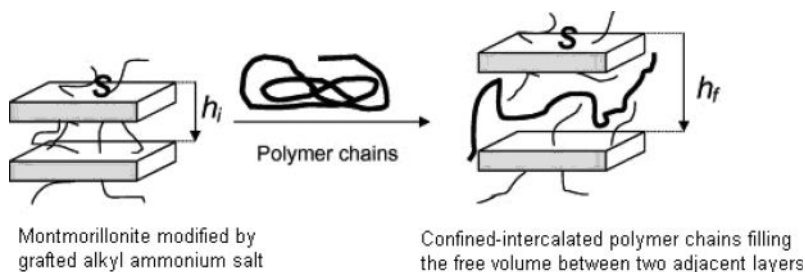
Evidence of the strong interaction between the EPM-g-DEM and the layered silicate was also provided with differential scanning calorimetry (DSC) and dielectric relaxation analyses. Initially, the insoluble toluene fraction was seen to have a glass transition temperature ( $T_g$ ) which was appreciably higher than that of the original composite. Furthermore, the dielectric relaxation analysis of nanocomposites indicated a reduction in both the dielectric strength and  $\alpha$ -relaxation frequency as the temperature was increased (Figure 13.7). As the dipolar relaxing units are the side DEM grafted groups, this phenomenon was explained by considering a partial immobilization of such groups on the silicate surface, as consequence of the nanoconfinement of polymer chains. The  $\alpha$ -relaxation was shown to disappear for the residue to the toluene extraction, while the cooperative dynamics of the dipolar groups of EPM-g-DEM were strongly reduced as they were interacting with the layers.

The amount of unextractable polymer, the existence of which confirms the polymer/OLS interactions, and can be related to an adsorbed/interacting confined polymeric fraction, was correlated (using a rough geometric model) to the volume occupied by trapped and intercalated macromolecules (Figure 13.8).



**Figure 13.7** Dielectric loss spectra of nanocomposite organo-layered silicate (OLS) 20wt% (closed symbols) and its residue to solvent extraction (open symbols) above the glass transition temperature. The same

symbol type corresponds to the same measurement temperature. Reproduced with permission from Ref. [84]; © 2008, Elsevier Ltd.



**Figure 13.8** Schematic model of polymer confinement. Reproduced with permission from Ref. [84]; © 2008, Elsevier Ltd.

This comparison between experimental and theoretical data provided evidence of the existence of different interaction levels between the polymer and the organophilic clay, which together caused the formation of an unextractable polymer, namely:

- polymer–surfactant interactions
- polymer–clay surface chemical and physical interactions
- intercalated polymer–bulk polymer interactions.

By applying this model, the PO/OLS nanocomposite can be considered as a system containing at least two phases: (i) the polymer matrix, which does not truly interact with the layers' surface (and thus is extractable with the same  $T_g$  of pristine PO); and (ii) a nanostructured phase containing polymer chains that strongly interact



and are “confined” (and thus are not extractable, with a higher  $T_g$  than pristine PO and the starting composite). Here, the Gordon–Taylor equation was employed to calculate the amounts of both polymer phases by considering the  $T_g$  of the polymer in the nanocomposite (as determined by the  $T_g$  of the free polymer), and of the confined polymer. This analysis provided results which, in terms of their behavior, were in agreement with experimental data.

Interestingly, it was demonstrated that the unextractable polymer was responsible for reductions in the oxygen permeability of LDPE and EPM/OLS nanocomposites prepared by using functionalized matrices [85]. In fact, by assuming a negligible oxygen permeability through the polymer phase adsorbed onto the surface or trapped inside the galleries of the OLS, these experimental data were finely correlated with the theoretical data predicted from mathematical models.

Besides the nature of the functional groups, it was also clear that the amount of functional groups grafted onto the PO could influence the final morphology of the PO/OLS nanocomposite. In fact, the hydrophilicity of the compatibilizer was seen to increase with the grafting level of MAH, thus improving the level of interaction between the polymer and the clay. In the case of the most common PO-g-MAH compatibilizers, the level of grafting ranged typically between 0.1 and 2 wt% [50, 85, 92, 93]. In the case of MAH-functionalized PO, there was seen to be a limit value for the grafting level (ca. 0.1 wt%), for achieving a good improvement in morphology. In the case of both PE and PP/OLS nanocomposites, if the grafting level was higher than this limit value, a shift or even a disappearance of the basal reflection peak of the OLS on the XRD diffraction pattern could be observed [51, 72, 77, 78, 92].

In general, because of the low grafting percentage of polar groups onto the common commercial compatibilizers, a large amount of functionalized polymer is added to the polyolefin matrix in order to achieve the necessary polarity and hence compatibility with the organoclay. Besides the degree of functionalization (DF), the molecular weight and structure of the compatibilizer, as well as its melt viscosity and rheological properties, are responsible for the composite final morphology [93, 94]. The best results are generally obtained by using a compatibilizer for which the rheological properties are similar to those of the matrix; otherwise, the miscibility between the two polymers might be compromised and the intercalation/exfoliation process inhibited. A typical example is that of PP, for which a high amount of compatibilizer is required to obtain an increase in the OLS basal spacing, but this may cause a deterioration in the properties of the nanocomposite due to the low molecular weight of the commonly used PP-g-MAH samples. Unfortunately, functionalized PPs with high molecular weights are yet not available commercially. The conventional radical functionalization process with peroxide and MAH in the case of PP causes a dramatic decrease in the molecular weight of the polymer, leading to severe damage of its rheological and mechanical properties. Notably, PP is very sensitive to degradation reactions when treated with peroxides above its melting temperature, even in the presence of commonly used maleate functionalizing agents [79–81, 94].

Consequently, conventional PP-g-MAH compatibilizers will in general have a low DF and molecular weight. The problem of obtaining appropriately functionalized PP can be overcome by a new radical functionalization approach involving the use of a furan derivative (BFA). This is added as coagent during the radical functionalization of PP with MAH, which can yield a wide range of PP-g-MAH samples with different DFs and molecular weights, by controlling the macroradical formation and content [86, 87]. These new functionalized PP samples were recently tested in the preparation of PP/OLS nanocomposites, both as a matrix or as a compatibilizer of the system, the aim being to study the effects of both polarity and chain structure/architecture on clay dispersion and the ultimate properties of the corresponding nanocomposites. The results showed that PP-g-MAH with a low molecular weight and a high DF (>2 mol%) had an excellent ability to disperse clay at the nanometric level, especially when used as the matrix of the corresponding nanocomposite. Those samples characterized by a high DF value (>2 mol%) and a branched structure/architecture produced nanocomposites with a lower degree of exfoliation. However, those nanocomposites with a composition of 90/5/5 PP/compatibilizer (the functionalized PP)/organomodified layered silicate, where the sample contained the compatibilizer characterized by a high DF; prepared using a grafting procedure to avoid PP degradation reactions) provided the best performance in terms of morphological and thermomechanical properties. These results not only confirmed the important role of the DF, but also highlighted the fact that the control of molecular weight and structure/architecture during functionalization ensures a good compatibility of the compatibilizer with the PP matrix, which in turn has a positive effect on the ultimate properties of the PP/OLS. In particular, elongation at break point (which usually are poor for similar systems) reached values in excess of 500%, with an excellent reproducibility [88].

### 13.2.3

#### **The One-Step Process**

In addition to a correctly selected OLS and compatibilizer, it is also necessary to utilize an effective mixing protocol (e.g., processing parameters such as mean residence time, screw speed, etc.) capable of promoting both high shear stress and shear rate, in order to assist the OLS dispersion into a PO matrix [82, 95]. It has been shown that the residence time and kneading force applied during extrusion can have a direct effect on the extent of the layered silicate exfoliation [96]. In the case of LDPE/OLS nanocomposites, a correct balance between dispersive and distributive actions, by fine-tuning the screw profile, allowed an optimal nanocomposite morphology [82]. A good dispersion of clay layers was assessed by preparing a master-batch PE-g-MAH/OLS, which highlighted the importance of the shear stress for dispersing, intercalating, and exfoliating lamellae when the correct interface interactions have been provided. A further improvement in dispersion degree was observed during a second processing step, as the melt viscosity of the two polymer components was accurately selected with the aim of improving their compatibility.

Besides the machine parameters, the method selected for feeding the extruder—and therefore also the order of addition for components—can influence the morphology of the final material. In most reports, the best stack delamination was observed when a master batch between the functionalized PO (compatibilizer) and a large proportion of clay (10–50 wt%) was first prepared, followed by dilution in the nonpolar PO matrix (master batch process). The advantage of this method, compared to a direct melt blending of all ingredients together, is that it facilitates the intercalation of the polar polymer chains between the clay stacks, thus obtaining a form of pre-intercalated material.

One rarely discussed aspect is the possibility of obtaining, in a single step, both functionalization of the PO and nanocomposite formation. Such a method would be especially interesting because its successful application would not only avoid selecting the compatibilizer but also save a preparative step. In fact, as noted above, selection of the best compatibilizer may require special care, as this must be sufficiently polar to allow interaction with the clay, but not so hydrophilic as to favor phase separations. Not least, it should have similar rheological properties as the matrix, in order to avoid any deterioration of the composite's ultimate mechanical properties.

Consequently, two different synthetic approaches were very recently compared for the preparation of EPM and PP OLS nanocomposites [89] (Figure 13.9):

- The first approach is a classical procedure where the dispersion of OLS is achieved by using, as the compatibilizer of the system or as a matrix, a previously functionalized PO bearing carboxylate groups on the backbone (two-step process, Method 1). This method involves a first step when the functionalized PO is prepared. Frequently, the traditional approach for the preparation of functionalized PO is by free radical grafting of polar unsaturated molecules.
- The second process is carried out by contemporaneously performing the functionalization of the PO (by using maleic anhydride and/or diethylmaleate and a peroxide as radical initiator) and the dispersion of the filler (one-step process, Methods 2 and 3).

The results obtained using the two-step process (Method 1) indicated that, by using the functionalized PO as matrix, only a fraction of the polar groups on the polyolefin macromolecules would be effective in establishing a bonding with the silicate surface. In order to facilitate the functionalized polymer–clay interactions, it seems convenient to perform the functionalization during mixing of the PO with the clay. In this way, the small polar molecules could more easily penetrate the clay channel, with grafting to the organic macromolecules occurring successively. Comparative experiments were also carried out according to the one-step procedure, following two different routes—Methods 2 and 3 (see Figure 13.9).

In Method 2, the functionalizing reagents and organically modified montmorillonite (OMMT) were premixed and added contemporarily to the molten polymer in a Brabender mixer, such that functionalization and intercalation/exfoliation could occur simultaneously. In Method 3, the functionalizing reagents (initiator,

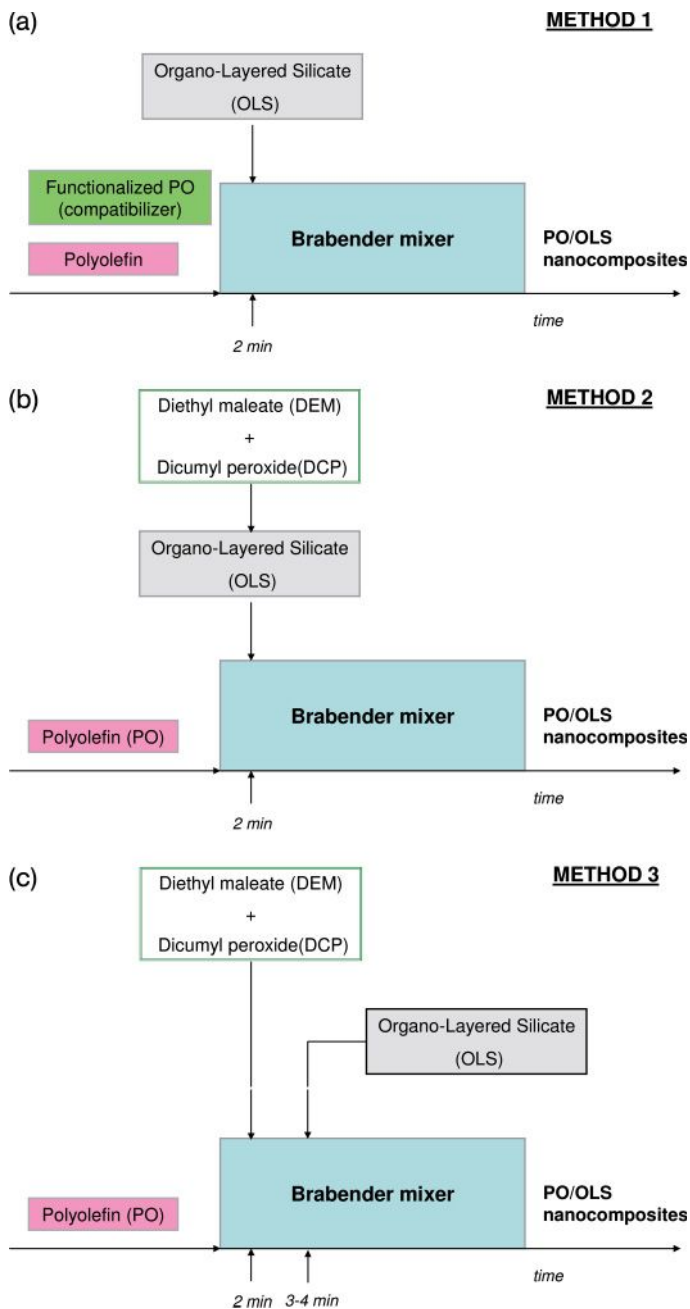


Figure 13.9 Different methods of preparation for compatibilized PO/OLS nanocomposites.

DEM and, occasionally, MAH) were added to the molten polymer, with the OMMT being added after a few minutes. In the former case, the operating conditions the aim essentially was first to have intercalation of the monomer, followed by grafting to the macromolecules. In the latter case, the procedure was essentially similar to the two-step method (Method 1), although for kinetic reasons there was a degree of overlapping within the time scale between the grafting of DEM to PO, and intercalation.

The results obtained indicated that, in terms of the role played by the different parameters (including the polyolefin chemical structure), the process was very complex. In the case of the random ethylene/propylene copolymer (EPM), the simultaneous addition of a functionalizing reagent and OMMT to the molten polymer (Method 2) was the most effective approach, even if an optimal ratio between the DF and clay basal spacing enlargement appeared to exist. In the case of PP, however, the application of Method 2 did not provide the same results, with a better dispersion being obtained via Method 3. Indeed, the polymer functionalization was seen to be favored, and degradation controlled, by the presence of clay. However, the best polymer chain intercalation was obtained when degradation was significant during the functionalization process of PP, indicating that a reduction in molecular weight which favored intercalation would probably be more effective than the presence of a larger amount of grafted polar groups.

### 13.3 Poly(Ethylene Terephthalate)-Based Nanocomposites

Poly(ethylene terephthalate) (PET), which is one of the most diffused polymers, is used in a wide variety of applications, notably the packaging and textile industries. The need to improve the stiffness, surface properties and/or gas barrier properties of PET has led to a plethora of investigations, in both academia and industry, into PET-based nanocomposites. Within this area, those nanocomposites which contain phyllosilicates are considered superior for providing improved gas barrier properties, due mainly to the strong effect of confinement as the result of a high surface:volume ratio (i.e., reducing chain mobility and permeability [35]), as well as to the enhancement of tortuosity [97] of the path required for small molecules to permeate through a polymer film due to the presence of silicate lamellae. Flame retardancy and gas barrier functions are much-required properties in the area of textiles, the main aim being to develop fabrics with flame self-extinguishing properties [98]. Consequently, many research groups have recently investigated PET/phyllosilicate nanocomposites in an attempt to provide solutions to these important technological problems [99–102].

One especially important field of application is that of recycling post-consumer PET [103]. The recovery of PET from post-consumer packaging products (e.g., beverage bottles) allows flakes to be obtained which have purity levels suitable for reprocessing. Unfortunately, in many countries (e.g., Italy) the recovered material

cannot be recycled via a bottle-to-bottle approach, as legislation decrees that post-consumer polymers cannot remain in contact with food. Consequently, there is a need to develop new materials based on post-consumer PET flakes, in order to achieve an effective recycling. At present, blending these flakes with other polymers, especially rubber [104–111], to achieve toughened blends, and/or adding fillers [112], represent the most frequently investigated strategies for producing materials with added value by utilizing post-consumer flakes. This final point is especially important because, if recycling cannot be used to provide materials that perform similarly to commonly used plastic materials, then landfilling or energy recovery using plastic wastes will become inevitable. Nanofillers—and in particular phyllosilicate-based nanocomposites—may well provide the means of modulating the mechanical, thermal, and flame-retardancy properties of post-consumer PET, thus broadening its field of application.

Today, both technological and environmental driving forces continue to attract the attention of scientific research towards PET–phyllosilicate nanocomposites.

### 13.3.1

#### **In Situ Polymerization**

The preparation of PET/MMT nanocomposites by *in situ* polymerization has been the object of several investigations. In particular, Hwang *et al.* [113] reported the preparation of PET nanocomposites containing pristine and organically modified MMT by *in situ* polymerization, since this technique has been shown to produce a homogeneous dispersion of MMT particles in the polymer matrix. The polymerization of PET was carried out through polycondensation [114, 115]. In an esterification tube, ethylene glycol and sodium or organically modified MMT and a catalyst of transesterification (zinc acetate) were subjected to ultrasonication before the ester interchange reaction was initiated. Dimethyl terephthalate was then added to the ethylene glycol slurry to obtain a homogeneously dispersed system. The mixture was then heated to 210°C to initiate esterification between the silicate layers in the clay. The ester exchange reaction was carried out for 3 h while continuously removing methanol. Finally, polycondensation was performed at reduced pressure, at temperatures between 180 and 285°C, by adding antimony (III) oxide catalyst as polycondensation catalyst.

The degree of exfoliation was determined by TEM measurements at 20 nm resolution; these showed a clear separation between the silicate layers of the clay, enhancing differences between the composites prepared using either sodium-MMT or OMMT which had been modified with dimethyl, benzyl, hydrogenated tallow, quaternary ammonium. The TEM images revealed the presence in 1% MMT composites of uniformly oriented sodium-MMT particles with complete layer stacks containing an average of 66 silicate sheets per particle, whereas particles in PET/OMMT were largely exfoliated, with a larger proportion of intercalated PET, as evidenced by significantly smaller particles composed of only four to five randomly oriented silicate sheets. Scanning electron microscopy (SEM) images of the nanocomposites confirmed that the

organophilic modifier had significantly improved the compatibility between PET and MMT.

DSC analyses showed that the crystallization temperature of PET/sodium-MMT during cooling gradually increased, while the degree of supercooling decreased with clay loading. This suggested that the sodium-MMT had acted as a nucleating agent and accelerated the crystallization rate of the PET matrix. In subsequent heating runs, the nanocomposites exhibited two melting peaks compared to pure PET. The lower melting temperature peak was attributable to the melting of imperfect crystals, which formed as a result of the nucleation effect of sodium-MMT during the cooling run. The higher melting temperature peak corresponded to melting of the melt-reorganized crystal.

DSC curves obtained for the PET/organophilic MMT exhibited an increase in the crystallization peak intensity during the cooling run at 0.5 wt% loading. This peak decreased with increasing clay content, although it maintained a higher intensity than that of neat PET. This indicated that the nucleating effect of organophilic MMT was lower than that of sodium-MMT. This may be attributable to interference by the alkyl groups on the organophilic MMT surfaces with secondary nucleation and diffusion of PET molecules, resulting in a decrease in the DSC crystallization peak.

The dispersion of rigid, exfoliated MMT layers served to enhance the macroscale stiffness of the composite material. Elongation at break values was drastically decreased due to increased stiffness and the formation of microvoids around the clay particles during tensile testing. The main factor contributing to the enhancement of mechanical properties in PET/clay nanocomposites was not the quantity of clay, but rather the degree of dispersion and exfoliation of the clay in the PET matrix.

A very similar *in situ* polymerization procedure was adopted by Chang and Mun [100], who prepared PET nanocomposites by using dodecyltriphenylphosphonium-modified MMT as a reinforcing filler in the fabrication of PET hybrid fibers. The group studied the properties of the composites obtained, for organoclay contents ranging from 0 to 5 wt%, by applying different draw ratios. The modified MMT displayed well-dispersed individual clay layers in the PET matrix, although some particles appeared to be agglomerated at size levels greater than approximately 10 nm.

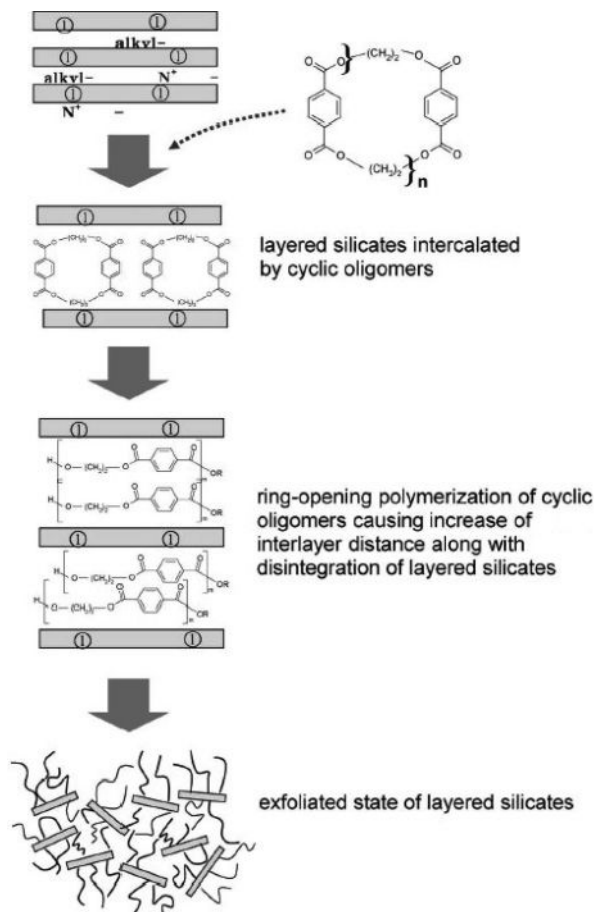
Ke *et al.* [116] also reported the properties of PET/MMT nanocomposites prepared by *in situ* polymerization of PET onto organophilic-modified MMT. The refined clay, reduced to particles of 40  $\mu\text{m}$  average diameter, was made into a slurry, and formed a solution with an intercalated reagent, which reacted directly with PET monomers in an autoclave [117, 118]. Although, this preparation method led mainly to intercalated nanocomposites, a similar nucleating effect with respect to the report of Chang and Munn was observed.

An alternative *in situ* polymerization method was provided by Lee *et al.* [118], who successfully polymerized ethylene terephthalate cyclic oligomers (ETCOs) to form a high-molecular-weight PET in the presence of OMMT by employing the advantages of the low viscosity of cyclic oligomers and lack of chemical emissions



during polymerization (Figure 13.10). Here, the OMMT was prepared via the cation exchange of sodium-MMT with *N,N,N*-trimethyl octadecylammonium bromide.

The application of ring-opening polymerization (ROP) is usually hindered by the limited efficiencies for synthesizing and isolating cyclic oligomers. Therefore, various types of preparative methods have recently been developed. The present authors followed the direct reaction of acid chlorides with glycols in dilute solution, which provides high yields of ETCs [119]. Subsequently, ETC, OMMT and  $\text{Ti}(\text{O}-1-\text{C}_3\text{H}_7)_4$  were dissolved in dichloromethane and the solution maintained at room temperature for 12 h. The oligomers, OMMT and  $\text{Ti}(\text{O}-1-\text{C}_3\text{H}_7)_4$ , dissolved in dichloromethane, were maintained at room temperature for 12 h; the solvent was



**Figure 13.10** Schematic representation of nanocomposites formation by ring-opening reaction of cyclic oligomers in-between silicate layers. Reproduced with permission from Ref. [118]; © 2005, Elsevier Ltd.

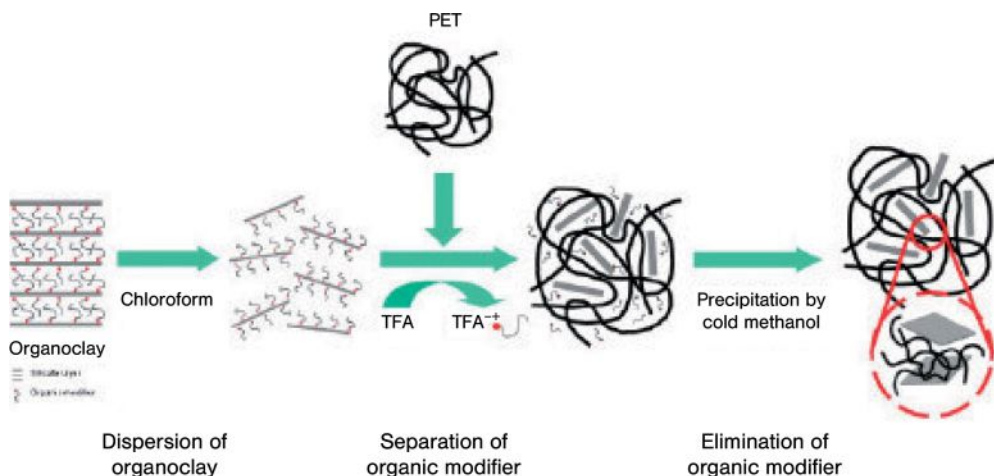
then removed, dried under reduced pressure and polymerized in a high-vacuum system at temperatures ranging from 240 to 310 °C.

Due to their low molecular weight and low viscosity, the ETCs are successfully intercalated into the clay galleries, as evidenced by XRD analyses which showed a down-shift of the basal plane peak of layered silicate, in good agreement with the results of TEM investigations. The successive ROP of ETCs in-between silicate layers yielded a PET matrix of high molecular weight, along with high disruption of the layered silicate structure and a homogeneous dispersion of the latter in the matrix. However, the coexistence of exfoliation and intercalation states of silicate layers was revealed by morphological investigations. Interestingly, the highest investigated polymerization temperature provided the nanocomposite with the PET having the greatest molecular weight (11 000 mol g<sup>-1</sup>).

### 13.3.2

#### Intercalation in Solution

To date, only one report has been made [120] detailing the preparation of PET/ phyllosilicate nanocomposites in solution. Exfoliated PET-layered silicate nanocomposites excluding and including organic modifiers were obtained by solution methods in chloroform/trifluoroacetic acid (TFA) mixtures, with and without solvent–nonsolvent systems, respectively. For this, the PET/OLS/chloroform/TFA solution was added dropwise to the cold methanol to obtain PET nanocomposites excluding an organic modifier; the precipitated materials were then collected by filtration and dried in a vacuum oven (Figure 13.11). In contrast, the PET



**Figure 13.11** Schematic illustration of the preparation of exfoliated PET nanocomposites excluding organic modifier by means of the solvent–nonsolvent system. Reproduced with permission from Ref. [120]; © 2008, John Wiley & Sons, Ltd.

nanocomposite including an organic modifier was prepared by removing both solvents from the prepared PET/OLS/chloroform/TFA solution.

Based on wide-angle X-ray diffraction (WAXRD) and high-resolution TEM analyses, both types of composite were found to have an exfoliated structure that was attributed to a sufficient dispersion of silicate in prepared solvents, regardless of the sample preparation method.

The DSC results indicated that both types of nanocomposite had higher degrees of crystallinity and shorter crystallization half-times than neat PET, since the dispersed silicate layers had acted as nucleating agents in both situations. However, those nanocomposites prepared with the organic modifier exhibited a lower degree of crystallinity and a longer half-time of crystallization than those without an organic modifier. This difference in crystallization behavior between the two nanocomposites was ascribed to the organic modifier, which may have acted as an inhibitor of crystallization.

### 13.3.3

#### **Intercalation in the Melt**

The most frequently reported method of intercalation has been within the melt, mainly because it is significantly more economical and simpler than other methods, and is also compatible with existing processes. In fact, melt processing allows nanocomposites to be formulated directly using ordinary compounding devices such as extruders or mixers, without the need to involve resin production. Consequently, nanocomposite production can be shifted downstream, providing end-use manufacturers with many degrees of freedom with regards to their final product specifications. Notably, melt processing is also environmentally friendly, as no solvents are required. It also enhances the specificity of intercalation of the polymer, by eliminating any competing host–solvent and polymer–solvent interactions.

One topic which has been widely investigated is the influence of an organophilic modification of nanoclay on the morphology of composites. Pegoretti *et al.* [121] compared the effect of a nonmodified natural MMT clay (Cloisite-Na<sup>+</sup>) and an ion-exchanged clay modified with quaternary ammonium salt (Cloisite 25A) (Table 13.5, row h) in a recycled PET matrix. The Cloisite 25A is a MMT modified with dimethyl, hydrogenated tallow, 2-ethylhexyl quaternary ammonium cations. Following preparation of the composites in an injection-molding machine, subsequent TEM images of the composite fracture surfaces indicated that the particles of Cloisite 25A were much better dispersed in the recycled PET matrix than those of Cloisite-Na<sup>+</sup>. Moreover, wide-angle X-ray scattering (WAXS) measurements indicated the intercalation of recycled PET between the silicate layers (lamellae) of the clay. In addition, improvements in mechanical properties were more evident in Cloisite 25A nanocomposites than in those containing Cloisite-Na<sup>+</sup>. More recently, the effects of different modified commercial MMTs on the morphology of PET composites prepared in a twin-screw extruder were investigated [122]. In particular, within a scale of increasing hydrophobicity of

**Table 13.5** Montmorillonites used for the preparation of polyesters/MMT nanocomposites by intercalation in the melt.

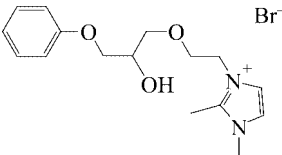
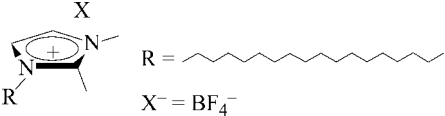
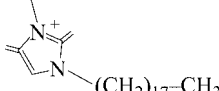
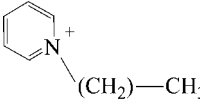
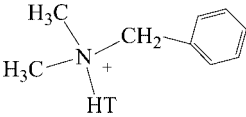
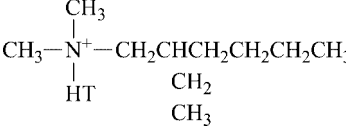
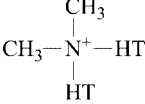
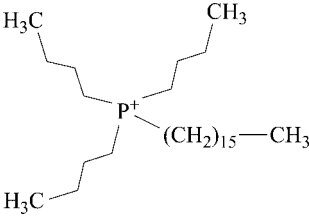
	Formula of the cation	Commercial name	Reference(s)
(a) Sodium montmorillonite	$\text{Na}^+$	Cloisite $\text{Na}^+$	[122–124]
(b) Methyl, tallow, bis-2-hydroxyethyl, quaternary ammonium montmorillonite	$\begin{array}{c} \text{CH}_2\text{CH}_2\text{OH} \\   \\ \text{CH}_3-\text{N}^+-\text{T} \\   \\ \text{CH}_2\text{CH}_2\text{OH} \end{array}$ <p>T is Tallow (~65% C18; ~30% C16; ~5% C14)</p>	Cloisite 30 B	[123, 125]
(c) 1-[2-(2-hydroxy-3-phenoxy-propoxy)-ethyl]-2,3-dimethyl-3H-imidazolium montmorillonite		–	[126]
(d) 1,2-dimethyl-3-N-hexadecyl imidazolium montmorillonite		–	[124]
(e) 1,3-Dioctadecyl imidazolium	$\text{H}_3\text{C}-(\text{CH}_2)_{17}$ 	–	[127]

Table 13.5 Continued.

	Formula of the cation	Commercial name	Reference(s)
(f) Hexadecyl pyridinium montmorillonite		–	[127]
(g) Dimethyl, benzyl, hydrogenated tallow, quaternary ammonium montmorillonite	 <p>HT = hydrogenated tallow</p>	Cloisite 10A Dellite 43B	[123]
(h) Dimethyl, dehydrogenated tallow, 2-ethylhexyl quaternary ammonium montmorillonite		Cloisite 25A	[122, 125]
(i) Dimethyl, dehydrogenated tallow, quaternary ammonium montmorillonite		Cloisite 20A (0.95 mg g <sup>-1</sup> clay) Cloisite 15A (1.25 mg g <sup>-1</sup> clay) Cloisite 6A (1.4 mg g <sup>-1</sup> clay) Dellite 72T	[127] [123, 125] [125]
(l) Tributyl hexadecyl phosphonium montmorillonite		–	[127]

the cation, sodium-MMT, methyl, tallow, bis-2-hydroxyethyl, quaternary ammonium-MMT (Cloisite 30B) (Table 13.5, row b), dimethyl, benzyl, hydrogenated tallow, quaternary ammonium-MMT (Cloisite 10A) (Table 13.5, row g) and dimethyl, dehydrogenated tallow, quaternary ammonium-MMT (Cloisite 15A) (Table 13.5, row i) were compared.

As revealed by both TEM and WAXD characterization, the shear in the extruder favored the exfoliation process, which resulted in both intercalated and exfoliated morphologies. PET nanocomposites obtained by using clay with polar modifiers showed intercalated and exfoliated morphologies, whereas tactoids were obtained when only apolar modifiers were present. The polymer–clay interactions and the extrusion conditions were sufficient to break the organized arrangement of the natural MMT, so as to disperse it in the polymer matrix. The organic modifier also appeared to sustain the exfoliated clay sheets flat since, in its absence, the intramolecular interactions were stronger and the platelets tended to roll due to their high flexibility. A comparison of these two reports [121, 122] showed contradictory results, however. As the recycled and virgin PET had practically identical structural characteristics (although the recycled form usually had a lower viscosity in the melt), the comparison mainly highlighted the strong effect of shear stresses on the morphology. In fact, the stronger shear stresses developed in the twin-screw extruder were most likely sufficient to achieve an exfoliated/intercalated structure, without using an organophilic modifier. In the study of Pegoretti *et al.* [121], the lower shear stresses of the injection-molding machine produced the opposite result, as in these conditions the main driving forces were the interactions of the hydrophobic chains with the polymer matrix, which were capable of producing a primary disaggregation of the filler.

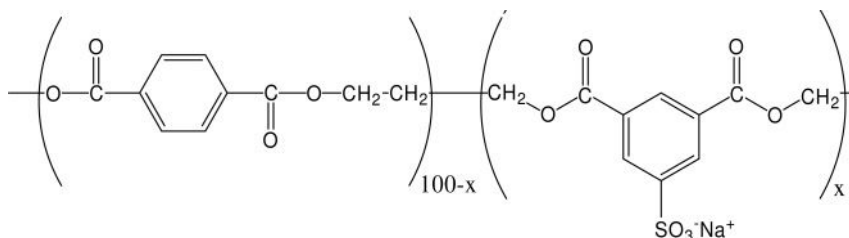
The strong effects of processing conditions and rheological properties on morphology were also reported by Krakalik *et al.* [123], who prepared composites in a co-rotating, twin-screw, microextruder by adding to recycled PET 5% (by weight) of different modified MMTs (Cloisite 6A, 15A, 20A, 25A, and 30B) (Table 13.5). Subsequently, these authors observed the partial exfoliation of Cloisite 25A, 30B, and 10A, which was in good agreement with the results observed by both Pegoretti *et al.* [121] and Calcagno *et al.* [122].

Davis *et al.* [125] investigated the effects of melt-processing conditions on the quality of PET/MMT nanocomposites prepared in a mini twin-screw extruder at 285 °C, and identified the need to use a highly stable ammonium salt in modified MMT. In fact, the use *N,N*-dimethyl-*N,N*-dioctadecylammonium-MMT led to the production of black PET nanocomposites as a result of ammonium salt degradation under the processing conditions. The most dispersed, exfoliated PET nanocomposite was achieved by melt-mixing at 21 radians per second for 2 min in a nitrogen atmosphere, after drying the polymer at 120 °C, and the clay at 150 °C. Alternative mixing conditions, longer residence times, and higher screw speeds resulted in poorer-quality nanocomposites. The alternative use of a hexadecyl imidazolium salt, which resulted in an intercalated/exfoliated morphology, allowed improvements in stability, as the imidazolium salt (which has a decomposition temperature of 350 °C) is stable under the conditions of

processing. The subject of modified MMT stability was recently investigated by Kim *et al.* [124], who synthesized an imidazolium salt with an aromatic group and an hydroxyl group (Table 13.5, row c), which was more stable than a quaternary ammonium salt. Such treatment was found to provide a similar dispersion with respect to Cloisite 15A and 30B, but with the advantage of a higher thermal stability.

More recently, Stoeffler *et al.* [126] used the surfactants alkyl phosphonium (Table 13.5, row l), alkyl pyridinium (Table 13.5, row f) and dialkyl imidazolium (Table 13.5, row e) as intercalating agents for the preparation of highly thermally stable organophilic MMTs, and compared these to commercial Cloisite 20A (Table 13.5, row i) from the point of view of thermal stability. Although the thermal stability of the former materials was improved with respect to the latter, a mass spectrometric analysis of the volatile products showed the evolution of chloromethane from Cloisite 20A above 200 °C, of pyridine from pyridinium-MMT above 250 °C, and of tributyl phosphine and/or tributyl phosphine oxide from phosphonium-MMT above 250 °C. Based on the toxicity of volatile products, the use of imidazolium or phosphonium derivatives proved unsatisfactory. Rather, the most interesting result obtained was the exfoliation of native sodium-MMT via the establishment of proper extrusion conditions [122].

In only one report [127] was the possibility considered of using a proper compatibilizer, namely a polyester ionomer (Figure 13.12), to improve the compatibility between an OMMT (Cloisite 20A) and PET. Here, the polyester ionomer was efficient in promoting intercalation (or intercalation/exfoliation if the ionomer/OMMT ratio was  $\geq 3$ ) of the OMMT in the PET matrix. Moreover, in terms of rheological behavior, the higher the filler content and/or the degree of intercalation/exfoliation of the OMMT, the more the nanocomposite behaved as a solid. With regards to rheological behavior, the higher the content of filler and/or degree of intercalation/exfoliation of the OMMT, the more the nanocomposite behaved as a solid because of the percolated structure formed by the OMMT layers, and the more the storage and loss modulus,  $G'$  and  $G''$ , became independent of the frequency at low frequencies.



**Figure 13.12** Structure of the polyester ionomer (PETi) used by Vidotti *et al.* [127]. ( $x = 0.13$ ).

## 13.4

### Poly(Lactide) (PLA)-Based Nanocomposites

Today, the development of renewable polymeric materials with excellent properties forms the subject of much active research interest worldwide [4]. Aliphatic polyesters are among the most promising materials for the production of high-performance, environment-friendly, biodegradable plastics [128]. Among these materials, PLA is a renewable and biodegradable polyester, the thermomechanical and gas-barrier properties of which prevent the replacement of traditional polymers in many areas of application. Consequently, innovative methods must be developed to modulate the properties of PLA, such as blending [129], plasticization [130], and the preparation of nanocomposites [131].

#### 13.4.1

##### Overview of Preparation Methods

###### 13.4.1.1 In Situ Polymerization

The preparation of some biodegradable polyesters, including PLA and PCL, is often achieved via ROP from corresponding lactones [132, 133]. In particular, the synthesis of PLA can be carried out starting either from the cyclic dimer, the lactide (3,6-dimethyl-1,4-dioxane-2,5-dione) by ROP, or by the condensation polymerization of lactic acid or its derivatives.

In terms of molecular weight control, the living ROP of lactide yields a linear relationship between monomer conversion and molecular weight and PLA with a narrow polydispersity index (PDI; defined as the ratio between the weight average and number average molecular weights,  $M_w/M_n$ ). In contrast, the step-growth condensation polymerization limits the practically accessible range of molecular weights, and leads to a PDI of 2.

The benefits of ROP in conjunction with a “living” method have enabled the controlled synthesis of block, graft, and star polymers [134], and this had led to the present consensus that living ROP represents a powerful and versatile method of addition–polymerization. In particular, coordination–insertion polymerization has been used extensively for the preparation of aliphatic polyesters with well-defined structure and architecture. The most widely used initiators include various aluminum and tin alkoxides and carboxylates. The covalent metal alkoxides or carboxylates with vacant d-orbitals react as coordination initiators by interacting with the oxygen of carbonyl group of the ester. These initiators are capable of producing stereoregular polymers of narrow molecular weight distribution and controlled molecular mass, with well-defined end groups.

Both, Kubies *et al.* [135] and Lepoittevin *et al.* [136, 137] studied the ROP of  $\epsilon$ -caprolactone ( $\epsilon$ -CL) onto modified MMTs. PCL-grafted layered silicate nanohybrids were thus prepared according to a controlled coordination–insertion mechanism. For this purpose, MMT was previously modified by an exchange of the constitutive Na cations by ammonium cations bearing one hydroxy function



((2-hydroxyethyl)dimethylhexadecylammonium), or simply trimethylhexadecylammonium [136]. In a successive study [137], Cloisite 30 B (Table 13.5, row b), modified with methyl, tallow, bis-2-hydroxyethyl, quaternary ammonium, was also employed.

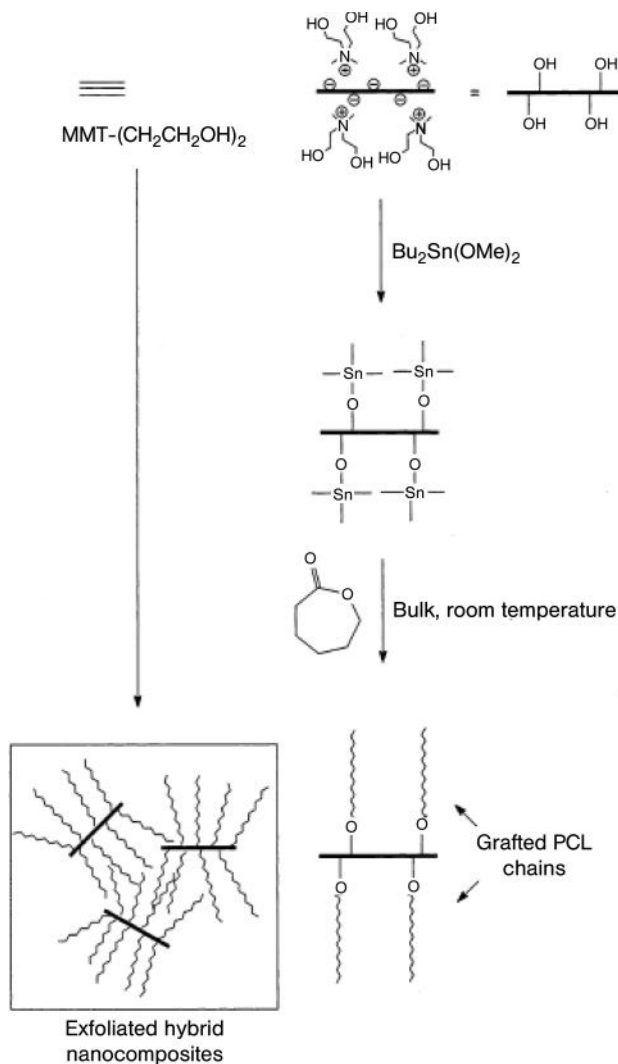
The modified MMT was then treated with aluminum or tin (II or IV) compounds [ $\text{AlEt}_3$ ,  $\text{Bu}_2\text{Sn}(\text{OMe})_2$  and  $\text{Sn}(\text{2-ethylhexanoate})_2$ ] to obtain the respective alkoxides, all of which are known to initiate the controlled polymerization of  $\epsilon$ -CL, by creating initiating species onto the MMT layers. The grafting of PCL onto the MMT was achieved in the presence of  $\epsilon$ -CL (Figure 13.13).

After polymerization, the molar mass of PCL, as determined by size-exclusion chromatography (SEC) after a reverse ion-exchange reaction with LiCl in tetrahydrofuran (THF), was found to decrease with the increasing content of hydroxy groups available at the clay surface. Indeed, the molar masses were 56 000, 47 000 and 28 000 for OH-deprived organomodified clay and clay containing 50 and 100% monohydroxylated ammonium cations, respectively. This observation suggests, at least qualitatively, that polymerization is initiated by the surface-anchored hydroxy groups activated in Sn(II) alkoxides by reaction with  $\text{Sn}(\text{2-ethylhexanoate})_2$ . In the absence of hydroxylated ammonium cations, polymerization is initiated by residual protic impurities (water, silanol, etc.). Polymerization initiation on the clay surface and PCL growth in a “grafting-from” manner each have strong effects on the morphology of the PCL/layered silicate nanocomposites, such that intercalated or exfoliated morphologies were obtained. However, extensive exfoliation occurred only when the silicate sheets were surface-modified with more than 25 wt% monohydroxylated ammonium [136]. Below this value, partially intercalated/partially exfoliated structures were found to coexist, and an intercalated structure was obtained, starting from sodium-MMT.

A good correlation was obtained between morphology and thermal stability, as the composites prepared with the clay that had been modified with hydroxyl groups were more stable than those deprived of them. Moreover, these composites were more stable than those containing sodium-MMT.

More recently, Chrissafis *et al.* [138] prepared PCL nanocomposites by following a similar approach, but used  $\text{Ti}(\text{OBu})_4$  as the coordination–insertion catalyst. Moreover, they performed ROPs not only onto sodium-MMT and Cloisite 20A (Table 13.5, row i), but also onto mica and fumed silica. In agreement with the above findings, there was also a decrease in the molecular weight of PCL obtained, compared to the pure material prepared in the absence of fillers. However, the mechanical properties (tensile strength at break, elastic modulus, elongation at break) of the nanocomposites were similar, or even slightly improved, compared to those of the pure PCL.

It appears that only two reports have been made concerning the synthesis of PLA using this method. For example, Paul *et al.* [139] synthesized PLA/layered aluminosilicate nanocomposites by ROP, using two different types of OMMT (Cloisite 30B and Cloisite 25A; see Table 13.5, rows b and h) for the preparation of nanocomposites. In a typical synthetic procedure, the clay was thoroughly dried and placed in the polymerization vial. The lactide solution in dried THF was then



**Figure 13.13** Scheme of the synthesis of PCL nanocomposites through *in situ* ROP onto montmorillonite modified with ammonium salt with hydroxyl groups. Reproduced with permission from Ref. [137]; © 2002, American Chemical Society.

transferred to the vial under nitrogen, and the solvent eliminated under reduced pressure. The polymerizations were conducted in bulk at 120 °C for 48 h, after 1 h of clay swelling in the monomer melt. When Cloisite 30B was used, the polymerization was cointiated by AlEt<sub>3</sub>, while Sn(2-ethylexanoate)<sub>2</sub> was used to catalyze the polymerization of lactide in the presence of Cloisite 25A. The clay Cloisite 30B led

to a fully exfoliated structure, whereas Cloisite 25A-based nanocomposites exhibited an intercalated morphology.

In the Cloisite 30B nanocomposites, the growing polymer chains were directly “grafted” onto the clay surface through the hydroxyl-functionalized ammonium cations, yielding exfoliated nanocomposites with an enhanced thermal stability. Notably, with increasing clay content the thermal stability was improved, with a maximum effect at a clay loading of 5 wt%. With a further increase of filler content, a decrease in thermal stability was observed—an effect explained by the relative extent of exfoliation as a function of the amount of organophilic MMT. Nonetheless, a decrease in PLA molecular weight was observed compared to that synthesized in the absence of filler.

A similar result was obtained more recently by Lee [140], who modified the clay surface (Cloisite 30B, Table 13.5 row b) by grafting low-molecular-weight PLA chains ( $M_n$  9400–21 600) through the *in situ* polymerization approach, following a preliminary activation of the hydroxyl sites with  $\text{Sn}(2\text{-ethylexanoate})_2$ . The composite obtained was then melt-blended with a high-molecular-weight PLA matrix. This novel clay/PLA nanocomposite showed a high shear-thinning behavior when the molecular weight of the grafted PLA was higher than the critical molecular weight of chain entanglement.

Today, the scientific investigations in this field are ongoing, with the *in situ* polymerization process clearly warranting further investigation. In particular, the ROP of lactide onto clay or organoclay may represent a promising approach for obtaining nanostructured PLA/layered silicate composites, allowing excellent control of the structural features of those materials prepared.

#### 13.4.1.2 Intercalation in Solution

Recently, several studies have focused on the preparation of PLA-layered silicate nanocomposites using intercalation from solution. Initially, Ogata *et al.* [141] dissolved the polymer in hot chloroform in the presence of OMMT, but observed that only microcomposites were formed. Marras *et al.* [142] adopted a similar method but, in contrast, obtained intercalated/exfoliated structures. The differences in experimental procedure here consisted of sonication of the organophilic MMT in chloroform, and of the solution containing both organophilic MMT and PLA. In the latter report, an increase in the  $d_{001}$  distance was cited as a function of the organophilic MMT modification, expressed as percentage of the CEC, when investigated over the range of 0 to 250%. The degree of organophilic modification was controlled by an ion-exchange reaction, using controlled amounts of hexadecylamine.

Krikorian and Pochan [143] prepared PLA nanocomposites using dichloromethane (DCM) as the polymer solvent and as the organophilic MMT dispersion medium (Cloisite 30B, 25A and 15A; Table 13.5, rows b, h, and i). These authors obtained intercalated or exfoliated nanocomposites, depending on the type of organophilic MMT used. Exfoliated nanocomposites were formed by using Cloisite 30B; that is, when hydroxyl groups were present in the organic modifier of the clay, due to the favorable enthalpic interaction between the

hydroxyl groups and the C–O bonds in the PLA backbone. Cloisite 25A, which showed the higher starting basal interlamellar distance, gave a  $d_{001}$  distance in the nanocomposites lower than Cloisite 30B. Hence, the starting basal interlamellar distance, which influences the capability of the organophilic MMT to be dispersed in a polyolefinic matrix, is a key factor but is less important in PLA-based nanocomposites.

Chang *et al.* [144] reported the preparation of PLA-based nanocomposites with different types of OMMT via solution intercalation using *N,N*-dimethylacetamide (DMA). The preparation method allowed the production of intercalated/exfoliated nanocomposites, providing material with an improved stiffness and barrier to oxygen compared to pure PLA.

#### 13.4.1.3 Intercalation in the Melt

To date, intercalation in the melt has attracted more attention than other intercalation processes, with different aspects being considered by various research groups with regards to melt blending. These include: the effects of different organophilic modifiers on morphology; the effects of the processing conditions; and the possibility of optimizing the processing and/or properties via blending or plasticization.

**Effect of Different Organophilic Modifiers** Di *et al.* [145] mixed two different organophilic MMTs (Cloisite 30B, Table 13.5, row b; and Cloisite 93A) in a PLA matrix by using an internal mixer. Cloisite 93A contains dimethyl-dihydrogenated tallow ammonium as modifier. It was observed that only the Cloisite 30B gave exfoliated nanocomposites, which was in good agreement with results obtained by Krikorian and Pochan [143] for nanocomposites obtained in solution. When Feijo *et al.* [146] compared two commercial organophilic MMTs, namely Dellite 43B (Table 13.5, row g) and Dellite 72T (Table 13.5, row i), the former material interacted more strongly with PLA, as confirmed by the better dispersion of the organoclay in the PLA matrix when compared to the neat PLA/Dellite 72T composites, which showed aggregates of only micrometric dimensions. Moreover, the PLA/Dellite43B nanocomposite exhibited a slightly higher thermal stability. Hence, replacement in the modifier of a long alkyl chain (hydrogenated tallow) with an aromatic ring renders the modifier more suitable for creating interactions between a modified nanofiller and the PLA polymer matrix. This result could, however, be ascribed to the higher polarity of the Dellite 43B ammonium salt.

**Effect of Processing Conditions** Pluta [147] investigated the processing of PLA and phyllosilicates by preparing, in a discontinuous laboratory mixer, nanocomposites containing 3% by weight of Cloisite 30B. In particular, the blending time (6.5, 10, 20, and 30 min) and rotor rate (50 and 100 r.p.m.) were varied in order to establish their effects on the morphology and properties of the nanocomposites. Molecular weight changes of the PLA matrices induced by melt compounding were determined using SEC. Whilst the molecular weight was marginally reduced by increasing the blending time, the level of dispersion of the filler into the matrix was

improved by increasing the blending time, as revealed by WAXD and TEM characterization.

The behavior of PLA during melt processing depends on many factors, including the grade of PLA used, the processing conditions applied (temperature, rotation speed, residence time, atmosphere, drying efficiency of the components), and the presence of additives and their chemical nature. Although pure PLA degrades slightly during blending, it was noticed that the degradation of PLA was enhanced by the presence of the nanofiller. This suggested important roles for both the shearing forces during compounding and the interaction of PLA with hydroxy groups of the organomodifier in determining the degradation of the PLA matrix. Moreover, the change in rotation speed adopted during nanocomposite preparation, from 50 to 100 r.p.m., caused a decrease in molecular weight but had no effect on the material's morphology and/or properties. It was also found that an increase in the degree of dispersion of the silicate layers led to a pronounced modification of the physical properties of the nanocomposites, via an increase in thermal stability, as revealed by TGA.

The rheological properties of the nanocomposites, as determined during a dynamic frequency sweep, appeared to be very sensitive to the nanostructure evolution. On investigating the rheological behavior of PLA during melt blending with Cloisite 30B, the apparent viscosity ( $\eta^*$ ) of the unfilled PLA was unchanged at low frequencies (indicating a Newtonian behavior), but this was followed by a shear-thinning response at a higher-frequency region. The  $\eta^*$  of the nanocomposites showed that, the higher the shear-thinning effect, the better the organoclay dispersion in the PLA matrix. These observed trends allowed an identification of the concentration of organoclay capable of providing a non-negligible interaction between nanoplatelets, based on rheology experiments. Similar results were obtained by Gu *et al.* [148], who explained the same trend as a function of the organophilic MMT content, by considering the formation of a "percolating network" resulting from reciprocity among the strongly related sheet particles. Because of this "percolating network," the values of entanglement molecular weight ( $M_e$ ), as calculated from master curves, were lower than that of pure PLA.

During such processing, Lewitus *et al.* [149] investigated the preparation and dilution of different types of masterbatch. The study results indicated the possibility of preparing PLA/Cloisite 25A nanocomposites via the preliminary preparation of a masterbatch which contained 20% by weight of the nanofiller and PLA. In particular, the most suitable PLA was that with the same grade as the final composite.

**Control of Processability and Properties by Blending and Plasticization** The addition of a reactive compatibilizer (e.g., an ethylene copolymer functionalized with maleic anhydride) during preparation in a discontinuous mixer of PLA/organophilic MMT nanocomposites was monitored by Pluta *et al.* [150]. When polylactide-based systems composed of an organoclay (Cloisite 30B; 3–10 wt%) and/or the compatibilizer were investigated, X-ray investigations revealed an exfoliated nanostructure in a 3 wt%-nanocomposite. The degree of exfoliation of the organoclay was notice-

ably enhanced by compatibilization, due to the combined interactions of the organoclay surfactant with the PLA chains and the MAH groups of the compatibilizer. In the 10wt%-nanocomposite, mixed (i.e., intercalated and exfoliated) nanostructures were detected due to the high concentration of the filler. Both, the rheological and mechanical properties suggested that a type of silicate network had been formed.

Sinha Ray *et al.* [151] noted that, although high-molecular-weight PCL was immiscible with PLA, oligomeric PCL was highly miscible (as indicated by a shift in  $T_g$ ). Consequently, the group used such an  $\alpha,\omega$ -hydroxy-terminated oligomeric PCL (0.2–3wt%) as compatibilizer when preparing PLA/octadecylammonium-modified MMT nanocomposites. The incorporation of a compatibilizer into the system led to a better parallel stacking of the silicate layers, and also to a much stronger flocculation as a result of the hydroxylated edge–edge interaction of the silicate layers. Owing to interaction between the clay particles and the PLA matrix with oligomeric PCL, the disk–disk interaction was considered to play an important role in determining the stability of the clay particles, and hence any enhancement of the mechanical properties of such nanocomposites. These systems, which were the first successful intercalated-type PLA/layered silicate nanocomposites, exhibited remarkable improvements in the materials properties of both solid and melt states when compared to the matrix without clay.

Shortly thereafter, Kubies *et al.* [152] prepared PCL-layered silicate nanocomposite masterbatches by the ROP of  $\epsilon$ -CL in the presence of the OMMT, Cloisite 30B. The masterbatch MB30 (28wt% MMT, PCL with  $M_w = 1800$ ) had an intercalated structure, while MB8 (7.5wt% MMT, PCL with  $M_w = 7500$ ) was exfoliated. Subsequently, high-molecular-weight PLLA nanocomposites containing 0.5–2.5wt% MMT were obtained by the melt-blending of PLLA ( $M_w = 4.5 \times 10^5$  Da) with PCL masterbatches or Cloisite 30B. The MMT particles in PLLA/Cloisite 30B and PLLA/MB30 nanocomposites were intercalated. In contrast to expectation, the exfoliated silicate layers of MB8 were not transferred into the PLLA matrix of the PLLA/MB8 nanocomposites. Due to a low miscibility of PCL and PLLA, MMT remained in the phase-separated masterbatch domains. The stress–strain characteristics of PLLA nanocomposites (i.e., Young's modulus), yield stress and yield strain, were decreased with increasing MMT concentration, associated with an increase in the PCL content (up to 35.4wt% in PLLA/MB8). The expected stiffening effect of the MMT was low, due to a low aspect ratio of its particles, and was obscured by both the plastifying effect of PCL and the low PLLA crystallinity. Interestingly, in contrast to the neat PLLA, ductility was enhanced in all PLLA/Cloisite 30B materials, and also in the PLLA/masterbatch nanocomposites with low MMT concentrations.

As reported Sinha Ray *et al.* [151], the miscibility of PCL with the PLA matrix plays a crucial role in its possible use as a compatibilizer. However, Yu *et al.* [153] more recently prepared PLA/PCL 90/10 blends containing different amounts (1–10wt%) of organophilic MMTs modified with bis-(2-hydroxyethyl)-methyl-(hydrogenated tallow alkyl) ammonium cations, by using a counter-rotating, discontinuous mixer. The silicate layers of the clay were intercalated and distributed

randomly in the matrix. The addition of organophilic MMT to the PLLA/PCL blend led to a significant improvement in the tensile properties and dynamic mechanical properties of the nanocomposites. In contrast, the layered silicate caused a clear improvement in the thermal stability of the PLLA/PCL blends when the organophilic MMT content was less than 5 wt%. SEM images confirmed that the addition of OMMT could reduce the size of the phase-separated particles, causing the material to become more uniform.

Interestingly, it has been suggested that OMMT might play the role of a compatibilizer, and a similar reduction in particle size in phase-separated blends was reported for a triblock PLA-PCL-PLA copolymer used as a compatibilizer in similar blend systems [154]. These authors ascribed this phenomenon to the intercalation of polymer molecules in OMMT, which increases the viscosity ratio and results in the retardation of coalescence of the dispersed phase-separated particles and an enhanced compatibility as a result of the intercalation of both PLLA and PCL molecules into the same OMMT gallery.

Hence, the possible use of a second polymeric phase as a compatibilizer should focus on the miscibility or compatibility between the two polymeric phases, in order to predict the morphology, as this depends not only on the level of dispersion of the lamellae in the polymeric matrix, but also on the phase distribution, which in turn influences the preferential distribution and orientation of the lamellae.

Recently, much interest has been expressed regarding not only the plasticization of PLA [130, 155, 156], but also the possible addition of a plasticizer to PLA/layered silicate nanocomposites. This subject is particularly attractive because it might allow a balance to be achieved between the mechanical and gas-barrier properties, since plasticization will in general provide an improved ductility but reduce the gas-barrier effects. In contrast, adding a nanofiller would improve the stiffness and gas-barrier properties of the PLA. Hence, the plasticization of PLA nanocomposites might provide a more ductile material, without either decreasing and/or improving its gas-barrier properties. Plasticized PLA-based nanocomposites were prepared by Paul *et al.* [157] by melt-blending the matrix with 20 wt% poly(ethyleneglycol) (PEG; number average molecular weight 1000) and different amounts of MMT, with or without organomodification. For this, four different (organo)clays were dispersed within the plasticized PLA matrix, after which the influence of the interlayer cations on the composite's morphological and thermal properties was studied while maintaining a constant level of inorganic material (3 wt% layered aluminosilicate).

Each of the MMTs studied, including the unmodified sodium-MMT, led to the formation of intercalated nanocomposites. Usually, melt-blending polymer matrices with sodium MMT results in the formation of a microcomposite, as most of the polymers are too highly hydrophobic to migrate into the hydrated Na<sup>+</sup> interlayer space. However, Vaia *et al.* [158] have reported on the intercalation of PEG between the aluminosilicate layers of an unmodified sodium-MMT that led to an increase in the interlayer distance which was similar to that observed by Paul *et al.* [157]. Clearly, in the presence of sodium-MMT, the PEG 1000 is able to intercalate preferentially with the interlayer spacing of the clay. This selective PEG

intercalation was further confirmed by an inability to form a nanocomposite by melt-blending nonplasticized PLA with sodium-MMT.

At a constant filler level it appears that, among all the clays studied (Cloisite Na+, Cloisite 30B, Cloisite 20A, and Cloisite 15A; see Table 13.5, rows a, b, and i, respectively), the MMT that had been organomodified with bis-(2-hydroxyethyl)-methyl-(hydrogenated tallow alkyl) ammonium cations (Cloisite 30B) brought about a greater effect in terms of improvements in dispersion level and thermal stability of the plasticized nanocomposites, and this was in good agreement with previous reports of PLA/MMT nanocomposites. It was noted, however, by using WAXS and DSC analyses, that there existed a real competition between PEG 1000 and PLA for intercalation into the interlayer spacing of the clay.

As also noted by Pluta *et al.* [159], who investigated the same system, SEC revealed a decrease in the molecular weight of the PLA matrix. This was more consistent at higher filler contents, but essentially independent of the type of organophilic modification of the MMT.

Thellen *et al.* [160] investigated the influence of MMT-layered silicate on plasticized PLA blown films. Here, the plasticized PLA MMT-layered silicate nanocomposites were compounded and blown film-processed, using a co-rotating, twin-screw extruder. The PLA was mixed with 10 wt% acetyltriethyl citrate ester as plasticizer and 5 wt% of an OMMT, at various screw speeds. Both, WAXD and TEM investigations showed that the compounded pellets and the blown-film PLA/OLS nanocomposites had intercalated. The effects of the processing screw speed on the barrier, thermal, mechanical, and biodegradation properties of the nanocomposites were also considered, and compared to the neat polymer. The nanocomposite films showed a 48% improvement in oxygen barrier, and a 50% improvement in water vapor barrier, when compared to PLA. A subsequent TGA revealed an overall 9°C increase in the decomposition temperature for all of the nanocomposites. A DSC analysis indicated that neither the glass transition, cold crystallization, nor melting point temperature was significantly influenced by the presence of MMT. The mechanical properties of the nanocomposites indicated a 20% increase in the Young's modulus, but that the ultimate elongation of the nanocomposites had not been sacrificed compared to the neat samples. Hence, the use of both plasticizers and nanofillers in a PLA matrix might effectively serve as a successful strategy for providing materials with modulated properties.

### 13.5 Conclusions

In this chapter we have compared the schemes used to prepare polymer/layered silicate nanocomposites from three classes of material, namely polyolefins, PET and PLA, and have reviewed certain interesting similarities and differences among these materials.

With regards to similarities, analogous synthetic approaches were described for the preparation of nanocomposites, with all three cases—*in situ* polymerization,



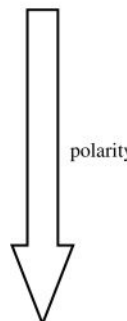
intercalation from solution, and intercalation in the melt—being investigated. For polyolefins, *in situ* polymerization appears less successful and less sustainable, with synthesis via catalytic polymerization perhaps proving to be a drawback, notably due to poor interactions between the inorganic filler and the polymeric matrix. To overcome this problem, the synthesis should include polyolefins bearing polar groups capable of interacting with the silicate layers. Many challenges remain, however. The catalytic polymerization of polar monomers with both traditional Ziegler–Natta and metallocene catalysts is not feasible, due mainly to catalyst deactivation, while the polymerization of polyesters via ROP onto layered silicates represents an interesting strategy for developing highly compatibilized organic–inorganic hybrid systems. The hydroxyl groups, whether typical of phyllosilicates or purposefully added via modification with hydroxyethyl functional ammonium salts, serve as initiating sites for the polymerization of lactide, or various lactones. Most importantly, polymerizations must be strictly controlled, with the length of the grafted chains being longer than the critical molecular weight of any chain entanglements.

Today, the number of reports describing the preparation of polyolefin-based nanocomposites exceeds that on the preparation of PET and PLA nanocomposites, essentially because preparing nanocomposites from polyolefins is much more difficult due to intrinsic incompatibilities between the polar matrix and the highly polar filler. Whilst for polyolefin-based nanocomposites, extensive data have been acquired by using apolar organophilic layered silicates, in the case of PET, exfoliated silicate nanocomposites were acquired via an extrusion process which utilized a nonmodified sodium-MMT.

It seems that the best structure for a modification agent depends on the polarity of the polymeric matrix. In the case of polyolefins, ammonium salts with long aliphatic chains can permit optimization of the dispersion level. For PLA, the methyl, hydrogenated tallow, bis(hydroxyethyl) ammonium salt seems to be the best dispersing agent for clay, whereas for PET, sodium-MMT, hydrogenated tallow, bis(hydroxyethyl) ammonium-MMT and dimethyl, hydrogenated tallow, benzyl ammonium-MMT, are each capable of providing exfoliated morphologies.

Another crucial point here is the need to use a compatibilizer. When preparing polyolefin/layered silicate nanocomposites, the addition of a compatibilizer is paramount, yet for PLA and PET nanocomposites the inclusion of a compatibilizer is rare. Thus, the polarity of a polymer matrix seems to be the main driving force of the preparation strategy, as summarized in Figure 13.14.

In general, the preparation of polymer/layered silicate nanocomposites requires parallel investigations concerning compatibilizers and processing aids. For polyolefin-based nanocomposites, the challenge resides in setting up and understanding the role of reactive compatibilizers to control and/or tailor the morphologies responsible for the improved material properties. But, for PET the main objective is—and will continue to be—the optimization of thermal stability, as organophilic modifiers are typically unstable at PET processing temperatures. Undoubtedly, improvements in the thermal stability and flame self-extinguishing properties of



	Best organophilic cations	Number of published papers dealing with compatibilizers
Polyolefin	With long aliphatic chains [71, 72]	16 [52, 56–58, 68, 76–79, 82–88]
PLA	$\begin{array}{c} \text{CH}_2\text{CH}_2\text{OH} \\   \\ \text{CH}_3-\text{N}^+-\text{T} \\   \\ \text{CH}_2\text{CH}_2\text{OH} \end{array}$ [148, 150]	3 [156–158]
PET	$\begin{array}{c} \text{Na}^+, [127] \\ \\ \begin{array}{c} \text{CH}_2\text{CH}_2\text{OH} \\   \\ \text{CH}_3-\text{N}^+-\text{T} \\   \\ \text{CH}_2\text{CH}_2\text{OH} \end{array} [128] \\ \\ \begin{array}{c} \text{H}_3\text{C} \\   \\ \text{N}^+ \\   \\ \text{H}_3\text{C} \end{array} \text{CH}_2-\text{C}_6\text{H}_5 \\ + \\ \text{HT} \end{array}$ [128]	1 [132]

**Figure 13.14** Schematic comparison of preparation methods for polymer/layered silicates nanocomposites.

PET will become technological necessities, notably in the development of new fibers and the preparation of nanocomposites. Meanwhile, PET recycling and the need to improve the properties of post-consumer materials remain major challenges for PET/layered silicate nanocomposites.

For PLA, and for biodegradable polyesters in general, new processing aids—developed from renewable resources—should be selected when preparing nanocomposites. Whilst the criteria of nanocomposite preparation are substantially similar to those for petrochemical polymers, the (preferential) need to use naturally derived compounds and polymers will surely lead to innovative methods of production. In particular, replacing commonly used commercial modifiers (ammonium salts) with cations that are not only more sustainable but also biodegradable should prove interesting. In attempts to develop new materials with modulated properties, melt-blending with biodegradable and/or renewable polymers, or perhaps the addition of highly sustainable plasticizers, should allow for the creation of innovative materials that are highly tunable in terms of their mechanical, thermal, gas-barrier, and biodegradation properties. Clearly, the behavior of nanolayers in a complex multiphase system will remain the object of increasing research attention for years to come.

### Acknowledgments

The authors thank Prof. Francesco Ciardelli, Stefania Castiello and Francesca Signorini (Dipartimento di Chimica e Chimica Industriale, Università di Pisa) for very helpful discussions. Financial support from MIUR (NANOPACK FIRB 2003

D. D. 2186 grant RBNE03R78E) and from CIPE (Toscana PC-RIPLAS project, 2008–2009) is also gratefully acknowledged.

## References

- 1 Gao, F. (2004) Clay/polymer composites: the story. *Mater. Today*, **7**, 50–5.
- 2 Zeng, Q.H., Yu, A.B., Lu, G.Q. and Paul, D.R. (2005) Clay-based polymer nanocomposites: research and commercial development. *J. Nanosci. Nanotechnol.*, **5**, 1574–1592.
- 3 Schadler, L.S., Brinson, L.C. and Sawyer, W.G. (2007) Polymer nanocomposites: a small part of the story. *JOM*, **3**, 53–60.
- 4 Yu, L., Dean, K. and Li, L. (2006) Polymer blends and composites from renewable resources. *Prog. Polym. Sci.*, **31**, 576–602.
- 5 Tsutsumi, N., Kono, Y., Oya, M., Sakai, W. and Nagata, M. (2008) Recent development of biodegradable network polyesters obtained from renewable natural resources. *Clean Soil, Air, Water*, **36**, 682–686.
- 6 Grim, R.E. (1968) *Clay Mineralogy*. 2nd edn, McGraw-Hill, New York, NY, USA.
- 7 Manocha, L.M. (2006) Composites with nanomaterials, in *Functional Nanomaterials* (eds K.E. Geckeler and E. Rosemberg), American Scientific Publishers, Stevenson Ranch, CA, USA.
- 8 Dong, H. (2005) Interstratified illite-smectite: a review of contributions of TEM data to crystal chemical relations and reaction mechanisms. *Clay Sci.*, **12** (Suppl. 1), 6.
- 9 Carnicelli, S., Mirabella, A., Cecchini, G. and Sanesi, G. (1997) Weathering of chlorite to a low charge expandable mineral in a spodosol on the Apennine Mountains, Italy. *Clays Clay Miner.*, **45**, 28.
- 10 Sakharov, B.A., Lindgreen, H., Salyn, A. and Drits, V.A. (1999) Determination of illite-smectite structures using multispecimen X-ray diffraction profile fitting. *Clays Clay Miner.*, **47** (5), 555–569.
- 11 Xu, W.B., Ge, M.L. and He, P.S. (2001) Nonisothermal crystallization kinetics of polyoxymethylene/montmorillonite nanocomposites. *J. Appl. Polym. Sci.*, **82**, 2281–2297.
- 12 Liu, J., Boo, W.-J., Clearfield, A. and Sue, H.-J. (2006) Intercalation and exfoliation: a review on morphology of polymer nanocomposites reinforced by inorganic layer structures. *Mater. Manufact. Process.*, **20**, 143–151.
- 13 Sinha Ray, S., Okamoto, K. and Okamoto, M. (2003) Structure–property relationship in biodegradable poly(butylene succinate)/layered silicate nanocomposites. *Macromolecules*, **36**, 2355.
- 14 Chen, B., Evans, J.R.G., Greenwell, H.C., Boulet, P., Coveney, P.V., Bowden, A.A. and Whiting, A. (2008) A critical appraisal of polymer–clay nanocomposites. *Chem. Soc. Rev.*, **37**, 568–594.
- 15 Samyn, F., Bourbigot, S., Jama, C., Bellayer, S., Nazare, S., Hull, R., Castrovinci, A., Fina, A. and Camino, G. (2008) Crossed characterisation of polymer-layered silicate (PLS) nanocomposite morphology: TEM, X-ray diffraction, rheology and solid-state nuclear magnetic resonance measurements. *Eur. Polym. J.*, **44**, 1642–1653.
- 16 Luo, Z.P. and Koo, J.H. (2008) Quantification of the layer dispersion degree in polymer layered silicate nanocomposites by transmission electron microscopy. *Polymer*, **49**, 1841–1852.
- 17 Drummy, L.F., Wang, Y.C., Schoenmakers, R., May, K., Jackson, M., Koerner, O.H., Farmer, B.L., Mauryama, B. and Vaia, R.A. (2008) Morphology of layered silicate- (NanoClay-) polymer nanocomposites by electron tomography and small-angle X-ray scattering. *Macromolecules*, **41**, 2135–2143.
- 18 Incarnato, L., Scarfato, P., Scatteia, L. and Acerno, D. (2004) Rheological behavior of new melt compounded

- copolyamide nanocomposites. *Polymer*, **45** (10), 3487–3496.
- 19 Lim, S.K., Kim, J.W., Chin, I., Kwon, Y.K. and Choi, H.J. (2002) Preparation and interaction characteristics of organically modified montmorillonite nanocomposite with miscible polymer blend of poly(ethylene oxide) and poly(methyl methacrylate). *Chem. Mater.*, **14**, 1989–1994.
  - 20 Kim, H.B., Choi, J.S., Lee, C.H., Lim, S.T., Jhon, M.S. and Choi, H.J. (2005) Polymer blend/organoclay nanocomposite with poly(ethylene oxide) and poly(methyl methacrylate). *Eur. Polym. J.*, **41**, 679–685.
  - 21 Ray, S.S., Pouliot, S., Bousmina, M. and Utracki, L.A. (2004) Role of organically modified layered silicate as an active interfacial modifier in immiscible polystyrene/polypropylene blends. *Polymer*, **45**, 8403–8413.
  - 22 Fang, Z., Harrats, C., Moussaif, N. and Groeninckx, G. (2007) Location of a nanoclay at the interface in an immiscible poly( $\epsilon$ -caprolactone)/poly(ethylene oxide) blend and its effect on the compatibility of the components. *J. Appl. Polym. Sci.*, **106**, 3125–3135.
  - 23 Gahleitner, M., Kretzschmar, B., Pospiech, D., Ingolic, E., Reichelt, N. and Bernreitner, K. (2006) Morphology and mechanical properties of polypropylene/polyamide 6 nanocomposites prepared by a two-step melt-compounding process. *J. Appl. Polym. Sci.*, **100**, 283–291.
  - 24 Vo, L.T. and Giannelis, E.P. (2007) Compatibilizing poly(vinylidene fluoride)/nylon-6 blends with nanoclay. *Macromolecules*, **40**, 8271–8276.
  - 25 Yurekli, K., Karim, A., Amis, E.J. and Krishnamoorti, R. (2003) Influence of layered silicates on the phase-separated morphology of PS-PVME blends. *Macromolecules*, **36**, 7256–7257.
  - 26 Filippone, G., Dintcheva, N.T., Acierno, D. and La Mantia, F.P. (2008) The role of organoclay in promoting co-continuous morphology in high-density poly(ethylene)/poly(amide) 6 blends. *Polymer*, **49**, 1312–1322.
  - 27 Chow, W.S., Mohd Ishak, Z.A., Karger-Kocsis, J., Apostolov, A.A. and Ishiaku, U.S. (2003) Compatibilizing effect of maleated polypropylene on the mechanical properties and morphology of injection molded polyamide 6/polypropylene/organoclay nano composite. *Polymer*, **44**, 7427–7440.
  - 28 Chow, W.S., Abu Bakar, A., Mohd Ishak, Z.A., Karger-Kocsis, J. and Ishiaku, U.S. (2005) Effect of maleic anhydride-grafted ethylene-propylene rubber on the mechanical, rheological and morphological properties of organoclay reinforced polyamide 6/polypropylene nanocomposites. *Eur. Polym. J.*, **41**, 687–696.
  - 29 Chow, W.S., Mohd Ishak, Z.A. and Karger-Kocsis, J. (2005) Atomic force microscopy study on blend morphology and clay dispersion in polyamide-6/polypropylene/organoclay systems. *J. Polym. Sci., Part B: Polym. Phys.*, **43**, 1198–1204.
  - 30 Chen, G.X. and Yoon, J.S. (2005) Thermal stability of poly(L-lactide)/poly(butylene succinate)/clay nanocomposites. *Polym. Degrad. Stab.*, **88**, 206–212.
  - 31 Pavlidou, S. and Papaspyrides, C.D. (2008) A review-layered silicate nanocomposites. *Prog. Polym. Sci.*, **33**, 1190–1198.
  - 32 Passaglia, E., Bertoldo, M., Ceriigi, S., Sulcis, R., Narducci, P. and Conzatti, L. (2008) Oxygen and water vapor barrier properties of MMT nanocomposites from low density polyethylene or EPM with grafted succinic groups. *J. Nanosci. Nanotechnol.*, **8** (4), 1690–1699.
  - 33 Lu, C. and Mai, Y.-W. (2005) Influence of aspect ratio on barrier properties of polymer-clay nanocomposites. *Phys. Rev. Lett.*, **95**, 088303.
  - 34 Xu, B., Zheng, Q., Song, Y. and Shangguan, Y. (2006) Calculating barrier properties of polymer/clay nanocomposites: effects of clay layers. *Polymer*, **47**, 2904–2910.
  - 35 Rittigstein, P., Priestley, R.D., Broadbelt, L.J. and Torkelson, J.M. (2007) Model polymer nanocomposites provide an understanding of confinement effects in real nanocomposites. *Nat. Mater.*, **6** (4), 257–258.

- 36 Gilman, J.W., Jackson, C.L., Morgan, A.B., Harris, R. Jr., Manias, E., Giannelis, E.P., Wuthenow, M., Hilton, D. and Phillips, S.H. (2000) Flammability properties of polymer-layered-silicate nanocomposites. Polypropylene and polystyrene nanocomposites. *Chem. Mater.*, **12**, 1866–1873.
- 37 Zanetti, M., Kashiwagi, T., Falqui, L. and Camino, G. (2002) Cone calorimeter combustion and gasification studies of polymer layered silicate nanocomposites. *Chem. Mater.*, **14**, 881–887.
- 38 Liu, T., Lim, K.P., Tjiu, W.C., Pramoda, K.P. and Chen, Z.-K. (2003) Preparation and characterization of nylon 11/ organoclay nanocomposites. *Polymer*, **44**, 3529–3535.
- 39 Harrats, C. and Groeninckx, G. (2008) Features, questions and future challenges in layered silicates clay nanocomposites with semicrystalline polymer matrices. *Macromol. Rapid. Commun.*, **29**, 14–26.
- 40 Xu, W., Ge, M. and He, P. (2001) Nonisothermal crystallization kinetics of polyoxymethylene/montmorillonite nanocomposite. *J. Appl. Polym. Sci.*, **82**, 2281–2289.
- 41 Giannelis, E.P., Krishnamoorti, R. and Manias, E. (1999) Polymer-silicate nanocomposites: model systems for confined polymers and polymer brushes. *Adv. Polym. Sci.*, **138**, 107–147.
- 42 Alexandre, M. and Dubois, P. (2000) Polymer-layered silicate nanocomposites: preparation, properties and uses of a new class of materials. *Mater. Sci. Eng., R*, **R28**, 1–63.
- 43 Pinnavaia, T.J. and Beall, G.W. (2000) *Polymer-Clay Nanocomposites*, John Wiley & Sons, Inc., New York.
- 44 Fischer, H. (2003) Polymer nanocomposites: from fundamental research to specific applications. *Mater. Sci. Eng., C*, **C23**, 763–772.
- 45 Ray, S.S. and Okamoto, M. (2003) Polymer/layered silicate nanocomposites: a review from preparation to processing. *Prog. Polym. Sci.*, **28**, 1539–1641.
- 46 Giannelis, E. (1996) Polymer layered silicate nanocomposites. *Adv. Mater.*, **8**, 29–35.
- 47 Tjong, S.C. (2006) Structural and mechanical properties of polymer nanocomposites. *Mater. Sci. Eng., R*, **R53**, 73–197.
- 48 Ciardelli, F., Coiai, S., Passaglia, E., Pucci, A. and Ruggeri, G. (2008) Nanocomposites based on polyolefins and functional thermoplastic materials. *Polym. Int.*, **57**, 805–836.
- 49 Vaia, R.A., Price, G., Ruth, P.N., Nguyen, H.T. and Lichtenhan, J. (1999) Polymer/layered silicate nanocomposites as high performance ablative materials. *J. Appl. Clay. Sci.*, **15**, 67–92.
- 50 Biswas, M. and Sinha Ray, S. (2001) Recent progress in synthesis and evaluation of polymer-montmorillonite nanocomposites. *Adv. Polym. Sci.*, **155**, 167–221.
- 51 Kawasumi, M., Hasegawa, N., Kato, M., Usuki, A. and Okada, A. (1997) Preparation and mechanical properties of polypropylene-clay hybrids. *Macromolecules*, **30**, 6333–6338.
- 52 Manias, E., Touny, A., Wu, L., Strawhecker, K., Lu, B. and Chung, T.C. (2001) Polypropylene/montmorillonite nanocomposites. Review of the synthetic routes and materials properties. *Chem. Mater.*, **13**, 3516–3523.
- 53 Liu, X.H. and Wu, Q.J. (2001) Polypropylene/clay nanocomposites prepared by grafting-melt. *Polymer*, **42**, 10013–10019.
- 54 García-López, D., Picazo, O., Merino, J.C. and Pastor, J.M. (2003) Polypropylene-clay nanocomposites: effect of compatibilizing agents on clay dispersion. *Eur. Polym. J.*, **39**, 945–950.
- 55 Usuki, A., Kato, M., Okada, A. and Kurauchi, T. (1997) Synthesis of polypropylene-clay hybrid. *J. Appl. Polym. Sci.*, **63**, 137–139.
- 56 Kato, M., Usuki, A. and Okada, A. (1997) Synthesis of polypropylene oligomer-clay intercalation compounds. *J. Appl. Polym. Sci.*, **66**, 1781–1785.
- 57 Oya, A., Kurokawa, Y. and Yasuda, H. (2000) Factors controlling mechanical properties of clay mineral/polypropylene nanocomposites. *J. Mater. Sci.*, **35**, 1045–1050.
- 58 Wang, Y., Chen, F.B., Li, Y.C. and Wu, K.C. (2004) Melt processing of

- polypropylene/clay nanocomposites modified with maleated polypropylene compatibilizers. *Composites Part B*, **35**, 111–124.
- 59 Sun, T. and Garcés, M.J. (2002) High-performance polypropylene-clay nanocomposites by in situ polymerization with metallocene/clay catalysts. *Adv. Mater.*, **14**, 128–130.
- 60 Hwu, J.M. and Jiang, G.J. (2005) Preparation and characterization of polypropylene-montmorillonite nanocomposites generated by in situ metallocene catalyst polymerization. *J. Appl. Polym. Sci.*, **95**, 1228–1236.
- 61 Ma, J.S., Qi, Z.N. and Hu, Y.L. (2001) Synthesis and characterization of polypropylene/clay nanocomposites. *J. Appl. Polym. Sci.*, **82**, 3611–3617.
- 62 He, A., Hu, H., Huang, Y., Dong, J.Y. and Han, C.C. (2004) Isotactic poly(propylene)/monoalkylimidazolium-modified montmorillonite nanocomposites: preparation by intercalative polymerization and thermal stability study. *Macromol. Rapid Commun.*, **25**, 2008–2013.
- 63 Alexandre, M., Dubois, P., Sun, T., Garcés, J.M. and Jerome, R. (2002) Polyethylene-layered silicate nanocomposites prepared by the polymerization-filling technique: synthesis and mechanical properties. *Polymer*, **43**, 2123–2132.
- 64 Osman, M.A., Rupp, J.E.P. and Suter, U.W. (2005) Effect of non-ionic surfactants on the exfoliation and properties of polyethylene-layered silicate nanocomposites. *Polymer*, **46**, 8202–8209.
- 65 Vaia, R.A. and Giannelis, E.P. (1997) Lattice model of polymer melt intercalation in organically-modified layered silicates. *Macromolecules*, **30**, 7990–7999.
- 66 Vaia, R.A. and Giannelis, E.P. (1997) Polymer melt intercalation in organically-modified layered silicates: model predictions and experiment. *Macromolecules*, **30**, 8000–8009.
- 67 Rogers, K., Takacs, E. and Thompson, M.R. (2005) Contact angle measurement of select compatibilizers for polymer-silicate layer nanocomposites. *Polym. Test.*, **24**, 423–427.
- 68 Borsacchi, S., Geppi, M., Ricci, L., Ruggeri, G. and Veracini, C.A. (2007) Interactions at the surface of organophilic-modified laponites: a multinuclear solid-state NMR study. *Langmuir*, **23**, 3953–3960.
- 69 Kádár, F., Százdi, L., Fekete, E. and Pukánszky, B. (2006) Surface characteristics of layered silicates: influence on the properties of clay/polymer nanocomposites. *Langmuir*, **22**, 7848–7854.
- 70 Balazs, A.C., Singh, C. and Zhulina, E. (1998) Modeling the interactions between polymers and clay surfaces through self-consistent field theory. *Macromolecules*, **31**, 8370–8381.
- 71 Balazs, A.C., Singh, C., Zhulina, E. and Lyatskaya, Y. (1999) Modelling the phase behaviour of polymer/clay nanocomposites. *Acc. Chem. Res.*, **32**, 651–657.
- 72 Wang, K.H., Choi, M.H., Koo, C.M., Choi, Y.S. and Chung, I.J. (2001) Synthesis and characterization of maleated polyethylene/clay nanocomposites. *Polymer*, **42**, 9819–9826.
- 73 Koo, C.M., Ham, H.T., Kim, S.O., Wang, K.H. and Chung, I.J. (2002) Morphology evolution and anisotropic phase formation of the maleated polyethylene-layered silicate nanocomposites. *Macromolecules*, **35**, 5116–5122.
- 74 Wang, Z.M., Nakajima, H., Manias, E. and Chung, T.C. (2003) Exfoliated PP/Clay nanocomposites using ammonium-terminated PP as the organic modification for montmorillonite. *Macromolecules*, **36**, 8919–8922.
- 75 Chrissopoulou, K., Altintzi, I., Anastasiadis, S.H., Giannelis, E.P., Pitsikalis, M., Hadjichristidis, N. and Theophilou, N. (2005) Controlling the miscibility of polyethylene/layered silicate nanocomposites by altering the polymer/surface interactions. *Polymer*, **46**, 12440–12451.
- 76 Moad, G., Dean, K., Edmond, L., Kukaleva, N., Li, G., Mayadunne, R.T.A., Pfaendner, R., Schneider, A., Simon, G.P. and Wermter, H. (2006) Non-ionic,

- poly(ethylene oxide)-based surfactants as intercalants/dispersants/exfoliants for poly(propylene)-clay nanocomposites. *Macromol. Mater. Eng.*, **291**, 37–52.
- 77** Hasegawa, N., Kawasumi, M., Kato, M., Usuki, A. and Okada, A. (1998) Preparation and mechanical properties of polypropylene-clay hybrids using a maleic anhydride-modified polypropylene oligomer. *J. Appl. Polym. Sci.*, **67**, 87–92.
- 78** Hasegawa, N., Okamoto, H., Kawasumi, M., Kato, M., Tsukigasa, A. and Usuki, A. (2000) Polyolefin–clay hybrids based on modified polyolefins and organoclay. *Macromol. Mater. Eng.*, **280/281**, 76–79.
- 79** Moad, G. (1999) The synthesis of polyolefin graft copolymers by reactive extrusion. *Prog. Polym. Sci.*, **24**, 81–142.
- 80** Passaglia, E., Coiai, S., Aglietto, M., Ruggeri, G., Rubertà, M. and Ciardelli, F. (2003) Functionalization of polyolefins by reactive processing: influence of starting reagents on content and type of grafted groups. *Macromol. Symp.*, **198**, 147–160.
- 81** Ciardelli, F., Aglietto, M., Coltelli, M.B., Passaglia, E., Ruggeri, G. and Coiai, S. (2004) Functionalization of polyolefins in the melt, in *Modification and Blending of Synthetic and Natural Macromolecules* (eds F. Ciardelli and S. Penczek), Kluwer Academic Publishers, The Netherlands.
- 82** Coiai, S., Scatto, M., Bertoldo, M., Conzatti, L., Andreotti, L., Sterner, M., Passaglia, E., Costa, G. and Ciardelli, F. (2009) Study of the compounding process parameters for morphology control of LDPE/layered silicate nanocomposites. *e-polymers*, accepted.
- 83** Passaglia, E., Sulcis, R., Ciardelli, F., Malvaldi, M. and Narducci, P. (2005) Effect of functional groups of modified polyolefins on the structure and properties of their composites with lamellar silicates. *Polym. Int.*, **54**, 1549–1556.
- 84** Passaglia, E., Bertoldo, M., Ciardelli, F., Prevosto, D. and Lucchesi, M. (2008) Evidences of macromolecular chains confinement of ethylene-propylene copolymer in organophilic montmorillonite nanocomposites. *Eur. Polym. J.*, **44**, 1296–1308.
- 85** Passaglia, E., Bertucelli, W. and Ciardelli, F. (2001) Composites from functionalized polyolefins and silica. *Macromol. Symp.*, **176**, 299–315.
- 86** Coiai, S., Passaglia, E., Aglietto, M. and Ciardelli, F. (2004) Control of degradation reactions during radical functionalization of polypropylene in the melt. *Macromolecules*, **37**, 8414–8423.
- 87** Augier, S., Coiai, S., Gagnoli, T., Passaglia, E., Pradel, J.L. and Flat, J.J. (2006) Coagent assisted polypropylene radical functionalization: monomer grafting modulation and molecular weight conservation. *Polymer*, **47**, 5243–5252.
- 88** Augier, S., Coiai, S., Pratelli, D., Conzatti, L. and Passaglia, E. (2009) New functionalized polypropylenes as controlled architecture compatibilizers for polypropylene layered silicates nanocomposites. *J. Nanosci. Nanotechnol.*, **9**, 4858–4869.
- 89** Passaglia, E., Bertoldo, M., Coiai, S., Augier, S., Savi, S. and Ciardelli, F. (2008) Nanostructured polyolefins/clay composites: role of the molecular interaction at the interface. *Polym. Adv. Technol.*, **19**, 560–568.
- 90** Ginzburg, V.V. and Balazs, A.C. (2000) Calculating phase diagrams for nanocomposites: the effect of adding end-functionalized chains to polymer/clay mixtures. *Adv. Mater.*, **23**, 1805–1809.
- 91** Sinsawat, A., Anderson, K.L., Vaia, R.A. and Farmer, B.L. (2003) Influence of polymer matrix composition and architecture on polymer nanocomposite formation: coarse-grained molecular dynamics simulation. *J. Polym. Sci., Part B: Polym. Phys.*, **41**, 3272–3284.
- 92** Marchant, D. and Jayaraman, K. (2002) Strategies for optimizing polypropylene-clay nanocomposite structure. *Ind. Eng. Chem. Res.*, **41**, 6402–6408.
- 93** Yang, K. and Ozisik, R. (2006) Effects of processing parameters on the preparation of nylon 6 nanocomposites. *Polymer*, **47**, 2849–2855.
- 94** Perrin-Sarazin, F., Ton-That, M.T., Bureau, M.N. and Denault, J. (2005) Micro- and nano-structure in



- polypropylene/clay nanocomposites. *Polymer*, **45**, 11624–11634.
- 95 Cho, J.W. and Paul, D.R. (2001) Nylon 6 nanocomposites by melt compounding. *Polymer*, **42**, 1083–1094.
- 96 Dennis, H.R., Hunter, D.L., Chang, D., Kim, S., White, J.L., Cho, J.W. and Paul, D.R. (2001) Effect of melt processing conditions on the extent of exfoliation in organoclay-based nanocomposites. *Polymer*, **42**, 9513–9522.
- 97 Neilson, L.E. (1967) Models for the permeability of filled polymer systems. *J. Macromol. Sci. Chem.*, **1** (5), 929.
- 98 Kashiwagi, T., Harris, R.H., Zhang, X., Briber, R.M., Cipriano, B.H., Raghavan, S.R., Srinivasa, R., Awad, W.H. and Shields, J.R. (2004) Flame retardant mechanism of polyamide 6–clay nanocomposites. *Polymer*, **45**, 881–891.
- 99 Jang, K.H., Kim, B.C., Hahm, W.G. and Kikutani, T. (2008) High-speed melt spinning of nanoparticle-filled high molecular weight poly(ethylene terephthalate). *Int. Polym. Process.*, **23** (4), 370–6.
- 100 Chang, J.-H. and Mun, M.K. (2007) Nanocomposite fibers of poly(ethylene terephthalate) with montmorillonite and mica: thermomechanical properties and morphology. *Polym. Int.*, **56**, 57–66.
- 101 Lange, J. and Wyser, Y. (2003) Recent innovations in barrier technologies for plastic packaging—a review. *Packaging Tech. Sci.*, **16** (4), 149–158.
- 102 Tzavalas, S., Drakonakis, V., Mouzakis, D.E., Fischer, D. and Gregoriou, V.G. (2006) Effect of carboxy-functionalized multiwall nanotubes (MWNT-COOH) on the crystallization and chain conformations of poly(ethylene terephthalate) PET in PET-MWNT nanocomposites. *Macromolecules*, **39**, 9150–9156.
- 103 Awaja, F. and Pavel, D. (2005) Recycling of PET. *Eur. Polym. J.*, **41**, 1453–1477.
- 104 Coltelli, M.B., Bianchi, S., Savi, S., Liuzzo, V. and Aglietto, M. (2003) Metal catalysis to improve compatibility at PO/PET blends interface. *Macromol. Symp.*, **204** (1), 227–236.
- 105 Aglietto, M., Coltelli, M.B., Savi, S., Lochiatto, F., Ciardelli, F. and Gianni, M. (2004) Post-consumer polyethylene terephthalate (PET)/ polyolefin blends through reactive processing. *J. Mater. Cycles Waste Manage.*, **6**, 13–19.
- 106 Coltelli, M.B., Savi, S., Della Maggiore, I., Liuzzo, V., Aglietto, M. and Ciardelli, F. (2004) A model study of  $Ti(OBu)_4$  catalyzed reactions during reactive blending of polyethylene (PE) and poly(ethylene terephthalate). *Macromol. Mater. Eng.*, **289**, 400–412.
- 107 Pracella, M., Pazzagli, F. and Galeski, A. (2002) Reactive compatibilization and properties of recycled poly(ethylene terephthalate)/polyethylene blends. *Polym. Bull.*, **48** (1), 67–74.
- 108 Coltelli, M.B., Della Maggiore, I., Savi, S., Aglietto, M. and Ciardelli, F. (2005) Modified styrene-*b*-ethylene-co-1-butene-*b*-styrene triblock copolymer as compatibiliser precursor in polyethylene/poly(ethylene terephthalate) blends. *Polym. Degrad. Stab.*, **90** (2), 211–223. Erratum (2006) *Polym. Degrad. Stab.*, **91**, 987–223.
- 109 Coltelli, M.-B. and Bianchi, S. (2007) Mauro aglietto, poly(ethyleneterephthalate) (PET) degradation during the Zn catalysed transesterification with dibutyl maleate functionalized polyolefins. *Polymer*, **48**, 1276–1286.
- 110 Coltelli, M.-B., Aglietto, M. and Ciardelli, F. (2008) Influence of the transesterification catalyst structure on the reactive compatibilization and properties of poly(ethylene terephthalate) (PET)/dibutyl succinate functionalized poly(ethylene) blends. *Eur. Polym. J.*, **44**, 1512–1524.
- 111 Coltelli, M.-B., Harrats, C., Aglietto, M. and Groeninckx, G. (2008) Phase morphology development in poly(ethylene terephthalate) (PET)/ low density poly(ethylene) (LDPE) blends: compatibilizer precursors effect. *Polym. Eng. Sci.*, **48**, 1424–1433.
- 112 Pegoretti, A. and Penati, A. (2004) Recycled poly(ethylene terephthalate) and its short glass fibres composites: effects of hygrothermal aging on the thermo-mechanical behavior. *Polymer*, **45**, 7995–8004.
- 113 Hwang, S.Y., Lee, W.D., Lim, J.S., Park, K.H. and Im, S.S. (2008) Dispersibility



- of clay and crystallization kinetics for in situ polymerized PET/pristine and modified montmorillonite nanocomposites. *J. Polym. Sci., Part B: Polym. Phys.*, **46**, 1022–1035.
- 114** Tomita, K. (1973) Studies on the formation of poly(ethylene terephthalate): 2. Rate of transesterification of dimethyl terephthalate with ethylene glycol. *Polymer*, **14**, 55–60.
- 115** Karayannidis, G.P., Roupakias, C.P., Bikiaris, D.N. and Achilias, D.S. (2003) Study of various catalysts in the synthesis of poly(propylene terephthalate) and mathematical modeling of the esterification reaction. *Polymer*, **44**, 931–942.
- 116** Ke, Y.C., Long, C.F. and Qi, Z.N. (1999) Crystallization, properties, and crystal and nanoscale morphology of PET–clay nanocomposites. *J. Appl. Polym. Sci.*, **71**, 1139–1146.
- 117** Ke, Y.C. and Qi, Z.N. (1997) Chinese Patent Application 97104294.6.
- 118** Lee, S.-S., Ma, Y.T., Rhee, H.-W. and Kim, J. (2005) Exfoliation of layered silicate facilitated by ring-opening reaction of cyclic oligomers in PET–clay nanocomposites. *Polymer*, **46**, 2201–2210.
- 119** Hubbard, P., Brittain, W.J., Mattice, W.L. and Brunelle, D.J. (1998) Ring-size distribution in the depolymerization of poly(butylene terephthalate). *Macromolecules*, **31**, 1518–1522.
- 120** Chung, J.W., Son, S.-B., Chun, S.-W., Kang, T.J. and Kwak, S.-Y. (2008) Nonisothermal crystallization behavior of exfoliated poly(ethylene terephthalate)-layered silicate nanocomposites in the presence and absence of organic modifier. *J. Polym. Sci., Part B: Polym. Phys.*, **46**, 989–999.
- 121** Pegoretti, A., Kolarik, J., Peroni, C. and Migliaresi, C. (2004) Recycled poly(ethylene terephthalate)/layered silicate nanocomposites: morphology and tensile mechanical properties. *Polymer*, **45**, 2751–2759.
- 122** Calcagno, C.I.W., Mariani, C.M., Teixeira, S.R. and Mauler, R.S. (2007) The effect of organic modifier of the clay on morphology and crystallization properties of PET nanocomposites. *Polymer*, **48**, 966–974.
- 123** Krácalík, M., Mikešová, J., Puffr, R., Baldrian, J., Thomann, R. and Friedrich, C. (2007) Effect of 3D structure on recycled PET/organoclay nanocomposites. *Polym. Bull.*, **58**, 313–319.
- 124** Kim, K.H., Kim, K.H., Huh, J. and Jo, W.H. (2007) Synthesis of thermally stable organosilicate for exfoliated poly(ethylene terephthalate) nanocomposite with superior tensile properties. *Macromol. Res.*, **15** (2), 178–184.
- 125** Davis, C.H., Mathias, L.J., Gilman, J.W., Schiraldi, D.A., Shields, J.R., Trulove, P., Sutto, T.E. and Delong, H.C. (2002) Effects of melt-processing conditions on the quality of poly(ethylene terephthalate) montmorillonite clay nanocomposites. *J. Polym. Sci., Part B: Polym. Phys.*, **40**, 2661–2666.
- 126** Stoeffler, K., Lafleur, P.G. and Denault, J. (2008) Thermal decomposition of various alkyl onium organoclays: effect on polyethylene terephthalate nanocomposites' properties. *Polym. Degrad. Stab.*, **93**, 1332–1350.
- 127** Vidotti, S.E., Chinellato, A.C., Hu, G.-H. and Pessan L.A. (2007) Preparation of poly(ethylene terephthalate)/organoclay nanocomposites using a polyester ionomer as a compatibilizer. *J. Polym. Sci., Part B: Polym. Phys.*, **45**, 3084–3091.
- 128** Tsutsumi, N., Kono, Y., Oya, M., Sakai, W. and Nagata, M. (2008) Recent development of biodegradable network polyesters obtained from renewable natural resources. *Clean Soil, Air, Water*, **36** (8), 682–86.
- 129** Signori, F., Coltelli, M.B., Bronco, S. and Ciardelli, F. (2009) Thermal degradation of poly(lactic acid) (PLA) and poly(butylene adipate-co-terephthalate) (PBAT) as a consequence of melt processing: effects on pure materials and their blends. *Polym. Degrad. Stab.*, **94**, 74–82.
- 130** Coltelli, M.B., Della Maggiore, I., Bertoldo, M., Bronco, S., Signori, F. and Ciardelli, F. (2008) Poly(lactic acid) (PLA) properties as a consequence of poly(butylene adipate-co-terephthalate)

- (PBAT) blending and acetyl tributyl citrate (ATBC) plasticization. *J. Appl. Polym. Sci.*, **110**, 1250–1262.
- 131** Sinha Ray, S. and Bousmina, M. (2005) Biodegradable polymers and their layered silicate nanocomposites: in greening the 21st century materials world. *Prog. Mater. Sci.*, **50**, 962–1079.
- 132** Lecomte, P., Riva, R., Jerome, C. and Jerome, R. (2008) Macromolecular engineering of biodegradable polyesters by ring opening polymerization and 'click' chemistry. *Macromol. Rapid Commun.*, **29** (12-13), 982–997.
- 133** Kamber, N.E., Jeong, W., Waymouth, R.M., Pratt, R.C., Lohmeijer, B.G.G. and Hedrick, J.L. (2007) Organocatalytic ring-opening polymerization. *Chem. Rev.*, **107** (12), 5813–5840.
- 134** Albertsson, A.C. and Varma, I.K. (2003) Recent developments in ring opening polymerization of lactones for biomedical applications. *Biomacromolecules*, **4**, 1466–1486.
- 135** Kubies, D., Pantoustier, N., Dubois, P., Rulmont, A. and Jerome, R. (2002) Controlled ring-opening polymerization of  $\epsilon$ -caprolactone in the presence of layered silicates and formation of nanocomposites. *Macromolecules*, **35**, 3318–3320.
- 136** Lepoittevin, B., Pantoustier, N., Alexandre, M., Calberg, C., Jerome, R. and Dubois, P. (2002) Polyester layered silicate nanohybrids by controlled grafting polymerization. *J. Mater. Chem.*, **12**, 3528–3532.
- 137** Lepoittevin, B., Pantoustier, N., Devalckenaere, M., Alexandre, M., Kubies, D., Calberg, C., Jerome, R. and Dubois, P. (2002) Poly( $\epsilon$ -caprolactone)/clay nanocomposites by in-situ intercalative polymerization catalyzed by dibutyltin dimethoxide. *Macromolecules*, **35**, 8385–8390.
- 138** Chrissafis, K., Antoniadis, G., Paraskevopoulos, K.M., Vassiliou, A. and Bikiaris, D.N. (2007) Comparative study of the effect of different nanoparticles on the mechanical properties and thermal degradation mechanism of in situ prepared poly( $\epsilon$ -caprolactone) nanocomposites. *Compos. Sci. Technol.*, **67**, 2165–2174.
- 139** Paul, M.-A., Alexandre, M., Degee, P., Calberg, C., Jerome, R. and Dubois, P. (2003) Exfoliated polylactide/ clay nanocomposites by in-situ coordination-insertion polymerization. *Macromol. Rapid Commun.*, **24** (9), 561–566.
- 140** Lee, S., Kim, C.H. and Park, J.-K. (2006) Improvement of processability of clay / polylactide nanocomposites by a combinational method: in situ polymerization of L-lactide and melt compounding of polylactide. *J. Appl. Polym. Sci.*, **101** (3), 1664–1669.
- 141** Ogata, N., Jimenez, G., Kawai, H. and Ogihara, T. (1997) Structure and thermal/mechanical properties of poly(L-lactide)-clay blend. *J. Polym. Sci., Part B: Polym. Phys.*, **35**, 389–396.
- 142** Marras, S.I., Tsimpliaraki, A., Zuburtikudis, I. and Panayiotou, C. (2007) Surfactant-induced morphology and thermal behavior of polymer layered silicate nanocomposites. *J. Phys.: Conf. Ser.*, **61**, 1366–1370.
- 143** Krikorian, V. and Pochan, D.J. (2003) Poly (L-lactic acid)/layered silicate nanocomposite: fabrication, characterization, and properties. *Chem. Mater.*, **15**, 4317–4324.
- 144** Chang, J.-H., Uk-An, Y. and Sur, G.S. (2003) Poly(lactic acid) nanocomposites with various organoclays. I. thermomechanical properties, morphology, and gas permeability. *J. Polym. Sci., Part B: Polym. Phys.*, **41**, 94–103.
- 145** Di, Y., Iannace, S., Di Maio, E. and Nicolais, L. (2005) Poly(lactic acid)/ organoclay nanocomposites: thermal, rheological properties and foam processing. *J. Polym. Sci., Part B: Polym. Phys.*, **43**, 689–698.
- 146** Feijoo, J.L., Cabedo, L., Gimenez, E., Lagaron, J.M. and Saura, J.J. (2005) Development of amorphous PLA-montmorillonite nanocomposites. *J. Mater. Sci.*, **40**, 1785–1788.
- 147** Pluta, M. (2006) Melt compounding of polylactide/organoclay: structure and properties of nanocomposites. *J. Polym. Sci., Part B: Polym. Phys.*, **44**, 3392–3405.
- 148** Gu, S.-Y., Ren, J. and Dong, B. (2007) Melt rheology of polylactide/ montmorillonite nanocomposites.

- J. Polym. Sci., Part B: Polym. Phys.*, **45**, 3189–3196.
- 149** Lewitus, D., McCarthy, S., Ophir, A. and Kenig, S. (2006) The effect of nanoclays on the properties of PLLA-modified polymers Part 1: mechanical and thermal properties. *J. Polym. Environ.*, **14**, 171–177.
- 150** Pluta, M., Jeszka, J.K. and Boiteux, G. (2007) Polylactide/montmorillonite nanocomposites: structure, dielectric, viscoelastic and thermal properties. *Eur. Polym. J.*, **43**, 2819–2835.
- 151** Sinha Ray, S., Maiti, P., Okamoto, M., Yamada, K. and Ueda, K. (2002) New polylactide/layered silicate nanocomposites. 1. Preparation, characterization, and properties. *Macromolecules*, **35**, 3104–3110.
- 152** Kubies, D., Scudla, J., Puffr, R., Sikora, A., Baldrian, J., Kovarova, J., Slouf, M. and Rypacek, F. (2006) Structure and mechanical properties of poly(L-lactide)/layered silicate nanocomposites. *Eur. Polym. J.*, **42**, 888–899.
- 153** Yu, Z., Yin, J., Yan, S., Xie, Y., Ma, J. and Chen, X. (2007) Biodegradable poly(L-lactide)/poly( $\epsilon$ -caprolactone)-modified montmorillonite nanocomposites: preparation and characterization. *Polymer*, **48**, 6439–6447.
- 154** Dell’Erba, R., Groeninckx, G., Maglio, G., Malinconico, M. and Migliozi, A. (2001) Immiscible polymer blends of semicrystalline biocompatible components. Thermal properties and phase morphology analysis of PLLA/PCL blends. *Polymer*, **42**, 7831–7840.
- 155** Piorowska, E., Kulinski, Z., Galeski, A. and Masirek, R. (2006) Plasticization of semicrystalline poly(L-lactide) with poly(propylene glycol). *Polymer*, **47**, 7178–7188.
- 156** Ljungberg, N., Colombini, D. and Wesslen, B. (2005) Plasticization of poly(Lactic acid) with oligomeric malonate esteramides: dynamic mechanical and thermal film properties. *J. Appl. Polym. Sci.*, **96**, 992–1002.
- 157** Paul, M.-A., Alexandre, M., Degeeé, P., Henrist, C., Rulmont, A. and Dubois, P. (2003) New nanocomposite materials based on plasticized poly(L-lactide) and organo-modified montmorillonites: thermal and morphological study. *Polymer*, **44**, 443–450.
- 158** Vaia, R.A., Vasudevan, S., Krawiec, W., Scanlon, L.G. and Giannelis, E.P. (1995) New polymer electrolyte nanocomposites. Melt intercalation of poly(ethylene oxide) in mica-type silicates. *Adv. Mater.*, **7**, 154–156.
- 159** Pluta, M., Paul, M.-A., Alexandre, M. and Dubois, P. (2006) Plasticized polylactide/clay nanocomposites. I. The role of filler content and its surface organo-modification on the physico-chemical properties. *J. Polym. Sci., Part B: Polym. Phys.*, **44**, 299–311.
- 160** Thellen, C., Orroth, C., Froio, D., Ziegler, D., Lucciarini, J., Farrell, R., D’Souza, N.A. and Ratto, J.A. (2005) Influence of montmorillonite layered silicate on plasticized poly(L-lactide) blown films. *Polymer*, **46**, 11716–11727.
- 161** Mainil, M., Alexandre, M., Monteverde, F. and Dubois, P. (2006) Polyethylene organo-clay nanocomposites: the role of the interface chemistry on the extent of clay intercalation/exfoliation. *J. Nanosci. Nanotechnol.*, **6**, 337–344.
- 162** Lertwimolnun, W. and Vergnes, B. (2005) Influence of compatibilizer and processing conditions on the dispersion of nanoclay in a polypropylene matrix. *Polymer*, **46**, 3462–3471.
- 163** Lertwimolnun, W. and Vergnes, B. (2006) Effect of processing conditions on the formation of polypropylene/organoclay nanocomposites in a twin screw extruder. *Polym. Eng. Sci.*, **46**, 314–323.
- 164** Qi, Z.N., Ke, Y.C. and Zhou, Y.Z. (1997) Chinese Patent Application 97104055.9.

# Advanced Nanomaterials

*Edited by*

*Kurt E. Geckeler and Hiroyuki Nishide*

*Volume 2*



WILEY-  
VCH

WILEY-VCH Verlag GmbH & Co. KGaA



**Advanced Nanomaterials**

*Edited by  
Kurt E. Geckeler and  
Hiroyuki Nishide*

## ***Further Reading***

Tjong, Sie Chin

### **Carbon Nanotube Reinforced Composites**

**Metal and Ceramic Matrices**

2009

ISBN: 978-3-527-40892-4

Zehetbauer, M. J., Zhu, Y. T. (eds.)

### **Bulk Nanostructured Materials**

2009

ISBN: 978-3-527-31524-6

Vollath, D.

### **Nanomaterials**

**An Introduction to Synthesis, Properties and Applications**

2008

ISBN: 978-3-527-31531-4

Astruc, D. (ed.)

### **Nanoparticles and Catalysis**

2008

ISBN: 978-3-527-31572-7

Lee, Yoon S.

### **Self-Assembly and Nanotechnology**

**A Force Balance Approach**

2008

ISBN: 978-0-470-24883-6

Eftekhari, Ali (Ed.)

### **Nanostructured Materials in Electrochemistry**

2008

ISBN: 978-3-527-31876-6

Lazzari, M. / Liu, G. / Lecommandoux, S. (eds.)

### **Block Copolymers in Nanoscience**

2006

ISBN: 978-3-527-31309-9

Kumar, Challa S. S. R. (Ed.)

### **Nanomaterials for the Life Sciences**

**10 Volume Set**

2010

ISBN: 978-3-527-32261-9

Kumar, Challa S. S. R. (Ed.)

### **Nanotechnologies for the Life Sciences**

**10 Volume Set**

2007

ISBN: 978-3-527-31301-3

Rao, C. N. R., Müller, A., Cheetham, A. K. (eds.)

### **Nanomaterials Chemistry**

**Recent Developments and New Directions**

2007

ISBN: 978-3-527-31664-9

# Advanced Nanomaterials

*Edited by*

*Kurt E. Geckeler and Hiroyuki Nishide*

*Volume 2*



WILEY-  
VCH

WILEY-VCH Verlag GmbH & Co. KGaA



## The Editors

### **Prof. Dr. Kurt E. Geckeler**

Department of Nanobio Materials and  
Electronics

World-Class University (WCU)

**and**

Department of Materials Science and  
Engineering

Gwangju Institute of Science and

Technology (GIST)

1 Oryong-dong, Buk-gu

Gwangju 500-712

South Korea

E-mail: keg@gist.ac.kr

### **Prof. Hiroyuki Nishide**

Department of Applied Chemistry

Waseda University

Ohkubo 3, Shinjuku

Tokyo 169-8555

Japan

E-mail: nishide@waseda.jp

**and**

Department of Nanobio Materials and  
Electronics

World-Class University (WCU)

Gwangju Institute of Science and

Technology (GIST)

1 Oryong-dong, Buk-gu

Gwangju 500-712

South Korea

■ All books published by Wiley-VCH are carefully produced. Nevertheless, authors, editors, and publisher do not warrant the information contained in these books, including this book, to be free of errors. Readers are advised to keep in mind that statements, data, illustrations, procedural details or other items may inadvertently be inaccurate.

**Library of Congress Card No.:** applied for

### **British Library Cataloguing-in-Publication Data**

A catalogue record for this book is available from the British Library.

### **Bibliographic information published by the Deutsche Nationalbibliothek**

The Deutsche Nationalbibliothek lists this publication in the Deutsche Nationalbibliografie; detailed bibliographic data are available on the Internet at <<http://dnb.d-nb.de>>.

© 2010 WILEY-VCH Verlag GmbH & Co. KGaA, Weinheim

All rights reserved (including those of translation into other languages). No part of this book may be reproduced in any form – by photoprinting, microfilm, or any other means – nor transmitted or translated into a machine language without written permission from the publishers. Registered names, trademarks, etc. used in this book, even when not specifically marked as such, are not to be considered unprotected by law.

**Composition** Toppan Best-set Premedia Limited

**Printing and Bookbinding** Strauss GmbH,  
Mörlenbach

**Cover Design** Schulz Grafik-Design, Fußgönheim

Printed in the Federal Republic of Germany

Printed on acid-free paper

**ISBN:** 978-3-527-31794-3

## Contents

<b>Preface</b>	<i>XV</i>
<b>List of Contributors</b>	<i>XVII</i>

### Volume 2

<b>14</b>	<b>Amphiphilic Poly(Oxyalkylene)-Amines Interacting with Layered Clays: Intercalation, Exfoliation, and New Applications</b>	<i>459</i>
	<i>Jiang-Jen Lin, Ying-Nan Chan, and Wen-Hsin Chang</i>	
14.1	Introduction	<i>459</i>
14.2	Chemical Structures of Clays and Organic-Salt Modifications	<i>460</i>
14.2.1	Natural Clays and Synthetic Layered-Double-Hydroxide (LDH)	<i>460</i>
14.2.2	Low-Molecular-Weight Intercalating Agents and X-Ray Diffraction <i>d</i> -Spacing	<i>461</i>
14.3	Poly(Oxyalkylene)-Polyamine Salts as Intercalating Agents, and Their Reaction Profiles	<i>462</i>
14.3.1	Poly(Oxyalkylene)-Polyamine Salts as Intercalating Agents	<i>462</i>
14.3.2	Critical Conformational Change in Confinement During the Intercalating Profile	<i>464</i>
14.3.3	Correlation between MMT <i>d</i> -Spacing and Intercalated Organics	<i>466</i>
14.4	Amphiphilic Copolymers as Intercalating Agents	<i>466</i>
14.4.1	Various Structures of the Amphiphilic Copolymers	<i>466</i>
14.4.2	Colloidal Properties	<i>469</i>
14.5	New Intercalation Mechanism Other than the Ionic-Exchange Reaction	<i>469</i>
14.5.1	Amidoacid and Carboxylic Acid Chelating	<i>469</i>
14.5.2	Intercalation Involving Intermolecular Hydrogen Bonding	<i>470</i>
14.6	Self-Assembling Properties of Organoclays	<i>471</i>
14.7	Exfoliation Mechanism and the Isolation of Random Silicate Platelets	<i>472</i>
14.7.1	Thermodynamically Favored Exfoliation of Na <sup>+</sup> -MMT by the PP-POP Copolymers	<i>472</i>
14.7.2	Zigzag Mechanism for Exfoliating Na <sup>+</sup> -MMT	<i>473</i>
14.8	Isolation of the Randomized Silicate Platelets in Water	<i>473</i>

14.9	Emerging Applications in Biomedical Research	475
14.10	Conclusions	477
	References	478
<b>15</b>	<b>Mesoporous Alumina: Synthesis, Characterization, and Catalysis</b>	<b>481</b>
	<i>Tsunetake Seki and Makoto Onaka</i>	
15.1	Introduction	481
15.2	Synthesis of Mesoporous Alumina	482
15.2.1	Experimental Techniques	482
15.2.1.1	Synthesis	482
15.2.1.2	Characterization	484
15.2.2	Examples of Synthesis	485
15.2.2.1	Neutral Surfactant Templating	486
15.2.2.2	Anionic Surfactant Templating	492
15.2.2.3	Cationic Surfactant Templating	495
15.2.2.4	Nonsurfactant Templating	498
15.3	Mesoporous Alumina in Heterogeneous Catalysis	500
15.3.1	Base-Catalyzed Reactions	508
15.3.2	Epoxidation	509
15.3.3	Hydrodechlorination	510
15.3.4	Hydrodesulfurization	512
15.3.5	Olefin Metathesis	513
15.3.6	Oxidative Dehydrogenation	517
15.3.7	Oxidative Methanol Steam Reforming	518
15.4	Conclusions and Outlook	519
	References	519
<b>16</b>	<b>Nanoceramics for Medical Applications</b>	<b>523</b>
	<i>Besim Ben-Nissan and Andy H. Choi</i>	
16.1	Introduction	523
16.2	Tissue Engineering and Regeneration	527
16.2.1	Scaffolds	527
16.2.2	Liposomes	531
16.3	Nanohydroxyapatite Powders for Medical Applications	532
16.4	Nanocoatings and Surface Modifications	535
16.4.1	Calcium Phosphate Coatings	535
16.4.2	Sol–Gel Nanohydroxyapatite and Nanocoated Coralline Apatite	538
16.4.3	Surface Modifications	540
16.5	Simulated Body Fluids	541
16.6	Nano- and Macroboceramics for Drug Delivery and Radiotherapy	546
16.6.1	Nanobioceramics for Drug Delivery	546
16.6.2	Microbioceramics for Drug Delivery	548
16.6.3	Microbioceramics for Radiotherapy	549
16.7	Nanotoxicology and Nanodiagnostics	551
	References	552

<b>17</b>	<b>Self-healing of Surface Cracks in Structural Ceramics</b>	<b>555</b>
	<i>Wataru Nakao, Koji Takahashi, and Kotoji Ando</i>	
17.1	Introduction	555
17.2	Fracture Manner of Ceramics	555
17.3	History	557
17.4	Mechanism	559
17.5	Composition and Structure	562
17.5.1	Composition	562
17.5.2	SiC Figuration	563
17.5.3	Matrix	566
17.6	Valid Conditions	567
17.6.1	Atmosphere	567
17.6.2	Temperature	568
17.6.3	Stress	571
17.7	Crack-healing Effect	573
17.7.1	Crack-healing Effects on Fracture Probability	573
17.7.2	Fatigue Strength	575
17.7.3	Crack-healing Effects on Machining Efficiency	577
17.8	New Structural Integrity Method	579
17.8.1	Outline	579
17.8.2	Theory	580
17.8.3	Temperature Dependence of the Minimum Fracture Stress Guaranteed	582
17.9	Advanced Self-crack Healing Ceramics	585
17.9.1	Multicomposite	585
17.9.2	SiC Nanoparticle Composites	587
17.10	Availability to Structural Components of the High Temperature Gas Turbine	588
	References	590
<b>18</b>	<b>Ecological Toxicology of Engineered Carbon Nanoparticles</b>	<b>595</b>
	<i>Aaron P. Roberts and Ryan R. Otter</i>	
18.1	Introduction	595
18.2	Fate and Exposure	596
18.2.1	General	596
18.2.2	Stability in Aquatic Systems	596
18.2.3	Bioavailability and Uptake	598
18.2.4	Tissue Distribution	600
18.2.5	Food Web	600
18.2.6	Effects on the Uptake of Other Contaminants	602
18.3	Effects	602
18.3.1	General	602
18.3.2	Oxidative Stress and Nanoparticles	602
18.3.3	Effects on Specific Tissues	606
18.3.3.1	Brain	606
18.3.3.2	Gills	607

- 18.3.3.3 Liver 607
- 18.3.3.4 Gut 608
- 18.3.4 Developmental Effects 608
- 18.4 Summary 609
- References 610

## **19 Carbon Nanotubes as Adsorbents for the Removal of Surface Water Contaminants 615**

*Jose E. Herrera and Jing Cheng*

- 19.1 Introduction 615
- 19.2 Structure and Synthesis of Carbon Nanotubes 616
- 19.3 Properties of Carbon Nanotubes 620
  - 19.3.1 Mechanical, Thermal, Electrical, and Optical Properties of Carbon Nanotubes 620
  - 19.3.2 Adsorption-Related Properties of Carbon Nanotubes 620
- 19.4 Carbon Nanotubes as Adsorbents 622
  - 19.4.1 Adsorption of Heavy Metal Ions 624
    - 19.4.1.1 Adsorption of Lead (II) 624
    - 19.4.1.2 Adsorption of Chromium (VI) 626
    - 19.4.1.3 Adsorption of Cadmium (II) 628
    - 19.4.1.4 Adsorption of Copper (II) 629
    - 19.4.1.5 Adsorption of Zinc (II) 630
    - 19.4.1.6 Adsorption of Nickel (II) 632
    - 19.4.1.7 Competitive Adsorption of Heavy Metals Ions 633
  - 19.4.2 Adsorption of Other Inorganic Elements 634
    - 19.4.2.1 Adsorption of Fluoride 635
    - 19.4.2.2 Adsorption of Arsenic 637
    - 19.4.2.3 Adsorption of Americium-243 (III) 638
  - 19.4.3 Adsorption of Organic Compounds 639
    - 19.4.3.1 Adsorption of Dioxins 639
    - 19.4.3.2 Adsorption of 1,2-Dichlorobenzene 640
    - 19.4.3.3 Adsorption of Trihalomethanes 642
    - 19.4.3.4 Adsorption of Polyaromatic Compounds 643
- 19.5 Summary of the Results, and Conclusions 644
- References 647

## **20 Molecular Imprinting with Nanomaterials 651**

*Kevin Flavin and Marina Resmini*

- 20.1 Introduction 651
  - 20.1.1 Molecular Imprinting: The Concept 651
    - 20.1.1.1 History of Molecular Imprinting 653
    - 20.1.1.2 Covalent Imprinting 654
    - 20.1.1.3 Noncovalent Imprinting 654
    - 20.1.1.4 Alternative Molecular Imprinting Approaches 656
  - 20.1.2 Towards Imprinting with Nanomaterials 656

20.2	Molecular Imprinting in Nanoparticles	657
20.2.1	Emulsion Polymerization	657
20.2.1.1	Core–Shell Emulsion Polymerization	657
20.2.1.2	Mini-Emulsion Polymerization	660
20.2.2	Precipitation Polymerization	661
20.2.2.1	Applications and Variations	662
20.2.2.2	Microgel/Nanogel Polymerization	664
20.2.3	Silica Nanoparticles	665
20.2.4	Molecularly Imprinted Nanoparticles: Miscellaneous	667
20.3	Molecular Imprinting with Diverse Nanomaterials	668
20.3.1	Nanowires, Nanotubes, and Nanofibers	668
20.3.2	Quantum Dots	669
20.3.3	Fullerene	670
20.3.4	Dendrimers	671
20.4	Conclusions and Future Prospects	672
	References	673
<b>21</b>	<b>Near-Field Raman Imaging of Nanostructures and Devices</b>	<b>677</b>
	<i>Ze Xiang Shen, Johnson Kasim, and Ting Yu</i>	
21.1	Introduction	677
21.2	Near-Field Raman Imaging Techniques	678
21.3	Visualization of Si–C Covalent Bonding of Single Carbon Nanotubes Grown on Silicon Substrate	682
21.4	Near-Field Scanning Raman Microscopy Using TERS	686
21.5	Near-Field Raman Imaging Using Optically Trapped Dielectric Microsphere	688
21.6	Conclusions	695
	References	695
<b>22</b>	<b>Fullerene-Rich Nanostructures</b>	<b>699</b>
	<i>Fernando Langa and Jean-François Nierengarten</i>	
22.1	Introduction	699
22.2	Fullerene-Rich Dendritic Branches	700
22.3	Photoelectrochemical Properties of Fullerodendrons and Their Nanoclusters	704
22.4	Fullerene-Rich Dendrimers	708
22.5	Conclusions	712
	Acknowledgments	712
	References	713
<b>23</b>	<b>Interactions of Carbon Nanotubes with Biomolecules: Advances and Challenges</b>	<b>715</b>
	<i>Dhriti Nepal and Kurt E. Geckeler</i>	
23.1	Introduction	715
23.2	Structure and Properties	715

- 23.3 Debundalization 716
- 23.4 Noncovalent Functionalization 718
- 23.5 Dispersion of Carbon Nanotubes in Biopolymers 719
- 23.6 Interaction of DNA with Carbon Nanotubes 720
- 23.7 Interaction of Proteins with Carbon Nanotubes 723
- 23.8 Technology Development Based on Biopolymer-Carbon Nanotube Products 729
  - 23.8.1 Diameter- or Chirality-Based Separation of Carbon Nanotubes 734
  - 23.8.2 Fibers 736
  - 23.8.3 Sensors 737
  - 23.8.4 Therapeutic Agents 738
- 23.9 Conclusions 738
  - Acknowledgments 738
  - References 739
  
- 24 Nanoparticle-Cored Dendrimers and Hyperbranched Polymers: Synthesis, Properties, and Applications 743**  
*Young-Seok Shon*
  - 24.1 Introduction 743
  - 24.2 Synthesis of Nanoparticle-Cored Dendrimers via the Direct Method, and their Properties and Application 745
  - 24.3 Synthesis of Nanoparticle-Cored Dendrimers by Ligand Exchange Reaction, and their Properties and Applications 753
  - 24.4 Synthesis of Nanoparticle-Cored Dendrimers by Dendritic Functionalization, and their Properties and Applications 758
    - 24.4.1 Nanoparticle-Cored Dendrimers by the Convergent Approach 759
    - 24.4.2 Nanoparticle-Cored Dendrimers by the Divergent Approach 761
  - 24.5 Synthesis of Nanoparticle-Cored Hyperbranched Polymers by Grafting on Nanoparticles 763
  - 24.6 Conclusions and Outlook 764
    - Acknowledgment 764
    - References 765
  
- 25 Concepts in Self-Assembly 767**  
*Jeremy J. Ramsden*
  - 25.1 Introduction 767
  - 25.2 Theoretical Approaches to Self-Organization 770
    - 25.2.1 Thermodynamics of Self-Organization 770
    - 25.2.2 The “Goodness” of the Organization 772
    - 25.2.3 Programmable Self-Assembly 773
  - 25.3 Examples of Self-Assembly 774
    - 25.3.1 The Addition of Particles to the Solid/Liquid Interface 774
      - 25.3.1.1 Numerically Simulating RSA 776

25.3.2	Self-Assembled Monolayers (SAMs)	776
25.3.3	Quantum Dots (QDs)	778
25.3.4	Crystallization and Supramolecular Chemistry	779
25.3.5	Biological Examples	780
25.3.6	DNA	781
25.3.7	RNA and Proteins	781
25.4	Self-Assembly as a Manufacturing Process	783
25.5	Useful Ideas	784
25.5.1	Weak Competing Interactions	784
25.5.2	Percolation	784
25.5.3	Cooperativity	785
25.5.4	Water Structure	786
25.6	Conclusions and Challenges	787
	References	787

## **26 Nanostructured Organogels via Molecular Self-Assembly** 791

*Arjun S. Krishnan, Kristen E. Roskov, and Richard J. Spontak*

26.1	Introduction	791
26.2	Block Copolymer Gels	793
26.2.1	Concentration Effects	793
26.2.2	Temperature Effects	801
26.2.3	Microdomain Alignment	804
26.2.4	Tensile Deformation	806
26.2.5	Network Modifiers	808
26.2.5.1	Inorganic Nanofillers	808
26.2.5.2	Polymeric Modifiers	810
26.2.6	Nonequilibrium Mesogels	812
26.2.7	Special Cases	814
26.2.7.1	Liquid Crystals	814
26.2.7.2	Ionic Liquids	815
26.2.7.3	Multiblock Copolymers	815
26.2.7.4	Cosolvent Systems	816
26.3	Organic Gelator Networks	816
26.3.1	Hydrogen Bonding	818
26.3.1.1	Amides	819
26.3.1.2	Ureas	820
26.3.1.3	Sorbitols	820
26.3.1.4	Miscellaneous LMOG Classes	822
26.3.2	$\pi$ - $\pi$ Stacking	822
26.3.3	London Dispersion Forces	824
26.3.4	Special Considerations	824
26.3.4.1	Biologically Inspired Gelators	824
26.3.4.2	Isothermal Gelation	825



26.3.4.3	Solvent Effects	826
26.4	Conclusions	827
	Acknowledgments	828
	References	828
<b>27</b>	<b>Self-assembly of Linear Polypeptide-based Block Copolymers</b>	<b>835</b>
	<i>Sébastien Lecommandoux, Harm-Anton Klok, and Helmut Schlaad</i>	
27.1	Introduction	835
27.2	Solution Self-assembly of Polypeptide-based Block Copolymers	837
27.2.1	Aggregation of Polypeptide-based Block Copolymers	837
27.2.1.1	Polypeptide Hybrid Block Copolymers	837
27.2.1.2	Block Copolypeptides	841
27.2.2	Polypeptide-based Hydrogels	842
27.2.3	Organic/Inorganic Hybrid Structures	842
27.3	Solid-state Structures of Polypeptide-based Block Copolymers	844
27.3.1	Diblock Copolymers	844
27.3.1.1	Polydiene-based Diblock Copolymers	844
27.3.1.2	Polystyrene-based Diblock Copolymers	845
27.3.1.3	Polyether-based Diblock Copolymers	850
27.3.1.4	Polyester-based Diblock Copolymers	851
27.3.1.5	Diblock Copolypeptides	851
27.3.2	Triblock Copolymers	852
27.3.2.1	Polydiene-based Triblock Copolymers	852
27.3.2.2	Polystyrene-based Triblock Copolymers	856
27.3.2.3	Polysiloxane-based Triblock Copolymers	857
27.3.2.4	Polyether-based Triblock Copolymers	858
27.3.2.5	Miscellaneous	862
27.4	Summary and Outlook	864
	References	865
<b>28</b>	<b>Structural DNA Nanotechnology: Information-Guided Self-Assembly</b>	<b>869</b>
	<i>Yonggang Ke, Yan Liu, and Hao Yan</i>	
28.1	Introduction	869
28.2	Periodic DNA Nanoarrays	871
28.3	Finite-Sized and Addressable DNA Nanoarrays	872
28.4	DNA Polyhedron Cages	874
28.5	DNA Nanostructure-Directed Nanomaterial Assembly	876
28.6	Concluding Remarks	877
	Acknowledgments	878
	References	878
	<b>Index</b>	<b>881</b>

## Volume 1

- 1 **Phase-Selective Chemistry in Block Copolymer Systems** 1  
*Evan L. Schwartz and Christopher K. Ober*
- 2 **Block Copolymer Nanofibers and Nanotubes** 67  
*Guojun Liu*
- 3 **Smart Nanoassemblies of Block Copolymers for Drug and Gene Delivery** 91  
*Horacio Cabral and Kazunori Kataoka*
- 4 **A Comprehensive Approach to the Alignment and Ordering of Block Copolymer Morphologies** 111  
*Massimo Lazzari and Claudio De Rosa*
- 5 **Helical Polymer-Based Supramolecular Films** 159  
*Akihiro Ohira, Michiya Fujiki, and Masashi Kunitake*
- 6 **Synthesis of Inorganic Nanotubes** 195  
*C.N.R. Rao and Achutharao Govindaraj*
- 7 **Gold Nanoparticles and Carbon Nanotubes: Precursors for Novel Composite Materials** 249  
*Thathan Premkumar and Kurt E. Geckeler*
- 8 **Recent Advances in Metal Nanoparticle-Attached Electrodes** 297  
*Munetaka Oyama, Akrajas Ali Umar, and Jingdong Zhang*
- 9 **Mesoscale Radical Polymers: Bottom-Up Fabrication of Electrodes in Organic Polymer Batteries** 319  
*Kenichi Oyaizu and Hiroyuki Nishide*
- 10 **Oxidation Catalysis by Nanoscale Gold, Silver, and Copper** 333  
*Zhi Li, Soorly G. Divakara, and Ryan M. Richards*
- 11 **Self-Assembling Nanoclusters Based on Tetrahalometallate Anions: Electronic and Mechanical Behavior** 365  
*Ishenkumba A. Kahwa*
- 12 **Optically Responsive Polymer Nanocomposites Containing Organic Functional Chromophores and Metal Nanostructures** 379  
*Andrea Pucci, Giacomo Ruggeri, and Francesco Ciardelli*

**13      Nanocomposites Based on Phyllosilicates: From Petrochemicals to  
Renewable Thermoplastic Matrices    403**

*Maria-Beatrice Coltelli, Serena Coiai, Simona Bronco,  
and Elisa Passaglia*

## Preface

Nanotechnology has found an incredible resonance and a vast number of applications in many areas during the past two decades. The resulting deep paradigm shift has opened up new horizons in materials science, and has led to exciting new developments. Fundamentally, nanotechnology is dependent on the existence or the supply of new nanomaterials that form the prerequisite for any further progress in this new and interdisciplinary area of science and technology. Evidently, nanomaterials feature specific properties that are characteristic of this class of materials, and which are based on surface and quantum effects.

Clearly, the control of composition, size, shape, and morphology of nanomaterials is an essential cornerstone for the development and application of nanomaterials and nanoscale devices. The complex functions of nanomaterials in devices and systems require further advancement in the preparation and modification of nanomaterials. Such advanced nanomaterials have attracted tremendous interest during recent years, and will form the basis for further progress in this area. Thus, the major classes of novel materials are described in the twenty-eight chapters of this two-volume monograph.

The initializing concept of this book was developed at the *3rd IUPAC International Symposium on Macro- and Supramolecular Architectures and Materials (MAM-06): Practical Nanochemistry and Novel Approaches*, held in Tokyo, Japan, 2006, within the framework of the biannual MAM symposium series. This monograph provides a detailed account of the present status of nanomaterials, and highlights the recent developments made by leading research groups. A compilation of state-of-the-art review chapters, written by over sixty contributors and well-known experts in their field from all over the world, covers the novel and important aspects of these materials, and their applications.

The different classes of advanced nanomaterials, such as block copolymer systems including block copolymer nanofibers and nanotubes, smart nanoassemblies of block copolymers for drug and gene delivery, aligned and ordered block copolymers, helical polymer-based supramolecular films, as well as novel composite materials based on gold nanoparticles and carbon nanotubes, are covered in the book. Other topics include the synthesis of inorganic nanotubes, metal nanoparticle-attached electrodes, radical polymers in organic polymer batteries, oxidation catalysis by nanoscale gold, silver, copper, self-assembling

nanoclusters, optically responsive polymer nanocomposites, renewable thermoplastic matrices based on phyllosilicate nanocomposites, amphiphilic polymer-clay intercalation and applications, the synthesis and catalysis of mesoporous alumina, and nanoceramics for medical applications.

In addition, this book highlights the recent progress in the research and applications of structural ceramics, the ecological toxicology of engineered carbon nanoparticles, carbon nanotubes as adsorbents for the removal of surface water contaminants, molecular imprinting with nanomaterials, near-field Raman imaging of nanostructures and devices, fullerene-rich nanostructures, nanoparticle-cored dendrimers and hyperbranched polymers, as well as the interactions of carbon nanotubes with biomolecules. The book is completed with a series of chapters featuring concepts in self-assembly, nanostructured organogels via molecular self-assembly, the self-assembly of linear polypeptide-based block copolymers, and information-guided self-assembly by structural DNA nanotechnology.

The variety of topics covered in this book make it an interesting and valuable reference source for those professionals engaged in the fundamental and applied research of nanotechnology. Thus, scientists, students, postdoctoral fellows, engineers, and industrial researchers, who are working in the fields of nanomaterials and nanotechnology at the interface of materials science, chemistry, physics, polymer science, engineering, and biosciences, would all benefit from this monograph.

The advanced nanomaterials presented in this book are expected to result in commercial applications in many areas. As the science and technology of nanomaterials is still in its infancy, further research will be required not only to develop this new area of materials science, but also to explore the utilization of these novel materials. All new developments impart risks, and here also it is important to evaluate the risks and benefits associated with the introduction of such materials into the biosphere and ecosphere.

On behalf of all contributors to we thank the publishers and authors on behalf of all contributors for granting copyright permissions to use their illustrations in this book. It is also very much appreciated that the authors devoted their time and efforts to contribute to this monograph. Last, but not least, the major prerequisite for the success of this comprehensive book project was the cooperation, support, and understanding of our families, which is greatly acknowledged.

The Editors

## List of Contributors

### **Kotoji Ando**

Yokohama National University  
Department of Material Science  
and Engineering  
79-1 Tokiwadai  
Hohogaya-ku  
Yokohama 240-8501  
Japan

### **Besim Ben-Nissan**

University of Technology  
Faculty of Science  
Broadway  
P.O. Box 123  
Sydney  
NSW 2007  
Australia

### **Simona Bronco**

CNR-INFM-PolyLab c/o  
Dipartimento di Chimica e  
Chimica Industriale  
Università di Pisa  
Via Risorgimento 35  
56126 Pisa  
Italy

### **Horacio Cabral**

The University of Tokyo  
Department of Materials Engineering  
Graduate School of Engineering  
7-3-1 Hongo, Bunkyo-ku  
Tokyo 113-8656  
Japan

### **Ying-Nan Chan**

National Taiwan University  
Institute of Polymer Science and  
Engineering  
Taipei 10617  
Taiwan

and

National Chung Hsing University  
Department of Chemical Engineering  
Taichung 40227  
Taiwan

### **Wen-Hsin Chang**

National Taiwan University  
Institute of Polymer Science and  
Engineering  
Taipei 10617  
Taiwan

***Jing Cheng***

The University of Western  
Ontario  
Department of Civil and  
Environmental Engineering  
London, ON N6A 5B9  
Canada

***Andy H. Choi***

University of Technology  
Faculty of Science  
Broadway  
P.O. Box 123  
Sydney  
NSW 2007  
Australia

***Francesco Ciardelli***

University of Pisa  
CNR-INFN-PolyLab  
c/o Department of Chemistry,  
and Industrial Chemistry  
Via Risorgimento 35  
56126 Pisa  
Italy

***Serena Coiai***

Centro Italiano Packaging and  
Dipartimento di Chimica e  
Chimica Industriale  
Università di Pisa  
Via Risorgimento 35  
56126 Pisa  
Italy

***Maria-Beatrice Coltelli***

Centro Italiano Packaging and  
Dipartimento di Chimica e  
Chimica Industriale  
Università di Pisa  
Via Risorgimento 35  
56126 Pisa  
Italy

***Claudio De Rosa***

University of Napoli "Federico II"  
Department of Chemistry  
Complesso Monte S. Angelo  
Via Cintia  
80126 Napoli  
Italy

***Soorly G. Divakara***

Colorado School of Mines  
Department of Chemistry and  
Geochemistry  
1500 Illinois St.  
Golden, CO 80401  
USA

***Kevin Flavin***

Queen Mary University of London  
School of Biological and Chemical  
Sciences  
Mile End Road  
London E1 4NS  
UK

***Michiya Fujiki***

Nara Institute of Science and  
Technology  
Graduate School of Materials Science  
8916-5 Takayama  
Ikoma  
Nara 630-0101  
Japan

***Kurt E. Geckeler***

Gwangju Institute of Science and  
Technology (GIST)  
Department of Materials Science and  
Engineering  
1 Oryong-dong, Buk-gu  
Gwangju 500-712  
South Korea

**Achutharao Govindaraj**

International Centre for  
Materials Science  
New Chemistry Unit and CSIR  
Centre of Excellence in  
Chemistry  
Jawaharlal Nehru Centre for  
Advanced Scientific Research  
Jakkur P. O.  
Bangalore 560 064  
India

and

Solid State and Structural  
Chemistry Unit  
Indian Institute of Science  
Bangalore 560 012  
India

**Jose E. Herrera**

The University of Western  
Ontario  
Department of Civil and  
Environmental Engineering  
London, ON N6A 5B9  
Canada

**Ishenkumba A. Kahwa**

The University of the West  
Indies  
Chemistry Department  
Mona Campus  
Kingston 7  
Mona  
Jamaica

**Johnson Kasim**

Nanyang Technological  
University  
School of Physical and  
Mathematical Sciences  
Division of Physics and Applied  
Physics  
Singapore 637371  
Singapore

**Kazunori Kataoka**

The University of Tokyo  
Department of Materials Engineering  
Graduate School of Engineering  
7-3-1 Hongo  
Bunkyo-ku  
Tokyo 113-8656  
Japan

and

The University of Tokyo  
Center for Disease Biology and  
Integrative Medicine  
Graduate School of Medicine  
7-3-1 Hongo  
Bunkyo-ku  
Tokyo 113-0033  
Japan

and

The University of Tokyo  
Center for NanoBio Integration  
7-3-1 Hongo  
Bunkyo-ku  
Tokyo 113-8656  
Japan

**Yonggang Ke**

Arizona State University  
Department of Chemistry and  
Biochemistry & The Biodesign  
Institute  
Tempe, AZ 85287  
USA

**Harm-Anton Klok**

Ecole Polytechnique Fédérale de  
Lausanne (EPFL)  
Institut des Matériaux, Laboratoire des  
Polymères  
STI-IMX-LP  
MXD 112 (Bâtiment MXD), Station 12  
1015 Lausanne  
Switzerland



**Arjun S. Krishnan**

North Carolina State University  
Department of Chemical &  
Biomolecular Engineering  
Raleigh, NC 27695  
USA

**Masashi Kunitake**

Kumamoto University  
Department of Applied  
Chemistry and Biochemistry  
2-39-1 Kurokami  
Kumamoto 860-8555  
Japan

**Fernando Langa**

Universidad de Castilla-La  
Mancha  
Facultad de Ciencias del  
Medio Ambiente  
45071 Toledo  
Spain

**Massimo Lazzari**

University of Santiago de  
Compostela  
Department of Physical  
Chemistry  
Faculty of Chemistry and  
Institute of Technological  
Investigations  
15782 Santiago de Compostela  
Spain

**Sebastien Lecommandoux**

University of Bordeaux  
Laboratoire de Chimie des  
Polymères Organiques (LCPO)  
UMR CNRS 5629  
Institut Polytechnique de  
Bordeaux  
16 Avenue Pey Berland  
33607 Pessac  
France

**Zhi Li**

Colorado School of Mines  
Department of Chemistry and  
Geochemistry  
1500 Illinois St.  
Golden, CO 80401  
USA

**Jiang-Jen Lin**

National Taiwan University  
Institute of Polymer Science and  
Engineering  
Taipei 10617  
Taiwan

**Guojun Liu**

Queens University  
Department of Chemistry  
50 Bader Lane  
Kingston Ontario K7L 3N6  
Canada

**Yan Liu**

Arizona State University  
Department of Chemistry and  
Biochemistry & The Biodesign  
Institute  
Tempe, AZ 85287  
USA

**Watoru Nakao**

Yokohama National University  
Department of Energy and Safety  
Engineering  
79-5 Tokiwadai  
Hodogaya-ku  
Yokohama 240-8501  
Japan

**Dhriti Nepal**

Gwangju Institute of Science  
and Technology (GIST)  
Department of Materials Science  
and Engineering  
1 Oryong-dong, Buk-gu  
Gwangju 500-712  
South Korea

and

School of Polymer  
Textile and Fiber Engineering  
Georgia Institute of Technology  
Atlanta, GA 30332  
USA

**Jean-François Nierengarten**

Université de Strasbourg  
Laboratoire de Chimie des  
Matériaux Moléculaires  
(UMR 7509)  
Ecole Européenne de Chimie  
Polymères et Matériaux  
25 rue Becquerel  
67087 Strasbourg, Cedex 2  
France

**Hiroyuki Nishide**

Waseda University  
Department of Applied  
Chemistry  
Tokyo 169-8555  
Japan

**Christopher K. Ober**

Cornell University  
Department of Materials Science  
and Engineering  
Ithaca, NY 14853  
USA

**Akihiro Ohira**

National Institute of Advanced  
Industrial Science and Technology  
(AIST)  
Polymer Electrolyte Fuel Cell Cutting-  
Edge Research Center (FC-Cubic)  
2-41-6 Aomi, Koto-ku  
Tokyo 135-0064  
Japan

**Makoto Onaka**

The University of Tokyo  
Department of Chemistry  
Graduate School of Arts and Sciences  
Komaba, Meguro-ku  
Tokyo 153-8902  
Japan

**Ryan R. Otter**

Middle Tennessee State University  
Department of Biology  
Murfreesboro, TN 37132  
USA

**Kenichi Oyaizu**

Waseda University  
Department of Applied Chemistry  
Tokyo 169-8555  
Japan

**Munetaka Oyama**

Kyoto University  
Graduate School of Engineering  
Department of Material Chemistry  
Nishikyo-ku  
Kyoto 615-8520  
Japan

**Elisa Passaglia**

University of Pisa  
Department of Chemistry and  
Industrial Chemistry  
Via Risorgimento 35  
56126 Pisa  
Italy

**Thathan Premkumar**

Department of Materials Science  
and Engineering  
Gwangju Institute of Science  
and Technology (GIST)  
1 Oryong-dong, Buk-gu  
Gwangju 500-712  
South Korea

**Andrea Pucci**

University of Pisa  
Department of Chemistry and  
Industrial Chemistry  
Via Risorgimento 35  
56126 Pisa  
Italy

**Jeremy J. Ramsden**

Cranfield University  
Bedfordshire MK43 0AL  
UK

and

Cranfield University at  
Kitakyushu  
2-5-4F Hibikino  
Wakamatsu-ku  
Kitakyushu 808-0135  
Japan

**C.N.R. Rao**

International Centre for Materials  
Science,  
New Chemistry Unit and CSIR Centre  
of Excellence in Chemistry  
Jawaharlal Nehru Centre for Advanced  
Scientific Research  
Jakkur P. O.  
Bangalore 560 064  
India

and

Solid State and Structural Chemistry  
Unit  
Indian Institute of Science  
Bangalore 560 012  
India

**Marina Resmini**

Queen Mary University of London  
School of Biological and  
Chemical Sciences  
Mile End Road  
London E1 4NS  
UK

**Ryan M. Richards**

Colorado School of Mines  
Department of Chemistry and  
Geochemistry  
1500 Illinois St.  
Golden, CO 80401  
USA

**Aaron P. Roberts**

University of North Texas  
Department of Biological Sciences &  
Institute of Applied Sciences  
Denton, TX 76203  
USA

**Kristen E. Roskov**

North Carolina State University  
 Department of Chemical &  
 Biomolecular Engineering  
 Raleigh, NC 27695  
 USA

**Giacomo Ruggeri**

University of Pisa  
 CNR-INFM-PolyLab  
 c/o Department of Chemistry  
 and Industrial Chemistry  
 Via Risorgimento 35  
 56126 Pisa  
 Italy

**Helmut Schlaad**

Max Planck Institute of Colloids  
 and Interfaces  
 MPI KGF Golm  
 14424 Potsdam  
 Germany

**Evan L. Schwartz**

Cornell University  
 Department of Materials Science  
 and Engineering  
 Ithaca, NY 14853  
 USA

**Tsunetake Seki**

The University of Tokyo  
 Department of Chemistry  
 Graduate School of Arts and  
 Sciences  
 Komaba, Meguro-ku  
 Tokyo 153-8902  
 Japan

**Ze Xiang Shen**

Nanyang Technological University  
 School of Physical and Mathematical  
 Sciences  
 Division of Physics and Applied  
 Physics  
 Singapore 637371  
 Singapore

**Young-Seok Shon**

California State University, Long Beach  
 Department of Chemistry and  
 Biochemistry  
 1250 Bellflower Blvd  
 Long Beach, CA 90840  
 USA

**Richard J. Spontak**

North Carolina State University  
 Department of Chemical &  
 Biomolecular Engineering  
 Raleigh, NC 27695  
 USA

and

North Carolina State University  
 Department of Materials Science &  
 Engineering  
 Raleigh, NC 27695  
 USA

**Koji Takahashi**

Kyushu University  
 Hakozaki  
 Higashi-ku  
 Fukuoka 812-8581  
 Japan

**Akrajas Ali Umar**

Universiti Kebangsaan Malaysia  
 Institute of Microengineering and  
 Nanoelectronics  
 43600 UKM Bangi Selangor  
 Malaysia

**Hao Yan**

Arizona State University  
Department of Chemistry and  
Biochemistry & The Biodesign  
Institute  
Tempe, AZ 85287  
USA

**Jingdong Zhang**

Huazhong University of Science and  
Technology  
College of Chemistry and Chemical  
Engineering  
Wuhan 430074  
China

**Ting Yu**

Nanyang Technological  
University  
School of Physical and  
Mathematical Sciences  
Division of Physics and Applied  
Physics  
Singapore 637371  
Singapore

## 14

# Amphiphilic Poly(Oxyalkylene)-Amines Interacting with Layered Clays: Intercalation, Exfoliation, and New Applications

Jiang-Jen Lin, Ying-Nan Chan, and Wen-Hsin Chang

### 14.1

#### Introduction

During recent years, organic–inorganic hybrid materials have attracted a great deal of research interest due to their promising industrial applications [1–3]. The successful development of Nylon-6/montmorillonite (MMT) nanocomposites by the Toyota research group [4, 5], reflects the importance of utilizing mineral clays for improving polymer properties [6–8], including fire retardation and gas barrier. One of the crucial issues for preparing these advanced polymers is to overcome the problem of incompatibility between the hydrophilic smectite-clays and hydrophobic polymers. Organic modification is the common method to convert the hydrophilic clay into an organophile [9–13]. Fine dispersion of the silicate particles in polymer matrices was then achieved for a variety of hydrophobic nanocomposites including polypropylene [14], polystyrene (PS) [15], polyurethane [16], polyester [17], epoxy [18–20], and polyimide [21].

In the past, many reviews have been devoted to the subject of clay nanocomposites [1–5, 21–25]. Significant progress in polymer engineering and the limitations of polymer compatibility to the nanoscale clays in intercalated and exfoliated forms are already well reviewed. Recent research developments on utilizing the layered silicate clays have also diversified into the areas of biotechnology [26], such as the use of anionic clays for gene therapy. Actually, recent advances in biomedical applications involve different types of nanomaterial, which can be generally classified into three categories according to their geometric dimensions: spherical (e.g., silver and titanium oxide particles) [27, 28]; fibril-shape (e.g., carbon nanotube) [29]; and sheet-like (e.g., natural and synthetic clays) nanomaterials. With at least one dimension that falls into the nanometer scale, all of these inorganic materials possess a high-aspect ratio surface area relative to their weight. For the sheet-like clays, each thin layer platelet with a thickness of approximately 1 nm (almost at the molecular level) and the lateral dimension of approximately 50 nm to several micrometers provides an extremely large specific surface ( $>500\text{ m}^2\text{ g}^{-1}$ ). Hence, the primary structure of the thin-layer clays is unique with respect to its

geometric shape as well as surface ionic charge, which could be important when interacting with biological materials such as proteins, nucleic acids, and microorganisms.

In this chapter, we review the synthetic aspects of organic modifications of smectite clays, with particular attention being paid to reports on the uses of various intercalation agents for the polymer–clay composite applications, without emphasizing their composite performance. Recent efforts on using high-molecular-weight poly(oxyalkylene)-diamines to tailor the layered-silicate spacing is particularly addressed [30–33]. The reaction profile of the intercalation via ion exchange by different equivalents of organic salt to clay exchange capacity, as well as the unconventional mechanisms involving metal-ion chelation and hydrogen bonding, are also reviewed. With the incorporation of hydrophobic amine-salts, the resulting organoclays may exhibit unusual colloidal properties [34, 35] as well as an ability to self-assemble into rigid-rod nanoarrays [36–38]. Furthermore, the method of exfoliating the layered-silicate clays into random platelets has been recently reported [39–41]. This process involved the use of polymeric amines via zigzag conformation or phase inversion mechanisms for the platelet randomization. The tailored organoclays are found to be suitable for embedding biomaterials such as protein [42, 43]. The aim of this chapter is to summarize the literature activities in clay utilization, with emphasis placed on the organic modifications and the emerging research in the areas of biomedical applications.

## 14.2

### Chemical Structures of Clays and Organic-Salt Modifications

#### 14.2.1

##### Natural Clays and Synthetic Layered-Double-Hydroxide (LDH)

Smectic clays are naturally abundant, with a well-characterized lamellar structure of multiple inorganic plates, a high surface area, and ionic charges on the surface [9–11]. The phyllosilicate clays of the 2:1 type, or smectites such as MMT, bentonite, saponite, and hectorite, are conventionally utilized as catalysts [44–46], adsorbents [47, 48], metal-chelating agents [49], fillers for polymer composites [1, 3, 21], and so on. The generic structure is composed of multiple layers of silicate/aluminum oxide, for example, with layers of two tetrahedron sheets sandwiching an edge-shared octahedral sheet [21]. Counter metal ions populate the composition with variation in isomorphic substitution of silicon or aluminum by divalent metal ions such as  $Mg^{2+}$ ,  $Ca^{2+}$ , or  $Fe^{2+}$ . These ionic charges are potentially exchangeable through further ionic exchange with alkali metal ions such as  $Na^+$  or  $Li^+$ , as well as with organic ions. Although these layered silicates are hydrophilic and swell in water, they often exist as aggregates in micrometer sizes from their primary stack units. In the case of MMT, the primary stack structure possesses multiple aluminosilicate plates of irregular polygonal shapes at average dimension of ca.  $100\text{ nm} \times 100\text{ nm} \times 1\text{ nm}$  for individual platelets [50]. For the ionic-exchange

reaction, the divalent counter-cations in most natural clays could be exchanged into different ions, including  $\text{Na}^+$ ,  $\text{Cu}^{2+}$ ,  $\text{Zn}^{2+}$ ,  $\text{Mg}^{2+}$ ,  $\text{Ca}^{2+}$  and an acidified  $\text{H}^+$  form [51]. The replacement priority for these cations are:  $\text{Al}^{3+} > \text{Ca}^{2+} > \text{Mg}^{2+} > \text{K}^+ = \text{NH}_4^+ > \text{Na}^+$  [46, 52]. According to this exchange order, organic quaternary ammonium salts can replace  $\text{Na}^+$  ions, but not with divalent cations in  $\text{Mg}^{2+}$ -MMT and  $\text{Ca}^{2+}$ -MMT. Therefore, for most natural clays, the sodium ion exchange is necessary to facilitate the subsequent organic ion intercalation.

Synthetic fluorine mica, which structurally is similar to sodium tetrasilicic micas, is prepared from the  $\text{Na}_2\text{SiF}_6$  treatment of talc at high temperature [53, 54]. The synthetic mica ( $\text{Na}^+$ -Mica) is water-dispersible and generally used as an inorganic thickener. This synthetic fluorinated mica has an average dimension of 300–1000 nm in 80–100 nm for MMT. Another class of synthetic clays, layered-double-hydroxided (LDHs), can be prepared from the coprecipitation of inorganic salts. The chemical structure is described as  $[\text{Mg}_6\text{Al}_2(\text{OH})_{16}]\text{CO}_3 \cdot 4\text{H}_2\text{O}$  in the example of magnesium/aluminum hydroxides. Various metal hydroxides, including Ni, Cu, or Zn for divalent and Al, Cr, Fe, V, or Ga for trivalent metal ions, and anions such as  $\text{CO}_3^{2-}$ ,  $\text{Cl}^-$ ,  $\text{SO}_4^{2-}$ ,  $\text{NO}_3^-$ , or other various organic anions, have been reported [55–58]. These LDHs are classified as anionic clays that can be organically modified through an anionic-exchange reaction, using substances such as carboxylic acids, anionic polymers, organic phosphoric acids, and so on [58]. These synthetic clays may have various applications, including heterogeneous catalysts, optical materials, biomimetic catalysts, separation agents, and DNA reservoirs [59–63]. Recently, Mg–Al LDHs were incorporated with poly(oxypropylene)-bis-amindocarboxylic acid salts (POP-acid) to result in a wide basal spacing of 92 Å [64]. This wide spacing, as well as the introduction of a hydrophobic POP backbone, may open up new applications for this class of anionic clays.

#### 14.2.2

##### Low-Molecular-Weight Intercalating Agents and X-Ray Diffraction $d$ -Spacing

The common strategy for utilizing smectite clays is to alter their inherent hydrophilic nature so that they become hydrophobic and organically compatible with polymers. For the synthesis of polymer–clay nanocomposites, organic oniums such as alkyl ammonium salts [22] are commonly used to intercalate the layered minerals. The resultant organoclays are then suitable for the consequent process of melt-blending with polymers and *in situ* polymerization. For example, sodium montmorillonite ( $\text{Na}^+$ -MMT), consisting of sodium ions on the silicate surface ( $\equiv\text{Si}-\text{O}^-\text{Na}^+$ ), can be intercalated with organic onium salts. The quaternary alkyl ammonium ( $\text{R}_4\text{N}^+\text{X}^-$ ) or alkyl phosphonium ( $\text{R}_4\text{P}^+\text{X}^-$ ) salts are the common intercalating agents because of their commercial availability. The incorporation of organic intercalating agents also resulted in a silicate gallery expansion. For example, the  $\text{C}_{18}$ -alkyl quaternary salts may intercalate  $\text{Na}^+$ -MMT, causing a layer space expansion to 20–30 Å basal spacing from the pristine 12 Å clay gallery. It is noteworthy that the same organic quaternary salt may not exchange with natural clays with divalent counter ions such as  $\text{M}^{2+}$ -MMT [65] (where  $\text{M}^{2+} = \text{Mg}^{2+}$  or  $\text{Ca}^{2+}$ ).



A large number of intercalating agents for modifying the cationic smectite clays have been described, and it is possible to classify these according to their chemical structures and organic functionalities (see Table 14.1). Low-molecular-weight alkyl ammonium and phosphonium salts are the common intercalating agents, and normally these may result in a widening of the basal spacing in the range of 13 to 50 Å. Thermally stable and reactive surfactant types of imidazolium salts (with C<sub>12</sub>, C<sub>16</sub> and C<sub>18</sub> alkyl groups) were reported for the preparation of polystyrene/MMT nanocomposites [93]. The general idea here is that the presence of alkyl imidazolium may contribute to the thermal stability of the composites. Other reactive cationic surfactants, such as vinylbenzyl dimethyldodecyl ammonium chloride and surfactants with 2-methacryloyl functionalities, have been reported for poly(methylmethacrylate) (PMMA) and PS–clay nanocomposites. The purpose of introducing a reactive functionality to the intercalating agent is to facilitate not only a layer exfoliation but also fine dispersion in the polymer matrices.

### 14.3

#### Poly(Oxyalkylene)-Polyamine Salts as Intercalating Agents, and Their Reaction Profiles

##### 14.3.1

#### Poly(Oxyalkylene)-Polyamine Salts as Intercalating Agents

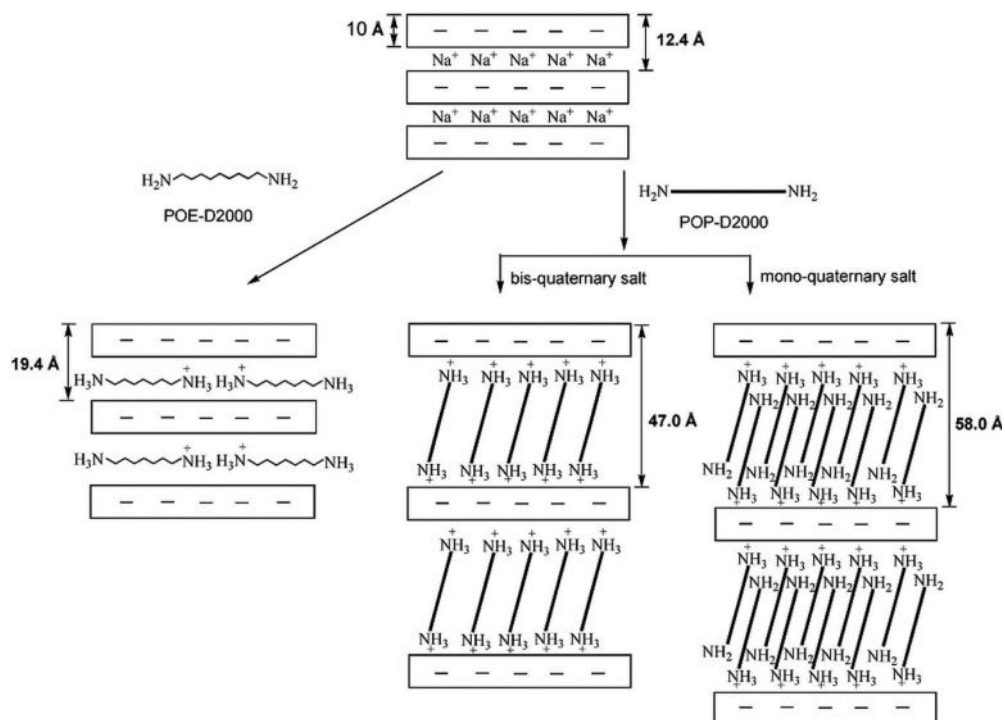
The uses of poly(oxyalkylene)-amines of M<sub>w</sub> 2000–4000 g mol<sup>-1</sup> for the intercalation of Na<sup>+</sup>-MMT to prepare organoclays with a large *d* spacing was reported in 2001 [30]. Poly(oxyalkylene)-diamines (POA-diamines) are commercially available polyether amines that are produced from the amination of polyols such as polyethylene glycols, polypropylene glycols, and their mixed poly(oxyethylene-oxypropylene) [99, 100]. Both, hydrophobic and hydrophilic types of POA-diamines, poly(oxypropylene)-amines (POP-amines) and poly(oxyethylene)-amines (POEamines), respectively, are available. By using the hydrophobic POP-diamines of 230, 400, 2000, and 4000 g mol<sup>-1</sup>, Na<sup>+</sup>-MMT was intercalated into organoclays at varied X-ray diffraction (XRD) basal spacings (15.0, 19.4, 58.0, and 92.0 Å, respectively). The lamellar expansion was found to be proportionally correlated with the POP molecular weights, through the POP tethering with silicate surfaces or the ionic-exchange reaction of the quaternary ammonium ions. Within the silicate confinement, the POP backbones may aggregate through a hydrophobic phase separation and consequently stretch out the basal spacing of the silicate interlayer gallery (Figure 14.1).

In contrast, the hydrophilic POE-diamine of M<sub>w</sub> 2000 g mol<sup>-1</sup> (POE2000) resulted in a spacing of 19.4 Å. The conclusion has been drawn that the intercalating agent requires a hydrophobic nature in order to expand the ionically charged platelets. The hydrophilic POE backbones or the  $-(\text{CH}_2\text{CH}_2\text{O})_x-$  structure, resulted in the organics associating tightly with the silicate surface. Only the hydrophobic POP backbone  $-(\text{CH}_2\text{CH}(\text{CH}_3)\text{O})_x-$  has shown an ability to generate a new “supporting” phase for widening the gallery space.

**Table 14.1** Representatives of the various intercalating agents described in the literature.

Functionality	Intercalating agent	Clay	XRD (Å)	Reference(s)
POA-diamine salt	Poly(oxypropylene)-diamine (2000 $M_w$ ), Poly(oxypropylene)-diamine (POP-amines, 4000 $M_w$ ), Poly(oxypropylene)-diamine (POP-amines, 5000 $M_w$ )	Li <sup>+</sup> -fluorohectorite, Na <sup>+</sup> -MMT, Na <sup>+</sup> -Mica	46–92	[12, 30, 35]
Polymeric amine	Amine-terminated PS surfactants, Amine-terminated butadiene acrylonitrile copolymers	Na <sup>+</sup> -MMT	10–155	[66–68]
Alkyl-amine salt	1-Hexadecylamine and octadecylamine	Na <sup>+</sup> -MMT	16–37	[69–76]
Amino acid	6-Aminohexanoic acid, 12-Aminododecanoic acid	Na <sup>+</sup> -MMT	17–49	[12, 77]
Acid	C <sub>18</sub> carboxylic acids and other acids, 2-Acrylamido-2-methyl-1-propanesulfonic acid	Mg <sup>2+</sup> - or Ca <sup>2+</sup> -MMT, Na <sup>+</sup> -MMT	35, Exfoliation	[65, 78–80]
Ammonium salt	Hexadecyltrimethylammonium bromide, Dioctadecyldimethyl ammonium bromide, Vinylbenzyl dimethyldodecylammonium chloride, Dialkyldimethylammonium salt from hydrogenated tallow	Na <sup>+</sup> -MMT	19–40	[69, 70, 81–86]
Phosphonium salts	10-[3,5-bis(methoxycarbonyl)phenoxy]decyltriphenylphosphonium bromide Dodecyltriphenyl phosphonium bromide, Hexadecyltributyl phosphonium bromide, Tetraoctyl phosphonium bromide	Na <sup>+</sup> -Mica, Li <sup>+</sup> -fluorohectorite, Na <sup>+</sup> -MMT	24–32	[72, 87–92]
Imidazolium salt	1,2-Dimethyl-3-(benzyl ethyl isobutyl polyhedral oligomeric silsesquioxane) imidazolium chloride (DMIPOSS), Dioctadecyl imidazolium, 1,2-Dimethyl-3-hexadecyl imidazolium, vinyl-alkyl-imidazolium (C <sub>12</sub> , C <sub>16</sub> and C <sub>18</sub> )	Na <sup>+</sup> -MMT	36	[93–96]
Stibonium salt	Triphenylhexadecyl stibonium trifluoromethyl sulfonate	Na <sup>+</sup> -MMT	20	[97]
Poly(ethylene glycol)	PEG400 vs. POP-amine <sup>a</sup>	Na <sup>+</sup> -MMT	17.7	[98]

<sup>a</sup> POP-amines: poly(oxyalkylene)-amines of  $M_w$  230–4000.



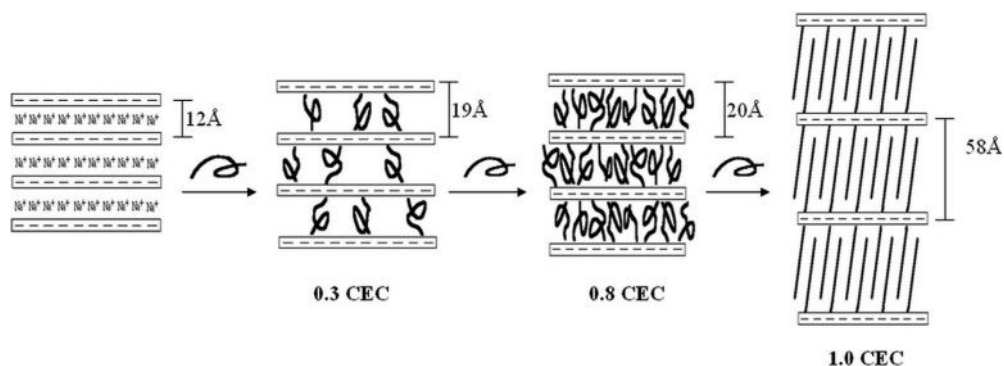
**Figure 14.1** Schematic representation of Na<sup>+</sup>-MMT intercalation by hydrophilic and hydrophobic poly(oxyalkylene)-diamine salts of the same molecular weight [31].

It was noted that formation of the hydrophobic POP phase in the silicate gallery could be understood by estimating the theoretical length of the fully stretched POP backbone. Based on calculations of the bond lengths (1.54 Å for C–C and 1.43 Å for C–O) and bond angles (109.6° and 112°, respectively), the theoretical length (77 Å) for POP2000 was longer than the value of 58.0 Å observed for those molecules in confinement. Apparently, the POPs were aggregated into hydrophobic phase but not fully extended at the molecular level, nor arranged in a tilting orientation in the gallery confinement.

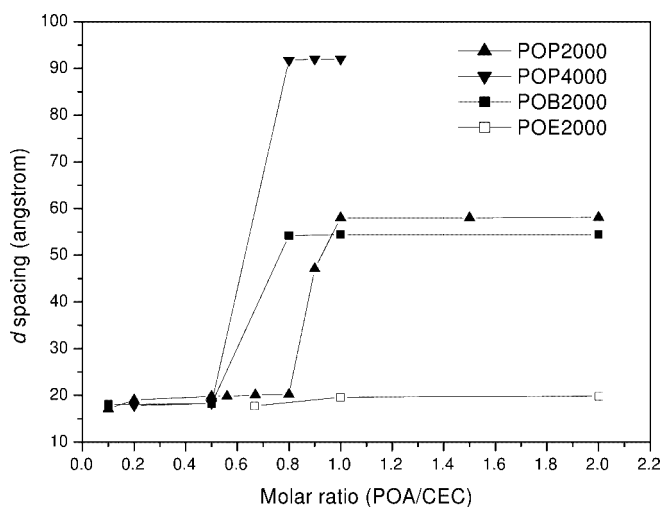
#### 14.3.2

##### Critical Conformational Change in Confinement During the Intercalating Profile [31]

The intercalation profile was studied by varying the equivalent ratios (from 0.2 to 1.0) of POP2000 salt to the clay CEC (120 mEq 100 g<sup>-1</sup>). Critical intercalation points were apparent, as shown in Figure 14.2, for the clay expansion with respect to the POP intercalants. Before the critical point, the basal spacing expansion was similar (19.0–20.2 Å) and in the range of amine addition, from 0.2 to 0.8 CEC equivalent.



**Figure 14.2** Schematic representation of POP-diamine forming a hydrophobic phase in a clay gallery [31].



**Figure 14.3** Critical points of poly(oxyalkylene)-diamine salts intercalating montmorillonite at different CEC ratios [31].

At 0.8 CEC equivalent, the POP addition expanded the  $d$  spacing suddenly to 58 Å in the case of POP2000 intercalation.

The critical concentration for the basal spacing expansion is generalized for several hydrophobic polyether-amines, as summarized in Figure 14.3. The POP4000 and poly(oxybutylene)diamine of  $2000 \text{ g mol}^{-1} M_w$  (POB2000) showed a critical point for the intercalation (Figure 14.3, ▼ and ■, respectively). The increases in basal spacing, from 20 Å to 92 Å for POP4000, and from 20 Å to 54 Å for POB2000, were observed and attributed to the molecular length, POP4000 > POP2000 > POB2000. The existence of a critical concentration was explained by the POP hydrophobic phase generated in the layer gallery. For the POE-backbone amine salt, there was no change in the critical basal spacing.

## 14.3.3

**Correlation between MMT *d*-Spacing and Intercalated Organics [32, 33]**

The basal spacing enlargement can only be achieved by a hydrophobic aggregation of the intercalating agents in the gallery. By taking in consideration the molecular end-to-end length in the confinement, a linear correlation was found for the basal spacing expansion. As the incorporated organics occupy the same volume as the measured silicate spacing, the relationship between the interlayer spacing ( $D$ ) and the organic weight fraction ( $R$  or w/w of POP-amine/MMT by weight) is expressed by the following equation [32]:

$$D = R \times \frac{1}{A \times \rho} + t \quad (14.1)$$

where  $A$  is the surface area of MMT,  $t$  is the plate thickness, and  $\rho$  is the density of the intercalant in the gallery. The XRD measurement is a function of the organics occupied in the gallery, and the relationship of gallery distance, volume, and organic fraction is predictable.

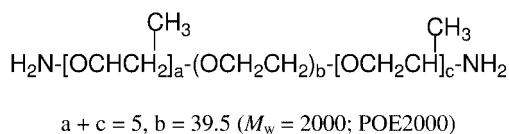
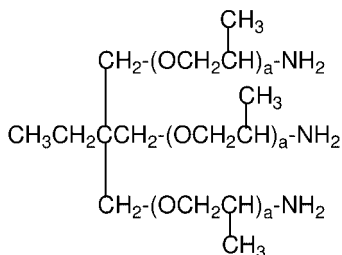
## 14.4

**Amphiphilic Copolymers as Intercalating Agents**

## 14.4.1

**Various Structures of the Amphiphilic Copolymers [34, 40, 101, 102]**

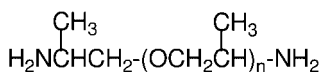
In order to tailor the hydrophobic nature for organoclays, several research groups have used amphiphilic copolymers as intercalating agents. For example, the copolymers of POP-amine grafting on poly(propylene) (PP) [34, 40], poly(styrene-ethylene/butadiene-styrene) (SEBS) [101] and poly(styrene-maleic anhydride) (SMA) [102] copolymers were reported. These copolymers, which comprised multiple amines as the pendant groups, were comb-like in shape and amphiphilic in nature (Figure 14.4). The copolymers, after treating with HCl, were able to form stable emulsions in water and to intercalate with  $\text{Na}^+$ -MMT. The generation of an emulsion at 670 nm diameter for the amine-grafted PP copolymer at ambient temperature, and at 560 nm at 75 °C in toluene/water, has also been reported [34]. The fine emulsion rendered the copolymers able to intercalate with  $\text{Na}^+$ -MMT. The pendant quaternary ammonium ions of the copolymers may undergo an ionic-exchange reaction to afford the silicates of 19.5 Å spacing. The layered silicate platelet gallery was widened and surrounded with hydrophobic copolymer backbones. The resultant silicate/copolymer hybrids resembled a single micelle structure containing a hydrophilic rigid silicate core and a hydrophobic organic corona. The hybrids were dispersible in toluene and were found to be approximately 500 nm in size in the example of PP-POP2000/MMT.

*Hydrophilic amine**Hydrophobic amines*

$$a = 4-5 (M_w = 400; \text{POPT}400)$$

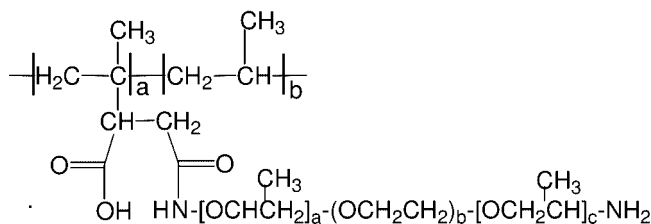
$$a = 16-17 (M_w = 3000; \text{POPT}3000)$$

$$a = 27-28 (M_w = 5000; \text{POPT}5000)$$



$$n = 5-6 (M_w = 400; \text{POPD}400)$$

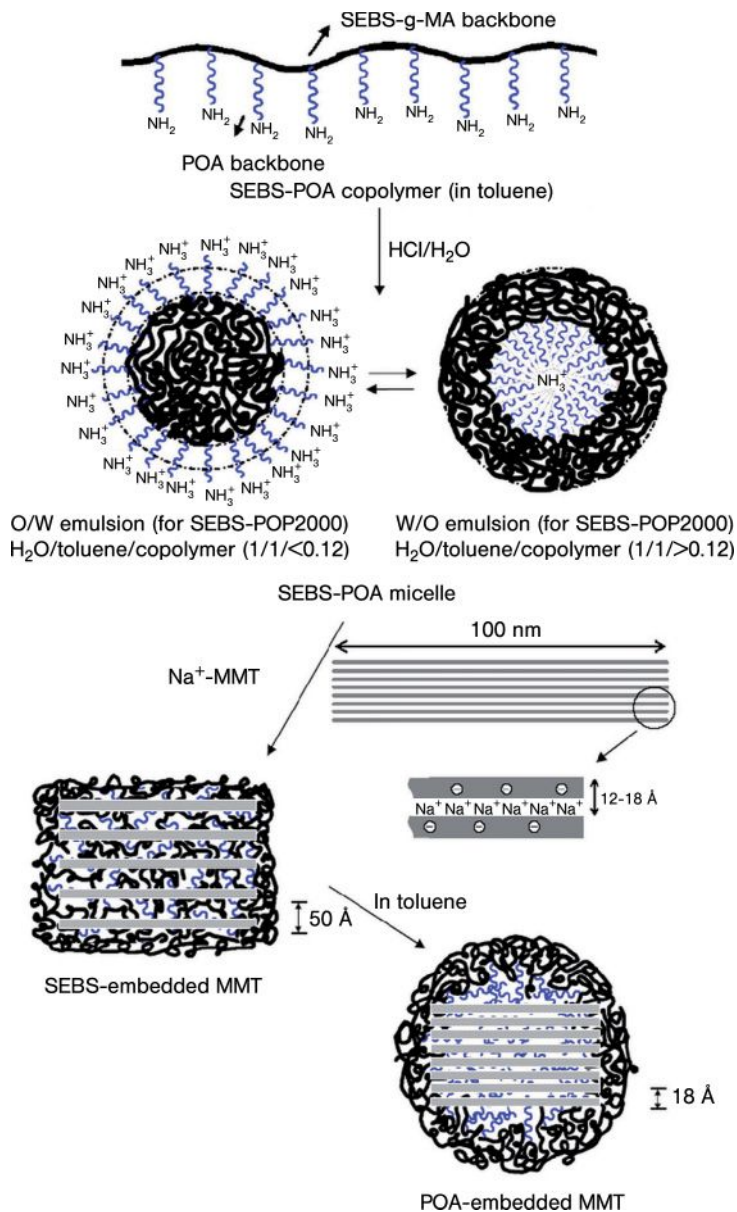
$$n = 33 (M_w = 2000; \text{POPD}2000)$$



**Figure 14.4** Chemical structures of POA-diamines and the grafted PP copolymers [34, 40].

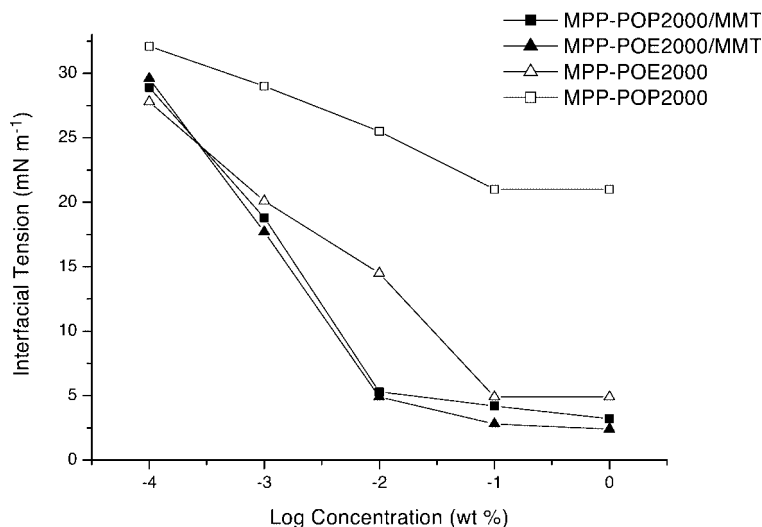
The POA-diamine grafting onto SEBS-*g*-MA generated another class of comb-like and amphiphilic polyamines. The particular SEBS-POA copolymer, with an average of nine amine pendants, is capable of forming a fine emulsion and intercalating with  $\text{Na}^+$ -MMT to afford a wide range of XRD  $d$  spacing, from 17 Å to 52 Å. The high  $d$  spacing was due to SEBS backbone intercalation, while the POA intercalation could result in only a low spacing. Thus, it was concluded that two different intercalating modes were present, the conceptual description of which is shown in Figure 14.5.

The amphiphilic properties of the copolymers can be better controlled by using poly(styrene-*co*-maleic anhydrides) (SMA) grafted with the POA-diamines. The



**Figure 14.5** Schematic representation of copolymer/clay hybrids in different forms of intercalation [101].

copolymers with different ratios of styrene/MA monomers provided a wide range of hydrophobic properties. The SMA-POP copolymers generated the intercalated organoclays with 12.9 Å to 78.0 Å basal spacing. Two types of intercalation were also observed for the SMA-POP intercalation.



**Figure 14.6** Interfacial tensions of the hybrids prepared from MMT intercalation with POP- or POE-grafted PP copolymers in toluene/water [34].

#### 14.4.2

##### Colloidal Properties

The silicate–copolymer hybrids, intercalated with hydrophobic organics, are dispersible in toluene and exhibit a surfactant property [34, 35, 101]. In Figure 14.6, the hybrids can be seen to exhibit an ability to reduce the toluene/water interfacial tension, from  $28 \text{ mN m}^{-1}$  to  $5 \text{ mN m}^{-1}$ . The critical micelle concentration (CMC) or critical aggregation concentration (CAC) was estimated as 0.01 wt%, by extrapolating from the interfacial tension versus concentration curve.

### 14.5

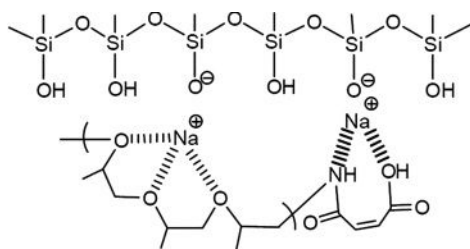
#### New Intercalation Mechanism Other than the Ionic-Exchange Reaction

##### 14.5.1

##### Amidoacid and Carboxylic Acid Chelating [65, 103]

The conventional method of modifying  $\text{Na}^+$ -MMT requires the use of organic onium salts, such as ammonium and phosphonium salts, for the ionic-exchanging intercalation. The driving force for the organic incorporation is via the ionic exchange reaction, the replacement of ammonium salts ( $-\text{NH}_3^+\text{Cl}^-$ ) for sodium ions ( $\equiv\text{Si}-\text{O}^-\text{Na}^+$ ). In the case of using poly(oxyalkylene)-amidoacids in the form of zwitterions as the intercalating agents, the intercalation of  $\text{Na}^+$ -MMT occurred [103]. The mechanism via a chelating intermediate between the amidoacid and the





**Figure 14.7** Schematic representation of sodium ion chelation via an oxypropylene-amidoacid [103].

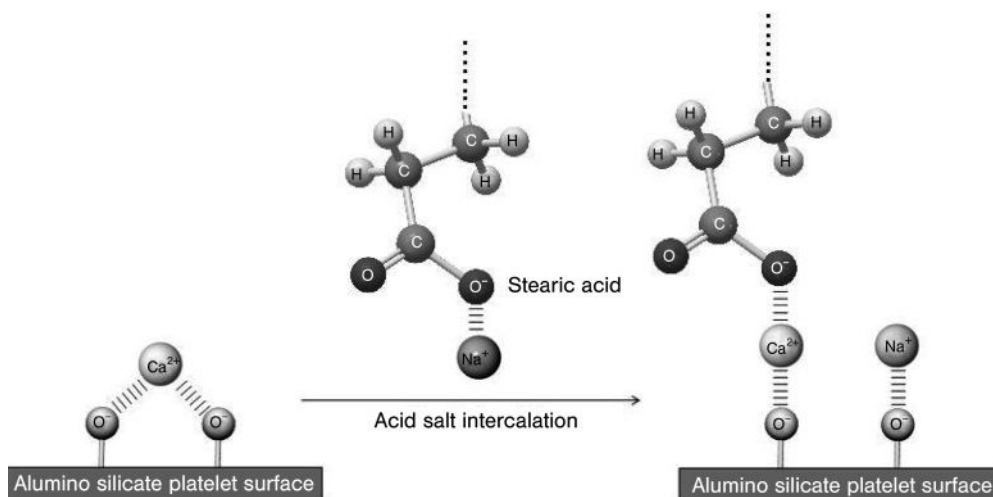
counter sodium ion in the clay gallery was proposed. The chelating intermediate is supposedly stable due to the formation of a cyclic, seven-membered ring structure (Figure 14.7).

Another mechanism [65] was reported for metal chelating in the clay gallery. Different alkyl lengths of alkyl-carboxylic acids,  $\text{CH}_3(\text{CH}_2)_n\text{COOH}$ , were allowed to intercalate into the clays that contained divalent metal counter ions. Conventionally, it was believed that the  $\text{C}_{12-18}$  carboxylic acids [e.g., lauric acid ( $n = 10$ ) and stearic acid ( $n = 16$ )] would be unable to incorporate into the silicate clays, such as the naturally occurring MMT. However, it was reported that the sodium or potassium salts of alkyl carboxylates could be incorporated into  $\text{Na}^+$ -MMT to afford a low organic embedment of 10–15 wt% organics, and an XRD basal spacing of 15 Å. However, the same intercalating carboxylate salts in fact intercalated the divalent  $\text{M}^{2+}$ -MMT (XRD = 10.1 Å) to achieve a wide spacing of up to 30 or 43 Å, in the example of the naturally occurring smectite silicates (K10), which comprised layered aluminosilicates and mostly divalent counter cations. The difference in intercalation between the  $\text{M}^{2+}$ -MMT and  $\text{Na}^+$ -MMT was explained by the complexes of divalent  $\text{M}^{2+}$  with carboxylate ( $-\text{COO}^-$ ) and  $\text{SiO}^-$  anions (Figure 14.8). Formation of the thermally stable complex served as the driving force for the organics to incorporate into the gallery.

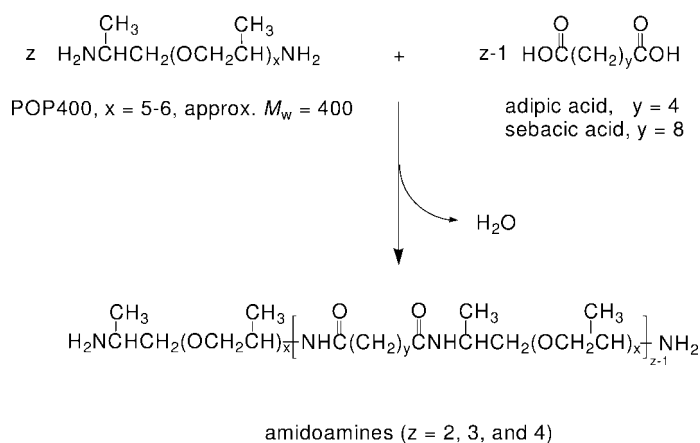
#### 14.5.2

##### Intercalation Involving Intermolecular Hydrogen Bonding [104]

Besides the chelating mechanism, hydrogen bonding of the intercalated organics (structures shown in Scheme 14.1) may serve as additional forces for the interaction, in similar fashion to the hydrophobic interaction described above. With the structure consisting of  $-(\text{CH}_2)_8-$  and amide functionalities, the intercalating agents may be further accumulated in the clay gallery. In the examples of the layered aluminosilicates of  $\text{Na}^+$  synthetic mica and MMT, in both cases intercalation with the POP-amidoamine quaternary salts afforded an enlarged basal spacing of up to 78 Å, with an organic embedment up to 70 wt% in the hybrids. The driving forces applied by the hydrogen bonding interaction were evidenced by using a stepwise intercalating method. Continuing addition of the POP-amidoamine salts after the



**Figure 14.8** Diagrammatic representation of a carboxylic acid salt complex through divalent cations on silicate K10 [65].



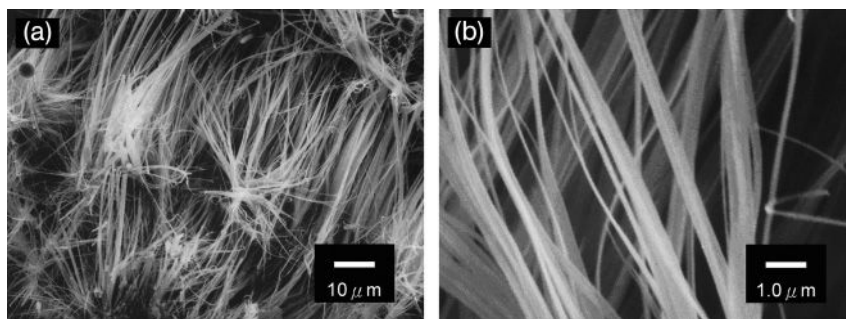
**Scheme 14.1** Representative structure of POP-amidoamines with hydrogen-bonding functionalities [104].

CEC equivalent amount led to the generation of hybrids, while the basal spacing was increased from 58 Å to 70–78 Å.

## 14.6

### Self-Assembling Properties of Organoclays [36, 37]

With the incorporation of hydrophobic POP, the MMT hybrids were amphiphilic in nature. For example, MMT/POP2000 at 58.0 Å basal spacing and 63 wt%



**Figure 14.9** (a, b) Scanning electron microscopy images of the self-assembly of a POP-modified clay [36].

organics was dispersible in toluene, and exhibited an ability to lower the toluene/water interfacial surface tension. The surfactant property was shown to depend on the hydrophobic–hydrophilic balance between the hydrophobic POP portion and the ionic character of the platelet. With varied amounts of organics in the clay, the amphiphilic nature of the hybrids can be tailored. Those hybrids with an organic content in the range of 22 to 63 wt%, and a corresponding  $d$  spacing of 19–58 Å, can easily be prepared. Among these hybrids, the POP/MMT hybrid with a balanced hydrophobic–hydrophilic ratio (19 Å  $d$  spacing, 26 wt% organics) enabled self-assembly into rod-like microstructures which were up to 40 μm in length [36] (Figure 14.9). These unique self-assemblies were observed using scanning electron microscopy (SEM). The POP-modified MMT hybrid was first dispersed in a water/toluene mixture at a concentration of 1.0 wt%, and then subjected to evaporation at 80 °C before the SEM observations were made. The formation of rod-like arrays [37] was uniform, with individual rod dimensions ranging from 100 to 800 nm in width, and from 2 to 10 μm as the average length. The mechanism for the formation of lengthy rods was proposed to be a two-directional growth of horizontal and vertical self-alignment, as illustrated conceptually in Figure 14.10. The correct balance between the POP hydrophobic aggregation and the silicate ionic charge attraction is important for forming orderly microstructures.

## 14.7

### Exfoliation Mechanism and the Isolation of Random Silicate Platelets

#### 14.7.1

##### Thermodynamically Favored Exfoliation of Na<sup>+</sup>-MMT by the PP-POP Copolymers [40]

The hybrids prepared from the intercalation of PP-POP2000 copolymers with Na<sup>+</sup>-MMT at 19.5 Å [34] could be further exfoliated under the conditions of 120 °C and 500 p.s.i. N<sub>2</sub> in a closed system, such that the layered structure of Na<sup>+</sup>-MMT was transformed into random platelets. The process required the copolymers to form

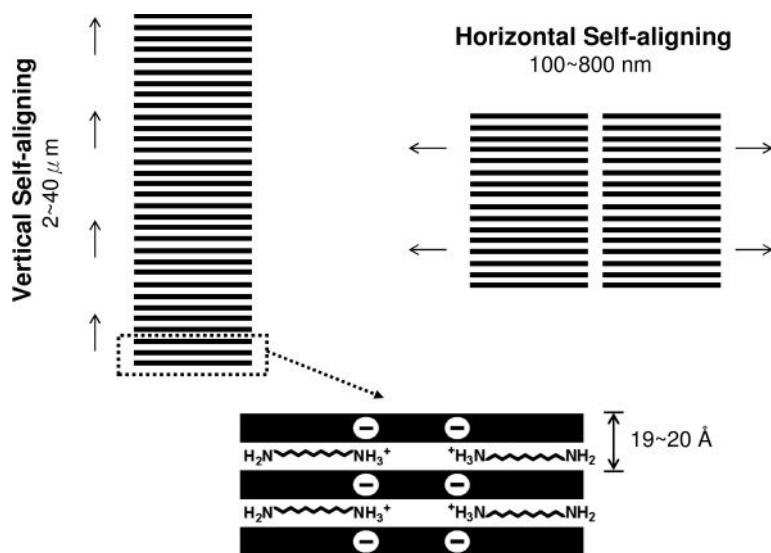


Figure 14.10 Schematic representation of the self-assembling mechanism [36].

a fine emulsion before interacting with the hydrophilic clays. Two types of intercalating hybrid may be involved, as shown conceptually in Figure 14.11. Transformation of the initial copolymer/layered silicate hybrid into the exfoliation could be explained by the relative stability of the water-in-oil (W/O) and oil-in-water (O/W) hybrid structures. An inversion from the W/O to the O/W hybrid was favored thermodynamically such that, ultimately, exfoliation of the clay-layered structure would occur.

#### 14.7.2

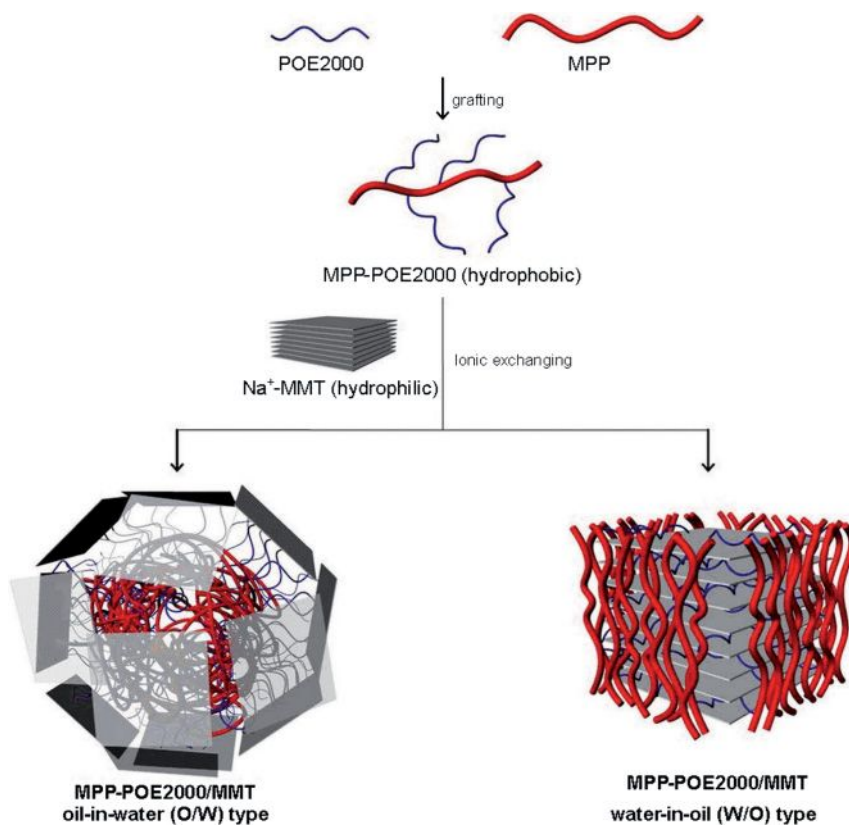
##### Zigzag Mechanism for Exfoliating Na<sup>+</sup>-MMT

An alternative mechanism of exfoliation was reported which used Mannich polyamines as the intercalating agents [39]; these were prepared from the reaction of *p*-cresol, formaldehyde, and POA-diamines. After being converted into the corresponding amine salts, the copolymers proved to be effective for exfoliating the layered silicates. Due to the presence of multiple amine sites in the polymer backbone for anchoring onto the silicate surface, a zigzag conformation of the copolymers within the confinement was proposed as the exfoliation mechanism. This process is illustrated schematically in Figure 14.12.

## 14.8

### Isolation of the Randomized Silicate Platelets in Water [41]

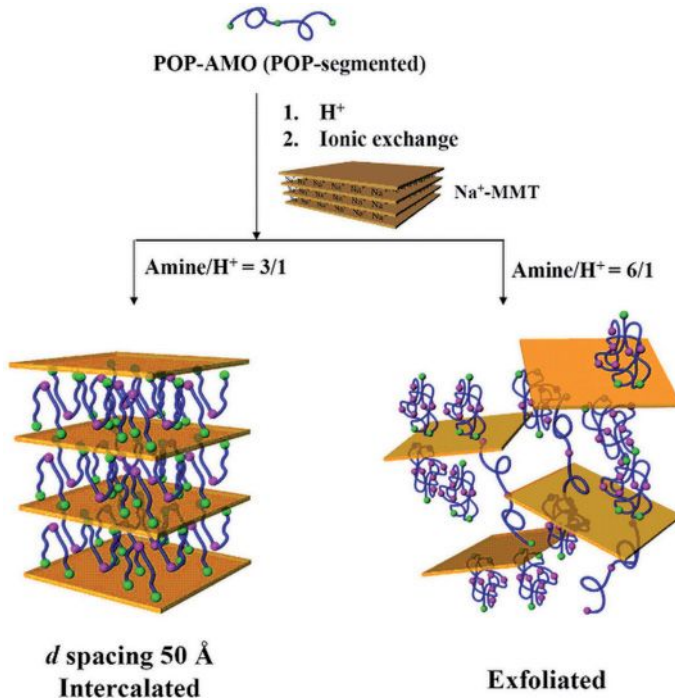
The process of exfoliation led to the next step of isolating random silicate platelets. As shown in Scheme 14.2), the layered Na<sup>+</sup>-MMTs were exfoliated through



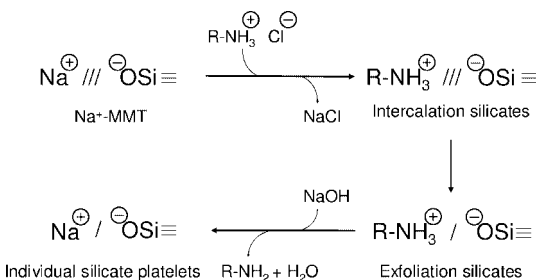
**Figure 14.11** Emulsion of the copolymers affecting Na<sup>+</sup>-MMT intercalation and exfoliation [40].

ionic-exchange reactions, while further Na<sup>+</sup> exchange permitted recovery of the organic amines.

The nature of the material of the random silicate platelets was confirmed by using XRD analysis, transmission electron microscopy (TEM), and atomic force microscopy (AFM). In particular, the material was shown to have a unique ionic character in water. Based on parameters of 1.2 mEqg<sup>-1</sup> CEC for Na<sup>+</sup>-MMT and a surface area of 720 m<sup>2</sup>g<sup>-1</sup>, the platelets were calculated to contain 20 000 ions per platelet, with an area per ion of 0.9 nm<sup>2</sup>, and with 4 × 10<sup>16</sup> platelets per gram. The intensive charges rendered the silicate plates with a high affinity for polar organics such as poly(ethylene glycol) (PEG) and water molecules. During measurement of the zeta potential (see Figure 14.13), a Na<sup>+</sup>-MMT suspension in water demonstrated a relatively constant charge character at -18 mV, over a pH range from 2 to 11. However, the zeta potential of the exfoliated platelets showed an isoelectric point of pH 6.4, and varied from 21 mV to -25 mV over the pH range from 5 to 8. It appeared that the platelet surface possessed different ionic potentials that were originally buried within the MMT layered structure.



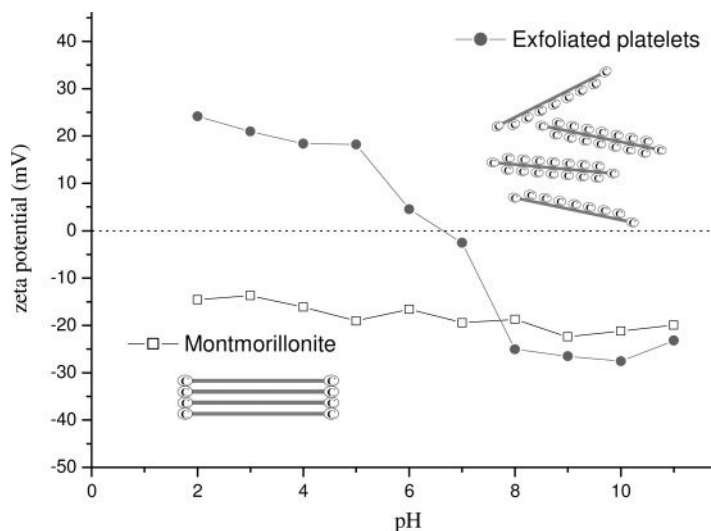
**Figure 14.12** Schematic representation of silicate stack and exfoliation by the presence of polyamine salts [39].



**Scheme 14.2** The scheme of stepwise intercalation, exfoliation, and isolation of random silicate platelets [41].

## 14.9 Emerging Applications in Biomedical Research

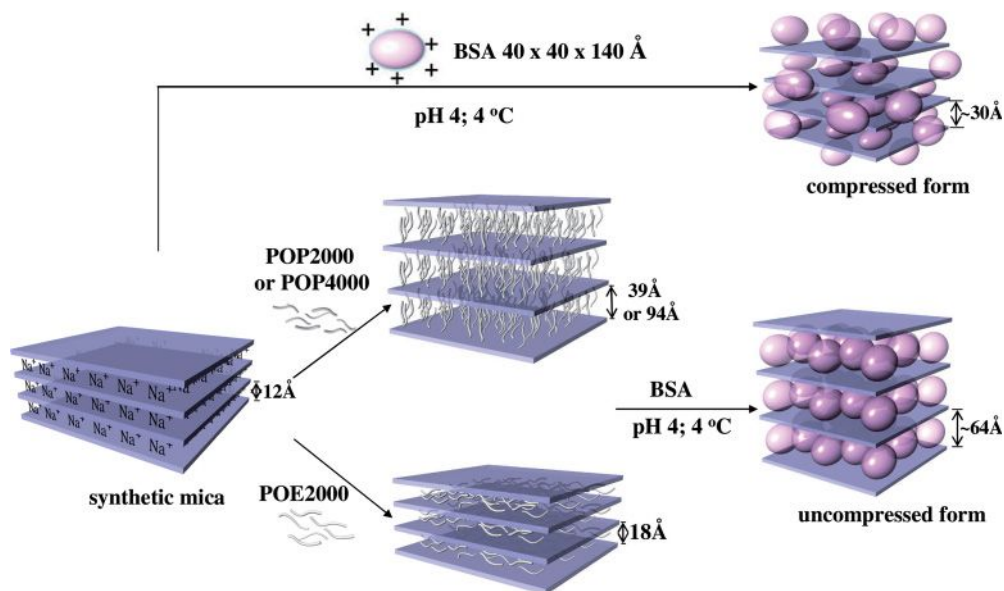
Both types of ionic clay, namely the anionic LDH and the cationic  $Na^+$ -MMT, have been recognized for their abilities to adsorb biomaterials [105], the key properties for this application being the high surface area, the ionic character, and the layered structure [106–108]. Previously reported examples have used clays as the support



**Figure 14.13** Zeta potentials of montmorillonite (□) and exfoliated silicate platelets (●) at different pH values [41].

for biomaterial adsorption [109], and DNA encapsulation for gene therapy [26]. In general, the key elements in this area of research are to specify the functions of encapsulating large molecules within the layered confinement. Earlier studies have revealed several examples of proteins complexing with naturally occurring clays, simply by their adsorption directly onto the clay surface [110, 111]. Such adsorption between proteins and silicates is affected by the properties of the clay, the ionic charges and the type of species, as well as the size of the protein and its isoelectric properties [111].

Recent improvements in this area have focused on the stability of the biomaterial, the controlled release profile, and targeting. Indeed, it has been reported that the incorporation of bovine serum albumin (BSA) into the layered spacing of MMT and synthetic fluorinated mica is possible via a step-wise ionic exchange reaction [42, 43], as shown in Figure 14.14. Specifically, the layer spacing of the synthetic mica was first expanded with a POA-amine salt of 2000 or 4000  $M_w$ , from the pristine 12 Å to the final 93 Å, and this was followed by BSA incorporation. By comparison, the direct incorporation of BSA into a clay interlayer was found to be relatively difficult, particularly for those micas with a larger platelet size. This stepwise process was performed at a suitable pH (less than the isoelectric point of 4.8 for BSA), at which point the protein structure was cationic ( $-\text{NH}_3^+/-\text{COOH}$ ); this proved to be ideal for the ionic-exchange intercalation with the counter ions in the silicate galleries. The stepwise intercalation can be generalized for embedding large biomolecules into the clay layer confinement. This synthetic methodology is considered to have practical applications, including biosensing for target molecular detection [112], as well as interface modification for drug delivery [113, 114] and tissue engineering [62, 115].



**Figure 14.14** Schematic representation of BSA intercalation into mica, via direct or step-wise processes [42].

## 14.10 Conclusions

The naturally abundant clays have been long recognized for their wide applications as catalysts, absorbents, metal-chelating agents, colloid stabilizers, and fillers for polymer composites. Recent developments in nanocomposite designs have required the preparation of organophilic clays, which may then become compatible with the ionic smectite clays. Since 2001, the present authors' group has explored tailoring of the basal spacing of the layered silicates, as well as the reaction profile and amphiphilic properties of these hybrids. By using a series of hydrophobic and hydrophilic POA-salts, it was possible to control the XRD basal spacing within the range of 20–92 Å and, for the first time, to observe a unique self-assembled morphology. During this time, the use of anionic LDH clays for a variety of applications, including gene therapy, has been suggested. With these spatially enlarged silicates, biomolecules such as proteins could be embedded in the clay gallery, which would retain its original size. It was also found that several comb-branched polyamines could randomize the layered structure into individual platelets. More recently, innovative families of polymer–clay hybrids have been identified with new properties of interfacial tension activity, compatibility to hydrophobic materials, and intensive affinity for biomacromolecules. It appears that the fundamental exploration of clay surface chemistry has in fact directed us towards a new horizon of biomedical research opportunities, including enzyme/drug encapsulation, wound surface anti-adhesives, and biosensors.



## References

- 1 Giannelis, E.P. (1996) *Adv. Mater.*, **8**, 29–35.
- 2 Utracki, L.A., Sepehr, M. and Boccaleri, E. (2007) *Polym. Adv. Technol.*, **18**, 1–37.
- 3 Alexandre, M. and Dubois, P. (2000) *Mater. Sci. Eng.*, **28**, 1–63.
- 4 Okada, A. and Usuki, A. (1995) *Mater. Sci. Eng. C*, **3**, 109–115.
- 5 Okada, A. and Usuki, A. (2006) *Macromol. Mater. Eng.*, **291**, 1449–1476.
- 6 Porter, D., Metcalfe, E. and Thomas, M.J.K. (2000) *Fire Mater.*, **24**, 45–52.
- 7 Wang, Z. and Pinnavaia, T.J. (1998) *Chem. Mater.*, **10**, 1820–1826.
- 8 Gilman, J.W. (1999) *Appl. Clay Sci.*, **15**, 31–49.
- 9 Theng, B.K.G. (1974) *The Chemistry of Clay-Organic Reactions*, 2nd edn, John Wiley & Sons, Inc., New York.
- 10 Van Olphen, H. (1977) *An Introduction to Clay Colloid Chemistry*, 2nd edn, John Wiley & Sons, Inc., New York.
- 11 Theng, B.K.G. (1979) *Formation and Properties of Clay-Polymer Complexes*, Elsevier, New York.
- 12 Triantafyllidis, C.S., LeBaron, P.C. and Pinnavaia, T.J. (2002) *Chem. Mater.*, **14**, 4088–4095.
- 13 Muzny, C.D., Butler, B.D., Hanley, H.J.M., Tsvetkov, F. and Peiffer, D.G. (1996) *Mater. Lett.*, **28**, 379–384.
- 14 Bohning, M., Goering, H., Fritz, A., Brzezinka, K.W., Turkey, G., Scholnhals, A. and Schartel, B. (2005) *Macromolecules*, **38**, 2764–2774.
- 15 Robello, D.R., Yamaguchi, N., Blanton, T. and Barnes, C. (2004) *J. Am. Chem. Soc.*, **126**, 8118–8119.
- 16 Tien, Y.I. and Wei, K.H. (2002) *J. Appl. Polym. Sci.*, **86**, 1741–1748.
- 17 Lepoittevin, B., Pantoustier, N., Alexandre, M., Calberg, C., Jerome, R. and Dubois, P. (2002) *J. Mater. Chem.*, **12**, 3528–3532.
- 18 Myskova, M.Z., Zelenka, J., Spacek, V. and Socha, F. (2003) *Macromol. Symp.*, **200**, 291–296.
- 19 Wang, M.S. and Pinnavaia, T.J. (1994) *Chem. Mater.*, **6**, 468–474.
- 20 Lan, T., Kaviratna, P.D. and Pinnavaia, T.J. (1996) *J. Phys. Chem. Sol.*, **57**, 1005–1010.
- 21 Ray, S.S. and Okamoto, M. (2003) *Prog. Polym. Sci.*, **28**, 1539–1641.
- 22 LeBaron, P.C., Wang, Z. and Pinnavaia, T.J. (1999) *Appl. Clay Sci.*, **15**, 11–29.
- 23 Giannelis, E.P. (1998) *Appl. Organomet. Chem.*, **12**, 675–680.
- 24 Zanetti, M., Lomakin, S. and Camino, G. (2000) *Macromol. Mater. Eng.*, **279**, 1–9.
- 25 Ishida, H., Campbell, S. and Blackwell, J. (2000) *Chem. Mater.*, **12**, 1260–1267.
- 26 Choy, J.H., Kwak, S.Y., Jeong, Y.J. and Park, J.S. (2000) *Angew. Chem. Int. Ed. Engl.*, **39**, 4041–4045.
- 27 Yi, Y., Wang, Y. and Liu, H. (2003) *Carbohydr. Polym.*, **53**, 425–430.
- 28 Fu, G., Vary, P.S. and Lin, C.T. (2005) *J. Phys. Chem. B*, **109**, 8889–8898.
- 29 Gu, L., Elkin, T., Jiang, X., Li, H., Lin, Y., Qu, L., Tzeng, T.R.J., Joseph, R. and Sun, Y.P. (2005) *Chem. Commun.*, 874–876.
- 30 Lin, J.J., Cheng, I.J., Wang, R. and Lee, R.J. (2001) *Macromolecules*, **34**, 8832–8834.
- 31 Lin, J.J., Cheng, I.J. and Chou, C.C. (2003) *Macromol. Rapid Commun.*, **24**, 492–495.
- 32 Chou, C.C., Shieu, F.S. and Lin, J.J. (2003) *Macromolecules*, **36**, 2187–2189.
- 33 Chou, C.C., Chang, Y.C., Chiang, M.L. and Lin, J.J. (2004) *Macromolecules*, **37**, 473–477.
- 34 Lin, J.J., Hsu, Y.C. and Chou, C.C. (2003) *Langmuir*, **19**, 5184–5187.
- 35 Lin, J.J. and Chen, Y.M. (2004) *Langmuir*, **20**, 4261–4264.
- 36 Lin, J.J., Chou, C.C. and Lin, J.L. (2004) *Macromol. Rapid Commun.*, **25**, 1109–1112.
- 37 Lin, J.J., Chu, C.C., Chou, C.C. and Shieu, F.S. (2005) *Adv. Mater.*, **17**, 301–304.
- 38 Lin, J.J., Chu, C.C., Chiang, M.L. and Tsai, W.C. (2006) *Adv. Mater.*, **18**, 3248–3252.
- 39 Chu, C.C., Chiang, M.L., Tsai, C.M. and Lin, J.J. (2005) *Macromolecules*, **38**, 6240–6243.
- 40 Chou, C.C. and Lin, J.J. (2005) *Macromolecules*, **38**, 230–233.

- 41 Lin, J.J., Chu, C.C., Chiang, M.L. and Tsai, W.C. (2006) *J. Phys. Chem. B*, **110**, 18115–18120.
- 42 Lin, J.J., Wei, J.C. and Tsai, W.C. (2007) *J. Phys. Chem. B*, **111**, 10275–10280.
- 43 Lin, J.J., Wei, J.C., Juang, T.Y. and Tsai, W.C. (2007) *Langmuir*, **23**, 1995–1999.
- 44 Cseri, T., Bekassy, S., Figueras, F. and Rizner, S. (1995) *J. Mol. Catal. A: Chem.*, **98**, 101–107.
- 45 Pinnavaia, T.J. (1983) *Science*, **220**, 365–371.
- 46 Ajjou, A.N., Harouna, D., Detellier, C. and Alper, H. (1997) *J. Mol. Catal. A: Chem.*, **126**, 55–60.
- 47 Celis, R., Hermosin, M.C., Carrizosa, M.J. and Cornejo, J. (2002) *J. Agric. Food Chem.*, **50**, 2324–2330.
- 48 Rawajfih, Z. and Nsour, N. (2006) *J. Colloid Interface Sci.*, **298**, 39–49.
- 49 Kiraly, Z., Veisz, B., Mastalir, A. and Kofarago, G. (2001) *Langmuir*, **17**, 5381–5387.
- 50 Usuki, A., Hasegawa, N., Kadoura, H. and Okamoto, T. (2001) *Nano. Lett.*, **1**, 271–272.
- 51 Sparks, D.L. (2003) *Environmental Soil Chemistry*, John Wiley & Sons, Ltd.
- 52 Wang, H., Zhao, T., Zhi, L., Yan, Y. and Yu, Y. (2002) *Macromol. Rapid Commun.*, **23**, 44–48.
- 53 Tateyama, H., Nishimura, S., Tsunematsu, K., Jinnai, K., Adachi, Y. and Kimura, M. (1992) *Clays Clay Miner.*, **40**, 180–185.
- 54 Kodama, T., Higuchi, T., Shimizu, T., Shimizu, K., Komarneni, S., Hoffbauer, W. and Schneider, H. (2001) *J. Mater. Chem.*, **11**, 2072–2077.
- 55 Rives, V. and Ulibarri, M.A. (1999) *Coord. Chem. Rev.*, **181**, 61–120.
- 56 Rives, V. (2002) *Mater. Chem. Phys.*, **75**, 19–25.
- 57 Khan, A.I. and O'Hare, D. (2002) *J. Mater. Chem.*, **12**, 3191–3198.
- 58 Aisawa, S., Takahashi, S., Ogasawara, W., Umetsu, Y. and Narita, E. (2001) *J. Solid State Chem.*, **162**, 52–62.
- 59 Iyi, N., Kurachima, K. and Fujita, T. (2002) *Chem. Mater.*, **14**, 583–589.
- 60 Choy, J.H., Kwak, S.Y., Park, J.S., Jeong, Y.J. and Portier, J. (1999) *J. Am. Chem. Soc.*, **121**, 1399–1400.
- 61 Leroux, F. and Besse, J.P. (2001) *Chem. Mater.*, **13**, 3507–3515.
- 62 Sels, B., Vos, D.D., Buntinx, M., Pierard, F., Mesmaeker, A.K.D. and Jacobs, P. (1999) *Nature*, **400**, 855–857.
- 63 Whilton, N.T., Vickers, P.J. and Mann, S. (1997) *J. Mater. Chem.*, **7**, 1623–1629.
- 64 Lin, J.J. and Juang, T.Y. (2004) *Polymer*, **45**, 7887–7893.
- 65 Chou, C.C., Chiang, M.L. and Lin, J.J. (2005) *Macromol. Rapid Commun.*, **26**, 1841–1845.
- 66 Beyer, F.L., Tan, N.C.B., Dasgupta, A. and Galvin, M.E. (2002) *Chem. Mater.*, **14**, 2983–2988.
- 67 Ha, Y.H., Kwon, Y., Breiner, T., Chan, E.P., Tzianetopoulou, T., Cohen, R.E., Boyce, M.C. and Thomas, E.L. (2005) *Macromolecules*, **38**, 5170–5179.
- 68 Kurian, M., Dasgupta, A., Galvin, M.E., Ziegler, C.R. and Beyer, F.L. (2006) *Macromolecules*, **39**, 1864–1871.
- 69 Yang, Y., Zhu, Z.K., Yin, J., Wan, X.Y. and Qi, Z.E. (1999) *Polymer*, **40**, 4407–4414.
- 70 Maiti, M., Bandyopadhyay, A. and Bhowmick, A.K. (2006) *J. Appl. Polym. Sci.*, **99**, 1645–1656.
- 71 Subramani, S., Lee, J.Y., Choi, S.W. and Kim, J.H. (2007) *J. Polym. Sci. B: Polym. Phys.*, **45**, 2747–2761.
- 72 Bourlinos, A.B., Jiang, D.D. and Giannelis, E.P. (2004) *Chem. Mater.*, **16**, 2404–2410.
- 73 Hotta, Y., Taniguchi, M., Inukai, K. and Yamagishi, A. (1996) *Langmuir*, **12**, 5195–5201.
- 74 Wang, K., Wang, L., Wu, J., Chen, L. and He, C. (2005) *Langmuir*, **21**, 3613–3618.
- 75 Szabo, A., Gournis, D., Karakassides, M.A. and Petridis, D. (1998) *Chem. Mater.*, **10**, 639–645.
- 76 Hotta, Y., Inukai, K., Taniguchi, M., Nakata, M. and Yamagishi, A. (1997) *Langmuir*, **13**, 6697–6703.
- 77 Byun, H.Y., Choi, M.H. and Chung, I.J. (2001) *Chem. Mater.*, **13**, 4221–4226.
- 78 Beatty, A.M., Granger, K.E. and Simpson, A.E. (2002) *Chem. Eur. J.*, **8**, 3254–3259.
- 79 Malakul, P., Srinivasan, K.R. and Wang, H.Y. (1998) *Ind. Eng. Chem. Res.*, **37**, 4296–4301.

- 80 Choi, Y.S., Choi, M.H., Wang, K.H., Kim, S.O., Kim, Y.K. and Chung, I.J. (2001) *Macromolecules*, **34**, 88978–88985.
- 81 Mahadevaiah, N., Venkataramani, B. and Prakash, B.S.J. (2007) *Chem. Mater.*, **19**, 4606–4612.
- 82 Vaia, R.A., Teukolsky, R.K. and Giannelis, E.P. (1994) *Chem. Mater.*, **6**, 1017–1022.
- 83 Hotta, S. and Paul, D.R. (2004) *Polymer*, **45**, 7639–7654.
- 84 Zeng, C. and Lee, L.J. (2001) *Macromolecules*, **34**, 4098–4103.
- 85 Fu, X. and Qutubuddin, S. (2001) *Polymer*, **42**, 807–813.
- 86 Fu, X. and Qutubuddin, S. (2000) *Mater. Lett.*, **42**, 12–15.
- 87 Imai, Y., Nishimura, S., Abe, E., Tateyama, H., Abiko, A., Yamaguchi, A., Aoyama, T. and Taguchi, H. (2002) *Chem. Mater.*, **14**, 477–479.
- 88 Chang, J.H., Jang, T.G., Ihn, K.J., Lee, W.K. and Sur, G.S. (2003) *J. Appl. Polym. Sci.*, **90**, 3208–3214.
- 89 Kim, M.H., Park, C.I., Choi, W.M., Lee, J.W., Lim, J.G., Park, O.O. and Kim, J.M. (2004) *J. Appl. Polym. Sci.*, **92**, 2144–2150.
- 90 Ijdo, W.L. and Pinnavaia, T.J. (1999) *Chem. Mater.*, **11**, 3227–3231.
- 91 Maiti, P., Yamada, K., Okamoto, M., Ueda, K. and Okamoto, K. (2002) *Chem. Mater.*, **14**, 4654–4661.
- 92 Xie, W., Xie, R., Pan, W.P., Hunter, D., Koene, B., Tan, L.S. and Vaia, R. (2002) *Chem. Mater.*, **14**, 4837–4845.
- 93 Bottino, F.A., Fabbri, E., Fragala, I.L., Malandrino, G., Orestano, A., Pilati, F. and Pollicino, A. (2003) *Macromol. Rapid Commun.*, **24**, 1079–1084.
- 94 Fox, D.M., Maupin, P.H., Harris, R.H. Jr., Gilman, J.W., Eldred, D.V., Katsoulis, D., Trulove, P.C. and DeLong H.C. (2007) *Langmuir*, **23**, 7707–7714.
- 95 Wang, Z.M., Chung, T.C., Gilman, J.W. and Manias, E. (2003) *J. Polym. Sci., B: Polym. Phys.*, **41**, 3173–3187.
- 96 Gilman, J.W., Awad, W.H., Davis, R.D., Shields, J., Harris, R.H. Jr., Davis, C., Morgan, A.B., Sutto, T.E., Callahan, J., Trulove, P.C. and DeLong, H.C. (2002) *Chem. Mater.*, **14**, 3776–3785.
- 97 Wang, D. and Wilkie, C.A. (2003) *Polym. Degrad. Stab.*, **82**, 309–315.
- 98 Greenwell, H.C., Harvey, M.J., Boulet, P., Bowden, A.A., Coveney, P.V. and Whiting, A. (2005) *Macromolecules*, **38**, 6189–6200.
- 99 Moss, P.H. (1964) Nickel-Copper-Chromia catalyst and the preparation thereof. US Patent 3, 152, 998.
- 100 Yeakey, E.L. (1972) Process for preparing polyoxyalkylene polyamines. US Patent 3, 654, 370.
- 101 Chang, Y.C., Chou, C.C. and Lin, J.J. (2005) *Langmuir*, **21**, 7023–7028.
- 102 Lin, J.J., Hsu, Y.C. and Wei, K.L. (2007) *Macromolecules*, **40**, 1579–1584.
- 103 Lin, J.J., Chang, Y.C. and Cheng, I.J. (2004) *Macromol. Rapid Commun.*, **25**, 508–512.
- 104 Lin, J.J., Chen, Y.M. and Yu, M.H. (2007) *Colloids Surf. A: Physicochem. Eng. Aspects*, **302**, 162–167.
- 105 Shan, D., Yao, W. and Xue, H. (2006) *Electroanalysis*, **18**, 1485–1491.
- 106 Zhou, Y., Hu, N., Zeng, Y. and Rusling, J.F. (2002) *Langmuir*, **18**, 211–219.
- 107 Kelleher, B.P., Oppenheimer, S.F., Han, F.X., Willeford, K.O., Simpson, M.J., Simpson, A.J. and Kingery, W.L. (2003) *Langmuir*, **19**, 9411–9417.
- 108 Baron, M.H., Revault, M., Servagent-Noinville, S., Abadie, J. and Quiquampoix, H. (1999) *J. Colloid Interface Sci.*, **214**, 319–332.
- 109 Naidja, A., Huang, P.M. and Bollag, J.M. (1997) *J. Mol. Catal. A: Chem.*, **115**, 305–316.
- 110 Causserand, C., Kara, Y. and Aimar, P. (2001) *J. Membr. Sci.*, **186**, 165–181.
- 111 Cristofaro, A.D. and Violante, A. (2001) *Appl. Clay Sci.*, **19**, 59–67.
- 112 Lvov, Y., Ariga, K., Ichinose, I. and Kunitake, T. (1995) *J. Am. Chem. Soc.*, **117**, 6117–6123.
- 113 Liu, Y.L., Hsu, C.Y., Su, Y.H. and Lai, J.Y. (2005) *Biomacromolecules*, **6**, 368–373.
- 114 Mezziani, M.J. and Sun, Y.P. (2003) *J. Am. Chem. Soc.*, **125**, 8015–8018.
- 115 Wang, Q., Gao, Q. and Shi, J. (2004) *J. Am. Chem. Soc.*, **126**, 14346–14347.

## 15 Mesoporous Alumina: Synthesis, Characterization, and Catalysis

*Tsunetake Seki and Makoto Onaka*

### 15.1

#### Introduction

The pore structure is one of the most important properties of heterogeneous catalysts that govern their activity, selectivity, and lifetime. Notably, not only the surface reactivity but also the mass transfer of reactants and products can be tuned by modifying the pore structure. Owing to the size of most reactant molecules capable of access to the internal surfaces, the values of pore diameter that are of most interest to catalyst chemists are the orders of nanometers, with a range of approximately 0 to 50 nm. By definition, the pores in this range are classified into two groups: “micropore,” with a diameter  $<2$  nm; and “mesopore,” with diameters in the range of 2 to 50 nm [1]. Since the mid-twentieth century, a large family of aluminosilicates known as zeolites have been synthesized and used as catalysts with regularly arrayed micropores [2]. On the other hand, the development of oxide frameworks with pore diameters within the mesoporous range lagged far behind, due to difficulties in their synthesis. In fact, such ordered mesoporous materials were not created successfully until 1992, when a team at the Mobil Research and Development Corporation first reported the successful synthesis of silica-based mesoporous molecular sieves (M41S) via a liquid crystal template (LCT) mechanism, where the surfactant liquid crystal phases served as the organic templates [3]. Since then, investigations to prepare organized mesoporous molecular sieves have been conducted not only for silica/aluminosilicate materials but also for oxides of Mg, Ti, Nb, Ta, and Al [4, 5]. For this, the electrostatic interaction between positively charged surfactants ( $S^+$ ) and negatively charged inorganic precursors ( $I^-$ ), charge-reversed interactions ( $S^- I^+$ ), counterion-mediated interactions ( $S^- M^+ I^-$  and  $S^+ X^- I^+$ ;  $M^+$  = metal cation,  $X^- = Cl^-, Br^-$ ), and neutral interactions ( $S^0 I^0$  and  $N^0 I^0$ ;  $N$  = nonionic organics) were used to assemble series of ordered mesopores [6].

Because of their high surface areas and strong adsorption abilities, aluminas with various morphologies have been widely used as catalysts and catalyst supports, both in the laboratory and in industry [7]. It seems natural, therefore, that

catalyst chemists would be prompted to investigate the behavior of these newly synthesized aluminas with uniform mesopores in a variety of catalytic reactions. The most likely major advantage of using mesoporous aluminas in catalytic reactions is that the regular mesoporous structures, which do not contain micropores, are free from the pore-plug problems caused by the formation of coke and other polymerized byproducts [8]. These problems, which have often been observed in catalysis by conventional aluminas, include a decrease in the surface areas and a disturbance of the diffusion of reactants and products within the porous networks. One other advantage includes the modification of surface reactivity by creating a uniform mesopore structure within the alumina. A warped bulk structure in mesoporous alumina may generate a unique surface reactivity (e.g., acidity and basicity) that is considerably different from that of normal alumina, and provides the opportunity to adjust the adsorption characteristics to optimum values by altering the mesopore sizes.

In this chapter, attention is focused on those aluminas with a regular mesoporosity, together with details of their synthesis and examples of their uses in catalytic reactions. In addition, a reference base of information up to early 2007 is included. Comparisons with conventional aluminas are frequently noted in order to emphasize the utility of mesoporous alumina as a catalytic material.

## 15.2

### Synthesis of Mesoporous Alumina

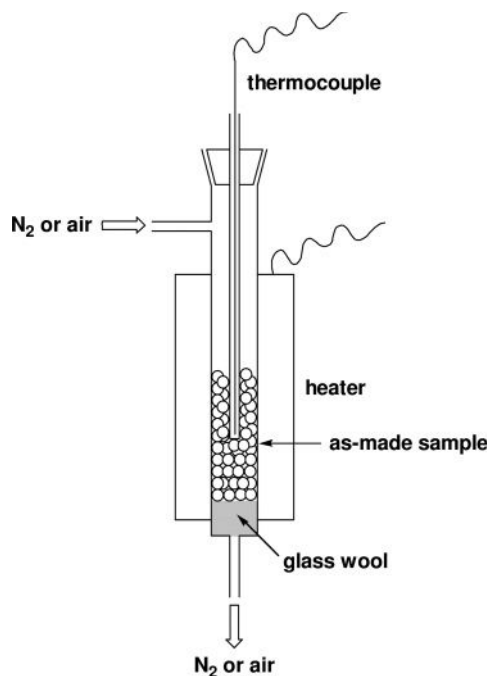
#### 15.2.1

##### Experimental Techniques

###### 15.2.1.1 Synthesis

The initial stage of mesoporous alumina synthesis is the hydrolysis of aluminum precursors in the presence of a template (a structure-directing agent) in a solvent to afford a precipitate or gel material; this material is subsequently filtered out, washed, and dried to provide the as-made material. It should be noted that special care is required when using water for any purpose in these procedures, as this may lead to a serious structural collapse of the samples. It is recommended, therefore, that anhydrous ethanol or propanols be used in any washing processes [9]. Moreover, when aluminum alkoxides are used as precursors, care must be taken when deciding on the amount of water required for the hydrolyses, as well as how the water should be contacted with the aluminum precursors, since the very rapid hydrolyses may proceed without being influenced by the template.

The as-made products are organic/inorganic biphasic composite materials in which the assembly of a hydrophobic group of templates helps to create the cylindrical inorganic walls. The template group is, on the other hand, adsorbed onto the surface of the inorganic walls by various interactions, including electrically neutral and electrostatic interactions. The most reliable way of removing the



**Figure 15.1** Apparatus for calcination of the as-made samples with organic/inorganic biphasic. Quartz-made glass should be used for the tubular vessel, due to its high thermal stability.

adsorbed templates is to burn off the organic phase by calcination in air; this also promotes dehydration of the inorganic wall, transforming the framework from aluminum hydroxide to aluminum oxide (alumina). An example of the apparatus suitable for the calcination of as-made samples is shown in Figure 15.1. This flow system allows a choice of calcination atmosphere simply by changing the type of flow gas. A muffle oven can also be used if the calcination steps are to be performed under air. The required temperature for burning off the adsorbed template molecules depends on the strength of the interaction between the molecules and the inorganic walls. Thus, whilst calcination can be carried out at lower temperatures for nonionic templates, any ionic templates that are strongly adsorbed onto the inorganic wall will require higher temperatures for their removal. It should be noted that increasing the calcination temperature will enhance removal of the templates, but also result in a structural collapse by sintering. Consequently, the use of templates that bond too strongly to the inorganic surface should be avoided. Some groups have experienced problems in removing the sulfate or sulfonate surfactants, whereby substantial amounts of sulfur and organic residues remained (even at calcination temperature) that caused the mesostructure to collapse [5b, 10].

### 15.2.1.2 Characterization

The structural properties of mesoporous alumina can be evaluated by  $N_2$  adsorption–desorption, powder X-ray diffraction (XRD), transmission electron microscopy (TEM), scanning electron microscopy (SEM), and  $^{27}\text{Al}$  magic angle spinning nuclear magnetic resonance (MAS-NMR) spectroscopy. The  $N_2$  adsorption–desorption method represents a powerful tool for characterizing the shape of mesoporous alumina. In Figure 15.2 the type IV isotherm is shown [11], which is typically observed for aluminas with organized mesopores.

The large uptake in the lowest partial pressure ( $P/P_0$ ) region is caused by a monolayer coverage of the surface, followed by a steep increase in adsorbed volume in the  $P/P_0$  range of 0.4–0.8, which corresponds to the filling of the mesopores. In the latter  $P/P_0$  region, the adsorption isotherm usually does not conform to the desorption isotherm, giving rise to a hysteresis loop which may be accounted for by the presence of ink-bottle-like mesopores [12]. A further increase in  $P/P_0$  leads to no further adsorption, which is represented by a horizontal plateau in the isotherm. In contrast, an additional steep increase is observed by the multilayer adsorption for the low-quality samples containing larger mesopores (i.e., pore diameter  $>8$  nm) and macropores. By applying the  $N_2$  adsorption–desorption data to the appropriate theories, it is possible to obtain the values of surface area, pore diameter, and pore volume. The Brunauer–Emmett–Teller (BET) method has been used for calculation of the surface areas [13], whilst values of pore diameter and pore volume have been calculated using the Barrett–Joyner–Halenda (BJH) or Dollimore–Heal (DH) methods [14, 15]. The Horváth–Kawazoe model, which was employed in the characterization of M41S by Beck and coworkers [3b], is not recommended because the model can give overestimated pore sizes [5a]. Čejka *et al.*, on the other hand, attempted to calculate the surface area and mesopore volume by employing a comparison plot in which the adsorption isotherm  $a(P/P_0)$  of a mesoporous alumina sample was transformed to a function  $a(a_{\text{ref}})$  of the amount  $a_{\text{ref}}$  adsorbed on a nonporous reference solid (Degussa Aluminiumoxid

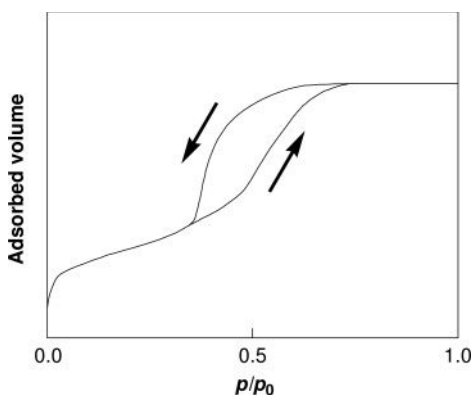


Figure 15.2 Type IV isotherm typically observed for mesoporous alumina.

C) at the same relative pressure [16]. The values obtained agreed well with those determined with the BET and BJH methods.

**Powder X-Ray Diffraction** Powder XRD provides information concerning the pore and framework structure. The recommendation is to use chromium as an X-ray source because of its longer wavelength compared to the more commonly used copper or cobalt [9]. Aluminas with a regular mesoporous structure usually exhibit a single intense diffraction line at a low-angle region ( $2\theta = 1\text{--}2^\circ$ ) without further diffraction lines, indicating a hexagonal or cubic symmetry. The position of the line is shifted to a lower angle for samples with larger pore sizes, and also when the sintering of a sample is promoted by calcination at higher temperatures. It should be noted that the appearance of this single diffraction line is not sufficient evidence for the presence of organized mesopores [5n]. Other approaches, including  $N_2$  adsorption–desorption measurements and TEM imaging, are also indispensable when discussing the quality of mesopores. The framework structure of a sample may be elucidated via the XRD pattern of the wide-angle region ( $2\theta = 10\text{--}80^\circ$ ). The detailed assignment of the XRD diffraction lines to the framework structures was described by Yanagida *et al.* [17].

**Transmission Electron Microscopy (TEM)** TEM enables a direct observation of the pore size and long-range channel order. In marked contrast to the long-range hexagonal arrangement of channels observed for MCM-41 [3], the mesoporous aluminas developed to date have exhibited a regular sponge- or worm-like channel motif, without any discernible long-range order.

**$^{27}\text{Al}$  MAS NMR Spectroscopy** This procedure provides information regarding the coordination number of aluminum in mesoporous alumina. When using this method, six-, five-, and four-coordinate aluminum centers produce a peak at  $\delta = \text{ca. } 0, 35, \text{ and } 75$ , respectively, although in some cases the peak from the five-coordinate form is invisible due to its low intensity. It is noteworthy that the ratio of four- and six-coordinate Al estimated via the NMR spectrum of a sample may provide evidence that the framework has a  $\gamma$ -phase structure [5i].

### 15.2.2

#### Examples of Synthesis

An early review introducing the synthetic methods of mesoporous alumina was provided by Čejka, and included those reports made up until 2002 [9]. Čejka classified the methods into three groups—namely neutral, anionic, and cationic synthesis—according to the type of electric state of the surfactant, while others used the abbreviations, *S* (surfactant), *I* (inorganic precursors), *N* (nonionic organics), with their electric charges, +, −, and 0, to express the synthetic pathways of mesophases [6]. Even though the electric charge of the surfactant is known, the detailed structure of the inorganic moiety that interacts with the surfactant has, in most cases, not been elucidated in published reports that describe mesoporous alumina



synthesis. For this reason, the synthetic methods are classified here as four groups, focusing only on the electric charge of the surfactant side: (i) neutral surfactant templating; (ii) anionic surfactant templating; (iii) cationic surfactant templating; and (iv) nonsurfactant templating. An overview of the various syntheses of mesoporous alumina is provided in Table 15.1.

#### 15.2.2.1 Neutral Surfactant Templating

The synthesis of mesoporous alumina using electrically neutral surfactant templates was first developed in 1996 by Bagshaw and Pinnavaia, who used poly(ethylene oxide)s (PEOs) or PEO/poly(propylene oxide) (PPO) copolymers as surfactant templates [5a]. The former templates involve the use of Tergitol® 15-S-9 with a formula of  $C_{11-15}[PEO]_9$ , while the latter templates involve Pluronic® L64 with a formula of  $[PEO]_{13}[PPO]_{30}[PEO]_{13}$ . In the presence of the surfactant, an aluminum source of aluminum *sec*-butoxide was hydrolyzed in 2-butanol solvent to give the as-synthesized surfactant–alumina mesophase. This was subsequently washed with ethanol, dried, and calcined at 500 °C to afford the mesoporous aluminas (denoted MSU-X, where X = 1–3 depending on the type of surfactant). The XRD reflections of the MSU-X aluminas at 1–3° (of which the intensity became large after calcination) were broad, signifying a greater degree of structural disorder compared to the disordered MCM-41, HMS, and MSU-X silicas (Figure 15.3).

Subsequent TEM images of the calcined MSU-X aluminas highlighted the regular wormlike channel motif in which the diameters of pores were more or less uniform (Figure 15.4). However, no discernible long-range order was observed, which was indicative of the randomness of packing of the channel system.

Characterization by  $N_2$  adsorption–desorption measurements showed hystereses in the isotherms of the MSU-X aluminas that had resulted from the condensation of  $N_2$  in the mesopores, and afforded pore diameters in the range of 2.4 to 4.7 nm, as estimated by the BJH model and in agreement with values obtained from TEM images (Figure 15.5). It was found that, on the basis of the BJH pore-sizes and the  $d_{100}$  values, a larger surfactant tended to give a longer pore diameter.

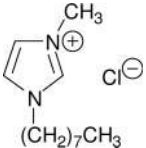
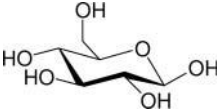
The MSU-X aluminas were also characterized using  $^{27}Al$  MAS NMR spectroscopy, which provides information concerning the coordination environment of aluminum (Figure 15.6). Three peaks appeared for both the as-synthesized and calcined samples at  $\delta$  0, 35, and 75, and these were attributed to the six-, five-, and four-coordinate aluminum centers, respectively. However, the calcination increased the peak intensities at  $\delta$  35 and 75 and decreased the intensity of the  $\delta$  0 peak through an enhancement of the dehydration and dehydroxylation.

In a succeeding study, the same group attempted to improve the thermal stability of the MSU-X aluminas by doping with rare earth ions such as  $Ce^{3+}$  and  $La^{3+}$  [5c]. In this case, the hydrolysis for the surfactant–alumina mesophase formation was performed in the presence of the corresponding rare earth nitrate. A PEO-based surfactant of Tergitol® 15-S-12 was used for synthesis of the  $Ce^{3+}$ -doped mesoporous alumina, while a PEO/PPO copolymer surfactant of Pluronic® P65 or P123 was employed for the  $La^{3+}$ -doping. The isotherms, BJH pore-sizes, XRD

**Table 15.1** Overview of representative synthetic methods of mesoporous alumina.

Mesoporous alumina denotation	Aluminum source (solvent)	Template: name; formula <sup>a</sup>	Surface area <sup>b</sup> (m <sup>2</sup> g <sup>-1</sup> )	Pore diameter <sup>c</sup> (nm)	Pore volume (ml g <sup>-1</sup> )	Reference(s)
I. Neutral surfactant templating						
MSU-1	Al[OCH(CH <sub>3</sub> )CH <sub>2</sub> CH <sub>3</sub> ] <sub>3</sub> (2-Butanol)	Tergitol <sup>®</sup> 15-S-9; C <sub>11-15</sub> [PEO] <sub>9</sub>	490	3.3	0.40	[5a, 5c]
MSU-2	Al[OCH(CH <sub>3</sub> )CH <sub>2</sub> CH <sub>3</sub> ] <sub>3</sub> (2-Butanol)	Triton <sup>®</sup> X-114; C <sub>8</sub> Ph[PEO] <sub>8</sub>	460	3.3	0.35	[5a, 5c]
MSU-3	Al[OCH(CH <sub>3</sub> )CH <sub>2</sub> CH <sub>3</sub> ] <sub>3</sub> (2-Butanol)	Pluronic <sup>®</sup> L64; [PEO] <sub>13</sub> [PPO] <sub>30</sub> [PEO] <sub>13</sub>	430	2.4	0.21	[5a, 5c]
MSU-γ	[Al <sub>13</sub> O <sub>4</sub> (OH) <sub>24</sub> (H <sub>2</sub> O) <sub>12</sub> ]Cl <sub>7</sub> (Water)	Pluronic <sup>®</sup> P84; [PEO] <sub>19</sub> [PPO] <sub>39</sub> [PEO] <sub>19</sub>	299	6.4	0.73	[5i]
MSU-γ	Al[OCH(CH <sub>3</sub> )CH <sub>2</sub> CH <sub>3</sub> ] <sub>3</sub> (2-Butanol)	Pluronic <sup>®</sup> P84; [PEO] <sub>19</sub> [PPO] <sub>39</sub> [PEO] <sub>19</sub>	306	9.0	1.15	[5i]
DL12	Al(NO <sub>3</sub> ) <sub>3</sub> (Water; pH = 7.01)	Poly(ethylene glycol) 1540; HO-(CH <sub>2</sub> CH <sub>2</sub> -O) <sub>1540</sub> -H	203	6.6	0.33	[5m]
DL54	Al <sub>2</sub> (SO <sub>4</sub> ) <sub>3</sub> (Water; pH = 10.0)	Poly(ethylene glycol) 1540; HO-(CH <sub>2</sub> CH <sub>2</sub> -O) <sub>1540</sub> -H	309	6.3	Not reported	[5m]
II. Anionic surfactant templating						
C <sub>A383</sub>	Al[OCH(CH <sub>3</sub> )CH <sub>2</sub> CH <sub>3</sub> ] <sub>3</sub> (1-Propanol)	Caproic acid; C <sub>5</sub> H <sub>11</sub> COOH	530	2.1	0.31	[5b]
L <sub>A383</sub>	Al[OCH(CH <sub>3</sub> )CH <sub>2</sub> CH <sub>3</sub> ] <sub>3</sub> (1-Propanol)	Lauric acid; C <sub>11</sub> H <sub>23</sub> COOH	710	1.9	0.41	[5b]
S <sub>A383</sub>	Al[OCH(CH <sub>3</sub> )CH <sub>2</sub> CH <sub>3</sub> ] <sub>3</sub> (1-Propanol)	Stearic acid; C <sub>17</sub> H <sub>35</sub> COOH	700	2.1	0.41	[5b]

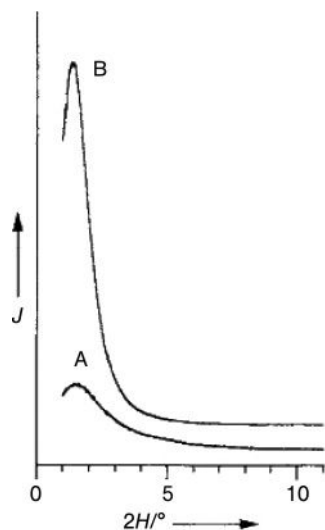
Table 15.1 Continued.

Mesoporous alumina denotation	Aluminum source (solvent)	Template: name; formula <sup>a</sup>	Surface area <sup>b</sup> (m <sup>2</sup> g <sup>-1</sup> )	Pore diameter <sup>c</sup> (nm)	Pore volume (ml g <sup>-1</sup> )	Reference(s)
III. Cationic surfactant templating						
ICMUV-1	Al[OCH(CH <sub>3</sub> )CH <sub>2</sub> CH <sub>3</sub> ] <sub>3</sub> (Triethanolamine)	Cetyltrimethylammonium bromide; CH <sub>3</sub> (CH <sub>2</sub> ) <sub>15</sub> N(CH <sub>3</sub> ) <sub>3</sub> <sup>+</sup> Br <sup>-</sup>	250–340	3.3–6.0	Not reported	[5d]
I, II	Al <sub>2</sub> Cl(OH) <sub>5</sub> (Water)	1-Methyl-3-octylimidazolium chloride; 	262–269	3.8–3.9	0.25–0.26	[5n]
IV. Nonsurfactant templating						
Al-TUD-1	Al[OCH(CH <sub>3</sub> ) <sub>2</sub> ] <sub>3</sub> (Ethanol and 2-propanol)	Tetra(ethylene glycol); HO(CH <sub>2</sub> CH <sub>2</sub> O) <sub>3</sub> CH <sub>2</sub> CH <sub>2</sub> OH	528	4.0	0.63	[5j]
Al <sub>2</sub> O <sub>3</sub> -X (X = 1–3)	Al[OCH(CH <sub>3</sub> ) <sub>2</sub> ] <sub>3</sub> (Water; pH = 4.5–5.5)	D-Glucose; 	337–422	3.8–5.1	0.43–0.66	[5k]
ID 7	Boehmite sol (Water)	Citric acid; HOC(COOH)(CH <sub>2</sub> COOH) <sub>2</sub>	320	4.1	0.44	[5l]

<sup>a</sup> Abbreviations: PEO, poly(ethylene oxide); PPO, poly(propylene oxide).

<sup>b</sup> Determined by the Brunauer–Emmett–Teller (BET) method.

<sup>c</sup> Determined by the Barrett–Joyner–Halender (BJH) method.

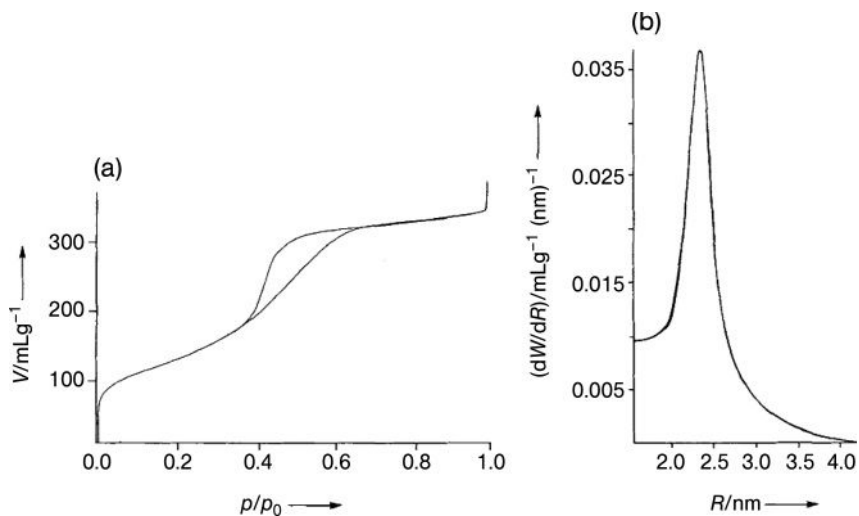


**Figure 15.3** Powder X-ray diffraction patterns of the MSU-3 alumina prepared with a surfactant of Pluronic® L64. The intensity  $I$  is in arbitrary units. Spectrum A represents the as-synthesized sample after air drying at room temperature for 16 h. Spectrum B represents the sample calcined at 500 °C in air for 6 h. Reprinted with permission from Ref. [5a].

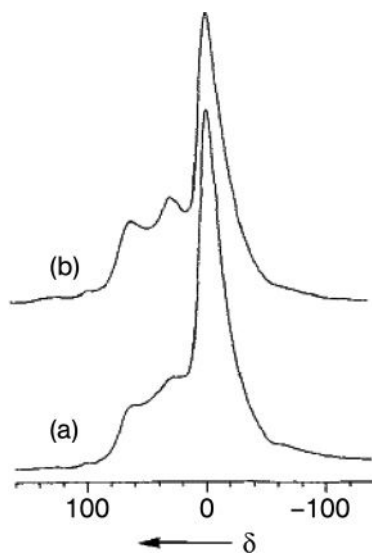


**Figure 15.4** Transmission electron microscopy image of the MSU-1 alumina prepared with a surfactant of Tergitol® 15-S-9 and calcined at 500 °C. Scale bar = 60 nm. Reprinted with permission from Ref. [5a].

basal spacings, and wormhole TEM images of the rare earth-stabilized MSU-X aluminas were equivalent to those observed for the pure MSU-X aluminas, which demonstrated that the incorporation of rare earth ions had not altered the original mesopore structures. However, the surface area after calcination at 500 or 600 °C was 35% higher for the 5 mol%  $\text{Ce}^{3+}$ -stabilized MSU-1 alumina than for the pure MSU-1 alumina. In addition, the 1 mol%  $\text{La}^{3+}$ -stabilized mesostructures formed



**Figure 15.5** (a)  $N_2$  adsorption–desorption isotherms for the MSU-3 alumina prepared with a surfactant of Pluronic® L64 and calcined at  $500^\circ\text{C}$  in air for 4 h; (b) BJH pore-size distribution determined from the  $N_2$  adsorption isotherm. Reprinted with permission from Ref. [5a].



**Figure 15.6**  $^{27}\text{Al}$  MAS NMR spectra of the MSU-3 alumina prepared with a surfactant of Pluronic® L64. Spectrum A represents the as-synthesized sample after air drying at room temperature for 16 h. Spectrum B represents the sample calcined at  $500^\circ\text{C}$  in air for 4 h. The chemical shifts are referenced to external  $[\text{Al}(\text{H}_2\text{O})_6]^{3+}$ . Reprinted with permission from Ref. [5a].

by the Pluronic surfactants also exhibited high surface areas after calcination at 500°C. The authors suggested that the incorporation of rare earth cations into the oxide framework took place during the assembly process of the mesostructures (but not during the calcination process), and that the site substitution of aluminum cations by rare earth cations reduces the lability of the oxide framework. These successes in increasing the thermal stability should greatly extend the potential applications of the MSU-X aluminas to catalytic reactions. González-Peña *et al.* later reported that thermally stable mesoporous aluminas could also be obtained by adding dipropylamine during formation of the surfactant–alumina mesophase [5f].

The synthesis of  $\gamma$ -Al<sub>2</sub>O<sub>3</sub> with mesostructured forms (denoted MSU- $\gamma$ ) was also accomplished with the neutral surfactants by the group led by Pinnavaia [5i]. The key to synthesizing these mesostructured aluminas composed of  $\gamma$ -Al<sub>2</sub>O<sub>3</sub> walls was the formation of a mesostructured surfactant/boehmite precursor (denoted MSU-S/B). The MSU-S/B (the structure of which was elucidated by XRD) could be formed by the hydrolysis of [Al<sub>13</sub>O<sub>4</sub>(OH)<sub>24</sub>(H<sub>2</sub>O)<sub>12</sub>]Cl<sub>7</sub>, AlCl<sub>3</sub>, or Al(O-*sec*-Bu)<sub>3</sub> in the presence of a PEO/PPO copolymer surfactant such as Pluoronic® P84, P123, and L64 with a formula of [PEO]<sub>19</sub>[PPO]<sub>39</sub>[PEO]<sub>19</sub>, [PEO]<sub>20</sub>[PPO]<sub>69</sub>[PEO]<sub>20</sub>, and [PEO]<sub>13</sub>[PPO]<sub>30</sub>[PEO]<sub>13</sub>, respectively. Calcination of the MSU-S/B precursors at 550°C afforded the MSU- $\gamma$  aluminas, and their  $\gamma$ -Al<sub>2</sub>O<sub>3</sub> walls were well-characterized by XRD, TEM, electron diffraction (ED), and <sup>27</sup>Al MAS NMR analysis. On the other hand, the XRD patterns in the small-angle region, N<sub>2</sub> adsorption–desorption isotherms, and BJH pore-size distributions of the MSU- $\gamma$  aluminas were those typically observed for mesoporous materials. A TEM image of the MSU- $\gamma$  alumina obtained through the hydrolysis of Al(O-*sec*-Bu)<sub>3</sub> in 2-butanol as solvent indicated that the nanoparticles were assembled into a scaffold-like array, whereas for those aluminas prepared from the Al<sub>13</sub> oligomer and AlCl<sub>3</sub> in aqueous media, parallel arrays were observed which gave a hierarchical, sheet-like morphology. The MSU- $\gamma$  alumina from the alkoxide had thicker and longer nanoparticles and a larger pore size and pore volume compared to those from the other aluminum sources. The pore size of the MSU- $\gamma$  aluminas was also correlated with the size of surfactant, indicative of the presence of the surfactant-induced assembly process of nanoparticles during the synthesis.

Zhao *et al.* investigated the effect of the addition of poly(ethylene glycol) (PEG) on the traditional precipitation synthesis using aluminum nitrate or sulfate and ammonium carbonate as an aluminum source and a precipitator, respectively [5m]. PEG 1540 was first mixed with an aqueous solution of aluminum nitrate or sulfate, followed by the slow addition of ammonium carbonate, an adjustment of the pH of the mixture using ammonia, and aging. Subsequent filtration, washing with water, and drying yielded the as-made material, which was calcined at 550°C in air to give the mesoporous alumina denoted DL12. A comparison of the TEM image of DL12 with that of the alumina synthesized in the absence of PEG showed that both materials exhibited a similar wormhole channel motif without any long-range order in their pore structure. The authors concluded that the PEG had not acted as a template in the synthesis process, and that the mesophase of

DL12 was formed by a self-assembly process of the inorganic precursor, which was more strongly affected by the ammonium carbonate precipitator. The main role of PEG as a surfactant in the synthesis was to create a slight enlargement of the mesopore size.

### 15.2.2.2 Anionic Surfactant Templating

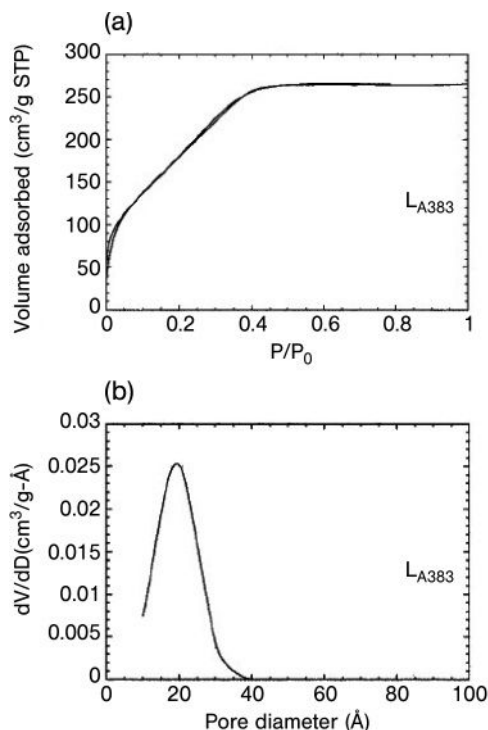
The anionic surfactant templating mechanism involves the coordination of negatively charged surfactant molecules with aluminum sites on freshly formed aluminum hydroxides, as well as cylindrical assemblies of the surfactant alkyl groups to form the corresponding mesophases. Anionic surfactants of types  $\text{RCOO}^-$ ,  $\text{R-XSO}_3^-$  ( $\text{R}$  = long alkyl chain;  $\text{X}$  =  $\text{O}$ ,  $\text{C}_6\text{H}_4$ ,  $\text{CH}_2$ ), and  $\text{R-OPO}_3^{2-}$  are plausible candidates as structure-directing agents, although to date the successful synthesis (including complete removal of the surfactant) has only been achieved with carboxylic acid surfactants.

Vaudry and Davis, in 1996, reported that carboxylic acids with long alkyl chains could be used as templates for the alumina mesostructure assemblies [5b]. The important parameters were the type of solvent, the synthesis temperature, and the thermal history of the as-made material (i.e., temperature and atmosphere for calcination), in addition to the type of alkyl group in the templates. Branched or normal carboxylic acids from  $\text{C}_3$  to  $\text{C}_{18}$  were found to afford mesophases, while suitable solvents were branched or normal alcohols, from  $\text{C}_1$  to  $\text{C}_9$ . The best mesoporous alumina (denoted  $\text{L}_{\text{A}383}$ ) was obtained by hydrolyzing aluminum *sec*-butoxide in 1-propanol solvent under the influence of lauric acid ( $\text{C}_{11}\text{H}_{23}\text{CO}_2\text{H}$ ), followed by heating at  $110^\circ\text{C}$  in a glass jar under static conditions. The solid was then filtered, washed with ethanol, and dried at room temperature to give the as-synthesized material, which was subsequently calcined at  $430^\circ\text{C}$  to give the  $\text{L}_{\text{A}383}$  alumina. An  $\text{N}_2$  adsorption-desorption isotherm and a BJH pore-size distribution of this alumina are shown in Figure 15.7.

The isotherm has no hysteresis loop and the distribution is centered at 1.9 nm. It was concluded, from the shape of distribution and the low-pressure hydrocarbon adsorption data (which showed that there was minimal difference between *n*-heptane uptake and neopentane uptake) that the mesoporous alumina  $\text{L}_{\text{A}383}$  possessed neither “zeolitic” micropores nor pores larger than 4.0 nm. Characterization of the  $\text{L}_{\text{A}383}$  alumina by XRD also showed a diffraction line in the small-angle region, which was attributed to the regular mesoporosity (Figure 15.8).

In addition, these figures show that the alumina is stable up to  $800^\circ\text{C}$ , even under an air/water atmosphere. The shift to a higher *d*-spacing was, however, striking for the calcination in the presence of water, and indicated that sintering had taken place with increasing Al-OH groups to collapse the mesoporous structure. The authors referred to a mechanism of the alumina mesophase formation, in which very small  $\text{AlO}(\text{OH})$  clusters with coordinated carboxylate ligands were first formed, followed by their rapid aggregation to produce the alumina mesophase (Scheme 15.1).

It should be noted that the alkyl chain of coordinated carboxylate is not in the straight-form but rather in bent-form. This is because the observed *d*-spacing of

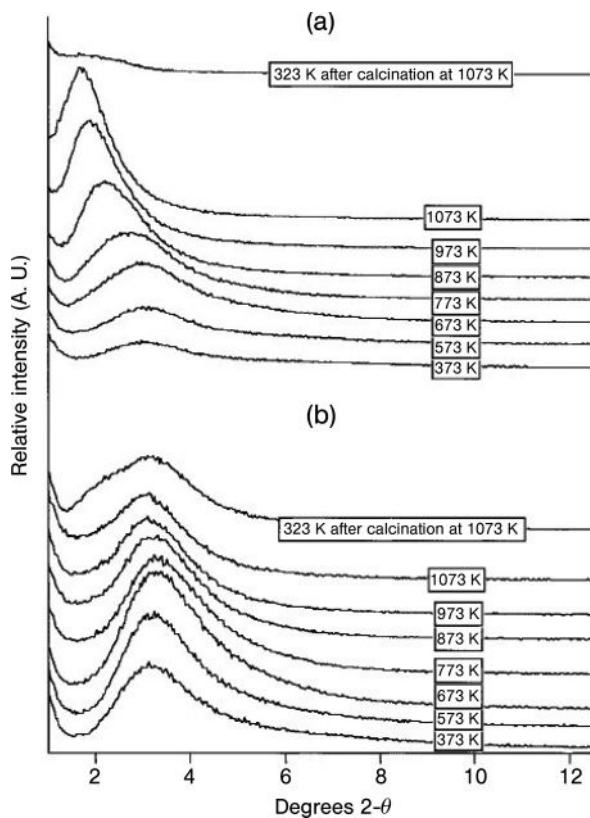


**Figure 15.7** (a) N<sub>2</sub> adsorption–desorption isotherm and (b) BJH pore-size distribution of the L<sub>A383</sub> alumina calcined at 430°C for 1.5 h. Reprinted with permission from Ref. [5b].

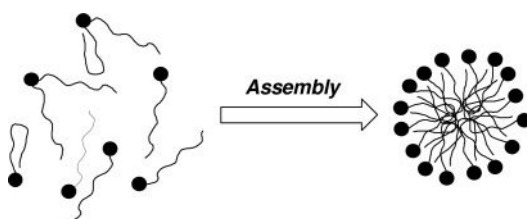
the as-made material (2.9 nm) is much shorter than the sum of the estimated aggregate diameter, assuming a straight alkyl-chain model (3.1 nm) and the wall average width (ca. 1.0 nm). On the other hand, the diameter assuming a curved alkyl-chain model (1.9 nm) is equal to the  $d$ -spacing by adding the wall width. The minimal effect of surfactant size on pore diameter can be seen more clearly in the calcined samples (see Table 15.1, II). The factor which controls the porous properties involving pore diameter is the extent of dehydration of the inorganic walls by calcination, which should also prevent pore-size control by the choice of surfactant size. Dehydration through calcination also drastically lowered the local order and symmetry of the aluminum, increasing the amount of four- and five-fold coordinated aluminum at the expense of the six-fold type, as demonstrated by <sup>27</sup>Al MAS NMR studies (Figure 15.9; see Section 15.2.1.2 for the peak assignments).

The synthesis of mesoporous alumina using sulfate or sulfonate surfactants has been attempted by several groups, but has usually proved unsuccessful owing to the low thermal stability and difficulties of surfactant removal. Vaudry and Davis added sodium dodecylbenzenesulfonate dissolved in formamide to an aqueous solution of hydrolyzed aluminum *sec*-butoxide, followed by aging of the mixture



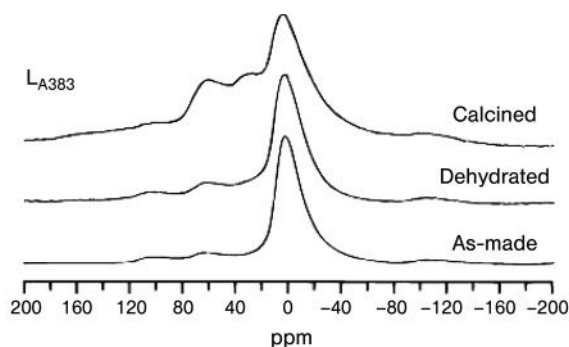


**Figure 15.8** Variation of the X-ray diffraction patterns with increasing temperature under (a) an air/water atmosphere and (b) an air atmosphere. Reprinted with permission from Ref. [5b].



**Scheme 15.1** Mechanism of the mesophase formation as proposed by Vaudry and Davis [5b]. The filled circles represent small clusters of AlO(OH), while the lines attached to the circles represent coordinated carboxylates.

at 110°C for 2 days [5b]. The resultant solid was filtered, washed with deionized water, and dried at room temperature. The as-made material thus obtained exhibited a low thermal stability, losing the XRD line at a high  $d$ -spacing above a calcination temperature of 510°C. In addition, the calcined solid still contained



**Figure 15.9**  $^{27}\text{Al}$  MAS NMR spectra of the as-made, dehydrated, and calcined solid  $L_{\text{A383}}$ . Reprinted with permission from Ref. [5b].

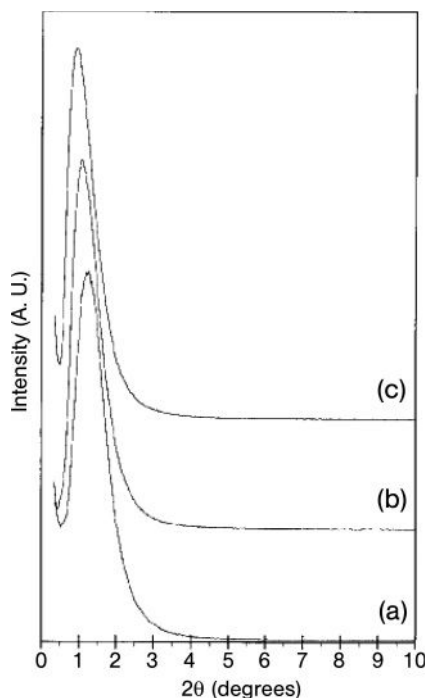
substantial amounts of sulfur components that might have reduced the stability to high-temperature treatment. The sulfonate surfactant also could not be removed from the as-synthesized material by extraction with HCl/ethanol, HCl/water, or AcOH/water solutions.

The use of sodium dodecyl sulfate as a surfactant template was reported by Yada and coworkers [10], who noted that an aluminum-based dodecyl sulfate mesophase possessing a hexagonal structure such as MCM-41 could be synthesized by the homogeneous precipitation method, using aluminum nitrate nonahydrate and urea as an aluminum source and a pH-controlling agent, respectively. The as-made solid obtained from the mixture, of which the components were Al:surfactant:urea:water (1:2:30:60), exhibited an XRD line at a high  $d$ -spacing even after calcination at  $600^\circ\text{C}$ , if it was heated up at a slow rate of  $1^\circ\text{C min}^{-1}$ . However, the content of sulfur impurities in the calcined sample was not reported, and thus the purity remained doubtful. In addition, the surface area—which was in the range  $93$  to  $365\text{ m}^2\text{ g}^{-1}$  depending on the calcination conditions—was much smaller than that of the mesoporous alumina synthesized with carboxylic acid surfactants.

The above two examples indicate that sulfate and sulfonate surfactants are not appropriate as structure-directing agents if the aim is to obtain pure mesoporous alumina with a high thermal stability. However, this approach may open the possibility that sulfated mesoporous alumina, which is an important material in the chemistry of strong acid catalysis, could be synthesized via a one-step process by using sulfate or sulfonate surfactants.

### 15.2.2.3 Cationic Surfactant Templating

Cabrera *et al.*, in 1999, first reported mesoporous alumina (denoted ICMUV-1) synthesized with a cationic surfactant template [5d]. A mixture of aluminum *sec*-butoxide and triethanolamine was added to cetyltrimethylammonium bromide (CTAB) dissolved in water, followed by aging of the resultant solution. The aged solid was filtered, washed with ethanol, dried, and calcined at  $500^\circ\text{C}$  in air to give

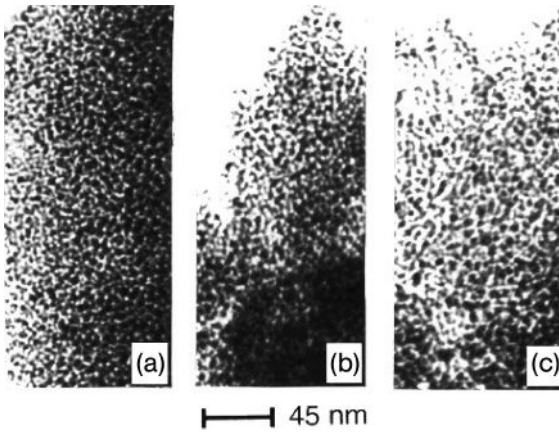


**Figure 15.10** X-ray diffraction patterns of calcined ICMUV-1 aluminas synthesized with water/triethanolamine ratios of 7.4 (pattern a,  $d = 6.9$  nm), 22.1 (pattern b,  $d = 7.9$  nm), and 44.5 (pattern c,  $d = 9.5$  nm). Reprinted with permission from Ref. [5d].

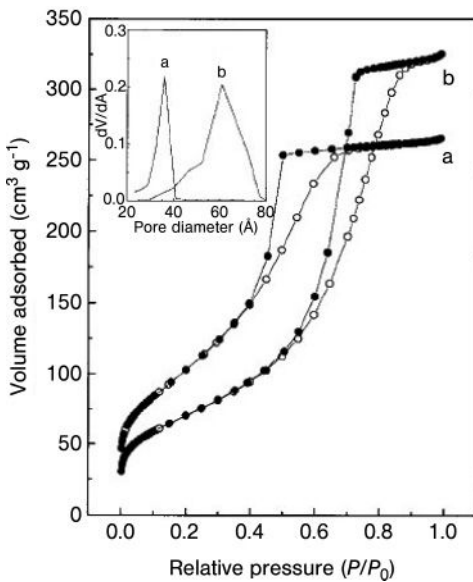
the ICMUV-1 alumina. The pore diameter and surface area of the alumina was found to be tailored by changing the Al:water:triethanolamine molar ratio in the solution from 2:111:15 to 2:195:4, while the Al:surfactant ratio was held at 2:1 for all the syntheses. Increasing the amount of water led to a monotonous increase in pore diameter, from 3.3 to 6.0 nm, whilst monotonously decreasing the surface area from 340 to 250 m<sup>2</sup> g<sup>-1</sup>. The XRD patterns of some samples are shown in Figure 15.10.

Each sample exhibited an XRD line with a high  $d$ -spacing that was attributed to the organized mesopore structures, and these peaks remained unaltered with increasing temperature up to 900 °C, indicative of the high thermal stability of the mesoporous aluminas. The TEM images of ICMUV-1 aluminas showed the worm-hole-like channel motif, without any apparent order in the pore arrangement (Figure 15.11).

The increase in pore diameter with an increase in water:triethanolamine ratio can be clearly seen in the images. The ICMUV-1 aluminas were also characterized using the N<sub>2</sub> adsorption-desorption method (Figure 15.12). The hysteresis loop in the isotherm indicates the presence of ink-bottle-type pores, while the volume at



**Figure 15.11** Transmission electron microscopy images of ICMUV-1 aluminas showing the wormhole-like channel motif. The aluminas were synthesized with water/triethanolamine ratios of 7.4 (a), 22.1 (b), and 44.5 (c). Reprinted with permission from Ref. [5d].



**Figure 15.12** N<sub>2</sub> adsorption-desorption isotherms of ICMUV-1 aluminas prepared with water:triethanolamine ratios of 7.4:1 (isotherm a) and 44.5:1 (isotherm b). The corresponding BJH pore-size distributions are shown in the inset. Reprinted with permission from Ref. [5d].

the saturation vapor pressure demonstrates the absence of any macroporosity in the aluminas. It is interesting to note that the pore wall widths were approximately 3.5 nm, regardless of the water:triethanolamine ratio. Unfortunately, the contents of nitrogen and bromide impurities in the calcined solids were not reported.

The authors suggested that formation of the  $(\text{HOCH}_2\text{CH}_2)_3\text{N}-\text{Al}[\text{OCH}(\text{CH}_3)\text{CH}_2\text{CH}_3]_3$  complex lowered the rate of hydrolysis, which allows the partially hydrolyzed inorganic moieties to be organized together with the surfactant molecules. In contrast, without triethanolamine, the hydrolysis of aluminum *sec*-butoxide proceeded too rapidly to be influenced by the surfactant, yielding the lamellar-type aluminum hydroxides. The fact that an increasing water:triethanolamine ratio increased the pore diameter should be attributed to a shift towards the formation of lamellar moieties.

Žilková and Čejka applied 1-methyl-3-octylimidazolium chloride to the synthesis of mesoporous alumina [5n]. To an aqueous solution of aluminum chlorohydrate and the cationic surfactant was added ammonium hydroxide solution drop-wise, followed by stirring, hydrothermal treatment, filtration of the precipitate, and washing the recovered solid with ethanol. The as-synthesized sample thus obtained was calcined at 560 °C with a temperature ramp of 1 °C min<sup>-1</sup> to give the mesoporous alumina (denoted I–III, depending on the Al:surfactant molar ratio). The effect of modifying the Al:surfactant molar ratio on the structural parameters was investigated by comparing the results of N<sub>2</sub> adsorption–desorption of the calcined solids. The aluminas I and II prepared with a respective Al:surfactant ratio of 5.8 and 3.3 exhibited similar values of surface area, mesopore volume, and pore diameter, but increasing the ratio to 12.0 (alumina III) drastically decreased the surface area and increased the pore volume and pore diameter remarkably. The latter exhibited an N<sub>2</sub> adsorption–desorption isotherm that is typically observed for dispersed materials composed of small particles, and also showed a broad pore-size distribution without maximum, whereas a single XRD line at a low-angle region was observed for this alumina. Thus, the authors referred to the risk of judging the mesoporosity of materials based on XRD data alone. The aluminas I and II, on the other hand, exhibited not only the XRD lines but also the BJH pore-size distributions, with clear maxima centered at 3.8 and 3.9 nm, respectively. The XRD peaks at higher-angle regions indicated that alumina I was composed of  $\gamma\text{-Al}_2\text{O}_3$ . A wormhole framework structure was observed for the alumina I by TEM. The  $S^+ X^- I^+$ -type interaction, which has been discussed in detail elsewhere [6], was proposed for the alumina mesophase formation, where  $S^+$ ,  $X^-$ , and  $I^+$  represent the  $\text{C}_{12}\text{H}_{23}\text{N}_2^+$ ,  $\text{Cl}^-$ , and cationic aluminum species, respectively.

#### 15.2.2.4 Nonsurfactant Templating

Shan *et al.* succeeded in synthesizing mesoporous alumina with a high thermal stability by utilizing tetraethylene glycol as a nonsurfactant template [5j]. A controlled amount of water was added stepwise to a mixture of aluminum isopropoxide and tetraethylene glycol dissolved in ethanol and 2-propanol to produce a suspension, which was subsequently aged at room temperature and then dried in air at 60–100 °C. The solid gel thus obtained was heated at 120–190 °C in an autoclave

and calcined at 600 °C to afford the mesoporous alumina (denoted Al-TUD-1). One of the most important parameters in the synthesis was the water : aluminum ratio. The wide-angle XRD patterns of the alumina prepared with an Al : H<sub>2</sub>O molar ratio of 1 : 10–20 indicated that the bulk structure of the alumina contained crystalline phases of  $\delta$ - or  $\theta$ -Al<sub>2</sub>O<sub>3</sub>. Even though this alumina also gave an intensive diffraction line at about 1.0°, the corresponding TEM image did not show any regular mesopores in the alumina particles. On the other hand, decreasing the amount of water to an Al : H<sub>2</sub>O molar ratio of 1 : 2 afforded the amorphous alumina with a sponge- or worm-like randomly three-dimensionally connected mesoporous network. The N<sub>2</sub> adsorption–desorption measurement of the latter alumina displayed the isotherm of type IV, with a hysteresis loop that indicated the presence of ink-bottle-like pores. In addition to the water content, the drying and heating conditions were also important, as they significantly affected the surface area and pore size of the final product. For instance, increasing the heating time of the solid gel resulted in a monotonous increase and decrease in pore size and surface area, respectively. Moreover, these two structural properties also could be tuned by changing the drying and heating temperature, although few examples were shown in the report and thus the tendencies remain unclear. The highlight of the Al-TUD-1 mesoporous alumina is its high stability toward high-temperature treatment. The alumina synthesized under the optimal conditions possessed a high surface area of 528 m<sup>2</sup> g<sup>-1</sup> after calcination at 600 °C, and of 414 m<sup>2</sup> g<sup>-1</sup> even after calcination at 700 °C, indicating the high potential of this material for practical uses.

Xu *et al.* synthesized mesoporous alumina in an aqueous medium using glucose as a structure-directing agent [5k]. To an aqueous solution of aluminum isopropoxide and glucose was added diluted aqueous nitric acid to adjust the pH value. After removal of the water by evaporation, the resulting solid material was calcined at 600 °C to give the mesoporous alumina (denoted Al<sub>2</sub>O<sub>3</sub>-X; X = 1–3). The pH value of the starting solution had a major effect on the structural property of the resultant alumina. The best alumina, Al<sub>2</sub>O<sub>3</sub>-2, was obtained when the solution pH was adjusted to 5.0, and showed a surface area, total pore volume, and BJH pore diameter of 422 m<sup>2</sup> g<sup>-1</sup>, 0.66 cm<sup>3</sup> g<sup>-1</sup>, and 5.1 nm, respectively. On the other hand, Al<sub>2</sub>O<sub>3</sub>-1 and 3, which were obtained from solutions at pH 4.5 and 5.5, exhibited smaller values of these parameters. The N<sub>2</sub> adsorption–desorption isotherm of Al<sub>2</sub>O<sub>3</sub>-2 was type IV, as typically observed for mesoporous materials; the isotherm contained a hysteresis loop, the shape of which was typical for ink-bottle-like pores. The most remarkable property of Al<sub>2</sub>O<sub>3</sub>-2 was its high thermal stability, with a high surface area of 225 m<sup>2</sup> g<sup>-1</sup> even after calcination at 800 °C. Such excellent thermal stability and simple preparation method imply a high potential for this material as a catalyst.

Zhang and coworkers reported the use of hydroxy carboxylic acids as structure-directing agents [5l]. Here, boehmite sol was first prepared by peptizing a water–boehmite suspension with nitric acid. To this sol was added a hydroxy carboxylic acid, and the mixture was then stirred at 30 °C. The resultant homogeneous mixture was dried and then calcined at 500 °C in air to give the corresponding

mesoporous alumina (denoted ID 1–11). The textural properties of the mesoporous alumina depended heavily on the content of hydroxy carboxylic acid and the drying temperature before calcination. When citric acid was used as a structure-directing agent, a citric acid : Al<sup>3+</sup> molar ratio in the range of 0.5 to 2.0, and a drying temperature of 100 °C, were found to be the optimal synthesis conditions. The use of excess citric acid decreased the surface area and pore volume of the mesoporous alumina, and led to a deterioration of the intrinsic crystalline structure of boehmite in the as-synthesized material. This effect was caused by the formation of larger aggregates of free citric acid molecules, as well as the enhancement of dissolution of boehmite particulates by the increased acidity of the synthetic mixture. The drying temperature, on the other hand, affected the pore structure by altering the coordination interaction between the citric acid molecules and boehmite. Raising the drying temperature increased the amount of hydroxy carboxylic acids coordinated with boehmite, but decreased the size of the aggregation of free hydroxy carboxylic acid molecules, owing to the decrease in free molecules. The size of the aggregation appeared to be crucial for the final structure of pores. Thus, the N<sub>2</sub> adsorption–desorption isotherm of the sample obtained by drying at 30 °C indicated the presence of larger mesopores, while that at 150 °C was analogous to the type I isotherm that is characteristic of microporous materials. Only the mesoporous alumina dried at 100 °C gave the type IV isotherm with a hysteresis loop that indicated the presence of ink-bottle-type pores. Unfortunately, the XRD patterns in the low-angle region were not reported, which makes the quality of the aluminas ambiguous.

### 15.3

#### Mesoporous Alumina in Heterogeneous Catalysis

Mesoporous alumina is superior to conventional alumina in that it possesses a larger surface area and organized mesopores that are not easily plugged by coke and other high-molecular-weight byproducts. The ideal structural properties of mesoporous alumina, however, are not always crucial factors when determining catalytic performance; the surface reactivity such as acidity and basicity is, in most cases, much more important. The reactivity of mesoporous alumina surface should depend heavily on the synthetic method, including the final calcination temperature, as is usually observed for most oxide catalysts. Unfortunately, most studies on mesoporous alumina have focused only on the synthesis and quality of mesoporous structure, and have not referred to the surface reactivity, which renders the potential for mesoporous alumina in catalysis ambiguous. At present, therefore, reliance must be placed on rather primitive trial-and-error methods to determine which mesoporous alumina is most suitable for the catalytic reaction under investigation. Nevertheless, continuous efforts are being made to utilize mesoporous alumina as a catalyst and catalyst support. In fact, the use of mesoporous alumina has in some cases led to better results than with conventional alumina, a topic which is introduced in the following sections (see Table 15.2).

**Table 15.2** Survey of reactions catalyzed by mesoporous alumina and modified mesoporous alumina.

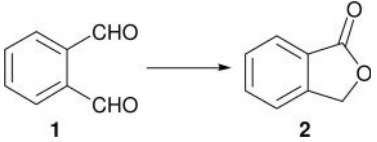
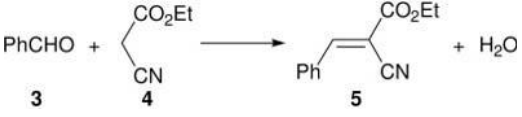
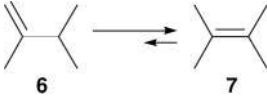
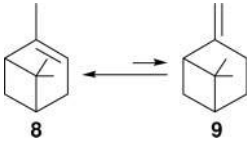
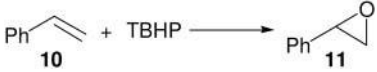
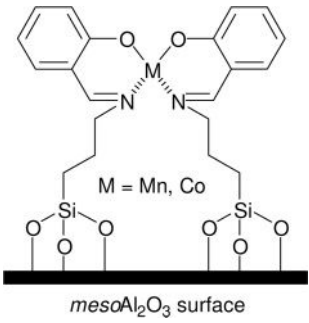


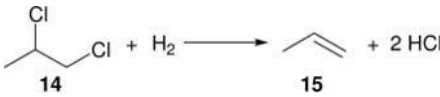
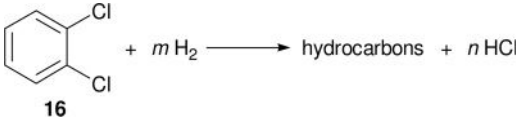
Catalyst <sup>a</sup>	Reaction equation	Conditions (Reactor type; solvent; reaction temperature; atmosphere)	Reference(s)
I. Base-catalyzed reactions			
A. Tishchenko reaction			
$mesoAl_2O_3$ ; $mesoAl_2O_3/SO_4^{2-}$		Batch; $scCO_2$ (8 MPa); 40 °C	[18]
B. Knoevenagel reaction			
$mesoAl_2O_3$		Batch; $scCO_2$ (8 MPa); 40 °C	[19]
C. Double-bond migration			
$Na/mesoAl_2O_3$		Batch; neat; 2 °C; <i>in vacuo</i>	[20]
$Na/mesoAl_2O_3$		Batch; neat; rt; <i>in vacuo</i>	[20]

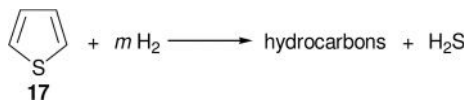


Table 15.2 Continued.

Catalyst <sup>a</sup>	Reaction equation	Conditions (Reactor type; solvent; reaction temperature; atmosphere)	Reference(s)
II. Epoxidation			
Au/ <i>meso</i> Al <sub>2</sub> O <sub>3</sub>	 $\text{Ph-CH=CH}_2 + \text{TBHP} \longrightarrow \text{Ph-CH(O)-CH}_2$	Batch; benzene; 82–83 °C	[21]
 <p>M = Mn, Co</p> <p><i>meso</i>Al<sub>2</sub>O<sub>3</sub> surface</p>	 $\text{Ph-CH=CH}_2 + \text{TBHP} \longrightarrow \text{Ph-CH(O)-CH}_2$	Batch; CH <sub>3</sub> CN; 60 °C	[22]
	 $\text{Cyclohexene} + \text{TBHP} \longrightarrow \text{Cyclohexene oxide}$		
III. Hydrodechlorination			
Ni/ <i>meso</i> Al <sub>2</sub> O <sub>3</sub>	 $\text{CH}_3\text{CHClCH}_2\text{Cl} + \text{H}_2 \longrightarrow \text{CH}_3\text{CH=CH}_2 + 2 \text{HCl}$	Continuous flow; 300 °C	[23, 24]
Ni–Mg/ <i>meso</i> Al <sub>2</sub> O <sub>3</sub> <sup>b</sup>	 $\text{C}_6\text{H}_4\text{Cl}_2 + m \text{H}_2 \longrightarrow \text{hydrocarbons} + n \text{HCl}$	Continuous flow; 300 °C	[25]

#### IV. Hydrodesulfurization

MoS<sub>2</sub>/mesoAl<sub>2</sub>O<sub>3</sub><sup>b</sup>



Continuous flow;  
280–400 °C; 1 MPa [26]

#### V. Olefin metathesis

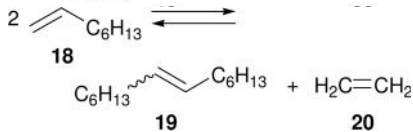
##### A. Terminal hydrocarbon olefins

Re<sub>2</sub>O<sub>7</sub>/mesoAl<sub>2</sub>O<sub>3</sub>



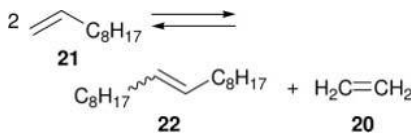
Batch; *n*-heptane; –1 °C; N<sub>2</sub> [27–29]  
Batch; neat; 40 or 60 °C; Ar

MTO/ZnCl<sub>2</sub>/mesoAl<sub>2</sub>O<sub>3</sub>



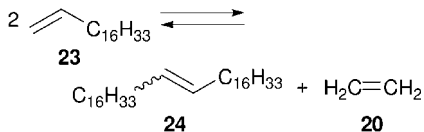
Batch; CH<sub>2</sub>Cl<sub>2</sub>; rt; N<sub>2</sub> [30]

Re<sub>2</sub>O<sub>7</sub>/mesoAl<sub>2</sub>O<sub>3</sub>



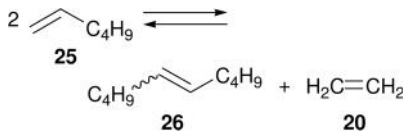
Batch; neat; 25, 40, or 60 °C; Ar [28–31]

Re<sub>2</sub>O<sub>7</sub>/mesoAl<sub>2</sub>O<sub>3</sub>



Batch; neat; 60 °C; Ar [28]

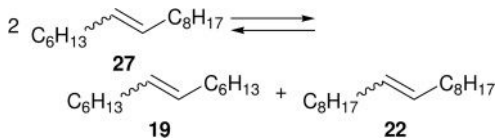
Re<sub>2</sub>O<sub>7</sub>/mesoAl<sub>2</sub>O<sub>3</sub>



Batch; dodecane; 40 °C; N<sub>2</sub> [32]

##### B. Internal hydrocarbon olefins

Re<sub>2</sub>O<sub>7</sub>/mesoAl<sub>2</sub>O<sub>3</sub>

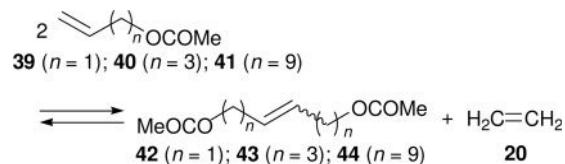


Batch; *n*-heptane; 50 °C; N<sub>2</sub> [27]

Table 15.2 Continued.

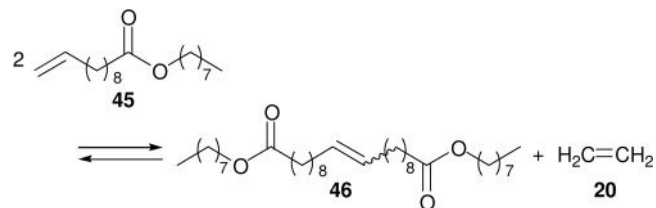
Catalyst <sup>a</sup>	Reaction equation	Conditions (Reactor type; solvent; reaction temperature; atmosphere)	Reference(s)
MTO/ZnCl <sub>2</sub> // <i>meso</i> Al <sub>2</sub> O <sub>3</sub>	$2 \text{ C}_6\text{H}_{13} \text{---} \text{CH}=\text{CH} \text{---} \text{C}_8\text{H}_{17} \rightleftharpoons \text{C}_6\text{H}_{13} \text{---} \text{CH}=\text{CH} \text{---} \text{C}_6\text{H}_{13} + \text{C}_8\text{H}_{17} \text{---} \text{CH}=\text{CH} \text{---} \text{C}_8\text{H}_{17}$ <p style="text-align: center;"> <span style="margin-right: 100px;"><b>27</b></span> <span><b>19</b></span> <span><b>22</b></span> </p>	Batch; CH <sub>2</sub> Cl <sub>2</sub> ; rt; N <sub>2</sub>	[30]
Re <sub>2</sub> O <sub>7</sub> / <i>meso</i> Al <sub>2</sub> O <sub>3</sub>	$2 \text{ CH}_3 \text{---} \text{CH}=\text{CH} \text{---} \text{C}_2\text{H}_5 \rightleftharpoons \text{CH}_3 \text{---} \text{CH}=\text{CH} \text{---} \text{CH}_3 + \text{C}_2\text{H}_5 \text{---} \text{CH}=\text{CH} \text{---} \text{C}_2\text{H}_5$ <p style="text-align: center;"> <span style="margin-right: 100px;"><b>28</b></span> <span><b>29</b></span> <span><b>30</b></span> </p>	Batch; neat; 25 °C; Ar	[29]
Re <sub>2</sub> O <sub>7</sub> / <i>meso</i> Al <sub>2</sub> O <sub>3</sub>	$2 \text{ CH}_3 \text{---} \text{CH}=\text{CH} \text{---} \text{C}_5\text{H}_{11} \rightleftharpoons \text{CH}_3 \text{---} \text{CH}=\text{CH} \text{---} \text{CH}_3 + \text{C}_5\text{H}_{11} \text{---} \text{CH}=\text{CH} \text{---} \text{C}_5\text{H}_{11}$ <p style="text-align: center;"> <span style="margin-right: 100px;"><b>31</b></span> <span><b>29</b></span> <span><b>32</b></span> </p>	Batch; neat; 40 °C; Ar	[29]
C. Terminal functionalized olefins Re <sub>2</sub> O <sub>7</sub> / <i>meso</i> Al <sub>2</sub> O <sub>3</sub> + Me <sub>4</sub> Sn	$2 \text{ MeO-C}_6\text{H}_4\text{-CH}_2\text{-CH}=\text{CH}_2 \rightleftharpoons \text{MeO-C}_6\text{H}_4\text{-CH}_2\text{-CH}=\text{CH-CH}_2\text{-C}_6\text{H}_4\text{-OMe} + \text{H}_2\text{C}=\text{CH}_2$ <p style="text-align: center;"> <span style="margin-right: 100px;"><b>33</b></span> <span><b>34</b></span> <span><b>20</b></span> </p>	Batch; toluene or decane; 25 °C; Ar	[31]
MTO/ZnCl <sub>2</sub> // <i>meso</i> Al <sub>2</sub> O <sub>3</sub>	$2 \text{ MeO}_2\text{C-(CH}_2\text{)}_n\text{-CH}=\text{CH}_2 \rightleftharpoons \text{MeO}_2\text{C-(CH}_2\text{)}_n\text{-CH}=\text{CH-(CH}_2\text{)}_n\text{-CO}_2\text{Me} + \text{H}_2\text{C}=\text{CH}_2$ <p style="text-align: center;"> <span style="margin-right: 100px;"><b>35</b> (<i>n</i> = 8); <b>36</b> (<i>n</i> = 9)</span> <span><b>37</b> (<i>n</i> = 8); <b>38</b> (<i>n</i> = 9)</span> <span><b>20</b></span> </p>	Batch; CH <sub>2</sub> Cl <sub>2</sub> ; rt; N <sub>2</sub>	[30]

MTO/ZnCl<sub>2</sub>//*meso*Al<sub>2</sub>O<sub>3</sub>



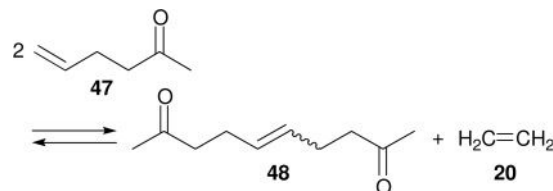
Batch; CH<sub>2</sub>Cl<sub>2</sub>; rt; N<sub>2</sub> [30]

MTO/ZnCl<sub>2</sub>//*meso*Al<sub>2</sub>O<sub>3</sub>



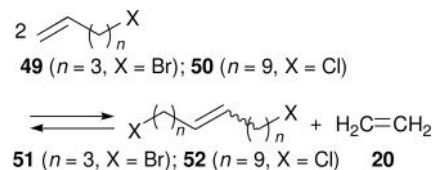
Batch; CH<sub>2</sub>Cl<sub>2</sub>; rt; N<sub>2</sub> [30]

MTO/ZnCl<sub>2</sub>//*meso*Al<sub>2</sub>O<sub>3</sub>



Batch; CH<sub>2</sub>Cl<sub>2</sub>; rt; N<sub>2</sub> [30]

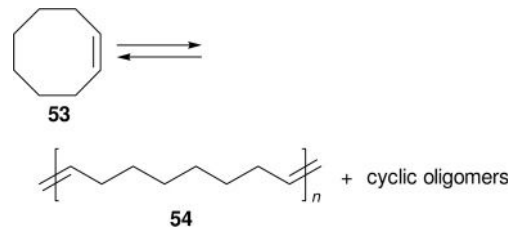
Re<sub>2</sub>O<sub>7</sub>/*meso*Al<sub>2</sub>O<sub>3</sub>



Batch; CH<sub>2</sub>Cl<sub>2</sub>; rt; N<sub>2</sub> [30]

D. Ring-opening metathesis polymerization (ROMP)

Re<sub>2</sub>O<sub>7</sub>/*meso*Al<sub>2</sub>O<sub>3</sub>



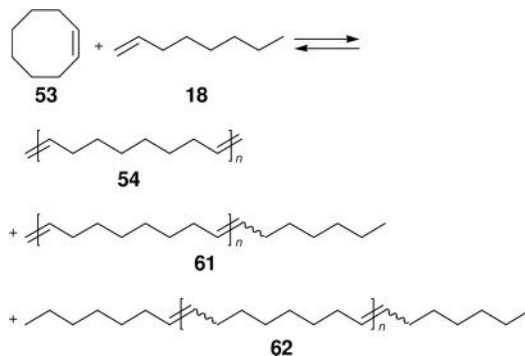
Batch; toluene; 40 °C; Ar [29]

Table 15.2 Continued.

Catalyst <sup>a</sup>	Reaction equation	Conditions (Reactor type; solvent; reaction temperature; atmosphere)	Reference(s)
E. Ring-closing metathesis (RCM) Re <sub>2</sub> O <sub>7</sub> /mesoAl <sub>2</sub> O <sub>3</sub>	<p style="text-align: center;"> <math display="block">\text{55} \rightleftharpoons \text{12} + \text{20}</math> </p>	Batch; neat or dodecane; 40 °C; Ar	[29]
Re <sub>2</sub> O <sub>7</sub> /mesoAl <sub>2</sub> O <sub>3</sub> + Me <sub>4</sub> Sn	<p style="text-align: center;"> <math display="block">\text{56} \rightleftharpoons \text{57} + \text{20}</math> </p>	Batch; toluene; 0–40 °C; Ar	[31]
F. Polymerization of terminal dienes Re <sub>2</sub> O <sub>7</sub> /mesoAl <sub>2</sub> O <sub>3</sub>	<p style="text-align: center;"> <math display="block">n \text{ 58} \rightleftharpoons \text{59} + n-1 \text{ 20}</math> </p>	Batch; toluene; 25 °C; Ar	[29]
Re <sub>2</sub> O <sub>7</sub> /mesoAl <sub>2</sub> O <sub>3</sub>	<p style="text-align: center;"> <math display="block">n \text{ 60} \rightleftharpoons \text{54} + n-1 \text{ 20}</math> </p>	Batch; toluene; 40 °C; Ar	[29]

G. Cross metathesis

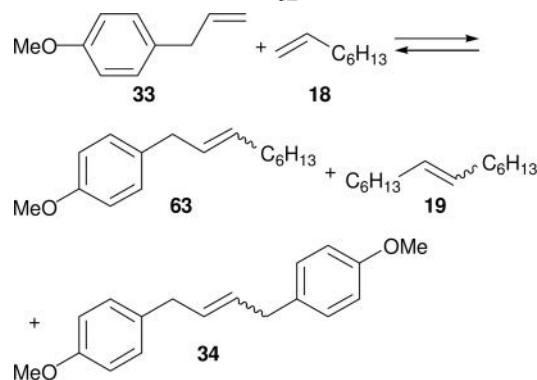
$\text{Re}_2\text{O}_7/\text{mesoAl}_2\text{O}_3$



Batch; neat; 40 °C; Ar

[29]

$\text{Re}_2\text{O}_7/\text{mesoAl}_2\text{O}_3 + \text{Me}_4\text{Sn}$



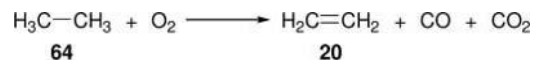
Batch; toluene; 40 °C; Ar

[31]

VI. Oxidative dehydrogenation

$\text{V}/\text{mesoAl}_2\text{O}_3^c$

$\text{Mo-V}/\text{mesoAl}_2\text{O}_3^c$

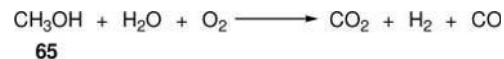


Continuous flow; 520–600 °C; atmospheric pressure

[33, 34]

VII. Oxidative steam reforming of methanol

$\text{Pd-Zn}/\text{mesoAl}_2\text{O}_3^c$



Continuous flow; 100–400 °C:

[35]

a  $\text{mesoAl}_2\text{O}_3$  represents mesoporous alumina.

b Products were not reported.

c Stoichiometries are not considered due to the complex reaction mechanism.

rt = room temperature.

## 15.3.1

**Base-Catalyzed Reactions**

Thermally activated alumina has long been recognized as a solid base catalyst [7b]. In fact, studies of the use of mesoporous alumina as a solid base catalyst were initiated by Seki and Onaka in their attempt to develop heterogeneous basic catalysis in supercritical CO<sub>2</sub> (scCO<sub>2</sub>). These authors found that mesoporous alumina synthesized in a similar manner to L-A<sub>383</sub> (see Table 15.1, II) and activated at 500 °C under vacuum (10<sup>-4</sup> Torr) exhibited a strong base catalysis for the Tishchenko reaction, even in the Lewis acidic medium of scCO<sub>2</sub> (Table 15.2, I, A) [18]. In addition, the activity could be increased by introducing SO<sub>4</sub><sup>2-</sup> ions into the alumina framework. Conventional  $\gamma$ -Al<sub>2</sub>O<sub>3</sub> and CaO, in contrast, showed quite low activities in scCO<sub>2</sub>, even though they were very active in benzene as solvent under nitrogen atmosphere. The phthalide **2** formation over the sulfated mesoporous alumina was accelerated remarkably by adding a small amount of tetrahydrofuran (THF) as a cosolvent, whereas the addition of acetic acid (or even much less-acidic methanol) led to a fatal deactivation of the catalyst due to strong poisoning. The former result was attributed to the improvement of solubility of phthalaldehyde **1** in scCO<sub>2</sub>, while the latter result suggested that the strong base sites on sulfated mesoporous alumina had promoted the reaction in scCO<sub>2</sub>. The infrared (IR) spectroscopy of adsorbed pyrrole implied that the average strength of base sites on sulfated mesoporous alumina was weaker than on conventional  $\gamma$ -Al<sub>2</sub>O<sub>3</sub>. However, the poisoning by methanol indicated that it still had a small number of strong base sites that functioned even in scCO<sub>2</sub>. It was concluded that the CO<sub>2</sub> molecules adsorbed onto the sulfated mesoporous alumina were less stable compared to those on conventional  $\gamma$ -Al<sub>2</sub>O<sub>3</sub>, due to the weaker surface basicity of the former, and thus could offer the active strong base sites to **1** much more easily through the surface diffusion, which in turn made a noticeable difference in activity.

In a subsequent study, the same authors reported that mesoporous alumina also exhibited a higher activity for the Knoevenagel reaction between benzaldehyde **3** and ethyl cyanoacetate **4** compared to conventional  $\gamma$ -Al<sub>2</sub>O<sub>3</sub> in scCO<sub>2</sub> (Table 15.2, I, B) [19]. Although the surface area of the mesoporous alumina employed was 2.7-fold larger than that of conventional form, the numbers of active base sites on the aluminas were almost equal according to the results of temperature-programmed desorption (TPD) of CO<sub>2</sub>. This indicated that the density of active base sites was much smaller for mesoporous alumina than for conventional  $\gamma$ -Al<sub>2</sub>O<sub>3</sub>. The authors thus suggested that the surface diffusion of CO<sub>2</sub> took place smoothly on mesoporous alumina owing to the large vacancy around the sites, while the CO<sub>2</sub> molecules adsorbed on the active base sites of conventional  $\gamma$ -Al<sub>2</sub>O<sub>3</sub> were jam-packed, thus retarding the surface diffusion with each other. As free active base sites should appear by moving the adsorbed CO<sub>2</sub>, it was concluded that the difference in facility of the surface diffusion of CO<sub>2</sub> accounted for the difference in activity between the two aluminas. In the same study, a careful examination was also made of the CO<sub>2</sub>-TPD in the high temperature range of 527–1000 °C. The results implied that mesoporous alumina had a small number of very strong

base sites, the strength of which was even higher than that of the base sites on conventional  $\gamma\text{-Al}_2\text{O}_3$ .

The double-bond migration of olefins is a simple, but important, process in chemical industry. Although both acid and base catalysts can promote double-bond migrations, base catalysts are usually much more selective, especially when cyclic olefins are used as the starting compounds. In addition, increasing the surface basicity increases the reaction rate, allowing the migrations to be performed even at a low reaction temperature (i.e., below zero region) by using superbase catalysts. Seki *et al.* attempted to enhance the surface basicity of mesoporous alumina by blowing an alkaline metal vapor against the activated alumina surface to improve the catalytic performance for the double-bond migrations (Table 15.2, I, C) [20]. It was revealed, via XRD and  $\text{N}_2$  adsorption–desorption analysis, that the sodium addition hardly collapsed the intrinsic mesoporosity and bulk structure of mesoporous alumina. Unfortunately, the double-bond migration of 2,3-dimethyl-1-butene **6** proceeded more slowly over sodium-doped mesoporous alumina than over sodium-doped conventional  $\gamma\text{-Al}_2\text{O}_3$ , which should be brought about by the lower density of active strong base sites on mesoporous alumina compared to conventional alumina. Nonetheless, sodium-doped mesoporous alumina could selectively yield 2,3-dimethyl-2-butene **7** at high yield (81%), even at a low reaction temperature (2°C), demonstrating that very strong base sites—including superbase sites—existed on the surface. The catalyst also promoted the reaction of  $\alpha$ -pinene **8** to give  $\beta$ -pinene **9** in excellent selectivities of 93–96%, while the selectivity fell to 58% and 89% for parent mesoporous alumina and sodium-doped conventional  $\gamma\text{-Al}_2\text{O}_3$ , respectively.

### 15.3.2

#### Epoxidation

Yin and coworkers investigated the catalysis of gold nanoparticles supported on mesoporous alumina for the epoxidation of styrene **10** with *tert*-butyl hydroperoxide (Table 15.2, II) [21]. Three types of mesoporous alumina were synthesized via neutral surfactant templating ( $\text{La}^{3+}$ -doped MSU-3) [5c], cationic surfactant templating (ICMUV-1; Table 15.1, III) [5d], and an original method using chitosan as the structure-directing agent. In addition, commercially available  $\gamma\text{-Al}_2\text{O}_3$  was employed for comparative purposes. Gold nanoparticles were subsequently loaded onto the aluminas via a homogeneous deposition precipitation method using  $\text{HAuCl}_4$  and urea as a gold source and precipitation agent, respectively. The as-made materials were reduced under an  $\text{H}_2/\text{He}$  flow before being used for the reactions. Among the catalysts thus prepared, the Au loaded on ICMUV-1 exhibited the highest catalytic performance, yielding styrene oxide **11** in 84.3% conversion and 69.0% selectivity. The major byproducts were benzaldehyde and phenyl acetaldehyde, which were given in 23.0% and 3.6% selectivity, respectively. Although the other catalysts yielded **11** in similar selectivities, they were inferior to Au/ICMUV-1 in terms of conversion. In addition to the high activity, the Au/ICMUV-1 catalyst exhibited a long lifetime and could be reused at least eight times, without losing



its high catalytic performance. X-ray photoelectron spectroscopy (XPS) measurements revealed that the preparation method gave Au(0) particles without any trace of higher-oxidized species, regardless of the type of support alumina. On the other hand, the CO<sub>2</sub>-TPD profiles and isoelectric points of the alumina supports showed that the ICMUV-1 alumina had the largest number of basic sites, which was advantageous for the formation and stabilization of smaller gold particles. The TEM image, in fact, showed that the size of gold particles on Au/ICMUV-1 was uniform and smaller (<4 nm) compared to those of other catalysts. The authors thus concluded that the presence of smaller gold particles with a uniform size accounted for the highest activity of Au/ICMUV-1, because the active sites for the epoxidation were considered to be low-coordinated Au atoms existing at the corner and edge of the particles. It was also noteworthy that the pure ICMUV-1 alumina could catalyze the epoxidation, giving **11** in 50.3% conversion and 66.9% selectivity.

Chaube *et al.* immobilized Mn- and Co-salen complexes onto mesoporous alumina and applied them to the catalytic epoxidation of **10** and cyclohexene **12** with *tert*-butyl hydroperoxide (Table 15.2, II) [22]. A synthetic method similar to that for the L<sub>A383</sub> (Table 15.1, II) was employed, but aluminum isopropoxide was used as an aluminum source. The mesoporous alumina thus obtained was first treated with 3-aminopropyltriethoxysilane to give the aminopropyl-modified mesoporous alumina, which was subsequently reacted with the precursor complexes, (bis-salicyl aldehyde)M (M = Mn, Co), to give the target catalysts. The IR band assignable to the C=N bond then appeared, indicating that the bis-salicyl aldehyde ligand had been converted into the salen-type ligand. The change in ligand was also demonstrated by the shift of characteristic peaks in UV-visible spectrum. A single XRD line in the low-angle region appeared, even after immobilization of the (bis-salicyl aldehyde)Co complex. In addition, the N<sub>2</sub> adsorption-desorption isotherm of type IV was obtained for the immobilized Co-salen complex catalyst, as well as for the parent mesoporous alumina. Moreover, thermal analysis indicated that the immobilized complexes decomposed at higher temperatures compared to the precursor complexes, which implied that the stabilities had been enhanced by the immobilizations. Thus, the entrapment of complex moieties inside the mesopores was proposed. The immobilized complexes were firmly fixed and did not dissolve into the solution during the reactions. In addition, the Mn catalyst was found to be used at least three times, without any significant loss in activity and selectivity. Unfortunately, however, the yields of the desired **11** (14–16%) and **13** (9–16%) were too low, rendering the potential of these catalysts for practical epoxide synthesis questionable.

### 15.3.3

#### Hydrodechlorination

Hydrodechlorination involves the cleavage of a C–Cl bond with H<sub>2</sub> under the influence of a catalyst, to yield useful hydrocarbons from hazardous chlorinated alkanes.

Kim *et al.* prepared nickel supported on mesoporous alumina and applied this to the hydrodechlorination of 1,2-dichloropropane **14** to propene **15** (Table 15.2, III) [23]. The mesoporous alumina was synthesized using stearic acid as a surfactant, using what has been termed a “post-hydrolysis” method [36]. The procedure was similar to that for the synthesis of  $S_{A383}$  alumina (Table 15.1, II), except that the hydrolyzed solution was dried directly without thermal treatment to produce the as-synthesized material that was subsequently calcined at 450°C. Nickel was loaded onto the mesoporous alumina using two different methods. The first method involved the vapor deposition of nickel acetylacetonate (denoted Ni-VD), followed by calcination, while the second method involved impregnation using an appropriate amount of aqueous solution of nickel nitrate (denoted Ni-IMP). Characterization by XPS, temperature-programmed reduction (TPR), and UV-diffuse reflectance spectroscopy (UV-DRS) revealed that the NiO species were dominant on the Ni-VD catalyst, whereas a large amount of  $Ni^{2+}$  ions was incorporated into the nickel aluminate spinels for Ni-IMP. It was proposed that such spinels were formed through the impregnation step in which a mixed adsorption occurred between  $Ni^{2+}$  ions of nickel nitrate and  $Al^{3+}$  ions that once were dissolved into the aqueous solution from the alumina surface. Both of the catalysts promoted the hydrodechlorination of **14** in a continuous-flow fixed-bed reactor, maintaining approximately 83% selectivity for at least 10 h. However, the conversion with Ni-VD was approximately twofold higher than that with Ni-IMP. The authors concluded that the NiO species could be reduced much more smoothly into active nickel metals compared to nickel aluminate species, as demonstrated by the TPR study, and thus Ni-VD exhibited a higher activity than Ni-IMP. The larger number of active nickel sites on Ni-VD was also clearly seen in the TPD measurement of 1,2-dichloropropane. Later, the same authors reported that the activity of Ni-IMP depended heavily on the molar ratio of surfactant/ $Al[OCH(CH_3)CH_2CH_3]_3$  in the preparation of the mesoporous alumina support [24]. It was observed that the amount of dissolved  $Al^{3+}$  ions during the impregnation increased as the ratio increased, leading to the formation of a larger amount of unfavorable nickel aluminate species. In fact, the Ni-IMP prepared with a lower ratio tended to exhibit a higher activity for the hydrodechlorination of **14**.

More recently, Kim *et al.* prepared nickel- and magnesium-containing mesoporous alumina as a catalyst for the hydrodechlorination of *o*-dichlorobenzene **16** (Table 15.2, III) [25]. Bimetallic nickel and magnesium stearate were used as structure-directing agents, as well as nickel and magnesium sources; these were first dissolved in 2-butanol with aluminum *sec*-butoxide, and the subsequent addition of water, drying, and calcination at 500°C yielded the catalyst. The bimetallic stearate was obtained by dissolving magnesium stearate and nickel nitrate in 2-butanol, after which the pH was adjusted with HCl or  $NH_4OH$ . The use of  $NH_4OH$  resulted in the precipitation of a solid bimetallic stearate, which yielded the most active catalyst (denoted NiMg-NP). A TPR study clearly demonstrated the presence of homogeneously mixed Ni metals on NiMg-NP that were the active sites for the hydrodechlorination, whereas on the catalyst

prepared via the HCl-treated surfactant (denoted NiMg-HS) there existed undesirable nickel aluminate species, in addition to nickel metal aggregates. Another factor that rendered NiMg-NP most active was a favorable modification of the electronic properties of Ni metals on NiMg-NP, caused by homogeneously mixed Mg. This was confirmed by H<sub>2</sub>-TPD profiles which revealed that only NiMg-NP showed an intense desorption peak below 400°C; this indicated that the Mg species had weakened the interaction between Ni metal surface and hydrogen. The Mg species also played an important role in extending the lifetime of the catalyst through the reaction with HCl; here, HCl was trapped on a partially formed basic MgO surface, inhibiting the conversion of active Ni metals into NiCl<sub>2</sub>.

#### 15.3.4

##### Hydrodesulfurization

Hydrodesulfurization is an industrially very important catalytic process for the removal of sulfur from natural gas and refined petroleum products. Such removal should lead to a reduction in SO<sub>2</sub> emissions from these fuels, and also extend the lifetime of the noble metal catalysts used in the subsequent reforming processes. Kaluža *et al.* employed the S<sub>A383</sub> mesoporous alumina (Table 15.1, II) as a support for an active MoS<sub>2</sub> species, although the calcination conditions were carefully modified from those reported originally (Table 15.2, IV) [26]. The mesoporous alumina, when finally calcined at 450°C, was found to serve as the best support. MoO<sub>3</sub> as a precursor was loaded onto the alumina by two different methods. The first method involved impregnation using an aqueous solution of (NH<sub>4</sub>)<sub>6</sub>Mo<sub>7</sub>O<sub>24</sub>, followed by drying at 50°C under vacuum (denoted 30Mo/MA(CIM); 30 wt% MoO<sub>3</sub>). The second method involved thermal spreading, where the mesoporous alumina was first ground with an appropriate amount of MoO<sub>3</sub> in an agate mortar and subsequently calcined at 500°C in a stream of air (denoted 30Mo/MA(TSM); 30 wt% MoO<sub>3</sub>). In both cases, the loaded MoO<sub>3</sub> was converted into active MoS<sub>2</sub> by treatment with an H<sub>2</sub>S/H<sub>2</sub> mixture at 400°C. The N<sub>2</sub> adsorption-desorption measurements revealed that the added MoO<sub>3</sub>, despite a very high loading, did not significantly block the texture of the parent alumina support. The rate constant of 30Mo/MA(CIM), when normalized to weight for the hydrodesulfurization of thiophene **17**, was almost twice as high as that of the commercial 15 wt% MoO<sub>3</sub>/Al<sub>2</sub>O<sub>3</sub> catalyst, whereas the rate constants of the two catalysts normalized to moles of Mo were almost equal. The authors concluded that the high surface area of mesoporous alumina was able to disperse a significantly higher amount of Mo than the conventional alumina. Although, the activity of 30Mo/MA(TSM) was inferior to that of 30Mo/MA(CIM), its rate constant (when normalized to weight) was still approximately 1.5-fold higher than that of the commercial catalyst, indicating that the high loading of MoO<sub>3</sub> could be realized also by thermal spreading. It should also be noted that 30Mo/MA(TSM) exhibited a long lifetime compared to the commercial catalyst for the hydrodesulfurization conducted at 370°C.

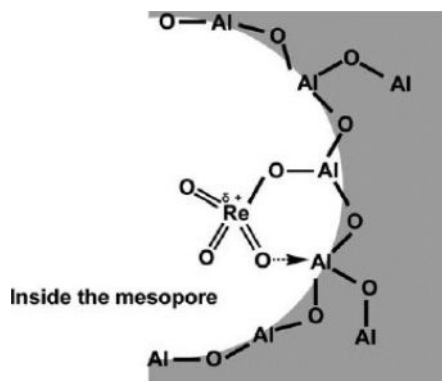
## 15.3.5

**Olefin Metathesis**

Olefin metathesis involves the mutual exchange of alkylidene fragments between two olefin molecules by the action of metal catalysts. Its use in organic synthesis, particularly of polymers and pharmaceuticals with various functional groups, has been explosively expanded by the respective discoveries of Mo- and Ru-based alkylidene complex catalysts by Schrock [37a] and Grubbs [37b], which led to these authors receiving the Nobel Prize in 2005. Heterogeneous olefin metathesis catalysts such as  $\text{WO}_3/\text{SiO}_2$ ,  $\text{MoO}_3/\text{Al}_2\text{O}_3$ , and  $\text{Re}_2\text{O}_7/\text{Al}_2\text{O}_3$ , on the other hand, have long been important in the petroleum industry for the manufacture of various olefins of pure hydrocarbons.

The use of mesoporous alumina in olefin metathesis was first attempted by Oikawa and Onaka (Table 15.2, V) [27]. These authors dispersed rhenium oxide,  $\text{Re}_2\text{O}_7$ , on the  $\text{L}_{\text{A}383}$  alumina (Table 15.1, II, calcined finally at  $600^\circ\text{C}$ ), using an impregnation method from the aqueous solution of  $\text{NH}_4\text{ReO}_4$ , with subsequent calcination at  $600^\circ\text{C}$ . Despite water being used as solvent, the loading did not significantly alter the structural properties of the parent support. The catalyst (denoted  $\text{Re}_2\text{O}_7/\text{meso-Al}_2\text{O}_3$ ) thus obtained was activated under vacuum at  $500^\circ\text{C}$ ; this step was found to be crucial for achieving a high conversion and selectivity. Compared to the conventional, 7 wt%  $\text{Re}_2\text{O}_7/\gamma\text{-Al}_2\text{O}_3$  catalyst, 7 wt%  $\text{Re}_2\text{O}_7/\text{meso-Al}_2\text{O}_3$  exhibited a higher conversion and selectivity for the metathesis of 1-octene **18** to 7-tetradecene **19** and ethylene **20** and of 7-hexadecene **27** to 7-tetradecene **19** and 9-octadecene **22**. In the case of the latter reaction, the lower conversion with a conventional catalyst was attributed to deactivation of the catalyst. The effect of changing the loading amount of  $\text{Re}_2\text{O}_7$  was investigated for the metathesis of **18**, and showed that 7 wt%  $\text{Re}_2\text{O}_7/\text{meso-Al}_2\text{O}_3$  exhibited a higher conversion and selectivity than 3.5 and 15 wt%  $\text{Re}_2\text{O}_7/\text{meso-Al}_2\text{O}_3$ . Characterization using X-ray adsorption spectroscopy (XAS) showed that rhenium oxide on both 7 wt%  $\text{Re}_2\text{O}_7/\text{meso-Al}_2\text{O}_3$  and 7 wt%  $\text{Re}_2\text{O}_7/\gamma\text{-Al}_2\text{O}_3$  were in the same oxidation state, and had the same structure. It was also revealed that the  $\text{ReO}_4$  species on the catalysts were greatly distorted from a regular tetrahedron by their fixation onto the alumina surfaces. The authors proposed that mesoporous alumina could produce a larger amount of active Re ions in partially reduced states compared to the conventional alumina, and that the difference in the amount of Re sites caused the difference in activity. An active rhenium site model, as depicted in Figure 15.13, was suggested, in which a rhenium ion is electronically activated not only by the Re–O–Al bond derived from an acidic hydroxyl group of mesoporous alumina but also by the coordination of a Re=O moiety to an adjacent Lewis acid site of  $\text{Al}^{3+}$ .

Balcar *et al.* employed the thermal spreading method to prepare rhenium oxide supported on mesoporous alumina (denoted Re/OMA) [28]. In this method, mesoporous alumina was first ground with  $\text{NH}_4\text{ReO}_4$  at room temperature, and then calcined at  $550^\circ\text{C}$ . Before use in a reaction, the catalyst was activated at  $500^\circ\text{C}$  in air. The rhenium oxide loading did not significantly affect the pore size of the parent mesoporous alumina. In addition, the decrease in surface area caused by



**Figure 15.13** Oikawa–Onaka model of surface rhenium oxide species on mesoporous alumina. Reprinted with permission from Ref. [27b].

the loading was much smaller for mesoporous alumina than for conventional alumina; this was due to the absence of micropores in the former case that may easily be plugged by rhenium oxide species. In the 1-decene **21** metathesis, the optimum Re loading was found to be between 9 and 15 wt%, and that the conversion depended heavily on the pore size of the catalysts. The rhenium oxide on conventional alumina (denoted Re/ALCOA) that had micropores exhibited a much lower conversion compared to Re/OMA. In addition, higher conversions were observed with Re/OMA with larger mesopores. Although the mesoporous alumina supports with different pore sizes were prepared by different methods, and thus the surface chemical properties might also be more or less different, it is reasonable to conclude that the pore size is the major factor that influences the conversion. The authors suggested that the active Re sites in larger pores may be much more easily accessible for long-chain olefin substrates, and that the larger pores were also favorable for product release from the mesoporous network.

The same group subsequently applied the Re/OMA catalysts to the metathesis of dienes and cycloalkenes to determine the effect of pore size on the product distributions [29]. One example that clearly showed the effect was the metathesis of 1,7-octadiene **55** to yield cyclohexene **12** and a small amount of 1,7,13-tetradecatriene. For this reaction, two types of mesoporous alumina-supported 9.3 wt% Re catalysts were tested; these were prepared using mesoporous aluminas with different pore diameters of 3.5 nm (denoted Re/OMA3.5) and 6.5 nm (denoted Re/OMA6.5). The yield of 1,7,13-tetradecatriene reached a maximum of approximately 5% in 25 min at 40°C over both catalysts, but began to decrease after 25 min over Re/OMA6.5, while remaining constant for 250 min with Re/OMA3.5. This indicated that the large mesopores of Re/OMA6.5 were sufficient for the triene molecules to re-enter and react with the internal Re species to give **12**. Another example was seen in the reaction of 1,9-decadiene **60** to the corresponding dimers, trimers, and tetramers (**54**,  $n = 2-4$ ), which was carried out

in toluene solvent using the same catalysts. The formation of these compounds occurred much more rapidly with Re/OMA6.5 than with Re/OMA3.5. In addition, the final amount of products was decreased in the order of dimers > trimers > tetramers > oligomers over Re/OMA3.5, whereas the order was changed to tetramers > trimers > dimers > oligomers over Re/OMA6.5. It is also noteworthy that the final conversion was higher for Re/OMA6.5 than for Re/OMA3.5. These results demonstrated that the larger mesopore of the Re/OMA6.5 was favorable for the reaction of larger-sized molecules. The authors stressed that the use of mesoporous alumina supports with different pore sizes provided the opportunity to tune the product distributions in olefin metathesis by using a “molecular sieving” effect.

Quite recently, Balcar *et al.* reported the metathesis of oxygen-containing terminal olefins promoted by the Re/OMA catalysts and Me<sub>4</sub>Sn as cocatalyst [31]. The main objective was, as in the former studies, to determine the effect of pore size on catalysis. The metathesis of *p*-allylanisole **33** at 25 °C in decane solvent proceeded only when Me<sub>4</sub>Sn was present in the reaction mixture, and gave the corresponding product **34** in 100% selectivity, regardless of the pore size of the mesoporous catalysts. Conversion at the initial and final stages of the reaction, on the other hand, was increased with as the pore size of the catalyst increased. It is also noteworthy that the conventional Re/ALCOA catalyst with micropores exhibited almost no activity for the metathesis at 25 °C in toluene solvent, whereas the conversions given by the Re/OMA catalysts under the same conditions exceeded 80% in 5 h, indicating that the presence of organized mesopores (and particularly of larger mesopores) is crucial in order to achieve a high catalytic performance. This tendency was the same as observed in previous studies of nonfunctionalized 1-decene metathesis [28], and was also seen in the cross-metathesis between **33** and **18**. The ring-closing metathesis (RCM) of diethyl diallylmalonate **56** was also tested with the Re/OMA–Me<sub>4</sub>Sn catalytic system. Under optimal conditions (i.e., a substrate:Re molar ratio of 40:1; reaction temperature 25 °C), a conversion of over 75% and 100% selectivity to **57** were achieved in 2 h with the Re/OMA catalysts, of which the parent supports had pore diameters of 4–7 nm. In contrast, a much lower conversion (ca. 50%) was observed for the Re/OMA prepared from the mesoporous alumina with a 3 nm pore diameter, again indicating the importance of larger mesopores also for this RCM reaction. It is of interest to note that **56** deactivated the Re/OMA catalysts more intensively than did **33**. Although the reason for this was not proposed, the present authors suggest that the strong interaction of the active Re sites with a polarized carbonyl group in **56** would inhibit the metathesis.

Aguado *et al.* investigated the metathesis of 1-hexene **25** over rhenium oxide supported on a commercially available alumina, and their original mesoporous alumina [32]. The commercial material was the MSU-type alumina synthesized with nonionic polyethylene oxides (Table 15.1, I), whereas the original alumina was prepared by the hydrolysis of aluminum isopropoxide in the presence of a cationic surfactant of CTAB at pH ≈ 1; the latter mixture was then heated at 80 °C, dried at 110 °C, and calcined at 550 °C. Rhenium oxide was loaded onto the alumi-

nas (using an impregnation method) from an aqueous solution of  $\text{HReO}_4$ , followed by drying at  $110^\circ\text{C}$ , calcination under a dry air flow, and cooling to room temperature under a dry  $\text{N}_2$  flow. The decrease in surface area after rhenium oxide loading was noticeable for the commercial mesoporous alumina (MSU), with the value changing from  $317$  to  $187\text{m}^2\text{g}^{-1}$ . In contrast, a much smaller decrease, from  $300$  to  $274\text{m}^2\text{g}^{-1}$ , was observed for the original alumina (SGAL). The pore sizes, on the other hand, were enlarged from  $5.3$  to  $7.4\text{nm}$  and from  $6.9$  to  $8.5\text{nm}$  for MSU and SGAL, respectively. The activity order for the metathesis of **25** performed at  $40^\circ\text{C}$ ,  $\text{Re}_2\text{O}_7/\text{MSU} > \text{Re}_2\text{O}_7/\text{SGAL} \gg \text{Re}_2\text{O}_7/\gamma\text{-Al}_2\text{O}_3$  (conventional), clearly demonstrated the superiority of mesoporous alumina as a support for rhenium oxide, where 9wt% of  $\text{Re}_2\text{O}_7$  was loaded onto each alumina. Selectivity for the self-metathesis product **26** exceeded 99% for all of these catalysts. It is also noteworthy that rhenium leaching was not observed by inductively coupled plasma (ICP) analysis for all of the reactions. The effect of modifying the solvent and  $\text{Re}_2\text{O}_7$  content in  $\text{Re}_2\text{O}_7/\text{SGAL}$  revealed dodecane to be the best solvent for the metathesis, and the optimum loading to be 6–10wt%. The authors examined the surface acidity of the catalysts in detail. Subsequent  $^{31}\text{P}$  MAS NMR spectroscopy using triethylphosphine oxide as a probe molecule indicated that the intensity of the peak at approximately 80ppm, which is attributed to the strongest Lewis acids sites, increased in the order of  $\text{Re}_2\text{O}_7/\text{MSU} > \text{Re}_2\text{O}_7/\text{SGAL} \gg \text{Re}_2\text{O}_7/\gamma\text{-Al}_2\text{O}_3$ , which was also in good agreement with the activity order for the metathesis. The absence of Brønsted acid sites on the catalysts was confirmed by the diffuse reflectance infrared Fourier transform (DRIFT) spectra of adsorbed pyridine. The authors concluded that the metathesis activity was mainly governed by the surface Lewis acidity, and insisted that the importance of the interaction between the monomeric rhenium species and the Lewis acid  $\text{Al}^{3+}$  sites on mesoporous alumina would generate active rhenium sites, as had been proposed by Oikawa *et al.* (see Figure 15.13).

It seems that the major task in heterogeneous catalytic olefin metathesis chemistry is to develop functional group-tolerant, highly active catalysts. As described above, Balcar *et al.* have reported that rhenium oxide, when supported on mesoporous alumina and with  $\text{Me}_4\text{Sn}$  as cocatalyst, will promote the metathesis of olefins containing oxygen atoms [31]. Oikawa and coworkers, on the other hand, have developed methyltrioxorhenium (MTO,  $\text{MeReO}_3$ ) doped on a  $\text{ZnCl}_2$ -modified mesoporous alumina as a functional group-tolerant, heterogeneous catalyst [30]. The mesoporous alumina used was the  $\text{L}_{\text{A}383}$  alumina (Table 15.1, II, calcined finally at  $600^\circ\text{C}$ ), while  $\text{ZnCl}_2$  was doped onto the alumina using an impregnation method from an ethanolic solution, followed by drying and calcination at  $400^\circ\text{C}$ . Subsequent characterization by  $\text{N}_2$  adsorption–desorption showed that the  $\text{ZnCl}_2$ -modified mesoporous alumina (denoted  $\text{ZnCl}_2//\text{meso-Al}_2\text{O}_3$ ) had regular mesopores with a relatively narrow pore-size distribution and a high surface area. The  $\text{ZnCl}_2//\text{meso-Al}_2\text{O}_3$  was suspended in  $\text{CH}_2\text{Cl}_2$ , and to the suspension was added a solution of MTO in  $\text{CH}_2\text{Cl}_2$  to yield the catalyst (denoted  $\text{MTO}/\text{ZnCl}_2//\text{meso-Al}_2\text{O}_3$ ). Typically, 3.0wt% MTO was loaded and an Al/Zn ratio of 16 was chosen. Olefins with ester (**35**, **36**, **39–41**, **45**), ketone (**47**), bromide (**49**), and chloride (**50**) groups were converted into the corresponding products at much higher yields with MTO/



ZnCl<sub>2</sub>//*meso*-Al<sub>2</sub>O<sub>3</sub> than with MTO/SiO-Al<sub>2</sub>O<sub>3</sub>, as developed previously by Herrmann *et al.* as a functional group-tolerant heterogeneous catalyst. When the effect of the pore size of the parent mesoporous alumina on catalytic performance was also investigated in the metathesis of methyl 10-undecenoate **35**, the results revealed that the mesoporous alumina with larger pore sizes and pore volumes would afford the corresponding product **37** at higher yields. This trend was in perfect accord with that observed by the Czech group [28, 29, 31].

The ZnCl<sub>2</sub>-modified mesoporous alumina (ZnCl<sub>2</sub>//*meso*-Al<sub>2</sub>O<sub>3</sub>) was designed in order that the mesoporous alumina should have a greater Lewis acidic character. The most interesting point here was that MTO, or a combination of MTO and ZnCl<sub>2</sub> in CH<sub>2</sub>Cl<sub>2</sub>, showed no catalytic ability for the olefin metathesis. However, when MTO contacted with the ZnCl<sub>2</sub>//*meso*-Al<sub>2</sub>O<sub>3</sub> support, the MTO/ZnCl<sub>2</sub>//*meso*-Al<sub>2</sub>O<sub>3</sub> catalyst promoted the metathesis efficiently because the MTO was activated by the Lewis acidic sites on ZnCl<sub>2</sub>//*meso*-Al<sub>2</sub>O<sub>3</sub>. This was the first example of a catalytic reaction in which organometallic intermediates were activated by Lewis acidic inorganic supports. The Lewis acid character of ZnCl<sub>2</sub>//*meso*-Al<sub>2</sub>O<sub>3</sub> provided another feature; in the metathesis of simple olefins such as 1-octene **18** and 7-hexadecene **27**, catalyzed by MTO/ZnCl<sub>2</sub>//*meso*-Al<sub>2</sub>O<sub>3</sub>, no olefin isomerization was observed because the Lewis acid sites had no ability to shift a double bond in the olefin. In contrast, MTO/SiO<sub>2</sub>-Al<sub>2</sub>O<sub>3</sub> (Herrmann's catalyst) produced a variety of olefins as SiO<sub>2</sub>-Al<sub>2</sub>O<sub>3</sub> was seen to be a typical Brønsted acid support and to promote olefin isomerization prior to or during the metathesis.

### 15.3.6

#### Oxidative Dehydrogenation

Oxidative dehydrogenation involves the catalytic dehydrogenation of alkanes to the corresponding alkenes in the presence of gaseous oxygen. One of the most active catalysts for this reaction is alumina-supported vanadium oxide, and this especially effective for ethane and propane. Concepción *et al.* employed mesoporous alumina as support and conducted the oxidative dehydrogenation of ethane **64** to ethylene **20** (Table 15.2, VI) [33]. The mesoporous alumina was synthesized using a method similar to that of Davis, with stearic acid as a surfactant (Table 15.1, II). Vanadium was loaded onto the alumina by impregnation from an ethanolic solution of vanadyl acetylacetonate, followed by drying with a rotary evaporator and calcination at 600 °C. The mesoporous structure was preserved up to a V-loading of 17.4 wt%. Analyses with UV-DRS and <sup>51</sup>V wide-line and MAS NMR spectroscopy indicated that the mesoporous alumina behaved similar to conventional alumina for the V-loading, except that it permitted the incorporation of a greater amount of vanadium atoms, without forming the polymeric vanadium species "bulk-type" V<sub>2</sub>O<sub>5</sub> composed of octahedral V<sup>5+</sup> species. This effect can be explained in terms of the larger surface area of mesoporous alumina compared to conventional alumina. Although the specific activity per vanadium atom was lower on mesoporous alumina than on conventional alumina, the mesoporous alumina-supported vanadium catalyst could afford higher space-time yields and selectivity for the oxidative



dehydrogenation of **64** to **20**, due to the larger number of active tetrahedral  $V^{5+}$  species. The mesoporous catalyst containing 9.7 wt% vanadium was best in terms of selectivity and showed a good catalytic performance at higher reaction temperatures. A V-content >9.7 wt% led to the formation of more octahedral  $V^{5+}$  species and Brønsted acid sites, which promoted an unfavorable deep oxidation of **64** and **20** to carbon oxides.

Later, the same group investigated the effect of molybdenum addition on the catalysis (Table 15.2, VI) [34]. Molybdenum (ammonium heptamolybdate) and vanadium were each loaded onto the mesoporous alumina in similar fashion, with a Mo/(Mo + V) ratio of 0.32 to 0.77. Increasing this ratio led to a decrease in the surface area, although the change was not significant (surface area range: 213–248  $m^2 g^{-1}$ ). Characterization by XRD and Raman spectroscopy revealed an absence of molybdovanadate species (i.e., mixed Mo–V–O species), indicative of the high metal dispersion on the catalysts due to the high surface area of mesoporous alumina. A synergetic effect between Mo and V was observed in terms of the better activity and selectivity compared to the pure Mo and V catalysts. The authors proposed two reasons for the favorable effect of Mo addition: (i) the coverage of nonselective sites of mesoporous alumina by molybdenum species, which suppressed the formation of carbon oxides and increased the selectivity to ethylene; and (ii) the formation of active molybdovanadate species, even though such species could not be observed with XRD and Raman spectroscopy. In all cases, the use of mesoporous alumina as a support led to a higher activity and selectivity than when using conventional  $\gamma-Al_2O_3$ , this being consistent with a former report [33].

### 15.3.7

#### Oxidative Methanol Steam Reforming

The oxidative steam reforming of methanol (OSRM) represents a promising catalytic process for the production of hydrogen from methanol, water, and oxygen. The process is a combination of the endothermic methanol steam reforming with the exothermic partial oxidation of methanol, with a zero net enthalpy. Lenarda *et al.* synthesized finely dispersed Pd–Zn on mesoporous alumina as catalyst for the OSRM reaction (Table 15.2, VII) [35]. The mesoporous alumina was synthesized with stearic acid as surfactant, using a method similar to that of Davis (Table 15.1, II, calcined finally at 500 °C). Palladium was then loaded onto the alumina by impregnation from an ethanolic solution of palladium acetate, and the resultant solid subsequently contacted with  $Zn(BH_4)_2$  in diethyl ether solvent, followed by drying. The as-made material (denoted PZBAA) was reduced in a hydrogen-flow at 500 °C to give the mesoporous alumina-supported Pd–Zn alloy catalyst (denoted PZBAAr), which contained 1.7 wt% Pd and 12.9 wt% Zn. Both the PZBAAr and PZBAA samples showed type IV isotherms with a hysteresis loop typical of mesoporous materials. The surface area and pore volume of PZBAAr were smaller than those of the parent mesoporous alumina, but the pore-sizes were almost the same. The XRD, XPS, and IR spectra of adsorbed CO revealed that the Pd–Zn alloy was not present on PZBAA, but formed only after a high-temperature treatment with hydrogen-flow (i.e., on PZBAAr). The OSRM was carried out with

a fixed-bed, continuous-flow reactor using the PZBAAr catalyst pretreated in a stream of O<sub>2</sub> at 400 °C, followed by H<sub>2</sub> at 400 °C. In order for the reaction to take place, a temperature above 250 °C was required, and the methanol conversion reached 100% at 350 °C, giving H<sub>2</sub> in a yield of 2.52% (defined as: (mol of H<sub>2</sub>)/(mol of CH<sub>3</sub>OH), theoretical value: 2.75). The reaction at 350 °C, however, also afforded 3% CO that was not the OSRM product. Both XPS and IR studies of CO adsorption implied the presence of metallic Pd on the surface, which could promote CO formation reactions such as the decomposition of methanol and the reverse water gas-shift reaction. The authors stressed that the high H<sub>2</sub> yield at 350 °C with the PZBAAr catalyst was unusual for such low active metal loadings.

## 15.4

### Conclusions and Outlook

Today, mesoporous alumina is becoming a relatively “common” catalyst and catalyst support, with several synthetic methods using various types of structure-directing agents having been developed. Nonetheless, the search continues to produce mesoporous alumina with better structural qualities. Whilst mesoporous alumina itself exhibits a unique catalytic performance, as seen in the base catalysis in scCO<sub>2</sub>, it serves as a much better support for metal-loading compared to conventional alumina, owing to its intrinsic high surface area. Interestingly, “molecular sieving,” which is well established in zeolite catalysis chemistry, has also been observed in several olefin-metathesis reactions promoted by mesoporous, alumina-supported Re catalysts. It is expected that these fundamental studies and future investigations in this area will lead to the practical use of mesoporous alumina as both catalyst and catalyst support in large-scale production processes in the chemical industry.

### References

- 1 Valenzuela Calahorra, C., Chaves Cano, T. and Gomez Serrano, V. (1972) IUPAC manual of symbols and terminology. Appendix 2, Part 1, Colloid and surface chemistry. *Pure Appl. Chem.*, **31**, 578.
- 2 (a) Breck, D.W. (1964) *J. Chem. Educ.*, **41**, 678.  
 (b) Csicsery, S.M. (1976) *Zeolite Chemistry and Catalysis* (ed. J.A. Rabo), ACS Monograph 171, American Chemical Society, p. 680.  
 (c) Weisz, P.B. (1980) *Pure Appl. Chem.*, **52**, 2091.  
 (d) Breck, D.W. (1984) *Zeolite Molecular Sieves*, Kreiger Publishing Company.  
 (e) Chen, N.Y., Garwood, W.E. and Dwyer, F.G. (1989) *Shape Selective Catalysis in Industrial Application*, Marcel Dekker.  
 (f) Baerlocher, C., Meier, W.M. and Olson, D.H. (2001) *Atlas of Zeolite Framework Types*, 5th edn, Elsevier, <http://www.iza-structure.org/databases/>.  
 (g) Cundy, C.S. and Cox, P.A. (2003) *Chem. Rev.*, **103**, 663.
- 3 (a) Kresge, C.T., Leonowicz, M.E., Roth, W.J., Vartuli, J.C. and Beck, J.S. (1992) *Nature*, **359**, 710.  
 (b) Beck, J.S., Vartuli, J.C., Roth, W.J., Leonowicz, M.E., Kresge, C.T., Schmitt, K.D., Chu, C.T.-W., Olson, D.H.,

- Sheppard, E.W., McCullen, S.B., Higgins, J.B. and Schlenker, J.L. (1992) *J. Am. Chem. Soc.*, **114**, 10834.
- 4 Synthesis of mesoporous oxides other than alumina: (a) For magnesium: Takenaka, S., Sato, S., Takahashi, R. and Sodesawa, T. (2003) *Phys. Chem. Chem. Phys.*, **5**, 4968.
- (b) For magnesium: Li, W.-C., Lu, A.-H., Weidenthaler, C. and Schüth, F. (2004) *Chem. Mater.*, **16**, 5676.
- (c) For titanium: Antonelli, D.M. and Ying, J.Y. (1995) *Angew. Chem. Int. Ed. Engl.*, **34**, 2014.
- (d) For titanium and niobium: Stone, V.F. Jr. and Davis, R.J. (1998) *Chem. Mater.*, **10**, 1468.
- (e) For titanium: Yu, J.C., Wang, X. and Fu, X. (2004) *Chem. Mater.*, **16**, 1523.
- (f) For niobium: Antonelli, D.M. and Ying, J.Y. (1996) *Angew. Chem. Int. Ed. Engl.*, **35**, 426.
- (g) For niobium: Antonelli, D.M., Nakahira, A. and Ying, J.Y. (1996) *Inorg. Chem.*, **35**, 3126.
- (h) For tantalum: Antonelli, D.M. and Ying, J.Y. (1996) *Chem. Mater.*, **8**, 874.
- 5 Synthesis of mesoporous alumina: (a) Bagshaw, S.A. and Pinnavaia, T.J. (1996) *Angew. Chem. Int. Ed. Engl.*, **35**, 1102.
- (b) Vaudry, F., Khodabandeh, S. and Davis, M.E. (1996) *Chem. Mater.*, **8**, 1451.
- (c) Zhang, W. and Pinnavaia, T.J. (1998) *Chem. Commun.*, 1185.
- (d) Cabrera, S., El Haskouri, J., Alamo, J., Beltrán, A., Beltrán, D., Mendioroz, S., Dolores Marcos, M. and Amorós, P. (1999) *Adv. Mater.*, **11**, 379.
- (e) Yao, N., Xiong, G., Zhang, Y., He, M. and Yang, W. (2001) *Catal. Today*, **68**, 97.
- (f) González-Peña, V., Diaz, I., Márquez-Alvarez, C., Sastre, E. and Pérez-Pariente, J. (2001) *Microporous Mesoporous Mater.*, **44–45**, 203.
- (g) Cruise, N., Jansson, K. and Holmberg, K. (2001) *J. Colloid Interface Sci.*, **241**, 527.
- (h) Yao, N., Xiong, G., Zhang, Y., He, M. and Yang, W. (2001) *Catal. Today*, **68**, 97.
- (i) Zhang, Z., Hicks, R.W., Pauly, T.R. and Pinnavaia, T.J. (2002) *J. Am. Chem. Soc.*, **124**, 1592.
- (j) Shan, Z., Jansen, J.C., Zhou, W. and Maschmeyer, T. (2003) *Appl. Catal. A*, **254**, 339.
- (k) Xu, B., Xiao, T., Yan, Z., Sun, X., Sloan, J., Gonzalez-Cortes, S.L., Alshahrani, F. and Green, M.L.H. (2006) *Microporous Mesoporous Mater.*, **91**, 293.
- (l) Liu, Q., Wang, A., Wang, X. and Zhang, T. (2006) *Microporous Mesoporous Mater.*, **92**, 10.
- (m) Zhao, R., Guo, F., Hu, Y. and Zhao, H. (2006) *Microporous Mesoporous Mater.*, **93**, 212.
- (n) Žilková, N., Zukal, A. and Čejka, J. (2006) *Microporous Mesoporous Mater.*, **95**, 176.
- 6 (a) Huo, Q., Margolese, D.I., Ciesla, U., Feng, P., Gier, T.E., Sieger, P., Leon, R., Petroff, P.M., Schüth, F. and Stucky, G.D. (1994) *Nature*, **368**, 317.
- (b) Huo, Q., Margolese, D.I., Ciesla, U., Demuth, D.G., Feng, P., Gier, T.E., Sieger, P., Firouzi, A., Chmelka, B.F., Schüth, F. and Stucky, G.D. (1994) *Chem. Mater.*, **6**, 1176.
- 7 (a) Ertl, G., Knözinger, H. and Weitkamp, J. (1997) *The Handbook of Heterogeneous Catalysis*, Wiley-VCH Verlag GmbH, Weinheim.
- (b) Kabalka, G.W. and Pagni, R.M. (1997) *Tetrahedron*, **53**, 7999.
- (c) Euzen, P., Raybaud, P., Krokidis, X., Toulhoat, H., Le Loarer, J.-L., Jolivet, J.-P. and Froidefond, C. (2002) *Handbook of Porous Materials* (eds F. Schüth, K. Sing and J. Weitkamp), Wiley-VCH Verlag GmbH, Weinheim, p. 1591.
- 8 Bartholomew, C.H. and Farrauto, R.J. (2006) *Fundamentals of Industrial Catalytic Process*, 2nd edn, John Wiley & Sons, Inc., Hoboken, New Jersey, p. 260.
- 9 Čejka, J. (2003) *Appl. Catal. A*, **254**, 327.
- 10 (a) Yada, M., Machida, M. and Kijima, T. (1996) *Chem. Commun.*, 769.
- (b) Yada, M., Hiyoshi, H., Ohe, K., Machida, M. and Kijima, T. (1997) *Inorg. Chem.*, **36**, 5565.
- 11 Brunauer, S., Deming, L.S., Deming, W.E. and Teller, E. (1940) *J. Am. Chem. Soc.*, **62**, 1723.
- 12 McBain, J.W. (1935) *J. Am. Chem. Soc.*, **57**, 699.

- 13 Brunauer, S., Emmett, P.H. and Teller, E. (1938) *J. Am. Chem. Soc.*, **60**, 309.
- 14 Barrett, E.P., Joyner, L.G. and Halenda, P.P. (1951) *J. Am. Chem. Soc.*, **73**, 373.
- 15 Dollimore, D. and Heal, G.R. (1964) *J. Appl. Chem.*, **14**, 109.
- 16 Čejka, J., Žilková, N., Rathouský, J. and Zukal, A. (2001) *Phys. Chem. Chem. Phys.*, **3**, 5076.
- 17 (a) Yamaguchi, G. and Yanagida, H. (1962) *Bull. Chem. Soc. Jpn.*, **35**, 1896.  
(b) Yanagida, H. and Yamaguchi, G. (1964) *Bull. Chem. Soc. Jpn.*, **37**, 1229.  
(c) Yanagida, H., Yamaguchi, H. and Kubota, J. (1965) *Bull. Chem. Soc. Jpn.*, **38**, 2194.
- 18 (a) Seki, T. and Onaka, M. (2005) *Chem. Lett.*, **34**, 262.  
(b) Seki, T. and Onaka, M. (2006) *J. Phys. Chem. B*, **110**, 1240.  
(c) Seki, T. and Onaka, M. (2006) *Catal. Surv. Asia*, **10**, 138.
- 19 Seki, T. and Onaka, M. (2007) *J. Mol. Catal. A*, **263**, 115.
- 20 Seki, T., Ikeda, S. and Onaka, M. (2006) *Microporous Mesoporous Mater.*, **96**, 121.
- 21 Yin, D., Qin, L., Liu, J., Li, C. and Jin, Y. (2005) *J. Mol. Catal. A*, **240**, 40.
- 22 Chaube, V.D., Shylesh, S. and Singh, A.P. (2005) *J. Mol. Catal. A*, **241**, 79.
- 23 Kim, P., Kim, Y., Kim, C., Kim, H., Park, Y., Lee, J.H., Song, I.K. and Yi, J. (2003) *Catal. Lett.*, **89**, 185.
- 24 Kim, P., Kim, Y., Kim, H., Song, I.K. and Yi, J. (2004) *J. Mol. Catal. A*, **219**, 87.
- 25 Kim, P., Kim, Y., Kim, H., Song, I.K. and Yi, J. (2005) *J. Mol. Catal. A*, **231**, 247.
- 26 Kaluža, L., Zdražil, M., Žilková, N. and Čejka, J. (2002) *Catal. Commun.*, **3**, 151.
- 27 (a) Onaka, M. and Oikawa, T. (2002) *Chem. Lett.*, 850.  
(b) Oikawa, T., Ookoshi, T., Tanaka, T., Yamamoto, T. and Onaka, M. (2004) *Microporous Mesoporous Mater.*, **74**, 93.
- 28 Balcar, H., Hamtil, R., Žilková, N. and Čejka, J. (2004) *Catal. Lett.*, **97**, 25.
- 29 Hamtil, R., Žilková, N., Balcar, H. and Čejka, J. (2006) *Appl. Catal. A*, **302**, 193.
- 30 Oikawa, T., Masui, Y., Tanaka, T., Chujo, Y. and Onaka, M. (2007) *J. Organomet. Chem.*, **692**, 554.
- 31 Balcar, H., Hamtil, R., Žilková, N., Zhang, Z., Pinnavaia, T.J. and Čejka, J. (2007) *Appl. Catal. A*, **320**, 56.
- 32 Aguado, J., Escola, J.M., Castro, M.C. and Paredes, B. (2005) *Appl. Catal. A*, **284**, 47.
- 33 Concepción, P., Navarro, M.T., Blasco, T., López Nieto, J.M., Panzacchi, B. and Rey, F. (2004) *Catal. Today*, **96**, 179.
- 34 Solsona, B., Dejoz, A., Garcia, T., Concepción, P., Lopez Nieto, J.M., Vázquez, M.I. and Navarro, M.T. (2006) *Catal. Today*, **117**, 228.
- 35 Lenarda, M., Moretti, E., Storaro, L., Patrono, P., Pinzari, F., Rodríguez-Castellón, E., Jiménez-López, A., Busca, G., Finocchio, E., Montanari, T. and Frattini, R. (2006) *Appl. Catal. A*, **312**, 220.
- 36 Kim, Y., Lee, B. and Yi, J. (2002) *Korean J. Chem. Eng.*, **19**, 908.
- 37 (a) Schrock, R.R. and Hoveyda, A.H. (2003) *Angew. Chem. Int. Ed. Engl.*, **42**, 4592.  
(b) Trnka, T.M. and Grubbs, R.H. (2001) *Acc. Chem. Res.*, **34**, 18.



## 16 Nanoceramics for Medical Applications

Besim Ben-Nissan and Andy H. Choi

### 16.1 Introduction

“Nanostructured materials” refer to certain materials which have delicate structures and sizes that fall within the range of 1 to 100 nm. As a consequence of this size, an extensive development of nanotechnology has taken place in the fields of materials science and engineering during the past decade. Yet, such developments have not come as a surprise, when it is appreciated that these nanostructured materials have the ability to be adapted and integrated into biomedical devices. This is possible because most biological systems, including viruses, membranes and protein complexes, exhibit natural nanostructures.

The microstructure and properties of nanostructured materials depend in an extreme manner on the method of their synthesis method, as well as on their processing route. Consequently, it is extremely important to select the most appropriate technique when preparing nanomaterials with desired properties and property combinations. The synthesis techniques most commonly used for the production of advanced ceramics include pressing, as well as wet chemical processing techniques such as co-precipitation and sol-gel, all of which have been used to produce nanoparticles, nanocoatings, and nanostructured solid blocks and shapes.

In modern ceramics technology, *pressing* is accomplished by placing the powder into a die and applying pressure to achieve compaction. Hot pressing (HP) and hot isostatic pressing (HIP) are the most common methods used to produce bioceramics. HIP can induce the higher densities and small grain structures required by bioceramics, whereby heat and pressure are applied simultaneously and the pressure is applied from all directions via a pressurized gas such as helium or argon. In contrast, flat plates or blocks and nonuniform components are relatively easily produced using HP.

*Sol-gel processing* is unique in that it can be used to produce different forms, such as powders, platelets, coatings, fibers and monoliths of the same composition, merely by varying the chemistry, viscosity, and other factors of a given solution. The advantages of the sol-gel technique are numerous:

- it is of the nanoscale
- it results in a stoichiometric, homogeneous and pure product, owing to mixing on the molecular scale
- high purity can be maintained as grinding can be avoided
- it allows reduced firing temperatures due to the small particle sizes with high surface areas
- it can be used to produce uniform, fine-grained structures
- it allows the use of different chemical routes (alkoxide or aqueous-based)
- it is easily applied to complex shapes with a range of coating techniques.

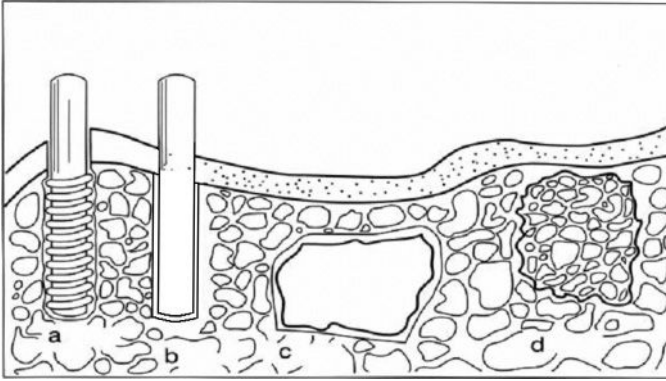
Sol–gel coatings also have the added advantages that the costs of the precursors are relatively unimportant, owing to the small amounts of materials required. Shrinkage up to a number of coatings, depending on the chemistry, is fairly uniform perpendicular to the substrate, and the coatings can dry rapidly without cracking. Shrinkage becomes an important issue, however, in monolith ceramic production.

At present, the most common materials in clinical use are those selected from a handful of well-characterized and available biocompatible ceramics, including metals, polymers, and their combinations as composites or hybrids. These unique production techniques, together with the development of new enabling technologies such as microscale, nanoscale, bioinspired fabrication (biomimetics) and surface modification methods, have the potential to drive at an unprecedented rate the design and development of new nanomaterials useful for medical applications.

The current focus is on the production of new nanoceramics that are relevant to a broad range of applications, including: implantable surface-modified medical devices for better hard- and soft-tissue attachment; increased bioactivity for tissue regeneration and engineering; cancer treatment; drug and gene delivery; treatment of bacterial and viral infections; delivery of oxygen to damaged tissues; imaging; and materials for minimally invasive surgery. A more futuristic view, which could in fact become reality within two decades, includes nanorobotics, nanobiosensors, and micronanodevices for a wide range of biomedical applications.

A *biomaterial*, by definition, is a nondrug substance that is suitable for inclusion in systems that augment or replace the function of bodily tissues or organs. A century ago, artificial devices made from materials as diverse as gold and wood were developed to a point where they could replace the various components of the human body. These materials were capable of being in contact with bodily fluids and tissues for prolonged periods of time, while eliciting little, if any, adverse reactions.

When these synthetic materials are placed within the human body, the tissues react towards the implant in a variety of ways. The mechanism of tissue interaction at a nanoscale level is dependent on the response to the implant surface, and as such three terms which describe a biomaterial, with respect to the tissues' responses, have been defined, namely *bioinert*, *bioresorbable*, and *bioactive* (Figure 16.1):



**Figure 16.1** Classification of bioceramics according to their bioactivity. (a) Bioinert (alumina dental implant); (b) Bioactive, hydroxyapatite ( $\text{Ca}_{10}(\text{PO}_4)_2(\text{OH})_2$ ) coating on a metallic dental implant; (c) Surface-active, bioglass or A-W glass; (d) Bioresorbable tricalcium phosphate implant [ $\text{Ca}_3(\text{PO}_4)_2$ ].

- *Bioinert* refers to any material that, once placed within the human body, has a minimal interaction with its surrounding tissue; examples include stainless steel, titanium, alumina, partially stabilized zirconia, and ultra-high-molecular-weight polyethylene.
- *Bioactive* refers to a material which, upon being placed within the human body, interacts with the surrounding bone and, in some cases, even soft tissue.
- *Bioresorbable* refers to a material that, upon placement within the human body, begins to dissolve or to be resorbed and slowly replaced by the advancing tissues (e.g., bone).

During the early 1970s, bioceramics were employed as implants to perform singular, biologically inert roles. The limitations of these synthetic materials as tissue substitutes were highlighted with the increasing realization that the cells and tissues of the body perform many other vital regulatory and metabolic roles. The demands of bioceramics have since changed, from maintaining an essentially physical function without eliciting a host response, to providing a more positive interaction with the host. This has been accompanied by increasing demands on medical devices that they not only improve the quality of life but also extend its duration. Most importantly, nanobioceramics—at least potentially—can be used as body interactive materials, helping the body to heal, or promoting the regeneration of tissues, thus restoring physiological functions.

The main factors in the clinical success of any biomaterial are its *biocompatibility* and *biofunctionality*, both of which are related directly to tissue/implant interface interactions. This approach is currently being explored in the development of a new generation of nanobioceramics with a widened range of medical applications. The improvement of interface bonding by nanoscale coatings, based



on biomimetics, has been of worldwide interest during the past decade, and today several companies are in early commercialization stages of new-generation, nanoscale-modified implants for orthopedic, ocular, and maxillofacial surgery, as well as for hard- and soft-tissue engineering.

*Biomimetic processing* is based on the notion that biological systems store and process information at the molecular level, and the extension of this concept to the processing of nanocomposites for biomedical devices and tissue engineering, such as scaffolds for bone regeneration, has been brought out during the past decade [1]. Several research groups have reported the synthesis of novel bone nanocomposites of hydroxyapatite (HAp) and collagen, gelatin, or chondroitin sulfate, through a self-assembly mechanism. These self-assembled experimental bone nanocomposites have been reported to exhibit similarities to natural bone in not only their structure but also their physiological properties [2].

The term *nanocomposite* can be defined as a heterogeneous combination of two or more materials, in which at least one of those materials should be on a nanometer-scale. By using the composite approach, it is possible to manipulate the mechanical properties such as strength and modulus of the composites closer to those of natural bone, with the help of secondary substitution phases. For example, HAp–polymer composites have been shown to have an elastic modulus close to that of bone.

The fabrication of a nanocomposite can be achieved by physically mixing or introducing a new component into an existing nanosized material, which allows for property modifications of the nanostructured materials and may even offer new material functions. For example, some biopolymers and biomolecules, such as poly(lactic acid) (PLA), poly(lactic-co-glycolic acid) (PLGA), polyamide, collagen, silk fibrin, chitosan, and alginate have been reported to mix into nanohydroxyapatite (nanoHAp) systems.

Another form of nanocomposite which has been developed for biomedical applications is the *gel system*. For this, nanostructured materials can be entrapped in to a gel (a three-dimensional (3-D) network immersed in a fluid), such that the properties of the nanomaterials can be improved and tailored to suit the specific needs of certain biomedical devices. A *nanogel*, which is a nanosized, flexible hydrophilic polymer gel [3], is an example of a gel that can be used in drug delivery carriers. These nanogels can bind and encapsulate spontaneously (through ionic interactions) any type of negatively charged oligonucleotide drug. A key advantage of nanogels is that they allow for a high “payload” of macromolecules (up to 50 wt%), a value which normally cannot be approached with conventional nanodrug carriers [4]. Recently, a novel intracellular biosensor has been fabricated by entrapping indicator dyes into an acrylamide hydrogel [5, 6], whilst a carbon nanotube (CNT) aqueous gel has been developed as an enzyme-friendly platform for use in enzyme-based biosensors [7].

This aim of this chapter is to provide information relating to the use of bioceramics for medical applications, including tissue engineering and regeneration using scaffolds and liposomes, nanoHAp powders for medical applications, calcium phosphate nanocoatings and other surface modification techniques, simu-

lated body fluids, and nano- and macrobioceramics for use in drug delivery and radiotherapy.

## 16.2

### Tissue Engineering and Regeneration

#### 16.2.1

##### Scaffolds

In the past, the development of bone tissue engineering has been directly related to changes in materials and nanotechnology. While the inclusion of materials requirements is standard in the design process of engineered bone substitutes, it is also critical to incorporate clinical requirements such that clinically relevant devices can be engineered.

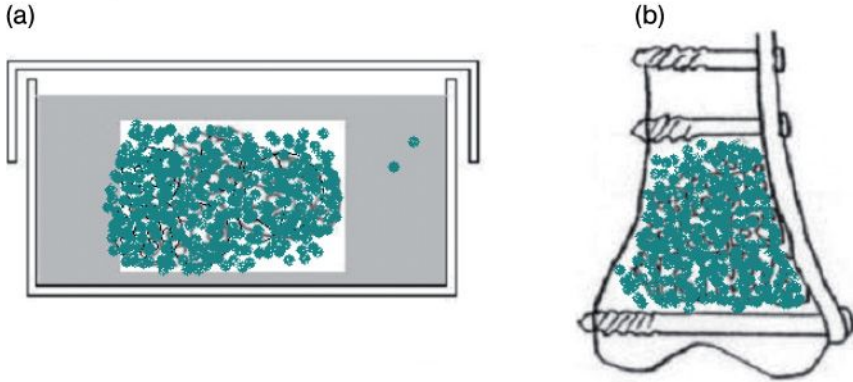
Multiple clinical reasons exist for the development of bone tissue-engineering alternatives, including a need for better filler materials when reconstructing large orthopedic defects, and for orthopedic implants that are mechanically more suitable to their biological environment. The traditional biological methods of bone-defect management include *autografting* and *allografting*.

Bone regeneration requires four components: (i) a morphogenetic signal; (ii) responsive host cells that will respond to the signal; (iii) a suitable carrier of this signal that can deliver it to specific sites then serve as scaffolding for the growth of the responsive host cells; and (iv) a viable—and most importantly—a well-vascularized host bed [8–10]. A *scaffolding material* is used either to induce the formation of bone from the surrounding tissue, or to act as a carrier or template for implanted bone cells or other agents.

The process of *bone regeneration* is common to the repair of fractures. The incorporation of bone grafts, the skeletal homeostasis and the cascading sequence of biological events are often described as the *remodeling cycle*. Stem cells have been incorporated into a range of bioceramics and when implanted, can combine with mineralized 3-D scaffolds to form highly vascularized bone tissue. These nanoscale cultured cell–bioceramic composites can be used to treat full-thickness gaps in long bone shafts, providing an excellent integration of the ceramic scaffold with bone, and a good functional recovery (Figure 16.2).

Peroglio *et al.* [11] have produced and characterized polycaprolactone (PCL)-coated alumina scaffolds to validate the concept of polymer–ceramic composites with increased fracture resistance. Alumina scaffolds were sintered using a foam replication technique, and the polymer coating was obtained by infiltrating the scaffold with either a PCL solution or nanodispersion.

*Bioactive glasses* are amorphous, silica-based materials that are biocompatible, bioactive, osteoconductive and even osteopductive. Sol–gel-derived bioactive glasses were developed by Hench *et al.* [12] to produce 3-D bioactive scaffolds with hierarchical interconnected pore morphologies similar to trabecular bone. The scaffolds consist of a pore network with macropores in excess of 500  $\mu\text{m}$



**Figure 16.2** Bone regeneration therapy using marrow mesenchymal cells for bone-graft applications for increased bioactivity. (a) The marrow cell/hydroxyapatite composite scaffold is cultured in an osteogenic medium; (b) After two to three weeks of culture, the cultured bone graft/hydroxyapatite composite is inserted into a bone defect.

that are connected by pore windows with diameters in excess of  $100\mu\text{m}$ , this being the minimum pore diameter required for tissue ingrowth and vascularization in the human body. The scaffolds also have textural porosity in the mesopore range (10–20 nm). The compressive strength reported was in the range of that for trabecular bone. In conclusion, Horsch *et al.* [12] stated that, by combining these properties with those inherent to sol–gel-derived bioactive glass, these scaffolds would have high potential as scaffolds for bone tissue engineering applications.

Considerable attention has also been paid during the past two decades to bioactive composite grafts that consists of a bioactive ceramic filler in a polymeric matrix. These bioactive composite grafts are designed essentially to achieve interfacial bonding between the graft and the host tissues. HAp/collagen, HAp/polyethylene (PE), and HAp/Ti-6Al-4V are notable examples of bioactive composite grafts [13, 14].

Of particular interest is the combination of HAp with collagen as a bioactive composite, as this appears to be a natural choice for bone grafting [15]. Skeletal bones comprise mainly collagen and carbonate-substituted HAp, both of which are osteoconductive components; consequently, an implant manufactured from such components is likely to behave in similar fashion. A composite matrix, when embedded with human-like osteoblast cells, showed better osteoconductive properties compared to monolithic HAp, and produced calcification of an identical bone matrix. In addition, collagen–HAp composites proved not only to be biocompatible in both humans and animals [16], but also to behave mechanically in a superior fashion to the individual components. Moreover, the ductile properties of collagen helped to increase the poor fracture toughness of HAp.

The reconstruction of bone tissue using nanocomposite bone grafts with structure, composition, physico-chemical, biomechanical, and biological features that

mimic those of natural bone, is a goal to be pursued. It is well known that natural bone consists of nanosized, plate-like crystals of HAp grown in intimate contact with an organic matrix which is rich in collagen fibers. One novel approach to fabricating nanocomposite bone grafts, using strategies found in Nature, has recently received much attention and is perceived to be beneficial over conventional methods. A variety of production methods have been employed for the formation of collagen–HAp composite gels, films, collagen-coated ceramics, ceramic-coated collagen matrices and composite scaffolds for spine and hard tissue repair [17].

*Stem cells* are cells from an embryo, fetus, or adult that have the ability to reproduce for long periods, and can also give rise to specialized cells that comprise the tissues and organs of the body. When implanted onto immunodeficient mice, stem cells were shown to combine with mineralized 3-D scaffolds to form a highly vascularized bone tissue. Cultured cell–bioceramic composites can be used to treat defects across the bone diaphysis, with excellent integration of the ceramic scaffold with bone, and a good functional recovery [18]. Excellent innovative studies with nanobioceramics are currently in progress, and clinical applications are becoming relatively common.

Vago and coworkers [19] have introduced a novel 3-D biomatrix obtained from the marine hydrocoral *Millepora dichotoma* as a scaffold for hard-tissue engineering. *M. dichotoma* was biofabricated under both field and laboratory conditions, and 3-D biomatrices prepared in order to convert mesenchymal stem cells (MSCs) to exemplify an osteoblastic phenotype. The effect of the biomatrices on the proliferation and differentiation of MSCs was then examined at 2, 3, 4, 7, 10, 14, 21, 28, and 42 days. The investigations included light microscopy, scanning electron microscopy (SEM) and energy dispersive spectroscopy (EDS), in addition to monitoring calcium incorporation into newly formed tissue (with Alizarin red staining), bone nodule formation (von Kossa staining), fat aggregate formation (oil red O staining), collagen type I immunofluorescence, DNA concentrations, alkaline phosphatase (ALP) activity, and osteocalcin concentrations. The MSCs seeded onto *M. dichotoma* biomatrices showed higher levels of calcium and phosphate incorporation, and higher type I collagen levels, than did control *Porites lutea* biomatrices. In addition, the ALP activity revealed that those MSCs seeded on *M. dichotoma* biomatrices were highly osteogenic compared to those on control biomatrices. The osteocalcin content of MSCs seeded on *M. dichotoma* remained constant for up to two weeks, before surpassing that of seeded *P. lutea* biomatrices after 28 days. The investigators reported that *M. dichotoma* biomatrices enhanced the differentiation of MSCs into osteoblasts, and hence showed excellent potential as bioscaffolding for hard-tissue engineering.

As emerging areas, both tissue and implant engineering are evolving to address the shortage of human tissue and organs. Feasible and productive strategies have been aimed at combining a relatively traditional approach, such as bioceramic implants, with the acquired knowledge applied to the field of cell growth and differentiation of osteogenic cells. The core of the tissue engineering and regenerative medicine is the fabrication of scaffolds, in which a given cell population is seeded,

proliferated, and differentiated with the introduction of functional cell types from many different sources [20].

Nanostructured materials and their modified forms offer some attractive possibilities in the fields of tissue and implant engineering, taking advantage of the combined use of living cells and 3-D ceramic scaffolds (Figure 16.2) to deliver vital cells to the damaged site of the patient. Recently, bone-like nanostructure scaffolds have been developed using the technology of composites to imitate natural bone in bone-tissue engineering [21].

The results of recent studies have suggested that *bone marrow stromal cells* might be a potential source of osteoblasts and chondrocytes, and can be used to regenerate damaged tissues using a tissue-engineering approach. However, these strategies require the use of an appropriate scaffold architecture that can support the formation *de novo* of bone and/or cartilage tissue, as in the case of osteochondral defects. Oliveira *et al.* [14, 22] developed a novel hydroxyapatite/chitosan (HAp/CS) bilayered scaffold by combining a sintering and a freeze-drying technique, aiming to show the potential of such scaffolds to be used in tissue engineering for osteochondral defects. Subsequently, *in vitro* (Phase 1) cell culture studies were carried out to evaluate the capacity of the HAp and CS layers to separately support the growth and differentiation of goat bone marrow stromal cells (GBMCs) into osteoblasts and chondrocytes, respectively. The data showed not only that the GBMCs were able to adhere and proliferate but also that the constructs exhibited a great potential for use in tissue-engineering strategies, leading to the formation of adequate tissue substitutes for the regeneration of osteochondral defects.

The effects of surface chemistry modifications of titanium alloy (Ti-6Al-4V) with zinc, magnesium, or alkoxide-derived nanocrystalline carbonate hydroxyapatite (CHAp) on the regulation of key intracellular signaling proteins in human bone-derived cells (HBDCs) cultured on these modified Ti-6Al-4V surfaces, have been investigated in Australia by Zreiqat *et al.* [23]. The surface modification with nanocrystalline CHAp was shown to contribute to successful osteoblast function and differentiation at the skeletal tissue–device interface.

The role of *gene therapy* in aiding wound healing and treating various diseases or defects has become increasingly important in the field of tissue engineering. The use of 3-D scaffolds in gene delivery has emerged as a popular and necessary delivery vehicle for obtaining controlled gene delivery. Ko *et al.* [24] described the techniques to synthesize composite scaffolds by combining natural polymers such as agarose and alginate with calcium phosphate (CaP). *Alginate* has been used extensively in various applications such as cell encapsulation seeding, gene delivery, and antibody or growth factor entrapment and release, while *agarose* has been used as a scaffold involved in cartilage repair. The incorporation of CaP into the agarose or alginate hydrogels was performed *in situ*. Ko *et al.* concluded that, by incorporating CaP into the agarose or alginate hydrogel, they were able to synthesize a scaffold that was mechanically strong and chemically suitable for use as a gene-delivery vehicle in tissue engineering.

For many implants, a sustained and controlled release of antibacterial agents into the wound site is desirable for combating infection. A further advantage of nanostructured sol–gel-derived glasses is that silver, which is known to have anti-

bacterial properties, can be incorporated into the glass composition. The addition of silver ions to bioactive glasses has also been investigated by Jones *et al.* [25], for the production of glasses with bactericidal properties. A bioactive glass scaffold containing 2 mol% silver was shown to release silver ions at a rate shown previously to be bactericidal in, but not cytotoxic to, bone cells.

### 16.2.2

#### Liposomes

Liposomes are the most clinically established nanometer-scale systems currently used to deliver nontoxic and antifungal drugs, genes, and vaccines; they are also being used as imaging agents. Liposomes consist of a single layer, or multiple concentric lipid bilayers, that encapsulate an aqueous compartment. The outstanding clinical profile of liposomes, compared to other delivery systems, is based on their biocompatibility, biodegradability, reduced toxicity, and capacity for size and surface manipulations [26].

Nanometer-sized particles, such as superparamagnetic iron oxides, semiconducting nanocrystals, silica nanoparticles, and calcium phosphate, each possess novel functions that include unique magnetic, optical, therapeutic, and medical properties. The encapsulation of these nanoparticles within liposomes may lead to an enhanced nanoparticle hydrophilicity, stability in plasma, and an overall improvement in their biocompatibility [26–28]. Furthermore, by utilizing the ability of liposomes to carry hydrophilic and hydrophobic moieties, combinatory therapy/imaging modalities can be achieved by incorporating therapeutics and diagnostic agents into a single liposome-delivery system [26].

Semiconductor nanocrystals, known as quantum dots (QDs) are fluorescent nanoparticles with a diameter in the range of 1 to 10 nm. QDs offer distinct spectrofluorometric advantages over traditional fluorescent organic molecules, with typical fluorescence characteristics 10 to 20-fold brighter than conventional dyes. QDs also exhibit a greater photostability, a broad excitation wavelength range, a size-tunable spectrum, and a narrow and symmetric emission spectrum. On the basis of these photophysical characteristics QDs are currently being investigated as potential imaging agents, primarily in fluorescence-based diagnostic applications [26].

The self-assembly of organized nanoscopic structures has been the subject of much interest in both colloidal and nanomaterials science. Indeed, some recent studies have shown that nanoscale liposomes can be used as a nanoscale template for the deposition of silica, so as to create a hollow silica nanoshell. These silicate materials have been used to encapsulate fluorescent dyes, enzymes, polymer particles, and liquids [27]. Moreover, the liposome–silica nanoparticle hybrid systems thus formed can be used in the design of biosensors, whereby the physical characteristics of silica can be matched with the biocompatibility and pharmaceutical and pharmacodynamic properties of liposomes [28].

Calcium phosphate-based hybrid nanoparticles have shown great promise as candidates for drug delivery and bone regeneration systems, based on the excellent biocompatibility of calcium phosphate [29]. Recently, hydroxyapatite-coated

liposomes (HACLs) were successfully manufactured and filled with a model hydrophobic (lipophilic) drug, namely indomethacin (IMC) [29]. In this process, the HAp layer was precipitated onto the liposomes, the aim being to provide the HACL with two functions: (i) that the inner core liposome provides a sustained drug release; and (ii) that the outer HAp layer provides the osteoconductivity for bone cells. The liposomes were formed from 1,2-dimyristoyl-*sn*-glycero-3-phosphate (DMPA) and 1,2-dimyristoyl-*sn*-glycero-3-phosphocholine (DMPC). The results reported by Xu *et al.* [29] indicated that precipitating HAp onto the liposome reduced the release rate of IMC compared to uncoated liposomes. In fact, under the conditions used, the 5 h period required to release 70% of the IMC from the liposomes was extended to 20 h when the liposomes were coated with HAp. Perhaps, more importantly, IMC release from the uncoated liposomes occurred more rapidly at pH 7.4 than at pH 4, whereas the HAp coating reduced the release rate at pH 7.4 compared to that at pH 4. Based on these findings, Xu *et al.* suggested that this effect might open up the possibility of creating “smart” (pH-controlled) targeted drug delivery devices.

When Hang *et al.* [30] used liposome-coated HAp and tricalcium phosphate as bone implants in the mandibular bony defect of miniature swine, they found the liposome-coated materials to be biocompatible. Moreover, the clinical endpoint was enhanced compared to that in the absence of liposomes. It was hypothesized that coating hydroxyapatite and tricalcium phosphate with negatively charged liposomes might improve the nucleation process for new bone formation. In experiments conducted in miniature swine, artificial bony defects on one side were implanted with either HAp-coated or tricalcium phosphate-coated liposomes, while defects on the other side served as controls. Histology and radiography performed at three and six weeks after surgery showed the coated liposome materials to be biocompatible. At three weeks, the implant material was surrounded by dense connective tissues, whilst by six weeks, new bone formation was visible near the implanted material. Liposomes immobilized in agarose gel and implanted in the defects also showed new bony bridge formation.

### 16.3

#### Nanohydroxyapatite Powders for Medical Applications

Bone mineral is composed of nanocrystals or, more accurately, nanoplatelets which originally were described as HAp, and similar to the mineral *dahllite*. Today, it is agreed that bone apatite may be better described as CHAp, and approximated by the formula  $(\text{Ca,Mg,Na})_{10}(\text{PO}_4\text{CO}_3)_6(\text{OH})_2$ . The composition of commercial CHAp is similar to that of bone mineral apatite. Bone pore sizes range from 1 to 100 nm in normal cortical bone, and from 200 to 400 nm in trabecular bone tissue, with the pores being interconnected.

*Orthopedic implants* used mainly for joint replacement and fracture fixation include metallic (cobalt chromium or titanium alloys) implants, screws, plates and nails, and their various permutations and combinations. The most important

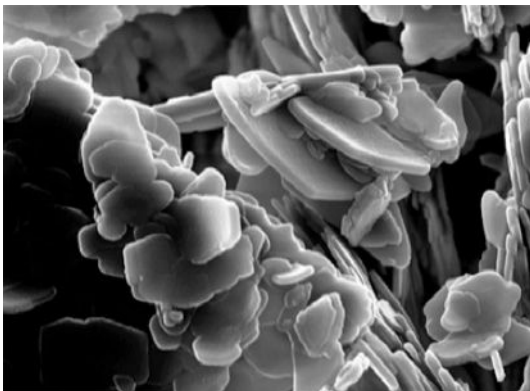


parameters for these implants are that they have the necessary wear resistance, allow for an adequate attachment to bone, and display the required strength, ductility, and elasticity. At a bone-implant-load-carrying interface, the greater the implant material stiffness, the greater load it can carry, compared to the surrounding tissues. This imbalance in load, which is known as *stress shielding*, can cause the bone tissue to be resorbed. An implant that is too rigid may also increase the likelihood of bone fracture, as the bone becomes osteoporotic (thinned) due to the excessive protection generated by the stress-shielding effect of the implant.

*Macro-textured implants* nanocoated with calcium phosphate and possessing the appropriate bioactivity characteristics, bonding ability, and design, may be the answer to this serious problem. A range of new nanomaterial production companies are in the process of applying this new technology in orthopedic, cardiovascular, and dental implants.

Nanotechnology has opened up novel techniques for the production of bone-like synthetic nanopowders and coatings of HAp. Indeed, the availability of HAp nanoparticles has opened up new opportunities for the design of superior biocompatible coatings for implants, and the development of high-strength orthopedic and dental nanocomposites.

Although, bone-like HAp nanopowders and nanoplatelets (Figure 16.3) can be synthesized by a range of production methods, one very promising approach is to synthesize these materials via a sol-gel solution. The results of earlier studies have shown that, while biphasic sol-gel HAp products are easily synthesized, monophasic HAp powders and coatings are more difficult to produce. Many companies have successfully synthesized HAp nanoparticles with diameters in the range of 15 to 20 nm, and with HAp coatings 70 nm thick (Nanocoatings Pty. Ltd., Australia). The nanoparticles and nanoplatelets of HAp provide excellent bioactivity for integration into bone, which arises from their very high surface areas [31, 32].



**Figure 16.3** Nanocrystalline carbonate apatite platelets formed by a sol-gel process.



Several new production and surface-modification techniques, including some sol-gel techniques, chemical vapor deposition (CVD), and plasma spray, have resulted in bonds with an excellent adhesive strength between the HAp and the substrate material, while others may be poor (e.g., electrophoretic deposition, various solution dip-coating systems, thermal spray). Currently, several companies and research groups are producing nanocomposites (e.g., NanoCoatings Pty Ltd, Australia; Mitsubishi Materials; ApaTech Ltd; Dentsply International; BioMet Int.; Wyeth BioPharmia; and Medtronic Sofamor Danek) that incorporate the macroparticles and nanoparticles of HAp and organic and biogenic materials (e.g., polyethylene, synthetic peptides and collagen, growth factors). Such a combination provides mechanical strength that is not achievable by using nanoparticles alone. In addition, for some of these materials an enhanced bioactivity and mechanical properties have been reported in orthopedic and dental applications, such as bone cements and dental fillings [33].

Saiz and coworkers [34] have focused on the sintering of porous HAp scaffolds fabricated using two techniques based on manipulation of the HAp slurries, namely *infiltration of the polymer foams* and *robocasting*:

- The first method involves the infiltration of a polymer sponge with a ceramic slurry until the inner polymer walls are completely coated by the ceramic powders. Subsequently, the sample is fired to remove the polymer and form a ceramic skeleton that is strengthened by sintering at high temperature.
- The second technique involves the use of computer-driven rapid prototyping techniques to produce porous ceramic with anisotropic microstructures. This so-called “robocasting” is a simple technique used to produce porous ceramic parts with complex shapes. In robocasting, a ceramic ink is extruded through a thin nozzle to build a part layer-by-layer, following a computer design. Sintering in air at temperatures ranging between 1100°C and 1200°C yields dense materials with narrow, grain-sized distributions.

It has been stated that both techniques can be used to fabricate scaffolds with an adequate pore size capable of promoting bone ingrowth.

Khalyfa and coworkers [35] have developed a powder mixture comprising tetracalcium phosphate (TTCP) as the reactive component and  $\beta$ -tricalcium phosphate ( $\beta$ -TCP) or calcium sulfate as a biodegradable filler, which can be printed with an aqueous citric acid solution. Two post-processing procedures—a sintering and a polymer infiltration process—were established to substantially improve the mechanical properties of the printed devices. Specimens of different shapes and sizes have been printed to study the usability of the developed powder-binder systems in the 3-D printing process; in this way a 3-D scaffold with a thoroughly open channel system was produced. The printing of a human cranial segment, together with all its filigree structures, was successfully achieved using both powder-binder systems, based on computed tomography scanning data of a human cranium. In all cases, the printed objects were strong enough to be handled manually, without damaging the integrity of the devices. Preliminary examinations on relevant application properties, including *in vitro* cytocompatibility testing, indi-

cated that the new powder-binder system represented an efficient approach to the creation of patient-specific ceramic bone substitutes and scaffolds for bone-tissue engineering.

Ordered tubular structures with open porosity were created by de Sousa and Evans [36] by using the microextrusion freeforming of a tubular latticework. The extrudate was a suspension of fine HAp powder in isopropyl alcohol with a polyvinyl butyral binder. The extruder consisted of a stepper-driven syringe fitted with a miniature tube extrusion die. In this way, tubular lattice scaffolds and microsponges were successfully prepared from crowded ceramic suspensions of HAp. The lattices were then sintered at 1250°C to produce a ceramic that had potential as a bone scaffold and could accommodate growth promoters in a slow release form.

## 16.4 Nanocoatings and Surface Modifications

### 16.4.1

#### Calcium Phosphate Coatings

When considering an ideal material to replace and mimic bone, synthetic calcium phosphates are an obvious choice, as they can replicate the structure and composition of HAp, a bone mineral. However, despite having a similar composition and chemistry to that of human bone, the mechanical properties of calcium phosphate are far from being close to those of human bone, which limits their use for load-bearing applications.

Today's solutions of materials for bone replacement are still far from ideal, with metallic implants remaining the first choice for load-bearing applications. As all metallic orthopedic and dental implants are bioinert and do not bond chemically to bone, the only means of fixation is by mechanical interlocks, whereby the implant must be manufactured in such a way that it possesses suitable surface roughness by micro- and macro-texturing. By increasing the surface roughness, the surface area is increased and this in turn increases the area of fixation. Other current methods for fixing implants firmly in place are the use of screws or bone cement, which are both used in dental and orthopedic implants.

Most published information on HAp is classified under calcium phosphate, to which HAp belongs. Therefore, the chemical properties will be viewed from the standpoint that HAp is calcium phosphate, although it will have different solubility and reactivities from other phosphates within the physiological environments.

Calcium phosphates are characterized by particular solubilities, such as when bonding to the surrounding tissues, and their ability to degrade and be replaced by advancing bone growth. As the calcium phosphate or HAp comes into contact with body fluid, its surface ions can be exchanged with those of the aqueous solution; alternatively, various ions and molecules, such as collagen and proteins, can be adsorbed onto the surface [31, 32].

The goal of calcium phosphate as a bioactive coating is to achieve a rapid biological attachment to bone. *Biological fixation* is defined as the process by which prosthetic components become firmly bonded to the host bone by bone in-growth, without the use of adhesive or mechanical fixation.

*Coatings* offer the possibility of modifying the surface properties of surgical-grade materials to achieve improvements in performance, reliability, and biocompatibility. More recently, techniques such as physical vapor deposition, thermal and electron beam evaporation, plasma metalorganic chemical vapor deposition (MOCVD), electrochemical vapor deposition, thermal or diffusion conversion and sol-gel processing have been used to produce both macro- and nanocoatings.

HAP-coated implants have demonstrated extensive bone apposition in animal models. The development of good implant-bone interfacial strength is thought to be a result of the biological interactions of released calcium and phosphate ions. Quality HAP-coated implants heal faster and attach more completely to the bone. The long-term performance of a calcium-phosphate-coated implant depends on coating properties such as thickness, porosity, phases and crystallinity, implant surface roughness, and overall design.

In addition to the effects of surface topography and chemistry, thin depositions of HAP or calcium phosphate crystals on implants were found to accelerate early bone formation and increase the strength of the bond between implant and bone. A histologic and histomorphometric evaluation of the implant-bone interface was carried out by Orsini and coworkers [37] to determine the effects of a novel surface treatment created by discrete crystalline deposition of nanometer-sized calcium phosphate particles added to the dual acid-etched surface of dental implants placed in the human posterior maxilla. The bone-implant contact evaluations indicated that an increase in osteoconduction along the calcium phosphate-treated surface occurs during the first two months after implant placement. These authors also stated that their results suggested that the nanometric deposition of calcium phosphate crystals could be clinically advantageous for shortening the implant healing period, providing earlier fixation, and minimizing micromotion, thus allowing earlier loading and restoration of function for implants placed in areas with low-density bone.

During the past 20 years, four general industrial coating methods have been adapted for the production of bioactive coatings:

- *Spray coating* was developed by Ducheyne and colleagues, who used relatively thick (100  $\mu\text{m}$  to 2 mm) calcium phosphate coatings for bone in-growth [38].
- *Thick bioglass coating* was initiated and developed by Hench and colleagues for surface bioactivity [39].
- The “self-assembly” of *biomimetics* by precipitation in a simulated body fluid (SBF) solution [40].
- *Nanocoatings*, using a range of methods including dipping in sol-gel HAP solutions to produce strong and bioactive coatings [31].

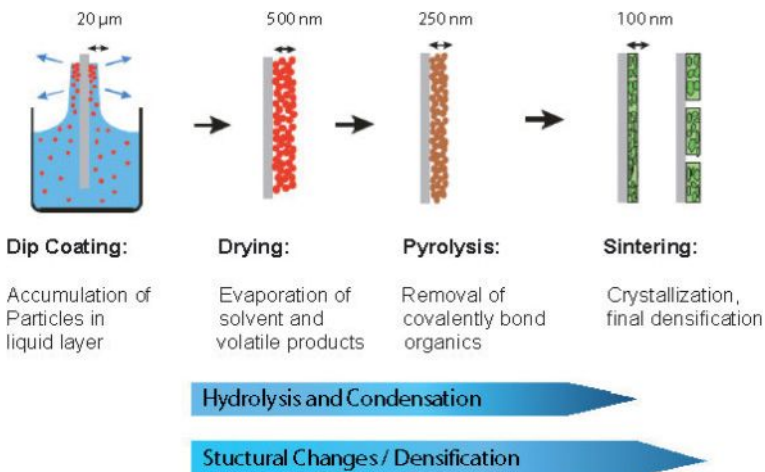
The sol-gel method in particular represents an attractive and versatile method, as it can be used to produce ceramic coatings from solutions by chemical means. It

is relatively easy to perform, and complex shapes can be coated. It has also been shown that the nanocrystalline grain structure results in improved mechanical properties. Sol-gel processing is also unique in that it can be used to produce different forms, such as powders, platelets, coatings, fibers, and monoliths of the same composition, merely by varying the chemistry, viscosity, and a number of factors of a given solution.

The advantages of the sol-gel technique are numerous: it is of the nanoscale; it results in a stoichiometric, homogeneous and pure product, owing to mixing on the molecular scale; high purity can be maintained as grinding can be avoided; it allows reduced firing temperatures due to its small particle sizes with high surface areas; it has the ability to produce uniform fine-grained structures; it allows the use of different chemical routes; and it is easily applied to complex shapes with a range of coating techniques, including dip, spin, and spray deposition (Figure 16.4). Furthermore, sol-gel coatings have the added advantages that the costs of precursors are relatively unimportant, owing to the small amounts of materials required [31].

The lower processing temperature has another advantage, namely that it avoids the phase transition ( $\sim 1156$  K) observed in titanium-based alloys used for biomedical devices.

Currently, companies are producing HAp nanoparticles with diameters in the range of 15 to 20 nm. Various sol-gel routes have been used for the production of synthetic HAp. A number of studies have been carried out on a range of precursors to produce pure nanocrystalline apatites for medical applications. A coating thickness in the range of 70–90 nm has been reported by some investigators [31, 32].



**Figure 16.4** Schematic showing the stages of the sol-gel dipping process and densification stages of nanocrystalline coating process.

Ti metal forms a nanoscale sodium titanate hydrogel layer on its surface, when it is soaked in 5 M NaOH solution at 60 °C for 24 h. In Japan, a large number of patients have been reported to receive artificial total hip joints of Ti alloy, modified with titanium beads subjected to NaOH treatments.

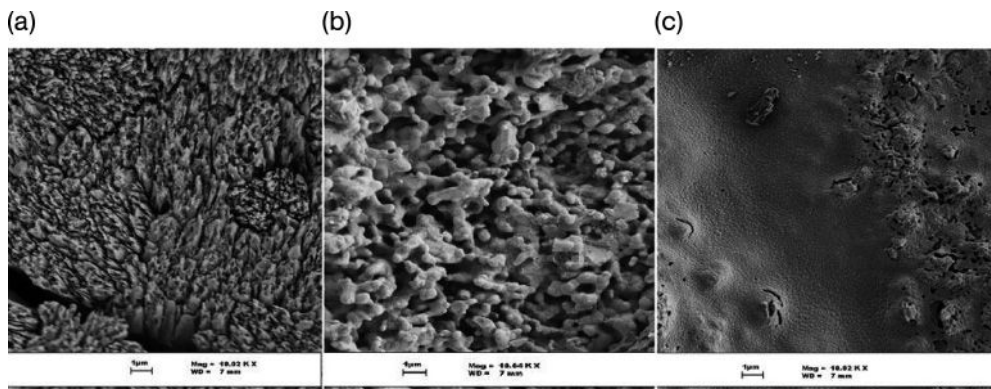
#### 16.4.2

##### Sol–Gel Nanohydroxyapatite and Nanocoated Coralline Apatite

Current bone graft materials are mainly produced from coralline HAP. Due to the nature of the conversion process, commercial coralline HAP has retained coral or  $\text{CaCO}_3$  and the structure possesses nanopores within the inter-pore trabeculae, resulting in high dissolution rates. Under certain conditions, these features reduce durability and strength, respectively, and are not utilized where high structural strength is required. To overcome these limitations, a new double-stage conversion technique was developed by Ben-Nissan and coworkers [23, 31, 32].

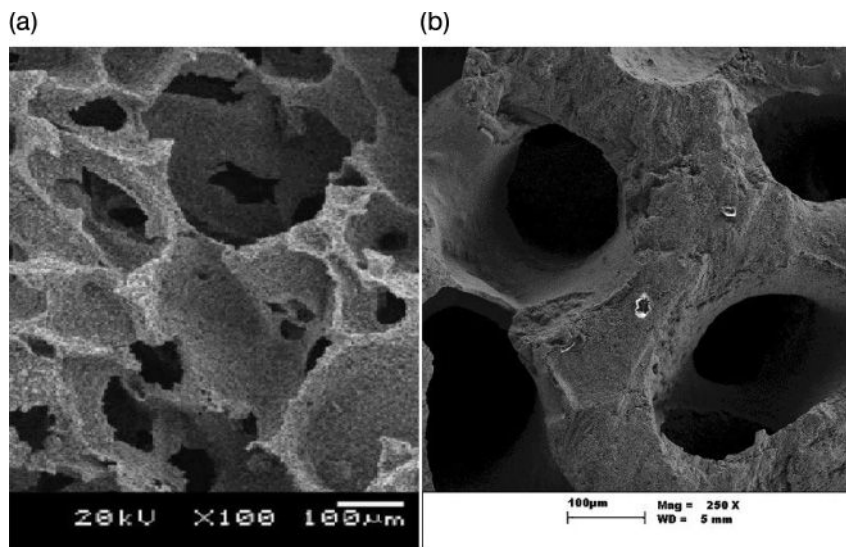
The current technique involves a two-stage application route whereby, in the first stage, a complete conversion of coral to pure HAP is achieved. In the second stage, a sol–gel-derived HAP nanocoating is applied directly to cover the meso- and nanopores within the intra-pore material, while maintaining the large pores for appropriate bone growth. The process is shown in Figure 16.5.

The compression and biaxial strengths, fracture toughness, and Young's modulus were each improved as a result of this unique double treatment. Application of the treatment method is expected to result in an enhanced bioactivity due to the nanograin size—and hence large surface area—that increases the reactivity of the nanocoating. It is anticipated that this new material could be applied to load-bearing bone-graft applications where high-strength requirements are pertinent.



**Figure 16.5** Stages of nanocrystalline hydroxyapatite-coated coralline apatite formation. (a) An enlarged micrograph of a coral skeleton spine area that has very sharp meso- and nanopore platelet regions;

(b) Surface morphological changes of the coral after conversion to hydroxyapatite with the hydrothermal method; (c) Stage 2 covering of the mesopores and nanopores with a nanohydroxyapatite coating.



**Figure 16.6** (a) Structural differences and morphology of (a) a synthetic tricalcium phosphate and (b) a natural Australian coral skeleton, showing pore size, distribution, and interconnectivity.

For these studies, the coral was obtained from the Australian Great Barrier Reef and contained micropores of 100 to 300  $\mu\text{m}$  size (Figure 16.6). The coral was shaped in the form of a block, and treated with boiling water and 5% NaClO solution. A hydrothermal conversion was carried out in a Parr reactor (Parr Instrument Company, USA) with a Teflon liner at 250  $^{\circ}\text{C}$  and 3.8 MPa pressure with excess  $(\text{NH}_4)_2\text{HPO}_4$ . A total conversion to HAP was achieved in this way.

Nanocrystalline ceramic coatings were produced using the sol-gel process. For this, the precursor solution was formed using the previously reported method. Coatings were formed using these solutions, followed by subsequent heat treatments. Mechanical testing involved a standard, four-point bend test according to ASTM C1161, to measure the flexural strength and flexural modulus of the natural coral. Comparative compression and biaxial strength tests were also carried out. Fracture surfaces were then viewed using SEM, which was performed on a LEO-Supra55VP instrument. Samples were analyzed using X-ray diffraction (XRD; Siemens D-5000, Karlsruhe, Germany), with scans being carried out from 20.0 to 60.0 in 0.020 steps at a step time of 2.0 s. A combined thermogravimetric analysis (TGA)/differential thermal analysis (DTA) was performed using a TA Instruments SDT 2960, at a heating rate of 10  $^{\circ}\text{C min}^{-1}$ .

Characterization studies of the natural and converted corals using XRD, SEM, DTA/TGA, nuclear magnetic resonance (NMR) and Raman spectroscopy have been reported previously.

These results showed a large increase in all mechanical properties, specifically the compression strength, due to hydrothermal conversion and nanocoating methods. The bioactivity was enhanced through the nanocrystalline formation, due to the HAp nanocoating.

#### 16.4.3

##### **Surface Modifications**

The surfaces of nanostructured materials can be modified and functionalized with different reagents, using a variety of physical, chemical, and/or biological methods. An enhanced solubility or stability of nanosized materials in aqueous media, as well as new material functions and properties, can be achieved via the surface modification of nanostructured materials.

A variety of physical, chemical, and biological surface modifications to increase bioactivity or mechanical properties have been proposed and investigated by many groups. Molecular coating, surface entrapment, and physical treating with plasma, ozone, or ultraviolet (UV) light have emerged as the leading strategies for surface modifications of nanostructured materials using physical methods. Through physical modifications, a range of functional molecules and entities, varying charges or active chemical groups can be introduced onto the surfaces of nanostructured materials, leading to functionalization and activation of the surfaces of materials.

Functional molecules may also be linked to the surfaces of nanostructured materials via certain chemical reactions. Compared to certain physical methods, a chemical modifications can be used not only to activate the surfaces of nanostructured materials to a greater extent, but also to offer stronger interactions between the linking molecules and the material surfaces through stable chemical bonds. A number of different chemical reagents and methods can be used for the surface modification of nanosized materials.

The biological modification of nanoparticle surfaces is often necessary for nanoparticle functionality. By employing chemical or physical methods, biospecific molecules and devices can be incorporated into the nanoparticles, thereby offering biospecific sites for the further immobilization of ligands specific to these molecules. The immobilizations of specific ligands can be performed through biologically specific reactions, for example antibody–antigen and receptor–ligand [21].

Different biomedical devices and applications require different properties and functions of materials. Therefore, methods to modify nanostructured materials in order to meet the needs of various biomedical systems will vary. A brief summary of the basic methods and technologies used to modify nanostructured materials for biomedical devices is presented below.

Today, highly porous scaffolds with an open structure represent the best candidates for cancellous bone substitution. In addition to natural and ceramic materials, many polymers have been proposed for medical applications. Each of these presents different biological and mechanical properties, allowing a choice of the correct polymer for the correct application. However, polymers usually present low



elastic modulus values, creep resistance and chemical constituents, compared to bone, and this is the major reason that limits their clinical use for hard- and soft-tissue substitution.

One example was that reported by Peroglio and coworkers [11], who produced PCL-coated alumina scaffolds that were then characterized to validate the concept of polymer–ceramic composites with an increased fracture resistance. The alumina scaffolds were processed using a classical foam replication technique, and then sintered to produce an open-porous structure with ~70% porosity and a mean pore size of 150  $\mu\text{m}$ . The polymer coating was obtained by infiltrating the scaffold with either a PCL solution or PCL nanodispersion. An emulsion–diffusion technique, using a nonionic surfactant, was used for the latter process. Subsequently, after infiltration with PCL, and irrespective of which quantity or infiltration technique was used, no change was seen in the Young's modulus. However, this was to be expected as the elastic modulus of PCL is negligible compared to that of alumina. Nonetheless, the addition of PCL completely altered the mechanical behavior of the scaffold during a four-point bending test, with a 10–20 vol% addition of PCL to the alumina scaffold leading to seven- to 13-fold increases in the apparent fracture energy. A further examination of the material, using SEM, indicated that the toughening was the result of the polymer fibrils bridging the cracks.

In recent years, nanoparticle systems have attracted increasing attention for use as potential drug-delivery systems. Despite the advantages of nanoparticles—such as their small size, which allows them to penetrate small capillaries and be taken up by cells—a number of problems, including a relatively short blood circulation time, have limited their clinical application. The efficiency and targeting ability of a nanoparticle drug-delivery system are often hampered by the rapid recognition of the carrier system by the body. As the main concern for nanoparticle drug carriers is a long circulation time in the blood, numerous approaches to the design and engineering of long-circulating-time carriers have been investigated. Among these, the surface modification of nanoparticles with a range of nonionic surfactant or polymeric macromolecules has proved to be the most successful for maintaining nanoparticle presence in the blood for prolonged periods [41]. Suitable and effective modifications of the nanoparticles are also required, however, to overcome a number of technical problems and possible issues of toxicity.

## 16.5 Simulated Body Fluids

Artificial materials implanted into bone defects might be encapsulated from time to time by a fibrous tissue, leading to their isolation from the surrounding bone. Any improvement in bone-implant bonding to the tissues requires the correct implant surface morphology and chemistry to generate a mechanical interlock and good surface activity. Interactions between the bone and the implant will be controlled with appropriate biological interactions.



During the past three decades, many investigators have proposed that the essential requirement for an artificial material to bond to living bone is the formation of a bone-like apatite on its surface when implanted in the living body. In 1991, Kokubo *et al.* proposed that *in vivo* apatite formation on the surfaces of many biomedical materials could be reproduced in a SBF with ion concentrations almost equal to those of human blood plasma. In essence, this means that the *in vivo* bone bioactivity of a material can be predicted from the apatite formation on its surface in SBF (Figure 16.7) [42].

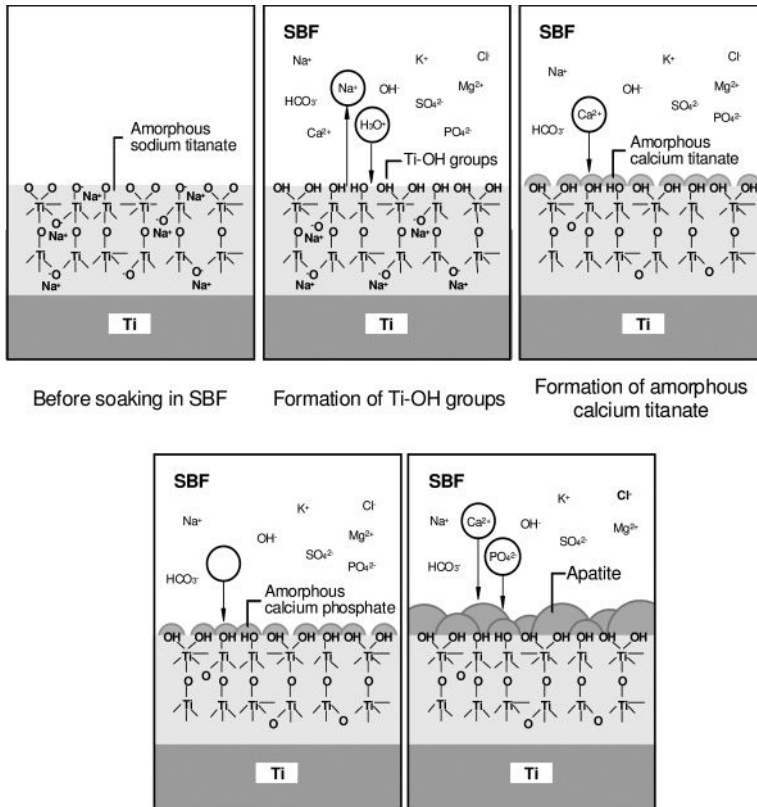
Hydroxyapatite layers can be easily produced on various organic and inorganic substrates when submerged in SBF and indeed, in 1989, Kokubo and Takadama [42] showed that, after immersion in SBF, a wide range of biomaterial surfaces initiated very fine crystallites of carbonate ion-containing apatite. Subsequently, many reports have described the ability of osteoblasts to proliferate and differentiate on this apatite layer. Based on these findings, other SBFs have been produced in order to provide insight into the reactivity of the inorganic component of blood plasma, and to predict the bioactivity of implants and bone scaffolds, as well as other novel biomaterials. SBF has also been used to prepare bioactive composites by forming HAp on various types of substrate.

The SBF solutions have been shown to induce apatitic calcium phosphate formation on any metal, ceramic, or polymer soaked in them. The SBF solutions, which closely resemble Hank's balanced salt solution (HBSS) [39], are prepared with the aim of simulating the ion concentrations present in human plasma. Hence, the solutions are prepared with relatively low calcium and phosphate ion concentrations (i.e., 2.5 and 1.0 mM, respectively), while the pH is adjusted to a physiological value of 7.4 by using organic buffers (e.g., Tris or HEPES).

Typically, a SBF solution will have ionic concentrations of 142.0 mM Na<sup>+</sup>, 5.0 mM K<sup>+</sup>, 1.5 mM Mg<sup>2+</sup>, 2.5 mM Ca<sup>2+</sup>, 147.8 mM Cl<sup>-</sup>, 4.2 mM HCO<sup>3-</sup>, 1.0 mM HPO<sup>4-</sup>, and 0.5 mM SO<sup>4-</sup>, with a pH of 7.4, all of these values being almost equal to those of human blood plasma at 36.5°C. The SBF is usually prepared by dissolving reagent-grade NaCl, NaHCO<sub>3</sub>, KCl, K<sub>2</sub>HPO<sub>4</sub>·3H<sub>2</sub>O, MgCl<sub>2</sub>·6H<sub>2</sub>O, CaCl<sub>2</sub> and Na<sub>2</sub>SO<sub>4</sub> in distilled water and buffering at pH 7.4 with Tris(hydroxymethyl)aminomethane ((CH<sub>2</sub>OH)<sub>3</sub>CNH<sub>3</sub>) and 1.0 M hydrochloric acid at 36.5°C.

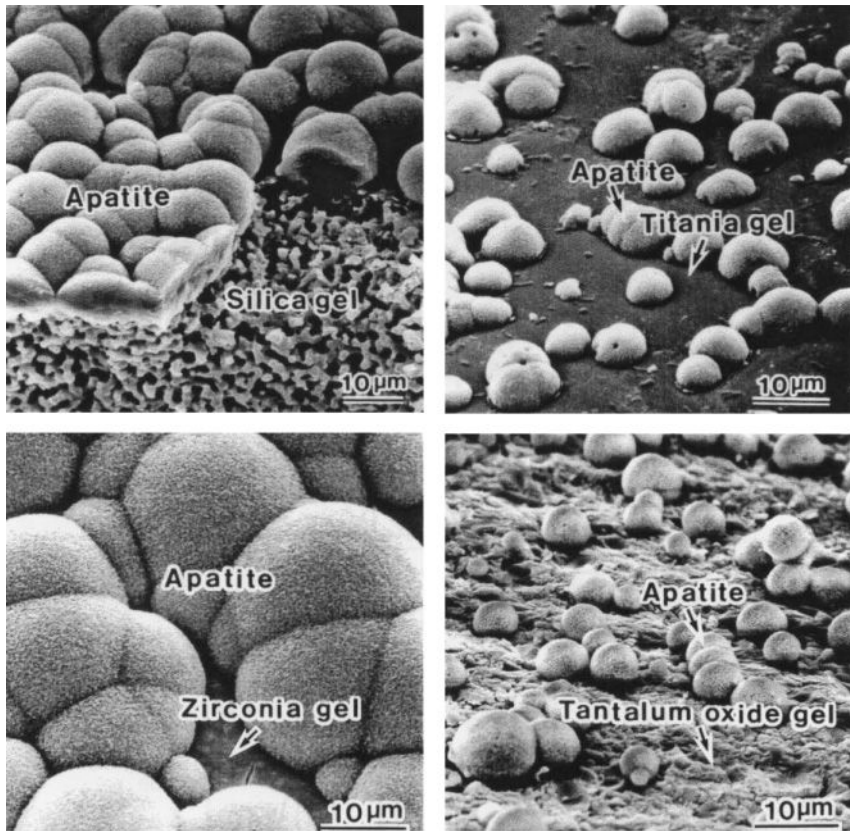
Since their ionic composition is more or less similar to that of human blood plasma, the HBSS or SBF formulations have only limited power with regards to the precipitation of apatitic calcium phosphates. As a direct consequence, the nucleation and precipitation of calcium phosphates from HBSS or SBF solutions is rather slow. The time taken to achieve total surface coverage of a 10 × 10 × 1 mm titanium or titanium alloy substrate immersed in a 1.5× or 2× SBF solution is typically two to three weeks, with frequent (every 36–48 h) replenishment of the solution [43].

Among the metallic oxide gels prepared using a sol-gel method, those consisting of SiO<sub>2</sub>, TiO<sub>2</sub>, ZrO<sub>2</sub>, and Ta<sub>2</sub>O<sub>5</sub> were found to have apatite formation on their surfaces in SBF, as shown in Figure 16.7. These results indicated that the Si-OH, Ti-OH, Zr-OH, and Ta-OH groups on the surfaces of these gels were effective in inducing apatite formation on their surfaces within the body environment (Figure 16.8).



**Figure 16.7** Treatment of a titanium alloy surface with NaOH to produce a bioactive surface on which hydroxyapatite particles nucleate and grow quite readily within the SBF solution [40].

A variety of studies have been conducted using SBF solutions to deposit apatite on both two-dimensional (2-D) and 3-D scaffolds. For example, Wu and coworkers [41] developed a novel bioactive, degradable and cytocompatible bredigite ( $\text{Ca}_7\text{MgSi}_4\text{O}_{16}$ ) scaffold with a biomimetic apatite layer (BTAP) for bone-tissue engineering. For this, porous bredigite scaffolds were first prepared using the polymer sponge method. A BTAP was then applied to the scaffolds by soaking them in SBF (pH 7.4) at  $37^\circ\text{C}$  for 10 days, with a solution volume-to-scaffold mass ratio of  $200\text{ mlg}^{-1}$ . After soaking, the scaffolds were dried at  $120^\circ\text{C}$  for one day, such that bredigite scaffolds with BTAPs were obtained. The porosity and *in vitro* degradability of the BTAP scaffolds were investigated. Likewise, the osteoblast-like cell morphology, proliferation and differentiation on BTAP scaffolds were evaluated and compared with those of  $\beta$ -tricalcium phosphate ( $\beta$ -TCP) scaffolds. The results showed that the bredigite scaffolds possessed a highly porous structure with a large pore size ( $300\text{--}500\mu\text{m}$ ). This biomimetic process mimics biomineralization and leads to the formation of a bone-like apatite layer on the scaffold



**Figure 16.8** Apatite formation on silica, titania, zirconia, and tantalum oxide gel-covered substrates within the SBF solution [40].

surface. The obtained BTA<sub>p</sub> scaffolds also possessed a high porosity (90%) and pore interconnectivity. When compared to  $\beta$ -TCP scaffolds, the cells on BTA<sub>p</sub> scaffolds showed a higher proliferation rate and differentiation level.

Cromme and coworkers [44] investigated the activation of regenerated cellulose 2-D model thin films and 3-D fabric templates with calcium hydroxide,  $\text{Ca}(\text{OH})_2$ . For this, the Langmuir–Blodgett (LB) film technique was applied to manufacture model thin films using a trimethylsilyl derivative of cellulose (TMS-cellulose). Regenerated cellulose films were obtained by treating the TMS-cellulose LB-films with hydrochloric acid vapors. For the 3-D templates, regenerated cellulose fabrics were used, and the templates activated with a  $\text{Ca}(\text{OH})_2$ -suspension and subsequently exposed to  $1.5\times$  SBF to induce the *in situ* formation of calcium phosphate phases. The calcium phosphates were identified using Fourier transform infrared (FTIR) and Raman spectroscopy as highly carbonated apatites (CA) lacking hydroxyl ions. Such 3-D fabric templates of regenerated cellulose covered with a

biomimetic coating of apatite might be of particular interest for novel scaffold architectures in bone repair and tissue engineering.

Lim and coworkers [45] noted that bone-like apatite could be more efficiently coated onto the scaffold surface by using polymer/ceramic composite scaffolds rather than polymer scaffolds, and by using an accelerated biomimetic process to enhance the osteogenic potential of the scaffold. The creation of a bone-like, apatite-coated polymer scaffold was achieved by incubating the scaffolds in SBF. Apatite growth on the porous poly(D,L-lactic-co-glycolic acid)/nanohydroxyapatite (PLGA/HAp) composite scaffolds was significantly faster than on the porous PLGA scaffolds. In addition, the distribution of coated apatite was more uniform on the PLGA/HAp scaffolds than on the PLGA scaffolds. After a five-day incubation period, the mass of apatite coated onto the PLGA/HAp scaffolds incubated in  $5\times$  SBF was 2.3-fold higher than on the PLGA/HAp scaffolds incubated in  $1\times$  SBF. Furthermore, when the scaffolds were incubated in  $5\times$  SBF for five days, the mass of apatite coated onto the PLGA/HAp scaffolds was 4.5-fold higher than on the PLGA scaffolds. These results indicated that the SBF-initiated apatite coating could be accelerated by using a polymer/ceramic composite scaffold and concentrated SBF. It was reported that, when seeded with osteoblasts, the apatite-coated PLGA/HAp scaffolds exhibited significantly higher cell growth, alkaline phosphatase (ALP) activity, and mineralization *in vitro* compared to the PLGA scaffolds coated only with HAp. In conclusion, the biomimetic apatite coating could be accelerated by both introducing nucleation sites into polymer scaffolds and using concentrated SBF. When seeded with osteoblasts, scaffolds with accelerated apatite coating significantly enhanced cell growth, ALP activity, and mineralization *in vitro*.

The SBF method was used by Kolos *et al.* [46] to fabricate calcium phosphate fibers for biomedical applications. A natural cotton substrate was first pretreated with phosphorylation and a  $\text{Ca}(\text{OH})_2$ -saturated solution, and then soaked in SBF of two different concentrations, namely  $1.5\times$  and  $5.0\times$  the ion concentration of blood plasma. The cotton was then burned out by sintering the ceramic coating at  $950^\circ\text{C}$ ,  $1050^\circ\text{C}$ ,  $1150^\circ\text{C}$ , and  $1250^\circ\text{C}$ , such that hollow calcium phosphate fibers approximately  $25\mu\text{m}$  in diameter and with a  $1\mu\text{m}$  wall thickness were successfully manufactured. However, the  $5.0\times$  SBF produced a thicker and more crystalline coat of greater uniformity. Kolos *et al.* further reported that osteoblastic cells were able to cover the entire surface of the cotton fibers; more surprisingly, the cell coverage seemed to be independent of the surface roughness and the fibers' Ca:P ratio.

Although of micron size rather than nanosize, a bioactive CHAp layer on cellulose fabrics was developed by Hoffman *et al.* [47]. Nonwoven cellulose (regenerated, oxidized) fabrics were coated with CHAp using a procedure based on the SBF method. For this, SBF with a high degree of supersaturation ( $5\times$  SBF) was applied to accelerate the biomimetic formation of bone-like apatite on the cellulose fabrics. After creating calcium phosphate nuclei on the cellulose fibers in an initial  $5\times$  SBF with high  $\text{Mg}^{2+}$  and  $\text{HCO}_3^-$  concentrations, the cellulose fabrics were additionally soaked in a second  $5\times$  SBF which was optimized with regards to

accelerated crystal growth by reduced  $\text{Mg}^{2+}$  and  $\text{HCO}_3^-$  concentrations. The carbonated apatite layer thickness was increased from  $6\mu\text{m}$  after a 4 h soaking in the latter solution, to  $20\mu\text{m}$  after 48 h. The amount of  $\text{CO}_3^{2-}$  substituting  $\text{PO}_4^{3-}$  in the HA $\mu$  lattice of the precipitates could be varied by changing the soaking time.

## 16.6

### Nano- and Macrobio-ceramics for Drug Delivery and Radiotherapy

#### 16.6.1

##### Nanobioceramics for Drug Delivery

For drug delivery, the primary aim is to target drugs to specific sites within the body, and to release them in a controllable fashion. However, for many current delivery systems the guest molecules are often released upon dispersion of the carrier/drug composites in water. This type of premature release is particularly undesirable and problematic when the guest molecule (e.g., an anti-tumor drug) is cytotoxic and might potentially harm healthy cells and tissues before being delivered to the affected sites [48].

In the case of ceramics, the critical pore and grain size may be varied from a few nanometers up to microns in order to control the ease of delivery and dispersion of a material to the targeted area. A variety of nanoceramic drug-delivery systems are currently undergoing clinical evaluation. In addition to reducing toxicity to nondiseased cells, these systems have the potential to increase drug efficiency, which translates to significant cost savings for the expensive drug treatments that currently are being engineered. On the basis of their physical size, nano drug-delivery systems also have the extraordinary characteristic of being able to target and control drug release with very high precision.

Mesoporous silica nanoparticle (MSN) materials, such as mobile composition of materials (MCM)-41/48, can be synthesized by utilizing surfactants as structure-directing templates to generate a range of mesoporous structures with high surface areas ( $>900\text{m}^2\text{g}^{-1}$ ), tunable pore sizes in the range of 2 to 20 nm, and uniform pore morphologies. Recent breakthroughs in terms of morphology control and the surface functionalization of MSN materials have resulted in a range of new materials that can be used as stimuli-responsive, controlled-release delivery-carriers for many biotechnological and biomedical applications. As with some other conventional drug-delivery agents with high loading capacities (e.g., polymer and liposomes), MSNs can encapsulate large quantities of drugs with various sizes, shapes, and functionalities [46]. In contrast to many biodegradable polymeric delivery systems, in which the loading of drug molecules requires organic solvents, the molecules of interest can be encapsulated inside the porous framework of the MSN by capping the openings of the mesoporous channels covalently with size-defined “caps,” which physically block the drugs from leaching out. Drug molecules loaded into the pores may then be released by the introduction of “uncapping triggers,” with the rate of release being controlled by the concentration of the

trigger molecules. Prior to uncapping, the capped MSN system exhibits a negligible release of drug molecules. This “zero-release” feature of a capped MSN delivery system, along with an ability to tune the rate of release by varying stimulant concentrations, are important prerequisites for developing delivery systems with many site-specific applications, such as highly toxic anti-tumor drugs, hormones, and neurotransmitters to certain cells types and tissues [48].

An MCM-41-type MSN-based, controlled-release delivery system has been synthesized and characterized using surface-derivatized cadmium sulfide (CdS) nanocrystals as chemically removable caps to encapsulate several drug molecules and neurotransmitters inside the organically functionalized MSN mesoporous framework. Lai and coworkers [49] studied the stimuli-responsive release profiles of vancomycin- and adenosine triphosphate (ATP)-loaded MSN delivery systems by using disulfide bond-reducing molecules, such as dithiothreitol (DTT) and mercaptoethanol (ME), as release triggers. The biocompatibility and delivery efficiency of the MSN system with neuroglial cells (astrocytes) *in vitro* was demonstrated. In contrast to many current delivery systems, the molecules of interest were encapsulated inside the porous framework of the MSN by capping the openings of the mesoporous channels with size-defined CdS nanoparticles, so as to physically prevent the drugs/neurotransmitters from leaching out.

Porous aluminosilicate ceramics were investigated by Byrne and Deasy [50] for their potential to act as extended-release drug-delivery systems. The aluminosilicate pellets were obtained either commercially, produced by extrusion-spheroization, or by cryopelletization. It was reported that each product had a highly interconnected porous microstructure, with the porosity and pore-size distribution being product-dependent. Drugs were loaded into the pellets using a vacuum impregnation technique, with the concentration of the drug loading solution and pellet porosity influencing the loading obtained. Each product provided an extended release of the incorporated drug, with the rate-determining step of release being the diffusion of the drug from the porous pellet interior into the bulk dissolution medium. Byrne and Deasy [50] showed that this rate was influenced by the pellet size, its porosity, pore-size distribution and porous microstructure, and by electrostatic interactions between the pellet surfaces and the drug. The solubility of the drug in the dissolution medium and its molecular weight also influenced the release rate. It was concluded that porous aluminosilicate pellets represent a particularly versatile class of extended-release drug-delivery system, as the drug is incorporated into the pellets after their production.

A new TiO<sub>2</sub> nanostructured bioceramic device was synthesized by López and coworkers [51], using a sol-gel process in order to control the pore-size distribution and particle size. The objective was to obtain a constant drug release rate for anti-epileptic drugs directly into the central nervous system (CNS). This method of drug delivery, using small reservoirs, is very important in pharmaceutical applications, as it offers advantages such as the elimination of secondary effects, a long duration of pharmacological activity, and protection of the drug against enzymatic degradation or pH variations. Among the best-developed and most studied materials, Titania has been shown to be an excellent candidate because of the possibility



to manipulate both the structure and the number of OH groups. Point defects were generated in the Titania network in order to obtain the desired interaction between a highly polar drug and the Titania device. The device contained an anti-convulsant drug, valproic acid (VPA), which could be released directly into the temporal lobe of the brain, at a constant rate. During the initial stage of the synthesis, VPA was added until a completely homogeneous solution was created; this solution was then maintained under constant stirring until a gel was formed. Under these conditions, the titanium dioxide underwent nucleation, whilst at the same time it was restructuring around the VPA in such a way that the chemical and polar properties of the anticonvulsant were preserved. The reaction was seen to take place under well-controlled conditions of pressure and temperature, which were purposely kept low. During the gelation period, both the electronic and molecular properties of the material were preserved. Finally, a dry gel was obtained, in which the anticonvulsant was occluded within the pore structure. The release of VPA into the temporal lobe of the brain, and its effect on epileptic rats, was observed by using the Kindling method. Several important conclusions were drawn from these studies, notably that a Titania device charged with an anticonvulsant drug could be successfully implanted in the rat's temporal lobe. Pore-blocking with higher concentrations of VPA led to a fall in the initial rate of drug release, while insertion of the device caused a drastic reduction in the animal's epileptic activity.

#### 16.6.2

##### **Microbioceramics for Drug Delivery**

The particulate forms of ceramic materials have found application in both medical and non-medical fields. Particles in the form of microspheres are especially applicable when treating tumors located in organs that are supplied by a single afferent arterial blood supply. More traditionally, microspheres and nanostructurally modified ceramics have been used in the targeted drug delivery of chemotherapeutic and radiotherapeutic agents.

In recent years, the preparation of surface-modified hollow microspheres has attracted considerable attention because of their unusual properties, notably their large specific surface area due to the nanolayer-modified surfaces, their low density and their encapsulation properties. Consequently, these materials should be very useful for novel applications such as drug- and protein-delivery systems. In certain applications, the efficacy of microparticulate materials can be greatly improved if they can act simultaneously as carriers for biologically active molecules. In this sense, porous and surface-modified materials have an advantage, as they present an additional surface area that greatly influences the loading capacity and release rates.

In dental clinical applications, such as the treatment of severe periodontitis, where massive alveolar bone loss occurs, bone defect filling and intensive systemic long-term antibiotics administration are often required. Nanohydroxyapatite microspheres intended for use as injectable bone filling material or as enzyme-

delivery matrices may also be used as antibiotic-releasing materials. Ferraz and coworkers [52] developed a novel injectable drug-delivery system with a drug-releasing capability for treating periodontitis. Their aim was to use HAp, loaded with an antibiotic, as a local drug-delivery system; consequently amoxicillin (with and without clavulanic acid) and erythromycin—both of which are used orally and parenterally to treat periodontitis—were tested. The results showed that the microspheres exhibited chemical compositions, porosities, and surface areas which provided adequate conditions for the sustained-release profile of the drugs investigated. Bactericidal tests indicated that the released antibiotics had an inhibitory effect on the bacteria present, while osteoblastic cells were seen to proliferate well on the surface of the microspheres, with cell growth being enhanced by the presence of antibiotics. Ferraz *et al.* concluded that these microspheres might also be considered as an alternative carrier system for antibiotics and to enhance bone regeneration while treating periodontitis.

### 16.6.3

#### Microbioceramics for Radiotherapy

The partial surgical removal of an organ afflicted with cancer generally results in a total or partial loss of organ function, that may or may not be recovered postoperatively. It would, therefore, be desirable to develop a cancer treatment that could destroy only cancerous cells, such that the normal healthy cells could regenerate after treatment and organ function be maintained. Although *radiotherapy* shows such potential, the irradiation is generally applied from an external source, often causing the cancer to receive an insufficient dose, especially if it is deep-seated. Moreover, the irradiation may cause severe damage to healthy tissues. In order to overcome this problem, microsphere-assisted radiation therapy is currently under development for a range of clinical applications, and has indeed shown a degree of success.

An *in situ* microsphere-assisted radiation method has been clinically applied using  $17\text{Y}_2\text{O}_3\text{-}19\text{Al}_2\text{O}_3\text{-}64\text{SiO}_2$  (mol%) (YAS) glass microspheres that have been prepared using a conventional melt-quench method. Although the yttrium-89 ( $^{89}\text{Y}$ ) in this glass is a nonradioactive isotope, neutron bombardment will activate  $^{89}\text{Y}$  to form the  $\beta$ -emitter  $^{90}\text{Y}$ , which has a half-life of 64.1 h. When radioactive glass microspheres 20–30  $\mu\text{m}$  in diameter are injected into a target organ (e.g., a liver tumor), they become trapped inside the small blood vessels in the tumor, blocking the nutritional supply to the tumor, and delivering a large, localized dose of short-range, highly ionizing  $\beta$ -rays. As the  $\beta$ -rays have a short penetration range of approximately 2.5 mm in living tissue, only minimal radiation damage will occur among the neighboring healthy tissues. These microspheres show a high chemical durability and, after their administration, the radioactive  $^{90}\text{Y}$  remains essentially within the microspheres so that it does not affect any neighboring healthy tissues. The radioactivity of  $^{90}\text{Y}$  decays to a negligible level within 21 days after its initial preparation; hence, the microspheres become inactive soon after the cancer treatment. These microspheres have been used clinically to treat liver cancer in Canada,



the USA, and China. Likewise, radioactive yttrium-containing resin microspheres 30–35  $\mu\text{m}$  in diameter have also been used clinically to treat liver cancer in Australia, China, New Zealand, and Singapore [53].

Kawashita and coworkers [53] have successfully prepared hollow  $\text{Y}_2\text{O}_3$  microspheres of 20–30  $\mu\text{m}$  diameter. For this, an aqueous carboxymethylcellulose sodium salt solution containing urease was atomized into an aqueous yttrium nitrate solution containing urea, using a spray gun located 2 m above the yttrium nitrate solution. The resultant solid materials were heat-treated at 1300 °C. An investigation of the structure and chemical durability of these microspheres showed the outer surfaces to be smooth and dense, and the inner parts to have a honeycomb structure. In SBFs at pH 6 and 7, the hollow  $\text{Y}_2\text{O}_3$  microspheres showed a high chemical durability.

It has been accepted that cancer cells generally perish at a temperature of approximately 43 °C because their oxygen supply via the blood vessels becomes insufficient; this is in contrast to normal cells, which do not suffer damage at higher temperatures of approximately 48 °C. A tumor is also more easily heated than the surrounding normal tissues, as its blood vessels and nervous system are poorly developed. It follows, therefore, that *hyperthermia* might represent a very effective treatment for cancer, with few adverse side effects. A variety of techniques has been employed to heat the tumors, including hot water, IR radiation, ultrasound, and microwaves but, unfortunately, deep-seated tumors cannot be heated either effectively or locally using these methods. Ferrimagnetic microspheres 20–30  $\mu\text{m}$  in diameter (and more recently nanospheres) have been shown to be valuable as *thermoseeds* for inducing hyperthermia in cancers, especially in those tumors located deep inside the body. In this situation, the spheres are implanted through the blood vessels and become entrapped in the capillary bed of the tumor. The application of an alternating magnetic field close to the tumor then causes the spheres to generate heat by their hysteresis loss; this results in the tumor being heated locally and strongly to a point where the cancerous cells are killed.

Kawashita *et al.* [54] prepared  $\text{Fe}_3\text{O}_4$  microspheres by melting powders in a high-frequency induction thermal plasma, and also by precipitation from an aqueous solution. The preparation in a high-frequency induction thermal plasma involved pure  $\text{Fe}_3\text{O}_4$  powders being completely melted in a plasma flame of argon gas, which was produced by high-frequency induction heating. The solidified products were sieved using a nylon mesh in order to obtain particles of 20–30  $\mu\text{m}$  in size. These particles were then heat-treated to 600 °C and allowed to cool under a reduced pressure of  $5.1 \times 10^3$  Pa.  $\text{Fe}_3\text{O}_4$  powders were added into 600 ml of a 1 wt% aqueous solution of hydrofluoric acid (HF) for the preparation of microspheres in aqueous solution. Silica glass microspheres of 12.4  $\mu\text{m}$  average diameter were soaked in Fe–HF solution at 30 °C for 24 days, with vigorous stirring. The products were then heat-treated at 600 °C for 1 h, and allowed to cool in a  $\text{CO}_2$ – $\text{H}_2$  gas atmosphere. The microspheres prepared in a high-frequency induction thermal plasma were shown to be composed mainly of  $\text{Fe}_3\text{O}_4$ , accompanied by a small amount of FeO. The surfaces of the microspheres were smooth before heat treat-

ment, but became slightly rough after treatment. This increase in surface roughness might be attributed to the formation of  $\alpha$ - $\text{Fe}_2\text{O}_3$  and/or the crystal growth of  $\text{Fe}_3\text{O}_4$ . The saturation magnetization of the microspheres was  $92 \text{ emu g}^{-1}$ . The heat generation was as low as  $10 \text{ W g}^{-1}$ , under 300 Oe and 100 kHz. Microspheres, 20–30  $\mu\text{m}$  in diameter, composed of small crystals of  $\text{Fe}_3\text{O}_4$  and 50 nm in size, were prepared by precipitation from an aqueous solution and subsequent heat treatment. Notably, the  $\beta$ - $\text{FeOOH}$  was seen to precipitate on the surface of silica glass microspheres, while its layer thickness increased with the increasing soaking period. The deposited  $\beta$ - $\text{FeOOH}$  was transformed into  $\text{Fe}_3\text{O}_4$  by heat treatment above  $400^\circ\text{C}$  in a  $\text{CO}_2$ – $\text{H}_2$  atmosphere. The silica glass microspheres soaked in  $\text{Fe}$ – $\text{HF}$  solution showed ferrimagnetism, with a saturation magnetization of  $53 \text{ emu g}^{-1}$ , a coercive force of 156 Oe and a heat generation of  $41 \text{ W g}^{-1}$ , under 300 Oe and 100 kHz, under the same magnetic field, which was fourfold higher than for pure  $\text{Fe}_3\text{O}_4$  microspheres prepared in a high-frequency induction thermal plasma.

## 16.7 Nanotoxicology and Nanodiagnostics

Today, nanomaterials and nanotechnologies represent a rapidly expanding discipline, with major potential to improve the lifestyle of humankind, notably by offering new solutions to many engineering and biomedical problems.

One major concern has arisen, however, regarding possible risks related to the impact of synthetic nanoparticulate matter on human health. However, at present insufficient data are available to make any accurate predictions concerning the long-term consequences of using these materials. Nevertheless, unintentional nanopollution is amply present in the current environment, and the use of nanomaterials for medical applications, as described here, is expected to increase as their benefits are recognized. Yet, it is somehow pertinent to mention that, there is no reason why unintentional pollution should differ from the intentional pollution, as far as its impact on health is concerned.

Gatti *et al.* [55], in their European project “Nanopathology” (QOL-2002-147), succeeded in developing a novel diagnostics tool which showed the presence of microsize and nanosized inorganic particles (including nanoceramics in pathological tissues) by using an environmental scanning electron microscope equipped with an X-ray microprobe of an energy-dispersive system. This study, which included approximately 700 tissues affected by cryptogenic pathologies, showed that in many cases where phlogosis (the inflammation of external parts) was dominant, then microsize and nanosized inorganic particles were present, and their elemental chemistry had been clearly identified and reported.

Among the pathologies investigated by Gatti *et al.* were cryptogenic granulomatosis and different forms of cancer, including lymphomas, carcinomas of the lung, colon and liver, and leukemia. Deep-vein thrombosis was also investigated, to demonstrate the possible thrombogenic activity of environmental pollutants. In

most cases, an inflammatory component was evident (e.g., in granulomas) when comparatively large particles (usually  $>10\mu\text{m}$ ) were identified. Particles the size of an erythrocyte or smaller were commonly found in thrombi, while particles down to 10 nm in size were identified in the cell nuclei. From a chemistry standpoint, Gatti *et al.* [55] identified a very wide variety of elemental compositions. As result of their investigations, the group advised that the use of biodegradable nanoceramics such as calcium phosphates should be seriously considered for biomedical applications, due to their non-nanotoxicity. However, they suggested that extreme care be taken with all other synthetic nanobiomaterial medical applications, until a better understanding and a more comprehensive combat strategy is available regarding these materials.

## References

- 1 Chang, M.C., Ko, C.C. and Douglas, W.H. (2003) *Biomaterials*, **24**, 2853.
- 2 Zhang, W., Liao, S.S. and Cui, F.Z. (2003) *Chem. Mater.*, **15**, 3221.
- 3 Vinogradov, S.V., Bronich, T.K. and Kabanov, A.V. (2002) *Adv. Drug Delivery Rev.*, **54**, 135.
- 4 Vinogradov, S.V., Batrakova, E.V. and Kabanov, A.V. (2004) *Bioconj. Chem.*, **15**, 50.
- 5 Clark, H.A., Hoyer, M., Philbert, M.A. and Kopelman, R. (1999) *Anal. Chem.*, **71**, 4831.
- 6 Park, E.J., Brasuel, M., Behrend, C., Philbert, M.A. and Kopelman, R. (2003) *Anal. Chem.*, **75**, 3784.
- 7 Gavalas, V.G., Law, S.A., Ball, J.C., Andrews, R. and Bachas, L.G. (2004) *Anal. Biochem.*, **329**, 247.
- 8 Croteau, S., Rauch, F., Silvestri, A. and Hamdy, R.C. (1999) *Orthopaedics*, **22**, 686–695.
- 9 Harakas, N.K. (1984) *Clin. Orthop. Rel. Res.*, **188**, 239–251.
- 10 Zhang, N., Nichols, H.L., Taylor, S. and Wen, X. (2007) *Mater. Sci. Eng.*, **27**, 599–606.
- 11 Peroglio, M., Gremillard, L., Chevalier, J., Chazeau, L., Gauthier, C. and Hamaide, T. (2007) *J. Eur. Ceram. Soc.*, **27**, 2679–2685.
- 12 Jones, J.R., Ehrenfried, L.M. and Hench, L.L. (2006) *Biomaterials*, **27**, 964–973.
- 13 Murugan, R. and Ramakrishna, S. (2005) *Compos. Sci. Technol.*, **65**, 2385–2406.
- 14 Oliveira, J.M., Rodrigues, M.T., Silva, S.S., Malafaya, P.B., Gomes, M.E., Viegas, C.A., Dias, I.R., Azevedo, J.T., Mano, J.F. and Reis, R.L. (2006) *Biomaterials*, **27**, 6123–6137.
- 15 TenHuisen, K.S., Martin, R.I., Klimkiewicz, M. and Brown, P.W. (1995) *J. Biomed. Mater. Res.*, **29**, 803–810.
- 16 Scabbia, A. and Trombelli, L. (2004) *J. Clin. Periodontol.*, **31**, 348–355.
- 17 Wahl, D.A. and Czernuszka, J.T. (2006) *Eur. Cell. Mater.*, **11**, 43–56.
- 18 Yoshikawa, T., Ohmura, T., Sen, Y., Iida, J., Takakura, Y., Nokana, I. and Ichijama, K. (2003) in *Bioceramics 15* (eds B. Ben-Nissan, D. Sher and W. Walsh), Trans Tech Publications, Uetikon-Zurich, pp. 383–386.
- 19 Abramovitch-Gottlieb, L., Geresh, S. and Vago, R. (2006) *Tissue Eng.*, **12**, 729–739.
- 20 Stock, U.A. and Vacanti, J.P. (2001) *Annu. Rev. Med.*, **52**, 443–451.
- 21 Xu, T., Zhang, N., Nichols, H.L., Shi, D. and Wen, X. (2007) *Mater. Sci. Eng. C*, **27**, 579–594.
- 22 Oliveira, A.L., Gomes, M.E., Malafaya, P.B. and Reis, R.L. (2003) in *Bioceramics 15* (eds B. Ben-Nissan, D. Sher and W. Walsh), Trans Tech Publications, Uetikon-Zurich, p. 101.
- 23 Zreiqat, H., Valenzuela, S.M., Ben-Nissan, B., Roest, R., Knabe, C., Radlanski, R.J., Renz, H. and Evans, P.J. (2005) *Biomaterials*, **26**, 7579–7586.

- 24 Ko, H.F., Sfeir, C. and Kumta, P.N. (2007) *Mater. Sci. Eng. C*, **27**, 479–483.
- 25 Jones, J.R., Ehrenfried, L.M., Saravanapavan, P. and Hench, L.L. (2006) *J. Mater. Sci.: Mater. Med.*, **17**, 989–996.
- 26 Al-Jamal, W.T. and Kostarelos, K. (2007) *Nanomedicine*, **2**, 85–98.
- 27 Schmidt, H.T. and Ostafin, A.E. (2002) *Adv. Mater.*, **14**, 532–535.
- 28 Moura, S.P. and Carmona-Ribeiro, A.M. (2006) *Cell. Biochem. Biophys.*, **44**, 446–452.
- 29 Xu, Q., Tanaka, Y. and Czernuszka, J.T. (2007) *Biomaterials*, **28**, 2687–2694.
- 30 Huang, J., Liu, K., Cheng, C., Ho, K., Wu, Y., Wang, C., Cheng, Y., Ko, W. and Liu, C. (1997) *Kaohsiung J. Med. Sci.*, **13**, 213.
- 31 Ben-Nissan, B. and Choi, A.H. (2006) *Nanomedicine*, **1**, 311–319.
- 32 Choi, A.H. and Ben-Nissan, B. (2007) *Nanomedicine*, **2**, 51–61.
- 33 Oonishi, H., Clarke, I.C., Good, V., Amino, H., Ueno, M., Masuda, S., Oomamiuda, K., Ishimaru, H., Yamamoto, M. and Tsuji, E. (2003) in *Bioceramics 15* (eds B. Ben-Nissan, D. Sher and W. Walsh), Trans Tech Publications, Uetikon-Zurich, p. 735.
- 34 Saiz, E., Gremillard, L., Menendez, G., Miranda, P., Gryn, K. and Tomsia, A.P. (2007) *Mater. Sci. Eng. C*, **27**, 546–550.
- 35 Khalyfa, A., Vogt, S., Weisser, J., Grimm, G., Rechtenbach, A., Meyer, W. and Schnabelrauch, M. (2007) *J. Mater. Sci.: Mater. Med.*, **18**, 909–916.
- 36 Gomes de Sousa, F.C. and Evans, J.R.G. (2005) *Adv. Appl. Ceram.*, **104**, 30–34.
- 37 Orsini, G., Piattelli, M., Scarano, A., Petrone, G., Kenealy, J., Piattelli, A. and Caputi, S. (2007) *J. Periodontol.*, **78**, 209–218.
- 38 Ducheyne, P., Beight, J., Cuckler, J., Evans, B. and Radin, S. (1990) *Biomaterials*, **11**, 244–254.
- 39 Hench, L.L. and West, J.K. (1990) *Chem. Rev.*, **90**, 33–72.
- 40 Kukobo, T., Kim, H.M., Kawashita, M. and Nakamura, T. (2000) *J. Aust. Ceram. Soc.*, **36**, 37–46.
- 41 Wu, C., Chang, J., Zhai, W. and Ni, S. (2007) *J. Mater. Sci.: Mater. Med.*, **18**, 857–864.
- 42 Kukobo, T. and Takadama, H. (2006) *Biomaterials*, **27**, 2907–2915.
- 43 Tas, A.C. and Bhaduri, S.B. (2004) *J. Mater. Res.*, **19**, 2742–2749.
- 44 Cromme, P., Zollfrank, C., Müller, L., Müller, F.A. and Greil, P. (2007) *Mater. Sci. Eng. C*, **27**, 1–7.
- 45 Kim, S.S., Park, M.S., Gwak, S.J., Choi, C.Y. and Kim, B.S. (2006) *Tissue Eng.*, **12**, 2997–3006.
- 46 Kolos, E.C., Ruys, A.J., Rohanizadeh, R., Nuir, M.M. and Roger, G. (2006) *J. Mater. Sci.: Mater. Med.*, **17**, 1179–1189.
- 47 Hofmann, I., Müllöer, L., Greil, P. and Müller, F.A. (2006) *Surf. Coat. Technol.*, **201**, 2392–2398.
- 48 Giri, S., Trewyn, B.G. and Lin, V.S.Y. (2007) *Nanomedicine*, **2**, 99–111.
- 49 Lai, C.Y., Trewyn, B.G., Jeftinija, D.M., Jeftinija, K., Xu, S., Jeftinija, S. and Lin, V.S.Y. (2003) *J. Am. Chem. Soc.*, **125**, 4451–4459.
- 50 Byrne, R.S. and Deasy, P.B. (2005) *J. Microencapsul.*, **22**, 423–437.
- 51 López, T., Ortiz, E., Quintana, P. and González, R.D. (2007) *Colloids Surf. A: Physicochem. Eng. Aspects*, **300**, 3–10.
- 52 Ferraz, M.P., Mateus, A.Y., Sousa, J.C. and Monteiro, F.J. (2007) *J. Biomed. Mater. Res. A*, **81**, 994–1004.
- 53 Kawashita, M., Takayama, Y., Kokubo, T., Takaoka, G.H., Araki, N. and Hiraoka, M. (2006) *J. Am. Ceram. Soc.*, **89**, 1347–1351.
- 54 Kawashita, M., Tanaka, M., Kokubo, T., Inoue, Y., Yao, T., Hamada, S. and Shinjo, T. (2005) *Biomaterials*, **26**, 2231–2238.
- 55 Gatti, A. and Montanari, S. (2005) in *Handbook of Nanostructured Biomaterials and Their Application in Nanobiotechnology* (ed. H.S. Nalwa), American Scientific Publishers, pp. 347–369.



## 17

### Self-healing of Surface Cracks in Structural Ceramics

*Wataru Nakao, Koji Takahashi, and Kotoji Ando*

#### 17.1

##### Introduction

Self-healing is the most valuable phenomenon to overcome the integrity decreases that are caused by the damages in service. Thus, self-healing should occur automatically as soon as the damages occur, and the healed zone should have high integrity as it was before damaging. When proposing self-healing materials, one must know the nature of the damage and the service, conditions of the materials. In the case of the structural ceramics, the severest damage is surface cracks, which is possible to be introduced by crash, fatigue, thermal shock, and corrosion during their service time. Over the past 30 years, ceramics have become the key materials for structural use at high temperature due to their enhanced quality and good processability. Structural ceramics are also expected to be applied in the corrosion environments such as air, because of its chemical stability. Thus, self-healing of surface cracks in the structural ceramics is an important issue to ensure the structural integrity of ceramic components.

In this chapter the mechanism and effects of self-healing of surface cracks in structural ceramics are introduced. Apart from this, the fracture manner of ceramics is also discussed. This will help the readers to understand the self-healing phenomena in ceramics and its benefits. The history of crack healing is also included in the text. Furthermore, new methodology to ensure the structural integrity using crack-healing effect and advanced ceramics having self-crack-healing ability are mentioned. Finally, it is assayed the self-healing ceramics can be applied to blades and nozzles of high-temperature gas turbine.

#### 17.2

##### Fracture Manner of Ceramics

Ceramics tend to have brittle fracture that usually occurs in a rapid and catastrophic manner. Brittle fracture is usually caused by the stress concentration at

the tip of the flaws. For brittle fracture under pure mode, I, loading, under which crack is subjected to opening, the failure criteria is that the stress intensity factor,  $K_I$ , is equal to the fracture toughness,  $K_{IC}$ . The stress intensity factor is an indicator of the magnitude of stress near a crack tip or the amplitude of the elastic field. The value of  $K_I$  can be obtained from the linear elastic mechanics as-follows:

$$K_I = \sigma \cdot Y \sqrt{\pi \cdot a} \quad (17.1)$$

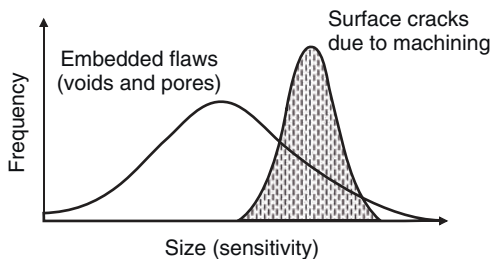
where  $a$  is the crack length,  $\sigma$  is the tensile stress applying to crack perpendicularly, and  $Y$  is a dimensionless parameter that is determined from the crack and loading geometries. Thus the stress at fracture is given by

$$\sigma_c = \frac{1}{Y} \cdot \frac{K_{IC}}{\sqrt{\pi \cdot a}} \quad (17.2)$$

From the fracture criterion, one can understand that the fracture strength of ceramic components is not intrinsic strength but is fracture toughness and crack geometry.

In general, ceramic components contain flaws at which the stress concentration causes brittle fracture before their end-use. These flaws have particular figurations and sizes and are introduced mainly during manufacturing. Figure 17.1 shows a schematic diagram of the flaw populations that could exist in ceramics. In this example, the severest flaws are surface cracks, perhaps resulting from machining. The next severest flaws are voids and pores introduced by sintering. Voids and pores would become the main fracture of origin, if the surface cracks are much smaller or removed, such as healed. The variation in the fracture sources leads to the large strength, distribution in ceramics.

There are few scenarios that can generate or introduce surface cracks during service. One possibility is by contact events, for example, impact, erosion, corrosion, and wear. Contact events may cause high stresses to the vicinity of the contact site, leading to crack formation. Sudden changes in temperature can also lead to stresses, known as *thermal stress* or *thermal shock*. The introduced surface cracks would be more severe than the pores and voids. As a result, these crackings cause



**Figure 17.1** Populations of the strength-controlling flaws.

large strength decrease to the component. If these scenarios occur again, it is possible that the component fractures catastrophically.

As mentioned above, ceramics usually fracture when  $K_I = K_{IC}$  but, in studies of fracture [1–3], it is sometimes found that crack growth can occur at lower value of  $K_I$ . The mechanisms have been analyzed to describe the slow crack growth behavior, including chemical reaction kinetics and interfacial diffusion. At the stressed crack tip, it is found that environmental species, for example, moisture, reacts and breaks the bonds at the crack tip resulting in stress corrosion cracking. The kinetics depends on the concentration of the environmental species. Actually it was found that the crack growth velocity in toluene is less than that in air [2]. This implies that the presence of moisture enhances the behavior. Furthermore, at high temperature, it is also found that the localized creep damage can give rise to the slow crack growth.

### 17.3 History

In 1966, the study on the strengthening behavior of ceramics by heat treatment was reported by Heuer and Roberts [4]. Then, Lange and Gupta [5] reported the strengthening of ZnO and MgO by heat treatment, and used the term “crack healing” for the first time in 1970. Now, we can find more than 200 reports on the strengthening effects by heat treatment for cracking ceramics. The crack-healing mechanisms in these reports can be roughly categorized into

1. re-sintering
2. relaxation of tensile residual stress at the indentation site
3. cracks bonding by oxidation.

Re-sintering [5–11], that is, diffusive crack-healing process, is an older crack-healing concept and commences with a degradation of the primary crack. This regression generates regular arrays of cylindrical voids in the immediate crack tip vicinity. Also, some studies [9–11] on the model and the kinetics of diffusive crack healing in single crystalline and polycrystalline ceramics have been proposed. However, as this crack healing requires the high crack-healing temperature, grain growth might also be generated. In some cases, the strength decreases than it before heat-treatment, although large strength recovery due to the crack healing is attained. The relaxation of the tensile residual stress at the indentation site leads to strength recovery. However, this phenomenon does not heal cracks. The crack bonding by oxidation has been first reported by Lange [12]. He investigated the strength recovery of the cracked polycrystalline silicon carbide (SiC) by heat treatment in air at 1.673 K, and reported that the average bending strength of the specimens heat-treated for 110h was 10% higher than that of the unheat-treated specimens. The same phenomenon in polycrystalline silicon nitride (Si<sub>3</sub>N<sub>4</sub>) was reported by Easier *et al.* [13]. The heat treatment temperature required for this crack-healing mechanism by oxidation is less than that required for the



re-sintering crack healing. The other important aspect is that the cracks healed by this mechanism are filled with the formed oxides. A further mechanism and method for crack-healing has been proposed. As an example, Chu *et al.* [14] proposed the crack-healing method using penetrating glasses. They succeeded to repair cracks in alumina ( $\text{Al}_2\text{O}_3$ ) and have found that the repaired part becomes even stronger than the base alumina.

As mentioned above, many other investigators have shown their interest on the crack healings of ceramics. In the field of ceramic nanocomposites, there are many reports also available on crack healing. The original impulsion for research in crack healings of ceramic nanocomposites originates from the works of Niihara and coworkers [15–17]. They observed that the strength of the alumina containing 5 vol% of submicrometer-sized SiC particles can be enhanced by annealing at 1573 K for 2 h in Argon. Since the original report, various mechanisms have been proposed to explain this phenomenon. Nowadays, this mechanism is confirmed to be driven by the oxidation of the dispersed SiC particles. Thompson *et al.* [18] observed that the partial healing of indentation cracks occurred when 5 vol%  $0.15\ \mu\text{m}$  SiC particles reinforced alumina were annealed at 1573 K for 2 h. Chou *et al.* [19] have also investigated the crack length and the lending strength of alumina/5 vol%  $0.2\ \mu\text{m}$  SiC particles nanocomposite after annealing at 1573 K for 2 h in Argon or air, concluding that the crack healing occurs by the oxidation of SiC particles. The similar conclusion was also derived by Wu *et al.* [20]. However, Chou *et al.* [19] noted that a uniform reaction layer was not formed between the crack walls, because the lower SiC content (only 5 vol%) results in a small quantity of the formed oxide.

Ando and coworkers observed that the similar crack healing in mullite ( $3\text{Al}_2\text{O}_3\cdot 2\text{SiO}_2$ ) [21–23],  $\text{Si}_3\text{N}_4$  [24–27] and alumina [28–31] based composites containing more than 15 vol% SiC particles can recover the cracked strength completely. They found that the healed zone is mechanically stronger than the base material and proposed the following requirements to obtain a strong healed zone:

1. Mechanically strong products (compared to the base material) should be formed by the crack-healing reaction.
2. The volume between crack walls should be completely filled with the products formed by the crack-healing reaction.
3. The bond between the product and crack wall should be strong enough.

Crack-healings reports can be classified into three generations. as shown in Table 17.1.

First generation, that is, the crack healing driven by the re-sintering is only to recover the cracked strength. Second generation, that is, the crack healing driven by oxidation of less than 10 vol% SiC can be triggered by damage and occur under service conditions, but the strength recovery is inadequate. Third generation, that is, the crack healing proposed by Ando *et al.* can be attained with all the requirements. Consequently, the third generation crack healing is confirmed to be “true” self-healing for structural ceramics.

**Table 17.1** Categorization of self-healing ceramics.

Types	Mechanism	Triggered by damage	Valid under service condition	Strong healed part
First generation	Re-sintering	No	No	Yes
Second generation	Oxidation of SiC (<5 vol% SiC)	Yes	Yes	No
Third generation	Oxidation of SiC (>10 vol% SiC)	Yes	Yes	Yes

## 17.4 Mechanism

To keep the structural integrity of ceramic, an efficient self-healing should occur. This is possible if healing the surface cracks obeys the following conditions:

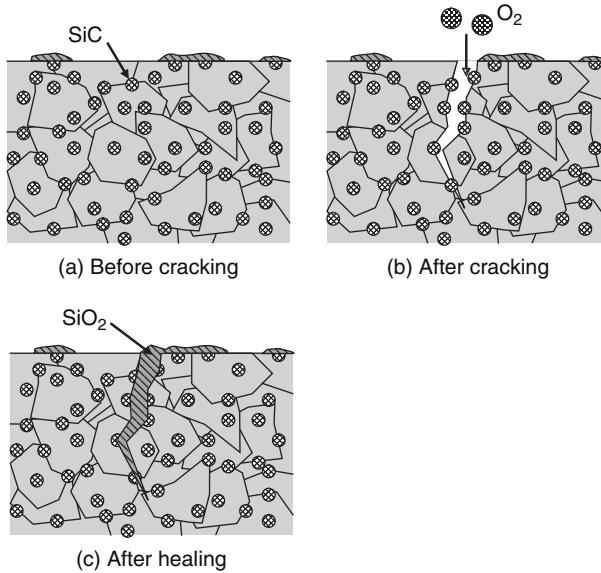
1. healing must be triggered by cracking;
2. healing must occur at high temperature [as structural ceramics are expected to typically operate at high temperature (~1273 K) in air] in the corrosion atmosphere, such as air;
3. Strength of the healed zone must be superior to the base material.

Self-crack healing driven by the oxidation of silicon carbide (SiC) can be qualitatively understood to satisfy the requirements 1 and 2. Figure 17.2 shows the schematic of the crack healing in the ceramics containing SiC particles heated at high temperature in the presence of air. Cracking allows the SiC particles located on the crack walls to react with oxygen in the atmosphere resulting in healing. The details of the valid conditions are discussed later (Section 17.6). Subsequently, the crack is completely healed as oxidation progresses. As mentioned earlier, if the three important conditions of achieving strong healed zone is satisfied, then fracture initiation changes from the surface crack to the other flaws such as embedded flaw. This behavior is well demonstrated in Figures 17.3a and b [29].

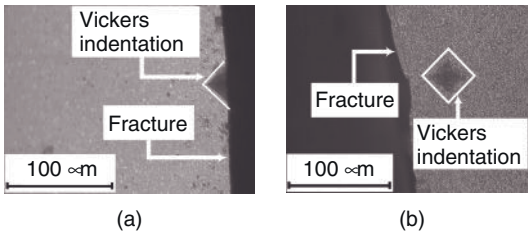
The following equation showing oxidation of SiC also supports the above findings.



There exist two important features in the above mentioned process. One is the increase in the volume of the condensed phase and the other is the generation of the huge exothermic heat. Because the mole number of silicon is held constant during the oxidation, the volume increase is found to be 80.1%. As the oxidation



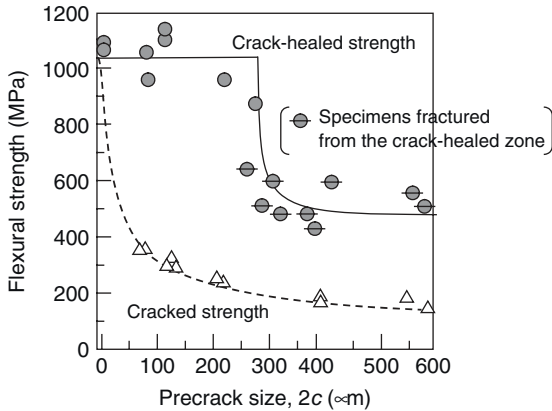
**Figure 17.2** Schematic illustration of crack-healing mechanism.



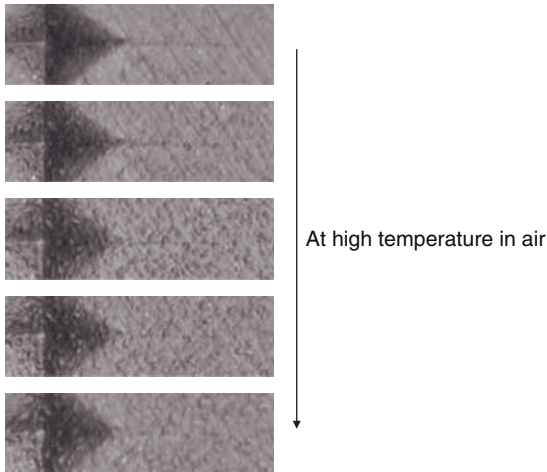
**Figure 17.3** Fracture initiation of alumina/15 vol%  $0.27\ \mu\text{m}$  SiC particles composite: (a) as-cracked and (b) crack healed at 1573 K for 1 h in the presence of air.

progresses, the crack walls are covered with the formed oxide. Finally, the space between the crack walls is completely filled with the formed oxide. For the complete infilling of the space between crack walls, it is necessary to contain more than 10 vol% SiC (Section 17.5). Another important parameter for attaining the complete infilling is the size of crack.

From Figure 17.4 [31], one can find the critical crack size that can be completely crack healed. As an example, the critical crack size of alumina/30 vol% SiC particles composite is  $300\ \mu\text{m}$ . This value is the surface length of a semi-elliptical crack with an aspect ratio (crack depth/half of surface length) of 0.9 introduced by indentation method. Below this value, the crack-healed specimens exhibit the same strength, because the space between crack walls is completely filled with the formed oxide and because the fracture initiates from an embedded flaw. When



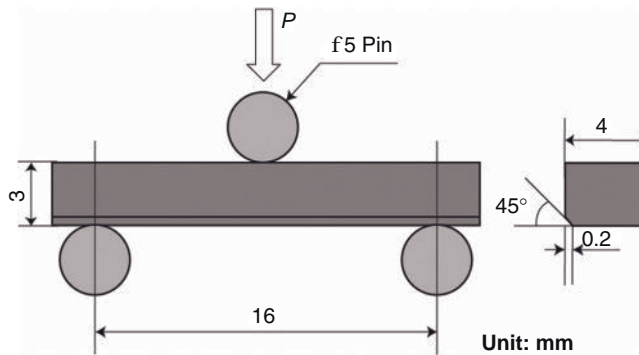
**Figure 17.4** Flexural strength of the crack-healed alumina/30vol% 0.27  $\mu\text{m}$  SiC particles composite as a function of surface length of a semi-elliptical crack.



**Figure 17.5** Photographs of *in situ* observation of crack healing, in which alumina/15vol% 0.27  $\mu\text{m}$  SiC particles composite containing cracks with an indentation is heat-treated at 1573 K in the presence of air.

the value is above the critical crack size, the space between the cracks walls is too large to be filled with the formed oxide.

Alternatively, the reaction heat makes the formed oxide and the base material to react or to once melt. The second low enthalpy change of the reaction can be evaluated to be  $-945 \text{ kJ}$  using the thermochemical data [32] of the pure substance. This phenomenon might lead to strong bonding between the reaction products and crack walls. The crack-healing mechanism is clearly demonstrated by *in situ* observation, as shown in Figure 17.5.



**Figure 17.6** Dimensions of three-point bending and the bar specimens.

The phenomenon was observed while alumina/15 vol% 0.27  $\mu\text{m}$  SiC particles composite containing an indentation crack was heat-treated at 1573 K in the presence of air. The features of the crack healing behavior are as follows: (i) the reaction products like sweats appear from the cracks and surface as the reaction progresses; (ii) cracks are perfectly covered and filled with the reaction products; (iii) the reaction products form with bubbling; and (iv) there are no changes in the indentation figuration. From the observation, it is noted that the high temperature makes the reaction products, as well as base material melting, and the bubble, including carbon monoxide (CO) gas, forming strong crack-healed zone.

Furthermore, to estimate the strength of the healed zone in detail, it is necessary to take account of the following issues, that is:

1. Effective volume should be so small that most fracture initiates at the crack-healed zone.
2. The strain energy at failure should be so low that fracture initiation is identified easily.

Ando and coworkers adapted a three-point bending method as shown in Figure 17.6 for fracture tests.

The span of the geometry is 14 mm less than that of Japan Industry Standard (JIS) [33]. The crack-healed specimens had higher strength than the smooth mirror-polished specimens (Section 17.6). Polishing was carried out according to JIS standard [33].

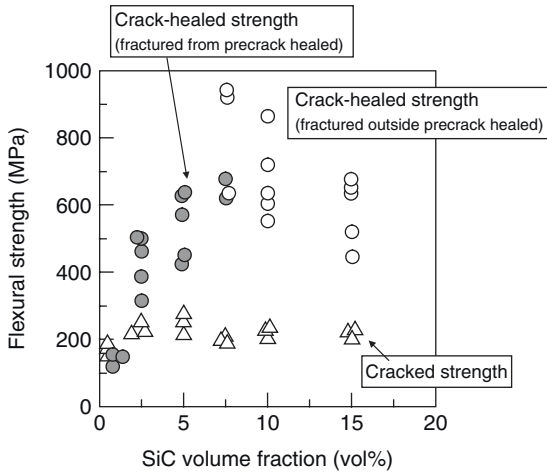
## 17.5

### Composition and Structure

#### 17.5.1

##### Composition

Most important factor to decide the self-crack-healing ability is the volume fraction of SiC. As mentioned in Section 17.4, it is necessary for achieving strong



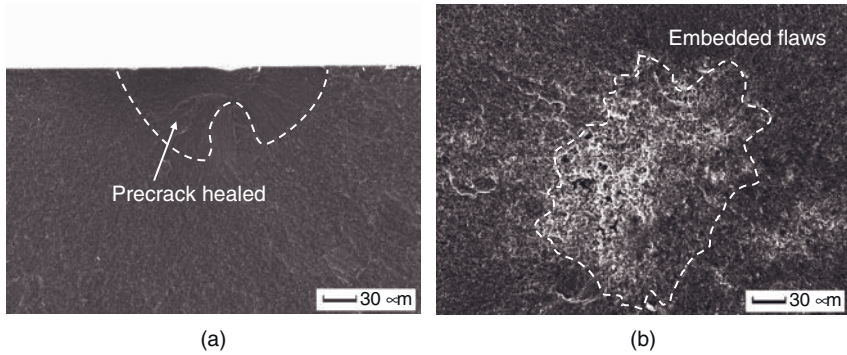
**Figure 17.7** Crack healed and cracked strength of alumina-SiC composites as a function of SiC volume fraction.

crack-healed zone that the volume between crack walls is completely filled with the products formed by the crack-healing reaction. Therefore, there is lower limit of the SiC volume fraction to endow with adequate self-cracking-healing ability. Figure 17.7 shows the cracked and crack-healed strengths of alumina containing various volume fractions of SiC particles, which has mean particle size of  $0.27\ \mu\text{m}$ . As a result, the crack-healed strength varies with SiC volume fraction and shows a maximum at SiC volume fraction of 7.5, as shown in Figure 17.7. From the strength dispersion, the crack-healing ability cannot be estimated by the strength recovery behavior alone. However, the fracture surface observations can reveal whether the crack is completely healed. There are two kinds of fracture mode. One is the fracture initiated from the crack-healed zone, as shown in Figure 17.8a. This means the formed oxide is not enough to heal the precrack completely. This fracture mode is observed in some specimens of the alumina mixed with 7.5 vol% SiC particles and all specimens that contain less than 5 vol% SiC particles. The other is the fracture initiated outside the crack-healed zone, as shown in Figure 17.8b. This means that the formed oxide is enough to heal the cracks. The enough quantity of the oxide is formed by the oxidation of more than 10 vol% SiC particles. From the results, the ceramics have to contain at least 10 vol% SiC to produce strong crack-healed zone.

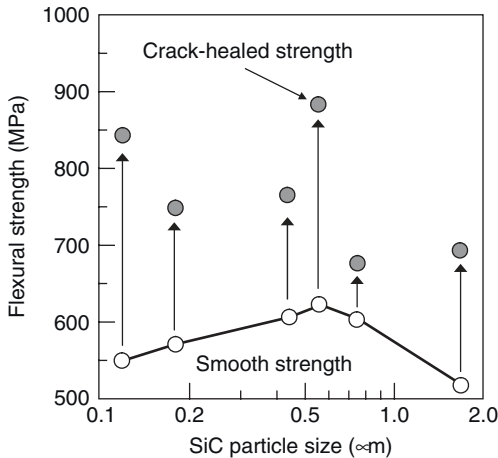
### 17.5.2

#### SiC Figuration

The SiC figuration also affects the crack-healing ability. Especially, SiC whisker that has high aspect ratio causes intrinsic change to the micromechanism of the crack healing.



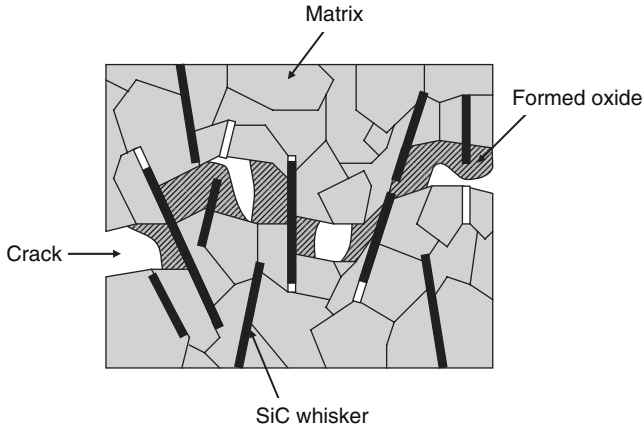
**Figure 17.8** Fracture initiations of (a) alumina/7.5vol% SiC particles composite in which fracture initiates from the precrack healed and (b) alumina/10vol% SiC particles composite in which fracture initiates from an embedded flaws.



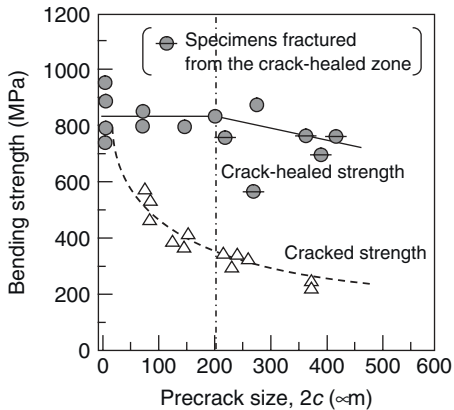
**Figure 17.9** Variation in crack-healed strength with SiC particle size in mullite containing 20vol% SiC particles composite.

Sato *et al.* [34] investigated the relation between SiC particle size and the crack-healed strength in the case of mullite ( $3\text{Al}_2\text{O}_3\cdot 2\text{SiO}_2$ )/20vol% SiC composite. From the results shown in Figure 17.9, they concluded that the crack healing at 1573 K for 1 h in the presence of air causes 100–300 MPa strength enhancement to all specimens, which shows a maximum with SiC particle size of 0.56 μm.

Ceramics containing SiC whiskers also show the self-crack-healing ability, but there are some differences between the crack-healing behaviors driven by oxidations of the SiC whiskers and that of SiC particles. This difference arises from the geometric relation between the SiC whiskers and the crack wall. The SiC whiskers



**Figure 17.10** Schematic illustration of crack-healing mechanism by SiC whiskers.



**Figure 17.11** Flexural strength of the crack-healed alumina/30vol% SiC whiskers (diameter = 0.8–1.0  $\mu\text{m}$ , length = 100  $\mu\text{m}$ ) composite as a function of surface length of a semi-elliptical crack.

stick out at the crack wall and bridge between the crack walls as illustrated in Figure 17.10.

Owing to this geometry, partial bondings between the crack walls can be formed despite the small amount of the oxide formation. The partial bondings [31, 35] was observed in the crack-healed zone of alumina/20vol% SiC whiskers (diameter = 0.8–1.0  $\mu\text{m}$ , length = 30–100  $\mu\text{m}$ ). The partial bondings enhance the strength recovery of the crack healing and at primary stage on large cracks, as shown in Figure 17.11 [31] (cf. Figure 17.4). Both in the primary stage and on large crack, the amount of the formed oxide is too less to completely fill the crack. In this situation, a large strength recovery could not be attained without the partial



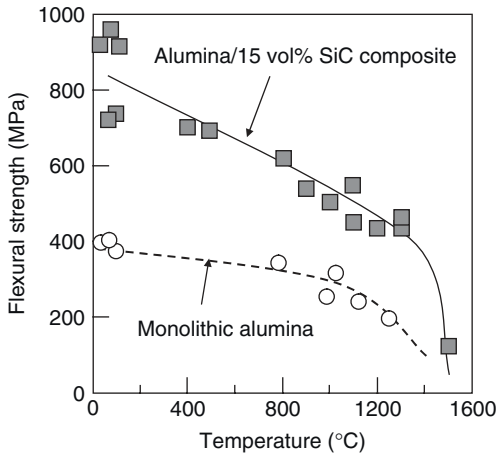
bonding. Therefore, composites with SiC whiskers do not only improve the fracture roughness but also have the advantage on crack-healing ability. However, the reliability of the crack-healed zone comprised by the partial bonding is inferior to that of the crack-healed zone completely filled with the formed oxide. Therefore, composites containing SiC whiskers as well as SiC particles show the excellent self-crack-healing ability.

### 17.5.3

#### Matrix

Since the self-crack-healing ability can only be seen in case of SiC composites, there is no restriction in selecting the matrix. Ando and coworkers succeeded to endow silicon nitride [24–27], alumina [28–31, 35], and mullite [21–23] with the self-crack-healing ability. Also monolithic SiC [36, 37] has excellent self-crack-healing ability.

These composites can be prepared from commercially available powders using ball mill mixing and hot pressing techniques. Sintering additives does not show any influence on the crack-healing ability. Moreover, a further improvement in mechanical properties can be obtained by employing the optimized sintering conditions. For example, the entrapped SiC particles [28] presented in the alumina matrix grains, when alumina containing 15 vol% SiC particles composite is hot pressed at 1873 K for 4 h. The entrapped SiC particles can inhibit the glide deformation of the alumina grains above 1273 K and this increases the temperature limit for bending strength, as shown in Figure 17.12 [28].



**Figure 17.12** Temperature dependence of the flexural strength of alumina containing 15 vol% SiC particles, which are entrapped in the alumina grains, compared with that of monolithic sintered alumina.

## 17.6 Valid Conditions

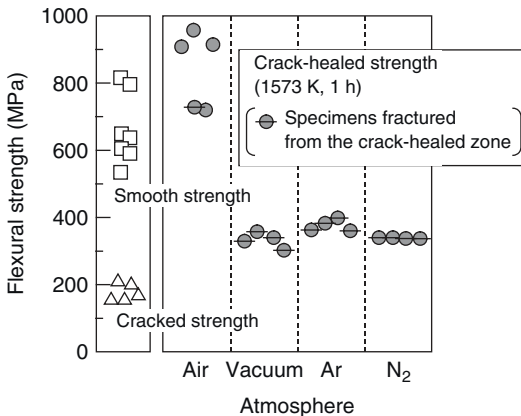
### 17.6.1 Atmosphere

The annealing atmosphere has an outstanding influence on the extent of the crack healing and the resultant strength recovery, as shown in Figure 17.13 [29].

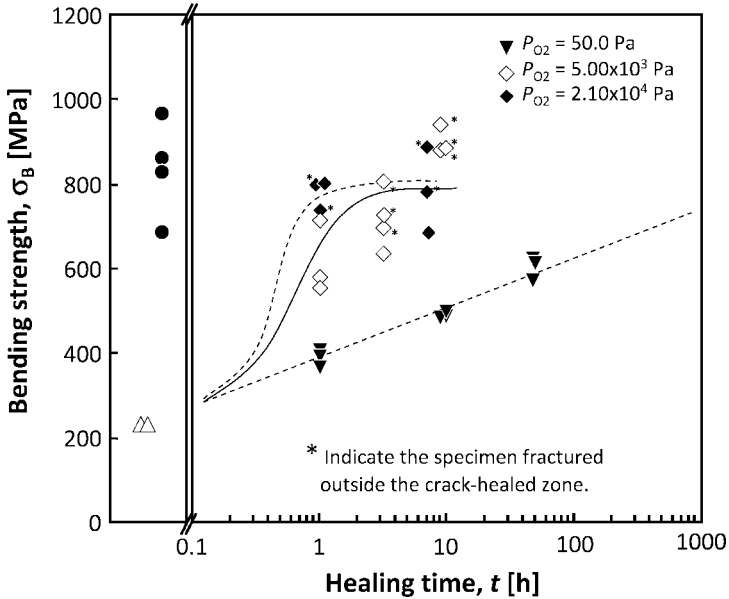
From the figure, it can be clearly seen that the presence of oxygen causes the self-healing phenomenon, as the crack healing is driven by the oxidation of SiC. However, the threshold oxygen partial pressure can be expected to be quite low. Therefore, the self-crack healing must be valid in the atmosphere, except in deoxygenated conditions, for example, the atmosphere containing hydrogen. Also embedded flaws cannot be healed, because the SiC particles present in the embedded flaws cannot react with oxygen.

Annealings in vacuum, argon (Ar), and nitrogen ( $N_2$ ) result in a slight strength recovery. Wu *et al.* [20] discussed this phenomenon to be the release of the tensile residual stress at the indentation site. Furthermore, Fang *et al.* [38] used a satellite indentation technique to show that, after 2 h at 1573 K, the degree of the annealing-induced relaxation in the stress intensity factor of the residual stress at the indentation site was ~26% for alumina/5 vol% SiC nanocomposite. Using this result, one can predict that annealing in atmosphere without oxygen leads to 10% strength recovery.

Recently, two large efforts [39, 40] made to know the quantitative influence of oxygen partial pressure on the self-healing behavior. From the results, the crack-healing rate is significantly decreased with decreasing oxygen partial pressure, as shown in Figure 17.14, in which the bending strengths of the alumina/20 vol%



**Figure 17.13** Crack-healing behavior of alumina/15 vol% 0.27 μm SiC particles composite under several atmospheres.



**Figure 17.14** Bending strength of the specimens crack-healed at 1573 K under several oxygen partial pressures as a function of the healing time, with the bending strength of healed smooth specimen and the as-cracked specimen.

SiC particles composite crack-healed under several oxygen pressure atmospheres. Moreover, the detail of the kinetics will be discussed later (Section 17.10).

### 17.6.2

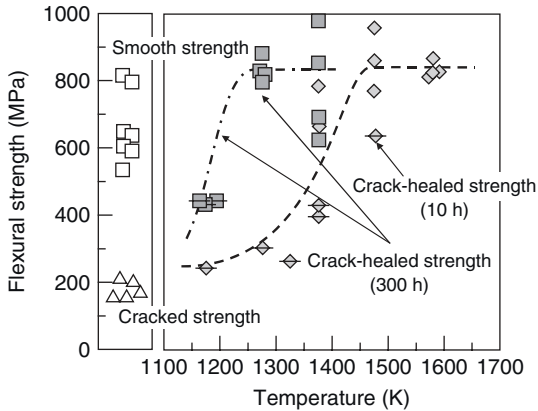
#### Temperature

The ceramic components are usually operated at high temperatures. The self-healing relies on the oxidation of SiC, thereby leading to the self-crack healing. Thus, it is important to know the valid temperature range for self-crack healing.

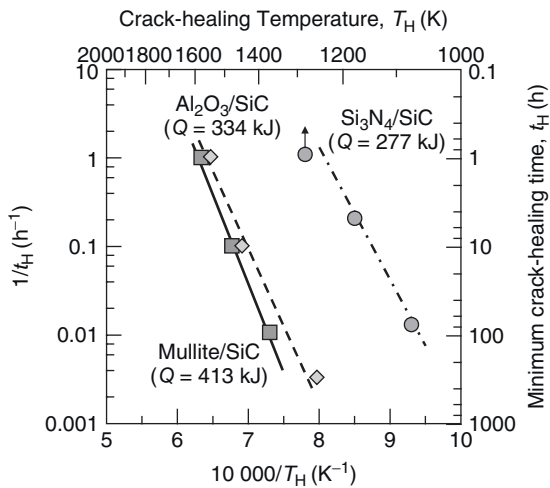
As the crack healing is induced by chemical reaction, the strength recovery rate decreases exponentially with decreasing temperature. For example, Figure 17.15 [28] shows the relationship between the crack-healing temperature and the strength recovery for alumina/15 vol% 0.27  $\mu\text{m}$  SiC parades composite.

In order to completely heal a semi-elliptical crack of 100  $\mu\text{m}$  in surface length within 1 h, heating above 1573 K is required. In the similar way, heating above 1473 and 1273 K is needed in order to completely heal the surface crack within 10 and 300 h, respectively. The relation between the crack-healing temperature and the strength recovery rate follows Arrhenius' equation.

Figure 17.16 [29] shows the Arrhenius plots on the crack healing of several ceramics having the self-crack-healing ability, in which the crack-healing rate is defined as the inverse of the time when complete strength recovery is attained at

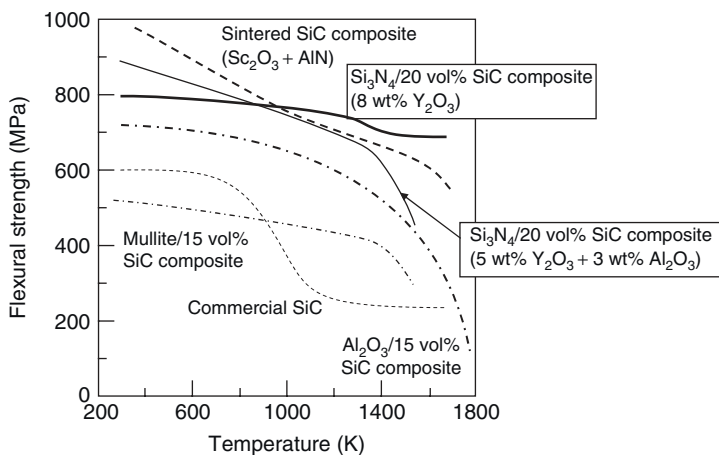


**Figure 17.15** Relationship between crack-healing temperature and strength recovery for alumina/15 vol%  $0.27\ \mu\text{m}$  SiC particles composite. (Centered line symbols indicate specimens fractured from the crack-healed zone.)



**Figure 17.16** Arrhenius' plots on the crack healing of several ceramics having the self-crack healing ability.

elevated temperatures. Apparent activation energies of the crack healing can be evaluated from Figure 17.16. The question is why the activation energy of  $\text{Si}_3\text{N}_4/\text{SiC}$  composite differs from those of alumina/SiC and mullite/SiC composites. The reason could be the crack healing of  $\text{Si}_3\text{N}_4/\text{SiC}$  composite is driven by the oxidation of SiC as well as  $\text{Si}_3\text{N}_4$ . Using these values, one can estimate the time for which a semi-elliptical crack of  $100\ \mu\text{m}$  in surface length can be completely healed at several temperatures.



**Figure 17.17** Temperature dependences of the flexural strength of several typical crack-healed ceramics.

The refractoriness of the crack-healed zone restricts the determination of the upper limit of the valid temperature range of self-crack healing. The temperature dependence of the flexural strength of the several typical ceramics crack healed [22, 25, 28, 36, 37] is shown in Figure 17.17. Except the dependence of  $\text{Si}_3\text{N}_4/20\text{ wt}\%$  SiC particles composite containing 8 wt%  $\text{Y}_2\text{O}_3$  as sintering additives, all dependences of the crack-healed specimens have the temperature at which the strength decreases abruptly, and this has been determined as the temperature limit for strength. The temperature limit is affected by the features of the oxide formed by the self-crack healing. The commercial sintered SiC [36] was found to have considerably low temperature limit of 873 K because the formed oxide is in glassy phase. Modifying the sintered additives to  $\text{Sc}_2\text{O}_3$  and AlN, Lee *et al.* [37] succeeded in improving the temperature limit of the crack-healed zone significantly. The similar behavior was observed in the  $\text{Si}_3\text{N}_4/20\text{ wt}\%$  SiC particles composites [25]. When the sintered additive is 5 wt%  $\text{Y}_2\text{O}_3$  and 3 wt%  $\text{Al}_2\text{O}_3$ , the formed oxide and grain boundary are in glassy phase. Alternatively  $\text{Si}_3\text{N}_4/20\text{ wt}\%$  SiC particles composite containing 8 wt%  $\text{Y}_2\text{O}_3$  as sintering additives forms the crystalline oxide, such as  $\text{Y}_2\text{Si}_2\text{O}_7$  by crack healing. The difference gives rise to the difference in the temperature limit. Both alumina containing 15 vol% SiC particles composite [28] and mullite containing 15 vol% SiC particles composite [22] form the crystalline phase because the formed oxide reacts with the matrix and forms mullite. These temperature limits are summarized in Table 17.2.

The temperature range at which the self-crack healing is valid is limited by the crack-healing rate and the high-temperature mechanical properties. Assuming that fracture by the second damage allows complete healing of surface cracks introduced by the first damage in 100h, one can evaluate the valid temperature range of the self-crack healing, as listed in Table 17.3.

**Table 17.2** Temperature limit of several ceramics.

Materials	Temperature limit (K)
Si <sub>3</sub> N <sub>4</sub> /20vol% SiC particles composite (8 wt% Y <sub>2</sub> O <sub>3</sub> )	1573
Si <sub>3</sub> N <sub>4</sub> /20vol% SiC particles composite (5 wt% Y <sub>2</sub> O <sub>3</sub> + 5 wt% Al <sub>2</sub> O <sub>3</sub> )	1473
Alumina/15 vol% SiC particles composite	1573
Mullite/15 vol% SiC particles composite	1473
SiC sintered with Sc <sub>2</sub> O <sub>3</sub> and A/N	1673
Commercial SiC sintered	873

**Table 17.3** Valid temperature region of self-crack healing for several ceramics.

Materials	Valid temperature range (K)
Si <sub>3</sub> N <sub>4</sub> /20vol% SiC particles composite (8 wt% Y <sub>2</sub> O <sub>3</sub> )	1073–1573
Alumina/15 vol% SiC particles composite	1173–1573
Mullite/15 vol% SiC particles composite	1273–1473
SiC sintered with Sc <sub>2</sub> O <sub>3</sub> and A/N	1473–1673

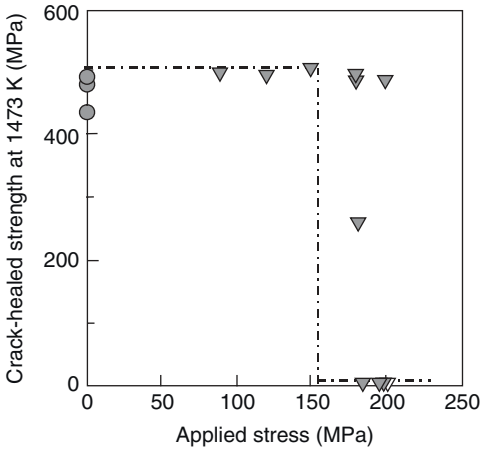
### 17.6.3

#### Stress

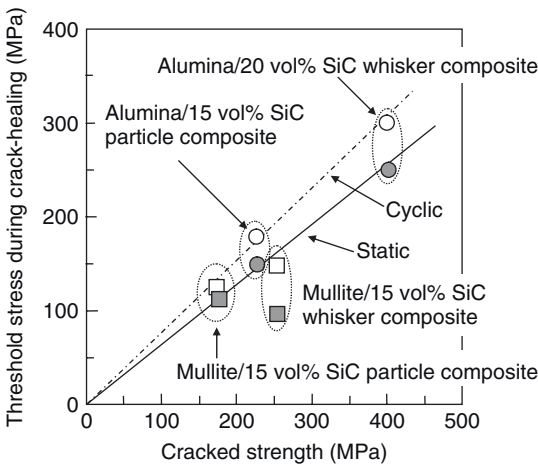
Stress applied to the components is also one of the most important factors to decide the valid condition of the self-crack healing. Structural components generally suffer various kinds of stresses. The applied stress is possible to cause the slow crack growth. If the applied stress exceeds the critical value, it would rise to catastrophic fracture. Therefore, it is important to know the threshold stress that could be safely applied to the cracks during self-crack healing.

Ando *et al.* [41] reported for the first time that the surface crack in the mullite containing 15 vol% SiC particles composite can be healed, although the tensile stress is applied to the cracks. Their results revealed that the crack healing occurs, although the precrack is grown by the applied stress, and the specimens crack healed under stress had the same strength as the specimens crack healed under no stress and at same temperature. Furthermore, Ando *et al.* [42] reported that surface cracks in the mullite containing 15 vol% SiC particles composite can be healed even though dynamic stress such as cyclic stress, opens and closes the crack.

Nakao *et al.* [43] investigated the threshold stresses during self-crack healing for several oxide ceramics. For example, the threshold static stress during crack healing for a semi-elliptical surface crack (surface length = 100 μm) in alumina containing 15 vol% SiC particles has been determined to be 150 MPa, as shown in Figure 17.18 [43].



**Figure 17.18** Crack-healing behavior at 1473 K under static stress for alumina/15 vol% SiC particles composite.



**Figure 17.19** Relation between threshold stress during crack healing and the corresponding cracked strength.

Figure 17.18 demonstrates that the tensile static stress of 180 MPa is possible to fracture the specimen during crack healing, whereas the stress less than 150 MPa never fractures the specimens during crack-healing.

Figure 17.19 shows the determined threshold stress as a function of the flexural strength of the specimen containing the same surface crack for several cracks in the oxide ceramics–SiC composite [43–46]. Except the threshold stresses of mullite containing 15 vol% SiC whiskers composite, all data satisfies the proportional relation, although the crack healings were subjected to different conditions. The crack healing ability for mullite containing 15 vol% SiC whiskers composite has been

found to be so low that the crack healing part was weaker than the other parts as only partly welding occurs, not satisfying the proportional relation. The proportional constants for the relations between the threshold static and cyclic stresses between the cracked strength have been found to be 64 and 76%, respectively. The threshold stress imposes an upper limit to the crack growth rate, thereby limiting the crack length to less than the critical crack length before the crack healing starts. This implied that the crack growth behavior of all specimens is time dependent rather than cyclic dependent at high temperature. Therefore, applying static stress could be confirmed to be the easiest condition for fracture during the crack healing under stress, and the threshold stresses of every condition during the crack healing have been found to be the threshold static stresses. The stress intensity factors at the tip of the precrack during the crack-healing treatment,  $K_{HS}$ , were estimated. Since a tensional residual stress was introduced during precracking by using an indentation method, it is necessary to consider the stress intensity factor of the residual stress,  $K_R$ , as expressed by the following equation:

$$K_{HS} = K_{ap} + K_R \quad (17.4)$$

where  $K_R$  can be evaluated by using the relation proposed by Kim *et al.* [47] and  $K_R = 0.35 \times K_{IC}$ . Also, by interpolating the threshold static stress during the crack healing and the geometry for the precrack into Newman–Raju equation [48], one can obtain  $K_{ap}$ . From the evaluation, it was found that ceramic components having the adequate crack healing ability can be crack healed under the stress intensity factor below 56% fracture toughness.

## 17.7

### Crack-healing Effect

#### 17.7.1

##### Crack-healing Effects on Fracture Probability

The crack-healing can simplify the complexity in the flaws associated with fracture, because surface cracks that are severest flaws in ceramic are completely healed. As a result, a fracture probability can be easily described after the crack-healing. Furthermore the crack-healing has a large contribution to decrease the fracture probability.

Fracture probability is one of the most important parameters for structural components. If the fracture probability is too high, one needs to either change the design or substitute high strength materials. The fracture probability can be obtained from the failure statistics. As indicated in Section 17.2, ceramics contain many flaws that can vary in size and figuration, causing the wide strength distribution. Thus the empirical approach needs to describe the strength distribution of a structural ceramic. Once the strength of a material is fitted to the distribution, the fracture probability can be predicted for any applied stress. A common empirical



approach to describe the strength distribution of a structural ceramic is the Weibull approach. The two-parameter Weibull function, which is given by

$$F(\sigma) = 1 - \exp\left\{-\left(\frac{\sigma}{\beta}\right)^m\right\} \quad (17.5)$$

can express the strength distribution of structural ceramics well, where  $F(\sigma)$  is the fracture probability at the tensile stress of  $\sigma$ ,  $m$  the Weibull modulus, and  $\beta$  the scale parameter. The Weibull modulus describes the width of the strength distribution. High Weibull modulus implies that the strength has a low variability. Values of  $m$  for ceramics are in the range of 5–20. The scale parameter describes the stress when  $F(\sigma) = 63.2\%$ . To analyze the strength distribution, Equation (17.5) is usually expanded as follows:

$$\ln \ln\left(\frac{1}{1-F(\sigma)}\right) = m \ln \sigma - m \ln \beta \quad (17.6)$$

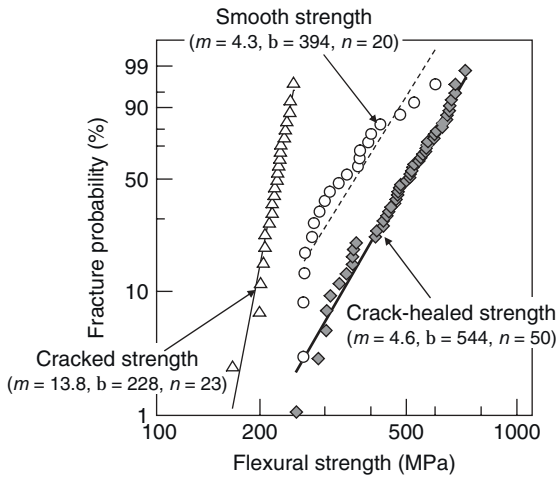
Thus, a plot of the left-hand side of Equation (17.6) has a linear relation versus the natural logarithm of the strength. In such a procedure, a fracture probability is needed for each test specimen. This is usually estimated using

$$F(\sigma) = \frac{i - 0.3}{n + 0.4} \quad (17.7)$$

The strength data of  $n$  specimens are organized from weakest to strongest and given a rank  $i$  with  $i = 1$  being the weakest specimen. Equation (17.7) is well known as *median rank method*.

As an example, the Weibull plot of the crack-healed alumina containing 20 vol% silicon carbide (SiC) particles composite is shown in Figure 17.20. The healed crack is a semi-elliptical surface crack having a surface length of 100  $\mu\text{m}$  and a depth of 45  $\mu\text{m}$ . In comparison, those of the as-cracked specimen and the smooth specimen having a mirror finish surface are shown in Figure 17.20. Assuming that the data obey the two-parameter Weibull function, one can apply a least-squares fitting. From the obtained line profiles, the values of  $m$  and  $\beta$  can be obtained for the crack-healed specimens, the as-cracked specimens, and the smooth specimens.

The crack-healing causes a slight increase to the value of  $m$  compared to the smooth specimens. Furthermore, the strength distribution of the crack-healed specimen is in a good agreement with the two-parameter Weibull function, although that of the smooth specimen differs from the function significantly. The flaw population in ceramics leads to this behavior. The Weibull modulus  $m$  of the crack-healed specimen was smaller than that of the as-cracked specimen. All the as-cracked specimens fractured from a crack introduced by the Vickers indentation, while fractures of most crack-healed specimens occurred outside of



**Figure 17.20** Weibull plot of the crack-healed alumina containing 20vol% silicon carbide (SiC) particles composite.

the crack-healed zone, as shown in Figure 17.3b, because cracks were completely healed. Since embedded flaws as the fracture initiation of the crack-healed specimens have different sizes, the fracture stresses exhibit a large scatter.

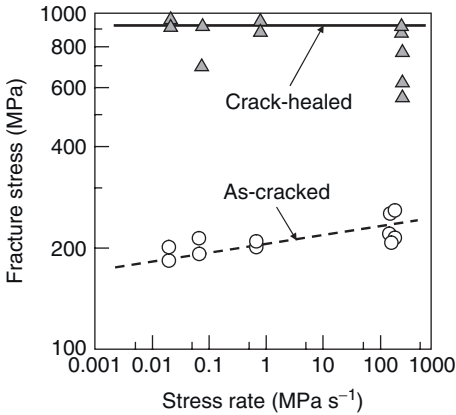
This specimen was tested at room temperature and exhibited the fracture stress of 526 MPa. To improve the reliability and the quality of the structural ceramics, it is therefore necessary to remove the specimens with large embedded flaws by proof test, even if surface cracks were completely healed. The scale parameter of the crack-healed specimens has a higher value than that of the as-cracked specimens as well as that of the smooth specimens, because cracks introduced by machinings which existed even in the smooth specimens, were also completely healed.

To show the considerable merit of the crack healing, the fracture probabilities of three specimens (smooth specimens, as-cracked specimens, and crack-healed specimens) for the proof test stress of 435 MPa were compared. The fracture probabilities of the smooth specimens, the as-cracked specimens, and the crack-healed specimens were 80, 100, and 30%, respectively. Therefore, it can be concluded that the crack healing drastically increases the survival probability by the proof test, and thus increases the working stress of structural ceramics.

### 17.7.2

#### Fatigue Strength

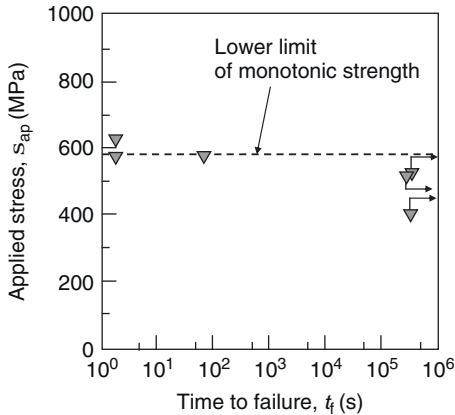
The effect of the self-crack healing on the fatigue strength is greater than that on the monotonic strength. The fatigue degradation of ceramics progresses by the stress corrosion cracking at the tip of cracks as mentioned in section 17.2. Therefore the presence of surface cracks affects strongly the fatigue strength. Figure 17.21 [50] shows the dynamic fatigue results of the crack-healed mullite containing



**Figure 17.21** Dynamic fatigue results of the crack-healed mullite containing 15 vol% SiC whiskers and 10 vol% SiC particles composite with that of the composite having a semi-elliptical crack of 100  $\mu\text{m}$  in surface length.

15 vol% SiC whiskers and 10 vol% SiC particles composite with that of the composite having a semi-elliptical crack of 100  $\mu\text{m}$  in surface length. From logarithmic plots of the dynamic strength versus stressing rate, the effect of the crack healing on the fatigue behavior can be clearly understood. The positive slope implies that the slow crack growth occurs. As the data on the specimens containing the surface crack shows the positive slope, the slow crack growth has been included in the fatigue behavior. On the other hand, the data on the crack-healed specimen is almost constant over the whole stressing rate. Therefore, the crack healing makes the fatigue sensitivity decrease significantly. Actually, the fracture initiator in the crack-healed mullite containing 15 vol% SiC whiskers and 10 vol% SiC particles composite under the every stressing rate is an embedded flaw, which did not grow under the applied stress.

In high temperature fatigue, there is another interesting phenomenon, in order that the self-crack healing occurs at the same time as fatigue damage. For example, Figure 17.22 [50] shows a logarithmic plot of life time in terms of the applied stress for the crack-healed mullite containing 15 vol% SiC whiskers and 10 vol% SiC particles composite at 1273 K. In general, that is, the slow crack growth is included, the life time increases as the applied stress decreases. However, all the crack-healed test specimens survived up to the finish time of 100 h obeying the JIS standard [51] under static stresses of 50 MPa less than the lower limit of the monotonic strength at the same temperature. Alternatively, the specimens fractured at less than 100 s under stresses corresponding to the lower limit of the flexural strength. This fracture is not fatigue, but rather rapid fracture. Therefore, it is confirmed that the crack-healed composite is not degraded by the static fatigue at 1273 K. The behavior would result from the fact that self-crack healing occurs rapidly compared with the fatigue damage.



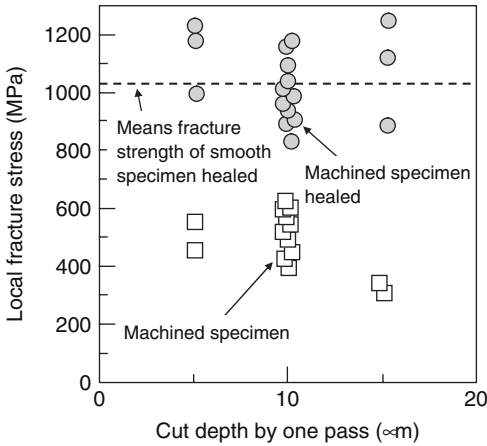
**Figure 17.22** Logarithmic plot of life time in terms of the applied stress for the crack-healed mullite containing 15 vol% SiC whiskers and 10 vol% SiC particles composite at 1273 K.

### 17.7.3

#### Crack-healing Effects on Machining Efficiency

An important alternative aspect is that the self-crack healing is a most valuable surface treatment. Applying the crack-healing process into the manufacturing for ceramic components can reduce the manufacturing cost. Machining processes included in the manufacturing reduce the reliability of the components [52] because it causes many cracks to the surface of the component. To remove the nonacceptable cracks, final machining processes, such as polishing and lapping, are generally required. Although these processes leave behind many minute cracks, these are expensive processes. It is, therefore, anticipated that substituting the crack-healing process for the final machining processes leads to economical manufacturing for ceramic components secured with high reliability.

Figure 17.23 [53] demonstrates that the nonacceptable cracks introduced by a heavy machining can be completely crack healed. The machining cracks were introduced at the bar specimens surface of alumina/20 vol% SiC whiskers composite by a ball-drill grinding. The ball-drill grinding was performed along the direction perpendicular to the long side of the specimens, as shown in shown in Figure 17.6, which consequently fabricated a semi-circular groove whose depth and curvature were 0.5 and 2 mm, respectively. As a result, the machined specimens contained many machining cracks perpendicular to the tensile stress at the bottom of the semi-circular groove. The horizontal variable is a cut depth by one pass, which is an indicator of the machining efficiency. For example, 14 to 40 cycles are needed to fabricate the semi-circular groove by the grinding with the cut depth by one pass of 15 and 5  $\mu\text{m}$ , respectively. Alternatively, the vertical axis indicates the local fracture stress of the machined specimens and the machined specimen healed. From the load as the specimens fractured,  $P_F$ , the section



**Figure 17.23** Effect of depths of cut by one pass on the local fracture stress at room temperature of the machined specimens healed.

modulus,  $Z$ , and the stress concentration factor,  $\alpha$ , the local fracture stress at the bottom of the semi-circular groove,  $\sigma_{LF}$ , was evaluated as follows:

$$\sigma_{LF} = \frac{\alpha P_f l}{4Z} \quad (17.8)$$

where  $l$  is a span length. Under this geometry, the value of  $Z$  and  $\alpha$  were 4.2 and 1.4 [54], respectively. The local fracture stress of the machined specimens decreased with increasing the cutting depth. This behavior implies that the cut depth by one pass also means the degree of the machining heaviness. Throughout the range of the cut depth by one pass a complete strength recovery was found to be attained by the crack-healing treatment for 10 h at 1673 K, because these average strengths were almost equal to that of the complete crack-healed specimens [35]. The crack healing is possible for relatively large cracks initiated by a heavy machining for cutting depths up to 15  $\mu\text{m}$ . However, the heavy machining for cutting depths above 15  $\mu\text{m}$  makes the diamond grain to drop out of the ball drill significantly, reducing the machining efficiency. Therefore, with a simple operation of heating, one can ensure the reliability over ceramic components machined by the limiting conditions of the grinding tool (ball-drill). To not cause the outstanding strength to decrease by fabricating the semi-circular groove, it is necessary to perform not only on machining with the cut depth by one pass of less than 5  $\mu\text{m}$  but also on lapping at the bottom. Thus, a high machining efficiency can be attained by the use of the crack-healing process.

It is important to note the difference in the optimized condition between the crack healing for indented cracks and the machining cracks. The optimized crack healing condition for the indentation cracks in alumina/20 vol% SiC whiskers composite was found to be 1573 K for 1 h [53]. However, the crack healing above

**Table 17.4** Weibull modulus ( $m$ ) and shape parameter ( $\beta$ ) of ball-grind alumina composites containing 20vol% of SiC whiskers.

Sample type	Weibull modulus, $m$ (MPa)	Shape parameter ( $\beta$ )
Machined specimen	6.69	549
Machined specimen healed at 1573 K for 1 h	6.70	796
Machined specimen healed at 1673 K for 10h	11.5	1026
Healed (1573 K for 1 h) smooth specimen	8.15	1075

1673 K for more than 10h is required to attain the complete strength recovery for the machined alumina/20vol% SiC whiskers composite. This behavior can be clearly understood by the statistical analysis using the two-parameter Weibull function given by Equation (17.5). Table 17.4 shows the Weibull modulus and the shape parameter evaluated from the analyses. The values of  $m$  and  $\beta$  of the machined specimen healed at 1673 K for 10h were 11.5 and 1026 MPa, respectively. The values were almost equal to those of complete crack-healed specimen. From this statistical and  $\chi^2$  analysis, it was found that the cracks introduced by machining were completely healed by the crack healing process at 1673 K for 10h. On the other hand, the machined specimen healed at 1573 K for 1h had lower values of  $m$  and  $\beta$  than those of the smooth specimen healed; thus, it can be concluded that this crack-healing condition is inadequate. Two approaches are confirmed to be reasonable to explain this difference: (i) the difference in the state of the subsurface residual stress associated with the different crack geometries and (ii) the oxidation of SiC by the heat generation during the machining. The machining crack was closed by the action of the compressive residual stress resulting in a reduction in the supply of oxygen to the crack walls. Moreover, before the crack-healing treatment, if SiC particles were already covered with a thin oxidation layer, by the grinding heat, this would lead to the decrease in the oxidation activity of the SiC particles.

Furthermore, it was found that the various cracks initiated by machining into various machined figurations could be healed by crack-healing treatment at 1673 K for 10h, as shown in Figure 17.24 [53].


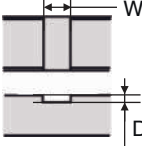
## 17.8

### New Structural Integrity Method

#### 17.8.1

##### Outline

A combination of the crack healing and the proof testing ultimately guarantees the structural integrity of the ceramic components. As mentioned above, by

		Means nominal fracture stress
Through hole		Machined 458 MPa
		Machined heated 728 MPa
Square groove		Machined 250 MPa
		Machined heated 728 MPa

**Figure 17.24** Effect of crack-healing condition on strength recoveries of various machined specimens.

eliminating not only the cracks introduced during manufacturing but also the cracks introduced during service, the crack healing can ensure perfectly against risk of the fracture initiated from surface flaws. The proof testing, in which components are over-stressed prior to use, can determine the maximum critical size of embedded flaws associated with fracture. Embedded flaws, such as voids, may be present in a material as a result of the processing, and could not be generated during service. Therefore, the minimum fracture stress caused by the embedded flaws [55, 56] or probabilistic fatigue S–N curves [57–59] has been estimated from the proof testing stress on the basis of the linear fracture mechanics.

However, two important points must be taken account of while using the proof testing. First is to ensure that engineering ceramics show the nonlinear fracture behavior [60, 61]. The other is that the evaluated minimum fracture stress is valid only at the proof testing temperature. Therefore, if ceramic components are used at high temperature, the proof testing must be conducted at the operating temperature. Ando *et al.* [62] proposed a theory to evaluate the temperature dependence of the guaranteed (minimum) fracture stress of a proof tested sample based on nonlinear fracture mechanics. This approach allows the ceramic components proof tested at room temperature to operate at the arbitrary temperatures.

### 17.8.2

#### Theory

On the basis of the process zone size failure criterion, the minimum fracture stress at high temperature can be guaranteed from the proof testing stress at room temperature. The criterion proposed by Ando *et al.* [62] has been obtained by the size of process zone, which is the plastic deformation region at the crack tip, well

expressing the nonlinear fracture behavior of ceramics. From the criterion, the process zone size at fracture  $D_C$ , is given by the following equation:

$$D_C = \frac{\pi}{8} \left( \frac{K_{IC}}{\sigma_0} \right)^2 = a_e \left\{ \sec \left( \frac{\pi \sigma_C}{2 \sigma_0} \right) - 1 \right\} \quad (17.9)$$

where  $\sigma_C$  and  $\sigma_0$  are the fracture stress at the fracture caused by the flaws having  $a_e$  and the fracture strength of the plain specimen (intrinsic bending strength), respectively.  $K_{IC}$  plane strain fracture toughness and  $a_e$ , equivalent crack length, which is given by the equation as

$$K_C = \sigma_C \sqrt{\pi a_e} \quad (17.10)$$

By expanding Equation 17.9 around  $a_e$ , one can write the equivalent crack size of the flaws associated with fracture as shown in the following equation:

$$a_e = \frac{\pi}{8} \left( \frac{K_{IC}}{\sigma_0} \right)^2 \left\{ \sec \left( \frac{\pi \sigma_C}{2 \sigma_0} \right) - 1 \right\}^{-1} \quad (17.11)$$

Since  $K_{IC}$  and  $\sigma_0$  is the function of temperature, the fracture strength associated with  $a_e$  needs to be also expressed as a function of temperature:

$$\sigma_C^T = \frac{2 \sigma_0^T}{\pi} \arccos \left\{ \frac{\pi}{8} \frac{1}{a_e} \left( \frac{K_{IC}^T}{\sigma_0^T} \right)^2 + 1 \right\}^{-1} \quad (17.12)$$

where the superscript  $T$  is the value at elevated temperature.

The maximum size of the flaw,  $a_e^p$ , that is able to present in the sample proof tested under  $\sigma_p$ , at room temperature can be given by

$$a_e^p = \frac{\pi}{8} \left( \frac{K_{IC}^R}{\sigma_0^R} \right)^2 \left\{ \sec \left( \frac{\pi \sigma_p}{2 \sigma_0^R} \right) - 1 \right\}^{-1} \quad (17.13)$$

where the superscript  $R$  is the value at room temperature. Assuming that the sizes of the residual embedded flaws do not vary with change in the temperature, one can determine the minimum fracture stress guaranteed of the proof tested sample,  $\sigma_G$ , as the fracture strength associated with  $a_e^p$  at arbitrary temperatures. Thus the value of  $\sigma_G$  can be expressed as

$$\sigma_G = \frac{2 \sigma_0^T}{\pi} \arccos \left\{ \left( \frac{K_{IC}^T}{K_{IC}^R} \right)^2 \left( \frac{\sigma_0^R}{\sigma_0^T} \right)^2 \left[ \sec \left( \frac{\pi \sigma_p}{2 \sigma_0^R} \right) - 1 \right] + 1 \right\}^{-1} \quad (17.14)$$

and can be evaluated from the data on the temperature dependences of  $K_{IC}$  and  $\sigma_0$ .



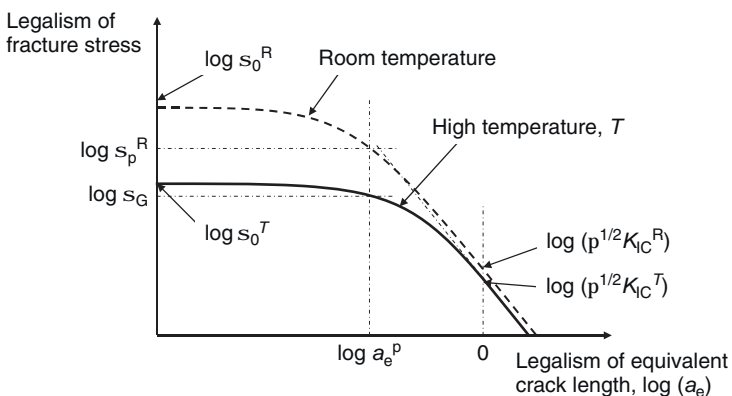
## 17.8.3

**Temperature Dependence of the Minimum Fracture Stress Guaranteed**

Using the above theory, one can estimate the minimum fracture stresses at elevated temperatures for the sample proof tested at room temperature. Ono *et al.* [49] (evaluated the temperature dependence of  $\sigma_G$  for alumina/20 vol% SiC particles composite. Moreover, by comparing the evaluated  $\sigma_G$  with the measured fracture stress of the proof tested sample at elevated temperature, the validity of this estimation was given by them. Their results and discussion are presented in the following text.

Before discussing the temperature dependence of  $\sigma_G$ , temperature dependences of the plane strain fracture toughness,  $K_{IC}$ , and the intrinsic bending strength,  $\sigma_0$ , are noticed. Ono *et al.* [49] investigated these temperature dependences for alumina/20 vol% SiC particles composite. The  $\sigma_0$ , which is determined as the average fracture stress of 5% of the highest strengths of the crack-healed specimens at the temperatures, has large temperature dependence and the tendency is almost linear and negative up to 1373 K. Moreover, the  $K_{IC}$  is almost constant against temperature. The features affect the correlativeness between the fracture stresses as a function of the equivalent crack length,  $a_e$ , at room temperature and at high temperature. The schematic is shown in Figure 17.25.

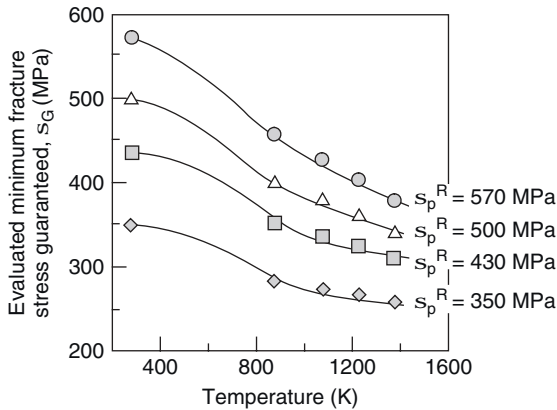
The fracture stress associated with small flaw, that is,  $a_e$  is low, is equal to the  $\sigma_0$ , and varies considerably as temperature varies. On the other hand, the fracture stress associated with large flaw, that is,  $a_e$  is high, is determined by linear fracture mechanics as expressed by Equation (17.10) and changes scarcely with temperature change. Therefore, the negative temperature gradient of the  $\sigma_G$  increases with increasing the proof testing stress,  $\sigma_p^R$ , as shown in Figure 17.26. Since high  $\sigma_p^R$  qualifies  $a_e^p$  to be a low value, the negative temperature gradient of the  $\sigma_G$  becomes considerably high. Alternatively, since low  $\sigma_p^R$  allows the large flaws to present



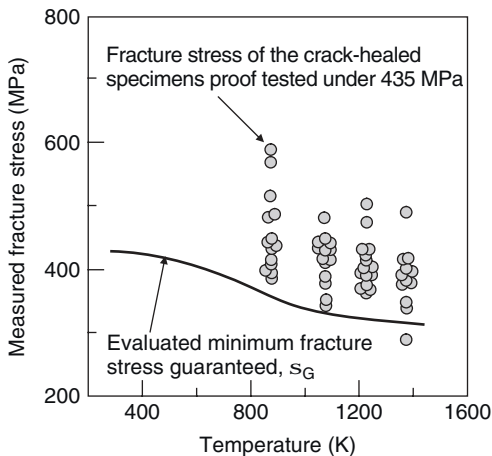
**Figure 17.25** Schematic illustration of proof-test theory and the effect of equivalent crack on fracture strength at room temperature and at high temperature.

in the proof tested specimen, the  $\sigma_G$  is almost constant as a function of temperature.

The values of the evaluated  $\sigma_G$  have good agreements with the measured minimum fracture stress of the proof tested specimens,  $\sigma_F^{\min}$ . Figure 17.27 shows the data on the fracture stress of the crack-healed and the proof-tested specimens as a function of temperature with the evaluated  $\sigma_G$  for the crack-healed alumina/20vol% SiC particles composite when  $\sigma_p = 435$  MPa. Except the data at 1373 K, all specimens have higher strength than the  $\sigma_G$  at all the temperature.



**Figure 17.26** Temperature dependence of minimum fracture stress guaranteed of the proof tested under several proof testing stress for alumina containing 20 vol% SiC particles composite.

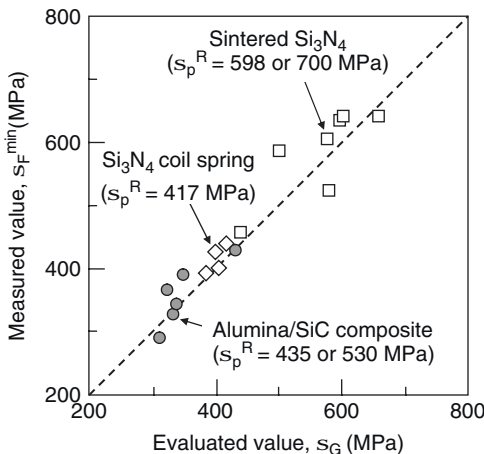


**Figure 17.27** Comparison between measured fracture stress and the evaluated minimum fracture stress guaranteed for the crack-healed alumina/20vol% SiC particles composite proof tested under 435 MPa.

Also, the minimum values of the experimental fracture stress are almost equal to the  $\sigma_G$  at all temperatures. At 1373 K, the  $\sigma_F^{\min}$  is 6.8% less than  $\sigma_G$ , but the value exists in the dispersion evaluated from the  $K_{IC}$  and the  $\sigma_0$  that have large scatters. Moreover, in the case of  $\sigma_p = 530$  MPa, the evaluated  $\sigma_G$  have good agreements with the  $\sigma_F^{\min}$  as well as with all the proof-tested specimens fractured under the tensile stress more than  $\sigma_G$ . Therefore, the results well demonstrate the validity of the guaranteed method.

Moreover, Ono *et al.* [49] and Ando *et al.* [62, 63] reported that the guaranteed theory can be applied to different conditions and the different materials. The obtained results can be seen in Figure 17.28, where the measured  $\sigma_F^{\min}$  is plotted as a function of the evaluated  $\sigma_G$ .  $N$  in the figure denotes the number of samples used to obtain  $\sigma_F^{\min}$ . Four open diamonds indicate the data on the ceramic coil spring made of silicon nitride. Also, a open square differs from the closed circles in the crack healing condition, that is, the open square employs 1373 K for 50 h and the closed circle employs 1573 K for 1 h. However, all  $\sigma_F^{\min}$  shows good agreement with  $\sigma_G$ . Therefore, using Equation (17.14) one can estimate the  $\sigma_G$  at higher temperatures of every material having the crack healing ability and every crack healing condition.

On the other point of view, it is interesting whether this estimation is reversible for temperatures, that is, the stress evaluated in Equation (17.14) can guarantee the minimum fracture stress at room temperature of the specimen proof tested at high temperature. For example, the  $\sigma_G$  at room temperature of the alumina/20 vol% SiC particles composite proof tested under 335 MPa ( $=\sigma_p$ ) at 1073 K is evaluated to be 435 MPa. Alternatively, the experimental minimum fracture stress was 410 MPa. The  $\sigma_G$  existed in the dispersion obtained from  $K_{IC}$  and  $\sigma_0$ , which have large scatters.



**Figure 17.28** Comparison between minimum fracture stresses guaranteed and measured minimum fracture stress.

## 17.9 Advanced Self-crack Healing Ceramics

### 17.9.1 Multicomposite

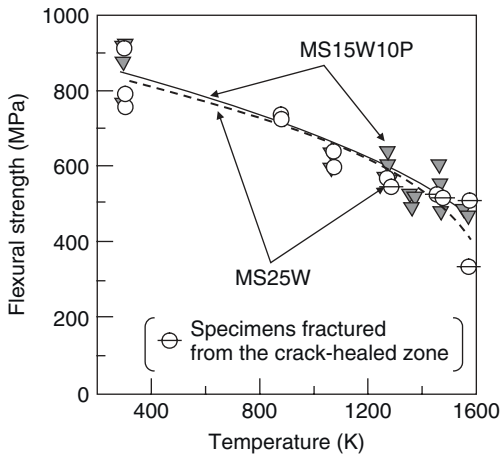
Ceramic composite containing both SiC whiskers and SiC particles, called SiC *multicomposite*, enhance fracture strength and toughness as well as endow the ceramics with the good self-crack healing ability. As mentioned in Section 17.5, the reinforcement by SiC whiskers can not only improve fracture toughness but can also generate the self-crack healing ability. However, it is difficult to disperse a large amount of SiC whiskers uniformly, and so the aggregated SiC whiskers decreases the fracture strength. SiC multicomposites containing both whiskers and particles improves the self-crack healing ability endowed by SiC whiskers alone without adversely affecting the composite strength. Therefore, ceramic–SiC multicomposites exhibit high strength, high fracture toughness, and excellent self–crack–healing ability.

Especially, SiC multicomposites perform better than the mullite-based composites. Mullite and mullite-based composites have been expected to be advanced ceramic spring because they exhibit the same low level elastic constant as metal and excellent oxidation resistance. However, mullite has remarkably low fracture toughness. Therefore, it is necessary to endow mullite with self–crack–healing ability for actualizing mullite-based ceramic springs. The mechanical properties of mullite/SiC composites [21, 46] and multicomposites [64] were investigated as shown in Table 17.5.

The fracture strength increases with SiC content increasing up to 20 vol%, above which it remains almost constant. The fracture toughness increased with an increase in SiC whiskers content. Clearly, it is confirmed that crack bridging and pulling out due to SiC whiskers lead to increase in fracture toughness. All the

**Table 17.5** Mullite/SiC composites having self-crack healing ability.

Sample descriptions	Content (vol%)		
	Mullite	SiC particle (diameter = 0.27 $\mu\text{m}$ )	SiC whisker (diameter = 0.8–1.0 $\mu\text{m}$ , length =30–100 $\mu\text{m}$ )
MS15P	85	15	0
MS15W	85	0	15
MS20W	80	0	20
MS25W	75	0	25
MS15W5P	80	5	15
MS15W10P	75	10	15



**Figure 17.29** Temperature dependence of the crack-healed strength of mullite/25 vol% SiC whiskers composite (MS25W) and mullite/15 vol% SiC whiskers/10 vol% SiC particles composite (MS15W10P), in which the center lined symbols indicate specimens fractured from the precrack healed.

mullite/SiC composites, which are listed in Table 17.5, can exhibit a large strength recover by the crack healing. However, mullite/15 vol% SiC whiskers composite (MS15W) [46] cannot attain the complete strength recovery despite the optimized crack healing condition. Complete strength recovery of the crack-healed specimens is defined as the strength of the specimens, whose fracture initiation is embedded flaw. This implies the complete elimination of surface cracks that can be attained and the strength of the crack healed part is superior to that of the base materials. The crack healed part in mullite/25 vol% SiC whiskers composite (MS25W) holds higher strength than the base materials below 1273 K, as shown in Figure 17.29 [64]. On the other hand, the crack healed part in mullite/15 vol% SiC whiskers/10 vol% SiC particles composite (MS15W10P) holds higher strength than the base materials at the whole of the experimental temperature region, as shown in Figure 17.29.

Figure 17.30 [64] shows the maximum shear strains of the mullite/SiC multi-composites as a function of SiC content. The maximum shear strain corresponds to the deformation ability as spring. The value of the maximum shear strain showed a maximum at a SiC content of 20 vol%, above which it slightly decreased because Young's modulus increased with an increase in SiC content, but the fracture strengths were almost constant above SiC content of 20 vol%. MS15W10P has the best potential as a material for the ceramic springs used at high temperatures, because it has a shear deformation ability that was almost two times greater than monolithic mullite as well as an adequate crack healing ability.

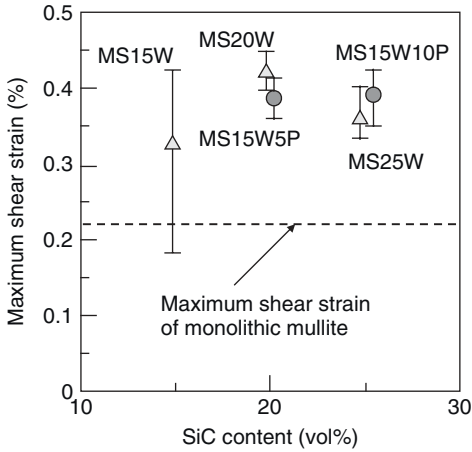


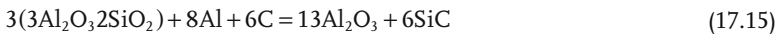
Figure 17.30 Maximum shear strains of mullite/SiC composites as a function of SiC content.

### 17.9.2

#### SiC Nanoparticle Composites

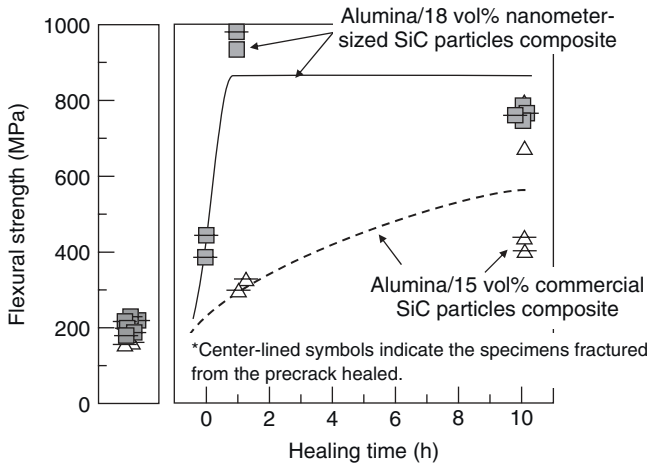
Nanometer-sized SiC fine particles enhance the self-crack healing rate because it gives a large increment in the reactive area and makes the surface of SiC particles active. This effect give a large benefit to the self-crack healing at relatively low temperatures at which the self-crack healing is completed in more than 100 h.

Reaction synthesis is a promising process for directly fabricating nanocomposites which are difficult to obtain by the normal sintering of nanometer-sized starting powder compacts. Reaction synthesis to fabricate alumina–SiC nanocomposites [65–71] were reported. Using the reaction synthesis (17.15)



Zhang *et al.* [71] succeeded in fabricating alumina nanometer-sized SiC particles nanocomposite, in which the formed SiC particles are mainly entrapped inside the alumina grains. Employing the similar process to prepare alumina–SiC nanocomposite, Nakao *et al.* [72] investigated the effect of nanometer-sized SiC particle on the crack-healing behavior, as shown in Figure 17.31.

The result demonstrates that the nanometer-sized SiC with particle size of 20 nm can significantly increase the self-crack healing rate compared to the commercial 270 nm SiC particles. Furthermore, the nano-SiC particles can attain the complete strength recovery within 10 h at 1023 K, which is a 250 K lower temperature compared to the commercial SiC particles. Although nanometer-sized SiC particles makes the crack-healing reaction activated at lower temperatures, it gives same level of refractoriness as the alumina containing commercial SiC particles



**Figure 17.31** Crack-healing behavior at 1373 K on alumina containing 18 vol% nanometer-sized SiC particles composite and alumina containing 15 vol% commercial SiC particles composite, in which center lined symbols indicate the specimen fractured from the precrack healed.

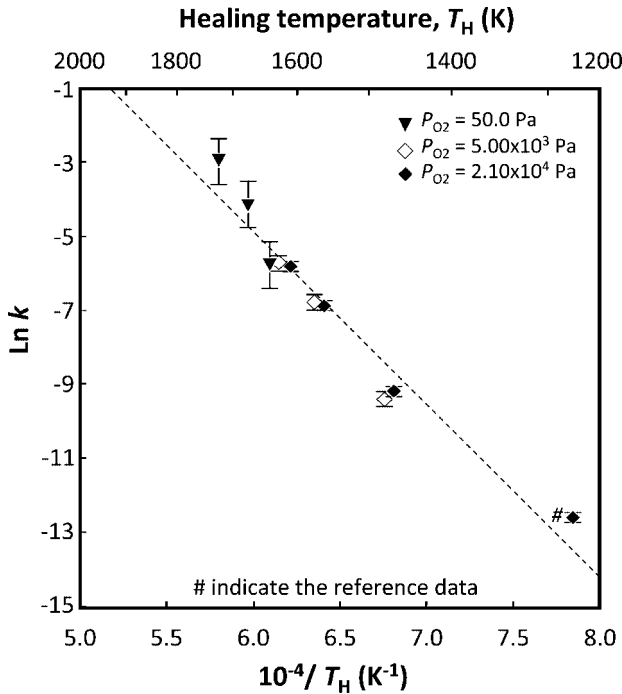
composite. Therefore, it is noted that the use of SiC nanoparticles is a most valuable route to enhance the valid temperature region of the self crack healing.

### 17.10

#### Availability to Structural Components of the High Temperature Gas Turbine

The structural component of the high temperature gas turbine is one of the most attractive applications for the self healing ceramics. The application requires high temperature durability and high mechanical reliability because of its service condition consisting of high temperature and oxidizing atmosphere, which is valid condition of the self-healing driven by the SiC oxidation. Actually the turbine nozzle and blade of the 1500 °C-class gas turbine are exposed in high temperatures ranging from 1273 to 1773 K and oxygen partial pressures ranging from 8000 to 10000 Pa. To discuss the availability of the self-healing driven by SiC oxidation to the turbine blades and nozzles requires knowing the self healing kinetics as a function of temperature and oxygen partial pressure, because the rate is sensitive to temperature and oxygen partial pressure changes.

Osada *et al.* [39] proposed the kinetics model in which the rate of self-crack healing,  $v_H$ , is expressed as a function of both the healing temperature,  $T_H$ , and oxygen partial pressure,  $P_{O_2}$ . Two assumptions of the kinetic model are that the reaction order,  $n$ , is independent on temperature and that obeying Arrhenius' law, the reaction constant,  $k$ , depends on only temperature. By using the kinetic model,  $k$  is expressed as a following function of  $T_H$  and  $P_{O_2}$ :



**Figure 17.32** Temperature dependence on natural logarithm of the rate constant,  $k$ , calculated from various levels of  $P_{O_2}$ .

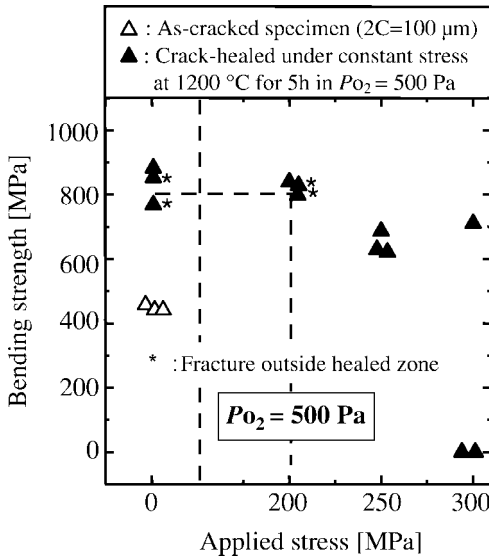
$$k = \frac{\nu_H}{P_{O_2}^n} = A \exp\left(-\frac{Q_H}{RT_H}\right) \quad (17.16)$$

where  $A$  is constant,  $Q_H$  activation energy, and  $R$  gas constant. Validity of the model was assayed from the experimental data on alumina/15 vol% SiC composite, as shown in Figure 17.32. The vertical axis indicates the logarithm of  $1/t_H \cdot P_{O_2}^n$ , corresponding to the logarithm of  $k$ , since where  $t_H$  is the minimum time until complete healing, and the value of  $\nu_H$  is determined to be the inverse of  $t_H$ . As all the plots can be fitted by only one straight line, it is confirmed that the proposed model can be available in the temperature region from 1273 to 1473 K. Furthermore, the minimum time for complete healing was obtained as;

$$t_H = 1.44 \times 10^{-6} \cdot P_{O_2}^{-0.835} \exp\left(\frac{4.65 \times 10^4}{T_H}\right) \quad (17.17)$$

Also it is important to know the threshold stress during self-crack healing under low oxygen partial pressure. Figure 17.33 show the bending strength of  $Si_3N_4/SiC$  composite crack-healed at 1473 K for 5 h in  $P_{O_2}$  of 500 Pa under several tensile stress. The tensile stress is applied by three point bending and applied to one face containing an indentation crack of 0.1 mm in surface length. The specimens





**Figure 17.33** Bending strength of crack-healed specimen as a function of applied stress during crack-healing in  $P_{O_2} = 500$  Pa.

applied stress of 200 MPa and 250 MPa survived during crack-healing process. For the applied stress of 200 MPa, the specimens fractured outside crack-healed zone, whereas the applied stress of 250 MPa the specimens fractured from crack-healed zone. The average values of bending strength of the specimens crack-healed under 200 MPa are comparable to those of the specimen healed without stress. Therefore, the threshold tensile stress for crack-healing at 1473 K in  $P_{O_2} = 500$  Pa is determined to be 200 MPa. In the same method, for the specimens crack-healed in  $P_{O_2} = 5000$  Pa and 21 000 Pa (air), the threshold tensile stresses for crack-healing were determined to be 200 MPa. From these results, the crack-healing can be achieved in low oxygen partial pressure of  $P_{O_2} = 500$  Pa and can elongate the lifetime and the reliability.

## References

- Williams, L.S. (1956) *Transactions of the British Ceramic Society*, 55 (5), 287–312.
- Evans, A.G. (1972) *Journal of Materials Science*, 7 (10), 1131–1146.
- Dwivedi, P.J. and Green, D.J. (1995) *Journal of the American Ceramic Society*, 78 (8), 2122–2128.
- Heuer, A.H. and Roberts, J.P. (1966) *Proceedings of the British Ceramic Society*, 6, 17–27.
- Lange, F.F. and Gupta, T.K. (1970) *Journal of the American Ceramic Society*, 53 (1), 54–55.
- Davies, L.M. (1966) *Proceedings of the British Ceramic Society*, 6, 29–53.
- Lange, F.F. and Radford, K.C. (1970) *Journal of the American Ceramic Society*, 53 (7), 420–421.
- Roberts, J.T.A. and Wrona, B.J. (1973) *Journal of the American Ceramic Society*, 56 (6), 297–299.

- 9 Bandyopadhyay, G. and Roberts, J.T.A. (1976) *Journal of the American Ceramic Society*, **59** (9–10), 415–419.
- 10 Gupta, T.K. (1976) *Journal of the American Ceramic Society*, **59** (9–10), 448–449.
- 11 Evans, A.G. and Charles, E.A. (1977) *Acta Metallurgica*, **25**, 919–927.
- 12 Lange, F.F. (1970) *Journal of the American Ceramic Society*, **53** (5), 290.
- 13 Easler, T.E., Bradt, R.C. and Tressler, R.E. (1982) *Journal of the American Ceramic Society*, **65** (6), 317–320.
- 14 Chu, M.C., Cho, S.J., Yoon, K.J. and Park, H.M. (2005) *Journal of the American Ceramic Society*, **88** (2), 491–493.
- 15 Niihara, K. and Nakahira, A. (1998) “Strengthening of oxide ceramics by SiC and Si<sub>3</sub>N<sub>4</sub> dispersions”, *Proceeding of the Third International Symposium on Ceramic Materials and Components for Engines*, American Ceramics Society, Westerville, pp. 919–926.
- 16 Niihara, K. (1991) *Journal of the Ceramic Society of Japan*, **9** (10), 974–982.
- 17 Niihara, K., Nakahira, A. and Sekino, T. (1993) *Materials Research Society Symposium Proceedings*, **286**, 405–412.
- 18 Thompson, A.M., Chan, H.M. and Harmer, M.P. (1995) *Journal of the American Ceramic Society*, **78** (3), 567–571.
- 19 Chou, I.A., Chan, H.M. and Harmer, M.P. (1998) *Journal of the American Ceramic Society*, **81** (5), 1203–1208.
- 20 Wu, H.Z., Lawrence, C.W., Roberts, S.G. and Derby, B. (1998) *Acta Materialia*, **46** (11), 3839–3848.
- 21 Chu, M.C., Sato, S., Kobayashi, Y. and Ando, K. (1995) *Fatigue and Fracture of Engineering Materials and Structures*, **18** (9), 1019–1029.
- 22 Ando, K., Tsuji, K., Hirasawa, T., Kobayashi, Y., Chu, M.C. and Sato, S. (1999) *Journal of the Society of Materials Science, Japan*, **48** (5), 489–494.
- 23 Ando, K., Tsuji, K., Ariga, M. and Sato, S. (1999) *Journal of the Society of Materials Science, Japan*, **48** (10), 1173–1178.
- 24 Ando, K., Ikeda, T., Sato, S., Yao, F. and Kobayashi, Y. (1998) *Fatigue and Fracture of Engineering Materials and Structures*, **21**, 119–122.
- 25 Ando, K., Chu, M.C., Kobayashi, Y., Yao, F. and Sato, S. (1991) *The Japan Society of Mechanical Engineering, International Journal Series A*, **65A**, 1132–1139.
- 26 Ando, K., Chu, M.C., Yao, F. and Sato, S. (1999) *Fatigue and Fracture of Engineering Materials and Structures*, **22**, 897–903.
- 27 Yao, F., Ando, K., Chu, M.C. and Sato, S. (2001) *Journal of the European Ceramic Society*, **21**, 991–997.
- 28 Ando, K., Kim, B.S., Chu, M.C., Saito, S. and Takahashi, K. (2004) *Fatigue and Fracture of Engineering Materials and Structures*, **27**, 533–541.
- 29 Kim, B.S., Ando, K., Chu, M.C. and Saito, S. (2003) *Journal of the Society of Materials Science, Japan*, **52** (6), 667–673.
- 30 Ando, K., Kim, B.S., Kodama, S., Ryu, S.H., Takahashi, K. and Saito, S. (2003) *Journal of the Society of Materials Science, Japan*, **52** (11), 1464–1470.
- 31 Nakao, W., Osada, T., Yamane, K., Takahashi, K. and Ando, K. (2005) *Journal of the Japan Institute of Metals*, **69** (8), 663–666.
- 32 Chase M.W. Jr. (ed.) (1998) *NIST-JANAF Thermochemical Tables*, 4th edn, American Chemistry Society and American Institute of Physics for the National Institute of Standards and Technology.
- 33 Japan Industrial Standard R1601 (1993) *Testing Method for Flexural Strength of High Performance Ceramics*, Japan Standard Association, Tokyo.
- 34 Sato, S., Chu, M.C., Kobayashi, Y. and Ando, K. (1995) *Journal of the Japan Society of Mechanical Engineers*, **61**, 1023–1030.
- 35 Takahashi, K., Yokouchi, M., Lee, S.K. and Ando, K. (2003) *Journal of the American Ceramic Society*, **86** (12), 2143–2147.
- 36 Lee, S.K., Ishida, W., Lee, S.Y., Nam, K.W. and Ando, K. (2005) *Journal of the European Ceramic Society*, **25** (5), 569–576.
- 37 Lee, S.K., Ando, K. and Kim, Y.W. (2005) *Journal of the American Ceramic Society*, **88** (12), 3478–3482.
- 38 Fang, J., Chan, H.M. and Harmer, M.P. (1995) *Materials Science and Engineering A*, **195**, 163–167.
- 39 Osada, T., Nakao, W., Takahashi, K., Ando, K. and Saito, S., (2009) *Journal of the American Ceramics Society*, **92** (4), 864–869.

- 40 Jung, Y.S., Nakao, W., Takahashi, K., Ando, K. and Saito, S., (2008) *Journal of the Society of the Materials Science Japan*, **57** (11), 1132–1137.
- 41 Ando, K., Furusawa, K., Chu, M.C., Hanagata, T., Tuji, K. and Sato, S. (2001) *Journal of the American Ceramic Society*, **84** (9), 2073–2078.
- 42 Ando, K., Furusawa, K., Takahashi, K., Chu, M.C. and Sato, S. (2002) *Journal of the Ceramic Society of Japan*, **110** (8), 741–747.
- 43 Nakao, W., Takahashi, K. and Ando, K. (2006) *Materials Letters*, **61**, 2711–2713.
- 44 Ando, K., Yokouchi, M., Lee, S.K., Takahashi, K., Nakao, W. and Suenaga, H. (2004) *Journal of the Society of Materials Science, Japan*, **53** (6), 599–606.
- 45 Nakao, W., Ono, M., Lee, S.K., Takahashi, K. and Ando, K. (2005) *Journal of the European Ceramic Society*, **25** (16), 3649–3655.
- 46 Ono, M., Ishida, W., Nakao, W., Ando, K., Mori, S. and Yokouchi, M. (2004) *Journal of the Society of Materials Science, Japan*, **54** (2), 207–214.
- 47 Kim, B.A., Meguro, S., Ando, K. and Ogura, N. (1990) *Journal of the High Pressure Institute of Japan*, **28**, 218–223.
- 48 Newman, J.C. and Raju, I.S. (1981) *Engineering Fracture Mechanics*, **15**, 185–192.
- 49 Ono, M., Nakao, W., Takahashi, K., Nakatani, M. and Ando, K. (2007) *Fatigue and Fracture of Engineering Materials and Structures*, **30** (7), 599–667.
- 50 Nakao, W., Nakamura, J., Yokouchi, M., Takahashi, K. and Ando, K. (2006) *Transactions of JSSE*, **51**, 20–26.
- 51 Japan Industrial Standard R1632 (1998) *Test Method for Static Bending Fatigue of Fine Ceramics*, Japan Standard Association, Tokyo.
- 52 Kanematsu, W., Yamauchi, Y., Ohji, T., Ito, S. and Kubo, K. (1992) *Journal of the Ceramic Society of Japan*, **100** (6), 775–779.
- 53 Osada, T., Nakao, W., Takahashi, K., Ando, K. and Saito, S. (2007) *Journal of the Ceramic Society of Japan*, **115** (4), 278–284.
- 54 Nishida, M. (1967) *Stress Concentration*, Morikita Publishing, Tokyo, pp. 572–574.
- 55 Ritter J.E. Jr., Oates, P.B., Fuller E.R. Jr. and Wiederhorn, S.M. (1980) *Journal of Materials Science*, **15**, 2275–2281.
- 56 Ritter J.E. Jr., Oates, P.B., Fuller, E.R. Jr. and Wiederhorn, S.M. (1980) *Journal of Materials Science*, **15**, 2282–2295.
- 57 Hoshide, T., Sato, T. and Inoue, T. (1990) *Journal of the Japan Society of Mechanical Engineers A*, **56**, 212–218.
- 58 Hoshide, T., Sato, T., Ohara, T. and Inoue, T. (1990) *Journal of the Japan Society of Mechanical Engineers A*, **56**, 220–223.
- 59 Ando, K., Sato, S., Sone, S. and Kobayashi, Y. “Probabilistic study on fatigue life of proof tested ceramics spring”, in *Fracture From Defects, Proceedings of ECF-12* (eds M.W. Brown, E.R. de los Rios and K.J. Miller), EMAS Publishing, London, 1998, pp. 569–574.
- 60 Ando, K., Kim, B.A., Iwasa, M. and Ogura, N. (1992) *Fatigue and Fracture of Engineering Materials and Structures*, **15**, 139–149.
- 61 Ando, K., Iwasa, M., Kim, B.A., Chu, M.C. and Sato, S. (1993) *Fatigue and Fracture of Engineering Materials and Structures*, **16**, 995–1006.
- 62 Ando, K., Shirai, Y., Nakatani, M., Kobayashi, Y. and Sato, S. (2002) *Journal of the European Ceramic Society*, **22**, 121–128.
- 63 Ando, K., Takahashi, K., Murase, H. and Sato, S. (2003) *Journal of the High Pressure Institute of Japan*, **41**, 316–326.
- 64 Nakao, W., Mori, S., Nakamura, J., Yokouchi, M., Takahashi, K. and Ando, K. (2006) *Journal of the American Ceramic Society*, **89** (4), 1352–1357.
- 65 Chaklader, A.C.D., Gupta, S.D., Lin, E.C.Y. and Gutowski, B. (1992) *Journal of the American Ceramic Society*, **75** (8), 2283–2285.
- 66 Borsa, C.E., Spiandorello, F.M. and Kiminami, R.H.G.A. (1999) *Materials Science Forum*, **299–300**, 57–62.
- 67 Amroune, A., Fantozzi, G., Dubois, J., Deloume, J.P., Durand, B. and Halimi, R. (2000) *Materials Science and Engineering A*, **290**, 11–15.

- 68 Amroune, A. and Fantozzi, G. (2001) *Journal of Materials Research*, **16**, 1609–1613.
- 69 Lee, J.H., An, C.Y., Won, C.W., Cho, S.S. and Chun, B.S. (2000) *Materials Research Bulletin*, **35**, 945–954.
- 70 Pathank, L.C., Bandyopadhyay, D., Srikanth, S., Das, S.K. and Ramachandrarao, P. (2001) *Journal of the American Ceramic Society*, **84** (5), 915–920.
- 71 Zhang, G.J., Yang, J.F., Ando, M. and Ohji, T. (2004) *Journal of the American Ceramic Society*, **87** (2), 299–301.
- 72 Nakao, W., Tsutagawa, Y. and Ando, K. *Journal of Intelligent Material Systems and Structures*, **19**, 407–410.



## 18

# Ecological Toxicology of Engineered Carbon Nanoparticles

Aaron P. Roberts and Ryan R. Otter

### 18.1

#### Introduction

Advancements in the science of engineered nanoparticles (materials with at least one dimension <100 nm) have created a great deal of promise for their application in a wide variety of fields. Today, the “nanosized” properties of a range of materials are being harnessed for use not only in industrial applications, but also in biomedical applications [1–3] and personal care products [4], among others. A great deal of concern has been expressed, however, regarding the potential safety of these materials to biological systems. Reviews in *Science* [5] as well as a United States National Research Council report [6] have noted a general lack of information on the potential human and environmental health effects of exposure to these compounds.

In particular, relatively few resources have been devoted to examining the potential ecological fate and effects of engineered nanoparticles, and there is a general lack of conclusive data regarding the fate and potential effects of these materials in natural ecosystems. Despite safeguards and environmental protection legislation, industrial and personal products are routinely deposited in the environment, including freshwater and marine ecosystems [7]. For example, Kolpin *et al.* [7] reported that in a study of 139 streams in the United States, 80% contained measurable levels of organic wastewater contaminants including caffeine, insecticides, cholesterol, antimicrobial agents, and fire retardants. With over 300 commercial products containing some type of nanotechnology currently available on the market [8], and growth expected to exceed US\$1 trillion by 2015 [5], it is likely that inputs of nanomaterials into the environment will increase over time [9].

In order to estimate the potential risk posed by engineered nanoparticles to ecological systems, several objectives must be met:

- **Realistic estimates of environmental discharge must be made:** Current research on the ecological effects of engineered nanoparticles is carried out without an estimate of what *environmentally relevant* concentrations of nanoparticles might be. Accurate environmental discharge estimates are necessary for ecotoxicologists

to refine test methods and ascertain mechanisms of toxicity which are most likely to occur in ecological settings.

- **The behavior of engineered nanoparticles in soils and water must be understood:** In order for toxic effects to occur, a material must be bioavailable and taken up by a biological organism. Thus, the environmental compartments that engineered nanomaterials move into, and how they behave within those compartments, must be understood in order to estimate biological–nanoparticle interaction.
- **The mechanisms by which engineered nanoparticles exert effects on ecologically important species must be understood:** Current research on the toxicity of engineered nanoparticles has focused on mammalian systems as a model for potential human health impacts. While biochemical, molecular, and tissue-level outcomes described by these studies are likely relevant for ecologically important species, other–more subtle–effects such as shifts in energetics or effects on organism behavior may also be significant and unexplored by the biomedical community.

In this chapter we will discuss some of these issues and how they relate to the potential ecological impacts of engineered carbon nanoparticles following their release into aquatic ecosystems.

## 18.2

### Fate and Exposure

#### 18.2.1

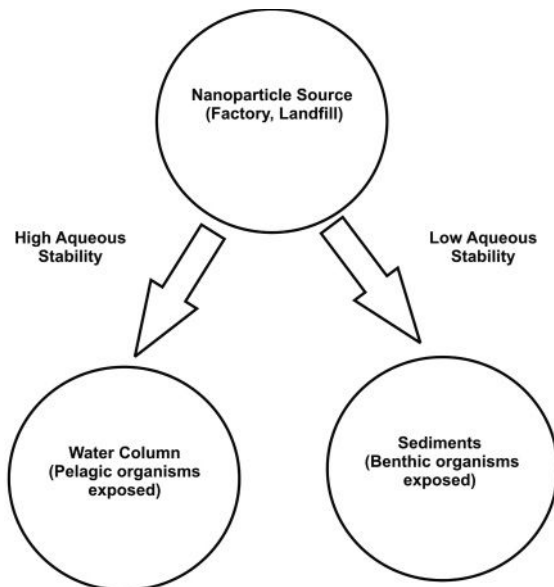
##### General

In order to assess the risk posed by engineered carbon nanomaterials to ecological systems, both the exposure scenarios as well as potential effects must be characterized. The behavior of engineered carbon nanoparticles in aqueous systems, their bioavailability to aquatic biota, and their potential to alter the transport and availability of co-occurring chemical contaminants, will be examined in the following sections.

#### 18.2.2

##### Stability in Aquatic Systems

The fate and behavior of engineered carbon nanoparticles in aquatic ecosystems depend on the specific properties of the individual material. Most carbon-derived nanoparticles are largely insoluble in water, and tend to aggregate into larger macroparticles which cannot maintain their place in the water column [10]. Thus, these materials, similar to many other organic chemical contaminants, are likely to partition into sediments following their discharge into aqueous environments (Figure 18.1). In the sediments, these materials will be available to benthic



**Figure 18.1** The potential fate of engineered carbon nanomaterials in aqueous systems.

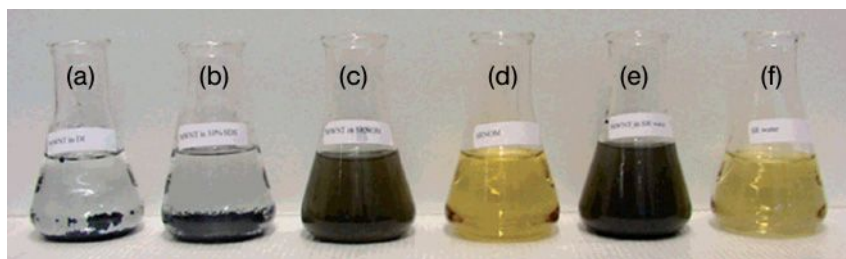
organisms and, possibly, to pelagic organisms through resuspension or food chain transport.

Potentially more relevant to aquatic ecotoxicology are engineered carbon nanoparticles which have been functionalized for technological applications that require increased stability in aqueous environments. Engineered carbon nanoparticles can be stabilized in aqueous environments using surfactants, organic solvents, and biomacromolecular coatings such as lipids and proteins [10–13]. However, little is known about how relevant these solubilization strategies are for natural systems, or how they influence the behavior of engineered carbon nanoparticles in freshwater and marine environments.

Perhaps more relevant for ecological systems is the discovery that some nanomaterials, including multiwalled carbon nanotubes (CNTs), can be stabilized in aqueous environments using natural organic matter (Figure 18.2) [10]. The latter is a complex mixture of organic molecules of varying size and chemical properties that originates from degraded plant and animal material, and is found at varying concentrations in virtually all aquatic ecosystems.

Natural organic matter contains both lipophilic and hydrophilic components which are able to interact with engineered carbon nanoparticles and thus increase their solubility and stability in aqueous environments. It is important to note that all of these methods (coatings, solvents, organic matter) often result in only stable *suspensions* and not true solutions. Thus, the suspended nanoparticles will come out of suspension over time. For example, Roberts *et al.* [12] found that lipid-coated single-walled CNTs, while far more stable in suspension than uncoated tubes, still





**Figure 18.2** Flasks containing: (a) organic-free water; (b) 1% sodium dodecylsulfate solution; (c) 100 mg natural organic matter (NOM) solution with  $500 \text{ mg l}^{-1}$  multi-walled nanotubes (MWNTs); and (e) river water containing NOM and  $500 \text{ mg l}^{-1}$  MWNTs. The 100 mg carbon per liter (C/L) SR-NOM solution and river water without MWNT addition are shown in flasks (d) and (f). Reproduced from Ref. [10].

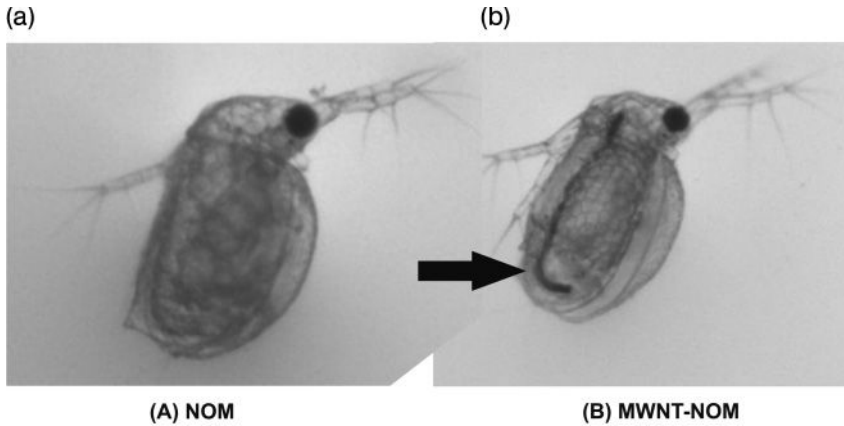
precipitated approximately 20% out of suspension in moderately hard freshwater over a 48 h period. Regardless, increased stability in aqueous environments will increase the period for which aquatic organisms are exposed to engineered carbon nanoparticles.

### 18.2.3

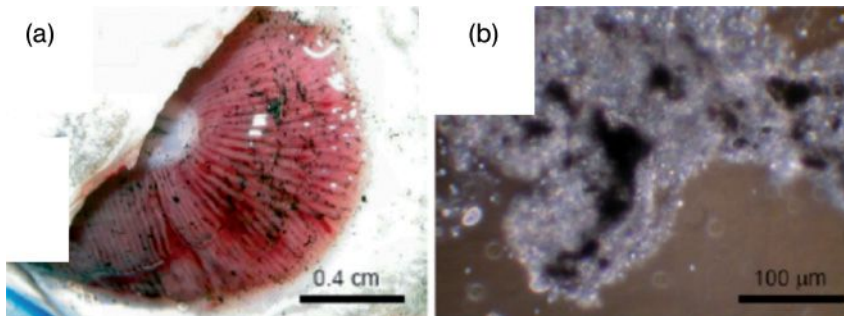
#### Bioavailability and Uptake

The term *bioavailable* refers to those chemical contaminants which can interact with, and be taken up by, an organism into its tissues. Bioavailable contaminants may enter an organism through a number of pathways, but the most common route is by uptake across the skin, the ingestion of contaminated food and water, or via respiratory processes. Not all contaminants in the environment are bioavailable. For example, the bioavailability of heavy metals such as cadmium and copper are reduced in aqueous environments with high water hardness [14, 15]. The bioavailability of metals in sediments can be reduced by the presence of acid-volatile sulfides [16]. Organic contaminants such as polycyclic aromatic hydrocarbons can be sequestered by dissolved organic carbon and natural organic matter, thus preventing their uptake by aquatic biota [17]. This reduction in bioavailability coincides with a reduction in toxic effects due to a decrease in the internal dose of the toxicant.

The potential bioavailability of engineered carbon nanoparticles in aquatic ecosystems is largely unknown, with few studies having been conducted to measure the uptake of engineered carbon nanoparticles by aquatic biota. Potential routes of exposure include uptake across the gills and skin, as well as ingestion [9]. Roberts *et al.* [12] demonstrated that grazing freshwater zooplankton (*Daphnia magna*) were able to ingest lipid-coated single-walled CNTs through their normal feeding behavior. The organisms were able to digest the lipid coating from the tubes and excrete the uncoated, insoluble nanotubes. Similar results were obtained



**Figure 18.3** Micrographs of the zooplankton *Ceriodaphnia dubia*, following exposure to (a) natural organic matter and (b) natural organic matter and multiwalled carbon nanotubes (MWCNTs). The dark line visible inside the organism in panel (b) is the intestinal tract (arrow), containing large amounts of MWCNTs.



**Figure 18.4** (a) Single-walled carbon nanotubes adhered to the mucous secretions around the gills of rainbow trout; (b) Phase-contrast micrograph of a mucus smear, showing nanotubes associated with the mucous proteins. Reproduced from Ref. [19].

with another smaller species (*Ceriodaphnia dubia*) using natural organic matter-stabilized multiwalled CNTs (Figure 18.3).

The dietary uptake of single-walled CNTs has also been reported in estuarine copepods (*Amphiascus tenuiremis*), another zooplankton species [18]. Also reported here was the presence of compact aggregations of nanotubes in the fecal pellets of the copepods. Fewer studies exist on the uptake of nanotubes by fish; in rainbow trout, nanotubes ingested from the water column were shown to adhere to the mucous secretions of the gill tissues (Figure 18.4) [19].

However, it is unknown what fraction (if any) of the nanotubes crossed the epithelium and were taken up into the soft tissues of the organisms in any of these studies, although this is largely due to a lack of effective methods for measuring nanotubes at the low concentrations found in biological tissues. The limit of detection for analytical methods requires samples to be concentrated to such a high degree that there may be great uncertainty in the accuracy of their determination.

Fullerenes and some fullerene-derivatives are known to be lipophilic [20]. Fullerenes are easily extracted from tissues using organic solvents, and their concentration determined using spectrophotometry. In one study, Oberdorster *et al.* [21] documented an increasing uptake of fullerenes by zooplankton from the water column over a 96 h period [21]. It has been suggested that adding functional groups to both fullerenes and nanotubes decreases their toxicity *in vitro* [22–24], though this may be due to alterations in the hydrophobicity and thus uptake of the material by cells [24].

#### 18.2.4

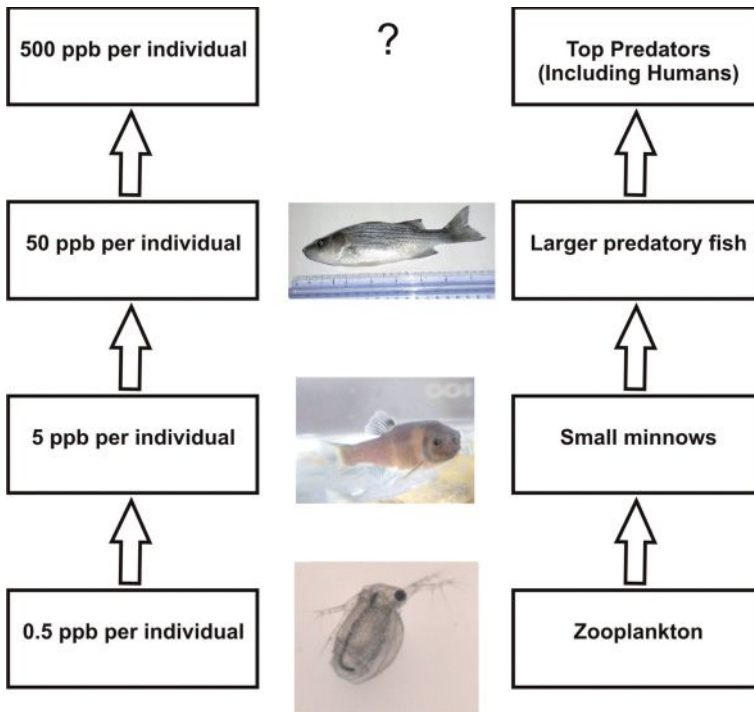
##### **Tissue Distribution**

Once internalized by the organism, chemical contaminants are distributed to the tissues via the circulatory system. Again, there is a paucity of data regarding the tissue distribution of carbon nanoparticles in aquatic organisms. Oberdorster *et al.* [21] found that exposure to uncoated fullerenes resulted in an increased oxidative stress in the brains of largemouth bass, leading to the possibility that the materials were able to cross the blood–brain barrier [11]. These results were supported by another study, in which the distribution of fluorescent, nanosized polystyrene spheres in the tissues of the medaka, an aquarium fish commonly used in aquatic toxicological studies, was investigated [25]. Kashiwada [25] found that fluorescing polystyrene nanoparticles accumulated within the gut and gills of the fish, and were also detected in the brain, testis, liver, and blood. However, the most intense fluorescence was observed in the gill tissues, indicating that uptake across the gill epithelium may be a major route of exposure. A previous study had shown that rats dosed orally with fullerenes excreted most of the material via the feces, whereas rats injected intravenously with fullerenes retained the materials for over one week, with the majority being distributed to the liver [26]. These findings support the hypothesis that, in fish, uptake across the gills may be a more important route of exposure than dietary ingestion.

#### 18.2.5

##### **Food Web**

Several chemical compounds found in the environment – and especially those which are not easily metabolized, such as mercury and polychlorinated biphenyls – have been shown to move through aquatic food chains [27–29]. These materials are taken up by organisms at low trophic levels such as bacteria, algae, and zooplankton and, because they are not easily metabolized and excreted, are passed



**Figure 18.5** Biomagnification through an aquatic food chain. Contaminants may be found at relatively low concentrations at lower trophic levels (zooplankton). Concentrations will increase as predatory organisms consume large numbers of prey items, but do not have the ability to metabolize or excrete the chemical contaminant.

on to higher trophic levels when those organisms are subsequently ingested by predators. This results in increasing concentrations of chemical within organisms at higher levels of the food chain, a process known as *biomagnification* (Figure 18.5).

The biomagnification of these materials can pose significant risks to the health of organisms located at higher trophic levels which might otherwise not be exposed, including humans [30–34]. For example, mercury consumption warnings in seafood are a result of biomagnification of methyl mercury through the food web.

Studies conducted by Templeton *et al.* [12] and Roberts *et al.* [18] have indicated that zooplankton in aquatic systems can ingest nanoparticles from their environment through normal feeding behavior. Bacteria, which form the bulk of aquatic biofilms, have also been shown to take up nanosized particles. Both, biofilms and zooplankton occupy lower trophic levels in aquatic ecosystems and provide an important food base for a variety of organisms, including fish. Considering the lipophilicity of some nanoparticles, and the lack of evidence of true metabolism, the potential for biomagnification clearly exists.

### 18.2.6

#### Effects on the Uptake of Other Contaminants

Due to the relative ease with which some engineered carbon nanoparticles are taken up by cells, there is also concern regarding the potential for these materials to facilitate the transport and uptake of other, adsorbed chemical contaminants into cells. Polycyclic aromatic hydrocarbons (PAHs) are a ubiquitous contaminant, and are discharged into the environment as a result of the incomplete combustion of fossil fuels. They are generally considered to be carcinogenic and to have a range of toxic effects [35–37]. Yang *et al.* [38] showed that PAHs readily adsorb to fullerenes and nanotubes [38], while Moore *et al.* [9] also found that coexposure to a model PAH (anthracene) and a nanosized polyester sucrose particle increased both the uptake and cellular toxicity of anthracene in mussels. Contaminants which are readily adsorbed onto carbon nanoparticles, or are closely associated with them as a result of manufacturing processes (such as transition metals), may be delivered more rapidly to cells in the presence of nanosized particles.

## 18.3

### Effects

#### 18.3.1

##### General

The limited data relating to the toxicological effects of engineered carbon nanoparticles has derived from research groups that have focused largely on mammalian models (both *in vitro* and *in vivo*). Such studies have been carried out primarily to determine whether these compounds cause, or have the potential to cause, human health effects following occupational exposure. Although there are exceptions, the bulk of the data suggests that engineered carbon nanoparticles are toxic to some degree, and points to oxidative stress, inflammatory reactions, and immunological effects as the key features of carbon nanoparticle toxicity [39, 40].

Relatively few studies, however, have been carried out regarding nanotoxicological effects on ecologically important aquatic species, such as fish and zooplankton (Table 18.1). The aim of this section is to summarize and review the ecotoxicological effects of engineered carbon nanoparticles, focusing primarily on aquatic eukaryotic systems (e.g., fish and zooplankton), as has the bulk of reports made to date.

#### 18.3.2

##### Oxidative Stress and Nanoparticles

Aerobic organisms use oxygen to oxidize (burn) carbon- and hydrogen-rich substrates (foods) to obtain the chemical and heat energy that is essential for life. However, when molecules are oxidized with oxygen, the oxygen molecule itself

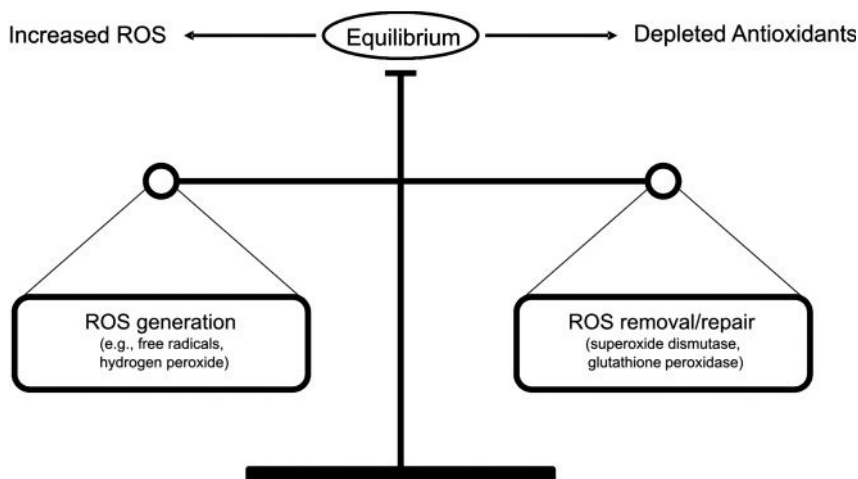
**Table 18.1** Summary of the ecotoxicological literature on nanoparticles.

Reference	Species	Nonmaterial tested	Preparation method	Concentrations tested	Endpoints examined
[11]	<i>Micropterus salmoides</i>	nC <sub>60</sub>	THF	0.5–1.0 ppm	Lipid peroxidation, protein oxidation, glutathione
[21]	<i>Daphnia magna</i> <i>Pimephales promelas</i> <i>Hyaella azteca</i> <i>Oryzias latipes</i>	nC <sub>60</sub>	Water-stirred	0.5–30 ppm	Mortality, CYP P450 isozymes, PMP70
[41]	<i>Daphnia magna</i>	nC <sub>60</sub>	Sonication THF	0.2–880 ppm	Mortality, behavior
[42]	<i>Daphnia magna</i> <i>Pimephales promelas</i>	nC <sub>60</sub>	Water-stirred THF	0.5 ppm	Lipid peroxidation, CYP2K1, CYP2M1
[42]	<i>Stylonychia mytilus</i>	MWCNT	AEDP	0.1–200 µg ml <sup>-1</sup>	Cytotoxicity cell morphology, structural alterations
[43]	<i>Danio rerio</i>	nC <sub>60</sub> nC <sub>70</sub> nC <sub>60</sub> (OH) <sub>24</sub>	DMSO DMSO DMSO	100–500 ppb 100–500 ppb 500–5000 ppb	Development effects, apoptosis

Table 18.1 Continued.

Reference	Species	Nonmaterial tested	Preparation method	Concentrations tested	Endpoints examined
[44]	<i>Bacillus subtilis</i> <i>Escherichia coli</i>	nC <sub>60</sub> nC <sub>60</sub> (OH) <sub>22-24</sub>	THF	0.04–4 mg l <sup>-1</sup> 5 mg l <sup>-1</sup>	Growth
[45]	<i>Danio rerio</i>	nC <sub>60</sub>	Stirring and sonication THF	Dilution of stock solution	Mortality, behavior, global gene expression
[12]	<i>Daphnia magna</i>	SWCNT-lipid coated	LPC	2.5–20 mg l <sup>-1</sup>	Mortality
[42]	<i>Danio rerio</i>	nC <sub>60</sub> nC <sub>60</sub> (OH) <sub>16-18</sub>	Acetone/benzene/ THF water	1.5 mg l <sup>-1</sup> 50 mg l <sup>-1</sup>	Mortality, developmental effects, hatching rate, heartbeat, pericardial edema
[19]	<i>Oncorhynchus mykiss</i>	SWCNT	SDS, sonication	0.1–0.5 mg l <sup>-1</sup>	Behavior, gill ventilation rates, plasma ions, histopathology, Na <sup>+</sup> K <sup>+</sup> -ATPase, oxidative stress
[46]	<i>Daphnia magna</i>	nC <sub>60</sub> nC <sub>20</sub> HxC <sub>20</sub> Hx	THF	260 ppb	Behavior

THF, tetrahydrofuran; AEDP, 2-Amino-ethylene-1,1-bis-phosphonic acid; LPC, lysophosphatidylcholine; SDS, sodium dodecylsulfate.



Arrows indicate a shift in balance

**Figure 18.6** Oxidative stress occurs naturally, but biological systems maintain an equilibrium by counteracting the deleterious effects of reactive oxygen species (ROS) with antioxidants. Increased oxidative stress, a common mode of action for a number of chemical toxicants, can occur through either a depletion of a biological system's antioxidants or an increase in the number of ROS.

becomes reduced and forms intermediates called reactive oxygen species (ROS); these include free radicals and hydrogen peroxide. *Oxidative stress* is the term used to describe the level of oxidative damage in a cell or tissue caused by ROS, the latter being a class of molecules that are derived from the metabolism of oxygen and which exist inherently in all aerobic organisms. In fact, ROS are produced constantly during normal aerobic metabolism, but are normally safely removed by a variety of biological antioxidants, such as superoxide dismutase (SOD), catalase, or glutathione (GSH) peroxidase. The amount of oxidative stress in a cell or tissue can be thought of as a balance between the overall generation and the overall removal/repair of ROS by antioxidants (Figure 18.6). Therefore, oxidative stress within a cell or tissue can result from two factors: (i) an increase in oxidant generation; and/or (ii) a decrease in antioxidant protection.

Research has shown that xenobiotics such as metals and hydrocarbons can shift the oxidative stress balance, thus causing an overproduction of ROS or the inhibition of antioxidant systems [47–49]. This shift in balance leads to excessive molecular damage and tissue injury, an example being lipid peroxidation. The latter process is defined as the free-radical oxidation of polyunsaturated fatty acids in biological systems, and can be used as an end-point to measure oxidative stress. The most common biomarkers used to measure oxidative stress include thiobarbituric acid reactive substances (TBARS), which measures the presence of lipid



peroxides and the reduction of GSH, an antioxidant which occurs naturally within cells and is known to scavenge ROS [49–52].

The majority of mammalian-based reports point to oxidative stress as the main mode of action of engineered carbon nanoparticles (e.g., Ref. [40]), and so the assumption is typically made that this is the main mode of action in all species. With the exception of one report [11], the present authors are unaware of any other *ecotoxicological* literature providing evidence that exposure to engineered carbon nanoparticles results in oxidative stress. These examinations provide insight into the possibility that carbon-engineered nanoparticles may affect aquatic organisms in a different way from mammalian systems. For example, Roberts *et al.* [12] have suggested an energetics mechanism and interference with normal feeding behavior in zooplankton.

One major issue which concerns all toxicological studies is to ensure that any observed effects can be attributed to the compound of interest, and not other confounding factors. This is of particular concern when using organic solvents to either solubilize or stabilize a material in aqueous media. Some carbon nanoparticles, including C<sub>60</sub>, have a very low solubility in water; consequently, organic solvents have been used (notably tetrahydrofuran; THF) to increase the solubility of engineered carbon nanomaterials. In the first report addressing the question of whether exposure to engineered carbon nanoparticles would result in ecotoxicological effects, Oberdorster [11] used THF to create nC<sub>60</sub> solutions for exposure to largemouth bass. These preliminary study results indicated that nC<sub>60</sub> caused significant lipid peroxidation in the brains of the exposed fish, since which time the preparation of nC<sub>60</sub> using THF has become common practice. However, data obtained by Henry *et al.* [45] indicated that, at least in zebrafish, observable toxic effects could be attributed to THF and its breakdown products, as opposed to fullerenes [45]. Although the exact mode of action of THF-prepared nanoparticles is unknown, it has been suggested that THF might cross the blood–brain barrier, unlike carbon nanoparticles [53], thus explaining the findings of Oberdorster [11].

It is also important to note that not all mammalian-based data have pointed to oxidative stress as the toxic mode of action of carbon nanoparticles. In fact, it has been suggested that nC<sub>60</sub> may function in an opposite manner, and act as a free-radical scavenger [53]. An *in vitro* experiment in rats investigated the antioxidant effect of nC<sub>60</sub> by pretreating rats with nC<sub>60</sub>, followed by an injection of carbon tetrachloride (CCl<sub>4</sub>), a chemical which is known to cause oxidative stress in the liver [53]. The study results showed that nC<sub>60</sub> protected the liver against oxidative stress, which led the research team to conclude that the mechanism behind the protective role of nC<sub>60</sub> could be attributed to the ability of nC<sub>60</sub> to scavenge large numbers of free radicals.

### 18.3.3

#### Effects on Specific Tissues

##### 18.3.3.1 Brain

The brain is arguably the most complex organ of all organisms, and may be incredibly sensitive to insult, with any disruption or interference with correct brain

functions possibly leading to a loss of fitness and/or death. Although the effects of engineered carbon nanoparticles on the brain are poorly understood, behavioral changes in multiple aquatic species exposed to engineered carbon nanoparticles have been observed and have provided evidence that these particles might impair normal brain function [19, 46]. For example, when Smith *et al.* [19] exposed rainbow trout (*Oncorhynchus mykiss*) to single-walled CNTs, they observed aggressive behavior in the exposed fish that led to severe fin nipping. Although no biochemical changes were observed in the brains of these fish, a histological analysis identified what appeared to be aneurysms (swelling of the blood vessels), which indicated that the blood supply—and hence the oxygen supply—of the brain may have been compromised. Behavioral effects were also observed in *Daphnia magna* after exposure to nC<sub>60</sub> [41, 46]. In these studies, both juvenile and adult *D. magna*, when exposed to nC<sub>60</sub>, showed an abnormal behavioral response to the exposure that resulted in sporadic swimming and disorientation.

Following initial studies conducted with mammalian cell lines, the investigations into the toxic mode of action focused on oxidative stress [5]. As noted above, Oberdorster [11] had suggested that nC<sub>60</sub> could be selectively transported to the brain, where it would cause toxic effects; this idea was based on the significant increase in lipid peroxidation that had been shown in the brains of largemouth bass exposed to nC<sub>60</sub>. Unfortunately, these results, and their subsequent interpretation, may have been compromised by the use of an organic solvent in the experiment.

#### 18.3.3.2 Gills

In fish, the gills function in similar fashion to the lungs in mammals, and are vital not only as the main site for gas exchange but also as an important component of ionoregulation. Carbon-engineered nanoparticles, based on their size and chemical properties, have the potential to cause harm in both a physical (e.g., abrasions) and chemical (e.g., disruption of gas exchange) manner. A study conducted by Smith *et al.* [19] documented increases in both ventilation rate and mucus secretion, as well as an enlargement of mucocytes on the gills of trout exposed to single-walled CNTs. This led the authors to conclude that the CNTs had clearly caused respiratory distress. Interestingly, the trout had responded to the exposure by increasing a natural defense mechanisms, namely an increased mucus secretion. This reaction is common in fish exposed to aqueous pollutants [54], and is a short-term defense mechanism designed to prevent the toxicant from reaching the sensitive gill epithelium [19].

#### 18.3.3.3 Liver

In higher-level organisms, such as fish (and humans), the liver performs the enormous duty of maintaining the metabolic homeostasis of the body. Its responsibilities include protein synthesis, nutrient homeostasis, and the filtration of particulates. The liver is also the main location for the detoxification of toxicants and is, therefore, susceptible to chemical exposure and toxicity. Results obtained from studies in mammals have shown that intravenously administered fullerenes can be retained in the body for up to one week, with the majority (>70%) lodging in the liver [26].

Whilst the potential effects of these compounds on correct liver function are relatively unknown, Smith *et al.* in 2007, observed apoptosis (programmed cell death) in the liver of trout following their exposure to single-walled CNTs. Although the exact toxic mode of action was unknown, the location of the injured liver cells (close to the blood vessels) raised concern that the nanoparticles were being delivered systemically via the blood supply [19].

#### 18.3.3.4 Gut

In theory, the gut would be expected to serve as the main site of uptake for nanoparticles associated with dietary exposure and drinking water. As noted earlier in the chapter, carbon-engineered nanoparticles are potentially bioavailable and can enter an organism via a number of pathways, including the ingestion of food and water. Although, observations have been made of carbon nanoparticle aggregates in the gut lumen of fish [19] and zooplankton [12], the bioavailability of these aggregates and their potential to cross the epithelial lining is largely unknown, as discussed previously.

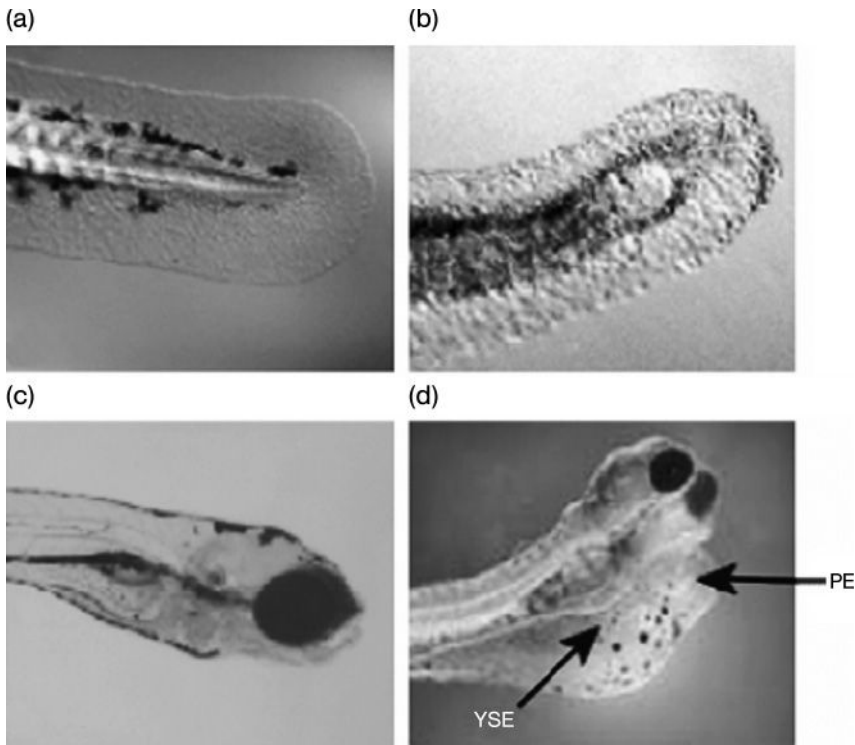
#### 18.3.4

#### Developmental Effects

Organisms are typically the most sensitive to insult (chemical or physical) during their early development and in the early life stages. Chemical compounds may disrupt cellular signaling, alter apoptosis patterns, or damage DNA, thus causing organisms to develop abnormally (*teratogenicity*). Teratogens can result in obvious effects such as physical deformities, or in more subtle changes such as behavioral abnormalities. These changes early in life can have profound effects on the ecological fitness of individuals, and result in deleterious population-level outcomes.

A host of investigations have utilized zebrafish embryos when investigating the developmental effects of engineered carbon nanoparticles [42, 43]. For example, Usenko *et al.* [43] observed delayed development, morphological malformations (e.g., of the body axis, eye, snout, jaw, otic vesicle, notochord, heart, brain, somite, and fins), pericardial edema (Figure 18.7), yolk sac edema (Figure 18.7), and behavioral abnormalities (e.g., hyperactivity, hypoactivity, paralysis) in fish exposed to nC<sub>60</sub>. Of particular interest in this study was the constant abnormal development of the fin regions in all exposed organisms, which was indicative of cell signaling perturbations during early development (Figure 18.7). In another study, Zhu *et al.* [42] found that hatching rates in nC<sub>60</sub>-exposed zebrafish embryos showed notable developmental delay and toxicity, slower heart rates, and increased pericardial edema.

The developmental effects such as those observed by Usenko *et al.* [43] and Zhu *et al.* [42] may have far-reaching implications since, in nature, individuals that experience abnormal development rarely survive to reproduce. Therefore, compounds found to cause developmental effects have the potential to affect entire populations and communities, and thus deserve special attention.



**Figure 18.7** (a,b) Representative images of the caudal fins for (a) control and (b) 200 ppb nC<sub>60</sub>-exposed animals; (c,d) Representative images of (c) 1% dimethylsulfoxide-exposed control larval head and (d) 200 ppb nC<sub>60</sub>-exposed larval head. The arrows indicate the pericardial edema (PE) and yolk sac edema (YSE). Reproduced from Ref. [43].

#### 18.4 Summary

The “nanotechnology revolution” has spurred interest and concern regarding the safety of engineered nanoparticles. In particular, attention has been paid to the potential effects that such materials might have on humans, either through the use of consumer products containing “nanotechnology,” or through occupational exposure during the manufacturing process. Unfortunately, less attention has been paid to the potential impacts that these materials might have on ecological systems, despite the increased manufacture of engineered carbon nanomaterials being likely to result in their deposition into aquatic ecosystems, either from spills or as a result of the waste stream, in a fashion similar to other chemicals and consumer products [7, 9]. As noted in this chapter, there is a paucity of data regarding the behavior and fate of engineered carbon nanoparticles in aquatic

ecosystems, their potential bioavailability to aquatic organisms, and the effects that they might have on those organisms.

The field of ecotoxicology generally operates within the framework of ecological risk assessment in order to determine the risk posed by a particular chemical to the natural environment. This framework relies on accurate exposure assessment—How much of the material is likely to be found in the environment and is the material bioavailable?—as well as accurate effects assessment—At what exposure concentrations does the material result in harm? Although preliminary investigations have indicated that fullerenes and nanotubes can be taken up by aquatic organisms, and result in deleterious effects under certain conditions, the realism of these exposure scenarios, and particularly of the exposure concentrations, is unknown. Are these exposure concentrations environmentally relevant? Are we likely to see these concentrations of fullerenes and nanotubes being discharged into aquatic systems? The effects that site-specific parameters such as pH, hardness, and temperature (which all have major impacts on the bioavailability of other contaminants) have on the bioavailability of engineered carbon nanomaterials are unknown. Until questions regarding these bioavailability and exposure scenarios are answered, it will remain difficult to ascertain the risk and potential effects that engineered carbon nanomaterials might have on aquatic ecosystems.

## References

- 1 Daroczi, B., Kari, G., McAleer, M.F., Wolf, J.C., Rodeck, U. and Dicker, A.P. (2006) In vivo radioprotection by the fullerene nanoparticle DF-1 as assessed in a zebrafish model. *Clin. Cancer Res.*, **12**, 7086–7091.
- 2 Kohli, P. and Martin, C.R. (2005) Template-synthesized nanotubes for biotechnology and biomedical applications. *J. Drug Deliv. Sci. Technol.*, **15**, 49–57.
- 3 Mroz, P., Pawlak, A., Satti, M., Lee, H., Wharton, T., Gali, H., Sarna, T. and Hamblin, M.R. (2007) Functionalized fullerenes mediate photodynamic killing of cancer cells: Type I versus Type II photochemical mechanism. *Free Radic. Biol. Med.*, **43**, 711–719.
- 4 Nohynek, G.J., Lademann, J., Ribaud, C. and Roberts, M.S. (2007) Grey goo on the skin? Nanotechnology, cosmetic and sunscreen safety. *Crit. Rev. Toxicol.*, **37**, 251–277.
- 5 Nel, A., Xia, T., Madler, L. and Li, N. (2006) Toxic potential of materials at the nanolevel. *Science*, **311**, 622–627.
- 6 Council, N.R. (2006) *A Matter of Size: Triennial Review of the National Nanotechnology Initiative*, National Academies Press, p. 130.
- 7 Kolpin, D.W., Furlong, E.T., Meyer, M.T., Thurman, E.M., Zaugg, S.D., Barber, L.B. and Buxton, H.T. (2002) Pharmaceuticals, hormones, and other organic wastewater contaminants in US streams, 1999–2000: a national reconnaissance. *Environ. Sci. Technol.*, **36**, 1202–1211.
- 8 Maynard, A.D., Aitken, R.J., Butz, T., Colvin, V., Donaldson, K., Oberdorster, G., Philbert, M.A., Ryan, J., Seaton, A., Stone, V., Tinkle, S.S., Tran, L., Walker, N.J. and Warheit, D.B. (2006) Safe handling of nanotechnology. *Nature*, **444**, 267–269.
- 9 Moore, M.N., Lowe, D.M., Soverchia, C., Haigh, S.D. and Hales, S.G. (1997) Uptake of a non-calorific, edible sucrose polyester oil and olive oil by marine mussels and their influence on uptake and effects of anthracene. *Aquat. Toxicol.*, **39**, 307–320.
- 10 Hyung, H., Fortner, J.D., Hughes, J.B. and Kim, J.H. (2007) Natural organic matter stabilizes carbon nanotubes in

- the aqueous phase. *Environ. Sci. Technol.*, **41**, 179–184.
- 11 Oberdorster, E. (2004) Manufactured nanomaterials (Fullerenes, C-60) induce oxidative stress in the brain of juvenile largemouth bass. *Environ. Health Perspect.*, **112**, 1058–1062.
  - 12 Roberts, A.P., Seda, B., Mount, A.S., Lin, S.J., Ke, P.C., Qiao, R. and Klaine, S.J. (2007) In vivo biomodification of a lipid coated carbon nanotube by *Daphnia magna*. *Environ. Sci. Technol.*, **41**, 3025–3029.
  - 13 Wu, Y., Hudson, J.S., Lu, Q., Moore, J.M., Mount, A.S., Rao, A.M., Alexov, E. and Ke, P.C. (2006) Coating single-walled carbon nanotubes with phospholipids. *J. Phys. Chem. B*, **110**, 2475–2478.
  - 14 Brinkman, S.F. and Hansen, D.L. (2007) Toxicity of cadmium to early life stages of brown trout (*Salmo trutta*) at multiple water hardnesses. *Environ. Toxicol. Chem.*, **26**, 1666–1671.
  - 15 Van Genderen, E., Gensemer, R., Smith, C., Santore, R. and Ryan, A. (2007) Evaluation of the Biotic Ligand Model relative to other site-specific criteria derivation methods for copper in surface waters with elevated hardness. *Aquat. Toxicol.*, **84**, 279–291.
  - 16 Ogendi, G.M., Brumbaugh, W.G., Hannigan, R.E. and Farris, J.L. (2007) Effects of acid-volatile sulfide on metal bioavailability and toxicity to midge (*Chironomus tentans*) larvae in black shale sediments. *Environ. Toxicol. Chem.*, **26**, 325–334.
  - 17 Weinstein, J.E. and Oris, J.T. (1999) Humic acids reduce the bioaccumulation and photoinduced toxicity of fluoranthene fish. *Environ. Toxicol. Chem.*, **18**, 2087–2094.
  - 18 Templeton, R.C., Ferguson, P.L., Washburn, K.M., Scrivens, W.A. and Chandler, G.T. (2006) Life-cycle effects of single-walled carbon nanotubes (SWNTs) on an estuarine meiobenthic copepod. *Environ. Sci. Technol.*, **40**, 7387–7393.
  - 19 Smith, C.J., Shaw, B.J. and Handy, R.D. (2007) Toxicity of single walled carbon nanotubes to rainbow trout (*Oncorhynchus mykiss*): respiratory toxicity, organ pathologies, and other physiological effects. *Aquat. Toxicol.*, **82**, 94–109.
  - 20 Braun, M. and Hirsch, A. (2000) Fullerene derivatives in bilayer membranes: an overview. *Carbon*, **38**, 1565–1572.
  - 21 Oberdorster, E., Zhu, S.Q., Blickey, T.M., McClellan-Green, P. and Haasch, M.L. (2006) Ecotoxicology of carbon-based engineered nanoparticles: effects of fullerene (C-60) on aquatic organisms. *Carbon*, **44**, 1112–1120.
  - 22 Cagle, D.W., Kennel, S.J., Mirzadeh, S., Alford, J.M. and Wilson, L.J. (1999) In vivo studies of fullerene-based materials using endohedral metallofullerene radiotracers. *Proc. Natl Acad. Sci. USA*, **96**, 5182–5187.
  - 23 Chen, X., Tam, U.C., Czaplinski, J.L., Lee, G.S., Rabuka, D., Zettl, A. and Bertozzi, C.R. (2006) Interfacing carbon nanotubes with living cells. *J. Am. Chem. Soc.*, **128**, 6292–6293.
  - 24 Qiao, R., Roberts, A.P., Mount, A.S., Klaine, S.J. and Ke, P.C. (2007) Translocation of C60 and its derivatives across a lipid bilayer. *Nano Lett.*, **7**, 614–619.
  - 25 Kashiwada, S. (2006) Distribution of nanoparticles in the see-through medaka (*Oryzias latipes*). *Environ. Health Perspect.*, **114**, 1697–1702.
  - 26 Yamago, S., Tokuyama, H., Nakamura, E., Kikuchi, K., Kananishi, S., Sueki, K., Nakahara, H., Enomoto, S. and Ambe, F. (1995) In-vivo biological behavior of a water-miscible fullerene-C-14 labeling, absorption, distribution, excretion and acute toxicity. *Chem. Biol.*, **2**, 385–389.
  - 27 Cleckner, L.B., Garrison, P.J., Hurley, J.P., Olson, M.L. and Krabbenhoft, D.P. (1998) Trophic transfer of methyl mercury in the northern Florida Everglades. *Biogeochemistry*, **40**, 347–361.
  - 28 Drevnick, P.E., Horgan, M.J., Oris, J.T. and Kynard, B.E. (2006) Ontogenetic dynamics of mercury accumulation in Northwest Atlantic sea lamprey (*Petromyzon marinus*). *Can. J. Fish. Aquat. Sci.*, **63**, 1058–1066.
  - 29 Johnson-Restrepo, B., Kannan, K., Addink, R. and Adams, D.H. (2005) Polybrominated diphenyl ethers and polychlorinated biphenyls in a marine foodweb of coastal Florida. *Environ. Sci. Technol.*, **39**, 8243–8250.

- 30 Donato, F., Magoni, M., Bergonzi, R., Scarcella, C., Indelicato, A., Carasi, S. and Apostoli, P. (2006) Exposure to polychlorinated biphenyls in residents near a chemical factory in Italy: The food chain as main source of contamination. *Chemosphere*, **64**, 1562–1572.
- 31 Drevnick, P.E. and Sandheinrich, M.B. (2003) Effects of dietary methylmercury on reproductive endocrinology of fathead minnows. *Environ. Sci. Technol.*, **37**, 4390–4396.
- 32 Drevnick, P.E., Sandheinrich, M.B. and Oris, J.T. (2006) Increased ovarian follicular apoptosis in fathead minnows (*Pimephales promelas*) exposed to dietary methylmercury. *Aquat. Toxicol.*, **79**, 49–54.
- 33 Langer, P., Kocan, A., Tajtakova, M., Petrik, J., Chovanova, J., Drobna, B., Jursa, S., Radikova, Z., Koska, J., Ksinantova, L., Huckova, M., Imrich, R., Wimmerova, S., Gasperikova, D., Shishiba, Y., Trnovec, T., Sebokova, E. and Klimes, I. (2007) Fish from industrially polluted freshwater as the main source of organochlorinated pollutants and increased frequency of thyroid disorders and dysglycemia. *Chemosphere*, **67**, S379–S385.
- 34 Tillitt, D.E., Ankley, G.T., Giesy, J.P., Ludwig, J.P., Kurita-Matsuba, H., Weseloh, D.V., Ross, P.S., Bishop, C.A., Sileo, L. *et al.* (1992) Polychlorinated biphenyl residues and egg mortality in double-crested cormorants from the Great Lakes. *Environ. Toxicol. Chem.*, **11**, 1281–1288.
- 35 Hoffmann, J.L. and Oris, J.T. (2006) Altered gene expression: a mechanism for reproductive toxicity in zebrafish exposed to benzo[a]pyrene. *Aquat. Toxicol.*, **78**, 332–3340.
- 36 Neff, J.M., (1979) *Polycyclic Aromatic Hydrocarbons in the Aquatic Environment*, Applied Science, London.
- 37 Oris, J.T. and Giesy, J.P. (1987) The photo-induced toxicity of polycyclic aromatic hydrocarbons to larvae of the fathead minnow *Pimephales promelas*. *Chemosphere*, **16**, 1395–1404.
- 38 Yang, K., Zhu, L.Z. and Xing, B.S. (2006) Adsorption of polycyclic aromatic hydrocarbons by carbon nanomaterials. *Environ. Sci. Technol.*, **40**, 1855–1861.
- 39 Lam, C.W., James, J.T., McCluskey, R. and Hunter, R.L. (2004) Pulmonary toxicity of single-wall carbon nanotubes in mice 7 and 90 days after intratracheal instillation. *Toxicol. Sci.*, **77**, 126–134.
- 40 Shvedova, A.A., Castranova, V., Kisin, E.R., Schwegler-Berry, D., Murray, A.R., Gandelsman, V.Z., Maynard, A. and Baron, P. (2003) Exposure to carbon nanotube material: assessment of nanotube cytotoxicity using human keratinocyte cells. *J. Toxicol. Environ. Health A*, **66**, 1909–1926.
- 41 Lovern, S.B. and Klaper, R. (2006) *Daphnia magna* mortality when exposed to titanium dioxide and fullerene (C-60) nanoparticles. *Environ. Toxicol. Chem.*, **25**, 1132–1137.
- 42 Zhu, X.S., Zhu, L., Li, Y., Duan, Z.H., Chen, W. and Alvarez, P.J.J. (2007) Developmental toxicity in zebrafish (*Danio rerio*) embryos after exposure to manufactured nanomaterials: Buckminsterfullerene aggregates (nC(60)) and fullerol. *Environ. Toxicol. Chem.*, **26**, 976–979.
- 43 Usenko, C.Y., Harper, S.L. and Tanguay, R.L. (2007) In vivo evaluation of carbon fullerene toxicity using embryonic zebrafish. *Carbon*, **45**, 1891–1898.
- 44 Fortner, J.D., Lyon, D.Y., Sayes, C.M., Boyd, A.M., Falkner, J.C., Hotze, E.M., Alemany, L.B., Tao, Y.J., Guo, W., Ausman, K.D., Colvin, V.L. and Hughes, J.B. (2005) C60 in water: nanocrystal formation and microbial response. *Environ. Sci. Technol.*, **39**, 4307–4316.
- 45 Henry, T.B., Menn, F.M., Fleming, J.T., Wilgus, J., Compton, R.N. and Saylor, G.S. (2007) Attributing effects of aqueous C-60 nano-aggregates to tetrahydrofuran decomposition products in larval zebrafish by assessment of gene expression. *Environ. Health Perspect.*, **115**, 1059–1065.
- 46 Lovern, S.B., Strickler, J.R. and Klaper, R. (2007) Behavioral and physiological changes in *Daphnia magna* when exposed to nanoparticle suspensions (titanium dioxide, nano-C-60, and C(60)HxC(70) Hx). *Environ. Sci. Technol.*, **41**, 4465–70.
- 47 Choi, J. and Oris, J.T. (2000) Anthracene photoinduced toxicity to PLHC-1 cell line (*Poeciliopsis lucida*) and the role of lipid

- peroxidation in toxicity. *Environ. Toxicol. Chem.*, **19**, 2699–2706.
- 48 Choi, J. and Oris, J.T. (2000) Evidence of oxidative stress in bluegill sunfish (*Lepomis macrochirus*) liver microsomes simultaneously exposed to solar ultraviolet radiation and anthracene. *Environ. Toxicol. Chem.*, **19**, 1795–1799.
- 49 Roberts, A.P. and Oris, J.T. (2004) Multiple biomarker response in rainbow trout during exposure to hexavalent chromium. *Comparative Biochemistry and Physiology C: Toxicology and Pharmacology*, **138**, 221–228.
- 50 Lehmann, D.W., Levine, J.F. and Law, J.M. (2007) Polychlorinated biphenyl exposure causes gonadal atrophy and oxidative stress in *Corbicula fluminea* clams. *Toxicol. Pathol.*, **35**, 356–365.
- 51 Possamai, F.P., Fortunato, J.J., Feier, G., Agostinho, F.R., Quevedo, J., Wilhelm, D. and Dal-Pizzol, F. (2007) Oxidative stress after acute and sub-chronic malathion intoxication in Wistar rats. *Environ. Toxicol. Pharmacol.*, **23**, 198–204.
- 52 Verlecar, X.N., Jena, K.B. and Chainy, G.B.N. (2007) Biochemical markers of oxidative stress in *Perna viridis* exposed to mercury and temperature. *Chem. Biol. Interact.*, **167**, 219–226.
- 53 Gharbi, N., Pressac, M., Hadchouel, M., Szwarc, H., Wilson, S.R. and Moussa, F. (2005) [60]Fullerene is a powerful antioxidant in vivo with no acute or subacute toxicity. *Nano Lett.*, **5**, 2578–2585.
- 54 Handy, R.D., Sims, D.W., Giles, A., Campbell, H.A. and Musonda, M.M. (1999) Metabolic trade-off between locomotion and detoxification for maintenance of blood chemistry and growth parameters by rainbow trout (*Oncorhynchus mykiss*) during chronic dietary exposure to copper. *Aquat. Toxicol.*, **47**, 23–41.





## 19

# Carbon Nanotubes as Adsorbents for the Removal of Surface Water Contaminants

*Jose E. Herrera and Jing Cheng*

### 19.1

#### Introduction

The level and complexity of water contamination worldwide has reached unprecedented levels in such a way that the complexity of this problem seems intractable. While there is a wide variety of different contaminant species, the US environmental protection agency divides most of the common contaminants found in surface water into six categories [1]:

- Inorganic compounds: these include toxic heavy metal ions (e.g., cadmium, chromium, lead, copper, mercury), oxoanions (arsenates, chromates) and nonmetal anions such as fluoride.
- Organic compounds: benzene, 1,2-dichloroethene (1,2-DCE), dioxins, polycyclic aromatic hydrocarbons (PAHs), tetrachloroethene (PCE), trichloroethene (TCE), polychlorinated biphenyls (PCBs), etc.
- Disinfection byproducts: trihalomethanes and haloacetic acids.
- Disinfectants: chlorine (as  $Cl_2$ ), chloramines (as  $Cl_2$ ) and chlorine dioxide.
- Radionuclide: atoms with unstable potentially radioactive nuclei, such as phosphorus-32, promethium-147 or americium-243.
- Microorganisms: these include bacteria, fungi and archaea, but not viruses nor prions.

Different methods employed for the removal of pollutants from water include chemical precipitation, membrane filtration, ion exchange, and adsorption. Many types of adsorbent, such as silica, alumina, activated carbon, rare earth oxides, amorphous iron hydroxide, polymers, ion-exchange fibers, and lanthanum-based compounds, have been developed as adsorbents for the removal of pollutants from water [2–7]. Recently, carbon nanotubes (CNTs) have been considered as materials for the removal of trace pollutants from water. A number of contributions in this field have been devoted to the experimental and theoretical study of contaminant

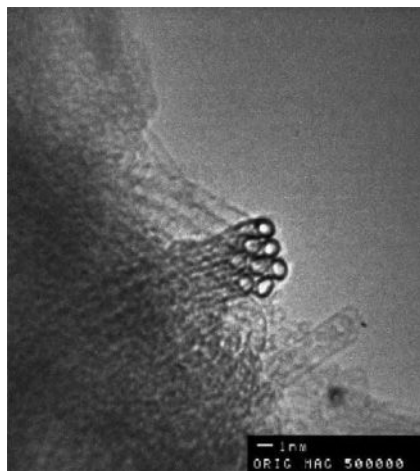
adsorption by CNTs. One of the earliest studies, conducted by Long *et al.* [8], reported that CNTs had a significantly higher dioxin removal efficiency than activated carbon. One year later Li *et al.* [9] suggested that CNTs had a high adsorption capacity for the removal of lead from water. The same group [10] also showed CNTs to be excellent fluoride adsorbents, with a removal capability superior to that of activated carbon. Peng *et al.* [11] indicated that CNTs were efficient adsorbents for the removal of 1, 2-dichlorobenzene (1, 2-DCB) from water, and could be used over a wide pH range. Lu and coworkers [12] noted that CNTs also displayed significant high trihalomethane removal efficiencies.

Together, the results of these studies have indicated that CNTs possess an enormous potential for applications in environmental remediation. Consequently, we present in this chapter a comprehensive overview of recent progress in laboratory studies of CNTs for contaminant removal from water. Particular aspects concentrate on the preparation, characterization and adsorption results of the nanotube materials, while specific examples of experimental studies with CNTs for the adsorption of common environmental contaminants in water are also discussed.

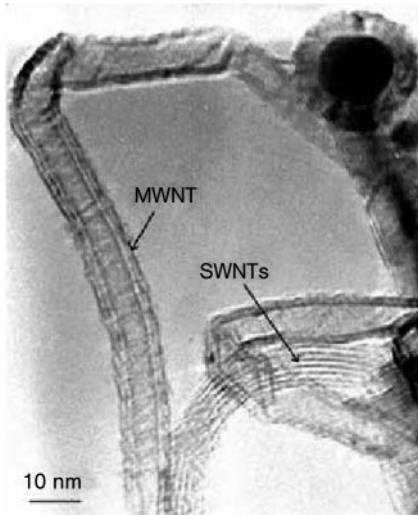
## 19.2

### Structure and Synthesis of Carbon Nanotubes

Carbon nanotubes can be formally depicted as a graphene honeycomb rolled either into a seamless single-walled cylinder or into several concentric cylinders. The former structure is termed single-walled nanotube (SWNT) (Figure 19.1), and the latter multi-walled nanotube (MWNT) (Figure 19.2). The diameter of a typical



**Figure 19.1** Transmission electronic microscopy image of a single-walled carbon nanotube rope. Reproduced from F.L. Darkrim, P. Malbrunot, G.P. Tartaglia, *Int. J. Hydrogen Energy* (2002), 27, 193–202.



**Figure 19.2** Multiwalled carbon nanotube (MWNT) as seen by transmission electron microscopy. The different walls constituting the material appear in a longitudinal view. A micrograph of a SWNT is included for comparison. Reproduced from B. Bai, A.-L. Hamon, A. Marrauda, B. Jouffrey, V. Zymlab, *Chem. Phys. Lett.* (2002), **365**, 184.

MWNT ranges from a few to a few tens of nanometers, while their length is of the order of one micron. In the case of SWNTs, the diameter is in the order of one nanometer, but the length can reach several micrometers, or more.

Each SWNT structure is fully described by two integers ( $n, m$ ) which specify the number of unit vectors  $\vec{a}_1$  and  $\vec{a}_2$  in the graphene structure that constitute the chiral vector  $\vec{v} = n\vec{a}_1 + m\vec{a}_2$ . The graphene structure is rolled-up in such a way that the chiral vector  $\vec{v}$  forms the nanotube circumference. These indices determine the nanotube diameter, and also the orientation of the carbon hexagons with respect to the nanotube axis; this orientation is termed the “chirality” of the nanotube.

Single-walled CNTs have unique chemical, electronic and mechanical properties, combined with a very light weight. Depending on their chirality and diameter, the nanotubes may be either electrically metallic or semiconductor. At the same time, they have shown evidence for high stiffness (Young’s modulus), a very high resilience, and an ability to reversibly buckle and collapse. These properties have led to SWNTs becoming promising candidates in the fabrication of strong fibers with a light weight and high electrical conductivity. Nanotubes can also be functionalized with different chemical moieties, and this greatly broadened the scope of their applications in fields ranging from conductive coatings to molecule-specific nanosensing.

The synthesis of CNT materials can be divided into high-temperature routes (laser ablation, arc discharge) [13–18] and medium-temperature processes, based on either catalytic decomposition or a carbon-containing molecule (a saturated or

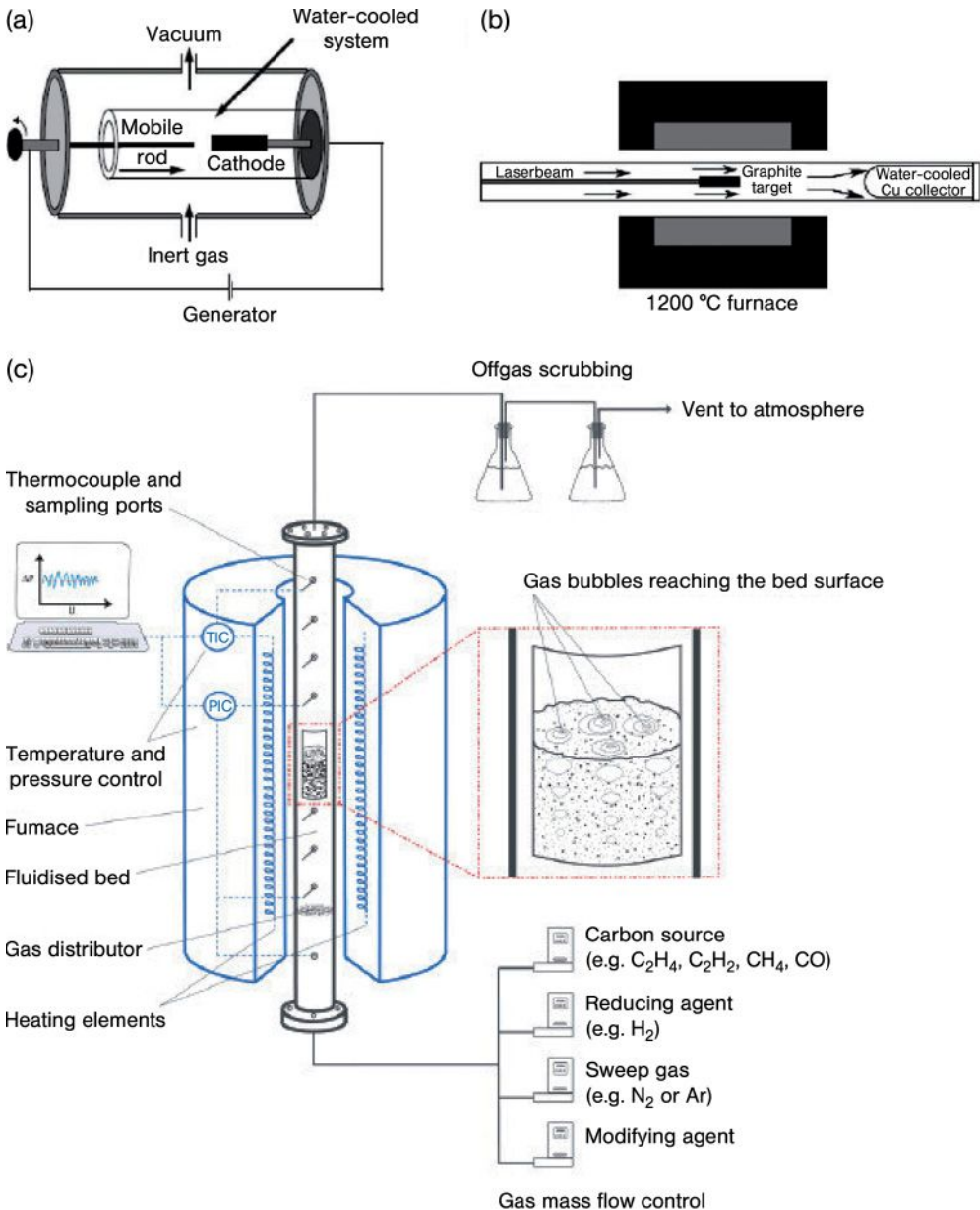
unsaturated hydrocarbon or carbon monoxide) [19, 20]. For the high-temperature routes, pure graphite or a mixture of graphite and a metallic catalyst are vaporized at very high temperatures (2000–4000 °C), and the nanotubes are formed during the cooling process at lower temperatures [21]. The catalytic decomposition of a carbon-containing molecule requires a relatively low temperature, and has the potential for high-yield productions.

Iijima [13] was the first to report the presence of multi-walled CNTs in the soot of an arc-discharge chamber. The tubes were produced using an electric arc-discharge evaporation method similar to that used for the synthesis of fullerene. In this method, an electric arc discharge is generated between two graphite electrodes under an inert atmosphere of helium or argon. (Figure 19.3a) [22]. The first successful production of MWNTs at the gram level was developed in 1992 by Ebbesen and Ajayan [23]. To synthesize SWNTs, a metal catalyst is required [24], and the first report of the synthesis of substantial amounts of these materials, by Bethune and coworkers, appeared in 1993 [25].

In 1996, Smalley and coworkers produced high yields (>70%) of SWNTs by utilizing the laser-ablation (vaporization) of graphite rods doped with small amounts of Ni and Co catalysts (Figure 19.3b) [26]. In this process, a piece of graphite is vaporized by laser irradiation under an inert atmosphere. The resultant soot containing the nanotubes is deposited on the walls of a quartz tube when the reaction mixture has cooled. Although this process is known to produce CNTs of the highest quality and highest purity, a purification step is generally required to eliminate any carbonaceous impurities from the as-produced material. This purification is normally achieved by carbon gasification.

Since 1960, carbon filaments and fibers have also been produced by the thermal decomposition of carbon-containing molecules (this process is also known as chemical vapor decomposition; CVD) in the presence of a catalyst [27, 28]. A similar approach was used by Yacaman [29] in 1993, and later by Nagy and collaborators [30, 31], to grow MWNTs. Following these initial reports, the CVD technique has been subsequently improved and optimized. In general, these processes involve the catalyst-assisted decomposition of hydrocarbons (usually ethylene or acetylene) in a tube reactor at temperatures between 550–1000 °C. The growth of CNTs occurs on the catalyst surface as the gas molecule decomposes (Figure 19.3c). This process has several advantages over the arc discharge and laser ablation techniques. In fact, its amenable nature has led to its use in the large-scale synthesis of aligned CNTs [32, 33].

Since all of these synthesis methods generate, in addition to the nanotubes, relatively large amounts of impurities, a number of techniques have been proposed to improve the quality of the materials through post-synthesis purification. These methods range from concentrated acid treatments, dispersion by sonication in a surfactant and filtration, to high-temperature heating under neutral or lightly oxidizing conditions [34, 35]. A detailed account of the different methods for CNT synthesis and purification is beyond the scope of this chapter, and these topics will be addressed only in the context of the synthesis or chemical treatment affecting the adsorption properties of the materials.



**Figure 19.3** Schematic representations of various processes used to produce CNTs. (a) Electric-arc method apparatus. Reproduced from Ref. [22]; (b) Schematic representation of an oven laser-vaporization apparatus. Reproduced from Ref. [26]; (c) A chemical vapor deposition set-up in which the catalytic bed is fluidized. Reproduced from C.H. See, A.T. Harris, *Ind. Eng. Chem. Res.* (2007), **46**, 997–1012.

### 19.3

#### Properties of Carbon Nanotubes

As described above, CNTs have unique structures, with remarkable properties that can be grouped as electronic, mechanical, thermal, and optical. Most of the physico-mechanical properties of CNTs are dependent on the  $sp^2$  bond network present on their structure [36] and their diameter, length, and chirality. As these properties have been discussed extensively elsewhere [37–39], some of the most important results in this area will be presented briefly, with emphasis placed on those properties that affect the adsorption capacity of these materials.

##### 19.3.1

#### Mechanical, Thermal, Electrical, and Optical Properties of Carbon Nanotubes

The mechanical properties of a solid must ultimately depend on the strength of its interatomic bonds. Both, experimental and theoretical, results have predicted that CNTs have the highest Young's modulus of all different types of nanostructures, with similar tubular forms such as BN,  $BC_3$ ,  $BC_2N$ ,  $C_3N_4$ , CN, and so on. Furthermore, due to the high in-plane tensile strength of graphite, both single and multiwalled CNTs, are expected to have large bending constants. The results of experimental and theoretical studies have indeed indicated that CNTs can be very flexible, able to elongate, twist, flatten, or bend into circles, before fracturing [37].

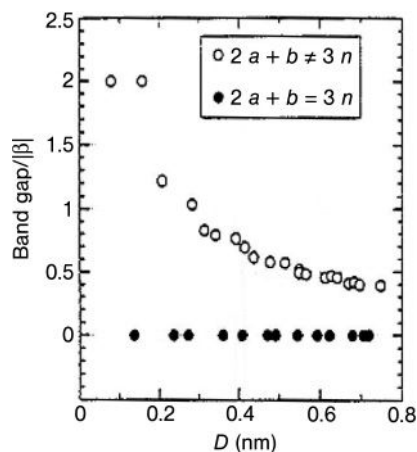
The thermal and electrical properties of CNTs include conductivity. The specific heat and thermal conductivity are determined primarily by the nanotube's electronic and phononic structures [38], with theoretical and experimental results demonstrating superior electrical properties for these materials. Carbon nanotubes have electric current-carrying capacities which are 1000-fold higher than that of copper wires [40]. In fact, theoretical calculations based on the tight-binding model approximation within the zone folding scheme show that one-third of the possible SWNT structures are metallic, while two thirds are semi-conducting (Figure 19.4) [37, 41].

##### 19.3.2

#### Adsorption-Related Properties of Carbon Nanotubes

Early studies investigating the adsorption of nitrogen onto both MWNTs [42, 43] and SWNTs [44] have highlighted the porous nature of these materials. Indeed, due to their uniformity in size and surface properties, CNTs are considered as ideal model sorbent systems to study the effect of nanopore size and surface morphology on sorption and transport properties.

The surface area of a CNT has a very broad range, depending on the nanotube number of walls, the diameter, length, wall defects and, in the case of SWNTs, the number of nanotubes in a nanotube bundle [45]. An isolated SWNT with an open end (this may be achieved through oxidation treatment) has a theoretical surface area equal to that of a single, flat graphene sheet of  $2700\text{m}^2\text{g}^{-1}$  [46]; however, reported experimental values indicate lower adsorption capacities [47]. In the case



**Figure 19.4** Band-gap values versus nanotube diameters defining SWNTs as metallic (●) or semi-conducting (○). Reproduced from Ref. [41].

**Table 19.1** Adsorption properties and type of adsorption sites in SWNTs and MWNTs. Reproduced from Ref. [49].

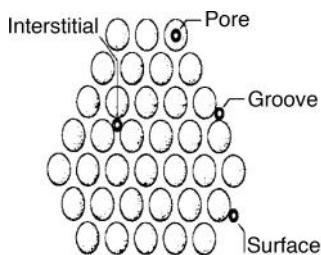
Type of nanotube	Porosity ( $\text{cm}^3 \text{g}^{-1}$ )	Surface area ( $\text{m}^2 \text{g}^{-1}$ )	Adsorption site	Surface area per site ( $\text{m}^2 \text{g}^{-1}$ )
SWNT bundle	Microporous $V_{\text{micro}}: 0.15\text{--}0.3$	400–900	Surface groove	483
			Pore	783
			Interstitial	45
MWNT	Mesoporous	200–400	Surface pore; aggregated pores	–

$V_{\text{micro}}$  = micropore volume.

of SWNTs, the diameters of the tubes and number of tubes in the bundle have the strongest effects on the nanotube surface area. In the case of MWNTs, chemical treatments are reported to be useful for promoting microporosity. Surface areas as high as  $1050 \text{ m}^2 \text{ g}^{-1}$  have been reported for MWNT subjected to alkaline treatment [48]. A two-step activation treatment (acid +  $\text{CO}_2$  activation) has been also reported to increase the specific surface area of MWNT materials. It has been proposed that these treatments open the ends of the nanotube structure, enabling adsorption onto the nanotube inner openings [49]. Some representative results of the surface area and pore volume of SWNTs and MWNTs are listed in Table 19.1.

An important issue to address when considering adsorption onto nanotubes is to identify the adsorption sites. For instance, the adsorption of gases into a SWNT bundle can occur inside the nanotubes (pore), in the interstitial triangular channels between the tubes, on the outer surface of the bundle, or in the grooves formed at the contacts between adjacent tubes outside of the bundle (Figure 19.5).





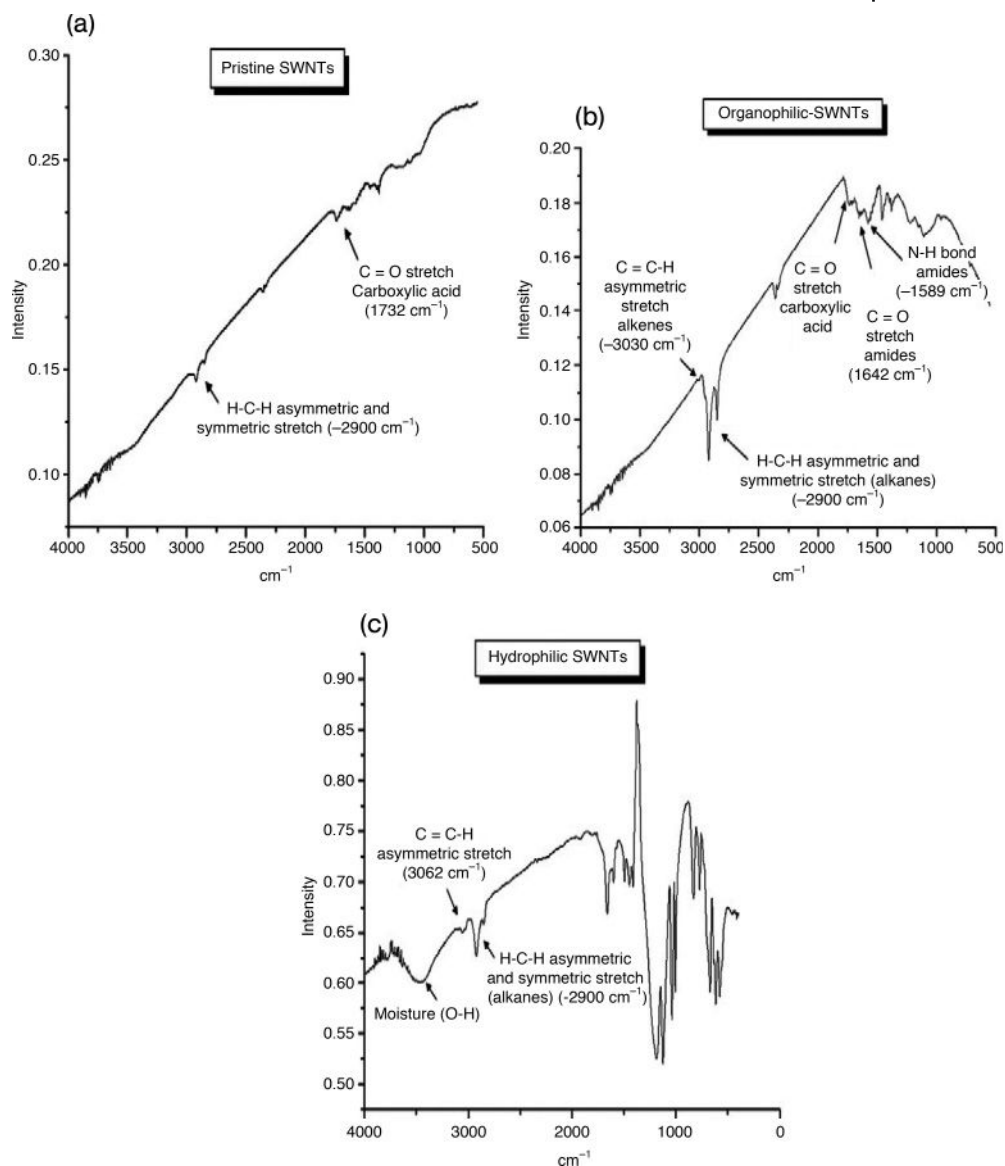
**Figure 19.5** Sketch of the cross-sectional view of a SWNT bundle, illustrating the four different adsorption sites. Reproduced from B. Bhushan, *Springer Handbook of Nanotechnology*, 2nd revision, Springer, Berlin, New York (2007).

In addition, the surface functionalization of CNTs by chemical methods has been found to be a powerful tool for improving the adsorption capacity. Selective adsorption can be achieved through a controlled modification of the nanotube's physical and chemical properties, such as surface area, hydrophilicity, and permeability. For instance, Vermisoglou and Georgakilas [50] have studied the sorption properties of pristine and chemically modified [functionalized with oleylamine and poly(sodium 4-styrene sulfonate)] nanotubes using adsorbates with different polarities. Based on their measurements, these authors concluded that the sorption behavior of the CNTs was greatly modified by chemical treatment. In fact, a chemical modification that increased the hydrophilicity of the nanotube walls enhanced the adsorption selectivity for water over *n*-hexane. Chemical modification of the nanotube wall was verified using infrared (IR) spectroscopy (Figure 19.6). When comparing the IR spectra of pristine SWNTs with those of chemically treated CNTs, new peaks corresponding to aliphatic chains were observed in the case of hydrophobic nanotubes, whereas peaks corresponding to more polar bonds were observed in the case of hydrophilic materials.

Yu *et al.* [51] have investigated the adsorptive performance on modified MWNTs by using mechanical ball milling. For these materials, the adsorptive performance for aniline in aqueous solution indicated that the adsorptive capacity of milled, short open-ended MWNTs increased from  $15 \text{ mg g}^{-1}$  to  $36 \text{ mg g}^{-1}$  compared to the unmilled MWNTs. The measurements of pore size distribution proved that the inner pore diameter of 3 nm remained constant after milling, but the aggregated pore diameter had decreased.

#### 19.4 Carbon Nanotubes as Adsorbents

Carbon nanotubes have superior capabilities for the adsorption of a wide range of toxic substances. The earliest reports of CNT use related to the removal of organic pollutants, notably dioxins, from water [8], though later they were reported also as



**Figure 19.6** Infrared spectra of (a) pristine and (b,c) modified CNTs, illustrating the characteristic peaks for hydrophilic (b) and organophilic (c) samples. Reproduced from Ref. [51].

having an exceptional ability to adsorb inorganic contaminants, such as fluoride [52]. In both cases, the CNTs displayed a superior performance compared to “traditional” adsorbents such as activated carbon. These pioneering studies opened a new field of CNT applications, with many subsequent reports noting CNTs to be excellent adsorbents for the removal of other contaminants. For example, CNTs

were shown to adsorb up to 30 mg of a trihalomethane molecule per gram from a 20 mg l<sup>-1</sup> solution [11]. Other reports indicated that SWNTs could act as “molecular sponges” for small organic molecules such as CCl<sub>4</sub> [53]. A similar case was demonstrated for inorganic contaminants, with CNTs again showing superior performance; measurements of the adsorption capacity of a MWNT material showed that it could adsorb 13.5-fold more fluoride than a typical high-surface-area alumina adsorbent (see below). These early results led to the suggestion that CNTs might indeed serve as effective adsorbents for removing polluting agents from water. Consequently during the past few years some extensive laboratory studies have established the role of CNTs as effective adsorbents for common contaminants from water, including a wide variety of organic compounds and inorganic ions. Although a large number of studies have been conducted into the use of CNTs as adsorbents of gas contaminants [54–56], this chapter will focus on the removal of contaminants from surface water (the process being complementary to the role of adsorbates in the gas phase). Consequently, below is presented a discussion of recent results demonstrating the huge potential of CNTs for the removal of contaminants from surface water.

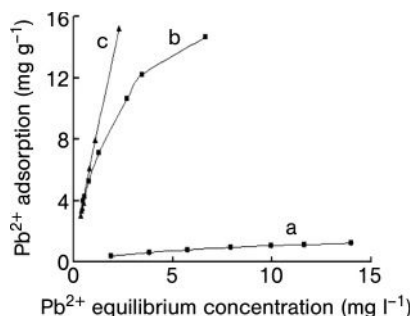
#### 19.4.1

##### **Adsorption of Heavy Metal Ions**

The effects of heavy metals such as lead, copper, zinc, nickel, and chromium on human health have been widely studied, based on findings that the ingestion of some of these species can cause accumulative poisoning, cancer, and nervous system damage [57]. A variety of technologies exist for the removal of heavy metals, including filtration, surface complexation, chemical precipitation, ion exchange, adsorption, electrode deposition, and membrane processing [58]. Among these procedures, adsorption is considered one of the most attractive processes for heavy metal removal from solution, as the adsorbents are generally easier to handle and provide a greater operating flexibility [59]. Recent increasingly stringent standards for the quality of drinking water have also catalyzed a growing effort in the development of new, highly efficient adsorbents. The high surface area and chemical stability of CNTs offer exciting possibilities for a new generation of adsorbents; hence, some recently acquired data relating to the adsorption of a wide variety of water contaminants are reviewed below. Here, emphasis is placed on the CNT processing method, the adsorption capacities observed, and the prospects for their successful application.

##### **19.4.1.1 Adsorption of Lead (II)**

Li and collaborators [9] were the first to report experimental data on lead adsorption from water using CNTs. Lead is ubiquitous in the environment, and its ingestion is extremely hazardous; the consumption of drinking water containing high levels of lead causes serious disorders, including anemia, kidney disease, and mental retardation [60]. Li and colleagues have shown CNTs to show exceptional adsorption capacities and a high adsorption efficiency of Pb(II) removal from



**Figure 19.7** Isotherms for Pb(II) adsorption by acid-refluxed CNTs at different pH values. Curve a, pH = 3.0; curve b, pH = 5.0; curve c, pH = 7.0. Reproduced from Ref. [9].

water. The CNTs used in these investigations were pretreated with nitric acid in order to increase the adsorption capacities and to remove most of the catalyst particles within the raw material. The amount of Pb(II) adsorbed onto the CNTs was determined by the difference between the initial Pb(II) concentration and the equilibrium Pb(II) concentration of the solution. The authors also monitored the effect of varying the pH of the solution on lead adsorption.

The acid treatment was seen to have a major impact on the nanotubes' adsorption capacities. For example, whereas pristine as-grown CNTs had an adsorption capacity for Pb(II) of  $1 \text{ mg g}^{-1}$  at pH 5, the capacity was increased remarkably (to  $15.6 \text{ mg g}^{-1}$ ) when the CNTs were refluxed with concentrated nitric acid, again at pH 5. It appears that acid oxidation of the CNTs leads to the introduction of many functional groups, such as hydroxyl, carboxyl, and carbonyl onto the CNT surface [61], which in turn leads to improved adsorption capacity. Li also reported that the removal of Pb(II) from water by acid-refluxed CNTs was highly dependent on the solution pH, as this affects the surface charge of the adsorbents and the degree of ionization and speciation of the adsorbates. The data in Figure 19.7 show that the Pb(II) adsorption capacity of the CNTs was increased as the pH value was increased from 3.0 to 7.0. It was proposed that, at low pH values, the adsorption of Pb(II) was very weak due to the competition of  $\text{H}^+$  with Pb(II) species for the adsorption sites (Figure 19.7, curve a). It was also proposed that, at pH 5, the adsorption capability had increased due to role of functional groups present on the nanotube surface (Figure 19.7, curve b), and was further increased at pH 7 (Figure 19.7, curve c). This might be the result of a combined effect of adsorption and a change in the speciation of the lead ions. The results of other experiments have indicated that, at pH 5 and room temperature, the amount of Pb(II) adsorbed onto the acid-refluxed CNTs increased rapidly during the first 8 min ( $16.4 \text{ mg g}^{-1}$  adsorbent, 81.6% removal), with equilibrium being reached after 40 min ( $17.5 \text{ mg g}^{-1}$ , 87.8% removal).

More recently, the same group [62] reported the adsorption thermodynamics and kinetics of Pb(II) adsorption on CNTs, by evaluating various thermodynamic parameters and employing a pseudo second-order kinetic model to describe the

**Table 19.2** Summary of results for lead adsorption in terms of nanotube surface area, pore specific volume, pore size distribution, and particle size distribution. Adapted from Ref. [63].

	$S_{\text{BET}}$ ( $\text{m}^2 \text{g}^{-1}$ )	$V_p$ ( $\text{cm}^3 \text{g}^{-1}$ )	$D_p$ ( $\text{cm}^3 \text{g}^{-1}$ )	$S_p$ ( $\mu\text{m}$ )
Sample 1	47	0.18	3.4	30 and 570
Sample 2	62	0.26	2.4 and 3.2	23 and 450
Sample 3	154	0.58	3.6	8 and 55
Sample 4	145	0.54	3.6	19 and 70

$S_{\text{BET}}$  ( $\text{m}^2 \text{g}^{-1}$ ) = BET surface area;  $V_p$  ( $\text{cm}^3 \text{g}^{-1}$ ) = pore specific volume;  $D_p$  ( $\text{cm}^3 \text{g}^{-1}$ ) = mean pore diameter;  $S_p$  ( $\mu\text{m}$ ) = particle size.

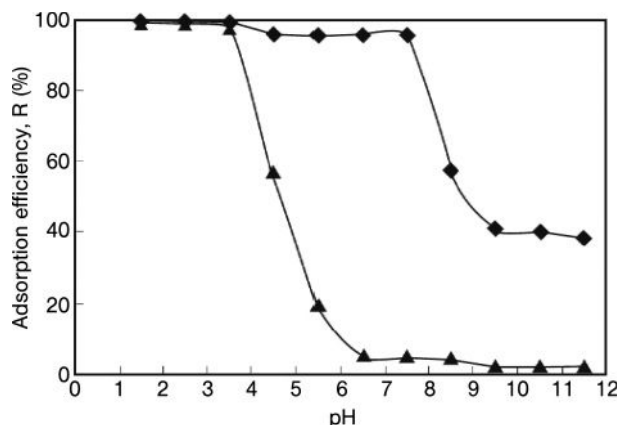
adsorption processes. Based on their results, the authors concluded that the adsorption of Pb(II) onto CNTs was endothermic; they also suggested that the CNT material not only possessed a larger adsorption capacity but also showed a good desorption rate. Such benefits could result in a significant reduction in the overall costs for adsorbent recycling. Desorption studies also revealed that Pb(II) could be easily removed from the CNTs by altering the pH values of the solution using both HCl and HNO<sub>3</sub>.

The results of another series of studies has further underlined the influence of the morphologies of CNTs on the removal of lead, in terms of specific surface area, particle size distribution, and type of functional group introduced to the CNT wall [63]. The specific surface area and pore volume of CNTs exposed to four different types of oxidation treatments were compared, and the pore and particle size distributions of the CNTs evaluated. The results (as summarized in Table 19.2) indicated that the CNTs with the highest surface area, smallest particle size and with a relative larger number of functional groups attached to their walls, showed a maximum adsorption capability of  $82.6 \text{ mg g}^{-1}$  from a solution with an initial lead concentration of  $10 \text{ mg l}^{-1}$ . Under the same conditions, the adsorption capacities of samples with a lower number of functional groups attached, and with larger wall defects, achieved adsorption capacities of only approximately  $10 \text{ mg g}^{-1}$ .

#### 19.4.1.2 Adsorption of Chromium (VI)

Chromium (VI) is one of the most toxic metals found in various industrial wastewaters. Public health considerations of chromium are mostly related to Cr(VI) compounds that are strong irritants due to their high solubility and diffusivity in tissue; certain Cr(VI) compounds have also been shown to be carcinogenic and mutagenic. The toxic effects of Cr(VI) ions in humans include liver damage, internal hemorrhages, respiratory disorders, dermatitis, skin ulceration, and chromosome aberrations [64].

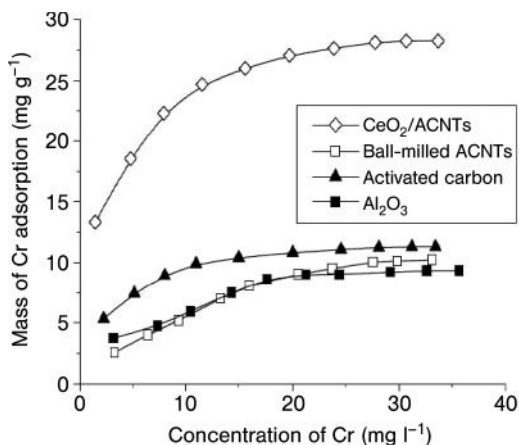
Di and collaborators [65] have investigated the suitability of CNTs for Cr(VI) (as dichromate oxoanion) adsorption, and compared their behavior to that of activated



**Figure 19.8** Adsorption of Cr(VI) ions onto CNTs (◆) and activated carbon (▲) as a function of pH. Cr(VI) ion concentration =  $5 \text{ mg g}^{-1}$  CNT; carbon nanotube concentration =  $1 \text{ g l}^{-1}$ ; contact time = 12 h. Reproduced from Ref. [65].

carbon. In these studies, following pretreatment of both as-prepared CNTs and activated carbon with nitric acid and hydrofluoric acid, the CNTs were shown to have superior adsorption capabilities and efficiencies for the removal of Cr(VI) ions from water over the pH range 4.0 to 7.5 (see Figure 19.8). Activated carbon was seen to adsorb chromate ions very rapidly at low pH values, but the adsorption capacity declined very sharply at pH 3.5. In contrast, the adsorption efficiency of the CNTs was maintained at over 90% over a wide pH range, although the Cr(VI) ion adsorption capacity of CNTs fell sharply at pH 8. The authors attributed this behavior to the influence of the nanotube's zeta potential. Subsequently, it was shown experimentally that the isoelectric point of the CNT material was 7.7; at higher pH values the surfaces of the CNTs became negatively charged and thus inaccessible to the chromate anions. The authors also proposed competition of the hydroxyl ions for the few adsorption sites available at these pH values. The data in Figure 19.8 indicate that the highest Cr(VI) ion adsorption capacity was observed over the pH range 4.0 to 7.5. At  $\text{pH} \leq 3$ , the CNTs and activated carbon showed a similar adsorption capacity, but at a higher pH the capacity of the CNTs was greater. The maximum CNT adsorption capacity ( $20.56 \text{ mg g}^{-1}$ ) occurred at pH 7.5, when the Cr(VI) concentration was  $33.28 \text{ mg l}^{-1}$ . The kinetic curves showed the adsorption rate of Cr(VI) ions to be relatively high over the first 20 min, reaching an adsorption capacity of  $15 \text{ mg g}^{-1}$ .

A few months later, improved values for chromium adsorption were reported in a new study [66]. Here, a composite of aligned CNTs supported in ceria nanoparticles ( $\text{CeO}_2/\text{CNTs}$ ) was used as the adsorbent, the material being prepared by the chemical reaction of  $\text{CeCl}_3$  with NaOH in the presence of a CNT suspension, followed by heat treatment. Scanning electron microscopy (SEM) images showed



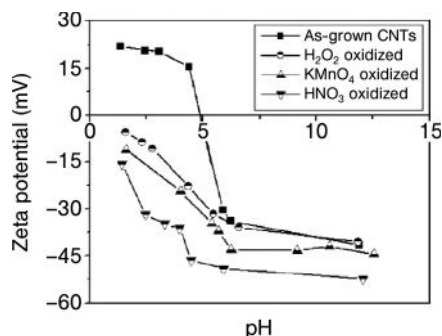
**Figure 19.9** Adsorption isotherms of Cr(VI) on CeO<sub>2</sub>/CNT materials compared with activated carbon, Al<sub>2</sub>O<sub>3</sub> and ball-milled CNTs (at pH 5.0 and 25 °C). Reproduced from Ref. [66].

that the CNT alignment was uniform, with lengths reaching 200  $\mu\text{m}$  and diameters ranging from 20 to 80 nm. Transmission electron microscopy (TEM) analysis indicated a homogeneous distribution on the ceria particles in the CNT network. Overall, the study results indicated that highest capacity for Cr(VI) adsorption occurred at pH values ranging from 3.0 to 7.4, with values of 30.3 mg Cr(VI) g<sup>-1</sup> nanotube being observed at pH 7.0. The authors also compared the Cr(VI) adsorption isotherm obtained on the CeO<sub>2</sub>/CNT material with those obtained on activated carbon and  $\gamma$ -Al<sub>2</sub>O<sub>3</sub>. As shown in Figure 19.9, the adsorption capacity of the CeO<sub>2</sub>/CNT material was 1.5-fold higher than that observed for activated carbon, and twofold larger than for Al<sub>2</sub>O<sub>3</sub>.

The authors proposed that the small size of the CeO<sub>2</sub> particles, and their uniform distribution on the surface of the aligned nanotubes, contributed to the observed high Cr(VI) adsorption. They also suggested that nanotube wall defects, produced by the CVD synthesis process, could offer active sites for Cr(VI) adsorption on the outer surfaces of the aligned nanotube array. The inner cavities and the opened ends present in the inter-aligned nanotube space might also have contributed to the effective adsorption of Cr(VI) ions.

#### 19.4.1.3 Adsorption of Cadmium (II)

Cadmium (II) represents a very high risk to human health due to its extremely high toxicity, even in very small quantities. Drinking water with a cadmium content in excess of permitted levels (0.005 mg l<sup>-1</sup>) can cause nausea, salivation, diarrhea, muscular cramps, renal degradation, lung insufficiency, bone lesions, cancer, and hypertension [67]. Li *et al.* [68] have analyzed the suitability of CNT materials for Cd(II) adsorption and its removal from water; the same group evaluated the efficacy of several chemical treatments using three different oxidizing agents, namely H<sub>2</sub>O<sub>2</sub>, KMnO<sub>4</sub>, and HNO<sub>3</sub>. The chemically treated CNTs were shown to have a larger



**Figure 19.10** Zeta potential curves versus pH for pristine and oxidized CNTs. Reproduced from Ref. [68].

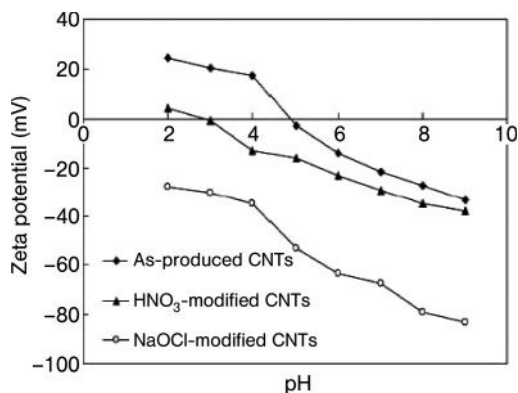
adsorption capacity for Cd(II) than did the pristine, as-grown CNTs. Subsequently, the authors measured the physico-chemical properties of oxidized CNTs and evaluated their Cd(II) adsorption capacity. The specific surface area and pore-size distributions of the as-grown and oxidized CNTs were measured using nitrogen adsorption, with the BET (Brunauer–Emmett–Teller) method. The functional groups on oxidized CNTs were assessed quantitatively using Boehm's titration method [69], and the zeta potentials of the as-grown and oxidized CNTs were also evaluated. Based on these results, it was proposed that the Cd(II) adsorption capacities for the three types of oxidized CNT were increased due to functional groups having been introduced by oxidation, compared to the as-grown, pristine CNTs. The observed Cd(II) adsorption capacity of the as-grown CNTs reached only  $1.1 \text{ mg g}^{-1}$ , compared to values of 2.6, 5.1, and  $11.0 \text{ mg g}^{-1}$  for nanotubes treated with  $\text{H}_2\text{O}_2$ ,  $\text{HNO}_3$  and  $\text{KMnO}_4$ , respectively. The authors linked these results to the increase in surface area observed following each chemical treatment. The data obtained regarding the particle size distribution and suspensibility of these materials indicated that oxidation with  $\text{H}_2\text{O}_2$  and  $\text{KMnO}_4$  only partially broke up the nanotubes, whilst oxidation with  $\text{HNO}_3$  cut short completely most of the CNTs.

The observed dependence of the zeta potential of the as-grown and oxidized CNTs on pH is shown graphically in Figure 19.10. At the same pH value, the zeta potential for the three types of oxidized CNTs followed the order  $\text{H}_2\text{O}_2 < \text{KMnO}_4 < \text{HNO}_3$ , and suggests that the amounts of acid-functional groups increase following the same order. The adsorption isotherms of Cd(II) also indicated that the functional groups introduced by oxidation improved the ion-exchange capabilities of the CNTs and thus led to corresponding increases in the Cd(II) adsorption capacities. A removal efficiency close to 100% at a CNT dosage of  $0.08 \text{ g } 100 \text{ ml}^{-1}$  was observed for the  $\text{KMnO}_4$ -oxidized CNTs, which suggested that this treatment represented an effective means of improving the Cd(II) adsorption capacity.

#### 19.4.1.4 Adsorption of Copper (II)

Despite being one of the most widespread environmental contaminants, copper is essential to human life and health, yet is potentially toxic in larger quantities. In humans, the ingestion of relative large quantities of copper salts may cause





**Figure 19.11** Zeta potential curves versus pH for pristine and oxidized CNTs. Reproduced from Ref. [70].

severe abdominal pain, vomiting, diarrhea, hemolysis, hepatic necrosis, hematuria, proteinuria, hypotension, tachycardia, convulsions, coma, and death. The major sources of copper in industrial effluents are metal cleaning and electroplating.

Wu [70] has evaluated the Cu(II) adsorption efficiency of pristine and chemically modified CNTs, the latter being functionalized using HNO<sub>3</sub> and NaOCl. This chemical treatment caused increases in both the pore volume and average pore size of the CNTs, while the value of the isoelectric point was shown to decrease. A comparison of the infrared spectra of the as-produced and modified CNTs indicated that several functional groups had been generated on the surface of modified CNTs. The zeta potential values of the as-produced and modified CNTs, as shown in Figure 19.11, indicated that the surface of the as-produced and HNO<sub>3</sub>-modified CNTs was positively charged in solution, whereas the zeta potentials of NaOCl-modified CNTs were all negative. These negatively charged surfaces would electrostatically favor the adsorption of Cu(II), as was observed by Wu and coworkers. Indeed, the Cu(II) adsorption capacity followed the order NaOCl-modified > HNO<sub>3</sub>-modified > as-produced CNTs. These findings suggest that modifying the surface of the CNTs may not only provide a more negatively charged and hydrophilic surface but also generate a variety of functional groups, markedly promoting the adsorption of Cu(II) onto the modified CNTs. The maximum adsorption capacities observed in this study at different temperatures are summarized in Table 19.3.

#### 19.4.1.5 Adsorption of Zinc (II)

Whilst zinc (II) is essential for human health, large amounts can be harmful. The consequences of a relatively large intake of Zn(II) include lethargy, light-headedness, ataxia, oropharyngeal cancer, gastric burns, epigastric tenderness, pharyngeal edema, hematemesis, and melena [71]. The suitability of CNTs (both MWNT and SWNT) to adsorb Zn(II) from water was studied by Lu *et al.* [72], whose data showed the adsorption capacity of CNTs to be greatly improved following a specific

**Table 19.3** Summary of copper adsorption capacities ( $q_m$ ) of CNTs at different temperatures in terms of the adsorbed mass of Cu(II) in solution (mg) per mass of nanotube (g). Reproduced from Ref. [70].

Temperature (°C)	Adsorption capacity ( $q_m$ ) (mg g <sup>-1</sup> )		
	As-produced CNTs	HNO <sub>3</sub> -modified CNTs	NaOCl-modified CNTs
7	6.39	12.46	44.64
17	7.87	13.10	45.87
27	8.25	13.87	47.39
37	9.34	15.11	49.02
47	10.17	16.04	51.81

chemical treatment that renders the CNTs more hydrophilic, and thus more effective in adsorbing Zn(II).

Lu and coworkers showed that the adsorption capacity of Zn(II) onto CNTs increased in line with a rising pH of the solution over the range 1 to 8, was maximal at pH 8 to 11, and then decreased at pH 12. A comparative study on the adsorption of Zn(II) between CNTs and commercially available, powdered activated carbon, was also conducted. The maximum adsorption capacities for Zn(II) observed were 43.66, 32.68, and 13.04 mg g<sup>-1</sup> with SWNTs, MWNTs, and activated carbon, respectively. The short contact time required to reach equilibrium, as well as the high adsorption capacity, suggests that both SWNTs and MWNTs possess a high potential for the removal of Zn(II) from water. The same group also suggested that the higher adsorption capacity observed for SWNTs over MWNTs might be due to the higher surface area observed for SWNTs (423 m<sup>2</sup> g<sup>-1</sup> compared to 297 m<sup>2</sup> g<sup>-1</sup> observed for MWNTs), and also to the larger proportion of defects present on the MWNTs (as observed using Raman spectroscopy).

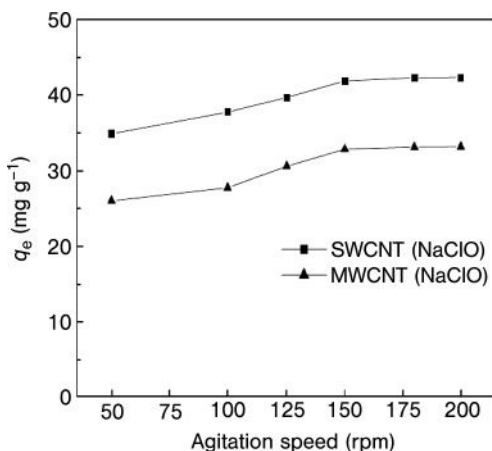
However, an interesting result was observed for the case of activated carbon. Although the surface areas of purified SWNTs and MWNTs were much lower than that of activated carbon, the adsorption capacities of Zn(II) onto purified SWNTs and MWNTs were much higher than was observed for activated carbon. This superior adsorption capacity was attributed to a larger number of hydrophilic groups present in the CNT walls.

Another study which focused on the adsorption kinetics and equilibrium of Zn(II) adsorbed onto CNTs nanotubes has also been reported [73]. This thermodynamic analysis revealed that the sorption of Zn(II) onto CNTs was endothermic and spontaneous, and that the Zn(II) ions could easily be removed from the surface sites of SWNTs and MWNTs by the action of a 0.1 M nitric acid solution. Moreover, the original adsorption capacity was maintained after 10 cycles of this sorption–desorption process. Such data suggest that both types of CNT material could be reused through many cycles of water treatment and regeneration.

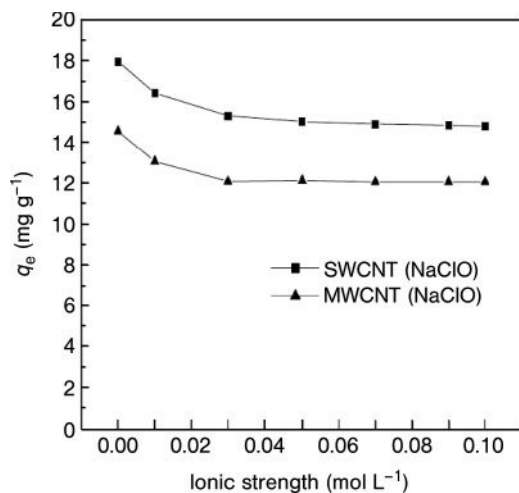
#### 19.4.1.6 Adsorption of Nickel (II)

Nickel is a toxic metal ion that is present in wastewaters. More than 40% of all nickel produced is used in steel factories, in nickel batteries, and in the production of some alloys, which leads to an increase in the Ni(II) burden on the ecosystem and a deterioration in water quality. If ingested, Ni (II) is harmful, and may cause vomiting, chest pain, and a shortness of breath [74].

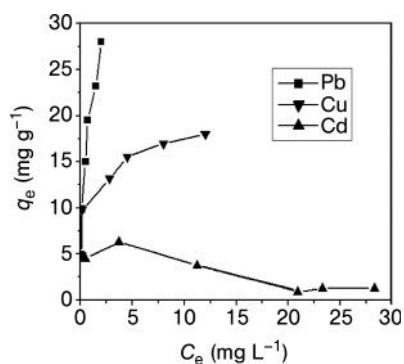
Lu *et al.* [75] have analyzed the effect of CNT mass, agitation speed, initial Ni(II) concentration, and solution ionic strength on the Ni(II) adsorption capacity of CNTs. The effects of agitation speed and solution ionic strength on Ni(II) sorption by oxidized CNTs are shown in Figures 19.12 and 19.13. The adsorption capacity of both SWNTs and MWNTs was shown to increase as the agitation speed increased, but to decrease when the ionic strength of the solution increased. The same group also reported that SWNTs showed a better performance for Ni(II) adsorption than did MWNTs. A similar conclusion was reached by Chen *et al.* [58], when studying the adsorption of Ni(II) onto oxidized MWNTs as a function of contact time, pH, ionic strength, MWNT amount, and temperature. The results showed that Ni(II) adsorption onto MWNTs was heavily dependent on the pH and, to a lesser extent, the ionic strength. Kinetic data showed the adsorption process to achieve equilibrium within 40 min, and that the process followed a pseudo second-order rate equation. The adsorption data fitted the Langmuir model and, together with thermodynamic data, indicated the spontaneous and endothermic nature of the process. The results of a desorption study showed that Ni(II) adsorbed onto oxidized MWNTs could easily be desorbed at pH <2. The authors proposed that ion exchange might be the predominant mechanism for Ni(II) adsorption on oxidized MWNTs.



**Figure 19.12** Effect of agitation speed on Ni(II) adsorption by oxidized CNTs. Reproduced from Ref. [75].



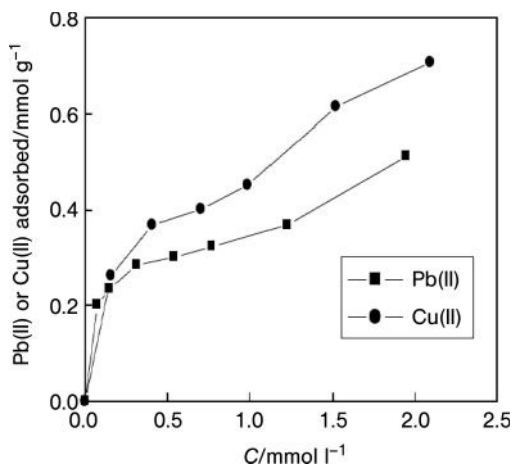
**Figure 19.13** Effect of solution ionic strength on Ni(II) adsorption by oxidized CNTs. Reproduced from Ref. [75].



**Figure 19.14** Competitive adsorption data for three ions of Pb(II), Cu(II) and Cd(II) onto CNTs at room temperature and pH 5.0. Reproduced from Ref. [76].

#### 19.4.1.7 Competitive Adsorption of Heavy Metals Ions

Whilst most reports on heavy metal adsorption using CNTs has focused on a single metal ion, Li and colleagues [76] were the first to conduct a study on the *competitive adsorption* of Pb(II), Cu(II) and Cd(II) onto HNO<sub>3</sub>-treated MWNTs. These studies showed the affinity order of these metal ions towards CNTs to vary in the order: Pb(II) > Cu(II) > Cd(II) (Figure 19.14). The Langmuir adsorption model represented the experimental data for Pb(II) and Cu(II) well, but did not provide a good fit for the adsorption data of Cd(II). It was also observed that, at a low pH, the adsorption percentages were negligible, but that at pH values between 1.8 and 6.0 the proportions of Pb(II) and Cu(II) increased sharply, almost attaining values of 100%, while only a small increase was noted for Cd(II).



**Figure 19.15** Adsorption data for Pb(II) and Cu(II) onto magnetic CNTs composites (pH = 5.0,  $T = 20^\circ\text{C}$ ). Reproduced from Ref. [78].

Another study, conducted by Hsieh *et al.* [77], focused on the competitive adsorption of Pb(II), Cu(II) and Cd(II) by CNTs grown on microsized  $\text{Al}_2\text{O}_3$  particles. The authors noted that the adsorption behavior of these metal ions on CNTs on  $\text{Al}_2\text{O}_3$  particles followed Langmuir's adsorption model, with observed adsorption capacities on the CNTs for Pb(II), Cu(II) and Cd(II) of 32, 18, and  $8\text{ mg g}^{-1}$ , respectively. These results confirmed that CNTs supported on  $\text{Al}_2\text{O}_3$  particles showed potential for the removal of soluble heavy metals from aqueous solutions.

Peng and collaborators [78] conducted a similar study to determine the adsorption capacity of Pb(II) and Cu(II) on CNT-iron oxide composites. These ferric composites offer the advantage of a continuous contaminant adsorption from a liquid effluent whilst, when adsorption is complete, the adsorbent can be separated from the liquid phase simply by using a magnet. Both, X-ray diffraction (XRD) and SEM studies indicated the presence of an entangled network of CNTs with attached iron oxide nanoclusters. The adsorption isotherms obtained for Pb(II) and Cu(II) adsorbed onto these magnetic composites are shown in Figure 19.15. The maximum adsorption capacities for Pb(II) and Cu(II) in the concentration range studied were 105.67 and  $45.12\text{ mg g}^{-1}$ . After adsorption, a magnetic separation process was carried out using a permanent magnet, providing a 98% recovery of the Pb(II) and Cu(II) ion mass adsorbed.

#### 19.4.2

##### Adsorption of Other Inorganic Elements

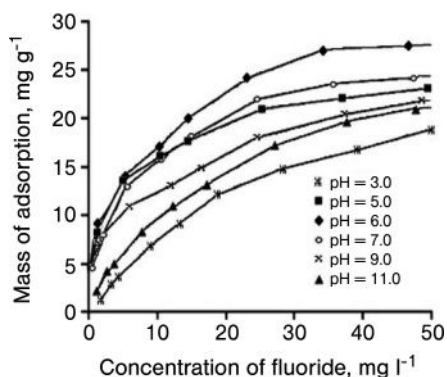
In addition to heavy metal ions, other common inorganic pollutants in drinking water include ionic forms of fluoride, arsenate, and americium-243(III). Although fluoride is added via drinking water, it is often present in surface waters due to

natural erosion or to discharges from fertilizers and aluminum factories. The ingestion of fluoride can cause bone disease and mottled teeth in children. Arsenate is occasionally present due to erosion of natural deposits, or it may be released into surface waters via the runoffs from orchards or from glass and electronics production wastes. Arsenate ingestion causes skin damage and circulatory problems; it is also a well-known carcinogen [2]. Americium-243(III) contributes significantly to the radiotoxicity of nuclear waste, and may be released into the environment during nuclear waste storage, processing, or disposal. Exposure to small traces of americium-243(III) increases the risk of cancer.

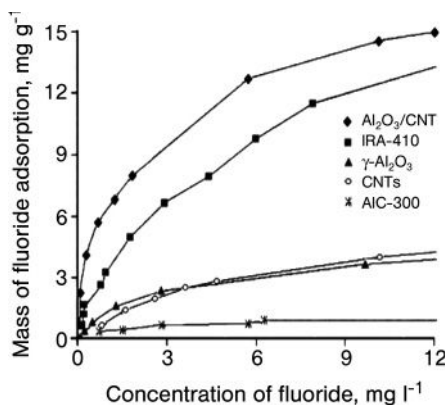
#### 19.4.2.1 Adsorption of Fluoride

The acceptable fluoride concentration in drinking water is generally in the range of 0.5 to 1.5 mg l<sup>-1</sup> [79]. Higher concentrations will affect the metabolism of calcium and phosphorus in the human body, and lead to dental and bone fluorosis [80]. Many methods have been adopted to remove excess fluoride from drinking water, the most common approach being adsorption with activated alumina, which has a good adsorption capacity and selectivity for fluoride. Unfortunately, the optimum capacity for fluoride removal in alumina occurs only at pH values below 6.0, which strongly limits the practical applications of this material [81].

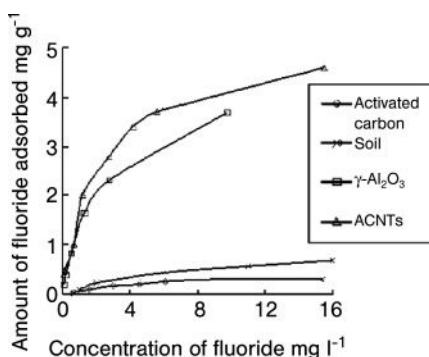
Li and collaborators [52] have reported that amorphous Al<sub>2</sub>O<sub>3</sub> supported on CNTs represents a major candidate for fluoride adsorption from water. These authors used CNTs as a supports for Al<sub>2</sub>O<sub>3</sub>, and showed the composite to have a high potential for removing fluoride from drinking water. Based on their adsorption isotherms (Figures 19.16 and 19.17), Li and coworkers found that Al<sub>2</sub>O<sub>3</sub>/CNT composites showed a high fluoride adsorption capacity over a pH range from 5.0 to 9.0. They also found the adsorption capacity for the Al<sub>2</sub>O<sub>3</sub>/CNT composite to be about 13.5-fold higher than that of activated carbon, fourfold higher than for  $\gamma$ -alumina, and also higher than that of the commercial polymeric resin, IRA-410. This broad range of pH values and high adsorption capacities observed for the Al<sub>2</sub>O<sub>3</sub>/CNT composite makes this material very attractive for fluoride removal from water.



**Figure 19.16** Effect of solution pH on fluoride adsorption onto an Al<sub>2</sub>O<sub>3</sub>/CNT composite. Reproduced from Ref. [52].



**Figure 19.17** Adsorption isotherms of fluoride on activated carbon (AIC-300), CNT,  $\gamma$ - $\text{Al}_2\text{O}_3$ , a commercial resin (IRA-410) and  $\text{Al}_2\text{O}_3$ /CNT composite. The data for activated carbon and IRA-410 were fitted with a Langmuir isotherm, while the data for CNT and  $\text{Al}_2\text{O}_3$ /CNTs were fitted with a Freundlich isotherm. Reproduced from Ref. [52].



**Figure 19.18** Adsorption isotherm of fluoride on CNTs (at pH 7 and 25°C) compared with  $\gamma$ - $\text{Al}_2\text{O}_3$ , soil, and activated carbon. Reproduced from Ref. [10].

A year later, the same group presented improved results using an array of aligned MWNTs [10]. For this, the authors studied the kinetics of the fluoride adsorption process, and the effect of pH on fluoride adsorption capacity. The kinetic data indicated that the fluoride adsorption rate was rapid during the first 60 min, and quickly reached an adsorption capacity of  $3.0 \text{ mg g}^{-1}$ , with equilibrium achieved after 180 min. A mild dependence of the adsorption capacity on the pH of the solution was also observed, with the highest adsorption capacity being observed at pH 7, and reaching  $4.5 \text{ mg g}^{-1}$  at fluoride concentrations of  $15 \text{ mg l}^{-1}$ . The adsorption isotherms obtained for this material, compared to those obtained in  $\gamma$ - $\text{Al}_2\text{O}_3$ , activated carbon, and a soil, are shown in Figure 19.18. At low fluoride

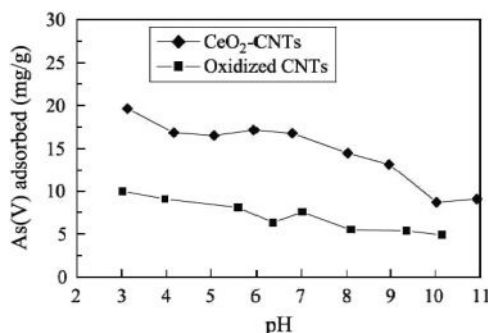
initial concentrations ( $<1 \text{ mg l}^{-1}$ ), the nanotube material and alumina had the same adsorption capacities, but at higher fluoride concentrations the fluoride adsorption capacity of the CNTs was higher. These results again indicated the potential of CNTs in fluoride removal.

#### 19.4.2.2 Adsorption of Arsenic

Arsenic is required as a micronutrient for the human body, yet it may be carcinogenic if consumed constantly. Thus, it is of great importance to remove arsenic from water before it is used for drinking. Two main forms of arsenic are encountered in natural water, namely trivalent (As(III), arsenite) and the higher-oxidized form, pentavalent (As(V), arsenate). Whilst either of these species can be found in natural waters, As(III) is more common in groundwater, and As(V) is more common in surface water [82].

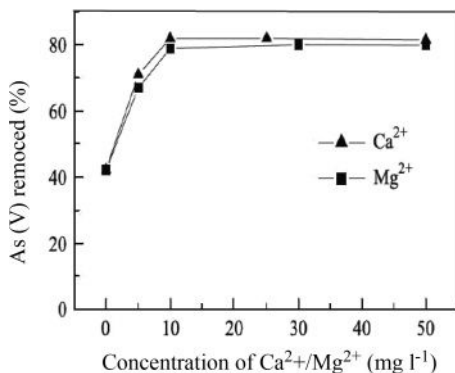
When a novel ceria–CNT composite was proposed as an alternative for the removal of arsenate from water [83], the results indicated that arsenate adsorption on these materials was pH-dependent. The presence of Ca(II) and Mg(II) also significantly enhanced the adsorption capacity. These very promising results suggest that these materials might represent a promising adsorbent for drinking water purification. The effect of pH on the adsorption of As(V) onto  $\text{CeO}_2/\text{CNT}$  is shown in Figure 19.19.

These results indicate that the adsorption of As(V) is pH-dependent, and that the pristine composite has a higher adsorption capacity than the chemically modified nanotubes. The authors proposed that the dependence of adsorption on pH was due to variations in the surface charge on the nanotube composites. This was corroborated by zeta potential measurements. Moreover, the authors also measured the influence of Ca(II) and Mg(II) on the adsorption capability of the  $\text{CeO}_2/\text{CNT}$  material. From the results shown in Figure 19.20 it is clear that both Ca(II) and Mg(II) significantly enhance the adsorption capacity of the nanotube composite. In fact, an increase from 0 to  $10 \text{ mg l}^{-1}$  in the concentration of Ca(II) and Mg(II) resulted in an almost one order of magnitude increase in the amount of As(V)

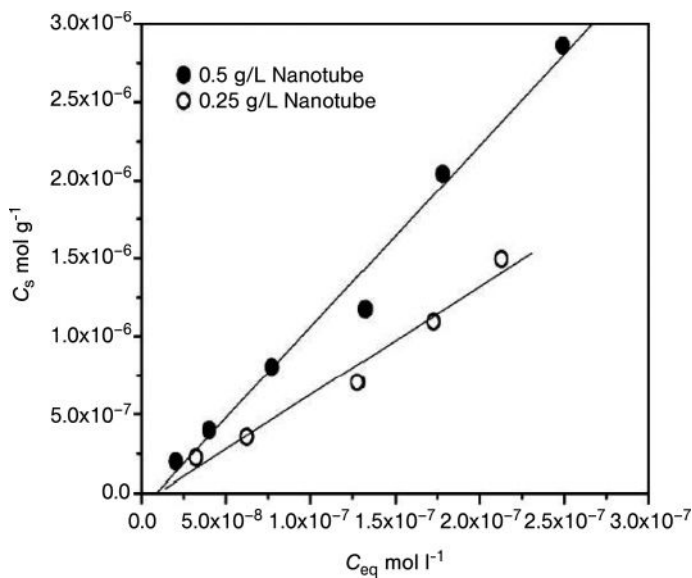


**Figure 19.19** Effect of pH on As(V) adsorption by chemically treated CNTs (■) and  $\text{CeO}_2/\text{CNT}$  composite (◆). Reproduced from Ref. [83].





**Figure 19.20** Effect of Ca(II) and Mg(II) on As(V) adsorption (initial concentration of As(V) = 20 mg l<sup>-1</sup>). Reproduced from Ref. [83].



**Figure 19.21** Adsorption isotherms for <sup>243</sup>Am(III) onto MWNTs in polyethylene tubes using Milli-Q water in the presence of 0.1 M NaClO. The contact time was 4 days. Reproduced from Ref. [85].

adsorbed. The authors explained this observed increase in adsorption capacity by proposing the formation of a ternary surface complex between calcium or magnesium, arsenate, and the ceria surface [84].

#### 19.4.2.3 Adsorption of Americium-243 (III)

Wang and collaborators [85] examined the use of MWNTs as adsorbents for the radionuclide americium-243 (III). The data obtained (see Figure 19.21) indicated

that the sorption isotherms were linear, and confirmed that the sorption of Am(III) onto MWNTs did not reach saturation under these conditions (up to  $3 \times 10^{-6} M$  of Am(III)). A dependence of  $^{243}\text{Am(III)}$  sorption by MWNTs on pH and ionic strength was also reported. Approximately 80% of  $^{243}\text{Am(III)}$  was adsorbed by the nanotubes at pH 5, and this increased to approximately 90% at pH 10. The authors explained this behavior in terms of surface complexation.

### 19.4.3

#### Adsorption of Organic Compounds

Although, as detailed above, CNTs have major potential for the removal of inorganic substances from water, the number of studies conducted on the adsorption of organic pollutants onto CNTs is relatively small. A report published by the U.S. Environmental Agency in 2002 [86] stated that the most common organic contaminants found in drinking water ranged from disinfection byproducts (e.g., trihalomethanes) to other organic chemicals, including carbon tetrachloride, benzene, polychlorinated benzenes, dioxins, and pesticides. The similar chemical characteristics of most of these organic pollutants give rise to similar acute health effects at high doses, with the primary target organ generally being the central nervous system. Sustained or very high exposures to these organic chemicals can be fatal. An overview of the results obtained on the removal of some of these chemicals from water, using CNTs as adsorbents, is provided in the following section.

##### 19.4.3.1 Adsorption of Dioxins

Dioxins and related compounds (e.g., polychlorinated dibenzofurans and biphenyls) are highly toxic pollutants. The toxicity of dioxins varies with the number of chlorine atoms; for example, 2,3,7,8-tetrachlorodibenzo-*p*-dioxin (TCDD) is a known human carcinogen. In addition to cancer, dioxins also adversely affect the immune and endocrine systems, as well as normal fetal development [87]. Dioxins are mainly generated from the combustion of organic compounds in waste incinerators. Due to the extreme toxicity and chemical inertness of dioxins, it is necessary to improve any current technologies based on activated carbon adsorption.

Long *et al.* [8] have reported that CNTs can attract and trap a large amount of dioxins in a more efficient manner than the activated carbon or other adsorbents currently used. Long's group attributed this observation to the stronger interaction forces that exist between dioxin molecules and the curved hydrophobic surface of the nanotubes. Another series of investigations, based on dioxin temperature-programmed desorption [8, 88], reported that the interaction of dioxins with CNTs is much stronger than that with activated carbon. The desorption temperatures, desorption activation energy and Langmuir constants obtained for dioxin desorption on CNTs, activated carbon and  $\gamma\text{-Al}_2\text{O}_3$  are listed in Table 19.4. These results clearly indicate that the interaction of dioxins with CNTs is significantly higher than with the other adsorbents.

A density functional theory (DFT) study conducted by Kang *et al.* [89] focused on the molecular interactions between dioxin and metal-doped (Li, Na, Fe) SWNTs. The calculations indicated that doping large-diameter SWNTs with calcium atoms

**Table 19.4** Position of the maximum in the dioxin temperature programmed desorption profiles of carbon nanotubes, activated carbon and alumina at different heating rates. Data for calculated values of activation energies for desorption and Langmuir constants are also presented. Reproduced from Refs [8] and [88].

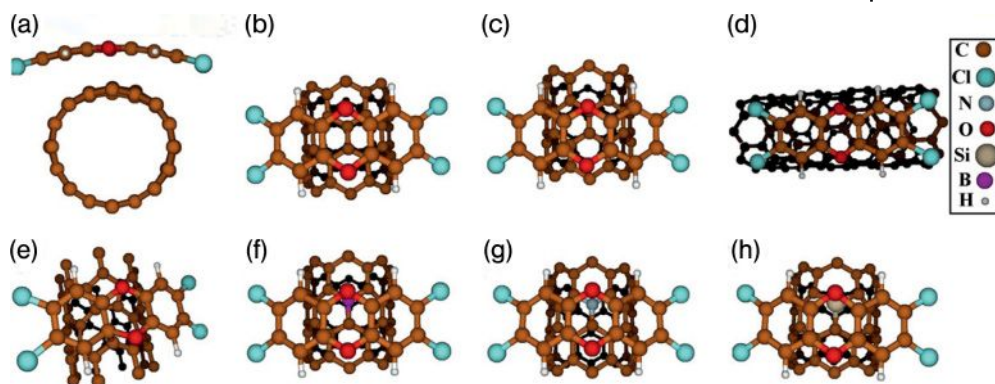
Sorbent	Peak desorption temp. (°C) at different heating rates				Desorption activation energy (kJ mol <sup>-1</sup> )	Langmuir constant <i>B</i> at 25 °C (latm <sup>-1</sup> )
	2 °C min <sup>-1</sup>	5 °C min <sup>-1</sup>	10 °C min <sup>-1</sup>	20 °C min <sup>-1</sup>		
Carbon nanotubes	588	609	620	634	315	$2.7 \times 10^{52}$
ZX-4 carbon (Mitsubishi)	481	517	543	?	119	$1.3 \times 10^{18}$
γ-Al <sub>2</sub> O <sub>3</sub>	306	353	394	?	47.9	$4.5 \times 10^5$

can introduce a strong cooperative binding of the carbon  $\pi$  system with the dioxin. A band structure analysis suggested that the charge transfer model could explain these observations. Iron atoms, which are commonly used as a catalyst for CNT synthesis, can also significantly facilitate dioxin binding. In a sense, this suggests that the adsorption of small molecules, particularly those with delocalized  $\pi$  electrons, can be significantly enhanced by the presence of metallic catalyst remnants following the accomplishment of SWNT synthesis.

More recently, a theoretical *ab initio* calculation of 2,3,7,8-tetrachlorinated dibenzo-*p*-dioxin interaction with pristine, “defective” as well as B-, N-, and Si-doped SWNTs, was reported by Fagan *et al.* [90]. Their results predicted that the interaction between SWNTs and dioxins would depend on the geometric configuration of the approaching dioxin (Figure 19.22), the dopant metal, and the number of defects in the nanotube wall. The results (see Table 19.5) suggested that the adsorption of dioxin was more effective for the case of defective nanotubes. This theoretical prediction shows promise from a practical point of view, as structural defects on the tube walls are naturally formed during nanotube growth and purification processes. Moreover, the results also indicated that doping with B, N, and Si does not improve the absorption capacities of dioxins.

#### 19.4.3.2 Adsorption of 1,2-Dichlorobenzene

Chlorobenzenes such as monochlorobenzene, dichlorobenzene (DCB), and trichlorobenzene, which are present in some surface and ground-waters, have been identified as priority pollutants by the US Environmental Protection Agency [91]. Among chlorobenzenes, DCB is one of the most chemically stable, and its degradation in soil and aquatic environments is extremely limited [92]. The widespread use of chlorinated aromatic chemicals over several decades has resulted in contamination of the environment and human exposure to DCB. The methods



**Figure 19.22** Schematic views of the most stable configurations of different SWNT/dioxin adsorption geometries. Views (b) to (d) show configurations for pristine SWNT interacting with a chlorinated dioxin in different configurations. View (a) depicts a

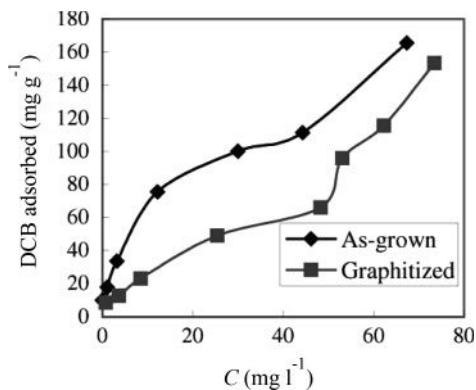
lateral view of the SWNT/dioxin configuration shown in (b). In view (e) the SWNT has a defect in the form of a vacancy. Views (f) to (h) show N-, B-, and Si-doped SWNTs interacting with dioxin, respectively. Reproduced from Ref. [90].

**Table 19.5** Calculated values for the binding energy for the SWNT/dioxin configurations shown in Figure 19.22. Reproduced from Ref. [90].

System <sup>a</sup>	Binding energy (eV)
SWNT/dioxin (Figure 19.1b)	-0.10
SWNT/dioxin (Figure 19.1c)	-0.35
SWNT/dioxin (Figure 19.1d)	-0.77
SWNT/vac_dioxin (Figure 19.1e)	-1.21
SWNT/B_dioxin (Figure 19.1f)	-0.43
SWNT/N_dioxin (Figure 19.1g)	-0.45
SWNT/Si_dioxin (Figure 19.1h)	-0.30

<sup>a</sup> Figure numbers relate to Ref. [90].

employed to remove DCB from water are either destructive oxidation or adsorption. Peng *et al.* [11] have reported the use of as-grown CNTs and graphitized CNTs as adsorbents to remove 1,2-DCB from water. The as-grown CNTs were prepared by catalytic pyrolysis of a propylene–hydrogen mixture at 750 °C using Ni particles as catalysts. The graphitized CNTs were prepared by treating the as-grown CNTs in a nitrogen atmosphere at 2200 °C for 2 h. The maximum amounts of DCB adsorbed by the as-grown and graphitized CNTs were 30.8 and 28.7 mg g<sup>-1</sup>, respectively. The short time required to achieve equilibrium suggested that the CNTs had very high adsorption efficiencies, with the removal rate remaining almost constant over a pH range from 3 to 10. The adsorption isotherms obtained are



**Figure 19.23** Isotherms for DCB adsorption onto as-grown and graphitized CNTs at 25 °C (pH = 5.5,  $t$  = 24 h). Reproduced from Ref. [11].

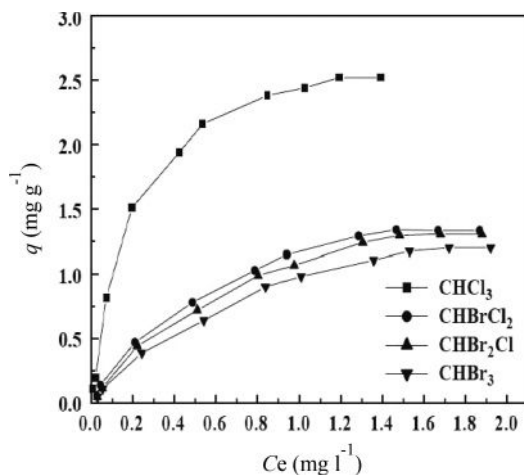
reproduced in Figure 19.23. Taken together, the results indicated that the as-grown CNTs were superior to the graphitized material in terms of DCB adsorption.

Recently, *ab initio* theoretical calculations of 1,2-DCB adsorption onto metallic SWNTs were reported by Fagan *et al.* [93]. The values for the binding energies obtained in terms of interaction between the DCB and SWNTs, indicated that a decrease in nanotube diameter and a consequent enhancement in tube curvature favored a more effective adsorption of DCB on the tube surface. Charge distribution calculations indicated that the adsorption of DCB occurred through  $\pi$ - $\pi$  stacking; the calculations also suggested that the DCB-SWNT interaction was larger for metallic nanotubes than for semi-conducting nanotubes.

#### 19.4.3.3 Adsorption of Trihalomethanes

Trihalomethanes (THMs) are generated during the disinfection of drinking water with chlorine [94], and are recognized as potentially hazardous and carcinogenic substances [95]. More stringent requirements for the removal of THMs from drinking water in recent years have led to the development of innovative, cost-effective alternatives to remove these byproducts.

In 2004, Lu *et al.* [12] reported the use of CNT materials to remove THMs from water, where the nanotube samples were fabricated by the catalytic decomposition of a  $\text{CH}_4/\text{H}_2$  mixture at 700 °C using Ni particles as catalyst. Based on FTIR spectra the authors noted that, after a mild acid treatment, the CNT material became more hydrophilic and effective for the adsorption of the relatively polar THMs molecules. It was also suggested that the diffusion mechanisms controlled the adsorption of THMs onto the CNTs. In fact, the smallest molecule,  $\text{CHCl}_3$ , was seen to adsorb preferentially onto the nanotubes, followed by  $\text{CHBrCl}_2$ ,  $\text{CHBr}_2\text{Cl}$ , and  $\text{CHBr}_3$ . The adsorption isotherms obtained in these studies are shown in Figure 19.24. The observed adsorption capacity for  $\text{CHCl}_3$  was highest, followed by  $\text{CHBrCl}_2$ ,  $\text{CHBr}_2\text{Cl}$  and  $\text{CHBr}_3$ . The maximum adsorbed amounts of  $\text{CHCl}_3$ ,



**Figure 19.24** Adsorption isotherms for four trihalomethanes onto CNTs. Reproduced from Ref. [12].

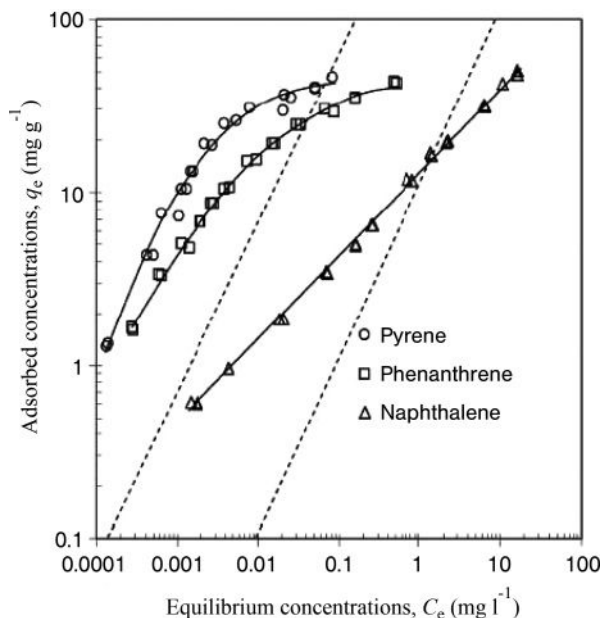
CHBrCl<sub>2</sub>, CHBr<sub>2</sub>Cl and CHBr<sub>3</sub> were 2.41, 1.23, 1.08 and 0.92 mg g<sup>-1</sup>, respectively, from an initial concentration of 1 mg l<sup>-1</sup> of each THM.

Another study conducted by the same group [96] included a comparison of the adsorption of THMs onto powdered activated carbon. In contrast to data obtained with CNTs, for activated carbon the largest molecule, CHBr<sub>3</sub>, was seen to be preferentially adsorbed, followed by CHBr<sub>2</sub>Cl, CHBrCl<sub>2</sub> and CHCl<sub>3</sub>. With an initial concentration of 1 mg l<sup>-1</sup>, the amounts of CHCl<sub>3</sub>, CHBr<sub>2</sub>Cl, CHBrCl<sub>2</sub> and CHBr<sub>3</sub> adsorbed were 1.2, 1.68, 2.19, and 2.75 mg g<sup>-1</sup> CNTs, respectively. The adsorption of THMs onto CNTs also occurred more rapidly compared to activated carbon. Although the surface area of the nanotube material (295 m<sup>2</sup> g<sup>-1</sup>) was much less than that for activated carbon (900 m<sup>2</sup> g<sup>-1</sup>), the adsorption capacity of CHCl<sub>3</sub> onto CNTs was approximately twice that for activated carbon.

The thermodynamic and kinetic parameters of the adsorption processes of THMs on MWNTs was also reported [96]. Here, the amount of THMs adsorbed onto CNTs was seen to decrease with a rise in temperature, with the highest adsorption capacities observed at 5 °C and 15 °C. Under the same conditions, the purified CNT material displayed two- to threefold greater adsorption capacities for CHCl<sub>3</sub> than did activated carbon. A thermodynamic analysis revealed the adsorption of THMs onto CNTs to be exothermic in nature.

#### 19.4.3.4 Adsorption of Polyaromatic Compounds

A recent study [97] investigating the adsorption of polycyclic aromatic hydrocarbons (PAHs) (e.g., naphthalene, phenanthrene, pyrene) from water onto six different carbon nanomaterials, including fullerenes, SWNTs, and MWNTs, has been reported. The results showed that the adsorption capacities of the nanomaterials for the different polycyclic aromatic molecules was related to the PAH



**Figure 19.25** Adsorption isotherms of pyrene, phenanthrene, and naphthalene onto MWNTs. Reproduced from Ref. [97].

molecular size (Figure 19.25), which prompted the authors to suggest that, due to their size, some of these aromatic molecules could not access the nanomaterial pores. Among the different carbon nanomaterials, adsorption appeared to relate well with the adsorbent surface area, micropore, and mesopore volume. Except for the SWNTs, a linear relationship was observed between the adsorbed capacity and the carbon nanomaterial.

## 19.5

### Summary of the Results, and Conclusions

Among the above-described data—some of which are summarized in Table 19.6—it appears that, except for those used by Peng *et al.* [11], all CNTs employed in these experiments have been purified by pretreating with acid, before adsorption measurements were made. Such pretreatment had a major impact on the adsorption capacity of the CNTs in terms of contaminant removal. An analysis of the aforementioned results indicated that the acid treatment not only removed the amorphous carbon that coats the CNT surface but also increased the specific nanotube surface area and pore volume. However, it seems that the most important factor responsible for the improved adsorption capacities seen with oxidized CNTs is the incorporation of surface functional groups (hydroxyl, carboxyl and carbonyl) generated by their treatment with oxidizing acids.

Table 19.6 Summary of selected cited results.

Reference(s)	Type of adsorbent used	Adsorbate	Pretreatment of adsorbent	Parameters affecting adsorption efficiency evaluated
[9]	Acid-refluxed CNTs	Pb(II)	Acid treatment	pH of solution
[62]	Acid-refluxed CNTs	Pb(II)	Acid treatment	Adsorption/desorption study
[63]	Oxidized CNTs	Pb(II)	Acid treatment	CNT morphology
[65]	Acid-refluxed CNTs	Cr(VI)	Acid treatment	pH of solution
[66]	CeO <sub>2</sub> /CNT composites	Cr(VI)	Acid treatment	pH of solution
[68]	Pristine and oxidized CNTs	Cd(II)	Oxidation by H <sub>2</sub> O <sub>2</sub> HNO <sub>3</sub> and KMnO <sub>4</sub>	CNT surface area CNT pore and particle size distribution CNT zeta potential Adsorbate/adsorbent ratio
[70]	Pristine and oxidized CNTs	Cu(II)	Oxidation by HNO <sub>3</sub> and NaClO	pH of solution CNT zeta potential



Table 19.6 Continued.

Reference(s)	Type of adsorbent used	Adsorbate	Pretreatment of adsorbent	Parameters affecting adsorption efficiency evaluated
[72, 73] [75]	Purified CNTs	Zn(II) Ni(II)	Acid treatment	Effect of consecutive adsorption/desorption cycles
[58] [76] [77]	Oxidized CNTs Oxidized	Ni(II) Pb(II),	Acid treatment	Agitation speed pH of solution
[78] [52] [10]	MWNTs Acid-treated CNTs	Cu(II) and Cd(II)	Acid treatment	Ionic strength of solution
[83]	Al <sub>2</sub> O <sub>3</sub> /CNT composite	Pb(II), Cu(II) and	Acid treatment	Adsorbate/adsorbent ratio Contact time
	FeOx/CNT magnetic composite	Cd(II) Pb(II),	Acid treatment	Desorption capacity
	Al <sub>2</sub> O <sub>3</sub> /CNT composite	Cu(II) fluoride	Acid treatment	pH of solution
	Acid-treated CNTs CeO <sub>2</sub> /CNT composite	fluoride Arsenic	Acid treatment	Ionic strength of solution
				Adsorbate/adsorbent ratio Competitive adsorption study
				Effect of consecutive adsorption/desorption cycles
				pH of solution
				pH of solution
				Influence of Ca(II) and Mg(II) as coadsorbates
[85] [8] [11]	MWNTs	243 Am(III)	Acid treatment	pH of solution
[90] [12] [96]	MWNTs	dioxin 1, 2-DCB	Acid treatment	Contact time
[97]	As-grown and graphitized CNTs Metallic SWNTs	1, 2-DCB THMs	Acid treatment	Structure and electronic properties of CNTs
	CNTs	THMs PAHs	Acid treatment	pH of solution
	MWNTs		Acid treatment	Theoretical study
	CNTs and fullerenes			pH of solution
				Temperature
				Adsorbed volume capacity Molecular size of adsorbate

The observed nanotube adsorption capacity is also dependent on pH, temperature, and contact time, whilst the effects of ionic strength, agitation speed, adsorbate initial concentration and CNT dosage have also been discussed. Zeta potential measurements have indicated that chemically treated CNTs have a larger number of negatively charged surface sites than do raw nanotube materials. The results of comparative studies have shown that CNTs exhibit much higher adsorption capabilities than other commonly used adsorbents. In a word, the excellent adsorption performance observed for CNTs indicates their high potential for water remediation applications. A number of fundamental issues remain, however, which limit the application of CNT materials for the removal of water contaminants, including their solubility in aqueous solution, their ultimate environmental fate, and the cost-effectiveness of a nanotube-based technology. Clearly, further field-scale studies must be conducted to determine not only the effectiveness of CNTs but also their potential, the target being to raise the limits currently faced by this technology.

## References

- 1 USEPA US Environmental Protection agency (NPL) (2007) Superfund National Priorities List. <http://www.epa.gov/superfund/sites/npl/index.htm> (accessed 7 January, 2008).
- 2 Raichur, A.M. and Panvekar, V. (2002) *Sep. Sci. Technol.*, **37**, 1095.
- 3 Wasay, S.A., Tokunaga, S. and Park, S.W. (1996) *Sep. Sci. Technol.*, **31**, 1501.
- 4 Pierce, M.L. and Moore, C.B. (1982) *Water Res.*, **16**, 1247.
- 5 Suzuki, T.M., Tanco, M.L. and Tanaka, D.A.P. (2001) *Sep. Sci. Technol.*, **36**, 103.
- 6 Liu, R., Guo, J. and Tang, H. (2002) *J. Colloid Interface Sci.*, **248**, 268.
- 7 Tokunaga, S., Wasay, S.A. and Park, S.W. (1997) *Water Sci. Technol.*, **35**, 71.
- 8 Long, R.Q. and Yang, R.T. (2001) *J. Am. Chem. Soc.*, **123**, 2058.
- 9 Li, Y.H., Wang, S., Wei, J., Zhang, X., Xu, C., Luan, Z., Wu, D. and Wei, B. (2002) *Chem. Phys. Lett.*, **357**, 263.
- 10 Li, Y., Wang, S., Zhang, X., Wei, J., Xu, C., Luan, Z. and Wu, D. (2003) *Mater. Res. Bull.*, **38**, 469.
- 11 Peng, X., Li, L., Di, Z., Wang, H., Tian, B. and Jia, Z. (2003) *Chem. Phys. Lett.*, **376**, 154.
- 12 Lu, C., Chung, Y.L. and Chang, K.F. (2005) *Water Res.*, **39**, 1183.
- 13 Iijima, S. (1991) *Nature*, **354**, 56.
- 14 Dillon, A.C., Jones, K.M., Bekkedahl, T.A., Kiang, C.H., Bethune, D.S. and Heben, M.J. (1997) *Nature*, **386**, 377.
- 15 Maddox, M.W. and Gubbins, K.E. (1995) *Langmuir*, **11**, 2988.
- 16 Maddox, M.W., Sowers, S.L. and Gubbins, K.E. (1996) *Adsorption*, **2**, 23.
- 17 Darkrim, F.L. and Levesque, D.J. (1998) *Chem. Phys.*, **109**, 4981.
- 18 Darkrim, F.L. and Levesque, D. (2000) *J. Chem. Phys.*, **104**, 6773.
- 19 Yan, H., Li, Q., Zhang, J. and Liu, Z. (2004) CVD Synthesis of SWNTs, in *The Chemistry of Nanostructured Materials* (ed. P. Yang), World Scientific Pub, pp. 101–26.
- 20 Colbert, D.T., Zhang, J., McClure, S.M., Nikolaev, P., Chen, Z., Hafner, J.H., Owens, D.W., Kotula, P.G., Carter, C.B., Weaver, J.H., Rinzler, A.G. and Smalley, R.E. (1994) *Science*, **266**, 1218.
- 21 Journet, C. and Bernier, P. (1998) *Appl. Phys. A*, **67**, 1.
- 22 Liu, Y. and Gao, L. (2005) *Carbon*, **1**, 47.
- 23 Ebbesen, T.W. and Ajayan, P.M. (1992) *Nature*, **358**, 220.
- 24 Iijima, S. and Ichihashi, T. (1993) *Nature*, **363**, 603.
- 25 Bethune, D.S., Kiang, C.H., de Vries, M.S., Gorman, G., Savoy, R. and Vazquez, J. (1993) *Nature*, **363**, 605.

- 26 Thess, A., Lee, R., Nikolaev, P., Dai, H., Petit, P., Robert, J., Xu, C., Lee, Y.H., Kim, S.G., Rinzler, A.G., Colbert, D.T., Scuseria, G.E., Tomane'k, D., Fischer, J.E. and Smalley, R.E. (1996) *Science*, **273**, 483.
- 27 Baker, R.T.K. (1989) *Carbon*, **27**, 315.
- 28 Tibbetts, G.G. (1989) *Carbon*, **27**, 745.
- 29 Yacamán, M.J., Yoshida, M.M., Rendon, L. and Santiesteban, J.G. (1993) *Appl. Phys. Lett.*, **62**, 202.
- 30 Ivanov, V., Nagy, J.B., Lambin, P., Lucas, A., Zhang, X.B., Zhang, X.F., Bernaerts, D., Van Tendeloo, G., Amelinckx, S. and Van Landuyt, J. (1994) *Chem. Phys. Lett.*, **223**, 329.
- 31 Amelinckx, S., Zhang, X.B., Bernaerts, D., Zhang, Z.F., Ivanov, V. and Nagy, J.B. (1994) *Science*, **265**, 635.
- 32 Li, W.Z., Xie, S.S., Qian, L.X., Chang, B.H., Zou, B.S., Zhou, W.Y., Zhao, R.A. and Wang, G. (1996) *Science*, **274**, 1701.
- 33 Zhang, L., Li, Z., Tan, Y., Lolli, G., Sakulchaicharoen, N., Requejo, F.G., Mun, B.S. and Resasco, D.E. (2006) *Chem. Mater.*, **18**, 5624.
- 34 Rinzler, A.G., Liu, J., Dai, H., Nikolaev, P., Human, C.B., Rodriguez-Macias, F.J., Boul, P.J., Lu, A.H., Heymann, D., Colbert, D.T., Lee, R.S., Fisher, J.E., Rao, A.M., Eklund, P.C. and Smalley, R.E. (1998) *Appl. Phys. A: Solids Surf.*, **67**, 29.
- 35 Vaccarini, L., Goze, C., Aznar, R., Micholet, V., Journet, C., Bernier, P., Metenier, K., Beghin, F., Gavillet, J. and Loiseau, A.C. (1999) *Sci. Paris*, **327 (IIb)**, 935.
- 36 Popov, V. (2004) *Mater. Sci. Eng. R.*, **43 (3)**, 61.
- 37 Dresselhaus, M.S., Dresselhaus, G. and Eklund, P.C. (1996) *Science of Fullerenes and Carbon Nanotubes*, Academic Press, San Diego, USA.
- 38 Ando, T. (2003) Physics of carbon nanotubes, in *Advances in Solid State Physics*, Vol. 43, Springer, Berlin/Heidelberg, p. 301.
- 39 Dresselhaus, M., Dresselhaus, G. and Saito, R. (1995) *Carbon*, **33 (7)**, 883.
- 40 Collins, P.G. and Avouris, P. (2000) *Sci. Am.*, **283**, 62.
- 41 Hamada, N., Sawada, S. and Oshiyama, A. (1992) *Phys. Rev. Lett.*, **68**, 1579.
- 42 Yang, Q.H., Hou, P.X., Bai, S., Wang, M.Z. and Cheng, H.M. (2001) *Chem. Phys. Lett.*, **345**, 18.
- 43 Inoue, S., Ichikuni, N., Suzuki, T., Uematsu, T. and Kaneko, K. (1998) *J. Chem. Phys.*, **102**, 4689.
- 44 Eswaramoorthy, M., Sen, R. and Rao, C.N.R. (2005) *Chem. Phys. Lett.*, **304**, 207.
- 45 Peigney, A., Laurent, C., Flahaut, E., Bacs, R.R. and Rousset, A. (2001) *Carbon*, **39**, 507.
- 46 Kuznetsova, A., Mawhinney, D.B., Naumenko, V., Yates, J.T. and Smalley, R.E. (2000) *Chem. Phys. Lett.*, **321**, 292.
- 47 Frackowiak, E., Delpeux, S., Jurewicz, K., Szostak, K., Cazorla-Amorou, D. and Beguin, F. (2002) *Chem. Phys. Lett.*, **336**, 35.
- 48 Raymundo, E.P., Azais, P., Cacciaguerra, T., Amorou, D.C., Solano, A.L. and Beguin, F. (2005) *Carbon*, **43**, 786.
- 49 Delpeux, S., Szostak, K., Frackowiak, E. and Beguin, F. (2005) *Chem. Phys. Lett.*, **404**, 374.
- 50 Vermisoglou, E.C., Georgakilas, V., Kouvelos, E., Pilatos, G., Viras, K., Romanos, G. and Kanellopoulos, N.K. (2007) *Microporous Mesoporous Mater.*, **99**, 98.
- 51 Yu, S., Ai, Z., Yin, Y., Yu, D., Cui, C., Zhang, X. and Hong, J. (2007) *Mater. Chem. Phys.*, **101**, 30.
- 52 Li, Y.H., Wang, S., Cao, A., Zhao, D., Zhang, X., Xu, C., Luan, A., Ruan, D., Liang, J., Wu, D. and Wei, B. (2001) *Chem. Phys. Lett.*, **350**, 412.
- 53 Kongdratyuk, P. and Yates, J.T. (2004) *Chem. Phys. Lett.*, **383**, 314.
- 54 Anastasios, I., Skoulidas, D., Sholl, J. and Karl, J. (2006) *J. Chem. Phys.*, **124**, 47.
- 55 Byl, O., Kondratyuk, P. and Yates, J.T. (2003) *J. Phys. Chem. B*, **107**, 4277.
- 56 Díaz, E., Ordóñez, S. and Vega, A. (2007) *J. Colloid Interface Sci.*, **305**, 7.
- 57 Friberg, L., Nordberg, G.F. and Vouk, B. (1979) *Handbook on the Toxicology of Metals*, Elsevier, Amsterdam.
- 58 Chen, C. and Wang, X. (2006) *Ind. Eng. Chem. Res.*, **45**, 9144.
- 59 Dabrowski, A. (2001) *J. Colloid Interface Sci.*, **93**, 135.
- 60 Calderon, J., Navarro, M.E., Jimenez-Capdeville, M.E., Santos-Diaz, M.A., Golden, A., Rodriguez-Leyva, I.,

- Borja-Aburato, V. and Diaz-Brriga, F. (2001) *Environ. Res.*, **85**, 69.
- 61 Denizli, A., Buyuktuncel, E., Tuncel, A., Bektas, S. and Genc, O. (2000) *Environ. Technol.*, **21**, 609.
- 62 Li, Y.H., Di, Z., Ding, J., Wu, D., Luan, Z. and Zhu, Y. (2005) *Water Res.*, **39**, 605.
- 63 Li, Y., Zhu, Y., Zhao, Y., Wu, D. and Luan, Z. (2006) *Diamond Relat. Mater.*, **15**, 90–4.
- 64 Katz, S.A. and Salem, H. (2006) *J. Appl. Toxicol.*, **13**, 217.
- 65 Di, Z.C., Li, Y., Luan, Z. and Liang, J. (2004) *Adsorpt. Sci. Technol.*, **22**, 6.
- 66 Di, Z.C., Ding, J., Peng, X.-J., Li, Y.-H., Luan, Z.-K. and Liang, J. (2006) *Chemosphere*, **62**, 861.
- 67 Mohan, D. and Singh, K.P. (2002) *Carbon*, **36**, 2304.
- 68 Li, Y., Wang, S., Luan, Z., Ding, J., Xu, C. and Wu, D. (2003) *Carbon*, **41**, 1057.
- 69 Toles, C.A., Marshall, W.E. and Johns, M.M. (1999) *Carbon*, **37**, 1207.
- 70 Wu, C.H. (2007) *J. Colloid Interface Sci.*, **311**, 338.
- 71 Rainbow, P.S., Hopkin, S.P. and Crane, M. (2001) *Forecasting the Environmental Fate and Effects of Chemicals*, John Wiley & Sons, Inc., New York.
- 72 Lu, C. and Chiu, H. (2006) *Chem. Eng. Sci.*, **61**, 1138.
- 73 Lu, C., Chiu, H. and Liu, C. (2006) *Ind. Eng. Chem. Res.*, **45**, 2850.
- 74 Kadirvelu, K., Senthilkumar, P., Thamaraiselvi, K. and Subburam, V. (2002) *Bioresour. Technol.*, **81**, 87.
- 75 Lu, C. and Liu, C. (2006) *Chem. Technol.*, **81**, 1932.
- 76 Li, Y., Ding, J., Luan, Z., Di, Z., Zhu, Y. and Xu, C. (2003) *Carbon*, **41**, 2787.
- 77 Hsieh, S.H., Horng, J.-J. and Tsai, C.-K. (2006) *J. Mater. Res.*, **5**, 1269.
- 78 Peng, X., Luan, Z., Di, Z., Zhang, Z. and Zhu, C. (2005) *Carbon*, **43**, 855.
- 79 Hichour, M., Persin, F., Molenat, J., Sandeaux, J. and Gavach, C. (1999) *Desalination*, **122**, 53.
- 80 Hichour, M., Persin, F., Sandeaux, J. and Gavach, C. (2000) *Sep. Purif. Technol.*, **18**, 1.
- 81 Bishop, P.L. and Sansoucy, G. (1978) *J. Am. Water Works Assoc.*, **70**, 554.
- 82 Buchanan, W.D. (1962) *Toxicity of Arsenic Compounds*, Amsterdam, New York.
- 83 Peng, X., Luan, Z., Ding, J., Di, Z., Li, Y. and Tian, B. (2005) *Mater. Lett.*, **59**, 399.
- 84 Zhang, Z., Liu, L., Zhao, H. et al. (1996) *J. Colloid Interface Sci.*, **182**, 158.
- 85 Wang, X., Chen, C., Hu, W., Ding, P., Xu, D. and Zhou, X. (2005) *Environ. Sci. Technol.*, **39**, 2856.
- 86 National Primary Drinking Water Regulations, U.S. Environmental Protection Agency 816-F-03-016, June 2003. <http://www.epa.gov/safewater/contaminants/index.html#listmcl>.
- 87 Hileman, B. (2000) *Chem. Eng. News*, **29**, 13.
- 88 Yang, R.T., Long, R.Q., Padin, J., Takahashi, A. and Takahashi, T. (1999) *Ind. Eng. Chem. Res.*, **38**, 2726.
- 89 Kang, H.S. (2005) *J. Am. Chem. Soc.*, **127**, 9839.
- 90 Fagan, S.B., Santos, E.J., Filho, A.G., Filho, J.M. and Fazzio, A. (2007) *Chem. Phys. Lett.*, **437**, 79.
- 91 Roberge, F., Gravel, M.J., Deschenes, L., Guy, C. and Samson, R. (2001) *Water Sci. Technol.*, **44**, 287.
- 92 Hill, G.A., Tomusiak, M.E., Quail, B. and Cleave, K.M.V. (1991) *Environ. Prog.*, **10**, 147.
- 93 Fagan, S.B., Gira, E.C., Mendesfilho, O.J. and Souzafilho, A.G. (2006) *Int. J. Quantum Chem.*, **106**, 2558.
- 94 Rook, J.J. (1974) *Water Treatment Exam.*, **23**, 234.
- 95 Bull, R.J., Brinbaum, L.S., Cantor, K.P., Rose, J.B., Butterworth, B.E., Pegram, R. and Tuomisto, J. (1995) *J. Fundam. Appl. Toxicol.*, **28**, 155.
- 96 Lu, C., Chung, Y. and Chang, K. (2006) *J. Hazard. Mater.*, **138**, 304.
- 97 Yang, K., Zhu, L. and Xing, B. (2006) *Environ. Sci. Technol.*, **40**, 1855.



## 20

# Molecular Imprinting with Nanomaterials

*Kevin Flavin and Marina Resmini*

### 20.1

#### Introduction

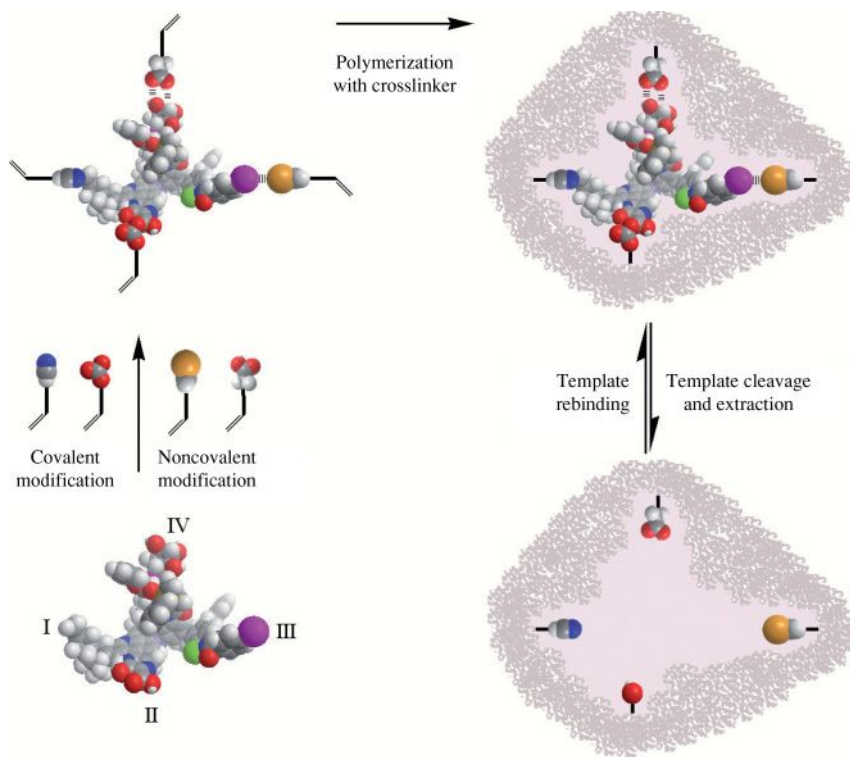
Molecular recognition plays a key role in the natural world, from DNA transcription to immune responses and enzyme substrate recognition. Important biological processes depend on the capability of small molecules to recognize their targets in a selective and efficient manner. During the past century, a great deal of research was performed involving molecular recognition, not only to further our comprehension of its role in biological processes but also to translate any findings to practical applications. The design of artificial receptors, capable of selective molecular recognition, has been a goal of research groups in different disciplines for use in a variety of processes such as catalysis, sensing, biological assaying, and the separation of complex chemical mixtures.

One interesting approach for the development of artificial receptors is molecular imprinting, and its application to polymeric materials. In this chapter we will discuss the concept of molecular imprinting, and highlight recent advances in the synthesis of molecularly imprinted polymers (MIPs) on the nanoscale. Included will be methodologies for the preparation of nanoparticles, with a view to a more rational and commercially viable receptor design, and imprinting methodologies which utilize various other nanomaterials, such as nanowires, quantum dots, fullerene, and dendrimers. The applications of these imprinted nanomaterials will be discussed, highlighting those properties which are advantageous to each application, together with details of the changes that will be needed in future in order to maintain the practical potential of molecular imprinting.

#### 20.1.1

##### Molecular Imprinting: The Concept

Molecular imprinting is a process where functional and crosslinking monomers are copolymerized in the presence of the target analyte (the imprint molecule), which acts as a molecular template [1]. The functional monomers initially form a



**Figure 20.1** Schematic representation of the imprinting process showing some of the interactions used in creating affinity in the binding site for the template. I, reversible covalent interaction; II, semicovalent method; III, electrostatic interaction with an oppositely charged monomer; IV, noncovalent H-bonding.

complex with the imprint molecule and, following polymerization, their functional groups are held in position by the highly crosslinked polymeric structure. Upon removal of the imprint molecule, a cavity or recognition site is created which is complementary to the original template used. A molecular memory is therefore created in the polymeric matrix, which is now capable of recognizing and rebinding the analyte with a very high specificity. The interaction between the template and the functional monomers can be either covalent, noncovalent, or combinations of both, and the choice is largely dependent on the chemical structure of both the template and monomers, and the intended application (Figure 20.1).

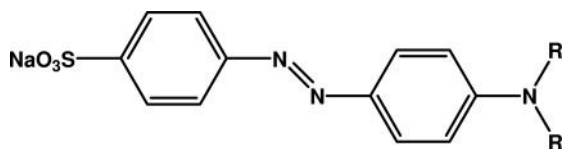
The evolution of molecular imprinting, as a technique, will be briefly discussed in the following sections, together with descriptions of some of the chemical strategies utilized for molecular imprinting, in terms of imprint molecule–monomer interactions.

### 20.1.1.1 History of Molecular Imprinting

Towards the beginning of the last century, much effort was devoted to the development of new materials and techniques for applications in chromatography [2]. Among many of those scientists active in this field was the soviet chemist M.V. Polyakov, who reported unexpected absorption properties in silica particles prepared by a novel synthetic procedure [3]. Silica prepared, in the presence of benzene, toluene or xylene, was observed to selectively reabsorb the additive present during the preparation [4, 5]. This appears to be the first point in the literature at which selective adsorption to polymeric materials had been observed and explained in terms of a template effect [6].

During the following decade, Pauling developed a theory of the structure and process of formation of antibodies that laid the foundations for the development of molecular imprinting [7]. Dickey, in 1949, reported the preparation of silica gel, having specific affinities for their predetermined substrates, using the same mechanistic approach described by Pauling [8]. Silica gels were prepared in the presence of four different dyes, namely methyl-, ethyl-, *n*-propyl- and *n*-butyl orange (Figure 20.2). The dye was subsequently removed and in rebinding experiments the presence of any of these “pattern molecules” would bind the pattern molecule in preference to the other three dyes. Several research groups pursued the preparation of specific adsorbents utilizing Dickey’s method [9, 10]. After a steady flow of publications for 15 years, interest in imprinted silica materials experienced a decline as a result of limitations in the stability of these preparations and the reproducibility of the results obtained [2].

The decline in research into imprinting with silica coincided with the publication of a report by Wulff and Sarhan in 1972, on the first example of molecular imprinting in synthetic organic polymers [11]. This report has been accredited with stemming the current interest in imprinted materials as artificial antibodies. By utilizing a covalent imprinting approach, Wulff and Sarhan succeeded in preparing polymers with chiral cavities for the separation of racemic mixtures. Research with imprinted materials accelerated when Mosbach *et al.* introduced a simpler synthetic approach, which utilized noncovalent interactions of the “template” species with the functional monomers [12]. At present, research groups worldwide are focusing attention on the preparation of novel imprinted polymers and new analytical and synthetic applications of molecularly imprinted materials. In the following sections, we describe the covalent and noncovalent imprinting approaches initially reported by Wulff and Mosbach, respectively, which are



**R = methyl, ethyl, *n*-propyl, *n*-butyl**

**Figure 20.2** Chemical structures of the alkyl orange dyes.



widely accredited to be the foundation for the field of molecular imprinting, as it is known today.

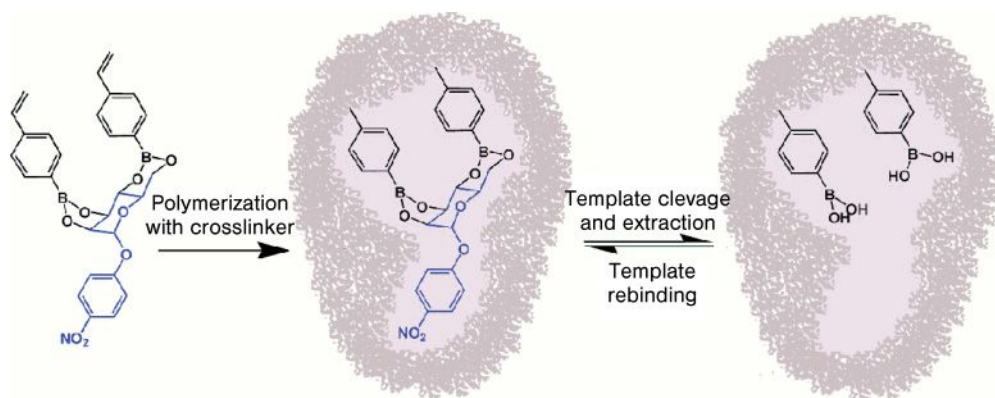
### 20.1.1.2 Covalent Imprinting

In the covalent imprinting strategy, the key step is the formation of a reversible covalent bond between the template and the functional monomer. After polymerization the template is removed, leaving the binding site with the functional group available for further covalent rebinding. Wulff utilized the reversible formation of boronate ester-linkages very successfully, initially for the imprinting of glyceric acid [11], and later for a number of carbohydrate derivatives [13, 14]. In one example, Wulff described the imprinting of a sugar (phenyl- $\alpha$ -D-mannopyranoside) which was coupled with a vinyl-derivatized phenylboronic acid [13]. The template monomer, illustrated in Figure 20.3, was polymerized by free radical initiation in the presence of a porogenic solvent and a large amount of crosslinking agent. The template was subsequently removed through hydrolysis with water or methanol, resulting in a template specific cavity.

The major advantage of the covalent approach is that the high-energy interactions will lead to high association constants, and therefore increase template recognition and reduce nonspecific binding between the template and polymer. Although, covalent strategies have been used successfully with boronate esters [13], Schiff's bases (imines) [15], ketals and acetals [16], only certain compounds such as alcohols, aldehydes, ketones, amines and carboxylic acids can be imprinted using this approach. Moreover, the synthetic difficulties associated with the preparation of a suitable polymerizable unit limit the applicability of this approach.

### 20.1.1.3 Noncovalent Imprinting

Currently, the most widely used technique to generate molecularly imprinted binding sites is represented by the noncovalent approach developed by Mosbach

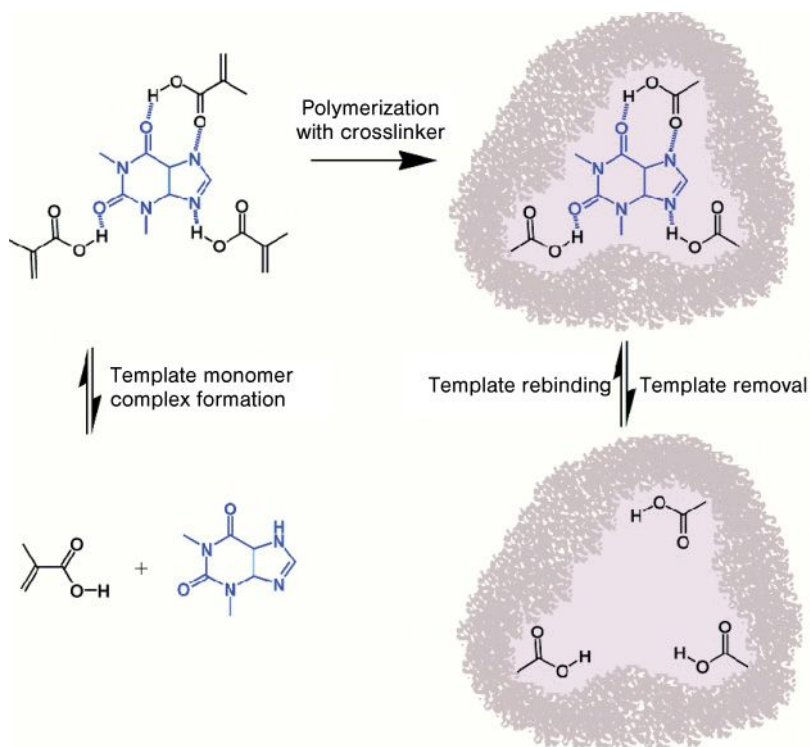


**Figure 20.3** Schematic representation of a covalent imprinting approach, using a sugar coupled with a vinyl-derivatized phenylboronic acid [13].

[17]. This is based on a noncovalent self-assembly of the template with functional monomers prior to polymerization with a crosslinking monomer and subsequent template extraction, followed by rebinding via noncovalent interactions, such as H-bonding, ion pairing, and dipole–dipole interactions. The most widely used functional monomer for noncovalent imprinting is methacrylic acid (MAA), which was initially proposed by Mosbach *et al.* [18]; however, many other functional monomers, such as 4-vinylpyridine [19] and acrylamide [20] are commercially available. A number of custom-designed functional monomers, such as *N,N'*-diethyl(4-vinylphenyl)amidine [21], for use in catalysis, and *trans*-4-[*p*-(*N,N*-Dimethylamino)styryl]-*N*-vinylbenzylpyridinium chloride [22], used for fluorescent sensing, have also been reported.

Figure 20.4 illustrates the well-known noncovalent imprinting strategy of theophylline using MAA as the functional monomer and ethylene glycol dimethacrylate as the crosslinker [23].

The monomer–template association complex can be obtained *in situ* simply by adding the components to the reaction mixture. After polymerization, the template is removed by extracting the polymer with acidified methanol. The guest binding



**Figure 20.4** Noncovalent imprinting of theophylline, using methacrylic acid as the functional monomer and ethylene glycol dimethacrylate as the crosslinker [23].

by the polymer occurs through the corresponding noncovalent interactions. The carboxylic acid function of the methyl methacrylate forms ionic interactions with the amino groups and hydrogen bonds with polar functions. Dipole–dipole and hydrophobic interactions are also thought to contribute.

The advantages of the noncovalent strategy are that the synthesis of covalent monomer–template conjugates is unnecessary, and that the imprint molecule is easily removed from the polymer under very mild conditions, as it is only weakly bound by noncovalent interactions. Also, guest binding and guest release via noncovalent interactions result in faster binding kinetics than occur in the covalent approach. The main disadvantages are that the imprinting process may not be very efficient, as the monomer–template adduct is labile and not strictly stoichiometric. In order to overcome these limitations, the polymerization conditions must be carefully chosen so as to maximize noncovalent adduct formation in the mixtures.

#### 20.1.1.4 Alternative Molecular Imprinting Approaches

The two most extensively used strategies for molecular imprinting have been the noncovalent and covalent approaches, respectively. However, a number of variations of these methods have been investigated in recent years, with the intention of overcoming the disadvantages inherent in each approach. One such strategy employs the stoichiometric noncovalent approach [24], in which the complex between the functional monomer and template is strong enough to ensure that the equilibrium lies well in favor of complex formation; this can be achieved when the association constant is  $\geq 10^3 M^{-1}$  [25]. Semicovalent imprinting is another frequently used strategy, which attempts to merge the advantages of the covalent and the noncovalent approach. In this method, the template is bound covalently to the functional monomer, either directly [26] or via a spacer [27]; however, rebinding occurs via noncovalent interactions only.

### 20.1.2

#### Towards Imprinting with Nanomaterials

The final application of a target-imprinted polymer plays a key role in determining the type of polymeric matrix to be used. Since the first report of an example of molecular imprinting, “bulk” polymerization has been the most frequently used method for the production of MIPs. However, in this method the “bulk” material must be ground mechanically, which results in a large size distribution of irregularly shaped particles and sieved; this is not only time-consuming but can also result in a substantial loss of material. Considerable advances have been made over the past decade, in the basic methodologies available for the production of receptor sites, and in the optimization of conditions for imprinting and subsequent rebinding [28]. In order to avoid the disadvantages associated with “bulk” polymerization, alternative polymeric materials have been used, for example, imprinted microbeads, films, and membranes [28, 29]. In the case of beads that are designed for chromatographic purposes, particle diameters of 25–38  $\mu\text{m}$  are

suitable for efficient separation with reasonable back-pressures [30]. However, when considering MIPs intended for catalysis, facilitated synthesis, sensing and assaying, a progression from the micro- to the nanoscale has been a major aim of many research groups. Aside from the obvious advantages that miniaturization presents, good accessibility to as many recognition sites as possible and shorter diffusion times to facilitate faster equilibrium between release and reuptake of the template in the cavity, are central to requirements [31]. Ultimately, improvements in the efficiency of synthetic receptors, with respect to response times and reaction rates, may depend on how closely the actual biological systems can be mimicked. To do so would require significant developments of MIPs on the nanoscale.

## 20.2 Molecular Imprinting in Nanoparticles

A variety of approaches for preparing imprinted particles in the nanometer size range have proved successful. In this section we will review the various approaches, and highlight recent developments and important applications.

### 20.2.1

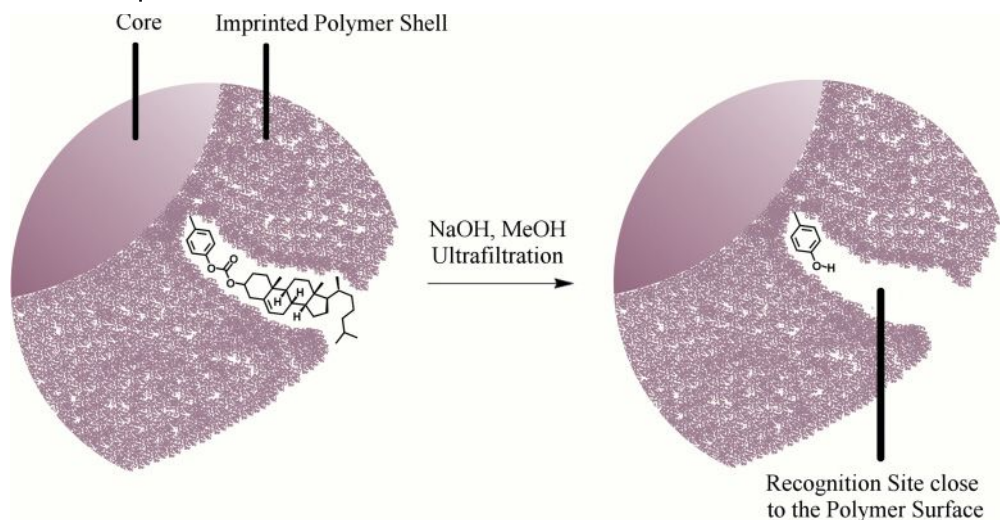
#### Emulsion Polymerization

The first reported synthesis of imprinted nanoparticles was over a decade ago by Takagi and coworkers [32], who successfully prepared a  $\text{Cu}^{2+}$ -selective resin using a novel template polymerization technique. Here, the target molecule (hydrophilic) and the host–monomer (amphiphilic) approach and arrange themselves at the interface of an oil-in-water emulsion. The oil phase, containing the monomer and crosslinker, was subsequently polymerized, the result being a resin with particle sizes ranging from 400 to 500 nm. Although standard emulsion polymerization has proved successful for molecular imprinting in nanoparticles [32–34], core–shell emulsion polymerization is probably a more useful approach, as it enables a much better control over particle size, polydispersity, and the location of recognition sites.

##### 20.2.1.1 Core–Shell Emulsion Polymerization

Core–shell emulsion polymerization consists of two steps that begin with the preparation of a core latex in the absence of an emulsifier. The core, which may be prepared from a variety of materials [35–37], is then mixed with another monomer or mixture of monomers that produces the shell. The core–shell particles possess two types of property, one being endowed by the core (spherical monodisperse nanoparticles) and the other by the shell (recognition layer).

Pérez *et al.* reported the synthesis of core–shell particles, in which a sacrificial spacer method was used, for the imprinting of cholesterol [38]. Initially, 30–40 nm MMA or styrene core particles were prepared, which were subsequently used in a second-stage polymerization with ethyleneglycol dimethacrylate (EGDMA), in

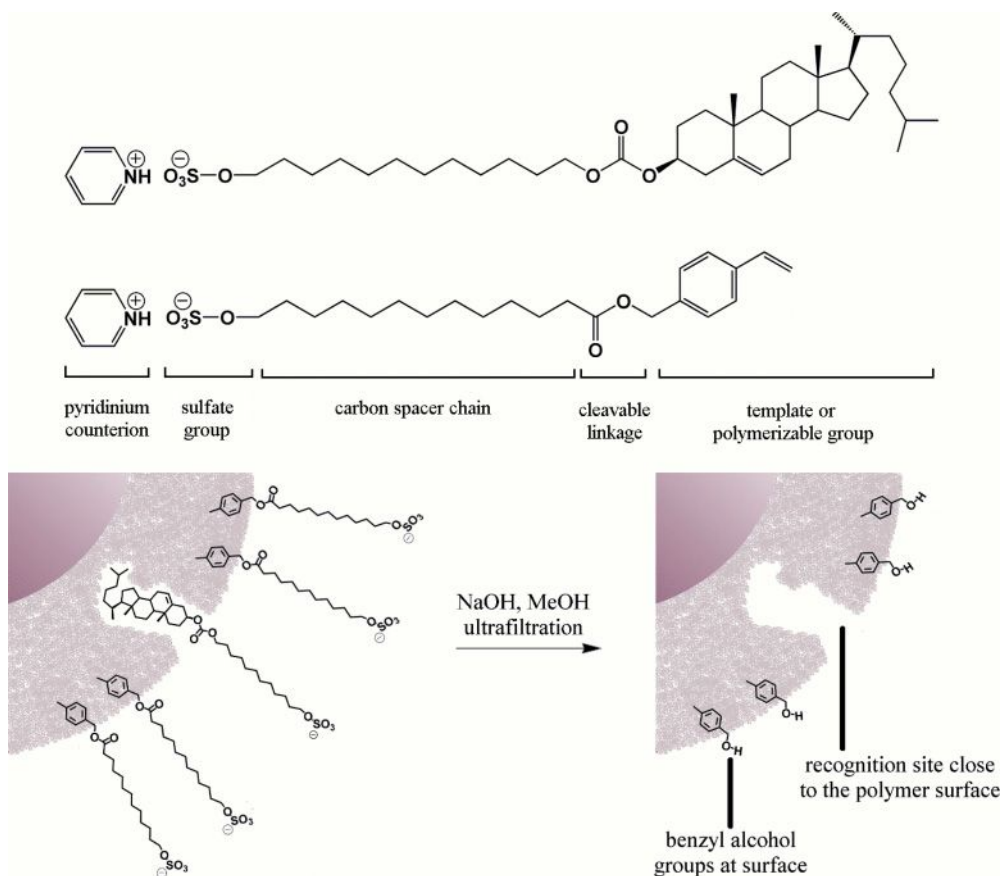


**Figure 20.5** Schematic diagram of core–shell nanoparticles with cholesterol-imprinted shells Adapted from Ref. [38].

the presence of a polymerizable cholesterol derivative (Figure 20.5). Following template cleavage (carbonate ester hydrolysis) and removal, the recognition properties of the imprinted core–shell polymers were evaluated.

On comparison of the imprinted and nonimprinted polymers, a considerably greater binding of cholesterol to the imprinted core–shells was evident. Similar imprinted nanoparticles were also prepared with a magnetic core, which demonstrated similar cholesterol rebinding properties to those particles prepared with nonmagnetic cores; however, in the presence of a magnetic field, a more efficient particle sedimentation—and thus removal from solution—was demonstrated. Subsequently, Pérez *et al.* reported the preparation of imprinted nanoparticles characterized by a poly(divinylbenzene) shell over a crosslinked poly(styrene) core [39]. In this case, the second-stage polymerization was performed in the presence of polymerizable surfactants (pyridinium 12-(4-vinylbenzyloxycarbonyl)dodecanesulfate (PS) and pyridinium 12-(cholesteryloxycarbonyloxy)dodecanesulfate (TS), that also acted as a template. Figure 20.6 illustrates the noncovalent imprinting approach used, where the surfactant-like template aligns itself at the polymer–water interface with the template region in the monomer phase. Following polymerization of the monomer phase, template removal creates hydrophobic recognition sites at the surface of the beads. As the polymerized surfactant tails are also hydrolyzed, a polar surface is exposed which differentiates it from the imprinted regions.

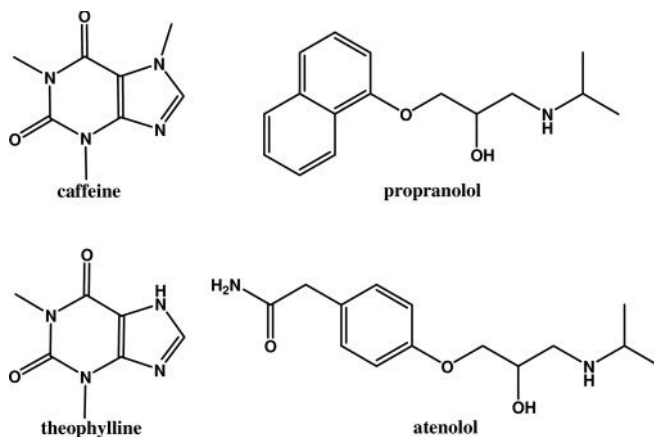
Pérez and Mayes subsequently reported the successful imprinting of propranolol by the more classical noncovalent approach in core–shell nanoparticles [40]. Although, the binding capacity was lower than that usually measured for bulk polymers imprinted with propranolol, this investigation proved that noncovalent imprinting in core–shell particles was possible, despite the fact that they were



**Figure 20.6** Schematic diagram of core-shell nanoparticles with cholesterol-imprinted shells accompanied by structures of the template surfactant and the polymerizable surfactant. Adapted from Ref. [38].

prepared in the presence of an aqueous continuous phase. The same group later reported the synthesis of similar propranolol-imprinted nanoparticles, where a fluorescent monomer was successfully incorporated into the particle core [41]. The presence of the imprinted shell had no effect on the fluorescence of the core; neither did the fluorescent monomer in the core affect the imprinting in the shell. This type of particle would be expected to find applications in assay technology.

Carter and Rimmer also used core-shell emulsion polymerization for the non-covalent imprinting of caffeine and propranolol [42–44]. The application of these nanoparticles is for the selective extraction of caffeine/propranolol from mixtures with a structural analogue theophylline/atenolol (Figure 20.7) [44]. Particles were prepared with a styrene/divinylbenzene core, and ranged in diameter from 180 to 214 nm. The shell was prepared with a mixture of EGDMA and binding monomer



**Figure 20.7** Chemical structures of template molecules (caffeine and propranolol) and their structural analogues (theophylline and atenolol).

(oley phenyl hydrogen phosphate) in the presence of template, and displayed thickness ranging from 2 to 20 nm.

#### 20.2.1.2 Mini-Emulsion Polymerization

A *mini-emulsion* is a type of emulsion, where the monomer droplet size is reduced to the range of 50 to 300 nm diameter by the application of sheer forces (ultrasonication or high-pressure homogenization) [45]. In order to stabilize the homogeneous dispersed phase, a costabilizer is added to prevent diffusion processes from occurring in the continuous phase. This in turn inhibits the occurrence of Ostwald ripening during the polymerization process. The main difference between emulsion and mini-emulsion polymerization is the solubility of the initiator. In mini-emulsion polymerization the initiator is only soluble in the dispersed phase, as opposed to emulsion polymerization where the initiator is soluble in the continuous phase [46]. Nucleation, as a consequence, occurs within the dispersed nanodroplets creating small “nanoreactors,” with the monomer and template already present at the start of the polymerization.

Tovar and coworkers have mainly used this method to prepare imprinted nanoparticles [47–50]. Initially, they produced nanoparticles (yield of  $98 \pm 2\%$ ) from varying ratios of EGDMA and MAA, imprinted with enantiomers of boc-phenylalanine anilide [47]. Although dynamic light scattering (DLS) indicated a particle diameter of  $200 \pm 20$  nm, transmission electron microscopy (TEM) verified a much larger polydispersity with particles ranging from 50 to 300 nm. During recognition studies, the quantity of L-boc-phenylalanine anilide that rebound was fourfold greater in the case of an L-imprinted MIP than in the corresponding NIP, and 10-fold greater than the binding of the D-enantiomer in the L-imprinted nanoparticles. This imprinting system was subsequently used to demonstrate the use of microcalorimetry, to monitor the heat of binding during rebinding experiments



with the nanoparticles, and to demonstrate the enthalpic basis of chiral recognition in molecularly imprinted polymers [48].

The imprinted nanoparticles produced by Tovar and coworkers were later used for the separation of enantiomers. Using the mini-emulsion approach, the imprinted nanoparticles were coated onto the surface of a polyamide membrane for enantiomeric separation [49]. The dense particle layer on the surface of the membrane resulted in a large imprinted surface area and a low flow rate, which was advantageous as the establishment of the chemical equilibrium due to selective rebinding is a time-consuming step. Adsorption experiments and binding isotherms were subsequently performed in order to establish a new mathematical model for the understanding and describing of the whole separation process by the composite membrane [50]. According to the authors, this should allow prediction of the most favorable configuration for the imprinted composite membrane, and thus allow an optimal performance.

More recently, Tan and Tong have attempted the imprinting of the protein ribonuclease A using mini-emulsion polymerization [51, 52]. In these studies, the preparation of protein surface-imprinted nanoparticles was described, with diameters ranging from approximately 40 to 80 nm. The major difficulty with the imprinting of proteins was optimization of the polymerization conditions in order to avoid protein denaturation [51]. Although, the high-shear homogenization demonstrated negligible disruption to the protein conformation, the initiators and the surfactants frequently used for mini-emulsion polymerization were singled out as possible sources of template denaturation, and suitable conditions were therefore investigated. The imprinted nanoparticles prepared under optimized, nondenaturing conditions (using a redox initiator and poly(vinyl alcohol) as surfactant) displayed a good imprinting efficiency that was absent from the imprinted polymer prepared through the conventional mini-emulsion polymerization using thermal or UV initiation and sodium dodecylsulfate as surfactant.

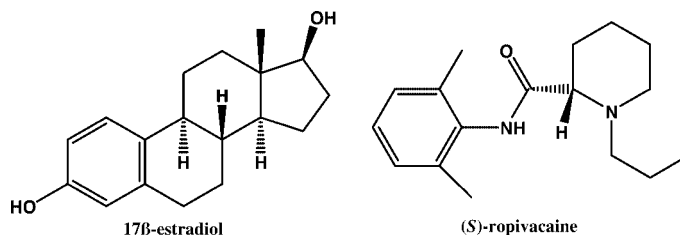
Tan and Tong also used a variation of this approach, where mini-emulsion polymerization was used in a core-shell approach [52]. In this case, larger particles of regular shape and 700–800 nm diameter were produced, which comprised a  $\text{Fe}_3\text{O}_4$  magnetite core and a surface-imprinted shell. The imprinted particles exhibited significant recognition and selectivity from aqueous solution, in addition to easy and efficient particle separation as a result of the magnetic core being present.

### 20.2.2

#### **Precipitation Polymerization**

In precipitation polymerization—unlike emulsion methods—the polymeric reaction begins in a homogeneous phase where the monomers, crosslinkers, and initiators are present in a dilute solution of porogenic solvent. As the polymerization proceeds, the expanding polymer becomes insoluble and aggregates into particles, which are stabilized against coagulation, either sterically or by their rigid crosslinked surfaces. Dispersion polymerization is another method for obtaining polymeric materials. Although the technique shows some differences





**Figure 20.8** Chemical structures of 17β-estradiol and (S)-ropivacaine.

from precipitation polymerization, these are not significant enough to justify discrimination between the two in the context of this chapter. More detailed information on this subject is available elsewhere, however [28, 46, 53].

The first reported synthesis of imprinted nanoparticles by precipitation polymerization was by Mosbach and coworkers [54]. In these studies, MAA and trimethylolpropane trimethacrylate (TRIM) were polymerized at high dilution in the presence theophylline and 17β-estradiol (Figure 20.8). These templates were chosen to demonstrate the applicability of the method toward targets with very different hydrophobicities. Imprinted nanoparticles, with yields of >85% and an average diameter of 300 nm, were isolated by centrifugation of the polymerization solution. Following template removal, the recognition properties were characterized using a radioligand-binding assay; the binding specificity of the polymers was found to be extremely high, with <1% crossreactivity between the two target molecules. Although, the imprinted nanoparticles bound three to four times more template than the corresponding reference material, a sixfold amount of imprinted polymer was necessary for effective absorption of the more hydrophobic template (17β-estradiol) in comparison with theophylline. This effect was, however, the result of a lower affinity constant between 17β-estradiol and the polymer when rebinding in an organic solvent.

The same group also studied the effect of crosslinker type and content on the preparation of imprinted nanoparticles by precipitation polymerization [55]. The results showed that nanoparticles prepared with TRIM (with three crosslinking vinyl groups) rather than with EGDMA (two crosslinking vinyl groups) allowed the incorporation of greater amounts of template and functional monomer, without compromising the rigidity of the particles. These polymers demonstrated higher load capacities, as a result of the increased amounts of functional monomer, but without any loss of specificity due to insufficient crosslinking. More recently, Ye and coworkers studied new synthetic conditions to obtain imprinted beads with controllable size in the nanometer to micrometer range [56]. A variation of particle size, while maintaining good recognition properties, was achieved by altering the ratio of the two different crosslinking monomers, in essentially the same precipitation polymerization system.

### 20.2.2.1 Applications and Variations

By using the precipitation method of imprinted nanoparticle formation, Ye and coworkers developed a new sensing approach using molecular imprinting and

proximity scintillation [57, 58]. The imprinting of (*S*)-propranolol was performed in the presence of a scintillation monomer, which fluoresces in the proximity of tritium-labeled target molecules. The authors showed that an enantioselective competitive binding assay was possible, without removal of the unbound ligand present in solution.

Nanoparticles produced by precipitation polymerization have also been used for various other applications, including the separation of enantiomers. Spégel *et al.* described the preparation of nanoparticles, which were used for separations in capillary electrochromatography [59, 60]. Two approaches for the preparation of the imprinted nanoparticles were used. The first was based on the mixing of two types of imprinted nanoparticle [(*S*)-propranolol and (*S*)-ropivacaine; Figure 20.8], while the second was based on the incorporation of two different templates during the preparation of imprinted nanoparticles. The imprinted nanoparticles were suspended in solutions of analyte, and both approaches resulted in a separation of the propranolol and ropivacaine enantiomers in one single chromatographic run.[60]

Zhu *et al.* also used the precipitation approach for the synthesis of 17 $\beta$ -estradiol-imprinted nanoparticles for use in chromatographic separations (high-performance liquid chromatography; HPLC) [61]. The functional monomer used in this case was 2-(trifluoromethyl)acrylic acid, and particles were obtained in the range of 300 to 1500 nm. The imprinted polymers, when packed into a column, demonstrated the separation of  $\alpha$ - and  $\beta$ -estradiol. Unfortunately, the report did not include any discussion of the general applicability of nanoparticles to HPLC, and the their implications in terms of flow rates and pressures.

Ciardelli and coworkers described the preparation of theophylline-imprinted nanospheres, with a view to developing materials with combined properties of drug delivery and rebinding, for clinical applications [62]. The result was that, by varying the percentage of MAA and MMA (methyl methacrylate) monomers, the properties of release and recognition of print molecules could be modulated. In subsequent investigations, the same group investigated an innovative approach to increase the binding and selective behavior of imprinted nanoparticles in aqueous media [63–65]. The recognition factor for theophylline and caffeine in physiological solution were found to be increased substantially when the imprinted nanoparticles were immobilized in an acrylic membrane [63]. It was suggested by the authors that the membrane had created a microenvironment that enhanced the affinity of the analyte for the imprinted nanosphere.

In a similar approach, as an alternative to incorporating the imprinted nanoparticles into a membrane, Ye *et al.* encapsulated within the polymer nanofibers that had been produced using an electrospinning technique [66]. The imprinted nanoparticles initially obtained were dissolved in dichloromethane with poly(ethylene terephthalate) (PET), which formed the matrix of the nanofiber. This solution was spun at high voltage to produce nanofibers with an average diameter of 150–300 nm. More recently, Ye and colleagues described an alternative precipitation method to prepare imprinted nanoparticles in the absence of organic solvents [67]. Using this approach, the noncovalent imprinting of propranolol was demonstrated under high-dilution conditions in supercritical carbon dioxide. The overall binding

performance of the imprinted nanoparticles was comparable to that of imprinted polymers prepared in conventional organic solvents.

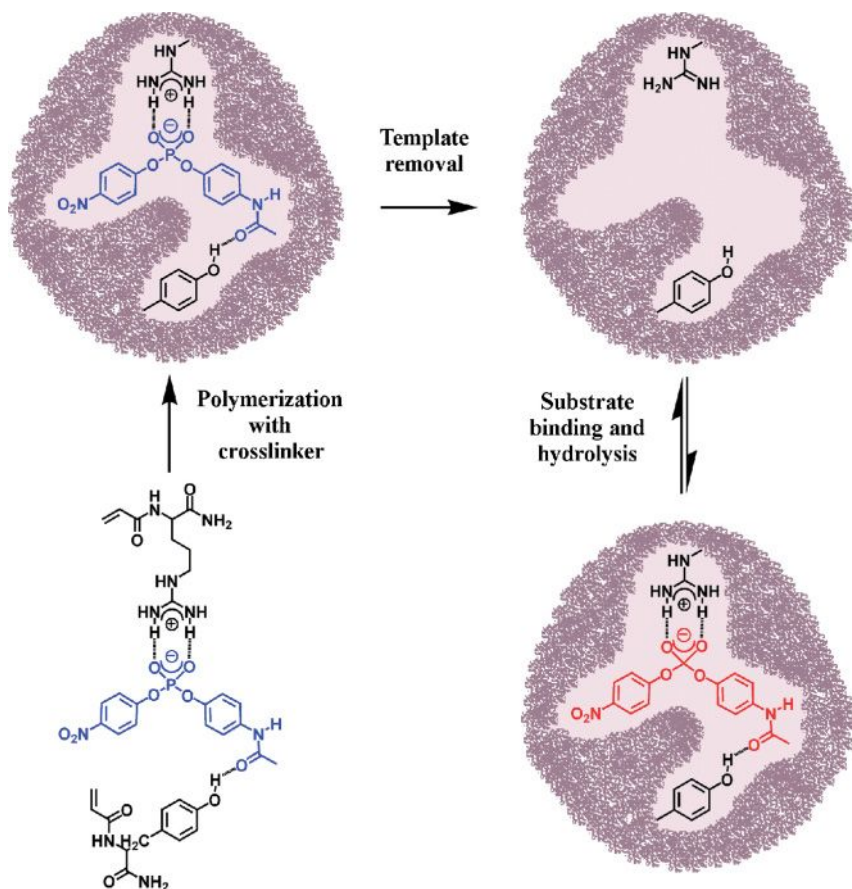
#### 20.2.2.2 Microgel/Nanogel Polymerization

Precipitation polymerization can be optimized to produce microgels and/or nanogels in the size range of 10 to 600 nm [68]. One characteristic of microgels/nanogels is that they are prepared in a suitable solvent system, based on solubility parameters, and produce a low-viscosity colloidal solution that never reaches the point of precipitation. The molecular mass may be varied in a simple, controllable manner from the low thousands (nanogels) to many millions (microgels), simply by the choice of concentration at which they are prepared. A number of research groups have recently shown interest in imprinting in microgels/nanogels given their unique properties, including their solubility [69–73].

Although, a number of groups have taken steps in this direction [74], Wulff and coworkers were the first to report investigations into the preparation of suitably crosslinked microgels with molecular recognition properties [69]. Covalently imprinted microgels were successfully synthesized with 70% EGDMA and 30% MMA in cyclohexanone, cyclopentanone and *N,N*-dimethylformamide at 1–4 wt% monomer concentrations. The microgels were characterized using gel permeation chromatography, viscometry, and membrane osmometry, and found to be highly crosslinked macromolecules with a molecular weight comparable to that of proteins. Although rebinding selectivities were low compared to the results achieved with insoluble crosslinked polymers, the success of this approach represented a step towards the development of “artificial enzymes.”

Although, at about the same time, Mosbach *et al.* produced theophylline-imprinted microgel spheres using a noncovalent approach [70], Resmini *et al.* were the first to report the preparation of imprinted soluble microgels, which acted as an enzyme mimic and displayed hydrolytic catalytic activity (Figure 20.9) [71, 72]. In these studies, a phosphate transition state analogue (TSA) was imprinted, by using two polymerizable amino acids (arginine and tyrosine) as functional monomers, in order to mimic the catalytic mechanism of hydrolytic antibodies and hydrolase enzymes with carbonate substrates. Imprinted microgels containing 70% crosslinker, and a monomer concentration of 1.5%, were found to display the highest rate enhancements of about an order of magnitude, over the uncatalyzed reaction.

More recently, Wulff and coworkers prepared phosphate-(TSA)-imprinted nanogels, with an average diameter of 20 nm, that were capable of carbonate hydrolysis, and where the  $k_{\text{cat}}/k_{\text{uncat}}$  value reached 2990 [73]. The group succeeded in imitating the natural enzymes by producing soluble nanogels that contained an average of one catalytically active site per polymeric macromolecule. Although, nanoparticles were produced with a single active site, higher-molecular-weight particles with a greater crosslink density and approximately 95 sites per particle demonstrated the greatest enhancement in catalytic activity. These results emphasized that the opposing factors which often are so critical in molecular imprinting are polymer rigidity and recognition/active site accessibility. Although, the polymer must



**Figure 20.9** Noncovalent imprinting of a phosphate transition-state analogue, using polymerizable arginine and tyrosine as functional monomers [71].

display sufficient flexibility to allow a rapid access to the binding sites, too much flexibility would compromise its rigidity and hence its recognition properties. It was for this reason that Haupt and colleagues prepared larger nanogels of approximately 180 nm, imprinted with 2,4-dichlorophenoxyacetic acid, which were used for a (pseudo-immuno) binding assay, where the requirements were different than for catalytic applications [75].

### 20.2.3

#### Silica Nanoparticles

To date, only a relatively small number of reports have been made describing successful imprinting in silica nanoparticles, and these all used different methods to form the recognition sites at the surface of the nanoparticle [76–80]. Markowitz

*et al.* used a template-directed method to imprint an  $\alpha$ -chymotrypsin TSA at the surface of silica nanoparticles (400–600 nm diameter) prepared from tetraethoxysilane and a number of organically modified silanes, for the incorporation of functionality [76]. Silica particle formation was performed in a microemulsion, where a mixture of a nonionic surfactant and the acylated chymotrypsin TSA (with the TSA acting as the headgroup at the surfactant–water interface) were used as a means of creating a cavity capable of hydrolyzing benzoyl-D-arginine-*p*-nitroanlyde, a trypsin substrate. The  $k_{\text{cat}}$  and turnover number for the nanoparticles were, however, not reported, as the authors had no means of calculating the active site concentrations. As an alternative,  $V_{\text{max}}/K_{\text{m}}$  was used as an estimate of the relative catalytic activity, which showed an increase in line with the increasing amounts of template used. Unexpectedly, the particles were highly selective for the D-isomer of the substrate, even though the imprint molecule had the L-isomer configuration.

In a subsequent study, Markowitz and coworkers investigated the effect that the addition of functional silanes had on the catalytic activity of the surface-imprinted nanoparticles [77]. It was suggested that a variation in the basicity of the functional monomers would affect the initial rates of hydrolysis, and that imprinted particles prepared with mixtures of functional monomers would show a cooperative effect promoting catalytic activity. Subsequently, the same group used a template-directed method for the imprinting of a hydrolysis product of soman (a nerve agent) at the surface of silica nanoparticles [78]. Again, a number of different functionalized silane precursors were used, and the binding characteristics of the imprinted particles investigated. The results showed the imprinted nanoparticles to display a significantly higher degree of specificity for the imprint molecule than did the structurally related organophosphates. It was also reported that variations in functionality incorporated into the particles had a definite effect on both the porosity and absorption capacity of the polymers.

Gao *et al.* reported an alternative surface functional monomer-directing strategy for the imprinting of trinitrotoluene (TNT) at the surface of silica nanoparticles [79]. The method employed a core–shell method in which monodisperse silica cores of 100 nm diameter were prepared using the Stöber process. The surface of the core particles was initially functionalized with aminopropyl groups which were, in turn, converted to acrylamide functions. An acrylate shell, composed of acrylamide and EGDMA in the presence of the template, was subsequently synthesized, around the silica particles. The acrylamide had a strong noncovalent, charge-transfer complexing interaction with the electron-deficient aromatic ring of the template molecule, which resulted in a significant shift in the UV-visible spectrum and allowed detection of the explosive. One interesting result of this synthetic method was the ability to control shell thickness between 10 and 30 nm by varying the total quantity of polymer precursors added during the shell preparation.

Kim and colleagues also used a core–shell approach, where a covalently imprinted aromatic polyimide layer of approximately 100 nm was coated to the surface of large silica spheres (~10  $\mu\text{m}$  diameter) [80]. The shell film adhered to the silica

spheres through electrostatic interactions between the carboxylic groups of the polymer chains and amino functional groups at the surface of the silica. The imprinted particles were packed into a column and used as a stationary phase in the HPLC separation of estrone and structural analogues.

#### 20.2.4

#### Molecularly Imprinted Nanoparticles: Miscellaneous

A number of interesting examples of imprinted nanoparticles have been reported that do not belong to the above-discussed categories, and these have been included in this section. One such approach, reported by Salam and Ulbricht, involved the imprinting of Boc-phenylalanine in “nanomonolithic” particles, that are formed by *in situ* polymerization in the nanosized pores of a polymeric membrane [81]. The authors claimed that the imprinted monoliths had a higher binding capacity and a higher enantioselectivity for the template than the reference monoliths, and suggested that the “nanomonolith” composite membranes might be used for continuous molecular-level separations with predetermined perm-selectivity.

Li *et al.* described a novel method in which uracil- and thiamine-imprinted polymeric nanospheres were prepared by diblock copolymer self-assembly [82]. Initially, a diblock copolymer was synthesized with one block containing functional groups for both hydrogen bond formation and crosslinking. In the presence of the template, the block copolymer was allowed to self-assemble to form spherical micelles in a selective solvent. This polymeric structure was then crosslinked, resulting in imprinted nanospheres of approximately 50 nm diameter, which were extracted to remove the template molecules. When compared to traditional monolithic-imprinted polymers, these imprinted nanospheres demonstrated a better solvent dispersibility, a higher capacity, and comparable selectivity. One possible drawback of this system was the presence of a hydrophobic shell around the imprinted core; however, the authors believed that hydrolysis of the shell would provide water-dispersible nanospheres with potential sensing and bioapplications.

Another novel method, which has been reported, is the preparation of covalently imprinted polymeric nanocapsules by microemulsion polymerization [83]. The polymerization of styrene and divinylbenzene in the presence of a monomer-template complex (a polymerizable derivative of estrone) was performed in oil-in-water microemulsion droplets. Following polymerization and phase separation in the micelle, the surfactant was removed, resulting in a hollow polymeric nanocapsule with diameters in the range of 20 to 25 nm. The template was thermally removed to produce highly accessible recognition sites that displayed moderate selectivity over structural analogues. However, the major interest here involved the use of these nanocapsules for controlled-release drug delivery. When the nanocapsules were incubated with a fluorescent probe (pyrene), prior to template removal, transfer of the pyrene into the interior of the capsule was not evident. Following template removal, however, a transfer of pyrene to the capsule interior was observed, confirming that the imprinted site had acted as a gateway to the

interior of the capsule, and could be opened and closed by template removal and rebinding.

### 20.3

#### Molecular Imprinting with Diverse Nanomaterials

In recent years, research into molecularly imprinted materials has focused on reducing the dimensions of these materials from the micro range to the nano. As a consequence, considerable effort has aimed at the development of new polymerization methods capable of producing imprinted nanoparticles. A number of research groups have, however, studied the application of the molecular imprinting approach to other types of nanomaterials, such as nanowires [84–87], nanotubes [86], nanofibers [88], quantum dots [89, 90], fullerene [91, 92], and dendrimers [93–95]. The most significant examples of these will be reviewed in the following sections.

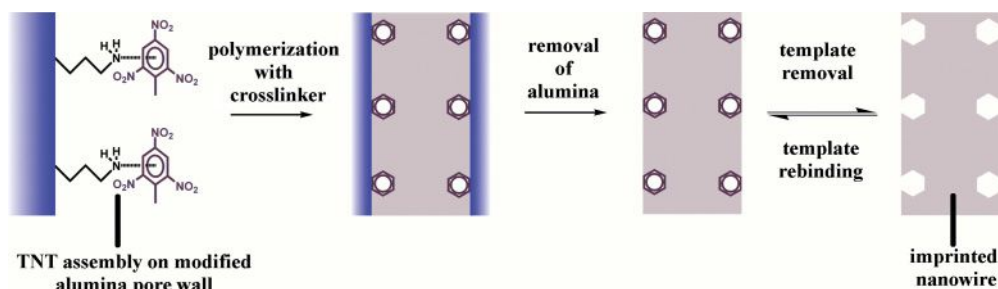
##### 20.3.1

#### Nanowires, Nanotubes, and Nanofibers

Wang and coworkers were the first to successfully prepare molecular recognition sites at the surface of nanowires using molecular imprinting technology [84]. In this approach, a commercially available nanoporous alumina membrane with a 100 nm pore diameter was used, with a sol–gel template synthesis being used to deposit silica nanotubes inside the pores of the alumina membranes. Initially, a silane precursor with aldehyde functionality was attached to the silica nanotubes, and the template—in this case glutamic acid—was immobilized on the inner walls of the nanotubes. The nanopores were subsequently filled with the monomer mixture (pyrrole in this case), polymerized, and both the alumina membrane and the silica nanotubes removed by chemical dissolution; this left behind polypyrrole nanowires with glutamic acid binding sites situated at the surface. The selectivity of the imprinted nanowires towards glutamic acid over phenylalanine and arginine was high, and similar to that observed from bulk polymers. However, a very high rate of analyte uptake was observed resulting from this surface imprinting technique.

The same group later used a similar protocol for the surface imprinting of a variety of proteins, including albumin, hemoglobin, and cytochrome c in nanowires [85]. On this occasion, acrylamide and *N,N'*-methylenebisacrylamide were used for the polymerization. There was an approximate sevenfold difference between rebinding of the template to the imprinted and control nanowires, which was complemented by a large binding capacity, observed as a result of the high surface area of the nanowires. Although the imprinted nanowires could not distinguish between bovine and horse cytochrome c, there was a definite distinction between bovine and human hemoglobin. In a subsequent report, the same group described the preparation of surface-imprinted nanowires toward theophylline, which were magnetic in nature [86]. Here, the nanopores were filled with a prepolymerization





**Figure 20.10** Schematic illustration of noncovalent imprinting of TNT at the surface of acrylate-based nanowires. Adapted from Ref. [87].

mixture containing the superparamagnetic  $\text{MnFe}_2\text{O}_4$  nanocrystallites. Unfortunately, the behavior or potential applications of the magnetic characteristics of the nanowires were not discussed to any great extent.

Xie *et al.* described the preparation of TNT surface-imprinted nanowires (Figure 20.10), where alumina membranes with pore diameters of 70 nm were prepared by electrochemical anodization [87]. In these studies, the authors also reported the first imprinted nanotubes, which were prepared in similar fashion to the nanowires, the main differences being a reduction in the monomer concentration and an increase in the quantity of initiator used. The binding capacities of the nanotubes and nanowires were almost 2.5-fold and threefold that of normal imprinted particles with 2–3  $\mu\text{m}$  diameter, respectively. This increase in binding capacity was attributed to the high ratio of surface-imprinted sites, the large surface-to-volume ratios, and the complete removal of TNT templates.

Ye and coworkers also described the incorporation of imprinted nanoparticles into electrospun nanofibers (as discussed previously in Section 20.2.2.1) [66]. The same group, however, also achieved the generation of artificial molecular recognition sites in the nanofiber itself by molecular imprinting [88]. The electrospun nanofibers were prepared from a solution mixture of PET and polyallylamine (which acts as a functional polymer) in the presence of a template molecule, 2,4-dichlorophenoxyacetic acid. Following template removal, the recognition properties of the imprinted nanofibers were identified using a radioligand-binding assay. The imprinted nanofibers displayed favorable binding characteristics in aqueous solution, where analyte binding to the imprinted nanofibers was fivefold that of the reference fibers. The authors predicted that this type of imprinted nanofiber would become highly applicable in the future for affinity-related separations.

### 20.3.2

#### Quantum Dots

Lin and coworkers are, to date, the only group to report the synthesis of molecularly imprinted polymers in conjunction with fluorescent semiconductor nanoparticles also known as quantum dots (QDs) [89, 90]. The first step of this

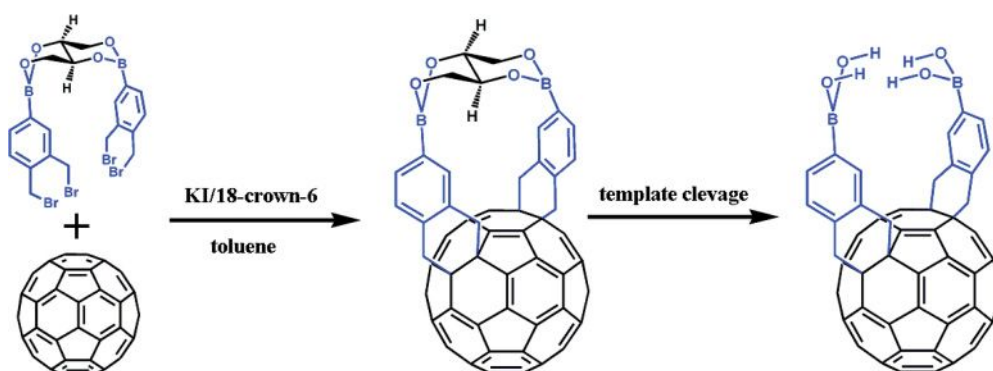


approach was the preparation of the CdSe/ZnS semiconductor nanoparticles. In order to ensure that the nanoparticles were incorporated covalently into the polymer, the surfaces of the QDs were functionalized with 4-vinylpyridine. The functionalized nanoparticles were polymerized with MAA and EGDMA in the presence of uracil, following spin coating of the initiated solution, to form a molecularly imprinted thin film [89]. In a subsequent study, the QDs were incorporated into bulk polymers, which were imprinted with a number of template molecules including caffeine, uric acid, L-cysteine, and estriol [90]. The authors showed that binding to recognition sites in the vicinity of the fluorescent nanoparticles caused quenching of the photoluminescence emission, presumably due to the fluorescence resonance energy transfer between the QDs and the template molecules. The imprinted polymers demonstrated good selectivity towards the template when compared to structurally related compounds and, according to the authors, the control polymers exhibited no response to the analyte.

### 20.3.3

#### Fullerene

The first “homogeneous nanoscale imprinting system,” wherein a saccharide was used as template and covalently bound by two boronic acid groups onto the surface of [60]fullerene, was described by Shinkai and coworkers [91]. This strategy was used in order to produce one single binding site per molecule and to avoid the creation of numerous binding sites with varying recognition properties (as illustrated in Figure 20.11) [92]. Initially, a template monomer complex, based on D,L-threitol, was synthesized which could undergo a regioselective and chiroselective double [4 + 2] cycloaddition with [60]fullerene. Subsequent cleavage of the template resulted in two optically active *cis-3 bis* adducts with opposite chirality in a ratio of 72:28. Competitive rebinding studies between D,L-threitol and the imprinted fullerene demonstrated that L-threitol-imprinted (<sup>l</sup>A)-4 and D-threitol-



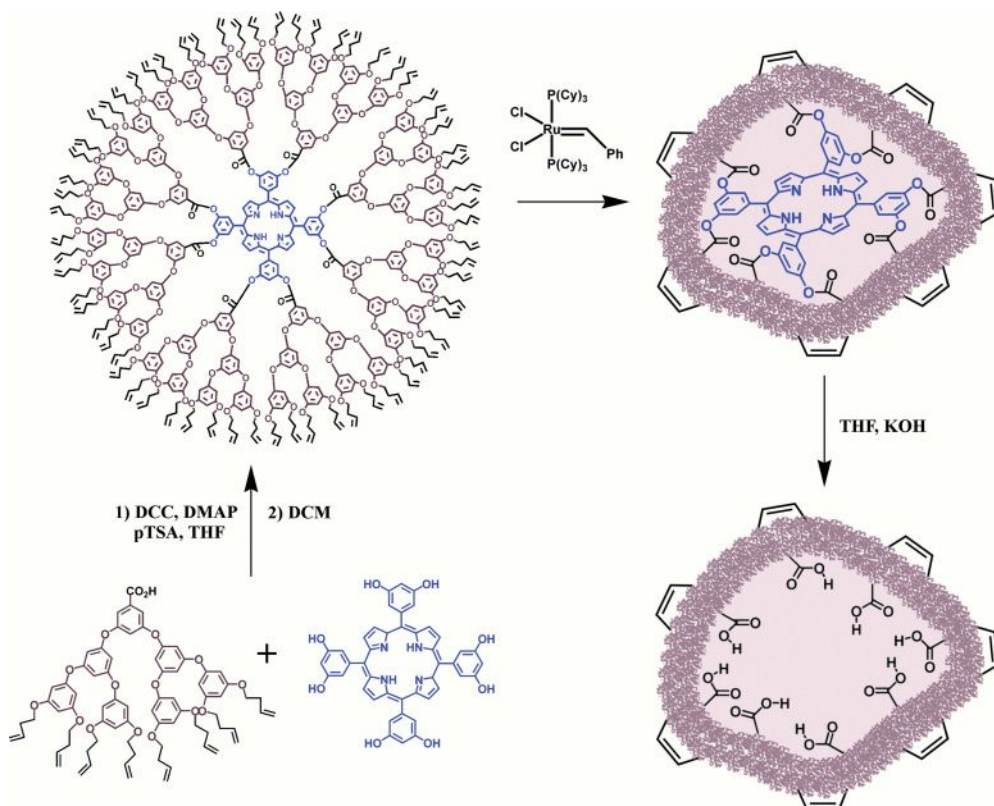
**Figure 20.11** Structural representation of a monomolecular covalent imprinting strategy with fullerene for the recognition of sugars. Adapted from Ref. [91].

imprinted ( $^{13}\text{C}$ )-4 rebound the original templates in diastereoselective fashion. Although, the selectivity in this system was not extraordinary, it should be emphasized that this was the first instance in which molecular imprinting was applied to a system with a soluble nanosized matrix in homogeneous solution.

#### 20.3.4

##### Dendrimers

Zimmerman *et al.* more recently used a different strategy, wherein a single porphyrin template was dynamically imprinted into a single macromolecule (dendrimer), in order to prepare molecularly homogeneous hosts each with a single recognition site [93]. For this, the authors used the covalent approach, where the porphyrin acted as the core and was covalently bound through ester linkages to eight third-generation dendrons to form the dendrimer. The porphyrin was cleaved by hydrolysis, following the crosslinking of homoallyl end groups at the exterior of the dendrimer by Grubbs ring-closing metathesis (Figure 20.12). Complexation



**Figure 20.12** Schematic diagram of a monomolecular covalent imprinting strategy with dendrimers for the recognition of porphyrins. Adapted from Ref. [96].

studies (where rebinding occurred noncovalently) demonstrated that >95% of the imprints were effective, and their binding properties homogeneous [96]. The imprinted dendrimer was also shown to be selective, and to bind porphyrins with at least four hydrogen bond donor/acceptor sites, in toluene as solvent. The imprinted cavity was also size-selective, and although the template itself was too large to bind, porphyrins of smaller physical size and appropriate functionality were able to complex strongly.

In a subsequent study, an imprinted dendrimer was prepared around a porphyrin with four reactive alcohol groups, which was covalently bound to four fourth-generation dendrons [94]. More recently, Zimmerman's group reported the preparation of an imprinted dendrimer with a less-symmetrical template molecule, with a view to producing an amine-selective sensor [95]. Here, very high affinity binding was perceived, from a three-point interaction, which included two hydrogen bonds and one covalent linkage to a reporter group that transduced binding by color change. This monomolecular imprinting approach resulted in properties that were difficult to achieve by conventional polymerization methods, such as high-efficiency imprinting, quantitative removal of the template, solubility of the imprinted material in common organic solvents, and possibility of separation of imperfectly assembled binding sites. However, the limitations of this approach were the need for a multistep synthesis of the dendrimers, the high dilution conditions required for the ring-closing metathesis reaction, and the incompatibility of many templates with this imprinting approach.

## 20.4

### Conclusions and Future Prospects

Nanomaterials represent one of the most important targets of the developing field of nanotechnology. The advanced scientific knowledge acquired for the synthesis and physical–chemical characteristics of these materials has led to a considerable increase in the number of their applications and commercial exploitations. The application of imprinting technologies to nanomaterials has provided a new insight, offering the possibility of creating tailored cavities with specific recognition properties.

Over the past decade, considerable effort has been devoted to developing novel synthetic strategies, and this has led to imprinted materials in a variety of formats. Attention has been mainly focused on the development of approaches to producing imprinted nanoparticles, and to providing reproducibility and efficiency among the polymerization methodologies used. Although, significant advances have been made in this area, the widespread commercialization of these materials has yet to be realized. Yet, ongoing developments in the field of nanomaterials have led to a range of promising polymeric formats, including soluble crosslinked imprinted dendrimers, microgels and nanogels, which more closely mimic the physical characteristics of enzymes and antibodies. Additional formats, such as nanofibers, nanowires and nanotubes, have arisen and have been used successfully in

conjunction with imprinting technologies. These materials exploit the advantages of high surface-to-volume ratios and often also the surface-imprinting techniques that allow an easy access of target molecules to recognition sites. The results obtained to date in this area have been the outcome of an increasing interest in molecular imprinting, by both academic and industrial enterprises, and will surely lead to their significant application in the near future.

## References

- 1 Haupt, K. and Mosbach, K. (2000) *Chem. Rev.*, **100**, 2495–2504.
- 2 Sellergren, B. (2003) *Molecularly Imprinted Polymers. Man-Made Mimics of Antibodies and Their Application in Analytical Chemistry*. Elsevier.
- 3 Polyakov, M.V. (1931) *Zh. Fiz. Khim.*, **2**, 799–805.
- 4 Polyakov, M.V., Stadnik, P., Paryckij, M., Malkin, I. and Duchina, F. (1933) *Zh. Fiz. Khim.*, **4**, 454–456.
- 5 Polyakov, M.V., Kuleshina, L. and Neimark, I. (1937) *Zh. Fiz. Khim.*, **10**, 100–112.
- 6 Alexander, C., Andersson, H.S., Andersson, L.I., Ansell, R.J., Kirsch, N., Nicholls, I.A., O'Mahony, J. and Whitcombe, M.J. (2006) *J. Mol. Recognit.*, **19**, 106–180.
- 7 Pauling, L. (1940) *J. Am. Chem. Soc.*, **60**, 2643–2657.
- 8 Dickey, F.H. (1949) *Proc. Natl Acad. Sci. USA*, **35**, 227–229.
- 9 Haldeman, R.G. and Emmett, P.H. (1955) *J. Phys. Chem.*, 1039–1043.
- 10 Beckett, A.H. and Anderson, P. (1957) *Nature*, **179**, 1074–1075.
- 11 Wulff, G. and Sarhan, A. (1972) *Angew. Chem. Int. Ed. Engl.*, **11**, 341.
- 12 Andersson, L., Sellergren, B. and Mosbach, K. (1984) *Tetrahedron Lett.*, **25**, 5211–5214.
- 13 Wulff, G., Vesper, W., Grobeinsler, R. and Sarhan, A. (1977) *Macromol. Chem. Phys.*, **178**, 2799–2816.
- 14 Wulff, G. and Schauhoff, S. (1991) *J. Org. Chem.*, **56**, 395–400.
- 15 Wulff, G. and Vietmeier, J. (1989) *Macromol. Chem. Phys.*, **190**, 1727–1735.
- 16 Shea, K.J. and Sasaki, D.Y. (1989) *J. Am. Chem. Soc.*, **111**, 3442–3444.
- 17 Arshady, R. and Mosbach, K. (1981) *Macromol. Chem. Phys. Makromol. Chem.*, **182**, 687–692.
- 18 Mosbach, K. (1994) *Trends Biochem. Sci.*, **19**, 9–14.
- 19 Kempe, M., Fischer, L. and Mosbach, K. (1993) *J. Mol. Recognit.*, **6**, 25–29.
- 20 Yu, C. and Mosbach, K. (1998) *J. Mol. Recognit.*, **11**, 69–74.
- 21 Strikovskiy, A.G., Kasper, D., Grun, M., Green, B.S., Hradil, J. and Wulff, G. (2000) *J. Am. Chem. Soc.*, **122**, 6295–6296.
- 22 Turkewitsch, P., Wandelt, B., Darling, G.D. and Powell, W.S. (1998) *Anal. Chem.*, **70**, 2025–2030.
- 23 Vlatakis, G., Andersson, L.I., Muller, R. and Mosbach, K. (1993) *Nature*, **361**, 645–647.
- 24 Wulff, G. and Schönfeld, R. (1998) *Adv. Mater.*, **10**, 957–959.
- 25 Mayes, A.G. and Whitcombe, M.J. (2005) *Adv. Drug. Deliv. Rev.*, **57**, 1742–1778.
- 26 Sellergren, B. and Andersson, L. (1990) *J. Org. Chem.*, **55**, 3381–3383.
- 27 Whitcombe, M.J., Rodriguez, M.E., Villar, P. and Vulfson, E.N. (1995) *J. Am. Chem. Soc.*, **117**, 7105–7111.
- 28 Pérez-Moral, N. and Mayes, A.G. (2001) *Bioseparation*, **10**, 287–299.
- 29 Brüggemann, O., Haupt, K., Ye, L., Yilmaz, E. and Mosbach, K. (2000) *J. Chromatogr. A*, **889**, 15–24.
- 30 Sellergren, B. (2001) *J. Chromatogr. A*, **906**, 227–252.
- 31 Wulff, G. (2002) *Chem. Rev.*, **102**, 1–27.
- 32 Kido, H., Miyajima, T., Tsukagoshi, K., Maeda, M. and Takagi, M. (1992) *Anal. Sci.*, **8**, 749–753.
- 33 Murata, M., Hijiya, S., Maeda, M. and Takagi, M. (1996) *Bull. Chem. Soc. Jpn.*, **69**, 637–642.

- 34 Yoshida, M., Uezu, K., Goto, M., Furusaki, S. and Takagi, M. (1998) *Chem. Lett.*, **27** (9), 925–926.
- 35 Eshuis, A., Leendertse, H.J. and Thoenes, D. (1991) *Colloid Polym. Sci.*, **269**, 1086–1089.
- 36 He, W.D., Cao, C.T. and CaiYuan, P. (1996) *J. Appl. Polym. Sci.*, **61**, 383–388.
- 37 Ferguson, C.J., Russell, G.T. and Gilbert, R.G. (2002) *Polymer*, **43**, 6371–6382.
- 38 Pérez, N., Whitcombe, M.J. and Vulfson, E.N. (2000) *J. Appl. Polym. Sci.*, **77**, 1851–1859.
- 39 Pérez, N., Whitcombe, M.J. and Vulfson, E.N. (2001) *Macromolecules*, **34**, 830–836.
- 40 Pérez-Moral, N. and Mayes, A.G. (2002) *Molecularly Imprinted Materials-Sensors and Other Devices*, Vol. 723 (eds K.J. Shea and M.J. Roberts), Materials Research Society, Warrendale, PA, pp. 61–66.
- 41 Pérez-Moral, N. and Mayes, A.G. (2004) *Langmuir*, **20**, 3775–3779.
- 42 Carter, S.R. and Rimmer, S. (2002) *Adv. Mater.*, **14**, 667–670.
- 43 Carter, S., Lu, S.Y. and Rimmer, S. (2003) *Supramol. Chem.*, **15**, 213–220.
- 44 Carter, S.R. and Rimmer, S. (2004) *Adv. Funct. Mater.*, **14**, 553–561.
- 45 Tovar, G.E.M., Kräuter, I. and Gruber, C. (2003) *Molecularly Imprinted Polymer Nanospheres as Fully Synthetic Affinity Receptors*, Springer, pp. 125–144.
- 46 Schillemans, J.P. and van Nostrum, C.F. (2006) *Nanomedicine*, **1**, 437–447.
- 47 Vaihinger, D., Landfester, K., Kräuter, I., Brunner, H. and Tovar, G.E.M. (2002) *Macromol. Chem. Phys.*, **203**, 1965–1973.
- 48 Weber, A., Dettling, M., Brunner, H. and Tovar, G.E.M. (2002) *Macromol. Rapid. Commun.*, **23**, 824–828.
- 49 Lehmann, M., Brunner, H. and Tovar, G.E.M. (2002) *Desalination*, **149**, 315–321.
- 50 Lehmann, M., Dettling, M., Brunner, H. and Tovar, G.E.M. (2004) *J. Chromatogr. B Analyt. Technol. Biomed. Life Sci.*, **808**, 43–50.
- 51 Tan, C.J. and Tong, Y.W. (2007) *Langmuir*, **23**, 2722–2730.
- 52 Tan, C.J. and Tong, Y.W. (2007) *Anal. Chem.*, **79**, 299–306.
- 53 Arshady, R. (1992) *Colloid Polym. Sci.*, **270**, 717–732.
- 54 Ye, L., Cormack, P.A.G. and Mosbach, K. (1999) *Anal. Commun.*, **36**, 35–38.
- 55 Ye, L., Weiss, R. and Mosbach, K. (2000) *Macromolecules*, **33**, 8239–8245.
- 56 Yoshimatsu, K., Reimhult, K., Krozer, A., Mosbach, K., Sode, K. and Ye, L. (2007) *Anal. Chim. Acta*, **584**, 112–121.
- 57 Ye, L. and Mosbach, K. (2001) *J. Am. Chem. Soc.*, **123**, 2901–2902.
- 58 Ye, L., Surugiu, I. and Haupt, K. (2002) *Anal. Chem.*, **74**, 959–964.
- 59 Spégel, P. and Nilsson, S. (2002) *Am. Lab.*, **34**, 29–33.
- 60 Spégel, P., Schweitz, L. and Nilsson, S. (2003) *Anal. Chem.*, **75**, 6608–6613.
- 61 Zhu, Q.J., Tang, J., Dai, J., Gu, X.H. and Chen, S.W. (2007) *J. Appl. Polym. Sci.*, **104**, 1551–1558.
- 62 Ciardelli, G., Cioni, B., Cristallini, C., Barbani, N., Silvestri, D. and Giusti, P. (2004) *Biosens. Bioelectron.*, **20**, 1083–1090.
- 63 Silvestri, D., Borrelli, C., Giusti, P., Cristallini, C. and Ciardelli, G. (2005) *Anal. Chim. Acta*, **542**, 3–13.
- 64 Silvestri, D., Barbani, N., Cristallini, C., Giusti, P. and Ciardelli, G. (2006) *J. Membr. Sci.*, **282**, 284–295.
- 65 Ciardelli, G., Borrelli, C., Silvestri, D., Cristallini, C., Barbani, N. and Giusti, P. (2006) *Biosens. Bioelectron.*, **21**, 2329–2338.
- 66 Chronakis, I.S., Jakob, A., Hagström, B. and Ye, L. (2006) *Langmuir*, **22**, 8960–8965.
- 67 Ye, L., Yoshimatsu, K., Kolodziej, D., Francisco, J.D. and Dey, E.S. (2006) *J. Appl. Polym. Sci.*, **102**, 2863–2867.
- 68 Graham, N.B. and Cameron, A. (1998) *Pure Appl. Chem.*, **70**, 1271–1275.
- 69 Biffis, A., Graham, N.B., Siedlaczek, G., Stalberg, S. and Wulff, G. (2001) *Macromol. Chem. Phys.*, **202**, 163–171.
- 70 Ye, L., Cormack, P.A.G. and Mosbach, K. (2001) *Anal. Chim. Acta*, **435**, 187–196.
- 71 Maddock, S.C., Pasetto, P. and Resmini, M. (2004) *Chem. Commun.*, 536–537.
- 72 Pasetto, P., Maddock, S.C. and Resmini, M. (2005) *Anal. Chim. Acta*, **542**, 66–75.
- 73 Wulff, G., Chong, B.O. and Kolb, U. (2006) *Angew. Chem. Int. Ed. Engl.*, **45**, 2955–2958.
- 74 Ohkubo, K., Funakoshi, Y. and Sagawa, T. (1996) *Polymer*, **37**, 3993–3995.
- 75 Hunt, C.E., Pasetto, P., Ansell, R.J. and Haupt, K. (2006) *Chem. Commun.*, 1754–1756.

- 76 Markowitz, M.A., Kust, P.R., Deng, G., Schoen, P.E., Dordick, J.S., Clark, D.S. and Gaber, B.P. (2000) *Langmuir*, **16**, 1759–1765.
- 77 Markowitz, M.A., Kust, P.R., Klaehn, J., Deng, G. and Gaber, B.P. (2001) *Anal. Chim. Acta*, **435**, 177–185.
- 78 Markowitz, M.A., Deng, G. and Gaber, B.P. (2000) *Langmuir*, **16**, 6148–6155.
- 79 Gao, D.M., Zhang, Z.P., Wu, M.H., Xie, C.G., Guan, G.J. and Wang, D.P. (2007) *J. Am. Chem. Soc.*, **129**, 7859–7866.
- 80 Kim, T.H., Do Ki, C., Cho, H., Chang, T.Y. and Chang, J.Y. (2005) *Macromolecules*, **38**, 6423–6428.
- 81 Salam, A. and Ulbricht, M. (2006) *Desalination*, **199**, 532–534.
- 82 Li, Z., Ding, J.F., Day, M. and Tao, Y. (2006) *Macromolecules*, **39**, 2629–2636.
- 83 Ki, C.D. and Chang, J.Y. (2006) *Macromolecules*, **39**, 3415–3419.
- 84 Yang, H.H., Zhang, S.Q., Tan, F., Zhuang, Z.X. and Wang, X.R. (2005) *J. Am. Chem. Soc.*, **127**, 1378–1379.
- 85 Li, Y., Yang, H.H., You, Q.H., Zhuang, Z.X. and Wang, X.R. (2006) *Anal. Chem.*, **78**, 317–320.
- 86 Li, Y., Yin, X.F., Chen, F.R., Yang, H.H., Zhuang, Z.X. and Wang, X.R. (2006) *Macromolecules*, **39**, 4497–4499.
- 87 Xie, C.G., Zhang, Z.P., Wang, D.P., Guan, G.J., Gao, D.M. and Liu, J.H. (2006) *Anal. Chem.*, **78**, 8339–8346.
- 88 Chronakis, I.S., Milosevic, B., Frenot, A. and Ye, L. (2006) *Macromolecules*, **39**, 357–361.
- 89 Lin, C.I., Joseph, A.K., Chang, C.K. and Lee, Y.D. (2004) *Biosens. Bioelectron.*, **20**, 127–131.
- 90 Lin, C.I., Joseph, A.K., Chang, C.K. and Lee, Y.D. (2004) *J. Chromatogr. A.*, **1027**, 259–262.
- 91 Ishi-i, T., Nakashima, K. and Shinkai, S. (1998) *Chem. Commun.*, 1047–1048.
- 92 Ishi-i, T., Iguchi, R. and Shinkai, S. (1999) *Tetrahedron*, **55**, 3883–3892.
- 93 Zimmerman, S.C., Wendland, M.S., Rakow, N.A., Zharov, I. and Suslick, K.S. (2002) *Nature*, **418**, 399–403.
- 94 Zimmerman, S.C., Zharov, I., Wendland, M.S., Rakow, N.A. and Suslick, K.S. (2003) *J. Am. Chem. Soc.*, **125**, 13504–113508.
- 95 Beil, J.B. and Zimmerman, S.C. (2004) *Chem. Commun.*, 488–489.
- 96 Zimmerman, S.C. and Lemcoff, N.G. (2004) *Chem. Commun.*, 5–14.



## 21

### Near-Field Raman Imaging of Nanostructures and Devices

*Ze Xiang Shen, Johnson Kasim, and Ting Yu*

#### 21.1

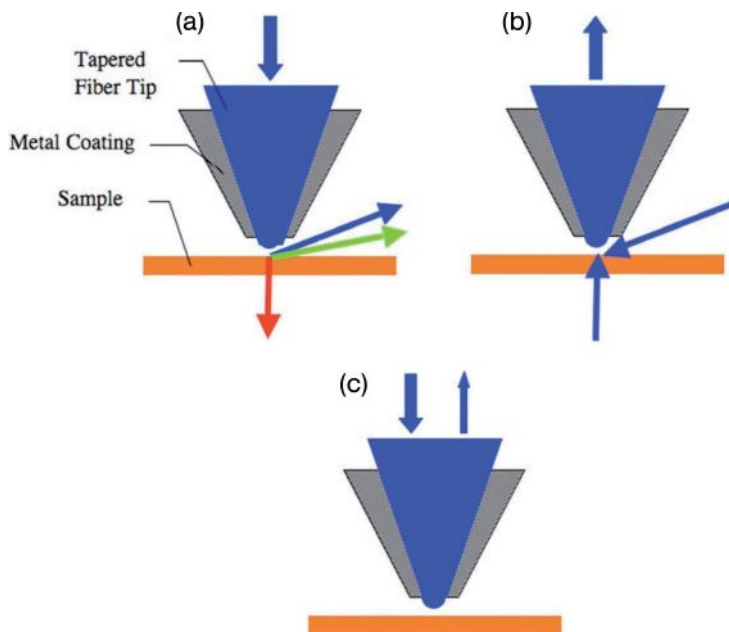
##### Introduction

Significant advances have been made in recent years in nanoscience and nanotechnology. Many applications which involve the use of nanomaterials and devices, and utilize their unique properties, have now been realized and more are expected in the near future. Despite these achievements, our understanding of nanomaterials and devices remains limited, due partly to the lack of suitable characterization techniques.

In Raman spectroscopy, molecular vibrations are measured that are determined by the structure and chemical bonding—as well as the masses—of the constituent atoms/ions. Raman spectra, as with infrared (IR) spectra, are unique in their chemical and structural identifications. The technique of Raman spectroscopy is nondestructive, sample preparation-free, there is no requirement for vacuum application, and it can be carried out in an aqueous/liquid environment. The technique can also easily be carried out at a different temperature, pressure, and electrical and magnetic fields. If it were possible to use Raman spectroscopy for nanocharacterization, it would provide critically important material-specific properties such as composition, chemical bonding, crystal and electronic structures and strain/stress, as well as supplementary information to other nanotechniques, such as scanning electron microscopy (SEM), atomic force microscopy (AFM), and transmission electron microscopy (TEM).

Conventional (far-field) micro-Raman spectroscopy has a spatial resolution of approximately  $0.5\ \mu\text{m}$ , which is governed by the theoretical diffraction limit, whereas IR spectrometry has at best a spatial resolution of approximately  $10\ \mu\text{m}$ , due to the longer wavelengths being utilized. Hence, the application of these techniques in nanoscience and nanotechnology is severely limited by their poor spatial resolution. Consequently, extensive efforts have recently been made to characterize structural information at the nanometer scale, utilizing near-field scanning optical microscopy (NSOM), the different operational modes of which are shown in Figure 21.1.





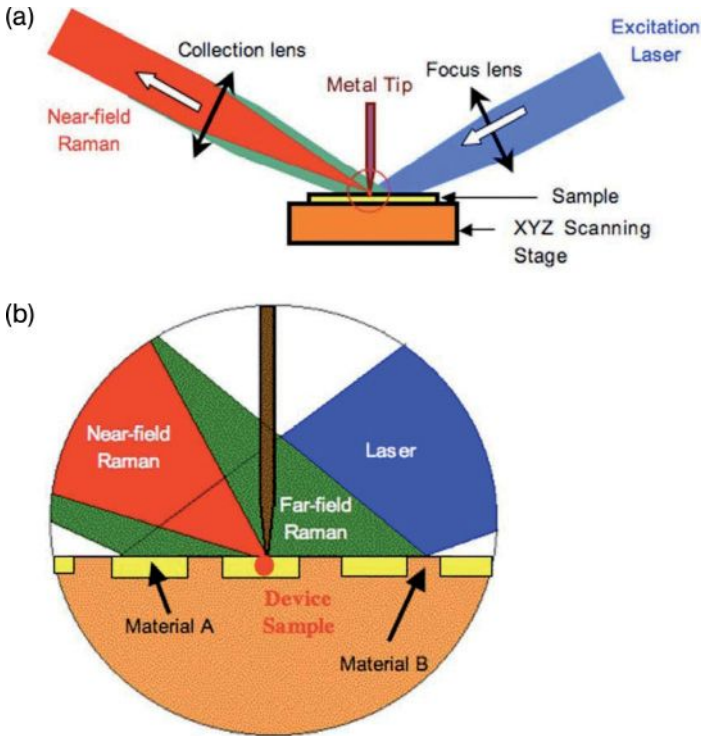
**Figure 21.1** Different operational modes of near-field scanning optical microscopy. (a) Illumination mode; (b) Collection mode; (c) Illumination and collection mode.

In this chapter, presented data have been acquired using both far-field and near-field Raman imaging. The aim is to demonstrate the importance of Raman imaging in materials and device research.

## 21.2 Near-Field Raman Imaging Techniques

There are three main approaches to near-field scanning Raman microscopy (NSRM). The first approach is based on the principle of NSOM [1–3], which is also known as “aperture near-field Raman.” It is embodied through an aperture NSOM, whereby an optical fiber tip with a small aperture (50–200 nm) is used to deliver laser light, while the fiber tip is held at a close distance (some tens of nanometers) above the sample surface. The Raman signal is collected in far-field through either a microscope objective or a lens [4–6]. The scattered light (Raman signal) is coupled to a Raman spectrometer, where the Raman spectra are recorded at each point on the sample by scanning the fiber tip across the sample surface. An NSRM image is constructed using these spectra.

The laser emerging from such a fiber tip is extremely weak (typically 100 nW) due to the low optical throughput of the fiber tip. Hence, aperture near-field Raman has been plagued by the poor signal-to-noise ratio (SNR) of the near-field



**Figure 21.2** (a) Schematic diagram of tip-enhanced Raman scattering in reflection geometry. The metal tip is brought to the sample surface by tuning fork or cantilever. The Raman signals can also be collected by the focus lens instead of the collection lens; (b) Magnified view of the tip region. The

far-field Raman signal comes from the whole laser-illuminated area (a few  $\mu\text{m}$ ) and is featureless, while the near-field Raman signal comes from only the tip region ( $<100\text{ nm}$ ) and carries information related to the device features.

Raman spectra. Although extensive efforts have been devoted to fabricate fiber tips with a higher throughput, the throughput is still very low, especially for tips with an aperture  $<200\text{ nm}$ . In addition, the Raman signal is intrinsically weak (typically less than 1 in  $10^7$  photons). A typical Raman spectrum takes several minutes to record when using the conventional near-field Raman method, which makes it prohibitive to construct a Raman image in this way. For example, when Webster *et al.* [7] used the aperture technique to study the stress distribution of a scratch on a Si crystal wafer, a period of about 9 hours was required to obtain a Raman image of  $26 \times 21$  points.

An alternative approach to near-field Raman microscopy is to use an aperture-less configuration (which is also known as tip-enhanced Raman scattering; TERS) [8–10], employing a metal or metal-coated tip (see Figure 21.2). In this configuration, the laser impinges on the apex of the metal tip, inducing a strong local electric field enhancement in the vicinity of the metal tip apex. In this case, the Raman

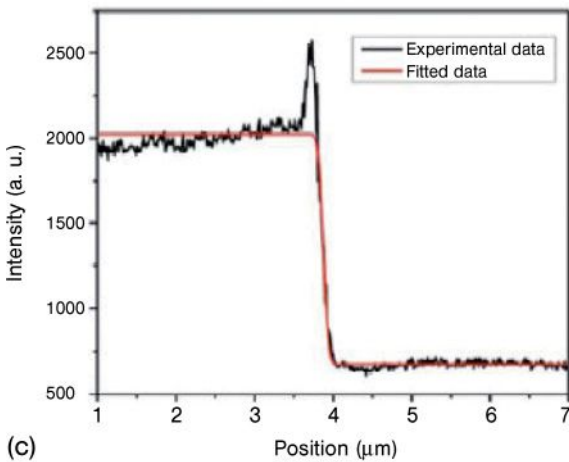
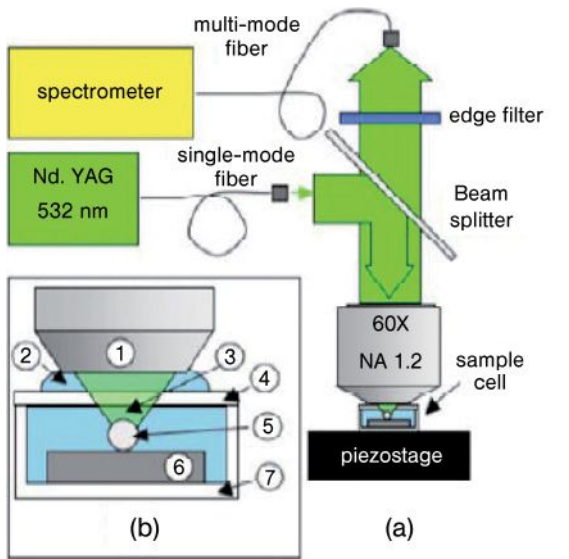
enhancement is a result of local field enhancement by the tip, or increased polarizability of the sample due to an interaction between the tip and sample, which is similar to surface-enhanced Raman scattering. As the laser is delivered to the sample surface by an objective lens rather than by a metal-coated fiber tip, the low optical throughput of conventional fiber tips can be overcome. With a suitable metal tip (usually Ag or Au), the Raman signal from the sample close to the tip can be enhanced by several orders of magnitude.

Besides the higher overall Raman throughput, TERS has several other merits over the apertureless configuration:

1. **A higher spatial resolution:** At least in principle, it is much easier to fabricate a sharp tip than a small aperture. A spatial resolution  $<10$  nm has been achieved using TERS.
2. **Fewer topographic artifacts:** In aperture configuration the tip is large, although its aperture may be small; therefore, the tip cannot follow the sample surface exactly. This is normally not a problem, and is less severe in TERS.
3. **A variety of potential tip materials:** In addition to noble metals, silicon and its oxides, nitrides, nanowires and nanotubes may represent good candidates for tips.
4. **A wider spectral response range:** Unlike the aperture technique, which usually functions in the visible region due to a need to use optical fibers to deliver the laser, TERS can extend its applications to a much wider range, for example from ultraviolet to IR.

Unfortunately, TERS also has some major disadvantages, the main challenge being to obtain reproducible near-field images. It is very difficult to achieve a consistent near-field enhancement in TERS, due to difficulties in controlling the geometry of the metal tip. The technique also encounters problems of wear and tear, oxidation, and contamination of the tip apex (e.g., by carbon) that may have severe adverse effects on the near-field enhancement. Another problem is that the laser spot, when focused on the tip apex, causes an intense background (far-field signal) that should be eliminated in order to achieve a better SNR [11, 12]. As a result, TERS is rarely used for routine characterization.

A third approach, developed by the present authors' group, uses a dielectric microsphere to focus the laser to a spot size that is smaller than the diffraction limit. Besides being used as the excitation source for Raman spectroscopy, the incident laser beam (linearly polarized Gaussian TEM<sub>00</sub> mode) is also used to trap the microsphere just above the sample surface, using the well-known "optical tweezers" mechanism. In these experiments, the sample and polystyrene microspheres (3  $\mu$ m diameter) were placed in a sample cell filled with deionized water. One microsphere was trapped at the center of the laser beam and was in contact with the surface of the sample during scanning. The experimental set-up is shown schematically in Figure 21.3a and b.



**Figure 21.3** (a) Schematic diagram of the near-field Raman microscope with microsphere; (b) Detailed description of the sample cell: 1 = water immersion lens (60 $\times$  NA = 1.2 water immersion), 2 = water, 3 = focused laser, 4 = cover glass, 5 = polystyrene microsphere (3  $\mu$ m), 6 = sample, 7 = sample cell' (c) Typical Si–Si Raman intensity versus position with the fitted data to determine the laser spot size.

### 21.3

#### Visualization of Si–C Covalent Bonding of Single Carbon Nanotubes Grown on Silicon Substrate

In this section, it is shown that Raman microscopy can be used to characterize nanoscale samples, using Si–C bonding between the carbon nanotubes (CNTs) and the Si substrate as an example. Recently, CNTs have attracted a great deal of interest on the basis of their extraordinary electrical, chemical, thermal, and mechanical properties [13–15], all of which make them promising materials for applications in nanometer-scale electronics and devices. For example, a unique property of CNTs is that they may be either metallic or semiconducting, depending on their chirality and diameters [16]. The tuning of electrical properties of single CNTs by inducing covalent bonding between the CNTs and the Si substrate has been predicted [17–22]. Such direct integration of CNTs into well-developed silicon technologies offers a new strategy of building nanoscale, or even single-molecule, electronic devices by selectively forming covalent bonding between the CNTs and the Si substrate.

Several groups have achieved Si–CNT bonding in ceramics with good mechanical properties by annealing Si nanoparticles together with CNTs, which served as a mechanical reinforcement [23]. The direct observation of Si–C covalent bonding on single CNTs on Si substrate samples has not been reported, due partly to a lack of suitable characterization techniques. However, it has been predicted that the interaction between Si and the CNT results in a rich variety of changes in the electronic structures of the CNT [19]. For example, when Miwa *et al.* studied the single-walled CNT adsorbed onto partially and fully hydrogenated Si (001) surfaces [19, 20], it could be shown that the removal of a few H-atoms along the adsorption sites would enhance the metallic character of the CNT. However, the removal of *all* H-atoms would transform the CNT to the semiconducting state. By using first-principle calculations, Peng *et al.* were able to determine the binding energies of CNTs adsorbed onto different sites on Si (001) surfaces [22]. In fact, their results showed that the absorption sites at the surface trench for CNTs parallel to the Si dimer rows, and between Si dimers for CNTs perpendicular to the Si dimer rows, were stable.

Such stability was also shown to depend heavily on the size (diameter) of the CNTs. When preparing these Si–CNT devices the first step is to fabricate Si–CNT covalent bonding on a large scale. Irrespective of which technique is used to characterize the sample, it must be capable of identifying those CNTs with Si–C bonds. In these studies, a micro-Raman imaging technique [24] was used that was capable of probing down to hundreds of nanometers, to investigate isolated single CNTs and their interaction with the Si substrate. The CNTs were grown on a silicon substrate at high temperature to achieve Si–CNT bonding, with Raman imaging showing that some of the single CNTs were attached covalently to the silicon wafer surface.

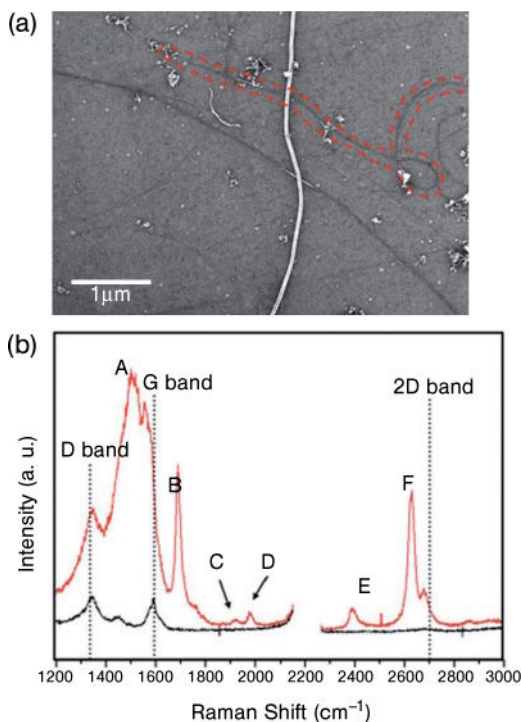
The CNTs were grown on the Si substrate using a thermal chemical vapor deposition (CVD) technique, the substrate having been cleaned using trichloroethylene,

acetone, and ethanol in turn, by ultrasonic agitation. An ultrathin Fe film to be used as the catalyst was deposited *in vacuo* ( $10^{-5}$  Torr) by ion beam sputtering. The substrates were pre-annealed at  $850^{\circ}\text{C}$  in a hydrogen-filled quartz tube furnace for 90 min. The CNTs were then grown at  $1000^{\circ}\text{C}$  for 20 min using methane, hydrogen, and argon with flow rates of 75, 20, and 100 sccm (standard  $\text{cm}^3\text{min}^{-1}$ ), respectively. The sample was cooled below  $300^{\circ}\text{C}$  before being exposed to ambient air, in order to avoid any damage caused by rapid cooling.

A JEOL JSM-6700F scanning electron microscope was used to study the surface morphology of samples and locations of interest for further Raman studies. The Raman spectroscopy and imaging were carried out using a WITec CRM200 confocal Raman system fitted with an Olympus microscope objective lens ( $100\times$  NA = 9.5). A double-frequency Nd:YAG laser (532 nm, 100 mW laser; CNI Laser) was used as the excitation source. The Raman scattered light was dispersed using a grating (1800 grooves per millimeter), and detected using a thermoelectrically cooled charge-coupled-device (CCD) cooled to  $-64^{\circ}\text{C}$ . A piezo-stage was used to scan the sample for the Raman imaging. The spatial resolution of the Raman imaging was approximately 250 nm.

The SEM image of the sample is shown in Figure 21.4a. It can be seen that all the CNTs were grown horizontally on the Si substrate, with random orientations. The various diameters of the CNTs may be due to the different sizes of the Fe catalyst. With assistance from markings on the Si substrate, Raman imaging was performed in the same region shown in the SEM image. A careful analysis of the Raman spectra in the Raman images revealed that the Raman spectra of the CNTs shown in Figure 21.4a could be indexed as two groups: (i) those consisting of only normal CNT peaks; and (ii) those with additional peaks, which can be assigned to Si–C bonds (this point is discussed later in the chapter). For simplicity, these two types of spectra are referred to as CNT spectra and Si–C spectra, respectively. Figure 21.4b shows the typical Raman spectra of the two groups. The CNT spectrum shows only Raman bands of normal CNTs: the D band ( $1344\text{cm}^{-1}$ ), G band, and 2D band ( $2681\text{cm}^{-1}$ ) [25]. The G band can be further identified as the G– band at  $1570^{-1}$  and the G+ band at  $1590\text{cm}^{-1}$ . For certain CNTs (such as the CNT highlighted by the broken line in Figure 21.4a), the Raman spectrum shows extra bands belonging to Si–C bonds at approximately  $1510\text{cm}^{-1}$  (band A),  $1692\text{cm}^{-1}$  (band B),  $1921\text{cm}^{-1}$  (band C),  $1981\text{cm}^{-1}$  (band D),  $2392\text{cm}^{-1}$  (band E), and  $2620\text{cm}^{-1}$  (band F). While several regions were tested in this study, it should be noted that the extra bands (A–F) were observed only for certain CNTs, which suggested that the Si–C bonds formed only for certain CNTs.

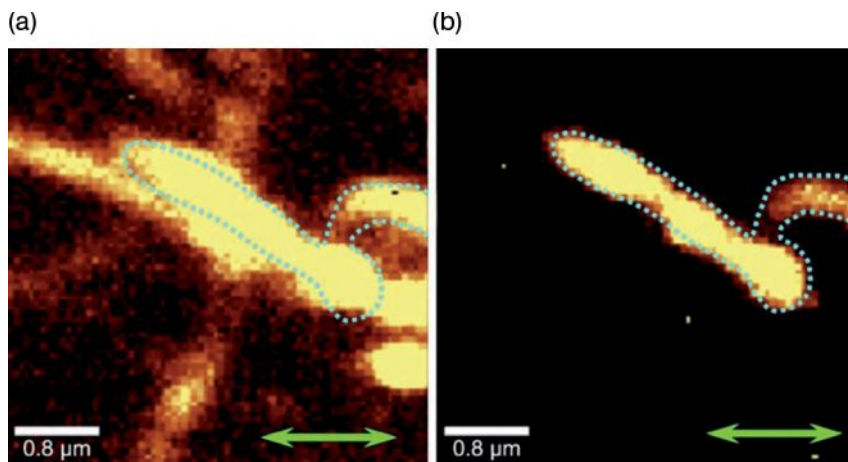
Raman imaging was performed in the sample region shown in Figure 21.4a with a scanning step size of 50 nm, and with the incident laser polarized in the plane of the substrate. Raman images constructed using different peak intensities are shown in Figure 21.5a–d. Figure 21.5a was generated by the G band (ca.  $1580\text{cm}^{-1}$ ) intensity of the CNTs. Brighter regions represent CNTs, which show an excellent correlation with those obtained using SEM. Images were also constructed using the intensity of the extra band A; the resultant image is shown in Figure 21.5b. The shape and position of the bright region matched perfectly the



**Figure 21.4** (a) Scanning electron microscope image showing the areas of interest. Raman bands belonging to Si–C bonds can be detected on a carbon nanotube (CNT), as indicated by the broken red line; (b) Comparison of Raman spectra obtained on normal CNTs (black) and the special CNT (red). The dashed lines represent the peak positions of the CNTs' D band, G band, and 2D band.

CNT, emphasized by the dashed curve in the SEM image (Figure 21.4a). Images generated using bands B and F (not shown) exhibited near-identical patterns to that of band A, clearly indicating that the three bands were all correlated to the same CNT marked in the SEM image.

In order to confirm that peaks A–F in Figure 21.4b were indeed related to Si–C covalent bonds, the Raman spectra were compared with those of bulk SiC, which have been well studied [26, 27]. Bulk SiC has several polytypes, which can give rise to the following first-order Raman peaks: TA mode between  $200\text{--}300\text{ cm}^{-1}$ , LA mode at around  $610\text{ cm}^{-1}$ , TO mode at around  $790\text{ cm}^{-1}$ , and LO mode at near  $970\text{ cm}^{-1}$  [28]. The TO mode at  $790\text{ cm}^{-1}$  is by far the strongest Raman peak in all polytypes, which is absent in the present sample (the reasons are given later). The peak positions and relative intensities of the SiC second-order Raman bands varied for different polytypes, with generally two characteristic bands: a broad band



**Figure 21.5** Raman images constructed using peak intensity of: (a) G band of CNTs and (b) Si–C band A at  $1510\text{cm}^{-1}$ . The Raman images generated using bands at  $1692\text{cm}^{-1}$  and  $2620\text{cm}^{-1}$  are identical to those in panel (b). The green arrow indicates the polarization of the incident laser. The blue dotted lines serve as a guide to the eye, and show the position and shape of the special CNT.

between  $1510\text{cm}^{-1}$  and  $1540\text{cm}^{-1}$ , and a narrower band around  $1710\text{cm}^{-1}$ . Both bands corresponded to multibands, resulting from the overlapping of different overtone phonons of the SiC vibration [27, 29, 30]. As shown in Figure 21.4b, both band A ( $1510\text{cm}^{-1}$ ) and band B ( $1692\text{cm}^{-1}$ ) observed in these Raman spectra showed a good agreement in shape and intensity with those two SiC characteristic bands. The slight shift to lower wavenumbers ( $\Delta\omega \sim 10\text{cm}^{-1}$ ) may be due to the small-size effect [31]. In addition, the weaker bands E and F also showed an agreement with the broad band of SiC at  $1930\text{cm}^{-1}$ . As there have been no reports on the Raman band of SiC above  $2000\text{cm}^{-1}$ , it was not possible to compare band F with that of bulk SiC. However, the excellent agreement between the Raman image using band F and those of band A and B showed that band F also belonged to the Si–C bonds in this sample.

The first-order Raman peak at  $790\text{cm}^{-1}$  is the strongest among all the Raman peaks in all polytypes of SiC, but was absent from these experiments. This can be explained by the substantial structural difference between the bulk SiC and the present CNT/Si system, where all the Si–C covalent bonds were formed at the Si–CNT interface. Such an unique arrangement deviates considerably from that in the bulk SiC, where the Si–C covalent bonds are arranged in three dimensions with a long-range order; in contrast, the bonds in the CNT/Si system showed a long-range order in only one dimension—that is, along the long axis of the CNTs.



## 21.4

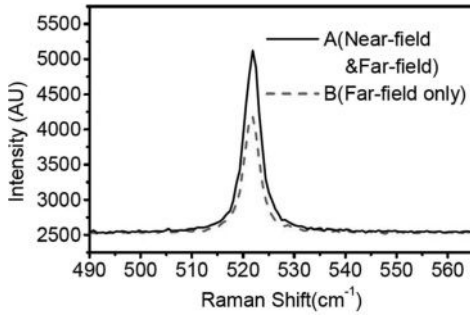
### Near-Field Scanning Raman Microscopy Using TERS

The NSRM system used in these experiments consisted of a standard Nanonics NSOM system and a Renishaw micro-Raman spectrometer. The Nanonics NSOM system uses a bent optic fiber tip (cantilevered tip), which makes the scanning head very compact. The compact design allows the easy integration of the spectrometer and NSOM by placing the scanning head under the microscope objective of the Renishaw system [32]. An argon ion laser (488 nm line) is focused onto the metal tip, which is made from tungsten wire through electrochemical etching [similar to the method used in scanning tunneling microscopy (STM) tip preparation], and then coated with silver through radiofrequency (RF)-sputtering [33].

The interaction between the tip and the laser enhances the local electrical field near the tip, which in turn enhances the Raman signal nearby. The same objective lens collects the Raman signal in the backscattering geometry, which is then directed into the Renishaw spectrometer by the coupling optics. In the configuration described above, both the near-field and far-field Raman signals are collected. In order to reduce the far-field component, the laser beam must be focused tightly to form a spot on the sample which is as small as possible. The collection efficiency of the optical system should also be high in order to obtain a good SNR, since the Raman signal is intrinsically weak. These two aspects require a lens or objective with a large numerical aperture (NA). In addition, the polarization direction and incident angle have strong effects on near-field enhancement, and these should be tuned carefully. The polarization direction is tuned by a  $\lambda/2$  plate, which is placed just before the laser and adjusted to be perpendicular to the beam. As shown by computer simulations, the near-field enhancement is not maximum when the laser beam is parallel to the tip axis. To maximize the near-field enhancement, two approaches can be used: the first approach is to set the tip oblique to the sample and use backscattering geometry; the second is to use a perpendicular tip and an oblique incident laser.

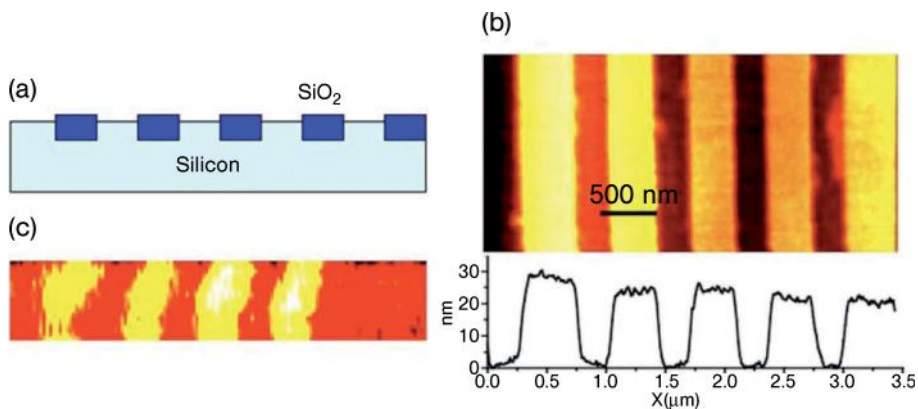
To observe the near-field enhancement, an experiment on single crystal silicon was performed. For this, the single crystal silicon was placed on the piezo scanning stage of the NSOM system, and the silicon Raman peak at  $520\text{ cm}^{-1}$  recorded for two tip positions: (i) with the tip “touching” the silicon surface to record the Raman spectrum, which includes both the near-field and far-field components; and (ii) with the tip lifted from the surface so as to record the far-field Raman spectrum. These are shown as spectra in Figure 21.6a and b, respectively. The near-field component is approximately 50% of the far-field signal.

It should be noted that the near-field Raman signal comes from a small region on the sample, while the far-field signal comes from a much larger volume (about  $2.5\ \mu\text{m}$  in diameter for our instrumental setup and the laser penetration of Si is about  $0.5\ \mu\text{m}$ ). Assuming that the diameter of the metal tip is several tens nanometers, say  $70\ \text{nm}$ , and the near-field enhancement occurs at a depth



**Figure 21.6** The silicon Raman spectra with the tip “touching” the sample surface (spectrum A) and the tip withdrawn (spectrum B).

of 20 nm of the Si sample. The far-field signal derives from a volume of  $V_{far} = \pi \left( \frac{2500}{2} \right)^2 \times 500 \text{ nm}^3$ , while the near-field signal is derived from a much smaller volume  $V_{near} = \pi \left( \frac{70}{2} \right)^2 \times 20 \text{ nm}^3$ . The enhancement factor can be estimated as  $\frac{I_{near}}{I_{far}} \times \frac{V_{far}}{V_{near}}$ , where  $I_{near} = 0.35I$  and  $I_{far} = (1 - 0.35)I$  are the measured near- and far-field Raman intensities, respectively. Such a simple estimation shows that the near-field enhancement factor is more than  $10^4$ . In another experiment, the improvement in spatial resolution was demonstrated by using a featured sample: a silicon device, which consists of  $\text{SiO}_2$  lines of 380 nm width, with 300 nm separations. The  $\text{SiO}_2$  lines were 30 nm higher than the silicon substrate (Figure 21.7a). By comparing the width of the  $\text{SiO}_2$  strips in the AFM profile and the real width (380 nm), the topographic spatial resolution of the set-up was derived as 34 nm (Figure 21.7b). Raman mapping ( $128 \times 20$  points) was performed on a strip, and the Raman image constructed using the Raman peak intensity, as shown in Figure 21.7c. The Raman spectra were collected with a 1 s integration time. In this experiment, the Raman spectrum contained both far-field and near-field components when the tip was on a Si-single crystal, but had only the far-field component when the tip was on  $\text{SiO}_2$ , where the  $\text{SiO}_2$  prevented the tip from coming close enough to the Si to excite its near-field Raman signal. Hence, the intensity variation of the Si Raman peak represented the near-field contribution, while the far-field contributed a constant background. The Raman intensity image shown in Figure 21.7c has a clear correlation with the Si device, as might be expected. This was the first two-dimensional (2-D) near-field Raman image of a real nanometer-sized device. The 1 s integration time required to record a good quality Raman spectrum is short enough to make NSRM a useful technique for imaging purposes. It should be noted that the  $\text{SiO}_2$  lines in the NSRM image are not straight, due to hysteresis and creep of the piezoelectric scanner, which is



**Figure 21.7** (a) Schematic cross-sectional diagram of the Si device sample; (b) Atomic force microscopy image of the Si device sample; (c) Raman intensity image of the Si device sample.

calibrated and linearized in normal AFM scanning. In Raman mapping, however, the scanning rate is much lower than that in normal AFM scanning, as the scanner must remain at each point for several seconds while the spectrometer records the Raman spectrum. Thus, the creep will become more obvious during the mapping process.

### 21.5 Near-Field Raman Imaging Using Optically Trapped Dielectric Microsphere

Recently, a new approach to near-field imaging has been developed, whereby the laser is focused to a spot size which is smaller than diffraction limit, by using a dielectric microsphere. In addition to being used as the excitation source for Raman spectroscopy, the incident laser beam (linearly polarized Gaussian TEM<sub>00</sub> mode) is also used to trap the microsphere just above the sample surface, through the well-known “optical tweezers” mechanism [34, 35]. Simulation studies have shown that subdiffraction-limited focusing can be achieved when the diameter of the dielectric microsphere is comparable to the wavelength of laser [36, 37]. In the experiments, the sample and polystyrene microspheres (3 μm diameter) in solution were placed in a sample cell filled with deionized water. One microsphere was trapped at the center of the laser beam, and was in contact with the surface of the sample during scanning. The schematic diagram of the experimental set-up is shown in Figure 21.3a. The near-field Raman microscopy set-up with polystyrene microsphere is based on the WITec CRM200 confocal Raman microscopy system

(25  $\mu\text{m}$  pinhole) with Olympus microscope objective (60 $\times$  NA = 1.2 water immersion). A double-frequency Nd:YAG laser (532 nm, 100 mW; CNI Laser) is used as the excitation laser, and coupled into a 3.5  $\mu\text{m}$ -core diameter single-mode fiber. The linearly polarized Gaussian beam (TEM00) that is used to excite the Raman signal is also used to trap the microsphere. The laser beam is incident on the sample through the microsphere. The sample is placed in a sample cell with diluted polystyrene microspheres in deionized water; the sample cell is then placed on a translation stage, which can be moved coarsely along the  $x$ - and  $y$ -axes (it can also be finely moved by using a piezostage). The Raman scattered light was directed to a 1800 grooves  $\text{mm}^{-1}$  grating, and detected using a TE-cooled CCD. Scanning electron microscopy images were recorded using field emission SEM (JEOL JSM-6700F).

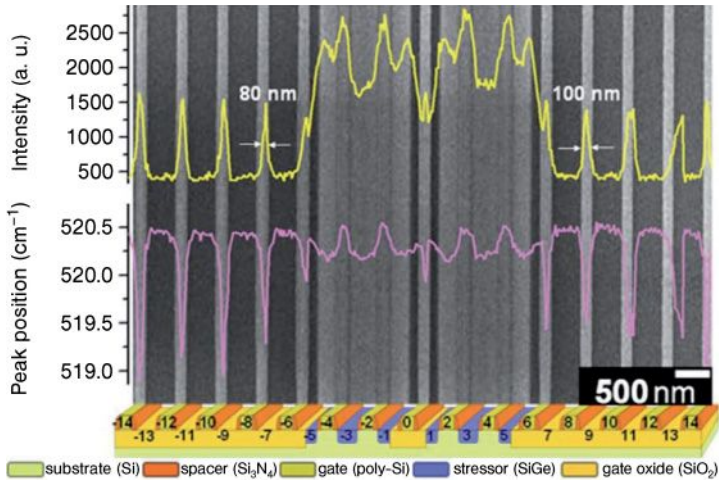
This technique has many advantages over the previous near-field techniques. The Raman signal collected with microsphere using the present technique is always much stronger than that without microsphere, typically two- to fivefold depending on the objective lens used. This is a critical advantage over the aperture near-field technique, which is orders of magnitude weaker than the corresponding far-field signal. As the laser light is focused on the sample through the microsphere, there is no background far-field signal in this experimental configuration, which has been one of the major problems in TERS. There is also no requirement to use a metal or metal-coated probe (e.g., a metal-coated AFM tip) to perform the experiment. The strong near-field Raman signal, and the simplicity in performing the experiment, make this technique attractive, easy, and fast. The reproducibility is also excellent, at near-100% level. Moreover, the technique can also be used on different types of sample.

The laser spot size of the near-field Raman technique was determined using a scanning-edge method [38]. For this, the trapped microsphere was scanned across a Si/SiO<sub>2</sub> structure and the scanning spectrum (Figure 21.3c) fitted with Equation 21.1:

$$I(x) = \frac{P}{2} \left\{ 1 + \operatorname{erf} \left( \frac{\sqrt{2}(x - x_0)}{w} \right) \right\} \quad (21.1)$$

where  $P$  is the total power contained in the laser beam,  $x$  is the position of the scanning edge,  $x_0$  is the center of the beam, and  $w$  is the  $1/e^2$  half-width. The spot size of the beam, the full width at half maximum (FWHM), was calculated to be  $\sim 80$  nm, from the following relationship:  $\text{FWHM} = \sqrt{2 \ln 2} w$ .

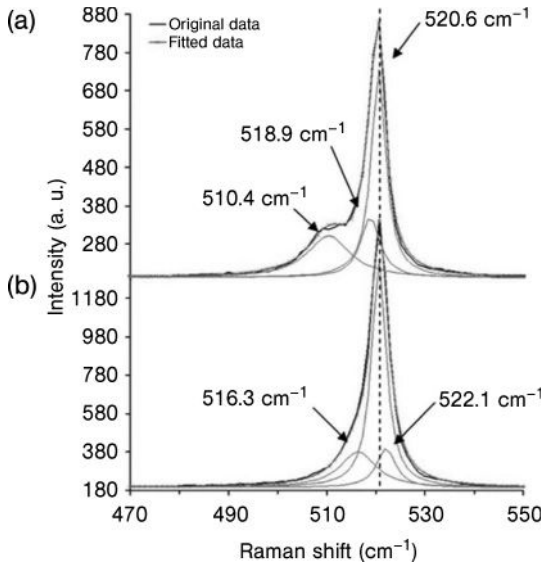
The system was used to study the SiGe/Si device sample with poly-Si gate and SiGe stressors, as shown in the electron micrograph in Figure 21.8. The patterned wafers used in this study were prepared using 65 nm device technology. After spacer formation and Si recess etching, the wafers were cleaned and the epitaxial SiGe growth was performed using a commercially available low-pressure chemical vapor deposition (LPCVD) system. The capability of the technique was also demonstrated by studying the strain on the channel below the poly-Si gates, which is compressively strained by the SiGe stressors.



**Figure 21.8** Scanning electron microscopy image with a cross-sectional diagram of the sample. The line scan of Raman Si intensity is shown in yellow, and the peak position in purple. The scanning step size was 20 nm with a 1 s integration time. The line width measured from the Si intensity profile was between 80 and 100 nm.

Straining the silicon can suppress the inter-valley scattering and reduce the effective carrier mass; the result is an improvement of the effective carrier mobility in the Si channel. In the past, the semiconductor industry has used mechanical strain as an alternative to physical scaling to improve transistor performance [39]. An appropriate strain, when applied to the channel region, can lead to a significant improvement in transistor performance. However, in the complementary metal-oxide-semiconductor (CMOS) transistor, the negative (n)-MOS and positive (p)-MOS must be strained differently. A compressive strain is known to be beneficial for p-MOS, while a tensile strain is known to improve n-MOS performance [40, 41]. It is for this reason that a technique to characterize strain with sub-100 nm resolution, on a reliable basis, is in such high demand.

Micro-Raman spectroscopy has long been a popular tool for strain measurements, because it is both nondestructive and quantitative [42–44]. Compressive strain shifts the Raman peak to higher frequency, while the tensile strain results in a red shift [45]. However, the spatial resolution of micro-Raman makes it impossible to be used for strain characterization in sub-100 nm semiconductor devices. Converging beam electron diffraction (CBED) in TEM can be used to characterize the strain with a nanometer-scale resolution [46, 47]. However, destructive and complicated sample preparations (which may alter the original strain field) have made this technique undesirable for large-scale strain characterization. Consequently, whilst the development of a reliable, nondestructive, quantitative assessment of strain on the nanometer-scale is critical, there is at present no

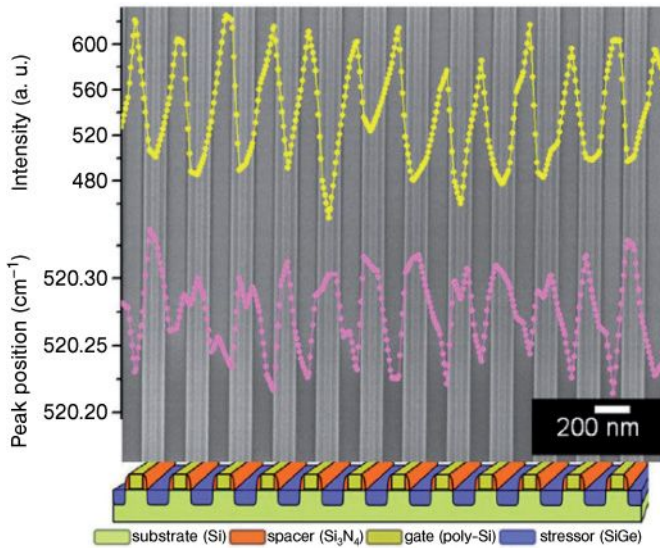


**Figure 21.9** Raman spectra from SiGe and poly-Si lines with fitted peaks using Lorentzian function. (a) The Raman peaks correspond to Si–Si phonon vibrations from the SiGe ( $\sim 510\text{ cm}^{-1}$ ), tensile-strained Si just below the SiGe ( $\sim 519\text{ cm}^{-1}$ ), and the Si substrate below ( $\sim 520\text{ cm}^{-1}$ ), respectively; (b) The Raman peaks correspond to Si–Si phonon vibrations poly-Si and bulk Si below ( $\sim 516\text{ cm}^{-1}$  and  $\sim 520\text{ cm}^{-1}$ ), and compressively strained Si in the channel region ( $\sim 522\text{ cm}^{-1}$ ).

such characterization technique available on the market. Here, we show the strain measurement on the 65 nm device lines with a much improved repeatability and SNR.

Figure 21.8 shows the SEM image as the background and the schematic cross-section diagram of the sample. This figure also shows the Raman line-scan Si intensity (yellow) and peak position (purple) profiles across the sample, with a scanning step size of 20 nm and a 1 s integration time. Both lines show an excellent correlation with the structure. Higher values of the intensity line scan correspond to positions of the poly-Si lines. It is important to note that the poly-Si lines of 45 nm width and 400 nm separations can easily be distinguished. The line-width measured from the FWHM of the Si-peak intensity is between 80 and 100 nm. The Si–Si peak position in regions below the poly-Si lines (purple line) is at a higher frequency, reflecting the fact that Si is under compressive strain exerted by the SiGe stressors. In other regions with SiGe lines (yellow line), the Si–Si peak position is at a lower frequency than that of the Si substrate, as would be expected for unstrained poly-Si lines. The difference between the center poly-Si line (marked 0) and its neighboring lines is also apparent, showing the high resolving power of the technique.

Figure 21.9a and b show the Raman spectra recorded in the SiGe line region and on top of the poly-Si line, respectively. Each spectrum was fitted with three



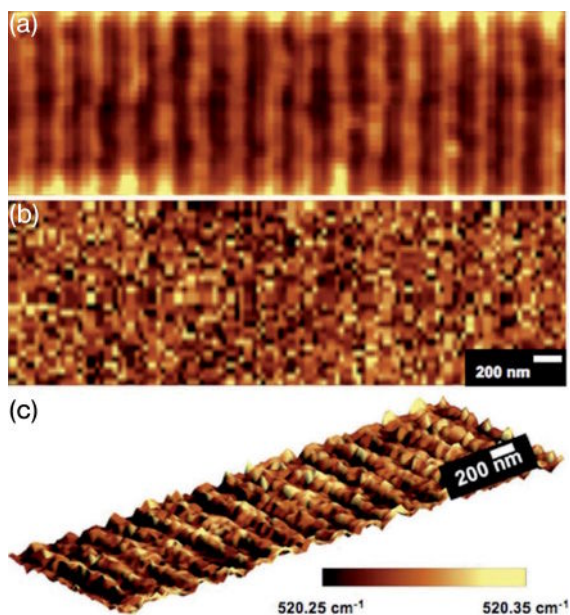
**Figure 21.10** Scanning electron microscopy image with a cross-sectional diagram of periodic poly-Si lines and SiGe stressors. The line scan of Raman Si–Si intensity from SiGe is shown in yellow, and the Si–Si peak position in purple. The line scans show excellent correspondence with the structure, and a good SNR.

Lorentzian peaks. In Figure 21.9a, the Raman peaks from SiGe line correspond to Si–Si phonon vibrations from the SiGe ( $\sim 510\text{ cm}^{-1}$ ), tensile-strained Si just below the SiGe ( $\sim 519\text{ cm}^{-1}$ ), and the Si substrate below ( $\sim 520\text{ cm}^{-1}$ ), respectively. Similarly, in Figure 21.9b, the Raman peaks correspond to the Si–Si phonon vibrations of poly-Si and bulk Si below ( $\sim 516\text{ cm}^{-1}$  and  $\sim 520\text{ cm}^{-1}$ ), and another one is from the compressively strained Si in the channel region ( $\sim 522\text{ cm}^{-1}$ ).

Figure 21.10 shows the SEM image of the device sample, together with the detailed illustration diagram. From this figure, the line profile of the intensity of Si–Si phonon vibrations from the SiGe (yellow), and the Si–Si peak position (purple), can be seen. The results show an excellent correspondence to the device structure, with a good SNR. The line profile data (intensity and peak positions) are extracted from an area of Raman mapping of  $4.0 \times 1.3\ \mu\text{m}^2$  ( $100 \times 32$  pixels), as shown in Figure 21.11, which took about 6 min to complete.

Figure 21.11a shows the Raman image from the intensity of Si–Si phonon vibrations from the SiGe of the structure shown in Figure 21.10. For comparison, Figure 21.11b shows the image from confocal Raman set-up (far-field imaging). It is clear that the present near-field technique can resolve the periodic lines with excellent repeatability that far-field technique cannot resolve. The three-dimensional (3-D) Raman image in Figure 21.11c is based on the peak position of Si–Si phonon vibration from Si at  $\sim 520\text{ cm}^{-1}$ . From this image, it is possible to study the higher compressive strain regions, which are under the poly-Si lines and



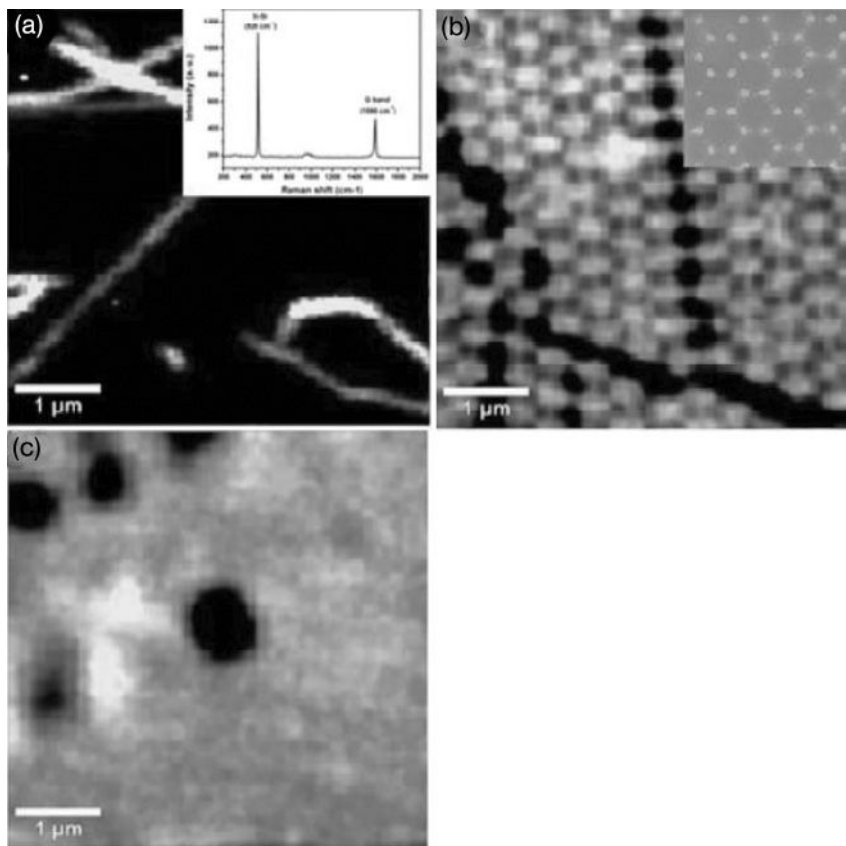


**Figure 21.11** Raman images ( $4.0 \times 1.3 \mu\text{m}^2$ ) of the periodic poly-Si lines and SiGe stressors obtained in approximately 6 min. (a) Near-field Raman image from the Si–Si peak intensity from SiGe; (b) Confocal Raman image from the Si–Si peak intensity from SiGe; (c) 3-D near-field Raman image from the Si–Si peak position, showing the relative strain at different regions.

are compressively strained by the SiGe stressors. The fact that it took only about 6 min to carry out the mapping means that the high-resolution Raman imaging using this technique can be performed within a reasonable time.

Apart from the device sample, in order to show the capability of the technique for other types of sample, Raman mapping was also performed on CNTs and gold nanopatterns. The purified HiPCO single-walled carbon nanotubes (SWNTs) were purchased from Carbon Nanotechnologies. The HiPCO SWNTs (10 mg) were dispersed in 100 ml  $\text{D}_2\text{O}$  solution with 1 wt% sodium dodecyl sulfate (SDS). The dispersion was then treated by probe sonication (Sonics & Materials Inc.; Model VCX 130) at a power level of 250 W for 30 min, followed by ultracentrifugation at  $140\,000\times g$  for 4 hours. The supernatant was drop-cast on a Si substrate and dried in air. Individual (or slightly bundled) tubes on Si were then obtained after rinsing the Si substrate with pure water. A gold nanopattern was also fabricated on a silicon substrate. For this, polystyrene microspheres (diameter  $0.5 \mu\text{m}$ ) in solution were dispersed on a silicon substrate, using the drop-coating method. The polystyrene microspheres self-assembled to form a monolayer, and a thin film of gold, of  $\sim 100 \text{ nm}$  thickness, was deposited onto the Si substrate, using DC magnetron sputtering. The sample was sonicated for 1 min in chloroform to remove the





**Figure 21.12** Raman images ( $5.0 \times 5.0 \mu\text{m}^2$  of the carbon nanotubes (CNTs) and gold nanopatterns. (a) Near-field Raman image from G band of CNTs; (b) Near-field Raman image from the Si–Si peak intensity; (c) Confocal Raman image from the gold nanopatterns. The inset in (a) is the Raman spectrum of the CNTs; the inset in (b) shows the SEM image of the gold nanopatterns, where the nanopattern size is  $\sim 100$  nm.

polystyrene microspheres, and then annealed in argon ambient at  $400^\circ\text{C}$  for 30 min. The size of the gold nanopattern was  $\sim 100$  nm.

Figure 21.12a–c show the  $5.0 \times 5.0 \mu\text{m}^2$  ( $100 \times 100$  pixels) Raman images of the CNTs and gold nanopattern. Figure 21.12a shows the Raman image from the G band ( $\sim 1590 \text{ cm}^{-1}$ ) of CNTs; the inset shows the Raman spectrum from the CNTs on a silicon substrate. Figure 21.12b shows the Raman image from the Si–Si peak intensity, where the darker regions correspond to the gold nanopatterns. It is clear that the  $\sim 100$  nm gold nanopattern can be clearly resolved using the new technique. The near-field Raman image corresponds well to the electron micrograph, as shown in the inset of Figure 21.12b. Figure 21.12c shows the confocal Raman image of the gold nanopatterns, which show no pattern details. Hence, the capability of this technique for various samples is proven.

## 21.6

## Conclusions

Characterization tools in the nanometer regime are very important to reveal and utilize the unique properties of nanomaterials, and Raman imaging is indeed a versatile tool for studying both materials and devices. In this chapter, we have illustrated the value of Raman imaging by using three techniques:

- *Micro-Raman imaging* for the detection of Si–C covalent bonding of CNTs grown on a Si substrate. The technique is simple and easy to perform, but is limited in its application to nanomaterials and devices by its limited spatial resolution.
- *Apertureless near-field Raman imaging*, where laser light is focused to the apex of a metal or metal-coated tip. This method is much superior to the aperture technique in terms of spatial resolution and SNR, but faces problems of wear and tear, oxidation, and contamination of the tip apex (e.g., by carbon). These may lead to severe adverse effects on the near-field enhancement. Far-field signals may also be problematic.
- *Microsphere near-field Raman imaging* [48], where laser is focused to a spot size smaller than the diffraction limit through a dielectric microsphere that is trapped using the optical tweezers principle. This method has many advantages over previous near-field techniques: the Raman signal is stronger; there is no background far-field signal; and the use of a metal or metal-coated tip is not required. The strong near-field Raman signal and simplicity in carrying out the experiments make this technique attractive, easy, and fast. The method's reproducibility is also excellent (close to 100%), and it can also be used on different types of sample.

## References

- 1 Pohl, D.W., Denk, W. and Lanz, M. (1984) Optical stethoscopy: image recording with resolution  $\lambda/20$ . *Appl. Phys. Lett.*, **44**, 651–653.
- 2 Frey, H.G., Bolwien, C., Brandenburg, A., Ros, R. and Aselmetti, D. (2006) Optimized apertureless optical near-field probes with 15 nm optical resolution. *Nanotechnology*, **17**, 3105–3110.
- 3 Kim, J.H. and Song, K.B. (2007) Recent progress of nano-technology with NSOM. *Micron*, **38**, 409–426.
- 4 Tsai, D.P., Othonos, A., Moskovits, M. and Uttamchandani, D. (1994) Raman spectroscopy using a fiber optic probe with subwavelength aperture. *Appl. Phys. Lett.*, **64**, 1768–1770.
- 5 Grausem, J., Humbert, B., Spajer, M., Courjon, D., Burneau, A. and Oswalt, J. (1999) Near-field Raman spectroscopy. *J. Raman Spectrosc.*, **30**, 833–840.
- 6 Hecht, B., Sick, B., Wild, U.P., Deckert, V., Zenobi, R., Martin, O.J.F. and Pohl, D.W. (2000) Scanning near-field optical microscopy with aperture probes: fundamentals and applications. *J. Chem. Phys.*, **112**, 7761–7764.
- 7 Webster, S., Batchelder, D.N. and Smith, D.A. (1998) Submicron resolution measurement of stress in silicon by near-field Raman spectroscopy. *Appl. Phys. Lett.*, **72**, 1478–1480.
- 8 Sun, W.X. and Shen, Z.X. (2003) Near-field scanning Raman microscopy

- using apertureless probes. *J. Raman Spectrosc.*, **34**, 668–676.
- 9 Anderson, N., Hartschuh, A. and Novotny, L. (2005) Near-field Raman microscopy. *Mater. Today*, **May**, 50–54.
  - 10 Saito, Y., Motohashi, M., Hayazawa, N., Iyoki, M. and Kawata, S. (2006) Nanoscale characterization of strained silicon by tip-enhanced Raman spectroscopy in reflection mode. *Appl. Phys. Lett.*, **88**, 143109.
  - 11 Lee, N., Hartschuh, R.D., Mehtani, D., Kisliuk, A., Maguire, J.F., Green, M., Foster, M.D. and Sokolov, A.P. (2007) High contrast scanning nano-Raman spectroscopy of silicon. *J. Raman Spectrosc.*, **38**, 789–796.
  - 12 Ossikovski, R., Nguyen, Q. and Picardi, G. (2007) Simple model for the polarization effects in tip-enhanced Raman spectroscopy. *Phys. Rev. B*, **75**, 045412.
  - 13 Iijima, S. (1991) Helical microtubules of graphitic carbon. *Nature*, **354**, 56–58.
  - 14 Tans, S.J., Devoret, M.H., Dai, H.J., Thess, A., Smalley, R.E., Geerligs, L.J. and Dekker, C. (1997) Individual single-wall carbon nanotubes as quantum wires. *Nature*, **386**, 474–477.
  - 15 Overney, G., Zhong, W. and Tomanek, D. (1993) Structural rigidity and low-frequency vibrational modes of long carbon tubules. *Z. Phys. D*, **27**, 93–96.
  - 16 Saito, R., Fujita, M., Dresselhaus, G. and Dresselhaus, M.S. (1992) Electronic structure of chiral graphene tubules. *Appl. Phys. Lett.*, **60**, 2204–2206.
  - 17 Albrecht, P.M., Barraza-Lopez, S. and Lyding, J.W. (2007) Scanning tunneling spectroscopy and *ab initio* calculations of single-walled carbon nanotubes interfaced with highly doped hydrogen-passivated Si(100) substrates. *Nanotechnology*, **18**, 095204.
  - 18 Albrecht, P.M. and Lyding, J.W. (2007) Local stabilization of single-walled carbon nanotubes on Si(100)- $2 \times 1$ :H via nanoscale hydrogen desorption with an ultrahigh vacuum scanning tunneling microscope. *Nanotechnology*, **18**, 125302.
  - 19 Miwa, R.H., Orellana, W. and Fazzio, A. (2005) Substrate-dependent electronic properties of an armchair carbon nanotube adsorbed on H/Si(001). *Appl. Phys. Lett.*, **86**, 213111.
  - 20 Miwa, R.H., Orellana, W. and Fazzio, A. (2005) Carbon nanotube adsorbed on hydrogenated Si(001) surfaces. *Appl. Surf. Sci.*, **244**, 124–128.
  - 21 de Brito Mota, F. and de Castilho, C.M.C. (2006) Carbon nanotube adsorbed on a hydrogenated Si-rich  $\beta$ -SiC(100) ( $3 \times 2$ ) surface: First-principles pseudopotential calculations. *Phys. Rev. B*, **74**, 165408.
  - 22 Peng, G.W., Huan, A.C.H., Liu, L. and Feng, Y.P. (2006) Structural and electronic properties of 4A carbon nanotubes on Si(001) surfaces. *Phys. Rev. B*, **74**, 235416.
  - 23 Wang, Y., Voronin, G.A., Zerda, T.W. and Winiarski, A. (2005) SiC-CNT nanocomposites: high pressure reaction synthesis and characterization. *J. Phys.: Condens. Matter*, **18**, 275–282.
  - 24 Mews, A., Koberling, F., Basche, T., Philipp, G., Duesberg, G.S., Roth, S. and Burghard, M. (2000) Raman imaging of single carbon nanotubes. *Adv. Mater.*, **12**, 1210–1214.
  - 25 Hiura, H., Ebbesen, T.W., Tanigaki, K. and Takahashi, H. (1993) Raman studies of carbon nanotubes. *Chem. Phys. Lett.*, **202**, 509–512.
  - 26 Nakashima, S., Katahama, H., Nakakura, Y. and Mitsuishi, A. (1986) Relative Raman intensities of the folded modes in SiC polytypes. *Phys. Rev. B*, **33**, 5721–5729.
  - 27 Olego, D. and Cardona, M. (1982) Pressure dependence of Raman phonons of Ge and 3C-SiC. *Phys. Rev. B*, **25**, 1151–1160.
  - 28 Nakashima, S. and Harima, H. (1997) Raman investigation of SiC polytypes. *Phys. Status Solidi A*, **162**, 39–64.
  - 29 Burton, J.C., Sun, L., Long, F.H., Feng, Z.C. and Ferguson, I.T. (1999) First- and second-order Raman scattering from semi-insulating 4H-SiC. *Phys. Rev. B*, **59**, 7282–7284.
  - 30 Windl, W., Karch, K., Pavone, P., Schutt, O., Strauch, D., Weber, W.H., Hass, K.C. and Rimai, L. (1994) Second-order Raman spectra of SiC: experimental and theoretical results from *ab initio* phonon calculations. *Phys. Rev. B*, **49**, 8764–8767.

- 31 Sasaki, Y., Nishina, Y., Sato, M. and Okamura, K. (1989) Optical-phonon states of SiC small particles studied by Raman scattering and infrared absorption. *Phys. Rev. B*, **40**, 1762–1772.
- 32 Sun, W.X. and Shen, Z.X. (2003) Apertureless near-field scanning Raman microscopy using reflection scattering geometry. *Ultramicroscopy*, **94**, 237–244.
- 33 Sun, W.X., Shen, Z.X., Cheong, F.C., Yu, G.Y., Lim, K.Y. and Lin, J.Y. (2002) Preparations of cantilevered W tips for atomic force microscopy and apertureless near-field scanning optical microscopy. *Rev. Sci. Instrum.*, **73**, 2942–2947.
- 34 Ashkin, A. (1980) Applications of laser radiation pressure. *Science*, **210**, 1081–1088.
- 35 Ashkin, A. (1997) Optical trapping and manipulation of neutral particles using lasers. *Proc. Natl Acad. Sci. USA*, **94**, 4853–4860.
- 36 Li, X., Chen, Z.G., Taflove, A. and Backman, V. (2005) Optical analysis of nanoparticles via enhanced backscattering facilitated by 3-D photonic nanojets. *Opt. Express*, **13**, 526–533.
- 37 Lecler, S., Takakura, Y. and Meyrueis, P. (2005) Properties of a three-dimensional photonic jet. *Opt. Lett.*, **30**, 2641–2643.
- 38 Veshapidze, G., Trachy, M.L., Shah, M.H. and DePaola, B.D. (2006) Reducing the uncertainty in laser beam size measurement with a scanning edge method. *Appl. Opt.*, **45**, 8197–8199.
- 39 Chidambaram, P.R., Bowen, C., Chakravarthi, S., Machala, C. and Wise, R. (2006) Fundamentals of silicon material properties for successful exploitation of strain engineering in modern CMOS manufacturing. *IEEE Trans. Electron. Dev.*, **53** (23), 944–964.
- 40 Paul, D.J. (2004) Si/SiGe heterostructures: from material and physics to devices and circuits. *Semicond. Sci. Technol.*, **19**, R75–R108.
- 41 Wu, S.L., Lin, Y.M., Chang, S.J., Lu, S.C., Chen, P.S. and Liu, C.W. (2006) Enhanced CMOS performances using substrate strained-SiGe and mechanical strained-Si technology. *IEEE Electron. Device Lett.*, **27**, 46–48.
- 42 Wolf, I.D., Maes, H.E. and Jones, S.K. (1996) Stress measurements in Si devices through Raman spectroscopy: bridging the gap between theory and experiment. *J. Appl. Phys.*, **79**, 7148–7156.
- 43 Nakashima, S., Yamamoto, T., Ogura, A., Uejima, K. and Yamamoto, T. (2004) Characterization of Si/Ge<sub>x</sub>Si<sub>1-x</sub> structures by micro-Raman imaging. *Appl. Phys. Lett.*, **84**, 2533–2535.
- 44 Mitani, T., Nakashima, S., Okumura, H. and Ogura, A. (2006) Depth profiling of strain and defects in Si/Si<sub>1-x</sub>Ge<sub>x</sub>/Si heterostructures by micro-Raman imaging. *J. Appl. Phys.*, **100**, 073511.
- 45 Anastassakis, E. and Liarokapis, E. (1987) Polycrystalline Si under strain: Elastic and lattice-dynamical considerations. *J. Appl. Phys.*, **62**, 3346–3352.
- 46 Senez, V., Armigliato, A., Wolf, I.D., Carnevale, G., Balboni, R., Frabboni, S. and Benedetti, A. (2003) Strain determination in silicon microstructures by combined convergent beam electron diffraction, process simulation, and micro-Raman spectroscopy. *J. Appl. Phys.*, **94**, 5574–5583.
- 47 Liu, H.H., Duan, X.F., Qi, X.Y., Xu, Q.X., Li, H.O. and Qian, H. (2006) Nanoscale strain analysis of strained-Si metal-oxide-semiconductor field effect transistors by large angle convergent-beam electron diffraction. *Appl. Phys. Lett.*, **88**, 263513.
- 48 Kasim, J., Yu, T., You, Y.M., Liu, J.P., See, A., Li, L.J. and Shen, Z.X. (2008) Near-field Raman imaging using optically trapped dielectric microsphere. *Opt. Express*, **16**, 7976.



## 22

### Fullerene-Rich Nanostructures

*Fernando Langa and Jean-François Nierengarten*

#### 22.1

##### Introduction

In recent years, the rapid advances in dendrimer synthetic chemistry have moved towards the creation of functional systems with increased attention to potential applications [1]. Among the large number of molecular subunits used for dendrimer chemistry,  $C_{60}$  has proven to be a versatile building block and fullerene-functionalized dendrimers – that is, *fullerodendrimers* [2] – have generated significant research activities in recent years [3, 4]. In particular, the peculiar physical properties of fullerene derivatives make fullerodendrimers attractive candidates for a variety of interesting features in supramolecular chemistry and materials science [5].  $C_{60}$  itself is a convenient core for dendrimer chemistry [3], and the functionalization of  $C_{60}$  with a controlled number of dendrons dramatically improves the solubility of the fullerenes [6]. Furthermore, variable degrees of addition about the fullerene core are possible, and its almost spherical shape leads to globular systems, even with low-generation dendrons [7]. On the other hand, specific advantages are brought about by the encapsulation of a fullerene moiety in the middle of a dendritic structure [8]. The shielding effect resulting from the presence of the surrounding shell has been found useful for optimizing the optical limiting properties of  $C_{60}$  derivatives [9], to obtain amphiphilic derivatives with good spreading characteristics [10], or to prepare fullerene-containing liquid crystalline materials [11]. Use of the fullerene sphere as a photoactive core unit has also been reported [12]. In particular, the special photophysical properties of  $C_{60}$  have been used to evidence dendritic shielding effects [13] and to prepare dendrimer-based, light-harvesting systems [14]. Whereas, the majority of the fullerene-containing dendrimers reported to date have been prepared with a  $C_{60}$  core, dendritic structures with fullerene units at their surface, or with  $C_{60}$  spheres in the dendritic branches, have been essentially ignored. This is mainly associated with difficulties related to the synthesis of fullerene-rich molecules [4]. Indeed, the two major problems for the preparation of such dendrimers are the low solubility of  $C_{60}$  and its chemical reactivity, which limits the range of reactions that can be used for the synthesis of

branched structures bearing multiple  $C_{60}$  units. The most recent developments on the molecular engineering of covalent and noncovalent fullerene-rich dendrimers will be presented in the chapter, the aim of which is not to provide an exhaustive review on such systems, but rather to present significant examples that illustrate the current state of fullerene chemistry for the development of new nanostructures.

## 22.2 Fullerene-Rich Dendritic Branches

Over the past years, Nierengarten and coworkers have developed synthetic methodologies allowing for the preparation of dendrons substituted with several fullerene moieties [15]. As a typical example, the convergent preparation of dendritic branches with fullerene subunits at the periphery is depicted in Figures 22.1–22.3. The starting fullerene derivative,  $G1CO_2tBu$ , is easily obtained on a multi-gram scale, and is highly soluble in common organic solvents, based on the presence of two long alkyl chains [16]. The iterative reaction sequence used in the preparation of the subsequent dendrimer generations relies upon successive cleavage of a *t*-butyl ester moiety under acidic conditions, followed by a *N,N*-dicyclohexylcarbodiimide (DCC)-mediated esterification reaction with the  $A_2B$  building block **1** possessing two benzylic alcohol functions and a protected carboxylic acid function [16].

Selective cleavage of the *t*-butyl ester group in  $G1CO_2tBu$  was achieved by treatment with an excess of  $CF_3COOH$  (TFA) in  $CH_2Cl_2$  to afford  $G1CO_2H$  in a quantitative yield. Reaction of the diol **1** with carboxylic acid  $G1CO_2H$  under esterification conditions using DCC, 4-*N*-dimethylaminopyridine (DMAP), and 1-hydroxybenzotriazole (HOBT) in  $CH_2Cl_2$  gave the protected dendron of second-generation  $G2CO_2tBu$  in 90% yield. Hydrolysis of the *t*-butyl ester moiety under acidic conditions then afforded the corresponding carboxylic acid  $G2CO_2H$  in a

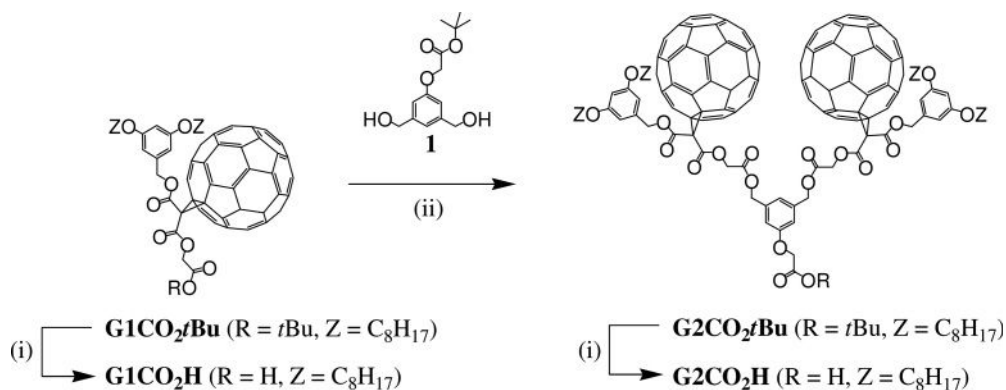


Figure 22.1 Reagents and conditions: (i) TFA,  $CH_2Cl_2$ ; (ii) DCC, DMAP, HOBT,  $CH_2Cl_2$ .

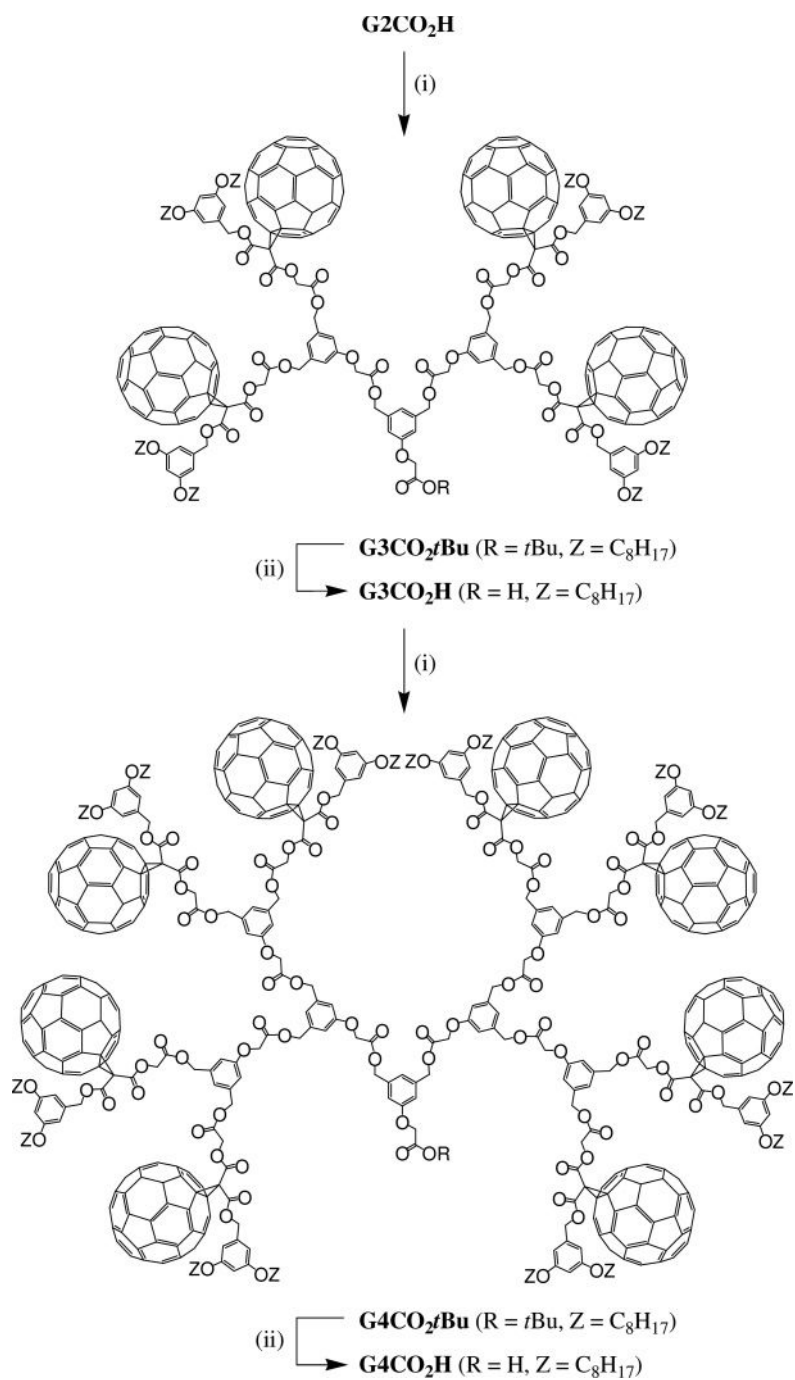
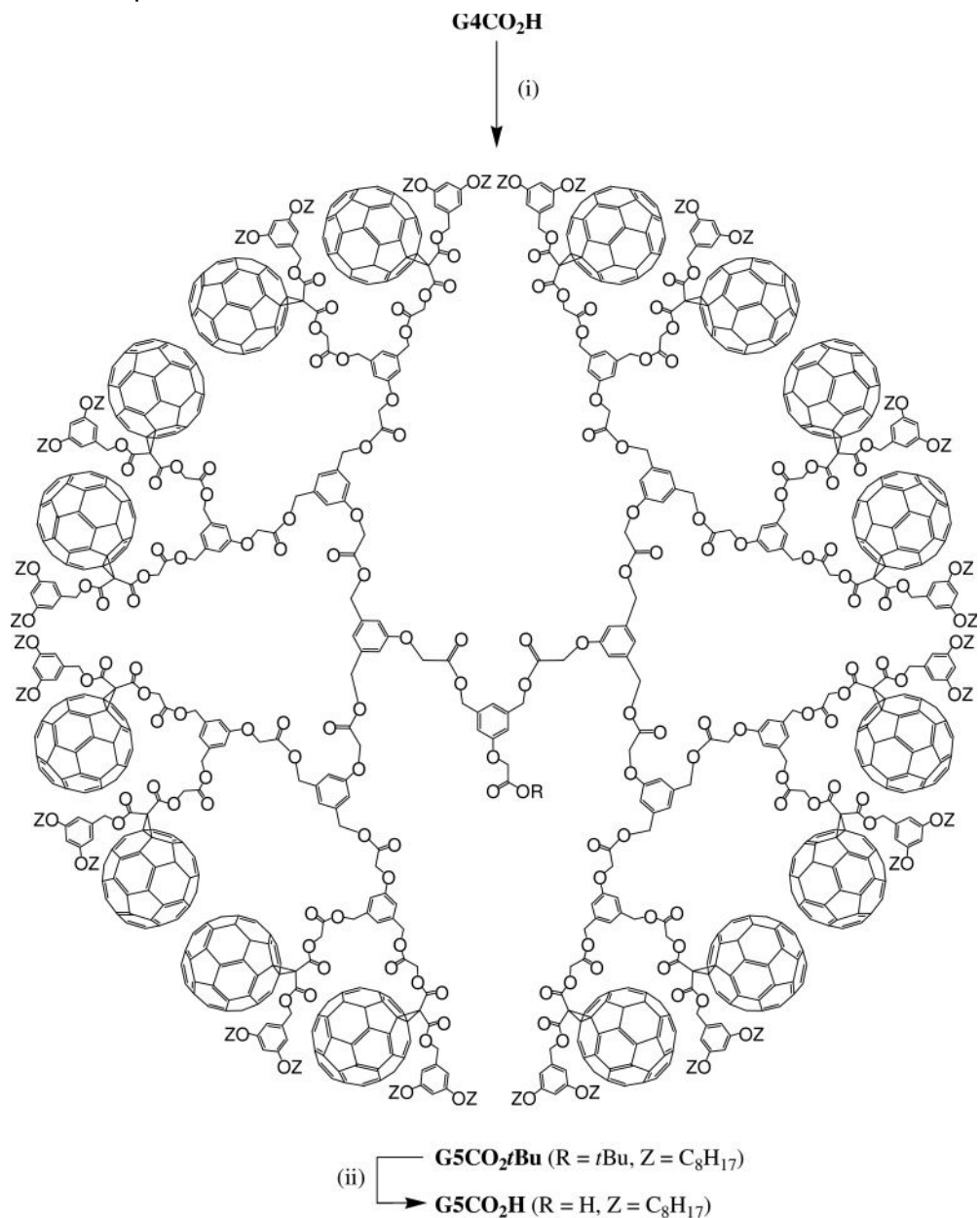


Figure 22.2 Reagents and conditions: (i) 1, DCC, DMAP, HOBT, CH<sub>2</sub>Cl<sub>2</sub>; (ii) TFA, CH<sub>2</sub>Cl<sub>2</sub>.





**Figure 22.3** Reagents and conditions: (i) 1, DCC, DMAP, HOBT, CH<sub>2</sub>Cl<sub>2</sub>; (ii) TFA, CH<sub>2</sub>Cl<sub>2</sub>.

quantitative yield. Esterification of G<sub>2</sub>CO<sub>2</sub>H with diol 1 (DCC, HOBT, DMAP) afforded the *t*-butyl-protected fullerodendron G<sub>3</sub>CO<sub>2</sub>*t*Bu in 87% yield (Figure 22.2). Selective hydrolysis of the *t*-butyl ester under acidic conditions afforded acid G<sub>3</sub>CO<sub>2</sub>H in 99% yield. Subsequent reaction of G<sub>3</sub>CO<sub>2</sub>H with the branching unit

1 in the presence of DCC, HOBt and DMAP afforded fullerodendron G4CO<sub>2</sub>tBu (95%), which after treatment with CF<sub>3</sub>CO<sub>2</sub>H gave G4CO<sub>2</sub>H (97%).

By repeating the same reaction sequence from G4CO<sub>2</sub>H, the fifth generation derivatives G5CO<sub>2</sub>tBu and G5CO<sub>2</sub>H were also prepared (Figure 22.3). Compounds G1-5CO<sub>2</sub>tBu and G1-5CO<sub>2</sub>H are highly soluble in common organic solvents such as CH<sub>2</sub>Cl<sub>2</sub>, CHCl<sub>3</sub>, or tetrahydrofuran (THF), and complete spectroscopic characterization was easily achieved.

The unequivocal characterization of these compounds also required their mass spectrometric analysis; this is quite difficult, as no structural features allow for easy protonation of the molecules. Several ionization techniques such as matrix-assisted laser desorption/ionization (MALDI), or fast-atom bombardment (FAB) have been applied for the characterization of fullerodendritic species [17]. These tools are, however, not always well adapted for C<sub>60</sub> derivatives of high molecular weight, such as G1-5CO<sub>2</sub>tBu and G1-5CO<sub>2</sub>H, as they lead to high levels of fragmentation. In contrast, electrospray mass spectrometry (ES-MS) has the ability to desolvate ions that preexist in solution, thus offering the possibility of transferring such ions into the gas phase without notable fragmentation [18]. Indeed, supramolecular cationic dendritic structures resulting from the self-assembly of fullerodendrons possessing an ammonium function at the focal point and bis-crown-ether receptors have been successfully characterized using ES-MS [19]. Unfortunately, fullerodendrons G1-5CO<sub>2</sub>tBu and G1-5CO<sub>2</sub>H are uncharged in solution, and therefore are not suitable for ES-MS analysis, at least in principle. However, it has been shown that an *in situ* reduction of fullerenes in the injection capillary of the electrospray mass spectrometer offers an interesting possibility to analyze neutral C<sub>60</sub> derivatives [17]. In other words, fullerene radical anions can be generated during the electrospray process, owing to the ability of the electrospray source to behave like an electrolysis cell [17]. Indeed, fullerodendrons G1-5CO<sub>2</sub>tBu and G1-5CO<sub>2</sub>H could be characterized by applying this technique. The ES mass spectra of the second-generation derivative G2CO<sub>2</sub>tBu is depicted in Figure 22.4. The mass spectrum obtained under mild conditions ( $V_c = 150$  V) is dominated by the doubly charged ion peak at  $m/z$  1343.2, which can be assigned to the radical di-anion of G2CO<sub>2</sub>tBu (calculated  $m/z$  1343.43). The experimental isotopic pattern of this ion is in perfect agreement with that calculated for the doubly reduced compound. A singly charged ion is also observed as minor signal at  $m/z$  2686.3, and corresponds to the singly reduced G2CO<sub>2</sub>tBu-structure. Finally, the minor peak observed at  $m/z$  1226.1 is ascribed to the fragment G1CO<sub>2</sub><sup>-</sup> resulting from the cleavage of a benzylic ester unit in G2CO<sub>2</sub>tBu. When the ES spectrum of G2CO<sub>2</sub>tBu was recorded under more harsher conditions ( $V_c = 300$  V), the characteristic peaks corresponding to the radical mono- and di-anions were still observed, but an additional signal could also be detected at  $m/z$  1124. This characteristic fragment was the same as that observed in the spectra of G1CO<sub>2</sub>tBu.

The analysis of the higher-generation compounds has been more difficult. Effectively, the response factor of the anions is reduced as their molecular weight is increased. In addition, the number of ester functions is higher, thus leading to more fragmentation. The resulting fragments having a lower molecular weight – and

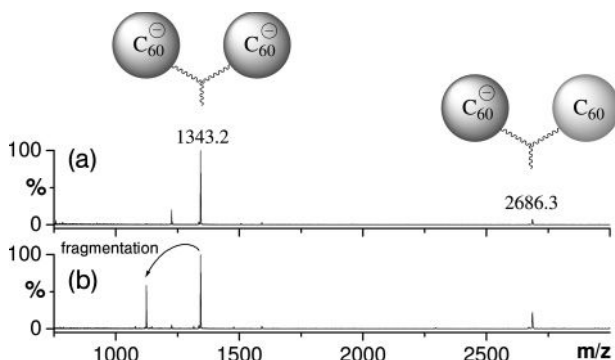


Figure 22.4 ES-MS spectra of  $G_2CO_2tBu$  recorded with  $V_c$  values of 150 (a) and 300 V (b).

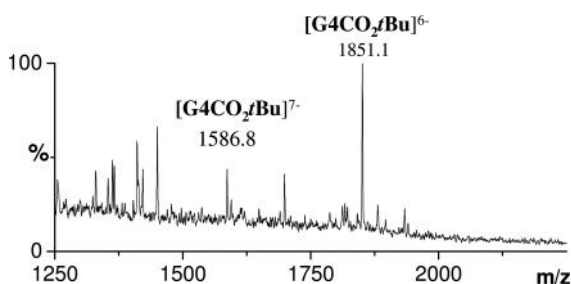


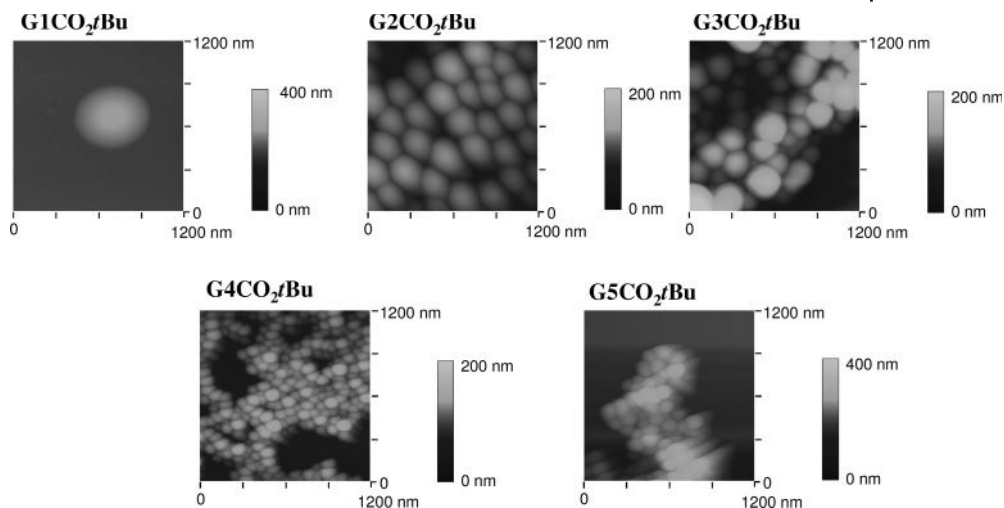
Figure 22.5 ES-MS spectrum of  $G_4CO_2tBu$  recorded with a  $V_c$  value of 150 V.

therefore a higher response factor—gave signals with significant intensities in all the spectra, regardless of the  $V_c$  value. However, peaks corresponding to nonfragmented ions could be clearly observed. As shown in Figure 22.5, two characteristic molecular ion peaks are observed at  $m/z$  1851.1 and 1586.8 in the ES-MS spectrum of  $G_4CO_2tBu$ . These correspond to the hexa- and hepta-anions of the fullerodendron, in which six or seven  $C_{60}$  units are reduced, respectively. Several fragment ions are also present in both cases, the low (100 V) and high (300 V) voltages. Importantly, their intensity relative to the molecular ion peaks is clearly increased when the  $V_c$  value was raised, thus showing that these additional signals result from a fragmentation of the dendrimer. Within this series of compounds, a general observation is a decrease in the absolute intensity of the signals arising from the fullerodendrons when the generation number is increased. As mentioned above, this is most likely due to the increased number of labile ester functions giving rise to more fragmentations, and to a decrease in the response factor when the molecular weight is increased.

### 22.3

#### Photoelectrochemical Properties of Fullerodendrons and Their Nanoclusters

The absorption spectra of  $G_1-5CO_2tBu$  in a toluene/acetonitrile (1/6, v/v) mixed solvent exhibit structureless broad absorption in the range of 300 to 800 nm. These



**Figure 22.6** Atomic force microscopy images of  $(G1-5CO_2tBu)_m$  on mica.

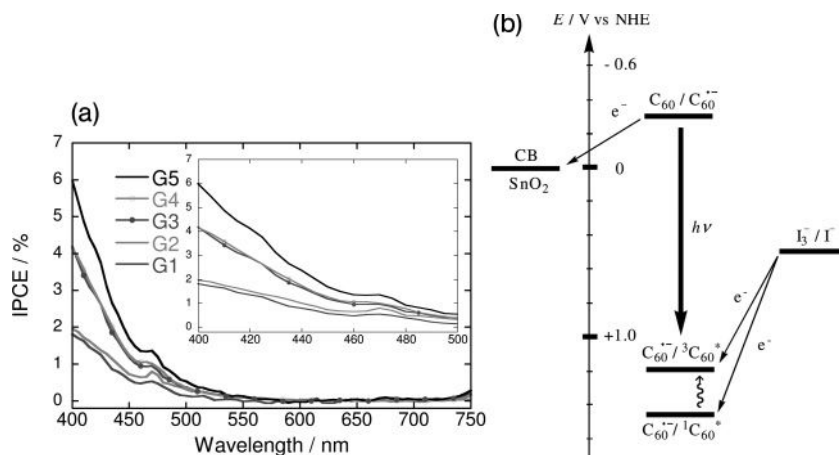
results suggest that such compounds aggregate and form large clusters in the mixed solvents [20]. The particle size of these clusters in the mixed solvent was measured using dynamic light scattering (DLS). In a mixture (1/6) of toluene/ acetonitrile at an incubation period of 15 min after injection of the toluene solution into acetonitrile, the size distribution of  $G1-5CO_2tBu$  was found to be relatively narrow, with different mean diameters of 790 nm for  $(G1CO_2tBu)_m$ , 210 nm for  $(G2CO_2tBu)_m$ , 170 nm for  $(G3CO_2tBu)_m$ , 100 nm for  $(G4CO_2tBu)_m$ , and 90 nm for  $(G5CO_2tBu)_m$ . The order of the mean diameters was not consistent with that of their molecular sizes. Both, dendrimers and dendrons are known to become compact, rigid structured as the generation number is increased [20]. This suggests that, in the process of cluster formation with the higher dendrimer generation, each dendritic branch is subject to interactions with branches belonging to the same dendrimer molecule (*intramolecular*), rather than to other molecules (*intermolecular*). This results in the formation of densely packed dendrimer clusters with a small, compact size (i.e., 90–100 nm). In other words, in the lower dendrimer generations, *intermolecular* interactions among branches prevail, leading to the formation of poorly packed dendrimer clusters with a large size. In order to assess the shape and morphology of  $(G1-5CO_2tBu)_m$  clusters, atomic force microscopy (AFM) measurements have been carried out. The AFM images of the clusters prepared by spin-coating of the  $(G1-5CO_2tBu)_m$  cluster solutions on mica surface are depicted in Figure 22.6. To remove solvent, the resulting substrates were heated under reduced pressure. The  $(G1-5CO_2tBu)_m$  clusters were spherical, with an average horizontal diameter of 900 nm for  $(G1CO_2tBu)_m$ , 200 nm for  $(G2CO_2tBu)_m$ , 200 nm for  $(G3CO_2tBu)_m$ , 100 nm for  $(G4CO_2tBu)_m$ , and 100 nm for  $(G5CO_2tBu)_m$ . The size of the clusters agreed well with the values obtained from the DLS measurements. The vertical size of the clusters on mica correlated largely with the horizontal size of the clusters, except in the case of  $(G1CO_2tBu)_m$ . The

AFM image of the  $(G1CO_2tBu)_m$  cluster revealed a rather disc-like structure with an average diameter of 900 nm and an average maximum thickness of 170 nm. Namely, the vertical size of the  $(G1CO_2tBu)_m$  cluster is much smaller than the horizontal size. Although detailed structure at the molecular level is not yet clear, self-organization of  $G1CO_2tBu$  in the mixed solvent would lead to the formation of multilayer vesicle. In such a case, solvent evaporation from the inner space of the multilayer vesicle may yield the disk-like structure. Similar proposed structures were reported for amphiphilic fullerene derivatives in water, mixed organic solvents, and cast films [21].

In order to determine if differences observed in the size of the nanoclusters obtained from  $G1-5CO_2tBu$  could have any influence on their macroscopic properties, photoelectrochemical cells have been prepared. For this, the clusters were deposited electrophoretically onto ITO/SnO<sub>2</sub> electrodes by applying a DC voltage to the electrode [20]. After the electrophoretic deposition, the ITO/SnO<sub>2</sub> electrode turned brown in color, whereas discoloration of the cluster solution took place. As a result, cluster films with a thickness of 4–5 μm could be obtained. AFM was used to evaluate the surface morphology of the films deposited on the electrodes. The ITO/SnO<sub>2</sub>/ $(G1-5CO_2tBu)_m$  films were composed of closely packed clusters with a size of 800 nm ( $G1CO_2tBu$ ), 200 nm ( $G2CO_2tBu$ ), 200 nm ( $G3CO_2tBu$ ), 100 nm ( $G4CO_2tBu$ ), and 100 nm ( $G5CO_2tBu$ ). The size of the clusters largely agreed with the diameters of the clusters on the mica obtained from the cluster solutions. These results also confirmed that fullerene dendrimer clusters could be successfully transferred onto the nanostructured SnO<sub>2</sub> electrodes. Photoelectrochemical measurements were performed in deaerated acetonitrile containing 0.5 M LiI and 0.01 M I<sub>2</sub> with ITO/SnO<sub>2</sub>/ $(G1-5CO_2tBu)_m$  as a working electrode, a platinum wire as a counterelectrode, and an I<sup>-</sup>/I<sup>3+</sup> reference electrode. The photocurrent responses were prompt, steady, and reproducible during repeated on/off cycles of visible light illumination. Blank experiments conducted with a bare ITO/SnO<sub>2</sub> electrode yielded no detectable photocurrent under similar experimental conditions. A series of photocurrent action spectra was recorded to evaluate the response of fullerodendrimer clusters towards photocurrent generation. The photocurrent action spectra of ITO/SnO<sub>2</sub>/ $(G1-5CO_2tBu)_m$  devices are shown in Figure 22.7. Incident photon-to-photocurrent efficiency (IPCE) was calculated by normalizing the photocurrent density for incident light energy and intensity using the expression:

$$IPCE (\%) = 100 \times 1240 \times i / (W_{in} \times \lambda)$$

where  $i$  is the photocurrent density ( $A\text{ cm}^{-2}$ ),  $W_{in}$  is the incident light intensity ( $W\text{ cm}^{-2}$ ), and  $\lambda$  is the excitation wavelength (nm). The action spectra of ITO/SnO<sub>2</sub>/ $(G1-5CO_2tBu)_m$  devices largely agreed with the absorption spectra on ITO/SnO<sub>2</sub>, supporting the involvement of the C<sub>60</sub> moieties for photocurrent generation. These results were consistent with the photoelectrochemical properties of the clusters of fullerene derivatives on SnO<sub>2</sub> electrodes [21]. When the IPCE values of ITO/SnO<sub>2</sub>/ $(G1-5CO_2tBu)_m$  devices were compared under the same conditions, the IPCE value



**Figure 22.7** (a) Photocurrent action spectra of ITO/SnO<sub>2</sub>/(G1-5CO<sub>2</sub>tBu)<sub>m</sub>. Applied potential = +0.11 V versus SCE; 0.5 M LiI and 0.01 M I<sub>2</sub> in acetonitrile; (b) Photocurrent generation diagram.

at an excitation wavelength of 400 nm were seen to increase with increasing the generation number: 1.7% for ITO/SnO<sub>2</sub>/(G1CO<sub>2</sub>tBu)<sub>m</sub>, 1.9% for ITO/SnO<sub>2</sub>/(G2CO<sub>2</sub>tBu)<sub>m</sub>, 4.1% for ITO/SnO<sub>2</sub>/(G3CO<sub>2</sub>tBu)<sub>m</sub>, 4.1% for ITO/SnO<sub>2</sub>/(G4CO<sub>2</sub>tBu)<sub>m</sub>, and 6.0% for ITO/SnO<sub>2</sub>/(G5CO<sub>2</sub>tBu)<sub>m</sub> devices.

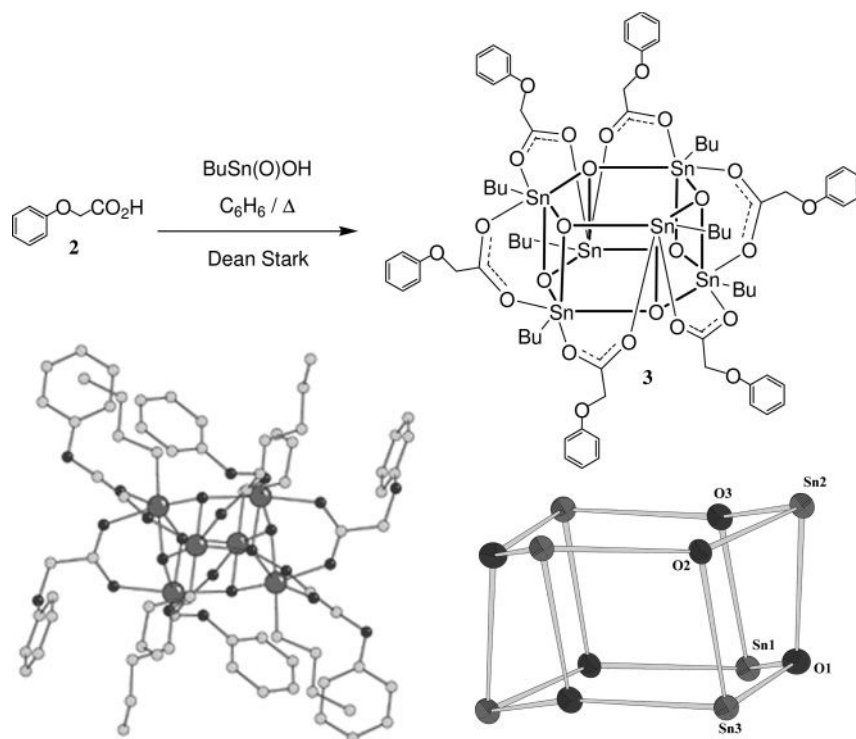
Based on previous studies on a similar photoelectrochemical system of C<sub>60</sub> and C<sub>60</sub> derivatives [22], photocurrent generation diagram is illustrated in Figure 22.7. The primary step in the photocurrent generation is initiated by photoinduced electron transfer from I<sup>-</sup> (I<sup>3-</sup>/I<sup>-</sup>, 0.5 V versus NHE) in the electrolyte solution to the excited states of fullerodendrimer clusters (C<sub>60</sub><sup>-•</sup>/<sup>1</sup>C<sub>60</sub><sup>\* = 1.45 V versus NHE, C<sub>60</sub><sup>-•</sup>/<sup>3</sup>C<sub>60</sub><sup>\* = 1.2 V versus NHE</sup> [20]. The electron transfer rate is controlled by the diffusion of I<sup>-</sup> (~10<sup>9</sup> s<sup>-1</sup>) in the electrolyte solution. The resulting reduced C<sub>60</sub> (C<sub>60</sub><sup>-•</sup>/C<sub>60</sub> = -0.3 V versus NHE) injects an electron directly into the SnO<sub>2</sub> nanocrystallites (ECB = 0 V versus NHE), or the electron is injected into the SnO<sub>2</sub> nanocrystallites through an electron-hopping process between the C<sub>60</sub> molecules [20]. The electron transferred to the semiconductor is driven to the counterelectrode via an external circuit so as to regenerate the redox couple. It is noteworthy that the IPCE values are dependent on the dendritic generation. With increasing the dendritic generation the IPCE value increases. The structural investigation on the fullerodendrimers revealed that the higher dendrimer generation led to the formation of densely packed clusters with a smaller, compact size (*vide supra*). Such structures of fullerene dendrimer clusters on ITO/SnO<sub>2</sub> in the higher generation would make it possible to accelerate the electron injection process from the reduced C<sub>60</sub> to the conduction band of SnO<sub>2</sub> via the more efficient electron hopping through the C<sub>60</sub> moieties, where the average distance between the C<sub>60</sub> moieties is smaller.</sup>

## 22.4 Fullerene-Rich Dendrimers

The results described in the previous section represent a powerful driving force to develop a new, efficient synthetic strategy for the preparation of large fullerene-rich dendritic molecules. In this respect, the self-assembly of dendrons using noncovalent interactions is particularly well suited to the preparation of fullerene-rich macromolecules [23, 24]. Indeed, the synthesis itself is restricted to the preparation of dendrons, and self-aggregation leads to the dendritic superstructure, thus avoiding tedious final synthetic steps with precursors incorporating potentially reactive functional groups such as C<sub>60</sub>. For example, Nierengarten and coworkers have shown that C<sub>60</sub> derivatives bearing a carboxylic acid function undergo self-assembly with *n*-butylstannonic acid (*n*BuSn(O)OH) to produce fullerene-rich nanostructures with a stannoxane core in near-quantitative yields [25]. The reaction conditions for the self-assembly of the stannoxane derivatives were first adjusted with model compound **2** (Figure 22.8). Under optimized conditions, a mixture of **2** (1 equiv.) and *n*BuSn(O)OH (1 equiv.) in benzene was refluxed for 12 h using a Dean–Stark trap. After cooling, the solution was filtered and evaporated to dryness to afford the hexameric organostannoxane derivative **3** in 99% yield. The drum-like structure of this compound, composed of a prismatic Sn<sub>6</sub>O<sub>6</sub> core, was confirmed by its <sup>119</sup>Sn nuclear magnetic resonance (NMR) spectrum recorded in C<sub>6</sub>D<sub>6</sub>, which showed a single resonance at –479.1 ppm. This chemical shift is characteristic of a drum-shaped structure with six equivalent Sn atoms coordinated by five oxygens and one carbon [26]. Crystals suitable for X-ray crystal-structure analysis were obtained by the slow diffusion of Et<sub>2</sub>O into a C<sub>6</sub>H<sub>6</sub> solution of **3**. Despite the disorder resulting from one of the flexible butyl chains, the central Sn<sub>6</sub>O<sub>6</sub> stannoxane core and the six peripheral 2-phenoxyacetate units of the structure were well resolved. As shown in Figure 22.8, the prismatic tin cage is formed by two, six-membered (SnO)<sub>3</sub> rings joined together by six Sn–O bonds [27]. The side faces of the cluster thus comprise six, four-membered (SnO)<sub>2</sub> rings, each of which is spanned by a carboxylate group that forms a bridge between two Sn atoms. A detailed observation of the stannoxane framework revealed that the six-membered rings had a chair-like conformation, with each Sn atom being bonded to three framework oxygen atoms, while the Sn–O bonds all had comparable lengths ranging from 208 to 210 pm. The six Sn atoms were seen to be hexacoordinated, with the coordination sphere being completed by a *n*-butyl group and two oxygen atoms from two different carboxylate groups. The Sn–O bonds to the bridging carboxylate atoms were longer than the core bonds, and ranged from 215 to 218 pm.

The reaction conditions used to prepare **3** from 2-phenoxyacetic acid were applied to the fullerene building blocks G1-3CO<sub>2</sub>H. The organostannoxane derivatives **4–6** were thus obtained in almost quantitative yields (Figures 22.9 and 22.10). These compounds are highly soluble in common organic solvents such as CH<sub>2</sub>Cl<sub>2</sub>, CHCl<sub>3</sub>, C<sub>6</sub>H<sub>6</sub> or toluene, and complete spectroscopic characterization was easily achieved. The <sup>1</sup>H and <sup>13</sup>C NMR spectra of **4–6** clearly revealed the characteristic





**Figure 22.8** Top: Preparation of compound 3. Bottom: X-ray crystal structure of 3 (C = pale gray, O = black, Sn = gray) and detailed view of the  $\text{Sn}_6\text{O}_6$  core. Selected bond lengths: Sn(1)-O(1): 2.084(3) Å, Sn(2)-O(1): 2.075(4) Å, Sn(2)-O(2): 2.097(3), Sn(2)-O(3): 2.093(3) Å, Sn(3)-O(1): 2.101(3) Å.

signals of the starting carboxylic acid precursors 4–6, as well as the expected additional resonances arising from the *n*-butyl chains. Importantly, the spectra clearly showed that all the peripheral fullerene subunits were equivalent in 4–6, as might be expected for a sixfold symmetric assembly with a drum-shaped organostannoxane core. In addition, a single resonance was observed at approximately  $-480$  ppm in the  $^{119}\text{Sn}$  NMR spectra of 4–6 recorded in  $\text{C}_6\text{D}_6$ . This characteristic signature of tin-drum clusters provided definitive evidence for the formation of 4–6.

The absorption spectra obtained from  $\text{CH}_2\text{Cl}_2$  solutions of compounds 4–6 were identical to those recorded for the corresponding starting carboxylic acid precursors; this demonstrated an absence of any significant influence of the stannoxane core on the electronic properties of the fullerene moieties. To further confirm that the characteristics of the fullerene subunits would be maintained for 4–6, their electrochemical properties were investigated using cyclic voltammetry (CV). For the sake of comparison, electrochemical measurements were also carried out with 3 and  $\text{G1CO}_2t\text{Bu}$ . All of these experiments were conducted at room temperature



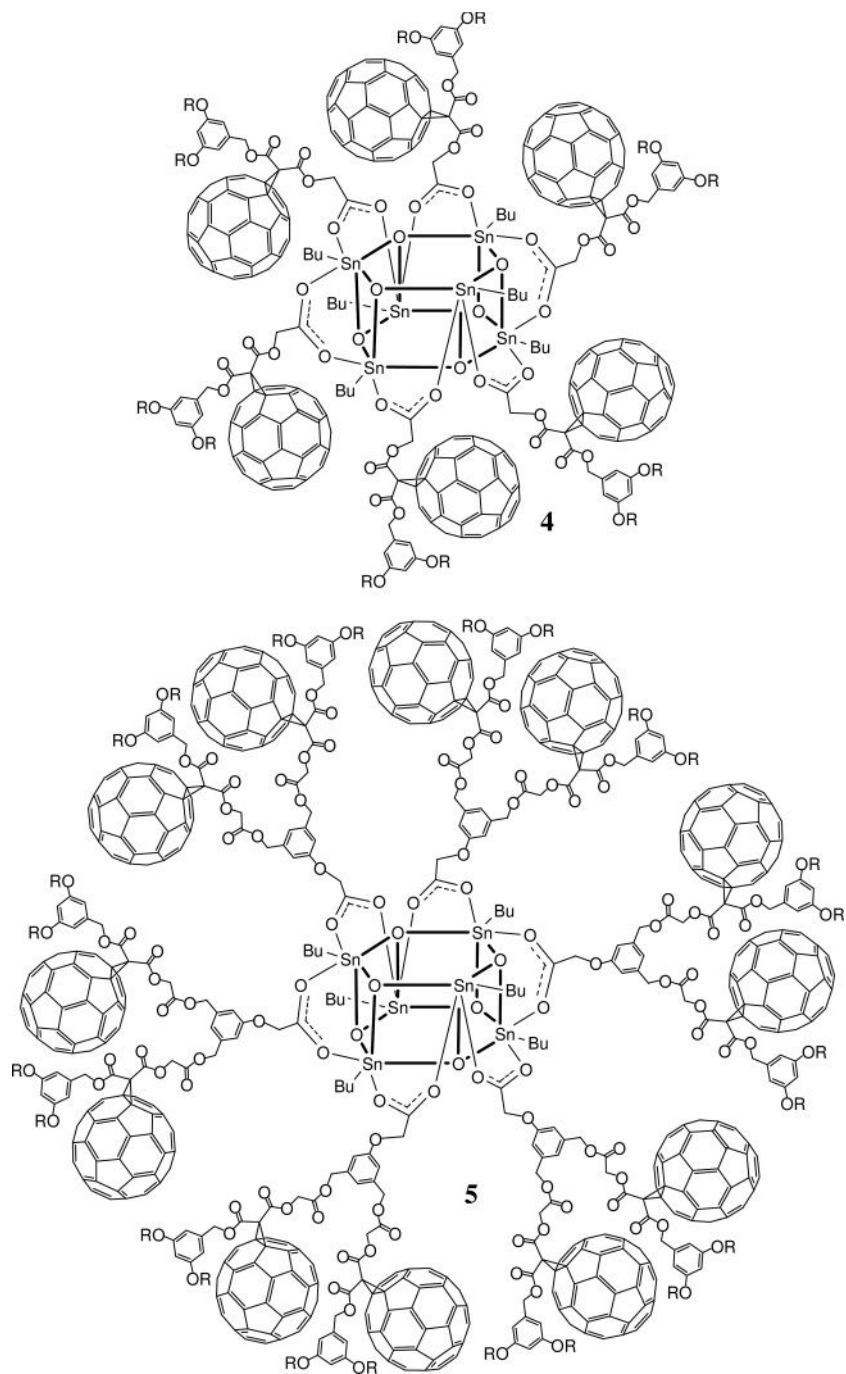
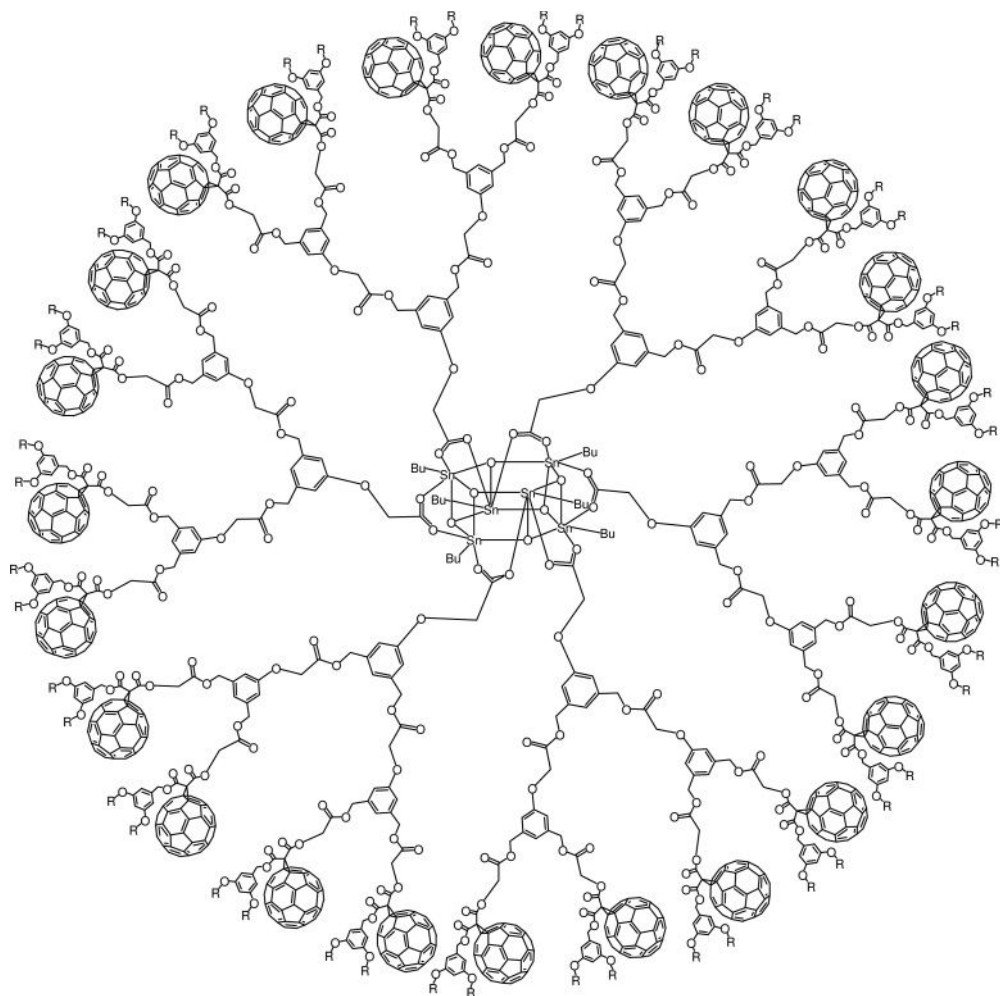


Figure 22.9 Structural formulae of compounds 4 and 5.



**Figure 22.10** Structural formula of compound 6.

in  $\text{CH}_2\text{Cl}_2$  solutions containing tetra-*n*-butylammonium tetrafluoroborate (0.1 M) as the supporting electrolyte, with a Pt wire as the working electrode and a saturated calomel electrode (SCE) as a reference. The potential data for all of these compounds are collected in Table 22.1.

In the anodic region, all of the studied compounds presented at least one irreversible peak at approximately +1.7–1.9 V versus SCE that could likely be attributed to oxidation of the dialkyloxyphenyl and/or alkyloxyphenyl units. Whereas, model compound 3 was found to be electrochemically silent in the cathodic region, the fullerene-substituted stannoxane derivatives 4–6 revealed the typical electrochemical response of fullerene derivatives [28]. Indeed, the electrochemical behavior of 4–6 appeared to be similar to that of the model compound  $\text{G1CO}_2t\text{Bu}$ . This

**Table 22.1** Electrochemical data on the reduction of **4–6** and  $\text{G1CO}_2t\text{Bu}$  determined by cyclic voltammetry on a Pt working electrode in  $\text{CH}_2\text{Cl}_2 + 0.1 \text{ M } n\text{Bu}_4\text{NBF}_4$  at room temperature. Values shown are for  $(E_{\text{pa}} + E_{\text{pc}})/2$  (in Volts) versus SCE and  $\Delta E_{\text{pc}}$  (in millivolts) (in parentheses) at a scan rate of  $0.1 \text{ V s}^{-1}$ .

	$E_1$	$E_2$	$E_3$
$\text{G1CO}_2t\text{Bu}$	−0.51 (75)	−0.89 (75)	−1.34 (65)
<b>4</b>	−0.53 (85)	−0.91 (80)	−1.35 (110)
<b>5</b>	−0.54 (75)	−0.92 (90)	−1.33 (110)
<b>6</b>	−0.54 (80)	−0.92 (90)	−1.34 (110)

indicated that all methanofullerene moieties in **4–6** behaved as independent redox centers, and that their electrochemical properties were not affected by the stannoxane core.

## 22.5

### Conclusions

The preparation of covalent, fullerene-rich dendrimers is difficult and involves a significant number of synthetic steps, thus limiting their accessibility and therefore their applications. Recent obtained results on the self-assembly of fullerene-containing components, by using supramolecular interactions rather than covalent bonds, have shown clearly that this strategy represents an attractive alternative for their preparation. Indeed, fullerene-rich derivatives are thus easier to produce, and the range of systems that can be prepared is not severely limited by the synthetic route. In this way, in-depth investigations of their properties are possible, and the use of fullerene-rich materials for specific applications can be envisaged. Despite some remarkable recent achievements, it is clear that the examples discussed in this chapter represent only the first steps towards the design of fullerene-rich molecular assemblies that can display functionality at the macroscopic level. Clearly, further research is required in this area to fully explore the possibilities offered by these materials, for example, in nanotechnology or in photovoltaics.

### Acknowledgments

These research studies were supported by the CNRS. The authors warmly thank all of their coworkers and collaborators for their outstanding contributions; their names are cited in the references.

## References

- 1 (a) Newkome, G.R., Moorefield, C.N. and Vögtle, F. (2001) *Dendrimers and Dendrons: Concepts, Syntheses, Applications*, Wiley-VCH Verlag GmbH, Weinheim.  
(b) Newkome, G.R., Moorefield, C.N. and Vögtle, F. (2001) *Dendrimers and Other Dendritic Polymers* (eds J.M.J. Fréchet and D.A. Tomalia), John Wiley & Sons, Ltd, Chichester.
- 2 Nierengarten, J.-F. (2000) *Chem. Eur. J.*, **6**, 3667.
- 3 Hirsch, A. and Vostrowsky, O. (2001) *Top. Curr. Chem.*, **217**, 51.
- 4 Nierengarten, J.-F. (2003) *Top. Curr. Chem.*, **228**, 87.
- 5 (a) Nierengarten, J.-F. (2004) *New J. Chem.*, **28**, 1177.  
(b) Imahori, H. and Fukuzumi, S. (2004) *Adv. Funct. Mater.*, **14**, 525.  
(c) Martin, N. (2006) *Chem. Commun.*, 2093.
- 6 (a) Wooley, K.L., Hawker, C.J., Fréchet, J.M.J., Wudl, F., Srdanov, G., Shi, S., Li, C. and Kao, M. (1993) *J. Am. Chem. Soc.*, **115**, 9836.  
(b) Hawker, C.J., Wooley, K.L. and Fréchet, J.M.J. (1994) *J. Chem. Soc. Chem. Commun.*, 925.  
(c) Nierengarten, J.-F., Habicher, T., Kessinger, R., Cardullo, F., Diederich, F., Gramlich, V., Gisselbrecht, J.-P., Boudon, C. and Gross, M. (1997) *Helv. Chim. Acta*, **80**, 2238.  
(d) Brettreich, M. and Hirsch, A. (1998) *Tetrahedron Lett.*, **39**, 2731.  
(e) Rio, Y., Nicoud, J.-F., Rehspringer, J.-L. and Nierengarten, J.-F. (2000) *Tetrahedron Lett.*, **41**, 10207.
- 7 (a) Camps, X. and Hirsch, A. (1997) *J. Chem. Soc. Perkin Trans. 1*, 1595.  
(b) Camps, X., Schönberger, H. and Hirsch, A. (1997) *Chem. Eur. J.*, **3**, 561.  
(c) Herzog, A., Hirsch, A. and Vostrowsky, O. (2000) *Eur. J. Org. Chem.*, 171.
- 8 Nierengarten, J.-F. (2003) *C. R. Chimie*, **6**, 725.
- 9 Rio, Y., Accorsi, G., Nierengarten, H., Rehspringer, J.-L., Hönerlage, B., Kopitkovas, G., Chugreev, A., Van Dorsselaer, A., Armaroli, N. and Nierengarten, J.-F. (2002) *New J. Chem.*, **26**, 1146.
- 10 (a) Cardullo, F., Diederich, F., Echegoyen, L., Habicher, T., Jayaraman, N., Leblanc, R.M., Stoddart, J.F. and Wang, S. (1998) *Langmuir*, **14**, 1955.  
(b) Zhang, S., Rio, Y., Cardinali, F., Bourgogne, C., Gallani, J.-L. and Nierengarten, J.-F. (2003) *J. Org. Chem.*, **68**, 9787.
- 11 Chuard, T. and Deschenaux, R. (2002) *J. Mater. Chem.*, **12**, 1944 and references therein.
- 12 Nierengarten, J.-F., Armaroli, N., Accorsi, G., Rio, Y. and Eckert, J.-F. (2003) *Chem. Eur. J.*, **9**, 36.
- 13 (a) Kunieda, R., Fujitsuka, M., Ito, O., Ito, M., Murata, Y. and Komatsu, K. (2002) *J. Phys. Chem. B*, **106**, 7193.  
(b) Murata, Y., Ito, M. and Komatsu, K. (2002) *J. Mater. Chem.*, **12**, 2009.  
(c) Rio, Y., Accorsi, G., Nierengarten, H., Bourgogne, C., Strub, J.-M., Van Dorsselaer, A., Armaroli, N. and Nierengarten, J.-F. (2003) *Tetrahedron*, **59**, 3833.
- 14 (a) Armaroli, N., Barigelletti, F., Ceroni, P., Eckert, J.-F., Nicoud, J.-F. and Nierengarten, J.-F. (2000) *Chem. Commun.*, 599.  
(b) Segura, J.L., Gomez, R., Martin, N., Luo, C.P., Swartz, A. and Guldi, D.M. (2001) *Chem. Commun.*, 707.  
(c) Accorsi, G., Armaroli, N., Eckert, J.-F. and Nierengarten, J.-F. (2002) *Tetrahedron Lett.*, **43**, 65.  
(d) Langa, F., Gómez-Escalonilla, M.J., Díez-Barra, E., García-Martínez, J.C., de la Hoz, A., Rodríguez-López, J., González-Cortés, A. and López-Arza, V. (2001) *Tetrahedron Lett.*, **42**, 3435.  
(e) Guldi, D.M., Swartz, A., Luo, C., Gomez, R., Segura, J.L. and Martin, N. (2002) *J. Am. Chem. Soc.*, **124**, 10875.  
(f) Pérez, L., Garcia-Martinez, J.C., Díez-Barra, E., Atienzar, P., Garcia, H., Rodriguez-Lopez, J. and Langa, F. (2006) *Chem. Eur. J.*, **12**, 5149.

- (g) Armaroli, N., Accorsi, G., Clifford, J.N., Eckert, J.-F. and Nierengarten, J.-F. (2006) *Chem. Asian J.*, **1**, 564.
- 15** (a) Nierengarten, J.-F., Felder, D. and Nicoud, J.-F. (1999) *Tetrahedron Lett.*, **40**, 269.  
 (b) Nierengarten, J.-F., Felder, D. and Nicoud, J.-F. (2000) *Tetrahedron Lett.*, **41**, 41.  
 (c) Nierengarten, J.-F., Eckert, J.-F., Rio, Y., Carreon, M.P., Gallani, J.-L. and Guillon, D. (2001) *J. Am. Chem. Soc.*, **123**, 9743.  
 (d) Gutiérrez-Nava, M., Accorsi, G., Masson, P., Armaroli, N. and Nierengarten, J.-F. (2004) *Chem. Eur. J.*, **10**, 5076.
- 16** Hahn, U., Hosomizu, K., Imahori, H. and Nierengarten, J.-F. (2006) *Eur. J. Org. Chem.*, 85.
- 17** Herschbach, H., Hosomizu, K., Hahn, U., Leize, E., Van Dorsselaer, A., Imahori, H. and Nierengarten, J.-F. (2006) *Anal. Bioanal. Chem.*, **386**, 46.
- 18** Felder, D., Nierengarten, H., Gisselbrecht, J.-P., Boudon, C., Leize, E., Nicoud, J.-F., Gross, M., Van Dorsselaer, A. and Nierengarten, J.-F. (2000) *New J. Chem.*, **24**, 687.
- 19** (a) Elhabiri, M., Trabolsi, A., Cardinali, F., Hahn, U., Albrecht-Gary, A.-M. and Nierengarten, J.-F. (2005) *Chem. Eur. J.*, **11**, 4793.  
 (b) Nierengarten, J.-F., Hahn, U., Trabolsi, A., Herschbach, H., Cardinali, F., Elhabiri, M., Leize, E., Van Dorsselaer, A. and Albrecht-Gary, A.-M. (2006) *Chem. Eur. J.*, **12**, 3365.
- 20** Hosomizu, K., Imahori, H., Hahn, U., Nierengarten, J.-F., Listorti, A., Armaroli, N., Nemoto, T. and Isoda, S. (2007) *J. Phys. Chem. C*, **111**, 2777.
- 21** Zhou, S., Burger, C., Chu, B., Sawamura, M., Nagahama, N., Toganoh, M., Hackler, U.E., Isobe, H. and Nakamura, E. (2001) *Science*, **291**, 1944.
- 22** (a) Kamat, P.V., Barazzouk, S., Thomas, K.G. and Hötchandani, S. (2000) *J. Phys. Chem. B*, **104**, 4014.  
 (b) Hotta, H., Kang, S., Umeyama, T., Matano, Y., Yoshida, K., Isoda, S. and Imahori, H. (2005) *J. Phys. Chem. B*, **109**, 5700.
- 23** Hahn, U., Cardinali, F. and Nierengarten, J.-F. (2007) *New J. Chem.*, **31**, 1128.
- 24** (a) Hahn, U., González, J.J., Huerta, E., Segura, M., Eckert, J.-F., Cardinali, F., de Mendoza, J. and Nierengarten, J.-F. (2005) *Chem. Eur. J.*, **11**, 6666.  
 (b) van de Coevering, R., Kreiter, R., Cardinali, F., van Koten, G., Nierengarten, J.-F. and Klein Gebbink, R.J.M. (2005) *Tetrahedron Lett.*, **46**, 3353.
- 25** Hahn, U., Gégout, A., Duhayon, C., Coppel, Y., Saquet, A. and Nierengarten, J.-F. (2007) *Chem. Commun.*, 516.
- 26** Chandrasekhar, V., Schmid, C.G., Burton, S.D., Holmes, J.M., Day, R.O. and Holmes, R.R. (1987) *Inorg. Chem.*, **26**, 1050.
- 27** Chandrasekhar, V., Gopal, K., Nagendram, S., Steiner, A. and Zacchini, S. (2006) *Cryst. Growth Des.*, **6**, 267.
- 28** (a) Nierengarten, J.-F., Habicher, T., Kessinger, R., Cardullo, F., Diederich, F., Gramlich, V., Gisselbrecht, J.-P., Boudon, C. and Gross, M. (1997) *Helv. Chim. Acta*, **80**, 2238.  
 (b) Boudon, C., Gisselbrecht, J.-P., Gross, M., Isaacs, L., Anderson, H.L., Faust, R. and Diederich, F. (1995) *Helv. Chim. Acta*, **78**, 1334.

## 23

### Interactions of Carbon Nanotubes with Biomolecules: Advances and Challenges

Dhriti Nepal and Kurt E. Geckeler

#### 23.1

##### Introduction

Carbon nanotubes (CNTs) are allotropes of carbon, composed up of rolled-up graphene sheets with a unique combination of properties that include excellent electrical, optical, and mechanical properties [1]. Such properties have opened up a great range of new possibilities for these fascinating materials in a wide range of research, including electronics, optics, high-performance fibers, composites, and biotechnology, as well as other fields of materials science.

#### 23.2

##### Structure and Properties

The chemical bonding of nanotubes is composed entirely of  $sp^2$  bonds, similar to those of graphite. The strength of the  $sp^2$  carbon-carbon bonds gives the CNTs amazing mechanical properties, as these bonds are much stronger than the  $sp^3$  bonds found in diamonds. Such properties, when coupled with the low specific weight of CNTs, provides these materials with great potential over a wide range of applications. The extraordinary electronic properties of CNTs are due to the quantum confinement effect, which is based on a unique structure that allows electrons to propagate only along the nanotube axis. Depending on how the two-dimensional (2-D) graphene sheet is “rolled up,” the CNTs may be either metals or semiconductors. Three types of nanotubes are possible, referred to as *armchair*, *zigzag*, and *chiral* nanotubes.

Despite the great potential that CNTs offer, many fundamental challenges remain to be met before such potential can be fully utilized. This includes the purification, dispersion, debundalization, and chiral-selective separation of nanotubes. The major hurdle results from the natural tendency of CNTs to remain in highly aggregated states, due to their intrinsic van der Waals interactions. In

fact, under normal conditions this property not only makes it practically impossible to solubilize the materials in any type of solvent but also hampers their electrical, optical, and mechanical properties. Consequently, the functionalization of nanotubes holds much promise as it provides processability and also helps when studying the materials' properties using solution-based techniques. In order to explore the potential of nanotubes, they have been functionalized in many ways, including direct covalent reaction with a variety of reagents, indirect reaction with different functional moieties starting from oxidized precursors, via organometallic routes, and noncovalent interactions. The reactions of nanotubes with polymers, whether by grafting or by using the nanotubes as an anchor to initiate polymerization, has led to the production of a range of nanotube-based polymer composites [2, 3]. Functionalization with well-defined chemistry has also helped in the design of nanotube-based "smart" devices, by modifying their properties.

Today, single-walled carbon nanotubes (SWNTs) are attracting increasing attention in biomedical research [4–6]. Because of their unique physical and chemical properties, they offer the promise for the development of novel diagnostic and therapeutic methods, high-sensitivity biosensors, and biofuel cells. When SWNTs absorb energy from near-infrared (NIR) light they emit heat—a property which can play important role in the design of novel biomedical devices or novel therapeutic agents. In developing such applications, the challenges of *in vivo* detection and biocompatibility are the most essential. The functionalization of biomolecules not only offers biocompatibility, but also provides new possibilities in the material world for the advancement of future technology. DNA and proteins represent major classes of biopolymers with extensive potential in both the natural as well as the synthetic world. In this chapter, an attempt has been made to summarize recent developments on the functionalization of CNTs using these polymers, with special attention on noncovalent functionalization. The aim also is to highlight some of the key challenges, and future prospects.

### 23.3 Debundalization

Due to their inherent van der Waals interactions and their special geometric structures, CNTs normally aggregate to form large bundles. Unfortunately, this process of "bundalization" causes the most outstanding characteristics of CNTs—namely their electrical [7], mechanical [8], and optical [9] properties—to be diminished. As an example, it has been shown experimentally that an individual SWNT has a tensile strain of ~280% and can undergo superplastic deformation by reducing its diameter 15-fold before breaking [10]. Yet, bundled SWNTs [11] and multi-walled carbon nanotubes (MWNTs) [12] will break at strains of less than ~6% and 12%, respectively. This provides a clear picture of the importance of including debundalized nanotubes in nanocomposites. Moreover, the develop-

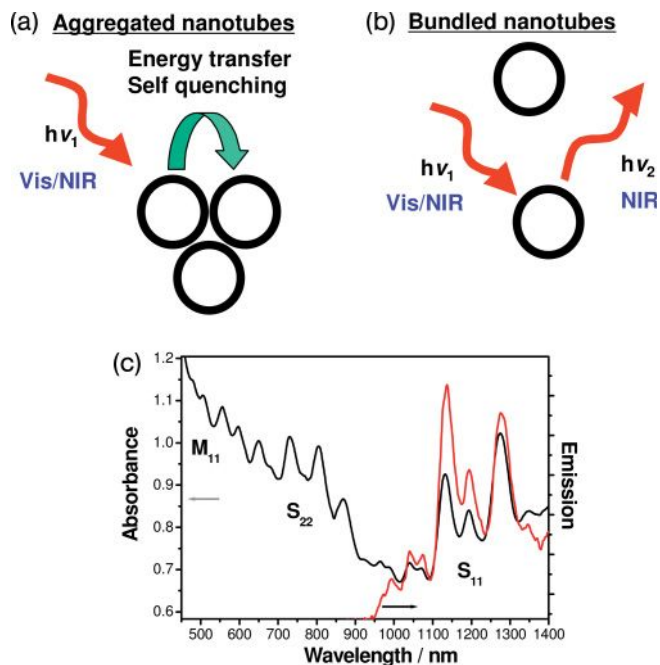
ment of efficient techniques to produce stable dispersions of debundalized nanotubes is a clear prerequisite to many applications, ranging from molecular electronics to nanocomposites.

In an effort to overcome these problems, many research groups worldwide have investigated the debundalization or individualization of SWNTs. The debundalization of SWNTs has been achieved via two routes, namely covalent [13] or noncovalent [14] modification/functionalization [3], with the former approach causing inevitable damage to the sidewalls of the nanotubes that altered their chemical and physical properties [15]. As a consequence, a range of studies has focused on noncovalent approaches to obtaining individual nanotubes by using different agents and polymers.

Previous studies have been focused on using synthetic polymers or surfactants. For example, Smalley and coworkers [9] obtained individual nanotubes by encasing each one in cylindrical micelles. This was made possible by ultrasonically agitating an aqueous dispersion of raw SWNTs in sodium dodecyl sulfate (SDS), followed by ultracentrifugation to remove tube bundles and residual catalyst. The absorbance spectra hold the key role to determining the degree of debundalization. The quasi-one-dimensionality of the SWNTs produces sharp van Hove peaks in the density of electronic states [16]. In this respect, for example in the case of HiPCO-SWNTs, the optical absorption spectrum consists of a series of transitions: first van Hove transitions of *met*-SWNTs (metallic-SWNT) ( $M_{11}$ ) (~400 and ~600 nm); second van Hove transitions of *sem*-SWNTs (semimetallic-SWNT) ( $S_{22}$ ) (~550 to 900 nm); and first van Hove transitions of *sem*-SWNTs ( $S_{11}$ ) (~800 to ~1600 nm). The well-resolved absorbance feature is a key indication of the debundalization, as otherwise the spectra are broadened (Figure 23.1).

In the bulk state, the individualization can be further confirmed by recording fluorescence spectra, which have been observed directly across the band gap of *sem*-SWNTs. A fluorescence spectrum can only be obtained in the debundalized state, because otherwise the presence of *met*-SWNTs will quench the electronic excitation on adjacent *sem*-SWNTs in the bundle, which prevents luminescence. This approach of direct fluorescence observation from individual SWNTs in solution has great importance for the development of SWNT-based optical devices. Different surfactants [17], synthetic polymers, and also biopolymers [3] were each found to be excellent dispersing agents for SWNTs, especially for making them disperse individually in aqueous media. A study was conducted to identify the best dispersing agent for SWNTs by comparing various anionic, cationic, and nonionic surfactants and polymers [17]. Each of these agents was compared with respect to their ability to suspend individual SWNTs, and the quality of the absorption and fluorescence spectra. For ionic surfactants, sodium dodecylbenzene sulfonate (SDBS) was found to provide well-resolved spectral features, and this correlated directly with the most favorable ionic surfactant for debundalization. For the nonionic systems, surfactants with a higher molecular mass could suspend more SWNT material and had more pronounced spectral features.





**Figure 23.1** Schematic diagram of the dispersion-dependent energy transfer in nanotubes, and evidence of isolated nanotubes by optical spectroscopy. (a) Model of energy-transfer quenching in a matrix with bundled nanotubes; (b) Model of fluorescent emission, if nanotubes are individually isolated; (c) Absorbance and emission spectra of individually isolated nanotubes in a protein solution.

#### 23.4 Noncovalent Functionalization

Covalent functionalization weakens the strength of all interband transitions in both the semiconducting and metallic SWNTs, because the saturated bonds function as defects. This perturbs the periodicity of the pseudo-one-dimensional (1-D) lattice and eventually destroys the electronic band structure altogether. However, the largest effects of covalent functionalization occur in metallic SWNTs, because the metallic state should be extremely sensitive to the occurrence of defects introduced by saturation of the delocalized electronic structure. In particular, these effects should be most strongly manifested in the transitions at  $E_F$  because these transitions are characteristic of a metal, which is a species without a gap in the energy band spectrum.

On the other hand, the noncovalent functionalization of CNTs represents one of the best alternatives for preserving the  $sp^2$ -structure of nanotubes and, thus, their electronic characteristics. The advantage is the possibility of attaching chemical functionalities to the surface, without disrupting the bonding network of the

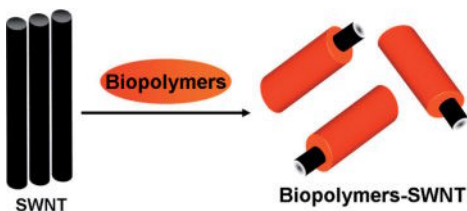
nanotubes. Thus, the noncovalent functionalization of CNT with different polymers or organic molecules has attracted great attention.

### 23.5

#### Dispersion of Carbon Nanotubes in Biopolymers

Synergetic effects with biomolecules on CNTs has attracted much attention for a wide range of biotechnological applications, including sensors, cancer therapy [18], drug delivery [19], tissue engineering, and antimicrobial surfaces [20]. The results of recent studies have shown CNTs to be compatible with mammalian cells and neurons [21], with CNT-based composites having been identified as excellent materials for scaffolds for neuron growth [22] and bone proliferation [23], as well as having potential for tissue engineering [24]. These types of bio-focused composites have been prepared using a variety of natural biopolymers, including different polysaccharides, polypeptides, and polynucleotides (Figure 23.2) [2]. Interestingly, the biopolymers have shown much promise, since “mother Nature” has provided an abundance of well-designed polymers for defined applications. The exploration of these molecules in conjunction with nanotubes not only facilitates the creation of suitable products from abundantly available resources, but also assists in mimicking their smart functions for the advancement of nanotube-based devices. For example, a degree of success has been achieved in preparing a unique supramolecular conjugate of nanotubes and lysozyme (LSZ), one of the most common proteins. In this way, novel properties could be induced (i.e., pH-sensitive dispersion and debundalization of the nanotubes) that directly gave their signal simply by switching photoluminescence. A similar success was achieved when nanotubes were individually dispersed, using different proteins.

Recently, biopolymer integration has attracted much attention due to their increased compatibility with biological systems compared to synthetic materials. Consequently, a variety of biopolymers was chosen in order to monitor their efficiency for the dispersion of CNTs. For example, Rozen *et al.* [25] used the water-soluble polysaccharide *gum arabica* to obtain a stable dispersion of individual, full-length tubes in an aqueous solution from as-produced SWNTs. Wenseleers *et al.* [26] reported an efficient isolation of pristine SWNTs in bile salts, such as the sodium salts of deoxycholic acid (DOC) and their taurine-substituted analogue



**Figure 23.2** Schematic diagram of the wrapping of single-walled carbon nanotubes by biopolymers.

taurodeoxycholic acid (TDOC), simply by stirring at room temperature. When using this process it is possible to avoid damage induced on the walls of the SWNTs during ultrasonication. The efficiency of debundalization of the SWNTs was monitored using NIR, fluorescence, and Raman spectroscopies. Most interestingly, a dramatically improved resolution of the radial breathing modes (RBMs) in the Raman spectra with multi-peaks was obtained with the bile salts, in contrast to the single peak obtained in most previous studies with arc discharge tubes. When the ability of the salts to disperse the SWNTs was compared with other common surfactants, by using NIR spectroscopy, among the most common surfactants, both DOC and TDOC (i.e., anionic, nonionic, cationic) showed the highest dispersion powers (five- to 20-fold higher).

A water-soluble product also has great potential in the design of an electrode for bioelectrochemical sensors, by taking advantage of the noncovalent interactions of chitosan with CNTs [27]. Hasegawa *et al.* showed that biopolymers such as Schizophyllan (s-SPG) and curdlan were capable of wrapping SWNTs, creating a “periodical” helical structure that reflected the helical nature of the SPG main-chain on the SWNT surface [28]. Kim *et al.* [28] reported a simple, but efficient, process for the solubilization of SWNTs with amylose in aqueous dimethylsulfoxide (DMSO), by using sonication. The former step separated the SWNT bundles, while the latter step provided a maximum cooperative interaction of SWNTs with amylose, leading to an immediate and complete solubilization. Both, scanning electron microscopy (SEM) and atomic force microscopy (AFM) images of the encapsulated SWNTs appeared as loosely twisted ribbons wrapped around the SWNTs, which were locally intertwined as a multiple twist; however, no clumps of the host amylose were seen on the SWNT capsules.

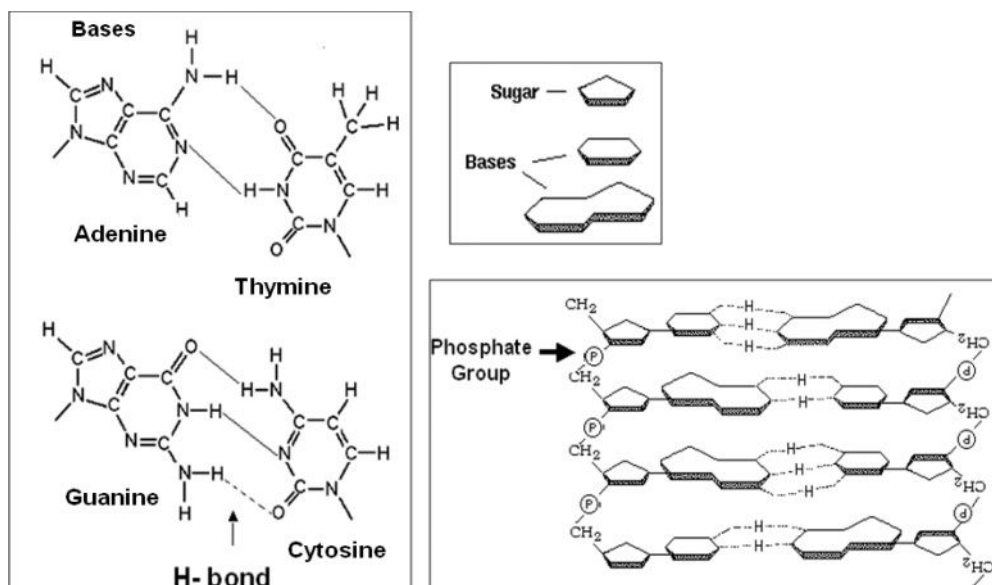
The potential of CNTs for the development of novel bioelectronic devices has been realized and, indeed, biomolecules have been immobilized on CNTs [29]. The major benefit in choosing biomolecules is to take advantage of their amphoteric nature to render the nanotubes processable, while simultaneously utilizing their unique properties to design novel artificial systems. In this respect, a variety of biomolecules hold great promise for this type of development.

Here, attention is focused on DNA and proteins for the interaction with CNTs. The major motivation to use these polymers includes: (i) their unique features and typical characteristics, as well as their diversity, which controls almost every living system in Nature; and (ii) the potential to bring about novel possibilities by uniting them, as this can have huge impact on both basic and applied research.

## 23.6

### Interaction of DNA with Carbon Nanotubes

The interaction of DNA with CNTs has been a major focus of recent research [30–32], due mainly to the unique structure of DNA (Figure 23.3) and its properties with regard to both biological and nonbiological applications. For instance, recent reports have already focused on several applications as a new material, including

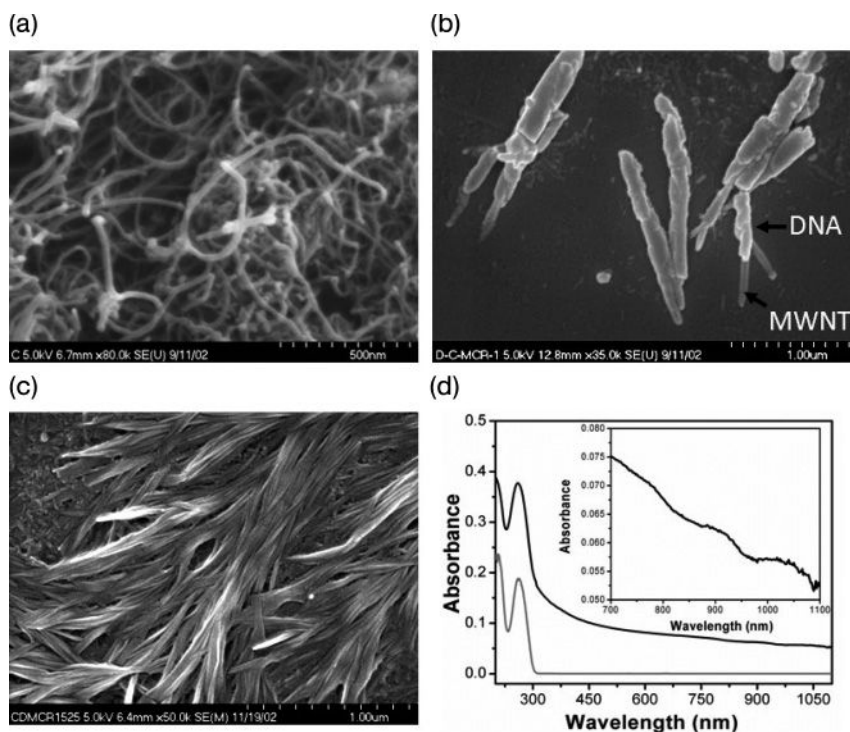


**Figure 23.3** Schematic showing the chemical structure of DNA, which is composed of the four different bases, sugar (ribose), and phosphate groups.

drug delivery [33, 34], molecular electronics, nanoscale robotics [35], computation [36], self-assembly, 1-D electron conduction [34], and photonics [37]. When considering the huge potential of CNTs, a combination of DNA with CNTs in the quest to identify new and advanced performances for a wide range of synthetic systems has been of vast interest. Yet, the major attraction for DNA has been based on a recent breakthrough which described its ability to individually disperse CNTs in aqueous solutions, under controlled conditions [32, 38, 39], and this has in turn led to many other possibilities.

The first report on the direct interaction of DNA with CNT was made by Tsang *et al.*, in a study which was based on the visualization of CNT by platinated oligonucleotides [40]. The major breakthrough in this field was based on the ability of DNA to disperse CNTs individually in water [30, 38], while others reported on a DNA-assisted dispersion of CNTs [39, 41]. All of these studies were based on the noncovalent functionalization of DNA with nanotubes. The covalent bonding of DNA with SWNTs [42] has been also reported, while field effect transistors [43] using such materials have also been studied.

Previously, the use of mechanochemical reactions has been suggested [44] as a generally efficient technique for various processes and, by using the same approach, supramolecular adducts of DNA–CNT conjugates have been reported [39]. Highly reactive centers generated on the CNTs by the mechanical energy in the solid state helped to promote good interactions with DNA (Figure 23.4), which in turn led to a short-length, highly water-soluble, CNT-based product in a single step. This



**Figure 23.4** Scanning electron microscopy images. (a) Pristine CNT; (b) CNT–DNA conjugate; (c) Self-assembly of the CNT–DNA conjugate; (d) UV-visible-NIR absorbance spectra of DNA (gray) and DNA–MWNT dispersion (black). The inset shows the van Hove transitions of the semiconducting nanotubes.

technique has also been used successfully to prepare both fullerene derivatives [45] and alcohol-functionalized CNTs [46]. Interestingly, this soluble CNT product appeared fully wrapped with DNA and seemed to differ from that described in previous reports on mechanochemical reactions for covalently functionalized products [46].

Zheng *et al.* obtained individual SWNTs in a solution of single-stranded DNA (ssDNA) [30, 38, 47]. Notably, removal of the free DNA by either anion-exchange column chromatography or nuclease digestion did not cause any flocculation of the nanotubes, indicating that binding of the DNA to the SWNTs was very strong. In order to obtain putative binding structures and to approximately quantify the thermodynamics of binding, Zheng's group simulated interactions between ssDNA molecules and nanotubes with a (10,0)-chiral vector. As a consequence, it appeared that the short ssDNA strands could bind in many ways to the nanotube surface, including helical wrapping with right- and left-handed turns, or simply by surface adsorption with a linearly extended structure. The bases could extend from the backbone and stack onto the nanotube, whereas the sugar-phosphate backbone could lead to solubilization of the SWNTs. The phosphate groups of the

product provided a negative charge density on the surface and affected the surface charge of the nanotubes, which was directly related to the electronic properties of the SWNTs. In this respect, DNA-*met*-SWNTs were found to have a lower surface charge than DNA-*sem*-SWNTs, due to the greater positive charge created in the *met*-SWNTs. This led to a successful separation of *met*-SWNTs from *sem*-SWNTs by using ion-exchange liquid chromatography. Moreover, by measuring the electronic absorption spectra for all fractions, a remarkable difference was noted between the early fractions, which were enriched with *met*-SWNTs, and the later fractions, which were enriched with *sem*-SWNTs.

## 23.7

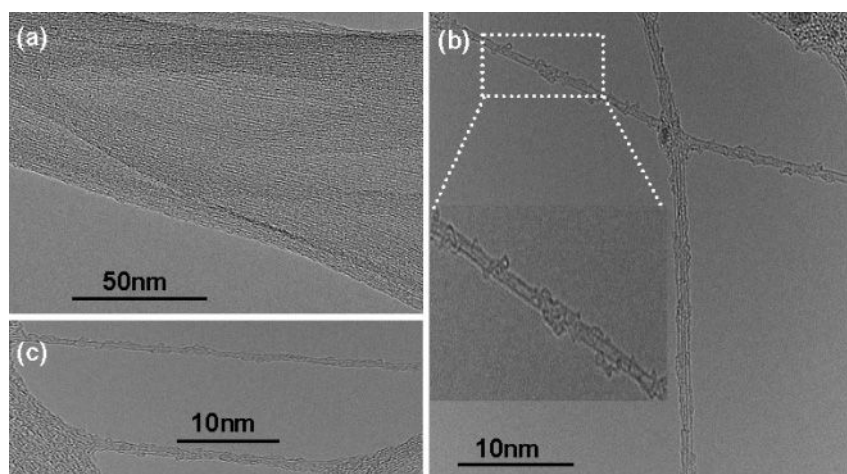
### Interaction of Proteins with Carbon Nanotubes

The main focus of preparing debundalized SWNTs with the aid of proteins was motivated by the outstanding properties that each of these proteins display in the natural environment. This offers the possibility to bring functionality into synthetic systems, if the correct technology were to be developed. A broad range of different types are available in Nature, which allows complicated synthetic procedures to be avoided and their compatibility with biological systems to be enhanced, when compared to synthetic materials. In addition, the intrinsic smart function in a synthetic system may be mimicked [2, 48]. Functionalization is possible by both the covalent and noncovalent approaches. For example, CNTs may be functionalized by the protein bovine serum albumin (BSA) via a diimide-activated amidation, under ambient conditions [49]. The nanotube–BSA conjugates thus obtained are highly water-soluble, and form dark-colored aqueous solutions. Results from characterizations using AFM, thermal gravimetric analysis (TGA), Raman spectroscopy and gel electrophoresis showed that the conjugate samples indeed contained both CNTs and BSA proteins, and that the protein species were intimately associated with the nanotubes. When the bioactivity of the nanotube-bound proteins was evaluated using a total protein microdetermination assay, the results showed that 90% of the protein species present in the nanotube–BSA conjugates remained bioactive [49].

Zorbas *et al.* [50] isolated long, individual SWNTs wrapped with a specially designed peptide in aqueous solution by sonication and centrifugation. Based on AFM studies, it was observed that the product contained SWNTs with an average length of  $1.2 \pm 1.1 \mu\text{m}$  and an average diameter of  $2.4 \pm 1.3 \text{ nm}$ . Furthermore, the peptide–peptide interactions apparently assisted the assembly of the SWNT structures, specifically in the formation of Y-, X-, and intraloop junctions. In this way, apart from the debundalization and biocompatibility of the peptide–SWNT product, their properties showed great potential for the development of SWNT-based, higher-ordered structures. Similarly, the importance of aromatic groups of the amino acid residues on the interaction with CNTs has been observed [51]. Various systematically designed peptides with different types of amino acid showed a stronger selectivity for CNTs than did peptides with a higher aromatic residue content.

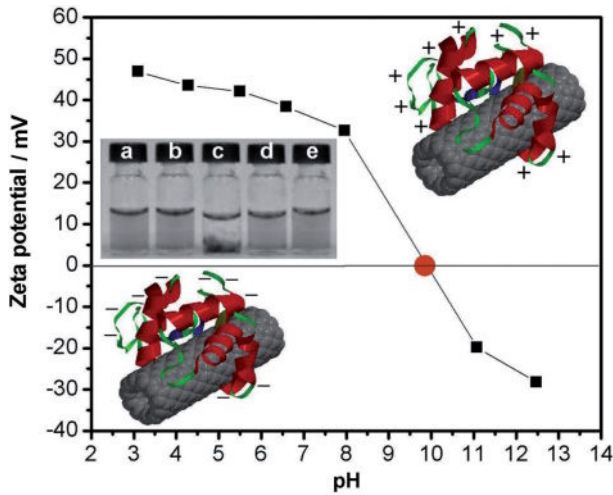
A study was conducted to evaluate the affinity of aromatic amino acids toward SWNTs in the absence of complications from peptide folding or self-association, by synthesizing a series of surfactant peptides [52]. Each surfactant peptide was designed with a lipid-like architecture: two Lys residues at the C-terminus as a hydrophilic head; five Val residues to form a hydrophobic tail; and the testing amino acid at the N-terminus. Both, Raman and circular dichroism (CD) spectroscopic studies revealed that the surfactant peptides had a large, unordered structural component, which was independent of the peptide concentration. This suggested that the peptides had undergone minimal association under experimental conditions, thus removing this interference from any interpretation of the peptide–CNT interactions. A lack of peptide self-association was also indicated by sedimentation equilibrium data. The optical spectroscopy of the peptide–CNT dispersions indicated that, among the three aromatic amino acids, tryptophan had the highest affinity for CNTs (both bundled and individual states), when incorporated into a surfactant peptide, while the Tyr-containing peptide was more selective for individual CNTs. A protein-assisted solubilization of nanotubes was also reported [53]. Although these recent findings have opened novel possibilities for nanobiohybrid systems, it remains an overt issue as to whether there is any selectivity and any effect of the proteins on the nanotubes. In addition, it is very important to note that these natural polyampholytes are highly pH-sensitive, and that their solubility and ionizability can easily be tuned with respect to pH. This, simultaneously, should influence the nanotube dispersion, which might offer novel options for the precise control of selectivity towards nanotubes.

The present authors studied highly dispersed and debundled CNTs (Figure 23.5), which had been prepared in an aqueous solution of LSZ, using a combina-

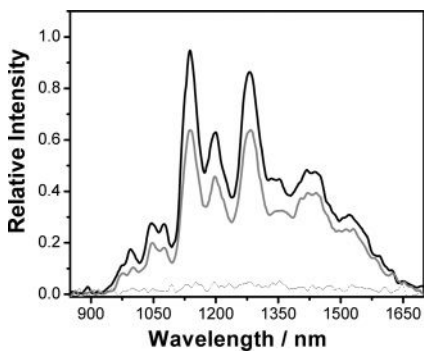


**Figure 23.5** High-resolution transmission electron microscopy images of (a) SWNT and (b, c) L-SWNT. The inset in (b) shows the magnified image of a nanotube.





**Figure 23.6** Zeta potential of L-SWNT at different pH values. The inset shows vials containing the products at different pH values: (a) 2.95; (b) 6.5; (c) 9.0; (d) 11.15; (e) 12.47.

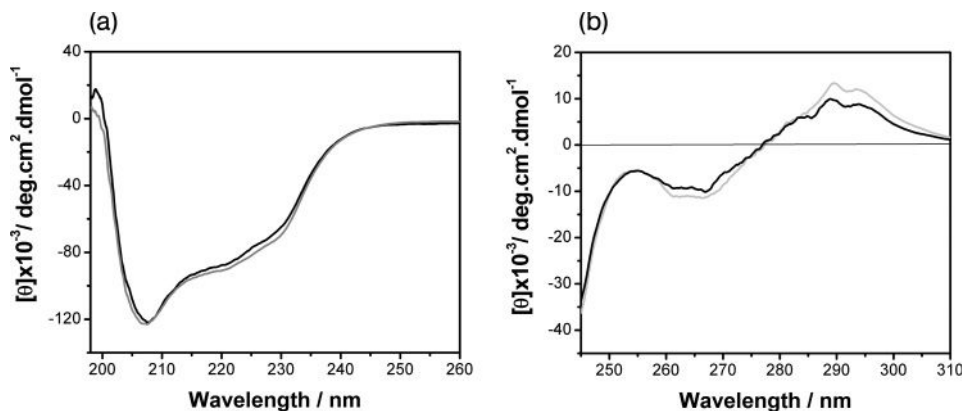


**Figure 23.7** Photoluminescence spectrum of L-SWNT, showing the pH-dependent reversibility in emission. The black (solid), black (dotted), and gray (solid) curves are from the solution at pH 12.5, same solution adjusted to pH 9.0, and again readjusted to pH 12.5, respectively.

tion of ultrasonication and ultracentrifugation [14]. The product showed a pH-sensitive dispersion, which remained in a highly dispersed state at  $\text{pH} < 8$  and  $\text{pH} > 11$ , and in an aggregated state at  $\text{pH} = 8\text{--}11$  (Figure 23.6). Photoluminescence measurements showed that, by changing the pH, a reversible conversion of the highly dispersed state to the aggregated state could be observed, or *vice-versa* (Figure 23.7).

It is important to understand the nature of the interactions involved between the LSZ and the SWNTs. LSZ has long been considered a structurally stable





**Figure 23.8** Far-UV-CD (a) and near-UV-CD (b) spectra of L-SWNT (black) and lysozyme (gray).

protein; hence, in order to appreciate the state of LSZ in the product, a CD analysis of the samples was carried out in the far- and near-UV regions (Figure 23.8). It has been well established that shorter wavelengths reflect the secondary structure, whereas longer wavelengths arise from the tertiary structure of proteins. A strong negative band was appeared in the range of 200–260 nm. The signal intensity at 208 nm was greater than at 222 nm, which was characteristic for an  $\alpha + \beta$  protein. These data confirmed that the secondary structure had remained intact in the product.

In an attempt to understand the efficiency of common proteins for SWNT dispersion, a selection of eight common proteins (histone [HST], hemoglobin [HBA], myoglobin [MGB], ovalbumin [OVB], bovine serum albumin [BSA], trypsin [TPS], glucose oxidase [GOX] and lysozyme [LSZ]), with a variety of molecular masses and isoelectric points, was selected. The basic physical data of the proteins are listed in Table 23.1. In a typical experiment, the SWNTs were ultrasonicated in an aqueous solution of the proteins, followed by a double-step ultracentrifugation process. This resulted in highly dispersed and debundalized SWNTs in the aqueous system. Schematic diagrams of the protein-stabilized SWNTs are shown in Figure 23.9.

The vials containing products from the different proteins are shown in Figure 23.10, each at three different pH values (intrinsic, acidic, and basic). It is clear from the figure that the color of the solution varies with respect to pH, ranging from a colorless-transparent liquid to a dark-gray solution. This color change corresponds directly to variations in the yields of nanotubes in the solutions.

Microscopic studies of the dispersed nanotubes using high-resolution transmission electron microscopy (HR-TEM) showed that the starting material consisted of bundled ropes assembled from a few tens to a hundred tubes, whereas HR-TEM images of the product HST-SWNT showed debundalized tubes, well separated

**Table 23.1** Comparison of the dispersion limits and yields of debundalized single-wall nanotubes (SWNTs) with different proteins, and some physical parameters of the proteins. The proteins are arranged in alphabetic order.

Protein	Code	Molar mass (kg mol <sup>-1</sup> ) <sup>a</sup>	Isoelectric point	Initial pH <sup>b</sup>	Final pH <sup>c</sup>	Dispersion limit (mg l <sup>-1</sup> ) <sup>d</sup>	Debundalized SWNTs (mg l <sup>-1</sup> ) <sup>e</sup>	Debundalization degree (DD) (%) <sup>f</sup>
Bovine serum albumin	BSA	69.293	4.7	1.8	1.5	2.44	0.98	1
				7.4	6.7	25.44	6.38	10
				11.4	11.2	132.71	43.41	65
Glucose oxidase	GOX	131.2764	4.2	1.6	1.8	0.33	0	0
				6.9	4.5	0.14	0	0
				11.2	11.3	1.39	0.01	0
Hemoglobin	HBA	61.933	9.4	1.7	1.5	179.96	36.46	55
				6.4	5.9	7.09	0.74	1
				11.5	11.1	134.52	27.09	41
Histone	HST	15.316	11.7	1.9	1.8	67.00	11.66	17
				5.7	4.2	196.78	66.70	100
				11.6	11.5	17.59	2.85	4
Lysozyme	LSZ	14.313	10.7	1.4	1.5	197.8	54.03	81
				6.5	4.7	255.3	58.97	88
				11.6	11.2	2.19	0.49	1
Myoglobin	MGB	16.953	7.2	1.9	1.6	91.93	28.96	43
				6.6	5.8	42.58	15.54	23
				11.6	11.5	119.42	37.12	56
Ovalbumin	OVB	42.861	4.6	1.6	1.6	67.78	20.53	31
				6.9	6.6	143.99	29.12	44
				11.2	11.2	153.40	45.49	68
Trypsin	TPS	23.783	9.2	1.8	1.7	0.13	0.01	0
				4.2	4.1	9.98	2.65	4
				11.8	11.6	42.78	12.56	19

**a** Molar masses were calculated based on the sequence downloaded from the protein data bank.

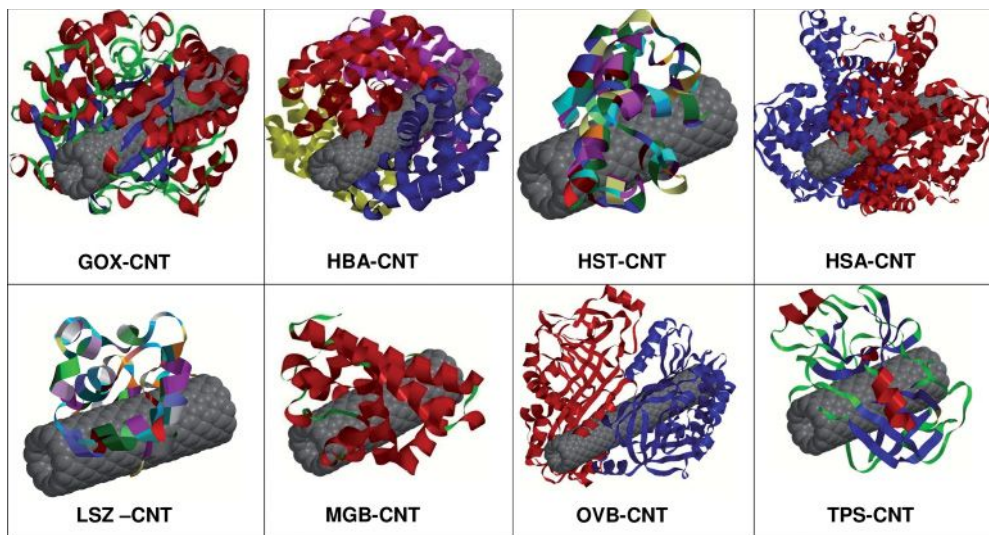
**b** pH of the solution before sonication.

**c** pH of the solution after sonication.

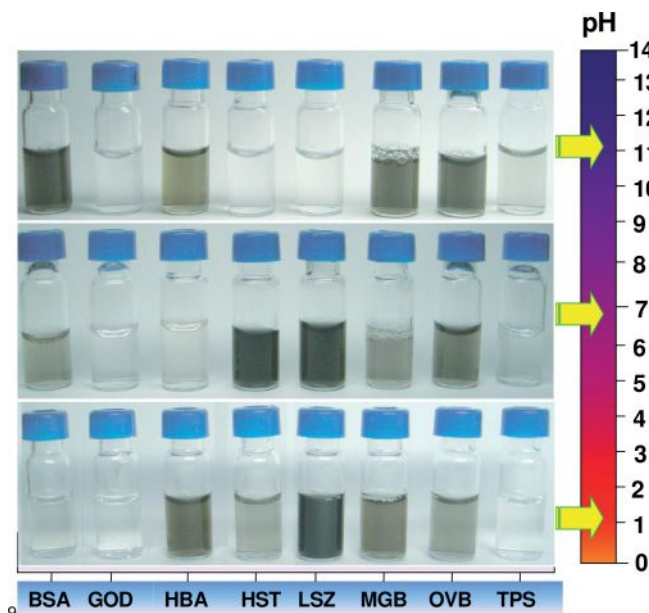
**d** Concentration of SWNTs in the supernatant solution from the first step (centrifugation for 3 h at 18 000×g).

**e** Concentration of SWNTs in the supernatant solution from the final step (centrifugation for 4 h at 120 000×g).

**f** HST-SWNT (which has the highest DD at the intrinsic pH) was considered as 100% DD; values for other products were calculated with respect to this value.



**Figure 23.9** Schematic representations of the single-walled carbon nanotube (SWNT) adducts with different proteins: glucose oxidase (GOX-SWNT), hemoglobin (HBA-SWNT), histone (HST-SWNT), human serum albumin (HSA-SWNT), lysozyme (LSZ-SWNT), myoglobin (MGB-SWNT), ovalbumin (OVB-SWNT), trypsin (TPS-SWNT). Color-coding: secondary structure for GOX, MGB, and TPS; amino acid residue sequence for HST and LSZ; and strand for HAS, HBA, and OVB.



**Figure 23.10** Vials containing the SWNT products obtained from different proteins at different pH values. From left: bovine serum albumin (BSA), glucose oxidase (GOX), hemoglobin (HBA), histone (HST), lysozyme (LSZ), myoglobin (MGB), ovalbumin (OVA), and trypsin (TPS). The arrow in each row indicates the pH range of the respective solutions.

from the bundles. The majority of the tubes were found to be individual, although small bundles of two to four tubes also existed. The irregular coating seen around the nanotube surface was the protein, as confirmed by the detection of nitrogen in the energy-dispersive X-ray (EDX) spectrum. Likewise, this confirmed that the nanotubes had become well dispersed in the protein solution. The AFM images of the product showed a nanotube diameter distribution of between 1 and 5 nm, with a majority of tubes being >3 nm in size. Similar observations were made for the other products. These data illustrate clearly that, during sonication, the nanotubes became simultaneously debundalized due to strong interactions of the proteins with the nanotube surface, and this resulted in highly dispersed protein–nanotube adducts in the aqueous systems. During high-speed ultracentrifugation, the bundled adducts were precipitated due to their higher density, and this resulted in highly individual or less-bundalized protein–nanotubes in the supernatant.

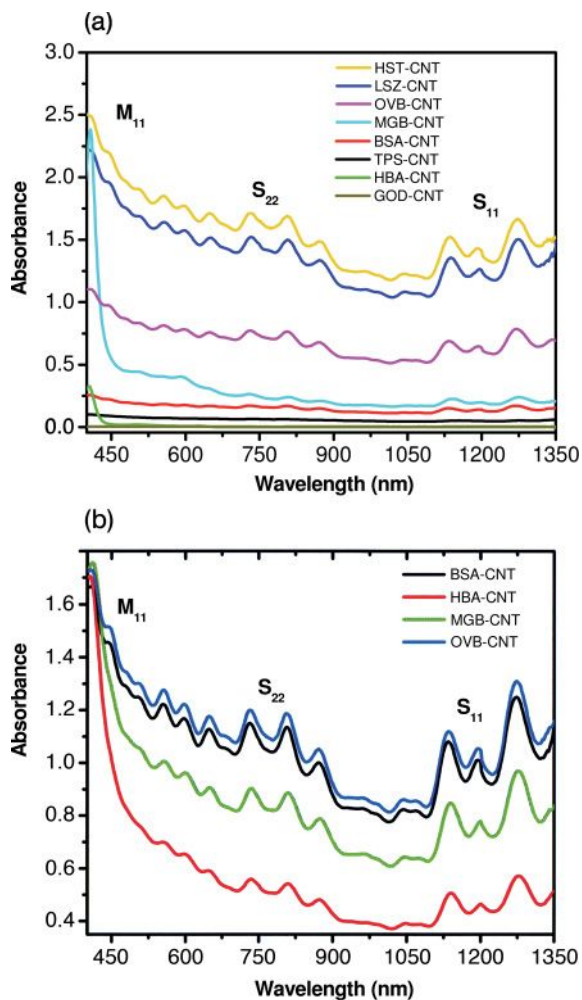
In order to quantify the yield and to check the efficiency of the proteins, the concentrations of nanotubes in the products were measured using absorbance spectroscopy at 500 nm (Figure 23.11). The concentrations were calculated using optical absorbance data fitted to a Beer–Lambert plot. The values (which are summarized in Table 23.1) showed clearly that the highest yield of debundalized nanotubes was obtained from HST at the intrinsic pH, followed by LSZ. However, the yield was exclusively dependent on the pH. In the cases of HBA, OVB, BSA, and MGB, the yields were much higher at basic pH. In contrast, under similar conditions TPS showed a slight improvement, but for GOX the value was almost zero.

In a bid to understand these diverse phenomena, the primary structure of these proteins was investigated. Numerous forces, including van der Waals, electrostatic, hydration, steric, hydrophobic, and chemically specific interactions, are known to act between the colloidal particles in solution. Proteins serve as a rich source of different functionalities due to the presence of different types of amino acid residues (Table 23.2) and the different interactions that are responsible for their interaction with substrates. Hence, the coordinates of these proteins were downloaded from a protein data bank and the different types of residues present in each sequence calculated (Table 23.3). For a better understanding of the major interactions responsible for the dispersion, an attempt was made to correlate the efficiency of proteins for the nanotube dispersion with the residues. The correlation of the debundalization degree (DD) of SWNTs at the intrinsic pH with respect to percentage of hydrophobic residues (HR), aromatic residues (ArR), polar residues (PR), acidic residues (AcR), basic residues (BR), and charged residues (CR) contained in each protein is shown as a three-dimensional plot in Figure 23.12.

## 23.8

### Technology Development Based on Biopolymer-Carbon Nanotube Products

A variety of novel materials has been developed by combining biopolymers with nanotubes. Some important contributions of these materials are outlined in the following sections.



**Figure 23.11** NIR absorbance spectra of the SWNT adducts with different proteins at (a) intrinsic pH, and (b) basic pH. At basic pH, the enhanced intensity of the nanotubes confirmed the high yield of nanotubes in the products.  $S_{11}$  and  $S_{22}$  correspond to the first and second interband transitions of semiconducting nanotubes;  $M_{11}$  corresponds to the first transition of metallic nanotubes.

**Table 23.2** Amino acid residues and their basic chemical and physical parameters.

Amino Acid	Symbol	Structure	Type(s)	Isoelectric point <sup>a</sup>
Alanine	A, Ala	$\begin{array}{c} \text{COO}^- \\   \\ ^+\text{H}_3\text{N}-\text{C}-\text{H} \\   \\ \text{CH}_3 \end{array}$	Hydrophobic	6.01
Arginine	R, Arg	$\begin{array}{c} \text{COO}^- \\   \\ ^+\text{H}_3\text{N}-\text{C}-\text{H} \\   \\ \text{CH}_2 \\   \\ \text{CH}_2 \\   \\ \text{CH}_2 \\   \\ \text{NH} \\   \\ \text{C}=\text{NH}_2^+ \\   \\ \text{NH}_2 \end{array}$	Basic Hydrophilic Polar	10.76
Asparagine	N, Asn	$\begin{array}{c} \text{COO}^- \\   \\ ^+\text{H}_3\text{N}-\text{C}-\text{H} \\   \\ \text{CH}_2 \\   \\ \text{C} \\ / \quad \backslash \\ \text{H}_2\text{N} \quad \text{O} \end{array}$	Hydrophilic Polar	5.41
Aspartic acid	D, Asp	$\begin{array}{c} \text{COO}^- \\   \\ ^+\text{H}_3\text{N}-\text{C}-\text{H} \\   \\ \text{CH}_2 \\   \\ \text{COO}^- \end{array}$	Acidic Polar Hydrophilic	2.85
Cysteine	C, Cys	$\begin{array}{c} \text{COO}^- \\   \\ ^+\text{H}_3\text{N}-\text{C}-\text{H} \\   \\ \text{CH}_2 \\   \\ \text{SH} \end{array}$	Hydrophobic Nonpolar	5.05
Glutamine	Q, Gln	$\begin{array}{c} \text{COO}^- \\   \\ ^+\text{H}_3\text{N}-\text{C}-\text{H} \\   \\ \text{CH}_2 \\   \\ \text{CH}_2 \\   \\ \text{C} \\ / \quad \backslash \\ \text{H}_2\text{N} \quad \text{O} \end{array}$	Hydrophilic Polar	5.65

Table 23.2 Continued.

Amino Acid	Symbol	Structure	Type(s)	Isoelectric point <sup>a</sup>
Glutamic acid	E, Glu	$  \begin{array}{c}  \text{COO}^- \\    \\  ^+\text{H}_3\text{N}-\text{C}-\text{H} \\    \\  \text{CH}_2 \\    \\  \text{CH}_2 \\    \\  \text{COO}^-  \end{array}  $	Acidic Hydrophilic Polar	3.15
Glycine	G, Gly	$  \begin{array}{c}  \text{COO}^- \\    \\  ^+\text{H}_3\text{N}-\text{C}-\text{H} \\    \\  \text{H}  \end{array}  $	Hydrophobic	6.06
Histidine	H, His	$  \begin{array}{c}  \text{COO}^- \\    \\  ^+\text{H}_3\text{N}-\text{C}-\text{H} \\    \\  \text{CH}_2 \\    \\  \text{C} \begin{array}{l} \text{N}^+ \\ \text{H} \end{array} \\  // \quad \backslash \\  \text{HC} \quad \text{CH} \\    \\  \text{H}  \end{array}  $	Basic Hydrophilic Polar	7.60
Isoleucine	I, Ile	$  \begin{array}{c}  \text{COO}^- \\    \\  ^+\text{H}_3\text{N}-\text{C}-\text{H} \\    \\  \text{H}-\text{C}-\text{CH}_3 \\    \\  \text{CH}_2 \\    \\  \text{CH}_3  \end{array}  $	Hydrophobic	6.05
Leucine	L, Leu	$  \begin{array}{c}  \text{COO}^- \\    \\  ^+\text{H}_3\text{N}-\text{C}-\text{H} \\    \\  \text{CH}_2 \\    \\  \text{CH} \\  / \quad \backslash \\  \text{H}_3\text{C} \quad \text{CH}_3  \end{array}  $	Hydrophobic	6.01
Lysine	K, Lys	$  \begin{array}{c}  \text{COO}^- \\    \\  ^+\text{H}_3\text{N}-\text{C}-\text{H} \\    \\  \text{CH}_2 \\    \\  \text{CH}_2 \\    \\  \text{CH}_2 \\    \\  \text{CH}_2 \\    \\  \text{NH}_3^+  \end{array}  $	Basic Hydrophilic Polar	9.60

Table 23.2 Continued.

Amino Acid	Symbol	Structure	Type(s)	Isoelectric point <sup>a</sup>
Methionine	M, Met	$  \begin{array}{c}  \text{COO}^- \\    \\  ^+\text{H}_3\text{N}-\text{C}-\text{H} \\    \\  \text{CH}_2 \\    \\  \text{CH}_2 \\    \\  \text{S} \\    \\  \text{CH}_3  \end{array}  $	Hydrophobic Nonpolar	5.74
Phenylalanine	F, Phe	$  \begin{array}{c}  \text{COO}^- \\    \\  ^+\text{H}_3\text{N}-\text{C}-\text{H} \\    \\  \text{CH}_2 \\    \\  \text{C}_6\text{H}_5  \end{array}  $	Hydrophobic Aromatic Nonpolar	5.49
Proline	P, Pro	$  \begin{array}{c}  \text{COO}^- \\    \\  ^+\text{H}_2\text{N}-\text{C}-\text{H} \\    \quad   \\  \text{H}_2\text{C} \quad \text{CH}_2 \\  \diagdown \quad / \\  \text{C} \\    \\  \text{H}_2  \end{array}  $	Hydrophobic Nonpolar	6.30
Serine	S, Ser	$  \begin{array}{c}  \text{COO}^- \\    \\  ^+\text{H}_3\text{N}-\text{C}-\text{H} \\    \\  \text{H}-\text{C}-\text{OH} \\    \\  \text{H}  \end{array}  $	Hydrophilic Polar	5.68
Threonine	T, Thr	$  \begin{array}{c}  \text{COO}^- \\    \\  ^+\text{H}_3\text{N}-\text{C}-\text{H} \\    \\  \text{H}-\text{C}-\text{OH} \\    \\  \text{CH}_3  \end{array}  $	Hydrophilic Polar	5.60
Tryptophan	W, Trp	$  \begin{array}{c}  \text{COO}^- \\    \\  ^+\text{H}_3\text{N}-\text{C}-\text{H} \\    \\  \text{CH}_2 \\    \\  \text{C} \\  // \quad   \\  \text{HC} \quad \text{N} \quad \text{C}_6\text{H}_4  \end{array}  $	Hydrophobic Aromatic Nonpolar	5.89



Table 23.2 Continued.

Amino Acid	Symbol	Structure	Type(s)	Isoelectric point <sup>a</sup>
Tyrosine	Y, Tyr	$  \begin{array}{c}  \text{COO}^- \\    \\  ^+\text{H}_3\text{N}-\text{C}-\text{H} \\    \\  \text{CH}_2 \\    \\  \text{C}_6\text{H}_4 \\    \\  \text{OH}  \end{array}  $	Aromatic Polar Hydrophilic	5.64
Valine	V, Val	$  \begin{array}{c}  \text{COO}^- \\    \\  ^+\text{H}_3\text{N}-\text{C}-\text{H} \\    \\  \text{CH} \\  / \quad \backslash \\  \text{H}_3\text{C} \quad \text{CH}_3  \end{array}  $	Hydrophobic	6.00

- a [http://en.wikipedia.org/wiki/Amino\\_acid](http://en.wikipedia.org/wiki/Amino_acid); Doolittle, R.F. (1989) Redundancies in protein sequences, in *Predictions of Protein Structure and the Principles of Protein Conformation* (G.D. Fasman, ed.) Plenum Press, New York, pp. 599–623; Nelson, D.L. and Cox, M.M. (2000) *Lehninger, Principles of Biochemistry*, 3rd ed., Worth Publishers.

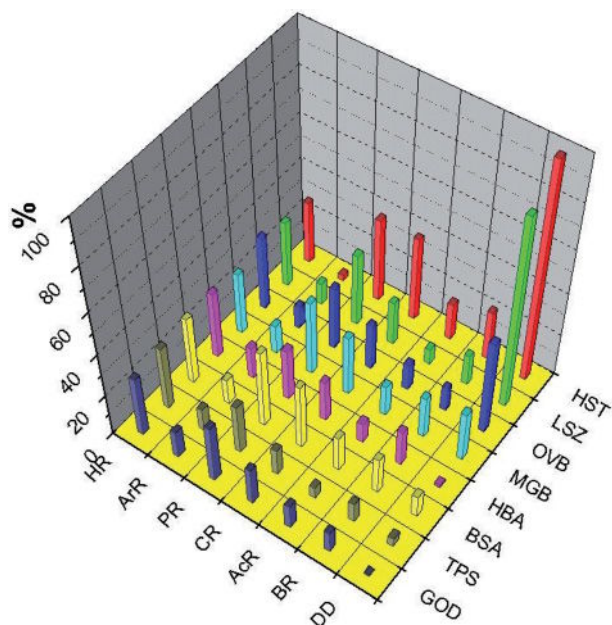
Table 23.3 Calculation of different types of residue content in different proteins.

Protein	Hydrophobic residue (V, I, L, M, F, W, C)	Aromatic residue (F, W, Y, H)	Basic residue (R, K, H)	Acidic residue (E, D)	Charged residue (R, K, E, D)	Polar residue (R, K, D, E, N, Q)
HST	28.9	2.8	23.1	17.3	39	39
LSZ	30.4	10.1	14	7	20.2	33.4
OVb	34.5	10.4	10.9	12.1	21.2	29.5
MGB	28.8	13.1	19.6	14.4	28.1	34.7
HBA	31.5	14.9	16.4	9.4	19.2	24.1
BSA	31.5	11.7	17	16.3	30.5	36.1
TPS	30	10.3	9	5.3	12.5	23.2
GOD	28.2	12.6	9.6	11	17.3	26.6

### 23.8.1

#### Diameter- or Chirality-Based Separation of Carbon Nanotubes

Another very important challenge remaining in nanotube research is the separation of nanotubes based on their electronic properties. This is feasible because, during the synthesis of nanotubes (notably of SWNTs) they may be semi-conducting, semi-metallic, or metallic, depending on the rolling vector. However, none of



**Figure 23.12** Three-dimensional plot showing the debundalization degree (DD) with respect to the percentage of hydrophobic residues (HR), aromatic residues (ArR), polar residues (PR), charged residues (CR), acidic residues (AcR), and basic residues (BR) contained in each protein.

the synthetic techniques reported to date can be used produce a single type of SWNT; rather, a heterogeneous mixture of SWNTs is usually obtained. More importantly, as the electrical and optical properties depend heavily on the chirality and diameter of the nanotubes, a separation of these tubes according to type is a prerequisite for further development of the technology. For example, when fabricating optical devices based on photoluminescence, *sem*-SWNTs are essential, but the presence of *met*-SWNTs leads to a quenching of these properties. Moreover, the problem is worsened due to the nature of nanotubes remaining in aggregation or bundalization, based on the strong van der Waals interactions of the parallel tubes. Although efforts have been made to overcome this problem, an effective and simple technique, which preferably could easily be scaled up, has yet to be developed. One of the major achievements when using DNA for the dispersion of nanotubes is its property to separate the nanotubes selectively, based on their electronic properties [47]. Different experiments have confirmed that the DNA-based approach using chromatography (both, ion-exchange and size exclusion) is highly effective for metal/semiconducting CNT separations, and single-chirality CNT enrichment for certain small-diameter tubes. Such separation is possible due to the selective interaction ability of the designed polynucleotide being synthesized with a specific sequence. For example, an improved metal/semiconductor separation was possible with shorter (guanine/thymine)<sub>n</sub> sequences.

**Table 23.4** Enrichment factors of metallic (*met*-SWNTs) and semiconducting (*sem*-SWNTs) single-wall carbon nanotubes (SWNTs) of small and large diameters in the products using the 532 nm and 632.8 nm Raman excitation laser lines.

Product	Enrichment factor <sup>d</sup>				<i>met:sem</i> <sup>a</sup>
	<i>(met)</i> <sub>s</sub> <sup>b</sup>	<i>(met)</i> <sub>L</sub> <sup>c</sup>	<i>(sem)</i> <sub>s</sub> <sup>c</sup>	<i>(sem)</i> <sub>L</sub> <sup>b</sup>	
BSA-SWNT <sup>d</sup>	1.71	1.31	0.44	1.09	1.08:1
HBA-SWNT <sup>e</sup>	1.42	1.31	0.53	1.23	1.68:2
HBA-SWNT <sup>d</sup>	1.24	1.54	0.5	1.55	1.57:2
HST-SWNT <sup>f</sup>	1.74	1.08	0.47	1	1:1
LSZ-SWNT <sup>e</sup>	1.45	1.62	0.34	1.36	1.12:1
LSZ-SWNT <sup>f</sup>	1.63	2.38	0.34	1.09	1.61:1
MGB-SWNT <sup>e</sup>	1.47	1.38	0.41	1.18	1.06:1
MGB-SWNT <sup>f</sup>	1.53	1.62	0.5	1.23	1.01:1
MGB-SWNT <sup>d</sup>	1.55	1	0.47	1.14	1.71:2
OVBSWNT <sup>f</sup>	1.68	1.46	0.38	1.09	1.23:1
OVBSWNT <sup>d</sup>	1.71	1.39	0.5	1.14	1.01:1
TRP-SWNT <sup>d</sup>	1.34	2	0.63	1	1.04:1

- a Calculated according to the method of Samsonidze, G.G., Chou, S.G., Santos, A.P. *et al.* (2004) *Appl. Physics Lett.* 85 (6), 1006–1008. *(met)*<sub>s</sub> = small diameter metallic SWNTs; *(met)*<sub>L</sub> = large diameter metallic SWNTs; *(sem)*<sub>s</sub> = small diameter semiconducting SWNTs; *(sem)*<sub>L</sub> = large diameter semiconducting SWNTs.
- b Calculated from 633 nm laser.
- c Calculated from 532 nm laser.
- d Basic pH.
- e Acidic pH.
- f Intrinsic pH.

By taking advantage of natural proteins under controlled conditions, it was possible to obtain metallic-enriched nanotubes in the final products, which ranged from ~33% (pristine nanotubes) to ~63% (final product) (Table 23.4). This unique and simple technique to enrich metallic nanotubes has had a major impact on metallic-semiconducting nanotube separation in bulk, on a large scale.

### 23.8.2 Fibers

Recently, DNA-dispersed nanotube products have been used to sort nanotubes based on chirality [30], to synthesize polymers [54], as well as serving as templates for nanoparticles [55]. In addition, these products have been shown to prepare liquid crystals [56], fibers [57], and coatings [20]. Whilst the future pros-

pects of CNTs in biomedical research continue to rise, the preparation of CNT-based biofibers has been introduced only recently [57–60]. DNA-based SWNT fibers were first produced via wet spinning using poly(vinyl alcohol) in the coagulation bath [57], this being possible only due to the excellent dispersion ability of DNA for the SWNTs. Typically, a concentration of 1 wt% SWNTs was able to disperse very well in 1 wt% salmon DNA, which made it feasible to produce DNA–SWNT fibers via wet spinning. Of note, this is almost impossible using surfactants, where ratios of surfactant to SWNTs of at least 2:1 [61] or 3:1 [62] are necessary. The fibers exhibited excellent mechanical properties, with a Young's modulus of up to 14–19 GPa—much higher than for the fibers obtained using sodium dodecyl sulfate (5 GPa), one of the most commonly used surfactants for CNT dispersion. Recently, other fibers based on heparin–SWNT, chitosan–SWNT, and hyaluronic acid–SWNT fibers have also been processed [58]. In this way, the unique nature of each of these biopolymers, and its effect on the CNTs, may open wide possibilities for future exploration. Indeed, combining the excellent conductivity and mechanical strength of CNTs with the inherent properties of different biomolecules might one day bring about new and exciting products.

### 23.8.3

#### Sensors

The size-dependent properties of nanomaterials have made them attractive for the development of highly sensitive sensors and detection systems. This is especially the case in the biological sciences, where the efficiency of a detection system is reflected by the size of the detector and the amount of sample required for detection. In this respect, CNTs hold much promise due to their typical size, which offers a great potential for enhancing the sensitivity of detection and diagnostics, while reducing the sample size (which may consist of a few individual proteins and antibodies). As carbon atoms dominate the surface of the SWNTs, the binding of proteins or antibodies to their surfaces can alter the surface state, and this in turn may result in a varied electrical and optical functionality. DNA-coated CNTs have a great potential in the design of a variety of sensors, and several research groups are currently working on this direction with electrochemical sensors [63]. In addition, protein- or DNA-incorporated CNTs can be used as a base for detecting biological surface reactions in a single protein or antibody attached to the CNT surface.

The other main advantages of nanotubes include their optical activity, as long as they are neither aggregated nor chemically altered. Under appropriate conditions, semiconducting SWNTs show a bandgap fluorescent emission in the NIR spectral region at wavelengths characteristic of their specific (n,m)-structure. As natural biomolecules are relatively transparent and nonemissive in this range, the sharp spectra of SWNTs can be detected even in a complex biological environment. By taking advantage of these properties different sensors have been designed, including those used to detect glucose [15].

## 23.8.4

**Therapeutic Agents**

Today, functionalized CNTs are emerging as a new family of nanovectors for the delivery of different types of therapeutic molecules. A recent study proved that functionalized CNTs can penetrate into cells, with the CNTs being loaded with bioactive molecules via stable covalent bonds or supramolecular assemblies based on noncovalent interactions. When the cargos have been carried into the different cells, tissues, and organs, they are able to express their biological function. Recently, Cheruki and coworkers [64] injected debundled, chemically pristine SWNTs into rabbits and monitored their characteristic NIR fluorescence. The nanotube concentration in the blood serum decreased exponentially, with a half-life of 1 h.

The ability of CNTs to convert NIR light into heat provides an opportunity to create a new generation of immunoconjugates for cancer phototherapy, with high performance and efficacy. The fact that biological tissue is relatively transparent to NIR suggests that targeting CNTs to tumor cells, followed by noninvasive exposure to NIR light, would cause tumor ablation within the range of accessibility of the NIR light. Recently, it was shown that antibody-functionalized SWNTs operated very efficiently to kill targeted tumor cells [65], this being achieved by a specific binding of antibody-coupled CNTs to tumor cells *in vitro*, followed by their highly specific ablation with NIR light. For this, biotinylated polar lipids were used to prepare the stable, biocompatible, and noncytotoxic CNT dispersions that were then attached to antibodies. Following exposure to NIR light, the CNT–antibody construct was shown to have killed the targeted cells with great specificity [65].

## 23.9

**Conclusions**

The functionalization of nanotubes with biopolymers has achieved good progress in a relatively short time. When compared to the programmed properties and functions they possess in a natural environment, the technological development achieved to date remains in its infancy. It may be premature at this stage to claim advancements of the different fields using these materials, and especially for the biotechnological sector, where issues of toxicity have not yet been fully resolved. Nonetheless, the vast potential for these materials will surely offer rapid research and development in this direction. There is also no doubt in anticipating that this field will bring future breakthroughs for the advancement of humankind.

**Acknowledgments**

This work was supported by the Ministry of Education (“Brain Korea 21” project) and a grant from the Institute of Medical System Engineering at GIST.

## References

- 1 Haddon, R.C. (2002) Carbon nanotubes. *Acc. Chem. Res.*, **35**, 997.
- 2 Nepal, D. (2006) PhD thesis. Dispersion, Individualization and Novel Supramolecular Adducts of Carbon Nanotubes. Department of Materials Science and Engineering 140, Gwangju Institute of Science and Technology (GIST), Gwangju.
- 3 Nepal, D. and Geckeler, K.E. (2006) Functional Nanomaterials. In: *Functionalization of Carbon Nanotubes*, (eds K.E. Geckeler and E. Rosenberg), American Scientific Publishers, Valencia, pp. 57–79.
- 4 Li, S.S., He, H., Jiao, Q.C. and Chuong, P.H. (2008) Applications of carbon nanotubes in drug and gene delivery. *Prog. Chem.*, **20**, 1798–1803.
- 5 Kim, S.N., Rusling, J.F. and Papadimitrakopoulos, F. (2007) Carbon nanotubes for electronic and electrochemical detection of biomolecules. *Adv. Mater.*, **19**, 3214–3228.
- 6 Prato, M., Kostarelos, K. and Bianco, A. (2008) Functionalized carbon nanotubes in drug design and discovery. *Acc. Chem. Res.*, **41**, 60–68.
- 7 Kovtyukhova, N.I., Mallouk, T.E., Pan, L. and Dickey, E.C. (2003) Individual single-walled nanotubes and hydrogels made by oxidative exfoliation of carbon nanotube ropes. *J. Am. Chem. Soc.*, **125**, 9761–9769.
- 8 Ajayan, P.M., Schadler, L.S., Giannaris, C. and Rubio, A. (2000) Single-walled carbon nanotube-polymer composites: strength and weakness. *Adv. Mater.*, **12**, 750–753.
- 9 O'Connell, M.J., Bachilo, S.M., Huffman, C.B., Moore, V.C., Strano, M.S., Haroz, E.H., Rialon, K.L., Boul, P.J., Noon, W.H., Kittrell, C., Ma, J., Haugl, R.H., Weisman, R.B., and Smalley, R.E. (2002) Band gap fluorescence from individual single-walled carbon nanotubes. *Science*, **297**, 593–596.
- 10 Huang, J.Y., Chen, S., Wang, Z.Q. *et al.* (2006) Superplastic carbon nanotubes. *Nature*, **439**, 281.
- 11 Yu, M.-F., Files, B.S., Arepalli, S. and Ruoff, R.S. (2000) Tensile loading of ropes of single wall carbon nanotubes and their mechanical properties. *Phys. Rev. Lett.*, **84**, 5552–5555.
- 12 Yu, M.-F., Lourie, O., Dyer, M.J., Moloni, K., Kelly, T.F. and Ruoff, R.S. (2000) Strength and breaking mechanism of multiwalled carbon nanotubes under tensile load. *Science*, **287**, 637–640.
- 13 Hudson, J.L., Casavant, M.J. and Tour, J.M. (2004) Water-soluble, exfoliated, nonroping single-wall carbon nanotubes. *J. Am. Chem. Soc.*, **126**, 11158–11159.
- 14 Nepal, D. and Geckeler, K.E. (2006) pH-sensitive dispersion and debundling of single-walled carbon nanotubes: lysozyme as a tool. *Small*, **2**, 406–412.
- 15 Barone, P.W., Baik, S., Heller, D.A. and Strano, M.S. (2005) Near-infrared optical sensors based on single-walled carbon nanotubes. *Nat. Mater.*, **4**, 86–92.
- 16 Saito, R., Dresselhaus, G. and Dresselhaus, M.S. (2000) Trigonal warping effect of carbon nanotubes. *Phys. Rev. B*, **61**, 2981.
- 17 Moore, V.C., Strano, M.S., Haroz, E.H., Hauge, R.H. and Smalley, R.E. (2003) Individually suspended single-walled carbon nanotubes in various surfactants. *Nano Lett.*, **3**, 1379–1382.
- 18 Zhang, Z.H., Yang, X.Y., Zhang, Y., Zeng, B., Wang, Z.J., Zhu, T.H., Roden, R.B.S., Chen, Y.S. and Yang, R.C. (2006) Delivery of telomerase reverse transcriptase small interfering RNA in complex with positively charged single-walled carbon nanotubes suppresses tumor growth. *Clin. Cancer Res.*, **12**, 4933–4939.
- 19 Hillebrenner, H., Buyukserin, F., Stewart, J.D. and Martin, C.R. (2006) Template synthesized nanotubes for biomedical delivery applications. *Nanomedicine*, **1**, 39–50.
- 20 Nepal, D., Balasubramanian, S., Simonian, A.L. and Davis, V.A. (2008) Strong antimicrobial coatings: single-walled carbon nanotubes armored with biopolymers. *Nano Lett.*, **8**, 1896–1901.
- 21 Dubin, R.A., Callegari, G.C., Kohn, J. and Neimark, A.V. (2008) Carbon nanotube fibers are compatible with mammalian

- cells and neurons. *IEEE Trans. Nanobioscience*, **7**, 11–14.
- 22 Hu, H., Ni, Y., Mandal, S.K., Montana, V., Zhao, B., Haddon, R.C. and Parpura, V. (2005) Polyethyleneimine functionalized single-walled carbon nanotubes as a substrate for neuronal growth. *J. Phys. Chem. B*, **109**, 4285–4289.
  - 23 Usui, Y., Aoki, K., Narita, N., Murakami, N., Nakamura, I., Nakamura, K., Ishigaki, N., Yamazaki, H., Horiuchi, H., Kato, H., Taruta, S., Kim, Y.A., Endo, M. and Saito, N. (2008) Carbon nanotubes with high bone-tissue compatibility and bone-formation acceleration effects. *Small*, **4**, 240–246.
  - 24 Harrison, B.S. and Atala, A. (2007) Carbon nanotube applications for tissue engineering. *Biomaterials*, **28**, 344–353.
  - 25 Bandyopadhyaya, R., Nativ-Roth, E., Regev, O. and Yerushalmi-Rozen, R. (2002) Stabilization of individual carbon nanotubes in aqueous solutions. *Nano Lett.*, **2**, 25–28.
  - 26 Wenseleers, W., Vlasov, I.I., Goovaerts, E., Obratzsova, E.D., Lobach, A.S. and Bouwen, A. (2004) Efficient isolation and solubilization of pristine single-walled nanotubes in bile salt micelles. *Adv. Funct. Mater.*, **14**, 1105–1112.
  - 27 Zhang, M., Smith, A. and Gorski, W. (2004) Carbon nanotube-chitosan system for electrochemical sensing based on dehydrogenase enzymes. *Anal. Chem.*, **76**, 5045–5050.
  - 28 Hasegawa, T., Fujisawa, T., Numata, M., Umeda, M., Matsumoto, T., Kimura, T., Okumura, S., Sakurai, K., and Shinkai, S. (2004) Single-walled carbon nanotubes acquire a specific lectin-affinity through supramolecular wrapping with lactose-appended schizophyllan. *Chem. Commun.*, 2150–2151.
  - 29 Star, A., Steurman, D.W., Heath, J.R. and Stoddart, J.F. (2002) Starched carbon nanotubes. *Angew. Chem. Int. Ed. Engl.*, **41**, 2508–2512.
  - 30 Zheng, M., Jagota, A., Strano, M.S., Santos, A.P., Barone, P., Chou, S.G., Diner, B.A., Dresselhaus, M.S., McLean, R.S., Onoa, G.B., Samsonidze, G.G., Semke, E.D., Usrey, M., and Walls, D.J. (2003) Structure-based carbon nanotube sorting by sequence-dependent DNA assembly. *Science*, **302**, 1545–1548.
  - 31 Cathcart, H., Quinn, S., Nicolosi, V., Kelly, J.M., Blau, W.J. and Coleman, J.N. (2007) Spontaneous debundling of single-walled carbon nanotubes in DNA-based dispersions. *J. Phys. Chem. C*, **111**, 66–74.
  - 32 Liu, Y., Chen, J., Anh, N.T., Too, C.O., Misoska, V. and Wallace, G.G. (2008) Nanofiber mats from DNA, SWNTs, and poly(ethylene oxide) and their application in glucose biosensors. *J. Electrochem. Soc.*, **155**, K100–K103.
  - 33 Jonganurakkun, B., Liu, X.D., Nodasaka, Y., Nomizu, M. and Nishi, N. (2003) Survival of lactic acid bacteria in simulated gastrointestinal juice protected by a DNA-based complex gel. *J. Biomater. Sci., Polym. Ed.*, **14**, 1269–1281.
  - 34 Fink, H.-W. and Schonenberger, C. (1999) Electrical conduction through DNA molecules. *Nature*, **398**, 407–410.
  - 35 Yan, H., Zhang, X., Shen, Z. and Seeman, N.C. (2002) A robust DNA mechanical device controlled by hybridization topology. *Nature*, **415**, 62–65.
  - 36 Turberfield, A. (2003) *Phys. World*, **16** (3), 43–46.
  - 37 Steckl, A.J. (2007) DNA—a new material for photonics? *Nat. Photonics*, **1**, 3–5.
  - 38 Zheng, M., Jagota, A., Semke, E.D., Diner, B.A., Mclean, R.S., Lustig, S.R., Richardson, R.E. and Tassi, N.G. (2003) DNA-assisted dispersion and separation of carbon nanotubes. *Nat. Mater.*, **2**, 338–342.
  - 39 Nepal, D., Sohn, J.-I., Aicher, W.K., Lee, S. and Geckeler, K.E. (2005) Supramolecular conjugates of carbon nanotubes and DNA by a solid-state reaction. *Biomacromolecules*, **6**, 2919–2922.
  - 40 Tsang, S.C., Guo, Z., Chen, Y.K., Green, M.L.H., Hill, H.A.O., Hambley, T.W. and Sadler, P.J. (1997) Immobilization of platinated and iodinated oligonucleotides on carbon nanotubes. *Angew. Chem. Int. Ed. Engl.*, **36**, 2198–2200.
  - 41 Nakashima, N., Okuzono, S., Murakami, H., Nakai, T. and Yoshikawa, K. (2003) DNA dissolves single-walled carbon nanotubes in water. *Chem. Lett.*, **32**, 456–457.
  - 42 Baker, S.E., Cai, W., Lasseter, T.L., Weidkamp, K.P. and Hamers, R.J. (2002) Covalently bonded adducts of

- deoxyribonucleic acid (DNA) oligonucleotides with single-wall carbon nanotubes: synthesis and hybridization. *Nano Lett.*, **2**, 1413–1417.
- 43 Keren, K., Berman, R.S., Buchstab, E., Sivan, U. and Braun, E. (2003) DNA-templated carbon nanotube field-effect transistor. *Science*, **302**, 1380–1382.
- 44 Drexler, K. (1992) *Nanosystems: Molecular Machinery, Manufacturing, and Computation*, John Wiley & Sons, Inc., New York.
- 45 Wang, G.-W., Komatsu, K., Murata, Y. and Shiro, M. (1997) Synthesis and X-ray structure of dumb-bell-shaped C120. *Nature*, **387**, 583–586.
- 46 Pan, H., Guo, Z.-X., Dai, L., Zhang, F., Zhu, D., Czerw, R. and Carroll, D.L. (2003) Carbon nanotubols from mechanochemical reaction. *Nano Lett.*, **3**, 29–32.
- 47 Tu, X. and Zheng, M. (2008) A DNA-based approach to the carbon nanotube sorting problem. *Nano Res.*, **1**, 185–194.
- 48 Kane, R.S. and Stroock, A.D. (2007) Nanobiotechnology: protein-nanomaterial interactions. *Biotechnol. Prog.*, **23**, 316–319.
- 49 Huang, W.J., Taylor, S., Fu, K.F., Lin, Y., Zhang, D.H., Hanks, T.W., Rao, A.M. and Sun, Y.P. (2002) Attaching proteins to carbon nanotubes via diimide-activated amidation. *Nano Lett.*, **2**, 311–314.
- 50 Zorbas, V., Ortiz-Acevedo, A., Dalton, A.B., Yoshida, M.M., Dieckmann, G.R., Draper, R.K., Baughman, R.H., Jose-Yacamán, M., and Musselman, I.H. (2004) Preparation and characterization of individual peptide-wrapped single-walled carbon nanotubes. *J. Am. Chem. Soc.*, **126**, 7222–7227.
- 51 Zorbas, V., Smith, A.L., Xie, H., Ortiz-Acevedo, A., Dalton, A.B., Dieckmann, G.R., Draper, R.K., Baughman, R.H., and Musselman, I.H. (2005) Importance of aromatic content for peptide/single-walled carbon nanotube interactions. *J. Am. Chem. Soc.*, **127**, 12323–12328.
- 52 Xie, H., Becraft, E.J., Baughman, R.H., Dalton, A.B. and Dieckmann, G.R. (2008) Ranking the affinity of aromatic residues for carbon nanotubes by using designed surfactant peptides. *J. Peptide Sci.*, **14**, 139–151.
- 53 Karajanagi, S.S., Yang, H., Asuri, P., Sellitto, E., Dordick, J.S. and Kane, R.S. (2006) Protein-assisted solubilization of single-walled carbon nanotubes. *Langmuir*, **22**, 1392–1395.
- 54 Ma, Y., Chiu, P.L., Serrano, A., Ali, S.R., Chen, A.M. and He, H. (2008) The electronic role of DNA-functionalized carbon nanotubes: efficacy for in situ polymerization of conducting polymer nanocomposites. *J. Am. Chem. Soc.*, **130**, 7921–7928.
- 55 Han, X., Li, Y. and Deng, Z. (2007) DNA-wrapped single walled carbon nanotubes as rigid templates for assembling linear gold nanoparticle arrays. *Adv. Mater.*, **19**, 1518–1522.
- 56 Badaire, S., Zakri, C., Maugey, M., Derre, A., Barisci, J.N., Wallace, G. and Poulin, P. (2005) Liquid crystals of DNA-stabilized carbon nanotubes. *Adv. Mater.*, **17**, 1673–1676.
- 57 Barisci, J.N., Tahhan, M., Wallace, G.G., Badaire, S., Vaugien, T., Maugey, M. and Poulin, P. (2004) Properties of carbon nanotube fibers spun from DNA-stabilized dispersions. *Adv. Funct. Mater.*, **14**, 133–138.
- 58 Lynam, C., Moulton, S.E. and Wallace, G.G. (2007) Carbon-nanotube biofibers. *Adv. Mater.*, **19**, 1244–1248.
- 59 Razal, J.M., Gilmore, K.J. and Wallace, G.G. (2008) Carbon nanotube biofiber formation in a polymer-free coagulation bath. *Adv. Funct. Mater.*, **18**, 61–66.
- 60 Shin, S.R., Lee, C.K., So, I.S. *et al.* (2008) DNA-wrapped single-walled carbon nanotube hybrid fibers for supercapacitors and artificial muscles. *Adv. Mater.*, **20**, 466–470.
- 61 Muñoz, E., Suh, D.-S., Collins, S., Selvidge, M., Dalton, A.B., Kim, B.G., Razal, J.M., Ussery, G., Rinzler, A.G., Martínez, M.T. and Baughman, R.H. (2005) Highly conducting carbon nanotube/polyethyleneimine composite fibers. *Adv. Mater.*, **17**, 1064–1067.
- 62 Kozlov, M.E., Capps, R.C., Sampson, W.M., Ebron, V.H., Ferraris, J.P. and Baughman, R.H. (2005) Spinning solid and hollow polymer-free carbon nanotube fibers. *Adv. Mater.*, **17**, 614–617.
- 63 Yogeswaran, U., Thiagarajan, S. and Chen, S.M. (2008) Recent updates of DNA incorporated in carbon nanotubes



- and nanoparticles for electrochemical sensors and biosensors. *Sensors*, **8**, 7191–7212.
- 64** Cherukuri, P., Gannon, C.J., Leeuw, T.K., Schmidt, H.K., Smalley, R.E., Curley, S.A. and Weisman, R.B. (2006) Mammalian pharmacokinetics of carbon nanotubes using intrinsic near-infrared fluorescence. *Proc. Natl Acad. Sci. USA*, **103**, 18882–18886.
- 65** Chakravarty, P., Marches, R., Zimmerman, N.S., Swafford, A.D.E., Bajaj, P., Musselman, I.H., Pantano, P., Draper, R.K., and Vitetta, E.S. (2008) Thermal ablation of tumor cells with antibody-functionalized single-walled carbon nanotubes. *Proc. Natl Acad. Sci. USA*, **105**, 8697–8702.

## 24

# Nanoparticle-Cored Dendrimers and Hyperbranched Polymers: Synthesis, Properties, and Applications

Young-Seok Shon

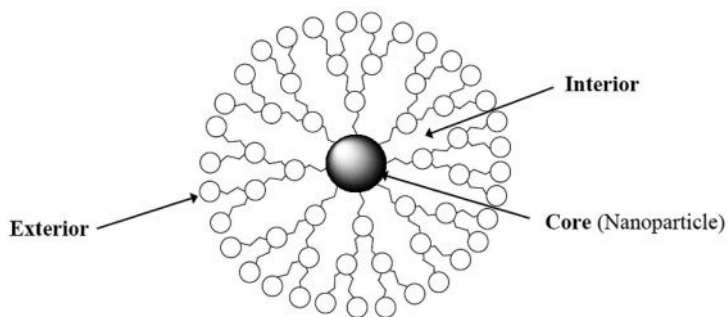
### 24.1

#### Introduction

Functionalized nanoparticles have attracted remarkable academic and industrial interest due to their unique chemical, biological, catalytic, optical, and electronic properties, as well as their potential applications in electronic devices, sensors, molecular reagents, and catalysis [1–3]. Nanoparticles protected by a polymeric ligand have been employed to prepare nanoscale building blocks for functional materials. Polymeric stabilizers such as thiolated polymers [4–6] and electrostatic polymer multilayers [7–9] have been used for the stabilization of metal nanoparticles. Nanoparticles have also been modified with polymer chains covalently bound to the surface using “grafting from” reactions, such as atom transfer radical (ATR) polymerization, living cationic ring-opening polymerization, and surface-immobilized ring-opening metathesis polymerization (ROMP) [10–12].

Dendrimers have attracted an intense interest because of their well-defined structures with interior cavities and chemical versatility [13–15]. Dendrimers also often have provided some of the most versatile tools to building blocks used in the construction of three-dimensional (3-D) organic/inorganic nanostructures [16]. The current research on dendrimers is mostly focused on the development of functionalized dendrimers with an active core or external surface groups [17–19]. These functional dendrimers have shown a variety of applications in the fields of medicinal chemistry (e.g., magnetic resonance imaging and drug delivery), host-guest chemistry, and catalysis [17–19]. Significant research progress has also been made in the use of dendritic frameworks to surround functional core molecules such as rotaxane, porphyrin, and fullerene [20–23].

Due to the interesting properties of metal nanoparticles [1], the incorporation of nanoparticles into the dendrimer templates has been attempted [24–33]. For example, monometallic nanoparticles of gold, palladium, platinum, copper, and silver were incorporated into the dendrimers by reduction of their metal salts with  $\text{NaBH}_4$  in the presence of “Tomalia-type” poly(amidoamine) dendrimers [24–26]. These materials were synthesized using a template approach in which metal ions



**Figure 24.1** General structure of nanoparticle-cored dendrimers (NCDs).

were first extracted into the interior of dendrimers and then subsequently reduced by chemical reactants to yield quite monodisperse particles having dimensions of less than 5 nm. Both, bimetallic and semiconductor nanoparticles have also been incorporated into the dendrimers by similar routes [28, 29]. These materials have a number of applications, but are especially useful in catalysis (e.g., hydrogenations, Heck coupling, Stille, and Suzuki reactions) [30–33]. Several reviews have been prepared detailing the synthesis, characterization, and application of dendrimer-encapsulated nanoparticles [23–25].

Structurally well-defined, inorganic, cluster-cored dendrimers have also attracted interest. Dendrimers supported by the  $[\text{Re}_6\text{Se}_8]^{2+}$  metal cluster were synthesized by Zheng and coworkers [34], this being the first example of utilizing metal clusters to construct cluster-cored metallodendrimers. These dendrimers exhibited dramatic color changes with only slight variations in the structure of dendrons, which suggested their interesting—and potentially important—optical tunability. Gorman *et al.* reported the synthesis and characterization of iron–sulfur  $[\text{Fe}_4\text{S}_4]$  cluster-cored dendrimers [35, 36]. Here, it was recognized that the iron–sulfur cluster employed as the core unit in these dendrimers displayed redox potentials that were very sensitive to environments such as the generation of dendrons and the solvent media. Dendrimers based on polyhedral oligomeric silsesquioxane (POSS) cores were also prepared, and provided an increased selectivity in hydroformylation reactions due to a positive dendrimer effect [37].

Nanoparticle-cored dendrimers represent an organic–inorganic hybrid nanostructure with a nanoparticle core and well-defined dendritic wedges (Figure 24.1) [38–58]. The preparation of nanoparticle-cored dendrimers represents an important advance in the control and preparation of new organized nanostructures. Dendritic scaffolds offer an enhanced stability and well-defined property to the materials, and can provide some segregation of external groups and internal nanoparticle core. While the external functionality mainly controls the overall solubility and reactivity of nanoparticle-cored dendrimers (NCDs), internal functionality provides a completely different environment for the nanoparticle core from that of the bulk solution and the exterior. Another important structural feature of NCDs

is the large void spaces present inside; these may act as guest cavities and also function as “reaction vessels” for catalytic reactions.

In this chapter we present a concise review of synthetic strategies for nanoparticle-cored dendrimers, along with their properties and applications. The most popular synthetic approach—the *direct method*—uses a modified Schiffrin reaction with dendrons containing thiols or disulfides [38–49]. In contrast, the *indirect method* involves two-step reactions, namely the synthesis of monolayer-stabilized nanoparticles followed by the ligand-place exchange of thiolated dendrons [47, 50–54]. A third synthetic strategy is also described, in which single or multistep organic reactions are employed to build dendritic architectures around a monolayer-protected metal nanoparticle [55–58]. Finally, the synthesis of nanoparticle-cored hyperbranched polymers is introduced as the convenient alternate for nanoparticle-cored dendrimers. In this approach, well-defined hyperbranched polymers are grafted onto a nanoparticle by self-organization [59–61]. The chemical and physical properties, and also the technological applications, of nanoparticle-cored dendrimers and hyperbranched polymers are described with regards to the synthetic methods for these nanostructures.

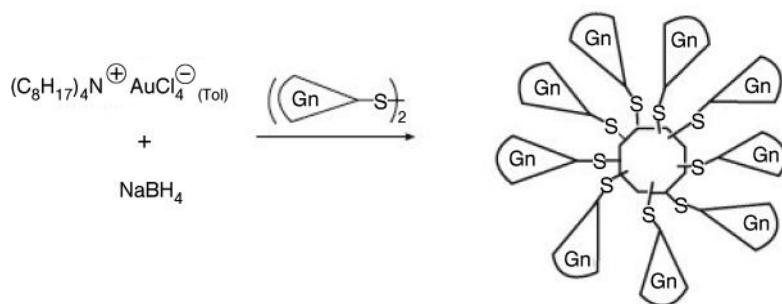
## 24.2

### Synthesis of Nanoparticle-Cored Dendrimers via the Direct Method, and their Properties and Application

When, in 1994, Schiffrin *et al.* reported the convenient two-phase synthesis of isolable and soluble alkanethiolate-protected gold nanoparticles, this had a major impact on nanoparticle research and development [1]. In this reaction,  $\text{AuCl}_4^-$  was transferred to toluene, using tetraoctylammonium bromide as the phase-transfer reagent. The addition of alkanethiol to organic-phase  $\text{AuCl}_4^-$ , followed by reduction with  $\text{NaBH}_4$ , generated alkanethiolate-protected gold nanoparticles. The first examples of nanoparticle-cored dendrimers were synthesized using a modified, two-phase Schiffrin protocol (Scheme 24.1).

Shultz, Linderman, Feldheim, and their coworkers reported that the alkene-terminated tripodal ligand (**1**; Figure 24.2), which contained a branched structure with a single thiolate group on one end and three alkene-terminated hydrocarbon chains on the other end, could be used for the stabilization of gold nanoparticles that were approximately 5 nm in diameter [38]. The alkene-terminated tripodal ligand was used in order to maximize polymeric crosslinking, which led to the formation of structurally rigid hollow capsules following removal of the gold nanoparticle. The dimensions of the capsules ( $\sim 10 \pm 2.5$  nm) agreed well with the diameter expected based on the size of the template gold nanoparticle and the length of the alkylthiol spacer. Crosslinking was carried out by olefin metathesis of the thiol-derivatized nanoparticles using a catalytic quantity of Grubbs catalyst [62].

Similarly, poly(oxymethyl) dendrons with a single thiol group (**2**; Figure 24.2) at the focal point were used as the stabilizer, and produced dendron-stabilized gold

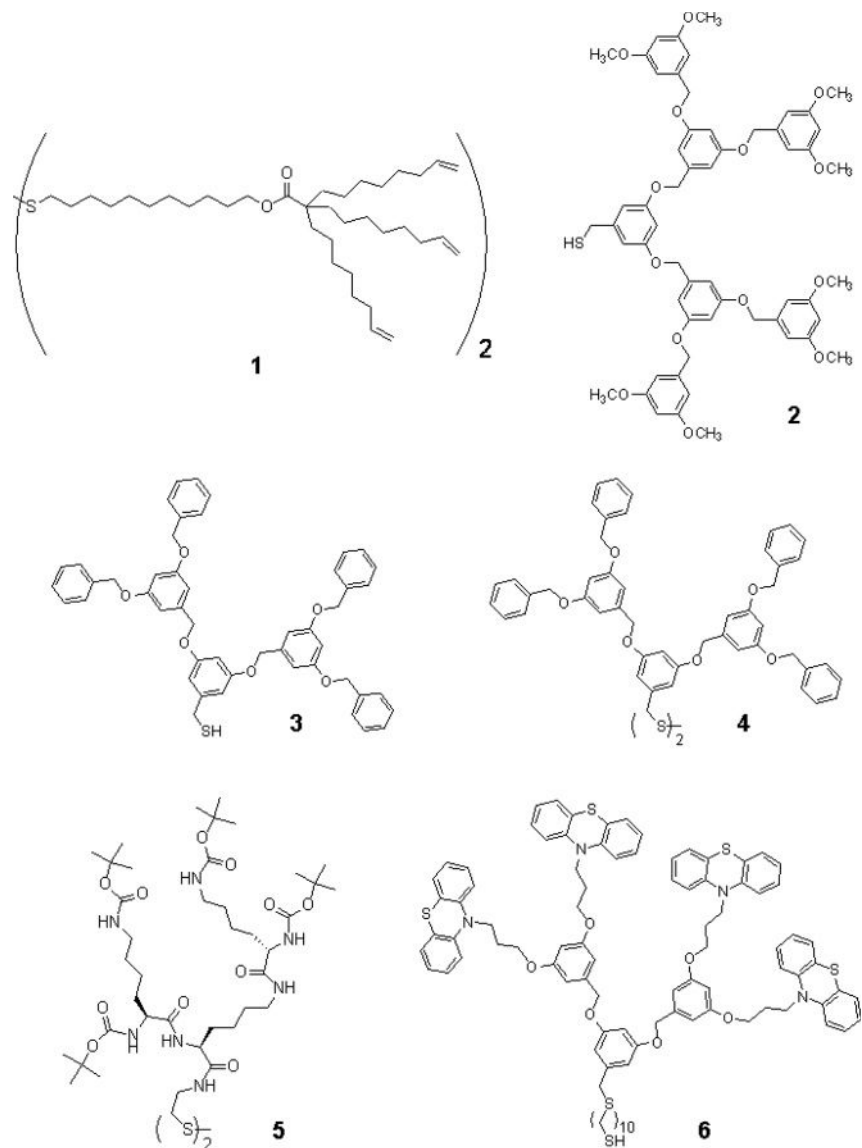


**Scheme 24.1** Synthesis and structure of nanoparticle-cored dendrimers (NCDs), where Gn represents a dendritic wedge of variable generation number. Reproduced with permission from Ref. [41]; © 2003, The American Chemical Society.

nanoparticles [39]. This approach afforded highly stable gold nanoparticles with average diameters of 2.4 to 3.1 nm. Generation-one [G-1], two [G-2], and three [G-3] dendron-stabilized gold nanoparticles were highly stable, both in solution and in the solid state. These NCDs remained unchanged after standing overnight at elevated temperatures (at 50 °C in solution, and at 160 °C in the solid state). The high stability of NCDs protected by dendrons with a thiol group was a clear improvement over that of dendrimer-encapsulated nanoparticles. The core size and size distribution of the nanoparticle-cored dendrimers, when examined with high-resolution transmission electron microscopy (HR-TEM), were not significantly affected by the use of different molar ratios of dendrons/ $HAuCl_4$  in this study [39].

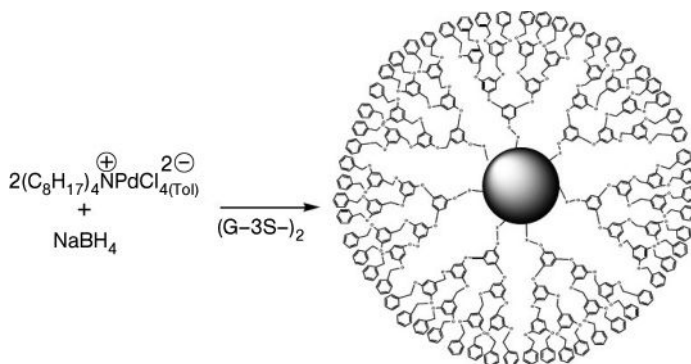
Torigoe *et al.* also used poly(oxyethylphenylene) dendrons (PPDs) (3; Figure 24.2) of generations 1–4 functionalized with a thiol group at the focal point as capping ligands for gold nanoparticle-cored dendrimers [40]. The average particle size was 1.5 and 1.4 nm for [G-1] and [G-2], respectively with a relatively small standard deviation. The particle size was increased for higher-generation dendrons (2.2 nm for [G-3] and 3.8 nm for [G-4]), with a much broader size distribution. The spontaneous formation of one-dimensional (1-D) arrays of [G-1] and [G-2] NCDs was observed over a larger area. This suggested that the dendron ligands had a strong tendency to crystallize due to an intermolecular  $\pi$ – $\pi$  stacking interaction of thiol-terminated PPDs, as in the case of the pyridine derivative system in which two-dimensional (2-D) superlattices have been observed [63]. The formation of 1-D arrays over a larger area would provide more elaborate nanoelectronic systems.

The systematic characterization of stable gold nanoparticle-cored dendrimers with different generations ([G-1] to [G-5]) prepared by the Schiffrin reaction using polyaryl ether dendritic disulfide as a capping reagent, was reported by Whitesell and Fox in 2003 (4; Figure 24.2) [41]. Results obtained with transmission electron microscopy (TEM) suggested that the nanoparticle core of NCDs exhibited a relatively high polydispersity. The average core sizes were increased from [G-1] NCDs to [G-4] NCDs, and then showed a decrease as the dendron wedge sizes increased to [G-5]. The structure and composition of NCDs were more carefully studied



**Figure 24.2** Dendron thiols and disulfides used for the synthesis of nanoparticle-cored dendrimers.

using ultraviolet (UV), Fourier transform infrared (FT-IR) and nuclear magnetic resonance (NMR) spectroscopies in this study. The surface plasmon bands (~520 nm) of these NCDs were similar to those for arenethiolate-protected clusters reported elsewhere [1, 3]. The IR spectra of NCDs and their dendritic disulfide precursors were almost identical. In the  $^1\text{H}$  NMR spectra, the peaks appeared very similar for dendrons and NCDs, except for broadened peaks in the bases. The

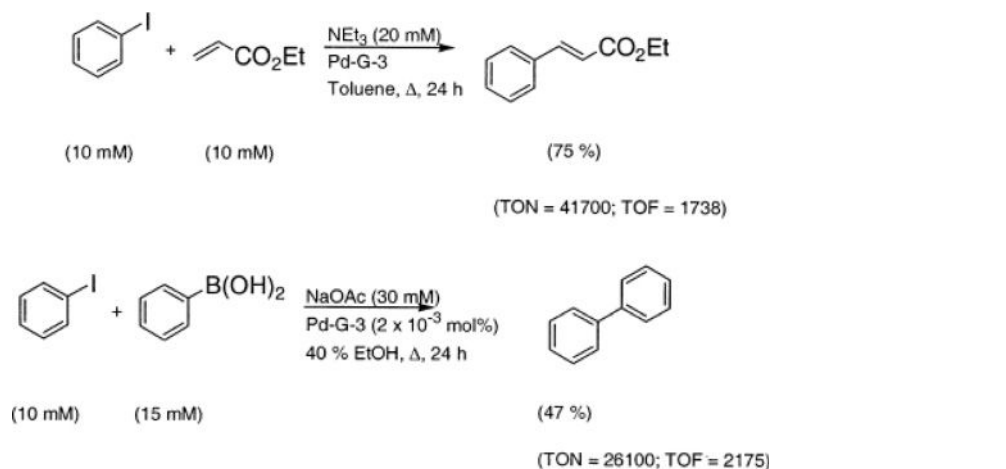


**Scheme 24.2** Synthesis of Pd-G-3 NCDs. Reproduced with permission from Ref. [42]; © 2003, The American Chemical Society.

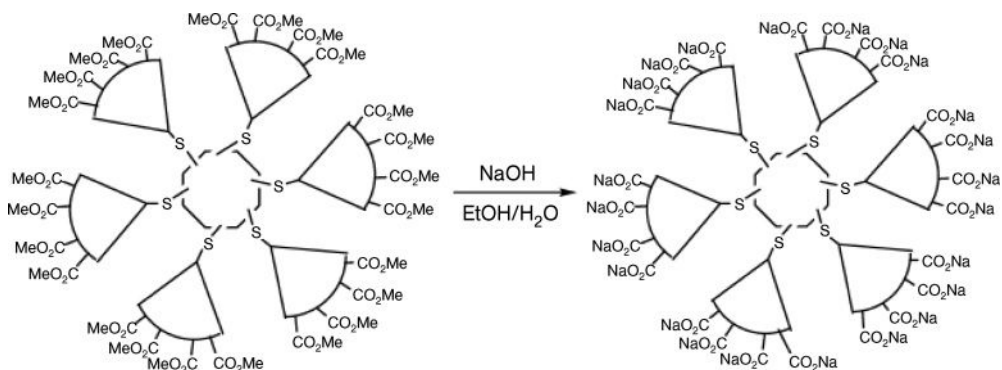
number of dendron units on a nanoparticle core, which was obtained via TEM and thermogravimetric analysis (TGA), decreased with the increased generation of the dendrons, with values falling from  $2.18 \text{ nm}^{-2}$  for [G-2] NCDs to  $0.27 \text{ nm}^{-2}$  for [G-5] NCDs. Therefore, for the higher-generation NCDs a large fraction of the surface area of the metal nanoparticle was not passivated and thus available for the catalytic reaction. Based on these characteristics, transition metal-based NCDs were recognized as being good catalysts for many organic reactions.

Whitesell and Fox prepared [G-3] Pd NCDs (as shown in Scheme 24.2) and investigated their catalytic properties [42]. A combination of data acquired using TEM and TGA showed that, for the Pd NCDs, more than 90% of the nanoparticle surface was unpassivated. If most of the unpassivated surface atoms were to be available for catalysis, and the required reagents could penetrate the dendritic exterior to reach the metal surface, then these NCDs might serve as excellent catalysts for many organic reactions. The Heck and Suzuki reactions (Scheme 24.3), both of which are normally carried out on Pd-phosphine catalysts, were tested on these Pd NCDs. The turnover number (TON; calculated as moles of product per mole catalyst) and turnover frequency (TOF; calculated as moles of product per mole catalyst per hour) for both the Heck and Suzuki reactions were very high. In addition, the absence of any side product other than the starting compound, products, and solvent for both reactions indicated the high efficiency of Pd NCDs as a new catalytic system.

Whitesell and Fox also reported the synthesis of NCDs stabilized by polyaryl ether dendrons with ester groups on the periphery, using the Schiffrin reaction [43]. The ester-terminated NCDs were converted to the corresponding carboxylate-functionalized NCDs by treatment with sodium hydroxide (Scheme 24.4). The sodium salts of carboxylate-terminated NCDs were soluble in water and exhibited micelle-like properties in solution; this was an important point because dendritic micelles can be used as catalysts in water and as drug-delivery agents. The micellar properties of NCDs were probed by the spectral shifts of dye molecules (Figure



**Scheme 24.3** Heck reaction (top) and Suzuki reaction (bottom) with Pd-G-3 NCDs. TON = turnover number; TOF = turnover frequency. Reproduced with permission from Ref. [42]; © 2003, The American Chemical Society.

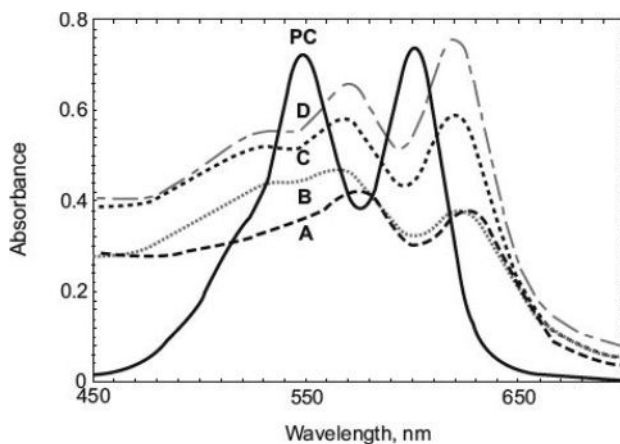


**Scheme 24.4** Basic hydrolysis of ester-terminated NCDs to produce unimolecular micelles. Reproduced with permission from Ref. [43]; © 2003, The American Chemical Society.

24.3). In aqueous solution, pinacyanol chloride (PC) showed absorption bands at 549 and 601 nm, but these were red-shifted to 564 and 610 nm, respectively, in NCD micelles. Such a result suggested that NCDs could act as micellar hosts and, potentially, also as water-soluble catalysts.

Chechik, Smith, and coworkers reported the synthesis of L-lysine based dendron-stabilized gold nanoparticles using the modified one-phase Schiffrin reaction (5; Figure 24.2) [44]. The size of the nanoparticle core was found to decrease with increasing dendron generation, a finding which contrasted with data reported for other NCD systems [39, 41, 45]. These differences suggested that the structure and

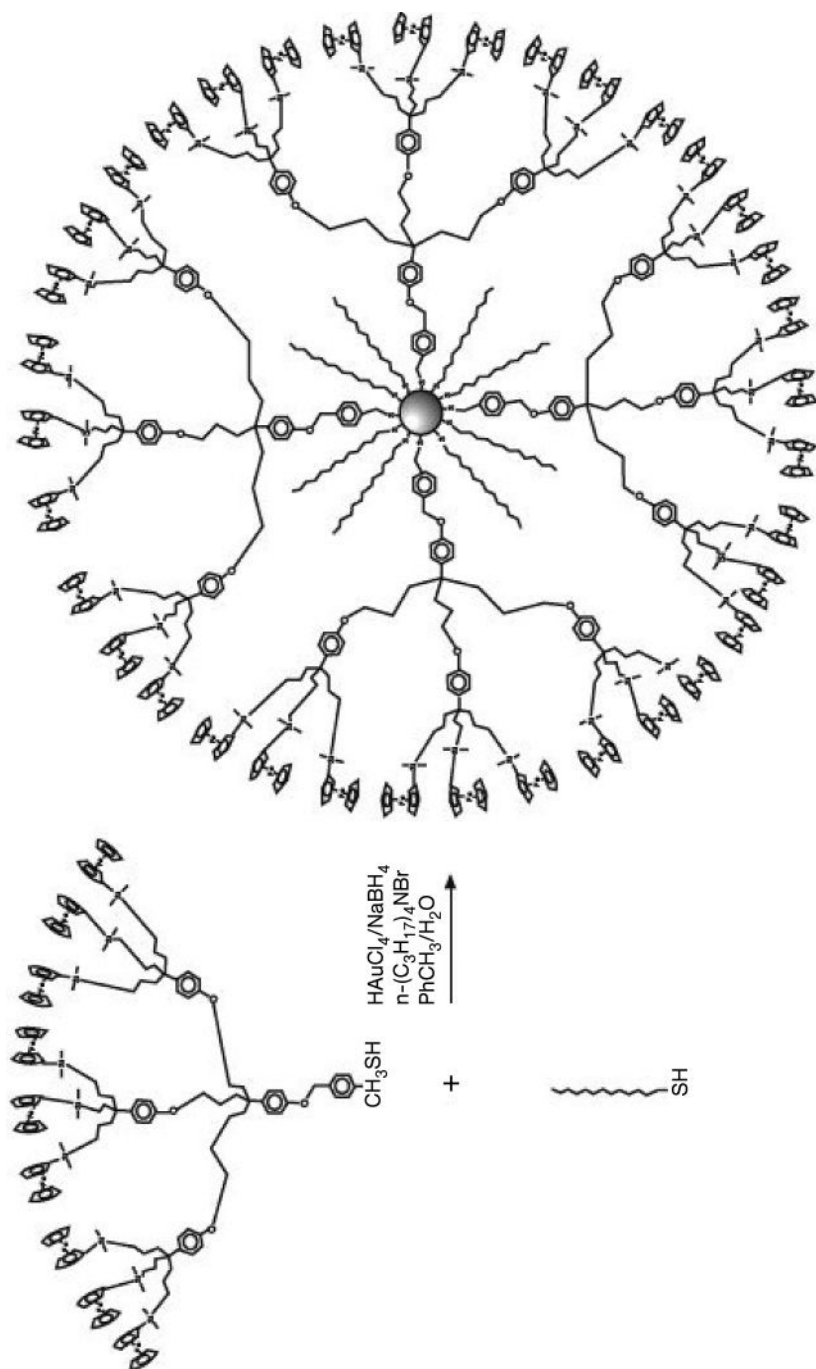




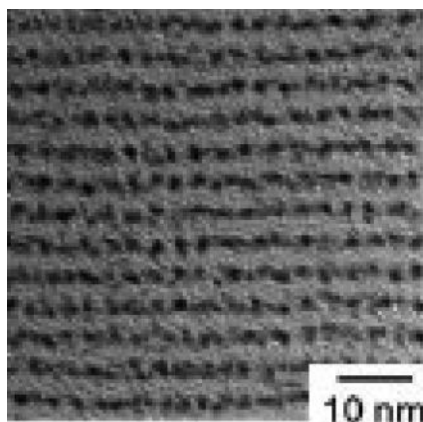
**Figure 24.3** Absorption spectra of pinacyanol chloride ( $1 \times 10^{-5}$  M) in water (PC) and in aqueous solutions of (a) Au-G1 ( $\text{CO}_2\text{Na}$ ), (b) Au-G2 ( $\text{CO}_2\text{Na}$ ), (c) Au-G3 ( $\text{CO}_2\text{Na}$ ), and (d) Au-G4 ( $\text{CO}_2\text{Na}$ ).  $[\text{Au-G}_n(\text{CO}_2\text{Na})]$  were  $\sim 0.1 \text{ mg ml}^{-1}$  water. Reproduced with permission from Ref. [43]; © 2003, The American Chemical Society.

functionality of the dendron ligands must play an important role in determining the characteristics of the gold core. Such a size relationship could be explained in terms of steric effects, as the much more bulky higher-generation dendritic system would be expected to pack more efficiently around a small core, thus favoring a smaller particle size. The thermal stability of the NCDs in solution was governed by the extent of branching in the surrounding dendron ligands. A different order of thermal ripening was observed at  $120^\circ\text{C}$ , which increased in size in the order  $[\text{G-1}] > [\text{G-2}] > [\text{G-3}]$ .

Astruc and colleagues synthesized redox-active NCDs using the Schiffrin reaction from a 1:1 mixture of dodecanethiol and nonaferrocenyl thiol dendrons (Scheme 24.5) [46, 47]. However, this approach resulted in NCDs without any open catalytic sites on the nanoparticle core. Smaller dodecanethiols could be coassembled on the nanoparticle surface, so that the integrity and solubility of NCDs was suitable for their applications in the electrochemical sensing of anions. The gold nanoparticle core was seen to be surrounded by  $\sim 360$  silylferrocenyl units, such that the general structure of these NCDs closely resembled that of large metal-lodendrimers. These redox-active NCDs were capable of selectively recognizing  $\text{H}_2\text{PO}_4^-$  anions and adenosine-5'-triphosphate ( $\text{ATP}^{2-}$ ) with a positive dendritic effect, even in the presence of other anions such as  $\text{Cl}^-$  and  $\text{HSO}_4^-$ . The titration of NCDs using anions resulted in a shift of the cyclic voltammetry (CV) wave to a less positive potential. The nonaferrocenyl thiol dendron-functionalized nanoparticles could be deposited on the Pt electrode by dipping it into the NCD solution. This modified electrode was quite robust and was capable of recognizing different anions. Moreover, the salt of these anions could be easily removed simply



**Scheme 24.5** Direct synthesis of NCDs containing the nonaferrocenyl thiol dendron. Reproduced with permission from Ref. [47]; © 2003, The American Chemical Society.

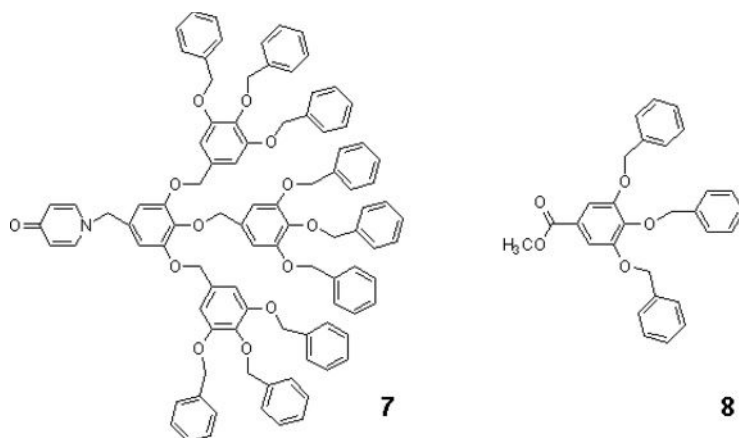


**Figure 24.4** Transmission electron microscopy image of one-dimensional arrays of phenothiazine-terminated NCDs. Reproduced with permission from Ref. [48]; © 2006, The Royal Society of Chemistry.

by dipping the electrode in  $\text{CH}_2\text{Cl}_2$ , the consequence being that the electrode could be re-used many times.

Phenothiazine-terminated NCDs were prepared by Fujihara and coworkers using the two-phase Schiffrin reaction (6; Figure 24.2) [48]. The gold nanoparticles with a higher-generation dendron bearing a long chain alkanethiol at the focal point had a smaller core size with a narrow size distribution. These NCDs underwent the spontaneous formation of 1-D arrays (Figure 24.4), and exhibited an interesting one-electron transfer behavior. The intermolecular  $\pi$ - $\pi$  stacking interaction of the thiol-terminated phenothiazine is believed to be the driving force for this self-organization. The 1-D assembly of redox-NCDs not only provides a good model to study the size-dependent electronic and optical properties of metal nanoparticles, but may also play an important future role in nanoelectronics.

Dendrons with another focal group that is capable of metal complexation were reported by Zheng *et al.* [45]. The  $\text{Oct}_4\text{N}^+\text{-AuCl}_4$  in toluene was reduced by  $\text{NaBH}_4$  in the presence of 4-pyridone-functionalized dendrons (7; Figure 24.5) as a capping reagent, and this resulted in stable, gold nanoparticle-cored dendrimers. There is no known example of monolayer formations of pyridone derivatives on bulk gold surfaces due to the chemical instability of such monolayers. Therefore, these results suggest that the high surface curvature of the gold nanoparticles can support the high-density packing of the capping ligands, which have only weak metal surface-binding properties. An examination using TEM highlighted the correlation between the particle size and the generation of dendrons, with higher-generation dendrons producing larger particles ([G-1], [G-2], [G-3] = 2.0, 3.3, 5.1 nm, respectively). However, the [G-3] NCDs were less stable than [G-1] and [G-2] NCDs, because the larger dendrons led to an increased open space between the ligands. The resultant weaker force between the dendrons and the particle caused a more rapid particle agglomeration of [G-3] NCDs.



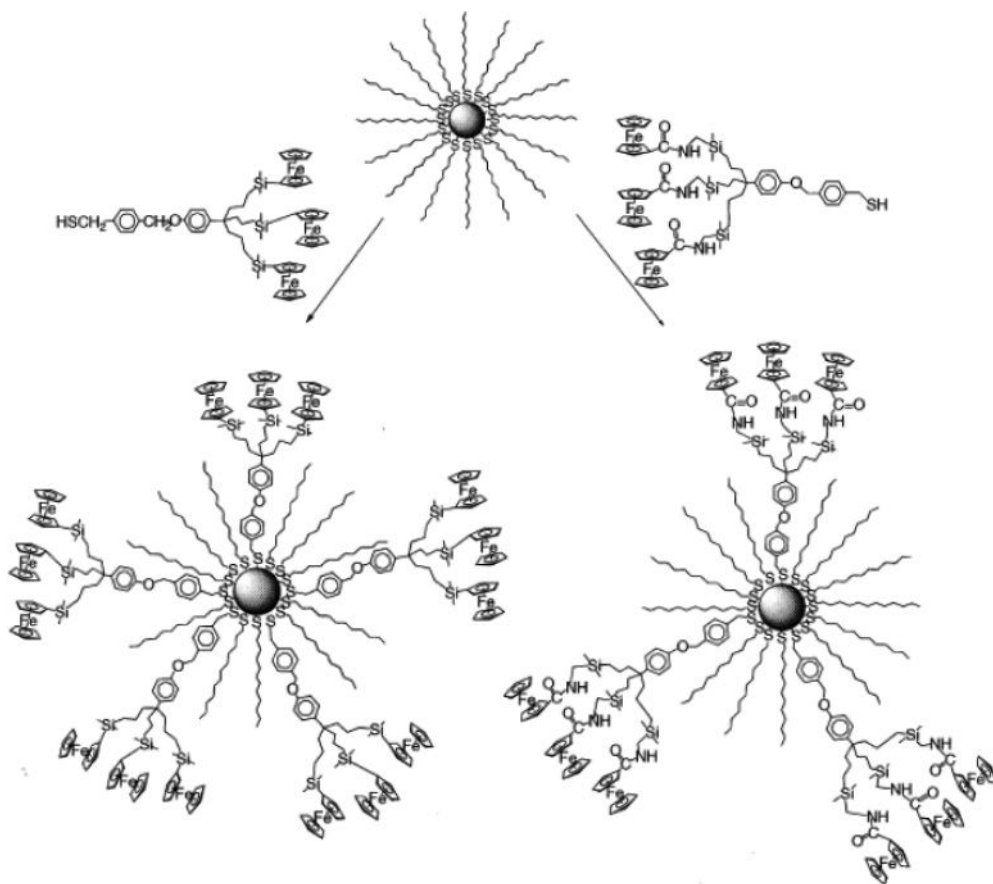
**Figure 24.5** Structure of dendrons with other functional groups used for the synthesis of nanoparticle-cored dendrimers.

Dendrons with an ester focal point were also used for the synthesis of polyaryl dendron-protected Pd nanoparticles (**8**; Figure 24.5) [49]. Briefly,  $\text{H}_2\text{PdCl}_4$  was phase-transferred into the organic phase using tetraoctylammonium bromide. The dendrons were then added to the reaction mixture before addition of  $\text{N}_2\text{H}_4$  as reducing agent. The resultant mixture was stirred under dry argon for an additional 24 h at room temperature. The Pd nanoparticle-cored dendrimers formed had mostly a spherical shape, and an average core size which ranged from ~10 to ~70 nm. The Pd core size was seen to increase with the decreasing molar ratio of dendrons to metal ions.

### 24.3

#### Synthesis of Nanoparticle-Cored Dendrimers by Ligand Exchange Reaction, and their Properties and Applications

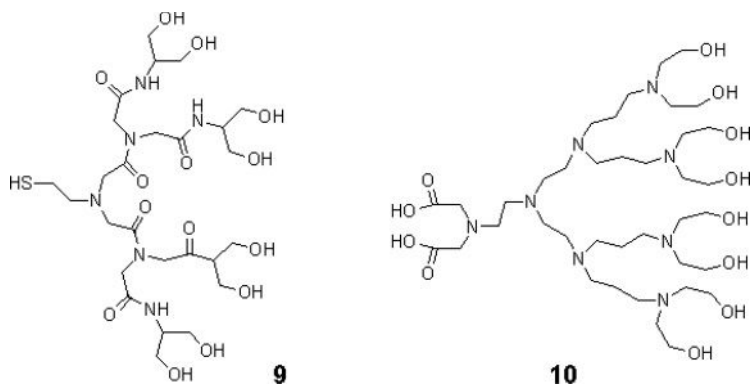
Nanoparticles with protecting monolayers composed of thiolate ligands can be functionalized by a partial ligand-replacement [1]. In this exchange reaction, the incoming ligands replace the thiolate ligands on nanoparticles by an associative reaction, while the displaced thiolate becomes a thiol. Ligand-exchange reactions of dodecanethiolate-protected gold nanoparticles with triferrocenyl thiol dendrons in dichloromethane were first reported by Astruc *et al.* (Scheme 24.6) [46, 47]. Although an excess of functional thiol dendrons was used, the percentages of dendron thiols introduced as ligands in dodecanethiolate-protected gold nanoparticles were less than 5% of the overall ligands. The limit of the ligand-exchange reaction was even greater with larger dendrons. Attempts to synthesize NCDs with nonaferrocenyl thiol dendrons resulted in the incorporation of very small amounts of dendrons (less than one per nanoparticle). As the rate of ligand-exchange



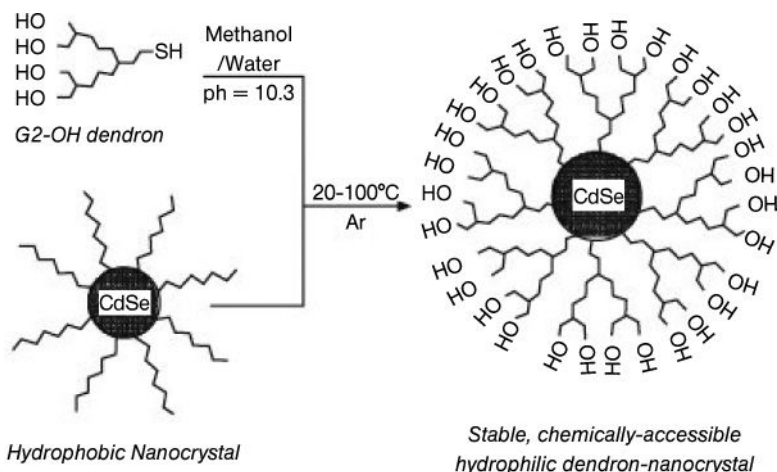
**Scheme 24.6** Synthesis of NCDs using the thiol-ligand exchange reaction. Reproduced with permission from Ref. [47]; © 2003, The American Chemical Society.

between thiols is dependent on the chain length and/or steric bulk of the initial monolayers on nanoparticles, the bulky or very small incoming ligands are difficult to replace the original ligands on the nanoparticle surface due to either kinetic (e.g., steric hindrance) or thermodynamic effects, respectively. Thus, the main short-coming of the ligand-exchange reaction, when using larger dendrons, was in fact quite consistent with previous results on ligand-place exchange reactions of alkanethiolate-protected nanoparticles [1, 3]. In contrast, the exchange between ligands having different functional groups was much more efficient.

Peng *et al.* synthesized hydrophilic NCDs by the ligand-exchange of citrate-capped gold nanoparticles using hydroxy-functionalized dendron thiols (**9**; Figure 24.6) [50]. The citrate reduction of  $\text{HAuCl}_4$  in water led to citrate-capped gold nanoparticles with core sizes that ranged from 10 to 150 nm [3]. Such nanoparticles

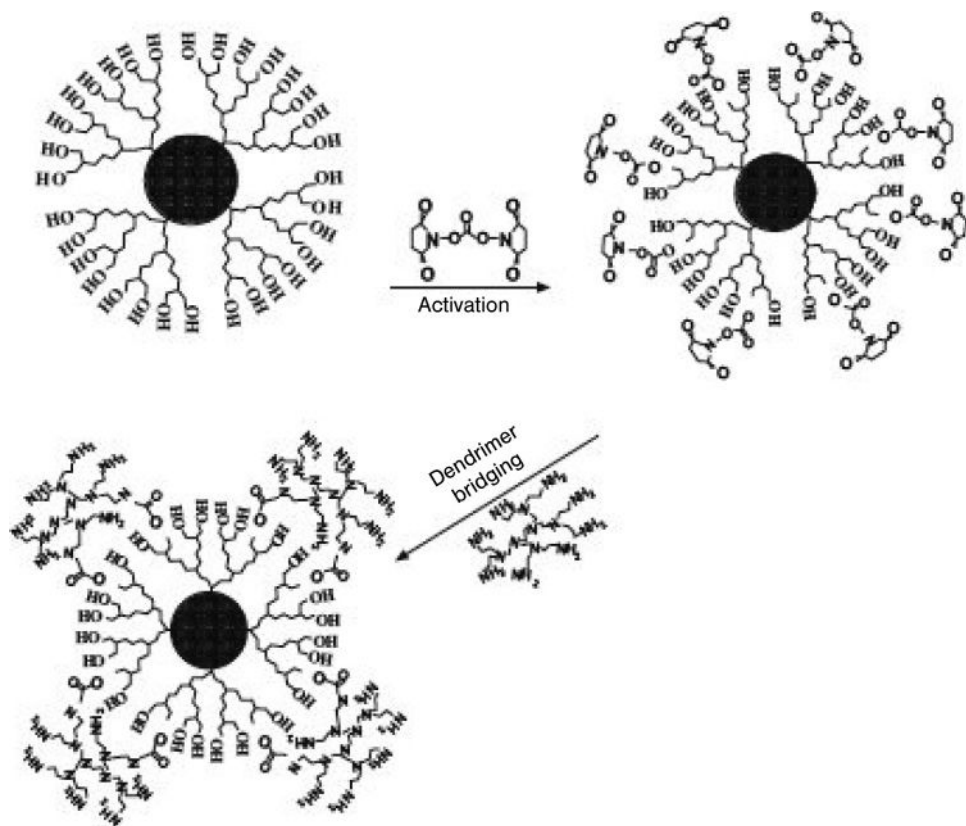


**Figure 24.6** Structure of hydroxy-functionalized dendrons used for the synthesis of nanoparticle-cored dendrimers.



**Scheme 24.7** Schematic process for converting hydrophobic semiconductor nanocrystals into hydrophilic and chemically processable NCDs. Reproduced with permission from Ref. [50]; © 2002, The American Chemical Society.

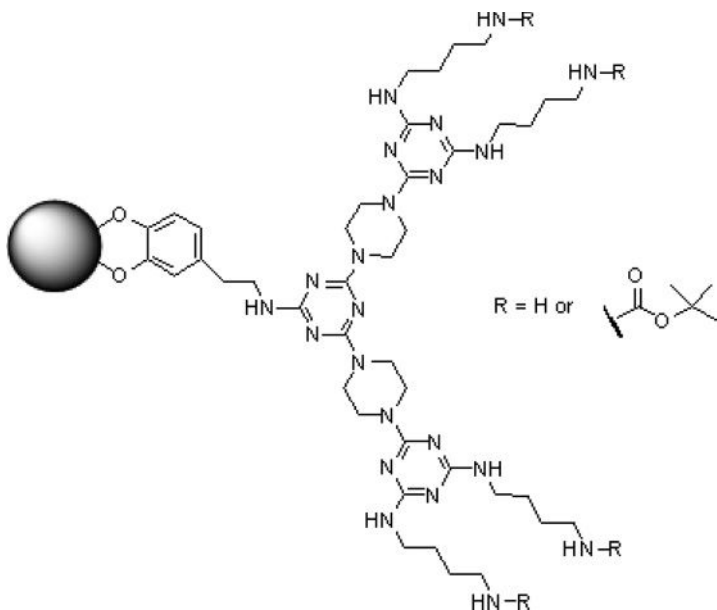
are typically useful when a rather loose shell of ligands is required around the gold core for ligand-exchange [64]. Peng also performed ligand-exchange reactions of trioctylphosphine oxide (TOPO)-capped CdSe nanoparticles with hydroxy-functionalized dendron thiols (Scheme 24.7) [50, 51]. Dendron thiols can rather easily replace the loosely bound TOPO groups, which have a weak binding property with CdSe nanoparticles. The chemistry related to CdSe NCDs can be applied for developing photoluminescence-based labeling reagents for biomedical applications. The photochemical, thermal, and chemical stability of both CdSe and Au NCDs was exceptionally good compared to that of the corresponding alkanethiolate-



**Scheme 24.8** Synthesis of amine-functionalized box nanoparticles. Reproduced with permission from Ref. [51]; © 2003, The American Chemical Society.

protected nanoparticles. The stability of CdSe NCDs could be further enhanced by a global crosslinking of the dendron ligands around a nanoparticle core [51]. Such crosslinking of alkene-terminated CdSe NCDs was achieved via ring-closing metathesis, and led to each nanoparticle being sealed in a dendron box. Another strategy—*dendrimer bridging*—was also reported by Peng for the simultaneous formation and functionalization of a biocompatible and bioaccessible dendron box with a semiconductor nanoparticle core [52] (Scheme 24.8). The dendrimer bridging involved an activation of the hydroxyl terminal groups of CdSe NCDs with a homobifunctional crosslinker, *N,N*-disuccinimidyl carbonate, followed by a crosslinking reaction with [G-2] polyamidoamine (PAMAM) dendrimers. The resulting amine box nanoparticles were very stable chemically, thermally, and photochemically. In addition, the amine groups on the surface of the box nanoparticles provided reactive sites for the conjugation of biological entities.





**Figure 24.7** Simanek (melamine)-type dendron-coated iron oxide nanoparticles.

Bioconjugation and biodetection using box nanoparticles were each successfully demonstrated with the avidin–biotin system [52].

Liu and Peng reported the synthesis of highly luminescent water-soluble CdSe/CdS core-shell NCDs by ligand-exchange reactions [53]. A dendron ligand with eight hydroxyl terminal groups and two carboxylate anchoring groups was found to replace alkylamine ligands on CdSe/CdS nanoparticles in toluene, and to convert the particles to water-soluble NCDs (**10**; Figure 24.6). The resultant water-soluble NCDs retained 60% of the photoluminescence value of the alkylamine-protected CdSe/CdS core-shell nanoparticles in toluene. Compared to the dendron thiol-protected NCDs, the photoluminescence value of these NCDs was much higher (about sixfold). Moreover, the UV-brightened photoluminescence could be retained for several months.

Dendron (with a shell of Simanek)-functionalized superparamagnetic (iron oxide) nanoparticles were prepared by Gao *et al.* using ligand-exchange methods (Figure 24.7) [54]. The resulting Fe<sub>2</sub>O<sub>3</sub> NCDs exhibited a switchable solubility in a variety of solvents, depending on the terminal groups of the dendritic shells, and were examined as soluble matrices for supporting magnetically recoverable homogeneous Pd catalysts for Suzuki crosscoupling reactions in organic solvents. For this, Gao immobilized a Pd-triphenyl phosphine moiety to the termini of dendron-protected iron oxide nanoparticles for catalysis. The Fe<sub>2</sub>O<sub>3</sub> NCDs were also investigated as potential contrast agents for magnetic resonance imaging (MRI) in aqueous media.

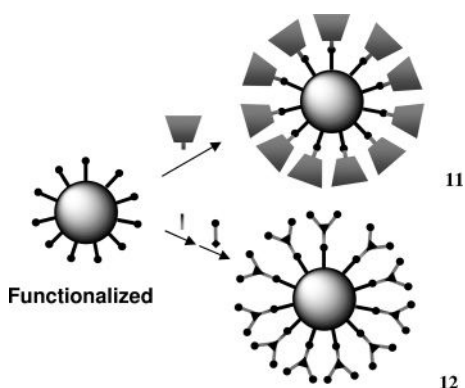


## 24.4

**Synthesis of Nanoparticle-Cored Dendrimers by Dendritic Functionalization, and their Properties and Applications**

The direct synthesis of NCDs was somewhat problematic because it required a large excess of dendronized thiols or disulfides, especially for the synthesis of NCDs with a small and monodispersed nanoparticle core [39–41]. The direct method also provided little control over the nanoparticle core dimension. NCDs with different core size were produced, when dendrons with different sizes (or generations) were used. In addition, the NCDs synthesized by the direct method often contained small amounts of trapped tetraoctylammonium bromide that could not be removed completely, even by repeated extraction with solvent. The indirect method using the ligand-exchange reaction was also somewhat limited considering a low exchange rate, especially for the synthesis of metal nanoparticle-cored dendrimers, as described in Section 24.3. A more convenient and cost-efficient synthetic methodology for the synthesis of NCDs with controlled particle core sizes, generations, and dendritic wedge density has been considered highly desirable for the basic understanding of structure–property relationships of these nanostructures.

The present authors' approach is based on a strategy in which the synthesis of monolayer-protected nanoparticles is followed by building the dendrimer architecture on the nanoparticle surface, using either the convergent or divergent approach (Scheme 24.9). A convergent synthesis of NCDs (**11**) can be accomplished by the coupling of reactive nanoparticles with functionalized dendrons. As the reaction only takes place at the functional groups on the surface of nanoparticles, this approach eliminates the need for a large excess of functionalized dendrons, and also maintains an intact core size for the synthesis of NCDs with different interior layers (generations) and dendritic wedge densities. The divergent approach



**Scheme 24.9** General reaction schemes for the synthesis of nanoparticle-cored dendrimers by (**11**) convergent and (**12**) divergent approaches.

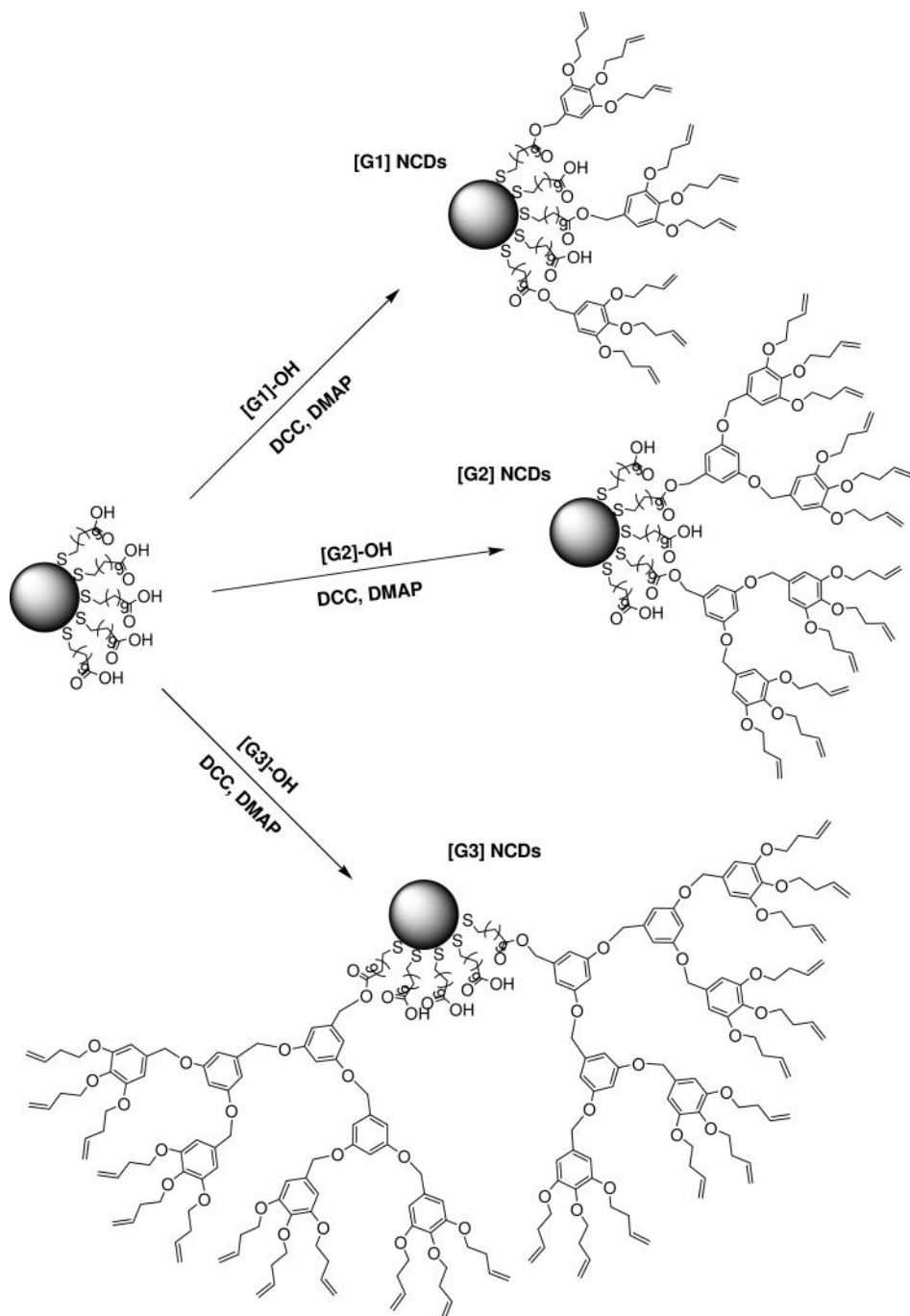
involves an iterative sequence of reaction steps, which lead to the addition of a branch (or branches) to the monolayer-protected cluster (MPC) framework (12).

#### 24.4.1

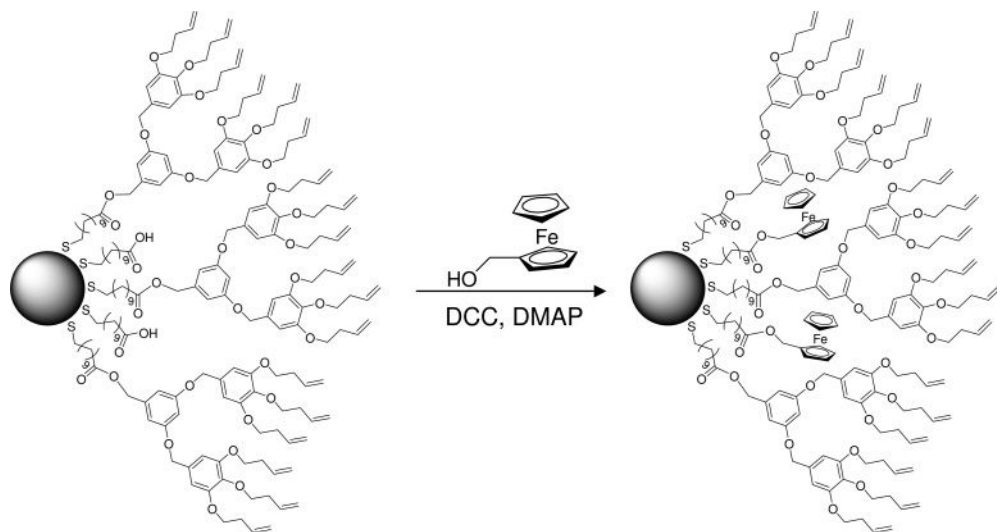
#### Nanoparticle-Cored Dendrimers by the Convergent Approach

The convergent synthesis of NCDs (Scheme 24.10) was accomplished by the ester coupling reaction of 11-mercaptoundecanoic acid-functionalized gold nanoparticles with hydroxy-functionalized “Fréchet-type” dendrons ([G-1]-OH, [G2]-OH, and [G-3]-OH) in the presence of ester coupling reagents (1,3-dicyclohexylcarbodiimide [DCC] and 4-dimethylaminopyridine [DMAP]) [56–58]. This synthetic approach provided an access to functionalized NCDs, which contain multiple reactive (COOH) functional groups inside dendritic wedges, even after the coupling of dendrons. These unreacted COOH groups resulted from the steric repulsion of dendrons during the synthesis of NCDs. The appearance of a new band at  $\sim 1735\text{ cm}^{-1}$  in FT-IR spectroscopy after the reaction indicated a formation of ester bonds due to a successful coupling reaction between 11-mercaptoundecanoic acids and [G-n]-OH. The  $^1\text{H}$  NMR results showed the same peak-broadening effect, as do monolayers of alkanethiolate-protected nanoparticles generated from alkanethiols. This peak-broadening effect also confirmed that [G-n]-OH was reacted with 11-mercaptoundecanoic acid-functionalized gold nanoparticles and bonded onto the surface of nanoparticles. The increased organic fractions were also observed by TGA.

The dendritic encapsulation of a functional molecule provides a site isolation, which mimics principles from biomaterials because dendritic scaffolds can provide the segregation of external and internal functionality. The incorporation of electroactive compounds onto the surfaces of nanoparticles in dendritic architecture should provide an opportunity to tune their electrochemical properties. The incorporation of redox-active groups in NCDs was achieved by a simple coupling reaction of ferrocene methanol with the remaining COOH groups inside dendritic wedges of NCDs ([G-2]<sub>conv</sub> NCDs), as shown in Scheme 24.11 [56, 58]. After an ester coupling reaction between [G-2]<sub>conv</sub> NCDs and ferrocene methanol, the IR spectrum of the NCD-encapsulated ferrocene (Fc@NCDs) showed an increase in the intensity of a band at  $1735\text{ cm}^{-1}$  (ester), in addition to the strong band around  $1450\text{ cm}^{-1}$  which indicated the presence of cyclopentadienyl groups. The NMR spectrum of Fc@NCDs showed additional broad bands at  $\sim 4.10\text{ ppm}$ , which was corresponding to the signals from cyclopentadienyl groups. Cyclic voltammetry was employed to compare electrochemical behaviors of ferrocene methanol and Fc@NCDs. Both, ferrocene methanol and Fc@NCDs exhibited well-defined voltammetric peaks corresponding to ferrocenyl groups. From the voltammogram of ferrocene methanol, it could be seen that there was a pair of voltammetric waves with a peak splitting of  $233\text{ mV}$  at  $100\text{ mV s}^{-1}$ , indicating a quasi-reversible electron-transfer processes. Interestingly, the peak splitting was found to be  $112\text{ mV}$  at  $100\text{ mV s}^{-1}$  for Fc@NCDs, which was only half of that for the ferrocene methanol; this was most likely due to either multielectron transfer or to the adsorption of particles onto the electrode.



**Scheme 24.10** Synthesis of  $[G-n]_{\text{conv}}$  NCDs by an ester coupling reaction.

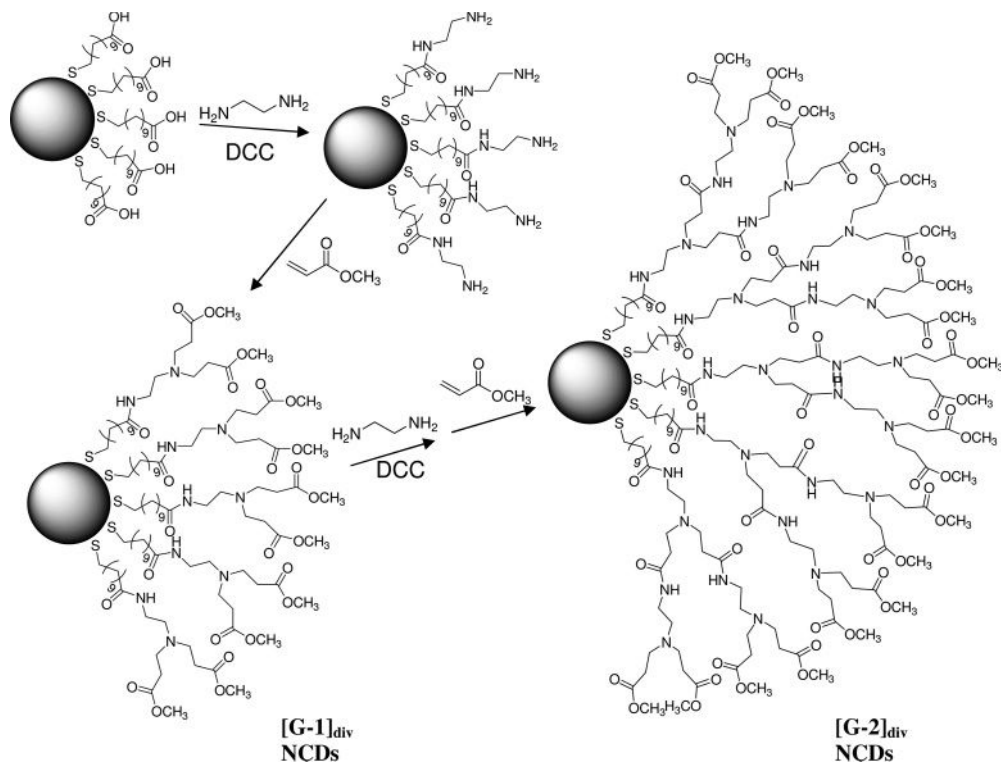


**Scheme 24.11** Incorporation of a ferrocene moiety in NCDs.

#### 24.4.2

##### Nanoparticle-Cored Dendrimers by the Divergent Approach

The NCDs (**6**) were grown in a stepwise manner from a central nanoparticle involving the amide coupling reaction with 1,2-diaminoethane ( $\text{NH}_2\text{CH}_2\text{CH}_2\text{NH}_2$ ) in the presence of DCC and the Michael addition reaction with methyl acrylate ( $\text{CH}_2\text{CH}=\text{CO}_2\text{CH}_3$ ) [11]. The repetition of the two reactions in the divergent approach was attempted for the synthesis of higher-generation NCDs (Scheme 24.12) [55, 57]. The IR spectra of 11-mercaptopundecanoic acid (MUA) MPCs showed a strong carbonyl ( $\text{C}=\text{O}$ ) stretching band at  $\sim 1710\text{ cm}^{-1}$ , the disappearance of which and the appearance of a new band at  $\sim 1650\text{ cm}^{-1}$ , after completion of the first reaction, indicated the formation of amide bonds. This was evidence of the successful coupling reaction between the  $\text{COOH}$  groups and 1,2-diaminoethane. The excess ( $10/1 = [\text{1,2-diaminoethane}]/[\text{COOH of MUA MPCs}]$ ) of 1,2-diaminoethane was used to prevent the intermolecular crosslinking of  $\text{COOH}$  groups on the clusters. These amine-functionalized MPCs ( $[\text{G-0.5}]_{\text{div}}$  NCDs) were reacted with excess methyl acrylate, such that the conjugate addition of the amine moiety occurred in “cascade” form (2:1 molar ratio of methyl acrylate to amine functional group) to generate  $[\text{G-1}]_{\text{div}}$  NCDs with terminal ester groups. The appearance of an ester band at  $\sim 1730\text{ cm}^{-1}$  was a clear indication of the successful addition reaction. The amide bands at  $\sim 1650\text{ cm}^{-1}$  indicated the presence of internal amide groups. Following the amide coupling reaction of  $[\text{G-1}]_{\text{div}}$  NCDs with 1,2-diaminoethane, the disappearance of the ester band at  $1730\text{ cm}^{-1}$  was clearly observed, indicating the



Scheme 24.12 Synthesis of  $[\text{G}-1]_{\text{div}}$  NCDs and  $[\text{G}-2]_{\text{div}}$  NCDs.

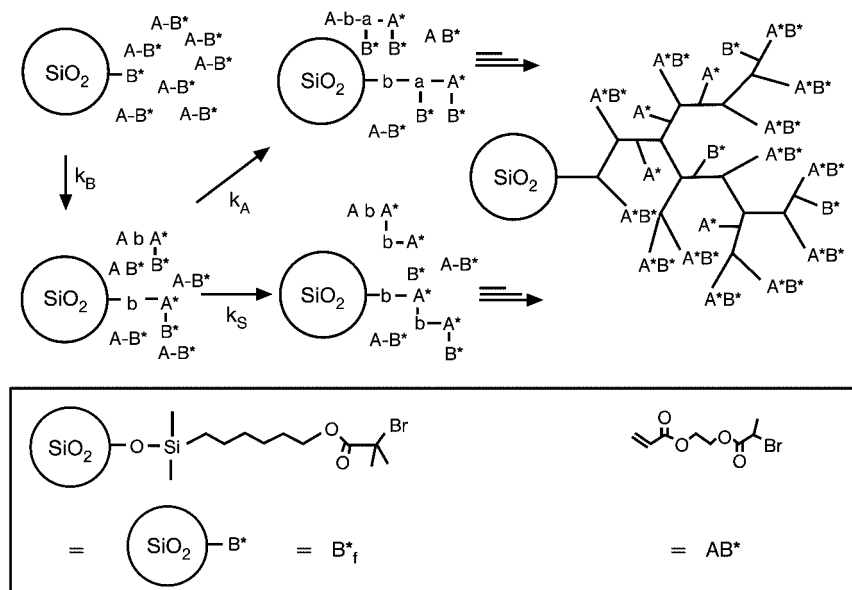
formation of amine-functionalized  $[\text{G}-1.5]_{\text{div}}$  NCDs. The reaction was again followed by the Michael addition reaction of  $[\text{G}-1.5]_{\text{div}}$  NCDs; this resulted in the reappearance of ester bands in the IR spectra of  $[\text{G}-2]_{\text{div}}$  NCDs. However, the relatively low intensity of this band suggested that the reaction had not been completed. Further iterative reactions of  $[\text{G}-2]_{\text{div}}$  NCDs were no longer effective and did not involve incorporation of methyl acrylate, as evidenced by an absence of ester bands in the IR spectra of  $[\text{G}-2]_{\text{div}}$  NCDs. A TEM image of the  $[\text{G}-1]$  NCDs showed the presence of slightly fused domains upon evaporation of the solvent. Additional TEM images of higher-generation NCDs prepared by the divergent approach showed that the multistep reactions of NCDs had resulted in the formation of large aggregates. Such aggregate formation prevented or minimized any further dendritic branching reactions for the higher-generation NCDs. This aggregation behavior of “Tomalia-type” NCDs during the iterative reactions probably resulted from the presence of strong inter-cluster hydrogen-bonding interactions.

## 24.5

## Synthesis of Nanoparticle-Cored Hyperbranched Polymers by Grafting on Nanoparticles

Further studies regarding the synthesis and characterization of NCDs are important for a fundamental understanding of nanostructures, and could also generate interesting technological applications in areas such as catalysis and sensing. However, one weakness of investigations involving NCDs is that multiple reaction steps and purification processes must be included in the synthesis of functionalized dendrons. As hyperbranched polymers may have properties and structures which are quite similar to those of dendrimers (even though the synthetic procedure requires only a direct, one-pot grafting reaction), the substitution of dendron-capping ligands with hyperbranched polymer ligands would definitely benefit in realizing some of the proposed technological applications in the real world, and the commercialization of these nanostructures. Some examples of grafting hyperbranched polymers on either silica or zinc oxide nanoparticle surfaces have recently been reported [59–61].

The first example of nanoparticle-cored hyperbranched polymers (NCHPs) was prepared by self-condensing vinyl polymerization via atom transfer radical polymerization (ATRP) from OH-functionalized silica nanoparticle surfaces (Scheme 24.13) [59]. For polymerization, the ATRP initiators were covalently attached to the



**Scheme 24.13** Synthesis of nanoparticle-cored hyperbranched polymers by self-condensing vinyl polymerization via atom transfer radical polymerization.

surface of silica nanoparticles. Well-defined hyperbranched polymer chains with multifunctional bromoester end groups were confirmed by gel permeation chromatography (GPC), GPC/viscosity, and NMR. These NCHPs can be designed to have a fairly open structure, allowing the functional materials (such as metal ions) to penetrate the ligands more easily than in conventional linear polymer layers. Therefore, a well-controlled synthesis for these NCHPs might lead to the creation of novel core-shell hybrids that are controllable on the nanoscopic scale, and have chemically sensitive interfaces.

A similar ATRP reaction involving a surface-initiated self-condensing vinyl polymerization of *p*-chloromethyl styrene was used for the preparation of NCHP from NH<sub>2</sub>-functionalized silica nanoparticles [60]. The surface Br atom of the NCHP could initiate another surface-initiated ATRP of methyl methacrylate and produce a dendritic-graft copolymer grafted onto silica nanoparticles. The same strategy was applied for the synthesis of ZnO nanoparticle-cored hyperbranched polymers with multifunctional chlorobenzyl functional end groups [61].

## 24.6 Conclusions and Outlook

Nanoparticle-cored dendrimers or hyperbranched polymers can be prepared using four different synthetic strategies: (i) a direct method, using a modified Schiffrin reaction; (ii) an indirect method, involving a ligand-place exchange reaction; (iii) the dendritic functionalization of nanoparticles; and (iv) the surface grafting of a hyperbranched polymer. The direct method is especially useful for the synthesis of nanoparticle-cored dendrimers with a large fraction of unpassivated metal nanoparticle surface, which is ideal for catalytic reaction. The indirect method, using a ligand-place exchange reaction, is ideal for the loading of functionalized dendrons on the surface of nanoparticle core. Dendritic functionalization is most versatile in terms of controlling the structure and composition of nanoparticle-cored dendrimers, while surface grafting of hyperbranched polymers might be the most convenient method as it can eliminate the multistep organic reactions involved in the synthesis of dendrons. Today, the synthetic procedures developed for nanoparticle-cored dendrimer preparation permits near-complete control over the critical molecular design parameters, such as core size, dendron wedge density, surface/interior chemistry, flexibility/rigidity, and solubility/micelle-like properties. The availability of effective methods to prepare distinct nanoparticle-cored dendrimers and hyperbranched polymers will allow investigators to exploit these materials in a variety of ways, including dendritic catalysis, energy storage, sensors, and drug delivery.

### Acknowledgment

These investigations were supported by a start-up grant and an SCAC grant from California State University, Long Beach, California, USA.

## References

- 1 Astruc, D. and Daniel, M.-C. (2004) *Chem. Rev.*, **104**, 293–346.
- 2 Pasquato, L., Pengo, P. and Scrimin, P. (2004) *J. Mater. Chem.*, **14**, 3481–3487.
- 3 Shon, Y.-S. (2004) Metal nanoparticles protected with monolayers: synthetic methods, in *Dekker Encyclopedia of Nanoscience and Nanotechnology*, Marcel Dekker, New York, pp. 1–11.
- 4 Zhu, M.-Q., Wang, L.-Q., Exarhos, G.J. and Li, A.D.Q. (2004) *J. Am. Chem. Soc.*, **126**, 2656–2657.
- 5 Lowe, A.B., Sumerlin, B.S., Donovan, M.S. and McCormick, C.L. (2002) *J. Am. Chem. Soc.*, **124**, 11562–11563.
- 6 Shimmin, R.G., Schoch, A.B. and Braun, P.V. (2004) *Langmuir*, **20**, 5613–5620.
- 7 Schneider, G. and Decher, G. (2004) *Nano Lett.*, **4**, 1833–1839.
- 8 Gittins, D.I. and Caruso, F. (2001) *J. Phys. Chem. B*, **105**, 6846–6852.
- 9 Caruso, F. and Möhwald, H. (1999) *J. Am. Chem. Soc.*, **121**, 6039–6046.
- 10 Werne, T. and Patten, T.E. (2001) *J. Am. Chem. Soc.*, **123**, 7497–7505.
- 11 Jordan, R., West, N., Ulman, A., Chou, Y.-M. and Nuyken, O. (2001) *Macromolecules*, **34**, 1606–1611.
- 12 Watson, K.J., Zhu, J., Nguyen, S.T. and Mirkin, C.A. (1999) *J. Am. Chem. Soc.*, **121**, 462–463.
- 13 Zeng, F. and Zimmerman, S.C. (1997) *Chem. Rev.*, **97**, 1681–1712.
- 14 Bosman, A.W., Janssen, H.M. and Meijer, E.W. (1999) *Chem. Rev.*, **99**, 1665–1688.
- 15 Fischer, M. and Vögtle, F. (1999) *Angew. Chem. Int. Ed. Engl.*, **38**, 884–905.
- 16 Tully, D.C. and Fréchet, J.M.J. (2001) *Chem. Commun.*, 1229–1239.
- 17 Fréchet, J.M.J. and Hecht, S. (2001) *Angew. Chem. Int. Ed. Engl.*, **40**, 74–91.
- 18 Adronov, A. and Fréchet, J.M.J. (2000) *Chem. Commun.*, 1701–1710.
- 19 Balzani, V., Ceroni, P., Gestermann, S., Kauffmann, C., Gorka, M. and Vögtle, F. (2000) *Chem. Commun.*, 853–854.
- 20 Amabilino, D.B., Ashton, P.R., Balzani, V., Brown, C.L., Credi, A., Fréchet, J.M.N., Leon, J.W., Raymo, F.M., Spencer, N., Stoddart, J.F. and Venturi, M. (1996) *J. Am. Chem. Soc.*, **118**, 12012–12020.
- 21 Stapert, H.R., Nishiyama, N., Jiang, D.L., Aida, T. and Kataoka, K. (2000) *Langmuir*, **16**, 8182–8188.
- 22 Herzog, A., Hirsch, A. and Vostrowsky, O. (2000) *Eur. J. Org. Chem.*, **2000**, 171–180.
- 23 Smith, D.K. (2006) *Chem. Commun.*, 34–44.
- 24 Crooks, R.M., Zhao, M., Sun, L., Chechik, V. and Yeung, L.K. (2001) *Acc. Chem. Res.*, **34**, 181–190.
- 25 Scott, R.W.J., Wilson, O.M. and Crooks, R.M. (2005) *J. Phys. Chem. B*, **109**, 692–704.
- 26 Ye, H., Scott, R.W.J. and Crooks, R.M. (2004) *Langmuir*, **20**, 2915–2920.
- 27 Floriano, P.N., Noble, C.O. IV, Scoonmaker, J.M., Poliakoff, E.D. and McCarley, R.L. (2001) *J. Am. Chem. Soc.*, **123**, 10545–10553.
- 28 Wilson, O.M., Scott, R.W.J., Garcia-Martinez, J.C. and Crooks, R.M. (2005) *J. Am. Chem. Soc.*, **127**, 1015–1024.
- 29 Lemon, B.I. and Crooks, R.M. (2000) *J. Am. Chem. Soc.*, **122**, 12886–12887.
- 30 Niu, Y., Yeung, L.K. and Crooks, R.M. (2001) *J. Am. Chem. Soc.*, **123**, 6840–6846.
- 31 Narayanan, R. and El-Sayed, M.A. (2004) *J. Phys. Chem. B*, **108**, 8572–8580.
- 32 Garcia-Martinez, J.C., Lezutekong, R. and Crooks, R.M. (2005) *J. Am. Chem. Soc.*, **127**, 5097–5103.
- 33 Rahim, E.H., Kamounah, F.S., Frederiksen, J. and Christensen, J.B. (2001) *Nano Lett.*, **1**, 499–501.
- 34 Wang, R. and Zheng, Z. (1999) *J. Am. Chem. Soc.*, **121**, 3549–3550.
- 35 Gorman, C.B. and Smith, J.C. (2000) *J. Am. Chem. Soc.*, **122**, 9342–9343.
- 36 Chasse, T.L., Sachdeva, R., Li, Q., Li, Z., Petrie, R.J. and Gorman, C.B. (2003) *J. Am. Chem. Soc.*, **125**, 8250–8254.
- 37 Ropartz, L., Morris, R.E., Foster, D.F. and Cole-Hamilton, D.J. (2001) *Chem. Commun.*, 361–362.
- 38 Wu, M., O'Neill, S.A., Brousseau, L.C., McConnell, W.P., Shultz, D.A., Linderman, R.J. and Feldheim, D.L. (2000) *Chem. Commun.*, 775–776.
- 39 Kim, M.-K., Jeon, Y.-M., Jeon, W.-S., Kim, H.-J., Hong, S.G., Park, C.G.



- and Kim, K. (2001) *Chem. Commun.*, 667–668.
- 40 Nakao, S., Torigoe, K. and Kon-No, K. (2002) *J. Phys. Chem. B*, **106**, 12097–12100.
- 41 Gopidas, K.R., Whitesell, J.K. and Fox, M.A. (2003) *J. Am. Chem. Soc.*, **125**, 6491–6502.
- 42 Gopidas, K.R., Whitesell, J.K. and Fox, M.A. (2003) *Nano Lett.*, **3**, 1757–1760.
- 43 Gopidas, K.R., Whitesell, J.K. and Fox, M.A. (2003) *J. Am. Chem. Soc.*, **125**, 14168–14180.
- 44 Love, C.S., Chechik, V., Smith, D.K. and Brennan, C. (2004) *J. Mater. Chem.*, **14**, 919–923.
- 45 Wang, R., Yang, J., Zheng, Z., Carducci, M.D., Jiao, J. and Seraphin, S. (2001) *Angew. Chem. Int. Ed. Engl.*, **40**, 549–552.
- 46 Astruc, D., Daniel, M.-C. and Ruiz, J. (2004) *Chem. Commun.*, 2637–2649.
- 47 Daniel, M.-C., Ruiz, J., Nlate, S., Blais, J.-C. and Astruc, D. (2003) *J. Am. Chem. Soc.*, **125**, 2617–2628.
- 48 Komine, Y., Ueda, I., Goto, T. and Fujihara, H. (2006) *Chem. Commun.*, 302–304.
- 49 Jiang, G., Wang, L., Chen, T., Yu, H. and Wang, J. (2004) *Nanotechnology*, **15**, 1716–1719.
- 50 Wang, Y.A., Li, J.J., Chen, H. and Peng, X. (2002) *J. Am. Chem. Soc.*, **124**, 2293–2298.
- 51 Guo, W., Li, J.J., Wang, Y.A. and Peng, X. (2003) *J. Am. Chem. Soc.*, **125**, 3901–3909.
- 52 Guo, W., Li, J.J., Wang, Y.A. and Peng, X. (2003) *Chem. Mater.*, **15**, 3125–3133.
- 53 Liu, Y., Kim, M., Wang, Y., Wang, Y.A. and Peng, X. (2006) *Langmuir*, **22**, 6341–6345.
- 54 Duanmu, C., Saha, I., Zheng, Y., Goodson, B.M. and Gao, Y. (2006) *Chem. Mater.*, **18**, 5973–5981.
- 55 Shon, Y.-S., Cutler, E.C., Chinn, L.E. and Garabato, B.D. (2004) *Polym. Mater. Sci. Eng.*, **91**, 1068.
- 56 Choi, D., Chinn, L.E. and Shon, Y.-S. (2005) *Polym. Mater. Sci. Eng.*, **93**, 739–740.
- 57 Cutler, E.C., Lundin, E., Garabato, B.D., Choi, D. and Shon, Y.-S. (2007) *Mater. Res. Bull.*, **42**, 1178–1185.
- 58 Shon, Y.-S. and Choi, D. (2006) *Chem. Lett*, **35**, 644–645.
- 59 Mori, H., Seng, D.C., Zhang, M. and Müller, A.H.E. (2002) *Langmuir*, **18**, 3682–3693.
- 60 Mu, B., Wang, T. and Liu, P. (2007) *Ind. Eng. Chem. Res.*, **46**, 3069–3072.
- 61 Liu, P. and Wang, T. (2007) *Poly. Eng. Sci.*, **47**, 1296–1301.
- 62 Beil, J.B., Lemcoff, N.G. and Zimmerman, S.C. (2004) *J. Am. Chem. Soc.*, **126**, 13576–13577.
- 63 Teranishi, T., Haga, M., Shiozawa, Y. and Miyake, M. (2000) *J. Am. Chem. Soc.*, **122**, 4237.
- 64 Watson, K.J., Zhu, J., Nguyen, S.B.T. and Mirkin, C.A. (1999) *J. Am. Chem. Soc.*, **121**, 462–463.

## 25

### Concepts in Self-Assembly

Jeremy J. Ramsden

#### 25.1

##### Introduction

This chapter begins with some basic definitions, followed by a review of the early studies conducted by Ashby and von Foerster. Some actual systems recognized as exemplars of self-assembly are then examined, after which self-assembly as a valid approach to nanofabrication is considered; in this context it is usually known as “bottom-up” manufacture. There follow some brief notes on useful ideas for understanding the self-assembly processes. The aim is not to discuss ordering related to phase transitions [1] (this will be detailed in a forthcoming article), or reaction-diffusion systems leading to striation and other regular patterns, nor phenomena such as spinodal dewetting [2] and other types of segregation (e.g., in block copolymers).

Assembly means gathering things together and arranging them (fitting them together) to produce an organized structure. A boy assembling a mechanism from “Meccano” captures the meaning, as does an assembly line where the workers and machines progressively build a complicated product such as a motor-car from simpler components; or when an editor assembles a newspaper from copy provided by journalists. In all of these examples the component parts are subject to constraints—otherwise they would not fit together—and their entropy  $S$  must necessarily decrease. Since the free energy  $\Delta G = \Delta H - T\Delta S$  must then necessarily increase, in general the process will not, by itself, happen spontaneously. On the contrary, a segregated arrangement will tend to become homogeneous. Hence, in order for self-assembly to become a reality, something else must be included. Typically, enthalpy  $H$  is lost through the formation of connections (bonds) between the parts, and provided that  $|\Delta H|$  exceeds  $|T\Delta S|$  there is at least the possibility that the process can occur spontaneously—which is presumably what is meant by “self-assembly.” The final result is generally considered to be in some sort of equilibrium.

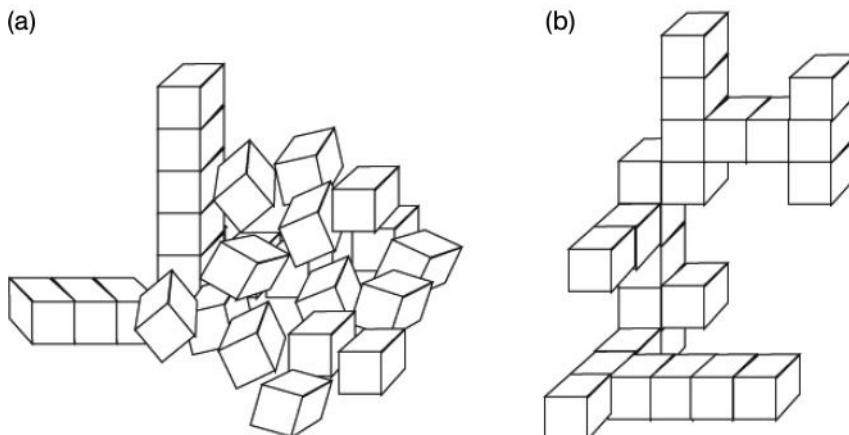
As *entropy* is always multiplied by the temperature  $T$  in order to compute the free energy, it should be noted that the relevant temperature is not necessarily what is measured with a thermometer. Rather, only the (typically small number

of) relevant degrees of freedom should be taken into account; the temperature is the mean energy per degree of freedom.

If slightly sticky granules are thrown into a rotating drum, or stirred in a mixing bowl, they will all eventually clump together to form a “random” structure (e.g., Figure 25.1a), but one which is evidently less random than the initial collection of freely flowing granules. An alternative example might be the dry ingredients of concrete (sand and cement) when thrown into a “cement mixer,” to which a small amount of water is added. Indeed the entropy is lowered, but each time the experiment is repeated the result will be different in detail. Thus, if the system were really ergodic, and if there were sufficient time to make all the repetitions, the ergodicity would only be broken because of insufficient time.

The goal of an ideal self-assembly process is for the same structure to be formed each time the constituent particles are mixed together (Figure 25.1b), as was imagined by von Foerster [3]. Of course, energy must be put into the system; in the “purest” form of self-assembly, the energy is thermal (random), but it could also be provided by an external field (e.g., electric or magnetic).

If we are satisfied by the constituent particles being merely joined together in a statistically uniform fashion and, moreover, the process happens spontaneously, then it is more appropriate to speak of “self-joining” or “self-connecting.” The mixing of concrete referred to above is, at least at first sight, an example of such a self-connecting process; more generally, one can refer to “gelation.” On approaching the phenomenon from a practical viewpoint, it is clear that gelation is almost always triggered by a change of external conditions imposed upon the system, such as a change of temperature, or dehydration, and the spontaneity implied by the prefix “self-” is absent. The only action that can be imposed upon the system without violating the meaning of “self-” is that of bringing the constituent particles



**Figure 25.1** (a) The result of mixing isotropically sticky cubelets; (b) Putative result of mixing selectively sticky cubelets.

together. Note that even here we diverge from the everyday meaning of the term “assembly,” which includes the gathering together of people, either spontaneously as when a group of people wish to protest against some new measure introduced by an authoritarian government, or by decree as in the case of the event with which the day is begun in many British schools.

If the process in which we are interested is deemed to begin at the instant the constituent particles are brought together, then we can place the mixing of concrete into the category of self-joining, because we could (although it is not usually done in this way) bring the wetted particles of sand and cement together, whereupon they would indeed spontaneously join together to form a mass. The meaning of self-joining (of which self-connecting is a synonym) is then the property possessed by certain particles of spontaneously linking together with their neighbors when they are brought to within a certain separation. One can also imagine there being kinetic barriers to joining, which can be overcome given enough time. Note that the particles each need more than one valency (unit of combining capacity), otherwise dimers would be formed and the process would then stop. A good example is when steam condenses to form water. We can suppose that the steam is first supercooled, which brings the constituent particles ( $\text{H}_2\text{O}$  molecules) together; the transition to liquid water is actually a first-order phase transition that requires an initial nucleus of water to be formed spontaneously. “Gelation” then occurs by the formation of weak hydrogen bonds (a maximum of four per molecule) throughout the system.

Strictly speaking, it is not necessary for all the constituent particles to be brought together instantaneously, as implied above. Once the particles are primed to be able to connect themselves to their neighbors, they can be brought together one by one. This is the model of diffusion-limited aggregation (DLA) [4]. In Nature, this is how biopolymers are formed—the monomers (e.g., nucleic acids or amino acids) are joined sequentially by strong covalent bonds to form a gradually elongating linear chain. The actual self-assembly into a compact three-dimensional (3-D) structure involves additional weak hydrogen bonds between neighbors that may be distant according to their positions along the linear chain (see Section 25.3.7); some of the weak bonds formed early are broken before the final structure is reached.

In the chemical literature, “self-assembly” is often used as a synonym of self-organization. A recapitulation of the examples already discussed shows, however, that the two terms cannot really be considered synonymous. The diffusion-limited aggregate is undoubtedly assembled, but can scarcely be considered to be organized, not least because every repetition of the experiment will lead to a result that is different in detail, and only the same when considered statistically. “Organized” is an antonym of “random”; therefore, the entropy of a random arrangement is high while that of an organized arrangement is low. It follows that inverse entropy may be taken as a measure of the degree of organization, and this notion will be further refined in the following section.

The diffusion-limited aggregate differs from the heap of sand only insofar as the constituent particles are connected to each other. An example of organization

is shown in Figure 25.1b. The impossibility of self-organization is proved by Ashby, as will be described in Section 25.2.2.

Before discussing self-organization, we must first discuss organization, of which self-organization is a part. If the elements in a collection (here we shall not say “system,” because that already implies a degree of organization) are organized to some degree, that implies they are in some way connected to each other, which can be considered as a kind of communication, and are hence subject to certain constraints. In other words, if the state of element B is dependent on the state of A to some extent, then we can say that B’s state is conditional on that of A. Likewise, the relationship between A and B may be conditional on the state of C. Whenever there is conditionality, there is *constraint*: B is not as free to adopt states as it would be in a totally unorganized system [5].

## 25.2 Theoretical Approaches to Self-Organization

### 25.2.1 Thermodynamics of Self-Organization

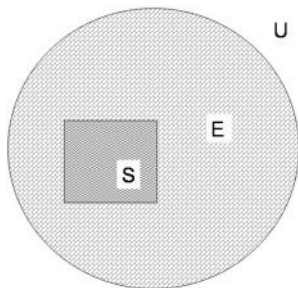
Consider a universe  $U$  comprising a system  $S$  and its environment  $E$ ; that is,  $U = S \cup E$  (Figure 25.2). Self-organization (of  $S$ ) implies that its entropy spontaneously diminishes; that is:

$$\delta S_S / \delta t < 0. \quad (25.1)$$

Accepting the Second Law of Thermodynamics, such a spontaneous change can only occur if, concomitantly,

$$\delta S_E / \delta t > 0, \quad (25.2)$$

with some kind of coupling to ensure that the overall change of entropy is greater than or equal to zero. If all processes were reversible, the changes could exactly



**Figure 25.2** Universe  $U$  comprising system  $S$  and its environment  $E$ .

balance each other, but since (inevitably, we may suppose) some of the processes involved will be irreversible, overall

$$\delta S_U / \delta t > 0. \quad (25.3)$$

Therefore, although the system itself has become more organized, overall it has generated more disorganization than the organization created, and it is more accurate to call it a *self-disorganizing system* [3]. Hence, the “system” must properly be expanded to include its environment: it is evidently intimately connected with it, since without it there could be no organization. Despite its true nature as a self-disorganizing system having been revealed, nevertheless we can still speak of a self-organizing *part*  $S$  of the overall system that consumes order (and presumably energy) from its environment. It follows that this environment must necessarily have structure itself, otherwise there would be nothing to be usefully assimilated by the self-organizing part.

The link between entropy (i.e., its inverse) and organization can be made explicit with the help of relative entropy  $R$  (called *redundancy* by Shannon); this is defined by

$$R = 1 - S/S_{\max}, \quad (25.4)$$

where  $S_{\max}$  is the maximum possible entropy. With this new quantity  $R$ , self-organization implies that  $\delta R / \delta t > 0$ . Differentiating Equation 25.4, we obtain

$$\frac{dR}{dt} = \frac{S(dS_{\max}/dt) - S_{\max}(dS/dt)}{S_{\max}^2}, \quad (25.5)$$

our criterion for self-organization (that  $R$  must spontaneously increase) is plainly

$$S \frac{dS_{\max}}{dt} > S_{\max} \frac{dS}{dt}. \quad (25.6)$$

The implications of this inequality can be seen by considering two special cases [3]:

1. The maximum possible entropy  $S_{\max}$  is constant; therefore  $dS_{\max}/dt = 0$  and  $dS/dt < 0$ . Now, the entropy  $S$  depends on the probability distribution of the constituent parts (at least, those that are to be found in certain distinguishable states); this distribution can be changed by rearranging the parts, which von Foerster supposed could be accomplished by an “internal demon” (see Ref. [6] for an updated description of James Clerk Maxwell’s original invention)
2. The entropy  $S$  is constant; therefore  $dS/dt = 0$  and the condition that  $dS_{\max}/dt > 0$  must hold; that is, the maximum possible disorder must increase. This could be accomplished, for example, by increasing the number of elements, but care must be taken to ensure that  $S$  then indeed remains constant, which

probably needs an “external” demon. Looking again at inequality (Equation 25.6), we see how the labor is divided among the demons:  $dS/dt$  represents the internal demon’s efforts, and  $S$  is the result;  $dS_{\max}/dt$  represents the external demon’s efforts, and  $S_{\max}$  is the result. There is therefore an advantage (in the sense that labor may be spared) in cooperating. For example, if the internal demon has worked hard in the past, the external demon can get away with putting in a bit less effort in the present. Yet, one should not underestimate the burden placed on the demons—particularly the external one—which must evidently possess an almost divine omnipotence.

### 25.2.2

#### The “Goodness” of the Organization

Examining again Figure 25.1, it can be asserted that both putative results of mixing slightly sticky cubelets together are organized, although most people would not hesitate to call the structure in (b) better organized than that in (a). Evidently, there is some meaning in the notion of “good organization,” even though it seems difficult to formulate an unambiguous definition. Can a system spontaneously (automatically) change from a bad to a good organization? This would be a reasonable interpretation of “self-organization,” but has been proved to be formally impossible [5]. Consider a device that can be in any one of three states, A, B or C, and the device’s operation is represented by some transformation, for example:

$$\begin{array}{ccc} \downarrow & A & B & C \\ & B & C & A \end{array}$$

Now suppose that we can provide an input  $f$  to the device, and that the output is determined by the value of  $f$ , for example:

$$\begin{array}{c|ccc} \downarrow & A & B & C \\ \hline f_A & B & C & A \\ f_B & A & A & A \\ f_C & A & B & C \end{array}$$

Spontaneous (automatic) operation means that the device is able to autonomously select its input. The different possible input values are here represented by a subscript indicating the state of the device on which the input now depends. However, this places severe constraints on the actual operation, because  $f_A(B)$  (for example) is impossible; only  $f_A(A)$ ,  $f_B(B)$  and  $f_C(C)$  are possible, hence the operation necessarily reduces to the simple transform, lacking any autonomy:

$$\begin{array}{ccc} \downarrow & A & B & C \\ & B & A & C \end{array}$$

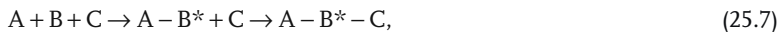
Any change in  $f$  must therefore come from an external agent.

## 25.2.3

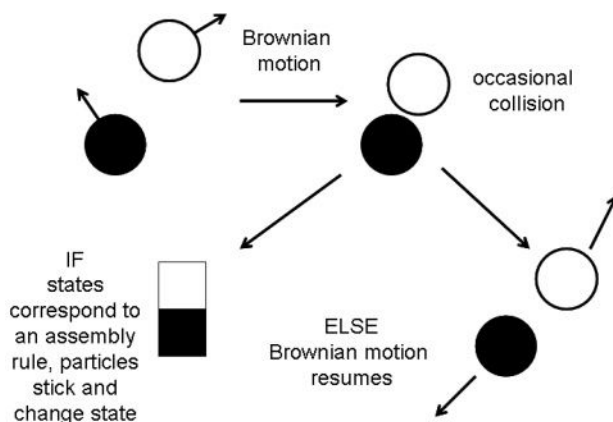
**Programmable Self-Assembly**

The results summarized in the two preceding subsections might well engender a certain pessimism regarding the ultimate possibility of realizing true self-assembly. Yet in biology, numerous examples are known (see also Section 25.3.5): the final stages of assembly of bacteriophage viruses [7], of ribosomes [8], and of microtubules [9], which occur not only *in vivo*, but which can also be demonstrated *in vitro* by simply mixing the components together in a test-tube. As apparent examples of what might be called “passive” self-assembly, in which objects possessing certain asymmetric arrangements of surface affinities are randomly mixed and expected to produce ordered structures [3], they seem to contradict the predictions of Sections 25.2.1 and 25.2.2.

It has long been known that biomolecules are constructions [10]; that is, they have a small number of macroscopic (relative to atomic vibrations) degrees of freedom, and can exist in a small number ( $\geq 2$ ) of stable conformations [11]. Without these properties, the actions of enzymes, active carriers such as hemoglobin, and the motors that power muscle, for example, are not understandable. Switching from one conformation to another is typically triggered by the binding or dissociation of a small molecule; for example, the “substrate” of an enzyme, or adenosine triphosphate (ATP) [12]. The initial collision of two particles is followed by a conformational change in one or both of them; for example:



where the asterisk denotes a changed conformation induced by binding to A; C has no affinity for B, but binds to  $B^*$  [7]. This process is illustrated in Figure 25.3, and is called “programmable self-assembly.” It has recently been modeled by *graph grammar*, which can be thought of as a set of rules encapsulating the outcomes of



**Figure 25.3** Illustration of programmable self-assembly, with a primitive local rule.



interactions between the particles [13, 14] (cf. stigmergic assembly; Section 25.3.5). The concept of graph grammar has brought about a significant advance in the formalization of programmable self-assembly, including the specification of minimal properties that must be possessed by a self-assembling system (e.g., the result implying that no binary grammar can generate a unique stable assembly [15]).

### 25.3

#### Examples of Self-Assembly

##### 25.3.1

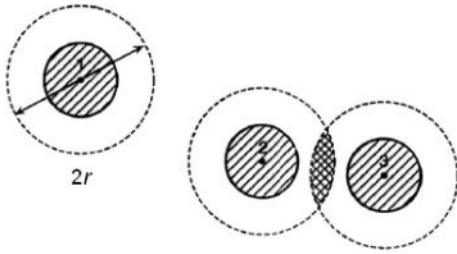
#### The Addition of Particles to the Solid/Liquid Interface

A chemically and morphologically unstructured surface of the solid substratum is prepared and brought into contact with a fluid medium. Self-assembly is initiated by replacing the pure fluid by a suspension of particles, the buoyancy of which in the fluid is such that they move purely by diffusion (Brownian motion) and are not influenced by gravity. Occasionally, those particles in the vicinity of the interface will strike it; the materials of substratum (1), fluid medium (2) and particle (3) are chosen such that the interfacial free energy  $\Delta G_{123}^{\parallel}$  is negative.<sup>1)</sup> In some cases  $\Delta G_{123}^{\parallel}$  is positive, but  $\Delta G_{13}^{\parallel}$  (i.e., when all the intervening fluid is eliminated) is negative. This signifies that there is an energy barrier hindering adsorption of the particle to the solid substratum. The rate of arrival of the particles at the substratum is proportional to the product of particle concentration  $c_i$  in the suspending medium and the diffusion coefficient  $D$  of a particle, the constant of proportionality depending on the hydrodynamic régime; this rate will be reduced by a factor  $1/\int_{\ell_0}^{\infty} [\exp(\Delta G_{123}(z)/k_B T) - 1] dz$  in the presence of an energy barrier; the reduction factor could easily be a hundred- or a thousand-fold.

Once a particle of radius  $r$  adheres to the substratum, evidently the closest the center of a second particle can be placed to the first one without overlapping it is at a distance  $2r$  from the center of the first; in effect, the first particle creates an *exclusion zone* around itself (Figure 25.4). If the particles interact with each other apart from via hard body (Born) repulsion, then the effective radius must be increased to the distance at which the particle–particle interaction energy  $\Delta G_{323}(z)$  equals the thermal energy  $k_B T$  [17]. A corollary of the existence of exclusion zones

1) Please refer to Ref. [16] for details of the calculation of  $\Delta G_{123}^{\parallel}$ . The subscript  $\parallel$  refers to the interfacial free energy between infinite parallel surfaces of materials 1 and 3 separated by the closest distance of approach  $\ell_0$ , when Born repulsion sets in (it is considered to be about 0.16 nm) and medium 2. The magnitude of the interfacial free

energy between an infinite planar surface of 1 and a sphere of 3 separated by an arbitrary distance  $z$  can be calculated from  $\Delta G_{123}^{\parallel}$  using the Derjaguin approximation [16]; for many purposes this might not even be necessary, especially if only the sign of the interfacial interaction is really needed.



**Figure 25.4** Diagram to illustrate the concept of exclusion zone, with twice the radius of the actual particle. The projected area of a spherical particle is hatched; the area enclosed by the dashed circles represents the exclusion zone, with twice the radius of the actual particle. The cross-hatched area marks the overlap of the exclusion zones of particles 2 and 3.

is that the interface will be jammed (i.e., unable to accept a further particle) at a surface coverage of substantially less than 100%. The actual value of the jamming limit depends on the shape of the particle; for spheres, it is about 54% of the complete surface coverage [18].

This process is known as random sequential addition (RSA). Although a random dispersion of particles in three dimensions is thereby reduced to a two-dimensional (2-D) layer, the positions of the particles remain random: the radial distribution function is totally unstructured [19]. Even if the particles can move laterally, allowing the interface to equilibrate in a certain sense, it is still jammed at a surface coverage of well below 100%. If, however, the particles can adhere to each other on the interface, the possibility for organizing arises. This has been very clearly demonstrated when lateral mobility was expressly conferred on the particles by covering the surface with a liquid-crystalline lipid bilayer and anchoring the particles (large spherical proteins) in the bilayer through a hydrophobic “tail” [20]. The particles structure themselves to form a 2-D ordered array. When such an affinity exists between the particles trapped at the interface, the exclusion zones are annihilated. From this fact alone (which can be very easily deduced from the kinetics of addition [20]), one cannot distinguish between random aggregation forming a diffusion-limited aggregate [4] (cf. reaction-limited aggregation [21]) and 2-D crystallization; these can generally be distinguished, however, by the fact that the crystal unit cell size is bigger than the projected area of the particle.<sup>2)</sup> The process of 2-D crystallization has two characteristic time scales, namely the interval  $\tau_a$  between the addition of successive particles to the interface

$$\tau_a = 1/[aF\phi(\theta)] \quad (25.8)$$

where  $a$  is the area per particle,  $F$  is the flux of particles to an empty surface (proportional to the bulk particle concentration and some power  $<1$  of the coefficient

<sup>2)</sup> This is especially to be expected if the particle is a protein; typically about 70% of the

volume of three-dimensional protein crystals is solvent.

of diffusion in three dimensions), and  $\phi$  is the fraction of the surface available for addition, which is some function of  $\theta$ , the fractional surface coverage of the particles at the interface; and the characteristic time  $\tau_D$  for rearranging the surface by lateral diffusion (with a diffusion coefficient  $D_2$ )

$$\tau_D = a/(D_2\theta). \quad (25.9)$$

If  $\tau_D \gg \tau_a$ , then lateral diffusion is encumbered by the rapid addition of fresh particles before self-organization can occur and the resulting structure is indistinguishable from that of random sequential addition. Conversely, if  $\tau_a \gg \tau_D$  there is time for 2-D crystallization to occur. Note that some affinity-changing conformational change must be induced by the interface; otherwise the particles would already aggregate in the bulk suspension. In the example of the protein with the hydrophobic tail, when the protein is dissolved in water the tail is buried in the interior of the protein, but partitions into the lipid bilayer when the protein arrives at its surface.

An intriguing example of interfacial organization is the heaping into cones of the antifreeze glycoprotein (AFGP) consisting of repeated alanine–alanine–glycosylated threonine triplets added to the surface of a solid solution of nanocrystalline  $\text{Si}_{0.6}\text{Ti}_{0.4}\text{O}_2$  [22]. Under otherwise identical conditions, on mica the glycoprotein adsorbs randomly sequentially. It is indeed possible that in this, as in other cases, we are seeing examples of programmable self-assembly (Sections 25.2.3 and 25.3.7), but current limitations in resolving the shapes of nanometer-sized biomolecules adsorbed at interfaces mean that it can only be inferred (e.g., from the overall kinetics of the assembly process), rather than observed directly.

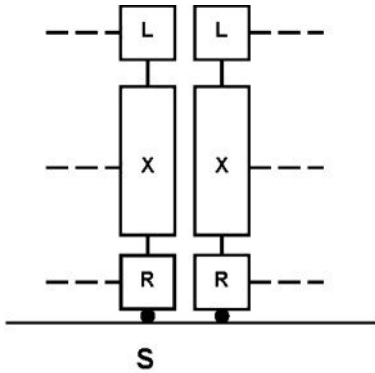
#### 25.3.1.1 Numerically Simulating RSA

The process is exceptionally easy to simulate. For each addition attempt, one selects a point at random: if it is further than  $2r$  from the center of any existing particle then a new particle is added (the available area for less symmetrical shapes may have to be computed explicitly), but if it is closer then the attempt is abandoned. The success of this simple algorithm is due to the fortuitous cancellation of two opposing processes: correlation and randomization. In reality, if a particle cannot be added at a selected position because of the presence of a previously added one, it will make another attempt in the vicinity of the first, because of the Rabinowitch (“cage”) effect [23]; successive attempts are strongly positionally correlated. On the other hand, as a particle approaches the interface through the bulk fluid, it experiences *hydrodynamic friction*, which exerts a randomizing effect; the two effects happen to cancel out each other [24].

#### 25.3.2

##### Self-Assembled Monolayers (SAMs)

If particles randomly and sequentially added to the solid–liquid interface are asymmetrical (i.e., elongated) and have an affinity for the solid substratum at only one



**Figure 25.5** A (fragment of a) self-assembled monolayer (SAM). The component molecules have the general formula LXR, where X is an apolar chain (e.g., alkyl), and R is a reactive group capable of binding to the substratum,

S. X can be functionalized at the end opposite from R with a group L to form molecules L–XR; the nature of L can profoundly change the wetting properties of the SAM.

end (but an ability to move laterally at the interface), and with the “tail” (the rest) poorly solvated by the liquid, they will tend to adsorb in a compact fashion, by strong lateral interaction between the tails (Figure 25.5).

Self-assembled monolayers were discovered by Bigelow *et al.* [25]. The original example was eicosyl alcohol ( $C_{20}H_{41}OH$ ) dissolved in hexadecane ( $C_{16}H_{34}$ ) adsorbing onto silica glass. Later, molecules with  $R = -SH$  (thiol or mercaptan), which bind strongly to metals such as Au, Ag, Cu, Hg, and so on, were investigated [26, 27], as well as organosilanes, which bind strongly (covalently) to silica. If the tail moiety X is poorly solvated by the liquid, its flexibility may enable it to be compactified while the molecule is in the bulk solution, tending to prevent self-aggregation, and only unfurling itself after R has attached to the solid surface; this can be seen as a rudimentary form of programming.

SAMs provide a very convenient way to change the wettability of a solid surface. Bigelow *et al.*'s monolayers were both hydrophobic and oleophobic. An octadecanethiol ( $L = -H$ ) film adsorbed onto gold would be both oil- and water-repellent; if  $L = -OH$  it would be hydrophilic. Equilibrium wetting is quantified by Young's equation; if wetting is complete, then the contact angle of a droplet of liquid L on solid S in the presence of vapor V is zero, and Young's equation becomes

$$0 = \gamma_{SV} - \gamma_{SL} - \gamma_{LV} \quad (25.10)$$

where  $\gamma_{LV}$  is the interfacial tension of liquid L (or an epitaxially grown solid) in contact with its vapor, and *mutatis mutandis* for the other symbols. Out of equilibrium, the spreading coefficient S introduced by Cooper and Nuttall [28] is useful:

$$S = \gamma_{SV} - \gamma_{SL} - \gamma_{LV} \quad (25.11)$$

where  $\gamma_{\text{SV}}$  is the interfacial tension of a *dry* (unwetted) solid S in contact with vapor V. Three régimes can be defined:

1.  $S > 0$ . This corresponds to  $\gamma_{\text{SV}} > \gamma_{\text{SV}}$ ; that is, the wetted surface has a lower energy than the unwetted one. Hence, wetting takes place spontaneously. The thickness  $h$  of the film is greater than monomolecular if  $S \ll \gamma_{\text{LV}}$ . The difference  $\gamma_{\text{SV}} - \gamma_{\text{SV}}$  can be as much as  $300 \text{ mJ m}^{-2}$  for water on metal oxides. Such systems therefore show enormous hysteresis between advancing and receding contact angles.
2.  $S = 0$ . This occurs if  $\gamma_{\text{SV}}$  practically equal to  $\gamma_{\text{SV}}$ , as is typically the case for organic liquids on molecular solids.
3.  $S < 0$ . This is partial wetting. Films thinner than a certain critical value, usually  $\sim 1 \text{ nm}$ , break up spontaneously into droplets.

More elaborate groups L can be incorporated into SAMs; however, if they are bulky the functionalized molecules should be mixed with unfunctionalized ones so as to avoid packing defects. Mixtures with different chain lengths (e.g.,  $X = \text{C}_{12}$  and  $\text{C}_{22}$ ) produce liquid-like SAMs.

The biologically ubiquitous lipid bilayer membrane could be considered to belong to this category. The component molecules are of type XR, where X is an alkyl chain as before, and R is a rather polar “head group,” the volume of which is typically roughly equal to that of X. Placing XR molecules in water and gently agitating the mixture will lead spontaneously to the formation of spherical bilayer shells called *vesicles*. The vesicles will coat a planar hydrophilic substratum with a lipid bilayer when brought into contact with it [29].

If the substratum is electrified (via the Gouy–Chapman mechanism) and the dissolved molecule is a polyion with an electrostatic charge of opposite sign, then it will adsorb onto the surface and invert the charge; the strong correlations within the polymeric ion render the Gouy–Chapman mechanism invalid [30]. The polyion-coated substratum can then be exposed to a different polyion of opposite sign, which will in turn be adsorbed and again invert the charge; this process can be repeated *ad libitum* to assemble thick films [31].

### 25.3.3

#### Quantum Dots (QDs)

Whereas SAMs can be prepared with very simple equipment, a somewhat analogous process—molecular beam epitaxy (MBE)—which was developed at the AT & T Bell Laboratories during the late 1960s, takes place in ultrahigh vacuum and requires elaborate and expensive equipment for its realization. In this process, the material to be assembled is evaporated from a source and beamed onto the substratum. A very slow deposition (a fraction of a nanometer per second) is the key to achieving epitaxy; ultrathin layers with atomically sharp interfaces are capable of being deposited. Equation 3.11 also applies. If  $S > 0$ , we have the Frank–van der Merwe régime, where the substratum is wet and layer-by-layer

growth takes place. If  $S < 0$ , we have the Volmer–Weber régime, where there is no wetting and three-dimensional (3-D) islands grow. But, if  $S > 0$ —for the first layer at least—and if there is a geometric mismatch between the lattices of the substratum and the deposited layer, then strain will build up in the latter, this being subsequently relieved by the spontaneous formation of monodisperse islands (the Stranski–Krastanov régime); it can be thought of as “frustrated wetting” [42]. The main application of this process is to fabricate QDs for lasers [43].<sup>3)</sup> In this application, the main difficulty is to ensure that the dots comprising a device are uniformly sized. If not, the density of states is smeared out and the behavior reverts to bulk-like. Initially, the QDs were prepared by conventional semiconductor processing [44], but it proved to be very difficult to eliminate defects and impurities. The Stranski–Krastanov self-assembly process does not introduce these problems.

#### 25.3.4

#### Crystallization and Supramolecular Chemistry

It is a remarkable fact that many (or even most) organic molecules, despite their usually very complicated shapes, are able spontaneously to form close-packed crystals. Perhaps only familiarity with the process prevents it from occupying a more prominent place in the world of self-assembly. In seeking to better understand this remarkable phenomenon, Kitaigorodskii formulated an Aufbau principle [32], according to which the self-assembly of complicated structures takes place in a hierarchical fashion in the following sequence:

- at stage zero, we have a single molecule (or a finite number of independent molecules)
- in stage one, single molecules join up to form linear chains
- in stage two, the linear chains are bundled to form 2-D monolayers
- in stage three, the 2-D monolayers are stacked to form the final 3-D crystal.

Many natural structures are evidently hierarchically assembled. Wood, for example, derives its structural strength from glucose polymerized to form cellulose chains, which are bundled to form fibrils, that are in turn glued together using lignin to form robust fibers. It should be noted that the interactions between the molecular components of the crystal may be significantly weaker than the covalent chemical bonds that hold the atomic constituents of the molecules together. Such weakness enables defects to be annealed by local melting of the partially formed structure.

There is an obvious analogy between “crystallization” in two dimensions and tiling a plane. Since tiling is connected to computation, self-assembly—which can

3) Quantum dot lasers are a development of quantum well lasers. The carriers are confined in a small volume and population inversion occurs more easily than in large

volumes, leading to lower threshold currents for lasing. The emission wavelength can be readily tuned by simply varying the dimensions of the dot (or well).

perhaps be regarded as a type of generalized crystallization—has in turn been linked to computation [33].

Just as QDs containing several hundred atoms can in some sense (e.g., with regard to their discrete energy levels) be regarded as “superatoms,” so can supramolecular assemblies (typically made up from very large and elaborate molecules [34]) be considered as “supermolecules.” The obtainable hierarchically assembled structures provide powerful demonstrations of the Kitaigorodskii Aufbau principle [35–39], and an enormous literature has subsequently accumulated. The use of metal ions as organizing centers in these assemblies has been a particularly significant practical development [35, 40, 41].

### 25.3.5

#### Biological Examples

The observation that preassembled bacteriophage components (head, neck, and legs) could be mixed in solution [7] provided profound inspiration for the world of “shake and bake” advocates. These components are essentially made up of proteins—heteropolymers made from irregular sequences chosen from the 20 natural amino acids of the general formula  $H_2N-C^{(\alpha)}HR-COOH$ , where R is naturally one of 20 different side chains (residues), ranging from  $R=H$  in glycine, the simplest amino acid, to elaborate heterocycles such as  $R=CH_2-[C_8NH_6]$  in tryptophan. The conformation—and hence affinity—of a protein depends on environmental parameters such as the pH and ionic strength of the solution in which it is dissolved [7]. Indeed, this is one mechanism for achieving programmability in assembly, as the local pH and ion concentration around a protein molecule will depend on the amino acids present at its surface. These factors also determine the conformation of the highly elongated, so-called “fibrous” proteins such as fibronectin, which are now known to consist of a large number of rather similar modules strung together [45]. Some other examples of biological self-assembly have already been mentioned in Section 25.2.3. A further example is provided by the remarkable S-layers with which certain bacteria are coated [46]. DNA is discussed in Section 25.3.6. Mention should also be made here of the oligopeptides found in fungi and the stings of bees and wasps, which self-assemble into pores when introduced into a bilayer lipid membrane (see, e.g., Ref. [47]). Yet, biological self-assembly and self-organization is by no means limited to the molecular scale: the development of an embryo consisting of a single cell into a multicellular organism is perhaps the most striking example of self-organization in the living world. The process of cell differentiation into different types can be very satisfactorily simulated on the basis of purely local rules enacted by the initially uniform cells (see Ref. [48] for the modeling of neurogenesis). On a yet larger scale, it is likely that the construction of nests by social insects such as ants and wasps relies on simple rules held and enacted by individual agents (the insects), according to local conditions [49]; this process has been called *stigmergy* and is evidently conceptually the same as the programmable self-assembly modeled by graph grammars (Section 25.2.3).

## 25.3.6

**DNA**

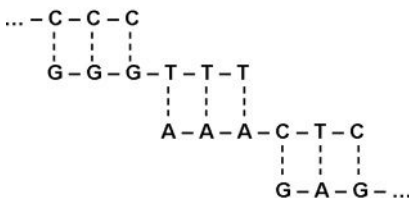
The importance of deoxyribonucleic acid (DNA), both as the quasi-universal carrier of genetic information in living creatures and as a sufficiently robust material to serve as the basis for synthetic self-assembling systems, warrants it having a subsection of its own. Similar to proteins, DNA is a heteropolymer, the monomers of which comprise an invariant backbone [in this case, of alternating sugar (deoxyribose) and phosphate units] and a variety of four “bases”, adenine (A), cytosine (C), guanine (G) and thymine (T). The rather specific base pairings between A and T, and between C and G, which are due to respectively two and three interbase hydrogen bonds [50], are responsible for the famous “double helix” [51] in which genetic information is stably stored in living cells and many viruses. The combinatorial uniqueness even of base strings of fairly modest length is exploited in the fabrication of “gene chips” [52] used to identify genes and genomes. In these devices, the sample to be identified (e.g., the nucleic acids extracted from bacteria found in the bloodstream of a patient) is dispersed over the surface of the chip, which comprises an array of contiguous microzones containing known oligomers of nucleic acids complementary to the sought-for sequences (e.g., the fragment GATTACA is complementary to CTAATGA).

Seeman was the first to point out that the specific complementary base pairing could form the basis of employing DNA as a structural nanomaterial [53, 54]: oligonucleotides could be artificially synthesized according to what are now straightforward, routine procedures and randomly stirred together, assembling in a unique fashion (Figure 25.6). This field has now grown enormously to encompass very elaborate constructions (e.g., Refs [55, 56]) and is connected with tile assembly and computation [57, 58]. Fragments of DNA have also been fastened to nanoparticles to confer selective affinity upon them (e.g., Ref. [59]).

## 25.3.7

**RNA and Proteins**

Although ribonucleic acid (RNA) differs only very slightly from DNA, heteropolymers formed from its four bases (the same as in DNA, except that uracil (U)



**Figure 25.6** Four oligonucleotides, which can only assemble in the manner shown. Long dashes represent strong covalent bonds; short dashed lines represent weak hydrogen bonds.



replaces thymine (T)) do not assemble into a double helix, but rather “fold.” That is, the linear polymer chain—each monomer of which is bonded covalently only to its two nearest neighbors—typically assembles into a compact 3-D structure (though not all sequences will do so) with additional base-pairing (A=U and C≡G) bonds between distant monomers. Predicting the final 3-D structure is *prima facie* a difficult problem. Energetics are clearly involved, because bonds between distant monomers form spontaneously (if geometric constraints are satisfied), releasing enthalpy and hence lowering the free energy. On the other hand, this raises the entropy because the chain becomes more constrained. At one time it was believed that the observed stable folded configurations were the result of minimizing the free energy of the molecule, and were found by systematically searching configuration space. It was, however, quickly realized that for a large molecule with thousands of atoms this was a practically impossible task that might take longer than the age of the universe. Both, *in vivo* and *in vitro*, it can be observed that biopolymers can typically fold within an interval of the order of seconds, and the only way that this can be achieved is for the system to find a pathway expeditiously leading to the goal (which is evidently some form of energy minimum, even if not the global one). This in turn suggests that a least-action principle might be operating. The action is the integral of the Lagrangian  $\mathcal{L}$  ( $= L - F$  for conservative systems, where  $L$  and  $F$  are respectively the kinetic and potential energies). The most expedient path is found by minimizing the action. This is, in fact, an inerrant principle for finding the correct solution of any dynamical problem; the difficulty lies in the fact that there is no general recipe for constructing  $\mathcal{L}$ , and it can often be found only by “fiddling around,” as has been remarked by Feynman.

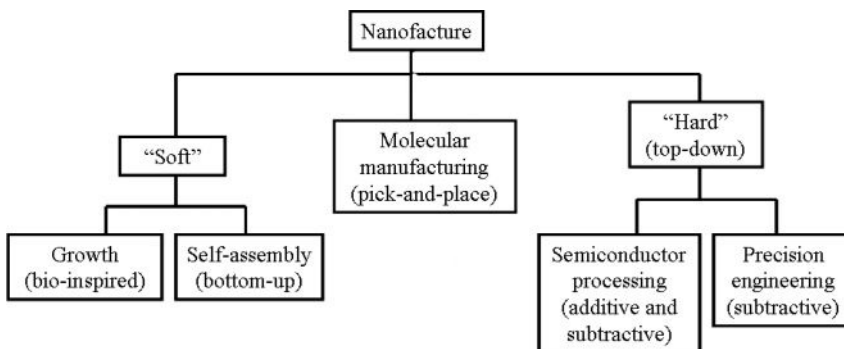
Folded RNA contains certain characteristic structures, notably loops and “hair-pins”. Loop closure is considered to be the most important folding event.  $F$  (the potential) is identified with the enthalpy; that is, the number  $n$  of base pairings (contacts), and  $L$  corresponds to the entropy [60]. At each stage in the folding process, as many as possible new favorable intramolecular interactions are formed, while minimizing the loss of conformational freedom (the principle of sequential minimization of entropy loss, SMEL [60]). The entropy loss associated with loop closure is  $\Delta S_{\text{loop}}$  (and the rate of loop closure  $\sim \exp(\Delta S_{\text{loop}})$ ); the function to be minimized is therefore  $\exp(-\Delta S_{\text{loop}}/R)/n$ , where  $R$  is the universal gas constant. A quantitative expression for  $\Delta S_{\text{loop}}$  can be found by noting that the  $N$  monomers in an unstrained loop ( $N \geq 4$ ) have essentially two possible conformations, pointing either inwards or outwards. For loops smaller than a critical size,  $N_0$ , the inward loops are in an apolar environment, as the nano-enclosed water no longer has bulk properties [61], while the outward loops are in polar bulk water. For  $N < N_0$ ,  $\Delta S_{\text{loop}} = -RN \ln 2$  (for  $N > N_0$ , the Jacobson–Stockmayer approximation based on excluded volume yields  $\Delta S_{\text{loop}} \sim R \ln N$  [60]).

A similar approach can be applied to proteins [62], although in proteins the main intramolecular structural connector (apart from the covalent bonds between successive amino acid monomers) is the backbone hydrogen bond. This form of hydrogen bond is responsible for the appearance of characteristic structures such

as the alpha helix but, being single, is necessarily weaker than the double and triple hydrogen bonds in DNA and RNA. They must therefore be protected from competition for hydrogen bonding by water, and this can be achieved by bringing amino acids with apolar residues to surround the hydrogen bonds [63]. This additional feature, coupled with the existence of multiple conformational states already referred to in Section 25.2.3, means that proteins are particularly good at engaging in programmable self-assembly—a possibility that is, of course, made abundant use of in Nature.

## 25.4 Self-Assembly as a Manufacturing Process

Practical, industrial interest in self-assembly is strongly driven by the increasing difficulty of reducing the feature sizes that can be fabricated by semiconductor processing technology [44]. Self-assembly is positioned as a rival to the so-called “top-down” processes, which also include precision engineering (Figure 25.7) [64]. For certain engineering problems, it may already be useful to manufacture regular structures such as dots or stripes over an indefinitely large area; passive self-assembly might be able to produce such structures with feature sizes at the molecular scale of a few nanometers. These could be used either as masks for photolithography (as a cheaper and faster method than electron beam writing for creating such small features), or they might be useful in their own right (e.g., as nanoporous membranes for separating vapors [65]). Self-assembly is a particularly attractive option for the fabrication of molecular electronic components [66, 67], for in this case—almost by definition—conventional semiconductor processing is useless.



**Figure 25.7** Different possible modes of nanomanufacture (nanofacture) [64].

## 25.5

### Useful Ideas

#### 25.5.1

##### Weak Competing Interactions

It is known from biological self-assembly (e.g., of compact RNA structures) that bonds must be broken and reformed before the final structure is achieved. This is particularly apparent because these molecules are synthesized as a linear polymer, which begins to fold spontaneously as soon as a few tens of monomers have been connected. As the chain becomes longer, some of these earlier bonds must be broken so as to allow connections between points more distant along the chain to be made. Since hydrogen bonds have only about one-tenth of the strength of ordinary covalent bonds, they have an appreciable probability of being melted (broken) even at room temperature. Furthermore, the polymer is surrounded by water, each molecule of which is potentially able to participate in four hydrogen bonds (although at room temperature only about 10% of the maximum possible number of hydrogen bonds in water are broken; see also Section 25.5.4). Hence, there is ceaseless competition between the intramolecular and intermolecular hydrogen bonds.

If the competing interactions have a different sign and range, then ordered structures can assemble spontaneously [68]. Consider nanoparticles suspended in water and weakly ionized, such that they all carry the same electrostatic charge. When the suspension is stirred, suppose that the repulsive electrostatic force is too weak to overcome the attractive van der Waals force when two particles happen to collide. Therefore, every collision will lead to sticking, and aggregates will slowly form. The van der Waals force is, however, very short ranged and can only act between nearest neighbors. The electrostatic force, on the other hand, has a much longer range, and can therefore be summed over the entire aggregate. Ultimately, the aggregate will become large enough for the summed electrostatic repulsion to exceed the van der Waals nearest-neighbor attraction; the result is monodisperse “superspheres” (i.e., aggregates of small, perhaps spherical, particles).

#### 25.5.2

##### Percolation

Percolation can be considered to be a formalization of gelation. Initially, in a flask we have isolated sol particles, which are gradually connected to each other in nearest-neighbor fashion until the gel is formed. Although the particles can be placed anywhere in the medium, subject only to the constraint of hard-body exclusion, it is convenient to consider them placed on a 2-D square lattice (imagine a Go board). Two particles are considered to be connected if they share a common side (this is called “site percolation”). Alternatively, neighboring lattice points are connected if they are bonded together (“bond percolation”).

In principle the lattice is infinite, but in reality it is merely very large. Percolation occurs if one can trace the continuous path of connections from one side to the

other. Initially, all the particles are unconnected. In site percolation, the lattice is initially considered to be empty, and particles are added. In bond percolation, initially all particles are unconnected and bonds are added. The problem is to determine what fraction of sites must be occupied, or how many bonds must be added, in order for percolation to occur.

In the remainder of this subsection we shall consider site percolation. Let the probability of a site being occupied be  $p$  (and of being empty,  $q = 1 - p$ ). The average number of singlets per site is  $n_1(p) = pq^4$  for the square lattice, as each site is surrounded by four shared sides. The average number of doublets per site is  $n_2(p) = 2p^2q^6$ , as there are two possible orientations. A triplet can occur in two shapes, straight or bent, and so on. Generalizing,

$$n_s(p) = \sum_t g(s, t) p^s q^t \quad (25.12)$$

where  $g(s, t)$  is the number of independent ways that an  $s$ -tuple can be put on the lattice, and  $t$  counts the different shapes. If there is no “infinite” cluster (i.e., one spanning the lattice from side to side) then

$$\sum_s s n_s(p) = p. \quad (25.13)$$

The first moment of this distribution gives the mean cluster size

$$S(p) = \frac{\sum_s s^2 n_s(p)}{p}. \quad (25.14)$$

Writing this as a polynomial in  $p$  using Equation 25.12, it will be noticed that for  $p < p_c$  the value of the series converges, but for  $p > p_c$  the value of the series diverges. The “critical” value  $p = p_c$  corresponds to the formation of the “infinite” cluster. For site percolation on a square lattice,  $p = p_c = 0.5$ ; the universal Galam–Mauger formula [69]

$$p_c = a[(d-1)(q-1)]^{-b}, \quad (25.15)$$

with  $a = 1.2868$  and  $b = 0.6160$  predicts, with less than 1% error, all known thresholds for lattices of connectivity  $q$  embedded in space of dimension  $d$ . The larger the lattice, the sharper the transition from not percolating to percolating. For a  $3 \times 3$  lattice there can be no percolation for two particles or less, but the probability of randomly placing three particles in a straight line from edge to edge is evidently one-third.

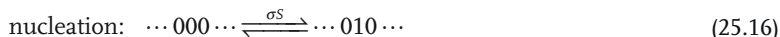
### 25.5.3

#### Cooperativity

When considering the interactions between precursors of a self-assembly process, it has tacitly been assumed that every binding event is independent. Similarly, when considering conformational switches, it has been assumed that each

molecule switches independently. This, however, is often not the case: switching or binding of one facilitates the switching or binding of neighbors, whereupon we have cooperativity (if it hinders rather than facilitates, then it is called *anticooperativity*).

A cooperative processes can be conceptualized as two subprocesses, nucleation and growth. Let our system exist in one of two states (e.g., bound or unbound, conformation A or B), which we shall label 0 and 1. We have [70]



and



Let  $\{1\} = \theta$  denote the probability of finding a “1”; we have  $\{0\} = 1 - \theta$ . The parameter  $\lambda^{-1}$  is defined as the conditional probability of “00”, given that we have a “0”, written as  $(00)$  and equal to  $\{00\}/\{0\}$ . It follows that  $(01) = 1 - (00) = (\lambda - 1)/\lambda$ .

According to the mass action law (MAL), for nucleation we have

$$S = \frac{\{011\}}{\{001\}} = \frac{(11)}{(00)} \quad (25.18)$$

from which we derive  $(11) = S/\lambda$ , and hence  $(10) = 1 - (11) = (\lambda - S)/\lambda$ . Similarly, for growth

$$S = \frac{(01)(10)}{(00)^2} = (\lambda - 1)(\lambda - S). \quad (25.19)$$

Solving for  $\lambda$  gives

$$\lambda = \left[ 1 + S + \sqrt{(1 - S)^2 + 4\sigma S} \right] / 2. \quad (25.20)$$

To obtain the sought-for relationship between  $\theta$  and  $S$ , we note that  $\theta = \{01\} + \{11\} = \{0\}(01) + \{1\}(11)$ , which can be solved to yield

$$\lambda = \frac{1 + (S - 1) / \sqrt{(1 - S)^2 + 4\sigma S}}{2}. \quad (25.21)$$

#### 25.5.4

##### Water Structure

So many self-assembly processes take place in water (not least all the biological ones) that it is advisable to bear some salient features of this remarkable liquid into account. Water (H–O–H) can participate in four hydrogen bonds (HB). The

two-electron lone pairs (LPs) on the oxygen atom are electron donors, and hence HB acceptors. The two hydrogens at the ends of the hydroxyl groups (OH) are HB donors, and hence electron acceptors. The equilibrium



is such that at room temperature about 10% of the OHs and LPs are nonbonded (i.e., free). It is especially noteworthy that the concentrations of the free species are seven to eight orders of magnitude greater than the concentrations of the perhaps more familiar entities  $\text{H}^+$  and  $\text{OH}^-$ , and their chemical significance is correspondingly greater.

The OH moiety has a unique infrared absorption spectrum, which differs according to whether it is hydrogen-bonded or free, and can therefore be used to investigate the reaction in Equation 25.22 (e.g., the effect of adding ionic cosolutes; see Ref. [16] for further discussion).

## 25.6

### Conclusions and Challenges

The most promising direction seems to be programmable self-assembly. Although some wholly synthetic examples have already been demonstrated [71], we can expect significant progress in the future to derive from the convergence of understanding of cooperative switching transitions in biomolecules with graph grammar or other formalisms for describing the assembly process. The final challenge will then be to reverse-engineer a device in order to specify the components (and environmental conditions) that should be stirred together for its assembly.

### References

- 1 Bray, A.J. (2002) Phase-ordering kinetics. *Adv. Phys.*, **51**, 481–587.
- 2 Higgins, A.M. and Jones, R.A.L. (2000) Anisotropic spinodal dewetting as a route to self-assembly of patterned surfaces. *Nature*, **404**, 476–478.
- 3 von Foerster, H. (1960) On self-organizing systems and their environments, in *Self-Organizing Systems* (eds M.C. Yorvitz and S. Cameron), Pergamon Press, Oxford, pp. 31–50.
- 4 Meakin, P. (1994) What do we know about DLA? *Heterogen. Chem. Rev.*, **1**, 99–102.
- 5 Ashby, R.W. (1962) Principles of the self-organizing system, in *Principles of Self-Organization* (eds H. von Foerster and G.W. Zopf), Pergamon Press, Oxford, pp. 255–278.
- 6 Maruyama, K., Nori, F. and Vedral, V. (2009) The physics of Maxwell's demon and information. *Rev. Mod. Phys.*, **81**, 1–23.
- 7 Kellenberger, E. (1972) Assembly in biological systems, in *Polymerization in Biological Systems*, CIBA Foundation Symposium 7 (new series), Elsevier, Amsterdam.

- 8 Culver, G.M. (2003) Assembly of the 30S ribosomal subunit. *Biopolymers*, **68**, 234–249.
- 9 Holy, T.E. and Leibler, S. (1994) Dynamic instability of microtubules as an efficient way to search in space. *Proc. Natl Acad. Sci. USA*, **91**, 5682–5685.
- 10 Blumenfeld, L.A. (1981) *Problems of Biological Physics*, Springer, Berlin.
- 11 Frauenfelder, H. (1984) From atoms to biomolecules. *Helv. Phys. Acta*, **57**, 165–187.
- 12 Ramsden, J.J. (2001) Biophysical chemistry, in *Encyclopaedia of Chemical Physics and Physical Chemistry* (eds J.H. Moore and N.D. Spencer), IOP, Philadelphia, PA, pp. 2509–2544.
- 13 Klavins, E. (2004) Directed self-assembly using graph grammars, in *Foundations of Nanoscience: Self-Assembled Architectures and Devices*, Snowbird, UT.
- 14 Klavins, E. (2004) Universal self-replication using graph grammars. International Conference on MEMs, NANOs and Smart Systems, Banff, Canada.
- 15 Klavins, E., Ghrist, R. and Lipsky, D. (2004) Graph grammars for self-assembling robotic systems. Proceedings, International Conference on Robotics and Automation, New Orleans, pp. 5293–5300.
- 16 Cacace, M.G., Landau, E.M. and Ramsden, J.J. (1997) The Hofmeister series: salt and solvent effects on interfacial phenomena. *Q. Rev. Biophys.*, **30**, 241–278.
- 17 Ramsden, J.J. and Máté, M. (1998) Kinetics of monolayer particle deposition. *J. Chem. Soc., Faraday Trans.*, **94**, 783–788.
- 18 Schaaf, P. and Talbot, J. (1989) Surface exclusion effects in adsorption processes. *J. Chem. Phys.*, **91**, 4401–4409.
- 19 Schaaf, P., Voegel, J.-C. and Senger, B. (1998) Irreversible deposition/adsorption processes on solid surfaces. *Ann. Phys.*, **23**, 3–89.
- 20 Ramsden, J.J., Bachmanova, G.I. and Archakov, A.I. (1994) Kinetic evidence for protein clustering at a surface. *Phys. Rev. E*, **50**, 5072–5076.
- 21 Meakin, P. and Family, F. (1988) Structure and kinetics of reaction-limited aggregation. *Phys. Rev. A*, **38**, 2110–2123.
- 22 Lavalle, Ph., DeVries, A.L., Cheng, C.-H.C., Scheuring, S. and Ramsden, J.J. (2000) Direct observation of postadsorption aggregation of antifreeze glycoproteins on silicates. *Langmuir*, **16**, 5785–5789.
- 23 Luthi, P.O., Ramsden, J.J. and Chopard, B. (1997) The role of diffusion in irreversible deposition. *Phys. Rev. E*, **55**, 3111–3115.
- 24 Bafaluy, J., Senger, B., Voegel, J.C. and Schaaf, P. (1993) Effect of hydrodynamic interactions on the distribution of adhering Brownian particles. *Phys. Rev. Lett.*, **70**, 623–626.
- 25 Bigelow, W.C., Pickett, D.L. and Zisman, W.A. (1946) Oleophobic monolayers. *J. Colloid Sci.*, **1**, 513–538.
- 26 Nuzzo, R.G., Fusco, C.O. and Allara, D.L. (1987) Spontaneously organized molecular assemblies. 3. Proportion and properties of solution-adsorbed monolayers of organic disulfides at surfaces. *J. Am. Chem. Soc.*, **109**, 2358–2368.
- 27 Sellers, H., Ulman, A., Shnidman, Y. and Eilers, J.E. (1993) Structure and binding of alkane thiolates on gold and silver surfaces. *J. Am. Chem. Soc.*, **115**, 9389–9401.
- 28 Cooper, W. and Nuttall, W. (1915) The theory of wetting and the determination of the wetting power of dipping and spraying fluids containing a soap basis. *J. Agric. Sci.*, **7**, 219–239.
- 29 Csúcs, G. and Ramsden, J.J. (1998) Interaction of phospholipid vesicles with smooth metal oxide surfaces. *Biochim. Biophys. Acta*, **1369**, 61–70.
- 30 Grosberg, A.Y., Nguyen, T.T. and Shklovskii, B.I. (2002) The physics of charge inversion in chemical and biological systems. *Rev. Mod. Phys.*, **74**, 329–345.
- 31 (a) Ramsden, J.J., Lvov, Y.A. and Decher, G. (1995) Optical and X-ray structural monitoring of molecular films assembled via alternate polyion adsorption. *Thin Solid Films*, **254**, 246–251.

- (b) Ramsden, J.J., Lvov, Y.A. and Decher, G. (1995) Optical and X-ray structural monitoring of molecular films assembled via alternate polyion adsorption. *Thin Solid Films*, **261**, 343–344.
- 32 Kitaigorodskii, A.I. (1961) *Organic Chemical Crystallography*, especially Chapters 3 and 4. Consultants Bureau, New York.
- 33 Winfree, E. (1996) On the computational power of DNA annealing and ligation, in *DNA-Based Computers* (eds R.J. Lipton and E.B. Baum), American Mathematical Society, Princeton, NJ, pp. 199–221.
- 34 Lehn, J.-M. (2000) Supramolecular polymer chemistry—scope and perspectives, in *Supramolecular Polymers* (ed. A. Ciferri), Dekker, New York, pp. 615–641.
- 35 Constable, E.C., Hannon, M.J., Edwards, A.J. and Raithby, P.R. (1994) Metallosupramolecular assembly of dinuclear double helicates incorporating a biphenyl-3,3' diyl spacer. *J. Chem. Soc., Dalton Trans.*, 2669–2677.
- 36 Fujita, M., Ibukuro, F., Hagihara, H. and Ogura, K. (1994) Quantitative self-assembly of a [2]catenane from two preformed molecular rings. *Nature*, **367**, 720–723.
- 37 Desiraju, G.R. (1995) Supramolecular synthons in crystal engineering. *Angew. Chem. Int. Ed. Engl.*, **34**, 2311–2327.
- 38 Kálmán, A., Argay, G., Fábrián, L. *et al.* (2001) Basic forms of supramolecular self-assembly organized by parallel and antiparallel hydrogen bonds in the racemic crystal structures of six disubstituted and trisubstituted cyclopentane derivatives. *Acta Crystallogr.*, **B57**, 539–550.
- 39 Lackinger, M., Griessl, S., Heckl, W.M. *et al.* (2005) Self-assembly of trimesic acid at the liquid-solid interface—a study of solvent-induced polymorphism. *Langmuir*, **21**, 4984–4988.
- 40 Barigelletti, F., Flamigni, L., Balzani, V. *et al.* (1994) Rigid rod-like dinuclear Ru(II)/Os(II) terpyridine-type complexes. *J. Am. Chem. Soc.*, **116**, 7692–7699.
- 41 Whittell, G.R. and Manners, I. (2007) Metallopolymers: new multifunctional materials. *Adv. Mater.*, **19**, 3439–3468.
- 42 Shchukin, V.A. and Bimberg, D. (1999) Spontaneous ordering of nanostructures on crystal surfaces. *Rev. Mod. Phys.*, **71**, 1125–1171.
- 43 Bimberg, D., Ledentsov, N.N., Grundman, M. *et al.* (1996) InAs-GaAs quantum pyramid lasers. *Jpn. J. Appl. Phys.*, **35**, 1311–1319.
- 44 Mamalis, A.G., Markopoulos, A. and Manolakos, D.E. (2005) Micro and nanoprocessing techniques and applications. *Nanotechnol. Percept.*, **1**, 63–73.
- 45 Rocco, M., Infusini, E., Daga, M.G., Gogioso, L. and Cuniberti, C. (1987) Models of fibronectin. *EMBO J.*, **6**, 2343–2349.
- 46 Pum, D., Sára, M., Schuster, B. and Sleytr, U.B. (2006) Bacterial surface layer proteins, in *Nanotechnology: Science and Computation* (eds J. Chen, N. Jonoska and G. Rozenberg), Springer, Berlin, pp. 277–290.
- 47 Schwarz, G., Stankowski, S. and Rizzo, V. (1986) Thermodynamic analysis of incorporation and aggregation in a membrane. *Biochim. Biophys. Acta*, **861**, 141–151.
- 48 Luthi, P.O., Preiss, A., Chopard, B. and Ramsden, J.J. (1998) A cellular automaton model for neurogenesis in *Drosophila*. *Physica D*, **118**, 151–160.
- 49 Theraulaz, G. and Bonabeau, E. (1995) Coordination in distributed building. *Science*, **269**, 686–688.
- 50 Ageno, M. (1967) Linee di ricerca in fisica biologica. *Accad. Naz. Lincei*, **102**, 3–58.
- 51 (a) Watson, J.D. and Crick, F.H.C. (1953) A structure for deoxyribose nucleic acid. *Nature*, **171**, 737–738.  
(b) Watson, J.D. and Crick, F.H.C. (1953) Genetical implications of the structure of deoxyribonucleic acid. *Nature*, **171**, 964–967.
- 52 Chumakov, S., Belapurkar, C., Putonti, C. *et al.* (2005) The theoretical basis of universal identification systems for bacteria and viruses. *J. Biol. Phys. Chem.*, **5**, 121–128.
- 53 Seeman, N.C. (1982) Nucleic-acid junctions and lattices. *J. Theor. Biol.*, **99**, 237–247.



- 54 Seeman, N.C. and Lukeman, P.S. (2005) Nucleic acid nanostructures: bottom-up control of geometry on the nanoscale. *Rep. Prog. Phys.*, **68**, 237–270.
- 55 Goodman, R.P., Schaap, I.A.T., Tardin, C.F. *et al.* (2005) Rapid chiral assembly of rigid DNA building blocks for molecular nanofabrication. *Science*, **310**, 1661–1665.
- 56 Rothemund, P.W.K. (2006) Folding DNA to create nanoscale shapes and patterns. *Nature*, **440**, 297–302.
- 57 Högberg, B. and Olin, H. (2006) Programmable self-assembly—unique structures and bond uniqueness. *J. Comput. Theor. Nanosci.*, **3**, 391–397.
- 58 Chen, J., Jonoska, N. and Rozenberg, G. (eds) (2006) *Nanotechnology: Science and Computation*, Springer, Berlin.
- 59 Mirkin, C.A., Letsinger, R.L., Mucic, R.C. and Storhoff, J.J. (1996) A DNA-based method for rationally assembling nanoparticles into macroscopic materials. *Nature*, **382**, 607–609.
- 60 Fernández, A. and Cendra, H. (1996) In vitro RNA folding: the principle of sequential minimization of entropy loss at work. *Biophys. Chem.*, **58**, 335–339.
- 61 Sinanoğlu, O. (1981) What size cluster is like a surface? *Chem. Phys. Lett.*, **81**, 188–190.
- 62 Fernández, A. and Colubri, A. (1998) Microscopic dynamics from a coarsely defined solution to the protein folding problem. *J. Math. Phys.*, **39**, 3167–3187.
- 63 Fernández, A. and Scott, R. (2003) Dehydron: a structurally encoded signal for protein interaction. *Biophys. J.*, **85**, 1914–1928.
- 64 Ramsden, J.J. (2009) *Nanotechnology*, Ventus, Copenhagen.
- 65 Ying, J.Y., Mehnert, C.P. and Wong, N.S. (1999) Synthesis and applications of supramolecular-templated mesoporous materials. *Angew. Chem. Int. Ed. Engl.*, **38**, 57–77.
- 66 Percec, V., Glodde, M., Bera, T.K. *et al.* (2002) Self-organization of supramolecular helical dendrimers into complex electronic materials. *Nature*, **417**, 384–387.
- 67 Grill, L., Dyer, M., Lafferentz, L. *et al.* (2007) Nano-architectures by covalent assembly of molecular building blocks. *Nat. Nanotechnol.*, **2**, 687–691.
- 68 Ramsden, J.J. (1987) The stability of superspheres. *Proc. R. Soc. Lond. A*, **413**, 407–414.
- 69 Galam, S. and Mauger, A. (1996) Universal formulas for percolation thresholds. *Phys. Rev. E*, **53**, 2177–2181.
- 70 Schwarz, G. (1970) Cooperative binding to linear biopolymers. *Eur. J. Biochem*, **12**, 442–453.
- 71 Bishop, J., Burden, S., Klavins, E., Kreisberg, R., Malone, W., Napp, N. and Nguyen, T. (2005) Programmable parts, in *International Conference on Intelligent Robots and Systems*, IEEE/RSJ Robotics and Automation Society.

## 26

### Nanostructured Organogels via Molecular Self-Assembly

Arjun S. Krishnan, Kristen E. Roskov, and Richard J. Spontak

#### 26.1

##### Introduction

Gels comprise an intermediate state of matter that is neither solid nor liquid. Generally speaking, gels are at least binary systems that consist of a crosslinked network swollen by a liquid, which constitutes the major component of the system. Due to their inherently high concentration of liquid, gels tend to be soft and possess the cohesive properties of a solid but the diffusive properties of a liquid [1]. Although they are largely liquid, gels behave mechanically as solids because the dominant liquid species is entrapped in a solid three-dimensional (3-D) network by capillary forces and adhesion. The underlying network responsible for gel behavior is stabilized by crosslink sites, and gels may be classified on the basis of the nature of their crosslinks. In *chemical gels*, the crosslinks are permanent (i.e., thermally irreversible) due to the formation of covalent bonds. Chemical gels are routinely produced by either connecting individual polymer chains with a bi- (or higher) functional crosslinking agent, or synthesizing macromolecular networks from small molecules in the presence of a crosslinking agent with at least trifunctionality [2]. In most cases, chemical gels are examples of molecular gels, wherein crosslink sites cannot be experimentally delineated from the remainder of the network.

*Physical gels*, the subject of this chapter, can be generated when microphase separation or weak physical interactions (e.g., hydrogen bonding, ion complexation, van der Waals forces, conformational changes and  $\pi$ - $\pi$  stacking) promote the formation of crosslinks and, hence, contiguous networks. Because microphase separation is generally enthalpically-driven and the interactions involved in creating such crosslinks are on the order of  $kT$  (where  $k$  denotes the Boltzmann constant and  $T$  the absolute temperature), the formation of crosslinks is usually thermoreversible, which means that physical gels frequently exist as liquids at elevated temperatures and undergo reversible gelation upon cooling. One of the best-known examples of a physical gel involves the protein *gelatin* in water. Gelatin molecules possess a random coil conformation at elevated temperatures, but spontaneously adopt a triple helix conformation at 37°C, thereby crosslinking

individual molecules and forming a thermoreversible network that can be dissolved upon reheating above 37°C [3, 4]. Although gelatin provides an excellent example of a system known to form a physical gel in water, only physical gels that develop in organic solvents (to yield so-called “organogels”) are considered here. Moreover, attention is focused specifically on systems capable of generating discrete nanoscale crosslink sites that can be experimentally interrogated.

While physical gels are often (and sometimes mistakenly) identified on the basis of a liquid-rich system undergoing solidification (at temperatures well above the fusion temperature of the liquid) upon cooling, a more scientifically rigorous, quantitative definition of a gel remains a matter of discipline-specific debate. One of the most widely accepted definitions of a gel derives from its response to dynamic mechanical deformation, and is thus of rheological origin. In dynamic rheology, a relatively soft specimen, such as a physical gel, is subjected to oscillatory shear deformation between two metal surfaces. The magnitude and frequency of deformation can be independently adjusted and used in concert to probe structure existing within the specimen. Measurements are normally expressed in terms of the dynamic storage modulus ( $G'$ ) and the dynamic loss modulus ( $G''$ ), which correspond to the in-phase and out-of-phase components, respectively, of the response of the specimen to oscillatory deformation [5]. In the specific case of classifying systems as gels, Kramer and coworkers [6] recommend the following criteria:

1. No experimentally discernible equilibrium modulus.
2. A storage modulus that exhibits a prominent frequency-independent plateau.
3. Frequency spectra wherein the  $G'$  plateau extends to time scales (i.e., reciprocal frequencies) on the order of seconds or more.
4. Values of  $G''$  that are lower than those of  $G'$  by an experimentally significant difference (at least one order of magnitude) over all frequencies.

Most physical gels relax at very low frequencies, eventually causing reductions in both  $G'$  and  $G''$ , and so the applicability of the definition offered above depends on the experimental time scale. In addition, some physical gels “ripen”—that is, the extent and stability of their network improves—over time under quiescent conditions, in which case sufficient time must be permitted for such gel networks to mature fully.

This chapter is divided into two sections on the basis of the type of nanostructured network that develops spontaneously in an organic solvent due to molecular self-assembly. While homopolymer molecules can undergo a variety of conformational transitions, such as helix formation—for example, a mixture of syndiotactic and isotactic poly(methyl methacrylate) (PMMA) in a variety of solvents [7], or atactic polystyrene (PS) in carbon disulfide [8]—or crystallization in organic solvents, these systems are not considered further due to the lack of a clearly identifiable network-forming nanostructure. For this reason, we likewise exclude liquid crystalline polymer solutions that can form gels due to intermolecular association between mesogenic groups along the backbone or in side chains [9]. Instead,

attention is first focused on macromolecular systems composed of chemically heterogeneous chains (e.g., block copolymers) that microphase-separate to form self-assembled micellar networks (SAMINs). A second section addresses physical organogels generated when low-molar-mass organic gelators (LMOGs) undergo specific interactions in organic solvents and organize into self-assembled fibrillar networks (SAFINs).

## 26.2

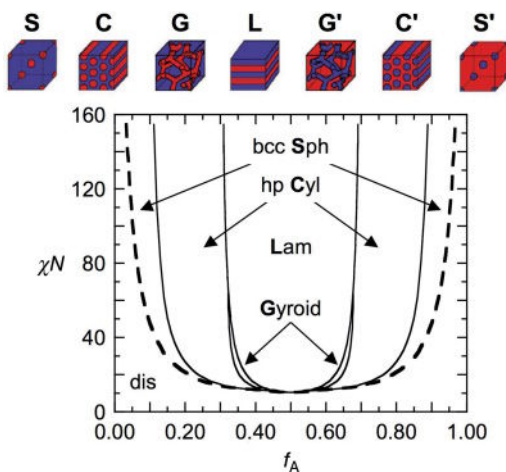
### Block Copolymer Gels

Block copolymers are macromolecules composed of long contiguous sequences (“blocks”) of chemically distinct repeating units that are covalently linked together. If the blocks are sufficiently incompatible, they can microphase-separate into a rich variety of periodic nanostructures, including spheres on a body- (or face-) centered cubic lattice, cylinders on a hexagonal lattice, bicontinuous channels exhibiting  $Ia\bar{3}d$  symmetry (the “gyroid”), or alternating lamellae [10, 11]. Microphase separation results from the competition between enthalpically-driven block stretching to reduce repulsive contacts and entropically-driven block elasticity to minimize chain deformation. The resultant morphology is generally dictated by chain packing along the interface that divides the chemically dissimilar microdomains. In many (but not all) cases, interfacial chain packing relates to molecular composition, expressed in terms of the number fraction ( $f$ ) of one of the blocks. As stated above, block copolymers microphase-separate if they are sufficiently incompatible, where thermodynamic incompatibility is given by the coupled parameter  $\chi N$  ( $\chi$  is the temperature-dependent Flory–Huggins interaction parameter and  $N$  is the number of repeat units along the copolymer backbone [12]). As illustrated in Figure 26.1 for an AB diblock copolymer composed of A and B repeat units [13], an increase in  $\chi N$  for a given  $f_A$  tends to favor microphase-ordering for  $\chi N > (\chi N)_{\text{ODT}}$ , where ODT denotes the order–disorder transition. Similar behavior is observed for block copolymers possessing different molecular architectures. The architecture of primary interest here is the linear ABA triblock design. Unlike their simple AB analogues, ABA copolymer molecules are capable of forming supramolecular networks by depositing their A endblocks in different microdomains. More specifically, the ABA copolymers discussed hereafter possess glassy (PS or PMMA) endblocks at ambient temperature, so that the A microdomains effectively serve as physical crosslinks upon gel formation.

#### 26.2.1

##### Concentration Effects

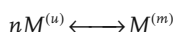
When an ABA triblock copolymer is dissolved in a B-selective organic solvent (i.e., the solvent is more compatible with, and thus preferentially swells, the B block), the A endblocks can, under propitious conditions, self-assemble to form microdomains that measure on the size scale of the endblocks [14–16]. Depending on



**Figure 26.1** Theoretical phase diagram predicted for a solvent-free AB diblock copolymer wherein the thermodynamic incompatibility ( $\chi N$ ) is presented as a function of copolymer composition ( $f_A$ ). Ordered morphologies are labeled in the

diagram and depicted schematically in order of increasing  $f_A$  above the diagram. The order–disorder transition (ODT) is denoted by the dashed bold line. Adapted from Ref. [13] and used with permission from the American Chemical Society.

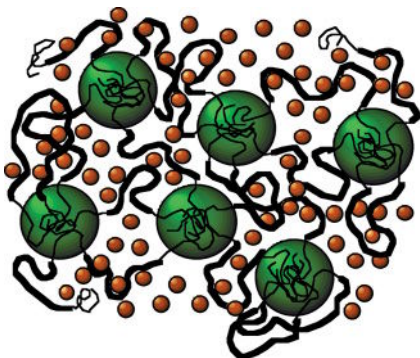
factors such as the copolymer composition ( $f_A$ ), copolymer chain length ( $N$ ) and copolymer concentration in the solvent ( $w_{BC}$ ), the microdomains will adopt a thermodynamically favored morphology at a given temperature (where  $T$  varies inversely with  $\chi$ ). In these studies, only solvated ABA systems composed of discrete micelles (SAMINs) with glassy, A-rich cores are considered further. At the critical micelle concentration (cmc), flower-like micelles first develop by a closed association mechanism characterized by dynamic equilibrium between unimers (u) and micelles (m) such that



where  $M$  denotes mass and  $n$  is the molecular association number of the micelle. In the case of a flower-like micelle, both A endblocks of each copolymer molecule co-reside in the same micelle so that the molecule forms a loop, or one endblock remains in the incompatible matrix to yield a dangling end. Although thermodynamically unfavorable, the effect of dangling ends on the phase behavior and ordering of molecularly asymmetric  $A_1BA_2$  triblock copolymers possessing A endblocks that differ in length ( $N_{A_1} \neq N_{A_2}$ ) has been systematically investigated [17] in copolymer melts. In solvated systems consisting of molecularly symmetric ABA copolymers, dangling ends may become energetically preferable due to the entropic penalty ( $F_{loop}$ ) associated with midblock looping in the micellar corona, which can be written as [18]

$$F_{\text{loop}} = \frac{1}{2}kT \ln(\pi\chi N_B) \quad (26.1)$$

At copolymer concentrations beyond the cmc, copolymer chains added to a solution predominantly form micelles [10]. The solvent molecules serve to increase the effective volume fraction of the copolymer midblock in the phase diagram, and concurrently decrease the effective  $\chi$  by screening repulsive A–B contacts [19]. Micellization is generally favored when the endblock size is large, and corresponding values of  $n$  may be high. Conversely, when the copolymer midblock is large, dangling ends are favored due to the high entropy of loop formation, which leads to smaller association numbers [20]. Conflicting trends of micelle association number and size with regards to block copolymer size and chemistry reported in independent studies [18, 21] can be attributed to variations in solvent–block interactions causing one of the blocks to dominate over the other. If the concentration of triblock copolymer is increased further, the number and size of micelles both increase, which results in a lower intermicellar spacing [22]. Due to their respective free energy penalties, the loops and dangling ends eventually form bridges wherein the endblocks locate in different micelles (cf. Figure 26.2), thereby generating a 3-D network stabilized by glassy micelles (SAMINs). The concentration at which a percolated SAMIN first develops is termed the critical gelation concentration (cgc) and is often significantly higher than the cmc under isothermal conditions. In the specific case of an ABA copolymer having glassy A endblocks and a rubbery B midblock, the neat copolymer is widely referred to as a thermoplastic elastomer (TPE), while the physically crosslinked, thermoreversible gel formed upon midblock-selective solvation has been previously termed [23] a thermoplastic elastomer gel (TPEG). Although TPEGs exhibit substantially lower moduli than their TPE



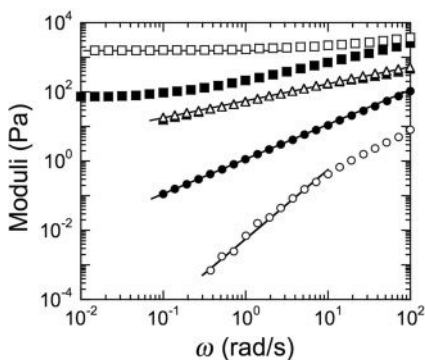
**Figure 26.2** Illustration of the micellar morphology that develops due to triblock copolymer self-assembly in SAMINs. The three distinct conformations depicted include the midblock loop, midblock bridge and dangling endblock (labeled).

precursors, they tend to display remarkable elasticity, as evidenced by elongations to break in excess of 2000% strain [24].

The effect of copolymer concentration on molecular conformation and, hence, midblock bridging and network formation, is elucidated by the frequency ( $\omega$ ) spectrum obtained from dynamic rheology. Below the cgc, the copolymer solutions exhibit terminal responses that are characteristic of a liquid:  $G' \sim \omega^2$  and  $G'' \sim \omega$ . At the sol–gel transition, however,  $G' \sim G'' \sim \omega^m$ , according to Winter and Chambon [25]. Experimental values of  $m$  commonly range from 0.4 to 0.7 [26], whereas percolation models predict values of  $m$  between 0.65 and 0.75 [27]. If the gel is self-similar, the Kramers–Kronig relationship can be invoked to yield  $\tan\delta = G''(\omega)/G'(\omega) = \tan(m\pi/2)$  [26]. At copolymer concentrations above the cgc,  $G'$  ultimately becomes independent of  $\omega$ , as required by the definition of a gel and evidenced in Figure 26.3. The plateau modulus  $G_0$  increases with increasing copolymer concentration ( $c$ ) as  $G_0 \sim c^\alpha$ . At low  $c$  ( $c > \text{cgc}$ ), the intermicellar distance of SAMINs is sufficiently large so that the micellar coronas remain unentangled and the modulus only incorporates contributions from bridged midblocks that behave as elastic springs in the unentangled-chain (Rouse) limit [28] with  $\alpha = 1$ . The corresponding plateau modulus depends on the molecular weight  $M_B$  of the bridge and is given by [29]

$$G_0^{\text{Rouse}} = \frac{RTc}{M_B} \quad (26.2)$$

At higher  $c$ , the midblock loops become entangled and  $\alpha$  theoretically increases to 2.25 in the presence of a good B-selective solvent [30]. While several studies [29, 31, 32] have demonstrated experimentally that  $\alpha$  can be close to this theoretical value, others [33, 34] have reported values of  $\alpha$  between 3 and 4 for copolymer concentrations just above the cgc. This variation is attributed to the presence of a large number



**Figure 26.3** Dynamic shear moduli ( $G'$ , open symbols;  $G''$ , filled symbols) provided as a function of oscillatory frequency ( $\omega$ ) for midblock copolymer organogels varying in copolymer concentration (in wt%): 1 (circles),

4 (triangles) and 10 (squares). The solid lines correspond to the scaling relationships discussed in the text. Adapted from Ref. [26] and used with permission from the American Chemical Society.

of clusters (or flocs) not physically attached to the network at the gel point. Roos and Creton [35] have derived an expression for the plateau modulus in this entangled regime by first considering the neat ABA triblock copolymer, which can be envisaged as an elastomer filled with hard spheres. If  $c_A$  represents the concentration of endblock microdomains (“hard spheres”), then, according to Guth [36],

$$G_0^{(\text{neat})} = \frac{\rho RT}{M_e} (1 + 2.5c_A + 14.1c_A^2) \quad (26.3)$$

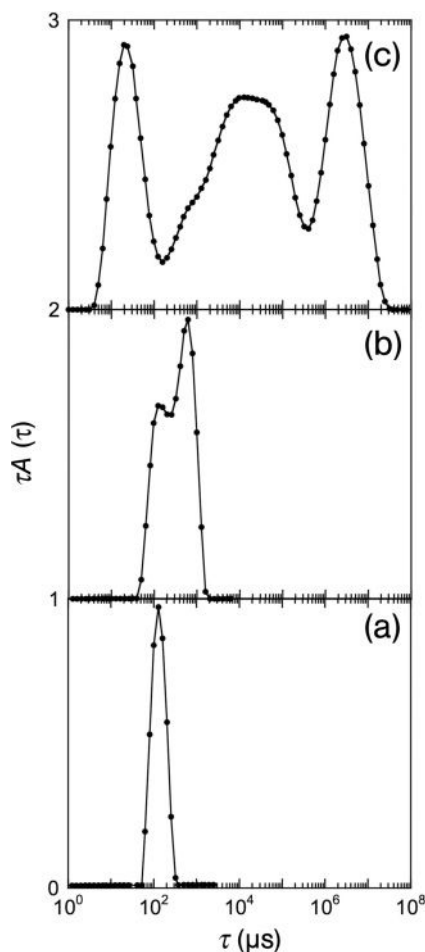
where  $\rho$  is the midblock density and  $M_e$  is the molecular weight between entanglements. The plateau modulus of the gel is consequently obtained by considering the copolymer in a B-selective solvent so that

$$G_0^{(\text{gel})} = \phi^{2.25} G_0^{(\text{neat})} \quad (26.4)$$

where  $\phi$  is the volume fraction of copolymer. More elaborate frameworks such as the Slip Tube Network (STN) model proposed by Rubinstein and Panyukov [37] to depict polymer networks subject to uniaxial tensile deformation provide a more physically realistic representation of block copolymer gels, and its applicability to such nanostructured gels varying in concentration and molecular weight has been recently established [31], as discussed in Section 26.2.4.

Koňák *et al.* [38, 39] have confirmed the presence of block copolymer clusters in the vicinity of the cgc by probing the dynamics of a styrenic triblock copolymer in a midblock-selective solvent (*n*-heptane) with dynamic light scattering (DLS). Different dynamic modes are observed in the relaxation time distributions,  $A(\tau)$  (cf. Figure 26.4), depending on whether the solution resides in the dilute or semi-dilute regimes, which are separated by the overlap concentration ( $c^*$ ). The overlap concentration is defined as  $3M/(4\pi N_A R_g^3)$ , where the gyration radius scales as  $M^\nu$  with  $0.5 < \nu < 0.6$  for good solvents. At  $c < c^*$ , the correlation function is a simple exponential decay that indicates a single diffusive dynamic mode. This single mode at low copolymer concentrations is attributed to the translational diffusion of flower-like micelles. However, as  $c \rightarrow c^*$ , the correlation function becomes the sum of several simple exponentials (corresponding to flower-like micelles) and a slower stretched exponential. These dynamics reveal that, close to the overlap concentration, individual micelles, as well as polydisperse clusters of connected micelles, undergo translational diffusion, with the diffusion mode of the clusters being slower than that of the micelles. At  $c > c^*$ , three different dynamic modes are identified. The slow and fast modes appear diffusive in nature, while the middle dynamic mode is a relaxation mode at low temperatures but a diffusive mode at temperatures above 40 °C. The authors have hypothesized that, for sufficiently high copolymer concentrations, a gel network forms, and the fast mode reflects the collective diffusion of networked micelles. The middle mode arises due to the relaxation of nodes comprising the network. When the temperature is increased, the network begins to break down as a consequence of endblock pullout, in which case the middle dynamic mode becomes diffusive. Although the slowest





**Figure 26.4** Relaxation time distributions, represented by  $A(\tau)$  where  $\tau$  denotes time, for triblock copolymer organogels varying in copolymer concentration (in wt%): (a) 0.49,

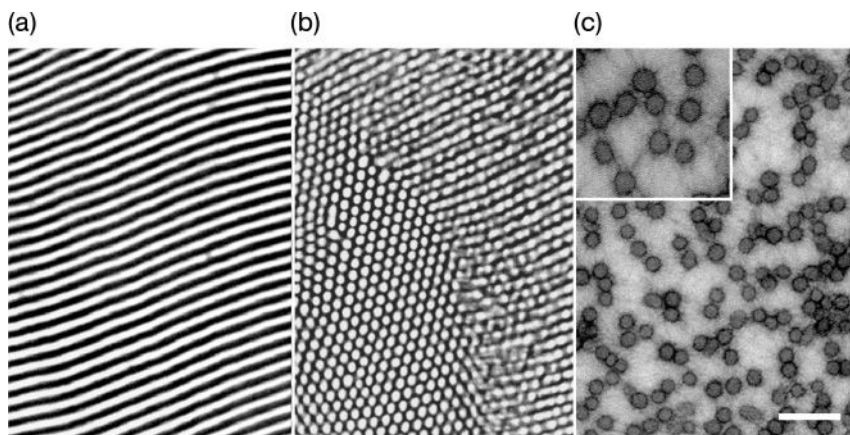
(b) 1.50, and (c) 5.50. The solid lines correspond to model fits, as discussed in the text. Adapted from Ref. [39] and used with permission from John Wiley & Sons, Inc.

diffusive mode has been previously observed [28], and is presumed to correspond to the presence of large-scale heterogeneities (impurities), its origin nonetheless requires further investigation.

Watanabe [40, 41] has developed a dielectric technique to experimentally ascertain the fraction of midblock loops ( $\phi_l$ ) in a triblock copolymer melt or solution. Dielectric properties are dependent on the polarization ( $\mathbf{P}$ ) of the system under investigation, which, in turn, depends on the arrangement of the dipoles present. *Cis*-polyisoprene molecules possess “type-A” dipoles, in which case their dipoles orient parallel to the polymer backbone and  $\mathbf{P}$  is proportional to the chain end-to-end vector. Thus, in a poly(styrene-*b*-isoprene-*b*-styrene) (SIS) triblock copolymer

system, dielectric measurements provide information regarding the relative movement of chain ends. Since the domain boundaries are immobilized in a quiescent state at ambient temperature, the SIS copolymer is dielectrically inert [40]. If dipole inversion is introduced at the center of the midblock,  $\mathbf{P}$  is proportional to the difference between the end-to-center vectors. This type of triblock (abbreviated as SIIS) is dielectrically active even under quiescent conditions. Quantitative comparison of the dielectric behavior of SIIS triblock and matched SI diblock copolymers yields [42] a simple expression for the fraction of looped midblocks ( $\phi_L$ ). For a triblock copolymer dissolved in *n*-tetradecane,  $\phi_L$  is found to decrease from 0.8 to 0.6 as the copolymer concentration is increased from 20 to 50 wt%. The contributions to the overall modulus provided by midblock loops, due to osmotic effects of microlattice formation, and midblock bridges, due to physical crosslinks, measure on the same order of magnitude, with the latter being larger by a factor of 2–3 $\times$ .

A block-selective solvent can induce morphological transitions in block copolymers because it serves to increase the effective volume fraction of the compatible block and reduce the effective  $\chi$  of the system by screening repulsive A–B monomer contacts. Thus, gels initially possessing a lamellar nanostructure will be transformed into gels with micellar nanostructures (cylindrical or spherical) by increasing the solvent fraction [43]. Representative transmission electron microscopy (TEM) images illustrating this morphological progression are provided in Figure 26.5, in which a microphase-separated SIS triblock copolymer swollen to different extents in mineral oil exhibits lamellar (Figure 26.5a), cylindrical (Figure 26.5b), and spherical (Figure 26.5c) morphologies. In these figures, the unsaturated

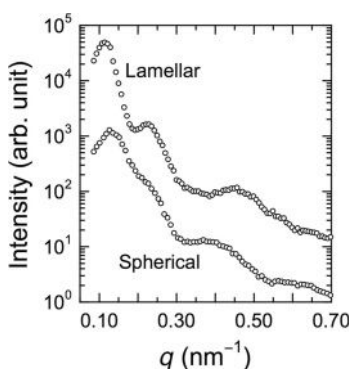


**Figure 26.5** Transmission electron microscopy images of SIS triblock copolymer organogels portraying several morphologies at different copolymer concentrations. (a) Lamellar; (b) Cylindrical; (c) Spherical. In all three images, the isoprenic midblocks are

selectively stained and appear dark. The inset in (c) is an enlargement that evinces the existence of fine structure in the solvent-rich matrix. Scale bar shown in (c) corresponds to 200 nm for (a) and (b), and 100 nm for (c).

isoprenic midblocks are selectively stained and appear dark. In Figure 26.5c, the coronas around the periphery of the micelles are delineated. It is important to recognize that nanoscale strands between and connecting neighboring micelles are evident in this image (and not in images wherein the styrenic endblocks are stained), which suggests that some bundles of bridged midblocks are sufficiently correlated that they become detectable upon staining. Morphological transitions in solvated triblock copolymer systems can be accompanied by abrupt changes in mechanical properties, such as the plateau or tensile moduli [44], and are readily identified by small-angle scattering patterns, such as those shown in Figure 26.6, due to signature peak ratios corresponding to various ordered morphologies [43]. While relatively few studies have systematically addressed the phase behavior of triblock copolymers in the presence of an organic solvent, Lodge and coworkers [19] have broadly scrutinized the effects of solvent concentration and selectivity on the phase behavior of diblock copolymers.

It is appropriate at this juncture to mention that several published reports [45, 46] describe diblock copolymer gels. Diblock copolymer molecules swollen in a selective solvent can self-organize into the same morphologies observed for solvated triblock copolymers, but there remains an important molecular-level difference. In a micellar morphology, for the sake of illustration, diblock copolymer molecules can only adopt a tail topology wherein the solvent-incompatible block forms the micellar core and the solvent-compatible block accounts for the solvent-swollen corona. Intermicellar bridging is not possible. At low copolymer concentrations, such systems behave as suspensions of soft particles. As the copolymer concentration is increased, the micelles order on a cubic lattice, a process that has been referred to as “microlattice structuring” [47]. Watanabe and Kotaka [48] have studied the microlattice formation of SI diblock copolymers in *n*-tetradecane, an I-selective solvent. In moderately concentrated solutions, overlapping coronas



**Figure 26.6** Small-angle X-ray scattering (SAXS) patterns acquired from SEPS triblock copolymer organogels varying in morphology (as labeled) due to differences in copolymer concentration at ambient temperature.

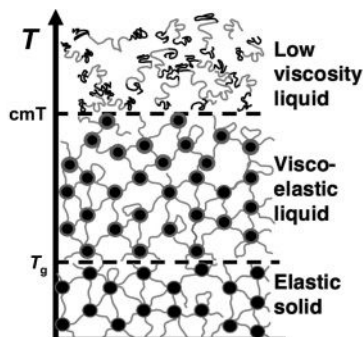
assume random conformations to maximize the conformational entropy, but are forced to maintain a uniform concentration distribution to minimize the free energy. A compromise yields mutually correlated microdomains with overlapping (and thus entangled) coronal blocks. When a small strain is applied, the local variation in concentration promotes an osmotic pressure gradient, which, in turn, generates a restoring force. Micellar solutions of diblock copolymers at moderate or high concentrations are elastic below a “yield” point. These systems, although gel-like at low strains, are not strictly considered organogels, as they undergo relaxation at ambient temperature. The presence of bridges in triblock copolymer organogels serves to increase relaxation times, so that at sufficiently high copolymer concentrations ( $c > c_{gc}$ ) and molecular weights, the copolymer network never relaxes at ambient temperature, which explains why  $G'$  is independent of frequency in rheological tests. Because of the copolymer network, SAMINs derived from triblock copolymers can undergo large strains and subsequently snap back to their original shape, indicating that they possess shape memory.

### 26.2.2

#### Temperature Effects

At ambient temperature, a TPEG behaves as an elastic solid with relatively little hysteresis (i.e., nonrecoverable, or permanent, strain) induced upon cycling. When the temperature is raised above the  $T_g$  of the endblocks, the network-stabilizing crosslinks soften, and the gel transforms into a viscoelastic liquid with a distinct yield stress due to pull-out of endblocks from their microdomains upon deformation. According to dynamic rheological analysis, the glass transition is manifested by a small decrease in the storage modulus ( $G'$ ) and a broad maximum in the loss modulus ( $G''$ ) [49]. Care must be taken, however, not to confuse the endblock glass transition with other copolymer transitions, such as order–order transitions (OOTs), corresponding to morphological transformations, and the order–disorder transition (ODT), sometimes termed the lattice-disordering transition. In the latter case, long-range (lattice) order is replaced by short-range (liquid-like) order, and  $G'$  is observed to drop precipitously. This progression [50] is illustrated schematically in Figure 26.7, in which  $cmT$  denotes the critical micelle temperature (i.e., the temperature at which micelles spontaneously form at constant concentration). Structural transitions such as OOTs and the ODT lie between the  $cmT$  and the endblock  $T_g$ . It must be recognized that all these transition temperatures depend on factors such as endblock size and endblock–solvent compatibility at elevated temperatures [22].

The dynamics of micelles in block copolymer gels have attracted considerable attention. In small-molecule (i.e., surfactant-based) micellar systems, micelle exchange is a well-documented phenomenon [51]. As alluded to above, under favorable conditions, block copolymer organogels can exhibit similar behavior. Watanabe and coworkers [52], for instance, have investigated network disruption and recovery of poly(butadiene-*b*-styrene-*b*-butadiene) (BSB) triblock copolymers



**Figure 26.7** Schematic diagram showing the effect of temperature on the micellar network formed in triblock copolymer organogels. Not included here is the order–disorder transition (ODT), if it exists at the copolymer

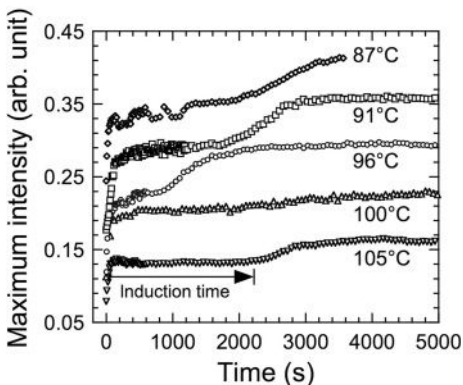
concentration of interest. This progression implicitly presumes that  $c > c_{gc}$ . Adapted from Ref. [50] and used with permission from the American Chemical Society.

in dibutyl phthalate, an S-selective solvent, using dielectric spectroscopy. Unlike conventional TPEGs with endblocks that form glassy crosslinks, solvated systems composed of BSB copolymer molecules consist of soft, deformable crosslinks that can experience chain pullout. When a large stress is applied at ambient temperature ( $T \gg T_g$  of the endblocks), flow is restricted to pre-existing lattice defects. During shear, bridges across the defect plane convert to loops, which has likewise been observed [53] in triblock copolymer melts. This change in chain conformation generates a force that causes the micelles to migrate away from the defect plane. Some loops produced in this fashion mix transiently with the matrix, thereby forming dangling ends. A full recovery of the network upon cessation of shear is achieved when the thermodynamically unequilibrated dangling ends reform into bridges. Thus, the time for recovery is a function of the thermodynamic stability of the dangling end, which is a shear-independent relationship.

Another aspect of organogel dynamics that warrants close examination pertains to the kinetics of ordering and disordering at temperatures in close proximity to the ODT. Bansil *et al.* [54] have employed time-resolved small-angle X-ray scattering (SAXS) to probe the kinetics associated with the nanostructural (dis)ordering of organogels containing 20 wt% poly[styrene-*b*-(ethylene-*co*-butylene)-*b*-styrene] (SEBS) triblock copolymer. In this case, the kinetics of ordering upon cooling are found to be much slower (on the order of hours) than those of disordering upon heating (on the order of seconds). Upon slow cooling ramps, the effective volume fraction of hard spheres deduced from the Percus–Yevick scattering model [55] initially increases to a maximum of  $\sim 0.52$  (indicating an increase in order) near the ODT, and then decreases slowly. At lower temperatures, Bragg peaks become discernible and increase in intensity, indicating that the system has ordered into a body-centered-cubic (bcc) lattice. This change is accompanied by a small, but abrupt, reduction in micelle size. The ordering transition has also been studied by performing a thermal quench from 140 °C (at which the gel is completely dis-

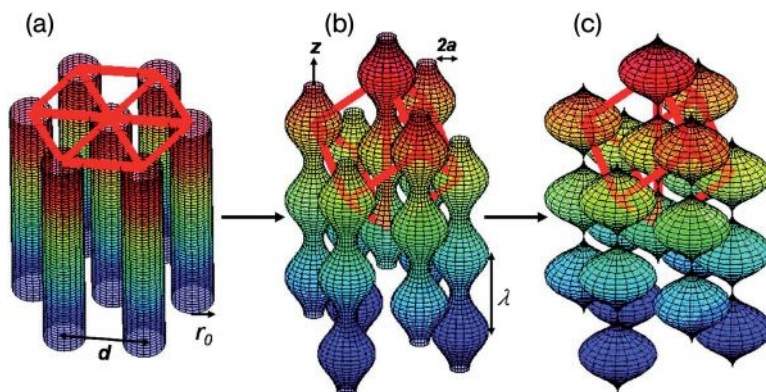
ordered) to a temperature below  $T_{\text{ODT}}$ , but above  $T_g$ . Two distinguishable stages are evident from the results, as shown in Figure 26.8. During an induction period ( $\sim 1000$  s or more after quenching), no change in the maximum SAXS intensity is evident, initially due to thermal equilibration and then to micelle supercooling. An analysis of the scattering curves by the Percus–Yevick model [56] indicates that the hard sphere volume fraction increases to  $\sim 0.53$ , which precedes the appearance of scattering reflections. Nucleation and growth of the ordered nanostructure occur during the second stage of structural development and account for an increase in scattering intensity at Bragg peak positions. The duration of the induction time depends on the depth of the thermal quench, exhibiting a minimum at an intermediate temperature between  $T_{\text{ODT}}$  and  $T_g$ . This observation suggests that a competition exists between the driving force for ordering, which increases at deeper quenches, and chain mobility, which is reduced at lower temperatures.

As alluded to earlier, block copolymer gels subjected to a thermal ramp can, under favorable conditions, also transform from one morphology to another at an OOT temperature. In this case, the initial morphology is either cylindrical or lamellar. Starting with a gel composed of a SEBS triblock copolymer swollen with a midblock-selective solvent and exhibiting the cylindrical morphology, Li *et al.* [57] have examined the transformation kinetics from hexagonally packed cylinders to bcc spheres by performing temperature-jump SAXS. Knowing the OOT and ODT temperatures (127 and 180 °C, respectively) from complementary rheological and SAXS measurements, temperature jumps between the OOT and ODT could be used to follow the mechanism of cylinder  $\rightarrow$  sphere transformation. For temperatures up to  $\sim 145$  °C, this structural evolution proceeds by a three-stage nucleation and growth process. In the first (incubation) stage, the cylinders retain their



**Figure 26.8** Time evolution of the maximum SAXS intensity for a triblock copolymer organogel with 20 wt% copolymer quenched from a temperature above the ODT to different temperatures (as labeled) below the ODT. The induction time (labeled for data

acquired at 105 °C) corresponds to the time before the maximum intensity undergoes a nearly stepwise increase. Adapted from Ref. [54] and used with permission from the American Chemical Society.



**Figure 26.9** Scheme depicting the temperature-induced time evolution of hexagonally packed cylinders to bcc spheres in triblock copolymer organogels. Initial and subsequently modulated cylinders are displayed in (a) and (b), respectively, whereas

cylinder break-up into spheres is portrayed in (c). The solid lines follow the accompanying crystallographic development discussed in the text. Reproduced from Ref. [57] and used with permission from the American Chemical Society.

shape, but a shift in the principal scattering peak indicates a reduction in the distance between cylinders. A critical number of cylinders rupture into modulated spheres during the second stage. These regions serve as nucleation sites to promote further rupture of cylinders and modulation of weakly correlated spheres in an outgoing ripple. Lastly, the spheres order on a bcc lattice so that the (100) plane of the hexagonal cylinders becomes the (110) plane of the bcc spheres and the cylinder axis evolves into the  $\langle 111 \rangle$  direction of the bcc spheres, as illustrated in Figure 26.9. At temperatures beyond  $150^\circ\text{C}$ , the first two stages coincide, and the mechanism commences via spinodal decomposition in which the cylinders transform directly into disordered spheres by correlated ripples. Above the ODT, the temperature jump permits formation of transient bcc spheres prior to disordering. Qualitatively similar results have been reported [58] for the transition from lamellae to cylinders in a triblock copolymer gel consisting of an endblock-selective solvent. Although no studies to date have examined the kinetics of OOTs in block copolymer gels upon cooling, corresponding efforts performed experimentally [59] and theoretically [60] on solvent-free copolymers have likewise revealed that the sphere  $\rightarrow$  cylinder transformation occurs by a nucleation and growth process, the details of which are sensitive to the depth of the thermal quench used to promote the transition.

### 26.2.3

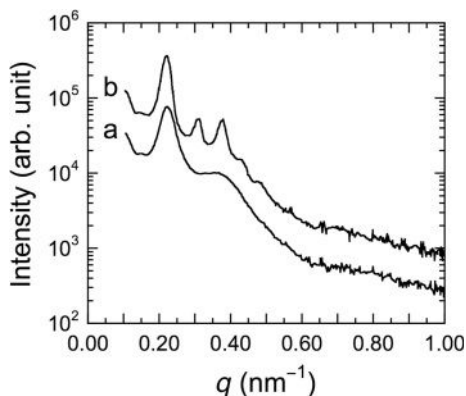
#### Microdomain Alignment

Microdomains that form by molecular self-organization in a block copolymer organogel, such as a TPEG, frequently appear deformed due to interfacial packing frustration that occurs during rapid solvent evaporation or thermal quenching. In either case, specimen processing can promote metastable conformations that



become frozen-in once the endblocks undergo vitrification. It immediately follows, then, that increasing the temperature of such gels above the endblock  $T_g$  should give the endblocks ample opportunity to relax and redistribute, and the nanostructure time to equilibrate. Quenching of such ordered gels to temperatures below the endblock  $T_g$  should again lock-in the morphology, even though it is nonequilibrium at the lower temperature. Independent efforts [32, 61, 62] have explored the effect of annealing on the morphologies and properties of organogels composed of SEBS copolymers. Laurer *et al.* [32] have directly observed moderately improved long-range order in annealed gels by TEM, whereas Soenen *et al.* [61, 62] have reported an increase in the number of peaks in SAXS patterns of gels upon annealing. Although annealing in the melt can enhance the nanostructural order of block copolymer organogels, it remains unclear that long-time annealing serves to either improve their mechanical properties or alter their phase behavior.

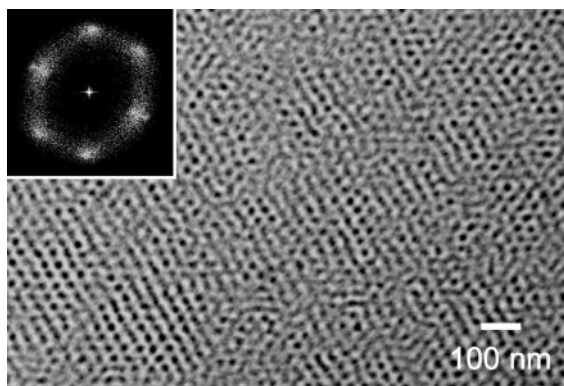
Similar structural results (cf. Figure 26.10) have been purported by Kleppinger *et al.* [63, 64], who have also shown that SAXS patterns acquired from gels, annealed or otherwise, retain a broad structure factor maximum at high temperatures, indicating that network clusters remain. For gels possessing intermicellar distances such that the midblocks behave as statistical coils, an abrupt transformation to the bcc morphology proceeds upon annealing in the melt [65, 66]. This morphology is preserved even after cooling below  $T_g$ . For gels with higher copolymer concentrations and compressed midblocks, the bcc morphology eventually forms upon longer annealing times. In this case, a temperature increase promotes an increase in midblock gyration radius, thus improving orientational order. At lower temperatures, this morphology is nonequilibrium, which may result in lattice distortion due to frustration of close-packed spheres. An alternative route to improved microdomain orientation in block copolymer gels involves shear-



**Figure 26.10** SAXS patterns obtained from triblock copolymer organogels with 20wt% copolymer under two different thermal conditions. (a) Quenched and unannealed; (b) Quenched and annealed at 90°C for 24 h.

The higher-order Bragg diffraction peaks in (b) identify the morphology as bcc spheres. Adapted from Ref. [63] and used with permission from John Wiley & Sons, Inc.





**Figure 26.11** Transmission electron microscopy image of a triblock copolymer organogel composed of 20wt% copolymer and subjected to large-amplitude oscillatory shear to induce nanostructural alignment. In

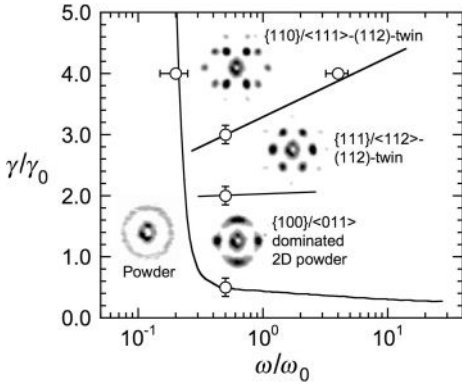
contrast to Figure 26.5, the styrenic endblocks are selectively stained and appear dark. The inset is a 2-D Fourier transform of the image to confirm the high degree of order in this specimen.

induced disordering and reordering [64]. After the gel has been preannealed to form a bcc morphology, a large-amplitude oscillatory shear is applied to disrupt the nanostructure. Upon reordering, the gel exhibits a highly ordered, single-crystal, twinned bcc morphology, as depicted in Figure 26.11. Thus, a combination of thermal and shear treatment can be used to achieve single-crystal order in block copolymer gels. By surveying a range of strain amplitudes and frequencies, Mortensen *et al.* [67] have developed a morphology diagram (cf. Figure 26.12) that establishes the conditions under which block copolymer gels can be highly oriented. Orientation refinement is found to occur only in the frequency range where  $G'' \approx G'$ , and long shear times are required for dislocation planes to form.

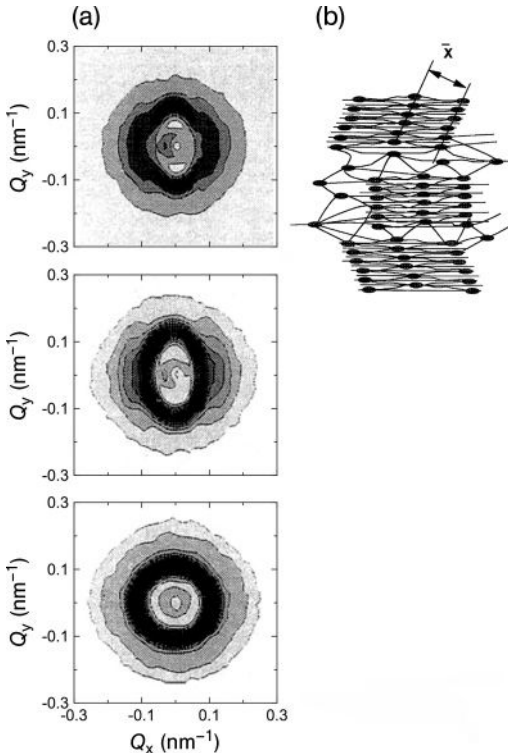
#### 26.2.4

##### Tensile Deformation

Reynaers and coworkers [68] have subjected disordered SEBS and poly[styrene-*b*-(ethylene-*co*-propylene)-*b*-styrene] (SEPS) gels to moderate uniaxial strains (up to 100%) and elucidated the resultant nanostructure by small-angle neutron scattering (SANS), as illustrated in Figure 26.13. Affine deformation of the supramolecular network is observed only at high copolymer concentrations, which favor entanglement of the copolymer midblocks. According to Prasman and Thomas [69], Poisson's ratio must remain constant to achieve affine deformation. At lower copolymer fractions, stretching in one direction up to 100% strain promotes the formation of distinct diffraction spots along the strain direction (Figure 26.13a) and well-defined layers of ordered micelles normal to the strain direction (Figure 26.13b). At higher strains (up to 1000%), however, the corresponding SANS patterns appear markedly different [70]. Between 200 and 400% strain, the patterns



**Figure 26.12** Normalized strain-frequency ( $\gamma\omega$ ) diagram revealing the dynamic shear conditions under which a triblock copolymer organogel can be highly oriented into a twinned bcc spherical morphology. Adapted from Ref. [67] and used with permission from the American Chemical Society.



**Figure 26.13** (a) 2-D SANS patterns of triblock copolymer organogels consisting of 18wt% SEPS copolymer and subjected to different uniaxial tensile strains: (bottom) 0%, (middle) 50%, (top) 100%; (b) A clustered micelle arrangement consistent with

experimental observations that SANS patterns do not change beyond a particular strain level. Adapted from Ref. [14] and used with permission from the American Chemical Society.

become more diffuse, clearly indicating distortion of the regular layers formed at lower strains. Above 400% strain, no structural changes are detectable at the length scales probed by SANS. This observation has been interpreted to mean that (i) the strained network consists of large, discrete clusters similar to those that develop at the sol–gel transition upon initial network formation; and (ii) these clusters vary in the extent of their connectivity. Cluster boundaries, for instance, possess fewer crosslink sites than the clusters themselves, and are thus more deformable than the clusters, which saturate and produce no further structural changes at high strains. Krishnan [71] has employed SAXS to examine the response of SEBS gels to biaxial tensile deformation up to  $300\% \times 300\%$  strain, and has found, by using the Percus–Yevick scattering model [72] incorporating a square-shoulder potential, that the micelles remain (for the most part) spherical and that the micellar coronas increasingly overlap with escalating strain. Kleppinger *et al.* [73] have likewise investigated the conditions responsible for affine behavior when SEBS gels are subjected to uniaxial strain. Affine behavior is observed in unannealed SEBS gels at high extension rates, while nonaffine behavior is dominant at low extension rates. If, however, a gel is preannealed so that the micellar nanostructure exhibits long-range order prior to deformation, then affine behavior is realized even at low extension rates.

Uniaxial tensile deformation of triblock copolymer gels deviates from the predictions of classical rubber elasticity [74], and is therefore often described in terms of the semi-empirical Mooney–Rivlin model [75, 76] that initially was developed for chemically crosslinked elastomers. A more recent attempt to relate the bulk physical behavior of triblock copolymer gels to their underlying nanoscopic network is the STN model [37], as introduced in Section 26.2.1. In this model, the measured nominal (or engineering) stress ( $\sigma$ ) is given by

$$\sigma = \left( G_c + \frac{G_e}{g(\lambda)} \right) \left( \lambda - \frac{1}{\lambda^2} \right) f(\phi, \Phi) \quad (26.5)$$

where  $G_c$  and  $G_e$  denote the contributions of permanent crosslinks and transient entanglements, respectively, to  $G$ . Here,  $g(\lambda) = 0.74\lambda + 0.61\lambda^{-1/2} - 0.35$ , where  $\lambda$  represents the extension ratio, and  $f(\phi, \Phi)$  depends on the concentration of hard filler ( $\phi$ )—for example, glassy micelles, governed by the composition of the copolymer—and the copolymer volume fraction ( $\Phi$ ). Shankar *et al.* [31] have demonstrated that this model can provide valuable insight into molecular factors, such as the copolymer chain length ( $N$ ), that influence gel network formation and properties.

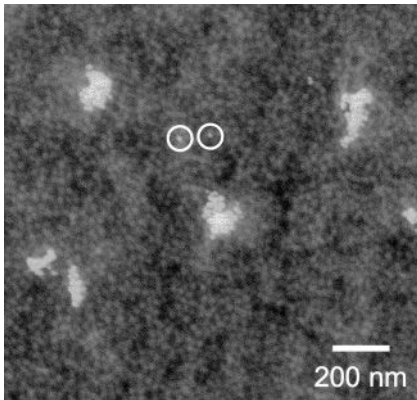
## 26.2.5

### Network Modifiers

#### 26.2.5.1 Inorganic Nanofillers

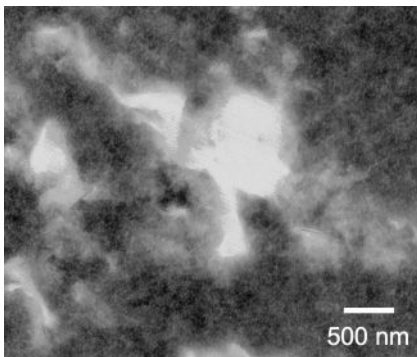
Due to a growing interest in hybrid organic–inorganic nanocomposites [77], several studies [49, 78–83] have recently addressed the effects of inorganic nano-

scale fillers on morphology and property development in block copolymer gels. Electron microscopy images of gels modified with colloidal silica nanoparticles and a surface-modified organoclay are provided in Figures 26.14 and 26.15, and indicate the extent to which the additives disperse, which is of paramount importance with regard to controllable property development. Mechanical properties are generally found to improve when surface-modified silicas [49, 78] and organoclays [78] are incorporated into the gel matrix. Efforts to use carbon nanotubes (CNTs) [78] have yielded less impressive results due to challenges associated with sufficient dispersion. An enhanced modulus is achieved when the additive is more



**Figure 26.14** Energy-filtered TEM image of a triblock copolymer organogel composed of 10wt% SEBS copolymer and modified with 3wt% colloidal silica nanoparticles. The styrenic micelles, stained by the vapor of

$\text{RuO}_4(\text{aq})$ , appear light, whereas the siliceous nanoparticles appear bright, due to imaging at an energy loss of 200 eV. Two neighboring individual nanoparticles are circled.



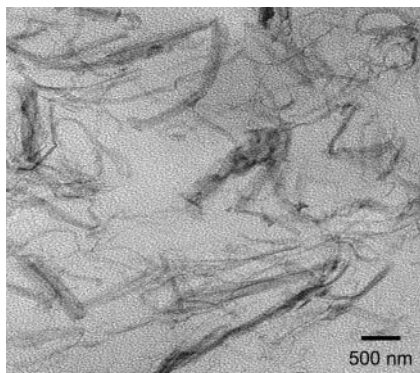
**Figure 26.15** Energy-filtered TEM image of the same triblock copolymer organogel pictured in Figure 26.14, but modified with 3 wt% organoclay. The siliceous clay platelets likewise appear bright due to imaging under the same conditions as those employed in the previous figure.

compatible with the matrix (solvent and midblock), as this renders improved dispersion and, consequently, more efficient stress absorption from the soft phase [49]. Properties are observed [79] to generally improve with increasing nanofiller content, even at surprisingly high (60 wt%) loading levels. The addition of nanoparticles may also expand the mechanical performance and stability of block copolymer organogels at high temperatures, especially if (i) the attractive interactions between the nanoparticles and matrix are particularly strong [49]; or (ii) the nanoparticles themselves form a secondary, load-bearing network that remains thermally stable [78].

#### 26.2.5.2 Polymeric Modifiers

**Endblock-Selective Homopolymer** In the previous section, the addition of inorganic nanofillers to a block copolymer gel resulted in a hybrid material wherein the nanofillers were highly dispersed to yield nearly discrete nanoscale particulates with an ultrahigh surface-to-volume ratio. For this reason, and to avoid macroscopic phase separation between the nanofillers and the gel, only very low nanofiller concentrations can be considered. The addition of an endblock-selective homopolymer to a block copolymer gel can likewise result in several different scenarios, depending on factors such as endblock compatibility, molecular weight disparity, and homopolymer concentration [84]. If the homopolymer is chemically identical (hA) to the endblocks of an ABA triblock copolymer, then only the molecular weight disparity ( $\alpha = N_{\text{hA}}/N_{\text{A}}$ ) and hA concentration constitute key design parameters. As in solvent-free block copolymers, if  $\alpha$  is large ( $>1$ ), the hA molecules will not be physically accommodated within the brush comprising the A-rich microdomains. In this case, the brush is said to remain *dry* due to the lack of penetration of homopolymer molecules [85]. This entropic penalty favors macrophase separation between the copolymer and homopolymer molecules even at relatively low hA concentrations. In this limit, hA-rich domains measuring on the order of micrometers or larger coexist with the gel network, and the accompanying mechanical properties are largely dictated by the separating interface. The incorporation of semicrystalline syndiotactic polystyrene (sPS) into a SEBS gel, for example, results in the formation of discrete sPS crystals, which appear as filaments and sheets (cf. Figure 26.16) that greatly improve the modulus due to adhesion between the crystals and the styrenic micelles [86].

As  $\alpha$  becomes smaller, however, due to a reduction in  $N_{\text{hA}}$  or an increase in  $N_{\text{A}}$ , the smaller hA molecules can locate within the A-rich microdomains and *wet* the compatible block brush. In this limit, added hA can serve to facilitate, or even induce, copolymer micellization because of the corresponding increase in the population of unfavorable A–B contacts [87], and it can likewise promote a change in interfacial curvature and, hence, gel morphology [88, 89]. Mechanical properties are found [90] to generally improve with increasing hA fraction up to a molecular-weight-dependent level, beyond which macrophase separation occurs. One way to lessen the propensity for macrophase separation and to ensure the encapsulation of a homopolymer within the endblock-rich microdomains responsible for stabiliz-

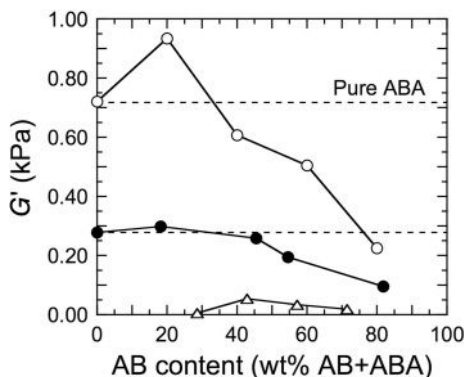


**Figure 26.16** TEM image of a triblock copolymer organogel composed of 8.5 wt% SEBS copolymer and 1.5 wt% syndiotactic polystyrene (sPS). The styrenic micelles and

crystalline sPS sheets and filaments are both selectively stained and appear dark. Adapted from Ref. [86] and used with permission from the American Chemical Society.

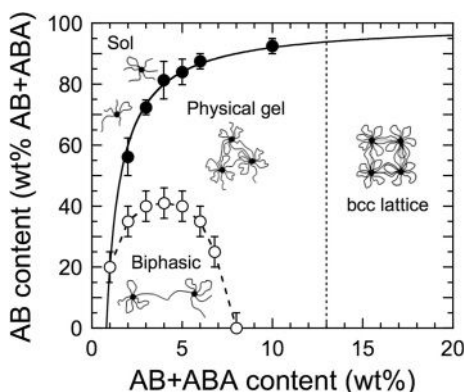
ing the gel network is to increase the homopolymer/endblock compatibility. In the case of gels composed of styrenic triblock copolymers (i.e., copolymers with PS endblocks), poly(2,6-dimethyl-1,4-phenylene oxide) (PPO) constitutes an ideal candidate in this regard, since  $\chi$  between these two polymers is negative over all compositions and a large temperature range [91]. Moreover, since PPO possesses a relatively high  $T_g$  ( $\sim 210^\circ\text{C}$ ), it may be added to improve the service temperature of styrenic SAMINs [92]. This increase has been reported [93] to be as high as  $\sim 30^\circ\text{C}$  upon the addition of 3 wt% PPO to a SEBS gel. At higher loading levels, the mechanical properties improve substantially and morphological transitions can be expected [91].

**Cosurfactant** Although a variety of midblock-selective homopolymers can be blended into block copolymer gels (e.g., polyolefins such as polypropylene [94] added to gels with a primarily aliphatic solvent) to modify process or application properties, such modification normally results in the formation of macrophase-separated systems consisting of homopolymer-rich and gel-rich domains that are discrete or cocontinuous, depending on the relative concentrations. For this reason, such multicomponent systems are not considered further here. Another means by which to alter gel properties at the molecular level involves the addition of an AB diblock copolymer as a cosurfactant to the ABA triblock copolymer network. In this scenario, the AB molecules, if sufficiently incompatible, are forced to coreside with their ABA analogues, resulting in submicrodomain stratification [95]. Due to the presence of AB molecules, the ABA molecules are entropically forced to form bridges (rather than re-enter to form loops) due to coronal volume exclusion, in which case addition of an AB copolymer in small quantities can improve mechanical properties even when  $c < c_{gc}$  for the parent ABA solution (cf.



**Figure 26.17** Dependence of  $G'$  on the fraction of AB diblock copolymer added to triblock copolymer organogels and solutions varying in total copolymer concentration (in wt%): 15 (○), 11 (●), and 7 (△). Note that a frequency-independent modulus indicative of

a gel network is not achieved in the system with 7 wt% copolymer until the diblock copolymer is added. The solid lines serve to connect the data. Adapted from Ref. [96] and used with permission from the American Chemical Society.



**Figure 26.18** Experimental phase diagram for an ABA triblock copolymer organogel modified with an AB diblock copolymer. The lines serve as guides for the eye. Adapted from Ref. [29] and used with permission from John Wiley & Sons, Inc.

Figure 26.17) [96, 97]. Complementary SAXS studies performed by Vega *et al.* [29] reveal that the presence of an AB copolymer could help to prevent macrophase separation due to a reduction in intermicellar distance, and could, in general, be used to tune to the phase behavior of the system (cf. Figure 26.18).

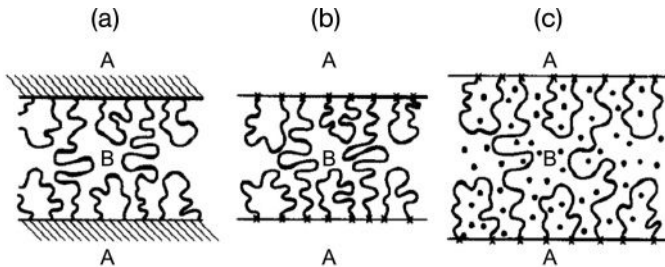
### 26.2.6

#### Nonequilibrium Mesogels

Thermoplastic elastomer gels are normally prepared by mixing a triblock copolymer and a low-volatility solvent, with or without a carrier solvent (to reduce viscos-

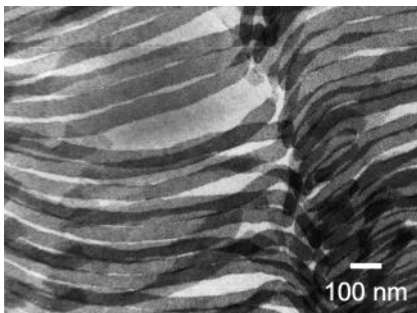


ity during mixing and evaporate thereafter), at elevated temperatures and then cooling the solution below the endblock  $T_g$  to induce glassy crosslinks that serve to stabilize the gel network. An alternative approach to preparing gels from the same copolymer and solvent pair is to introduce a solvent directly into the ordered copolymer by diffusion at temperatures below the endblock  $T_g$ . As the solvent-incompatible endblocks—and hence their microdomains—are glassy, they do not dissolve as the midblocks swell. Midblock swellability depends on both the solubility of the solvent in the midblock and the extent to which the midblocks stretch (which is entropically unfavorable), as shown schematically in Figure 26.19. Gels produced in this fashion from an ordered copolymer have been referred [99] to as “mesogels” because they retain the characteristics of the neat copolymer mesophase, since fabrication occurs under nonequilibrium conditions. King *et al.* [100] have observed that, on progressive swelling, such gels derived from a copolymer possessing the lamellar morphology retain highly swollen lamellae, as evidenced by the TEM image shown in Figure 26.20, even at solvent concentrations that



**Figure 26.19** Schematic illustration of the procedure to generate lamellar mesogels from midblock-selective solvation of ABA triblock copolymers. (a) Microphase ordering of the copolymer from solvent casting or melt processing; (b) Reduction in temperature so

that the A lamellae are rigid (i.e., glassy or semicrystalline); (c) Diffusion of solvent into the B lamellae to induce swelling while retaining a layered morphology. Reproduced with permission from Ref. [98]; © American Chemical Society.



**Figure 26.20** Transmission electron microscopy image of a triblock copolymer mesogel demonstrating that the procedure depicted in Figure 26.19 yields intact styrenic

lamellae (stained) in a solvent-swollen midblock matrix. Reproduced with permission from Ref. [100]; © American Chemical Society.



would have otherwise induced morphological transformations. Li *et al.* [101] have expanded earlier theoretical efforts [98, 99, 102] designed to model mesogels in terms of swollen brushes by simulating the equilibrium swelling volume fraction as a function of morphology, bridge fraction and midblock–solvent interaction parameter. It is interesting to note that the extension and compression behavior of lamellar mesogels are predicted [102] to be dissimilar. During extension, chain elasticity dominates, whereas osmotic pressure governs compression. In general, however, mesogels tend to exhibit improved mechanical properties (expressed in terms of modulus [100]) relative to their equilibrium counterparts at the same gel composition.

## 26.2.7

### Special Cases

#### 26.2.7.1 Liquid Crystals

Generally speaking, liquid crystals (LCs) can be envisaged as anisotropic, rod-like molecules that are capable of developing orientational and/or positional order in the liquid state [103]. Of the three commonly encountered types of liquid crystalline mesophases reported (nematic, smectic and cholesteric, or twisted nematic), the nematic, wherein the molecules align along a single direction with no positional order, constitutes the simplest [104]. *Thermotropic* LCs are temperature-sensitive, and an increase in temperature causes the nematic mesophase to disorder into an unstructured, isotropic liquid. Kornfield and coworkers [105] have successfully synthesized thermoresponsive triblock copolymer gels containing a midblock-selective LC solvent. To ensure sufficient compatibility between the copolymer and nematic solvent (4-cyano-4-*n*-pentylbiphenyl; known commercially as 5CB) and to avoid macrophase separation, the copolymer molecule is designed to have glassy (styrenic) endblocks and a midblock functionalized with a nematic side group. In this case, the copolymer midblock is soluble in both the LC and isotropic phases of 5CB. At low copolymer concentrations, the copolymer endblocks are soluble in the isotropic phase, but aggregate in the nematic phase due to endothermic mixing and a low entropy of mixing. Unlike isotropic solvents, in which the solvent quality changes gradually with temperature, this LC solvent undergoes an abrupt change in solvent quality at the relatively sharp isotropic  $\rightarrow$  nematic phase transition [106]. In essence, the gel exhibits an “on–off” LC response at this transition temperature, thereby imparting the gel with added functionality. At higher copolymer concentrations (20 wt%), the endblocks also become insoluble in the isotropic phase of 5CB, in which case the gel network remains intact even at temperatures above the nematic  $\rightarrow$  isotropic transition. Mesogels of LC triblock copolymers swollen by a nematic solvent have likewise been investigated [107]. An interesting finding is that the modulus of the gel can be reversibly changed by applying an electric field. The gel can also be sheared by applying a field above a certain threshold value, thus evincing quasi-piezoelectricity.

### 26.2.7.2 Ionic Liquids

Ionic liquids (ILs) constitute an emerging class of functional compounds that exhibit electrical conductivity and possess negligibly low vapor pressure, as well as broadly tunable physical properties [108]. Lodge and coworkers [26] have fabricated thermoreversible block copolymer gels by dissolving a poly(styrene-*b*-ethylene oxide-*b*-styrene) (SEOS) triblock copolymer in an IL at elevated temperatures, and allowing the glassy endblocks to self-organize and vitrify upon cooling. The IL used in this study remains liquid at ambient temperature. It is interesting to note that the same type of copolymer, with a polar midblock, has been used [109] to prepare mesogels in conjunction with poly(ethylene glycol) (PEG) for enhanced carbon dioxide separation. Characterization of the IL-based copolymer gel, for which the cgc is 4 wt% at 10 °C, reveals that the temperature dependence of the ionic conductivity is comparable to that of the bulk ionic liquid in the absence of the copolymer network. Similar gels have also been produced [110] with a poly(*N*-isopropyl acrylamide-*b*-ethylene oxide-*b*-*N*-isopropyl acrylamide) triblock copolymer, which possesses temperature-sensitive endblocks. Gelation in this system can be induced due to the lower critical solution temperature (LCST) behavior of the endblock in the IL solvent. Pioneering efforts such as these are charting the course for future research in the bottom-up design of conductive gels, especially as the copolymers and solvents can be further modified to improve both electrical and mechanical properties.

### 26.2.7.3 Multiblock Copolymers

Thus far, nanostructured organogels composed exclusively of ABA triblock copolymers have been considered. Multiblock copolymers generically designated as  $(A_nB_n)_m$  copolymers are likewise expected to form stabilizing network structures in an A- or B-selective solvent. Similar to triblock copolymer gels containing cosurfactant (diblock copolymer) molecules (cf. Section 26.2.5.2), each microdomain in a multiblock copolymer consists of dangling endblocks, as well as looped and bridged midblocks, in proportions that depend only on  $n$  [111]. While the morphological and property attributes of solvent-free multiblock copolymers have received considerable attention [112, 113], few studies have explored the utility of well-defined multiblock copolymer gels. Bansil and coworkers, for instance, have examined an ABABA pentablock copolymer in two different solvents: 1,4-dioxane [114], a slightly good solvent for A and a  $\theta$  solvent for B; and *n*-hexane [115], a strongly selective solvent for the B blocks. In 1,4-dioxane solutions, the marginally less-soluble B blocks appear to be physically connected by swollen A blocks. An interesting result is that a gel network does not develop in these solutions, even at the highest copolymer concentrations studied, due possibly to (i) an insufficiently low fraction of microphase-separated B blocks; or (ii) insufficient solvent selectivity. In the presence of *n*-hexane, macrophase separation occurs at low copolymer concentrations, whereas gelation is accompanied by solvent expulsion at higher concentrations. Gindy *et al.* [116] have attempted to explain this result by performing Monte Carlo simulations and have proposed that, in dilute solutions, macrophase separation occurs when the ratio  $m/n$  exceeds a critical value (as observed

experimentally in *n*-heptane). Gelation at higher copolymer concentrations is attributed to the association of collapsed insoluble microdomains, similar to multiplets in ionomers. More complicated gel systems derived from randomly coupled multiblock copolymers possessing broad block and chain polydispersities (e.g., polyurethanes [117]) have likewise been generated and studied, but their nanostructures are typically not well-defined, which is why they are not considered further here.

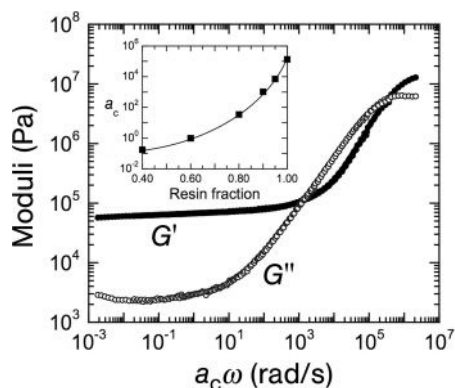
#### 26.2.7.4 Cosolvent Systems

Although ABA triblock copolymer gels normally consist of a single, low-volatility solvent that is selected to be sufficiently B-selective and A-incompatible, a mixture of miscible solvents can certainly be employed to fine-tune solvent quality and controllably alter the phase behavior and physical properties of the resultant gel [118]. More recent studies [71] have demonstrated that this strategy can likewise be used to adjust the time-responsive dynamic nature of such gels. The addition of a triblock copolymer to a saturated tackifying resin, which possesses saturated ring groups and a  $T_g$  near or slightly above ambient temperature, yields a time-dependent viscoelastic system that, upon uniaxial or biaxial deformation, slowly returns to its original shape. In this case, the elastic restoring force of the copolymer network is thwarted by the high viscosity of the solvent matrix. Results acquired from dynamic rheology confirm that both  $G'$  and  $G''$  are strong functions of frequency, indicating that these systems are not gels according to the rheological criteria listed earlier. The addition of a low- $T_g$  aliphatic oil to the system, however, results in a composition-dependent progressive shift of the frequency spectrum to higher frequencies. This apparent time-composition equivalence is similar in effect to time-temperature equivalence [5] and permits the construction of a superpositioned frequency spectrum over a broader range than could be measured experimentally (cf. Figure 26.21). As frequency relates to reciprocal time, the behavior of the cosolvent gel at very long or very short times can be accurately assessed at ambient temperature by simply changing the cosolvent composition.

### 26.3

#### Organic Gelator Networks

Organic gelling agents, or *gelators*, with molecular masses of less than  $\sim 2 \text{ kg mol}^{-1}$  are referred to as low molar-mass organic gelators (LMOGs), and constitute a growing class of compounds that provides fundamental insight into molecular self-organization and practical use for applications requiring responsive materials [1, 119, 120]. In stark contrast to solvated block copolymers that form gels by microphase separation, LMOGs are generally classified according to their molecular structure and the intermolecular interactions that promote physical gelation. In this case, the organogel networks are stabilized via noncovalent physicochemical interactions such as hydrogen bonds,  $\pi$ - $\pi$  stacking, or London dispersion forces. As with block copolymer gels, gels produced by LMOGs are thermorevers-

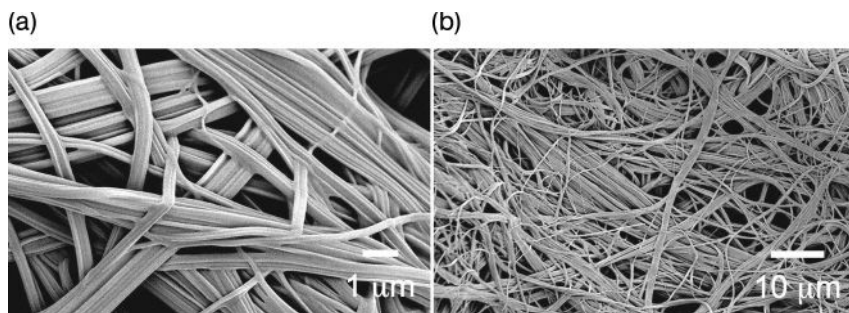


**Figure 26.21** Frequency spectra shown as master curves for  $G'$  and  $G''$  measured from triblock copolymer organogels composed of 25 wt% copolymer and a cosolvent (mineral oil/tackifying resin) that varies in composition, thereby demonstrating that a

ternary SAMIN system exhibits time–composition equivalence. The composition-dependent shift factor ( $a_c$ ), determined using a reference composition of 60 wt% tackifying resin, is included as a function of resin fraction in the inset.

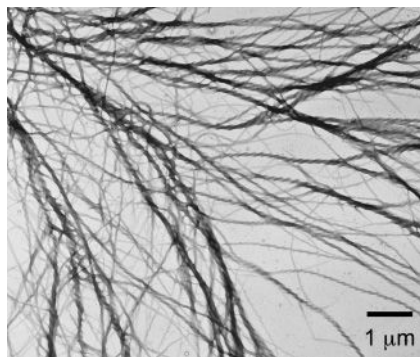
ible, in which case the load-bearing networks dissolve into the surrounding liquid matrix upon heating above a composition-dependent dissolution temperature ( $T_{\text{dis}}$ ), but reform upon cooling. Physical gels are typically generated by first heating a relatively low concentration (typically a few percent by mass) of the LMOG in an organic solvent or low- $T_g$  polymeric liquid until all the components become a solution, or *sol*, and then cooling the sol to below the gelation temperature ( $T_{\text{gel}}$ ). The value of  $T_{\text{gel}}$  is identified as the temperature at which flow is no longer discernible over long periods [119]. It is important to recognize that  $T_{\text{gel}}$  is generally lower than  $T_{\text{dis}}$ , since more thermal energy is required to break apart and dissolve the gel network than to form it. Conversely, gel network formation may require a finite degree of supercooling to initiate either (i) crystallization; (ii) precipitation; or (iii) aggregation of the LMOG, thereby producing a gel [121].

The resultant gels consist of 3-D self-assembled fibrillar networks (SAFINs) that are characterized by entangled nanoscale fibrils exhibiting a high surface-to-volume ratio. These networks have been visualized by a variety of imaging methods, including scanning electron microscopy (SEM), TEM and atomic force microscopy (AFM). Representative examples of SEM [122] and TEM [123] images of SAFINs are provided in Figures 26.22 and 26.23, respectively, and demonstrate that the fibrils can range in size from nanometers to micrometers in width, and from micrometers to millimeters in length. Due to the large solid–liquid interfacial area, the matrix solvent is effectively entrapped by capillary forces within the network. At the macroscopic level, the total volume of solvent is immobilized, resulting in a solid-like material [124]. Because the networks do not consist of long, elastic chains (as in block copolymer gels), LMOG-based gels tend to be exquisitely shear-sensitive, and their networks readily break apart during steady or large-amplitude



**Figure 26.22** Scanning electron microscopy images collected at (a) high and (b) reduced magnification from a polycatenar organogel consisting of 3 wt% gelator, illustrating the

morphology representative of SAFIN organogels. Reproduced with permission from Ref. [122]; © American Chemical Society.



**Figure 26.23** Transmission electron microscopy image acquired from a 1-acetonitrile organogel consisting of 0.07 wt% gelator, confirming the existence of nanofibrils (measuring 40–70 nm in diameter),

some of which exhibit helical twist with a pitch of ~150 nm. To improve contrast, the nanofibrils have been selectively stained. Adapted from Ref. [123] and used with permission from John Wiley & Sons, Inc.

oscillatory shear, but reform upon cessation of shear. The kinetics of network healing depend on the chemistry (and interaction mechanism) of the LMOG, the concentration of the LMOG, and the quality of the solvent matrix. As gels produced with LMOGs depend on specific intermolecular interactions, this section is divided into three types of interactions that LMOGs require to promote physical gelation, namely hydrogen bonding,  $\pi$ - $\pi$  stacking, and London dispersion forces.

### 26.3.1

#### Hydrogen Bonding

Hydrogen bonding is the attractive force that exists between an electronegative atom and a hydrogen attached to another electronegative atom, thereby imparting the hydrogen with a partial positive charge. The electronegative atom must possess

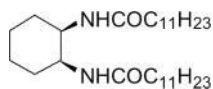
one or more unshared electron pairs, and thus has a partial negative charge. Hydrogen bonding can occur *intermolecularly*, between molecules, or *intramolecularly*, between parts of the same molecule. Hydrogen bonding is weaker than covalent or ionic bonds, but stronger than van der Waals forces. Originally thought to be a random event, hydrogen bonding constitutes an example of a highly ordered occurrence and is ubiquitous throughout nature [125, 126]. Characteristics that are common to almost all gelators include [123]:

- Molecular factors, such as the presence of long alkyl substituents, that promote one-directional growth which prohibits the formation of 3-D crystal structure.
- The ability of SAFINs to branch and entangle, often due to active functional groups that promote intermolecular interactions, and thus develop a 3-D network capable of immobilizing the solvent.
- At least one chiral center within the molecule.

It should be noted that, while this list provides guidelines for known gelators, the existence of any or all of these traits in a molecule does not guarantee that it can gel organic solvents. Meléndez *et al.* [127] have suggested three common features of efficient gelators that self-assemble via hydrogen bonding: (i) the presence of one or more hydrogen-bonding groups; (ii) long alkyl substituents; and (iii) stereogenic centers within the molecule. Although these types of interaction unquestionably contribute to the ability of a molecule to induce gelation, this section focuses on the functional groups, chirality, and the self-aggregated structure of several important families of gelators. The aim here is to identify the common features that are responsible for gelation, and to classify LMOGs on the basis of their chemical similarity. As it is not possible to include all gelators at this point, several excellent reviews [119, 128, 129], each dedicated to LMOGs and their organogels, are recommended to the reader.

#### 26.3.1.1 Amides

The presence of two electronegative atoms in amides allows them to produce highly ordered hydrogen-bonded networks that can extend in linear arrays, as well as form eight-membered ring dimers [130]. The addition of long alkyl chains to an amide can help to prevent crystallization [123], thereby resulting in an effective gelling agent. Cyclic amide derivatives possessing butyl chains, for instance, are less effective at promoting gelation than the same derivatives with chains possessing ten or more carbons [131]. The formation of extended molecular sheets due to gelation of a diaminocyclohexane constitutes another example of how hydrogen bonding promotes the entanglement of SAFINs through complementary functional groups [123]. Chirality in amides can also play a critical role when determining which enantiomeric form can induce gelation in an organic or organic-containing solvent. *Trans*-cyclohexane-1,2-diamide (see Figure 26.24) is an efficient gelator of polydimethylsiloxane (silicone) oil and liquid paraffin, whereas the *cis* enantiomer is unable to produce a gel [132]. This difference in gelling efficacy is attributed to the fact that the *trans* molecule can exist in an anti-parallel arrangement that



**Figure 26.24** Chemical structure of *trans*-cyclohexane-1,2-diamide, an example of an efficient LMOG for SAFIN organogels.

maximizes the self-complementary interaction of hydrogen-bonding groups. Other types of amide gelators include aromatic polyamides [133], synthetic peptides [134], and perfluorinated amides [135].

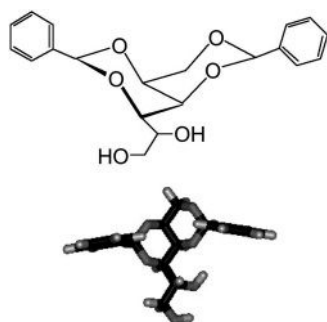
#### 26.3.1.2 Ureas

Ureas (also referred to as *carbamides*) have attracted much attention as another family of LMOGs. More specifically, bis-urea molecules have been used as organic gelators that assemble into thin rectangular sheets by hydrogen bonding and form thermoreversible gels [136]. Similar to many other organic gelators, only one enantiomeric form, *trans* bis-urea, is capable of promoting gelation because, unlike its *cis* analogue, it can self-aggregate into an anti-parallel arrangement and thus form linear aggregates [137]. A practical challenge with urea gelators is that the minimum temperature, at which the gels are stable, is much higher than ambient temperature ( $\sim 100^\circ\text{C}$ ) [127]. Hamilton [138] has, however, successfully established that a group of bis-urea–amino acid conjugates can gel solvents as low as  $5^\circ\text{C}$ , which is unique for this molecule and highly advantageous for industrial applications. “Spacer” moieties such as azobenzenes, thiophenes and bithiophene groups have been incorporated between two urea molecules to synthesize new urea-based gelators [139–141]. These designer molecules self-assemble into highly ordered monolayers by hydrogen bonding between the urea groups [137].

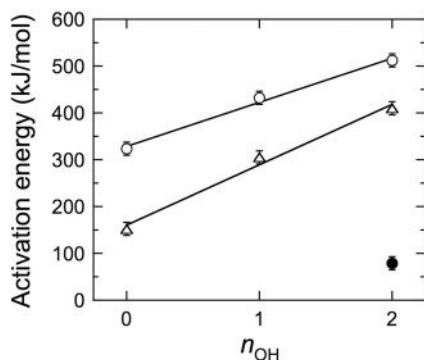
#### 26.3.1.3 Sorbitols

Sorbitol is a sugar alcohol used in diverse applications in the food and medical industries. One commercial derivative of sorbitol is 1,3:2,4-dibenzylidene sorbitol (DBS), which is an effective LMOG due to its solubility in a broad range of organic solvents and polymers at elevated temperatures and the low concentrations of DBS necessary to induce gelation. The DBS molecule (Figure 26.25) is both chiral and amphiphilic, and is often described as “butterfly-like” due to its sorbitol body and two phenyl “wings.” The two hydrophobic phenyl groups are largely responsible for the solubility of DBS in various polymers and organic solvents, while the hydroxyl and acetal oxygen functionalities induce intermolecular hydrogen bonding between DBS molecules, resulting in nanofibril formation [142]. Network formation is achieved by the aggregation of DBS nanofibrillar strands or bundles, which is strongly influenced by both DBS concentration and solvent polarity [143]. The primary unit size of DBS nanofibrils has been repeatedly measured to be about 9–10 nm in diameter. Using dynamic rheology, Wilder *et al.* have investigated the time–temperature equivalence principle of DBS in polypropylene glycol and PEGs differing in endblock chemistry and, hence, polarity [144]. The extraction of activation energies from shift factors discerned during the analysis reveals





**Figure 26.25** Chemical structure (top) and energy-minimized molecular configuration (bottom) of the commercial gelator 1,3:2,4 dibenzylidene sorbitol (DBS).



**Figure 26.26** Activation energy discerned as a function of solvent polarity (expressed in terms of the number of hydroxyl endgroups,  $n_{OH}$ ) from the time–temperature equivalence of frequency spectra collected from DBS organogels containing functionalized polyethylene glycol at two different DBS concentrations ( $\circ$ , 2 wt%;  $\triangle$ , 5 wt%) and polypropylene glycol ( $\bullet$ ) at a DBS concentration of 0.4 wt%. The solid lines are linear regressions of the data.

that DBS gelation is most energetically favored (with relatively low activation energies) in nonpolar solvents (cf. Figure 26.26).

The reason for this behavior is that, as the polarity of the solvent increases, the DBS molecules can hydrogen bond—even if only transiently—with solvent molecules rather than with other DBS molecules, thus reducing the gelation effectiveness and increasing the time required for gelation. Although through independent experimental and theoretical efforts, much insight has been gained into the macroscopic properties of DBS organogels, little is known regarding the precise molecular mechanism by which DBS induces gelation. Since *D,L*-DBS, a racemate of DBS with equal mixtures of *D* and *L* forms, is unable to form gels [145], the chirality of the DBS molecule appears to constitute a critical consideration in elucidating the self-assembly behavior of DBS molecules. Fourier-transform infrared (FTIR) spectroscopy has likewise confirmed that DBS molecules self-assemble via hydro-



gen bonding by the appearance of a broad spectral peak at  $3250\text{ cm}^{-1}$  [145, 146], although molecular modeling [143] suggests that phenyl stacking may also play an important role. One of the reasons why DBS is singled out here, other than its commercial availability, is that it is capable of inducing gelation in both nonpolar solvents and molten polymers [147] at relatively low concentrations (ca. 0.25 wt%), which makes it attractive for scientific enquiry and technological applications.

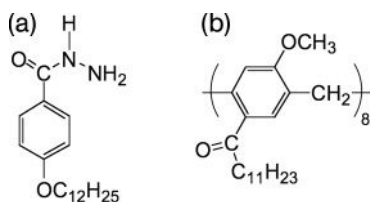
#### 26.3.1.4 Miscellaneous LMOG Classes

*Hydrazides* are hydrazine derivatives possessing a N–N covalent bond with four substituent groups, at least one of which is an acyl group. Tan *et al.* [148] have reported that long-chain substituted benzoic acid hydrazides (cf. Figure 26.27a) can form stable gels in organic solvents. Spectroscopic analysis confirms that the molecules self-assemble via hydrogen bonding due to the synergistic interactions between the carbonyl and amine groups, and the growth of the resultant SAFINs in one dimension is attributed to self-alignment of the long alkyl group. Although it is typically essential that LMOGs possess a chiral center, Bai *et al.* [149] have successfully synthesized achiral hydrazides. These compounds, composed of a core hydrazide unit with three exterior alkoxy chains of varying length, self-assemble due to intermolecular hydrogen bonding into columnar aggregates that are capable of efficiently gelling a variety of nonpolar organic solvents. *Calixarenes*, which are cup-shaped LMOGs characterized by several repeat units (each of which possesses a long acyl group at the *para* position of an aromatic ring; see Figure 26.27b), have likewise been shown [150] to generate stable gels in organic liquids such as alkanes, alcohols, carbon tetrachloride, and aromatic solvents. Physical gelation due to hydrogen bonding is attributed to the carbonyl in the acyl group, since alkyl groups in the *para* position do not gel common organic liquids. Because of the large number of possible binding sites available on calixarenes, the addition of metal ions provides a viable route by which to produce stable metalogels [151].

#### 26.3.2

##### $\pi$ - $\pi$ Stacking

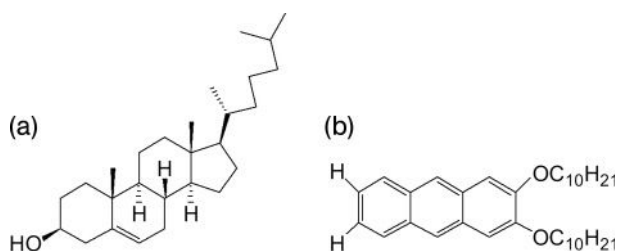
Aromatic interactions, also known as  $\pi$ - $\pi$  stacking, refer to noncovalent intermolecular interactions between organic compounds that contain phenyl units. This type of interaction is caused by overlapping *p*-orbitals in  $\pi$ -conjugated systems,



**Figure 26.27** Chemical structures of two LMOGs with long alkyl-chain substitution. (a) A benzoic acid hydrazide; (b) A calixarene.

and  $\pi$ - $\pi$  interactions are strongest for flat, polycyclic aromatic hydrocarbons such as anthracene, triphenylene or coronene, due to the numerous delocalized  $\pi$ -electrons residing in these molecules. Sufficiently strong interactions may develop between coplanar aromatic rings so that these groups on neighboring molecules stack, in which case the molecules consequently self-assemble to form SAFINs. One of the most diverse classes of LMOGs that rely on  $\pi$ - $\pi$  stacking for network formation derives from the cholesterol, a steroid of which the backbone consists of hydrocarbons arranged in three six-membered rings and one five-membered ring (cf. Figure 26.28a). Although cholesterol is amphiphilic due to a polar hydroxyl head group and hydrophobic body and tail groups, it alone is incapable of gelling organic liquids. Relatively simple synthetic derivatives of cholesterol, however, constitute excellent examples of LMOGs. Lin *et al.* [152, 153] have established that molecules composed of an aromatic (A) unit connected to a steroidal (S) group through a functionalized linkage (L) serve as efficient and predictable ALS-type gelators, and numerous variations of the ALS design motif have been investigated since its introduction. The aromatic group is essential for gelation to ensure  $\pi$ - $\pi$  stacking. On a side note, the delocalized  $\pi$ -electrons in the aromatic ring may likewise impart resultant organogels with electronic and optical properties that provide added functionality. While the stacking of aromatic units in ALS-type molecules is generally responsible for the formation of linear aggregates, cholesterol derivatives, in particular, tend to self-assemble so that the aromatic groups are arranged helically, facing outward, at the periphery of a columnar core, as experimentally verified by the AFM observations of Song *et al.* [154, 155].

Even if the linker between the A and S segments is relatively long, ALS-type LMOGs still produce stable organogels due to  $\pi$ - $\pi$  interactions. The development of intercolumnar aromatic-aromatic interactions further stabilizes the gel network. Other factors affecting the stability of the gel network include the size and shape of the aromatic group. For example, large porphyrin rings or simple phenyl rings yield relatively weak gels unless they are simultaneously stabilized by other intermolecular interactions induced by (i) coexisting functionalities to promote, for



**Figure 26.28** Chemical structures of two highly aromatic compounds used as LMOGs alone or modified.

(a) Cholesterol, which requires derivatization (cf. the ALS approach discussed in the text); (b) 2,3-di-*n*-alkoxyanthracene, which can gel polar solvents.

instance, hydrogen bonding [143]; or (ii) chemical additives such as metal ions, amines or nucleobases [156]. It is interesting to note that the sol–gel transition in ALS systems can be controlled by UV irradiation, as well as by temperature. The *trans*-isomer of an azobenzene ALS, for example, is able to promote gelation of organic solvents. Upon irradiation, it switches to the *cis*-isomer, which is incapable of producing a gel [157]. Over the past decade, cholesterol-based gels have become more chemically complex through the strategic incorporation of inorganic complexes [158, 159], novel linker groups [160, 161], and multiple LS moieties [124]. In the event that gelation relies exclusively on aromatic interactions, however, LMOGs such as dialkoxybenzenes (cf. Figure 26.28b) perform more effectively if they are symmetrically substituted [162, 163]. Using SANS, Terech *et al.* [164] have ascertained that the molecules which fit into this classification tend to self-assemble into bundles possessing a hexagonal or square symmetry, which suggests that the molecules are shifted radially to maximize  $\pi$ – $\pi$  interactions. Unlike other LMOGs that rely to different extents on hydrogen bonding, these molecules form gel networks solely on the basis of nonpolar interactions and can thus gel polar organic liquids.

### 26.3.3

#### London Dispersion Forces

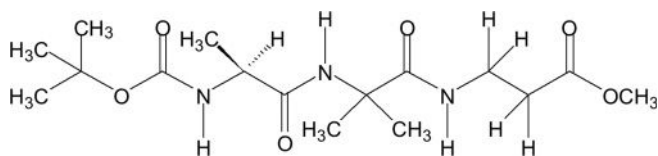
London dispersion forces are weak compared to other noncovalent interactions and arise from induced dipoles between two molecules, regardless of their intrinsic polarity. They are typically stronger between molecules that (i) can be easily polarized; or (ii) contain large or electron-dense atoms. While it has been suggested previously in this chapter that SAFINs require chemically complex LMOGs, simpler LMOGs based on functionalized long-chain *n*-alkanes are also capable of gelling organic liquids due to London dispersion forces. Most of these alkanes are at least partially fluorinated or possess N or S heteroatoms incorporated along the backbone [165, 166]. Perfluoroalkylalkanes with a chemical structure of the form  $F(CF_2)_n(CH_2)_mH$  constitute examples of LMOGs that undergo self-assembly due to thermodynamic incompatibility between the chemically dissimilar fluorinated and hydrocarbon segments. Due to this incompatibility, the two segments microphase-separate into lamellar nanostructures and form gel networks stabilized only by London dispersion forces as a consequence of the strong dipole of the fluorinated segment [167]. The SAFINs generated by perfluoroalkylalkanes, which inherently possess a low surface energy [168], have been utilized to create superhydrophobic surfaces in conjunction with organic solvents [169].

### 26.3.4

#### Special Considerations

##### 26.3.4.1 Biologically Inspired Gelators

Amino acid derivatives constitute another class of organogelators that are becoming increasingly important due to their ability to gel both organic and aqueous



**Figure 26.29** Chemical structure of the tripeptide LMOG Boc-Ala-( $\alpha$ -aminoisobutyric acid)-( $\beta$ -Ala)-Ala-Ome.

liquids [1]. Even in polar solvents, these compounds self-assemble via hydrogen bonding due to the large number of donor sites available per molecule, and the gelation efficacy improves as the number of peptide units increases. The thermodynamic balance between the hydrophobic alkyl substituent and the hydrophilic amide segment governs how these molecules self-assemble. According to UV-visible spectroscopy, these molecules can organize into one of three morphologies: lamellar spheres (multilamellar vesicles); helical ribbons; or tubules. Discrete tubules and ribbons become entangled as the solution approaches the sol-gel transition, which consequently promotes network formation via hydrogen bonding [170]. Lamellar spheres, on the other hand, are unstable and incapable of forming a gel network. One amino acid commonly used as an organogelator is L-lysine, which can bind with long aliphatic chains to form fibrillar micelles [171], a unique organogel nanostructure. Further studies [172] with L-Lysine have yielded binary gels. An interesting feature of this system is that, while neither  $\alpha,\omega$ -diaminoalkane alone can form a gel, together the two species can mutually self-assemble and promote network formation. This discovery of organogels derived from amino acid derivatives greatly facilitates control over the conditions responsible for gelation, including the sol-gel transition temperature.

Both, linear and cyclopeptides are capable of gelling a variety of organic solvents and aqueous systems. In the same vein as amino acid derivatives, their gelation effectiveness is due, for the most part, to the large number of hydrogen-bonding donor sites located on these molecules. Oligopeptide-based gelators and tripeptides (cf. Figure 26.29) have attracted much attention due to their ability to self-assemble through intermolecular hydrogen bonding into anti-parallel  $\beta$ -sheets, which can be envisaged as an entangled network of rodlike fibrils [173, 174]. Hirst *et al.* [175] have investigated mixing different molecular building blocks of dendritic peptides to identify the key factors that influence the self-assembly of such LMOGs. These authors have reported that mixtures of molecules differing in size and chirality can self-organize, whereas mixing molecules differing in shape, defined as the length of the spacer connecting the peptide head groups, reduces the propensity for supramolecular organization. Findings such as these regarding LMOG mixtures are beneficial to the rational design of organogels with tailorable properties.

#### 26.3.4.2 Isothermal Gelation

Although all organogels discussed thus far are generated by a change in temperature, some can be formed isothermally by bubbling  $\text{CO}_2$  and  $\text{N}_2$  through solutions

of primary *n*-alkanamines [176]. This distinctive gelation process has been shown to be chemically reversible, which allows the sol to be recovered. Another type of latent organogel is achieved by bubbling HCl through amino acid derivatives of cholesterol to protonate the amino groups [177]. Organogelation can also be performed *in situ* in the presence of highly reactive solvents. This route not only eliminates the need for thermal treatment, but also shortens the gelation time as the crystalline state is bypassed during formation of the 3-D fibrillar network [178].

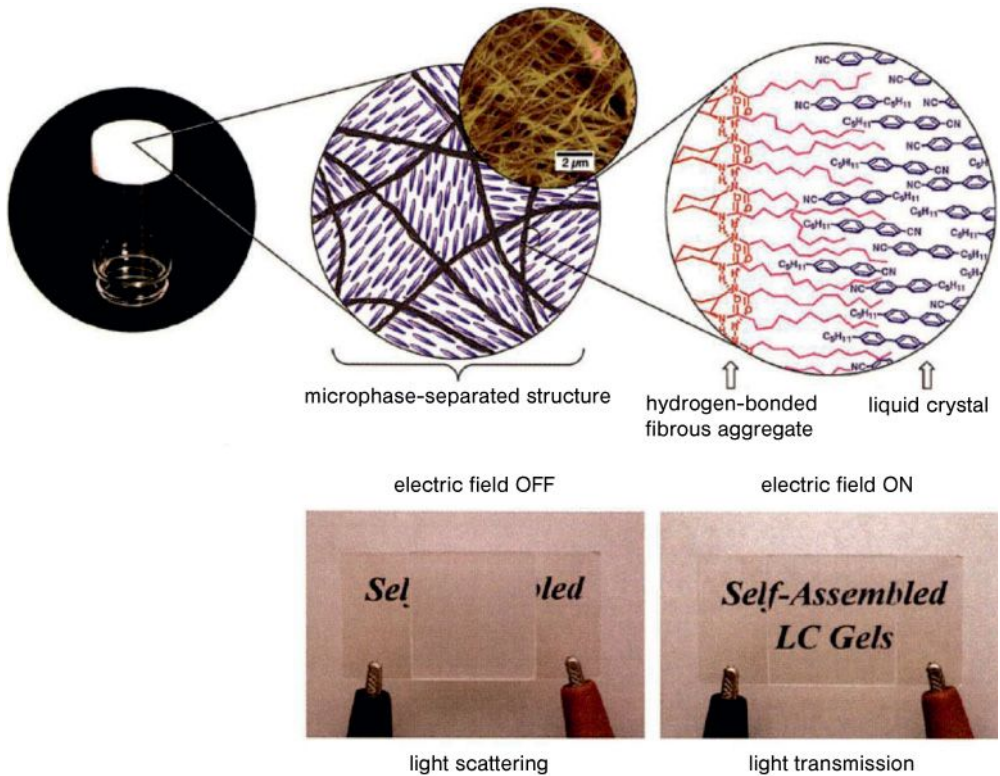
#### 26.3.4.3 Solvent Effects

Solvent polarity plays a critical role in the hydrogen-bonding (and hence gelation) efficacy of many LMOGs. The degree to which the binding sites in a gelator are solvated affects the strength of the gel network, which explains why dramatically different properties can be realized with a single LMOG in different solvents. A recent study [179] has addressed the ability of the disaccharide trehalose to gel organic solvents on the basis of the Hildebrand solubility parameter theory. Gelation is found to improve markedly as solvent–gelator interactions decrease and solvent polarity is low; this is consistent with the findings of Wilder *et al.* [143] regarding the gelation effectiveness of DBS in polyethers differing in polarity due to endgroup substitution. Zhu and Dordick [179] have likewise demonstrated that, when the solvent–gelator interactions are low, the gel network forms from thin, entangled fibrils. Yet, in the presence of strong solvent–gelator interactions, clusters of gelator molecules form thick, rigid fibrils. In addition to solvent polarity, two other criteria must be considered when matching a solvent with an appropriate LMOG to form a stable organogel:

- The boiling and melting temperatures of the solvent and pure LMOG, respectively, must be high so as to avoid undesirable loss of material due to vaporization.
- The solubility of the LMOG in the solvent of choice must be low so as to avoid bulk crystallization of the LMOG [120].

The organic solvents considered thus far in the design of SAFINs have all been isotropic liquids, but this requirement is relaxed below as we again consider organogel networks containing LCs (cf. Section 26.2.7.1).

Because the ability of LC molecules to reorient depends on external conditions such as temperature and electromechanical fields [180], they are used as active displays in watches, televisions, computer monitors, and projectors. Attempts to better control these functional liquids have shown [181] that organogels produced from LCs in the presence of LMOGs can yield fast electro-optical responses due to the low concentrations of gelator required for network formation. As in conventional SAFINs, the LMOG is first dispersed in an isotropic LC solution wherein the LMOG can, upon cooling, self-assemble into fibrils to form a thermoreversible gel network containing immobilized LCs [182]. Unlike other physical gels with only two thermoreversible states (sol and gel), however, LC gels possess three distinct states: isotropic liquid, isotropic gel, and liquid-crystalline gel [182]. Results obtained with FTIR spectroscopy reveal [183, 184] that, while hydrogen bonds are absent in the isotropic liquid state, such interactions develop at the sol–gel transi-



**Figure 26.30** Top: Schematic illustrations of organogels containing a nanostructured liquid crystal (LC) solvent, wherein the SAFIN entraps the anisotropic LC molecules (labeled). Bottom: Images of LC organogel films with an applied electric field off (light

scattering, left) and on (light transmission, right), demonstrating the field-responsive optical nature of these organogels.

Reproduced with permission from Ref. [180]; © American Association for the Advancement of Science.

tion. Deindörfer *et al.* [185] have recently reported on the formation of photosensitive gels composed of smectic LCs and capable of responding elastically to small stresses. The scattering of light from LC physical gels is also of tremendous scientific and technological interest, as the degree of transparency can be controlled electrically without using a polarizer (see Figure 26.30) [186, 187]. Such gels may likewise display anisotropic mechanical responses and recovery, which can be strongly affected by temperature [188].

## 26.4 Conclusions

Nanostructured organogels developed from SAMINs (through, for instance, the use of selectively solvated triblock copolymers) or SAFINs (through the use of

sparingly soluble LMOGs) afford a new class of soft materials [189–191] that possess a broad range of interesting and useful properties. In the first case, supramolecular networks stabilized by nanoscale micelles are readily generated by allowing an incompatible block copolymer possessing at least one midblock to self-organize into discrete micelles in the presence of a midblock-selective solvent. If the micelle-forming blocks are glassy, the micelles effectively behave as physical crosslinks that can endow this genre of organogels with remarkable elasticity and shape memory, depending on factors such as copolymer composition and molecular weight. Because of their unique property attributes, SAMINs are currently under investigation [24, 31, 192, 193] as next-generation dielectric elastomers designed for use as synthetic muscle in microrobotics and as pumps in microfluidics. Through judicious selection of the midblock-selective solvent, SAMINs can likewise exhibit temperature-responsive optical [105] or conductivity [26] properties. In the case of SAFINs, high-melting LMOGs form (nano)fibrillar networks in various organic solvents through site-specific intermolecular interactions such as hydrogen bonds,  $\pi$ - $\pi$  stacking or London dispersion forces. Unlike SAMINs, however, the stability of SAFINs tends to be exquisitely sensitive to mechanical deformation, as well as to temperature. Once the supramolecular network of a SAFIN is broken under shear, for instance, the solvent can flow. Upon cessation of shear, the network begins to reform so that, over a system-specific period of time, the initial SAFIN may be fully recovered. In addition to such mechanically responsive properties, SAFINs have been designed with unique optical properties and can be produced through nonconventional routes, such as exposure to light [194]. Taken together, these two families of nanostructured organogels afford tremendous versatility in the fabrication of soft materials exhibiting designer properties for use in a wide range of mature and emerging (nano)technologies [121].

### Acknowledgments

These studies were supported by Eaton Corporation and the U.S. National Science Foundation. The authors thank Mr Arif O. Gozen for his editorial services, and the various authors who contributed their results to this work.

### References

- 1 Weiss, R.G. and Terech, P. (2006) *Molecular Gels: Materials with Self-Assembled Fibrillar Networks*, Springer, Dordrecht.
- 2 Painter, P.C. and Coleman, M.M. (1997) *Fundamentals of Polymer Science: An Introductory Text*, 2nd edn, Technomic Pub. Co., Lancaster, PA.
- 3 Joly-Duhamel, C., Hellio, D., Ajdari, A. and Djabourov, M. (2002) *Langmuir*, **18**, 7158–7166.
- 4 Joly-Duhamel, C., Hellio, D. and Djabourov, M. (2002) *Langmuir*, **18**, 7208–7217.
- 5 Larson, R.G. (1999) *The Structure and Rheology of Complex Fluids*,



- Oxford University Press, New York.
- 6 Admal, K., Dyre, J., Hvidt, S. and Kramer, O. (1993) *Polym. Gels Networks*, **1**, 5–17.
  - 7 Spěváček, J. and Schneider, B. (1987) *Adv. Colloid Interface Sci.*, **27**, 81–150.
  - 8 Bui, H.S. and Berry, G.C. (2007) *J. Rheol.*, **51**, 915–945.
  - 9 Franse, M.W.C.P., Nijenhuis, K.T. and Picken, S.J. (2003) *Rheol. Acta*, **42**, 443–453.
  - 10 Hamley, I.W. (1998) *The Physics of Block Copolymers*, Oxford University Press, Oxford, New York.
  - 11 Bates, F.S. and Fredrickson, G.H. (1999) *Phys. Today*, **52**, 32–38.
  - 12 Leibler, L. (1980) *Macromolecules*, **13**, 1602–1617.
  - 13 Matsen, M.W. and Bates, F.S. (1996) *Macromolecules*, **29**, 1091–1098.
  - 14 Lindman, B. and Alexandridis, P. (2000) *Amphiphilic Block Copolymers: Self-Assembly and Applications*, 1st edn, Elsevier, Amsterdam, New York.
  - 15 Alexandridis, P. and Spontak, R.J. (1999) *Curr. Opin. Colloid Interface Sci.*, **4**, 130–139.
  - 16 Hamley, I.W. (2005) *Block Copolymers in Solution: Fundamentals and Applications*, John Wiley & Sons, Ltd, Chichester, England and Hoboken, NJ.
  - 17 Hamersky, M.W., Smith, S.D., Gozen, A.O. and Spontak, R.J. (2005) *Phys. Rev. Lett.*, **95**, 168306.
  - 18 Balsara, N.P., Tirrell, M. and Lodge, T.P. (1991) *Macromolecules*, **24**, 1975–1986.
  - 19 Lodge, T.P., Pudil, B. and Hanley, K.J. (2002) *Macromolecules*, **35**, 4707–4717.
  - 20 Giacomelli, F.C., Riegel, I.C., Petzhold, C.L., da Silveira, N.P. and Spěváček, P. (2009) *Langmuir*, **25**, 731–738.
  - 21 Quintana, J.R., Jáñez, M.D. and Katime, I. (1998) *Polymer*, **39**, 2111–2117.
  - 22 Seitz, M.E., Burghardt, W.R., Faber, K.T. and Shull, K.R. (2007) *Macromolecules*, **40**, 1218–1226.
  - 23 Laurer, J.H., Bukovnik, R. and Spontak, R.J. (1996) *Macromolecules*, **29**, 5760–5762.
  - 24 Shankar, R., Ghosh, T.K. and Spontak, R.J. (2007) *Adv. Mater.*, **19**, 2218–2223.
  - 25 Winter, H.H. and Chambon, F. (1986) *J. Rheol.*, **30**, 367–382.
  - 26 He, Y.Y., Boswell, P.G., Bühlmann, P. and Lodge, T.P. (2007) *J. Phys. Chem. B*, **111**, 4645–4652.
  - 27 Yu, J.M., Jérôme, R., Overbergh, N. and Hammond, P. (1997) *Macromol. Chem. Phys.*, **198**, 3719–3735.
  - 28 Raspaud, E., Lairez, D., Adam, M. and Carton, J.P. (1996) *Macromolecules*, **29**, 1269–1277.
  - 29 Vega, D.A., Sebastian, J.M., Loo, Y.L. and Register, R.A. (2001) *J. Polym. Sci., B: Polym. Phys.*, **39**, 2183–2197.
  - 30 de Gennes, P.-G. (1979) *Scaling Concepts in Polymer Physics*, Cornell University Press, Ithaca, NY.
  - 31 Shankar, R., Krishnan, A.K., Ghosh, T.K. and Spontak, R.J. (2008) *Macromolecules*, **41**, 6100–6109.
  - 32 Laurer, J.H., Mulling, J.F., Khan, S.A., Spontak, R.J. and Bukovnik, R. (1998) *J. Polym. Sci., B: Polym. Phys.*, **36**, 2379–2391.
  - 33 Yu, J.M., Dubois, P., Teyssié, P., Jérôme, R., Blacher, S., Brouers, F. and L'Homme, G. (1996) *Macromolecules*, **29**, 5384–5391.
  - 34 Inomata, K., Nakanishi, D., Banno, A., Nakanishi, E., Abe, Y., Kurihara, R., Fujimoto, K. and Nose, T. (2003) *Polymer*, **44**, 5303–5310.
  - 35 Roos, A. and Creton, C. (2005) *Macromolecules*, **38**, 7807–7818.
  - 36 Guth, E. (1945) *J. Appl. Phys.*, **16**, 20–25.
  - 37 Rubinstein, M. and Panyukov, S. (2002) *Macromolecules*, **35**, 6670–6686.
  - 38 Koňák, Č., Helmstedt, M. and Bansil, R. (2000) *Polymer*, **41**, 9311–9315.
  - 39 Koňák, Č., Fleischer, G., Tuzar, Z. and Bansil, R. (2000) *J. Polym. Sci., B: Polym. Phys.*, **38**, 1312–1322.
  - 40 Watanabe, H. (1995) *Macromolecules*, **28**, 5006–5011.
  - 41 Watanabe, H. (2001) *Macromol. Rapid Commun.*, **22**, 127–175.
  - 42 Watanabe, H., Sato, T. and Osaki, K. (2000) *Macromolecules*, **33**, 2545–2550.
  - 43 Laurer, J.H., Khan, S.A., Spontak, R.J., Satkowski, M.M., Grothaus, J.T., Smith, S.D. and Lin, J.S. (1999) *Langmuir*, **15**, 7947–7955.
  - 44 Ceaușescu, E., Bordeianu, R., Ghioca, P., Buzdugan, E., Stancu, R. and



- Cerchez, I. (1984) *Pure Appl. Chem.*, **56**, 319–328.
- 45 Watanabe, H. (1997) *Acta Polym.*, **48**, 215–233.
- 46 Hamley, I.W. (2001) *Phil. Trans. R. Soc. A*, **359**, 1017–1044.
- 47 Hashimoto, T., Shibayama, M., Kawai, H., Watanabe, H. and Kotaka, T. (1983) *Macromolecules*, **16**, 361–371.
- 48 Watanabe, H. and Kotaka, T. (1983) *J. Rheol.*, **27**, 223–240.
- 49 Theunissen, E., Overbergh, N., Reynaers, H., Antoun, S., Jérôme, R. and Mortensen, K. (2004) *Polymer*, **45**, 1857–1865.
- 50 Drzal, P.L. and Shull, K.R. (2003) *Macromolecules*, **36**, 2000–2008.
- 51 Zana, R. (2005) *Dynamics of Surfactant Self-Assemblies: Micelles, Microemulsions, Vesicles, and Lyotropic Phases*, Taylor & Francis, Boca Raton.
- 52 Tan, H., Watanabe, H., Matsumiya, Y., Kanaya, T. and Takahashi, Y. (2003) *Macromolecules*, **36**, 2886–2893.
- 53 Morrison, F.A. and Winter, H.H. (1989) *Macromolecules*, **22**, 3533–3540.
- 54 Nie, H.F., Bansil, R., Ludwig, K., Steinhart, M., Koňák, Č. and Bang, J. (2003) *Macromolecules*, **36**, 8097–8106.
- 55 Percus, J.K. and Yevick, G.J. (1958) *Phys. Rev.*, **110**, 1–13.
- 56 Kinning, D.J. and Thomas, E.L. (1984) *Macromolecules*, **17**, 1712–1718.
- 57 Li, M., Liu, Y., Nie, H., Bansil, R. and Steinhart, M. (2007) *Macromolecules*, **40**, 9491–9502.
- 58 Liu, Y.S., Li, M.H., Bansil, R. and Steinhart, M. (2007) *Macromolecules*, **40**, 9482–9490.
- 59 Sota, N., Sakamoto, N., Saijo, K. and Hashimoto, T. (2006) *Polymer*, **47**, 3636–3649.
- 60 Matsen, M.W. (2001) *J. Chem. Phys.*, **114**, 8165–8173.
- 61 Soenen, H., Berghmans, H., Winter, H.H. and Overbergh, N. (1997) *Polymer*, **38**, 5653–5660.
- 62 Soenen, H., Liskova, A., Reynders, K., Berghmans, H., Winter, H.H. and Overbergh, N. (1997) *Polymer*, **38**, 5661–5665.
- 63 Kleppinger, R., Mischenko, N., Reynaers, H.L. and Koch, M.H.J. (1999) *J. Polym. Sci., B: Polym. Phys.*, **37**, 1833–1840.
- 64 Kleppinger, R., Mischenko, N., Theunissen, E., Reynaers, H.L., Koch, M.H.J., Almdal, K. and Mortensen, K. (1997) *Macromolecules*, **30**, 7012–7014.
- 65 Reynders, K., Mischenko, N., Kleppinger, R., Reynaers, H., Koch, M.H.J. and Mortensen, K. (1997) *J. Appl. Crystallogr.*, **30**, 684–689.
- 66 Kleppinger, R., Reynders, K., Mischenko, N., Overbergh, N., Koch, M.H.J., Mortensen, K. and Reynaers, H. (1997) *Macromolecules*, **30**, 7008–7011.
- 67 Mortensen, K., Theunissen, E., Kleppinger, R., Almdal, K. and Reynaers, H. (2002) *Macromolecules*, **35**, 7773–7781.
- 68 Reynders, K., Mischenko, N., Mortensen, K., Overbergh, N. and Reynaers, H. (1995) *Macromolecules*, **28**, 8699–8701.
- 69 Prasman, E. and Thomas, E.L. (1998) *J. Polym. Sci., B: Polym. Phys.*, **36**, 1625–1636.
- 70 Mischenko, N., Reynders, K., Mortensen, K., Overbergh, N. and Reynaers, H. (1996) *J. Polym. Sci., B: Polym. Phys.*, **34**, 2739–2745.
- 71 Krishnan, A.S. (2010) Morphological, property and phase studies of multicomponent triblock copolymer networks, PhD thesis, North Carolina State University.
- 72 Sharma, R.V. and Sharma, K.C. (1977) *Physica A*, **89**, 213–218.
- 73 Kleppinger, R., van Es, M., Mischenko, N., Koch, M.H.J. and Reynaers, H. (1998) *Macromolecules*, **31**, 5805–5809.
- 74 Flory, P.J. (1953) *Principles of Polymer Chemistry*, Cornell University Press, Ithaca.
- 75 Mooney, M. (1940) *J. Appl. Phys.*, **11**, 582–592.
- 76 Rivlin, R.S. (1948) *Phil. Trans. R. Soc. A*, **241**, 379–397.
- 77 Krishnamoorti, R. and Vaia, R.A. (2002) *Polymer Nanocomposites: Synthesis, Characterization, and Modeling*, American Chemical Society, Washington, DC.
- 78 van Maanen, G.J., Seeley, S.L., Capracotta, M.D., White, S.A., Bukovnik, R.R., Hartmann, J., Martin,

- J.D. and Spontak, R.J. (2005) *Langmuir*, **21**, 3106–3115.
- 79 Drzal, P.L. and Shull, K.R. (2005) *Eur. Phys. J. E*, **17**, 477–483.
- 80 Jin, J. and Song, M. (2005) *Thermochim. Acta*, **438**, 95–101.
- 81 Mishra, J.K., Ryou, J.H., Kim, G.H., Hwang, K.J., Kim, I. and Ha, C.S. (2004) *Mater. Lett.*, **58**, 3481–3485.
- 82 Mishra, J.K., Kim, G.H., Kim, I., Chung, I.J. and Ha, C.S. (2004) *J. Polym. Sci., B: Polym. Phys.*, **42**, 2900–2908.
- 83 Paglicawan, M.A., Balasubramanian, M. and Kim, J.K. (2007) *Macromol. Symp.*, **249–250**, 601–609.
- 84 Spontak, R.J. and Patel, N.P. (2004) Phase behavior of block copolymer blends, in *Developments in Block Copolymer Science and Technology* (ed. I.W. Hamley), John Wiley & Sons, Inc., New York, pp. 159–212.
- 85 Leibler, L., Ajdari, A., Mourran, A., Coulon, G. and Chatenay, D. (1994) Spreading of homopolymers on copolymer modified surfaces, in *Ordering in Macromolecular Systems* (eds A. Teramoto, M. Kobayashi and T. Norisuye), Springer-Verlag, Berlin, p. 353.
- 86 Walker, T.A., Semler, J.J., Leonard, D.N., van Maanen, G.J., Bukovnik, R.R. and Spontak, R.J. (2002) *Langmuir*, **18**, 8266–8270.
- 87 Quintana, J.R., Jáñez, M.D. and Katime, I. (1996) *Langmuir*, **12**, 2196–2199.
- 88 Flosenzier, L.S., Rohlfling, J.H., Schwark, A.M. and Torkelson, J.M. (1990) *Polym. Eng. Sci.*, **30**, 49–58.
- 89 Flosenzier, L.S. and Torkelson, J.M. (1992) *Macromolecules*, **25**, 735–742.
- 90 Quintana, J.R., Díaz, E. and Katime, I. (1998) *Langmuir*, **14**, 1586–1589.
- 91 Mazard, C., Benyahia, L. and Tassin, J.F. (2003) *Polym. Int.*, **52**, 514–521.
- 92 Barbe, A., Bökamp, K., Kummerlowe, C., Sollmann, H., Vennemann, N. and Vinzelberg, S. (2005) *Polym. Eng. Sci.*, **45**, 1498–1507.
- 93 Jackson, N.R., Wilder, E.A., White, S.A., Bukovnik, R. and Spontak, R.J. (1999) *J. Polym. Sci., B: Polym. Phys.*, **37**, 1863–1872.
- 94 Sengupta, P. and Noordermeer, J.W.M. (2005) *Macromol. Rapid Commun.*, **26**, 542–547.
- 95 Kane, L., Norman, D.A., White, S.A., Matsen, M.W., Satkowski, M.M., Smith, S.D. and Spontak, R.J. (2001) *Macromol. Rapid Commun.*, **22**, 281–296.
- 96 Spontak, R.J., Wilder, E.A. and Smith, S.D. (2001) *Langmuir*, **17**, 2294–2297.
- 97 Wilder, E.A., White, S.A., Smith, S.D. and Spontak, R.J. (2003) Gel network development in AB, ABA and AB/ABA block copolymer solutions in a selective solvent, in *Polymer Gels: Fundamentals and Applications*, Vol. 833, American Chemical Society, pp. 248–261.
- 98 Zhulina, E.B. and Halperin, A. (1992) *Macromolecules*, **25**, 5730–5741.
- 99 Halperin, A. and Zhulina, E.B. (1991) *Europhys. Lett.*, **16**, 337–341.
- 100 King, M.R., White, S.A., Smith, S.D. and Spontak, R.J. (1999) *Langmuir*, **15**, 7886–7889.
- 101 Li, B.Q. and Ruckenstein, E. (1998) *Macromol. Theory Simul.*, **7**, 333–348.
- 102 Halperin, A. (1996) *J. Adhes.*, **58**, 1–13.
- 103 de Gennes, P.-G. and Prost, J. (1993) *The Physics of Liquid Crystals*, 2nd edn, Oxford University Press, Oxford, New York.
- 104 Li, M.H., Keller, P., Yang, J.Y. and Albouy, P.A. (2004) *Adv. Mater.*, **16**, 1922–1925.
- 105 Kempe, M.D., Scruggs, N.R., Verduzco, R., Lal, J. and Kornfield, J.A. (2004) *Nat. Mater.*, **3**, 177–182.
- 106 Kempe, M.D., Verduzco, R., Scruggs, N.R. and Kornfield, J.A. (2006) *Soft Matter*, **2**, 422–431.
- 107 Halperin, A. and Williams, D.R.M. (1994) *Phys. Rev. E*, **49**, R986–R989.
- 108 Welton, T. (1999) *Chem. Rev.*, **99**, 2071–2083.
- 109 Patel, N.P. and Spontak, R.J. (2004) *Macromolecules*, **37**, 2829–2838.
- 110 He, Y. and Lodge, T.P. (2007) *Chem. Commun.*, 2732–2734.
- 111 Spontak, R.J. and Smith, S.D. (2001) *J. Polym. Sci., B: Polym. Phys.*, **39**, 947–955.
- 112 Wu, L.F., Cochran, E.W., Lodge, T.P. and Bates, F.S. (2004) *Macromolecules*, **37**, 3360–3368.

- 113 Smith, S.D., Spontak, R.J., Satkowski, M.M., Ashraf, A., Heape, A.K. and Lin, J.S. (1994) *Polymer*, **35**, 4527–4536.
- 114 Bansil, R., Nie, H.F., Koňák, Č., Helmstedt, M. and Lal, J. (2002) *J. Polym. Sci., B: Polym. Phys.*, **40**, 2807–2816.
- 115 Nie, H.F., Li, M.H., Bansil, R., Koňák, Č., Helmstedt, M. and Lal, J. (2004) *Polymer*, **45**, 8791–8799.
- 116 Gindy, M.E., Prud'homme, R.K. and Panagiotopoulos, A.Z. (2008) *J. Chem. Phys.*, **128**, 164906.
- 117 Florez, S., Muñoz, M.E. and Santamaria, A. (2005) *J. Rheol.*, **49**, 313–325.
- 118 Quintana, J.R., Jáñez, M.D., Hernández, E.Z., García, A. and Katime, I. (1998) *Macromolecules*, **31**, 6865–6870.
- 119 Terech, P. and Weiss, R.G. (1997) *Chem. Rev.*, **97**, 3133–3159.
- 120 George, M. and Weiss, R.G. (2006) *Acc. Chem. Res.*, **39**, 489–497.
- 121 Sangeetha, N.M. and Maitra, U. (2005) *Chem. Soc. Rev.*, **34**, 821–836.
- 122 Lim, G.S., Jung, B.M., Lee, S.J., Song, H.H., Kim, C. and Chang, J.Y. (2007) *Chem. Mater.*, **19**, 460–467.
- 123 Hanabusa, K., Yamada, M., Kimura, M. and Shirai, H. (1996) *Angew. Chem. Int. Ed. Engl.*, **35**, 1949–1951.
- 124 Žinic, M., Vögtle, F. and Fages, F. (2005) *Top. Curr. Chem.*, **256**, 39–76.
- 125 Etter, M.C. (1991) *J. Phys. Chem.*, **95**, 4601–4610.
- 126 Zaworotko, M.J. (1994) *Chem. Soc. Rev.*, **23**, 283–288.
- 127 Meléndez, R.E., Carr, A.J., Linton, B.R. and Hamilton, A.D. (2000) Controlling hydrogen bonding: from molecular recognition to organogelation, in *Molecular Self-assembly Organic versus Inorganic Approaches*, Vol. 96, Springer, Berlin, pp. 31–61.
- 128 Dastidar, P. (2008) *Chem. Soc. Rev.*, **37**, 2699–2715.
- 129 Abdallah, D.J. and Weiss, R.G. (2000) *Adv. Mater.*, **12**, 1237–1247.
- 130 Leiserowitz, L. and Schmidt, G.M.J. (1969) *J. Chem. Soc. A*, 2372–2382.
- 131 Fan, E.K., Yang, J., Geib, S.J., Stoner, T.C., Hopkins, M.D. and Hamilton, A.D. (1995) *J. Chem. Soc., Chem. Commun.*, 1251–1252.
- 132 Hanabusa, K., Tanaka, R., Suzuki, M., Kimura, M. and Shirai, H. (1997) *Adv. Mater.*, **9**, 1095–1097.
- 133 Ohishi, T., Sugi, R., Yokoyama, A. and Yokozawa, T. (2008) *Macromolecules*, **41**, 9683–9691.
- 134 Lockwood, N.A., van Tankeren, R. and Mayo, K.H. (2002) *Biomacromolecules*, **3**, 1225–1232.
- 135 George, M., Snyder, S.L., Terech, P. and Weiss, R.G. (2005) *Langmuir*, **21**, 9970–9977.
- 136 van Esch, J.H. and Feringa, B.L. (2000) *Angew. Chem. Int. Ed.*, **39**, 2263–2266.
- 137 Fages, F., Vögtle, F. and Žinic, M. (2005) *Top. Curr. Chem.*, **256**, 77–131.
- 138 Carr, A.J., Meléndez, R.E., Geib, S.J. and Hamilton, A.D. (1998) *Tetrahedron Lett.*, **39**, 7447–7450.
- 139 van der Laan, S., Feringa, B.L., Kellogg, R.M. and van Esch, J. (2002) *Langmuir*, **18**, 7136–7140.
- 140 de Loos, M., van Esch, J., Kellogg, R.M. and Feringa, B.L. (2001) *Angew. Chem. Int. Ed.*, **40**, 613–616.
- 141 Schoonbeek, F.S., van Esch, J.H., Wegewijs, B., Rep, D.B.A., de Haas, M.P., Klapwijk, T.M., Kellogg, R.M. and Feringa, B.L. (1999) *Angew. Chem. Int. Ed.*, **38**, 1393–1397.
- 142 Thierry, A., Straupé, C., Wittmann, J.C. and Lotz, B. (2006) *Macromol. Symp.*, **241**, 103–110.
- 143 Wilder, E.A., Spontak, R.J. and Hall, C.K. (2003) *Mol. Phys.*, **101**, 3017–3027.
- 144 Wilder, E.A., Hall, C.K., Khan, S.A. and Spontak, R.J. (2003) *Langmuir*, **19**, 6004–6013.
- 145 Yamasaki, S., Ohashi, Y., Tsutsumi, H. and Tsujii, K. (1995) *Bull. Chem. Soc. Jpn.*, **68**, 146–151.
- 146 Smith, T.L., Masilamani, D., Bui, L.K., Khanna, Y.P., Bray, R.G., Hammond, W.B., Curran, S., Belles, J.J. and Bindercastelli, S. (1994) *Macromolecules*, **27**, 3147–3155.
- 147 Wilder, E.A., Hall, C.K., Khan, S.A. and Spontak, R.J. (2002) *Recent Res. Dev. Mat. Sci.*, **3**, 93–115.
- 148 Tan, C.H., Su, L.H., Lu, R., Xue, P.H., Bao, C.Y., Liu, X.L. and Zhao, Y.Y. (2006) *J. Mol. Liq.*, **124**, 32–36.
- 149 Bai, B.L., Wang, H.T., Xin, H., Zhang, F.L., Long, B.H., Zhang, X.B., Qu, S.N.

- and Li, M. (2007) *New J. Chem.*, **31**, 401–408.
- 150 Aoki, M., Murata, K. and Shinkai, S. (1991) *Chem. Lett.*, 1715–1718.
- 151 Xing, B.A., Choi, M.F., Zhou, Z.Y. and Xu, B. (2002) *Langmuir*, **18**, 9654–9658.
- 152 Lin, Y.C. and Weiss, R.G. (1987) *Macromolecules*, **20**, 414–417.
- 153 Lin, Y., Kachar, B. and Weiss, R.G. (1989) *J. Am. Chem. Soc.*, **111**, 5542–5551.
- 154 Song, X.D., Geiger, C., Farahat, M., Perlstein, J. and Whitten, D.G. (1997) *J. Am. Chem. Soc.*, **119**, 12481–12491.
- 155 Song, J.H. and Sailor, M.J. (1997) *J. Am. Chem. Soc.*, **119**, 7381–7385.
- 156 Shoji, Y., Tashiro, K. and Aida, T. (2004) *J. Am. Chem. Soc.*, **126**, 6570–6571.
- 157 Murata, K., Aoki, M., Suzuki, T., Harada, T., Kawabata, H., Komori, T., Ohseto, F., Ueda, K. and Shinkai, S. (1994) *J. Am. Chem. Soc.*, **116**, 6664–6676.
- 158 Llusar, M. and Sanchez, C. (2008) *Chem. Mater.*, **20**, 782–820.
- 159 Kawano, S., Fujita, N. and Shinkai, S. (2004) *J. Am. Chem. Soc.*, **126**, 8592–8593.
- 160 Xue, M., Liu, K.Q., Peng, J.X., Zhang, Q.H. and Fang, Y. (2008) *J. Colloid Interface Sci.*, **327**, 94–101.
- 161 Lu, L.D., Cocker, T.M., Bachman, R.E. and Weiss, R.G. (2000) *Langmuir*, **16**, 20–34.
- 162 Clavier, G., Mistry, M., Fages, F. and Pozzo, J.L. (1999) *Tetrahedron Lett.*, **40**, 9021–9024.
- 163 Pozzo, J.L., Desvergne, J.P., Clavier, G.M., Bouas-Laurent, H., Jones, P.G. and Perlstein, J. (2001) *J. Chem. Soc., Perkin Trans.*, **2**, 824–826.
- 164 Terech, P., Clavier, G., Bouas-Laurent, H., Desvergne, J.P., Demé, B. and Pozzo, J.L. (2006) *J. Colloid Interface Sci.*, **302**, 633–642.
- 165 Ku, C.Y., Nostro, P.L. and Chen, S.H. (1997) *J. Phys. Chem. B*, **101**, 908–914.
- 166 Abdallah, D.J., Lu, L.D. and Weiss, R.G. (1999) *Chem. Mater.*, **11**, 2907–2911.
- 167 Nostro, P.L. and Chen, S.H. (1993) *J. Phys. Chem.*, **97**, 6535–6540.
- 168 Hozumi, A. and Takai, O. (1997) *Thin Solid Films*, **303**, 222–225.
- 169 Yamanaka, M., Sada, K., Miyata, M., Hanabusa, K. and Nakano, K. (2006) *Chem. Commun.*, 2248–2250.
- 170 Selinger, J.V., MacKintosh, F.C. and Schnur, J.M. (1996) *Phys. Rev. E*, **53**, 3804–3818.
- 171 Fuhrhop, J.H., Spiroski, D. and Boettcher, C. (1993) *J. Am. Chem. Soc.*, **115**, 1600–1601.
- 172 Huang, B.Q., Hirst, A.R., Smith, D.K., Castelletto, V. and Hamley, I.W. (2005) *J. Am. Chem. Soc.*, **127**, 7130–7139.
- 173 Das, A.K. and Banerjee, A. (2006) *Macromol. Symp.*, **241**, 14–22.
- 174 Maji, S.K., Malik, S., Drew, M.G.B., Nandi, A.K. and Banerjee, A. (2003) *Tetrahedron Lett.*, **44**, 4103–4107.
- 175 Hirst, A.R., Huang, B.Q., Castelletto, V., Hamley, I.W. and Smith, D.K. (2007) *Chem. Eur. J.*, **13**, 2180–2188.
- 176 George, M. and Weiss, R.G. (2001) *J. Am. Chem. Soc.*, **123**, 10393–10394.
- 177 Li, Y.G., Liu, K.Q., Liu, J., Peng, J.X., Feng, X.L. and Fang, Y. (2006) *Langmuir*, **22**, 7016–7020.
- 178 Suzuki, M., Nakajima, Y., Yumoto, M., Kimura, M., Shirai, H. and Hanabusa, K. (2004) *Org. Biomol. Chem.*, **2**, 1155–1159.
- 179 Zhu, G.Y. and Dordick, J.S. (2006) *Chem. Mater.*, **18**, 5988–5995.
- 180 Kato, T. (2002) *Science*, **295**, 2414–2418.
- 181 Mizoshita, N., Hanabusa, K. and Kato, T. (1999) *Adv. Mater.*, **11**, 392–394.
- 182 Kato, T., Kutsuna, T., Hanabusa, K. and Ukon, M. (1998) *Adv. Mater.*, **10**, 606–608.
- 183 Yabuuchi, K., Rowan, A.E., Nolte, R.J.M. and Kato, T. (2000) *Chem. Mater.*, **12**, 440–443.
- 184 Kato, T., Hirota, N., Fujishima, A. and Fréchet, J.M.J. (1996) *J. Polym. Sci., Part A: Polym. Chem.*, **34**, 57–62.
- 185 Deindörfer, P., Eremin, A., Stannarius, R., Davis, R. and Zentel, R. (2006) *Soft Matter*, **2**, 693–698.
- 186 Mizoshita, N., Hanabusa, K. and Kato, T. (2003) *Adv. Funct. Mater.*, **13**, 313–317.
- 187 Suzuki, Y., Mizoshita, N., Hanabusa, K. and Kato, T. (2003) *J. Mater. Chem.*, **13**, 2870–2874.
- 188 Pakula, T. and Zentel, R. (1991) *Makromol. Chem.*, **192**, 2401–2410.

- 189** Jones, R. (2002) *Soft Condensed Matter*, Oxford University Press, New York.
- 190** Hamley, I.W. (2007) *Introduction to Soft Matter*, John Wiley & Sons, Ltd, Chichester.
- 191** Ozin, G.A., Arsenault, A.C. and Cademartiri, L. (2009) *Nanochemistry: A Chemical Approach to Nanomaterials*, 2nd edn, Royal Society of Chemistry, Cambridge.
- 192** Shankar, R., Ghosh, T.K. and Spontak, R.J. (2007) *Soft Matter*, **3**, 1116–1129.
- 193** Shankar, R., Ghosh, T.K. and Spontak, R.J. (2007) *Macromol. Rapid Commun.*, **28**, 1142–1147.
- 194** George, M. and Weiss, R.G. (2003) *Chem. Mater.*, **15**, 2879–2888.

## 27

### Self-assembly of Linear Polypeptide-based Block Copolymers

*Sébastien Lecommandoux, Harm-Anton Klok, and Helmut Schlaad*

#### 27.1

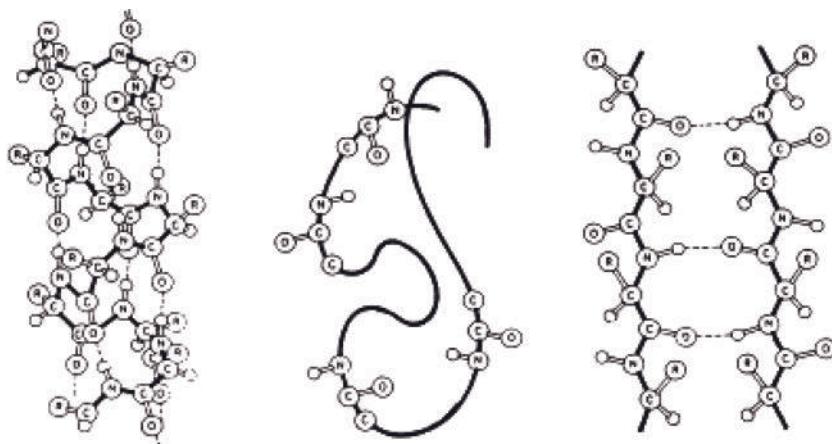
##### Introduction

Now that the fundamental principles that underlie the self-assembly of block copolymers have been addressed in numerous theoretical and experimental studies, these materials are finding increasing interest in several nanotechnology applications, such as nanostructured membranes, templates for nanoparticle synthesis and high-density information storage [1–3]. The self-assembly of block copolymers composed of two (A and B) or more (A, B, C, ...) chemically incompatible, amorphous segments is determined by the interplay of two competitive processes [4, 5]. On the one hand, in order to avoid unfavorable monomer contacts, the blocks segregate and try to minimize the interfacial area. Minimization of the interfacial area, however, involves chain stretching, which is entropically unfavorable. It is the interplay between these two processes that determines the final block copolymer morphology. Depending on the volume fractions of the respective blocks, amorphous AB diblock copolymers can form lamellar, hexagonal, spherical and gyroid structures. More complex morphologies can also be generated, but these require alternative strategies. One possibility is to increase the number of different blocks [6]. Other strategies to create more complex block copolymer nanostructures include the introduction of more rigid or (liquid) crystalline blocks [7, 8]. Often, such conformationally restricted segments introduce additional secondary interactions, such as electrostatic, hydrogen bonding or  $\pi$ - $\pi$  interactions, which have an impact on the block copolymer self-assembly. In particular, rod-coil type block copolymers composed of a rigid (crystalline) block and a flexible (amorphous) segment have attracted increased interest over the past years [9, 10]. Morphological studies on rod-coil block copolymers have revealed several unconventional nanoscale structures, which were previously unknown for purely amorphous block copolymers. These findings underline the potential of manipulating chain conformation and interchain interactions to further engineer block copolymer self-assembly.

The self-assembly of amphiphilic block copolymers in solution, driven by the incompatibility of constituents, into ordered structures in the sub-micrometer

range is a current topic in colloid and materials science [11–15]. The basic structures of diblock copolymers in solution are, in the order of decreasing curvature, spherical and cylindrical micelles and vesicles; the curvature of the core–corona interface is essentially determined by the volume fractions of comonomers and environmental factors (solvent, ionic strength, etc.) [16]. Polymer vesicles, often also referred to as “polymersomes”, are particularly interesting as mimetics for biological membranes [17–20]. Deviation from this conventional aggregation behavior and appearance of more complex superstructures occur, as in biological systems, when specific non-covalent interactions, chirality and secondary structure effects come into play [21, 22]. Particularly interesting are block copolymers that combine advantageous features of synthetic polymers (solubility, processability, rubber elasticity, etc.) with those of polypeptides or polysaccharides (secondary structure, functionality, biocompatibility, etc.).

This chapter discusses the solid-state and solution structures, organization and properties of polypeptide-based block copolymers. Most of the block copolymers studied so far are composed of a synthetic block and a peptide segment and are an interesting class of materials, both from a structural and a functional point of view [23, 24]. Peptide sequences can adopt ordered conformations, such as  $\alpha$ -helices or  $\beta$ -strands (Figure 27.1). In the former case, this leads to block copolymers with rod–coil character. Peptide sequences with a  $\beta$ -strand conformation can undergo intermolecular hydrogen bonding, which also offers additional means to direct nanoscale structure formation compared with purely amorphous block copolymers. Combining peptide sequences and synthetic polymers, however, is not only interesting to enhance control over nanoscale structure formation, but can also result in materials that can interface with biology. Such biomimetic hybrid polymers or molecular chimeras [25] may produce sophisticated superstructures



**Figure 27.1** Illustration of the basic secondary structure motifs of polypeptides: (a)  $\alpha$ -helix, (b) random coil and (c) antiparallel  $\beta$ -sheet.

with new materials properties. “Smart” materials based on polypeptides may reversibly change the conformation and, along with it, properties in response to an environmental stimulus, such as a change in pH or temperature [26]. Also, polypeptide block copolymers may be used as model systems to study generic self-assembly processes in natural proteins. Obviously, such materials would be of great potential interest for a variety of biomedical and bioanalytical applications.

## 27.2

### Solution Self-assembly of Polypeptide-based Block Copolymers

#### 27.2.1

##### Aggregation of Polypeptide-based Block Copolymers

###### 27.2.1.1 Polypeptide Hybrid Block Copolymers

**Corona-forming Polypeptides** Block copolymers with soluble and thus corona-forming polypeptide segments include linear diblock and triblock copolymer samples. In most cases, studies on the aggregation behavior were carried out in aqueous solutions with samples consisting of a soft polybutadiene (PB) or polyisoprene (PI) (exhibiting a glass transition temperature,  $T_g$ , below the freezing point of water) and an  $\alpha$ -helical poly(L-glutamate) (PLGlu) or poly(L-lysine) (PLLys) segment.

The first study, reported in 1979 by Nakajima *et al.* [27], dealt with the structure of aggregates of symmetric triblock copolymers consisting of a coiled *trans*-1,4-PB middle-block and two  $\alpha$ -helical poly( $\gamma$ -benzyl L-glutamate) outer-blocks, PBLGlu<sub>53-188</sub>-*b*-PB<sub>64</sub>-*b*-PBLGlu<sub>53-188</sub> (subscripts denote number averages of repeat units,  $P_n$ ), so-called “once-broken rods”, in chloroform. The shape and dimensions of the aggregates in solution were calculated on the basis of simple thermodynamic considerations by taking into account chain conformation and the interfacial free energy. Predictions were found to be in good agreement with the structures (of solvent-cast films) observed by transmission electron microscopy (TEM). Depending on the composition of the copolymer, aggregates had a spherical, cylindrical or lamellar structure with a characteristic size of about 25–45 nm. Similar data were also obtained for block copolymers based on poly( $\gamma$ -methyl L-glutamate) (PMLGlu) and poly( $N^{\epsilon}$ -benzyloxycarbonyl L-lysine) (PZLLys) [28]. These results suggest that the aggregation of rod-coil block copolymers might be treated in the same way as conformationally isotropic samples [29], provided that the rigid segment is dissolved in the continuous phase.

Schlaad and coworkers [30] and Lecommandoux and coworkers [31] investigated the aggregates of PB<sub>27-119</sub>-*b*-PLGlu<sub>20-175</sub> in aqueous saline solution by dynamic and static light scattering (DLS/SLS), small-angle neutron scattering (SANS) and TEM. Copolymers were found to form spherical micelles with a hydrodynamic radius of  $R_h < 40$  nm (70–75 mol-% glutamate) or unilamellar vesicles with  $R_h = 50$ –90 nm



(17–54 mol-% glutamate); cylindrical micelles have not been observed so far. Against all expectations, however, Klok and Lecommandoux and coworkers [32, 33] earlier reported not micelles but vesicles for a  $PB_{40}\text{-}b\text{-PLGlu}_{100}$  containing 71 mol-% glutamate.

DLS and SANS showed that any pH-induced changes of the secondary structure of poly(L-glutamate) from a random coil (pH > 6) to an  $\alpha$ -helix (pH < 5) (CD spectroscopy) did not have a severe impact on the morphology (curvature) of the aggregates. SANS further suggested that aggregation numbers remained the same [31], despite equilibration of the sample and a dynamic exchange of polymer chains between aggregates [30]. Coiled and  $\alpha$ -helical polypeptide chains seem to have similar spatial requirements at the core-corona interface (see also [27]). However, as the contour length of an all-*trans* polypeptide chain is more than twice that of an  $\alpha$ -helix, in particular the hydrodynamic size of the aggregates might decrease when decreasing the pH of the solution. A decrease of the hydrodynamic radius by 20% or less could be observed for  $PB_{48}\text{-}b\text{-PLGlu}_{56\text{--}145}$  [31] but, however, not for  $PB_{27\text{--}119}\text{-}b\text{-PLGlu}_{24\text{--}64}$  [30].  $PI_{49}\text{-}b\text{-PLLys}_{123}$  micelles in saline, also reported by Lecommandoux and coworkers [34], exhibited a hydrodynamic radius of  $R_h \approx 44$  nm at pH 6 (coil) and of 23 nm at pH 11 (helix) (DLS), which corresponds to a decrease in size by almost 50%. Interestingly, although the polypeptide segment is of nearly the same length, the effect seen for  $PI_{49}\text{-}b\text{-PLLys}_{123}$  micelles is much larger than that for  $PB_{48}\text{-}b\text{-PLGlu}_{114}$  ( $\approx 8\%$ ). A possible explanation might be that the PLGlu helices are disrupted [28] and/or folded and hence less stretched as PLLys helices.

It is worth noting that the coronae of micelles of  $PB_{48}\text{-}b\text{-PLGlu}_{114}$  and  $PI_{49}\text{-}b\text{-PLLys}_{178}$  could be stabilized using 2,2'-(ethylenedioxy)bisethylamine and glutaric dialdehyde as cross-linking agents, respectively (Lecommandoux *et al.* [35]). The size and morphology of the aggregates were not affected by the chemical modification reaction.

Ouchi and coworkers [36] studied the aggregation of poly(L-lactide)-*block*-poly(aspartic acid),  $PLL_{95,270}\text{-}b\text{-PAsp}_{47\text{--}270}$ , in pure water and in 0.2 M phosphate buffer solution at pH 4.4–8.6. Irrespective of the chemical composition of the copolymer (21–74 mol-% aspartic acid), however, only spherical aggregates with  $R_h = 10\text{--}80$  nm could be observed [DLS and scanning force microscopy (SFM)]. The aggregation behavior of the samples was rationalized in terms of a balance between hydrophobic interactions in the PLL core and electrostatic repulsion and hydrogen-bridging interactions in the PAsp corona. That the aggregates might be non-equilibrium structures being kinetically trapped in a “frozen” state due to semi-crystallinity of PLL chains was not considered. Metastability could be an explanation for the exclusive formation of spherical micelles in addition to the seemingly arbitrary changes of the size of aggregates in buffer solutions at different pH.

Klok and coworkers [37] used DLS/SLS, SANS and analytical ultracentrifugation (AUC) for the analysis of aggregates formed by  $PS_{8,10}\text{-}b\text{-PLLys}_{9\text{--}72}$  (PS = polystyrene) in dilute aqueous solution at neutral pH; at this pH, PLLys was in a random coil conformation. They observed, however, cylindrical micelles regardless of the

length of the PLLys segment. A conclusive explanation of this unexpected aggregation behavior could not be given.

**Core-forming Polypeptides** Aggregates with an insoluble polypeptide core have been prepared with block or random copolymers having linear or branched architecture. Most studies focused on aqueous systems (designated for use as drug carriers in biomedical applications), and the only inverse systems investigated to date are PB-*b*-PLGlu in dilute tetrahydrofuran (THF) and CH<sub>2</sub>Cl<sub>2</sub> solution and PS-*b*-PZLLys in CCl<sub>4</sub>.

Harada and Kataoka [38–40] were the first to investigate the formation of polyion complex (PIC) micelles in an aqueous milieu from a pair of oppositely charged linear polypeptide block copolymers, namely of PEG<sub>113</sub>-*b*-PAsp<sub>18,78</sub> polyanions and PEG<sub>113</sub>-*b*-PLLys<sub>18,78</sub> polycations [PEG = poly(ethylene glycol)]. Complexation studies were carried out at pH 7.29, where both block copolymers had the same degree of ionization ( $\alpha = 0.967$ ) and were thus double-hydrophilic in nature and did not form aggregates in water. Mixing of the copolymers at a 1:1 ratio of amino acid residues resulted in the formation of stable and monodispersed spherical core-shell assemblies of 30 nm in diameter (DLS). Another interesting feature connected with PIC micelles is that of “chain-length recognition” [40]. PIC micelles are exclusively formed by matched pairs of chains with the same block lengths of polyanions and polycations, even in mixtures with different block lengths. The key determinants in this recognition process are considered to be the strict phase separation between the PIC core and the PEO corona, requiring regular alignment of the molecular junctions at the core–corona interface, and the charge stoichiometry (neutralization).

Yonese and coworkers [41] studied the aggregation behavior of PEG<sub>113</sub>-*b*-PMLGlu<sub>20,50</sub> and lactose-modified PEG<sub>75</sub>-*b*-PMLGlu<sub>32</sub> in water. As shown by DLS, the copolymers formed large aggregates with a hydrodynamic radius of  $R_h \approx 250$  nm. Contrary to what was claimed by these workers, it seems more likely that these aggregates were vesicles rather than spherical micelles. Key in the aggregation behavior might be the association of  $\alpha$ -helical PMLGlu segments, as evidenced by CD spectroscopy, promoting the formation of plane bi-layers which then close into vesicles [15]. Further systematic studies on this system and detailed analysis of structures are lacking.

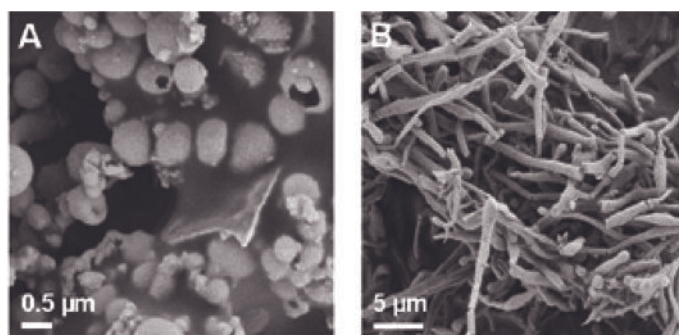
Closely related to this system are PEO<sub>272</sub>-*b*-PBLGlu<sub>38–418</sub> and PNIPAAm<sub>203</sub>-*b*-PBLGlu<sub>39–123</sub> [PEO = poly(ethylene oxide), PNIPAAm = poly(*N*-isopropylacrylamide)] described by Cho and coworkers [42, 43]. The aqueous polymer solutions, prepared by the dialysis of organic solutions against water, contained large spherical aggregates ( $R_h \approx 250$  nm) with a broad size distribution (DLS). Although the size suggested a vesicular structure of the aggregates, aggregation numbers ( $Z < 100$ , method of determination not specified) were far below the values of several thousands typically being reported for polymer vesicles [18]. It is also worth noting that the PNIPAAm chains exhibit LCST (lower critical solution temperature) behavior. However, raising the temperature to the LCST ( $\approx 34^\circ\text{C}$ ) had no serious impact on the size of the aggregates.

Dong and coworkers described symmetric triblock copolymers with a glyco methacrylate middle block and two outer poly(L-alanine) (PLAla) or PBLGlu blocks [44, 45]. The aggregates formed in dilute aqueous solution were spherical in shape and were 200–700 nm in diameter (TEM). TEM further revealed a compact structure of the aggregates as with multi-lamellar vesicles. The dimensions of the particles, however, were found to decrease with increasing concentration of the copolymer.

Naka *et al.* [46] studied the aggregation behavior of poly(acetylminoethylene)-*block*-poly(L-phenylalanine), PAEI<sub>41</sub>-*b*-PLPhe<sub>4,8</sub>, in a 0.05 M phosphate buffer at pH 7. Aggregates were observed despite the very low number of hydrophobic L-phenylalanine units, and the size of which was in the order of  $R_h = 425$  nm (DLS). The seemingly high tendency of these polymers to form aggregates was attributed to the establishment of hydrogen bridges between the amino acid units, as shown by IR spectroscopy, in addition to hydrophobic interactions. Visualization of the aggregates with TEM strongly suggested the presence of coacervates or large clusters of small micelles but no vesicles.

The existence of vesicles could be demonstrated for PS<sub>258</sub>-*b*-PZLLys<sub>57</sub> in dilute CCl<sub>4</sub> solution (Losik and Schlaad [47]). Scanning electron microscopy (SEM) showed collapsed hollow spheres of about 300–600 nm in diameter, indicative of vesicles, and also sheet-like structures, supposedly bi-layers that are not yet closed to vesicles (Figure 27.2A) [15]. The preference for a lamellar structure might be, as in the previous examples, attributed to a stiffening of the core by the 2D-arrangement of crystallizable PZLLys  $\alpha$ -helices. PS<sub>258</sub>-*b*-PZLLys<sub>109</sub>, on the other hand, was found to form large compact fibrils being hundreds of nanometers in diameter and several tens of microns in length (Figure 27.2B); these aggregates might be cylindrical multi-lamellar vesicles. However, the processes involved in the formation of these structures are not yet known.

Likewise, Lecommandoux and coworkers [31] found vesicles for PB<sub>48</sub>-*b*-PLGlu<sub>20</sub> in THF and in CH<sub>2</sub>Cl<sub>2</sub> solution ( $R_h = 106$ –108 nm, DLS/SLS). The formation of



**Figure 27.2** SEM images of the aggregates formed by (A) PS<sub>258</sub>-*b*-PZLLys<sub>57</sub> and (B) PS<sub>258</sub>-*b*-PZLLys<sub>109</sub> in dilute CCl<sub>4</sub> solution; specimens were prepared by shock-freezing a 0.2 wt-% polymer solution with liquid nitrogen and subsequent freeze-drying [47].

vesicles rather than micelles was attributed to the  $\alpha$ -helical rod-like secondary structure of the insoluble PLGlu that forms a planar interface.

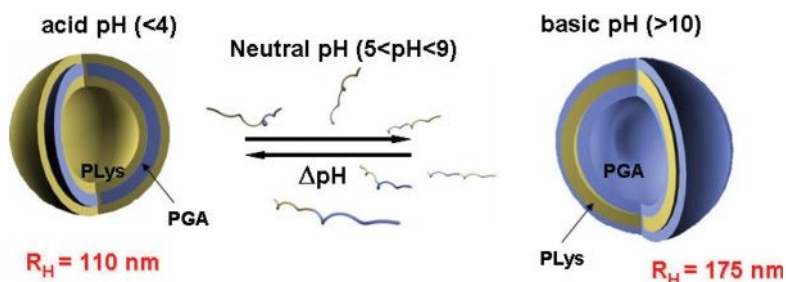
### 27.2.1.2 Block Copolypeptides

Besides the polypeptide hybrid block copolymers described earlier, a few purely peptide-based amphiphiles and block/random copolymers (copolypeptides) exist. In the latter case, both the core and corona of aggregates consist of a polypeptide. All of the studies reported so far have dealt with aggregation in aqueous media.

Doi and coworkers [48, 49] observed the spontaneous formation of aggregates of PMLGlu<sub>10</sub> with a phosphate (P) head group in water. Immediately after sonication, the freshly prepared solution contained globular assemblies (diameter: 50–100 nm, TEM), which after 1 h transformed into fibrous aggregates, promoted by intermolecular hydrogen bonding between peptide chains. After one day, these fibrils assembled into a twisted ribbon-like aggregate (TEM). As its thickness was  $\approx$  4 nm, which is close to the contour length of PMLGlu<sub>10</sub>-P in a  $\beta$ -sheet conformation (CD and FT-IR spectroscopy), these workers concluded that the formation of the ribbon was driven by a stacking of anti-parallel  $\beta$ -sheets via hydrophobic interactions (see above) [22].

Lecommandoux and coworkers [50] showed that zwitterionic PLGlu<sub>15</sub>-*b*-PLLys<sub>15</sub> in water can self-assemble into unilamellar vesicles with a hydrodynamic radius of greater than 100 nm (Figure 27.3). A change in the pH from 3 to 12 induced an inversion of the structure of the membrane (NMR) and was accompanied by an increase in the size of vesicles from 110 to 175 nm (DLS).

Non-ionic block copolypeptides made of L-leucine and ethylene glycol modified L-lysine residues, PLLeu<sub>10–75</sub>-*b*-PELLys<sub>60–200</sub>, were described by Deming and coworkers [51]. The copolymers adopted a rod-like conformation, due to the strong tendency of both segments to form  $\alpha$ -helices, as confirmed by CD spectroscopy. The self-assembled structures observed in aqueous solutions included (sub-) micrometer vesicles, sheet-like membranes and irregular aggregates. Here again, it was shown that the vesicle formation is related to the systematic presence of the polypeptide in a rod-like conformation in the hydrophobic part of the membrane, inducing a low interfacial curvature and as a result a hollow structure.



**Figure 27.3** Schematic representation of the self-assembly of zwitterionic PLGlu<sub>15</sub>-*b*-PLLys<sub>15</sub> in water into unilamellar vesicles [50].

Meyrueix and coworkers [52] performed the selective precipitation of PLLeu<sub>180</sub>-*b*-PLGlu<sub>180</sub> and obtained nanoparticles, which could be purified and further suspended in water or in a 0.15 M phosphate saline buffer at pH 7.4. The colloidal dispersions were stable, due to the electrosteric stabilization of the particles by poly(sodium L-glutamate) brushes, containing spherical or cylindrical micelles, besides the large hexagonally-shaped platelets with a diameter of about 200 nm (TEM). Different shapes of particles were due to the heterogeneity of copolymer chains with respect to chemical composition (NMR): glutamate-rich chains formed micelles and leucine-rich ones formed platelets. CD spectroscopy and X-ray diffraction suggested that the core of platelets consisted of crystalline, helical PLLeu segments, and the structural driving force was thus related to the formation of leucine zippers in a three-dimensional array.

### 27.2.2

#### **Polypeptide-based Hydrogels**

Protein-based hydrogels are used for many applications, ranging from food and cosmetic thickeners to support matrices for drug delivery and tissue replacement. These materials are usually prepared using proteins extracted from natural resources, which can give rise to inconsistent properties unsuitable for medical applications.

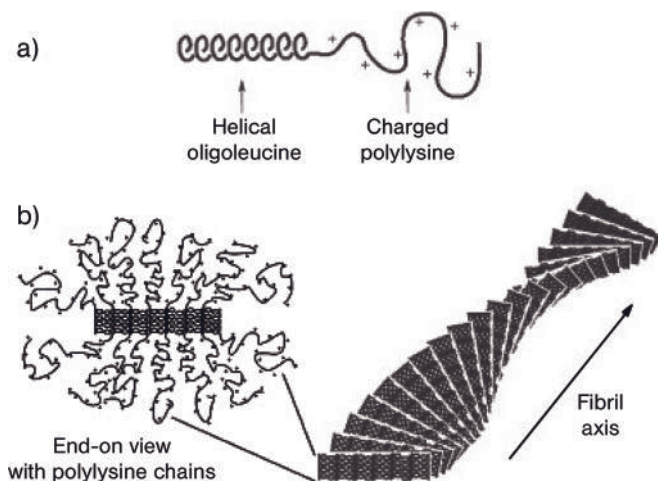
Recently, Deming and coworkers [53–56] designed and synthesized diblock copolypeptide amphiphiles containing charged and hydrophobic segments. It was found and demonstrated that gelation depends not only on the amphiphilic nature of the polypeptides, but also on chain conformation, meaning  $\alpha$ -helix,  $\beta$ -strand or random coil. Specific rheological measurements were performed to evidence the self-assembly process responsible for gelation [55]: the rod-like helical secondary structure of enantiomerically pure PLLeu blocks is instrumental for gelation at polypeptide concentrations as low as 0.25 wt-%. The hydrophilic polyelectrolyte segments have stretched coil configurations and stabilize the twisted fibrillar assemblies by forming a corona around the hydrophobic cores (Figure 27.4).

Interestingly, these hydrogels can retain their mechanical strength up to temperatures of about 90 °C and recover rapidly after stress. This new mode of assembly was found to give rise to polypeptide hydrogels with a unique combination of properties, such as heat stability and injectability, making them attractive for applications in foods, personal care products and medicine. In this context, their potential application as tissue engineering scaffolds has been recently studied [57].

### 27.2.3

#### **Organic/Inorganic Hybrid Structures**

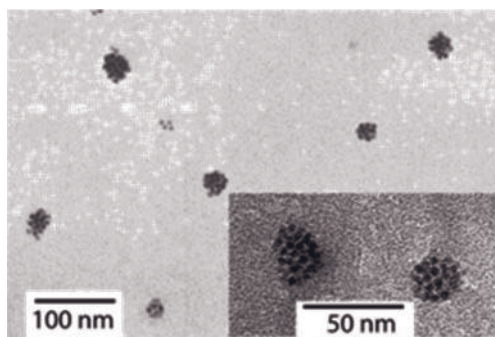
Recently, polypeptide-based copolymers have also been used for the stabilization or synthesis of inorganic species. As a first example, Stucky and coworkers [58] used block copolypeptides to direct the self-assembly of silica into spherical and columnar morphologies at room temperature and neutral pH.



**Figure 27.4** Drawings showing (a) representation of a block copolypeptide chain and (b) proposed packing of block copolypeptide amphiphiles into twisted fibrillar tapes, with helices packed perpendicular to the fibril axes. Polylysine chains were omitted from the fibril drawing for clarity (reprinted from [55] with permission of The American Chemical Society).

Stucky, Deming and colleagues [59] also designed a double-hydrophilic block copolypeptide poly{ $N^{\epsilon}$ -2[2-(2-methoxyethoxy)ethoxy]acetyl L-lysine} $_{100}$ -*b*-poly(sodium L-aspartate) $_{30}$  (PELLys-*b*-PNaLAsp) that can direct the crystallization of calcium carbonate into microspheres. They incorporated PLAsp in the diblock because domains of anionic aspartate residues are known to nucleate calcium carbonate crystallization. This effect is believed to be caused by matching interactions between aspartate and the atomic spacing of certain crystal faces in the growing mineral.

Also worth mentioning is the application of polypeptide-based copolymers in the production of magnetic nanocomposite materials. Lecommandoux *et al.* [60] obtained stable dispersions of super-paramagnetic micelles and vesicles by combining an aqueous solution of PB $_{48}$ -*b*-PLGlu $_{56-145}$  with a ferrofluid consisting of maghemite ( $\gamma$ -Fe $_2$ O $_3$ ) nanoparticles. Incorporation of one mass equivalent of ferrofluid into the hydrophobic core of aggregates did not alter their morphology, as deduced from SLS and SANS data, but caused a substantial increase in the outer diameter by a factor of 6 (DLS). Interestingly, the hybrid vesicles underwent deformation under a magnetic field, as shown by 2D-SANS experiments. Held and coworkers [61] earlier reported that monodisperse, highly crystalline maghemite nanoparticles in organic solvents could be transferred into an aqueous medium using tetramethylammonium hydroxide stabilized at neutral pH. Combination of the aqueous maghemite solution with PELLys $_{100}$ -*b*-PAsp $_{30}$  led to the formation of uniform clusters comprising approximately 20 nanoparticles (Figure 27.5).



**Figure 27.5** TEM images of clusters of maghemite nanoparticles deposited from dispersions in water in the presence of PELLys<sub>100</sub>-*b*-PASP<sub>30</sub> (reprinted from [61] with permission of The American Chemical Society).

## 27.3

### Solid-state Structures of Polypeptide-based Block Copolymers

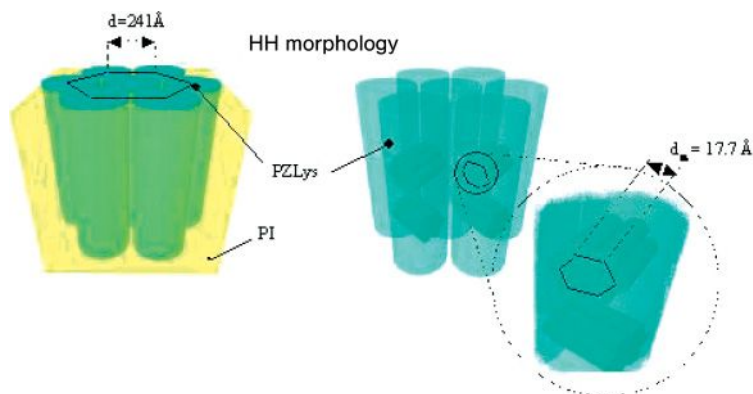
#### 27.3.1

##### Diblock Copolymers

###### 27.3.1.1 Polydiene-based Diblock Copolymers

One of the first reports on the nanoscale solid-state structure of peptide–synthetic hybrid block copolymers was published by Gallot and coworkers [62] in 1976. In this publication, the solid-state structure of a series of PB-*b*-PBLGlu and PB-*b*-PHLGLn diblock copolymers was investigated using a combination of techniques, including infrared and CD spectroscopy, X-ray scattering and TEM. The block copolymers covered a broad composition range with peptide contents ranging from 19 to 75%. Interestingly, SAXS revealed a well-ordered lamellar superstructure characterized by up to four higher-order Bragg spacings for all of the investigated samples. The lamellar superstructure was confirmed by electron microscopy experiments, which were carried out on OsO<sub>4</sub>-stained specimens. The intersheet spacings determined from the electron micrographs were in good agreement with the diffraction data. Wide-angle X-ray scattering (WAXS) experiments indicated that the  $\alpha$ -helical peptide blocks were assembled in a hexagonal array. For a number of block copolymer samples it was found that the calculated length of the peptide helix was larger than the thickness of the polypeptide layer. To accommodate this difference, it was proposed that the peptide helices were folded in the peptide layer. The lamellar structure consists of plane, parallel equidistant sheets. Each sheet is obtained by superposition of two layers: (1) the PB chains in a more or less random coil conformation and (2) the  $\alpha$ -helical polypeptide blocks in a hexagonal array of folded chains. The hexagonal-in-lamellar structure was also found for PB-*b*-PZLLys and PB-*b*-PLLys block copolymers by the same





**Figure 27.6** Schematic model representation of the hexagonal (HH) morphology obtained for  $PI_{49}\text{-}b\text{-}PZLLys_{178}$  copolymer cast from dioxane solution.

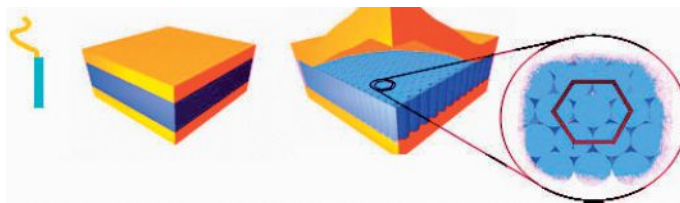
workers [63–66]. In the case of the PB-PLLys block copolymers, no periodic arrangement of the PLLys chains in the peptide layer was found. This is due to the fact that the polypeptide segments in these block copolymers are not exclusively  $\alpha$ -helical but are composed roughly of 50% random coil, 35%  $\alpha$ -helix and 15%  $\beta$ -strand domains [63].

More recently, the solid-state nanoscale structure of  $PI\text{-}b\text{-}PZLLys$  diblock copolymers was reported [34]. Diblock copolymers composed of a P1 block with a number-average degree of polymerization of 49 and a PZLLys block containing 61–178 amino acid residues were investigated with dynamic mechanical analysis and X-ray scattering. For the  $PI_{49}\text{-}b\text{-}PZLLys_{35}$ ,  $PI_{49}\text{-}b\text{-}PZLLys_{61}$  and  $PI_{49}\text{-}b\text{-}PZLLys_{92}$ , the X-ray scattering data were in agreement with a hexagonal-in-lamellar morphology. Interestingly, for  $PI_{49}\text{-}b\text{-}PZLLys_{92}$  the lamellar spacing was found to decrease when the samples were prepared from dioxane instead of THF/*N,N*-dimethylformamide (DMF) and suggested folding of the peptide helices. For  $PI_{49}\text{-}b\text{-}PZLLys_{123}$  and  $PI_{49}\text{-}b\text{-}PZLLys_{178}$  a hexagonal-in-hexagonal structure was found. This morphology is illustrated in Figure 27.6. This structure is unprecedented for polydiene-based peptide hybrid block copolymers, but has also been found for low molecular weight  $PS\text{-}b\text{-}PBLGlu$  copolymers [73].

### 27.3.1.2 Polystyrene-based Diblock Copolymers

In an early study, Gallot and coworkers [64] reported on the bulk nanoscale structure of  $PS\text{-}b\text{-}PZLLys$  diblock copolymers, which were based on a PS block with a number-average molecular weight of  $M_n = 37\text{ kg mol}^{-1}$  and had peptide contents ranging from 18 to 80 mol-%. X-ray scattering patterns of dry samples that had been evaporated from dioxane showed two sets of signals, characteristic of a hexagonal-in-lamellar superstructure. At very low angles, Bragg spacings characteristic of a layered superstructure were found, whereas at somewhat larger angles,





**Figure 27.7** Schematic model representation of the hexagonal-in-lamellar (HL) morphology obtained for polypeptide-based rod-coil diblock copolymers cast from solutions.

there was a second set of reflections pointing towards a hexagonal arrangement of peptide helices. For several samples, the calculated length of the peptide helix was larger than the peptide layer thickness as determined from the X-ray data. In these cases, it was proposed that the helical PZLLys chains were folded in the peptide layer. Thus, the bulk nanoscale structure of the PS-*b*-PZLLys copolymers can be described in terms of the same hexagonal-in-lamellar model as was also proposed for the PB-based block copolymer described earlier (Figure 27.7).

Removal of the of the side-chain protective groups of the peptide segment resulted in PS-*b*-PLLys diblock copolymers [63]. These copolymers were not water soluble, but formed mesomorphic gels at water contents of less than 50%. The X-ray scattering patterns indicated a lamellar superstructure, both in the gel state and the dry samples. In contrast to the side-chain protected block copolymers, no evidence for a periodic arrangement of the peptide chains was found. This is not too surprising considering that IR spectra indicated that roughly 50% of the peptide blocks have a random coil conformation, 35% an  $\alpha$ -helical secondary structure and 15% a  $\beta$ -strand conformation.

Along the same lines, Douy and Gallot [66] also studied the bulk nanoscale organization of PS-*b*-PBLGlu. For block copolymers composed of a PS block with  $M_n = 25 \text{ kg mol}^{-1}$  and containing 31–94 mol-% peptide, the same hexagonal-in-lamellar morphology as described above for the PS-*b*-PZLLys was found. The biocompatibility of PS-*b*-PBLGlu copolymers has been discussed in two publications [67, 68]. Mori *et al.* [68] studied diblock copolymers composed of a PS block with a number-average degree of polymerization of 87 and PBLGlu segments with number-average degrees of polymerization of 23, 52 or 83. Thrombus formation was assessed by exposing films of the diblock copolymers and the corresponding homopolypeptides to fresh canine blood. It was found that thrombus formation on the diblock copolymer films was reduced compared with the corresponding homopolymers. For the block copolymers, thrombus formation decreased with decreasing PBLGlu block length. Also, adsorption of plasma proteins such as bovine serum albumine, bovine  $\gamma$ -globulin and bovine plasma fibrinogen was reduced on the block copolymers compared with PS homopolymer.

The characterization of the solid-state nanoscale organization of PS-polypeptide hybrid block copolymers has recently been refined in a series of publications by

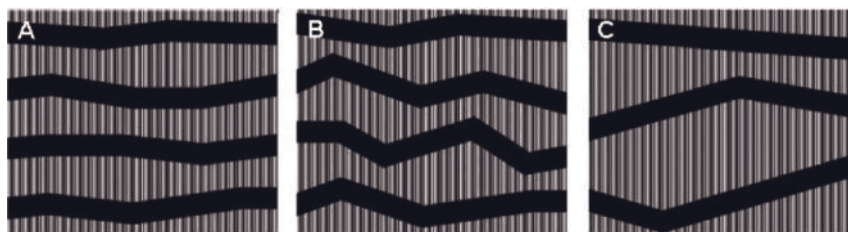
Schlaad and coworkers [69–71]. In a first report, three PS-*b*-PZLLys diblock copolymers with peptide volume fractions of 0.48, 0.74 and 0.82 were investigated [69]. SAXS patterns recorded from DMF cast films confirmed the hexagonal-in-lamellar morphology published earlier by Gallot and coworkers [64]. In their paper, Schlaad and coworkers went a step further and analyzed their SAXS data using the interface-distribution concept and the curvature-interface formalism. These evaluation techniques suggested that the bulk nanoscale structure of the PS-*b*-PZLLys diblock copolymers does not consist of plain but of undulated lamellae. The concept of the interface-distribution function and the curvature-interface formalism were also applied to compare the solid-state structures of two virtually identical PS based diblock copolymers; PS<sub>52</sub>-*b*-PZLLys<sub>111</sub> ( $\phi_{\text{peptide}} = 0.82$ ) and PS<sub>52</sub>-*b*-PBLGlu<sub>104</sub> ( $\phi_{\text{peptide}} = 0.79$ ) [70]. Analysis of the SAXS data obtained on DMF-cast films indicated a hexagonal-in-undulated (or zigzag) lamellar morphology for both block copolymers. However, the X-ray data also revealed two striking differences between the samples. The first difference concerns the thickness of the layers, which are a factor of three smaller for PS<sub>52</sub>-*b*-PBLGlu<sub>104</sub> as compared with PS<sub>52</sub>-*b*-PZLLys<sub>111</sub>. Whereas the PZLLys helices are fully stretched, the PBLGlu helices are folded twice in the layers. As peptide folding increases the area per chain at the PS-PBLGlu interface, the thickness of the PS layers also has to decrease in order to cover the increased interfacial area. The second difference concerns the packing of the peptide helices. For the PZLLys-based diblock copolymer it was estimated that about 180 peptide helices form an ordered domain. The level of ordering, however, was considerably lower for the peptide blocks of PS<sub>52</sub>-*b*-PBLGlu<sub>104</sub> and only  $\approx 80$  helices were estimated to form a single hexagonally ordered domain.

In addition, the influence of the polydispersity of the polypeptide block on the solid-state morphology of PS-*b*-PZLLys diblock copolymers has also been studied [71]. To this end, a series of five diblock copolymers was prepared from an identical  $\omega$ -amino-polystyrene macroinitiator ( $P_n = 52$ ; polydispersity index, PDI = 1.03). The peptide content in these diblock copolymers varied between 0.43 and 0.68 and the PDI ranged from 1.03 to 1.64. Evaluation of the SAXS data with the interface-distribution function and the curvature-interface formalism confirmed, as expected, the hexagonal-in-undulated (or zigzag) lamellar solid-state morphology. Fractionation of the peptide helices according to their length leads (locally) to the formation of an almost plane, parallel lamellar interface, which is disrupted by kinks (undulations). The curvature at the PS-PZLLys interface, however, was found to be strongly dependent on the chain length distribution of the peptide block. Block copolymers with the smallest molecular weight distribution produced lamellar structures with the least curvature. Increasing the chain length distribution of the peptide block (block copolymers with PDI  $\approx 1.25$ ) leads to larger fluctuations in the thickness of the PZLLys layers, which increases the number of kinks and the curvature at the lamellar interface. At even larger polydispersities (PDI  $\approx 1.64$ ), however, the number of kinks decreases again. With increasing polydispersity of the peptide block, the thickness fluctuations become larger and larger, as does the interfacial area. At a certain point, at sufficiently high polydispersity, the system tries to

compensate for the increased interfacial tension and minimizes the number of kinks (Figure 27.8).

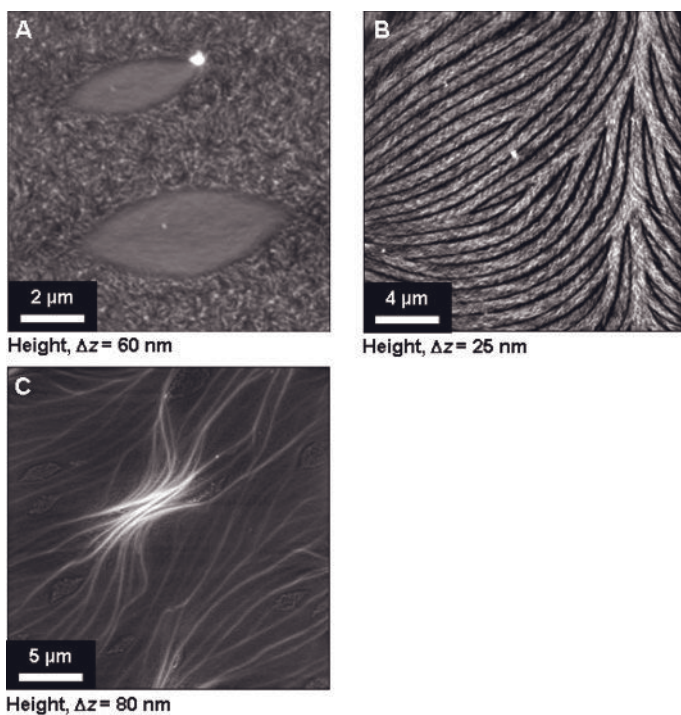
Ludwigs *et al.* [72] used SFM to investigate the formation of hierarchical structures of PS<sub>52</sub>-*b*-PBLGlu<sub>104</sub> in thin films. Thin films with a thickness of  $\approx 4$  and 40 nm were prepared by spin-coating of dilute polymer solutions on silicon substrates and were subsequently annealed in saturated THF vapor to achieve a controlled crystallization of the  $\alpha$ -helical PBLGlu. On the smallest length-scale, the structure was found to be built of short ribbons or lamellae of interdigitated polymer chains. PBLGlu helices were fully stretched in thin films, in contrast to what has been observed in the 3D organized bulk mesophase (see above). Depending on the time of solvent annealing, different ordered structures on the micrometer length-scale could be observed (Figure 27.9).

The examples discussed so far have all involved relatively high molecular weight diblock copolymers. In these cases, the molecular weight of the polypeptide block is usually sufficiently high so that it forms a stable  $\alpha$ -helix and the common hexagonal-in-lamellar morphology is found. The situation changes, however, when the molecular weight of the block copolymers is significantly decreased. The influence of molecular weight on the solid-state organization of polystyrene-based peptide–synthetic hybrid block copolymers has been studied for a series of low-molecular weight PS-*b*-PBLGlu and PS-*b*-PZLLys [73, 74]. These diblock copolymers consisted of a short PS block with  $P_n \approx 10$ , a polypeptide block containing  $\approx 10$  to 80 amino acid repeat units and were characterized by means of variable temperature FT-IR spectroscopy and X-ray scattering. These experiments allowed the construction of “phase diagrams”, which are shown in Figure 27.10. The phase diagrams reveal a number of interesting features. At temperatures below 200 °C and for sufficiently long polypeptide blocks, a hexagonal arrangement of the diblock copolymers was found, analogous to the hexagonal-in-lamellar morphology of the high-molecular weight analogues. Upon decreasing the length of the peptide block, however, several novel solid-state structures were discovered. For very short peptide block lengths (PS<sub>10</sub>-*b*-PBLGlu<sub>10</sub>, PS<sub>10</sub>-*b*-PZLLys<sub>20</sub>, PS<sub>10</sub>-*b*-PZLLys<sub>40</sub> and PS<sub>10</sub>-*b*-PZLLys<sub>60</sub>) a lamellar supramolecular structure was found. This is



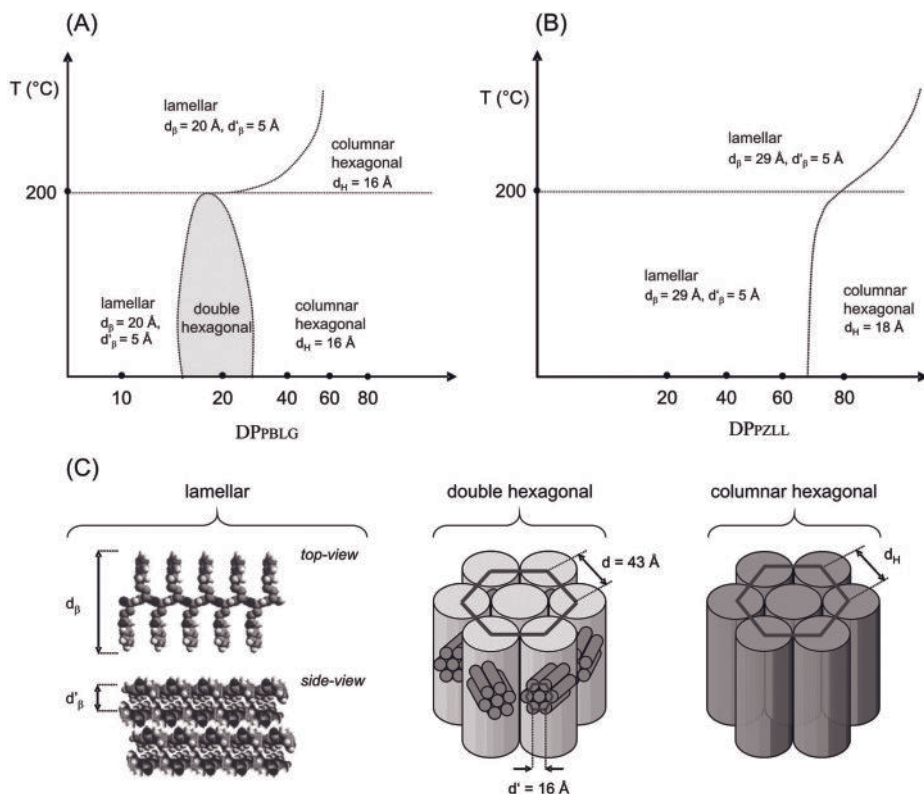
**Figure 27.8** Schematic representation of the disordered zigzag lamellar morphology formed by polypeptide-based diblock copolymers with low (A), moderate (B) and high polydispersity (C) with respect to the

length of helices. Polypeptide helices are represented as cylinders, and polyvinyl sheets are depicted in black (reprinted from [71] with permission of The American Chemical Society).



**Figure 27.9** SFM height images of a film of  $\text{PS}_{52}\text{-}b\text{-PBLGlu}_{104}$  obtained by spin-coating from a  $5 \text{ mg mL}^{-1}$  THF solution and subsequent exposure to saturated THF vapor for 3.5 (A), 22.5 (B) and 42 h (C) (reprinted from [72] with permission of The American Chemical Society).

due to the fact that for such short peptide block lengths, a substantial fraction of the peptide blocks adopts a  $\beta$ -strand secondary structure. Self-assembly of these diblock copolymers in a  $\beta$ -sheet type fashion results in the lamellar structures observed by SAXS. For  $\text{PS}_{10}\text{-}b\text{-PBLGlu}_{20}$  a peculiar and until then unprecedented structure was found. This structure that consisted of hexagonally packed diblock copolymer molecules, which are organized in a hexagonal superlattice, has been referred to as the double hexagonal or hexagonal-in-hexagonal morphology. Apart from several unconventional solid-state nanoscale structures, another factor that distinguishes the phase diagrams in Figure 27.10 from those of most conventional, conformationally isotropic block copolymers is the influence of temperature. For a number of diblock copolymers, increasing the temperature above  $200^\circ\text{C}$  results in a change from a hexagonal-in-hexagonal ( $\text{PS}_{10}\text{-}b\text{-PBLGlu}_{20}$ ) or hexagonal ( $\text{PS}_{10}\text{-}b\text{-PBLGlu}_{40}$ ,  $\text{PS}_{10}\text{-}b\text{-PZLLys}_{80}$ ) to a lamellar morphology. FT-IR spectroscopy experiments suggested that these morphological transitions are induced by an increase in the fraction of peptide blocks that have a  $\beta$ -strand conformation.



**Figure 27.10** Phase diagrams describing the solid-state nanoscale structure of (A) PS-*b*-PBLGlu and (B) PS-*b*-PZLLys diblock copolymers; (C) illustration of the lamellar, double hexagonal and hexagonal

morphologies found for the low molecular weight hybrid block copolymers (reprinted from [73, 74] with permission of The American Chemical Society).

### 27.3.1.3 Polyether-based Diblock Copolymers

PEG–polypeptide block copolymers are of particular interest, from both a structural and a functional point of view. Unlike the hybrid block copolymers discussed in the previous paragraphs, which were based on amorphous synthetic polymers, PEG is a semi-crystalline polymer. In addition to microphase separation and the tendency of the peptide blocks towards aggregation, crystallization of PEG introduces an additional factor that can influence the structure formation of these hybrid block copolymers. Ma and coworkers [75] have investigated the solid-state structure and properties of three PEG-*b*-PAla copolymers that were prepared from a PEG macroinitiator with  $M_n = 2 \text{ kg mol}^{-1}$ . The diblock copolymers contained 39.8, 49.6 and 65.5 mol-% alanine. From FT-IR spectra and DSC measurements, these workers proposed a microphase-separated bulk structure.

AB diblock and ABA triblock copolymers composed of PEG as the A block and random coil segments of poly(D,L-valine-co-D,L-leucine) as the B block(s) were

investigated by Cho and coworkers [76]. DSC experiments revealed PEG crystallization and showed that the PEG melting temperature was decreased compared with that of the PEG homopolymer. TEM micrographs suggested a lamellar microphase-separated structure for one of the triblock copolymer samples.

#### 27.3.1.4 Polyester-based Diblock Copolymers

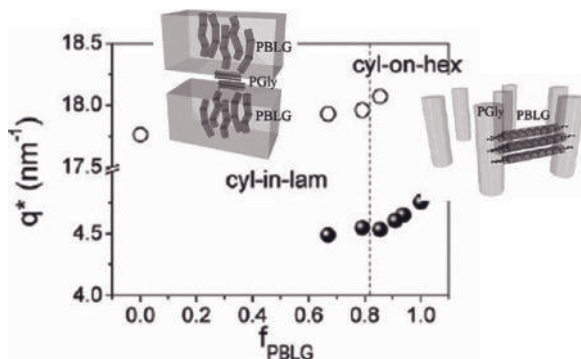
One of the first studies focusing on the solid-state properties of polypeptide–polyester synthetic hybrid block copolymers was reported by Jérôme and coworkers [77]. DSC experiments on a poly( $\epsilon$ -caprolactone)<sub>50</sub>-*block*-poly( $\gamma$ -benzyl L-glutamate)<sub>40</sub> (PCL<sub>50</sub>-*b*-PBLGlu<sub>40</sub>) diblock copolymer revealed two endotherms. The first endotherm was found at 60°C and is due to the melting of the PCL. The second endotherm, which was located at 110°C, was, mistakenly, interpreted as the melting transition of PBLGlu. This transition, however, is not a melting transition, but instead reflects the conformational transition of the PBLGlu helix from a 7/2 to an 18/5 helical structure. Although no further structural investigations were carried out, the observation of two separate endotherms occurring at temperatures identical to the transitions found for the respective homopolymers was a first indication for the existence of a microphase-separated structure. Similar results were reported by Chen and coworkers [78] who investigated the thermal properties of a series of PCL-*b*-PBLGlu copolymers composed of PCL blocks containing 13–51 repeat peptide segment units with and 22–52 amino acid repeat units.

Caillol *et al.* [79] have studied the solid-state structure and properties of a series of PLL-*b*-PBLGlu [PLL = poly(L-lactide)] copolymers. The PLL block in these copolymers contained 10–40 repeat units and the peptide segments were composed of 20–100 repeat units. DSC thermograms of the block copolymers revealed three transitions corresponding to the  $T_g$  of PLL ( $\approx 50^\circ\text{C}$ ), the 7/2 to 18/5 helix transition of PBLGlu ( $\approx 100^\circ\text{C}$ ) and the melting temperature of PLL ( $\approx 160^\circ\text{C}$ ), respectively. This observation was already providing a first hint towards a microphase-separated bulk morphology. SAXS experiments, which were performed at 100°C, indicated the existence of hexagonally ordered assemblies of  $\alpha$ -helical PBLGlu chains. With decreasing glutamate content, the peaks corresponding to this hexagonal organization decreased in intensity and another scattering peak appeared, which was ascribed to a lamellar assembly of PBLGlu chains with a  $\beta$ -strand secondary structure. Increasing the temperature to 200°C not only resulted in melting of PLL, but also led to a decrease in intensity of the diffraction peaks corresponding to the hexagonally ordered  $\alpha$ -helical PBLGlu segments and an increase in the fraction of PBLGlu segments that are ordered in a lamellar  $\beta$ -strand fashion.

#### 27.3.1.5 Diblock Copolypeptides

A step forward in the design of hierarchically ordered structures with biofunctionality has been the subject of recent reports on the synthesis of block copolymers based on polypeptides. In the first such report [80], organo-nickel initiators rather than amines were used to avoid the unwanted  $\alpha$ -amino acid *N*-carboxyanhydrides (NCA) side reactions, which had, for more than 50 years, hampered the formation of well-defined copolypeptides. This approach gave rise to various peptidic-based





**Figure 27.11** Dependence of the WAXS peak positions on the PBLGlu (PBLG) volume fraction, corresponding to the distance between PBLGlu  $\alpha$ -helices (filled circles) and PGly  $\beta$ -sheets (open circles). The interhelix (inter-sheet) distance increases (decreases) with increasing polypeptide volume fraction. The vertical line separates the two nanodomain morphologies.

block copolymers that have mainly been studied in solution (see previous section). A second approach addressed the side reaction problem directly by using amines in combination with high-vacuum techniques, to ensure the necessary conditions for the living polymerization of NCAs: PBLGlu-*b*-PGly (PGly = polyglycine) were prepared for the first time with this methodology [81].

Despite these important synthetic efforts, the solid-state morphology of purely peptidic block copolymers is largely unexplored. Hadjichristidis and coworkers [81] recently investigated the self-assembly of a series of narrow polydispersity PBLGlu-*b*-PGly diblock copolymers within the composition range  $0.67 < f_{\text{PBLGlu}} < 0.97$  and the temperature range  $303 < T < 433$  K. SAXS and WAXS,  $^{13}\text{C}$  NMR and DSC were used for the structure investigation coupled with dielectric spectroscopy for both the peptide secondary structure and the associated dynamics. These techniques not only provided insight into the nanophase morphology but also gave information about the type and persistence of peptide secondary structures. Particular evidence has been found for hexagonal-in-lamellar and cylinder-on-hexagonal nanostructures (Figure 27.11). The thermodynamic confinement of the blocks within the nanodomains and the disparity in their packing efficiency results in multiple chain folding of the PGly secondary structure that effectively stabilizes a lamellar morphology for high  $f_{\text{PBLGlu}}$ . Nanoscale confinement proved to be important in controlling the persistence length of secondary peptide motifs.

### 27.3.2

#### Triblock Copolymers

##### 27.3.2.1 Polydiene-based Triblock Copolymers

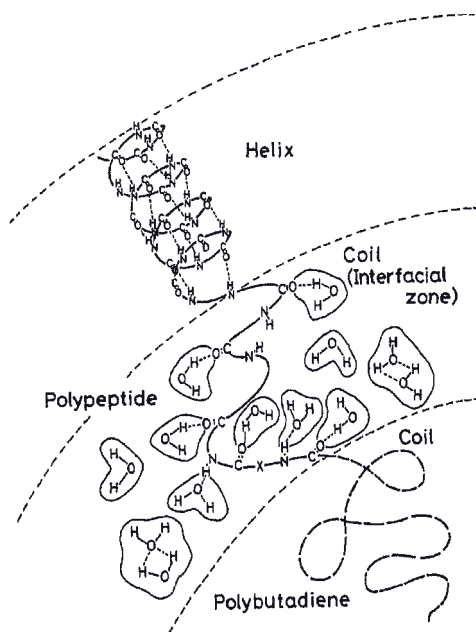
Whereas Gallot and coworkers have mainly studied the solid-state organization of PB-based diblock copolymers, Nakajima *et al.* concentrated on ABA-type hybrid block copolymers containing PB as the B component (“once-broken rods”). In a

first series of publications, the structure and properties of PBLGlu-*b*-PB-*b*-PBLGlu triblock copolymers containing 7.5–32.5 mol-% (= 3.0–14.3 vol-%) PB were investigated [82–84]. Infrared spectroscopy and WAXS experiments on films of the triblock copolymers indicated that the PBLGlu blocks were predominantly  $\alpha$ -helical. From the WAXS experiments, it was concluded that the PBLGlu blocks assembled into different structures, depending on the type of solvent that was used to cast the films. In benzene cast films, the peptide helices were relatively poorly ordered, similar to the so-called form A morphology of PBLGlu [85]. In contrast, the PBLGlu segments in films cast from  $\text{CHCl}_3$  were well ordered and contained paracrystalline and mesomorphic regions. Based on TEM, a cylindrical microstructure was proposed for a triblock copolymer containing 8 vol-% PB. Electron micrographs for other samples were not reported, but based on volume fraction considerations it was predicted that triblock copolymers containing 12 and 14 vol-% PB would form either cylindrical or lamellar superstructures [83]. Interestingly, copolymers having the same composition but polypeptide segments made of either enantiomerically pure or racemic  $\gamma$ -benzyl glutamate exhibited not only different secondary structures ( $\alpha$ -helix or random coil, respectively; FTIR and WAXS) but also different superstructures (TEM). A cylindrical or lamellar morphology was proposed in the first case and a more spherical superstructure in the second [86].

Further support for the microphase-separated structure of the PBLGlu-*b*-PB-*b*-PBLGlu triblock copolymers was obtained from dynamic mechanical spectroscopy and water permeability experiments [84]. The temperature dependence of the dynamic modulus and the loss modulus could be explained well by assuming a microphase-separated structure. Furthermore, the hydraulic permeability of water through membranes prepared from the copolymers was approximately three orders of magnitude larger compared with a pure PBLGlu membrane. The hydraulic water permeability was found to increase with increasing PB content in the block copolymers. This was explained in terms of microphase-separated structure and the presence of an interfacial zone that separates the ordered domains formed by the  $\alpha$ -helical PBLGlu chains from the unordered PB phase (Figure 27.12). The interfacial zone consists of amino acid residues that are located close to the N-terminus of the peptide block and in the vicinity of the PB segment. The amino acid residues in the interfacial zone do not form regular secondary structures. As the amide groups of the peptide chains in the interfacial zone are not involved in intramolecular hydrogen bonding, they are able to bind water molecules. Consequently, increasing the interfacial zone, e. g., by increasing the PB content, leads to an increase in the water permeability.

The bulk and surface structure of solvent-cast films from a series of PBLGlu-*b*-PB-*b*-PBLGlu triblock copolymers with much higher PB contents (50–80 mol-%) than the samples discussed above have been described by Gallot and coworkers [87]. The organization of these copolymers was compared with that of three other triblock copolymers with approximately the same PB content ( $\approx 50$  mol-%) but which were composed of poly( $N^{\epsilon}$ -trifluoroacetyl L-lysine) (PTLLys), poly( $N^5$ -hydroxyethyl L-glutamine) (PHLGln) or polysarcosine (PSar) as the peptide block. For any





**Figure 27.12** Hydrogen-bonded water and water clusters in an interfacial zone formed by unordered peptide chains that separate the PB domains from the helical PBLGlu phase in films of ABA triblock copolymers.

sample investigated, X-ray scattering experiments indicated a hexagonal-in-lamellar bulk morphology. X-ray photoelectron spectroscopy (XPS) measurements revealed that for the triblock copolymers with hydrophobic peptide blocks, i. e., PBLGlu or PTLlys, the surface composition was identical with that in the bulk of the sample. In contrast, the surfaces of films prepared from the triblock copolymers with the more hydrophilic peptide segments, i.e., PHLGln or PSar, were PB enriched. Furthermore, the XPS data suggested that the lamellar superstructures formed by the triblock copolymers were perpendicular to the air–polymer interface.

In addition, the solid-state organization and properties of PZLLys-*b*-PB-*b*-PZLLys triblock copolymers have been investigated. Nakajima and coworkers [88, 89] have studied copolymers composed of a central PB block with  $M_n = 3.6 \text{ kg mol}^{-1}$  and PB contents ranging from 12 to 52 mol-%. WAXS patterns obtained from solution-cast triblock copolymer films were in agreement with the  $\alpha$ -helical secondary structure of the peptide blocks. The bulk microphase-separated structure of the five different block copolymer samples could be successfully characterized by means of TEM. For the samples with the largest PB volume fraction (56 and 65 vol-%), a lamellar superstructure was found. However, the electron micrographs suggested cylindrical and spherical microphase-separated structures for triblock copolymers with smaller PB volume fractions.

Other polybutadiene-based ABA type triblock copolymers that have been investigated include PMLGlu-*b*-PB-*b*-PMLGlu and PMGlu-*b*-PB-*b*-PMGlu [PMGlu = poly( $\gamma$ -methyl D,L-glutamate)] [86, 90]. Infrared spectroscopy experiments on solvent-cast films indicated that the incorporation of 50% of the D-isomer disrupts the  $\alpha$ -helical secondary structure and induces a random coil conformation in significant portions of the peptide blocks. From the infrared spectra and WAXS experiments, it was estimated that the helix content of a PMGlu homopolypeptide was about 60% of that of the corresponding PMLGlu. TEM images of OsO<sub>4</sub> stained samples provided evidence for the microphase-separated solid-state structure. Interestingly, different morphologies were observed when comparing the images of PMLGlu-*b*-PB-*b*-PMLGlu and PMGlu-*b*-PB-*b*-PMGlu samples with the same PB content ( $\approx$ 30 mol-%). A cylindrical morphology was proposed for the first and a spherical structure for the second [86] (see above). The difference in morphology was ascribed to the less regular secondary structure of the peptide block in the case of the D,L-triblock copolymer, which prevents a highly ordered organization of the peptide domains and facilitates the formation of spherical PB domains. The ATRIR spectra further showed that adsorption of bovine serum albumine (BSA) and bovine fibrinogen (BF) did not lead to denaturation. From these observations, these workers concluded that the surfaces of the PMGlu-*b*-PB-*b*-PMGlu membranes interact only weakly or reversibly with these plasma proteins and it was predicted that this may also lead to a good overall biocompatibility.

The solid-state structure and properties of PELGlu-*b*-PB-*b*-PELGlu [PELGlu = poly( $\gamma$ -ethyl L-glutamate)] triblock copolymers containing 31.5–94.5 mol-% (= 17–88 vol-%) PELGlu have been studied using the same techniques as described above for the other triblock copolymers [91, 92]. The secondary structure of the PELGlu blocks was found to be predominantly  $\alpha$ -helical and the helix content in the triblock copolymers decreased from 95 to 60% upon decreasing the peptide content from 95 to 61%. Interestingly, the WAXS data suggested that the PELGlu helices were packed in a pseudo-hexagonal, i.e., monoclinic, arrangement instead of the hexagonal structure observed for most of the other investigated peptide–synthetic hybrid block copolymers. TEM experiments on OsO<sub>4</sub> stained films indicated a microphase-separated structure. Based on the electron micrographs, a spherical microphase-separated structure was proposed for the copolymer containing 17 vol-% PB, while cylindrical and lamellar morphologies were suggested for triblock copolymers containing 28 and 44 vol-%, respectively, 68 and 88 vol-% PB. The biocompatibility of the PELGlu-*b*-PB-*b*-PELGlu triblock copolymers was assessed by coating the samples onto a polyester mesh fiber cloth, which was subsequently subcutaneously implanted in mongrel dogs for four weeks. It was found that the foreign body reaction and degradation of the PELGlu-*b*-PB-*b*-PELGlu samples were less pronounced as compared with PMLGlu-*b*-PB-*b*-PMLGlu, PBLGlu-*b*-PB-*b*-PBLGlu and PZLLys-*b*-PB-*b*-PZLLys triblock copolymers.

The bulk nanoscale structure of a series of PBLGlu-*b*-PI-*b*-PBLGlu copolymers containing 37.4–81.1 mol-% PBLGlu was studied by means of infrared spectroscopy, WAXS, dynamic mechanical analysis and electron microscopy [93]. Based

on the electron micrographs, a cylindrical morphology was proposed for triblock copolymers containing 74.6 and 81.1 mol-% PBLGlu. Water permeability measurements also supported the microphase-separated bulk morphology [94]. Further insight into the bulk morphology of the PBLGlu-*b*-PI-*b*-PBLGlu triblock copolymers was obtained from pulsed proton NMR experiments [95]. The NMR signals of the block copolymers were composed of three components with different spin-spin relaxation times ( $T_2$ ). The three different  $T_2$  values were attributed to the microphase-separated structure, which consists of three regions (the ordered helical peptide domains, the unordered interfacial peptide region and the rubbery PI phase) with different molecular mobility. The spin-lattice relaxation times ( $T_1$ ) that were obtained provided insight into the domain sizes, which were in good agreement with the results from TEM. The surface structure of  $\text{CHCl}_3$ -cast films was studied by XPS and contact angle measurements [96]. It was found that the chemical composition of the microphase-separated films at the surface was different from that in the bulk. The PI content at the film surface was higher than that in the bulk. Water contact angle measurements indicated that the block copolymer films were wetted easier than the respective homopolymers for the same reasons as the previous samples.

Treatment of a PBLGlu-*b*-PI-*b*-PBLGlu film with a mixture of 3-amino-1-propanol and 1,8-octamethylenediamine led to the formation of hydrophilic, cross-linked PHLGln-*b*-PI-*b*-PHLGln membranes being obtained [97]. The swelling ratio of these membranes in pseudoextracellular fluid (PECF) was found to decrease with increasing PI content and increasing cross-link density. Tensile tests in PECF revealed that the triblock copolymer membranes had a larger Young's modulus, increased tensile strength and elongation at breaking compared with membranes prepared from PBLGlu homopolymer. Enzymatic degradation experiments using papain showed that the triblock copolymer films were more resistant towards degradation than the corresponding homopolypeptide membranes. The half-times for sample degradation increased with decreasing peptide content, which was in agreement with the swelling behavior of the membranes.

### 27.3.2.2 Polystyrene-based Triblock Copolymers

Tanaka and coworkers studied ABA type triblock copolymers composed of a central PS block flanked by two polypeptide segments (PBLGlu, PZLLys or PSar) [98]. TEM of a  $\text{CHCl}_3$ -cast film of PBLGlu<sub>25</sub>-*b*-PS<sub>165</sub>-*b*-PBLGlu<sub>25</sub> that was stained with phosphotungstic acid revealed a lamellar phase separated structure. In contrast, no microphase separation was observed in a film of PSar<sub>73</sub>-*b*-PS<sub>421</sub>-*b*-PSar<sub>73</sub>. These workers proposed that the different block copolymer morphologies could be related to the different secondary structure of the peptide block; while the PBLGlu segments are predominantly helical, the PSar may not form any regular secondary structure. Fibrinogen adsorption on the block copolymer films was studied with ATR-IR spectroscopy and compared with that on the corresponding homopolymer films [98]. It was found that fibrinogen adsorption on PS and PSar homopolymer films and on PSar-*b*-PS-*b*-PSar triblock copolymer films led to denaturation of the protein. In contrast, protein adsorption on the

microphase-separated PBLGlu-*b*-PS-*b*-PBLGlu surfaces was reported to stabilize the protein's secondary structure. Blood clotting tests suggested that thrombus formation was retarded compared with the respective homopolymers.

Samyn and coworkers [99] extended the investigations of ABA triblock copolymers and studied the solid-state organization of three different PBLGlu-*b*-PS-*b*-PBLGlu copolymers containing 34, 55 and 92 wt-% PBLGlu. TEM micrographs of ultramicrotomed and RuO<sub>4</sub> stained specimens and SAXS experiments indicated a lamellar morphology for the copolymers with 34 and 55 wt-% PBLGlu. The sample containing 92 wt-% PBLGlu did not form a lamellar structure. WAXS patterns yielded *d*-spacings reflecting the intermolecular distance between neighboring peptide  $\alpha$ -helices. Ion permeability measurements on dioxane-cast films indicated that the bulk morphology influences the membrane properties [100]. The membranes prepared from the lamellae forming 34 and 55 wt-% PBLGlu containing triblock copolymers showed cation selectivity. In contrast, the membrane prepared from the triblock copolymer containing 92 wt-% PBLGlu did not show such selectivity. It was proposed that uptake of cations into the triblock copolymer membranes was facilitated by the interactions between the cations and the ester functions in the block copolymers. The difference in selectivity was explained in terms of the interfacial zone (as discussed earlier), which separates the PS and PBLGlu domains only in the films generated by the former two triblock copolymers.

### 27.3.2.3 Polysiloxane-based Triblock Copolymers

Imanishi and coworkers [101] have studied the structure, antithrombogenicity and oxygen permeability of ABA triblock copolymers composed of poly(dimethylsiloxane) (PDMS) as the B block and PBLGlu, PBGLu [poly( $\gamma$ -benzyl D,L-glutamate)], PZLLys or PSar as the A block. Several series of triblock copolymers were prepared using bifunctional PDMS macroinitiators and targeting various peptide block lengths. TEM images of DMF-cast films provided evidence for a microphaseseparated morphology for PZLLys<sub>49</sub>-*b*-PDMS<sub>400</sub>-*b*-PZLLys<sub>49</sub> and PZLLys<sub>91,160</sub>-PDMS<sub>256</sub>-PZLLys<sub>91,160</sub>. The images revealed a spherical morphology composed of PDMS islands in a PZLLys matrix. The formation of these spherical domains was attributed to the solvent that was used for sample preparation. While DMF is a good solvent for PZLLys, it is a poor solvent for PDMS. In a separate publication, the same workers also described non-spherical microphase-separated structures [102]. In CH<sub>2</sub>Cl<sub>2</sub>-cast films of a triblock copolymer with a very high PDMS content (PBLGlu<sub>48</sub>-*b*-PDMS<sub>508</sub>-*b*-PBLGlu<sub>48</sub>, 83 mol-% PDMS) more extended, rod-like PBLGlu aggregates in a matrix of PDMS were observed. The TEM experiments also provided insight into the effects of peptide secondary structure and the nature of the casting solvent on the thin film morphology [101].

Thin films of PBLGlu<sub>42</sub>-*b*-PDMS<sub>148</sub>-*b*-PBLGlu<sub>42</sub> prepared from DMF showed a spherical morphology. Changing the solvent from DMF (a good solvent for PBLGlu) to CH<sub>2</sub>Cl<sub>2</sub> (a fairly non-selective solvent) resulted in coarsening of the microphase-separated structures. PBGLu<sub>42</sub>-*b*-PDMS<sub>148</sub>-*b*-PBGLu<sub>42</sub> films prepared from CH<sub>2</sub>Cl<sub>2</sub> also showed a microphase-separated structure in which spherical

PDMS domains were embedded in a PBGLu matrix. The dimensions of the spherical domains, however, were much smaller than those observed by TEM. These different morphologies reflect the influence of the peptide secondary structure on the block copolymer self-assembly; PBLGlu<sub>42</sub> adopts an  $\alpha$ -helical conformation and PBGLu<sub>42</sub> a random coil conformation. Studies on adsorption/denaturation of proteins and oxygen permeation measurements from these triblock copolymers also tend to describe the relationship between the film morphology and these properties. In addition, a detailed study of the gas permeation properties of PBLGlu-*b*-PDMS-*b*-PBLGlu films cast from CH<sub>2</sub>Cl<sub>2</sub> and DMF solution with PDMS contents ranging from 46 to 83 mol-% has been reported [103] and revealed that the oxygen permeability of the triblock copolymer films in water was found to increase exponentially with increasing PDMS content, in agreement with a microphase-separated morphology of the membranes. Similar results were reported by Kugo *et al.*, who studied oxygen and nitrogen transport across PBLGlu-*b*-PDMS-*b*-PBLGlu triblock copolymers containing 63–81 mol-% PBLGlu [104].

#### 27.3.2.4 Polyether-based Triblock Copolymers

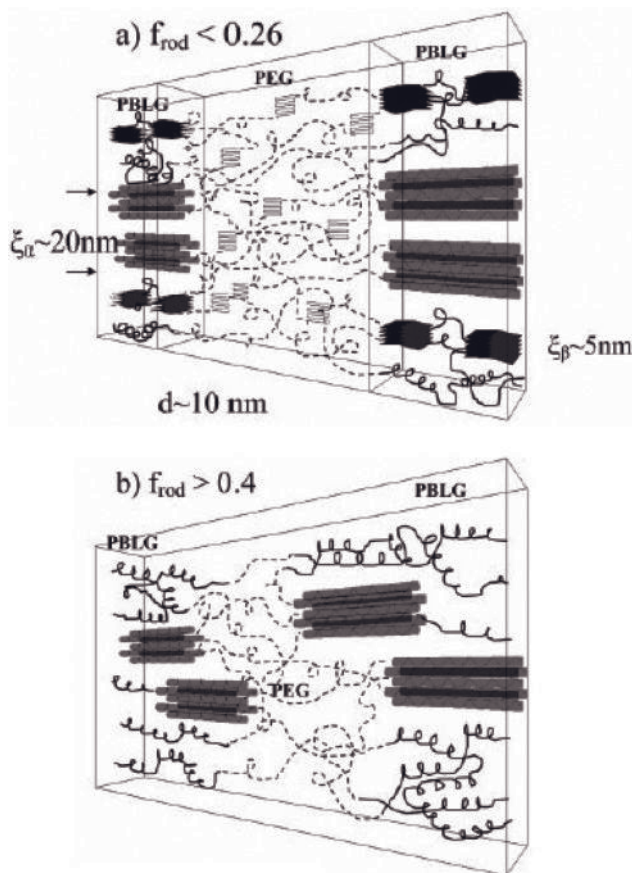
Inoue and coworkers [105, 106] studied the adhesion behavior of rat lymphocytes on solvent-cast films of PBLGlu-*b*-PEG-*b*-PBLGlu triblock copolymers. The triblock copolymers were prepared from  $\alpha,\omega$ -bis-amino functionalized PEG macroinitiators with molecular weights of 1.0 and 4.0 kg mol<sup>-1</sup> and had PEG contents varying from 11 to 33 wt-%. Rat lymphocyte adhesivity was found to decrease with increasing PEG content. At the same PEG content, the adhesivity of the triblock copolymers based on the macroinitiator with a molecular weight of 4 kg mol<sup>-1</sup> was lower than that of samples based on the macroinitiator with 1 kg mol<sup>-1</sup>. In addition to overall lymphocyte adhesivity, these workers also studied the adhesion of specific subpopulations: B-cells and T-cells. All triblock copolymers showed a preference towards B-cells. These experiments, however, revealed that the observed differences in cell adhesion behavior were neither due to differences in the conformation of the peptide blocks, nor could they be attributed to differences in surface hydrophilicity. It was therefore proposed that the observed effects were caused by differences in the higher order surface structures, i.e., in terms of the microphase-separated morphology and/or PEG crystallinity.

Kugo *et al.* [107] studied the solid-state conformation of the peptide segment of a series of PBLGlu-*b*-PEG-*b*-PBLGlu copolymers containing a PEG segment with a molecular weight of 4 kg mol<sup>-1</sup> and 36–86 mol-% PBLGlu. FT-IR spectroscopy experiments on CHCl<sub>3</sub>-cast films revealed that the PBLGlu blocks, which had degrees of polymerization of 25–276, had an  $\alpha$ -helical secondary structure. The helix content of the triblock copolymer containing PBLGlu<sub>276</sub> blocks was found to be similar to that of the PBLGlu homopolymer. Swelling the triblock copolymer films with water resulted in a decrease in helix content, as indicated by the CD spectra. This decrease in helicity was attributed to competition of water clusters to form hydrogen bonds with the peptide backbone. The effect was even more pronounced when pseudo-extracellular fluid was used instead of water.

A first detailed study of the solid-state nanoscale structure of peptide-PEG hybrid block copolymers was published by Cho *et al.* [108]. They investigated thin,  $\text{CHCl}_3$ -cast films of PBLGlu-*b*-PEG-*b*-PBLGlu copolymers, which were composed of a PEG block of  $2\text{ kg mol}^{-1}$  and contained 25–76 mol-% PBLGlu. TEM micrographs of  $\text{RuO}_4$ -stained specimens revealed a lamellar morphology for triblock copolymers containing 25–64 mol-% PBLGlu. The microphase-separated structure was proposed to consist of chain folded, crystalline PEG domains and helical PBLGlu domains (IR). WAXS patterns were consistent with the ordered, crystalline-like solid-state modification C of PBLGlu. In contrast, in films cast from benzene, the peptide blocks only formed poorly ordered arrays. The sensitivity of the organization of the PBLGlu blocks towards the nature of the casting solvent is identical with the behavior of the PBLGlu homopolymer.

In a separate study, the enzymatic degradation behavior of PBLGlu-*b*-PEG-*b*-PBLGlu triblock copolymers was investigated [109]. The rate of degradation was found to increase with increasing PEG content in the triblock copolymers from 1.4 to 3.1 to 13.6 mol-%. A similar dependence on PEG content was observed for the level of swelling. Exposure of the triblock copolymer samples to a PBS solution without the enzyme did not result in measurable weight loss, indicating that hydrolytic degradation did not take place.

While the data reported by Cho *et al.* described the structure and organization of thin solvent cast films of PBLGlu-*b*-PEG-*b*-PBLGlu, Floudas *et al.* have extensively studied the bulk nanoscale organization of these materials [110]. To this end, a series of triblock copolymers with PBLGlu volume fractions ( $f_{\text{PBLGlu}}$ ) ranging from 0.07 to 0.89 was investigated using SAXS/WAXS, polarizing optical microscopy (POM), DSC and FT-IR spectroscopy. For triblock copolymers with  $f_{\text{PBLGlu}} \leq 0.25$ , PEG crystallization was observed, however, with significant undercooling. Triblock copolymers with  $f_{\text{PBLGlu}} \geq 0.43$  did not show PEG crystallization. SAXS experiments, which were carried out at 373 K, i.e., above the melting point of PEG, also revealed a different behavior for triblock copolymers with small and large PBLGlu volume fractions. For triblock copolymers with  $f_{\text{PBLGlu}} \geq 0.43$  only a weakly phase separated structure was found, whereas for samples with  $f_{\text{PBLGlu}} \leq 0.25$  the SAXS data clearly indicated a microphase-separated structure. WAXS patterns showed that in the microphase-separated state the PEG phase was semi-crystalline and the peptide phase consisted of hexagonally ordered assemblies of PBLGlu  $\alpha$ -helices that coexisted with  $\beta$ -sheet structures. For triblock copolymers with  $f_{\text{PBLGlu}} \geq 0.43$ , PEG is amorphous and interspersed with aggregates of  $\alpha$ -helical PBLGlu segments and unordered peptide chains. These different bulk structures are illustrated schematically in Figure 27.13. This figure illustrates how the competing interactions that promote the bulk self-assembly of the PBLGlu-*b*-PEG-*b*-PBLGlu triblock copolymers lead to the formation of hexagonally ordered structures covering different length scales. At the smallest length scale, hydrogen-bonding interactions stabilize peptide secondary structures ( $\alpha$ -helices and  $\beta$ -strands) and PEG chain folding occurs. On the next higher level, peptide  $\alpha$ -helices and  $\beta$ -strands form hexagonal assemblies and  $\beta$ -sheet structures, respectively. Finally,



**Figure 27.13** Highly schematic model of the phase state in the PBLGlu-*b*-PEG-*b*-PBLGlu triblock copolymers. (a) Phase state corresponding to low peptide volume fractions depicting a microphase-separated copolymer consisting of all the peptide and

PEG secondary structures. (b) Phase state corresponding to  $f_{rod} > 0.4$  depicting phase mixing resulting in the appearance of only one ( $\alpha$ -helical) secondary structure (reprinted from [110] with permission of The American Chemical Society).

the mutual incompatibility of the peptide and PEG block leads to microphase separation.

Additional insight into the solid-state nanoscale organization of the triblock copolymers just discussed was obtained by combining SAXS/WAXS with various microscopic techniques (TEM and AFM) [111]. A “broken lamellar” morphology was observed in the TEM micrographs of PBLGlu<sub>58</sub>-*b*-PEG<sub>90</sub>-*b*-PBLGlu<sub>58</sub> ( $f_{\text{PBLGlu}} = 0.58$ ). Annealing converted this metastable structure into a nonuniform microphase-separated pattern, which was proposed to consist of “pucklike” PEG domains in a PBLGlu matrix. For PBLGlu<sub>105</sub>-*b*-PEG<sub>90</sub>-*b*-PBLGlu<sub>105</sub> ( $f_{\text{PBLGlu}} = 0.67$ ), a lamellar morphology was found in the as-cast film, which was transformed into



a “broken lamellar” structure upon annealing. Based on these results, a morphology map was constructed.

In addition to PBLGlu-*b*-PEG-*b*-PBLGlu, PZLLys-*b*-PEG-*b*-PZLLys triblock copolymers have also been studied. Cho *et al.* [112] reported on the solid-state structure of a series of PZLLys-*b*-PEG-*b*-PZLLys composed of a PEG block with  $M_n = 2 \text{ kg mol}^{-1}$  and PZLLys contents of 25.2, 49.9 and 83.0 mol-% (= 68, 86 and 98 vol-%). Infrared spectra of  $\text{CHCl}_3$ -cast films were in agreement with a helical secondary structure of the peptide blocks. DSC experiments provided a first hint for the existence of a microphase-separated structure and revealed two  $T_g$  values for all samples. The higher  $T_g$  was very close to that of the PZLLys homopolymer and the lower  $T_g$  approximately 20 °C higher than that of PEG homopolymer. A PEG melting transition was not observed. These results were interpreted in terms of a microphase-separated structure with hard, crystalline PZLLys domains and soft, amorphous PEG segments. The presence of a microphase-separated structure was confirmed by TEM micrographs of  $\text{RuO}_4$ -stained thin films.

Akashi and coworkers [113] reported on the solid-state nanoscale structure of ABA type triblock copolymers composed of a central PEG block flanked by two poly( $\beta$ -benzyl L-aspartate) (PBLAsp) blocks. The molecular weight of the central PEG block was 11 or 20  $\text{kg mol}^{-1}$  and the degrees of polymerization of the peptide blocks ranged from 12 to 32. WAXS and POM studies on  $\text{CH}_2\text{Cl}_2$ -cast films showed PEG crystallization in all samples. The intensity of the crystalline PEG reflection peak, however, was found to decrease with increasing length of the PBLAsp block. The observation of PEG crystallization was interpreted as a first indication for microphase separation. In addition to the PEG signal, the WAXS patterns also contained reflections at  $2\theta = 5.9^\circ$  ( $= 15 \text{ \AA}$ ), which were assigned to a hexagonally packed array of PBLAsp helices, a result confirmed by FT-IR spectroscopy. In the SAXS patterns of PBLAsp<sub>25</sub>-*b*-PEG<sub>250</sub>-*b*-PBLAsp<sub>25</sub>, PBLAsp<sub>25</sub>-*b*-PEG<sub>454</sub>-*b*-PBLAsp<sub>25</sub> and PBLAsp<sub>32</sub>-*b*-PEG<sub>454</sub>-*b*-PBLAsp<sub>32</sub> broad and weak diffraction peaks were observed, indicating the formation phase separated structures. Thermal analysis of the triblock copolymers, however, revealed several interesting properties. DSC experiments showed that the melting temperature of the crystalline PEG domains decreased linearly with increasing PBLAsp content, reflecting the strong influence of the peptide segments on PEG crystallization. More interestingly, these workers found that heating the as-cast films above 333 K and cooling down to 303 K, converted a certain fraction of the  $\alpha$ -helical PBLAsp chains into  $\beta$ -strands and was accompanied by a decrease in PEG crystallinity. On a macroscopic level, this led to increased strength and elasticity of the films.

Cho *et al.* [114] have studied triblock copolymers composed of a middle block of poly(propylene glycol) (PPG) with a molecular weight of 2  $\text{kg mol}^{-1}$  flanked by two PBLGlu segments. Three triblock copolymer samples were investigated with PPG contents of 17.0, 26.0 and 60.0 mol-%, respectively. According to infrared spectra that were recorded from  $\text{CHCl}_3$ -cast films, the PBLGlu blocks possessed an  $\alpha$ -helical secondary structure. WAXS patterns revealed a 12.5  $\text{\AA}$  interhelical spacing and were in agreement with a solid-state modification C of PBLGlu. No further details on the solid-state nanoscale structure and the possibility of microphase



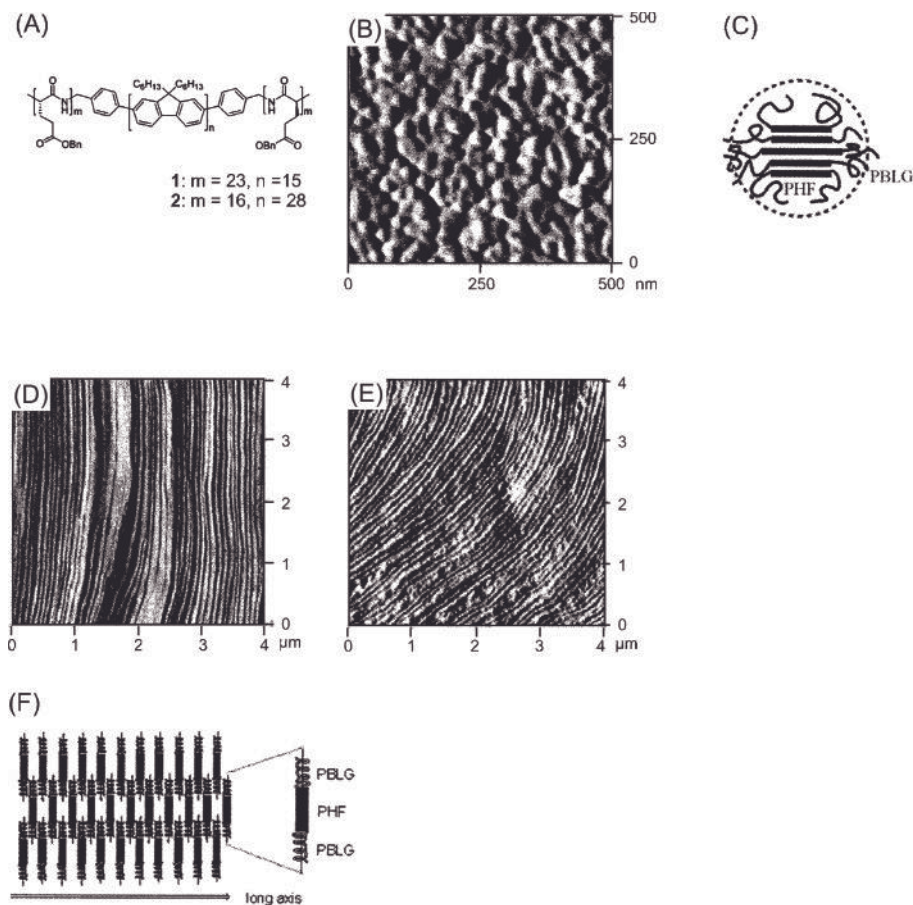
separation were reported. Platelet adhesion on glass beads coated with block copolymers containing 33 or 47 mol-% PPG was reduced compared with beads modified with PMLGlu homopolymer or block copolymers with 70.0 mol-% PPG. These differences were attributed to differences in surface composition and morphology, which, unfortunately, were not discussed further. Finally, Hayashi *et al.* [115] have reported on PMLGlu-*b*-PTHF-*b*-PMLGlu [PTHF = poly(tetrahydrofuran)] triblock copolymers that were prepared from an amino-functionalized PTHF macroinitiator with a molecular weight of  $9.6 \text{ kg mol}^{-1}$ . Three different triblock copolymers were studied with PMLGlu contents and degrees of polymerization of 86.8 mol-%/460, 89.7 mol-%/605 and 91.3 mol-%/730, respectively. With respect to the solidstate structure and organization, only infrared spectra and WAXS data were discussed.

#### 27.3.2.5 Miscellaneous

The structure and properties of an ABA triblock copolymer composed of a poly(ether urethane urea) (PEUU) B block with  $M_n = 15.8 \text{ kg mol}^{-1}$  and two PBLGlu<sub>29</sub> B blocks were described by Ito *et al.* [116]. DSC thermograms showed a single endotherm located between the  $T_g$  of the PEUU and the 7/2 to 18/5 helix transition of PBLGlu, suggesting that there was no phase separation. Platelet adhesion on DMF-cast films of the triblock copolymer was significantly reduced compared with the respective homopolymers and a PEUU/PBLGlu blend. Thrombus formation on block copolymer films was found to be  $\approx 50\%$  less compared with a glass surface. However, no significant difference in antithrombogenicity between PEUU, PBLGlu, their blend and the block copolymer was observed.

Another, very early study focused on two PBLGlu-*b*-PBAN-*b*-PBLGlu [PBAN = poly(butadiene-*co*-acrylonitrile)] triblock copolymers [117]. These block copolymers were composed of a PBAN block with  $M_n = 3.4 \text{ kg mol}^{-1}$  and two PBLGlu segments containing either 80 or 160 repeat units. TEM micrographs of OsO<sub>4</sub>-stained films cast from dioxane, which is a selective solvent for PBLGlu, revealed a lamellar morphology. When the non-selective solvent CHCl<sub>3</sub> was used for the preparation of the TEM specimens, the images were more homogeneous and phase separation was less distinct. This suggests that, depending on the solvent conditions, the PBAN block can affect PBLGlu secondary structure.

Electro- and photoactive peptide-synthetic hybrid triblock copolymers have been prepared using bis(benzyl amine)-terminated poly(9,9-dihexylfluorene-2,7-diyl) (PHF) as a macroinitiator for the ring-opening polymerization of BLGlu-NCA [118]. The electroactive and photoactive properties of the triblock copolymers were similar to those of the PHF homopolymer, indicating that the introduction of the PBLGlu segments did not interfere with charge injection and transport and other material properties. FT-IR spectra of CHCl<sub>3</sub>-cast films of PBLGlu<sub>23</sub>-*b*-PHF<sub>15</sub>-*b*-PBLGlu<sub>23</sub> indicated an  $\alpha$ -helical secondary structure. The FT-IR spectra of PBLGlu<sub>16</sub>-*b*-PHF<sub>28</sub>-*b*-PBLGlu<sub>16</sub> displayed, however, an additional peak at  $1630 \text{ cm}^{-1}$ , indicating the coexistence of  $\alpha$ -helical and  $\beta$ -strand conformations. The thin film morphologies of the triblock copolymers were investigated with AFM using different casting solvents (Figure 27.14). When 2,2,2-trifluoroacetic acid (TFA)-



**Figure 27.14** (A) Chemical structure of PBLGlu-*b*-PHF-*b*-PBLGlu triblock copolymers **1** and **2**; (B) AFM image of a thin film of **1** cast from TFA-CHCl<sub>3</sub> 30/70 (v/v); (C) schematic representation of the spherical nanostructures that can be observed in (B); (D) and (E) AFM images of triblock copolymers **1** (D) and **2** (E) cast from TFA-CHCl<sub>3</sub> 3/97 (v/v); (F) model proposed for the self-assembly of **1** and **2** in the fibrillar structures shown in (D) and (E) (reprinted from [118] with permission of The American Chemical Society).

CHCl<sub>3</sub> 30/70 (v/v) was used for the preparation of samples, globular or spherical aggregates with diameters of about 32 and 40 nm were observed for PBLGlu<sub>23</sub>-*b*-PHF<sub>15</sub>-*b*-PBLGlu<sub>23</sub> and PBLGlu<sub>16</sub>-*b*-PHF<sub>28</sub>-*b*-PBLGlu<sub>16</sub>, respectively. In this solvent mixture, the PBLGlu chains have a random coil conformation and the triblock copolymers were proposed to form spherical nanostructures composed of a PHF core and a PBLGlu shell. When the solvent was changed to TFA-CHCl<sub>3</sub> 3/97 (v/v), the SFM images revealed parallel fibrillar structures being  $79 \pm 25$  nm (PBLGlu<sub>23</sub>-*b*-PHF<sub>15</sub>-*b*-PBLGlu<sub>23</sub>) and  $83 \pm 17$  nm (PBLGlu<sub>16</sub>-*b*-PHF<sub>28</sub>-*b*-PBLGlu<sub>16</sub>) in width and 4–10 μm in length. Under these conditions, PBLGlu adopts an  $\alpha$ -helical secondary

structure. As the widths of the fibrils were much larger than the extended length of the triblock copolymers, a side-by-side antiparallel stacking was proposed to explain the fibril formation.

## 27.4

### Summary and Outlook

In summary, the first part of this chapter described and discussed the phase behavior of biomimetic polypeptide-based copolymers in solution with respect to the occurrence of secondary structure effects. Evidently, incorporation of crystallizable polypeptide segments inside the core of an aggregate has an impact on the curvature of the core–corona interface and promotes the formation of fibrils or vesicles, or other flat superstructures. Spherical micelles are not usually observed. Copolymers with soluble polypeptide segments, on the other hand, seem to behave as conventional block copolymers. A pH-induced change of the conformation of coronal polypeptide chains only affects the size of aggregates, not their shape. It is evident that the biomimetic approach using polypeptide hybrid polymers is very successful in the creation of novel superstructures with hierarchical order. However, although begun about 30 years ago in the mid-1970s, this field is still in a premature state. Most systematic studies on aggregation in solution have been reported only during the last five to ten years. A comprehensive picture of the processes involved in the formation of hierarchical structures is still lacking. The application potential of polypeptide copolymers has also not been exhausted. Most studies deal with ordinary micelles for the controlled delivery of drugs or genes. Not much attention has been, for whatever reason, paid to gel structures and other colloidal systems, such as emulsions, polymer latexes and inorganic–organic hybrid nanoparticles.

The solid-state structure, organization and properties of peptide–synthetic hybrid block copolymers were discussed in the second part. The most notable difference between peptide-based block copolymers and their fully synthetic and amorphous analogues is their hierarchical solid-state organization. In contrast to most synthetic amorphous block copolymers, which typically exhibit structural order only over a single length scale, peptide-based block copolymers can form hierarchically organized nanoscale structures that cover several different length scales. At the smallest length scale, peptide sequences fold into regular secondary structures, such as  $\alpha$ -helices or  $\beta$ -strands. On the next higher level, peptide  $\alpha$ -helices and  $\beta$ -strands can assemble into hexagonal superstructures and  $\beta$ -sheets, respectively. Finally, phase separation between the peptide and synthetic blocks leads to the formation of ordered domains with the largest characteristic length scales. For a large number of peptide-based block copolymers, lamellar phase separated morphologies have been observed. These lamellar structures, however, are often found over a much broader range of compositions compared with regular, fully amorphous diblock copolymers. This behavior, as in solution, can be explained easily considering the flat interface that is generated from the rod–rod

packing. In addition to these more conventional morphologies, structural investigations on peptide-based hybrid block copolymers have also led to the discovery of various novel phase separated structures, which were not previously known for fully amorphous diblock copolymers. Both observations reflect the fact that the solid-state structure formation of peptide hybrid block copolymers is not solely dictated by phase separation, as is the case for amorphous diblock copolymers, but is also influenced by other factors such as intra- and intermolecular hydrogen bonding and chain conformation. While much of the early interest in peptide–synthetic hybrid block copolymers was driven by their potential use as membrane materials or for the development of antithrombogenic surfaces, more recent studies revealed that these materials can also have interesting mechanical properties [113].

The major drawback of most of the block copolymers discussed in this chapter is that they have been prepared via the conventional amine-initiated NCA polymerization. The polymerization of NCAs under these conditions does not allow very accurate control over polymer chain length, results in rather broad molecular weight distributions and is also not very useful for preparing defined block copolypeptides [119, 120]. It is obvious that these limitations possibly restrict further engineering of the structure and organization of peptide–synthetic hybrid block copolymers and could also hamper the exploration of their full practical potential. Over recent years, however, a number of alternative NCA polymerization strategies have been developed, which provide enhanced control over polypeptide chain length and chain length distribution and also allow access to defined block copolypeptides [121–123]. In the last 5 years, a great deal of effort has been focused on controlling the synthesis and understanding the structural behavior of these polypeptide-based block copolymers. These systems, which have been known for a long time, are currently gaining more and more attention due to the possibilities of making highly ordered materials on the nano- to micrometer-length scale and bio-compatible aggregates that respond to external stimuli. The door to new innovations in materials science is now open.

This chapter has been published previously in:

Lazzari, Massimo/Liu, Guojun/Lecommandoux, Sébastien (eds.)

**Block Copolymers in Nanoscience**

2006

ISBN-13: 978-3-527-31309-9-Wiley-VCH, Weinheim

**References**

- 1 Park, C., Yoon, J. and Thomas, E.L. (2003) *Polymer*, **44**, 6725.
- 2 Hamley, I.W. (2003) *Nanotechnology*, **14**, R39.
- 3 Lazzari, M. and López-Quintela, M.A. (2003) *Adv. Mater.*, **15**, 1583.
- 4 Bates, F.S. and Fredrickson, G.H. (1990) *Annu. Rev. Phys. Chem.*, **41**, 525.
- 5 Hamley, I.W. (1998) *The physics of block copolymers*, Oxford University Press, Oxford, New York, Tokyo.

- 6 Bates, F.S. and Fredrickson, G.H. (1999) *Phys. Today*, **52**, 32.
- 7 Walther, M. and Finkelmann, H. (1996) *Progr. Polym. Sci.*, **21**, 951.
- 8 Mao, G. and Ober, C.K. (1997) *Acta Polym.*, **48**, 405.
- 9 Klok, H.-A. and Lecommandoux, S. (2001) *Adv. Mater.*, **13**, 1217.
- 10 Lee, M., Cho, B.K. and Zin, W.C. (2001) *Chem. Rev.*, **101**, 3869.
- 11 Förster, S. and Antonietti, M. (1998) *Adv. Mater.*, **10**, 195.
- 12 Bates, F.S. and Fredrickson, G.H. (1999) *Phys. Today*, **52**, 32.
- 13 Cölfen H. (2001) *Macromol. Rapid Commun.*, **22**, 219.
- 14 Förster, S. and Konrad, M. (2003) *J. Mater. Chem.*, **13**, 2671.
- 15 Antonietti, M. and Förster, S. (2003) *Adv. Mater.*, **15**, 1323.
- 16 Choucair, A. and Eisenberg, A. (2003) *Eur. Phys. J. E*, **10**, 37.
- 17 Discher, B.M., Won, Y.-Y., Ege, D.S., Lee, J.C.-M., Bates, F.S., Discher, D.E. and Hammer, D.A. (1999) *Science*, **284**, 1143.
- 18 Discher, D.E. and Eisenberg, A. (2002) *Science*, **297**, 967.
- 19 Taubert, A., Napoli, A. and Meier, W. (2004) *Curr. Opin. Chem. Biol.*, **8**, 598.
- 20 Kita-Tokarczyk, K., Grumelard, J., Haefele, T. and Meier, W. (2005) *Polymer*, **46**, 3540.
- 21 Cornelissen, J.J.L.M., Rowan, A.E., Nolte, R.J.M. and Sommerdijk, N.A.J.M. (2001) *Chem. Rev.*, **101**, 4039.
- 22 Löwik, D.W.P.M. and van Hest, J.C.M. (2004) *Chem. Soc. Rev.*, **33**, 234.
- 23 Vandermeulen, G.W.M. and Klok, H.-A. (2004) *Macromol. Biosci.*, **4**, 383.
- 24 Klok, H.-A. (2005) *J. Polym. Sci. Part A Polym. Chem.*, **43**, 1.
- 25 Schlaad, H. and Antonietti, M. (2003) *Eur. Phys. J. E*, **10**, 17.
- 26 Rodríguez-Hernández, J., Chécot, F., Gnanou, Y. and Lecommandoux, S. (2005) *Progr. Polym. Sci.*, **30**, 691.
- 27 Nakajima, A., Kugo, K. and Hayashi, T. (1979) *Macromolecules*, **12**, 844.
- 28 Hayashi, T. (1985), in *Developments in block copolymers*, ed. Goodman, I., Elsevier Applied Science Publishers, London, p. 109.
- 29 Förster, S., Zisenis, M., Wenz, E. and Antonietti, M. (1996) *J. Chem. Phys.*, **104**, 9956.
- 30 Kukula, H., Schlaad, H., Antonietti, M. and Förster, S. (2002) *J. Am. Chem. Soc.*, **124**, 1658.
- 31 Chécot, F., Brület, A., Oberdisse, J., Gnanou, Y., Mondain-Monval, O. and Lecommandoux, S. (2005) *Langmuir*, **21**, 4308.
- 32 Chécot, F., Lecommandoux, S., Gnanou, Y. and Klok, H.-A. (2002) *Angew. Chem., Int. Ed. Engl.*, **41**, 1340.
- 33 Chécot, F., Lecommandoux, S., Klok, H.-A. and Gnanou, Y. (2003) *Eur. Phys. J. E*, **10**, 25.
- 34 Babin, J., Rodríguez-Hernández, J., Lecommandoux, S., Klok, H.-A. and Achard, M.-F. (2005) *Faraday Discuss.*, **128**, 179.
- 35 Rodríguez-Hernández, J., Babin, J., Zappone, B. and Lecommandoux, S. (2005) *Biomacromolecules*, **6**, 2213.
- 36 Arimura, H., Ohya, Y. and Ouchi, T. (2005) *Biomacromolecules*, **6**, 720.
- 37 Lübbert, A., Castelletto, V., Hamley, I.W., Nuhn, H., Scholl, M., Bourdillon, L., Wandrey, C. and Klok, H.-A. (2005) *Langmuir*, **21**, 6582.
- 38 Harada, A. and Kataoka, K. (1995) *Macromolecules*, **28**, 5294.
- 39 Harada, A. and Kataoka, K. (1997) *J. Macromol. Sci.-Pure Appl. Chem.*, **A34**, 2119.
- 40 Harada, A. and Kataoka, K. (1999) *Science*, **283**, 65.
- 41 Toyotama, A., Kugimiya, S-i, Yamanaka, J. and Yonese, M. (2001) *Chem. Pharm. Bull.*, **49**, 169.
- 42 Cheon, J.-B., Jeong, Y.-I. and Cho, C.-S. (1998) *Korea Polym. J.*, **6**, 34.
- 43 Cheon, J.-B., Jeong, Y.-I. and Cho, C.-S. (1999) *Polymer*, **40**, 2041.
- 44 Dong, C.-M., Sun, X.-L., Faucher, K.M., Apkarian, R.P. and Chaikof, E.L. (2004) *Biomacromolecules*, **5**, 224.
- 45 Dong, C.-M., Faucher, K.M. and Chaikof, E.L. (2004) *J. Polym. Sci., Part A: Polym. Chem.*, **42**, 5754.
- 46 Naka, K., Yamashita, R., Nakamura, T., Ohki, A. and Maeda, S. (1997) *Macromol. Chem. Phys.*, **198**, 89.
- 47 Losik, M. and Schlaad, H. unpublished results.

- 48 Doi, T., Kinoshita, T., Kamiya, H., Tsujita, Y. and Yoshimizu, H. (2000) *Chem. Lett.* 262.
- 49 Doi, T., Kinoshita, T., Kamiya, H., Washizu, S., Tsujita, Y. and Yoshimizu, H. (2001) *Polym. J.*, **33**, 160.
- 50 Rodríguez-Hernández, J. and Lecommandoux, S. (2005) *J. Am. Chem. Soc.*, **127**, 2026.
- 51 Bellomo, E.G., Wyrsta, M.D., Pakstis, L., Pochan, D.J. and Deming, T.J. (2004) *Nat. Mater.*, **3**, 244.
- 52 Constancis, A., Meyrueix, R., Bryson, N., Huille, S., Grosselin, J-M, Gulik-Krzywicki, T. and Soula, G. (1999) *J. Colloid. Interf. Sci.*, **217**, 357.
- 53 Deming, T.J. (2005) *Soft Matter*, **1**, 28.
- 54 Nowak, A.P., Breedveld, V., Pakstis, L., Ozbas, B., Pine, D.J., Pochan, D. and Deming, T.J. (2002) *Nature (London)*, **417**, 424.
- 55 Breedveld, V., Nowak, A.P., Sato, J., Deming, T.J. and Pine, D.J. (2004) *Macromolecules*, **37**, 3943.
- 56 Pochan, D.J., Pakstis, L., Ozbas, B., Nowak, A.P. and Deming, T.J. (2002) *Macromolecules*, **35**, 5358.
- 57 Pakstis, L.M., Ozbas, B., Hales, K.D., Nowak, A.P., Deming, T.J. and Pochan, D. (2004) *Biomacromolecules*, **5**, 312.
- 58 Cha, J.N., Stucky, G.D., Morse, D.E. and Deming, T.J. (2000) *Nature (London)*, **403**, 289.
- 59 Euliss, L.E., Trnka, T.M., Deming, T.J. and Stucky, G.D. (2004) *Chem. Commun.*, 1736.
- 60 Lecommandoux, S., Sandre, O., Chécot, F., Rodríguez-Hernández, J. and Perzynski, R. (2005) *Adv. Mater.*, **17**, 712.
- 61 Euliss, L.E., Grancharov, S.G., O'Brien, S., Deming, T.J., Stucky, G.D., Murray, C.B. and Held, G.A. (2003) *Nano Lett.*, **3**, 1489.
- 62 Perly, B., Douy, A. and Gallot, B. (1976) *Makromol. Chem.*, **177**, 2569.
- 63 Billot, J.-P., Douy, A. and Gallot, B. (1976) *Makromol. Chem.*, **177**, 1889.
- 64 Billot, J.-P., Douy, A. and Gallot, B. (1977) *Makromol. Chem.*, **178**, 1641.
- 65 Douy, A. and Gallot, B. (1977) *Polym. Eng. Sci.*, **17**, 523.
- 66 Douy, A. and Gallot, B. (1982) *Polymer*, **23**, 1039.
- 67 Gallot, B., Douy, A., Hayany, H. and Vigneron, C. (1983) *Polym. Sci. Technol.*, **23**, 247.
- 68 Mori, A., Ito, Y., Sisido, M. and Imanishi, Y. (1986) *Biomaterials*, **7**, 386.
- 69 Schlaad, H., Kukula, H., Smarsly, B., Antonietti, M. and Pakula, T. (2002) *Polymer*, **43**, 5321.
- 70 Losik, M., Kubowicz, S., Smarsly, B. and Schlaad H. (2004) *Eur. Phys. J. E*, **15**, 407.
- 71 Schlaad, H., Smarsly, B. and Losik, M. (2004) *Macromolecules*, **37**, 2210.
- 72 Ludwigs, S., Krausch, G., Reiter, G., Losik, M., Antonietti, M. and Schlaad, H. (2005) *Macromolecules*, **38**, 7532.
- 73 Klok, H.-A., Langenwalter, J.F. and Lecommandoux, S. (2000) *Macromolecules*, **33**, 7819.
- 74 Lecommandoux, S., Achard, M.-F., Langenwalter, J.F. and Klok, H.-A. (2001) *Macromolecules*, **34**, 9100.
- 75 Zhang, G., Ma, J., Li, Y. and Wang, Y. (2003) *J. Biomater. Sci. Polym. Edn.*, **14**, 1389.
- 76 Cho, I., Kim, J.-B. and Jung, H.-J. (2003) *Polymer*, **44**, 5497.
- 77 Degée, P., Dubois, P., Jérôme, R. and Theysssié, P. (1993) *J. Polym. Sci. Part A Polym. Chem.*, **31**, 275.
- 78 Rong, G., Deng, M., Deng, C., Tang, Z., Piao, L., Chen, X. and Jing, X. (2003) *Biomacromolecules*, **4**, 1800.
- 79 Caillol, S., Lecommandoux, S., Mingotaud, A.-F., Schappacher, M., Soum, A., Bryson, N. and Meyrueix, R. (2003) *Macromolecules*, **36**, 1118.
- 80 Deming, T.J. (1997) *J. Am. Chem. Soc.*, **119**, 2759.
- 81 Papadopoulos, P., Floudas, G., Schnell, I., Aliferis, T., Iatrou, H. and Hadjichristidis, N. (2005) *Biomacromolecules*, **6**, 2352.
- 82 Nakajima, A., Hayashi, T., Kugo, K. and Shinoda, K. (1979) *Macromolecules*, **12**, 840.
- 83 Nakajima, A., Kugo, K. and Hayashi, T. (1979) *Macromolecules*, **12**, 844.
- 84 Nakajima, A., Kugo, K. and Hayashi, T. (1979) *Polymer J.*, **11**, 995.
- 85 McKinnon, A.J. and Tobolsky, A.V. (1968) *J. Phys. Chem.*, **72**, 1157.
- 86 Hayashi, T., Chen, G.-W. and Nakajima, A. (1984) *Polymer J.*, **16**, 739.



- 87 Gervais, M., Douy, A., Gallot, B. and Erre, R. (1988) *Polymer*, **29**, 1779.
- 88 Kugo, K., Hayashi, T. and Nakajima, A. (1982) *Polymer J.*, **14**, 391.
- 89 Kugo, K., Hata, Y., Hayashi, T. and Nakajima, A. (1982) *Polymer J.*, **14**, 401.
- 90 Kugo, K., Murashima, M., Hayashi, T. and Nakajima, A. (1983) *Polymer J.*, **15**, 267.
- 91 Chen, G.-W., Hayashi, T. and Nakajima, A. (1981) *Polymer J.*, **13**, 433.
- 92 Sato, H., Nakajima, A., Hayashi, T., Chen, G.-W. and Noishiki, Y. (1985) *J. Biomed. Mater. Res.*, **19**, 1135.
- 93 Yoda, R., Komatsuzaki, S., Nakanishi, E. and Hayashi, T. (1995) *Eur. Polym. J.*, **31**, 335.
- 94 Yoda, R., Komatsuzaki, S. and Hayashi, T. (1996) *Eur. Polym. J.*, **32**, 233.
- 95 Yoda, R., Shimoda, M., Komatsuzaki, S., Hayashi, T. and Nishi, T. (1997) *Eur. Polym. J.*, **33**, 815.
- 96 Yoda, R., Komatsuzaki, S. and Hayashi, T. (1995) *Biomaterials*, **16**, 1203.
- 97 Yoda, R., Komatsuzaki, S., Nakanishi, E., Kawaguchi, H. and Hayashi, T. (1994) *Biomaterials*, **15**, 944.
- 98 Imanishi, Y., Tanaka, M. and Bamford, C.H. (1985) *Int. J. Biol. Macromol.*, **7**, 89.
- 99 Janssen, K., Van Beylen, M., Samyn, C., Scherrenberg, R. and Reynaers, H. (1990) *Makromol. Chem.*, **191**, 2777.
- 100 Janssen, K., Van Beylen, M., Samyn, C. and Van Driessche, W. (1989) *Makromol. Chem. Rapid. Commun.*, **10**, 457.
- 101 Kumaki, T., Sisido, M. and Imanishi, Y. (1985) *J. Biomed. Mater. Res.*, **19**, 785.
- 102 Kang, I.-K., Ito, Y., Sisido, M. and Imanishi, Y. (1988) *Biomaterials*, **9**, 138.
- 103 Kang, I.-K., Ito, Y., Sisido, M. and Imanishi, Y. (1988) *Biomaterials*, **9**, 349.
- 104 Kugo, K., Nishioka, H. and Nishino, J. (1987) *Chem. Express*, **2**, 21.
- 105 Nishimura, T., Sato, Y., Yokoyama, M., Okuya, M., Inoue, S., Kataoka, K., Okano, T. and Sakurai, Y. (1984) *Makromol. Chem.*, **185**, 2109.
- 106 Yokoyama, M., Nakahashi, T., Nishimura, T., Maeda, M., Inoue, S., Kataoka, K. and Sakurai, Y. (1986) *J. Biomed. Mater. Res.*, **20**, 867.
- 107 Kugo, K., Ohji, A., Uno, T. and Nishino, J. (1987) *Polymer J.*, **19**, 375.
- 108 Cho, C.-S., Kim, S.-W. and Komoto, T. (1990) *Makromol. Chem.*, **191**, 981.
- 109 Cho, C.-S. and Kim, S.U. (1988) *J. Control. Release*, **7**, 283.
- 110 Floudas, G., Papadopoulos, P., Klok, H.-A., Vandermeulen, G.W.M. and Rodríguez-Hernandez, J. (2003) *Macromolecules*, **36**, 3673.
- 111 Parras, P., Castelletto, V., Hamley, I.W. and Klok, H.-A. (2005) *Soft Matter*, **1**, 284.
- 112 Cho, C.S., Jo, B.-W., Kwon, J.-K. and Komoto, T. (1994) *Macromol. Chem. Phys.*, **195**, 2195.
- 113 Tanaka, S., Ogura, A., Kaneko, T., Murata, Y. and Akashi, M. (2004) *Macromolecules*, **37**, 1370.
- 114 Cho, C.-S., Kim, S.-W., Sung, Y.-K. and Kim, K.-Y. (1988) *Makromol. Chem.*, **189**, 1505.
- 115 Hayashi, T., Kugo, K. and Nakajima, A. (1984) *Cont. Topics Polym. Sci.*, **4**, 685.
- 116 Ito, Y., Miyashita, K., Kashiwagi, T. and Imanishi, Y. (1993) *Biomater. Artif. Cells Immob. Biotechnol.*, **21**, 571.
- 117 Barenberg, S., Anderson, J.M. and Geil, P.H. (1981) *Int. J. Biol. Macromol.*, **3**, 82.
- 118 Kong, X., Jenekhe, S.A. (2004) *Macromolecules*, **37**, 8180.
- 119 Kricheldorf, H.R. (1987)  *$\alpha$ -Aminoacid-N-carboxyanhydrides and related heterocycles*, Springer-Verlag, Berlin, Heidelberg, New York.
- 120 Deming, T.J. (2000) *J. Polym. Sci. A Polym. Chem.*, **38**, 3011.
- 121 Deming, T.J. (1997) *Nature (London)*, **390**, 386.
- 122 Dimitrov, I. and Schlaad, H. (2003) *Chem. Commun.*, 2944.
- 123 Aliferis, T., Iatrou, H. and Hadjichristidis, N. (2004) *Biomacromolecules*, **5**, 1653.

## 28

# Structural DNA Nanotechnology: Information-Guided Self-Assembly

*Yonggang Ke, Yan Liu, and Hao Yan*

### 28.1

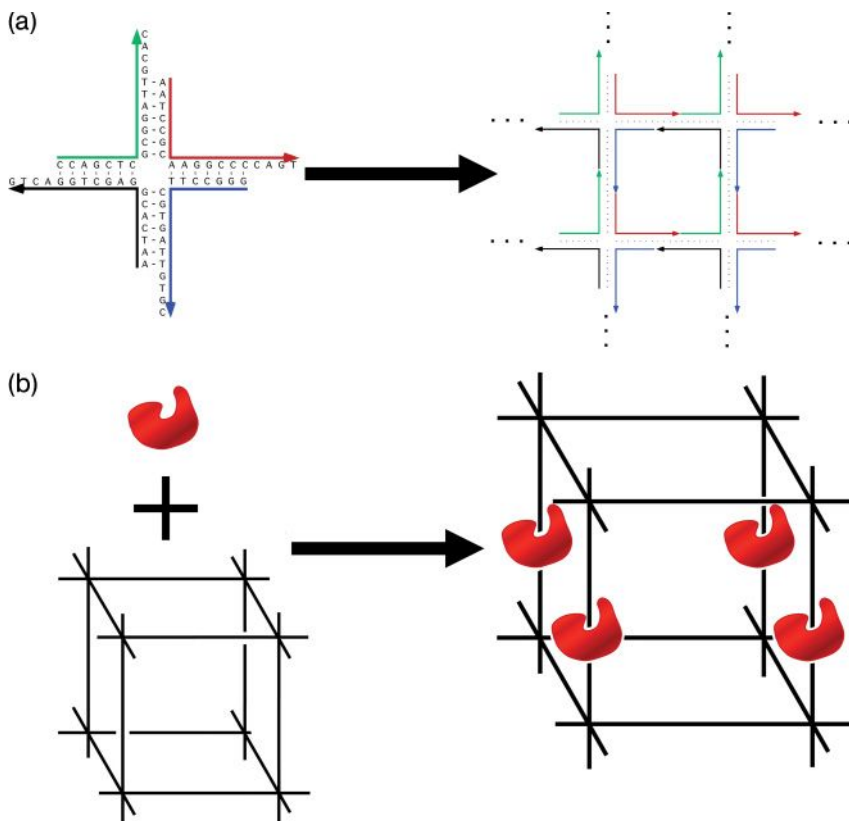
#### Introduction

Although the Watson–Crick double helical model [1] of DNA has imparted major impacts on modern biology for more than 50 years, the significance of this simple–yet very elegant–model is not limited to one particular area. In 1982 [2], Ned Seeman proposed the building of nanostructures from DNA, an idea which led to the origination of the field now known as “structural DNA nanotechnology.” During the past decade, this field has witnessed much significant progress, and in this chapter we will discuss the basic concepts and major research directions of structural DNA nanotechnology, the important progress that has been made in recent years, and some future perspectives of the field.

DNA, which serves as the genetic information carrier in most organisms on Earth, is also an ideal candidate for structural nanotechnology, which targets at controlling and organizing matter at the nanometer scale. First, DNA is a nanometer-scale object itself, with a diameter of 2 nm and a helical repeat of 10–10.5 nucleotide pairs, or ~3.5 nm for the common B-form DNA. Second, DNA hybridization is highly predictable because of the well-known Watson–Crick base-pairing that guanine (G) pairs with cytosine (C), and adenine (A) with thymine (T). Third, whilst single-stranded DNA is quite flexible, the DNA duplex is more rigid and has a persistence length of approximately 50 nm. It is this combined flexibility and rigidity that permits the design of DNA structures to form different geometric shapes. Furthermore, as a result of advances in modern chemistry and molecular biology, DNA molecules with any designed lengths, sequences, and a variety of functionalities can now be synthesized conveniently, and also manipulated by using the wide range of enzymes that are available for the cleavage, ligation and amplification of DNA. All of these facilities have provided scientists with an extreme degree of control for building DNA nanostructures and maneuvering DNA nanomachines.

Topologically speaking, DNA duplex is a one-dimensional (1-D) molecule. In order to create a two-dimensional (2-D) or three-dimensional (3-D) structure, it is





**Figure 28.1** Ned Seeman's original proposal of construction of a periodic DNA array and its application. (a) Four-arm junction DNA tiles with sticky ends are connected together to form a 2-D periodic array through self-assembly process; (b) A 3-D DNA lattice templated protein array could be used for X-ray crystallography.

necessary to use branched objects. For example, Seeman proposed techniques that would allow DNA strands to assemble into branched junctions that could further self-assemble into periodic, 2-D arrays [3] (Figure 28.1a).

The basic building block here is the branched four-arm junction consisting of four single-stranded DNA oligonucleotides. To enable DNA junction building blocks to form higher ordered objects and lattices, single stranded DNA overhangs called “*sticky ends*” are used to bring DNA junction molecules together. These sticky ends carries base sequences that are complementary to each other; for example, the red sticky end is complementary to the black end, and the green end is complementary to the blue end (Figure 28.1a). As a result, sticky end cohesion will cause the individual four-arm junctions to be “glued” together to form the 2-D array. Yet, this simple scheme illustrated a powerful method for building

DNA nanostructures: first, to design the branched DNA building blocks or “tiles”, and then to assemble them together using sticky end cohesion.

Although other cohesions have also been used for mortaring DNA nanostructures—for example, paranemic crossovers (PX) cohesion [4] and edge-sharing [5]—sticky end cohesion is by far the most extensively used in DNA nanostructure design. Studies of crystal structures have revealed that the duplex formed by complementary sticky ends has an exactly identical structure to B-DNA [6], a feature which allows designers to predict and control the relative orientations of the DNA tiles. It is interesting to note that for sticky ends that are  $N$ -bases long, the number of unique sticky ends can be up to  $4^N$ , which provides a library of programmable molecular interactions.

Ideally, the DNA sequences of a DNA nanostructure should be designed to achieve the highest stability, so that all other less-stable competitive structures will be less likely to form. On a practical basis, it is necessary to choose a set of optimized sequences that minimizes sequence symmetry at the branch points [7] so as to prevent the branch migration of DNA strands.

As originally proposed by Seeman, one potential application of structural DNA nanotechnology would be to use the highly ordered self-assembling DNA scaffolds to organize other types of macromolecule into 3-D crystals. Moreover, if the macromolecule could be attached to a 3-D DNA nanostructure (Figure 28.1b), the self-assembly of DNA would facilitate the organization of macromolecules into a periodic lattice, the periodicity and parameters of which could be well defined. This would in turn facilitate macromolecule structural analysis using X-ray diffraction.

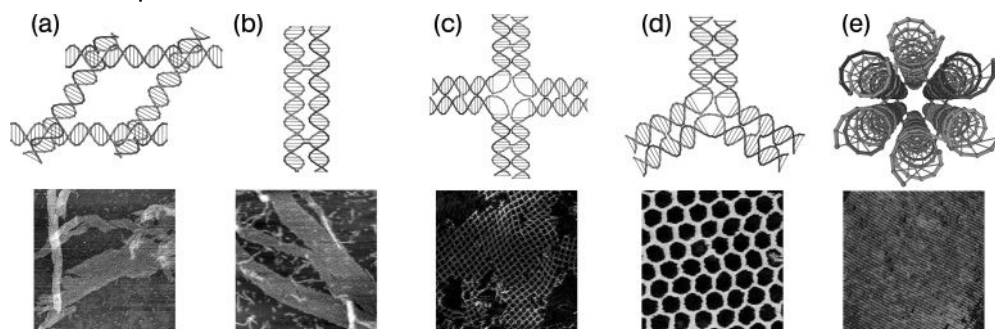
Besides the above-described potential application, the DNA nanostructure might also be used as a scaffold to organize different nanomaterials. An example of this is the organization of nanoelectronic components into an addressable fashion, leading to the construction of DNA-templated nanoelectronics/nanophotonics devices. Indeed, recent developments in the use of 1-D and 2-D DNA nanostructures to template nanoparticles into rationally designed patterns have paved the way towards this goal.

## 28.2

### Periodic DNA Nanoarrays

Seeman’s original proposal has inspired many research groups to construct a variety of DNA tiles with different sizes and geometries, and assemble them into 2-D periodic arrays (Figure 28.2). For example, Mao *et al.* designed and constructed DNA parallelograms that would grow into micrometer-sized 2-D arrays (Figure 28.2a) [8].

A series of DNA tile molecules termed double crossover [9] (DX) DNA molecules were originally created by Seeman, and subsequently utilized in many of the later studies. The DX tile consists of two parallel DNA helices, joined together by two crossovers through strand exchange. Winfree *et al.* successfully built DNA 2-D



**Figure 28.2** DNA tiles and their 2-D periodic arrays formed through sticky end cohesion. (a) A DNA parallelogram tile consisting of four Holliday junction structures; (b) A double crossover (DX) tile; (c) A  $4 \times 4$  cross-shaped tile. Each arm of the cross is a four-arm DNA junction; (d) A three-point-star tile; (e) A six-helix-bundle tile.

arrays through the self-assembly of DX tiles (Figure 28.2b) [10]. A similar design strategy, learned from the DX tile construction, was then used by different groups when designing DNA tiles containing multiple parallel DNA helices; these included triple crossover tiles [11], and four-, eight-, and 12-helix tiles [12, 13].

Yan *et al.* used four four-arm DNA junctions to design a cross-shaped tile, named “ $4 \times 4$ ” tile [14]. In this design, four four-arm junctions are tethered together by a long central strand with a  $dT_4$  loop in between (Figure 28.2c); the  $4 \times 4$  tiles then self-assembled into a 2-D square lattice. By removing one arm from, or adding two more arms to the  $4 \times 4$  tile, Mao’s group were able to construct a three-point-star [15] and a six-point star tile [16] that could self-assemble into 2-D lattices with hexagonal and triangular cavities (Figure 28.2d).

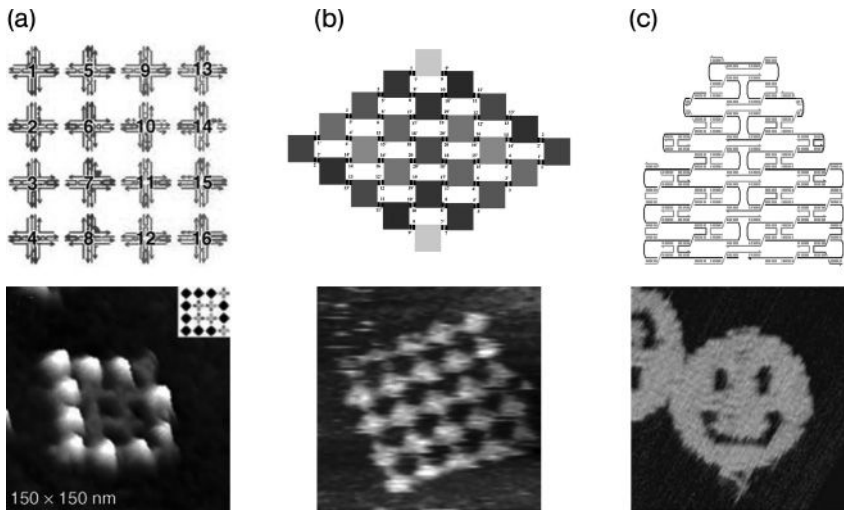
Another family of tiles are tube-like tiles, including three-helix [17], six-helix [18] (Figure 28.2e), and eight-helix bundles [19]. With different sticky end designs, these tubes tile can be assembled to either 1-D tubes, 2-D arrays, or even 3-D lattices.

### 28.3

#### Finite-Sized and Addressable DNA Nanoarrays

For the purpose of DNA-directed macromolecule crystallization, the periodic arrays represent an excellent choice. However, to build a functional DNA nanoelectronic device, it must be possible to control the size of a DNA array and to attach functional species at particular locations on the array. Such needs have driven research teams to develop methods for building finite-sized and addressable arrays.

Park *et al.* [20] reported the construction of a square-shaped, addressable array consisting of sixteen  $4 \times 4$  tiles (Figure 28.3a) through an hierarchical assembly



**Figure 28.3** DNA finite-sized and addressable arrays. (a) A  $4 \times 4$  tile array consisting of 16 distinctive  $4 \times 4$  tiles. This is a fully addressable array on the level of individual tiles. Streptavidin protein was attached onto certain DNA tiles to display a letter “D”; (b) A  $5 \times 5$  tile array consisting of 25 eight-helix tiles. The number of distinctive tiles was reduced from 25 to 13 by taking advantage of the array’s  $C_2$  symmetry; (c) Schematic of Rothmund’s scaffolded DNA self-assembly and atomic force microscopy image of a nanometer-scale “smiley face.” The black strand is the scaffold DNA that is folded by other short “staple” strands into the designed shape.

process. In order to demonstrate that the 16-tile array was fully addressable on the level of individual tiles, Park and colleagues first functionalized a few tiles on the array with biotin groups, and then attached streptavidin molecules to the array. In this way, the protein molecules could be organized to display the letters, “D”, “N” and “A.”

It is costly to make every tile in an array unique; moreover, the more complex the system, the greater the chances of self-assembly errors occurring. In order to build finite-sized arrays in a cost-efficient way, Liu *et al.* [21] demonstrated a strategy to utilize the geometric symmetry of the array to reduce the number of unique tiles. For a  $N$ -tile finite-size array with  $C_m$  symmetry, the number of unique tiles required is  $N/m$ , if  $N/m$  is an integral number, or  $\text{Int}(N/m) + 1$ , if  $N/m$  is a non-integral number. Consequently, Liu and coworkers demonstrated two 25-tile array examples with  $C_2$  and  $C_4$  fold symmetry. The  $5 \times 5$  array with  $C_2$  symmetry required 13 unique tiles instead of 25 (Figure 28.3b), while the  $5 \times 5$  array with  $C_4$  symmetry required only seven unique cross-shaped tiles instead of 25.

When comparing these two finite-size addressable arrays, it is possible to understand the dilemma that research groups often face when designing a DNA structure. On one hand, the addressability of an array can be increased by introducing more unique sequences/tiles into the system, although a low yield and a high error rate will be expected. On the other hand, the symmetry can be utilized to reduce

complexity of the system so as to achieve a high yield and a low assembly error rate, but the high addressability would be lost. Thus, depending on the purpose of a DNA nanostructure, it is important for a designer to identify a good balance between the complexity and addressability of the system.

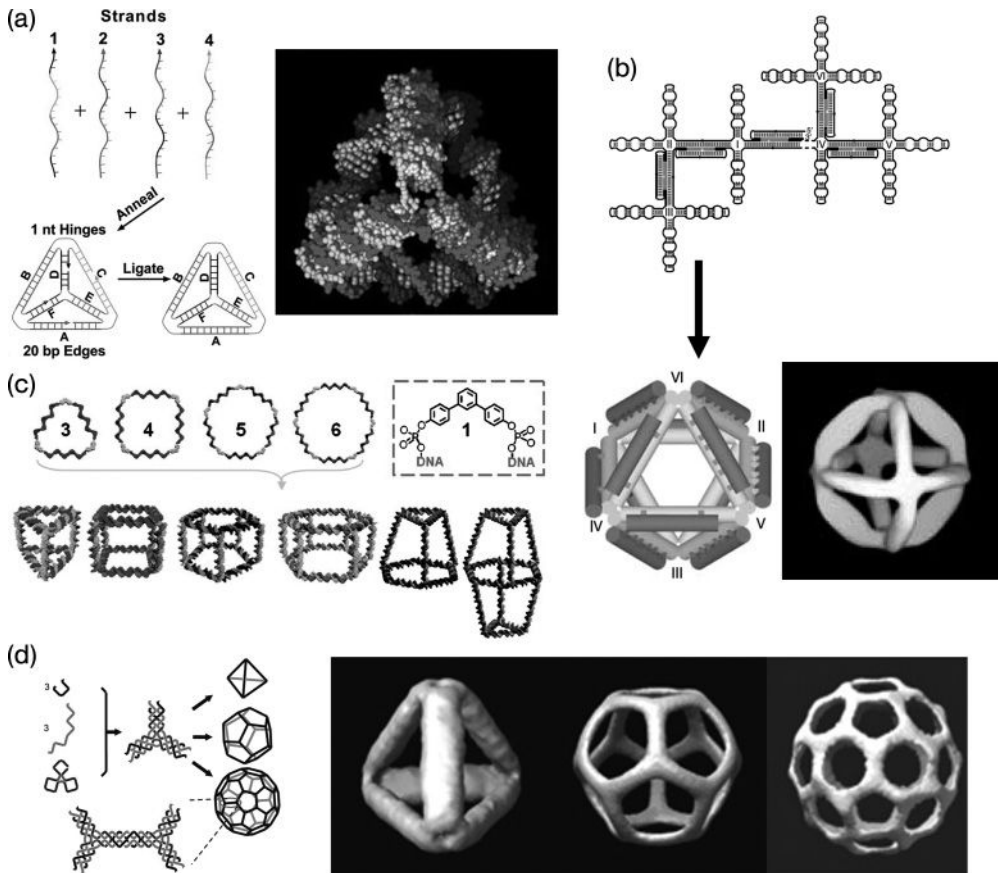
Another important approach when building an addressable DNA nanoarray is “nucleated DNA self-assembly.” This method uses a long natural or synthetic DNA strand, which serves as a scaffold, to direct the DNA strands or tiles self-assembly. Yan *et al.* demonstrated the use of this technique by efficiently assembling DX tiles together into barcode-patterned lattices [22]. In 2006, Paul Rothemund reported an exciting breakthrough, in which he used more than 200 short “staple” DNA strands to fold 7249 base long, single-stranded M13 viral DNA into 2-D arrays (“DNA Origami”) with a variety of shapes [23]. Every staple has its unique sequence, and can only hybridize with predefined parts of M13 according to a predetermined folding path (Figure 28.3c). The array resulted is fully addressable at the position of each individual staple strand. In theory, if the scaffold strand is long enough, it is possible to design any arbitrarily shaped 2-D DNA array and to functionalize staples at any position on that array.

## 28.4

### DNA Polyhedron Cages

One branch of structural DNA nanotechnology focuses on the construction of 3-D DNA “cages.” Potentially, DNA cages can be used for applications such as target-specific drug delivery or nanoparticle site-specific functionalization. For delivery purposes, the cages can be made to encapsulate cargos during their self-assembly and to display target recognition tags outside the cages. Because DNA duplex is linear, it is not surprising that most of the DNA cages built to date are polyhedral, using DNA duplex(es) as straight edges and branching point(s) at the vertices. When Chen and Seeman assembled the first DNA polyhedron, a cube consisting of ten DNA strands [24], they used endonucleases to cleave specific edges of the cube to prove the tube topology with polyacrylamide gel electrophoresis. Many years later, several groups have only recently developed a number of methods to build DNA polyhedral cages and more direct ways to prove their formation (Figure 28.4).

Goodman *et al.* built a DNA tetrahedron by hybridizing four single-stranded DNAs together in a one-step annealing process (Figure 28.4a) [25, 26]. In a later study, the same group built hairpin loops into the tetrahedron and demonstrated that the edge of this cage could be opened/closed by the addition of “fuel DNA” strands [27]. This mechanism would allow cargos to diffuse into the structure at the open stage, and to be captured in the close stage. Shih *et al.* used a 1.7 kilobase and five short, single-stranded DNAs to construct an octahedron (Figure 28.4b) [28] where the edges of the octahedron were double crossovers (DX) or paranemic crossovers (PX) DNA motifs. One noteworthy feature of this octahedron was that the 1.7 kilobase DNA was formed through polymerase chain reaction (PCR), which



**Figure 28.4** DNA polyhedron cages. (a) DNA tetrahedron: schematic drawing and a physical model; (b) DNA octahedron model and 3-D reconstruction image from cryo-electron microscopy (EM) experiments; (c) A series of DNA polyhedra. Organic molecules are incorporated into the DNA circular strands to help the structures form. (d) DNA tetrahedron, dodecahedron, and buckyball assembled from three-point-star tiles. A 3-D reconstruction of the cryo-EM images of these polyhedra is shown on the right.

in turn means that the DNA could be easily amplified to produce large amounts of the DNA octahedron.

Aldaye *et al.* recently developed a new approach for building different-shaped DNA cages [29]. They introduced organic molecules into the circular single-stranded DNA during the DNA synthesis process (Figure 28.4c). This allowed the building of a series of DNA polygons with repeated sequences at each edge and branched organic molecules at the corners. Linker strands were then used to bring two or three polygons together to form the DNA cages.

Mao's group reported the design and formation of tetrahedron, dodecahedron, and buckyballs through hierarchical DNA assembly (Figure 28.4d) [30]. All three polyhedra shared the same basic building unit, namely the three-point-star

[15], although at low concentrations (50–75 nM) the tile tended to form discrete 3-D polyhedra rather than a 2-D array. Another variable in such a design was the length of the single-stranded loops at the center part of the tile, which provided a variable flexibility to the tile and controlled the angle at which the arms could bend out of the plane. Longer loops seemed to provide a higher flexibility at the center of tiles and allowed them to form polyhedra that required larger bending angles at the vertexes. For example, five-base loops were found to promote the formation of tetrahedrons, while three-base loops were suitable for the formation of dodecahedrons. By linking two of the three-point-star tiles, a tile with four arms was created that could self assemble into a buckyball-shaped DNA structure. In a later study, a five-point-star tile was shown to self-assemble into an icosahedron, using a similar design/assembly strategy [31].

## 28.5

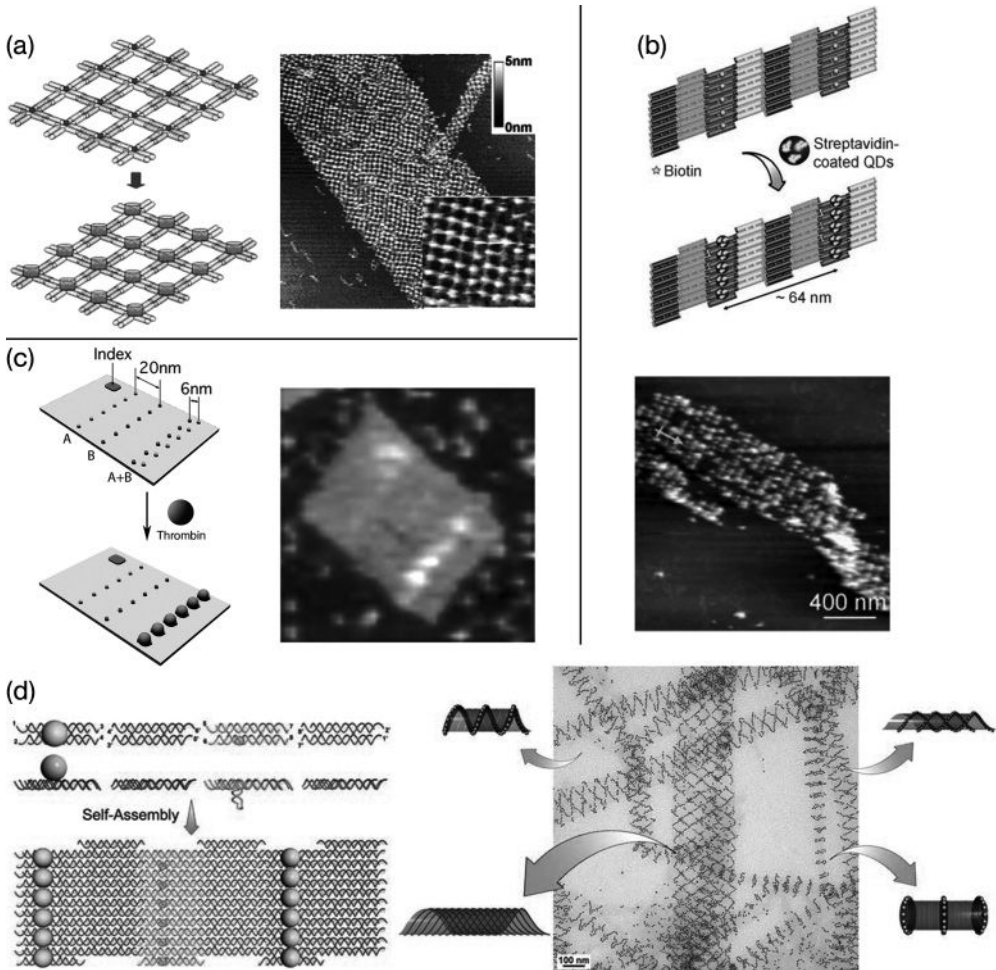
### DNA Nanostructure-Directed Nanomaterial Assembly

As noted at the start of this chapter, one central task of DNA nanotechnology is to control functional materials at the nanometer scale, and the DNA templated self-assembly of nanomaterials represents an important direction towards this goal. Until now, several groups have demonstrated the assembly of nanometer-scale materials such as metallic nanoparticles, quantum dots (QDs) and proteins on DNA nanostructures (Figure 28.5). The recognition events used to capture these functional materials included protein–protein/small molecule/aptamer (*in vitro* selected short DNA or RNA that can specifically bind to certain protein) interactions, functionalized metallic nanoparticle–DNA interactions, and DNA–DNA hybridization.

By using the well-known interaction between streptavidin and biotin, streptavidin protein molecules can be organized onto 2-D DNA nanoarrays with a controlled periodicity and spacing [32]. The streptavidin–biotin interaction has also been shown to be useful for organizing nanoparticles. For example, Sharma *et al.* successfully built a patterned QD array by reacting streptavidin-coated QDs with biotin groups on the 2-D DNA nanoarray [33]. By attaching single/multiple copies of DNA onto the Au nanoparticle surface [34–36], Au nanoparticles could be rationally organized onto self-assembled DNA nanoarrays through DNA–DNA hybridization. Recently, Yan’s group demonstrated that different-sized Au nanoparticles could be used to control the conformation of DNA nanotubes (Figure 28.5d) [37].

Liu *et al.* incorporated thrombin-binding aptamers into a linear, three-helix DNA tile array and used aptamer/protein recognition to capture thrombin proteins into periodic arrays [38]. Recently, Rinker *et al.* [39] were able to take one step further by displaying two different thrombin aptamers, each target at a distinctive site of the protein, on a DNA array. The distances between the two aptamers were systematically tuned such that a ~5.7 nm spacing led to an optimal “multivalent binding,” which has much higher binding affinity than does any of the single aptamers (Figure 28.5c).





**Figure 28.5** DNA nanostructure-directed nanomaterial assembly. (a) Streptavidin assembly on DNA  $4 \times 4$  periodic 2-D array; (b) Quantum dot assembly on a double crossover (DX) array; (c) Thrombin line assembled on M13 viral DNA scaffolded 2-D array; (d) Gold nanoparticles were assembled on a DX 2-D array and forced the array to form tubes with different spiral patterns.

## 28.6 Concluding Remarks

The field of structural DNA nanotechnology has witnessed numerous breakthroughs during the past decade, although only a small fraction of the prominent studies are outlined here. In that time, the complexity of the DNA structures has grown dramatically, from less than 100 nucleotides (four-arm DNA junction) to more than 10 000 nucleotides (“DNA Origami”), with series of 3-D objects having



been built and characterized. Today, the capability is available to attach proteins, metallic and semi-conducting nanoparticles onto DNA arrays so as to create a variety of patterns of these materials. An increasing knowledge of the rules to design DNA structures has led to the building of more-complex DNA self-assemblies, and with fewer errors. With such progress, there is much optimism that DNA nanotechnology can potentially be applied to build DNA nanostructure-based nanocircuits and to control chemical/biochemical reactions in an ordered fashion that mimics enzyme cascade reactions. Nonetheless, many challenges remain. Although some functional materials have been successfully patterned by DNA arrays, the key ability is still lacking to create well-controlled, multicomponent nanoarchitectures. Whilst the current success with DNA 3-D objects has been limited to the building of polyhedron cages for purposes such as protein encapsulation and drug delivery, the task remains to create a universal strategy for building highly ordered 3-D structures. The “designer DNA” nanostructures produced, with their controlled geometry and topology, might find their use in biological applications such as interfacing cellular components through DNA scaffolds. Yet, much remains to be done in studying the biocompatibility, delivery, and stability of DNA nanostructures inside living systems. With the field of nanotechnology having successfully “borrowed” DNA from biological systems, it will not be surprising to see DNA nanotechnology contribute to the *in vivo* applications of nanotechnology in the future.

### Acknowledgments

These studies were supported by grants from the National Science Foundation (NSF), the Army Research Office (ARO), and the Technology and Research Initiative Fund from Arizona State University to Y.L., and by grants from NSF, ARO, Air Force Office of Scientific Research, Office of Naval Research, and the National Institute of Health to H.Y.

### References

- 1 Watson, J.D. and Crick, F.H.C. (1953) A structure for deoxyribose nucleic acid. *Nature*, **171**, 737–738.
- 2 Seeman, N.C. (1982) Nucleic acid junctions and lattices. *J. Theor. Biol.*, **99**, 237–247.
- 3 Holliday, R. (1964) A mechanism for gene conversion in fungi. *Genet. Res.*, **5**, 282–304.
- 4 Zhang, X., Yan, H., Shen, Z. and Seeman, N.C. (2002) Paranemic cohesion of topologically-closed DNA molecules. *J. Am. Chem. Soc.*, **124**, 12940–12941.
- 5 Yan, H. and Seeman, N.C. (2003) Edge-sharing motifs in structural DNA nanotechnology. *J. Supramol. Chem.*, **1**, 229–237.
- 6 Qiu, H., Dewan, J.C. and Seeman, N.C. (1997) A DNA decamer with a sticky end: the crystal structure of d-CGACGATCGT. *J. Mol. Biol.*, **267**, 881–898.
- 7 Seeman, N.C. (1990) De novo design of sequences for nucleic acid structural engineering. *J. Biomol. Struct. Dyn.*, **8**, 573–581.

- 8 Mao, C., Sun, W. and Seeman, N.C. (1999) Designed two-dimensional DNA Holliday junction arrays visualized by atomic force microscopy. *J. Am. Chem. Soc.*, **121**, 5437–5443.
- 9 Fu, T.J. and Seeman, N.C. (1993) DNA double-crossover molecules. *Biochemistry*, **32**, 3211–3220.
- 10 Winfree, E., Liu, F., Wenzler, L.A. and Seeman, N.C. (1998) Design and self-assembly of two-dimensional DNA crystals. *Nature*, **394**, 539–544.
- 11 LaBean, T.H., Yan, H., Kopatsch, J., Liu, F., Winfree, E., Reif, J.H. and Seeman, N.C. (2000) Construction, analysis, ligation, and self-assembly of DNA triple crossover complexes. *J. Am. Chem. Soc.*, **122**, 1848–1860.
- 12 Reishus, D., Shaw, B., Brun, Y., Chelyapov, N. and Adleman, L. (2005) Self-assembly of DNA double-double crossover complexes into high-density, doubly connected, planar structures. *J. Am. Chem. Soc.*, **127**, 17590–17591.
- 13 Ke, Y., Liu, Y., Zhang, J. and Yan, H. (2006) A study of DNA tube formation mechanisms using 4-, 8-, and 12-helix DNA nanostructures. *J. Am. Chem. Soc.*, **128**, 4414–4421.
- 14 Yan, H., Park, S.H., Finkelstein, G., Reif, J.H. and LaBean, T.H. (2003) DNA-templated self-assembly of protein arrays and highly conductive nanowires. *Science*, **301**, 1882–1884.
- 15 He, Y., Chen, Y., Liu, H., Ribble, A.E. and Mao, C. (2005) Self-assembly of hexagonal DNA two-dimensional (2D) arrays. *J. Am. Chem. Soc.*, **127**, 12202–12203.
- 16 He, Y., Tian, Y., Ribble, A.E. and Mao, C. (2006) Highly connected two-dimensional crystals of DNA six-point-stars. *J. Am. Chem. Soc.*, **128**, 15978–15979.
- 17 Park, S.H., Barish, R., Li, H., Reif, J.H., Finkelstein, G., Yan, H. and LaBean, T.H. (2005) Three-helix bundle DNA tiles self-assemble into 2D lattice or 1D templates for silver nanowires. *Nano Lett.*, **5**, 693–696.
- 18 Mathieu, F., Liao, S., Kopatsch, J., Wang, T., Mao, C. and Seeman, N.C. (2005) Six-helix bundles designed from DNA. *Nano Lett.*, **5**, 661–665.
- 19 Kuzuya, A., Wang, R., Sha, R. and Seeman, N.C. (2007) Six-helix and eight-helix DNA nanotubes assembled from half-tubes. *Nano Lett.*, **7**, 1757–1763.
- 20 Park, S.H., Pistol, C., Ahn, S.J., Reif, J.H., Lebeck, A.R., Dwyer, C. and LaBean, T.H. (2006) Finite-size, fully addressable DNA tile lattices formed by hierarchical assembly procedures. *Angew. Chem. Int. Ed. Engl.*, **45**, 735–739.
- 21 Liu, Y., Ke, Y. and Yan, H. (2005) Self-assembly of symmetric finite-size DNA nanoarrays. *J. Am. Chem. Soc.*, **127**, 17140–17141.
- 22 Yan, H., LaBean, T.H., Feng, L. and Reif, J.H. (2003) Directed nucleation assembly of DNA tile complexes for barcode-patterned lattices. *Proc. Natl Acad. Sci. USA*, **100**, 8103–8108.
- 23 Rothmund, P.W.K. (2006) Folding DNA to create nanoscale shapes and patterns. *Nature*, **440**, 297–302.
- 24 Chen, J. and Seeman, N.C. (1991) The electrophoretic properties of a DNA cube and its substructure catenanes. *Electrophoresis (Weinheim)*, **12**, 607–611.
- 25 Goodman, R.P., Berry, R.M. and Turberfield, A.J. (2004) The single-step synthesis of a DNA tetrahedron. *Chem. Commun.*, 1372–1373.
- 26 Goodman, R.P., Schaap, I.A.T., Tardin, C.F., Erben, C.M., Berry, R.M., Schmidt, C.F. and Turberfield, A.J. (2005) Rapid chiral assembly of rigid DNA building blocks for molecular nanofabrication. *Science*, **310**, 1661–1665.
- 27 Goodman, R.P., Heilemann, M., Doose, S., Erben, C.M., Kapanidis, A.N. and Turberfield, A.J. (2008) Reconfigurable, braced, three-dimensional DNA nanostructures. *Nat. Nanotechnol.*, **3**, 93–96.
- 28 Shih, W.M., Quispe, J.D. and Joyce, G.F. (2004) A 1.7-kilobase single-stranded DNA that folds into a nanoscale octahedron. *Nature*, **427**, 618–621.
- 29 Aldaye, F.A. and Sleiman, H.F. (2009) Modular access to structurally switchable 3D discrete DNA assemblies. *J. Am. Chem. Soc.*, **129**, 13376–13377.
- 30 He, Y., Ye, T., Su, M., Zhang, C., Ribble, A.E., Jiang, W. and Mao, C. (2008) Hierarchical self-assembly of DNA into

- symmetric supramolecular polyhedra. *Nature*, **452**, 198–201.
- 31** Zhang, C., Su, M., He, Y., Zhao, X., Fang, P., Ribble, A.E., Jiang, W. and Mao, C. (2008) Conformational flexibility facilitates self-assembly of complex DNA nanostructures. *Proc. Natl Acad. Sci. USA*, **105**, 10665–10669.
- 32** Park, S.H., Yin, P., Liu, Y., Reif, J.H., LaBean, T.H. and Yan, H. (2005) Programmable DNA self-assemblies for nanoscale organization of ligands and proteins. *Nano Lett.*, **5**, 729–733.
- 33** Sharma, J., Ke, Y., Lin, C., Chhabra, R., Wang, Q., Nangreave, J., Liu, Y. and Yan, H. (2008) DNA-tile-directed self-assembly of quantum dots into two-dimensional nanopatterns. *Angew. Chem. Int. Ed. Engl.*, **47**, 5157–5159.
- 34** Sharma, J., Chhabra, R., Liu, Y., Ke, Y. and Yan, H. (2006) DNA-templated self-assembly of two-dimensional and periodical gold nanoparticle arrays. *Angew. Chem. Int. Ed. Engl.*, **45**, 730–735.
- 35** Sharma, J., Chhabra, R., Andersen, C.S., Gothelf, K.V., Yan, H. and Liu, Y. (2008) Toward reliable gold nanoparticle patterning on self-assembled DNA nanoscaffold. *J. Am. Chem. Soc.*, **130**, 7820–7821.
- 36** Sharma, J., Chhabra, R., Yan, H. and Liu, Y. (2008) A facile in situ generation of dithiocarbamate ligands for stable gold nanoparticle-oligonucleotide conjugates. *Chem. Commun.*, 2140–2142.
- 37** Sharma, J., Chhabra, R., Cheng, A., Brownbell, J., Liu, Y. and Yan, H. (2009) Control of self-assembly of DNA tubules through integration of gold nanoparticles. *Science*, **323**, 112–116.
- 38** Liu, Y., Lin, C., Li, H. and Yan, H. (2005) Aptamer-directed self-assembly of protein arrays on a DNA nanostructure. *Angew. Chem. Int. Ed. Engl.*, **44**, 4333–4338.
- 39** Rinker, S., Ke, Y., Liu, Y. and Yan, H. (2008) Self-assembled DNA Nanostructures for distance dependent multivalent ligand-protein binding. *Nat. Nanotechnol.*, **3**, 418–422.

## Index

### a

- active center transformation 14
- acylnitroxide 328
- adenosine-5'-triphosphate 750, 773
  - MSN material 547
- adipic acid 347
- adsorbent 460
  - carbon nanotube 622ff.
  - removal of surface water contaminant 615ff.
- adsorption
  - <sup>243</sup>americium(III) 638
  - arsenic 637
  - cadmium(II) 628
  - chromium(VI) 626
  - competitive 633
  - copper(II) 629
  - 1,2-dichlorobenzene (1,2-DCB) 640f.
  - dioxin 639
  - fluoride 635
  - heavy metal ion 624ff.
  - lead(II) 624
  - nickel(II) 632
  - trihalomethane 642
  - zinc(II) 630
- Ag, *see* silver
- alcohol
  - oxidation 350ff.
- aldehyde
  - oxidation 350ff.
- alginate 530
- alkyl phosphonium 438
- alkyl pyridinium 438
- alkyltrimethyl ammonium cation 414
- allografting 527
- ALS approach 823
- aluminium
  - <sup>27</sup>Al MAS NMR spectroscopy 485ff.
- aluminium oxide (alumina) 566
  - $\gamma$ -Al<sub>2</sub>O<sub>3</sub> 343, 491, 508f., 635ff.
  - Al<sub>2</sub>O<sub>3</sub> 343ff., 558, 570, 635
  - Al<sub>2</sub>O<sub>3</sub>/CNT composite 635
  - Al<sub>2</sub>O<sub>3</sub> nanotube 220ff.
  - 3Al<sub>2</sub>O<sub>3</sub> 2SiO<sub>2</sub> 558ff.
  - Al<sub>2</sub>O<sub>3</sub>-X 499
  - Al-TUD-1 499
  - alumina membrane (AM) 196, 228, 669
  - Au/Al<sub>2</sub>O<sub>3</sub> 353
  - DL12 491
  - ICMUV-1 495f., 509
  - ID 1–11 500
  - I-A<sub>383</sub> 492
  - mesoporous 481ff.
  - MSU- $\gamma$  491
  - MSU-X 486, 509
  - PCL-coated 541
  - SGAL 516
- aluminogermanate nanotube 234
- aluminosilicate 406
- <sup>243</sup>americium(III) 638
- amide 819
- amidoacid chelating 469
- amine
  - hydrophilic 467
  - hydrophobic 467
  - selective sensor 672
- amino acid residue
  - chemical and physical parameter 731
- (S)-(-)-2-amino-3-phenylpropan-1-ol (APP) 215
- (3-aminopropyl)trimethoxysilane (APS, APTMS) 199, 298
- ammonium-MMT
  - quaternary 437
- amoxicillin 549
- anthracene (AN) 130ff., 602
  - PS-*b*-PEP-*b*-PE 141ff.
  - triaryl amine-terminated diimide 388

- antibody-coupled CNT 738
  - anticooperativity 786
  - antifreeze glycoprotein (AFGP) 776
  - antimony
    - SbPS<sub>4-x</sub>Se nanotube 238
  - apatite layer
    - biomimetic (BTAp) 543
  - aperture near-field Raman 678
  - apertureless near-field Raman imaging 695
  - aptamer/protein recognition 876
  - 1-D architecture
    - helical polymer-based 161, 176
  - 2-D architecture
    - helical polymer-based 161, 176
  - array
    - self-organized 173f., 218
  - arsenic
    - adsorption 637
  - ascorbic acid 300
  - atenolol 659f.
  - atom transfer radical (ATR) polymerization (ATRP) 12, 743, 763
  - atomic force microscopy (AFM) 161
    - visualization of 1-D rod, semi-circle and circle structure 162
    - visualization of 2-D self-organized array 173
  - atomic layer deposition (ALD) 218ff.
    - in alumina membrane 228
    - gas-phase 220
  - Au, *see* gold
  - autografting 527
  - azobenzene 51f., 105
    - light-active azobenzene block copolymer vesicle 52
    - mesogen 51
    - photoisomerization 105
    - photoresponsive 122
  - azobenzene-poly(methacrylate)-*block*-poly(acrylic acid) 105
- b**
- backbone modification 81
  - barium titanate (BaTiO<sub>3</sub>) nanotube 233
  - Barrett–Joyner–Halenda (BJH) method 484
  - basal plane spacing 407
  - base-catalyzed reaction 508
  - battery 319ff.
    - “see-through” 329
  - BCN nanotube 237
  - bentonite 460
  - benzoic acid (BA) 129
    - crystal 130ff.
    - PS-*b*-PEP-*b*-PE 141ff.
  - ( $\gamma$ -benzyl L-glutamate)-*N*-carboxyanhydride (BLGlu-NCA) 862
  - bilayer system
    - spin-coated 185ff.
  - N,N'*-bi(2-mercaptoethyl)-perylene-3,4,9,10-tetra-carboxylic diimide (MEPTCDI) 279
  - biocompatibility 525
  - biofunctionality 525
  - biomagnification 601
  - biomaterial 524
  - biomedical application 475
  - biomimetic hybrid polymer 836
  - biomimetic processing 526
  - biomimetics 524, 536
  - biomolecule
    - AuNP/ITO electrode 315
  - biopolymer 782
    - dispersion of CNT 719
    - interaction with CNT 715ff.
  - biosensor 50, 289
  - bis(benzoxazolyl) stilbene (BBS) 383ff.
  - bis-(2-hydroxyethyl)-methyl-(hydrogenated tallow alkyl) ammonium cation 445
  - bismuth
    - Bi<sub>2</sub>S<sub>3</sub> nanotube 211f.
    - Bi<sub>2</sub>Te<sub>3</sub> nanotube 212
  - blending 444
  - block copolymer (BCP) 1ff.
    - alignment 111ff.
    - azobenzene containing 51ff.
    - drug delivery vesicle 52
    - film thickness 127
    - fluorinated 48
    - gel 793
    - holographic material 52
    - interface-active 48
    - linear polypeptide-based 835ff.
    - lithographic system 15
    - microdomain structure 126ff.
    - multilevel resist strategy 29
    - nanofibre 67ff.
    - nanolithographic template 17
    - nanoporous block polymer template 20
    - nanoporous film 36
    - nanoporous monolith 34
    - nanoreactor 44
    - nanotube 67ff.
    - rod-coil 7
    - self-assembling 1ff.
    - self-assembly 835
    - semi fluorinated 49
    - structure direction 34
    - surface interaction 127
    - synthesis 9

- thin film 126
  - triblock 4
  - block copolymer micelle
    - nanolithography 47
  - block copolymer morphology
    - alignment and ordering 111ff.
  - block copolymer system 1ff.
    - phase-selective chemistry 1ff.
  - block copolypeptide 841
  - block-selective solvent 72
  - blood–brain barrier (BBB) 606
  - BN nanotube 235ff.
  - boc-phenylalanine 667
  - boehmite nanotube 234
  - bone regeneration 527
  - bottom-up fabrication 321, 334, 767
  - bovine serum albumin (BSA) 476, 723ff.
  - brain
    - effect of engineered carbon nanoparticle 607
  - breidigite 543
  - broken lamellar morphology 860
  - Brunauer–Emmett–Teller (BET) method 484, 629
  - 3-D bulk phase 175
    - self-organized array 175
  - bulk polymerization 656
  - bundalization 716
  - tert*-butoxycarbonyl (TBOC) protecting group 50
  - t*-butyl methacrylate (*t*BMA)-*block*-3-methacryloxy-propyl pentamethyldisiloxane (SiMA) 33
  - n*-butylstannic acid 708
- c**
- cadmium
    - Cd(II) adsorption 628ff.
    - CdCl<sub>2</sub> nanotube 240
    - CdO nanotube 223
    - CdSe nanotube 206ff.
    - CdSe-ZnS quantum dot 286
    - CdTe nanotube 210
    - trioctylphosphine oxide (TOPO)-capped CdSe nanoparticle 755
  - cadmium sulfide CdS
    - nanotube 206
    - surface-derivatized nanocrystal 547
  - caffeine 659ff.
  - calcination 483
  - calcium phosphate (CaP) 530
    - coating 535
  - calixarene 822
  - cancer 551, 738
    - ε-caprolactam 347
    - ε-caprolactone (ε-CL) 347
    - carbamide 820
    - carbide nanotube 240
    - carbodiimide reagent 268
    - carbon dioxide (CO<sub>2</sub>) 508
      - supercritical (scCO<sub>2</sub>) 508
    - carbon monoxide (CO) 337f., 562
      - selective oxidation 337ff.
    - carbon nanoparticle
      - bioavailability 598
      - developmental effect 608
      - ecological toxicology 595ff.
      - engineered 595ff.
      - food web 600
      - stability in aquatic system 596
      - tissue distribution 600
      - toxicological effect 602
      - uptake 598
    - carbon nanotube (CNT) 220, 249ff., 597f., 615ff.
      - adsorbent 620ff.
      - <sup>243</sup>americium(III) 638
      - anchoring of metal nanoparticle 289
      - arsenic adsorption 637
      - AuNP composite 255ff.
      - B<sub>2</sub>O<sub>3</sub>-coated 236
      - bamboo-like (BCNT) 276f.
      - chirality-based separation 734
      - composite material 249
      - covalent linkage 268
      - deposition of AuNP 256
      - diameter-based separation 734
      - 1,2-dichlorobenzene adsorption 640
      - dioxin adsorption 639
      - dispersion in biopolymer 719
      - DNA coated 737
      - DNA conjugate 721
      - electrical property 620
      - emitter 289
      - fluoride adsorption 635
      - functionalized 738
      - heavy metal adsorption 624ff.
      - hydrogen bonding 271
      - hydrophobic interaction 271
      - interaction with biomolecules 715ff.
      - interaction with DNA 720f.
      - interaction with modified AuNP 267
      - interaction with protein 723
      - mechanical property 620
      - memory element 289
      - multiwalled (MWNT) 251ff., 597, 616ff., 716
      - nanotube aquator 289

- noncovalent functionalization 718
- optical property 620
- polyaromatic compound adsorption 643
- property 620ff.
- removal of surface water
  - contaminant 615ff.
- sensor 289
- silicon substrate 682
- single-walled (SWNT) 251ff., 598, 616ff., 716ff.
- $\pi$ - $\pi$ -stacking interaction 277ff.
- structure 616
- supramolecular interaction 271
- synthesis 616
- thermal property 620
- TiO<sub>2</sub> nanotube 240
- trihalomethane adsorption 642
- visualization of Si-C bonding 682
- carbonate hydroxyapatite (CHAp) 530ff.
- carbonated apatite (CA) 544
- N-carboxyanhydride (NCA) 851
- carboxylic acid chelating 469
- catalysis
  - AuNP 288
  - heterogeneous 500
  - oxidation 333ff.
- catalyst 337, 460
- cation exchange 413
- cation exchange capacity (CEC) 407, 442, 464ff.
- ceramic component
  - structural integrity 579
- ceramics
  - fracture 555
  - microboceramics 548f.
  - multicomposite 585
  - nanobioceramics 546
  - nanoceramics 523ff.
  - self-crack healing 559ff., 585
  - Si-CNT bonding 682
  - structural 555ff.
  - temperature 571
- cerium hydroxide Ce(OH)<sub>3</sub> nanorod 233
- cerium oxide (CeO<sub>2</sub>, ceria) 339ff.
  - adsorbent 627
  - CNT composite 637
  - nanotube 233
- cesium
  - [(18C6)Cs(18C6)Cs(18C6)]<sup>+</sup> 375
- cetyltrimethylammonium bromide (CTAB) 222, 299ff., 495
- chemical gel 791
- chemical sensor
  - AuNP 288
  - chemical valve effect 43
  - chemical vapor deposition (CVD) 196, 221ff., 618
    - low-pressure (LPCVD) 689
    - microwave plasma-enhanced 236
    - plasma-enhanced (PECVD) 265
  - chirality-based separation of CNT 734
  - chiroptical inversion 178ff.
  - chiroptical memory 178ff.
    - helical polysilane film 178
  - chiroptical switch 178
  - chiroptical transfer 185
  - chlorite 404
  - chloroaluminum phthalocyanine (AlClPc) 95
  - cholesterol 823
    - imprinted shell 658
  - chromium(VI) 626ff.
    - adsorption 626ff.
    - carbon nanotube 626ff.
  - chromophore
    - dispersed phase 380
    - organic 380
  - cinnamoyloxyethyl methacrylate (CEMA) 39
  - circle structure 162ff.
  - clay 404ff.
    - chemical structure 460
    - ionic 475
    - layered 459ff.
    - natural 460
    - organophilic 477
  - Cloisite-Na<sup>+</sup> 434
  - Cloisite 6A 437
  - Cloisite 10A 437
  - Cloisite 15A 437ff.
  - Cloisite 20A 438
  - Cloisite 25A 437ff.
  - Cloisite 30B 437ff.
  - Cloisite 93A 443
  - cluster
    - infinite 785
    - nucleation 46
    - size 785
  - CNT, *see* carbon nanotube
  - coating 535f.
    - calcium phosphate 535
    - nanocoating 535f.
    - spray 536
    - thick bioglass 536
  - cobalt
    - microtubule 200
    - salen complex 510
    - [(Tl(18C6))<sub>4</sub>(CoCl<sub>4</sub>)]<sub>2</sub>[TiCl<sub>4</sub>]<sub>2</sub> · nH<sub>2</sub>O 371

- cobalt oxide
    - Co<sub>3</sub>O<sub>4</sub> nanotube 228f.
    - nanowire 322
  - collagen
    - HAp/collagen 528f.
  - colloidal gold, *see* gold nanoparticle
  - colloidal nanoparticle 333
  - compatibilizer 410ff., 425ff., 438ff.
  - competing interaction
    - weak 784
  - complementary metal-oxide-semiconductor (CMOS) transistor 690
  - composite, *see also* micro- or nanocomposite
    - morphology 408
    - polymer–clay composite 408
    - property 411
  - composite graft
    - bioactive 528
  - concentration effect 793
  - conductor
    - electronic 160
    - ionic 160
  - contour length 163
  - convergent synthesis
    - NCD 759
  - converging beam electron diffraction (CBED) 690
  - cooperativity 785
  - coordination–insertion catalyst 440
  - copolymer 466ff.
    - amphiphilic 466
    - IL-based gel 815
    - volume fraction 808
  - copper
    - catalyst 343ff.
    - Cu(II) adsorption 629ff.
    - CuS nanotube 206ff.
    - CuSe nanotube 210
    - nanocatalyst 335
  - coralline apatite
    - nanocoated 538
  - core–shell emulsion polymerization 657
  - core–shell morphology 39
  - core–shell nanoparticle 658
  - cosolvent system 816
  - cosurfactant 811
  - covalent imprinting 654
  - crack
    - bonding by oxidation 557
  - crack healing 557ff.
    - atmosphere 567
    - ceramics 559ff., 585
    - effect 573ff.
    - fracture probability 573
    - machining efficiency 577
    - temperature 568
  - critical aggregation concentration (CAC) 469
  - critical electric field strength 119
  - critical micelle concentration (CMC) 95, 469, 794
  - critical micelle temperature (CMT) 104
  - critical radius 46
  - cross-polarization-magic angle spinning (CP-MAS) 375
  - crown ether 366
    - [(A(18C6))<sub>4</sub>(MX<sub>4</sub>)] [BX<sub>4</sub>]<sub>2</sub> · nH<sub>2</sub>O 366ff.
    - rotation 374
  - crystallization 129, 779
    - 2-D 172
    - epitaxy 140
    - directional 126ff.
    - graphoepitaxy 138
  - Cu, *see* copper
  - curdlan 720
  - cyano-oligo(*p*-phenylene vinylene) (cyano-OPV) 382f.
  - 4-cyano-4-*n*-pentylbiphenyl (5CB) 814
  - cyclic voltammetry (CV) 750
  - [2+2] cycloaddition 41
  - cyclohexane 349
  - trans*-cyclohexane-1,2-diamide 819
  - L-cysteine 670
- d**
- d*-spacing 461ff., 492ff.
  - dahllite 532
  - debundalization 716
    - degree 729
  - decorated phase 5
  - deep ultraviolet (DUV) radiation 22
  - degree of functionalization (DF) 425
  - Dellite 43B 443
  - Dellite 72T 443
  - dendrimer 671, 699ff.
    - bimetallic nanoparticle 744
    - bridging 756
    - cluster-cored 744
    - fullerene-functionalized 699
    - fullerene-rich 708
    - gold nanoparticle-cored 746ff.
    - nanoparticle-cored (NCD) 743ff.
    - poly(amidoamine) (PAMAM) 756
    - polyhedral oligomeric silsesquioxane (POSS) core 744
    - semiconductor nanoparticle 744
  - dendritic branch
    - fullerene-rich 700



- dendritic functionalization 758
  - dendron
    - Fréchet-type 759
    - poly(oxymethylphenylene) (PPD) 746
    - 4-pyridone-functionalized 752
    - Simanek-functionalized
      - superparamagnetic nanoparticle 757
  - density functional theory (DFT) 121, 343
  - deoxycholic acid (DOC) 720
  - deposition–precipitation (DP) 337ff.
  - 2,3-di-*n*-alkoxyanthracene 823
  - dialkyldimethyl ammonium cation 414
  - dialkyl imidazolium 438
  - diameter-based separation of CNT 734
  - 1,3:2,4-dibenzylidene sorbitol (DBS) 820f.
  - diblock copolymer 1, 800, 844
    - polydiene-based 844
    - polyester-based 851
    - polyether-based 850
    - polystyrene-based 845
  - diblock copolypeptide 851
  - 1,2-dichlorobenzene (1,2-DBC) 616, 640f.
  - SWNT interaction 642
  - N,N'*-dicyclohexyl-carbodiimide (DCC) 268, 759
  - dielectric material
    - silicon dioxide 34
  - N,N'*-diethyl(4-vinylphenyl)amidine 655
  - differential scanning calorimetry (DSC) 423
  - diffuse reflection infrared Fourier transform (DRIFT) spectrum 516
  - diffusion coefficient 326
  - diffusion-limited aggregation (DLA) 769
  - N,N*-dimethylacetamide (DMA) 443
  - 1-[3-(dimethylamino)propyl]-3-ethylcarbodiimide hydrochloride (EDCI) 86
  - 4-dimethylaminopyridine (DMAP) 700, 759
  - trans*-4-[*p*-(*N,N*-dimethylamino)styryl]-*N*-vinylbenzylpyridinium chloride 655
  - N,N*-dimethyl-*N,N*-dioctadecylammonium-MMT 437
  - 1,2-dimyristoyl-*sn*-glycero-3-phosphate (DMPA) 532
  - 1,2-dimyristoyl-*sn*-glycero-3-phosphocholine (DMPC) 532
  - dioxin
    - adsorption 639
  - dispersed phase 380
    - metal nanostructure 389
    - organic chromophore 380
  - divergent synthesis
    - NCD 761
    - DL12 491
  - DNA (deoxyribonucleic acid) 781, 869
    - base pair mismatch 288
    - biosensor 270
    - CNT conjugate 721
    - dispersed nanotube 736
    - double crossover (DX) 871ff.
    - filament 172
    - interaction with CNT 720
    - *met*-SWNT 723
    - nanostructure design 871
    - origami 874ff.
    - paranemic crossover (PX) 871ff.
    - periodic DNA nanoarray 871
    - polyhedron cage 874
    - self-assembly 874ff.
    - sticky end 870
    - SWNT fiber 737
    - transfer 96
  - DNA assembly 878
    - hierarchical 875
  - DNA nanoarray 871ff.
    - addressable 872
    - finite-sized 872
    - nucleated DNA self-assembly 874
    - periodic 871
    - self-assembled 876
  - DNA nanotechnology
    - information guided self-assembly 869ff.
    - structural 869ff.
  - Dollimore–Heal (DH) method 484
  - dopamine 300
  - doxorubicin (DOX)
    - polymeric micelle 94, 107
  - Drude–Lorentz–Sommerfeld theory 389
  - drug delivery 663
    - light-active azobenzene block copolymer vesicle 52
    - microboceramics 548
    - nanoassembly of block copolymer 91ff.
    - nanoboceramics 546
    - pH-sensitive nanoassembly 93
  - dynamic light scattering (DLS) 797
- e**
- ecological toxicology 595ff.
    - engineered carbon nanoparticle 595ff.
  - elastin-like polypeptide (ELP)
    - nanoassembly 397
  - GNR–ELP 397
  - electric field 118
  - electrode
    - AgNP/ITO 309
    - AuNP/ITO 300ff., 315

- biomolecule 315
- inorganic electrode-active material 322
- metal nanoparticle-attached 297ff.
- organic polymer battery 319ff.
- organic radical polymer electrode 324
- PtNC/GC 313
- PtNP/ITO 313
- electrodeposition 212
- electrohydrodynamic (EHD) film
  - instability 119
- electron beam lithography (EBL) 124
- electron hopping 321
- electron-withdrawing group (EWG) 328
- electronic device
  - AuNP 288
- electroporation
  - MWNT 288
- electrospinning 118
- emitter
  - CNT 289
- emulsion polymerization 657
  - core–shell 657
- end functionalization 85
- endblock-selective homopolymer 810
- endocytosis 93f.
- endogenous trigger 93ff.
- energy dispersive spectroscopy (EDS) 529
- energy storage device 319ff.
- enhanced permeability and retention (EPR) effect 93
- entropy 767ff.
  - relative 771
- epinephrine 300
- 2-D epitaxial array 172
- epitaxial control 129
- epitaxy 126ff.
  - directional crystallization 140
- EPM, *see* ethylene–propylene (random) copolymer
- epoxidation reaction 344ff., 509
  - gold catalyst 344
- 17 $\beta$ -estradiol 662
- estriol 670
- etch resistance 16
- 1-ethyl-3-(3-dimethyl-amino-propyl)-carbodiimide (EDC) 268
- ethylene carbonate/diethylcarbonate (EC/DEC) 319
- ethylene glycol dimethacrylate (EGDMA) 657
- ethylene terephthalate cyclic oligomer (ETCO) 431

- ethylene–propylene (random) copolymer (PE–PP rubber, EPM) 410
  - EPM/OLS nanocomposite 421ff.
  - functionalized with diethyl maleate (EPM-g-DEM) 421ff.
  - functionalized with maleic anhydride (EPM-g-MAH) 410
- excimer formation 380
- exclusion zone 774
- exfoliation 427, 472f.
  - zigzag mechanism 473
- external stimulus 102
- extreme ultraviolet interferometric lithography 124
- extreme ultraviolet (EUV) radiation 17

## **f**

- fast Fourier transform (FFT) power spectrum 133ff.
- fatigue strength 575
- Fe, *see* iron
- ferrocene
  - NCD-encapsulated 759
  - nonaferrocenyl thiol dendron-functionalized nanoparticle 750
- ferrocenyl-polyethylene glycol (FPEG) 100
- fiber 736
  - DNA-based SWNT 737
- fibrillar micelle 825
- field-emission scanning electron microscopy (FESEM) 267, 299
- flocculation 408
- Flory–Huggins interaction 793
- fluorescent sensing 655
- fracture 556
  - criterion 556
  - probability 573
  - strength 581
  - stress 581ff.
- Frank-van der Merwe régime 778
- [60]fullerene (C<sub>60</sub>) 285, 670, 699ff.
  - nanostructure 699ff.
- fullerodendrimer 699
- fullerodendron 702ff.
  - photoelectronic property 704
- functional film 177
  - helical polymer-based 177
- functionalization
  - dendritic 758
  - noncovalent 718

## **g**

- G1CO<sub>2</sub>tBu 700ff.
- G1–5CO<sub>2</sub>tBu 703ff.

- G1CO<sub>2</sub>H 700
- G2CO<sub>2</sub>tBu 700ff.
- G2CO<sub>2</sub>H 700
- G3CO<sub>2</sub>tBu 702ff.
- G3CO<sub>2</sub>H 702
- G4CO<sub>2</sub>tBu 703ff.
- G4CO<sub>2</sub>H 703
- G5CO<sub>2</sub>tBu 703
- G5CO<sub>2</sub>H 703
- Galam–Mauger formula 785
- GaN nanotube 237
- gas phase catalytic process 252
- gel
  - chemical 791
- gelatin 791
- gelation 768f.
  - isothermal 825
- gelator 816ff.
  - biologically inspired 824
  - oligopeptide-based 825
- gene delivery
  - nanoassembly of block copolymer 91ff.
- gene therapy 530
- geometry
  - confining 135
- giant polymer chain 75
- gill
  - engineered carbon nanoparticle 607
- glass
  - bioactive 527
  - transition temperature 22
- glassy carbon (GC)
  - attachment of AuNP 306
  - attachment of PtNP 312ff.
- glucose biosensor 289
- glucose oxidase (GOx) 100, 726ff.
- (3-glycidyloxypropyl) trimethoxysilane ((glycidoxypropyl)trimethoxy silane, GLYMO) 35, 411
- goethite nanorod 199
- gold
  - anion cluster 337
  - Au/Al<sub>2</sub>O<sub>3</sub> 353
  - Au/ICMUV-1 509
  - nanocatalyst 335ff.
  - nanopattern 693f.
  - nanowire 285
  - polymer composite 393
  - silver alloy catalyst 342
  - tubule 196
- gold catalyst 337ff., 349ff.
  - epoxidation reaction 344ff.
  - titan dioxide 344
- gold nanoparticle (AuNP) 249ff., 297
  - alkanethiolate-capped 274
  - attachment on GC 306
  - attachment on ITO 302ff.
  - attachment onto mesoporous TiO<sub>2</sub> film 307
  - AuNP-cored dendrimer 746ff.
  - AuNP-directly attached ITO (AuNP/ITO) 300ff.
  - catalysis 288
  - chemical sensor 288
  - CNT composite 255ff.
  - covalent linkage 268
  - dendrimer 746
  - deposition on the CNT surface 256
  - dibenzo[24]crown-modified 275
  - dodecane-thiol-modified 275
  - electrode 298ff., 315
  - electronic device 288
  - growth 306
  - growth on ITO 302ff.
  - hydrogen bonding 271
  - hydrophobic interaction 271
  - interaction between modified AuNP and CNT 267
  - 11-mercaptopundecanoic acid-functionalized 759
  - MWNT composite 281
  - seed-mediated growth method 298ff.
  - silica-coated 282
  - supramolecular interaction 271
  - tetraoctylammonium bromide stabilized 272
  - thiol-stabilized 288
  - water-dispersible AuNP–MWNT hybrid 279
- gold nanorod (GNR)
  - elastin-like polypeptide (ELP) nanoassembly 397
- gold nanoshell
  - goethite nanorod 199
- gold nanotube 197ff.
  - 3-D 197
  - reactive ion etching 197
- grafting on nanoparticle 763
- graphite substrate 174
- graphoepitaxy 124, 135ff.
  - directional crystallization 138
- group transfer polymerization (GTP) 13
- growth 46
- gum arabica 719
- gyration radius 77
- gyroid network structure 4

**h**

- hard–soft, acid–base (HSAB) principle 44f.  
 healing temperature 588  
 hectorite 407, 460  
 helical polymer-based 1-D architecture 161, 176  
 helical polymer-based 2-D architecture 161, 176  
 helical polymer-based functional film 177ff.  
 helicity 170ff.  
 helix–coil transition 178ff.  
 helix–helix (PM) transition 167, 177f.  
 hemoglobin (Hb) 300, 726ff.  
 heterogeneous catalysis 500  
*trans*-[2-(2,2,3,3,4,4,4-heptafluorobutylamino)ethyl][2-[4-(4-hexylphenylazo)phenoxy]ethyl] dimethylammonium ( $C_3F_7\text{-Azo}^+$ ) 234  
 hexadecyltrimethylammonium bromide 407  
 high-density polyethylene (HDPE) 390f.  
 high-pressure carbon monoxide (HiPCO) – method 252  
 – HiPCO-SWNT 693, 717  
 high-temperature gas turbine 588  
 highest occupied molecular orbital (HOMO) – nanotube 261  
 highly oriented pyrolytic graphite (HOPG) 172ff., 342  
 Hildebrand solubility parameter theory 826  
 histone 726  
 holography 53  
 – azobenzene containing block copolymer 52f.  
 homochiral intermolecular interaction 169ff.  
 – superhelical assembly 169ff.  
 homopolymer 810  
 Horvath–Kawazoe model 484  
 hot isostatic pressing (HIP) 523  
 hot pressing (HP) 523  
 Huggins coefficient 78  
 hybrid structure  
 – organic/inorganic 842  
 hybrid triblock copolymer  
 – electro- and photoactive peptide 862  
 hydrazide 822  
 hydrocarbon  
 – selective oxidation 347ff.  
 hydrocoral 529  
 hydrodechlorination 510  
 hydrodesulfurization 512  
 hydrogel  
 – polypeptide-based 842  
 hydrogen bonding 271, 818  
 hydrogen peroxide  
 – direct synthesis 353  
 – mediator-free sensor 301  
 hydrogen plasma 48  
 hydrophobic interaction 271  
 1-hydroxy-benzotriazole (HBA) 86  
 hydroxyapatite (HAp) 526ff.  
 – antibiotic 549  
 – coralline apatite 538  
 – HAp/chitosan (CS) 530  
 – HAp/collagen 528  
 – HAp/polyethylene 528  
 – HAp/Ti-6Al-4V 528  
 – liposome 532  
 – nanocoating 538  
 – nanoparticle 537  
 – nanopowder 533  
 – nanoplatelet 533  
 hyperthermia 550  
 hypsochromic shift 389f.

**i**

- ICMUV-1 495f.  
 ID 1–11 500  
 IL, *see* ionic liquid  
 illite 404  
 imidazolium salt 463  
 implant  
 – macro-textured 533  
 – orthopedic 532  
*in situ* intercalative polymerization 412f.  
*in situ* polymerization 430ff.  
 incompatibility parameter 5  
 indentation 557ff.  
 indigo carmine derivative 323  
 indium  
 –  $InVO_4$  nanotube 234  
 – nanotube 205  
 indium oxide  
 –  $In_2Ge_2O_7$  nanotube 234  
 –  $In_2O_3$  nanotube 230f.  
 indium tin oxide (ITO) 298  
 – attachment of AgNP 309  
 – attachment of Au nanoplate 308  
 – attachment of AuNP 302ff.  
 – attachment of PdNP 311  
 – AuNP-directly attached ITO (AuNP/ITO) 300ff.  
 – electrochemical application 300, 315  
 – electrode 300ff., 315  
 – growth of AuNP 302ff.

- growth of AgNP 309
- growth of PdNP 311
- ITO/SnO<sub>2</sub> 706
- ITO/SnO<sub>2</sub>/(G1–5CO<sub>2</sub>tBu)<sub>m</sub> film 706
- metal NP-attached ITO 315
- nonlinear optical property 315
- seed-mediated growth method 298ff.
- indomethacin (IMC) 532
- inductively coupled plasma (ICP) 516
- infiltration
  - polymer foam 534
- inorganic nanotube
  - general synthetic strategy 196
  - synthesis 195ff.
- intercalating agent 461ff.
  - low molecular weight 461
- intercalation 408, 460ff.
  - exfoliation 427
  - intermolecular hydrogen bonding 470
  - melt 434ff.
  - solution 433, 442
- interfacial energy 119
- interlayer distance 407
- interlinker 277ff.
- intermaterial dividing surface (IMDS) 7
- inversion 180
- ionic liquid (IL) 815
- IRA-410 635
- iron nanotube 204
- iron oxide
  - dendron with Simanek-functionalized superparamagnetic nanoparticle 757
  - $\alpha$ -Fe<sub>2</sub>O<sub>3</sub> 551
  - $\alpha$ -Fe<sub>2</sub>O<sub>3</sub> nanotube 228
  - $\gamma$ -Fe<sub>2</sub>O<sub>3</sub> 843
  - $\gamma$ -Fe<sub>2</sub>O<sub>3</sub> nanotube 228
  - Fe<sub>3</sub>O<sub>4</sub> microspheres 550
  - $\beta$ -FeOOH 551
  - $\alpha$ -FeOOH nanotube 234
- iron(II) phthalocyanine 276
- iron–sulfur [Fe<sub>4</sub>S<sub>4</sub>] cluster-cored dendrimer 744
- cis-trans* isomerization 51, 105
- N*-isopropylacrylamide (NIPAAm) 95
- ITO, *see* indium tin oxide

**j**

- Jacobson–Stockmayer approximation 782

**k**

- KA-oil 347
- kaolinite 404
- Kramer–Kronig relationship 796

**l**

- L<sub>A383</sub> 492
- lamellar spheres 825
- lanreotide nanotube 215
- lanthanum
  - La<sub>0.5</sub>Sr<sub>0.5</sub>CoO<sub>3</sub> nanotube 235
- Laponite® 407
- large amplitude oscillatory shear (LAOS) 117
- lattice 785, 793
- layer-by-layer (LBL) self-assembly technique 270, 281ff.
- layered-double hydroxide (LDH) 460f., 475f.
  - clay 476
- LDPE/OLS nanocomposite 426
- lead(II) 624f.
  - adsorption 624ff.
  - carbon nanotube 626
- lead zirconate titanate (PZT) nanotube 233
- length distribution function 75
- ligand exchange reaction
  - NCD 753
- light
  - polymeric assembly 105
- light scattering (LS) 75
- linear low density polyethylene (LLDPE) 381
- liposome 531
  - hydroxyapatite coated (HACL) 531f.
- liquid crystal (LC) 814
  - chiral nematic 159
  - lyotropic 205
  - thermotropic 814
- liquid crystal template (LCT) mechanism 481
- liquid crystalline (LC)
  - behavior 7
  - diblock copolymer 122
  - phase 200
- lithium cobalt oxide 320
- lithium ion battery 319
- lithium ion conducting electrolyte layer 319
- lithium ion intercalating anode 319
- lithography 15
  - block copolymer 15
  - top-down positive and negative tone 29
- liver
  - engineered carbon nanoparticle 607
- living polymerization technique 9
  - block copolymer synthesis 9
- LLDPE, *see* linear low density polyethylene
- local fracture stress 578

- London dispersion forces 824
- low-molecular mass organic gelator (LMOG) 793, 816ff.
- low-pressure chemical vapor deposition (LPCVD) 689
- lower critical solution temperature (LCST) 102, 839
- lowest unoccupied molecular orbital (LUMO)
- nanotube 261
- luminescence decay dynamics 374
- luminescence spectroscopy
- $[(A(18C6))_4(MnX_n)] [TlX_4]_2 \cdot nH_2O$  372
- luminescent dye 381ff.
- lysozyme (LSZ) 719ff.
- m**
- macroinitiator 11ff.
- macrophase 3
- maghemite 843
- magnesium oxide nanotube 230
- magnesium silicate 406f.
- magnetic field 118
- maleic anhydride (MAH) 415
- manganese
- $Mn_2P_2S_6$  214
  - $[(Rb(18C6))_4(MnCl_4)] [TlCl_4]_2 \cdot nH_2O$  371
  - salen complex 510
- material
- amphiphilic 8
  - bioactive 524f.
  - bioinert 524f.
  - bioresorbable 524f.
- matrix 566
- mechanical flow field 117
- mechanical stress
- polymeric indicator 381
- median rank method 574
- medical application 523ff.
- nanoceramics 523ff.
- melt intercalation 413, 434
- membrane pore
- electrodeposition 196
- memory 178
- chiroptical 178ff.
  - element 289
  - helical polysilane film 178
  - Re-Writable mode 178
  - Write-once Read Many (WORM) mode 182
- 3-mercaptopropionic acid (MPA) 302
- 3-mercaptopropyl-trimethoxysilane (MPTMS) 298, 309
- 11-mercaptoundecanoic acid (MUA) 761
- mesogel 813
- nonequilibrium 812
- mesogen 51
- mesoporous alumina 481ff.
- base-catalyzed reaction 508
  - characterization 484f.
  - epoxidation 509
  - heterogeneous catalysis 500
  - hydrodechlorination 510
  - hydrodesulfurization 512
  - olefin metathesis 513ff.
  - oxidative dehydrogenation 517
  - oxidative methanol steam reforming 518
  - synthesis 482ff.
- mesoporous molecular sieve (M41S) 481
- mesoporous silica nanoparticle (MSN)
- material 546
  - vancomycin- and adenosine triphosphate (ATP)-loaded 547
- mesoscale radical polymer 319ff.
- mesostructured material 319ff.
- bottom-up fabrication 321
- metal chalcogenide nanotube 206
- metal nanoassembly
- optical property 389
- metal nanoparticle (NP) 297
- use 391
- metal nanorod 395
- metal nanostructure 379ff.
- dispersed phase 389
  - optically responsive polymer nanocomposite 379ff.
- metal oxide nanotube 214
- metal–boron nanotube 205
- metal-chelating agent 460
- metal-oxide-silicon (MOS) capacitor 25
- metal/semiconducting CNT separation 735
- methacrylic acid (MAA, MAAC) 95, 655
- methylloxirane 289
- methyltrioxorhenium (MTO,  $MeReO_3$ ) 516
- $SiO-Al_2O_3$  517
  - $ZnCl_2/meso-Al_2O_3$  516f.
- mica 404
- micelle 72, 794ff.
- formation 8
  - PEG-*b*-PPO-*b*-PEG poloxamer 107
  - polymeric 93ff.
- micro-Raman imaging technique 683ff.
- microbioceramics 548
- drug delivery 548
  - radiotherapy 549
- microcomposite 408
- microcontact printing ( $\mu$ -CP) 220

- microdomain 115ff.
    - alignment 127, 804f.
    - lamellar 135
  - microgel 664
    - polymerization 664
  - microlattice structuring 800
  - micromagnetics 140
  - microphase 3
  - microphotonics 140
  - Millepora dichotoma* 529
  - mini-emulsion polymerization 660
  - minimum fracture stress 582f.
    - temperature dependence 582
  - molecular beam epitaxy 778
  - molecular imprinted polymer (MIP) 651
  - molecular imprinting 651ff.
    - nanomaterial 651ff.
  - molybdenum
    - 30Mo/MA(CIM) 512
    - 30Mo/MA(TSM) 512
    - ammonium heptamolybdate 518
    - MoS<sub>2</sub> 206
  - molybdovanadate species 518
  - monolayer-protected cluster (MPC)
    - amine-functionalized 761
    - framework 759
    - MUA 759
  - monolith
    - nanoporous 34
  - montmorillonite (MMT) 404ff., 460f.
    - *d*-spacing 466
    - MMT/POP2000 471
    - organophilic 442
  - Mooney–Rivlin model 808
  - MSN, *see* mesoporous silica nanoparticle
  - MSU- $\gamma$  491
  - MSU-X 486ff.
  - MUA, *see* 11-mercaptoundecanoic acid
  - mullite 558ff.
    - silicon carbide composite 585f.
  - multiblock copolymer 815
  - multilevel resist strategy
    - block copolymer 2
  - multiwall carbon nanotube (MWCNT, MWNT) 240, 251ff., 597, 616ff., 716
    - alkylthiol-modified 273
    - AuNP composite 281
    - carboxy-modified 275
    - cation-modified 275
    - competitive adsorption of heavy metal ion 633
    - electroporation 288
    - electrostatic interaction 280
    - emitter 289
    - memory element 289
    - nanotube aquator 289
    - nitrogen-doped 280
    - noncovalent functionalization 286
    - sensor 289
    - water-dispersable AuNP–MWNT hybrid 279
  - myoglobin 726ff.
  - Mytilus edulis* 1f.
- n**
- nano-object
    - photo-crosslinkable 41
  - nanoassembly
    - oxidation- and reduction-sensitive 99
    - pH-sensitive 93
    - thermosensitive 102
  - nanobioceramics 546
    - drug delivery 546
  - nanocatalyst 335
    - Ag 335
    - Au 335ff.
    - Cu 335
  - nanoceramics 523ff.
    - medical application 523ff.
  - nanocluster
    - [(A(18C6))<sub>4</sub>(MX<sub>4</sub>)] [BX<sub>4</sub>]<sub>2</sub> · nH<sub>2</sub>O 366ff.
    - electronic and mechanical behavior 365ff.
    - self-assembling 365ff.
    - tetrahalometallate anion 365ff.
  - nanocoating 535
  - nanocomposite 526
    - exfoliated 408
    - intercalated 408
    - metal nanostructure 379ff.
    - optically responsive polymer 379ff.
    - organic functional chromophore 379ff.
    - phyllosilicate 403ff.
    - poly(ethylene terephthalate) (PET)-based 429
    - polyolefin (PO)-based 411
    - polylactide (PLA)-based 439
    - processing condition 443
  - nanocomposite-based indicator
    - mechanical stress 391
  - nanodiagnostics 551
  - nanoelectromechanical system (NEMS) 253
  - nanoelectronic device 253
  - nanofiber 67ff.
    - block copolymer 67ff.
    - catalytic 83
    - chemical reaction 81ff.

- molecular imprinting 668
- preparation 69ff.
- superparamagnetic 83
- water-dispersible 83
- nanofiller
  - inorganic 808
- nanogel 526, 664
  - polymerization 664
- nanogold, *see* gold nanoparticle
- nanohand 44
  - optical magnetic 88
- nanohydroxyapatite (nanoHAp) 526ff.
  - microspheres 548
- nanolithographic template 17
  - block copolymer 17
- nanomaterial
  - block copolymer 1ff.
  - molecular imprinting 651ff.
- nanomaterial assembly
  - DNA nanostructured-directed 876
- nanomonolithic particle 667
- nanoparticle (NP) 297
  - calcium phosphate-based hybrid 531
  - core–shell 658
  - dendrimer 743ff.
  - dendron with Simanek-functionalized superparamagnetic NP 757
  - engineered carbon 595ff.
  - grafting 763
  - hydroxyapatite (HAp) 533
  - molecular imprinted 667
  - nonaferrocenyl thiol dendron-functionalized 750
  - silica 665
  - silicon carbide composite 587
  - trioctylphosphine oxide-capped CdSe 755
- nanoparticle-cored dendrimer (NCD) 743ff.
  - CdSe/CdS core–shell 757
  - Fe<sub>2</sub>O<sub>3</sub> 757
  - [G-1]<sub>div</sub> NCD 761
  - [G-2]<sub>conv</sub> NCD 759
  - [G-2]<sub>div</sub> NCD 762
  - micellar property 748
  - phenothiazine-terminated 752
  - redox-active 750
  - synthesis 745ff., 758ff.
  - Tomalia-type 762
- nanoparticle-cored hyperbranched polymer (NCHP) 763
  - grafting on nanoparticle 763
- nanopatterned surface 123
  - templated self-assembly 123
- nanoplate
  - gold nanoplate on ITO 308
- nanoplatelet
  - hydroxyapatite (HAp) 533
- nanopore size tunability 36
- nanoporous monolith
  - block copolymer system 34
- nanoporous surface
  - functionalized 38
- nanoreactor 44, 660
  - block copolymer 44
- nanorobotic system 253
- nanoshell 104
  - photoactive gold 104
- nanospheres 42
- nanostucture
  - fullerene-rich 699ff.
  - near-field Raman imaging 677ff.
  - polymeric self-assembled 92
  - stimulus-responsive 92
- nanotest-tube 82
- nanotoxicology 551
- nanotube 42, 195ff.
  - aquator 289
  - array 218
  - block copolymer 67ff.
  - chemical reaction 81ff.
  - complex inorganic nanostructure 240
  - DNA-dispersed 736
  - Fe(II)-containing 82
  - HOMO 261
  - inorganic 195ff.
  - LUMO 261
  - metal 196
  - metal disulfide 206
  - molecular imprinting 668
  - niobate-based 233f.
  - preparation 72ff.
  - reinforced material 253
  - spiral 234
  - synthesis 195ff.
  - titanate 233
  - transition metal oxide 228
  - triselenide 206
  - trisulfide 206
- nanowire
  - molecular imprinting 668
- N-(1-naphthyl)ethylenediamine 280
- NCD, *see* nanoparticle-cored dendrimer
- near-field Raman imaging 677ff.
  - optically trapped dielectric microsphere 688
- near-field scanning optical microscopy (NSOM) 677ff.



- near-field scanning Raman microscopy (NSRM) 678
  - TERS 686
  - network modifier 808
  - nickel
    - microtubule 200
    - Ni(II) adsorption 632
    - NiMg–NP 511f.
    - nitrate (Ni-IMP) 511
    - oxide NiO nanotube 230
  - nicotinamide adenine dinucleotide hydrate (NADH) 302
  - niobate-based nanotube 233
  - niobium oxide nanotube 225ff.
  - nitroxide
    - polymer 328
    - radical 328
  - nonaferrocenyl thiol dendron-functionalized nanoparticle 750
  - noncovalent imprinting 654
  - nonsurfactant templating 498ff.
  - norepinephrine 300
  - nucleic acid transfer 96
  - nylon-6 (PA6) 347, 410
    - PA6/PP blend 410
    - PA6-g-PP phase 410
  - 6,6-nylon 347
- o**
- octadecyltrichlorosilane (OTS) 220
  - olefin metathesis 513ff.
  - oligo(*p*-phenylene vinylene) 381ff.
  - OMMT, *see* organically modified montmorillonite
  - once-broken rod 837, 852
  - one-electron-electrode reaction 324
  - one-step process 426
  - optical magnetic nanohand 88
  - optical tweezer mechanism 688
  - optically responsive polymer nanocomposite 379ff.
    - metal nanostructure 379ff.
    - organic functional chromophore 379ff.
  - optically trapped dielectric microsphere 688
    - near-field Raman imaging 688
  - order–disorder transition (ODT) 801
  - order–order transition (OOT) 801
  - organic electrode fabrication
    - bottom-up strategy 323ff.
  - organic functional chromophore 379ff.
  - organic gelator network 816
  - organic polymer battery 319ff.
  - organic radical polymer electrode 324
  - organic/inorganic hybrid structure 842
  - organically modified montmorillonite (OMMT) 427ff., 442
  - organics
    - intercalated 466
  - organization
    - good 772
  - organoclay 444, 809
    - self-assembling 471
  - organogel
    - nanostructured 791ff.
  - organophilic clay 414
  - organophilic layered silicate (OLS) 413ff.
    - dispersion 426
  - organophilic modifier 443
  - orientation
    - external field 116
  - ovalbumin 726ff.
  - oxidation
    - alcohol 350ff.
    - aldehyde 350ff.
    - crack bonding 557
    - selective 337ff.
  - oxidation catalysis 333ff.
    - nanoscale Ag 333
    - nanoscale Au 333
    - nanoscale Cu 333
  - oxidative dehydrogenation 517
  - oxidative steam reforming of methanol (OSRM) 518
  - oxidative stress 602ff.
    - nanoparticle 602
  - ozonolysis 34
- p**
- $\pi$ – $\pi$ -stacking interaction 277ff., 746ff., 822ff.
  - palladium
    - catalyst 354
    - CNT 263
    - G-3 Pd NCD 748
    - nanostructure 200
    - Pd(II) 83ff.
    - PZBAA 518
    - PZBAAr 518
  - palladium nanoparticle (PdNP) 311
    - attachment on ITO 311
    - growth on ITO 311
  - pattern molecule 653
  - patterning surface energy 49
  - pentadecylphenol (PDP) 37
  - peptide amphiphile (PA) nanofiber 214
  - peptide–CNT interaction 724

- peptide–synthetic hybrid block copolymer 844ff., 855ff.
- percolating network 444
- percolation 784
- Percus–Yevick scattering model 802ff.
- periodontitis 549
- perylene derivative 384
- petrochemical 403
- phase 2
- dispersed 380
  - isotropic 7
  - nematic 7
  - smectic 7
- phase-selective chemistry 1ff.
- block copolymer system 1ff.
- phase separation 113ff.
- PHEMA 52
- phosphate-TSA-imprinted nanogel 664
- phosphonium salt 463
- photo-crosslinkable nano-object 41
- photoacid generator (PAG) 28
- photoactive gold nanoshell 104
- photocyclodimerization 41
- photoisomerization 51ff., 105
- photolithographic technique 18
- photoluminescence 735, 757
- photon-to-photocurrent efficiency (IPCE) 706f.
- photonic crystal
- 2-D 136
- photoresist 16, 50, 124
- etch-resistant 30
  - resolution 16
- photoswitchable surface energy 51
- phyllosilicate 403ff.
- clay 460
  - nanocomposite-based 403ff.
  - structure 404
- pinacyanol chloride (PC) 749
- plasma-enhanced chemical vapour deposition (PECVD) 265
- plasticization 444
- platinum
- CNT 263
  - nanocluster dispersedly-attached GC (PtNC/GC) electrode 313
  - nanocluster film (PtNCF) 313
  - nanotube 199f.
  - PtPd alloy nanotube 199
- platinum nanoparticle (PtNP) 312
- attachment on ITO 312f.
  - attachment on GC 312ff.
- PLLA nanocomposite 445
- Plumber’s Nightmare morphology 36
- Pluronic® L64 486ff.
- Pluronic® P65 486
- Pluronic® P84 491
- Pluronic® P123 203, 486ff.
- pnictide nanotube 235
- polarization 798
- polarizing optical microscopy (POM) 859
- poloxamer 107
- polyacetylene fiber
- double-stranded 159
  - hierarchical helical 159
- poly(acetyliminoethylene-*block*-L-phenylalanine) (PAEI-*b*-PLPhe) 840
- PAEI<sub>41</sub>-*b*-PLPhe<sub>4,8</sub> 840
- poly(acrylic acid) (PAA) 210
- polyL-alanine (PLAAla) 840
- poly(amidoamine) (PAMAM) dendrimer
- Tomalia-type 743
- poly(4-(2-aminoethyl)styrene-*block*-styrene-*block*-4-(2-aminoethyl)styrene) (PAES-*b*-PS-*b*-PAES) 85
- poly( $\beta$ -benzyl L-aspartate) (PBLAsp) 861
- poly( $\beta$ -benzyl L-aspartate-*block*-ethylene glycol-*block*- $\beta$ -benzyl L-aspartate) (PBLAsp-*b*-PEG-*b*-PBLAsp) 861
- PBLAsp<sub>25</sub>-*b*-PEG<sub>250</sub>-*b*-PBLAsp<sub>25</sub> 861
  - PBLAsp<sub>25</sub>-*b*-PEG<sub>454</sub>-*b*-PBLAsp<sub>25</sub> 861
  - PBLAsp<sub>32</sub>-*b*-PEG<sub>454</sub>-*b*-PBLAsp<sub>32</sub> 861
- poly( $\gamma$ -benzyl D,L-glutamate) (PBGlu) 857
- poly( $\gamma$ -benzyl L-glutamate) (PBLGlu) 837, 856
- poly( $\gamma$ -benzyl L-glutamate-*block*-butadiene-*block*- $\gamma$ -benzyl L-glutamate) (PBLGlu-*b*-PB-*b*-PBLGlu) 853
- PBLGlu<sub>53-188</sub>-*b*-PB<sub>64</sub>-*b*-PBLGlu<sub>53-188</sub> 837
- poly( $\gamma$ -benzyl L-glutamate-*block*-butadiene-*co*-acrylonitrile-*block*- $\gamma$ -benzyl L-glutamate) (PBLGlu-*b*-PBAN-*b*-PBLGlu) 862
- poly( $\gamma$ -benzyl L-glutamate-*block*-9,9-dihexylfluorene-2,7-diyl-*block*- $\gamma$ -benzyl L-glutamate) (PBLGlu-*b*-PHF-*b*-PBLGlu) 862
- PBLGlu<sub>16</sub>-*b*-PHF<sub>28</sub>-*b*-PBLGlu<sub>16</sub> 862f.
  - PBLGlu<sub>23</sub>-*b*-PHF<sub>15</sub>-*b*-PBLGlu<sub>23</sub> 862f.
- poly( $\gamma$ -benzyl L-glutamate-*block*-dimethylsiloxane-*block*- $\gamma$ -benzyl L-glutamate) (PBLGlu-*b*-PDMS-*b*-PBLGlu) 858
- poly( $\gamma$ -benzyl L-glutamate-*block*-ethylene glycol-*block*- $\gamma$ -benzyl L-glutamate) (PBLGlu-*b*-PEG-*b*-PBLGlu) 858ff.
- PBLGlu<sub>58</sub>-*b*-PEG<sub>90</sub>-*b*-PBLGlu<sub>58</sub> 860
  - PBLGlu<sub>105</sub>-*b*-PEG<sub>90</sub>-*b*-PBLGlu<sub>105</sub> 860

- poly( $\gamma$ -benzyl L-glutamate-*block*-glycine) (PBLGlu-*b*-PGly) 852
- poly( $\gamma$ -benzyl L-glutamate-*block*-isoprene-*block*- $\gamma$ -benzyl L-glutamate) (PBLGlu-*b*-PI-*b*-PBLGlu) 855f.
- poly( $\gamma$ -benzyl L-glutamate-*block*-styrene-*block*- $\gamma$ -benzyl L-glutamate) (PBLGlu-*b*-PS-*b*-PBLGlu) 856f.
- PBLGlu<sub>25</sub>-*b*-PS<sub>165</sub>-*b*-PBLGlu<sub>25</sub> 856
- poly(N<sup>ε</sup>-benzyloxycarbonyl L-lysine) (PZLLys) 837, 856
- poly(N<sup>ε</sup>-benzyloxycarbonyl L-lysine-*block*-butadiene-*block*-N<sup>ε</sup>-benzyloxycarbonyl L-lysine) (PZLLys-*b*-PB-*b*-PZLLys) 854f.
- poly(N<sup>ε</sup>-benzyloxycarbonyl L-lysine-*block*-dimethylsiloxane-*block*-N<sup>ε</sup>-benzyloxycarbonyl L-lysine) (PZLLys-*b*-PDMS-*b*-PZLLys) 857
- PZLLys<sub>42</sub>-*b*-PDMS<sub>148</sub>-*b*-PZLLys<sub>42</sub> 857
- PZLLys<sub>48</sub>-*b*-PDMS<sub>508</sub>-*b*-PZLLys<sub>48</sub> 857
- PZLLys<sub>49</sub>-*b*-PDMS<sub>400</sub>-*b*-PZLLys<sub>49</sub> 857
- PZLLys<sub>91,160</sub>-*b*-PDMS<sub>256</sub>-*b*-PZLLys<sub>91,160</sub> 857
- poly(N<sup>ε</sup>-benzyloxycarbonyl L-lysine-*block*-ethylene glycol-*block*-N<sup>ε</sup>-benzyloxycarbonyl L-lysine) (PZLLys-*b*-PEG-*b*-PZLLys) 861
- poly(bisphenyl A carbonate) (PC) 385
- poly(butadiene) (PB) 837, 853
- poly(butadiene-*block*-N<sup>ε</sup>-benzyloxycarbonyl L-lysine) (PB-*b*-PZLLys) 844
- poly(butadiene-*block*-L-glutamate) 837ff.
- PB<sub>27-119</sub>-*b*-PLGlu<sub>20-175</sub> 837
- PB<sub>48</sub>-*b*-PLGlu<sub>56-145</sub> 843
- poly(butadiene-*block*-N<sup>5</sup>-hydroxyethyl L-glutamine) (PB-*b*-PHLGln) 844
- poly(butadiene-*block*-L-lysine) (PB-*b*-PLLys) 844
- poly(butadiene-*block*-styrene-*block*-butadiene) (BSB) 801
- poly(butadiene-*co*-acrylonitrile) (PBAN) 862
- poly(*tert*-butyl acrylate-*co*-acrylic acid)-*block*-azo methacrylate) 57
- poly(butyl methacrylate-*block*-2-cinnamoyloxyethyl methacrylate-*block*-*tert*-butyl acrylate) (PbMA-*b*-PCEMA-*b*-P*t*BA) 42
- poly(*tert*-butyl methacrylate) 33
- poly(1,4-butylene succinate) (PBS) 384
- poly( $\epsilon$ -caprolactone) (PCL) 439ff.
- alumina 527, 541
- immiscible blend PCL/PEO 410
- poly( $\epsilon$ -caprolactone-*block*- $\gamma$ -benzyl L-glutamate) (PCL-*b*-PBLGlu) 851
- PCL<sub>50</sub>-*b*-PBLGlu<sub>40</sub> 851
- poly(chloromethylstyrene) 32
- poly(cinnamoyl ethyl methacrylate-*block*-*tert*-butyl acrylate) 57
- poly(2-cinnamoyloxyethyl methacrylate) (PCEMA) 41
- polycondensation catalyst 430
- polycyclic aromatic hydrocarbon (PAH) 602, 643
- carbon nanomaterial 643
- poly(cyclo-octene) (PCO) 386
- poly(*n*-decyl-*i*-butylsilane) 185
- poly(*n*-decyl-*(S)*-2-methylbutylsilane) 168, 185
- poly(*n*-decyl-3-methylbutylsilane) 185
- poly(diallyldimethylammonium chloride) (PDDA) 231, 280
- polydiene-based diblock copolymer 844
- polydiene-based triblock copolymer 852ff.
- poly(9,9-dihexylfluorene-2,7-diyl) (PHF) 862
- bis(benzyl amine)-terminated 862
- poly(2-(dimethylamino)ethylmethacrylate) (PDAEMA) 14
- poly(*(R)*-3,7-dimethyloctyl-3-methylbutylsilane) 167
- poly(*(S)*-3,7-dimethyloctyl-3-methylbutylsilane) 167
- poly(*(S)*-3,7-dimethyloctyl-3-methylpentylsilane) 178
- poly(*(S)*-3,7-dimethyloctyl-*n*-propylsilane) 178
- poly(2,6-dimethyl-1,4-phenylene oxide) (PPO) 811
- poly(dimethylsiloxane) (PDMS) 32, 390ff., 819, 857
- polydispersity index (PDI) 439
- poly(divinylbenzene) shell 658
- polyelectrolyte 231, 281ff., 329
- polyester
- biodegradable 439
- polyester ionomer (PETi) 438
- polyester-based diblock copolymer 851
- polyether-based diblock copolymer 850
- polyether-based triblock copolymer 858
- poly(ether urethane urea) (PEUU) 862
- PEUU/PBLGlu blend 862
- poly( $\gamma$ -ethyl L-glutamate) (PELGlu) 855
- poly( $\gamma$ -ethyl L-glutamate-*block*-butadiene-*block*- $\gamma$ -ethyl L-glutamate) (PELGlu-*b*-PB-*b*-PELGlu) 855
- polyethylene (PE) 129f., 382, 410
- EPM/OLS nanocomposite 421ff.
- lamellae 130ff., 141ff.
- linear low density (LLDPE) 381
- matrix 392

- PE-g-MAH/OLS 426
- PE/OLS nanocomposite 414
- PE–PP rubber (EPM), *see* ethylene–propylene (random) copolymer
- poly(ethylene-*block*-ethylene propylene-*block*-ethylene) (PE-*b*-PEP-*b*-PE) 130
- poly(ethylene glycol) (PEG) 463ff., 491, 815
- poly(ethylene glycol-*block*-alanine) (PEG-*b*-PAla) 850
- poly(ethylene glycol-*block*-alkyl acrylate-co-methacrylic acid) (PEG-*b*-(PAA-co-MAAc)) 95
- poly(ethylene glycol-*block*-aspartic acid) (PEG-*b*-P(Asp)) 94
- PEG<sub>113</sub>-*b*-PASP<sub>18,78</sub> 839
- poly(ethylene glycol-*block*-(*N*'-citraconyl-2-aminoethyl)aspartamide) (PEG-*b*-P(Asp(EDA-Cit))) 98
- poly(ethylene glycol-*block*-(ethylenediamine) aspartic acid) (PEG-*b*-P[Asp(DET)]) 98
- poly(ethylene glycol-*block*- $\gamma$ -methyl L-glutamate)
  - PEG<sub>75</sub>-*b*-PMLGlu<sub>32</sub> 839
  - PEG<sub>113</sub>-*b*-PMLGlu<sub>20,50</sub> 839
- poly(ethylene glycol-*block*-L-histidine) (PEG-*b*-P(His)) 95
- poly(ethylene glycol-*block*-lactic acid) (PEG-*b*-PLA) 95
- poly(ethylene glycol-*block*-L-lysine) 839
  - PEG<sub>113</sub>-*b*-PLLys<sub>18,78</sub> 839
- poly(ethylene glycol-*block*-(3-morpholinopropyl) aspartamide-*block*-L-lysine) (PEG-*b*-PMPA-*b*-P(Lys)) 98
- poly(ethylene glycol-*block*-(2-nitrobenzyl methacrylate) (PEG-*b*-PNBM) 105
- poly(ethylene glycol)-oligodeoxynucleotide conjugate (PEG-ODN) 97
  - acid-labile linkage 97
  - lactosylated (Lac-PEG-ODN) 97
- poly(ethylene glycol-*block*-propylene oxide-*block*-ethylene glycol) (PEG-*b*-PPO-*b*-PEG) poloxamer micelle 107
- poly(ethylene glycol-*block*-propylene sulfide-*block*-ethylene glycol) (PEG-*b*-PPS-*b*-PEG) 100
- poly(ethylene glycol-*block*-(D,L-valine-co-D,L-leucine)) 850
- poly(ethylene glycol-*block*-(D,L-valine-co-D,L-leucine)-*block*-ethylene glycol) 850
- poly(ethylene imine) (PEI) 96, 283f.
- poly(ethylene oxide) (PEO) 486
  - poly(ethylene oxide-*block*- $\gamma$ -benzyl L-glutamate)
    - PEO<sub>272</sub>-*b*-PBLGlu<sub>38-418</sub> 839
  - poly(ethylene oxide-*block*-isoprene) (PEO-*b*-PI) 79
  - poly(ethylene oxide-*block*-propylene oxide-*block*-ethylene oxide) (PEO-*b*-PPO-*b*-PEO, Pluronics®) 35, 222
    - [PEO]<sub>13</sub>[PPO]<sub>30</sub>[PEO]<sub>13</sub> 486
    - [PEO]<sub>19</sub>[PPO]<sub>39</sub>[PEO]<sub>19</sub> 491
    - [PEO]<sub>20</sub>[PPO]<sub>69</sub>[PEO]<sub>20</sub> 491
  - poly(ethylene terephthalate) (PET) 200, 386, 448, 663
    - MMT nanocomposite 430f.
    - nanocomposite 429f.
    - OMMT 430f.
    - phyllosilicate nanocomposite 429f.
    - sodium-MMT 431
  - poly( $\gamma$ -L-glutamate) 160ff.
    - 2-D crystallization on surfaces 172
  - poly( $\gamma$ -L-glutamate) derivative 162
    - thermotropic behavior 160
  - poly(L-glutamate) (PLGlu) 837
  - poly(L-glutamate-*block*-L-lysine) (PLGlu-*b*-PLLys) 841
    - PLGlu<sub>15</sub>-*b*-PLLys<sub>15</sub> 841
  - poly(glyceryl methacrylate-*block*-2-cinnamoyloxyethyl methacrylate-*block*-acrylamide) (PGMA-*b*-PCEMA-*b*-PAA) 86
  - polyglycine (PGly) 852
  - polyhedral oligomeric silsesquioxane (POSS) core
    - dendrimer 744
  - poly(*n*-hexyl isocyanate) (PHIC) 74
  - poly(hexyl isocyanate-*block*-styrene) (PHIC-*b*-PS) 7
  - poly(*N*<sup>5</sup>-hydroxyethyl L-glutamine) (PHLGln) 853
  - poly(*N*<sup>5</sup>-hydroxyethyl L-glutamine-*block*-isoprene-*block*-*N*<sup>5</sup>-hydroxyethyl L-glutamine) (PHLGln-*b*-PI-*b*-PHLGln) 856
  - poly(hydroxystyrene) (PHOST) 28f.
  - polyion complex (PIC) micelle 97ff., 839
  - polyisocyanide
    - helical 159
  - polyisoprene (PI) 837
  - poly(isoprene-*block*-*N*<sup>6</sup>-benzyloxycarbonyl L-lysine) (PI-*b*-PZLLys) 845
    - PI<sub>49</sub>-*b*-PZLLys<sub>35</sub> 845
    - PI<sub>49</sub>-*b*-PZLLys<sub>61</sub> 845
    - PI<sub>49</sub>-*b*-PZLLys<sub>92</sub> 845

- poly(isoprene-*block-tert*-butyl acrylate-*block*-  
(cinnamoyloxyethyl methacrylate-*co*-2-  
hydroxyethyl methacrylate)-*block*-glyceryl  
methacrylate)  
(PI-*b*-P*t*BA-*b*-P(CEMA-*co*-HEMA)-*b*-  
PGMA) 83
- poly(isoprene-*block*-cinnamoyloxyethyl  
methacrylate-*block-tert*-butyl acrylate)  
(PI-*b*-PCEMA-*b*-P*t*BA) 39
- PI<sub>130</sub>-PCEMA<sub>130</sub>-P*t*BA<sub>800</sub> 72
- poly(isoprene-*block*-ethylene oxide)  
(Pi-*b*-PEO) 35, 56
- poly(*N*-isopropylacrylamide)  
(PNIPAAm) 102f., 839
- poly(*N*-isopropylacrylamide-*block-γ*-benzyl  
L-glutamate)  
– PNIPAAm<sub>203</sub>-*b*-PBLGlu<sub>39,123</sub> 839
- poly(*N*-isopropylacrylamide-*block*-butyl  
methacrylate) (PNIPAAm-*b*-PBMA) 102
- poly(*N*-isopropylacrylamide-*block*-ethylene  
oxide-*block-N*-isopropylacrylamide) 815
- poly(*N*-isopropylacrylamide-*block*-styrene)  
(PNIPAAm-*b*-PS) 102
- poly(*N*-isopropylacrylamide-*co*-  
dimethylacrylamide)  
(PNIPAAm-*co*-PDMAAm) 103
- poly(2-isopropyl-2-oxazoline) (PiPrOx) 104
- poly(lactic acid) (PLA) 526
- poly(butylene succinate) (PBS) blend 411
- poly(lactic acid-*co*-glycolic acid) (PLGA) 526
- poly(D,L-lactic acid-*co*-glycolic acid)/  
nanohydroxyapatite (PLGA/HAp) 545
- poly(lactide) (PLA) 439ff.
- PLA-based nanocomposite 439
- PLA/MMT nanocomposite 447
- PLA/PCL 445
- poly(L-lactide-*block*-aspartic acid)  
– PLL<sub>95,270</sub>-*b*-PAsp<sub>47,270</sub> 838
- poly(L-lactide-*block-γ*-benzyl L-glutamate)  
(PLL-*b*-PBLGlu) 851
- poly(lactide-*block-ε*-caprolactone-*block*-lactide)  
(PLA-*b*-PCL-*b*-PLA) 446
- poly(L-leucine) (PLLeu) 841f.
- poly(L-leucine-*block*-L-glutamate)  
(PLLeu-*b*-PLGlu) 842
- PLLeu<sub>180</sub>-*b*-PLGlu<sub>180</sub> 842
- poly(L-leucine-*block-N*<sup>ε</sup>-2[2-(2-methoxyethoxy)  
ethoxy]acetyl L-lysine)  
– PLLeu<sub>10,75</sub>-*b*-PELLys<sub>60,200</sub> 841
- poly(L-lysine) (P(Lys), PLLys) 97, 837
- ethylene glycol-modified (PELLys) 841ff.
- polymer
- alkyl side chain 175
- compatibilizer 413ff.
- conjugated 323
- electrode-active material 323
- helical 160ff.
- hyperbranched 743ff.
- matrix 392
- metal nanostructure 379ff.
- molecular imprinted (MIP) 651ff.
- nanoparticle-cored hyperbranched  
(NCHP) 763
- optically responsive polymer  
nanocomposite 379ff.
- organic functional chromophore 379ff.
- organic polymer battery 319ff.
- organosilicon-containing 30
- polymer chain
- 1-D architecture 166
- dynamics 165
- giant 75
- visualization of single chain 167
- polymer composite
- filler 460
- polymer foam
- infiltration 534
- polymer intercalation 412f.
- polymer-analogous chemistry 50
- polymer-analogous reaction 14
- polymer-clay composite 408
- polymer/layered silicates  
nanocomposite 449
- polymer-metal solubility 44
- polymer/particle interface 46
- polymer-Pd hybrid catalytic nanofiber 83
- polymer-Pd-Ni superparamagnetic  
nanofiber 83
- polymer-wrapping technique 282
- polymeric indicator
- mechanical stress 381ff.
- thermal stress 385ff.
- polymeric micelle 93ff.
- DOX-loaded 102f.
- polymeric modifier 810
- polymerization
- anionic 10f.
- atom transfer radical (ATRP) 12, 743,  
763
- backbiting 11
- bulk 656
- degree 3ff.
- emulsion 657ff.
- filling technique 413
- group transfer (GTP) 13
- *in situ* 430
- intrachain cyclization 11
- living 9

- microgel 664
- nanogel 664
- precipitation 661
- reversible addition–fragmentation chain transfer (RAFT) 12
- ring opening (ROP) 432ff.
- ring-opening metathesis (ROMP) 13, 743
- stable free radical 11
- polymersome 836
- poly(methacrylic acid) (PMA) 105
- poly((3-methacryloxy) propyl pentadimethyldisiloxane) 33
- poly((3-methacryloxy) propyl pentadimethyldisiloxane-*block-tert*-butyl acrylate) 56
- poly{N<sup>ε</sup>-2[2-(2-methoxyethoxy)ethoxy]acetyl L-lysine-*block*-sodium L-aspartate}
  - PELLys<sub>100</sub>-*b*-PNaLASp<sub>30</sub> 843
- poly(γ-methyl L-glutamate) (PMLG, PMLGlu) 175, 837
  - aggregate with phosphate (PMLGlu<sub>10</sub>-P) 841
  - poly(γ-methyl L-glutamate-*block*-butadiene-*block*-γ-methyl D,L-glutamate) (PMLGlu-*b*-PB-*b*-PMGLu) 855
  - poly(γ-methyl L-glutamate-*block*-butadiene-*block*-γ-methyl L-glutamate) (PMLGlu-*b*-PB-*b*-PMLGlu) 855
  - poly(γ-methyl L-glutamate-*block*-tetrahydrofuran-γ-methyl L-glutamate) (PMLGlu-*b*-PTHF-*b*-PMLGlu) 862
- poly(methyl methacrylate) (PMMA) 22ff., 385, 462
  - chain scission 24
  - miscible system PMMA/PEO 409
  - syndiotactic and isotactic 792
- poly(α-methylstyrene-*block*-hydroxystyrene) (Pα-MS-*b*-HOST) 27, 56ff.
- polynorbornene
  - TEMPO-substituted 325
- poly(norbornene-*block*-vinylalcohol) 14
- polyolefin (PO)
  - matrix 414
  - PO-g-MAH compatibilizer 425
  - PO/OLS nanocomposite 414ff., 428
  - preparation method of PO/layered silicates nanocomposite 412ff.
- poly(oxyalkylene)-amidoacid 469
- poly(oxyalkylene)-amine 462ff.
  - amphiphilic 459ff.
  - salt 463
- poly(oxyalkylene)-diamine (POA-diamine) 462ff.
  - salt 464
- poly(oxyalkylene)-polyamine salt 462
  - intercalating agent 462
- poly(oxybutylene)-diamine (POB-diamine) 465
  - POB2000 465
- poly(oxyethylene)-amine (POE-amine) 462
- poly(oxyethylene)-diamine (POE-diamine) 462
  - POE2000 462
- poly(oxymethyl) dendron 745
- poly(oxymethylphenylene) dendron (PPD) 746
  - thiol-terminated 746
- poly(oxypropylene)-amine (POP-amine) 462
  - POP2000 464f.
  - POP4000 465
  - POP/MMT hybrid 472
- poly(oxypropylene)-bis-amindocarboxylic acid salt (POP-acid) 461
- polypeptide 836
  - core-forming 839
  - corona-forming 837
  - hybrid block copolymer 837
- polypeptide-based block copolymer 835ff.
  - aggregation 837
  - linear 835
  - self-assembly 835ff.
  - solid-state structure 844
  - solution self-assembly 837
- polypeptide-based hydrogel 842
- polyplex 98
- polypropylene (PP) 383, 466
  - functionalized with maleic anhydride (PP-g-MAH) 410, 425f.
  - immiscible system PP/PS 409
  - PP/OLS nanocomposite 421ff.
  - PP/PA blend 410
  - PP-POP2000 copolymer 472
- poly(propylene glycol) (PPG) 861
- poly(propylene sulfide) 100
- polysaccharide 719, 836
- polysarcosine (PSar) 853ff.
- poly(sarcosine-*block*-styrene-*block*-sarcosine) (PSar-*b*-PS-*b*-PSar) 856
- polysilane 160ff.
  - 1-D architecture on surfaces 162
  - binary helical film 185
  - fluoroalkyl-containing 162
  - helical 161f.
  - optically active 167
- polysiloxane-based triblock copolymer 857
- poly(sodium L-glutamate) 842
- poly(sodium 4-styrene sulfonate) (PSS) 282

- polystyrene (PS)  
 – atactic 792  
 – clay nanocomposite 462  
 – core 658  
 – dinitroxide functionalized 329  
 polystyrene-based diblock copolymer 845  
 polystyrene-based triblock copolymer 856  
 poly(styrene-*block*- $\gamma$ -benzyl L-glutamate)  
 (PS-*b*-PBLGlu) 846ff.  
 – PS<sub>10</sub>-*b*-PBLGlu<sub>10</sub> 848  
 – PS<sub>10</sub>-*b*-PBLGlu<sub>20</sub> 849  
 – PS<sub>10</sub>-*b*-PBLGlu<sub>40</sub> 849  
 – PS<sub>52</sub>-*b*-PBLGlu<sub>104</sub> 848  
 poly(styrene-*block*-N<sup>ε</sup>-benzyloxycarbonyl  
 L-lysine) (PS-*b*-PZLLys) 839ff.  
 – PS<sub>10</sub>-*b*-PZLLys<sub>20</sub> 848  
 – PS<sub>10</sub>-*b*-PZLLys<sub>40</sub> 848  
 – PS<sub>10</sub>-*b*-PZLLys<sub>60</sub> 848  
 – PS<sub>10</sub>-*b*-PZLLys<sub>80</sub> 849  
 – PS<sub>52</sub>-*b*-PZLLys<sub>111</sub> 847  
 – PS<sub>258</sub>-*b*-PZLLys<sub>57</sub> 840  
 – PS<sub>258</sub>-*b*-PZLLys<sub>109</sub> 840  
 poly(styrene-*block*-butadiene) (PS-*b*-PB) 20,  
 55, 123  
 poly(styrene-*block*-butadiene-*block*-styrene)  
 (PS-*b*-PB-*b*-PS) 116  
 poly(styrene-*block*-1,2-butadiene)  
 – modified 58  
 poly(styrene-*block*-2-cinnamoyloxyethyl  
 methacrylate) (PS-*b*-PCEMA) 69ff.  
 – nanofibre 69ff.  
 poly(styrene-*block*-2-cinnamoyloxyethyl  
 methacrylate-*block*-acrylamide)  
 (PS-*b*-PCEMA-*b*-PAA) 73  
 –  $\gamma$ -Fe<sub>2</sub>O<sub>3</sub> hybrid nanofiber 87  
 – nanotube 82ff.  
 – PS<sub>690</sub>-*b*-PCEMA<sub>170</sub>-*b*-PtBA<sub>200</sub> 73  
 poly(styrene-*block*-2-cinnamoyloxyethyl  
 methacrylate-*block*-*tert*-butyl acrylate)  
 (PS-*b*-PCEMA-*b*-PtBA) 43  
 poly(styrene-*block*-ethylene) (PS-*b*-PE) 147f.  
 poly(styrene-*block*-ethylene-*co*-butadiene-*block*-  
*block*-styrene) (SEBS) 466, 802ff.  
 – SEBS-POA copolymer 467  
 poly(styrene-*block*-ethylene-*co*-  
 propylene) 390  
 poly(styrene-*block*-(ethylene-*co*-propylene)-  
*block*-styrene) (SEPS) 806  
 poly(styrene-*block*-ethylene oxide) (PS-*b*-PEO)  
 14, 40, 116ff.  
 poly(styrene-*block*-ethylene oxide-*block*-  
 styrene) (PS-*b*-PEO-*b*-PS, SEOS) 815  
 poly(styrene-*block*-ethylene propylene)  
 (PS-*b*-PEP) 117  
 poly(styrene-*block*-ethylene propylene-*block*-  
 ethylene) (PS-*b*-PEP-*b*-PE) 141ff.  
 – anthracene 141ff.  
 – benzoic acid 141ff.  
 poly(styrene-*block*-ferrocenyldimethylsilane)  
 (PS-*b*-PFS) 27, 123, 136  
 poly(styrene-*block*-hydroxyethyl methacrylate-  
*block*-methyl methacrylate)  
 (PS-*b*-PHEMA-*b*-PMMA) 120  
 poly(styrene-*block*-isoprene) (PS-*b*-PI) 7ff.,  
 50ff., 120, 148  
 – asymmetric 133  
 – nanofibre 70ff.  
 – PS<sub>130</sub>-*b*-PI<sub>570</sub> 80  
 poly(styrene-*block*-isoprene-*block*-styrene)  
 (PS-*b*-PI-*b*-PS, SIS) 798f.  
 poly(styrene-*block*-lactic acid) (PS-*b*-  
 PLA) 27, 40  
 poly(styrene-*block*-L-lactide) 56  
 poly(styrene-*block*-L-lysine)  
 (PS-*b*-PLLys) 846  
 – PS<sub>8,10</sub>-*b*-PLLys<sub>9,72</sub> 838  
 poly(styrene-*block*-methyl methacrylate)  
 (PS-*b*-PMMA) 18ff., 55ff., 115ff.  
 – surfactant-assisted orientation 128  
 – symmetric diblock copolymer 132ff.  
 poly(styrene-*block*-methyl methacrylate-*block*-  
 ethylene oxide) (PS-*b*-PMMA-*b*-PEO) 116  
 poly(styrene-*block*-perfluoro-octylethyl  
 methacrylate) (PS-*b*-PFOMA) 37  
 poly(styrene-*block*-dimethylacrylamide-*block*-  
 lactide) (PS-*b*-PDMA-*b*-PLA) 39  
 poly(styrene-*block*-2-vinylpyridine)  
 (PS-*b*-P2VP) 47  
 – diblock copolymer 136  
 poly(styrene-*block*-2-vinylpyridine-*block*-*tert*-  
 butyl acrylate) (PS-*b*-P2VP-*b*-PtBA) 115  
 poly(styrene-*block*-4-vinylpyridine) (PS-*b*-  
 P4VP) 37, 55, 123  
 poly(styrene-*co*-maleic anhydride)  
 (SMA) 466f.  
 – grafted with POA-amine 467  
 – SMA-POP copolymer 468  
 poly(styrene sulfonate) (PSS) 231  
 polytetrafluoroethylene (PTFE) crystal 136  
 polytetrahydrofuran (PTHF) 862  
 polythiophene-based conjugated  
 polymer 323  
 poly(N<sup>ε</sup>-trifluoroacetyl L-lysine)  
 (PTLLys) 853  
 poly(vinyl alcohol) (PVA) 286, 390f.  
 poly(vinyl methylether) (PVME)/polystyrene  
 (PS) 410  
 poly(vinylpyridine) (PVP) 45

- poly(vinyl pyrrolidone) (PVP) 199, 308, 390  
poly(*N*-vinyl-2-pyrrolidone) 353  
poly(vinylidene fluoride) (PVDF)/nylon-6 (PA6) blend 410  
porous anodic alumina (PAA) 265  
porphyrin 671  
post polymerization modification 14  
potassium hexaniobate nanotube 234  
powder X-ray diffraction 485  
precipitation polymerization 661  
17-(1-prenyl)-13-oxo-hepta-decanethiol (PHT) 277f.  
preparation method  
– biodegradable polyester 439  
– PO/layered silicates  
nanocomposite 412ff.  
pressing 523  
principle of independent surface action 49  
pristine PO 424  
pristine SWNT 622, 719  
process zone size failure criterion 580  
processability 444  
propranolol 659ff.  
protein 781f.  
– interaction with CNT 723  
protein kinase A (PKA) 101f.  
proton sponge effect 96  
pseudoextracellular fluid (PECF) 856  
pyrene 667  
pyrene chromophore  
– photolabile 105  
pyrene fluorophore 280  
1-pyrenemethylamine 280  
pyridinium 12-(cholesteryloxycarbonyloxy) dodecanesulfate (TS) 658  
pyridinium 12-(4-vinylbenzyloxycarbonyl) dodecanesulfate (PS) 658  
PZBAA 518  
PZBAAr 518f.
- q**  
quantum dot (QD) 531, 778  
– CdSe–ZnS 286  
– molecular imprinting 669  
quartz crystal microbalance (QCM) 325ff.
- r**  
radical group  
– C-centered 324  
– N-centered 324  
– NO-centered 324  
– O-centered 324  
radical polymer  
– mesoscale 319ff.  
– organic radical polymer electrode 324  
radiofrequency (RF)-sputtering 686  
radiotherapy 549  
– microbioceramics 549  
random sequential addition (RSA) 775f.  
re-sintering 557  
– crack healing 558  
reactive ion etching (RIE) 20, 136  
reactive oxygen species (ROS) 605  
redox capacity 329  
redox polymer layer 321  
redundancy 771  
relative Kuhn's dissymmetry ratio 179ff.  
relative viscosity 78  
relaxation 557  
 $\alpha$ -relaxation frequency 423  
remodeling cycle 527  
renewable thermoplastic matrix 403ff.  
resist  
– negative-tone 17  
– positive-tone 17  
reversible addition–fragmentation chain transfer (RAFT) polymerization 12  
Re-Writable (RW) mode 178  
rhenium  
– [Re<sub>6</sub>Se<sub>6</sub>]<sup>2+</sup> metal cluster 744  
rhenium oxide (Re<sub>2</sub>O<sub>7</sub>) 513ff.  
– Re/ALCOA 514f.  
– Re/OMA 513ff.  
– Re/OMA3.5 514f.  
– Re/OMA6.5 514f.  
– Re<sub>2</sub>O<sub>7</sub>/ $\gamma$ -Al<sub>2</sub>O<sub>3</sub> 513  
– Re<sub>2</sub>O<sub>7</sub>/*meso*-Al<sub>2</sub>O<sub>3</sub> 513  
ring opening metathesis polymerization (ROMP) 13, 743  
ring opening polymerization (ROP) 432ff.  
RNA (ribonucleic acid) 781  
– transfer 96  
robocasting 534  
rod structure 162ff.  
rod–coil block copolymer 7  
(*S*)-ropivacaine 662f.  
rubidium  
– [(Rb(18C6))<sub>4</sub>(MnCl<sub>4</sub>)] [TiCl<sub>4</sub>]<sub>2</sub> · *n*H<sub>2</sub>O 371  
ruboxyl  
– pluronic micelle 107  
rutile nanotube 220
- s**  
S<sub>A383</sub> 512  
saponite 460



- Sb, *see* antimony
- SBA-15 343ff.
- scaffolding material 527
- scandium oxide ( $\text{Sc}_2\text{O}_3$ ) 570
- scanning electron microscopy (SEM) 430, 529
- scanning force microscopy (SFM) 120
- scanning probe microscopy (SPM) 161
- scanning tunnel microscopy (STM) 161
- scattering angle 77
- schizophyllan (SPG)
- single-stranded (s-SPG) 720
- seed-mediated growth method 298ff.
- AuNP on ITO 298ff.
- selenium nanostructure 205
- selected area diffraction (SAD) 141
- selected area electron diffraction (SAED) 203
- self-assembled fibrillar network (SAFIN) 793, 817ff.
- self-assembled micellar network (SAMIN) 793ff., 827f.
- self-assembled monolayer (SAM) 124, 220, 776ff.
- self-assembled supramolecular  $\text{C}_{32}\text{H}_{70}\text{N}_2\text{ZnO}_4$  nanotube 235
- self-assembling nanocluster
- tetrahalometallate anion 365ff.
- self-assembling synthetic material 2
- self-assembly
- biomimetics 536
  - concept 767ff.
  - enantiopure 172
  - gold nanoparticle 198
  - information guided 869ff.
  - layer-by-layer (LBL) 270, 281ff.
  - linear polypeptide-based block copolymer 835ff.
  - manufacturing process 783
  - molecular 791ff.
  - nanostructured organogel 791ff.
  - nucleated DNA 874
  - passive 773
  - programmable 773
  - smectic 159
  - solution 837
  - Stranski–Krastanov 779
  - structural DNA nanotechnology 869ff.
  - surfactant 215
  - templated 123
- self-connecting 768
- self-consistent mean field 3
- self-crack healing 559ff.
- self-disorganizing system 771
- self-healing 555ff.
- atmosphere 567
  - ceramics 555ff., 588
  - composition 562
  - fatigue strength 575
  - mechanism 559
  - structure 562f.
  - surface crack in structural ceramics 555ff.
  - temperature 568
- self-joining 768f.
- self-organization 772
- thermodynamics 770ff.
- self-organized array 173f.
- 3-D bulk phase 175
  - intermolecular weak van der Waals interaction 175
  - orientation 174
  - visualization 173
- semi circle structure 162ff.
- semiconductor nanocrystal 531
- sensor 737
- CNT 289
- sequential minimization of entropy loss (SMEL) 782
- shape memory polymer (SMP) 386
- shear-thinning effect 78
- silicate
- copolymer hybrid 466ff.
  - layered 460
  - organophilic layered (OLS) 413ff.
  - random platelet 472
- silicon
- SiGe 689ff.
  - visualization of Si–C bonding 682
- silicon carbide (SiC) 557ff.
- bulk 684
  - composite 569
  - figuration 563
  - mullite composite 585f.
  - multicomposite 585
  - nanoparticle composite 587
  - nanowire 240
  - particle composite 571
  - SiC/SiO<sub>2</sub> core–shell nanocable 240
  - whisker 563ff., 585
- silicon dioxide (silica)
- dielectric material 34
  - double-walled nanotube 215
  - hybrid nanotube 215
  - liposome–silica nanoparticle hybrid system 531
  - molecular imprinting 653
  - nanoparticle 665

- nanotube 214f.
- Raman spectrum 687
- surface-modified 809
- silicon nitride ( $\text{Si}_3\text{N}_4$ ) 557f.
- composite 569f.
- nanotube 238
- silicone oil 819
- silver
  - Ag nanoparticle (AgNP) 309
  - Ag nanowire 199, 211
  - $\text{Ag}_2\text{Se}$  nanotube 211
  - $\text{Ag}_2\text{Te}$  nanotube 211
  - gold–silver alloy catalyst 342
  - nanocatalyst 335
  - nanoparticle 393
  - nanorod 395
  - PVA nanocomposite 394
  - silver catalyst 342ff., 351ff.
    - epoxidation reaction 346f.
  - simulated body fluid (SBF) 541ff.
  - single-walled carbon nanotube (SWNT) 251ff., 598, 616ff., 716ff.
    - AuNP 286
    - CdSe–ZnS quantum dot 286
    - DNA-*met*-SWNT 723
    - emitter 289
    - interaction with protein 723
    - LSZ 725f.
    - memory element 289
    - metallic (*met*-SWNT) 717ff., 735
    - nanotube aquator 289
    - noncovalent functionalization 718
    - semimetallic (*sem*-SWNT) 717, 735
    - sensor 289
  - siRNA transfer 96
  - size-exclusion chromatography (SEC) 440
  - slip tube network (STN) 797
  - small angle neutron scattering (SANS) 806, 837
  - small angle X-ray scattering (SAXS) 120, 409, 802
  - smectite 404, 460
  - sodium
    - $[(\text{Na}(15\text{C}5))_n\text{Br}][\text{TlBr}_4]_3$  368
  - sodium dodecyl benzene sulfonate (SDBS) 279, 717
  - sodium dodecyl sulfate (SDS) 215, 234, 286, 301ff., 495
  - sodium montmorillonite ( $\text{Na}^+$ -MMT) 461ff.
    - exfoliating 473
  - sodium poly(acrylate) 390
  - sol–gel method 196, 216ff., 233ff., 536ff.
  - sol–gel nanohydroxyapatite 538
  - sol–gel processing 523
  - solid/liquid interface 774
  - solidification
    - directional 140
  - solution
    - intercalation 412f.
    - lyotropic 7
    - self-assembly 837
  - solution–liquid–solid (SLS) method 234
  - solvated metal atom dispersion (SMAD) 265
  - solvent
    - effect 826
    - evaporation 122
  - sono-electrochemical method 210
  - sorbitol 820
  - spacer 820
  - spin-coating technique 186
  - spin–lattice relaxation time 856
  - spirobenzopyran (SBP) 107
  - stable free radical polymerization (SFRP) 11
  - $\pi$ – $\pi$ -stacking interaction 277ff., 746ff., 822ff.
  - standing wave effect 30
  - stannoxane 708ff.
  - stearyldimethylbenzylammonium chloride 407
  - stem cell 529
  - stencil 18
  - stigmergy 780
  - stress 556, 571, 808
  - stress intensity factor 556, 573
  - stress shielding 533
  - strontium
    - $\text{La}_{0.5}\text{Sr}_{0.5}\text{CoO}_3$  nanotube 235
    - $\text{SrAl}_2\text{O}_4$  nanotube 235
  - structural ceramics 555ff.
    - self-healing of surface crack 555ff.
  - structural DNA nanotechnology 869ff.
    - information guided self-assembly 869ff.
  - substrate-enhanced electroless deposition (SEED) 260
  - sugar recognition 670
  - superconducting oxide 365
  - superconducting quantum interference device (SQUID) 325
  - superhelical assembly
    - homochiral intermolecular interaction 169
    - mesoscopic 2-D hierarchical 167
  - super-paramagnetism 43
  - supersaturation
    - degree 46
  - superspheres 784

- supersurfactant 86
  - supramolecular assembly
    - helical polymer 160
  - supramolecular chemistry 85, 779
  - supramolecular film
    - helical polymer-based 159ff.
  - supramolecular interaction
    - AuNP and CNT 271
  - supermolecule 780
  - suprapolymer 75
  - surface
    - low-energy 48
    - fluorinated block copolymer 48
    - modification 540
    - nanopatterned 123
    - relief grating 54
  - surface crack
    - self-healing in structural ceramics 555ff.
  - surface energy 49
    - photoswitchable 51
  - surface interaction 126
    - homogeneous 126
    - preferential wetting 126
  - surface plasmon resonance (SPR)
    - frequency 389
  - surface water contaminant 615ff.
    - CNT as adsorbent 615ff.
  - surface-enhanced Raman scattering 680
  - surface-responsive material 2
  - surfactant 86, 222, 286, 395
    - anionic surfactant templating 492ff.
    - cationic surfactant templating 495ff.
    - CNT dispersion 737
    - intercalating agent 438
    - ionic 717
    - neutral surfactant templating 486ff.
    - polymerizable 658
    - self-assembly 215
  - switch
    - helical polysilane film 178
    - helix–coil transition 182
    - reversible 180
  - SWNT, *see* single-walled carbon nanotube
  - synthetic material
    - self-assembling 1
- t**
- taurodeoxycholic acid (TDOC) 720
  - tellurium nanostructure 205
  - temperature
    - dependence of minimum fracture stress 582f.
    - effect 801
    - polymeric assembly 102ff.
  - temperature-programmed desorption (TPD) 508
  - temperature-programmed reduction (TPR) 511
  - template 17, 482
    - effect 653
    - nanolithographic 17
    - nanoparticle 736
    - nanoporous block copolymer 20
  - templating
    - anionic surfactant 492ff.
    - cationic surfactant 495ff.
    - neutral surfactant 486ff.
    - nonsurfactant 498ff.
  - tensile deformation 806ff.
  - teratogenicity 608
    - engineered carbon nanoparticle 608
  - Tergitol® 15-S-9 486
  - Tergitol® 15-S-12 486
  - tetracalcium phosphate (TTCP) 534
  - 2,3,7,8-tetrachlorodibenzo-*p*-dioxin (TCDD) 639
  - tetraethoxysilane (TEOS) 199
  - tetraethylorthosilicate (TEOS) 35
  - 2,2,6,6-tetramethylpiperidine-1-oxyl (TEMPO) derivative 325
  - tetrakis(hydroxymethyl)phosphonium chloride (THPC) 199
  - tetramethoxymethyl glycoluril (TMMGU) 28
  - thallium
    - $[(Tl(18C6))_4(MCl_4)][TlCl_4]_2 \cdot nH_2O$  369
  - theophylline 659ff.
  - therapeutic agent 738
  - thermal annealing 114
  - thermal gradient 122
  - thermal shock 556
  - thermal stress 385ff., 556
  - thermoplastic elastomer (TPE) 795
    - gel (TPEG) 795ff.
  - thermoseeds 550
  - thiobarbituric acid reactive substance (TBARS) 605
  - thrombin aptamer 876
  - time-dependent indicator (TTI) 386
  - tin
    - Sn(2-ethylhexanoate)<sub>2</sub> 440ff.
  - tin oxide (SnO<sub>2</sub>) nanotube 232
  - tip-enhanced Raman scattering (TERS) 679ff.
  - tissue distribution
    - carbon nanoparticle 600
  - tissue engineering 527ff.
  - tissue interaction 524

- titanium
- Ti6Al-4V 528ff.
  - Ti(O-1-C<sub>3</sub>H<sub>7</sub>)<sub>4</sub> 432
- titanium dioxide (TiO<sub>2</sub>, titania)
- attachment of AuNP 307
  - Brookite-type nanotube 221
  - nanostructured bioceramic 547
  - nanotube 216ff.
  - sulfur-doped nanotubular array 220
- tone chemistry
- negative 18
  - positive 18
- top-down process 334, 783
- topology 161f.
- rod, semi-circle and circle structure 162
  - switching 165
- toroid-like architecture 166
- toxicology
- ecological 595ff.
  - engineered carbon nanoparticle 595ff.
- transition state analogue (TSA) 664ff.
- transition temperature 179f.
- transmission electron microscopy (TEM) 202, 409, 485
- triblock copolymer (tri-BCP) 3, 39, 852
- organogel 803
  - polydiene-based 852ff.
  - polyether-based 858
  - polysiloxane-based 857
  - polystyrene-based 856
- β-tricalcium phosphate (β-TCP) 534, 543f.
- trihalomethane (THM) 642
- CNT 642f.
- N,N,N*-trimethyl octadecylammonium bromide 432
- trimethylolpropane trimethacrylate (TRIM) 662
- trinitrotoluene (TNT) 666
- triethylphosphine oxide (TOPO)
- CdSe nanoparticle 755
- triphenylsulfonium triflate 28
- tris(8-hydroxyquinoline) gallium organic nanowire (GaQ<sub>3</sub>) 224
- trypsin 726ff.
- tumor 93
- tungsten
- WS<sub>2</sub> 206
- tungsten oxide
- WO<sub>3</sub> nanotube 230
  - WO<sub>3</sub>-H<sub>2</sub>O nanotube 234
- turnover frequency (TOF) 748
- turnover number (TON) 748
- u**
- ultra-high molecular-weight polyethylene (UHMWPE) 390
- uncapping trigger 546
- ureas 820
- uric acid 300, 670
- UV-diffuse reflectance spectroscopy (UV-DRS) 511
- v**
- valproic acid (VPA) 548
- vanadium 518
- vanadium oxide
- VO<sub>x</sub> nanotube 225f.
  - V<sub>2</sub>O<sub>5</sub> bulk-type 517
  - V<sub>2</sub>O<sub>5</sub> · *n*H<sub>2</sub>O nanotube 225f.
- vapor-liquid-solid (VLS) mechanism 230
- Vickers indentation 560, 574
- 4-vinylpyridine 670
- viscometry 75
- viscosity 78, 444
- index 168
- Volmer-Weber régime 779
- w**
- W, *see* tungsten
- water structure 786
- Weibull function 574
- Weibull modulus 574
- wide-angle X-ray diffraction (WAXD) 172, 415
- wide-angle X-ray scattering (WAXS) 434, 844
- Write-once Read Many (WORM) mode 178ff.
- x**
- X-ray diffraction (XRD) 461
- *d*-spacing 461
  - pattern 237
  - powder 485
  - wide-angle (WAXD) 172, 415
- X-ray lithography 17
- X-ray photoelectron spectroscopy (XPS) 510, 854
- y**
- Yamakawa-Fujii-Yoshizaki (YFY) theory 78
- yttrium
- YBa<sub>2</sub>Cu<sub>3</sub>O<sub>7</sub> 365
- yttrium oxide (Y<sub>2</sub>O<sub>3</sub>) 550, 570
- nanotube 232
  - 17Y<sub>2</sub>O<sub>3</sub>-19Al<sub>2</sub>O<sub>3</sub>-64SiO<sub>2</sub> (YAS) 549

**z**

- zeolitic micropore 492
- zigzag mechanism
  - exfoliating Na<sup>+</sup>-MMT 473
- zinc
  - Pd-Zn alloy catalyst (PZBAAr) 518f.
  - Zn(II) adsorption 630f.
  - ZnAl<sub>2</sub>O<sub>4</sub> spinel nanotube 235
  - ZnCl<sub>2</sub>//*meso*-Al<sub>2</sub>O<sub>3</sub> 516f.
  - ZnO nanorod array 240
  - ZnO nanotube 221ff.
  - ZnO–ZnS nanocable 240
  - ZnS 206ff.
- zirconium oxide
  - ZrO<sub>2</sub> nanotube 232
- zirconium titanate (ZrTiO<sub>3</sub>) nanotube 233